COMPOSITE STRUCTURES

EDITOR: I.H. MARSHALL

Special Issue

Seventh International Conference
on Composite Structures

DTIC
ELECTE
SEP 3 0 1993
S A D

ELSEVIER
APPLIED
SCIENCE

Best
Available
Copy

COMPOSITE STRUCTURES

The past few decades have seen outstanding advances in the use of composite materials in structural applications. There can be little doubt that, within engineering circles, composites have revolutionised traditional design concepts and made possible an unparalleled range of new exciting possibilities as viable materials of construction. *Composite Structures*, an International Journal, disseminates knowledge between users, manufacturers, designers and researchers involved in structures or structural components manufactured using composite materials.

The journal publishes papers which contribute to knowledge in the use of composite materials in engineering structures. Papers may be on design, research and development studies, experimental investigations, theoretical analyses and fabrication techniques relevant to the application of composites in load-bearing components for assemblies. These could range from individual components such as plates and shells to complete composite structures.

COMPOSITE STRUCTURES

VOL. 25 1993

SPECIAL ISSUE

Seventh International Conference
on Composite Structures

EDITOR

I. H. MARSHALL

ELSEVIER APPLIED SCIENCE

Contents

Session 6 — Damage tolerance B

Session 7 — Localised effects

Session 8 — Shell structures A

Session 9 — Materials aspects B

Session 10 — Joints

Session 11 — Metal matrix composites

Session 12 — Impact studies

Session 13 — Materials aspects A

Session 14 — Shell structures B

Session 15 — Design and development

Session 16 — Failure analysis

Session 17 — Buckling studies

Session 18 — Smart structures

Session 24 — Finite element analysis B

Session 25 — Aircraft structures

Session 26 — Composite beams B

Preface

Herein are contained the papers presented at the Seventh International Conference on Composite Structures (ICCS/7) held at the University of Paisley in July 1993. The Conference was sponsored by the University of Paisley with co-sponsorship kindly provided by Scottish Enterprise, the National Engineering Laboratory, the US Air Force European Office of Aerospace Research and Development, the US Army Research, Development and Standardisation Group—UK, Strathclyde Business Development and Renfrew District Council. It forms a natural and ongoing progression from the highly successful ICCS/1, 2, 3, 4, 5 and 6 held in Paisley in 1981, 1983, 1985, 1987, 1989 and 1991 respectively.

After more than a decade of both 'Composite Structures' Conferences and the *Journal of Composite Structures* it is appropriate to reflect on the rapid growth in this technology and the universally accepted maturity it has achieved in that period. At the time of the first Conference in 1981 papers pertaining to the Space Shuttle Programme were heralding blood-stirring achievements. Likewise the *Journal of Composite Structures* has blossomed from 9 papers published at its inception in 1983 to 70 published last year. Nowadays we tend to accept that still existing technology with an unfortunate, almost commonplace, acceptance. I wonder how the prophetic Jules Verne would have reacted!

Although the aforementioned comments are by no means exhaustive parameters of progress they do nevertheless underscore feelings of a rapidly expanding adult technology. Moreover it is a technology that is becoming increasingly international and interdisciplinary in outlook with lead times between research and industrial implementation rapidly diminishing.

What of the future? If this rate of progress is to be sustained it is important that knowledge is efficiently disseminated by the written and spoken word. The present Proceedings Volume will go a little way to addressing the former and it is hoped that the latter will be assisted by both open forum discussion at the conference and subsequent feedback to colleagues throughout the world.

To authors, session chairmen and contributors go our sincere thanks for their efforts, without which there would be no conference. As always, an International Conference can only succeed through the willing and enthusiastic assistance of a group of individuals. In particular, grateful thanks go to the following:

THE INTERNATIONAL ADVISORY PANEL

W. M. Banks — *University of Strathclyde, UK*
A. M. Brandt — *Polish Academy of Sciences, Poland*
A. R. Bunsell — *Ecole des Mines de Paris, France*
W. S. Carswell — *University of Paisley, UK*
T. Hayashi — *Japan Plastic Inspection Association, Japan*
R. M. Jones — *Virginia Polytechnic and State Institute, USA*
A. Miravete — *University of Zaragoza, Spain*
J. Rhodes — *University of Strathclyde, UK*

THE LOCAL ORGANISING COMMITTEE

J. S. Paul
J. M. Thompson

THE CONFERENCE SECRETARY

Ms C. A. MacDonald

Grateful thanks are due to many other individuals who contributed to the success of the event. As always a final thanks to Nan, Simon, Louise and Richard for their support throughout the conference.

I. H. Marshall

The role of biaxial stresses in discriminating between meaningful and illusory composite failure theories

L. J. Hart-Smith

Douglas Aircraft Company, McDonnell Douglas Corporation, 3855 Lakewood Boulevard, Long Beach, CA 90846, USA

The irrelevance of most composite failure criteria to conventional fiber-polymer composites is claimed to have remained undetected primarily because the experiments that can either validate or disprove them are difficult to perform. Uniaxial tests are considered inherently incapable of validating or refuting any composite failure theory because so much of the total load is carried by the fibers aligned in the direction of the load. The Ten-Percent Rule, a simple rule-of-mixtures analysis method, is said to work well only because of this phenomenon. It is stated that failure criteria can be verified for fibrous composites only by biaxial tests, with orthogonal in-plane stresses of the same, as well as different signs, because these particular states of combined stress reveal substantial differences between the predictions of laminate strength made by various theories. Three scientifically plausible failure models for fibrous composites are compared, and it is shown that only the in-plane shear test, orthogonal tension and compression, is capable of distinguishing between them. This is because most theories are 'calibrated' against the measured uniaxial tension and compression tests, and any cross-plied laminate tests dominated by those same states of stress must inevitably 'confirm' the theory.

BACKGROUND

For several years, the author has tried to expose and rectify serious fundamental deficiencies in the most widely taught 'failure theories' for composite laminates. This has proved to be a most difficult task, mainly because of a widespread reluctance to use any method not already coded on a computer or to challenge any output from the computer. The difficulty of generating valid test data with which to accept or reject any theory is also a factor.

The issue of computer codes for the new theory is being addressed in another paper. The emphasis here is on the need to validate theories by tests on structural laminates, particularly under biaxial in-plane loads. Unfortunately, there is only a limited appreciation of difficulties with the design and execution of even the standard uniaxial tests on cross-plied laminates. These problems are exacerbated by a failure to recognize that gross oversimplifications have been made in the model used to formulate most composite failure criteria.

Consequently, most biaxial test coupons fail prematurely outside the test section in areas of uniaxial stress because the target biaxial strengths have been badly underestimated.

Some promoters of abstract mathematical failure models for composite materials have taken advantage of these experimental difficulties. They do not find it necessary to conduct experiments at the structural laminate level to validate predictions made by theory. Instead, they characterize the material by a series of tests at the lamina coupon level, relying on a theory with sufficient adjustable and sometimes unmeasurable parameters to match the lamina test results. Since no mathematical approximations are made in the derivations, it is implied that there is no need for further tests which, if conducted for a sufficiently wide range of stress states, might expose inconsistencies in the predictions when the model used for the theory does not represent physical reality. Conversely, redundant testing would inevitably validate a scientifically sound theory unless the experiments were faulty. If 10 successful tests

were run to deduce eight unknown properties, the same properties should be predicted no matter which eight tests were selected for the analysis. The scheme of ensuring that redundant tests will not be conducted so that one's theory can *never* be challenged has also been used in bolted composite joint studies. The technique has been applied so artfully that few would question it.

Such thinking has not only led most composite structural analysts to refrain from questioning the foundations of their computer codes for strength prediction, but has also deluded some who would apply theories of anisotropic elasticity for *homogeneous* materials to distinctly *heterogeneous* fiber-polymer composites into believing that there is nothing wrong with such a 'simplifying' assumption, merely because the individual fibers in the composite are microscopic.

Others have justified the need for such simplifications by the complexity of micromechanics, suggesting that *some* simpler theory had to be developed for all those who would not use *any* theory far more complicated than what they used for metallic structures. This problem is not helped by the widespread use of finite-element procedures without ensuring that both the model and the boundary conditions simulate reality. But, to be fair, the most potent argument against micromechanical analyses is the large number of material properties that cannot be easily determined experimentally but are needed to implement the more realistic failure models.

The end result of all this is that few if any composite failure theories have *ever* been properly verified by experiment.

This by no means implies that all composite structures designed and built so far are unsafe; typically, less than 1% of composite structures on large aircraft is actually governed by *unnotched* laminate strengths. The rest is dominated by joints, damage tolerance, and stiffness requirements. Empirical interpretations of data are needed for joint strength and damage tolerance, while the laminate stiffnesses are not in doubt because lamination theory works for even heterogeneous materials. At least the predicted elastic constants are right, even if the strengths are wrong.

Further, nearly all composite structures built so far have been certified by test rather than by analysis. And things are likely to stay this way unless better, more realistic theories are developed.

HOW MANY MEASUREMENTS ARE NEEDED TO CHARACTERIZE THE STRENGTH OF A FIBROUS COMPOSITE LAMINATE?

Considerable confusion exists as to the number of measurements needed to characterize the strength of composite materials. The seemingly reasonable position that it is necessary to characterize longitudinal and transverse strengths, in both the tensile and compressive directions, and to have some measure of the shear strength would suggest that five measurements are needed. Many composite failure models have been based on such an assumption, adopted because of the apparent ease with which those particular measurements could be made. But if one were to consider the real physics of the situation instead, one would conclude that only *one* measurement is needed to characterize *each mode* of failure. If the same mode of failure, such as yielding in ductile metal alloys, occurred under different states of combined stress, measurements made under different states of stress would be *equivalent* and not independent. The value of redundant tests would be to demonstrate a consistency confirming that the theory was sound.

Thus, the five strength measurements would be appropriate *only* if there were precisely five modes of failure to be characterized. And, *under no circumstances* could these five measurements be integrated into a *single* smooth, continuous failure envelope. They should represent five *superimposed* envelopes, truncating each other locally so that one or another would govern as the state of stress varied.

It is clear, then, that the unstated simplifying assumptions of traditional composite failure theories are so contradictory to basic laws of physics that the theories should be discarded. However, it is commonly held that any new and better theory must inevitably be *more complicated* than older theories and need additional data for its implementation. A claim that an entire failure envelope can be constructed from a *single* test result and simultaneously be more accurate than older theories based on measurements of *four* distinct measurements of strength seems difficult to accept, even when it is explained that additional failure modes can be covered, if needed, at the rate of one test per failure mechanism. The conclusion seems to run contrary to tradition: the new theory needs, at most, measurements of the longi-

tudinal strength of the lamina in tension and compression, whereas older theories needed transverse strengths as well, and the *omission* of the transverse measurements *improves* the accuracy of the theory. The transverse-tension strength measured on a unidirectional lamina has no relevance to any in-plane strength of a multidirectional structural laminate, whether the failure be matrix-dominated or fiber-dominated. However, an empirically deduced 'effective' transverse-tension strength can be used to provide a *separate* failure characteristic truncating the fiber-failure envelope locally throughout part of the tension-tension stress quadrant (see Ref. 1).

Separate failure envelopes for shear failures of the fibers and in-plane shear failures for the matrix can be superimposed at the lamina level, as shown in Fig. 1. Their origins are offset to account for residual thermal stresses induced by curing at elevated temperatures. Apart from traditional elastic constants such as Young's moduli and the various Poisson's ratios, Fig. 1 would be based on *only two* measurements of strength, one for the fibers and one for the matrix.

THE INVALIDITY OF ASSOCIATING COMPOSITE FAILURE CRITERIA WITH HILL'S WORK ON PLASTICITY IN METALS

Many composite failure theories have been falsely likened to the *unrelated* work of Hill on the plastic yielding of slightly anisotropic ductile metals. The very name Tsai-Hill for one of the early composite failure theories implies such an association. In fact, there is absolutely *no similarity* between the two situations. Hill's theory of plasticity characterizes the yielding of a *homogeneous* material under various states of combined stress by a *single* mechanism, while the other theory and its innumerable clones refer to failures by at least four and sometimes five different mechanisms of a distinctly *heterogeneous* composite.

If Hill had tried to adapt his own methods to predicting the strength of fibrous composite laminates, he would most likely have developed a *separate* curve for each possible failure mechanism. One or another mechanism would prevail, depending on the state of combined stresses, and the failure 'envelope' would have been kinked wherever the failure mechanism changed. Instead, today, industry and academia alike have what can only be described as a plethora of *meaningless smooth curves passed through unrelated data points* as the 'characterization' of unidirectional composites. These curves then serve as the basis for predicting the strength of cross-plied composite laminates.

This misunderstanding is highlighted in Fig. 2, in a different context, to illustrate the absurdity of the conventional composite failure model shown in Fig. 3. Figure 4 shows a further variation of this theme. In every case, some meaning can be ascribed to the axes themselves, no matter how difficult they may be to measure; the problem is in interpreting intermediate points, as indicated by the question mark in each of the figures.
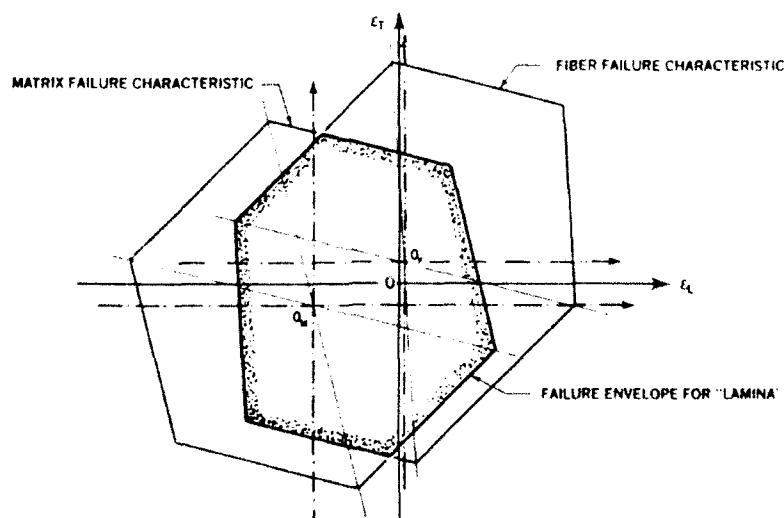
Fig. 1. Separate failure characteristics for fibers and matrix.
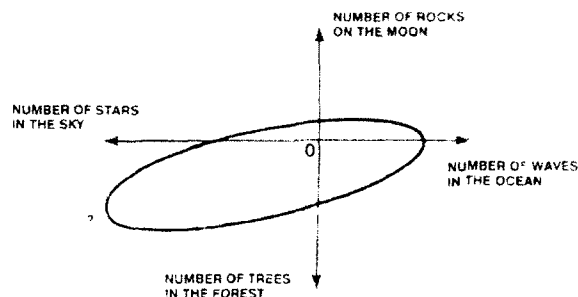
Fig. 2. One example of a meaningless curve drawn through unrelated data points.
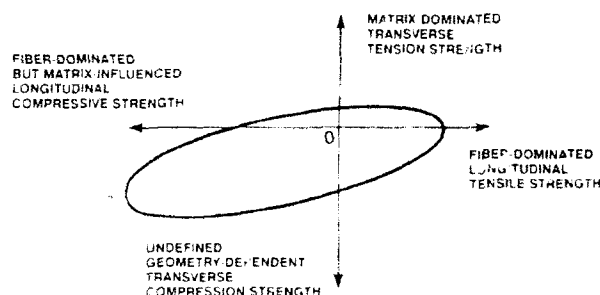
Fig. 3. An equally meaningless curve drawn through unrelated data points.
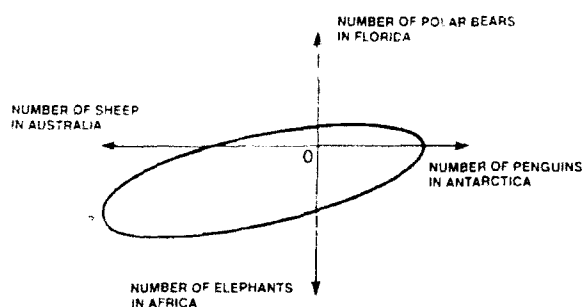
Fig. 4. Another example of a meaningless curve drawn through unrelated data points.

Hill's use of *three* parameters to characterize his failure surface for mildly anisotropic materials may seem to contradict the author's assertion that only one should be needed when only one failure mode is involved. However, while it takes only two points to specify a straight line, the line may be specified by three or more points, provided that they are merely redundant and not contradictory. The Tresca and von Mises' criteria for ductile materials require only *one* parameter each to characterize the yield of a ductile material under *any* set of combined stresses. Logic suggests that, if one were to perform the necessary algebra, one could also deduce an equivalent *single* parameter for orthotropic materials, pro-

vided that only one failure mechanism were involved. The other two parameters would be replaced by elastic constants characterizing the degree of anisotropy. Hill found a way of circumventing such tedious work. In all probability, he arrived at a far more elegant expression of essentially the same result, or an extremely close approximation to it.

If three distinct modes of failure had been involved for different states of stress — yielding under shear, short-transverse-grain delaminations, and brittle fracture, for example — no *single* characterization of the strength would be possible. But neither would Hill's three parameters suffice since they would merely represent the redundant specification of *one* mode of failure. These three different modes of failure would certainly be associated with three different strengths along the principal material axes, but that is the end of the similarity. Their characterization would require *three* physically independent parameters and the failure surface would certainly *not* be smooth.

Rowlands, in an excellent summary of the history of composite strength failure theories, reveals the extent of misinterpretation of Hill's work. He states that 'Hill's theory was adapted by Azzi and Tsai as a strength criterion for composites' (p. 76), and later states 'While it is not common to use Equation 43 (one particular formulation of Hill's theory) with composites, this concept does form the basis of several composite strength criteria' (p. 90). But, later on the same page he states that 'Unlike the maximum stress or strain criteria, Equation 43 contains interaction among the stresses and *therefore involves combined modes of failure*' (emphasis added). Rowlands also states (pp. 90 and 91) that 'This led Hill (1950) to propose *an* orthotropic yield condition' (emphasis added). How does this imply 'combined modes of failure?'

Nothing in Hill's work addresses more than one mode of failure and he should therefore be spared the ignominy of association with the many abstract mathematical failure theories for composite materials. Yet, in the UK and Europe, Tsai's misinterpretation of Hill's theory of anisotropic plasticity is referred to as the 'modified Hill theory'.

Earlier, Rowlands states (p. 86) that 'Yielding normally does not occur in fiber-reinforced plastics in the same sense as in metals. Nevertheless, many of the orthotropic strength theories are anisotropic extensions of isotropic yield criteria'. He also states (p. 96) 'In an effort to more accu-

rately predict experimental results Tsai and Wu (1971) proposed a lamina failure criterion having additional stress terms not appearing in theories such as the Hill analysis'.

What is involved is a simple curve-fit, which has no association with the physics of the situation. Additional tests are needed to provide data for each additional term included in the theoretical failure model. Ironically, as is well known, the Tsai–Wu failure model[5] contains one interaction term for which no reliable measurement has been found. Instead, it is customarily assigned the value of 0·5 or zero.

THE NEED FOR BIAXIAL RATHER THAN UNIAXIAL LAMINATE TESTS TO VALIDATE FAILURE THEORIES

Unfortunately, the characteristics of fiber–polymer composites in which strong, stiff fibers are embedded in relatively soft matrices are such that 'failure theories' can *never* be validated, or even repudiated, by uniaxial testing alone. Indeed, the author's Ten-Percent Rule[6] for preliminary design by mental arithmetic works as well as it does *only* because of the dominance of the load carried by fibers aligned with the applied load. Only the *biaxial* strengths of cross-plied laminates provide a means of differentiating between good and bad methods. And it transpires that at least *two* theories can be validated if attention is confined to

only those biaxial in-plane stresses in which the stress components have the *same* sign. Of all the possible states of stress with which to assess composite failure theories, the in-plane shear state is the most crucial. But a theory cannot be validated without also considering biaxial stresses of the same sign.

The criticality of the in-plane-shear state of stress in differentiating between plausible and implausible failure models is explained in Fig. 5. Except for the tension–compression shear quadrants, virtually the same composite laminate strengths would be predicted by the author's generalized maximum-shear-stress failure criterion, the maximum-strain model, and a combination of flaw-sensitive fracture in tension and some form of instability in compression. The other predicted strengths are similar because all three models are empirically forced to pass through the *same* measured tensile and compressive strengths under uniaxial loads. The theories predict different strengths only under in-plane shear loads, so that is the *only* test capable of validating or repudiating any of these proposed failure mechanisms.

On the other hand, agreement between test and the predictions in all the stress quadrants using the author's failure model does not actually prove that flaw-sensitive fracture could not occur under tensile loads alone. All that can be said with certainty is that the other models cannot possibly be valid throughout *all* states of combined stresses.

COMMON MEASURED UNIAXIAL COMPRESSION STRENGTH

CUTOFF FOR FIBER FAILURE IN ORTHOGONAL DIRECTION

PRESUMED FLAW-SENSITIVE (CONSTANT STRESS) BEHAVIOR

COMMON MEASURED UNIAXIAL TENSION STRENGTH

MAXIMUM-SHEAR-STRESS FAILURE CRITERION

MAXIMUM-STRAIN FAILURE MODEL

OVER-ESTIMATED IN-PLANE SHEAR STRENGTH

ASSUMED MICROBUCKLING (CONSTANT STRAIN) CUTOFF
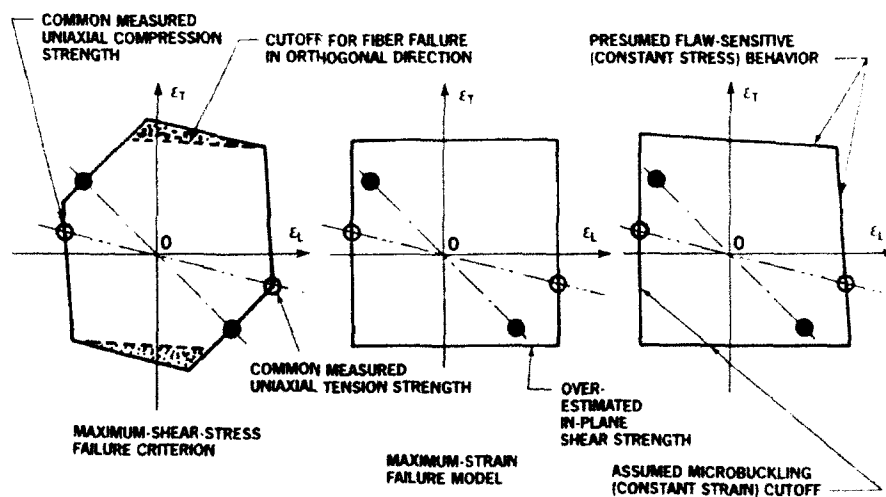
NOTE: ONLY THE IN-PLANE SHEAR TEST CAN DISTINGUISH BETWEEN THESE PHYSICALLY DIFFERENT FAILURE MODELS SINCE THE UNIAXIAL TENSION AND COMPRESSION STRENGTHS (OPEN SYMBOLS) ARE COMMON THROUGHOUT

Fig. 5. Importance of biaxial testing to distinguish between failure mechanisms.

USE OF MATRIX 'FAILURES' TO TRUNCATE PREDICTED FIBER-DOMINATED STRENGTHS

A number of theories postulate that the maximum-strain theory is valid for the fibers but that it sometimes needs truncating to allow for matrix-dominated failures. This concept appears to result from a perception that the fiber-based maximum-strain theory is in such close agreement with tests for some states of stress that it must be a valid basis for a composite failure criterion, even if it does need some minor adjustment for other states of stress.

Perhaps the best known of these works on failure criteria with multiple characterizations is by Puck, who has influenced others to follow his rationale. In one respect, he is quite correct in separating the failure criteria for the fibers and the resin, although he seems to have been unaware that he could not possibly characterize the state of stress in the resin with a simple theory that does not provide for residual curing stresses. Similar, more complex treatments such as those of Grant and Sanders' have also relied on presumed matrix failures to modify the maximum-strain failure model for shear- and compression-dominated loads.

As with much of Tsai's work, use of postulated matrix failures to truncate a fiber-failure envelope seems quite plausible. And, under other circumstances, such truncations are undoubtedly true. However, in this specific case, the cutoffs are not consistent with other test data. The very highest measured in-plane shear strength of an all $\pm45°$ laminate has the fibers failing at barely *half* the axial strain at which they fail under uniaxial loads. This implies that the matrix strains are also barely half as high, which leads to the following question: How can a matrix failure be used to explain a fiber-dominated in-plane shear strength when both the matrix and the fiber can withstand *twice* as much load under uniaxial tension or compression?

Researchers such as Puck, and Grant and Sanders must have been aware that the fiber-dominated maximum-strain failure model predicted excessive strengths for in-plane shear-dominated loads since their 'matrix' failure equations truncated those regions — and sometimes the compression-dominated regions — without changing predictions for the tension-tension quadrant. It seems strange that these authors and others did not accept the same fiber-dominated maximum-strain failure model as a basis for a complete failure criterion and modify the *fiber* failure criterion for those states of stress for which the model was inadequate. This would have produced an even better theory and avoided the need to introduce many other experimentally determined reference strengths for the theory.

The truncated maximum-strain theory proposed in Ref. 9 is almost indistinguishable from the author's generalized maximum-shear-stress failure criterion for orthotropic materials such as carbon fibers, and differs from the original untruncated maximum-strain model only for in-plane shear-dominated loads. This approach limits predicted in-plane shear strengths just as effectively as matrix cutoffs, but without doubling the number of input properties needed for the analysis. In any case, it is more in keeping with the physics of the problem.

Curiously, work by Grimes *et al.* at Northrop[10] included a cutoff with similar consequences but for entirely different reasons. Grimes imposed a limit on the shear deformation a resin matrix could withstand if there were no fibers in some direction to restrict the strain. He set the limit in the form of a shear strain between the $0°$ and $90°$ directions for either a woven or unidirectional layer of composite material. He intended to confine the matrix to elastic deformations only; the shear strain limit was set slightly higher than that associated with the unidirectional tension state of stress, so as not to undercut that seemingly valid test result. But, although he was not aware of this at the time, the in-plane shear cutoff also *implied* a limit on the axial strains of any fibers in the $\pm45°$ directions to far below the fiber strains which the maximum-strain failure model would have permitted. Indeed, Grimes's cutoff has virtually the same effect on predicted fiber-dominated strengths in the tension–compression quadrant as the author's own theory. And to think that it all originated from a desire to prevent the matrix from cracking! Nevertheless, the linear limit on design shear strains in the matrix implies that the actual ultimate failure would occur at higher loads. There is no evidence to support this.

In the late 1960s, long before Grimes's work was published, entirely empirical truncations for in-plane shear strengths were made at Grumman Aircraft on the lamina rather than on the fiber or matrix, to achieve a similar end.[11]

These works, as well as that by Black,[12] shown in Fig. 6, are noteworthy because they imply (i) an acknowledgment that classical composite failure

AXIAL STRAINS ESTABLISHED BY TEST AND CHECKED BY MAXIMUM-STRAIN COMPUTER CODE

SHEAR STRAIN LIMIT DEDUCED EMPIRICALLY AND CHECKED BY HAND WHENEVER ABOVE COMPUTER OUTPUT INDICATES LARGE STRAINS OF OPPOSITE SIGNS

STRESSING CONSISTS OF THREE SIMPLE INDEPENDENT CHECKS ON TENSILE, COMPRESSIVE, AND IN-PLANE SHEAR STRAINS FOR FIBER-DOMINATED FAILURES OF *ANY* COMPOSITE LAMINATE

FIBER REFERENCE DIRECTION

Fig. 6. Black's[?] fibrous composite failure criterion, as used on the C-17.

theory is inferior to empirical modifications of the popular maximum-strain failure model for fiber–polymer composites, and (ii) an acceptance of predicted strengths similar to those later predicted by the author using a generalization of the maximum-shear-stress failure criterion as his physical model.

Despite a paucity of publications on this topic and a lack of agreement on a single failure model, the aerospace industry has found reliable empirical techniques to predict the strength of composite laminates quite independently of the neoclassical mathematical theories of anisotropic elasticity for truly homogeneous materials.

THE TEN-PERCENT RULE

The many abstract mathematical theories surveyed by Rowlands[4] that purport to be capable of predicting the strength of structural composite laminates would seem to suggest that there is something difficult and mysterious about the task. On the contrary, provided that one does not lose track of physical realism in the model, it is easy to generate plausible sets of uniaxial and biaxial predicted strengths with the simplest of mathematical techniques, as the following approximate methods developed by the author are intended to show. Admittedly, it is necessary to restrict the theory to fiber-dominated failures *a priori*, but no skilled composite designer would knowingly waste expensive fibers in inferior structures in which the inexpensive matrix really does fail first. This theory is also restricted to fiber–polymer

composites in which strong stiff fibers are embedded in relatively soft matrices. But this limitation also is met by the great majority of composite materials, such as carbon–epoxy, fiberglass–epoxy, and boron–epoxy. There is also the customary restriction to fibers patterns in the 0, ±45°, and 90° family, with equal numbers of fibers in the +45° and −45° directions. Some of the simplifications are lost for arbitrary laminate patterns, and a computer code is needed to apply the same physical model in such cases.

The basis of the simple analysis is that, for a load in the 0° direction, the longitudinal strength and stiffness of cross-plied laminates can be deduced by applying a simple factor to the appropriate unidirectional 0° strength and modulus of a unidirectional tape laminate. The reference strength and stiffness are adjusted for the effects of the environment and must be established experimentally, as for any other composite failure theory. The strengths may need to account for the load direction (tension or compression) as well. Laminates made from biwoven fabrics can be analyzed the same way by first analytically decomposing the cloth into equivalent orthogonal tape layers. This simple theory is set apart from the others by its ease in computing the scaling factor. Each 0° ply counts as one unit of strength and stiffness, while every cross-ply[‡] contributes

---

‡ Here, the author is using the term cross-ply in its general form, to denote *any* ply other than a 0° ply. This is contrary to efforts to confine the designation to only 90° plies and to use the confusing term 'angle ply' to designate all other directions *except* 0° and 90°.

only one-tenth as much to the strength and stiffness. On that basis, a 0°/90° laminate would have $(1 + 0 \cdot 1)/2 = 0 \cdot 55$ as much strength and stiffness as an all-0° laminate. Likewise, a quasi-isotropic laminate would be predicted to have $(1 + 3 \times 0 \cdot 1)/4 = 0 \cdot 325$ as much strength and stiffness as an all-0° laminate. An all-90° or entirely ±45° laminate would be expected to have about one-tenth of the strength and stiffness of the all-0° laminate, but those particular properties are really matrix-dominated and the predictions may not always be relied on for such plies in isolation.

Biaxial strengths for stresses having the same sign are then predicted on the basis of the maximum-strain theory for fibrous composites. For uniaxial loads with a strain ε in the 0° direction, any 90° fibers would be strained by $-\nu\varepsilon$, while ±45° fibers would develop an axial strain of $1 - \nu\varepsilon/2$ times the strain in the 0° fibers, as explained in Fig. 4 of Ref. 13. Here, the Poisson's ratio ν refers to ν_{xy} of the laminate. For a quasi-isotropic laminate, ν_{xy} is inevitably very close to $0 \cdot 33$, as derived in Ref. 6, while it is only $0 \cdot 05$ for the 0°/90° laminate but almost $0 \cdot 8$ for an entirely ±45° laminate.

Consequently, a uniaxial 0° load on a quasi-isotropic laminate would strain the ±45° fibers to only one-third of their ultimate capacity. Since the stress on those fibers would contribute only half as much after rotation to the reference 0° direction, an improved estimate of the scaling factor for the strength and stiffness of this laminate would be $(1 \cdot 0 + 0 \cdot 1 + 2 \times 0 \cdot 333 \times 0 \cdot 5)/4 = 0 \cdot 358$, a value adequate for design purposes. However, if we examine the biaxial rather than the uniaxial stress state, *all* the fibers must now be stressed equally and the scaling factor would then become $(1 \cdot 0 + 0 \cdot 1 + 2 \times 1 \times 0 \cdot 5)/4 = 0 \cdot 525$, or some 50% *higher* than the strength under a uniaxial load.

This easily established increase in strength can *never* be demonstrated by the common kind of 'biaxial' test specimen shown in Fig. 4 of Rowlands' work (see Ref. 4), the key features of which are summarized in Fig. 7 of this paper. The biaxially loaded interior of the test coupon cannot possibly experience a higher stress than that needed to fail the uniaxially loaded fingers around the periphery. The most obvious demonstration of this deficiency is testing for the biaxial strength of a ±45° laminate which, by definition, must be the same as for a 0°/90° laminate. The surrounding ±45° fingers would have less than one-fifth of the required strength to fail the interior test section of this specimen. Even the quasi-isotropic
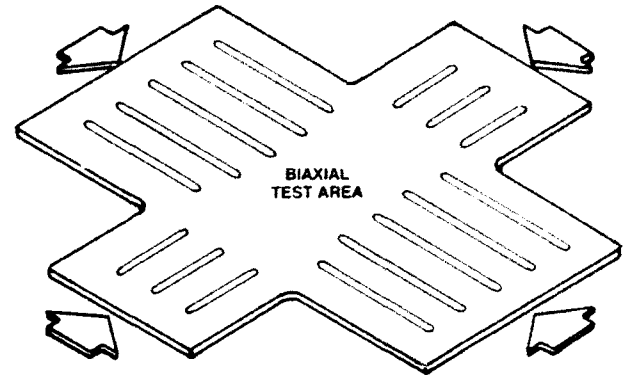
BIAXIAL STRESSES DEVELOPED IN TEST SECTION CAN NEVER EXCEED
THE UNIAXIAL STRENGTH OF THE SURROUNDING FINGERS

Fig. 7. Defective biaxial test specimen.

laminate is 50% stronger under equal biaxial stressing than when loaded uniaxially.

This widespread error in trying to experimentally determine the biaxial strength of composite materials using test coupons which are inherently incapable of providing the correct result has been a major reason why so many scientifically unsound composite 'failure theories' have not been exposed.

In Ref. 14, the author proves that biaxial testing would indeed be a very difficult task, requiring a large circular sandwich plate supported around its periphery and loaded by lateral pressure, as shown in Fig. 8, if premature failure at some uniaxially stressed area is not to precede failure in the biaxially loaded central test section. Such an expensive specimen has yet to be tested, although the author is confident that it will eventually be used by those who design and build submarines since knowing the true biaxial compressive strength of composite laminates is so critical to the success of their activities.

However, in Ref. 15, Swanson and Nelson used pressurized tubes with varying tensile axial loads to prove beyond any reasonable doubt that the maximum-strain theory is acceptable — and unlikely to be improved upon — for carbon–epoxy composites in the tension–tension quadrant (see Fig. 9). Interestingly, their finding that the Tsai–Wu 'last-ply' failure model was totally inconsistent with Swanson's test data as long ago as 1986 seems to have had even less effect on the technical community than this author's efforts.

Some test data in the compression–compression quadrant seem to support the author's predictions about the straight-sided form of the failure envelope. However, the strengths measured are all too low, as are Swanson's in this
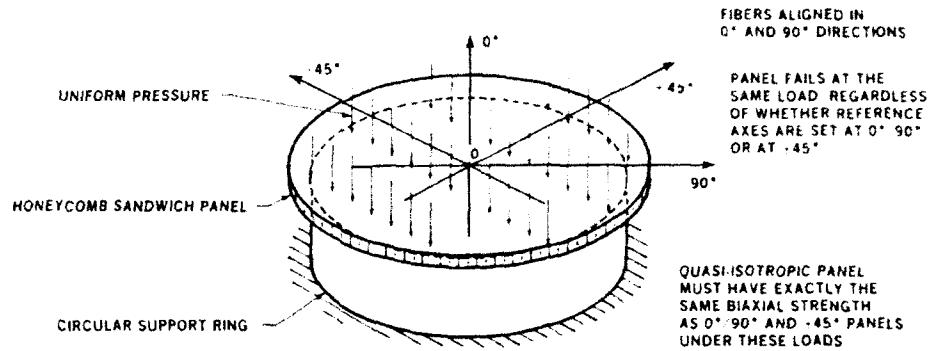
Fig. 8. Biaxial test specimen demonstrating identical biaxial strengths of 0°/90° and ±45° laminates.
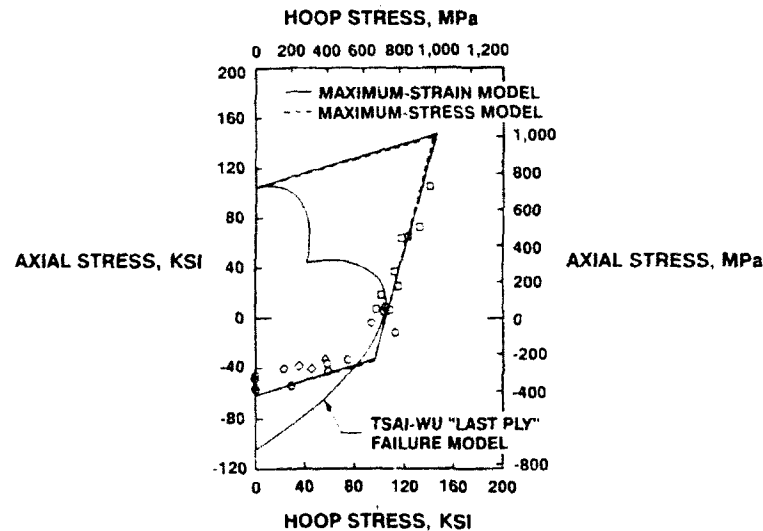
SOURCE: SWANSON, OF THE UNIVERSITY OF UTAH

Fig. 9. Swanson's comparison of laminate failure theories with failure stresses in quasi-isotropic cylinders.

stress domain. New tests are needed to truly characterize composite materials under biaxial compressive stresses.

Nevertheless, the author contends that there is really no need to directly measure the biaxial strengths of fibrous composites since they can be determined with an extremely high confidence level from uniaxial testing of 0°/90° flat laminates. Because the Poisson's ratio is almost zero in this case, the biaxial strength cannot differ significantly from the uniaxial strength. According to the maximum-strain model, the biaxial strength would be higher than the uniaxial by the ratio $1/(1-\nu)$, or about 1·05. Now, the biaxial strength of an entirely ±45° laminate must be precisely the *same*

because the only difference is the reference direction for the fiber axes (see Fig. 8). Similarly, the biaxial strength of a quasi-isotropic laminate must also be the same, since it must be the average of these two identical quantities.

This biaxial strength serves as a kind of magic number for *all* laminates containing the same number of 0° and 90° fibers, with the remainder shared equally between the +45° and −45° directions. Once the biaxial strength has been obtained, the uniaxial strength is derived with great precision by multiplying the biaxial strength by $(1-\nu)$, as explained below, there being only one Poisson's ratio for this family of doubly symmetric laminates.

In the case of the 0°/90° laminate, one would expect the normalizing factor with respect to the unidirectional lamina strength to be 0·55/ 1−0·05 = 0·575, quite close to the 0·525 deduced earlier. Likewise, the uniaxial strength of the quasi-isotropic laminate would be (1 − 0·33) × 0·575 = 0·383, again only slightly above the 0·325 deduced above by treating the Ten-Percent Rule in its simplest form as a rule of mixtures and the factor 0·358 deduced by resolving and summing the stresses in the various fiber directions. These various forms of simplified analysis are self-consistent, the result of being based on a physically realistic model.

Turning now to the in-plane shear strength for the same family of doubly symmetric laminates, the author has suggested a strength be selected that is equal to *half* the unidirectional strength of the complementary fiber pattern, with 0°/90° and ±45° fiber contents interchanged.[16] Thus, the fiber-dominated in-plane shear strength of an entirely ±45° laminate would be half the unidirectional tension or compressive strength, whichever is greater, of a 0°/90° laminate. The scaling factor for this laminate, with respect to the uniaxial strength of a unidirectional laminate, would be 0·5 × 0·55 = 0·275. Similarly, the factor for a quasi-isotropic laminate would be 0·5 × 0·325 = 0·163, although either of the higher estimates for the second factor would be equally acceptable. The prediction of 0·5 × 0·1 = 0·05 for the in-plane shear strength of an all-0°/90° laminate happens to be nearly correct, but is really suspect because that particular property is obvi-

ously matrix-dominated rather than fiber-dominated and so contravenes the original simplifying assumptions.

Failure envelopes for these three fiber patterns, based on the Ten-Percent Rule, are shown in Fig. 10, which is not at all similar to the predictions of Tsai's theories in Fig. 11.

This simple procedure, developed by the author for predicting in-plane shear strengths, has been criticized as being unscientific and unworthy of publication. However, when a paper advocating this approach was presented in 1987,[16] structural designers had neither reliable test specimens nor credible theoretical methods with which to establish in-plane shear strengths for laminates. What was desperately needed was something at least good enough for preliminary design. And, if this controversial idea inspired others to improve both the test specimen designs and the analysis methods, the paper would have served an even greater purpose. Now that such predictions can be made scientifically,[17] the crude approximations of in-plane shear strength by the Ten-Percent Rule are still close enough to the best analyses to be used for formal stressing. For a comparison between tests and theories, see Fig. 15 of Ref. 17.

Even the maximum-strain model of Ref. 18, which is outstanding in the tension–tension and compression–compression quadrants, grossly *overestimates* in-plane-shear strengths, typically by 60%. Figure 9 of Ref. 6 shows that, for the maximum-strain failure model, the in-plane shear strength is (1 − ν)/(1 + ν) times as high as the bi-axial strength for *all* doubly symmetric cross-
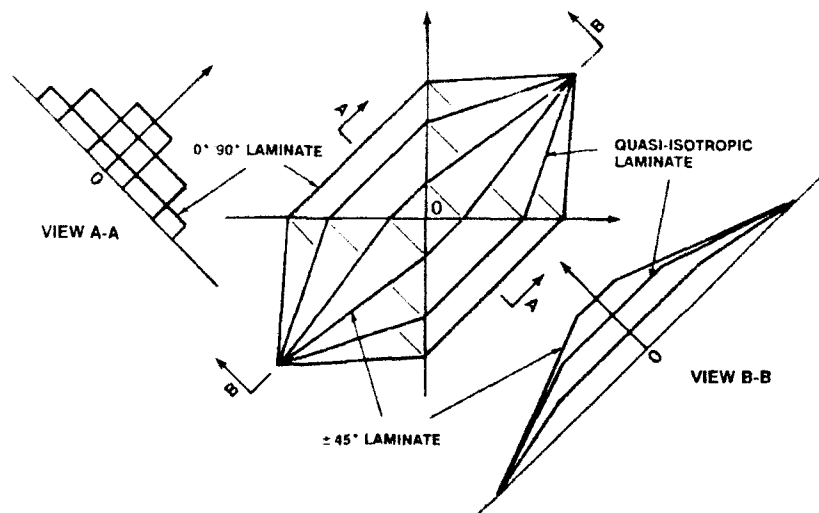
Fig. 10. Failure envelopes according to the Ten-Percent Rule.
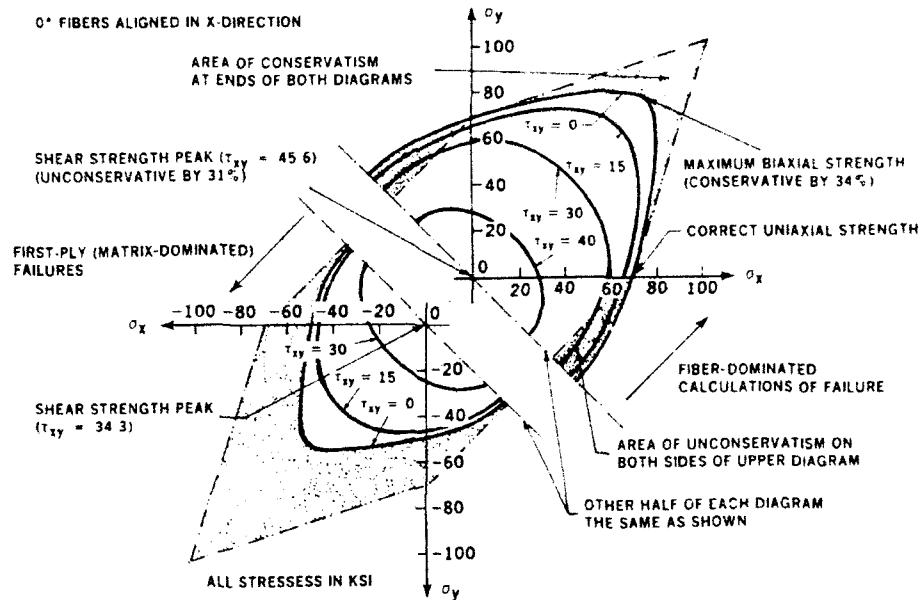
Fig. 11. Failure envelope for quasi-isotropic carbon-epoxy laminates — Tsai-Hill and Tsai-Wu theories.

plied laminate patterns. Therefore, in place of the factors 0·275, 0·163, and 0·05 above, the maximum-strain model would overestimate the in-plane-shear strength via the factors [1 − 0·05 /
1 + 0·05] × 0·55 / 1 − 0·05 = 0·524, [1 − 0·33 /
1 + 0·33] × 0·55 / 1 − 0·05 = 0·290, and [1 − 0·8 /
1 + 0·8] × 0·55 / 1 − 0·05 = 0·064, respectively.

While the sample solutions here are confined to doubly symmetric fiber patterns for simplicity's sake, the original derivations of the simplified analysis methods also cover fiber patterns with different 0° and 90° fiber contents, but the evaluation of the biaxial strengths for these laminates requires a pocket calculator rather than mental arithmetic.

COMPARISON WITH OTHER PREDICTIONS OF BIAXIAL COMPOSITE STRENGTHS

This section reveals gross deficiencies in corresponding predictions from a widely promoted computer code based on mathematical theories of anisotropic elasticity for homogeneous materials. Although the illustrative examples refer to only one such computer program, that of Tsai,[19] the criticisms apply equally to all similar codes as well, many of which are cited in Ref. 8.

Figure 12 contains first- and last-ply failure predictions published by Tsai[19] for a quasi-isotropic carbon-epoxy laminate. Tsai advocates

accepting the larger estimate for monotonically loaded test coupons on pp. 12-16 of his work, as shown on the right of this figure. This recommendation is based on his proposed progressive-failure models. The author's corresponding predictions, using the *same* input properties but ignoring those for which there was no call, are given in Fig. 13 for comparison. There are great differences, particularly with respect to the first-ply failure predictions, which do not even permit agreement under uniaxial loads. The agreement with the last-ply failure predictions is better, but the failure envelope is far from smooth and continuous at the laminate level, which encourages one to question the importance of such a constraint at the unidirectional lamina level.

Tsai's first-ply predictions fall far short of the strengths predicted by the author throughout the tension-tension quadrant and greatly exceed them throughout the compression-compression quadrant. Remarkably, the strains to failure under biaxial compressive loads exceed the input unidirectional compressive strain limit by a factor of nearly 2! No explanation of this is provided and, in the author's opinion, none ever could be. And the justification given by Tsai for reducing these acknowledged excessive estimates *requires* the kind of matrix degradation that could occur *only* during some prior application of *tensile* loads in order to crack the matrix and reduce its ability to support longitudinally compressed fibers in a *subsequent* application of load.

(NOTE: COMPRESSIVE STRAIN USED IN ANALYSIS IS 8.29 μIN./IN.)

SOURCE: TSAI   -●- FPF   -O- LPF   -■- ULT
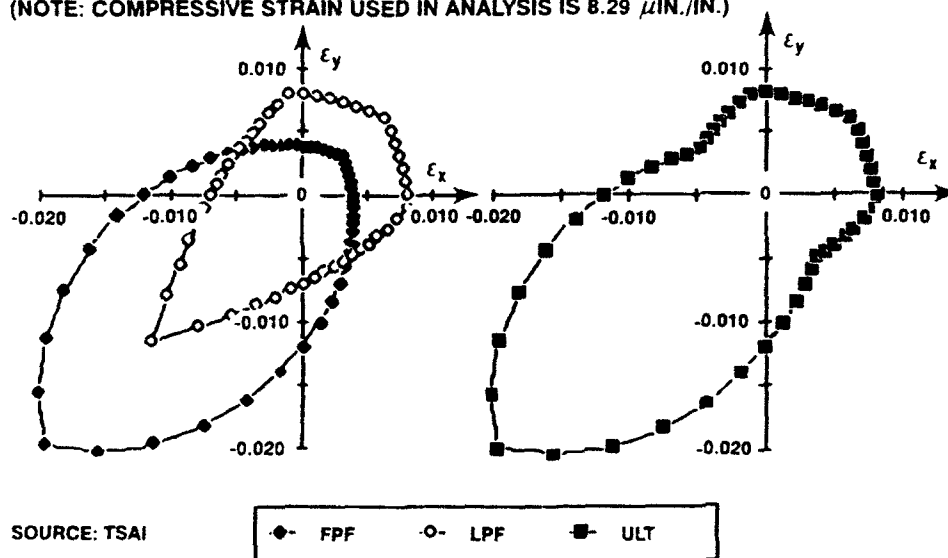
(a) FPF AND LPF ENVELOPES OF QUASI-ISOTROPIC T300/N5208 CFRP LAMINATE AND
(b) THE ULTIMATE STRENGTH ENVELOPE DEFINED BY THE OUTERMOST BOUNDARY OF
    THE FPF AND LPF ENVELOPES

Fig. 12.   Tsai's first- and last-ply failure analyses.

ε_0 = 8.29 μIN./IN.

α = ARCTAN 0.28
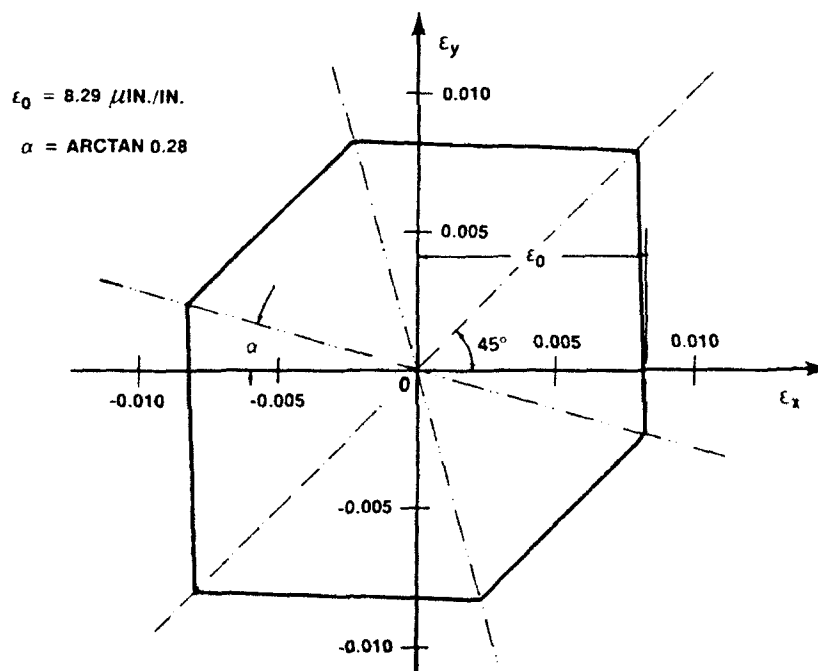
Fig. 13.   Hart-Smith's[16] failure envelope for a quasi-isotropic carbon-epoxy laminate.

Further, the predicted last-ply biaxial tension strength still falls short of the author's prediction, even when the transverse properties have been adjusted to match the uniaxial tensile strengths reasonably well. Surprisingly, the best agreement seems to be with the in-plane shear (equal and opposite tension and compression) state of stress.

It is difficult to make concrete comparisons with any theory using a progressive failure model because, as indicated in Fig. 14, also taken from Tsai's *Composite Design* book, his failure envelope will collapse onto that for the maximum strain theory if one presupposes the necessary amount of matrix degradation. (There seems to be
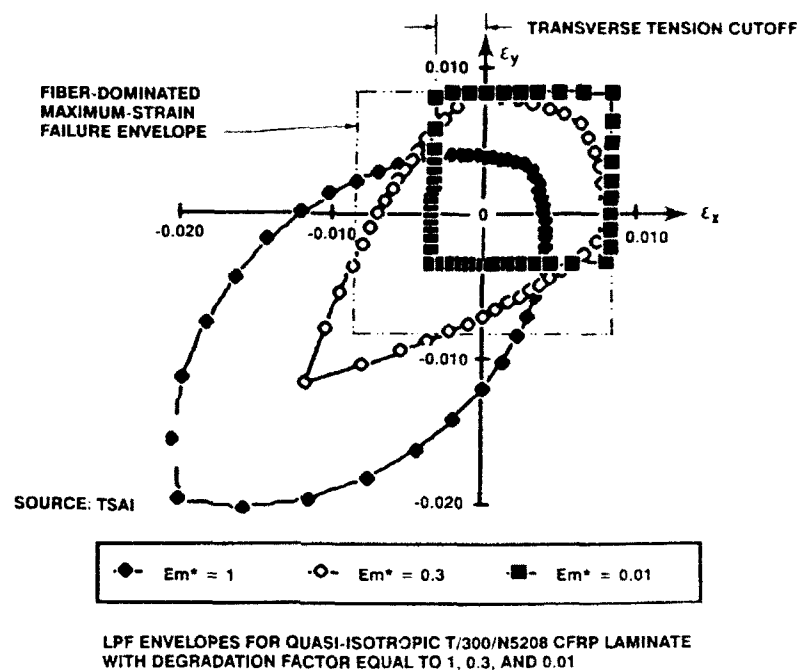
Fig. 14. Tsai's first- and last-ply failure analyses showing progressive transformation into maximum-strain failure envelope.

an error in coding his program because the strain in the compression–compression quadrant has collapsed onto the value of strain entered for transverse tension, not longitudinal compression. However, the agreement achieved in the tension–tension quadrant by invoking matrix degradation has invalidated the agreement previously reached for the in-plane shear loads.

Given the difficulty of making comparisons with a moving target, as the degree of matrix degradation is altered, one is entitled to ask whether or not it would have been easier to go directly to the maximum-strain failure model instead of arriving at it indirectly via adjustments to the transverse properties entered into some other failure model which would not at first give acceptable answers. The abuse of progressive failure theories to 'enhance' predicted composite laminate strengths will be discussed in a future work.

A comparison of Figs 12–14 indicates that no matter what degree of matrix degradation is assumed, no *single* set of input properties for Tsai's theory will *simultaneously* match the author's predictions for uniaxial *and* biaxial states of stress. Even when the transverse properties are suitably 'adjusted' to match the uniaxial tensile and compressive strengths, the predicted biaxial tension strength will still be too small and the biaxial compressive strength too large.

In theory, one could always add two more adjustable parameters to the lamina failure model, to be set to match the biaxial testing of two cross-plied laminates. Ashizawa[20] did so by using a cutoff based on measured fiber-dominated in-plane shear strengths of $\pm 45°$ laminates. However, while this technique worked whenever the measured shear strength was accurate, the predictions were obviously inconsistent whenever the shear measurement was far too low. Unless one had a valid physical model to guide the process, it is likely that those particular biaxial tests would be inconsistent with predictions based on *other* biaxial tests. And, if one really did have a reliable physical model, one would not need any additional terms.

The quadratic 'failure criteria' for fibrous composites are not the first unsound theories which are capable of predicting *some* numerically correct answers to problems despite a consistent inability to solve *other* problems. The beliefs of the Flat Earth Society come readily to mind. While the old idea that the sun revolves around the earth is no longer taught, *many* celestial and seasonal observations were explained at the time by use of this model. The author can only hope that it will take less time to recognize the correct way to predict the strength of composite laminates than it took to reach agreement on a model for the solar system.

Another failing of these abstract mathematical failure 'criteria' is exposed by a physical assessment of the most severe 'triaxial' stresses that can be applied. Actually, it is the combination of biaxial in-plane direct loads with additional in-plane shear, so it is really a case of biaxial loads with respect to different axes. As the author noted in 1985 (Fig. 13 of Ref. 13), the cross-section of the failure envelope looking along the biaxial stress line *must* be rectangular, as shown in Fig. 10. For the case of a quasi-isotropic laminate, the specific load of equal and opposite σ_x and σ_y stresses in the absence of any in-plane shear stress τ_{xy} induces *no* load in either the $+45°$ or $-45°$ fibers. Most of it is reacted by axial tension in the $0°$ fibers, for example, and simultaneous compression in the $90°$ fibers. A very small fraction of the load is reacted by shearing the resin matrix. On the other hand, the application of a pure in-plane shear load to the same laminate, with respect to the same reference axes, would load up the $\pm45°$ fibers while leaving the $0°$ and $90°$ fibers unloaded. This particular cross-section of the failure envelope is therefore rectangular because there is essentially *no* interaction between the loads, one of which is carried by the $0°/90°$ fibers while the other is resisted by the $\pm45°$ fibers. The form of the abstract mathematical failure envelopes in Fig. 11 is in stark contrast to Fig. 10, being smoothly curved all over.

The failure envelopes in Fig. 11 are obviously also in error at the biaxial tension and biaxial compression points. Since *all* fibers are equally strained under those conditions, it is physically impossible to add in-plane shear loads without decreasing the in-plane direct loads. The ends of the failure envelope must be *pointed*, not rounded as they are in Fig. 11.

The reason for these errors is that Tsai's fictitious failure criterion, cited on p. 11-5 of Ref. 19, contains a mixture of unrelated reference strengths, some pertaining to the fiber and others to the matrix. Tsai's formula and its many clones are restricted in validity to truly homogeneous materials exhibiting only *one* failure mechanism for *all* the states of combined stresses being considered. And, under such circumstances, the use of four or five test measurements to characterize the strength of the material should not be necessary. For distinctly heterogeneous materials such as fiber–polymer composites, on the other hand, it is necessary to write *separate* failure criteria against the fibers, the matrix, and possibly also the interface between the two. Further, additional

criteria are needed whenever multiple failure modes are possible for any constituent.

There should perhaps be additional interlaminar criteria for the immediate proximity of any boundaries, but this refinement is customarily ignored, along with stacking-sequence effects, which is why every so often composite laminates with excessive clustering of parallel fiber layers delaminate during cooldown before they are even removed from the autoclave. And more often than not, a laminate was designed that way because some computer 'optimization' program was used to identify the most 'suitable' laminate instead of allowing accumulated experience to dictate that there be a minimum percentage of plies in each of the four standard directions and that there be strict limits on the clustering of parallel plies. Tsai's position on this matter is stated on p. 7-1 of Ref. 19. 'For symmetric laminates subjected to in-plane loads only, the stacking sequence of plies is not important.' He accounts for stacking sequence only when studying the bending of laminates and all but ignores the issue of edge delaminations, while concentrating on intraply failures.

A major difference between the author's methods of predicting the strength of fibrous composites and those typified by the works of Tsai is that, in the author's case, minor changes in 'lamina' properties do not affect the basic *form* of the failure envelopes. The failure envelope has remained characteristically flat-faceted since the very first report on the subject in 1984.[21] Each facet has been defined by the failure of one particular fiber direction under a uniform failure mode throughout. The intersections of the facets denote the simultaneous failure of two or three fiber directions, depending on how many facets intersect. Reference 22 even includes parametric studies showing the small effects of systematic variations in material properties. Yet a study of Ref. 19, for example, will show an endless variety of shapes, some associated with different fiber patterns but many caused merely by a change in the level of 'degradation' due to matrix 'cracking'. Such variability does not inspire confidence in a theory.

The author's failure model for composite laminate analysis has been criticized as being too simplistic by some well-regarded researchers. A particular stumbling block is that the final failure envelope shows only *one* line for compressive failures while there is considerable evidence that several failure modes are possible. This is not

germane to the level of analysis being performed here. Also, the critics seem to have missed the very clear coverage of both shear failures of the fibers and some not necessarily defined form of compressive instability, depending on the particular composite material under investigation. The author is interested in only the *weakest* of the possible failure mechanisms, whatever it may be. It might even change with operating environment and certainly changes between unidirectional and cross-plied laminate patterns. There is no need for the author to address this issue of multiple possibilities for any one facet of the failure envelope because the experimentally derived input data will automatically identify the weakest mechanism provided that the test coupon and fixture are representative of the real structure.

The reluctance to admit that the art of predicting the strengths of composite laminates has not been perfected is apparent in a response to the author's attempts to find interest in improving the analytical techniques. If one were to believe the predictions of the Tsai–Wu 'failure theory', for example, one would be forced to conclude that the underwater compressive strength of a composite submarine hull could be increased substantially by *reducing* the interlaminar and hence transverse-tension strength of the lamina, as explained in Fig. 15. While many got the message, one response was: 'That sounds like a great idea. How do we reduce the interlaminar tension strength?'

A MAJOR INCONSISTENCY IN STANDARD COMPOSITE FAILURE THEORIES

Analytical predictions of strength based on a combination of orthogonal unidirectional tape layers have no resemblance whatever to the predicted strengths of the same fibers in the same resin, in the form of a cloth laminate, even when the two laminates have precisely the same elastic constants and the fibers have precisely the same failure stress or strain. The issue has nothing to do with kinks in the woven fabric; the dissimilarity also exists when the bidirectional lamina is made from unkinked dry stitched preforms which are subsequently impregnated with resin.

Figure 16 illustrates this point very clearly. The irreconcilability is quantified in Fig. 17 by various analyses of 0° and 90° and 0°/90° laminates. The analyses are symmetric about the diagonal running from the lower left to the upper right, so only
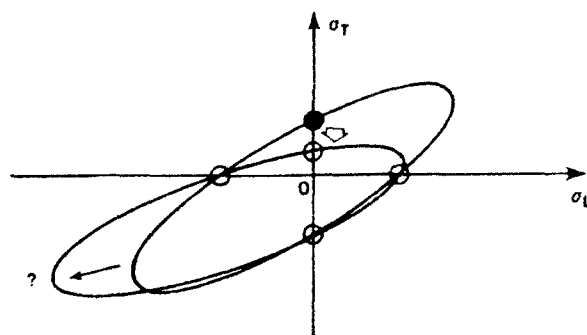
ULD ANYONE BELIEVING THIS ANALYSIS BE WILLING TO PUT TO SEA FOR THE DIVING TRIALS?

Fig. 15. 'Improved' composite material for submarine hulls by decreasing transverse-tension strength of unidirectional lamina.
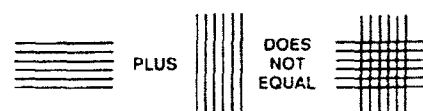
Fig. 16. Fatal flaw in tensor-polynomial composite failure criteria.

half of each is shown, with the 'tape' analyses in the lower right and the equivalent 'cloth' analyses in the upper left. Precisely the same fiber strains-to-failure are used throughout the analyses, and the output of the tape laminates analysis is used to define the elastic constant inputs for the cloth analysis. The first-ply failure (FPF) analyses on the right of the figure show a gross underestimation of the tensile strengths,† with respect to both the author's theory and the well-known maximum-strain failure model, which is compensated for by a gross overestimation of the compressive strengths. The computer code then 'modifies' the tape material properties and recalculates last-ply failures (LPF) which appear to agree much better with the author's theory. Tsai's reduction in transverse stiffness to achieve this transformation is directly equivalent to the author's recommendations in Ref. 22. There was concern that the predictions of the BLACKART computer code would be invalidated by premature transverse-tension failures of the type responsible for the distortion of the FPF envelope in Fig. 17. But the author's approach has been described as merely a

---

† The cusp at the biaxial tension point in Fig. 9 results from Swanson's interpretation that if all the laminae are *equally* critical according to the FPF analysis, no enhancement of strength is possible under an LPF analysis. Only the transverse ply properties were degraded in Fig. 17.
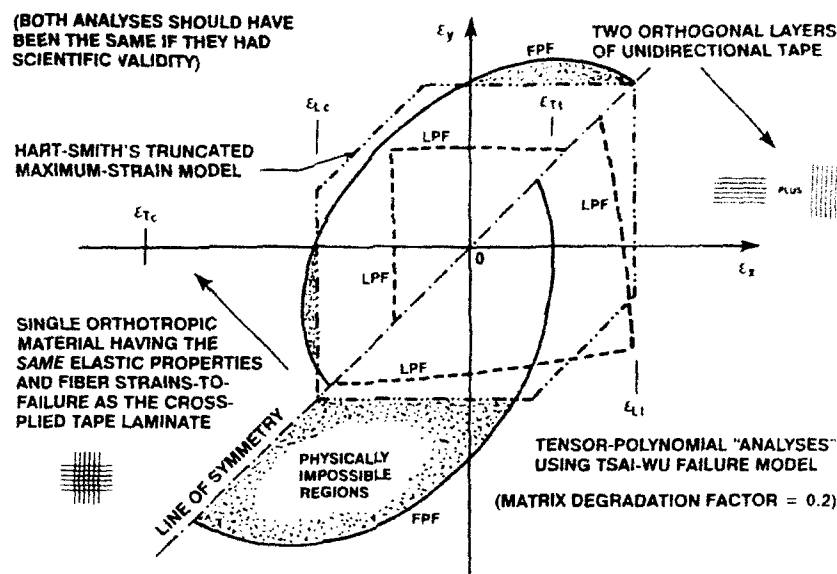
Fig. 17.   Conflicting analyses of the same 0°/90° composite laminate.

fudge. Perhaps it would have appeared more scientific if it had been accomplished by a computer code.

The FPF predictions shown in the upper left of Fig. 17 should correspond to fiber-dominated failures and, indeed, they agree well with the author's predictions, apart from the minor problem of physically impossible small overestimations of strength whenever the two in-plane stress components have the same rather than opposite signs. However, this apparent reconciliation is undermined by further computer coding in the form of LPF predictions for the cloth laminate which are significantly weaker. No justification for this second analysis has been found in Tsai's book, and no physical explanation is given in the text accompanying the computer code.

However, the good agreement between the 'cloth' FPF analysis in Fig. 17 and the author's analysis reinforces the author's repeated claims over the years that the mechanical properties needed for predicting the strength of cross-plied composite laminates are those prevailing in the cross-plied laminate, not those for the unidirectional tape laminate in isolation. If, instead of proceeding from the tape to a cloth analysis, the process had been reversed to establish representative in-situ mechanical properties for the unidirectional tape *in the presence of orthgonal fibers*, the 'tape' analysis for the combination of unidirectional 0° and 90° plies would also have been correct *because all the predicted failures would have been fiber-dominated*. The only thing found

wrong would be the original hypothesis that it was appropriate to create a composite failure model based on measured tensile and compressive strengths in the longitudinal and transverse directions for a unidirectional tape laminate.

CONCLUSIONS

One would have to conclude from the simplicity of the author's Ten-Percent Rule for approximate analysis of fibrous composite laminates that it should be extremely difficult to develop computerized composite 'failure theories' that are incapable of correctly predicting the uniaxial strengths under tension and compression. Surprisingly, the literature on the subject shows that many authors have failed to predict even these simplest of laminate strengths.

Of the well-established failure models, only the empirical maximum-strain model has been found by the author and others to lead to acceptable predictions for even the simplest load cases. This same theory has already been confirmed by experiment to be valid throughout the tension–tension quadrant. And the author expects that it will eventually be proven equally valid throughout the compression–compression quadrant when reliable test data re generated. However, this theory has been shown to be unacceptably unconservative, typically by 60%, for the in-plane-shear loads in which the biaxial stresses are of opposite sign.

If it were not for this in-plane-shear case, there would be no criterion by which to distinguish between the maximum-strain theory and the author's generalization of the Tresca maximum-shear-stress failure model. This particular biaxial stress state is *crucial* in selecting one of the two theories. The criticality applies equally in assessing other physically plausible failure models, some of which have considerable experimental support for *other* states of stress. For instance, as shown in Fig. 5, a failure model based on a combination of notch sensitivity in the tension–tension quadrant and some form of compressive instability throughout the compression–compression domain cannot be challenged except for the need to find a third mechanism to eliminate unacceptably unconservative predictions throughout the tension–compression shear states of biaxial stress. Neither the author nor anyone else is in a position to challenge such theories if they are not assessed for *all* states of uniaxial and biaxial stresses.

In applying and presenting the generalized maximum-shear-stress failure model, the author has already acknowledged the need to provide for at least one *different* failure mechanism, that of compressive instability for the newer high-strain carbon fibers of very small diameters. Expressing his new failure theory with respect to the strain plane, even though it is really a stress-based criterion, makes it easy to superimpose additional realistic failure modes. The author also acknowledges the need to provide for but only rarely used transverse matrix cracking for such composite materials as S-glass fibers in a brittle polymer matrix.

The author's failure model is set apart from the numerous abstract mathematical theories of anisotropic elasticity by additional failure modes that can be superimposed on the basic shear failure envelope for the fibers *without* altering the predicted strengths for other failure modes. With the fictitious smooth curves drawn through four unrelated measured strengths, on the other hand, a change in any *one* of these four calibration points alters *every* predicted strength except for the other three reference strengths. A weakness in transverse tension strength, for example, would be expected to cause predicted increases in the biaxial compression strength, while premature compressive failure by instability would be associated with a prediction that the biaxial tension strength had been enhanced.

It should now be evident that the innumerable abstract mathematical 'failure theories' for fibrous composites, which have been acknowledged as unreliable by their own originators the moment they had to invoke 'progressive failure' models to achieve agreement with even the uniaxial tests, are beyond redemption as useful structural design tools when one also considers the biaxial stress states.

ACKNOWLEDGEMENT

REFERENCES

1. Hart-Smith, L. J., Some observations on the analysis of in-plane matrix failures in fibrous composite laminates. Douglas Paper 8858, presented at 4th ASTM Symposium on Composite Materials: Fatigue and Fracture, Indianapolis, IN, USA, 6–7 May 1991.
2. Hill, R., *The Mathematical Theory of Plasticity*. Oxford University Press, London, UK, 1971, pp. 317–40.
3. Tsai, S. W., Strength characteristics of composite materials. NASA CR-224, Apr. 1965.
4. Rowlands, R. E., Strength failure theories and their experimental correlation. In *Handbook of Composites. Vol. 3 — Failure mechanics of composites*, ed. G. C. Sih & A. M. Skudra. North-Holland, Amsterdam, The Netherlands, 1985, pp. 71–125.
5. Tsai, S. W. & Wu, E. M., A general theory of strength for anisotropic materials. *J. Comp. Mater.*, **5** 1971 58–80.
6. Hart-Smith, L. J., Simple methods for predicting the strength of cross-plied fibrous composite laminates. Douglas Paper 8377, presented at SAMPE Composites Seminar on Repair, Maintainability and Supportability, San Diego, CA, USA, 19 Oct. 1989.
7. Puck, A., Festigkeitsberechnung an Glasfaser-Kunstoff-Laminaten bei zusammengesetzter Beanspruchung (Stress analysis of glass fiber in composite laminates). *Kunstoffe*, **59** 1969 780–7.
8. Anon., Failure criteria for an individual layer of a fibre reinforced composite laminate under in-plane loading. Engineering Sciences Data Unit, Item 83014, June 1986.
9. Hart-Smith, L. J., A new approach to fibrous composite laminate strength prediction. In *Proceedings of the 8th DoD/NASA/FAA Conference on Fibrous Composites in Structural Design*, 1989, NASA CP-3087, Part 2, pp. 663–93.

10. Grimes, G. C., Ranger, K. W. & Brunner, M. D., Element and subcomponent tests. In *Engineered Materials Handbook Vol. 1 - Composites*, ed. C. A. Dostal. ASM International, Metals Park, OH, USA, 1987, pp. 313–45.

11. Hadcock, R. N., Saurez, J. & Whiteside, J. B., *Advanced Composite Wing Structures Boron-Epoxy Design Data Vol. 1, Design data summary*. Grumman Aerospace Corporation, Technical Report AC-SM-ST-8085, March 1970.

12. Black, J. B., Jr, Failure Criterion No. 1,075,372, internal Douglas document dated 4-22-88.

13. Hart-Smith, L. J., Simplified estimation of stiffnesses and biaxial strengths for design of carbon-epoxy composite structures. In *Proceedings of 7th DoD/NASA Conference on Fibrous Composites in Structural Design*, 1985, AFWAL-TR-3094, pp. V.a.-17 to V.a.-52.

14. Hart-Smith, L. J., A biaxial-strength test for composite laminates using circular honeycomb panels. In *Proceedings of 33rd International SAMPE Symposium and Exhibition*, 1988, pp. 1485–98.

15. Swanson, S. R. & Nelson, M., Failure properties of carbon-epoxy laminates under tension-compression biaxial stress. In *Composites '86: Recent Advances in Japan and the United States*, ed. K. Kawata, S. Umekawa & A. Koyabashi, Proceedings of the Third Japan-US Conference on Composite Materials, Tokyo, Japan, June 23–25, 1986, pp. 279–86.

16. Hart-Smith, L. J., A radical proposal for in-plane shear testing of fibrous composite laminates. In *Proceedings of 32nd International SAMPE Symposium and Exhibition*, pp. 349–59; reprinted in *SAMPE Quart.* **19** 1, 1987, 7–13.

17. Hart-Smith, L. J., Fibrous composite laminate strength predictions demystified. In *Proceedings of 11th European SAMPE Meeting*, ed. H. I. Hornfeld, Basel, Switzerland, 1990, pp. 365–80.

18. Waddoups, M. E., Characterization and design of composite materials. In *Composite Materials Workshop*, ed. S. W. Tsai, J. C. Halpin & N. J. Pagano, Technomic, CT, USA, 1968, pp. 254–308.

19. Tsai, S. W., *Composites Design*, 4th edn. Think Composites, Dayton, OH, USA, 1988.

20. Ashizawa, M., Semi-empirical approach to failure criteria for laminated composites. In *Proceedings of 7th DoD/NASA Conference on Fibrous Composites in Structural Design*, 1985, pp. V.a.-53 to V.a.-73.

21. Hart-Smith, L. J., Approximate analysis methods for fibrous composite laminates under combined biaxial and shear loading, Douglas Aircraft IRAD Technical Report MDC-J9898, March 1984.

22. Peterson, D. A. & Hart-Smith, L. J., A rational development of lamina-to-laminate analysis methods for fibrous composites. In *Proceeding of 9th ASTM Symposium on Composite Materials Testing and Design*, ed. S. P. Garbo, ASTM STP 1059, February 1990, pp. 86–120.

An evaluation of equivalent-single-layer and layerwise theories of composite laminates

J. N. Reddy

Department of Mechanical Engineering, Texas A&M University, College Station, TX 77843-3123, USA

A review of equivalent-single-layer and layerwise laminate theories is presented and their computational models are discussed. The layerwise theory advanced by the author is reviewed and a variable displacement finite element model and the mesh superposition techniques are described. The variable displacement finite elements contain several different types of assumed displacement fields. By choosing appropriate terms from the multiple displacement field, an entire array of elements with different orders of kinematic refinement can be formed. The variable kinematic finite elements can be conveniently connected together in a single domain for global-local analyses, where the local regions are modeled with refined kinematic elements. In the finite element mesh superposition technique an independent overlay mesh is superimposed on a global mesh to provide localized refinement for regions of interest regardless of the original global mesh topology. Integration of these two ideas yields a very robust and economical computational tool for global-local analysis to determine three-dimensional effects e.g. stresses within localized regions of interest in practical laminated composite structures.

1 INTRODUCTION

Numerous laminate theories have been proposed to date to describe the kinematics and stress states of composite laminates. Most of these theories are extensions of the conventional, single-layer plate theories, which are based on assumed variation of either stresses or displacements through the plate thickness:

$$\phi_i(x, y, z, t) = \phi_i^0(x, y, t) + z\phi_i^1(x, y, t)$$
$$+ z^2\phi_i^2(x, y, t) + \dots$$
$$= \sum_{j=0}^{N} z^j \phi_i^j(x, y, t) \qquad (1)$$

where $\phi_i(x, y, z, t)$ denotes either a stress or a displacement component in the plate, (x, y) are the inplane coordinates, z is the thickness coordinate, t denotes time, and ϕ_i^j, $(j = 0, 1, 2, \dots, N)$ are functions of x, y, and t. The series in eqn (1) can be terminated at a desired degree of the thickness coordinate, i.e. select the value of N ($N = 1$, 2, and so on). The spirit of these theories is to reduce a three-dimensional problem to a two-dimensional one; see Refs 1–13 for pioneering works in the field. A review of refined theories of plates can be found in an article by Noor and Burton[14] and the author.[15]

The governing equations of motion associated with the assumed displacement or stress field can be obtained using an appropriate principle of virtual work.[16] For example, when ϕ_i, $i = 1, 2, 3$ is a displacement component, the dynamic version of the principle of virtual displacements is used to derive $3(N + 1)$ equations of motion, which are usually expressed in terms of stress resultants through the thickness:

$$R_i^j \equiv \int_{-h/2}^{h/2} (z)^j \sigma_i \, dz, \qquad j = 0, 1, 2, \dots, N \qquad (2)$$

where σ_i denotes the ith stress component $(i = 1, 2, \dots, 6)$.

$$\sigma_{xx} = \sigma_1, \ \sigma_{yy} = \sigma_2, \ \sigma_{zz} = \sigma_3, \ \sigma_{yz} = \sigma_4,$$
$$\sigma_{xz} = \sigma_5, \ \sigma_{xy} = \sigma_6 \qquad (3)$$

The stress components are assumed to be known in terms of the displacement functions ϕ_i^j through the strain–displacement relations and the stress–strain relations. When ϕ_i, $(i = 1, 2, \dots, 6)$ is a stress component, the dynamic version of the principle of virtual forces is used to derive $6(N + 1)$ equations of motion. Of course, mixed variational principles can be used to derive the governing equations associated with assumed independent expansions of displacements and

21

stresses. Stress-based theories[6-8] are seldom used in practice because of the difficulty in developing reliable finite element models. The displacement-based theories[11-13] have received the most attention from the computational mechanics community. In the rest of this paper only the displacement-based theories are discussed.

2 DISPLACEMENT-BASED SINGLE-LAYER THEORIES

The displacement-based theory of order 1 (i.e. $N = 1$) is derived using the displacement field:

$$u_1(x, y, z, t) = u_1^0(x, y, t) + z\phi_1(x, y, t)$$

$$u_2(x, y, z, t) = u_2^0(x, y, t) + z\phi_2(x, y, t)$$

$$u_3(x, y, z, t) = u_3^0(x, y, t) + z\phi_3(x, y, t) \qquad (4)$$

where u_i is the displacement component along the x-coordinate direction ($x_1 = x$, $x_2 = y$, $x_3 = z$). The displacement field in eqn (4) implies that straight lines normal to the $x - y$ plane before deformation remain straight after deformation. Comparing eqns 1 and 4, we have the following:

$$\phi_i^0 = u_i^0, \qquad \phi_i^1 = \phi_i, \qquad (i = 1, 2, 3) \qquad (5)$$

It is clear from the displacement field in eqn (4) that u, v, w are the displacements of a point on the $z = 0$ plane in the three coordinate directions:

$$u_i^0 = u_i(x, y, z, t)|_{z=0} \qquad (6a)$$

Also, we note that

$$\phi_i = \left[\frac{\partial u_i}{\partial z}\right]_{z=0} \qquad (6b)$$

Geometrically, ϕ_1 and $-\phi_2$ denote rotations about the y and x axes, respectively, and ϕ_3 denotes the elongation of a transverse normal at the point (x, y). There will be six equations of motion in the six generalized displacements (u_i^0, ϕ_i). The most commonly used *first-order plate theory*,[16,17] is based on the displacement field of eqn (4) with $\phi_3 = 0$ (i.e. transverse normals are inextensible); the number of equations of motion reduce to five in terms of $(u_1^0, u_2^0, u_3^0, \phi_1, \phi_2)$. Since the transverse shear strains are constant through the thickness, the transverse stresses would also be constant through the thickness — a contradiction with the elasticity solution. This discrepancy is remedied in the energy sense by introducing the *shear correction factors*.

The *classical plate theory* is also based on the displacement field in eqn (4), but with the additional assumption concerning the slopes ϕ_1 and ϕ_2:

$$\phi_1 = -\frac{\partial u_3^0}{\partial x}, \qquad \phi_2 = -\frac{\partial u_3^0}{\partial y} \qquad (7)$$

i.e. transverse normals before deformation remain normal to the deformed surface at $z = 0$. In summary, the classical plate theory is based on the hypothesis, known as the *Love–Kirchhoff hypothesis*, that straight lines normal to the $x - y$ plane before deformation, (i) remain straight, (ii) inextensible, and (iii) normal to the $z = 0$ plane after deformation. The classical plate theory is governed by three equations of motion in terms of u_1^0, u_2^0, u_3^0.

The second-order[18,19] and third-order theories[20-30] introduce additional unknowns that are difficult to interpret in physical terms. All theories in which the normality condition in eqn (7) is not invoked account for transverse shear and normal strains. If inextensibility of transverse normals is assumed, the transverse normal strain becomes zero. For example, the *third-order theory of Reddy*[27,28] is based on the displacement field,[20-26]

$$u_1(x, y, z, t) = u_1^0(x, y, t) + z\phi_1(x, y, t)$$
$$+ z^3\left(-\frac{4}{3h^2}\right)\left[\phi_1(x, y, t) + \frac{\partial u_3^0}{\partial x}\right]$$

$$u_2(x, y, z, t) = u_2^0(x, y, t) + z\phi_2(x, y, t)$$
$$+ z^3\left(-\frac{4}{3h^2}\right)\left[\phi_2(x, y, t) + \frac{\partial u_3^0}{\partial y}\right]$$

$$u_3(x, y, z, t) = u_3^0(x, y, t) \qquad (8)$$

The displacement field accommodates quadratic variation of transverse shear strains (and hence stresses) and vanishing of transverse shear stresses on the top and bottom of a general laminate composed of orthotropic layers. Thus, there is no need to use shear correction factors in a third-order theory. The theory was generalized in Ref. 31.

Theories higher than third order are not used because the accuracy gained is so little that the effort required to solve the equations is not justified. In all conventional displacement-based

theories, one single expansion for each displacement component is used through the entire thickness, and therefore, the transverse strains are continuous through the thickness — a strain state appropriate for homogeneous plates.

3 EQUIVALENT-SINGLE-LAYER LAMINATE THEORIES

Extension of the single-layer theories of homogeneous plates to laminated composite plates is straightforward.[16,17,20-42] The only difference is in accounting for the varying layer thicknesses and material properties in the evaluation of the integrals in eqn (2). In carrying out the integration it is tacitly assumed that the layers are perfectly bonded. For laminated composite plates, this amounts to replacing the heterogeneous laminate with a statically equivalent (in the integral sense) single layer whose stiffnesses are a weighted average of the layer stiffnesses through the thickness. Therefore, such laminate theories are termed *equivalent single layer* (ESL) theories.

For many applications, the ESL theories provide a sufficiently accurate description of the global laminate response (e.g. transverse deflection, fundamental vibration frequency, critical buckling load, force and moment resultants). The main advantages of the ESL models are their inherent simplicity and low computational cost due to the relatively small number of dependent variables that must be solved for. However, the ESL models are often inadequate for determining the three-dimensional stress field at the ply level. The major deficiency of the ESL models in modeling composite laminates is that the transverse strain components are continuous across interfaces between dissimilar materials; thus, the transverse stress components (ε_{13}, ε_{23}, ε_{33}) are discontinuous at the layer interfaces. To see this, consider the linear strain-displacement relations for the first-order shear deformation laminated plate theory.[16,17]

$$\varepsilon_i = \varepsilon_i^0 + z\varepsilon_i^1 \quad (i = 1, 2, 6, 4, 5) \tag{9a}$$

where

$$\varepsilon_1^0 = \frac{\partial u_1^0}{\partial x}, \quad \varepsilon_1^1 = \frac{\partial \phi_1}{\partial x}$$

$$\varepsilon_2^0 = \frac{\partial u_2^0}{\partial y}, \quad \varepsilon_2^1 = \frac{\partial \phi_2}{\partial y}$$

$$\varepsilon_6^0 = \frac{\partial u_1^0}{\partial y} + \frac{\partial u_2^0}{\partial x}, \quad \varepsilon_6^1 = \frac{\partial \phi_1}{\partial y} + \frac{\partial \phi_2}{\partial x}$$

$$\varepsilon_3^0 = 0, \quad \varepsilon_3^1 = 0 \quad \varepsilon_4^0 = \frac{\partial u_3^0}{\partial y} + \phi_2, \quad \varepsilon_4^1 = 0$$

$$\varepsilon_5^0 = \frac{\partial u_3^0}{\partial x} + \phi_1, \quad \varepsilon_5^1 = 0 \tag{9b}$$

We note from eqn (9a) that the strains vary linearly through the laminate thickness, and they are independent of the lamination scheme as noted earlier. For a fixed value of z, the strains vary only with respect to the x and y coordinates. The transverse stresses according to the stress–strain relations of the kth lamina are given by

$$\begin{Bmatrix} \sigma_4 \\ \sigma_5 \end{Bmatrix}^k = \begin{bmatrix} Q_{44} & Q_{45} \\ Q_{45} & Q_{55} \end{bmatrix}^k \begin{Bmatrix} \varepsilon_4 \\ \varepsilon_5 \end{Bmatrix}^k \tag{10a}$$

or

$$\{\sigma\}^k = [Q]^k \{\varepsilon\}^k \tag{10b}$$

where

$$\varepsilon_3 = \varepsilon_{33}, \quad \varepsilon_4 = 2\varepsilon_{23}, \quad \varepsilon_5 = 2\varepsilon_{13} \tag{11}$$

and $[Q]^k$ represents the matrix of material stiffnesses of the kth layer referred to the global coordinates of the laminate. Thus, the stresses at the interface of the kth and $(k+1)$st layer, called *interlaminar stresses*, are not continuous because $[Q]^k \neq [Q]^{k+1}$ and $\{\varepsilon\}^k = \{\varepsilon\}^{k+1}$. This deficiency is most evident in relatively thick laminates, in localized regions of complex loading, or near geometric and material discontinuities.

While the inplane stresses (σ_{xx}, σ_{yy}, σ_{xy}) can be computed only through stress–strain relations, the transverse stresses (σ_{xz}, σ_{yz}, σ_{zz}) can be computed through either the constitutive equations or the equilibrium equations of three-dimensional elasticity. As shown above, the constitutive equations give discontinuous interlaminar stresses. Alternatively, the equations of stress equilibrium

$$\frac{\partial \sigma_{xx}}{\partial x} + \frac{\partial \sigma_{xy}}{\partial y} + \frac{\partial \sigma_{xz}}{\partial z} = 0 \tag{12a}$$

$$\frac{\partial \sigma_{xy}}{\partial x} + \frac{\partial \sigma_{yy}}{\partial y} + \frac{\partial \sigma_{yz}}{\partial z} = 0 \tag{12b}$$

$$\frac{\partial \sigma_{xz}}{\partial x} + \frac{\partial \sigma_{yz}}{\partial y} + \frac{\partial \sigma_{zz}}{\partial z} = 0 \tag{12c}$$

can be used to compute the interlaminar stresses, when the inplane stresses $(\sigma_{xx}, \sigma_{yy}, \sigma_{xy})$ are known. Integration of eqns (12a,b) with respect to z gives $(\sigma_{xz}, \sigma_{yz})$, which then can be used in eqn (12c) to determine σ_{zz}. It is found that even this approach gives inaccurate, but continuous, stress fields at the layer interfaces for thick composites. This inaccuracy is attributed to inaccurate representation of the inplane stress components in ESL theories.

Fig. 1. Schematic of a laminate and layerwise discretization

4 LAYERWISE LAMINATE THEORIES

Unlike the ESL theories, the layerwise theories assume separate displacement field expansions within each material layer, thus providing a kinematically correct representation of the strain field in discrete layer laminates, and allowing accurate determination of ply level stresses. Numerous displacement-based, layerwise laminate theories have appeared in the literature.[33-50] In most of these layerwise theories, displacement continuity across layer interfaces is enforced via constraint equations that allow some of the dependent variables to be eliminated during the model development. However, in the layerwise theory of Reddy,[45-50] the transverse variation of the displacement field is defined in terms of a one-dimensional, Lagrangian, finite element representation that automatically enforces C^0 continuity of the displacement components through the thickness, resulting in transverse strains that are layerwise continuous through the thickness. The variation of the displacements through the thickness can be represented to any desired level of accuracy by simply increasing the number of one-dimensional finite elements (i.e. numerical layers) or increasing the order of the transverse interpolation polynomials. Thus, the layerwise theory of Reddy provides a generalization of the layerwise displacement field concept.

The layerwise theory of Reddy is based on the following displacement expansion through the laminate thickness. The ith displacement component is expressed as (see Fig. 1),

$$u_i(x, y, z, t) = \sum_{I=1}^{N} U_i^I(x, y, t)\Phi_I(z) \qquad (13)$$

where ($i = 1, 2, 3$). N is the number of subdivisions (e.g. finite-element discretization) through the thickness of the laminate, and Φ_I are known functions of the thickness coordinate, z. The resulting
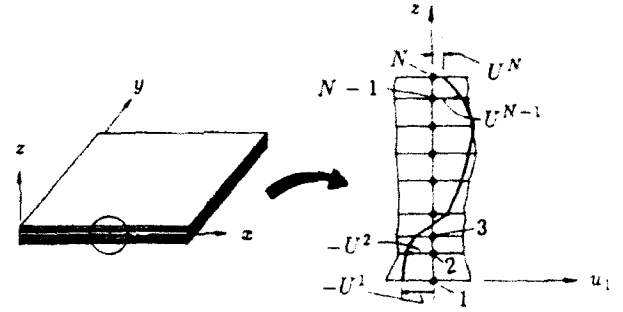
theory will have $3N$ variables and as many differential equations in two dimensions. An advantage of this layerwise theory is that it requires only two-dimensional finite elements while incorporating the kinematics of three-dimensional elasticity.

While the same interpolation functions are used in eqn (13) for all three displacements for simplicity, independent interpolation of the displacements (especially u_3) can be used. The functions Φ_I are piecewise continuous functions, defined only on two adjacent layers, and can be viewed as the global Lagrange interpolation functions associated with the Ith interface of the layers through the laminate thickness, and U_i^I denotes the nodal values of u_i at the nodes through the thickness. Because of this local nature of Φ_I, the displacements are continuous through the thickness but their derivatives with respect to z are not continuous. This implies that the transverse strains can be discontinuous at a point P on the discrete layer interfaces, $(\varepsilon_{ip}^k \neq \varepsilon_{ip}^{k-1})$, leaving the possibility that the interlaminar stresses computed from the layer constitutive equations at the point from the two layers can be continuous:

$$[Q]^k \{\varepsilon\}_P^k = [Q]^{k-1} \{\varepsilon\}_P^{k-1}$$

The inplane strains ε_i will be continuous and therefore the inplane stresses σ_i will be discontinuous at layer interfaces, as they should, because of the difference in material properties of adjacent layers.

The choice of N in eqn (13) provides the analyst with many options and flexibility in modeling. When N is chosen such that at least one element per layer is used, the interlaminar stress distributions can be determined accurately. The sublaminate concept can be used to model several identical layers of the laminate as one equivalent layer by choosing one element through the layers.

On the other hand, a layer can be modeled with more than one element to represent matrix splits or to capture local effects. In addition, the layer-wise theory of Reddy can be used to model imbedded delaminations between layers[51] and study their growth.

The linear strain–displacement relations associated with the layerwise displacement field of eqn (13) are

$$\varepsilon_{xx} = \frac{\partial U_1^I}{\partial x}\Phi_I, \quad \varepsilon_{yy} = \frac{\partial U_2^J}{\partial y}\Phi_J, \quad \varepsilon_{zz} = U_3^I\frac{d\Phi_J}{dz},$$

$$2\varepsilon_{xz} = U_2^I\frac{d\Phi_J}{dz} + \frac{\partial U_3^J}{\partial y}\Phi_I,$$

$$2\varepsilon_{xz} = U_1^I\frac{d\Phi_J}{dz} + \frac{\partial U_3^J}{\partial x}\Phi_I,$$

$$2\varepsilon_{xy} = \left(\frac{\partial U_1^I}{\partial y} + \frac{\partial U_2^J}{\partial x}\right)\Phi_J \qquad (14)$$

where summation on repeated indices is assumed.

The governing equations for the nodal variables (U_1^I, U_2^I, U_3^I) can be derived using the principle of virtual displacements. The equations of motion of the layerwise theory are

$$\frac{\partial M_{xx}^I}{\partial x} + \frac{\partial M_{xy}^I}{\partial y} - Q_x^I = M_{IJ}\ddot{U}_1^I,$$

$$\frac{\partial M_{xy}^I}{\partial x} + \frac{\partial M_{yy}^I}{\partial y} - Q_y^I = M_{IJ}\ddot{U}_2^I,$$

$$\frac{\partial K_{xx}^I}{\partial x} + \frac{\partial K_{yy}^I}{\partial y} - Q_z^I = M_{IJ}\ddot{U}_3^I \qquad (15)$$

for $I = 1, 2, \ldots, N$, where the resultants are defined by

$$(M_{xx}^I, M_{yy}^I, M_{xy}^I) = \int_{-h/2}^{h/2} (\sigma_{xx}, \sigma_{yy}, \sigma_{xy})\Phi_I(z)\,dz,$$

$$(Q_x^I, Q_y^I, Q_z^I) = \int_{-h/2}^{h/2} (\sigma_{xz}, \sigma_{yz}, \sigma_{zz})\frac{d\Phi_I}{dz}\,dz,$$

$$(K_{xx}^I, K_{yy}^I) = \int_{-h/2}^{h/2} (\sigma_{xz}, \sigma_{yz})\Phi_I\,dz,$$

$$M_{IJ} = \int_{-h/2}^{h/2} \rho\Phi_I\Phi_J\,dz \qquad (16)$$

where h is the total thickness of the laminate and ρ is the material density.

Fiber-reinforced composite laminates are constructed of orthotropic layers, with the material principal axes (x_1, x_2) of each layer oriented at an angle with respect to the global coordinate system (x, y) while the material principal coordinate x_3 of all layers coincide with the global z axis. In the layerwise theory, the stress–strain relations of three-dimensional elasticity are used. For a typical lamina, we have,[17]

$$\begin{Bmatrix} \sigma_{xx} \\ \sigma_{yy} \\ \sigma_{zz} \\ \sigma_{xz} \\ \sigma_{yz} \\ \sigma_{xy} \end{Bmatrix}^k =$$

$$\begin{bmatrix} C_{11} & C_{12} & C_{13} & 0 & 0 & C_{16} \\ & C_{22} & C_{23} & 0 & 0 & C_{26} \\ & & C_{33} & 0 & 0 & C_{36} \\ & & & C_{44} & C_{45} & 0 \\ & & & & C_{55} & 0 \\ \text{sym.} & & & & & C_{66} \end{bmatrix}^k \begin{Bmatrix} \varepsilon_{xx} \\ \varepsilon_{yy} \\ \varepsilon_{zz} \\ 2\varepsilon_{xz} \\ 2\varepsilon_{yz} \\ 2\varepsilon_{xy} \end{Bmatrix}^k \quad (17)$$

The stresses can be written in terms of the displacements by means of eqns (14) and (17), and the resultants in (16) can be written in terms of the displacements (U_I, V_I, W_I) by substituting for stresses into eqn (16). Thus, the governing differential equations can be ultimately written in terms of the displacements, (U_1^I, U_2^I, U_3^I) and their derivatives with respect to x and y.

5 VARIABLE KINETIC FINITE ELEMENTS

While layerwise finite elements allow accurate determination of three-dimensional stress fields, they are computationally expensive to use due to the large number of degrees of freedom per element, comparable to stacks of three-dimensional finite elements. Thus, it is often impractical to discretize an entire laminate with layerwise finite elements. Further, for many laminate applications, the indiscriminate use of layerwise elements is a waste of computational resources since significant three-dimensional stress states are usually present only in localized regions of complex loading or geometric and material discontinuities. A logical idea is to subdivide the laminate into regions that can be adequately described by ESL models and other regions that require some type of layerwise model (i.e. a simultaneous *global–local* strategy). In this way, the most appropriate model is chosen for each region, thereby increasing solution

economy without compromising solution accuracy. Such global–local schemes can be developed using established finite element technology;[52] however, currently available methods make implementation extremely cumbersome. The primary source of difficulty is the enforcement of displacement continuity across boundaries that separate incompatible subdomains. Currently established methods of achieving displacement continuity between incompatible regions include (i) multi-point constraint equations via Lagrange multipliers, (ii) penalty function methods, and (iii) special transition elements. Each of these methods is too cumbersome for extensive use under a wide variety of operating conditions. Thus, there is a need for the development of a global–local analysis procedure that provides greater robustness, simpler computer implementation, and wider applicability to practical composite structures.

To overcome the limitations of the current procedures used in the global–local finite element analysis, a variable displacement field concept was proposed by the author and his colleagues.[53-56] The variable displacement field is a sum of all admissible displacement fields, single layer as well as layerwise, so that appropriate part of the displacement field can be invoked in a given region of the domain. The finite elements based on different displacement fields can be connected together in a single domain for global–local analysis. To further reduce the computational effort the mesh superposition is employed. In the mesh superposition technique, an independent overlay mesh is superimposed on a global mesh to provide localized refinement for regions of interest regardless of the original global mesh topology. Integration of variable kinematic elements and mesh superposition technique yields a very robust, economical analysis for global–local analysis of practical laminated composite structures.

The variable kinematic, finite element is developed by superimposing several types of assumed displacement fields within the finite element domain. In general, the multiple assumed displacement field can be expressed as

$$u_i(x, y, z) = u_i^{\text{ESL}}(x, y, z) + u_i^{\text{LW}}(x, y, z),$$

$$(i = 1, 2, 3) \qquad (18)$$

where u_1 and u_2 are the local inplane displacement components and u_3 is the local transverse displacement component. The coordinates (x, y) represent the inplane coordinates and z is the transverse coordinate. The underlying foundation of the displacement field is provided by u_i^{ESL} which represents the assumed displacement field for any desired equivalent-single-layer theory (e.g. the first-order shear deformation theory). The second term u_i^{LW} represents the assumed displacement field for any desired layerwise theory (e.g. the layerwise theory of Reddy). The layerwise displacement field is included as an incremental enhancement to the basic ESL displacement field, so that the element can have full three-dimensional modeling capability when needed. Depending on the desired level of accuracy, the element can use all, part, or none of the layerwise field to create a series of different elements having a wide range of kinematic complexity. For example, discrete layer transverse shear effects can be added to the element by including u_1^{LW} and u_2^{LW}, resulting in a layerwise element, which we denote as the LW1 element. Further, discrete layer transverse normal effects can be added to the element by also including u_3^{LW}, resulting in another layerwise element which we denote as the LW2 element. Displacement continuity is maintained between these different types of elements by simply enforcing certain homogeneous essential boundary conditions (see Fig. 2), thus eliminating the need for multi-point constraints, penalty function methods, or special transition elements. Such variable kinematic plate elements have been developed by Robbins and Reddy[54-57] and show much potential for a wide variety of global–local analysis of composite plate problems.

6 MESH SUPERPOSITION TECHNIQUE

The use of hierarchical, variable kinematic, finite element concept provides a convenient means of
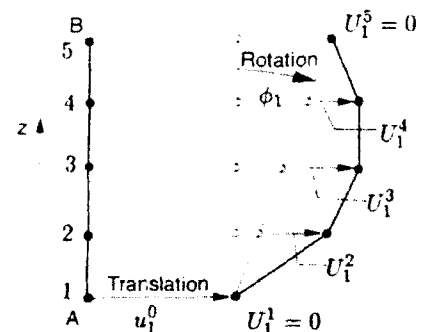
Fig. 2. Superposition of the first-order shear deformation theory displacement field and layerwise displacement field. Deformation of the transverse normal AB in the xz plane.

simultaneously discretizing subregions of a single computational domain with different theories. Thus, the analyst can use the most appropriate theory for each subregion of the domain. However, the efficiency of a global–local analysis based solely on variable kinematic elements is still strongly dependent on *a priori* knowledge of the locations of subregions that require the more powerful layerwise elements. This limitation is due to the requirement that the inplane discretizations of adjacent subregions must be compatible across subregion boundaries. The removal of this restriction would result in a very general, robust global–local computational model. In keeping with the hierarchical modeling philosophy of the previous section, the finite element mesh superposition technique (see, for example, the recent paper by Fish[58]) is chosen as the means to remove the strong dependence of initial mesh topology upon global–local solution efficiency.

The mesh superposition method is an adaptive refinement technique that creates refined areas within a chosen crude finite element mesh by superimposing independent, refined meshes (overlay meshes) on the original mesh. No changes are made to the original mesh during the superposition process. The mesh superposition method is adaptive in the sense that the size, shape and ultimate location of the overlay mesh is based on the solution provided by the original mesh alone. The overlay mesh and the original mesh need not have a compatible discretization; the overlay mesh can be used to provide enhanced interpolation capability precisely where it is most needed, regardless of the original mesh.

To illustrate the mesh superposition idea,[57] consider the two-dimensional, displacement-based, finite element model of an elastic solid shown in Fig. 3. The original coarse mesh occupies a region
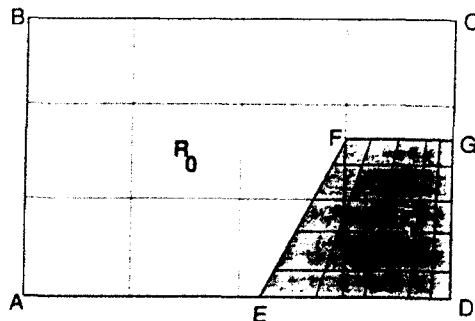
Fig. 3. Finite element mesh superposition showing a coarse 4×3 global mesh and an independent, refined, 5×5 overlay mesh (shaded).

R_0 with boundary S_0 (i.e. the rectangle ABCD). Assume that a solution obtained with the original 4×3 mesh indicates high displacement gradients in a subregion R_1 enclosed by boundary S_1 (i.e. the quadrilateral region EFGD). An independent overlay mesh is then constructed corresponding to the subregion R_1 and this overlay mesh is superimposed on the original mesh to form a composite mesh. The total displacement field **u** for the resulting composite mesh is then defined as follows:

$$\mathbf{u} = \mathbf{u}^0 + \mathbf{u}^1 \quad \text{in } R_1 \tag{19a}$$

and

$$\mathbf{u} = \mathbf{u}^0 \quad \text{in } R_0 - R_1 \tag{19b}$$

where **u** is the total displacement field, $\mathbf{u}^0$ is the displacement field interpolated on the original 4×3 mesh, and $\mathbf{u}^1$ is the additional displacement field interpolated on the 5×5 overlay mesh. Note that $\mathbf{u}^1$ serves as an incremental enhancement to the global solution within region R_1. A new solution is then computed based on the multiple displacement field, which permits an enhanced representation of the solution within subregion R_1. Note that the process of forming a composite mesh does not require altering the original mesh. An important consequence of the multiple displacement fields is that the original mesh and the overlay mesh need not have compatible discretizations along the boundary S_1, since C_0 continuity of the displacements across S_1 is imposed by prescribing homogeneous essential boundary conditions on the additional displacement field $\mathbf{u}^1$:

$$\mathbf{u}^1 = 0 \quad \text{on } S_1 \not\subset S_0 \tag{20}$$

(i.e. along EFG). Homogeneous essential boundary conditions on $\mathbf{u}^1$ are not required along the boundary $S_1 \in S_0$ (i.e. along EDG) unless EDG happens to be part of a Dirichlet boundary (i.e. boundary where the solution **u** is specified) for the problem as a whole. By circumventing the mesh compatibility requirement along S_1, a tremendous amount of flexibility is provided for the construction of the overlay mesh, and the adaptive refinement process can proceed in an optimal manner regardless of the original mesh topology.

The assembled finite element equations of the global–local analysis with mesh superposition technique are of the form,

$$\begin{bmatrix} [K_{11}] & [K_{12}] \\ [K_{21}] & [K_{22}] \end{bmatrix} \begin{Bmatrix} \{d_1\} \\ \{d_2\} \end{Bmatrix} = \begin{Bmatrix} \{F_1\} \\ \{F_2\} \end{Bmatrix} \tag{21}$$

where $[K_{11}]$ and $[K_{22}]$ represent the independent stiffness matrices for the global mesh and local overlay mesh respectively, the submatrices $[K_{12}]$ and $[K_{21}]$ represent the stiffness matrices associated with the coupling between the global and overlay meshes, and $\{d_1\}$ and $\{d_2\}$ denote the nodal degrees of freedom associated with the global and local meshes respectively. Thus, the process of creating a composite mesh by adding an overlay mesh to an original global mesh destroys the banded nature of the composite system of equations. This process is illustrated in Figs 4 and 5. In Fig. 4, one quadrant of a 2×2 global mesh is superposed by an independent 2×2 local mesh to form a composite mesh. The local elements can be different from the global elements, both in terms of the degree of interpolation as well as the theory (or mathematical model) on which they are based. In the composite stiffness matrix, Fig. 5 shows the composite stiffness matrix in terms of zero and nonzero entries for the composite mesh of Fig. 4. While both $[K_{11}]$ and $[K_{22}]$ retain the usual banded form, the presence of the coupling

stiffnesses ($[K_{12}]$ and $[K_{21}]$) destroys the banded nature of the composite stiffness matrix, thus a conventional direct banded equation solver is inefficient. Due to the incremental additive nature of the variables interpolated on the overlay mesh, $\{d_2\} = \{0\}$ provides a reasonable starting estimate for $\{d_2\}$. Thus, the following iterative method is used to solve the composite system of equations:

Step 1. Set $\{d_2\} = \{0\}$

Step 2. Solve $[K_{11}]\{d_1\} = \{F_1\} - [K_{12}]\{d_2\}$
for $\{d_1\}$

Step 3. Solve $[K_{22}]\{d_2\} = \{F_2\} - [K_{21}]\{d_1\}$
for $\{d_2\}$

Step 4. Repeat steps 2 and 3 until convergence is achieved.

7 NUMERICAL RESULTS

7.1 Accuracy of the layerwise theory

Numerical results are presented here to illustrate the accuracy of the layerwise theory. The numerical results were obtained using a displacement finite element model of the layerwise theory described above. The reader is referred to the paper by Robbins and Reddy[50] for a description of the finite element model and additional numerical results.

Consider a cross-ply laminate (0/90/0) subjected to sinusoidal transverse load at the top surface of the plate. This problem has the three-dimensional elasticity solution.[36] The plies are of equal thickness ($h/3$), and the material properties of each ply are

$$E_1 = 25 \text{ msi}, E_2 = 1 \text{ msi}, E_3 = E_2, G_{12} = 0.5 \text{ msi},$$

$$G_{13} = G_{23} = 0.2 \text{ msi}, \nu_{12} = \nu_{13} = \nu_{23} = 0.25 \quad (22)$$

The intensity of the sinusoidally distributed load is denoted q_0. Two different finite element meshes are used. The two meshes differ from each other only in the mesh refinements through the thickness. A 2×2 mesh of eight-node quadratic elements is used in a quadrant of the laminate. The mesh used through the thickness are as follows (see Fig. 6):

Mesh 1 — three quadratic elements through the thickness (441 dof).

Mesh 2 — six quadratic elements through the thickness (969 dof).

$$\begin{bmatrix} [K_{11}] & [K_{12}] \\ [K_{21}] & [K_{22}] \end{bmatrix} \begin{Bmatrix} \{d_1\} \\ \{d_2\} \end{Bmatrix} = \begin{Bmatrix} \{F_1\} \\ \{F_2\} \end{Bmatrix}$$
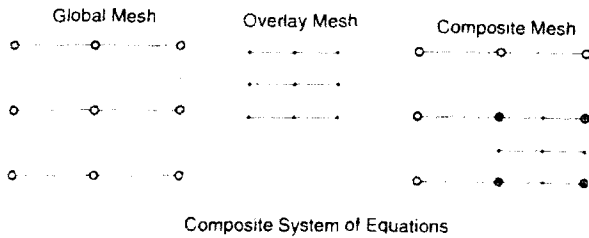
Fig. 4. Finite element mesh superposition showing the structure of the composite system of equations.
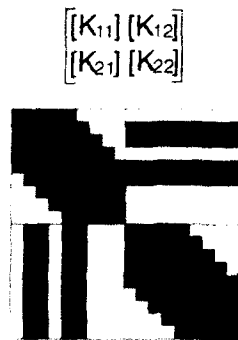
Fig. 5. Form of the stiffness matrix for the composite mesh. Nonzero entries are indicated by dark areas. Banded nature is lost due to extensive coupling between global and overlay meshes.
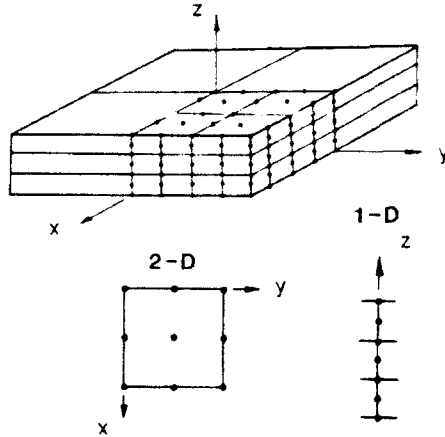
Fig. 6. Finite element meshes of layerwise elements used for a three-layer (0/90/0), simply-supported square laminate under sinusoidal transverse load. Mesh 1 is shown in the figure; mesh 2 differs only in doubling the number of layerwise elements through the thickness.
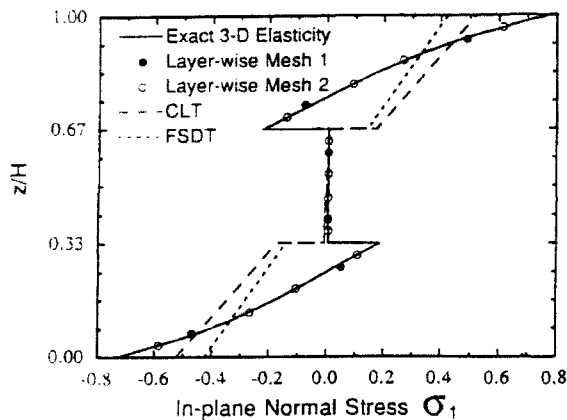
Fig. 7. Distribution of inplane normal stress σ_{xx} through the thickness of a three-layer (0/90/0), simply-supported square laminate under sinusoidal transverse load.
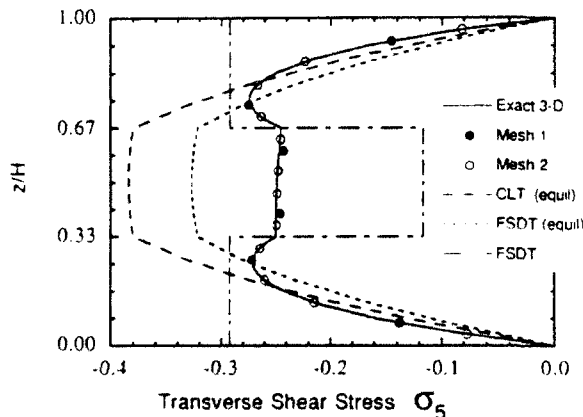
Fig. 8. Distribution of transverse shear stress σ_{xz} through the thickness of a three-layer (0/90/0), simply-supported square laminate under sinusoidal transverse load.

Figures 7 and 8 contain plots of nondimensional stresses $(\sigma_{xx}, \sigma_{xz})$ through the thickness of the square, thick, laminate $(b/h = 4)$. The stresses are nondimensionalized as follows:

$$\bar{\sigma}_{xx} = \sigma_{xx}(a_c, a_c, z)h^2/(b^2 q_0)$$

$$\bar{\sigma}_{xz} = \sigma_{xz}(b_c, a_c, z)h/(bq_0) \tag{23}$$

where $a_c = 0.105662(b/2)$, $b_c = 0.894338(b/2)$ are the (reduced order) Gauss points closest to the points of maximum stresses. The coordinate system is taken in the midplane of the laminate, with the origin of the coordinate system being at the center of the laminate. In Figs 6 and 7, the solid line represents the three-dimensional elasticity solution of Pagano,[36] the solid circles represent the finite element stresses at the Gauss points for mesh 1, the open circles represent the finite element solution at the Gauss points for mesh 2 (refined), and broken lines correspond to the classical and first-order theories. Excellent agreement is found between the three-dimensional elasticity results and the finite element results based on the layerwise laminate theory. The deflection $u_3^0(x, y)$ coincides with the exact three-dimensional elasticity solution and is not shown here.

All stresses in the layerwise theory were computed in the post-computation using the displacement field, linear strain–displacement relations, and linear constitutive relations. The inplane normal stress (σ_{xx}) in the classical laminate theory (CLT) and the first-order shear deformation (FSD) theory were post-computed at the Gauss points using the constitutive equations. The transverse shear stress σ_{xz} in the CLT was post-computed from the first two equilibrium equations of the three-dimensional elasticity, whereas they were post-computed in the FSD both from constitutive and three-dimensional elasticity equations.

From the plot of the inplane normal stress σ_{xx}, it is seen that both CLT and FSD predict wrong sign of the stress at the layer interfaces. This is due to the fact that the stress is approximated in the classical and first-order theories by a linear expansion. In trying to best approximate the nonlinear stress distribution by a linear variation, both CLT and FSDT yield wrong interface stress values. This can lead to inaccurate prediction of failure load and failure mode. The equilibrium-based stress σ_5 from the single-layer theories is in considerable error compared to the three-dimensional elasticity solution; in fact, they predict maximum value of σ_{xz} in the middle layer while

the three-dimensional elasticity gives in the outer layers. Note that the error introduced in the computation of the inplane stresses $(\sigma_{xx}, \sigma_{yy}, \sigma_{xy})$ through constitutive equations will influence the accuracy of the transverse stresses computed using the equilibrium equations. The transverse shear stress computed in the FSD by constitutive equations is in qualitative agreement with the three-dimensional elasticity results. For all stresses, the layerwise theory yields accurate results.

7.2 Global-local analysis with variable kinematic elements

To demonstrate the accuracy and efficiency of the variable kinematic finite elements, a global-local analysis is performed to determine the nature of the free edge stress field of the free edge effect in a thick, symmetric angle-ply laminate under imposed axial extension.[55] Consider a thick, symmetric, angle-ply laminate $(45/-45)_s$ subjected to axial displacements on the ends. The laminate has a length of $2L$, width $2W$, and thickness $4h$, with $L=10W$ and $W=8h$ (see Figs 9 and 10). Each of the four material layers is of equal thickness h, and is idealized as a homogeneous, orthotropic material with the following properties expressed in the material coordinate system:

$$E_L = 20 \times 10^6 \text{ psi}, \quad E_T = E_z = 2 \cdot 1 \times 10^6 \text{psi},$$

$$G_{LT} = G_{Lz} = 0 \cdot 85 \times 10^6 \text{ psi},$$

$$\mu_{LT} = \mu_{Lz} = \mu_{Tz} = 0 \cdot 21 \tag{24}$$

where subscript L denotes the direction parallel to the fibers, subscript T denotes the inplane direction perpendicular to the fibers, and subscript z denotes the out-of-plane direction. The origin of the global coordinate system coincides with the centroid of the three-dimensional composite laminate. The x-coordinate is taken along the length of the laminate; the y-coordinate is taken along the width of laminate; and the z-coordinate is taken through the thickness of the laminate. Since the laminate is symmetric about the xy-plane, only the upper half of the laminate is modeled. Thus the computational domain is defined by $(-L\leq x\leq L, \; -W\leq y\leq W, \; 0\leq z\leq 2h)$. The displacement boundary conditions for this problem are:

$$u_1(L, y, z) = u_0, \quad u_1(-L, y, z) = 0,$$

$$u_2(-L, 0, 0) = 0, \quad u_2(L, 0, 0) = 0,$$

$$u_3(x, y, 0) = 0 \tag{25}$$

The variable kinematic finite elements are used in a global-local analysis to determine interlaminar free edge stresses near the middle of one of the two free edges (see Figs 9 and 10). The global region is modeled using first order shear deformable elements; the local region is modeled with *LW2* elements in order to capture the three-dimensional stress state near the free edge. Five different finite element meshes are used. The inplane discretization for all five meshes is exactly the same, consisting of a 5×11 mesh of eight-node quadratic two-dimensional finite elements. All elements have the same length $(2L/5)$. However, the width of the elements decreases as the free edge at (x, W, z) is approached. The widths of the eleven rows of elements, as one moves away from the refined free edge are $h/16$, $h/16$, $h/8$, $h/4$, $h/2$, h, h, $2h$, $3h$, $3h$, $5h$, where h is the ply thickness. The five meshes differ only in the size of the local region that is discretized with *LW2* elements. The *LW2* elements used in the local region employ eight quadratic layers through the
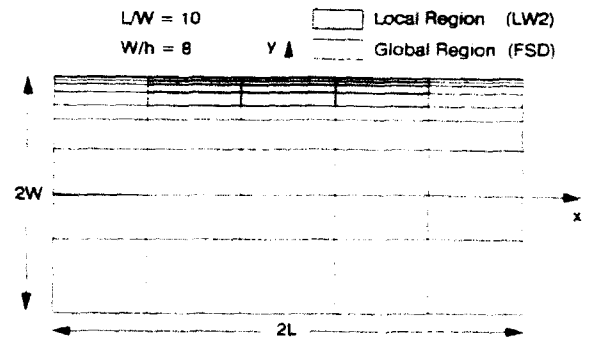
Fig. 9. Inplane discretization of a $(+45/-45)_s$ laminate under axial extension.
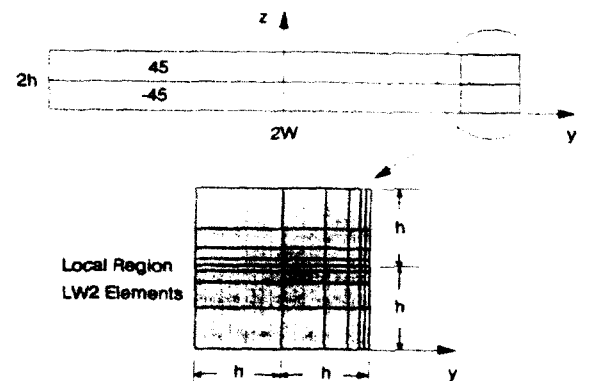
Fig. 10. Layerwise discretization of the local region (through the thickness) near the free edge of a $(+45/-45)_s$ laminate under axial extension.

laminate thickness (four per material layer). The thickness of the numerical layers decreases as the (+45/−45) interface is approached. From bottom to top, the layer thicknesses are $0.533h$, $0.267h$, $0.133h$, $0.083h$, $0.083h$, $0.133h$, $0.267h$, $0.533h$ (see Fig. 9).

The five meshes used in this problem are summarized below (see Table 1).

- *Mesh 1* — 3×4 local mesh of $LW2$ elements, centered about the point $(0, W, 0)$. The $LW2$ elements extend a distance of $h/2$ away from the free edge (2354 active global dof).

- *Mesh 2* — 3×5 local mesh of $LW2$ elements, centered about the point $(0, W, 0)$. The $LW2$ elements extend a distance of h away from the free edge (2740 active global dof).

- *Mesh 3* — 3×6 local mesh of $LW2$ elements, centered about the point $(0, W, 0)$. The $LW2$ elements extend a distance of $2h$ away from the free edge (3226 active global dof).

- *Mesh 4* — 3×7 local mesh of $LW2$ elements, centered about the point $(0, W, 0)$. The $LW2$ elements extend a distance of $3h$ away from the free edge (3512 active global dof).

- *Mesh 5* — 5×11 mesh of $LW2$ elements in the entire domain. This mesh is used as a control mesh for comparison (9116 active global dof).

Figures 11 and 12 show the distribution of the interlaminar stress σ_{xz} and σ_{zz} respectively, through the laminate thickness. All stresses are nondimensionalized by multiplying them by the factor $(20\epsilon_0/E_T)$, where ϵ_0 is the nominal applied axial strain of $(u_0/2L)$. The stresses are computed

at the reduced Gauss points nearest the middle of the refined free edge, i.e. along the line $(−0.115L, 0.998W, z)$. In Fig. 11, all four global–local meshes compare very well with the control mesh. In Fig. 12, meshes 1 and 2 show some error, indicating that σ_{zz} is more sensitive to the mesh and the boundary layer thickness is larger than that of σ_{xz}. Meshes 3 and 4 are practically indistinguishable from the control mesh.

Figures 13 and 14 show the distribution of the interlaminar stresses σ_{xz} and σ_{zz}, respectively, across the width of the laminate near the (+45/−45) interface. The stresses are computed at the reduced Gauss points closest to the line $(0, y, h)$, i.e. along the line $(−0.115L, y, 1.014h)$. In both Figs 13 and 14, the interlaminar stresses computed with meshes 3 and 4 are very close to the stresses obtained with the control mesh. Once again, the stresses computed with meshes 1 and 2 show a slight error; however, the distributions are qualitatively similar to the other meshes.
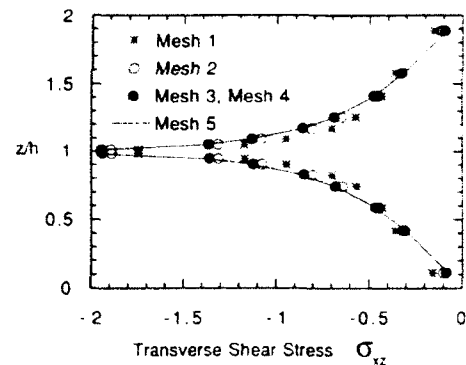
Fig. 11. Interlaminar shear stress σ_{xz} distribution near the free edge of a symmetric (+45/−45) laminate under axial extension.
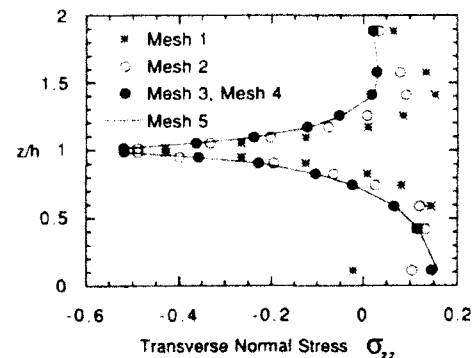
Fig. 12. Interlaminar normal stress σ_{zz} distribution near the free edge of a symmetric (+45/−45) laminate under axial extension.

Table 1. Global–local finite element meshes used in the study of the free edge problem*

	Number of elements in local region	Width of local region	Total active dof
Mesh 1	3×4	$h/2$	2354
Mesh 2	3×5	h	2740
Mesh 3	3×6	$2h$	3226
Mesh 4	3×7	$3h$	3512
Mesh 5	5×11	$16h$	9116

*The total inplane discretization for all five global–local meshes is 5×11.
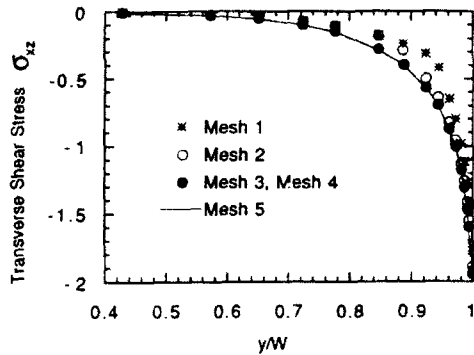
Fig. 13. Interlaminar shear stress σ_{xz} distribution across the width of a $(+45/-45)$ laminate under axial extension.

Fig. 15. Cylindrical bending of a cantilever plate with a surface bonded piezoelectric actuator strain induced in the actuator $= -10^{-3}$.

Piezoelectric thickness = 0.2 in . Actuation strain = 0.001
Adhesive thickness = 0.01 in

Fig. 14. Interlaminar normal stress $\sigma_{zz} = -0.115 L_1$, y, $1.014h$ distribution across the width of a $(+45/-45)$ laminate under axial extension.

Global Region. 8 FSD elements

Local Region. 13 LW2 elements
4 layers through piezoelectric
3 layers through adhesive
4 layers through aluminum
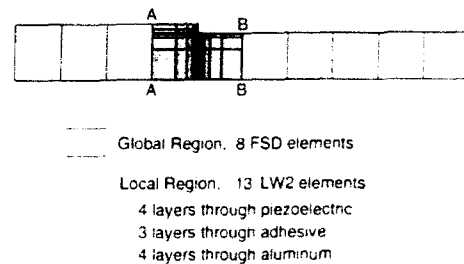
Fig. 16. Finite element mesh used to model the cylindrical bending of a cantilever plate with a surface bonded piezo-electric actuator. Variable kinematic elements are used to permit the simultaneous use of two different mathematical models (or theories).

7.3 Variable kinematic elements and mesh superposition

To illustrate the utility of combining the variable kinematic element concept with the mesh super-position technique, consider the cylindrical bending of a cantilever plate by a surface bonded piezoelectric actuator shown in Fig. 15. The objective of the analysis is to determine the transverse stresses in the thin adhesive layer near the end of the actuator. The local region of interest, where significant three-dimensional stresses are expected, is shown in Fig. 15. If this problem is to be solved by variable kinematic finite elements, in order to capture these local three-dimensional stresses while maintaining an overall economical solution, the majority of the plate should be discretized using FSD elements while the local region of interest be discretized using the $LW2$ elements (see Fig. 16).

Figure 17 shows the computed transverse stresses in the center of the adhesive layer verses

Fig. 17. Distribution of transverse stresses along the center of the adhesive layer near the free edge of the actuator, as determined using a mesh of variable kinematic finite elements.

y. Several points of interest should be noted. First, both of the transverse stresses approach zero as the global–local boundary AA is approached (i.e. as y decreases toward 3.0); this suggests that the size of the local region is sufficient to capture all

of the free edge stresses near the end of the actuator. Secondly, the transverse shear stress appears to satisfy the traction free boundary conditions at the free edge of the actuator and adhesive. Third, a significant transverse normal stress exists in the adhesive layer near the free edge of the actuator. This transverse normal stress is of particular concern since many adhesives are relatively weak in tension. It is also interesting to note that if this problem is solved using FSDT elements only, then both the transverse shear stress and transverse normal stress are predicted to be zero over the entire domain.

To illustrate the utility of combining the variable kinematic element concept with the mesh superposition technique, consider once again the example problem shown in Fig. 15. Figure 18 shows the global mesh, the local overlay mesh and the resulting composite mesh used to solve this problem. The global mesh is a coarse uniform mesh of ten FSD elements. To capture the local three-dimensional stress field in the adhesive layer near the end of the actuator, an independent local overlay mesh of 13 $LW2$ layerwise elements are used. The $LW2$ elements used to form the overlay mesh contain four layers through the aluminum substrate, three layers through the adhesive, and four layers through the piezoelectric actuator. The local overlay mesh is superimposed over the fourth and fifth global elements to achieve the composite mesh. The composite mesh shown in Fig. 18 has the exact same interpolating capability as the mesh shown in Fig. 16. Thus, it is not surprising that the solution obtained from the composite mesh of Fig. 18 is exactly the same as the previous solution obtained using variable kinematic elements only; therefore the results are not repeated here. The advantage of the present model over the previous model is that the same global mesh can be used in the investigation of many different local regions of interest. For each new local region of interest, an independent local overlay mesh of variable kinematic elements is formed and superimposed on the global mesh. Since the global and overlay meshes need not be compatible, the effectiveness of the global-local analysis is not strongly tied to the global mesh topology.

8 CONCLUSIONS

A review of the single-layer theories of composite laminates is presented, and the layerwise theory
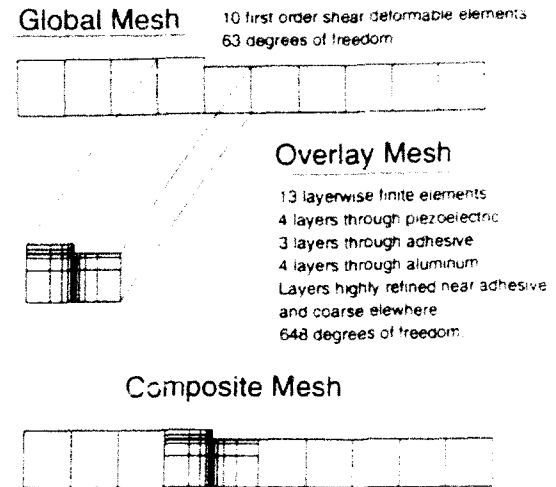
Fig. 18. Finite element mesh superposition showing the coarse global mesh of FSD elements, the independent overlay mesh of $LW2$ elements, and resulting composite mesh.

proposed by the author is described. A finite element modeling methodology is presented for the hierarchical, global-local analysis of laminated composite plates. The method incorporates a new variable kinematic, displacement-based, finite element that is based on a multiple assumed displacement field approach. The variable kinematic elements provide a great degree of flexibility in defining the transverse through thickness variation of the assumed displacement field. The resulting finite element model permits different subregions of the computational domain to be described by different mathematical models. Enforcing displacement continuity along subregion boundaries requires only the specification of certain homogeneous essential boundary conditions, thus avoiding multi-point constraints, penalty function methods, or special transition elements.

To increase the utility of the variable finite elements, an integration of the variable kinematic element concept with the finite element mesh superposition technique is developed. The resulting global-local model permits selected local subregions in a composite plate to be conveniently discretized with an independent refined overlay mesh composed of FSDT, $LW1$, and/or $LW2$ elements. Due to the independent nature of the local overlay mesh, the present integrated method allows several different local regions of interest to be accurately and conveniently investigated regardless of the original global mesh topology. The computational procedure described

herein offers greater flexibility in modeling and it can be used in a variety of applications.

ACKNOWLEDGEMENT

REFERENCES

1. Cauchy, A. L., Sur l'equilibre et le mouvement d'une plaque solide. *Exercises de Mathematique*, **3** (1828) 328–55.

2. Poisson, S. D., Memoire sur l'equilibre et le mouvement des corps elastique. *Mem. Acad. Sci.*, **8** (1829) 357.

3. Kirchhoff, G., Uber das Gleichgwich und die Bewegung einer Elastischen Scheibe, *J. Angew. Math.*, **40** (1850) 51–88.

4. Basset, A. B., On the extension and flexure of cylindrical and spherical thin elastic shells. *Phil. Trans. Royal Soc.* London, Ser. A, **181** (6) (1890) 433–80.

5. Goodier, J. N., On the problem of the beam and the plate in the theory of elasticity. *Trans. Royal Soc. Canada*, **32** (1938) 65.

6. Reissner, E., On the theory of bending of elastic plates. *J. Math. Physics*, **23** (1944) 184–91.

7. Reissner, E., The effect of transverse shear deformation on the bending of elastic plates. *J. Appl. Mech.*, **12** (1945) 69–77.

8. Reissner, E., Reflections on the theory of elastic plates. *Appl. Mech. Rev.*, **38** (11) (1985) 1453–64.

9. Bollé, E., Contribution au probleme lineare de flexion d'une plaque elastique. *Bull. Tech. Suisse. Romande.*, **73** (1947) 281–5 and 293–8.

10. Hencky, H., Uber die Berucksichtigung der Schubverzerrung in ebenen Platten. *Ing.-Arch.*, **16** (1947) 72–766.

11. Hildebrand, F. B., Reissner E. & Thomas, G. B., *Notes on the Foundations of the Theory of Small Displacements of Orthotropic Shells.* NASA TN-1833. Washington, DC, USA, 1949.

12. Mindlin, R. D., Influence of rotatory inertia and shear on flexural motions of isotropic, elastic plates. *J. Appl. Mech., Trans. ASME*, **18** (1951) 31–8.

13. Vlasov, B. F., Ob uravneniyakh teovii isgiba plastinok (on the equations of the theory of bending of plates), *Izv. Akd. Nauk SSR*, OTN, **4** (1958) 102–9.

14. Noor, A. K. & Burton, W. S., Assessment of shear deformation theories for multilayered composite plates. *Appl. Mech. Rev.*, **42** (1) (1989) 1–13.

15. Reddy, J. N., A review of refined theories of laminated composite plates. *Shock & Vibration Digest*, **22** (7) (1990) 3–17.

16. Reddy, J. N., *Energy and Variational Methods in Applied Mechanics.* John Wiley and Sons, New York, USA, 1984.

17. Ochoa, O. O. & Reddy, J. N., *Finite Element Analysis of Composite Laminates.* Kluwer, Dordrecht, The Netherlands, 1992.

18. Lo, K. H., Christensen, R. M. & Wu, E. M., A higher-order theory plate deformation. Part 1: Homogeneous plates. *J. Appl. Mech., Trans. ASME*, **44** (4) (1977) 663–8.

19. Lo, K. H., Christensen, R. M. & Wu, E. M., A higher-order theory of plate deformation. Part 2: Laminated plates. *J. Appl. Mech.*, **44** (4) (1977) 669–76.

20. Librescu, L., *Elastostatics and Kinetics of Anisotropic and Heterogeneous Shell-type Structures.* Noordhoff, Leyden, Netherlands, 1975.

21. Jemeilita, G., Techniczna teoria plyt S'redniej Grubosci (Technical theory of plates with moderate thickness). *Rozprawy Inzynierskie (Engrg. Trans.), Polska Akad. Nauk*, **23** (3) (1975) 483–99.

22. Schmidt, R., A refined nonlinear theory of plates with transverse shear deformation. *J. Ind. Math. Soc.*, **27** (1) (1977) 23–38.

23. Krishna Murty, A. V., Higher order theory for vibration of thick plates. *AIAA J.*, **15** (12) (1977) 1823–4.

24. Levinson, M., An accurate, simple theory of the statics and dynamics of elastic plates. *Mech. Res. Comm.*, **7** (6) (1980) 343–50.

25. Seide, P., An improved approximate theory for the bending of laminated plates. *Mech. Today*, **5** (1980) 451–66.

26. Murthy, M. V. V., An improved transverse shear deformation theory for laminated anisotropic plates. *NASA Tech. Paper 1903*, 1981, pp. 1–37.

27. Reddy, J. N., A simple higher-order theory for laminated composite plates. *J. Appl. Mech.*, **51** (1984) 745–52.

28. Reddy, J. N., A refined nonlinear theory of plates with transverse shear deformation. *Int. J. Solids and Structures*, **20** (9/10) (1984) 881–96.

29. Bhimaraddi, A. & Stevens, L. K., A higher order theory for free vibration of orthotropic, homogeneous, and laminated rectangular plates. *J. Appl. Mech.*, **51** (1984) 195–8.

30. Di Sciuva, M., A refined transverse shear deformation theory for multilayered anisotropic plates. *Atti Accad Sci. Torino*, **118** (1984) 279–95.

31. Reddy, J. N., A general non-linear third-order theory of plates with transverse shear deformation. *J. Non-Linear Mech.*, **25** (6) (1990) 677–86.

32. Stavsky, Y., On the theory of symmetrically heterogeneous plates having the same thickness variation of the elastic moduli. In *Topics in Applied Mechanics*, E. Schwerin Memorial Volume. ed. D. Abir, F. Ollendorff & M. Reiner. Elsevier, New York, USA, 1965, pp. 105–66.

33. Yang, P. C., Norris, C. H. & Stavsky, Y., Elastic wave propagation in heterogeneous plates. *Int. J. Solids and Structures*, **2** (1966) 665–84.

34. Whitney, J. M., The effect of transverse shear deformaton in the bending of laminated plates. *J. Comp. Mater.*, **3** (1969) 534–47.

35. Whitney, J. M. & Pagano, N. J., Shear deformation in heterogeneous anisotropic plates. *J. Appl. Mech.*, **37** (4) (1970) 1031–6.

36. Pagano, N. J., Exact solutions for rectangular bidirectional composites and sandwich plates. *J. Comp. Mater.*, **4** (1970) 20–34.

37. Whitney, J. M., Shear correction factors for orthotropic laminates under static load. *J. Appl. Mech.*, **40** (1) (1973) 302–4.

38. Reissner, E., A consistent treatment of transverse shear deformations in laminated anisotropic plates. *AIAA J.*, **10** (5) (1972) 716–18.

39. Reissner, E., Note on the effect of transverse shear deformation in laminated anisotropic plates. *Comp. Meth. Appl. Mech. Engng.*, **20** (3) (1979) 203–9.

40. Librescu, L. & Reddy, J. N., A critical review and generalization of transverse shear deformable aniso-

tropic plates theories. In *Euromech Colloquium 219, Refined Dynamical Theories of Beams, Plates and Shells and their Applications.* ed. I. Elishakoff & H. Irretier. Springer-Verlag, Berlin, Germany, 1987, pp. 32-43.

41. Di Sciuva, M., Bending, vibration and buckling of simply supported thick multilayered orthotropic plates: an evaluation of a new displacement model. *J. Sound & Vibration,* **105** (3)(1986) 425-42.

42. Di Sciuva, M., An improved shear deformation theory for moderately thick multilayered anisotropic shells and plates. *J. Appl. Mech.,* **54** (3)(1987) 589-96.

43. Sreenivas, S., A refined analysis of composite laminates. *J. Sound & Vibration,* **30** (4)(1973) 495-507.

44. Mau, S. T., A refined laminated plate theory. *J. Appl. Mech.,* **40** (2)(1973) 606-7.

45. Epstein, M. & Glockner, P. G., Nonlinear analysis of multilayered shells, *Int. J. Solids and Structures,* **13** (1977) 1081-9.

46. Murakami, H., Laminated composite plate theory with improved in-plane responses. *J. Appl. Mech.,* **53** (3) (1986) 661-6.

47. Hinrichsen, R. L. & Palazotto, A. N., Nonlinear finite element analysis of thick composite plates using cubic spline functions. *AIAA J.,* **24** (11)(1986) 1836-42.

48. Reddy, J. N., A generalization of two-dimensional theories of laminated composite plates. *Comm. Appl. Numerical Methods,* **3** (1987) 173-80.

49. Reddy, J. N., On the generalization of displacement-based laminate theories. *Appl. Mech. Rev.,* **42** (11) (2) (1989) S213-22.

50. Robbins, D. H. & Reddy, J. N., On the modeling of free-edge stress fields and delaminations in thick composite laminates. In *Composites Structures for Aerospace Applications,* ed. J. N. Reddy & A. V. Krishna Murty. Narosa Publishing House, New Delhi, India, 1992, pp. 33-74.

51. Barbero, E. J. & Reddy, J. N., Modeling of delamination in composite laminates using a layer-wise plate theory. *Int. J. Solids and Structures,* **28** (3)(1991) 373-88.

52. Reddy, J. N., On computational schemes for global-local stress analysis. *Workshop on Computational Methods for Structural Mechanics and Dynamics,* NASA Langley Research Center. Hampton, VA, USA, 1985, pp. 29-31.

53. Robbins, D. H. & Reddy, J. N., Modeling of thick composites using a layerwise laminate theory. *Int. J. Numerical Methods Engng,* **36** (1993) 655-77.

54. Robbins, D. H. & Reddy, J. N., Global/local analysis of laminated composite plates using variable kinematic finite elements. Paper presented at AIAA/ASME/ASCE/AHS/ASC 33rd Structures, Structural Dynamics, and Materials (SDM) Conference. Dallas, TX, USA, 13-15 April 1992.

55. Reddy, J. N., Robbins, D. H. & Reddy, Y. S. N., Analysis of interlaminar stresses and failures using a layer-wise laminate theory. *Local Mechanics Concepts for Composite Material Systems,* ed. J. N. Reddy & K. L. Reifsnider. Springer-Verlag, New York, USA, 1992, pp. 307-39.

56. Reddy, J. N. & Robbins, D. H., Analysis of composite laminates using variable kinematic finite elements. In *Proceedings of the 7th Brazilian Symposium on Piping and Pressure Vessels (SIBRAT),* ed. C. A. C. Selke & C. S. Baecellos. University of Santa Catarina, Florianopolis, Brazil, 1992, pp. 47-68.

57. Robbins, D. H. & Reddy, J. N., Modeling of actuators in laminated composite structures. Paper presented at the North American Conference on Smart Structures and Materials, Albuquerque, NM, USA, 31 Jan.-3 Feb. 1993.

58. Fish, J., The s-version of the finite element method. *Computers and Structures,* **43** (3)(1992) 539-47.

The influence of trigger configurations and laminate lay-up on the failure mode of composite crush cylinders

H. G. S. J. Thuis & V. H. Metz

National Aerospace Laboratory, Voorsterveg 31, 8316 PR Marknesse, The Netherlands

In this paper the results are presented of a test program on the energy absorption of composite cylinders loaded in compression. The influence of the laminate lay-up and of the trigger configuration were determined. Two different failure modes for the different laminates and triggers were observed: a splaying mode and a fragmentation mode. The splaying mode is more efficient in absorbing energy. The failure mode did not change during the crushing process.

1 INTRODUCTION

The increasing importance of improved safety and crashworthiness in aerospace and automotive vehicles leads to additional design requirements. To meet these new design requirements without severe weight penalties designers are searching for new materials and structural concepts which can absorb a large amount of crush energy.[1] Composite materials have a large potential in absorbing crush energy. Unlike metals, which absorb energy by plastic deformation, composites absorb crush energy by multiple microfracture of the fibres.[2,3]

In order to establish a large amount of energy absorption in composites it is important to:

(1) Trigger the failure of the structure. When the failure of the structure is not triggered, a peak load occurs before crushing is established (see Fig. 1) and an undesirable failure mode may be generated which has a negative effect on the energy absorption. Furthermore a high peak load leads to high acceleration levels which are undesirable in the case of a crash, whereas the peak load is only a small contribution to the total amount of absorbed energy.

(2) Create a stable crush zone that will propagate through the material, because this will assure a process of continuous high energy absorption. The occurrence of such a stable crush zone must be achieved by the right choice of laminate lay-up and trigger configuration.

In an experimental study, performed at the NLR,[4] the influence of different trigger mechanisms and laminate lay-ups on the crush characteristics of composite sine-wave beams was investigated. The fabrication of the sine-wave beams is cumbersome, however, and not suitable for studying the influence of the different trigger configurations and laminate lay-ups. Hence, in this study the crush characteristics were evaluated by testing cylinders loaded in compression.

The test program on the cylinders was conducted in two phases. In the first phase the influence of different laminate lay-ups and trigger configurations on the energy absorption of the composite cylinders was determined. In the second phase the different failure modes introduced two different trigger configurations which were investigated. In this second test program the crush zones were analysed in detail.

2 TEST SPECIMENS AND MATERIALS

The specimens were composite cylinders with a inner diameter of 42·2 mm, a length of 100 mm and a wall thickness of 1·2 mm or 1·26 mm (depending on the laminate used).

The specimens were composed of a combination of hybrid carbon/aramid fabric at the outside

of the laminate, and unidirectional carbon layers on the inside of the laminate. The materials used and their mechanical properties are listed in Table 1. The laminates used are listed in Table 2. These laminates were used also in the experimental program of Ref. 4. The aramid fibres in the laminates provide post-crush integrity which is desirable for materials in crashworthy structures.

3 FABRICATION OF THE SPECIMENS

The specimens were made by the trapped rubber moulding technique. The inner part of the mould consisted of the TYGAVAC moulding rubber RTV 60. The outer part of the mould consisted of two steel form blocks and two steel caul plates which could be bolted together (see Fig. 2). The specimens were made of prepreg layers. The prepreg layers were laminated with an overlap (see Fig. 3) to prevent a zone of pure resin. The laminate was rolled around the inner mould. This package was placed in the steel mould and the mould was closed. The closed mould was put into an oven and heated to 120°C at which curing of the laminate took place. After curing the cylinder ends were sandpapered flat and parallel.
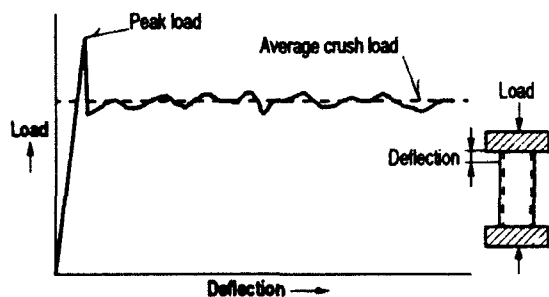
Fig. 1. Typical load–deflection curve of a cylinder loaded in compression.

4 TRIGGER CONFIGURATIONS

In this program five different trigger configurations were examined (see Fig. 4):

Inplane triggers:
(1) Shortening of the three unidirectional carbon layers, located in the centre of the laminate, by 0, 2 and 4 mm respectively.
(2) Shortening of the middle layer of the unidirectional carbon layers by 10 mm.
(3) Removing squares of 5 mm × 5 mm from the unidirectional carbon layers.
(4) Shortening of the unidirectional carbon layers by 10 mm and filling the gap with unidirectional carbon layers at 90°.

Out-of-plane trigger:
(5) Adding a flange to one end of the cylinder. A radius of 5 mm is applied as shown in Figs 2 and 4. This trigger simulates the web–flange connection in a sine-wave beam.

5 TEST PROGRAM

5.1 Test matrix and test set-up for the first test phase

During the first test program the cylinders were loaded in compression between two flat plates using a 250 kN, mechanically driven test machine. The loads were applied under displacement control with a velocity of 50 mm/min. During the tests the applied load and the shortening of the cylinders were measured and plotted. The (specific) energy absorption of the specimens was determined. The failure modes of the specimens were photographed. Table 3 presents the different specimen configurations which were used in the

Table 1. Material properties

Code	Type	Material	Ply thickness (mm)	Specific mass (kg/m³)
TenCate CD-553/8475	Unidirectional tape	Carbon/epoxy prepreg	0·154	1500
TenCate CV-170-40-8475	Crowfoot weave fabric	(60/40) Carbon/aramid epoxy prepreg	0·20	1430

Table 2. Laminate composition

Laminate no.	Stacking sequence[a]	Thickness (mm)
1	[Fa$_{\pm 45}$, Fa$_{0/90}$, Fa$_{\pm 45}$]$_s$	1·20
2	[Fa$_{\pm 45}$, Fa$_{0/90}$, (UD$_0$)$_3$, Fa$_{0/90}$, Fa$_{\pm 45}$]	1·26
3	[Fa$_{\pm 45}$, Fa$_{\pm 45}$, (UD$_0$)$_3$, Fa$_{\pm 45}$, Fa$_{\pm 45}$]	1·26
4	[Fa$_{0/90}$, Fa$_{0/90}$, (UD$_0$)$_3$, Fa$_{0/90}$, Fa$_{0/90}$]	1·26

[a]Fa, fabric; Fa$_{x/y}$, fabric in the x/y direction; [ ]$_s$, symmetric; UD, unidirectional tape; UD$_x$, unidirectional tape in the x direction; (UD)$_n$, number of unidirectional tape layers; 0° direction, longitudinal direction of the cylinder; 90° direction, hoop direction of the cylinder.
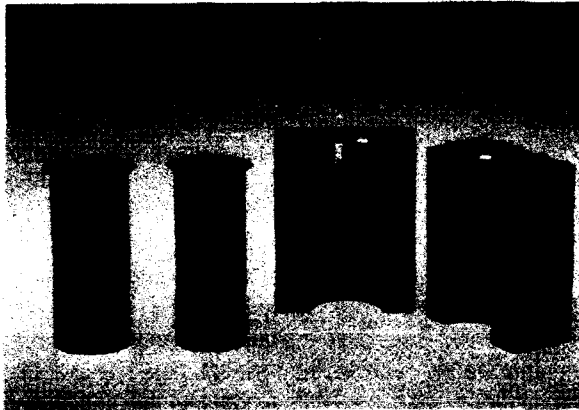
Fig. 2. Steel form blocks, rubber inner mould and specimen with trigger no. 5.
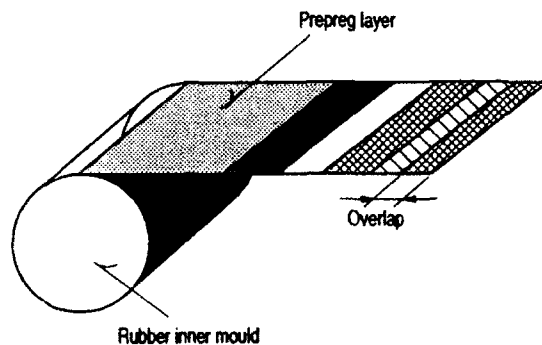
Fig. 3. Laminating the prepreg layers with an overlap on the inner rubber mould.

first test program. Of each configuration three specimens were tested.

5.2 Test matrix and test set-up for the second test program

During the second test program two different cylinder configurations were tested (see Table 3). The cylinders were tested on the same test machine as was used during the first test program.
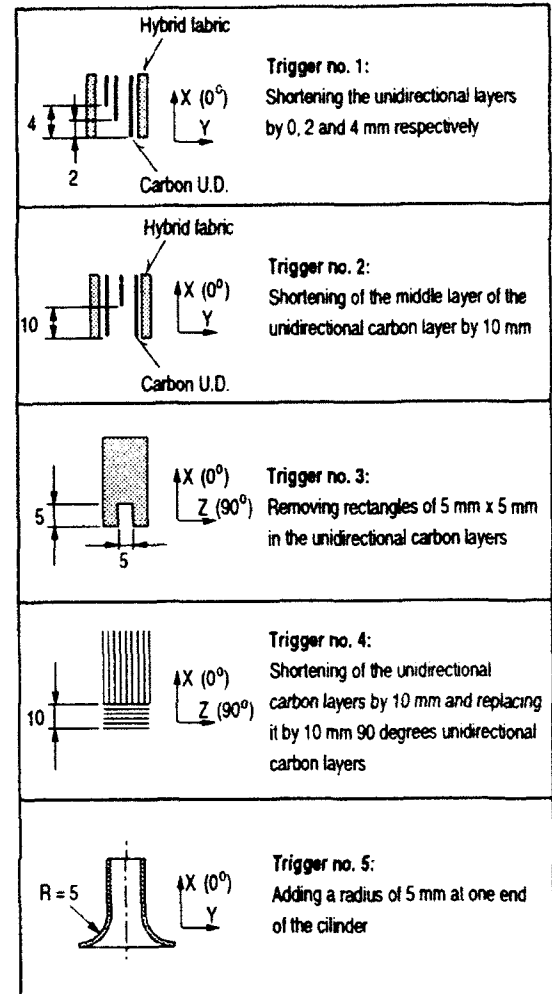
Fig. 4. Different trigger configurations.

The loads were applied under displacement control with a velocity of 5 mm/min. Of each configuration 10 specimens were tested. The specimens were crushed over increasing distances, ranging from 1 mm to 10 mm (the first specimen 1 mm, the second specimen 2 mm, the third specimen 3 mm and so on). After the specimens were crushed the crush zones were potted in a resin while the specimens remained under compression. After curing of the potting resin the cylinders were cut and the crush zones were analysed.

6 TEST RESULTS

6.1 Failure modes

According to Ref. 5 laminates can fail basically in two different modes (see Fig. 5): fragmentation of

Table 3. Test matrix
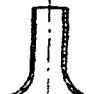
	No trigger	Trigger no. 1	Trigger no. 2	Trigger no. 3	Trigger no. 4	Trigger no. 5
Laminate no. 1	Prog. 1					
Laminate no. 2	Prog. 1	Prog. 1 and 2	Prog. 1	Prog. 1	Prog. 1	Prog. 1 and 2
Laminate no. 3	Prog. 1	Prog. 1	Prog. 1	Prog. 1	Prog. 1	Prog. 1
Laminate no. 4	Prog. 1	Prog. 1				

Fig. 5. Different failure modes, induced by different laminate compositions.

the laminate (cylinder on the left in Fig. 5) or splaying of the laminate (remaining cylinders on the right in Fig. 5).

6.1.1 Fragmentation failure mode

This failure mode occurred in specimens with laminate no. 1 with lay-up [$Fa_{\pm45}$, $Fa_{0/90}$, $Fa_{\pm45}$] (see Fig. 5 cylinder on the left). The crushed carbon fibres in the fabric fractured in many small pieces, whereas the aramid fibres show a lot of wrinkling. Because of the presence of the aramid fibres some post-crush integrity was accomplished.

6.1.2 Splaying failure mode

In the splaying mode the laminate is split by a wedge of debris which forces the laminate into two parts, one part folding outwards and one part folding inwards. The way the unidirectional fibres will bend depends on the way they are supported by the fabric layers. The more hoop fibres present in the fabric the better the unidirectional fibres are supported. This will lead to a decrease in bending radius of the unidirectional fibres during crushing. A small bending radius induces large bending stresses and an increase in the number of fractures in the unidirectional layers. This will lead to an increase in energy absorption. Three different possible splaying failure modes will be discussed, observed for three laminates. In the discussion the

test results of the specimens with trigger no. 1 were used.

6.1.2.1 Fracture behaviour of laminate no. 2: [$Fa_{\pm45}$, $Fa_{0/90}$, $(UD_0)_3$, $Fa_{0/90}$, $Fa_{\pm45}$] (see Fig. 6).

The fabric layers which are forced outwards have to stretch (increase in diameter). The fabric layer $Fa_{\pm45}$ can do this by increasing the orientation angle of the fibres. This leads to high interlaminar shear stresses and the fabric layer ($Fa_{\pm45}$) is separated from the rest of the laminate and pushed over the remaining cylinder like a sock (see Fig. 6). The fabric layer $Fa_{0/90}$ which is forced to bend outwards can only increase in diameter by fracturing the hoop fibres. Figure 5 shows that the fabric layer $Fa_{0/90}$ is not separated from the axial (splitted) unidirectional carbon layers. The crushed carbon fibres in the fabric fractured in many small pieces, whereas the aramid fibres show a lot of wrinkling.

6.1.2.2 Fracture behaviour of laminate no. 3: [$Fa_{\pm45}$, $Fa_{\pm45}$, $(UD_0)_3$, $Fa_{\pm45}$, $Fa_{\pm45}$] (see Fig. 7).

The fabric layers which bend inwards (decrease in diameter) showed a decrease in fibre angle orientation. The fabric layers which bend outwards (increase in diameter) showed an increase in fibre angle orientation. Figure 7 shows that the carbon fibres in the fabric fractured in many small pieces. A number of these fragments remain bonded to the unidirectional carbon fibres. The picture shows that the aramid fibres (light grey fibres in the photograph) are no longer interrupted by the carbon fibres (black fibres). Axial splits occur at a more frequently repeated interval than the axial splits in laminate no. 2. Because of the aramid fibres some post crush integrity was established.

6.1.2.3 Fracture behaviour of laminate no. 4: [$Fa_{0/90}$, $Fa_{0/90}$, $(UD_0)_3$, $Fa_{0/90}$, $Fa_{0/90}$] (see Fig. 8).

Figure 8 shows that the fabric layers which are
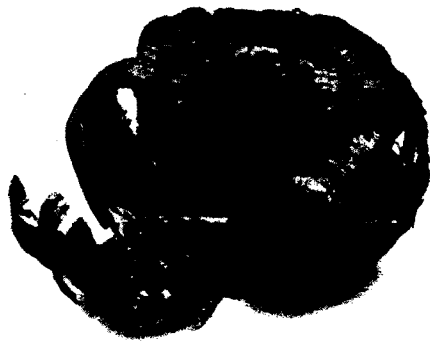
Fig. 6. Fracture mode in cylinder with laminate no. 2: $[Fa_{\pm 45}, Fa_{0,90}, (UD_0)_3, Fa_{0,90}, Fa_{\pm 45}]$.

Fig. 8. Fracture mode in cylinder with laminate no. 4: $[(Fa_{0,90})_2, (UD_0)_3, Fa_{0,90})_2]$.

Fig. 7. Fracture mode in cylinder with laminate no. 3: $[(Fa_{\pm 45})_2, (UD_0)_3, (Fa_{\pm 45})_2]$.

Table 4. Peak loads and crushing loads of the diferent specimens of the first test program

Specimen	Laminate no.	Trigger no.	Peak load kN	Crush load kN
1·1	1	—	26·7	16·6
2·1	2	—	42·3	27·0
2·2	2	1	35·6	26·6
2·3	2	2	40·4	24·3
2·4	2	3	37·7	26·6
2·5	2	4	30·1	20·4
2·6	2	5	26·9	19·4
3·1	3	—	33·6	21·2
3·2	3	1	31·8	20·6
3·3	3	2	28·4	18·6
3·4	3	3	36·6	21·0
3·5	3	4	25·8	21·6
3·6	3	5	23·1	15·2
4·1	4	1	29·9	25·0

forced to bend outwards are not separated from the axial carbon layers. The increasing curvature in the layers which bend outwards leads to fracture of the hoop fibres and axial splitting of the axial carbon fibres.

6.2 Effect of the different trigger configurations on the peak load

Table 4 presents the peak and the crush loads which were measured during the tests on the cylinders in the first test phase. Figure 9 shows the efficiency of the triggers used. The trigger efficiency is defined as the ratio of the peak load and the average crush load (see Fig. 1). In the case of an ideal trigger this ratio should be close to one. Figure 9 shows that it is difficult to reach a trigger efficiency of 1·0 with the triggers used. Figure 9 also shows that trigger nos 1, 4 and 5 have the best trigger efficiency.

6.3 Effect of laminate lay-up on the specific energy absorption

In Fig. 10 the effect of the laminate lay up on the specific energy absorption can be found. The specific energy absorption is defined as the area under the load–displacement curve (see Fig. 1) divided by the crushed mass of the specimen. Figure 10 shows that laminate no. 1 (pure fabric) has poor energy absorption. This is probably caused by the absence of axial carbon layers and the absence of the splaying mode during fracture. Figure 10 shows that laminate no. 2 can absorb more energy than laminate no. 3. This is probably caused by the large hoop constraint of the fabric layers $Fa_{0,90}$.
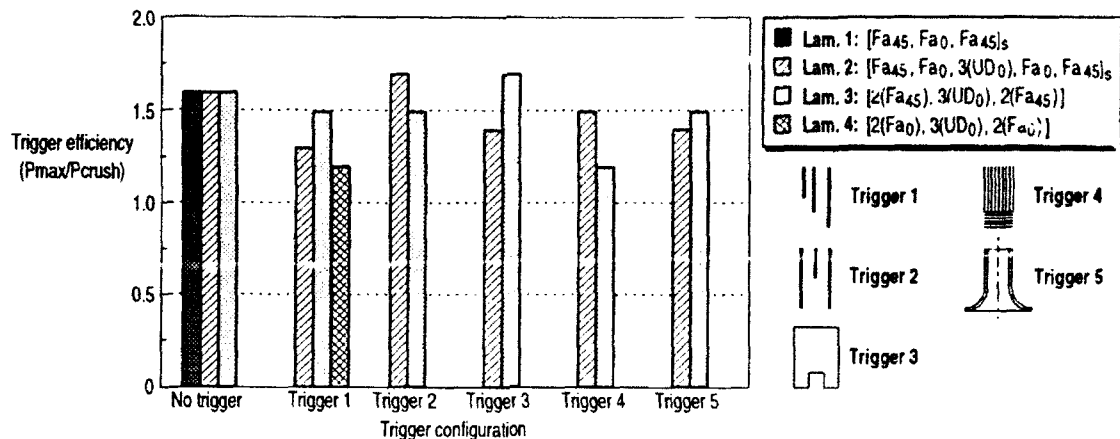
Fig. 9.   Trigger efficiency of different trigger configurations.
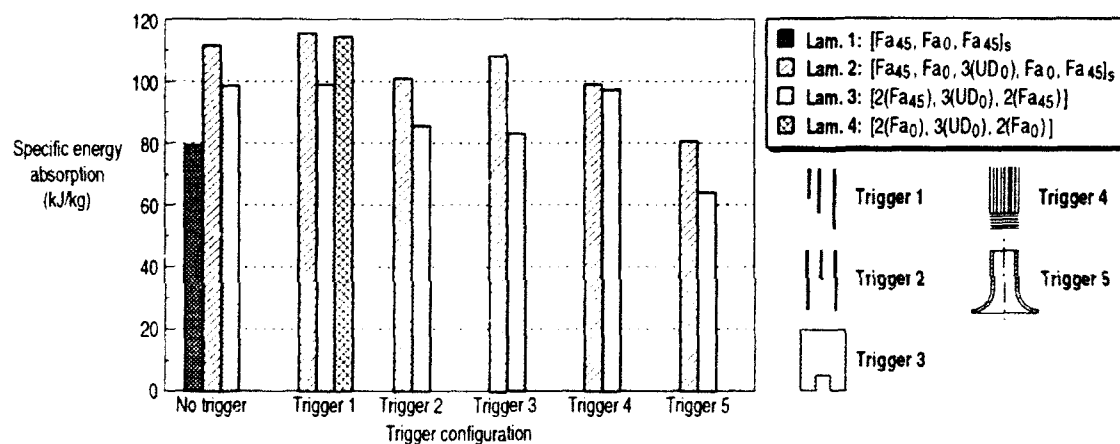
Fig. 10.   Effect of laminate structure and trigger configuration on the energy absorption.

Fig. 11.   Splaying mode in specimen with laminate no. 2 and trigger no. 1.
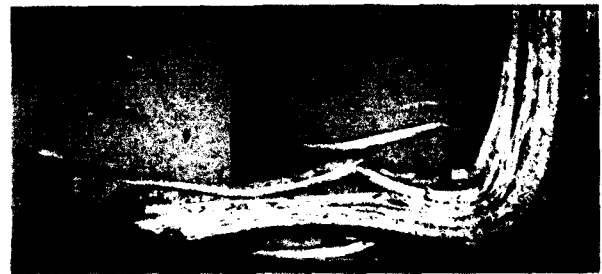
Fig. 12.   Bending of the out-of-plane trigger in a specimen with laminate no. 2 and trigger no. 5 after crushing of 3 mm.

6.4 Effect of trigger configuration on the energy absorption

Figure 10 shows the effect of different trigger configurations on the energy absorption. Specimens

with equal laminates absorb more energy with trigger 1 than with trigger 5.

Figure 11 shows the failure mode of a cylinder with laminate no. 2 ($[Fa_{\pm 45}, Fa_{0/90}, (UD_0)_3, Fa_{0/90}, Fa_{\pm 45}]$) and trigger no. 1 (shortening of the three inner unidirectional carbon layers by 0, 2 and

Fig. 13. Fracture of the out-of-plane trigger in a specimen with laminate no. 2 and trigger no. 5 after crushing of 4 mm.

Fig. 14. Failure mode in specimen with laminate no. 2 and trigger no. 5 after crushing of 10 mm.

4 mm respectively). The cylinder was crushed over 9 mm. The picture shows the wedge of debris which causes the splaying mode.

Figures 12 and 13 show the development of the failure mode in a cylinder with laminate no. 2 ($[Fa_{\pm45}, Fa_{0/90}, (UD_0)_3, Fa_{0/90}, Fa_{\pm45}]$) and trigger 5 (adding a flange to one end of the cylinder). Figure 12 shows the bending of the out of plane trigger. In Fig. 13 this out-of-plane trigger fractured. Because of the fractured out-of-plane trigger the remaining uncrushed laminate is no longer in direct contact with the platens of the test machine. Figure 14 shows a concentration of fractured material at the outside of the cylinder.

Because the remaining laminate is no longer in contact with the plates of the test machine, this laminate is forced to bend inwards by the congestion of fractured material at the outside of the cylinder. This leads to a large bending radius in the remaining laminate and therefore to a reduced number of fractures in the unidirectional fibres. This results in a reduction in energy absorption.

It can be concluded that a trigger with a good efficiency (trigger 5: adding a flange to one end of the cylinder) does not necessarily lead to a high energy absorption level, as the subsequent progressive failure may be unfavourable.

7 CONCLUSIONS

A study of the influence of several trigger configurations and laminate structures on the energy absorption of composite cylinders was conducted. Composite cylinders were fabricated and tested in compression. From the tests the following conclusions are drawn:

(1) By using hybrid carbon/aramide fabric post crush integrity can be accomplished.
(2) Cylinders which fail in the splaying mode can absorb more energy than cylinders which fail in the fragmentation mode.
(3) Cylinders with axial and hoop fibres can absorb more energy than cylinders which have no hoop fibres.
(4) To achieve a splaying mode, the use of axial unidirectional fibres is essential.
(5) The trigger configuration affects the failure mode during crushing.
(6) The trigger configuration affects the amount of energy absorption during crushing.
(7) The trigger configuration which simulates the chamfer has the best trigger efficiency.

REFERENCES

1. Untersuchungen zur Crash-Sicherheit von Hubschraubern. Lehrgang *Neue technologie für Hubschrauber.* Carl-Cranz Gesellschaft, DLR Braunschweig, 13–17 Nov., 1989.
2. Sigalas, I., Kumosa, M. & Hull, D., Trigger mechanism in enery-absorbing glass cloth epoxy tubes. *Composite Science and Technology,* **40** (1991) 265–87.
3. Farly, Gary L., Effect of fibre and matrix maximum strain on the energy absorption of composite materials. US Army Aviation Research and Technology Activity (AVSCOM) Langly Research Centre, Hampton, Virginia. *Journal of Composite Materials,* **20** (July 1986).
4. Thuis, H. G. S. J. & Wiggenraad, J. F. M., The influence of trigger mechanisms and geometry of the crush characteristics of sine-wave beams. National Aerospace Laboratory NLR, The Netherlands, NLR CR 92133 C.
5. Hull, D., A unified approach to progressive crushing of fibre-reinforced composite tubes. *Composite Science and Technology,* **40** (1991) 377–421.

Comparison between the short and long term behaviour of fibre reinforced and unreinforced concrete beams

J. A. Purkiss

Department of Civil Engineering, Aston University, Birmingham, B4 7ET, UK

&

P. Blagojević

Faculty of Civil Engineering, University of Niš, Beogradska, 18 000 Niš, Yugoslavia

The paper deals with the results of tests on concrete beams with and without steel fibres, reinforced (with high yield flexural steel only) and without any reinforcement loaded statically both long and short term. Tests were carried out for both serviceability and ultimate limit states. Measurements were taken of load, strains, crack width and crack pattern, and deflection. For short term loading the beams were loaded incrementally to failure, whilst for the long term tests were loaded incrementally to their service load which was maintained for 28 days before being increased to failure. From the long term tests the effects of creep can be determined.

A total of 15 beams were tested over 28 days. The fibres were stainless steel with an aspect ratio of 55 and a volume fraction of 1·5%. In all cases the results indicate successively better performances as fibre reinforcement and bar reinforcement were added.

INTRODUCTION

Designers are becoming much more aware that serviceability, and as a result the need to limit crack widths, is becoming increasingly important in the design of reinforced concrete structures. The extent that fibre reinforcement can play in this has not been properly evaluated, although Swamy[1] provides some indication of the potential benefits of such reinforcement. It should be realised that there is also a certain amount of prejudice within the construction industry to be overcome, in that fibre reinforced concrete is perceived to produce problems on site.

This paper evaluates the benefit both on short term static loading and long term loading that the addition of steel fibres has on the strength and serviceability of reinforced and plain concrete.

MIX DETAILS

The mix proportions used were those that have been established over a period during various projects carried out at Aston and were, by weight,

1:1·18:0·86 OPC:10 mm coarse aggregate (crushed gravel): sand (zone 2), with a batched water–cement ratio of 0·4. The actual water–cement ratio was slightly lower as the coarse aggregate has an adsorption of around 3%. The fibres used were Stainless Steel Melt Extract fibres (Fibrex SS35) 35 mm long, with an equivalent diameter of 0·64 mm and an aspect ratio of 55 (supplied by Fibretech, Nottingham, UK). A constant volume fraction of 1·5% was used.

The mix constituents were mixed dry for 3 min before the addition of water, after which mixing continued for another 2 min. The test beams were cast in timber moulds and vibrated with a poker vibrator.

All specimens were demoulded after 24 h with the control specimens cured in water and the test beams cured in the laboratory, all for 28 days before testing.

CONTROL TEST DATA

All control tests were carried out in accordance with the relevant section of BS 1881.[2] The results of the control tests are given in Table 1.

45

Table 1. Control test results

Test	No fibres		With fibres	
	Mean (MPa)	Std. dev. (MPa)	Mean (MPa)	Std. dev. (MPa)
Compression	66·9	4·0	68·9	2·8
Split cylinder	4·2	0·4	6·1	1·0
Modulus of rupture	8·0	0·5	10·7	2·2

Cube strength

It will be noted that the cube strength of the fibre reinforced concrete is only marginally higher than that of the plain concrete.

Splitting tensile test

The fibres increase the splitting tensile strength by around 46% over the plain concrete.

Flexural tensile test

Here the increase in strength is less marked (32%). This difference between the two tensile test results is common.

TEST DETAILS

Specimen details

All the beams were 2000 mm long by 100 mm wide by 176 mm deep. For all the tests except for the long term fibre reinforced only beams three beams were cast. In the case of the long term fibre reinforced test it was only possible to test a single beam, and thus the results of this test will need treating with a certain amount of caution. The beams with bar reinforcement had two 8 mm high yield bars ($f_y = 550$ MPa) at an effective depth of 162 mm. None of the beams had any shear reinforcement.

Test procedure

The beams were loaded hydraulically through a spreader beam to give loading at the third points of the beam. Short term loading and the load in the long term test was applied at the rate of 10 kN/h in 1 kN increments. For the short term tests the load was taken directly up to failure, whereas

in the long term tests the beams with bar reinforcement were incrementally loaded to 22·5 kN, the load was then held constant for 28 days before being finally taken to failure. The load for the beams with fibres only was 8 kN representing a similar fraction of ultimate load.

Test measurements

Besides recording values of the applied load, the following measurements were taken:

(1) Deflection
This was determined using dial gauges at centre span and under each load point.

(2) Strain
Values of strain were obtained at the positions shown in Fig. 1 using electrical resistance strain gauges. Also in some of the tests strain gauges were attached to the reinforcement.

(3) Cracking
For all the tests, except the long term tests with fibre reinforcement, the crack widths were monitored using demountable strain (displacement) gauges, and the crack propagation was noted by eye.

RESULTS

Short term static loading

The ultimate loads for each of the beam types is given in Table 2, where it is observed that the beams reinforced with fibres only are 72% stronger than those without any fibres, and that the beams reinforced with bar and fibre reinforcement are 13% stronger than those with bar reinforcement only. Swamy[1] indicates that the addition of fibres gives larger increases in moment capacity, but his results are based on a fibre length of 50 mm.

The load–deflection characteristics are plotted in Fig. 2a for the beams with no bar reinforcement and in Fig. 2b for beams with bar reinforcement. For the beams with no bar reinforcement the addition of fibres increases the load to non-linearity and allows a certain amount of post-crack deformation. For the beams with bar reinforcement, the addition of fibres increases the linear portion of the loading characteristic and produces a very clear second linear portion of
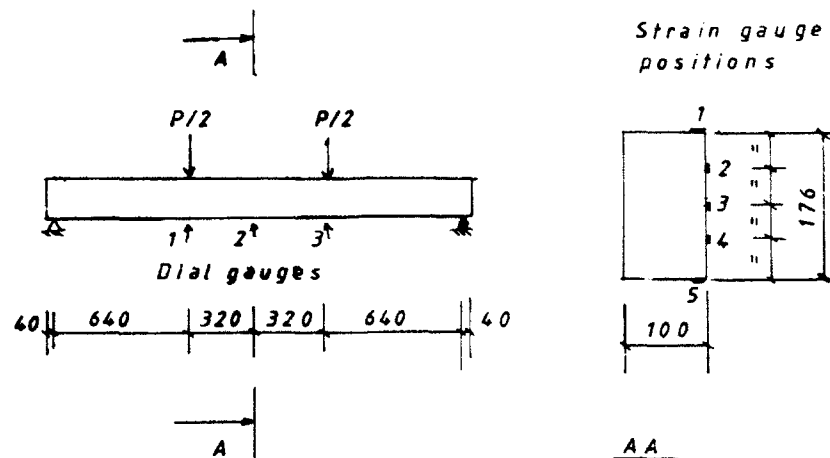
Fig. 1. Details of the tests with the locations of dial and strain gauges.

Table 2. Beam test loads

Test type	Load (kN)	Plain concrete		Reinforced concrete	
		No fibres	Fibres	No fibres	Fibres
Short term tests	Failure	8·0	13·0	32·0	36·0
		6·5	11·0	30·0	35·0
		7·5	13·0	33·0	36·0
	Average	7·33	12·33	31·67	35·67
	First crack			12·0	18·0
				12·0	18·0
				12·0	17·0
	Average			12·0	17·67
Long term tests	Failure (mean)			32·84	39·17
	First crack			12·0	18·0
				12·0	18·0
				11·0	17·0
	Average			11·67	17·67

steeper slope indicating a degree of extra stiffening not apparent in the beams with bar reinforcement only. There is, however, a slight anomaly in that the beams without fibres appear to have a greater capacity for post yield deformation. A comparison between the deflection profiles at the design service loads and ultimate loads is given in Figs 3a and 3b.

For the bar reinforced beams with and without fibres the load to first observed crack is also given in Table 2, when it is noted that the addition of fibres increases the load to first crack by some 47%.

Measurements of crack width were taken on the beams reinforced with bars with and without fibres in both the short term tests and the long term tests during the loading phase and are given

in Table 3. The results from the short and long term loading tests are generally comparable. In Table 3 the average for all t beams in a test series is quoted. This is reasonab. since cracking is a statistical phenomenon as cracks will tend to occur at points of apparent weakness in the matrix.

Long term static loading

Measurements of deflection under a constant load of 22·5 kN for all specimens were taken over a period of 28 days after application of the load. Following the 28 day period the beams were loaded to failure. These failure loads are noted in Table 2 when it will be observed that the failure loads from the long term tests showed only a very
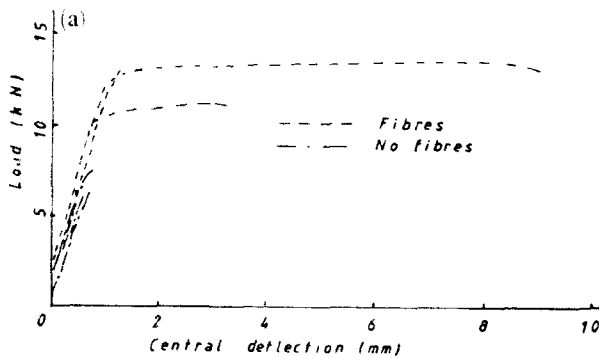
Fig. 2a. Load-deflection characteristics for beams with no bar reinforcement.
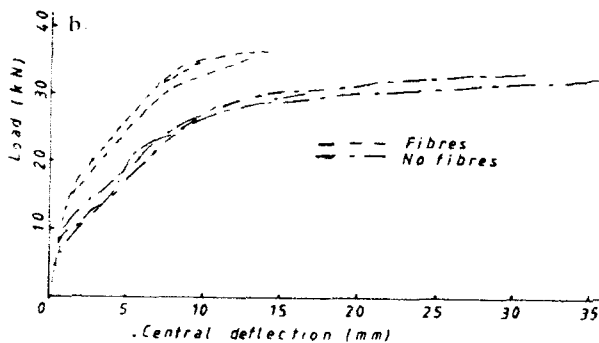
Fig. 2b. Load-deflection characteristics for beams with bar reinforcement.
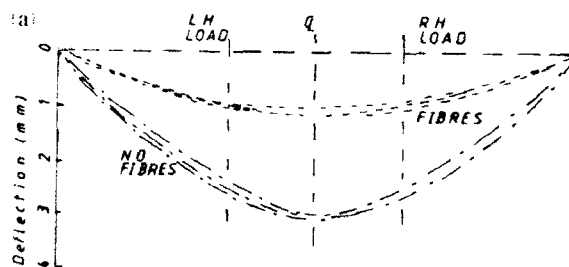
Fig. 3a. Deflection profile at design service loading.
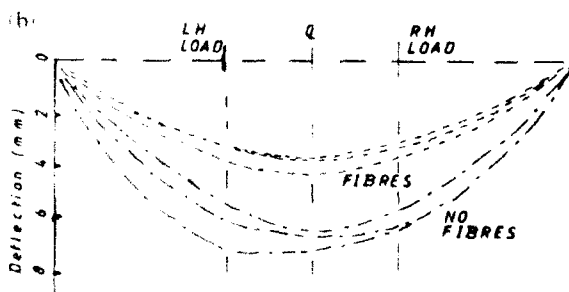
Fig. 3b. Deflection profile at design ultimate loading.

slight increase for the beams with bar reinforcement only, but an increase of 10% higher for those with bar and fibre reinforcement over those from the short term tests. The deformation–time responses are plotted in Fig. 4. For all the tests the deflection profile was initially sharply curved followed by a sensibly linear portion. The slope of the linear portion for the bar reinforced beams either with or without fibres was similar, i.e. the addition of fibres did not appear to have a significant effect in these tests on the rate of creep. This result is explained by the fact that the predominant mechanism governing the rate of creep is the compressive stress level in the concrete which is the same in both tests and that the elastic properties of concrete are little affected by the addition of fibres unless cracking occurs.

The single result for a beam reinforced by fibres alone is included as a comparison, but it is not advisable to draw too much conclusion as there is no indication of repeatability, except that a very similar profile is obtained. It should be noted that the single fibre reinforced beam failed at a load of 11 kN.

Table 3. Crack width development

Load (kN)	Crack width (mm) Reinforcement type			
	Fibres only		Bar and fibres	
	Short term test	Long term test	Short term test	Long term test
11·0	0·16	0·11	0	0
13·0	0·19	0·15	0	0
15·0	0·22	0·21	0	0
17·0	0·25	0·24	0·03	0·06
19·0	0·28	0·27	0·05	0·07
20·0	0·31	0·30	0·06	0·09
22·5	0·33	0·33	0·10	0·14
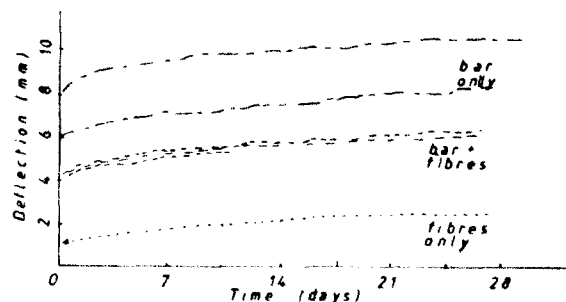
Fig. 4. Deformation–time responses for the long term 28 day creep tests.

Table 4. Deflection rates

Beam type	Load (kN)	δ_e (mm)	δ_{28} (mm)	$\delta_{28}-\delta_e$ (mm)	$(\delta_{28}-\delta_e)/\delta_e$	$(\delta_{28}-\delta_e)/P$ (mm/kN)
Fibres only	8·0	0·96	2·56	1·60	1·67	0·20
Bar only	22·5	7·36	10·6	3·29	0·45	0·15
	22·5	5·61	8·47	2·86	0·51	0·13
Bar + fibres	22·5	2·82	5·29*	2·47	0·88	0·11
	22·5	3·80	6·14	2·34	0·62	0·10
	22·5	3·95	6·34	2·39	0·60	0·11

*This beam failed after 11 days under load.

Table 4 gives the absolute and percentage change in central deflection for all the long term tests. It will be noted that although the absolute change in deflection for the beams reinforced with fibres and bars is lower, it is a higher percentage of the short term elastic deflection as this is much lower than the equivalent for beams with bar reinforcement only. The change in deflection per unit applied load, which can be taken as a measure of specific creep, is also smaller for the beams with bars and fibres compared with that from beams with bars only, and as would be expected is at its highest for the beam with fibres only.

As expected the crack widths in the beams increased during the tests. If the crack widths for the reinforced beams are compared at the point at which the 22·5 kN loading had been just applied and 10 days later, then for the beams with bar reinforcement only the crack width had progressed from 0·33 mm to 0·40 mm and for the beams with bar reinforcement and fibres from 0·12 mm to 0·15 mm. There only appeared in both cases to be a slight increase in crack widths by the end of the 28 day period.

CONCLUSIONS

(1) The addition of fibres to conventional reinforced concrete beams increases the flexural strength, and also decreases the deflection and amount of cracking.

(2) In the long term the introduction of fibres reduces the amount of creep but appears not to affect significantly the creep rate.

ACKNOWLEDGEMENTS

REFERENCES

1. Swamy, R.N., Steel fibre concrete for bridge deck and building floor application. *Structural Engineer*. **64A** (1986) 149–57.
2. BS 1881. *Methods of Testing Concrete, Part 116: Method of determination of compressive strength of concrete cubes, 1983; Part 117: Method of determination of tensile splitting strength, 1983; Part 118: Method of determination of flexural strength, 1983.* British Standards Institution Milton Keynes.

Examples of the multicriteria optimization of cement-based composites

A. M. Brandt & M. Marks

Institute of Fund. Technical Research, Sweitokrzyska 21, 00-049, Warsaw, Poland

The materials considered in the paper are called concrete-like composites or materials with cement-based matrices. These are not only ordinary and high performance concretes, but also materials with different admixtures, dispersed fibre reinforcement, polymers, etc.

The selection of the most appropriate material composition and internal structure is proposed using the methods of the optimal design. In the paper basic methods of mathematical optimization are briefly discussed and applied to the formulation and solution of six different problems.

The main aim of the paper is to demonstrate how the optimization approach may be used in practical situations of the design of high performance concretes.

INTRODUCTION

Optimization as a part of the design process is a direct way in which the goal and main conditions are formulated and the best solution is looked for. In that case the search for the solution is conducted in an objective and rational way, independent of the intuition, experience or particular abilities of the designer. Thus, optimization takes over that part of the process of material design which consists of selecting proportions and distribution of basic components, and subsequently of checking that imposed criteria and conditions are met.

There are many analogies with structural optimization, which is relatively more advanced than the material one. Optimization of materials is related to the mechanics and to mathematical optimization theory and makes use of methods and results developed in both these disciplines. In particular, for brittle matrix composites the fracture mechanics, general damage theory and all knowledge of the mechanical properties and behaviour of materials are exploited.

Optimization of composite materials deals with the selection of values of several independent variables which determine the composition, internal structure, but also methods of production and curing.

In this paper the optimization approach is limited to materials with cement-based matrices, like ordinary plain concretes, fibre reinforced concretes, polymer concretes, etc. Its importance is increasing when applied to high performance concretes. The properties of these materials are related in a very complicated way to their internal structure and composition and determine their utility in building and civil engineering structures. A short list of papers on the optimization of different composite materials is given and commented on by Brandt.[1,2] The approach initiated in both these papers is developed here to present a general formulation for multicriteria optimization and to demonstrate it on a few examples of cement-based composites.

BASIC CONCEPT OF MATERIAL OPTIMIZATION

An optimal material is described by a set of decisive variables $x_i (i = 1, 2, ..., n)$ which extremize an optimization criterion.

Variables x_i are considered as independent and together with arbitrary selected parameters they determine the object of the optimization: a material, i.e. characteristics of the components, their mass or volume proportions and distribu-

51

tion, also their reciprocal relations (e.g. adherence).

The decisive variables belong to a feasible set. It means their values beyond imposed limits cannot be accepted in the problem for constructional, functional or other reasons. The constraints may have the form of equalities or inequalities

$$g_p(x_i) = 0, \qquad p = 1, 2, \ldots, r$$
$$h_s(x_i) \leq 0, \qquad s = 1, 2, \ldots, t \qquad (1)$$

or simply limit values may be imposed

$$\underline{x}_i \leq x_i \leq \bar{x}_i, \quad i = 1, 2, \ldots, n$$

lower and upper bars indicate lower and upper limit values, respectively. For example, the variables which describe the components are limited to available materials (cement, sand, gravel, etc.) and their possible properties. All constraints determine the domain of feasible solutions.

The variables may be defined as continuous or discontinuous (discrete) ones. The quantities of particular components are continuous variables, e.g. volume contents. Discrete components are represented by discontinuous variables, e.g. two or three different kinds of Portland cement may be considered as variables in an optimization problem.

The properties of the components as well as their effective distribution in a composite material are random variables. Their final values and their nominal values determined by testing are subjected to unavoidable scatter. When in an optimization problem only design and nominal values are considered, then that is a deterministic approach. In the opposite case, when the distribution functions are taken into account, the stochastic problem of optimization is formulated.

Optimization criteria describe the basic properties of materials. They are also called objective functions. In material optimization the objective functions describe selected properties which are considered as important and decisive for the quality and applicability of the designed material. The solution consists of the determination of these values of the design variables which extremize the objective functions. As material properties, all physical, chemical and other properties may be considered. For engineering materials particularly important are mechanical properties such as strength, Young's modulus, specific fracture energy, durability but also specific cost.

When a set of independent variables x_i, ($i = 1, 2, \ldots, n$) is considered the optimization criterion is expressed by these variables as a function $F(x_i)$, subject to constraints of different kinds and forms, e.g. the limited volume of material may be presented as an integral.

If the problem is formulated with one single criterion $F(x_i)$ with the constraints (1), then the necessary conditions for a solution are derived from the Kuhn–Tucker theorem and have following form:

$$x_i \frac{\partial F^*(x_i)}{\partial x_i} = 0 \quad \frac{\partial F^*(x_i)}{\partial x_i} \leq 0 \quad \frac{\partial F^*(x_i)}{\partial \mu_p} = 0$$
$$(2)$$
$$\mu_s \frac{\partial F^*(x_i)}{\partial \mu_s} = 0 \quad \frac{\partial F^*(x_i)}{\partial \mu_s} \geq 0$$

$$x_i \geq 0, i = 1, 2, \ldots, k$$

here $\mu_s \geq 0, s = 1, 2, \ldots, t$, and $\mu_p, p = 1, 2, \ldots, r$, are so-called Lagrange multipliers, and

$$F^*(x_i) = F(x_i) + \sum_{p=1}^{r} \mu_p g_p(x_i) + \sum_{s=1}^{t} \mu_s h_s(x_i) \qquad (3)$$

The problems are correctly formulated when criteria, constraints and variables are defined. Sometimes the design variants are imprecisely called 'optimal solutions'. Calculation of a few cases and selection of the best one is not an optimization approach. There is no optimal solution without clear determination in what sense and within what feasible region.

It should be also emphasized that the optimization problem is solved not on real materials, but on their approximate models. The results of an optimization procedure are dependent on assumptions and approximations admitted for these models, e.g. materials may be assumed as elastic and homogeneous.

The optimization does not replace entirely the material design, because it may not cover certain aspects and requirements, which determine the material completely. The omission of secondary aspects is justified by necessary simplification of the optimization problem. In the next step of the material design, on the other hand all requirements concerning safety, serviceability, economy, etc., should be satisfied. That is why the material optimization, like the structural optimization, does not replace the design but is its part, in which some intuitive procedures are avoided.

Determination of constraints and objective functions is important in the formulation of the problem: it is based on given conditions, but

sometimes an objective function may be replaced by a constraint or vice versa. It occurs also that a small modification of a constraint may influence considerably the objective function. In such a case the resignation of preliminary assumptions concerning constraints may be justified.

In rare problems it is admissible to limit the optimization to one single criterion, e.g. a structure of minimum cost or a material of maximum strength may be looked for as an appropriate solution. In general, such a formulation has a somewhat academic character or is a simplified example for a preliminary explanation of the problem. In most cases the existence and necessity of several criteria is obvious as presented below.

MULTICRITERIA OPTIMIZATION OF MATERIALS

Let us consider an n-dimensional space of variables x_i in which objective functions $F_j(x_i)$, $j = 1, 2, \ldots, k$, are determined, here k is the number of objective functions or functionals. It means that a solution of the problem should satisfy k objective functions and the problem may be formulated as follows: 'determine an n-dimensional vector in the space of decisive functions which satisfies all constraints and ensures that the functions F_k have their extrema or limit values'.

The decisive functions are the components of the vector $\mathbb{X}^N$ in the n-dimensional space. Every point of that space indicates one particular material defined by n decisive variables. The feasible region Q is a part of the n-dimensional space and is defined by the constraints (1).

The space of the objective functions R^K has k dimensions. Every point of that space corresponds to one vector of the objective function $F_k(x_i)$. In that space the feasible region Q is represented by a region $F(Q)$. Without giving all mathematical formulations which may be found elsewhere, it may be proved that the points of the feasible region Q are represented by the points in the region $F(Q)$. An example of regions Q and $F(Q)$ are shown in Fig. 1 in the case of $k = 2$ and a two-dimensional region.

The optimization problem formulated in this way may have several solutions and the solution appropriate for the given conditions should be selected using other arguments. To present that procedure a few definitions are necessary.

The ideal solution is an extremum for all objective functions. Because a characteristic feature in
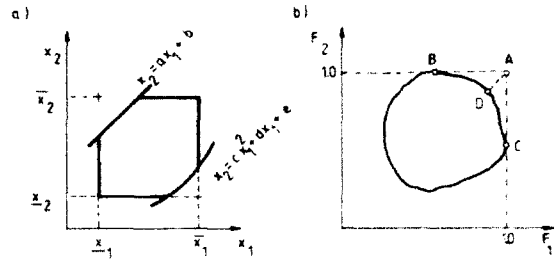
Fig. 1. Feasible regions: (a) in variable space; (b) in objective functions space.

multiobjective optimization is that the criteria are in conflict, then the ideal solution is outside the feasible region. That is indicated in Fig. 1 by point A, in which both objective functions F_1 and F_2 have their maximal values.

The solutions of the problem are situated on section BDC of the boundary of the feasible region. These are called the nondominated solutions, Pareto ideal solutions or the compromise set, it means that no one objective function can be increased without causing a simultaneous decrease of at least one other function. In effect, the difficulty is that there is an infinite number of Pareto solutions along section BDC. It is therefore necessary to apply another procedure for the selection of one solution, called the preferable solution.

The compromise set is a rigorous and strict solution of the problem, but the next step, i.e. selection of the preferable solution is based on a subjective decision. Different preferable solutions may be found using different assumptions and methods. For example, when strength and cost are two conflicting objective functions, then the compromise set contains all possible solutions. For one application the cheapest solution may be selected, and for the other the strongest one. In general, a system of arbitrary weights may be assumed for each objective function, it means that some functions are considered as more important than others. A further development of that method is the creation of a utility function, by which the weights of various criteria are introduced.

Another method is based on the selection of a point on the curve of Pareto solutions which is closest to the ideal solution in the space of normalized functions. That second method is applied in the examples below. For explanation of other methods the reader is referred to manuals of mathematical optimization.

APPLICATION OF MULTICRITERIA OPTIMIZATION TO DESIGN OF CEMENT COMPOSITES

The application of the optimization approach to cement-based composite materials requires selection of appropriate decisive functions and objective functions. Effective solutions of such problems are possible only when the relations between these functions may be presented in an analytical form. These relations should be based either on verified models of materials or on experimental results, presented in a form of approximate functions.

The decisive functions (variables) and objective functions (criteria) are presented in Table 1, which is only an example and may be completed by other variables and criteria. It is not possible to present all of them, and this does not even seem necessary. Table 1 is shown here as a general indication of how the problems may be formulated. The subsequent examples may be related to different parts of Table 1.

EXAMPLES OF MATERIAL OPTIMIZATION

Example 1

A simple optimization problem is considered in which there is only one variable and one objective function. The problem has been solved in Refs 1 and 2 and is only briefly described here.

A composite element shown in Fig. 2 is subjected to direct tension. The only variable is angle ϑ which determines the direction of parallel fibres (1D) reinforcing the considered element. The objective function is the fracture energy W accumulated in the element at the limit state, which is formulated as corresponding to the appearance of a crack of given width r_o.

The energy W is expressed as a function of one independent variable ϑ and of several given parameters characterizing the mechanical properties of the matrix and fibres and the matrix–fibre bond

$$W = W^{1D}(\vartheta)$$

The analytical function W was derived from a complex model in Ref. 2. The solution is obtained from the equation $dW/d\vartheta = 0$ in the region $0° \le \vartheta \le 90°$ and is shown in Fig. 3. It may be observed that the optimal value of angle ϑ is equal to 36° approximately for a given set of parameters

describing materials used and $W_{opt} = 2·57$ N mm^{-2}.

Example 2

The same problem as for Example 1 is considered in a more general way. Namely, with the same objective function two other variables are added: the length of a single fibre l and its diameter D. The optimization problem has been published more in detail in Ref. 3. The constraints for the variables are:

$$0 \le \vartheta \le \frac{\pi}{2}; \quad \underline{l} \le l \le \bar{l}; \quad \underline{D} \le D \le \bar{D}$$

where $\underline{l} = 10$ mm, $\underline{D} = 0·1$ mm, $\bar{l} = 100$ mm, $\bar{D} = 1·0$ mm. These limits for length and diameter of a single fibre are imposed by an assortment of available fibres and by construction requirements.

To solve the problem an auxiliary function $F^*(2)$ was constructed with Lagrange constants and the solution obtained for the same set of numerical values of the parameters as in Example 1 is:

$$\vartheta \cong 19°5', \quad l = 100 \text{ mm}, \quad D = 0·1 \text{ mm},$$
$$W_{opt} = 17·68 \text{ Nmm}^{-2}$$

Two variables should have their maximum values corresponding to the boundaries of the feasible region and angle ϑ is smaller than in Example 1 and the value of objective function is much higher. This reflects the influence of the two other independent variables.

Example 3

Example 2 is further completed with a second objective function which expresses the loading capacity of the element $P = P(\vartheta)$ which should reach its maximum, cf. Ref. 3. The function $P(\vartheta)$ is based on experimental results and is presented in the form of a polynomial

$$P(\vartheta) = 28 - 8·94185\vartheta - 0·318293\vartheta^2$$
$$+ 0·445299\vartheta^3$$

It is assumed that P does not depend on the other two variables. The constraints imposed on variables ϑ, l and D are the same as in Example 2.

That is the problem of multicriteria optimization. For determination of the compromise set an auxiliary function is constructed and the Kuhn–Tucker theorem for multicriteria optimiza-

Table 1. Examples of criteria (objective functions) and design variables in optimization of cement-based composites (after Ref. 3)

Criteria objective functions	Design variables												
	Basic components				Dispersed reinforcement (fibres)				Admixtures				Other
	Cement	Water	Sand	Aggreg.	Steel	Glass	Polymeric	Other	Superplast.	Air-entr.	Polymers	Other	
Strength													
Compressive													
Tensile													
Elastic modulus													
Other													
Energy													
Tough.index I5													
Tough.index I10													
Impact													
Fracture energy													
Other													
Economy													
Specific cost													
Execution cost													
Energy													
Other													
Other													

Fig. 2. Fibre reinforced (1D) concrete element subjected to axial tension before and after the crack opening (Example 1, after Ref. 1).

Fig. 4. Compromise set BC and preferable solution D for Example 3 (A is ideal solution, after Ref. 3).

Fig. 3. Diagram of the fracture energy W^{1D} as a function of angle ϑ; here W_1, W_2,.... are energy components (Example 1, after Ref. 2).

tion is applied. With the numerical values of the parameters as in previous examples the compromise set has the form as shown in Fig. 4. The preferable solution in the space of normalized functions with $W_1 = 0.9625$, $P_1 = 0.9544$ corresponds to the following values of variables:

$$\vartheta = 8°9', \ l = 100 \text{ mm}, D = 0.1 \text{ mm},$$
$$W_{\text{opt}} = 17.02 \text{ N mm}^{-2}, P_{\text{opt}} = 26.72 \text{ kN}$$

It may be observed that due to the second criterion the angle ϑ obtained is much smaller than in Examples 1 and 2 and value of W_{opt} is smaller than in Example 2.

Example 4

This example is taken from Ref. 4 and is based also on modification of the problem in Example 1. Two objective functions are introduced: the maxi-

mum of the fracture energy in an element subjected to tension and the minimum cost of that element, which is made of brittle matrix and is reinforced with parallel fibres (1D) with angle $\vartheta = 0°$. There are two variables: volume fraction of fibres β and factor τ_0 determining the quality of the fibres:

$$\tau_0 = \frac{\tau_{\text{max}}}{\underline{\tau}_{\text{max}}}$$

here τ_{max} is the actual characteristic value of the pull-out test for selected fibres and $\underline{\tau}_{\text{max}}$ is this characteristic value for the fibres which are the least effective for the fibre/matrix bond. The values of β and τ_0 may be selected from the ranges $\underline{\beta} \leq \beta \leq \bar{\beta}$ and $\underline{\tau}_0 \leq \tau_0 \leq \bar{\tau}_0$, respectively. The quality of the bond of the fibres is reflected in their cost and the total cost of the composite materials is expressed in the following form:

$$K(\beta, \tau_0) = k_c V_c + k_f[\tau_0 + (\tau_0 - \underline{\tau}_0) 0.25] V_f$$
$$+ g(\beta) V_f$$

here k_c, k_f, V_c and V_f are unit costs of concrete matrix and of fibres and their volumes, respectively. The function $g(\beta) = b_1 \beta^2 + b_2 \beta$ is proposed to account for the increased cost of material technology related to the application of fibres. This function is assumed to be nonlinear, because the increased volume of fibres introduced to the matrix causes additional complications to the execution of the composite material. Here b_1 and b_2 are constants which are selected according to the local conditions of construction.

In the problem considered the numerical values of the parameters are as in Example 1 and the following constraints are assumed:

a)

b)
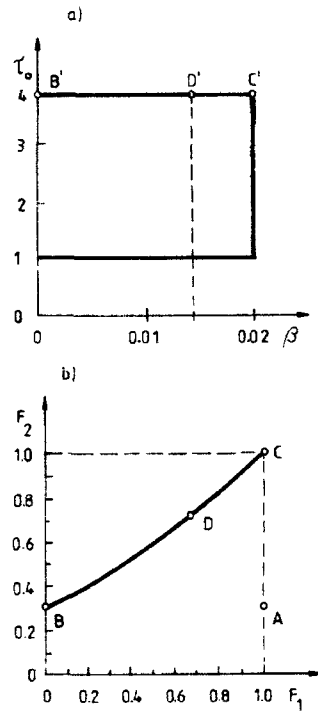
Fig. 5. Compromise set BC with ideal solution A and preferable solution D: (a) in objective functions space for Example 4; (b) in variable functions space (point D' indicates preferable solution, after Ref. 3).

$\underline{\beta} = 0$, $\hat{\beta} = 0.02$, $\underline{\tau}_o = 1$, $\hat{\tau}_o = 4$

The cost of the components is characterized by the values

$k_c = 8 \times 10^5$, $k_f = 36.57 \times 10^6$, $b_1 = 4 \times 10^{10}$, $b_2 = 6 \times 10^8$

taking into account particular unit costs of basic materials and workmanship.

The compromise set is presented in Fig. 5(b). In the space of decisive variables it is represented by the corresponding section B'C' in Fig. 5(a). The ideal point A is determined by its coordinates (1·0, 0·30488). As the preferable solution it is proposed to be a point which is the closest to the ideal solution A in the space of normalized functions. It is point D with coordinates $F_1 = 0.6819$ and $F_2 = 0.7145$ (Fig. 5(b)). In the space of the variables the solution is obtained in point D' in Fig. 5(a) for $\beta = 0.014$ and $\tau_o = 4$. This means that in the preferable solution the volume fraction of the fibres is $\beta = 1.4\%$ and the best possible fibres with $\tau_o = 4$ should be applied.

Example 5

Let us consider a cement-based matrix with a hybrid reinforcement composed of steel and

carbon fibres, cf. Ref. 5. The elements made of this composite material are subjected to bending. In the problem there are the following three objective functions:

1. Ratio of the fracture energy of the composite material to the energy for the plain matrix, which should be maximal, it means that the best effect of the reinforcement is sought:

$$F_1(x_i) = \frac{G_f(x_i)}{G_f(x_i = 0)} = \max F_1.$$

2. Ratio of the first crack composite stress to the stress for the plain matrix should be maximal. Again the maximal effect of the reinforcement is expected:

$$F_2(x_i) = \frac{\sigma_c(x_i)}{\sigma_c(x_i = 0)} = \max F_2$$

3. The total cost of fibre reinforcement should reach its minimum:

$$F_3(x_i) = k_1 x_1 + k_2 x_2 = \min F_3$$

Here x_1 and x_2 are the volume fractions of carbon and steel fibres, respectively, and these are the only variables, k_1 and k_2 being the specific costs of these fibres. The additional constraints

$$x_1 + x_2 \leq c, \quad x_i \geq 0, \quad i = 1, 2$$

mean that the total volume fraction of both kinds of fibres is limited by the good workability of the fresh mix required and that these volumes are expressed by nonnegative values. In the solution the volume fractions of both kinds of fibres should be determined in such a way, that the effects of reinforcement in the sense of the fracture energy and the first crack strength are a maximum and the cost of reinforcement is a minimum. Here several simplifying assumptions are accepted, among others:

— that the matrix properties do not depend on the kind of reinforcement,
— that the cost of reinforcement may be expressed as proportional to their volume fractions.

The functions $F_1(x_i)$ and $F_2(x_i)$, $i = 1, 2$, are determined from the test results and represented by two polynomials.[5]

The feasible region for the design variables is shown in Fig. 6. The maxima of functions F_1 and F_2 are determined by the Kuhn–Tucker theorem. All seven solutions are shown as points in Fig. 6.
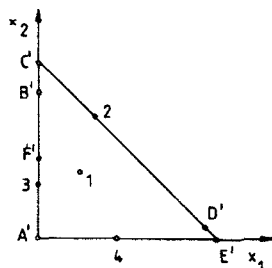
Fig. 6. Feasible region in Example 5 (after Ref. 5).

These are the solutions inside the feasible region in point 1 and on the constraints in points 2, 3, 4 and A', C' and E'. The maxima of functions F_1 and F_2 are obtained only from the solutions which satisfy the necessary conditions. The function F_3 is linear with respect to variables x_1 and x_2 and has its minimum in point $x_1 = 0, x_2 = 0$.

The solution of an optimization problem for three criteria is the compromise set, the ideal solution and the preferable solution. In the dimensionless space of objective functions the ideal solution is in the point $(1\cdot0, 1\cdot0, 0\cdot0)$. In the problem considered for imposed $c = 5\%$ and $k_1/k_2 = 10$, the maximum of the normalized function Φ_1 is obtained for $x_1 = 0$ and $x_2 = 4\cdot0975$ (point B' in Fig. 6). The maximum of function Φ_2 is for $x_1 = 5$ and $x_2 = 0$ (point E'). The minimum of function Φ_3 is for $x_1 = 0$ and $x_2 = 0$ (point A).

The set of compromises may be determined using one of the methods proposed in any manual for mathematical optimization. Its projections on all three planes $\phi_3 = 0$, $\phi_2 = 0$ and $\phi_1 = 0$ are shown in Fig. 7. The preferable solution is determined as the point nearest to the ideal solution. Its coordinates are: $\phi_{1pr} = 0\cdot9629$, $\phi_{2pr} = 0\cdot4774$, $\phi_{3pr} = 0\cdot10$. This point is projected on the planes in Fig. 7. In the space of the design variables point C' with coordinates $x_1 = 0$, $x_2 = 5$ (Fig. 6) is the preferable solution. The optimum composite is reinforced with a volume fraction of steel fibres equal to 5% and without the carbon fibres which are assumed 10 times more expensive.

If the conditions are modified in such a way that the difference in the cost of fibres is neglected and $k_1/k_2 = 1$, then the solution is 2·37% of steel fibres and also without carbon fibres (point F '). In the case when the cost of fibres is completely neglected and $k_1 = k_2 = 0$, then the solution is: 4·83% of carbon fibres and 0·17% of steel fibres (point D' in Fig. 6). It is interesting how the conditions imposed on the cost determine the solution.

Example 6

The optimization problem was formulated on the basis of data obtained from testing of concrete used for the construction of piers of a highway bridge across the Vistula near Zakroczym. The text which follows is based on Ref. 6.

Two criteria were used: maximum compressive strength and minimum specific cost. Five independent variables were selected as mass fractions of: p, sand (0–2 mm), z, gravel (2–8 mm), g, crushed stone (8–16 mm), c, cement and w, water.

Using experimental data approximated by the least squares method and a set of curves from the design method applied in the UK for mix design the compressive strength was presented as a second order function of five independent variables $f_c(c, p, g, w, z)$.

The specific cost was proposed as a sum of the costs of particular components (water was excluded) multiplied by a nonlinear coefficient α related to the content of cement and representing the increased cost of high strength concrete. The cost function has the following form:

$$F(c, p, g, z) = \alpha(540c + 12p + 20z + 40g)$$

where the numerical coefficients are the approximate cost of components in PLZ per 1 kg and the coefficient α was proposed as

$$\alpha = \frac{9\cdot025 \times 10^{-3}c^{-2} - 2\cdot28c + 423\cdot75}{1\cdot425c + 52\cdot5}$$

The constraints were taken from effective mixes used on the site where the conditions of workability were taken into account. Using similar mathematical methods as in previous Examples, the solution obtained is shown in Fig. 8. Section BC in the space of normalized functions Φ is the compromise set and points C and B represent solutions for maximum compressive strength and minimum cost, respectively. The preferred solution in point D was selected as the one closest to the ideal solution in point A. Points with numbers indicate the test mixes realized on the site.

It is interesting to note that the compressive strength of optimum concrete appeared to be 9 MPa higher than the average taken from 10 samples of the test mixes. At the same time the specific cost turned out to be 6% lower than the actual mix Nr 6 on the construction site. That mix was the closest to the calculated optimum solution, but it was weaker.

The results of this Example show that useful information may be obtained from the solution of
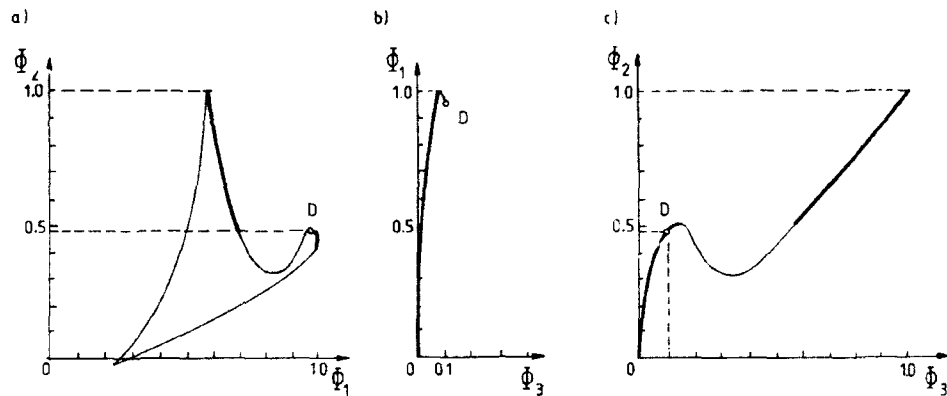
Fig. 7. Compromise set: (a) for functions ϕ_1 and ϕ_2 in Example 5; (b) for functions ϕ_1 and ϕ_3; (c) for functions ϕ_2 and ϕ_3 (after Ref. 5).

an optimization problem even though a rather simplified model was adopted for calculations.

CONCLUDING REMARKS

The problems were solved as examples of the optimization approach to design of cement-based composites. The examples were selected for explanation of the proposed procedures in a simple way. In all cases only one method of determination of the preferable solution from the Pareto compromise set was applied: in the space of normalized objective functions a point closest to the ideal solution was found as representing the preferable solution. It is possible to determine the preferable solution in many other ways, e.g. using numerical factors as weights which represent the importance of each particular objective function. By that method a so-called utility function may be created which represents all objective functions with their weights in the form:

$$\Phi = \Phi_1 k_1 + \Phi_2 k_2 + \Phi_3 k_3 + \dots$$

where Φ_i are objective functions and k_i are their weights.

The principal difficulty in the problems of material optimization is their correct formulation from which effective and useful solutions may be derived. Here the sensitivity of the objective function with respect to the variables is a separate question. The next difficulty is the determination of analytical relations between objective functions and variables. Such relations may be established from various test results available from publications. It is not necessary to execute experimental
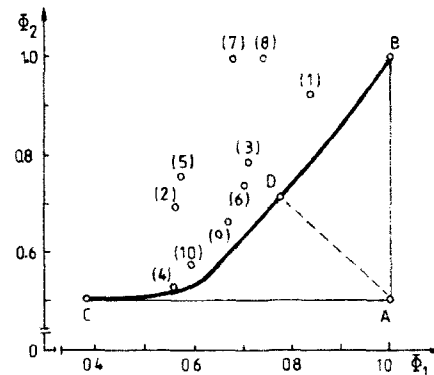
Fig. 8. Compromise set, ideal solution A and preferable solution D in Example 6 (after Ref. 6).

research in each case when an optimization problem is formulated. Often, however, the relations between all variables and objective functions are not given explicitly and special methods should be applied to obtain approximate solutions from incomplete test results.

The last difficulty in these problems is the effective solution of the equations obtained.

Further development of the optimization approach for cement-based composites should be directed at consideration of various objective functions and variables. Mechanical models which express optimization criteria as functions of independent variables should be considerably improved and random variables should be also considered in the optimization approach. The optimization for the least cost seems to be of particular importance because of the increasing cost of both material components and sophisticated technologies applied to the composite materials.

REFERENCES

1. Brandt, A. M., On the optimization of the fiber orientation in cement based composite materials. *Proc. Int. Symp. 'Fiber Reinforced Concrete'*, Detroit, 1982, ed. G. C. Hoff. ACI SP 81-13, 1984, pp. 267–85.

2. Brandt, A. M., On the optimal direction of short metal fibres in brittle matrix composites. *J. Mater. Sci.*, **20** (1985) 3831–41.

3. Brandt, A. M. & Marks, M., Optimization of the material structure and composition of cement based composites (in Polish). *Proc. 38th Conf. in Civ. Engng, Vol. 3*. Krynica, 1992, pp. 7–12.

4. Brandt, A. M. & Marks, M., Optimization of cement based composites. In *Proc. Int. Conf. 'Concrete 92'*, Tehran 1992, pp. 429–41.

5. Brandt, A. M., Glinicki, M. A. & Marks, W., Optimization of cement based composites reinforced with carbon fibres. In *Proc. 2nd Int. Symp. 'Textile Composites in Building Construction', part 1*. Pluralis, Lyon, 1992, pp. 17–28.

6. Marks, W. & Potrzebowski, J., Multicriteria optimization of structural concrete mix. *Civ. Engng Arch.*, **34** (4) Warsaw, 1992 (in press).

A simplified tensile damage analysis method for composite laminates using a quasi-three-dimensional model

Tsuyoshi Nishiwaki,[a] Atsushi Yokoyama,[b] Zen-ichiro Maekawa,[c] Hiroyuki Hamada,[c]
Yoshinori Maekawa[d] & Sadaki Mori[a]

[a]ASICS Corp., Takatsukadai, Nishi-ku, Kobe, Japan
[b]Faculty of Education, Mie University, Kamihamacho, Tsu, Mie, Japan
[c]Faculty of Textile Science, Kyoto Institute of Technology, Matsugasaki, Sakyo-ku, Kyoto, Japan
[d]Faculty of Information Science, Osaka Sangyo University, Nakakakiuchi, Daito, Osaka, Japan

Measurement of the strength of laminated composites is very difficult because their failure processes imply various failure modes, which are, for example, an interlaminar delamination, a destruction of matrix and an interfacial fracture between fiber and matrix. However, that strength is one of the most important characteristics in structural design using laminated composites. Hence we try a fractural progress analysis of laminated composites using a quasi-three-dimensional analysis method under a tensile load. The quasi-three-dimensional model is constructed of shell elements and beam elements which represent fiber and matrix respectively. The fractural progress analyses of the laminated composites are carried out to evaluate this proposed model. The precision is very good. Therefore we confirm that this proposed model can simulate a transverse crack and an interlaminar delamination.

INTRODUCTION

There is considerable interest in many industries in the use of carbon-reinforced plastics as substitutes for the conventional metallic materials. This is because of the benefits of high specific strength and specific stiffness. The other advantages such as high corrosion resistance and design flexibility are added attractions. Particularly a laminated composite fabricated from unidirectional reinforced prepregs is widely used. Therefore we can read many reports for experimental estimation of their characteristics. The tensile strength is considered to be one of the most important factors in structural designs and estimation of tensile strength is not very difficult. However it is very difficult for experiments to consider a situation of a damage process, the effects of fiber and matrix and interface on the damage process. Moreover the estimation of a critical tensile load for a laminated composite with holes is more difficult because of stress concentration in the vicinity of the hole.[1] Accordingly the consideration of the tensile fractural mechanism by using the finite

element method is an important guide to the design of structures with laminated composites. The use of three-dimensional solid elements is considered to be most proper for the simulation of the behaviors of laminated composites since the behaviors have complex three-dimensional deformations with Poisson's effect. Therefore the simulation of the fractural process of laminated composites by using a three-dimensional element requires a very small element and a huge number of elements, because the fractural process consists of local failures such as interlaminar delamination. On the other hand, assuming the laminated composite as a single equivalent stiffness plate by means of Classical Lamination Theory, we cannot simulate the in-layer fracture and the interlaminar delamination separately. Hence we need to consider a new numerical model by constructing shell and beam elements which represent fiber and matrix respectively. And we call this model the quasi-three-dimensional model. We reported that the quasi-three-dimensional model is effective for the estimation of various static stiffnesses of the virgin laminated composites. Moreover we con-

firmed that the quasi-three-dimensional model was appropriate for damaged laminates enough to simulate the eigen-frequencies by deleting beam elements. In this study we try to estimate the tensile strength of fair types of quasi-isotropic CFRP plates. We also investigate the estimation of tensile strength for holed CFRP plates.

QUASI-THREE-DIMENSIONAL MODEL

As already mentioned, conventional models are not good enough to simulate the strengths of laminated composites. The main reason is that the laminated composite is modeled by assuming it to be a homogeneous object though it has a heterogeneous nature. Therefore one of the aims of our new numerical model is to take into account the heterogeneity of laminated composites. Our proposed model is constructed of orthotropic shell elements and isotropic beam elements, which represent fiber and matrix respectively.

Figure 1(a) shows a cross-section of single layer of the laminated composite. The cross-section is usually modeled as a homogeneous material. However according to our concept, this cross-section is considered to be heterogeneous as shown in Fig. 1(b). Namely we divide each layer into a fiber area and two resin areas. In the fiber area of Fig. 1(b), we assume that the array of fibers is hexagonal. By means of this assumption, the fiber fraction V_f is:

$$V_f = \frac{\pi}{2\sqrt{3}} \left(\frac{r}{R} \right)^2 \tag{1}$$

where $2R$ is the distance between fiber and fiber, and $2r$ is the diameter of the fiber. When R is equal to r in eqn (1), the fiber volume fraction V_f becomes the maximum value V_{fmax}. And V_{fmax} is equal to 0·907.[3] Thus we model the fiber area of orthotropic shell elements whose V_f is 0·907 and the resin area of isotropic beam elements whose V_f is 0. In this case the thickness of the shell elements in the individual plies h1 is:

$$h1 = h0 \times \frac{V_{f0}}{0·907} \tag{2}$$

where h0 is the thickness of the ply, and V_{f0} is the fiber volume fraction in the ply under consideration. The material properties of the shell and the beam elements used in our proposed model are obtained by means of Tsai's equation[4] and a hand-

book[5] respectively. Figure 2 shows our proposed model, known as the quasi-three-dimensional model. In Fig. 2 the distance between each ply is equal to the thickness of each ply h0 because the shell elements are placed on the neutral surface of each ply. Then we connect the shell elements with the beam elements along the thickness direction in order to produce an interlamina. The material properties of these beam elements correspond to the resin used. Figure 3 shows a top figure of the quasi-three-dimensional model. As shown in Fig. 3 the beam elements have various cross-sections depending on their positions. Figure 4 shows a quasi-three-dimensional model of the eight-layer laminate. Using a quasi-three-dimensional model, we hope that the calculation time is very short as compared with that of the three-dimensional analysis because the quasi-three-dimensional model need hardly consider the aspect ratio.
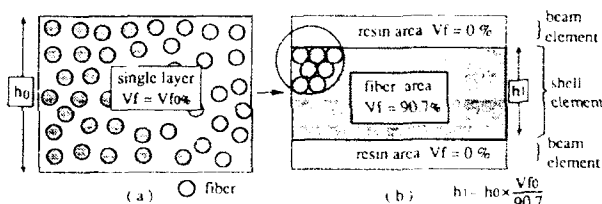
Fig. 1. Basic concept for quasi-three-dimensional model.

Composite Laminate (4 layers)   Quasi-3Dimensional model
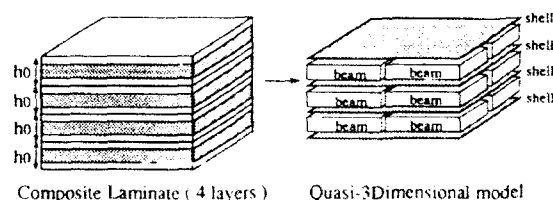
Fig. 2. Example of making quasi-three-dimensional model.

O Beam Element   Shell Element
                Sectional Area (Beam)
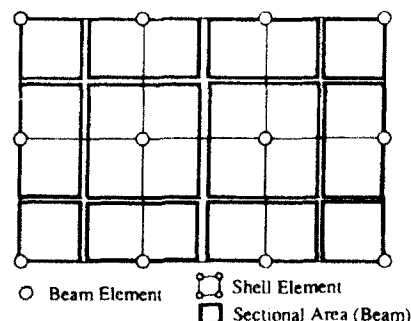
Fig. 3. Top figure of quasi-3-dimensional model.
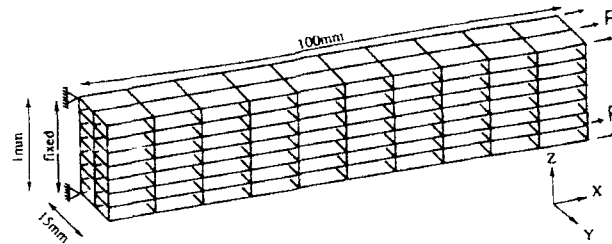
Fig. 4. Mesh division of virgin laminate.

TENSILE DAMAGE ANALYSIS FOR VIRGIN LAMINATES

Analysis procedure

The CFRP plates analyzed in this study were set up to form an eight-layer quasi-isotropic plate. The stacking sequences were of four kinds as shown in Table 1. The overall length of the model was 100 mm, the width 15 mm and the thickness 1 mm. On the other hand, we carried out an experiment to investigate the appropriateness of our quasi-three-dimensional analyses. The specimens tested were fabricated from unidirectional prepregs. These were supplied by TOHO-rayon and consisted of 'HTA-7' carbon fiber embedded in common epoxy resin 'No. 114'. The fiber volume fraction (V_f) was equal to 57% constantly.

Figure 4 shows the quasi-three-dimensional model of the virgin laminated composite used in this study. Here the X, Y and Z axes show the loading, width and thickness direction, respectively. The load condition is that the outermost layers (first and eighth layers) are tensioned by a load incremental method. And we calculate the components of the normal and shear stresses separately with every load increment. Figure 5 shows the analytical results for an A-type laminated composite. Two kinds of failures appear in the quasi-three-dimensional model with an increase in the tensile load. At first, when the transverse stress value σ_1 on 90° layers reaches the transverse strength F_t with $V_1 = 90.7\%$ (point A in Fig. 5),[3] a failure called a 'transverse crack' appears. Also this point is usually called the 'knee-point'. We define the tensile stress on point A as the 'first analytical failure stress'. We must consider that the redistribution of the stress field in the laminated composite is caused by the transverse crack. Accordingly after the tensile stress reaches the first failure stress, we continue the analysis by reducing the transverse elastic

Table 1. Stacking sequence

	Type A	Type B	Type C	Type D
8th layer	0 deg.	90 deg.	45 deg.	45 deg.
7th layer	90 deg.	0 deg.	−45 deg.	−45 deg.
6th layer	45 deg.	45 deg.	0 deg.	90 deg.
5th layer	−45 deg.	−45 deg.	90 deg.	0 deg.
4th layer	−45 deg.	−45 deg.	90 deg.	0 deg.
3rd layer	45 deg.	45 deg.	0 deg.	90 deg.
2nd layer	90 deg.	0 deg.	−45 deg.	−45 deg.
1st layer	0 deg.	90 deg.	45 deg.	45 deg.
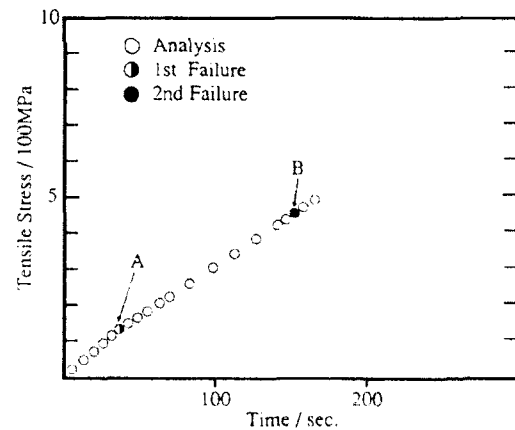
Fig. 5. Analytical result for type A.

modulus on 90° layers E_T^{90} to the resin elastic modulus E_m. As the tensile load increases, the beam elements representing the interlamina begin to yield (point B in Fig. 5). Here we apply 'Von-Mises law' to the yield condition of the beam elements.[6] When the first of the beam elements yields, we define the tensile stress as 'second analytical failure stress'. Moreover we investigated the yielding progress of the beam elements after the second failure stress. On the other hand, we carried out a tensile experiment in order to evaluate the appropriateness of the above analytical method. For the experiment, we used an
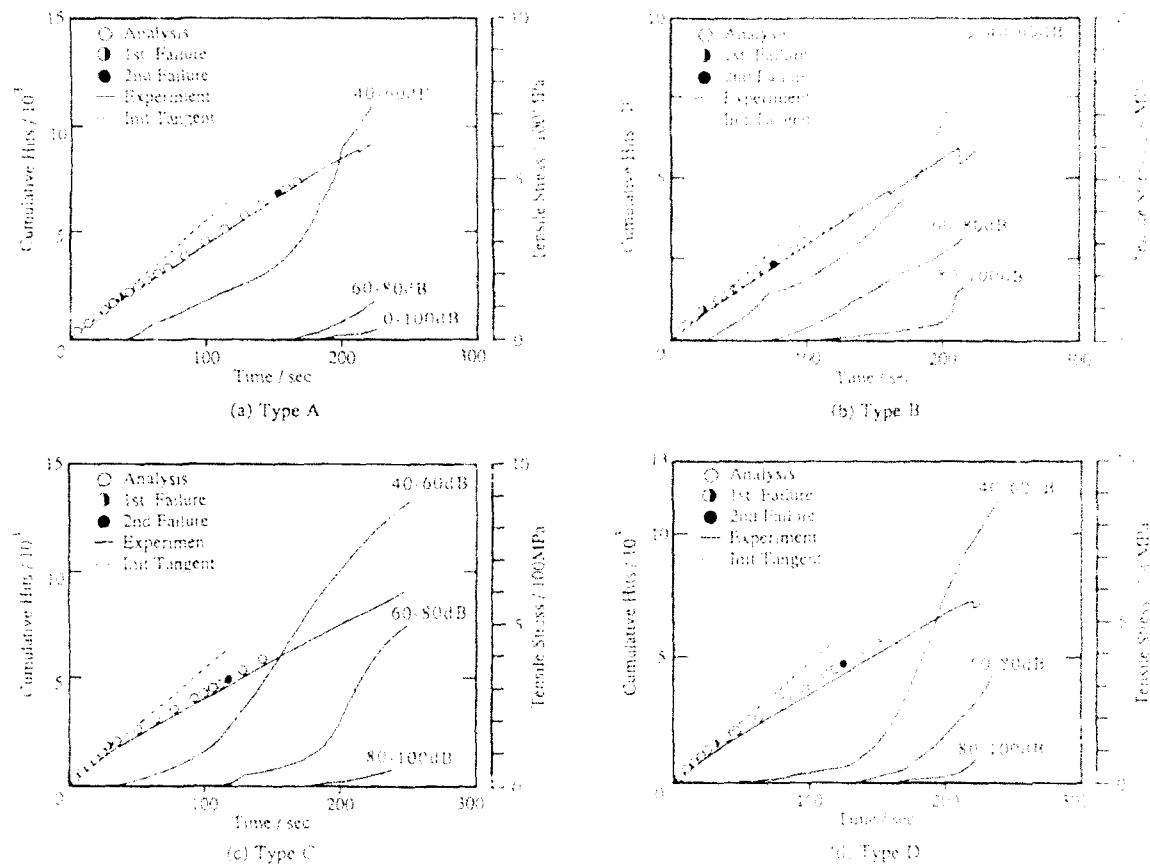
Fig. 6. Comparison of analytical and experimental results for virgin laminate.

INSTRON testing machine with computer control, and was carried out an Acoustic Emission measurement with a 40 dB threshold at the same time. For the AE results, we measured the cumulative hit counts at low amplitude (40–60 dB), middle amplitude (60–80 dB) and high amplitude (80–100 dB) separately.

Table 2. Stress values of yielded beam elements at first analytical failure stress

Type	Position of the 1st yielded beam	σ_y MPa	τ_y MPa
A	45/90 interlamina	−1·16	14·12
B	90/0 interlamina	−1·14	14·13
C	0/90 interlamina	−5·40	13·80
D	−45/90 interlamina	−3·21	14·02

Results and discussion

Figure 6 shows both analytical and experimental results. In Fig. 6, it is evident that there is good agreement between the analytical and experimental stress-strain behavior of virgin laminates. The first analytical failure stress is in accordance with experimental positions of the 'knee-point' for all four types; and they are associated with the start of the low-amplitude events for the AE measurements. These events indicate the occurrence of micro-cracks in the resin region. We decided that the transverse crack appears at the first analytical failure stress level, because of the

agreement with the starting of the low amplitude events and the first analytical failure stress level. For A–D types, we confirm that the first analytical failure stress values are almost constant at 131·0, 120·0, 128·4 and 128·5 MPa respectively. Then the middle-amplitude events appear at the second analytical failure stress for all four types. These events indicate interlaminar delamination. Accordingly we confirm that the yielding of beam elements corresponds to interlaminar delamination because of the agreement between the events and the second analytical failure stress level. Table

(1) at 456 MPa Loading   (2) at 484 MPa Loading

(3) at 497 MPa Loading   (4) at 525 MPa Loading

▮ Yielded Beam Element
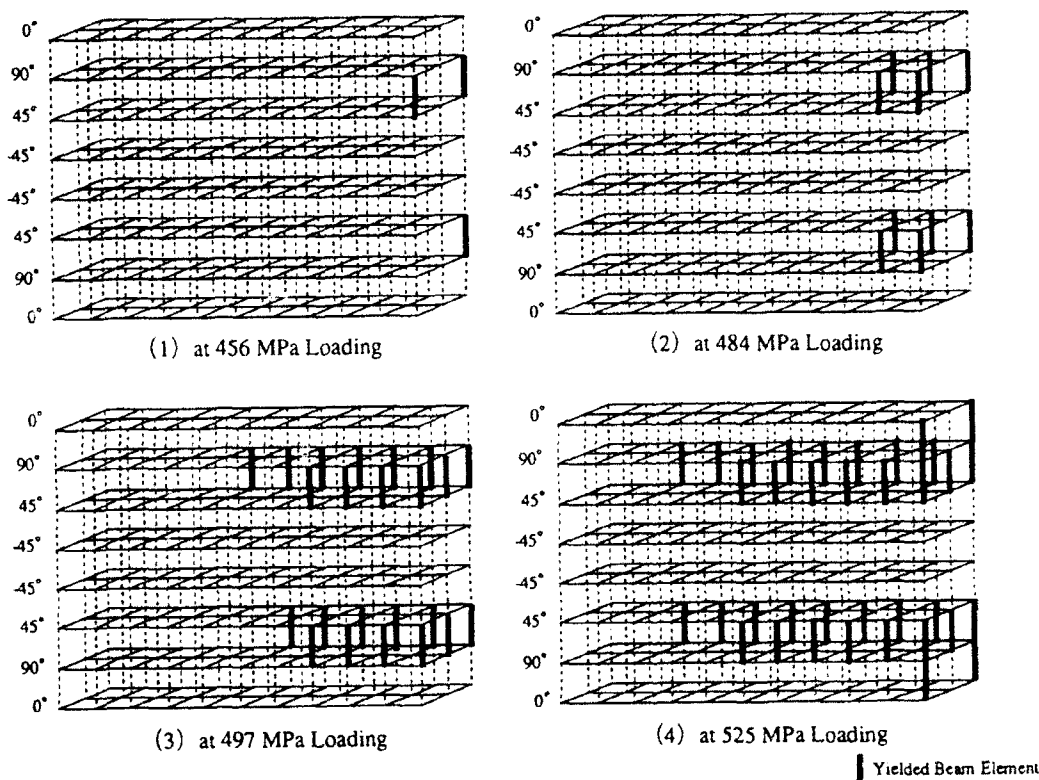
Fig. 7. Yield progress for virgin type A.

2 shows the stress values of the first yielded beam elements and the positions of their beam elements under the second analytical failure stress level. Judging from Table 2, the yielding of beam elements is controlled by shear stress and the positions of yielding are the interlaminas connected with 90° layers for all types. Figure 7 shows a series of features of beam element yielding progress in four stages for A type. Judging from Fig. 7. the yielding starts at the edge of the 90/45 interlamina, then the yielding spreads in the same interlamina in proportion to the tensile stress increase. In consequence of modeling the fiber and matrix separately such as in the quasi-three-dimensional model, we confirm that the different fractural phenomena such as the transverse crack and the interlaminar delamination can be simulated at the same time. On the other hand, the partition of the different fractural phenomena may be impossible using the conventional solid elements because the use of them indicates that the laminated composite is assumed to be homogeneous. Therefore we believe firmly that application of the quasi-three-dimensional model to tensile damage analyses is effective.

TENSILE DAMAGE ANALYSIS FOR HOLED LAMINATE

As already mentioned, we can simulate the transverse crack and interlaminar delamination for virgin laminates using the quasi-three-dimensional model. In this section, we try to apply this model to a holed laminate whose strength is more difficult to measure as compared with the virgin laminate.[8-11] Because the holed laminate has variable stress values in each layer. The objects analysed are the same laminated composites as shown in Table 1 with $\phi = 6$ mm center hole. The quasi-three-dimensional model of the holed laminate is shown in Fig. 8.

Results and discussion

Figure 9 shows both the analytical and experimental results for holed laminates. We confirm that the first and second analytical fractural stress levels are interrelated with the experimental occurrences of the 'knee-point' and middle-amplitude AE events, respectively. Moreover Fig. 10 shows a series of beam elements yielding progress

in three stages for an A type. Judging from Fig. 10, we confirm that beam element yielding starts at the edges of the center hole along the direction transverse to the loading in the 90/45 interlamina.

Then, as the tensile load increases, the yielding propagates along the loading direction. At the second analytical fractural stress level, the start of beam element yielding is in the 90/45, 90/0, 0/90 and −45/90 interlaminas for A-D types, respectivley. These interlaminar positions are the same as those for virgin laminates. Judging from the above results, we confirm the quasi-three-dimensional model is effective for the estimation of damage progress in holed laminates.

CONCLUSION

Using the quasi-three-dimensional model we performed tensile stress analyses and both analytical and experimental results were compared. The results are summarized as follows:

(1) We could simulate the stress–strain relationship up to the second analytical fractural stress level for CFRP virgin laminates.

Fig. 8.   Mesh division of holed laminate.

(a) Type A

(b) Type B

(c) Type C
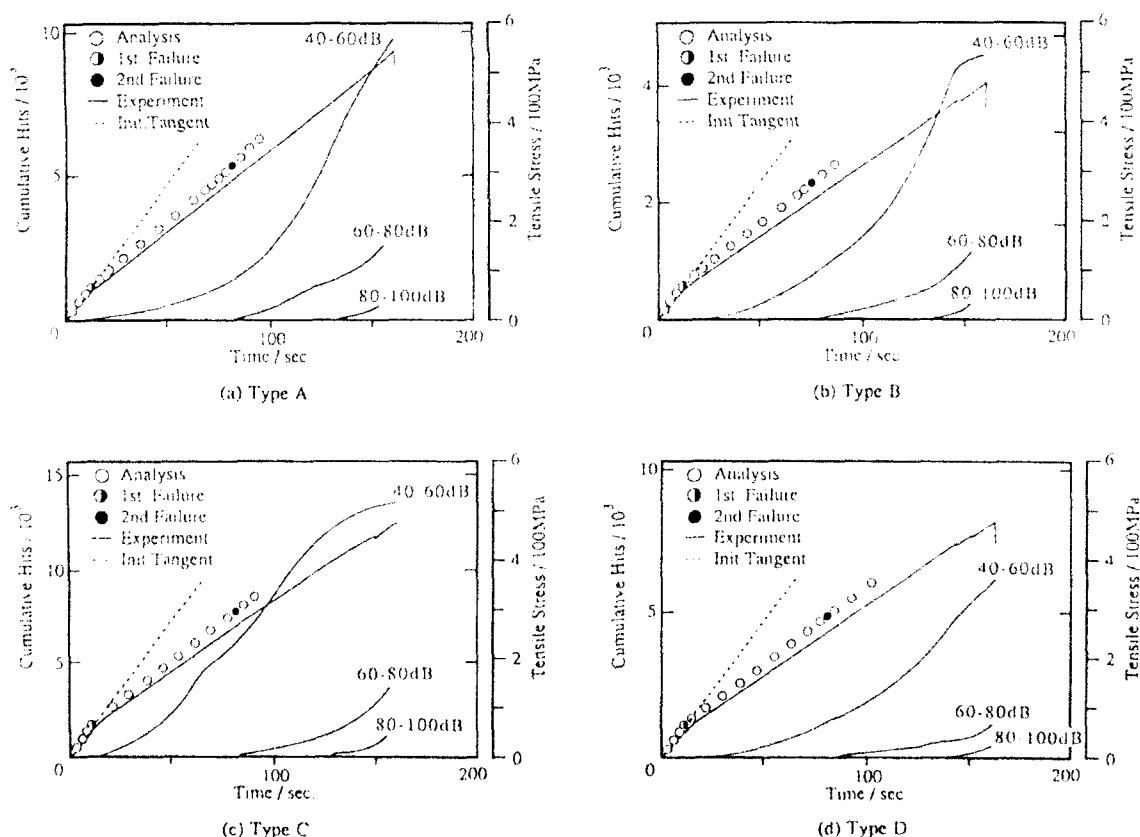
(d) Type D

Fig. 9.   Comparison of analytical and experimental results for holed laminate.
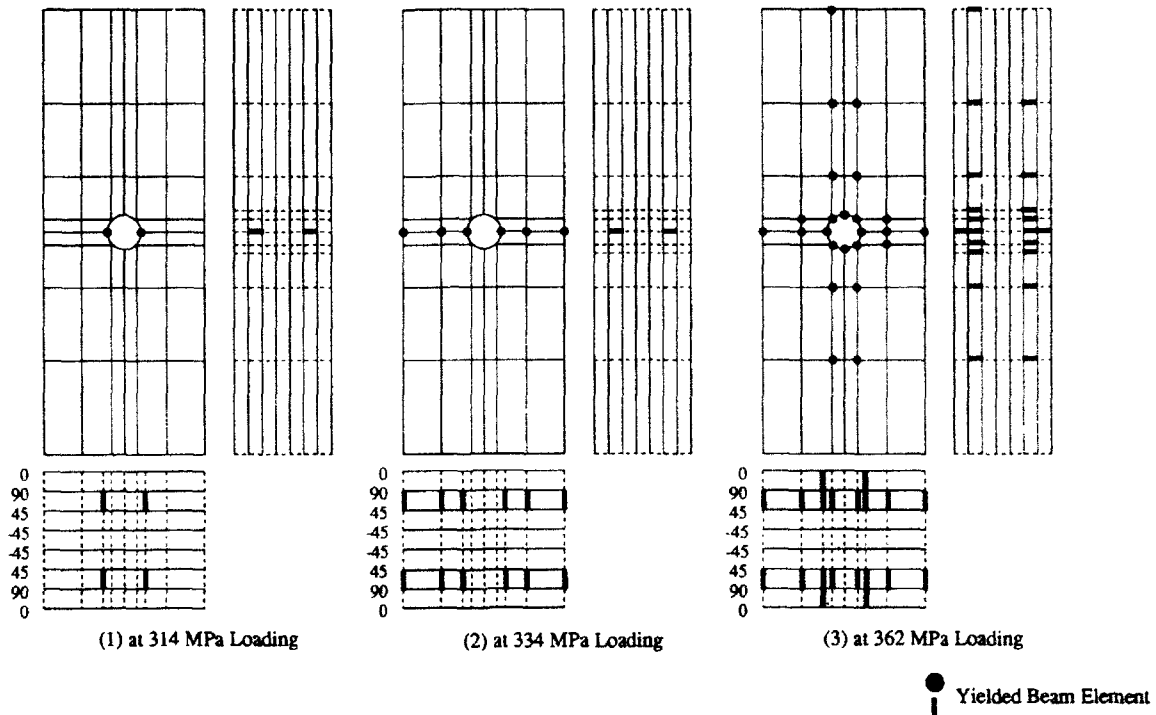
Fig. 10. Yield progress for holed type A.

Also the transverse crack, interlaminar delamination and interlaminar damage propagation could be estimated.

(2) We could also simulate the stress–strain relation of holed CFRP laminates with stress concentration.

REFERENCES

1. Pipes, R. B., *J. Comp. Mater.*, **13** (1979) 148–62.
2. Nishiwaki, T. & Yokoyama, A., A quasi-3-dimensional vibration analysis method for composite laminates. *J. Soc. Mech. Engrs*, **58-554A** (1990) 1895–9.
3. Hull, D., *An Introduction to Composite Materials*. Cambridge Solid State Science Series, 1987, pp. 60–4.
4. Jones, R. M., *Mechanics of Composite Materials*. McGraw-Hill, New York, 1975, pp. 173–86.
5. Ito, K., *Plastic Data Handbook*. Kogyo Chosakai Publishing Co. Ltd, 1980, pp. 308–29.
6. Owen, D. R. J. & Hinton, E., *Finite Element in Plasticity*. Pineridge Press, 1987, pp. 227–38.
7. Ohtsu, M., *Characteristic and Theory for Acoustic En s-sion*. Morikita Press, 1986, p. 179.
8. Lin, J. K. & Ueng, C. E. S., Stress concentrations in orthotropic laminates containing two elliptical holes. *Compos. Struct. 4*, **2** (1987) 2.419–2.430.
9. Sundaresan, M. J. & Lakshminarayana, H. V., Stress concentration around circular cutouts in laminated composites. *J. Aeronaut Soc. India*, **35** (1)(1983) 13–22.
10. Marshall, I. H., Little, W. & El-Tayeby, M. M., Membrane stress distributions in post-buckled composite plates with circular holes. *Compos. Struct.*, *4*, **5** (1987) 5.57–5.68.
11. Burns, S. W. & Herakovich, C. T., Failure modes for compression loaded angle-ply plates with holes. *Compos. Struct.*, *4* **2** (1987) 2.175–2.191.

A reduced basis approach to quantifying damage dependent dynamic response of laminated composite structures

John J. Engblom & Qinghui Yang

Mechanical and Aerospace Engineering Department, Florida Institute of Technology, Melbourne, Florida 32901, USA

A finite element (FE) based formulation is utilized to represent the damage-dependent response of laminated composite structures. An internal-state-variable (ISV) approach provides a definition of the stiffness reduction caused by intralaminar crack propagation at the ply level. These ISVs are combined with simple stress criteria to accommodate ply property changes caused by fiber fracture, fiber microbuckling and interior delaminations. A set of orthogonal Ritz vectors are chosen as basis vectors to transform the dynamical equations of motion to a reduced coordinate space. The reduced basis form of the equations provides significant numerical efficiencies, especially for large ordered systems. Furthermore, damping and its variation with damage can be generally represented in any number of vibratory modes. The Newmark integration operator is used to solve the dynamic equations of motion, and equilibrium iterations are performed in each incremental time step to assure convergence. Results are given for laminated beam and plate geometries subjected to dynamic loads.

INTRODUCTION

When fiber-reinforced laminated composite structures are subjected to either static or time-varying loading conditions, a multitude of damage modes can initiate and propagate. These modes may, for example, include some combination of matrix (intralaminar) cracking, fiber fracture, fiber microbuckling and delamination (interlaminar cracking). A general capability to model such damage modes at the macro-mechanics level would provide a much needed capability in the optimal design of composite structures. Furthermore, such modeling capability would be required in many 'smart structures' applications, e.g. those aimed at sensing the structural integrity of a component. In the present finite element (FE) formulation, an internal state variable (ISV) approach is used to represent the smooth transition in ply stiffness properties due to intralaminar crack propagation. These properties vary smoothly due to the nature of intralaminar crack distributions, i.e. as cracks develop in a given ply the material between cracks remains bonded to adjacent plys resulting in a gradual reduction in moduli and Poisson's ratio values. The ISV ply-level matrix

cracking model, incorporated in the FE formulation, is an extension of Talreja's laminate damage model,[1] i.e. extended to treat variation in the constitutive properties at the ply rather than at the laminate level. In combination with the ISVs, stress criteria, e.g. those developed by Hashin,[2] Lee[3] and Greszczuk,[4] are utilized to accommodate ply property changes due to fiber fracture, fiber microbuckling and interior delaminations. A set of orthogonal Ritz vectors are chosen as basis vectors to transform the dynamical equations of motion to a reduced basis.[5,6] Response of the full model is obtained as a re-expansion of the reduced system solution. The approach is similar to the modal superposition method, except that the basis vectors are the Ritz vectors proposed by Wilson *et al.*[7] These vectors have some advantages, e.g. they can be generated with much more computational efficiency than can the eigenvectors (mode shapes), which is especially significant for large ordered systems. Furthermore, unlike eigenvectors, Ritz vectors can account for the spatial load distribution. Not only does this reduced basis approach provide an efficient incremental solution of the dynamic equations of motion, it also provides an effective numerical

method for representing damping and its variation with damage, in any number of modes. The proposed approach, therefore, does not have the limitation associated with proportional damping, i.e. that only two modal damping factors can be prescribed independently. The Newmark integration operator is used to solve for the dynamic response in the reduced coordinate space, and equilibrium iterations are performed within each incremental time step to assure convergence. It is important to emphasize that the damage model presented herein requires a significant experimental database. The ISV approach requires that matrix cracking thresholds and saturation levels be established and related to ply stresses. Unidirectional ply properties must also be available, i.e. tension, compression and shear strengths. When damping properties are an important consideration, both baseline modal damping parameters and changes related to damage should be measured for a particular laminate geometry and loading condition of interest.

UNREDUCED EQUATIONS OF MOTION

The 'unreduced' equations of motion governing the dynamical system can be given in the incremental form

$$M\Delta\ddot{U}_{T+\Delta T} + C_T\Delta\dot{U}_{T+\Delta T} + K_T\Delta U_{T+\Delta T}$$
$$= \Delta P_{T+\Delta T} + I_T \qquad (1)$$

Here, M is the mass matrix, C_T is the equivalent viscous damping matrix at time T, K_T is the stiffness matrix evaluated at time T, $\Delta U_{T+\Delta T}$ is the incremental displacement vector, $\Delta P_{T+\Delta T}$ is the incremental applied load vector at time $T+\Delta T$ and I_T is the residual (unbalanced) load vector. The dot and double-dot superscripts on ΔU represent the first and second derivatives of the incremental displacement vector with respect to time, i.e. incremental velocity and acceleration vectors, respectively. Furthermore, the residual load vector relates to the equilibrium balance at time T and is given as

$$I_T = P_T - M\ddot{U}_T - C_T\dot{U}_T - F_T \qquad (2)$$

where P_T is the applied load vector at time T, F_T is the vector of forces corresponding to the internal element stresses at time T and the time derivatives of the displacement vector U_T represent the velocity and acceleration vectors evaluated at time T. Note that the number of equations

in (1) is simply equal to the total number of unrestrained degrees of freedom in the FE model. Through use of the Newmark integration scheme,[8] eqns (1) can be written in a form appropriate for solution of the incremental displacement vector, i.e.

$$K_T^*\Delta U_{T+\Delta T} = \Delta P_{T+\Delta T}^* \qquad (3)$$

where the effective stiffness matrix K_T^* is defined as

$$K_T^* = K_T + \frac{2}{\Delta T}C_T + \frac{4}{\Delta T^2}M \qquad (4)$$

and the effective incremental load vector has the form

$$\Delta P_{T+\Delta T}^* = \Delta P_{T+\Delta T} + I_T$$
$$+ M\left(\frac{4}{\Delta T}\dot{U}_T + 2\ddot{U}_T\right) + 2C_T\dot{U}_T \qquad (5)$$

where the term ΔT in these equations represents the incremental time step used in the solution process.

DAMAGE MODEL

In the present formulation, damage is accounted for at the layer level. Note that the term 'layer' herein represents a ply or a subset of adjacent plies of equal fiber orientation. Stress criteria[2-4] provide the numerical basis for reducing the appropriate ply properties for fiber fracture, fiber microbuckling and interior delaminations. The solution assumes step changes in ply properties when such failures are predicted. In combination with these stress failure criteria, the ISV representation[9] of intralaminar cracking takes the form of a smooth variation of the ply moduli and major Poisson's ratio as given below

$$E_2 = \frac{(1-D)}{(1-D_{TH})}E_2^o + \frac{(D-D_{TH})}{(1-D_{TH})}E_2^f$$

$$G_{12} = \frac{(1-D)}{(1-D_{TH})}G_{12}^o + \frac{(D-D_{TH})}{(1-D_{TH})}G_{12}^f \qquad (6)$$

$$v_{12} = \frac{(1-D^r)}{(1-D_{TH}^r)}v_{12}^o + \frac{(D^r-D_{TH}^r)}{(1-D_{TH}^r)}v_{12}^f$$

where E_2 is the transverse ply modulus, G_{12} the ply shear modulus and v_{12} the ply Poisson's ratio.

The r superscript represents the order of variation in v_{12}, and the o and f superscripts are indicative of the initial (undamaged) and final (crack saturated) properties, respectively. Note that D is a damage parameter which has significance in the range $D_{TH} < D < 1$. Here, D_{TH} is the threshold value of the damage parameter, below which no matrix cracking has occurred in the ply of interest. The ply damage parameter is implicitly related to both average crack density and crack dimension. Rather than attempt to directly account for these crack characteristics, the approach taken here is to utilize the ISV formulation to define the form of smooth ply moduli variation and then to allow the damage parameter to depend on the state of stress in the ply. This approach requires that the threshold value D_{TH} be determined from experiment, i.e. based on the observance of crack initiation in the ply of interest, and relating such observation to the state of ply stress. Additionally, a ply constraint factor should be determined if needed to adjust the damage parameter D to have a value of 1 at crack saturation. The dependence of D on stress state is assumed to be based on the Hashin (matrix cracking) stress criteria.[2] For example, in the case of in-plane tensile loading the damage parameter takes the form

$$D = \alpha \left[\left(\frac{\sigma_{22}}{\sigma_{22MAX}} \right)^2 + \left(\frac{\sigma_{12}}{\sigma_{12MAX}} \right)^2 \right] \qquad (7)$$

where σ_{22} and σ_{12} are the in-plane transverse and shear stress in the layer. σ_{22MAX} and σ_{12MAX} are the in-plane transverse and shear failure stresses as obtained from unidirectional specimen tests and α is the ply constraint factor based on the experimentally determined ply stresses at matrix crack saturation. As previously noted, other forms of damage typically follow the intralaminar cracking and are accounted for in the present FE formulation at the layer level by the use of stress criteria.

NUMERICAL CONSIDERATIONS

The unreduced incremental equations (3) have been directly solved, using the Newmark integration scheme, with the damage effects on stiffness reduction included in the formulation.[10] Including the effects of damping in the direct solution of these unreduced equations, i.e. through definition of an equivalent viscous damping matrix C_I, can present significant numerical difficulties when modal damping parameters are to be used in

specifying C_I. A classical approach is to assume that C_I is proportional to mass and/or stiffness, in which case at most two modal damping parameters can be matched with experimental data. An alternative approach, which allows for any number of modal damping parameters to be represented in the solution, involves definition of the equivalent viscous damping matrix in the following manner.

$$C_I = M \Phi [2\zeta\omega] \Phi^T M \qquad (8)$$

where Φ is a matrix of eigenvectors (mode shapes), which are orthogonalized with respect to the mass matrix M. The matrix in brackets is diagonal and includes the modal damping parameters ζ and the undamped natural frequencies ω. Also, the T superscript simply implies the transpose of a matrix. It is apparent from the matrix form given in (8) that this form of equivalent damping yields the appropriate modal damping parameters when eqns (3) are transformed to the reduced modal coordinate space. That is, the equivalent viscous damping matrix in (8) can be transformed to modal coordinates via the transformation below

$$\Phi^T C_I \Phi = \Phi^T M \Phi [2\zeta\omega] \Phi^T M \Phi = [2\zeta\omega] \qquad (9)$$

Note that the matrix form of (9) is diagonal, i.e. each term relates to damping in each of the independent modes of vibration. Unfortunately, this approach to a more generalized definition of damping has a serious shortcoming when direct solutions of eqns (3) are of interest, i.e. the equivalent viscous damping matrix given in (8) yields a 'full' rather than 'banded' damping matrix. This fact presents a formidable storage problem for large ordered models when a direct solution technique is employed to solve the unreduced equations of motion (3). Note that the mass and stiffness matrices are banded and, therefore, banded solvers are normally utilized in obtaining direct solutions. A representation of equivalent viscous damping similar to that given in (8) is utilized in the present reduced basis formulation.

REDUCED EQUATIONS OF MOTION

In order to include the effects of damping in any number of modes and to avoid numerical difficulties, equations of motion (3) are transformed to reduce coordinate space. Displacement increment ΔU, of order n, can be represented by m linearly independent basis vectors via the coordin-

ate transformation below

$$\Delta U = \psi \Delta \eta \tag{10}$$

The basis vectors ψ chosen in this work are the Ritz vectors which have been shown to have great utility in obtaining solutions for highly nonlinear dynamic systems.[5,6] Here, $\Delta \eta$ represents incremental displacements in reduced coordinates. Note that typically $n \gg m$, i.e. the set of governing equations in the reduced coordinate space (m) is quite small relative to the number of degrees of freedom (n) of the finite element model. Parenthetically, the Ritz vectors can be combined with eigenvectors and even with the derivatives of basis vectors.[5,6] Using the coordinate transformation given in (10), eqns (3) can be transformed to the reduced form

$$\tilde{K}_T^* \Delta \eta_{T+\Delta T} = \Delta \tilde{P}_{T+\Delta T}^* \tag{11}$$

where the reduced effective stiffness matrix has the form

$$\tilde{K}_T^* = \tilde{K}_T + \frac{2}{\Delta T} \tilde{C}_T + \frac{4}{\Delta T^2} \tilde{M} \tag{12}$$

and it follows that the reduced stiffness, damping and mass matrices have the form

$$\tilde{K}_T = \psi^T K_T \psi$$
$$\tilde{C}_T = \psi^T C_T \psi \tag{13}$$
$$\tilde{M} = \psi^T M \psi = I$$

where ψ contains the Ritz basis vectors and I is the identity matrix, i.e. M orthogonality is enforced. Additionally, the reduced effective incremental load vector is obtained from the matrix multiplication given below

$$\Delta \tilde{P}_{T+\Delta T}^* = \psi^T \Delta P_{T+\Delta T}^* \tag{14}$$

If it is assumed that the unreduced equivalent viscous damping matrix takes the matrix form

$$C_T = M \psi \phi [2 \zeta \omega] \phi^T \psi^T M \tag{15}$$

where ϕ represents a sub-set of the eigenvectors (mode shapes) in reduced coordinate space, it follows that the reduced damping matrix defined in (13) would yield appropriate damping coefficients in 'reduced' modal coordinate space, i.e.

$$\phi^T \tilde{C}_T \phi = \phi^T \tilde{M} \phi [2 \zeta \omega] \phi^T \tilde{M} \phi = [2 \zeta \omega] \tag{16}$$

which is analogous to the expression in (9), except that here the diagonalized damping terms are based on the 'reduced' eigenvectors. When experimentally determined modal damping coefficients ζ are assigned to each of the reduced coordinates,

care must be taken to assure that the appropriate order is defined, i.e. the Ritz vectors do not simply represent an ordered set of eigenvectors (modes). In the reduced basis approach, therefore, it is not necessary to assemble and to store the unreduced damping matrix C_T. The reduced effective stiffness matrix simply includes a reduced equivalent viscous damping matrix of the form

$$\tilde{C}_T = \phi [2 \zeta \omega] \phi^T \tag{17}$$

Of course, C_T does appear on the right-hand side of (11), i.e. in the reduced effective incremental load vector, see (5) and (14). However, the numerical procedure utilized in this work avoids defining C_T explicitly by combining the vector term in (5) involving C_T with the definition of C_T in (15). This gives

$$2 C_T \dot{U}_T = 2 M \psi \phi [2 \zeta \omega] \phi^T \psi^T M \dot{U}_T \tag{18}$$

and if the following definition is used

$$\Gamma = M \psi \tag{19}$$

eqn (18) simplifies to

$$2 C_T \dot{U}_T = 2 \Gamma \phi [2 \zeta \omega] \phi^T \Gamma^T \dot{U}_T \tag{20}$$

so that the matrix array Γ of order $n \times m$ must be computed, and a sequence of matrix multiplications performed in obtaining the vector defined in (18). Fortunately, the full matrix C_T of order $n \times n$ need not be explicitly defined. On the basis of the formulation presented here, the reduced basis approach provides both a numerically efficient method for including damping in the dynamic solution, as well as a general approach, i.e. any number of modal damping factors can be represented. Furthermore, variation in damping with damage can be included in the incremental solution by allowing the damping factors to vary with damage. Both baseline and 'damage related' values of the modal damping parameters would be needed for a particular laminate geometry and loading condition of interest. Simple pre-damaged specimen geometries can be subjected to sinusoidally varying axial/bending loads to obtain useful damping data. The approach taken here is to allow the damping parameters to vary linearly on the basis of such experimentally determined values.

RESULTS

Results are presented for the damage dependent damped-transient response of selected composite

beam and plate geometries. For the composite beam solutions, the material is a graphite/epoxy with the moduli and strength properties given below

$E_1 = 138$ GPa; $E_2 = 10.6$ GPa;

$G_{12} = G_{13} = G_{23} = 6.4$ GPa

$\nu_{12} = \nu_{13} = \nu_{23} = 0.30$;

$\sigma_{11MAX} = 1500$ MPa;

$\sigma_{22MAX} = 41$ MPa (tension)

$\sigma_{22MAX} = 249.8$ MPa (compression);

$\sigma_{12MAX} = \sigma_{13MAX} = \sigma_{23MAX} = 67.4$ MPa

While for the composite plate solution, the material is a glass/epoxy with properties defined as

$E_1 = 41.7$ GPa; $E_2 = 13$ GPa;

$G_{12} = G_{13} = G_{23} = 3.4$ GPa

$\nu_{12} = \nu_{13} = \nu_{23} = 0.30$;

$\sigma_{11MAX} = 128.8$ MPa; $\sigma_{22MAX} = 46$ MPa (tension)

$\sigma_{22MAX} = 174.3$ MPa (compression);

$\sigma_{12MAX} = \sigma_{13MAX} = \sigma_{23MAX} = 44.8$ MPa

Comparisons are made between direct and reduced basis solutions in each of the following cases.

The first case considered is that of a simply supported beam with an aspect ratio of 50 (length/height); the beam has a laminate geometry of $[90_2, -30_2, 30_2, 0_2]_s$; and is modeled using eight shear deformable plate elements[11] along its length. The beam is excited by a centrally applied rectangular load pulse of short time duration, i.e. having a loading period equal to the eighth (undamaged) natural period of the model. Parameters utilized in the damage model are based on experiments and are defined as

$$E_2^t = G_{12}^t = \nu_{12}^t = 0; \ D_{TH} = 0.93; \ r = 2; \ \alpha = 1$$

Displacement and stress results are given in Figs 1 and 2 for the case of damage progression and no damping. Three curves are given, i.e. linear response (no damage), response based on using the direct solution, and response based on using the reduced basis (5 Ritz vectors) solution. It is clear that there is a significant difference between the linear and nonlinear (damage) results, and also that the reduced basis approach provides results in good agreement with those obtained from the direct solution. The damage exhibited in this case is in the form of matrix cracking in the outer 90° plies. Note that it has not been necessary to update the basis vectors in this case, as well as in the following cases, during the solution process.

Fig. 1. Displacement of simply supported $[90_2, -30_2, 30_2, 0_2]_s$ beam, without damping, load pulse, eighth period.
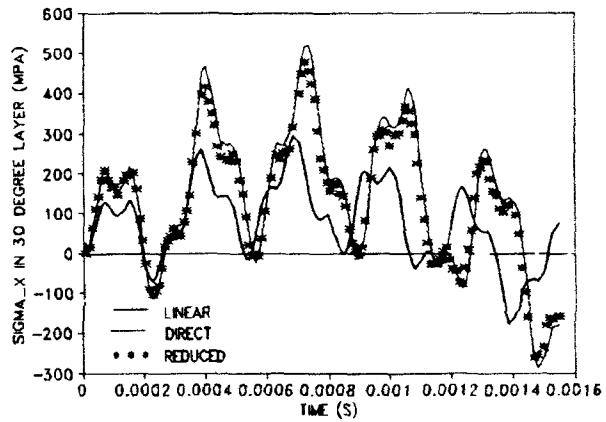
Fig. 2. Stress in 30° layer of simply supported $[90_2, -30_2, 30_2, 0_2]_s$ beam, without damping, load pulse, eighth period.

Of course, equilibrium iterations have been performed in each incremental time step in both the direct and the reduced basis solutions.

Figures 3 and 4 present similar results to those previously discussed; however, equivalent viscous damping is included in the linear and nonlinear (damage) cases. Baseline (undamaged) modal damping coefficients are specified for normal modes 1, 3, 5, 8 and 10 of the model, i.e. these modes are consistent with the subspace defined by the first five Ritz vectors. The baseline values for these coefficients are defined as

$\zeta_1^0 = 0.0175; \ \zeta_2^0 = 0.0309; \ \zeta_3^0 = 0.0823;$

$\zeta_4^0 = 0.166; \ \zeta_5^0 = 0.299$

where these coefficients are allowed to vary linearly with D (the matrix cracking damage parameter). Note also that the first two values of ζ and their variation are based on experiments with simple laminated beams of the present geometry.
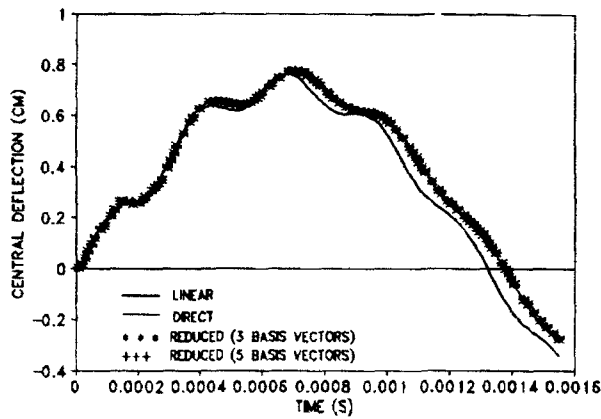
Fig. 3. Displacement of simply supported $[90_2,-30_2,30_2,0_2]_k$ beam, with damping, load pulse, eighth period.
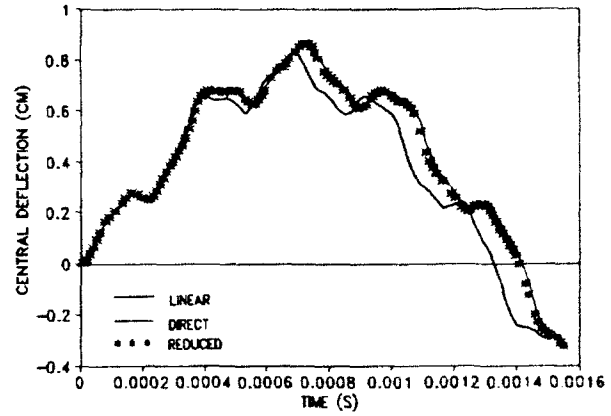

Fig. 5. Displacement of simply supported $[90_2,-30_2,30_2,0_2]_k$ beam, with damping, load pulse, fifth period.

Fig. 4. Stress in 30° layer of simply supported $[90_2,-30_2,30_2,0_2]_k$ beam, with damping, load pulse, eighth period.

Fig. 6. Stress in 30° layer of simply supported $[90_2,-30_2,30_2,0_2]_k$ beam, with damping, load pulse, fifth period.

and the higher three values are based on the proportional damping model, i.e.

$$\zeta_j = \frac{\alpha + \beta\omega_j^2}{2\omega_j} \qquad j = 1, m \qquad (21)$$

where α and β are the constants of proportionality relating damping to mass and stiffness, respectively. This approach is utilized to allow a comparison between the reduced basis and direct solutions. It is emphasized that while the direct approach is limited to this prescription of damping, i.e. limited to two independently defined modal damping factors, the reduced basis approach is not limited in this manner. As is apparent in Figs 3 and 4, the reduced basis approach gives excellent results for both displacements and stress. Comparison of the reduced basis results for three versus five basis vectors is quite interesting. The smaller number of Ritz
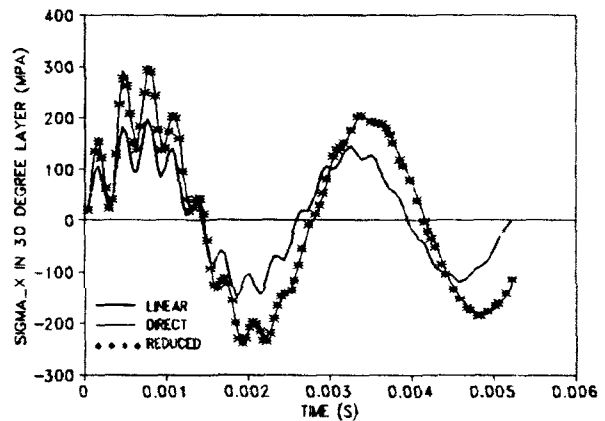
vectors gives poorer results in the first half cycle of stress response; but otherwise, the results are nearly identical for three versus five Ritz vectors.

Similar results are given in Figs 5 and 6 for the simply supported beam subjected to a rectangular load pulse of longer time duration, i.e. load period approximately equal to the fifth (undamaged) natural period. These direct and reduced basis (five Ritz vectors) results include both damage progression (matrix cracking) and damping. Again, the displacement and stress results obtained via the reduced basis approach are in excellent agreement with those obtained from the direct solution.

The final case considered is that of a simply supported square glass/epoxy plate with an aspect ratio of 20 (width/height); the plate has a laminate geometry of $[0,90,45,-45]_k$; and is modeled with four shear deformable elements in a quadrant. The plate is excited by a centrally applied
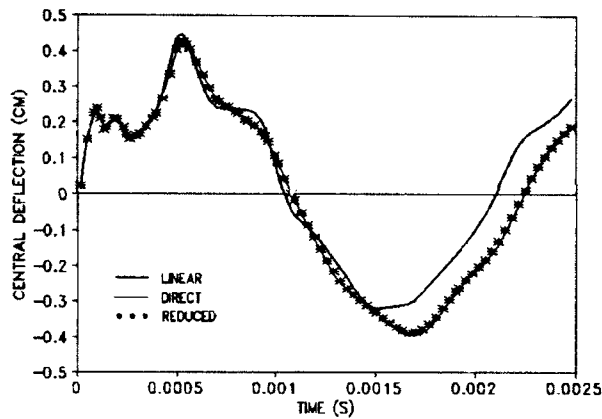
Fig. 7. Displacement of simply supported $[0,90,45,-45]_s$ plate, with damping, load pulse, tenth period.
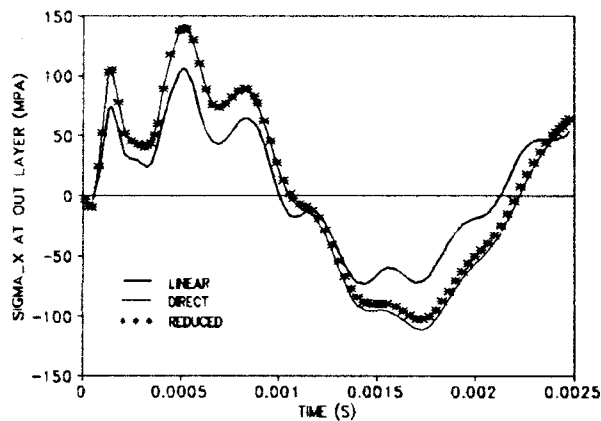
Fig. 8. Stress in outer layer of simply supported $[0,90,45,-45]_s$ plate, with damping, load pulse, tenth period.

rectangular load pulse of time duration about equal to the tenth (undamaged) natural period of the plate. The assumed damage model parameters are defined as

$$E_2^f = G_{12}^f = v_{12}^f = 0; \ D_{TH} = 0.45; \ r = 2; \ \alpha = 1$$

and the baseline damping factors for seven Ritz basis vectors are assumed to have the values

$$\zeta_1^0 = 0.0206; \ \zeta_2^0 = 0.0306; \ \zeta_3^0 = 0.0836;$$
$$\zeta_4^0 = 0.0337; \ \zeta_5^0 = 0.0549; \ \zeta_6^0 = 0.209; \ \zeta_7^0 = 0.117$$

As in the previous cases, these damping factors are allowed to vary linearly with the matrix cracking damage parameter. Displacement and stress results are given in Figs 7 and 8 for the plate model. In each of these figures, results are shown for damping included without damage and for the combination of damping and damage. Reduced basis results are again in excellent agreement with results obtained via the direct solution. While not presented here, residual dynamic properties can

be determined, e.g. shifts in natural frequencies due to damage.

CONCLUSIONS

Excellent results have been obtained using a reduced basis approach for determining the damage dependent response of laminated beam and plate geometries. The approach is numerically efficient and provides the general analytical capability of being able to represent damping coefficients in any number of modes.

ACKNOWLEDGEMENT

REFERENCES

1. Talreja, R., Damage mechanics of composite materials. Danish Center of Applied Mathematics and Mechanics. Report S32, 1986.
2. Hashin, Z., Failure criteria for unidirectional fiber composites. *Journal of Applied Mechanics*, 47 (1980) 329–34.
3. Lee, J. D., Three dimensional finite element analysis of damage accumulation in composite laminate. *Computers and Structures*, 15 (3) (1982) 335–50.
4. Greszczuk, L. B., Microbuckling of lamina-reinforced composites, ASTM STP 546. ASTM, Philadelphia, PA, 1974.
5. Chang, C. & Engblom, J. J., Nonlinear dynamical response of impulsively loaded structures: a reduced basis approach. *AIAA Journal*, 29 (4) (April 1991) 613–18.
6. Chang, C. & Engblom, J. J., Reduced basis alternatives to the solution of nonlinear dynamical systems. *Journal of Aircraft* (Sept./Oct. 1992), 760–7.
7. Wilson, E. L., Yuan, M. W. & Dickens, J. M., Dynamic analysis by direct superposition of Ritz vectors. *Earthquake Engineering and Structural Dynamics*, 10 (1982) 813–21.
8. Newmark, N. M., A method of computation for structural dynamics. *Transactions ASCE*, 127 (1) (1962) 1406–35.
9. Engblom, J. J., Modeling the effects of intraply cracking in composite laminates at the sublaminate level, design and analysis of composite material vessels, ASME PVP-V.121. ASTM, Philadelphia, PA, 1987, pp. 105–10.
10. Engblom, J. J., Yang, Q., Abdul-Samad, N. & Havelka, J. J., Residual property predictions for laminated composite structures: FE based internal state variable approach. *Proceedings of 33rd Structures, Materials and Dynamics Conference*, 1992, pp. 21–8.
11. Engblom, J. J., Fuehne, J. P. & Hamdallah, J. M., Transverse stress calculations for laminated composite shell structures using plate/shell finite element formulations. *Journal of Reinforced Plastics and Composites*, 8 (5) (1989) 446–57.

Free vibration of generally-laminated, shear-deformable, composite rectangular plates using a spline Rayleigh–Ritz method

D. J. Dawe & S. Wang

School of Civil Engineering, The University of Birmingham, Edgbaston, Birmingham UK, B15 2TT

A Rayleigh–Ritz method is presented for predicting the natural frequencies of flat rectangular laminates which can have arbitrary lay-up. The effects of through-thickness shear deformation are included in the analysis. The displacement field utilises B-spline functions in what has been referred to in earlier work as a $B_{k,k-1}$-spline Rayleigh–Ritz method and the approach is versatile in the specification of boundary conditions. The results of a number of applications are presented in the form of studies showing the convergence of frequency values with increase in the number of spline sections used. The analysis procedure is seen to have good convergence characteristics when dealing with laminates of thin and thick geometry.

1 INTRODUCTION

The analysis of the vibration of fibre-reinforced, composite laminated, rectangular plates is made difficult by the complications introduced by arbitrary lamination, which may lead to aniso-tropic material behaviour and to coupling between in-plane and out-of-plane behaviours. Even when conducting analyses on the basis of classical plate theory (CPT), there are only strictly limited circumstances in which exact solutions can be obtained. The situation is further complicated if account is taken of through-thickness shear effects, which are known to be important for other than very thin laminates, by conducting analyses on the basis of shear deformation plate theory (SDPT).

In general situations, then, in seeking to determine the natural frequencies of laminated plates recourse must be made to approximate numerical methods. For single plates the traditional single-field Rayleigh–Ritz method (RRM) can be employed if displacement fields can be proposed which are appropriate for the complete plate and which allow satisfaction of the relevant boundary conditions. The related multi-field procedures, the finite strip method (FSM) and finite element method (FEM), are more versatile, and capable of use in analysing plate structures as well as single

plates, but are likely to be more expensive computationally, especially so for the FEM.

The RRM has been used frequently in the past in the analysis of the free vibration of rectangular plates but almost always in the context of CPT and usually only for homogeneous isotropic plates. Different types of trial functions have been employed in displacement fields within the context of CPT. The most popular of these have perhaps been Bernoulli–Euler beam functions as used by, for instance, Warburton[1] and Leissa[2] and, for composite laminates, as described in the text of Whitney.[3] However, polynomial functions have been used to some extent. Antes[4] has used a spline-function RRM in static bending problems and Mizusawa *et al.*[4-6] have considered the vibration of skew plates using a similar method. In an analysis directed specifically to generally laminated composite plates Baharlou and Leissa[7] have used simple polynomials as their trial functions.

In the context of SDPT the vibration and stability of rectangular isotropic plates and composite laminates have been analysed using the RRM by Dawe *et al.*[8-12] wherein Timoshenko beam functions are employed as trial functions in the displacement field. It has been shown in numerical applications that this approach, which will be referred to here as the Beam RRM, is very efficient in the analysis of isotropic and symmetric-

ally-laminated (or balanced) orthotropic laminates. However, there are difficulties in some circumstances in allowing the proper satisfaction of some natural boundary conditions at the edges of anisotropic laminates. Furth~r, the approach is somewhat lacking in versatility since it relies on the use of trial functions which need to be changed every time the boundary conditions are changed, and this becomes onerous especially for unbalanced laminates where five independent fundamental displacement quantities are involved.

To complement the accurate but restricted Beam RRM the authors[13] examined the use of versatile B-spline polynomial functions[14] as trial functions in RRM (and FSM) analyses of the free vibration of balanced laminates in the context of SDPT. In this earlier study[13] cubic B_3-spline functions were used to represent each of the three fundamental quantities, namely the deflection w and the two cross-sectional rotations ψ_x and ψ_y, along the x- and y-directions, respectively. It was found that this particular approach yielded results of good accuracy for moderately thick laminates but that the accuracy decreased significantly for thin laminates due to shear-locking behaviour.

More recently the authors have examined in detail the occurrence of shear-locking behaviour when considering the free vibration of shear deformable beams[15] and of balanced, orthotropic laminated plates.[16] It has been demonstrated that shear-locking behaviour can be effectively eliminated using an approach which is termed the $B_{k,k-1}$-spline RRM. In this approach w is represented by spline functions of polynomial order k in each co-ordinate direction, ψ_x is represented by spline functions of order $k-1$ in the x-direction and of order k in the y-direction, and ψ_y is represented by spline functions of order k in the x-direction and of order $k-1$ in the y-direction. The $B_{k,k-1}$-spline RRM has been shown to yield accurate results, and good convergence characteristics, for thick and thin balanced, orthotropic laminates.

In the present work the $B_{k,k-1}$-spline RRM is extended to apply to the analysis, in the context of SDPT, of the vibration of unbalanced and anisotropic laminated plates. The material properties that are allowed are very general and now five fundamental quantities are involved in the displacement field, namely the in-plane displacements u and v plus w, ψ_x and ψ_y.

2 ANALYSIS

A rectangular plate with its co-ordinates and displacement quantities is shown in Fig. 1. Components of translational displacement at a general point are $\bar{u}$, $\bar{v}$ and $\bar{w}$ whilst ψ_x and ψ_y are components of rotation along the x and y axes respectively. The plate is of uniform thickness h and, in general, is made up of a number of layers, each consisting of unidirectional fibre-reinforced composite material. The lay-up of layers is arbitrary, admitting the possibility of coupling between in-plane and out-of-plane behaviours and of anisotropy.

During vibration the displacements at a general point in the plate are assumed, within the context of SDPT,[17,18] to have the form

$$\bar{u}(x, y, z, t) = u(x, y, t) + z\psi_x(x, y, t)$$

$$\bar{v}(x, y, z, t) = v(x, y, t) + z\psi_y(x, y, t) \tag{1}$$

$$\bar{w}(x, y, z, t) = w(x, y, t)$$
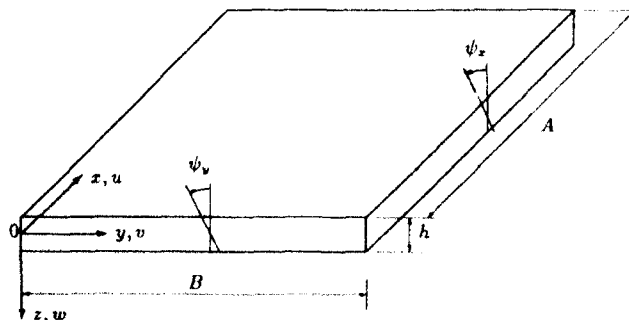
Fig. 1. Plate geometry.

where t is the time dimension. The quantities u, v, w, ψ_x and ψ_y are middle-surface reference quantities and are the fundamental quantities whose variations over the plate middle surface are to be assumed in the Rayleigh–Ritz approach.

The constitutive equations for an arbitrary laminate, within the context of SDPT, are

$$
\begin{Bmatrix} N_x \\ N_y \\ N_{xy} \\ M_x \\ M_y \\ M_{xy} \\ Q_y \\ Q_x \end{Bmatrix} = \begin{bmatrix} A_{11} & & & & & & & \\ A_{12} & A_{22} & & \text{Symmetric} & & & & \\ A_{16} & A_{26} & A_{66} & & & & & \\ B_{11} & B_{12} & B_{16} & D_{11} & & & & \\ B_{12} & B_{22} & B_{26} & D_{12} & D_{22} & & & \\ B_{16} & B_{26} & B_{66} & D_{16} & D_{26} & D_{66} & & \\ 0 & 0 & 0 & 0 & 0 & 0 & A_{44} & \\ 0 & 0 & 0 & 0 & 0 & 0 & A_{45} & A_{55} \end{bmatrix} \begin{Bmatrix} \partial u/\partial x \\ \partial v/\partial y \\ \partial u/\partial y + \partial v/\partial x \\ \partial \psi_x/\partial x \\ \partial \psi_y/\partial y \\ \partial \psi_x/\partial y + \partial \psi_y/\partial x \\ \partial w/\partial y + \psi_y \\ \partial w/\partial x + \psi_x \end{Bmatrix} \tag{2}
$$

or in more compact form

$$
\sigma^* = \begin{bmatrix} \mathbf{A} & \mathbf{B} & \mathbf{0} \\ \mathbf{B} & \mathbf{D}_h & \mathbf{0} \\ \mathbf{0} & \mathbf{0} & \mathbf{D}_s \end{bmatrix} \varepsilon^* \tag{3}
$$

Here N_x, N_y and N_{xy} are the membrane direct and shearing forces per unit length; M_x, M_y and M_{xy} are the bending and twisting moments per unit length; and Q_x and Q_y are the through-thickness shear forces per unit length. The quantities σ^* and ε^* are column matrices of generalized stress resultants and of strains, whose definitions will be clear on comparing eqns (2) and (3). Similarly the definitions of the submatrices appearing in eqn (3) will be clear on comparison with eqn (2).

The laminate stiffness coefficients are defined as

$$
(A_{ij}, B_{ij}, D_{ij}) = \int_{-h/2}^{h/2} Q_{ij}(1, z, z^2)\, dz \quad i, j = 1, 2, 6 \tag{4}
$$

and

$$
A_{ij} = k_i k_j \int_{-h/2}^{h/2} Q_{ij}\, dz \quad i, j = 4, 5 \tag{5}
$$

Here Q_{ij} for $i, j = 1, 2, 6$ are plane-stress reduced stiffnesses and Q_{ij} for $i, j = 4, 5$ are through-thickness shear stiffnesses. The $k_i k_j$ are shear correction factors, determined here usually according to the procedures of Whitney.[19]

During free vibration the fundamental quantities vary harmonically with time, with circular frequency p. Let u, v, w, ψ_x and ψ_y now be regarded as amplitudes of the motion. Then the maximum strain energy of the plate is

$$
U_{\max} = \frac{1}{2} \int_0^B \int_0^A \sigma^{*\mathrm{T}} \varepsilon^* \, dx\, dy = \frac{1}{2} \int_0^B \int_0^A \varepsilon^{*\mathrm{T}} \begin{bmatrix} \mathbf{A} & \mathbf{B} & \mathbf{0} \\ \mathbf{B} & \mathbf{D}_h & \mathbf{0} \\ \mathbf{0} & \mathbf{0} & \mathbf{D}_s \end{bmatrix} \varepsilon^* \, dx\, dy \tag{6}
$$

The maximum kinetic energy is

$$
T_{\max} = \frac{1}{2} p^2 \int_0^B \int_0^A \rho h \left(u^2 + v^2 + w^2 + \frac{h^2}{12} [\psi_x^2 + \psi_y^2] \right) dx\, dy \tag{7}
$$

where ρ is the material density, which is assumed here to be uniform throughout the volume of the plate. The expression for T_{max} clearly includes rotary inertia terms.

In applying the spline RRM the assumed spatial displacement field is based on separate assumptions for u, v, w, ψ_x and ψ_y and each of these is expressed as a summation of a series of terms which are products of one-dimensional B-spline functions in the x- and y-directions. A full description of one-dimensional B-spline functions, with equally-spaced knots, is given in the earlier work by the authors dealing with beam analysis.[15] There, use is made of linear, quadratic, cubic, quartic and quintic B-spline functions and details are recorded of the form of the functions. Consideration is also given, in the earlier work, to the way in which prescribed kinematic boundary conditions can be applied and in the present analysis the modified B-spline basis[15] will be used.

In using the unidirectional B-spline functions in a RRM analysis of the vibration of the rectangular plate shown in Fig. 1, the plate dimensions A and B are imagined to be divided into M and N equal sections, respectively and a corresponding grid of knots is set up as shown in Fig. 2. There will be some knots located outside the boundary of the plate as a necessary requirement of satisfying the kinematic boundary conditions but these external knots are not shown since their number will depend on the order of the B-spline functions that are used.

In a similar, but extended, fashion to the approach described in an earlier study by the authors[16] the complete spatial displacement field of the rectangular plate of Fig. 1 is expressed as

$$u(x,y) = (\hat{\boldsymbol{\theta}}_k \otimes \hat{\boldsymbol{\beta}}_k) \mathbf{d}_1$$

$$v(x,y) = (\hat{\boldsymbol{\theta}}_k \otimes \hat{\boldsymbol{\beta}}_k) \mathbf{d}_2$$

$$w(x,y) = (\hat{\boldsymbol{\theta}}_k \otimes \hat{\boldsymbol{\beta}}_k) \mathbf{d}_3 \qquad\qquad\qquad (8)$$

$$\psi_x(x,y) = (\hat{\boldsymbol{\theta}}_{k-1} \otimes \hat{\boldsymbol{\beta}}_k) \mathbf{d}_4$$

$$\psi_y(x,y) = (\hat{\boldsymbol{\theta}}_k \otimes \hat{\boldsymbol{\beta}}_{k-1}) \mathbf{d}_5$$

Here $\hat{\boldsymbol{\theta}}_k$ is a row matrix containing all the $\hat{\theta}(x)$ modified local spline functions of polynomial order k, in the x-direction, associated with the ith knot in the x-direction. The $\hat{\boldsymbol{\theta}}_{k-1}$ is defined similarly but the local spline functions are of polynomial order $k-1$. The $\hat{\boldsymbol{\beta}}_k$ and $\hat{\boldsymbol{\beta}}_{k-1}$ are corresponding row matrices containing all the $\hat{\beta}(y)$ modified local spline functions of polynomial orders k and $k-1$, respectively, associated with the jth knot in the y-direction. The $\otimes$ symbol denotes a tensor product, such that $\hat{\boldsymbol{\theta}}_k \otimes \hat{\boldsymbol{\beta}}_k$, for instance, represents all possible linear combinations of $\hat{\theta}(x)$ and $\hat{\beta}(y)$, with these latter local spline functions being of polynomial order k. The $\mathbf{d}_1 \ldots \mathbf{d}_5$ are column matrices of generalized displacement parameters associated with $u \ldots \psi_y$, respectively.

The above displacement field corresponds to what the authors have termed the $B_{k,k-1}$-spline RRM.[15,16] This means specifically that the spline functions used to represent ψ_x in the x-direction are of one order less than the functions used to represent w in the x-direction. Similarly in the y-direction ψ_y is
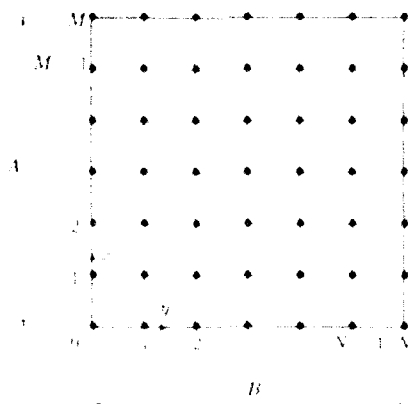

Fig. 2.   Spline knots and sections

represented by spline functions of one order less than that used to represent *w*. As mentioned earlier, this procedure eliminates shear locking.

To generate the elastic stiffness matrix **K** and consistent mass matrix **M** of the plate, the displacement field of eqns (8) is substituted into the expressions for maximum strain energy (eqn (6)) and maximum kinetic energy (eqn (7)), respectively.

To determine the elastic stiffness matrix the column matrix $\boldsymbol{\varepsilon}^*$ is first expressed through use of eqns (8) as

$$\boldsymbol{\varepsilon}^* = \begin{bmatrix} \mathbf{B}_m \\ \mathbf{B}_b \\ \mathbf{B}_s \end{bmatrix} \begin{Bmatrix} \mathbf{d}_1 \\ \mathbf{d}_2 \\ \mathbf{d}_3 \\ \mathbf{d}_4 \\ \mathbf{d}_5 \end{Bmatrix} = \begin{bmatrix} \mathbf{B}_m \\ \mathbf{B}_b \\ \mathbf{B}_s \end{bmatrix} \mathbf{d} \tag{9}$$

where **d** is the column matrix of all generalized displacement parameters. Further

$$\mathbf{B}_m = \begin{bmatrix} \dot{\boldsymbol{\theta}}_k \otimes \boldsymbol{\beta}'_k & 0 & 0 & 0 & 0 \\ 0 & \boldsymbol{\theta}'_k \otimes \dot{\boldsymbol{\beta}}_k & 0 & 0 & 0 \\ \boldsymbol{\theta}'_k \otimes \dot{\boldsymbol{\beta}}_k & \dot{\boldsymbol{\theta}}_k \otimes \boldsymbol{\beta}'_k & 0 & 0 & 0 \end{bmatrix} \tag{10}$$

$$\mathbf{B}_b = \begin{bmatrix} 0 & 0 & 0 & \boldsymbol{\theta}'_{k-1} \otimes \boldsymbol{\beta}_k & 0 \\ 0 & 0 & 0 & 0 & \boldsymbol{\theta}_k \otimes \boldsymbol{\beta}'_{k-1} \\ 0 & 0 & 0 & \boldsymbol{\theta}_{k-1} \otimes \boldsymbol{\beta}'_k & \boldsymbol{\theta}'_k \otimes \boldsymbol{\beta}_{k-1} \end{bmatrix} \tag{11}$$

and

$$\mathbf{B}_s = \begin{bmatrix} 0 & 0 & \bar{\boldsymbol{\theta}}_k \otimes \boldsymbol{\beta}'_k & 0 & \bar{\boldsymbol{\theta}}_k \otimes \boldsymbol{\beta}_{k-1} \\ 0 & 0 & \boldsymbol{\theta}'_k \otimes \bar{\boldsymbol{\beta}}_k & \boldsymbol{\theta}_{k-1} \otimes \bar{\boldsymbol{\beta}}_k & 0 \end{bmatrix} \tag{12}$$

The prime(') denotes differentiation with respect to the co-ordinate in which a function is expressed, i.e. with respect to *x* for $\boldsymbol{\theta}$ and with respect to *y* for $\boldsymbol{\beta}$. On substituting eqn (9) into eqn (6) the maximum strain energy can be expressed as

$$U_{max} = \frac{1}{2} \mathbf{d}^t \mathbf{K} \mathbf{d} \tag{13}$$

where

$$\mathbf{K} = \int_0^H \int_0^L (\mathbf{B}_m^t \mathbf{A} \mathbf{B}_m + \mathbf{B}_m^t \mathbf{B} \mathbf{B}_b + \mathbf{B}_b^t \mathbf{B} \mathbf{B}_m + \mathbf{B}_b^t \mathbf{D}_b \mathbf{B}_b + \mathbf{B}_s^t \mathbf{D}_s \mathbf{B}_s) \, dx \, dy \tag{14}$$

is the elastic stiffness matrix. Here the first term on the right-hand side of eqn (14) is the in-plane contribution, the last two terms are out-of-plane bending and through-thickness shearing contributions, and the other two terms are contributions from coupling between in-plane and out-of-plane actions. All these terms are evaluated individually and then summed to yield **K**.

Using eqns (7) and (9) the maximum kinetic energy can be expressed as

$$T_{max} = \frac{1}{2} p^2 \mathbf{d}^t \mathbf{M} \mathbf{d} \tag{15}$$

where

$$M = \rho \int_0^B \int_0^A G^T H G \, dx \, dy \tag{16}$$

is the consistent mass matrix. Here H is the diagonal matrix

$$H = \left[h \quad h \quad h \quad \frac{1}{12} h^3 \quad \frac{1}{12} h^3 \right] \tag{17}$$

and G can also be expressed in diagonal form as

$$G = \left[\bar{\theta}_k \otimes \bar{\beta}_k \quad \bar{\theta}_k \otimes \bar{\beta}_k \quad \bar{\theta}_k \otimes \bar{\beta}_k \quad \bar{\theta}_{k-1} \otimes \bar{\beta}_k \quad \bar{\theta}_k \otimes \bar{\beta}_{k-1} \right] \tag{18}$$

The final forms of K and M will not be presented here but are available in Ref. 20.

In evaluating K and M the necessary integrals are determined using a systematic scheme which involves the use of Gauss quadrature but with sufficient integrating points to yield effectively exact values of the integrals.

The set of equations governing the free vibration problem is generated by minimising the functional $(T_{max} - U_{max})$, i.e. by partial differentiation of this functional with respect to each of the generalized displacement parameters. The result is the standard set of equations.

$$(K - p^2 M) d = 0 \tag{19}$$

In the present study the QR method is used to obtain solutions to this eigenproblem in the form of natural frequencies and associated modes.

It has been remarked that in the spline function approach the same basic functions are used whatever the boundary conditions, since such conditions are met by local modifications only. The approach is very versatile and can accommodate readily any combinations of kinematic conditions related both to in-plane and out-of-plane behaviours, by setting to zero, or leaving free, any or all of u, v, w, ψ_x and ψ_y at an edge. There are a total of five boundary conditions, of the kinematic and natural kind, associated with each edge, and hence a very considerable number of edge conditions can be specified. In the next section the applications considered are concerned with plates which have individual edges which are either clamped or simply supported type 1, or simply supported type 2. In terms of the displacement type quantities, the conditions that these definitions imply at an edge parallel to the y-axis, for instance, are as follows

Clamped (C): $u = v = w = \psi_x = \psi_y = 0$ (20)

Simply supported type 1(S1): $u \neq 0$, $v = 0$, $w = 0$, $\psi_x \neq 0$, $\psi_y = 0$ (21)

Simply supported type 2(S2): $u = 0$, $v \neq 0$, $w = 0$, $\psi_x \neq 0$, $\psi_y = 0$ (22)

3 APPLICATIONS

The $B_{k,1}$-spline Rayleigh-Ritz method described in Section 2 has been programmed for the computer with allowance made for $k = 3$ or 4 or 5. Here, however, all the applications described in what follows are based on the use of $k = 3$ and the approach is described as the B_3-spline Rayleigh-Ritz method or, in short, the B_3SRRM. It bears recalling that this means that cubic splines are used to represent each of u, v, w, ψ_x and ψ_y in each co-ordinate direction, except that the representations of ψ_x in the x-direction and of ψ_y in the y-direction are by quadratic splines.

The applications considered here involve square plates and in using the B_3SRRM the number of spline sections within a plate in each of the x- and y-directions is the same, and is $M = N = q$. The number of degrees of freedom used in obtaining a solution, after boundary conditions have been applied, is denoted as NDOF.

The performance of the B_3SRRM has been examined in detail in Ref. 16 when considering the free vibration of isotropic plates and balanced orthotropic laminates having combinations of simply supported, clamped and free edges. It has been shown that the B_3SRRM is efficient in calculating the natural frequencies of such plates

of thin and thick geometry and that it appears to be completely free of shear-locking difficulties. Convergence to known exact, or highly accurate, results has been demonstrated.

Here, as a first example (not detailed in Ref. 16), we document in Table 1 details of the convergence with q of the B_{32}SRRM frequency predictions for the first four modes of balanced orthotropic, square laminates of thick $(h/A = 0.1)$ and thin $(h/A = 0.01)$ geometry. The laminates are five-layer symmetric cross-ply laminates with $0°/90°/0°/90°/0°$ lay up. The thickness of each $0°$ layer is $h/6$ and that of each $90°$ layer is $h/4$. The material properties of all layers are $E_L/E_T = 30$, $G_{LT}/E_T = 0.6$, $G_{TT}/E_T = 0.5$, $\nu_{LT} = 0.25$ in the standard terminology. The shear correction factors used are $k_4^2 = 0.591\,39$ and $k_5^2 = 0.873\,23$. The laminate edges $x = 0$, A are simply supported and the edges $y = 0$, B are clamped. In analysing these balanced SCSC laminates, consideration is given only to out-of-plane behaviour, involving w, ψ_x and ψ_y. The B_{32}SSRM results in Table 1 show good convergence toward comparative values generated using the Beam RRM[11] which, for this balanced orthotropic laminate, are expected to be highly accurate: the Beam RRM results are based on the use of five series terms in each coordinate direction (i.e. $r = 5$) in representing each of w, ψ_x and ψ_y. Also quoted in Table 1 are CPT solutions which are seen to be slightly high for the thin laminate and very high for the thick laminate, reflecting the significance of through-thickness shear deformation.

The next problems considered concern square anisotropic plates composed of a single layer of an orthotropic material oriented with the principal axis of orthotropy at $30°$ from the x-axis. The

material properties of the layer are $E_1/E_2 = 10$, $G_{LT}/E_T = 0.25$, $G_{TT}/E_1 = 0.25$, $\nu_{LT} = 0.3$. The shear correction factors k_4^2 and k_5^2 are taken to be $5/6$. Two values of thickness-to-length ratios are considered, namely $h/A = 0.1$ and 0.01. For the single-layer plate there is, of course, once more no coupling between in-plane and out-of-plane behaviour and here only out-of-plane modes are considered.

Table 2 gives details of a convergence study of calculated values of a frequency parameter for the first four modes of vibration of thick and thin plates with all edges simply supported. It is seen from Table 2 that convergence of the B_{32}SRRM results is orderly and quite rapid for both the thin and thick plates, given that the mode shapes of the anisotropic plates are relatively complicated. The comparative results recorded as Beam RRM results in Table 2 are based on the use of simple sine and cosine functions, with $r = 10$. It is noted that for all modes considered in Table 2 the present converged B_{32}SRRM values are significantly lower, and hence more accurate, than the corresponding Beam RRM values. The Beam RRM anisotropic plate model is, in fact, overconstrained due to an inability to allow the condition of zero normal moment to be met at the plate edges. No such difficulty exists in using the B_{32}SRRM.

Table 3 is of similar form to Table 2 but now the anisotropic plate is fully clamped at all edges. Three sets of comparative frequency values are quoted, two based on the use of SDPT (the Beam RRM, with $r = 6$, and the Beam FSM values) and one on the use of CPT[21] (which is also a Rayleigh–Ritz approach, using seven Bernoulli–Euler beam functions in each coordinate direc-

Table 1. Values of frequency parameter Ω for SCSC balanced cross-ply, square plates

$$\left(\Omega = p\,\frac{A^2}{h}\left[\frac{\rho}{(Q_{11})_1}\right]^{1/2}\ \text{where}\ (Q_{11})_1 = 155.3236\right)$$

q	NDOF	$h/A = 0.1$ Mode				$h/A = 0.01$ Mode			
		1	2	3	4	1	2	3	4
2	27	4.516	9.217	10.10	12.91	6.264	37.19	17.87	85.71
3	48	4.496	7.978	9.270	11.42	6.208	14.72	14.70	20.25
4	75	4.491	7.939	9.234	11.36	6.191	14.59	14.57	20.04
5	108	4.490	7.920	9.221	11.34	6.181	14.45	14.53	19.90
6	147	4.489	7.914	9.216	11.33	6.185	14.40	14.51	19.86
Beam RRM[11]		4.489	7.911	9.213	11.33	6.184	14.37	14.50	19.83
CPT[11]		6.215	14.55	14.61	20.06	6.215	14.55	14.61	20.06

Table 2. Values of frequency parameter Ω for simply supported anisotropic square plates

$$\left(\Omega = p \frac{A^2}{h} \left[\frac{12(1 - \nu_{11}\nu_{11})}{E_1} \right]^{1/2} \right)$$

q	NDOF	$h/A = 0.1$ Mode				$h/A = 0.01$ Mode			
		1	2	3	4	1	2	3	4
2	33	10·17	20·74	27·33	33·50	11·98	26·62	44·94	49·83
3	56	10·07	18·05	24·23	29·75	11·86	22·44	36·40	43·12
4	85	10·04	17·80	23·84	28·00	11·81	22·02	35·50	37·81
5	120	10·02	17·72	23·69	27·57	11·78	21·90	35·19	36·75
6	161	10·01	17·70	23·64	27·42	11·76	21·86	35·05	36·42
7	208	10·00	17·69	23·62	27·37	11·75	21·84	34·99	36·30
Beam RRM		10·34	18·21	24·45	27·81	12·02	22·28	35·44	36·83

Table 3. Values of frequency parameter Ω for clamped, anisotropic square plates

$$\left(\Omega = p \frac{A^2}{h} \left[\frac{12(1 - \nu_{11}\nu_{11})}{E_1} \right]^{1/2} \right)$$

q	NDOF	$h/A = 0.1$ Mode				$h/A = 0.01$ Mode			
		1	2	3	4	1	2	3	4
2	21	14·47	30·63	33·09	42·60	24·03	294·6	295·7	416·7
3	40	14·06	22·19	27·06	33·25	22·16	37·47	56·93	75·22
4	65	13·97	21·71	26·52	31·44	21·53	34·50	54·10	56·85
5	96	13·95	21·55	26·31	30·91	21·33	33·44	52·27	52·79
6	133	13·94	21·50	26·24	30·72	21·25	33·11	51·16	51·56
7	176	13·93	21·48	26·22	30·65	21·21	32·98	50·58	51·27
8	225	13·93	21·47	26·20	30·61	21·19	32·92	50·35	51·13
Beam RRM[11]		14·63	22·50	27·55	31·24	21·25	33·02	50·33	51·30
Beam FSM[11]		14·28	22·24	26·64	31·01	21·22	33·00	50·45	51·21
CPT solution[21]		21·35	33·18	50·72	51·87	21·35	33·18	50·72	51·87

tion). The convergence rate for the present B$_{12}$SRRM is somewhat slower for the clamped anisotropic plate than for the simply supported plate but nevertheless is satisfactory in a difficult application. It is seen that for the thin plate there is close agreement between the converged results of the present approach and the comparative results: as expected the CPT values are a little higher than the SDPT values. For the thick plate the CPT results are gross overestimates due to the neglect of through-thickness shear effects. The Beam RRM and Beam FSM results for the thick plate are higher (and hence less accurate) than the B$_{12}$SRRM results, due again to overconstraint at the edges of the anisotropic plate. (The overconstraint affects the Beam RRM more than the Beam FSM since it involves all four edges in the RRM and only two edges in the FSM.)

Bert and Chen[22] have considered the vibration of antisymmetric angle-ply laminated plates and have developed exact, closed-form solutions for plates with S2 simple supports on all four edges, within the context of SDPT. Exact solutions in the context of CPT are also quoted in Ref. 22. A problem detailed by Bert and Chen concerns a square plate with $+45°/-45°/+45°/-45°$ lay-up. All layers are of the same thickness and have properties defined as $E_1/E_T = 40$, $G_{11}/E_1 = G_{TT}/E_T = 0.6$, $\nu_{11} = 0.25$ with shear correction factors taken to be $k_4^2 = k_5^2 = 5/6$. For this un-balanced lay-up the coupling terms that are present are B_{16} and B_{26}. Table 4 gives convergence details for the B$_{12}$SRRM for plates with $h/A = 0.1$ and $h/A = 0.01$, and records the exact solutions, together with solutions obtained using the Beam RRM ($r = 6$) for the thicker geometry. For the

thick plate there is very close comparison between the present $B_{32}SRRM$ results and the exact (and Beam RRM) results. It is noted, though, that the second mode is an in-plane (uv) mode which is not recorded in Ref. 22. For the thin plate it should be noted that the quoted exact results are in the context of CPT and hence are a little higher than the values towards which the $B_{32}SRRM$ results are converging.

Further consideration is given to angle-ply, square laminates of the type just described but now with a variable, but even, number of layers and with the edge conditions changed to S1 simple supports. The object is to examine the effect that the B_{16} and B_{26} coupling coefficients have on natural frequencies. Figure 3 shows how the first four frequencies change with the A/h ratio varying from 5 to 100 for antisymmetric laminates having 2, 4, 6 and 8 layers, and for the corresponding orthotropic laminate (with B_{16} and B_{26} set to zero) which corresponds to an antisymmetric laminate with an infinite number of layers. The curves in Fig. 3 are based on the use of the $B_{32}SRRM$ with $q = 5$. The frequency parameter Ω is as defined in Table 4 and nl denotes the number of layers. It is clear from Fig. 3 that the presence of the B_{16} and B_{26} coupling coefficients reduces natural frequencies very considerably for small values of nl but has little effect above $nl = 8$. For the particular case of $A/h = 10$, Fig. 4 confirms this conclusion in graphs showing the variation of Ω with nl for the first four frequencies.

Finally, the same four-layer, angle-ply, square plate of Bert and Chen[22] is reconsidered, now with all edges clamped (a CCCC plate) or with one pair of opposite edges clamped and the other

pair having S1 simple supports (a SCSC plate). For both cases $h/A = 0.1$. Table 5 shows the good convergence of the $B_{32}SRRM$ results and gives comparative Beam RRM results ($r = 7$). These latter results are generally higher than are the corresponding $B_{32}SRRM$ results, due to some difficulty in satisfying the edge conditions when using the Beam RRM in the presence of the B_{16} and B_{26} stiffness coefficients.

4 CONCLUSIONS

The use of the $B_{k,k-1}$-spline Rayleigh–Ritz method for the prediction of the natural fre-
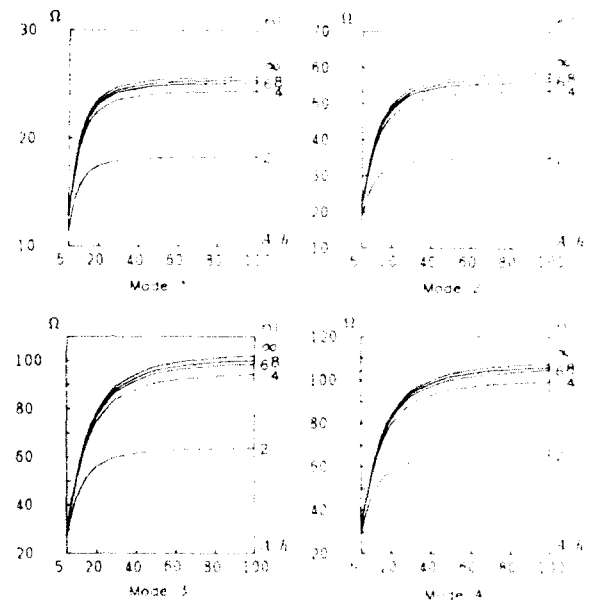
Fig. 3. The effect of B_{16} and B_{26} on natural frequencies of simply supported square anti-symmetric angle-ply laminates.

Table 4. Values of frequency parameter Ω for simply supported (S2), unbalanced angle-ply, square plates

$$\left(\Omega = p\,A^2\left[\frac{\rho}{E_1 h^3}\right]^{1/2}\right)$$

q	NDOF	$h/A = 0.1$ Mode				$h/A = 0.01$ Mode			
		1	2(u,v)	3	4	1	2	3	4
2	63	18·48	34·56	37·76	53·37	23·49	60·59	104·2	113·8
3	104	18·47	34·43	35·10	50·67	23·46	53·90	93·64	127·6
4	155	18·46	34·42	34·95	50·58	23·46	53·55	93·20	100·7
5	216	18·46	34·42	34·90	50·54	23·46	53·43	93·03	98·86
6	287	18·46	34·41	34·89	50·53	23·45	53·40	92·98	98·18
Exact[22]		18·46	—	34·87	50·52	23·53	53·74	94·11	98·87
Beam RRM		18·46	—	34·89	50·52	—	—	—	—

Table 5. Values of frequency parameter Ω for CCCC and SCSC, unbalanced angle-ply, thick ($h/A = 0.1$), square plates

$$\left(\Omega = pA^2\left[\frac{\rho}{E_1 h^3}\right]^{1/2}\right)$$

| q	NDOF	CCCC plate Mode				NDOF	SCSC plate Mode			
		1	2	3	4		1	2	3	4
2	39	22·90	44·80	59·34	63·15	51	20·75	38·32	44·11	55·51
3	72	22·73	38·84	52·72	66·68	88	20·66	35·47	38·46	51·57
4	115	22·69	38·58	52·50	57·64	135	20·64	35·31	38·24	51·43
5	168	22·68	38·48	52·41	57·14	192	20·63	35·25	38·14	51·37
6	231	22·67	38·44	52·38	56·89	259	20·63	35·24	38·11	51·35
7	304	22·67	38·43	52·37	56·79	336	20·63	35·23	38·10	51·34
Beam RRM		23·42	39·64	52·87	57·81	—	21·00	35·78	39·15	51·32
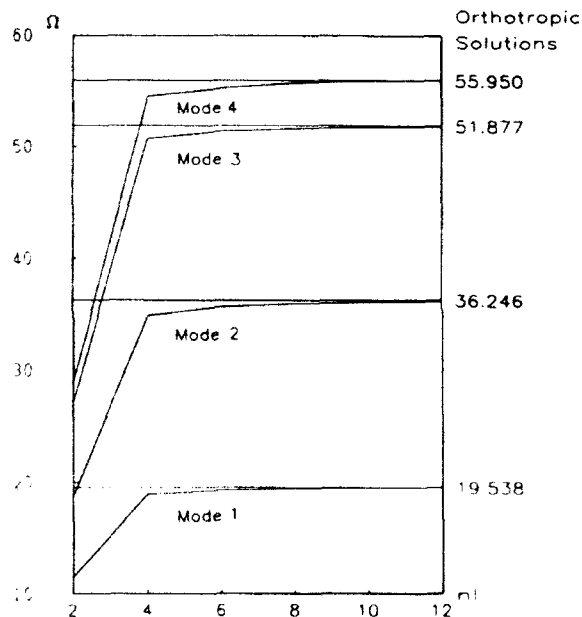
Fig. 4. Frequency variation of simply supported square anti-symmetric angle-ply laminates with the number of layers.

quencies of shear-deformable rectangular laminates of arbitrary lay-up has been detailed. In specific applications attention has been restricted to the case of $k = 3$, i.e. to the B_{32}SRRM. The procedure has been shown to have good convergence characteristics for anisotropic and unbalanced laminates of thin and thick geometry.

The use of spline functions in a Rayleigh–Ritz approach provides a versatile analysis procedure, since boundary, or interior support, conditions can be accommodated readily by only local modification of the spline functions. Beyond the scope of the current study, it is possible to use the spline

Rayleigh–Ritz method in analysing skew plates or plates with non-homogeneous boundary conditions and/or interior supports.[20] Furthermore, the $B_{k,k-1}$-spline approach can be incorporated into the finite strip analysis of shear deformable laminated plates[20] and prismatic plate structures.[23]

REFERENCES

1. Warburton, G. B., The vibration of rectangular plates. *Proc. Inst. Mech. Eng., Series A*, **168** (1954) 371–84.
2. Leissa, A. W., The vibration of rectangular plates. *J. Sound Vib.*, **31** (1973) 257–93.
3. Whitney, J. M., *Structural Analysis of Laminated Anisotropic Plates*. Technomic, Lancaster, PA, 1987.
4. Antes, H., Bicubic fundamental splines in plate bending. *Int. J. Num. Meth. Engng*, **9** (1974) 503–11.
5. Mizusawa, T., Kajita, T. & Naruoka, M., Vibration of stiffened skew plates by using B-spline functions. *Comp. Struct.*, **10** (1979) 821–6.
6. Mizusawa, T. & Kajita, T., Vibration of skew plates resting on point supports. *J. Sound Vib.*, **115** (1987) 243–51.
7. Baharlou, B. & Leissa, A. W., Vibration and buckling of generally laminated composite plates with arbitrary edge conditions. *Int. J. Mech. Sci.*, **29** (1987) 545–55.
8. Dawe, D. J. & Roufaeil, O. L., Rayleigh–Ritz vibration analysis of Mindlin plates. *J. Sound Vib.*, **69** (1980) 345–59.
9. Roufaeil, O. L. & Dawe, D. J., Rayleigh–Ritz vibration analysis of rectangular Mindlin plates subjected to membrane stress. *J. Sound Vib.*, **85** (1982) 263–75.
10. Dawe, D. J. & Craig, R. J., The influence of shear deformation on the natural frequencies of laminated rectangular plates. In *Composite Structures — 3*, ed. I. H. Marshall. Elsevier Applied Science, London, 1985, pp. 660–76.
11. Craig, T. J. & Dawe, D. J., Flexural vibration of symmetrically-laminated composite, rectangular plates, including transverse shear effects. *Int. J. Solids Struct.*, **22** (1986) 155–69.
12. Dawe, D. J. & Craig, T. J., The vibration and stability of

symmetrically-laminated composite rectangular plates subjected to in-plane stress. *Comp. Struct.*, **5** (1986) 281–307.

13. Wang, S. & Dawe, D. J., The use of spline functions in calculating the natural frequencies of anisotropic rectangular laminates. In *Composite Structures*, ed. I. H. Marshall. Elsevier Applied Science, London, 1987, pp. 1.447–1.460.

14. Prenter, P. M., *Splines and Variational Methods.* John Wiley, New York, 1975.

15. Dawe, D. J. & Wang, S., Vibration of shear-deformable beams using a spline-function approach. *Int. J. Num. Meth. Engng*, **33** (1992) 819–44.

16. Wang, S. & Dawe, D. J., Vibration of shear-deformable rectangular plates using a spline-function Rayleigh–Ritz approach. *Int. J. Num. Meth. Engng.* **36** (1993) 695–711.

17. Mindlin, R. D., Influence of rotary inertia and shear on flexural motions of isotropic elastic plates. *J. Appl. Mech.*, **18** (1951) 31–8.

18. Yang, P. C., Norris, C. H. & Stavsky, Y., Elastic wave propagation in heterogeneous plates. *Int. J. Solids Struct.*, **2** (1966) 665–84.

19. Whitney, J. M., Shear correction factors for orthotropic laminates under static load. *J. Appl. Mech.*, **40** (1974) 302–4.

20. Wang, S., The use of spline functions in the analysis of composite laminated plates. PhD thesis, The University of Birmingham, 1990.

21. Ashton, J. E. & Whitney, J. W., *Theory of Laminated Plates.* Technomic, Stanford, CA, 1970.

22. Bert, C. W. & Chen, T. L. C., Effect of shear deformation on vibration of antisymmetric angle-ply laminated rectangular plates. *Int. J. Solids Struct.*, **14** (1978) 465–73.

23. Dawe, D. J. & Wang, S., Buckling and vibration of composite prismatic plate structures using a spline finite strip approach. Report to RAE Farnborough, under Agreement Number No. 2027/209/MA, December, 1992.

Flutter analysis of cantilevered curved composite panels

R. M. V. Pidaparti

Department of Mechanical Engineering, Purdue University at Indianapolis, Indianapolis, IN 46202, USA

A 48 degrees of freedom (dof) doubly curved quadrilateral thin shell finite element is used for studying the supersonic flutter of cantilevered curved composite panels. The composite material behavior is included using classical lamination theory and supersonic aerodynamic behavior is included using linearized piston theory. To reduce the number of dof of the finite element aeroelastic system, a normal mode approach is adopted. Results are presented to illustrate the behavior of flutter characteristics for composite curved cylindrical panels. The effects of fiber orientation and flow angle on the flutter characteristics are presented for selected examples. The accuracy, efficiency, and applicability of the present finite element method is demonstrated by illustrative examples with some results comparing well with the available alternate solutions in the literature.

1 INTRODUCTION

Composite curved panels are being used in a variety of engineering fields. For example, fan and impeller blades in turbomachinery and in many civil and aerospace engineering structures. Aeroelastic analysis requires accurate evaluation of free vibration characteristics and unsteady aerodynamic loads. A vast amount of literature exists regarding vibration of turbomachinery blades treating them as beams. However, for accurate prediction, the blades should be treated as curved panels/shells.

Early works on panel flutter were concerned mainly with conventional isotropic panels. The research progress and some of the references can be found, for example, in the textbooks by Fung,[1] Bisplinghoff and Ashley,[2] and Dowell *et al.*[3,4] Early reviews on panel flutter can be found, for example, in Refs 5 and 6. Olson,[7] Sander *et al.*,[8] Yang and Sung,[9] and Mei,[10] among others, studied the flutter of isotropic flat panels using the finite element method. Some studies were also devoted to the flutter of composite panels, see, among others, Refs 11–16. Ketter[11] considered the effects of boundary conditions and fiber angle of panels on the flutter boundaries. Rosettes and Tong[12] applied a hybrid stress finite element method and used linearized piston theory to analyze the flutter of anisotropic cantilever plates. Their results indicate that flutter characteristics

are strongly dependent upon the composite fiber angle and anisotropy. Srinivasan and Babu[13] studied the panel flutter of cross-ply laminated composites by using the integral equations method. Lin *et al.*[14] used an 18 degrees of freedom (dof) high-precision triangular finite element to perform a flutter analysis of symmetrically laminated composite panels. Their studies included the effects of composite fiber angle, orthotropic modulus ratio, flow direction, and aerodynamic damping on the flutter boundaries. Sawyer[15] used the Galerkin method to study both the flutter and buckling problems of general laminated plates with simply supported boundary conditions. Oyibo[16] presented an analytical approach by combining classical plate theory and Ackeret's aerodynamic strip theory to study the flutter behavior of an orthotropic panel.

For the purpose of more general application, it appears plausible to use the curved quadrilateral shell finite elements to study flutter behavior of curved composite panels by including the effects of supersonic aerodynamic forces and laminated composite materials. With the use of such quadrilateral elements, the configuration of the panel is no longer limited to being flat or shallow. Furthermore, it seems of interest to explore in depth the effects of different material properties, lay-up schemes, and various flow angles on the flutter behavior as there is a renewed interest in supersonic transport aircraft.

This paper presents an accurate and efficient high-precision quadrilateral shell finite element for the supersonic flutter analysis of laminated composite curved panels. To establish the validity of the present formulation and computer program, flutter examples of composite plates were first studied, and the results were compared with existing alternative solutions. to illustrate and demonstrate the applicability of the present formulation and computer program, flutter examples of laminated composite cantilevered cylindrical panels were studied. The effects of flow angles and fiber angles on the flutter boundaries and modes are presented. The fiber orientation and flow angle have an interesting effect on the flutter/divergence behavior of cantilevered composite curved panels.

2 FORMULATION

A high-precision 48 dof quadrilateral shell finite element[17] is extended to include the property of composite materials based on classical lamination theory and also to include the effect of supersonic flow based on linearized piston theory for the flutter analysis of laminated composite curved panels. Some of the details of the element development are available in Ref. 17.

The shell finite element is quadrilateral in shape and has four nodal points with a total of 48 dof. The element nodal displacement vector is given as

$$\{\mathbf{q}\}^T = \lfloor u, u_\xi, u_\eta, u_{\xi\eta}, v, v_\xi, v_\eta, v_{\xi\eta}, w, w_\xi, w_\eta, w_{\xi\eta} \rfloor \tag{1}$$

where u, v, and w are the displacement components in three curvilinear directions, ξ, η, and z, respectively. Bicubic Hermitian polynomials are used to interpolate each of the displacement components.

The strain–displacement relations are represented in terms of curvilinear coordinates. The laminated anisotropic behavior is included using classical lamination theory. The shell is made up of an arbitrary number of layers. Each layer is assumed to be orthotropic with its principal material axes at an angle to the local coordinate axes. The stress–strain relations for each layer are transformed to be written in terms of the reference coordinate system. The stress and moment resultants are then related to the middle surface strains and the changes of curvature as[18]

$$\begin{Bmatrix} \mathbf{N} \\ \mathbf{M} \end{Bmatrix} = \begin{bmatrix} A & B \\ B & D \end{bmatrix} \begin{Bmatrix} \varepsilon \\ \kappa \end{Bmatrix} \tag{2}$$

The vector $\{\mathbf{N}\}$ contains the resultant tangential forces, the vector $\{\mathbf{M}\}$ contains the resultant moments, the vector $\{\varepsilon\}$ contains the middle surface strains, the vector $\{\kappa\}$ contains the changes of curvature, and the coefficients in matrices $[A]$, $[B]$ and $[D]$ are given as

$$[A_{ij}, b_{ij}, D_{ij}] = \int_{-h/2}^{h/2} [Q_{ij}](1, z, z^2)\, dz$$
$$(i, j = 1, 2, 3) \tag{3}$$

where $[Q_{ij}]$ is the 3×3 plane–stress stiffness matrix for each individual layer and h is the total thickness of the plate or the shell.

The derivation of the mass and stiffness matrices can be obtained using the stationary principle of kinetic and potential energies, respectively. The details of the 48×48 stiffness and consistent mass matrices can be found in Ref. 17. The aerodynamic stiffness and damping matrices are derived by considering the virtual work done by the aerodynamic forces.

$$\delta W = \int_A p\,\delta w\, dA \tag{4}$$

where A is the area of the element which the pressure is acting on.

Assuming a first-order, high Mach number (M_∞) approximation to the linear piston theory,[19,20] the aerodynamic pressure acting on a curved surface area dA is given by

$$p = \left[\beta \frac{\partial}{\partial \xi} + \mu \frac{\partial}{\partial t} - \frac{\beta}{2r\sqrt{(M_\infty^2 - 1)}} \frac{\partial}{\partial t} \right] w \tag{5}$$

with

$$\beta = \frac{2q}{\sqrt{(M_\infty^2 - 1)}}; \qquad \mu = \beta \frac{1}{V} \frac{M_\infty^2 - 2}{M_\infty^2 - 1} \tag{6}$$

where p is the free stream aerodynamic pressure, V is the free stream velocity defined as parallel to the ξ axis, q is the free stream dynamic pressure, r is the radius of curvature of the shell element, and β and μ are the free stream dynamic pressure and aerodynamic damping parameters, respectively.

The aerodynamic virtual work can be written in terms of the element nodal vector as

$$\delta W = \{\delta q\}^T [k_a]\{q\} - \{\delta \dot{q}\}^T [c_a]\{\dot{q}\} \tag{7}$$

with

$$[k_a] = -\beta \int_A \{f\} \frac{\partial \{f\}^T}{\partial \xi} \, dA \tag{8}$$

$$[c_a] = \left(-\mu + \frac{\beta}{2r\sqrt{(M_\infty^2 - 1)}}\right) \int_A \{f\}\{f\}^T \, dA \tag{9}$$

where $\{\dot{q}\}$ denotes the time derivative of the nodal vector. The matrices $[k_a]$ and $[c_a]$ are known as the aerodynamic stiffness and damping matrices, respectively. The aerodynamic stiffness matrix $[k_a]$ is asymmetric whereas the damping matrix $[c_a]$ is symmetric.

The aeroelastic system of equations for the structure is obtained by assembling the element matrices which can be symbolized by capital letters as

$$[M]\{\ddot{Q}\} + [C_a]\{\dot{Q}\} + \{[K] + [K_a]\}\{Q\} = 0 \tag{10}$$

The above system of equations is solved as an eigenvalue problem by assuming $\{Q\}$ to be

$$\{Q\} = \{\bar{Q}\} e^{st} \tag{11}$$

where s is a complex number and $s = s_r + is_i$.

To reduce the aeroelastic system of equations, the normal modes approach is used. First, free vibration analysis is performed to obtain the natural frequencies and mode shapes. Then, using a sufficient number of lowest modes for the aeroelastic system, eqn (10) can be reduced by premultiplying by $[\Phi]_t$ and post-multiplying by $[\Phi]$,

$$\{\omega_s\} + [\bar{K}_a]\{\bar{Q}\} = \{k\}\{\bar{Q}\} \tag{12}$$

$$[\bar{K}_a] = [\Phi]^T [K_a][\Phi] \tag{13}$$

where $[k]$ is a diagonal matrix containing complex eigenvalues $(k_r + ik_i)$, the matrix $[\Phi]$ is the modal matrix constructed by retaining the selected lowest natural modes of the structure and $[\omega_s]$ is a diagonal matrix containing the squares of the structural natural frequencies as diagonal elements.

The system of equations in eqn (12) results in an eigenvalue problem corresponding to a given value of the dynamic pressure parameter β. If the aerodynamic damping factor μ is neglected, the flutter boundary is obtained when the two relative lowest eigenvalues coalesce to give a critical value of β_{cr}. When $\mu > 0$, the flutter solution is obtained

when

$$\frac{\overline{k_i^2}}{\overline{k_r}} \geq \frac{\mu^2}{\rho D} \tag{14}$$

with

$$D = \frac{E_2 h^3}{12(1 - \nu_{12}^2)} \tag{15}$$

When presenting the subsequent results, the following nondimensional parameters are used: $\beta^* = \beta a^3/E_2 h^3$; $\omega^* = \omega a^2\sqrt{\rho h/E_2 h^3}$; and $\lambda^2 = -\omega^2 - \mu \omega a^4/E_2 h^3$.

3 RESULTS AND DISCUSSION

A general computer program was developed for the present composite shell finite element formulation as applied to supersonic panel flutter analysis. As part of the evaluation process, the natural frequencies and flutter solutions were first obtained for those isotropic and composite plates for which alternative solutions were available. For every example a convergence study was performed by computing the four lowest natural frequencies related to the flutter frequencies and observing their convergence trends while the meshes were being successively refined. It was found that for the square plates and curved panels, the values for the four lowest frequencies converged at the 6×6 mesh level. Thus, a 6×6 mesh was used to model the curved panels. All computations were carried out using a CYBER 205 vectorized supercomputer at Purdue University.

First, an isotropic square plate of length $L = 10$ in and thickness $h = 0.1$ in (1 in ≈ 2.54 cm) was studied. Table 1 shows the natural frequency parameter (ω^*) and flutter bounds $(\lambda_{cr}$ and $\beta_{cr})$ for the cantilevered square plate. The present finite element results are compared with other available solutions in Table 1. It can be seen that the present natural frequency parameter and flutter bounds agree well with those of Refs 12 and 13. Figure 1 shows the three lowest natural frequency parameters for a four layered $(\theta/-\theta/-\theta/t$ graphite–epoxy cantilevered composite plate. The material properties used for the graphite–epoxy composite material are as follows: $E_1 = 20.02 \times 10^6$ psi (1 psi ≈ 6.9 kPa); $E_2 = 1.3 \times 10^6$ psi; $G_{12} = 1.03 \times 10^6$ psi; $\rho = 0.148 \times 10^{-3}$ lb-s^2/in^4; and $\nu_{12} = 0.3$. The present results of

natural frequencies are compared to those of Ref.
21 as there are no results of flutter bounds avail-
able for comparison. A good agreement is found
for the natural frequencies. Divergence instead of

Table 1. Comparison of natural frequency parameters (ω^*)
and flutter boundaries (λ_{cr} and β_{cr}) for an isotropic square
cantilever plate

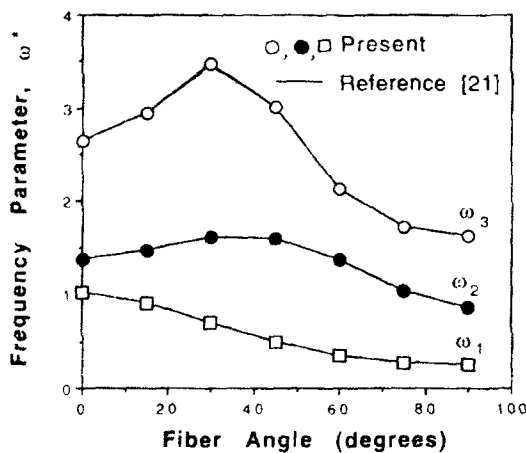| Reference	Natural frequency parameters ω^*					Flutter bounds	
	ω_1^*	ω_2^*	ω_3^*	ω_4^*	ω_5^*	λ_{cr}	β_{cr}
Ref. 13	3·40	8·48	20·77	26·73	30·67	58·35	6·43
Ref. 12	3·43	8·23	20·87	27·22	—	61·15	6·23
Present 6×6 mesh	3·47	8·51	21·30	27·21	30·98	52·78	6·07

Fig. 1. Lowest three natural frequency parameters for a
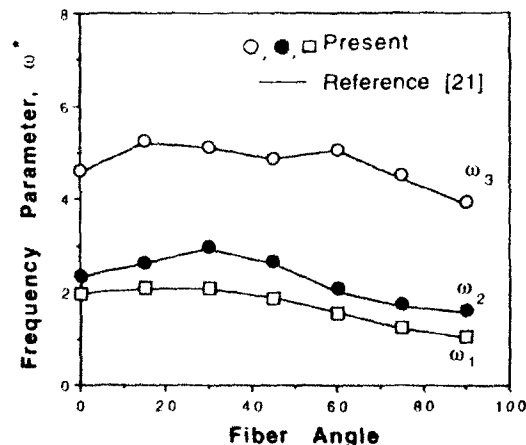$\theta/-\theta/-\theta/\theta$ graphite-epoxy laminated cantilevered com-
posite plate.

Fig. 2. Lowest three natural frequency parameters for a
$(\theta/-\theta/-\theta/\theta)$ graphite-epoxy laminated cantilevered cylin-
drical curved panel.

flutter occurs for all the fiber orientations consid-
ered. For the same problem, divergence occurs
when the flow direction is changed.

Figure 2 shows the three lowest natural fre-
quency parameters for a four layered $(\theta/-\theta/-\theta/\theta)$ graphite-epoxy cantilevered cylindrical
composite panel. The present results of natural
frequencies are in good agreement with those of
Ref. 21. Divergence instead of flutter occurs for
all the fiber orientations considered in this
example. Figure 3 shows the results of flutter
boundaries (β^* and ω^*) for a graphite-epoxy $[0°/\pm45°/90°]$ laminated cylindrically curved panel at
various flow angles. It can be seen from Fig. 3 that
as the flow angle is increased, the flutter bounds
(β_{cr} and ω_{cr}) decrease. It should be noted that
flutter occurs when modes 1 and 2 coalesce for
flow angles less than 30°, whereas modes 2 and 3
coalesce for flow angles greater than 30°. Diver-
gence occurs at 90° flow angle.

Figure 4 shows the results of flutter boundaries
(β^* and ω^*) for a graphite-epoxy $[0°/90°/0°]$
laminated cylindrically curved panel at various
flow angles. It can be seen from Fig. 4 that as the
flow angle is increased, the flutter bounds (β_{cr} and
ω_{cr}) decrease. It is observed that flutter occurs
when modes 2 and 3 coalesce for the flow angles
considered in this example. Divergence occurs at
0° and 90° flow angles. It can be seen from Figs 3
and 4 that mode coalesce will be different for
different laminated curved composite panels. In
general, for the two examples considered, the
trends for flutter behavior are similar. It should be
mentioned that for the various cases considered,
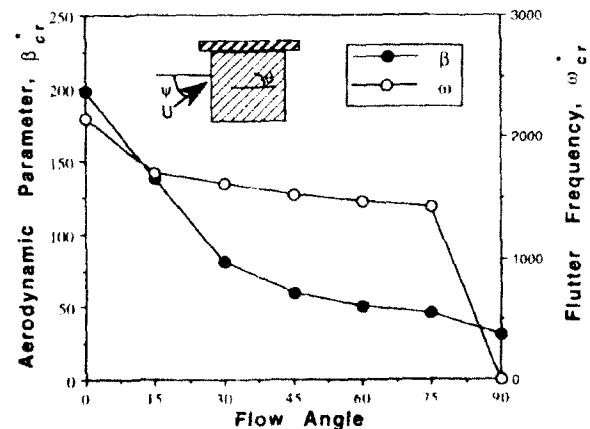divergence instead of flutter occurs.

Fig. 3. Effect of flow angle on flutter bounds (β_{cr} and ω_{cr})
for a $[0/\pm45°/90°]$ graphite-epoxy laminated cantilevered
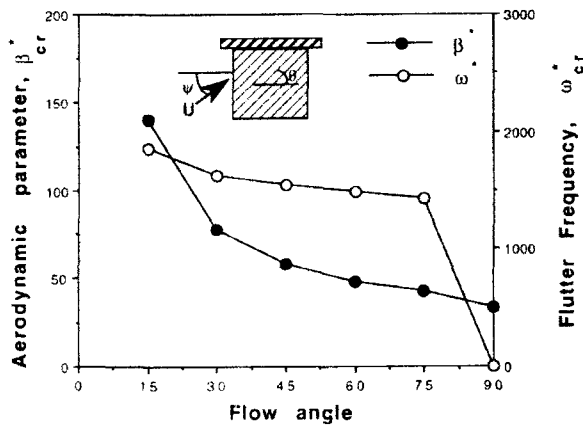cylindrical curved panel.

Fig. 4. Effect of flow angle on flutter bounds (β_{cr} and ω_{cr}) for a $0 - 0 - 0/0$ graphite–epoxy laminated cantilevered cylindrical curved panel.

4 CONCLUDING REMARKS

A supersonic flutter analysis of laminated composite plates and shells is carried out using a doubly curved quadrilateral thin shell finite element, developed on the basis of the Kirchhoff–Love thin shell theory, classical lamination theory, and linear piston aerodynamic theory. Numerical results are obtained for isotropic and laminated composite plates and curved panels. Good agreement of some of the obtained solutions with existing results serves to establish the validity of the present formulations for supersonic flutter analysis of laminated composite curved panels. The present results quantitatively illustrate the effects of flow angle and fiber orientation on the flutter bounds and mode shapes for cantilevered composite curved panels.

REFERENCES

1. Fung, Y. C., *The Theory of Aeroelasticity*. John Wiley & Sons, New York, USA, 1955.
2. Bisplinghoff, R. Y. & Ashley, H., *Principles of Aeroelasticity*. Dover Publications, New York, USA, 1962.
3. Dowell, E. H., *Aeroelasticity of Plates and Shells*. Noordhoff International Publishing, Leyden, The Netherlands, 1975.
4. Dowell, E. H., Curtiss, Jr. H. C., Scanlan, R. H. & Sisto, F., *A Modern Course in Aeroelasticity*. Sijthoff & Noordhoff, The Netherlands, 1978.
5. Fung, Y. C., Some recent contributions to panel flutter research. *AIAA J.*, 1 (4) (1963) 898–909.
6. Dowell, E. H., Panel flutter: a review of the aeroelastic stability of plates and shells. *AIAA J.*, 8 (3) (1970) 385–99.
7. Olson, M. D., Some flutter solutions using finite elements. *AIAA J.*, 8 (4) (1970) 747–52.
8. Sander, G., Bon, C. & Geradin, M., Finite element analysis of supersonic panel flutter. *Int. J. Numerical Methods Engng*, 7 (3) (1973) 379–94.
9. Yang, T. Y. & Sung, S. H., Finite element flutter in three-dimensional supersonic unsteady potential flow. *AIAA J.*, 15 (12) (1977) 1677–83.
10. Mei, C., A finite element approach for non-linear panel flutter. *AIAA J.*, 15 (8) (1977) 1107–10.
11. Ketter, D. J., Flutter of flat, rectangular, orthotropic panels. *AIAA J.*, 8 (2) (1967) 116–24.
12. Rossettos, J. N. & Tong, P., Finite element analysis of vibration and flutter of cantilever anisotropic plates. *J. Appl. Mech., ASME*, 41 (4) (1974) 1075–80.
13. Srinivasan, R. S. & Babu, B. J., Free vibration and flutter of laminated quadrilateral plates. *Computers and Structures*, 27 (2) (1987) 297–304.
14. Lin, K. J., Lu, P. J. & Tam, J. Q., Flutter analysis of composite panels using high-precision finite elements. *Computers and Structures*, 33 (2) (1989) 561–74.
15. Sawyer, J. W., Flutter and buckling of general laminated plates. *J. Aircraft*, 14 (4) (1977) 387–93.
16. Oyibo, G. A., Flutter of orthotropic panels in supersonic flow using affine transformations. *AIAA J.*, 21 (3) (1983) 283–9.
17. Yang, T. Y., High-order rectangular shallow shell finite elements. *J. Eng. Mech. Div., ASCE*, 99 (EM1) (1973) 157–81.
18. Jones, R. M., *Mechanics of Composite Materials*. McGraw Hill, New York, USA, 1975.
19. Lighthill, M. J., Oscillating airfoils at high Mach number. *J. Aerospace Sci.*, 20 (6) (1953) 402–6.
20. Voss, H. M., The effect of an external supersonic flow on the vibration characteristics of thin cylindrical shells. *J. Aerospace Sci.*, 12 (1961) 945–56.
21. Qatu, M. S. & Leissa, A. W., Natural frequencies for cantilevered doubly-curved laminated composite shallow shells. *J. Comp. Structures*, 10 (1991) 227–55.

Weight change mechanism of randomly oriented GFRP panel immersed in hot water

Tohru Morii,[a] Hiroyuki Hamada,[b] Zen-ichiro Maekawa,[b] Toshio Tanimoto,[a] Takahiro Hirano[c]
& Kenji Kiyosumi[c]

[a]*Shonan Institute of Technology, Tsujido-Nishikaigan, Fujisawa 251, Japan*
[b]*Kyoto Institute of Technology, Matsugasaki, Sakyo-ku, Kyoto 606, Japan*
[c]*Sekisui Plant System Co., Ltd, Dojimahama, Kita-ku, Osaka 530, Japan*

This study deals with the weight changes of the fiber/matrix interface and the weight change mechanisms of the randomly oriented E-glass fiber continuous strand m   reinforced unsaturated polyester panels. The weight changes were evaluated by introducing the weight gain due to water absorption (M_g) and the weight loss due to matrix dissolution (M_l). The weight changes of the fiber/matrix interface $(M_{gi}$ and $M_{li})$ were obtained from the difference of M_g and M_l between GFRP and neat resin. Water absorption of the interface occurred after water absorption of matrix resin reached saturation. Weight loss due to dissolution of binder on glass-fiber mat and matrix from the interface occurred after water penetration into the interface. The debondings at the fiber/matrix interface occurred due to water penetration, and as a result, the binder and matrix dissolved easily in the water through the interface. The weight changes of the GFRP panel were classified into three phases. In phase I, only the resin matrix absorbed water. In phase II, the fiber/matrix interface absorbed water. After that phase, water absorption into the fiber/matrix interface and matrix dissolution from the interface occurred simultaneously.

INTRODUCTION

Glass-fiber reinforced plastics (GFRP) have been used as the structural materials in a wet environment, because GFRP has excellent corrosion resistance as well as high specific modulus and strength. In particular, GFRP panels such as continuous strand mat reinforced plastics, SMC, etc., have been widely used as water tanks. During long-term use in a water environment, the weight of GFRP is changed by water absorption and matrix dissolution, and it induces a serious reduction in the mechanical properties.[1-4] Water is mainly absorbed in the matrix resin and the fiber/matrix interface consisting of GFRP.[5] The weight change behavior of matrix resin only can be evaluated easily by exposure of a neat resin specimen to a wet environment.[6,7] However, it is difficult to evaluate the weight change behavior of the fiber/matrix interface in GFRP. Therefore the studies dealing with the weight change behavior of the interface are very few, and the role of the interface in the weight change behavior has not been clari-

fied well.[5] It is generally said that water penetrates into the interface by capillary action, however, the quantitative evaluation of weight changes of the interface has never been done.

We have studied the degradation behavior of a randomly oriented GFRP panel immersed in hot water.[8,9] In our previous papers, we evaluated the weight changes of a GFRP panel by introducing the weight gain due to water absorption and the weight loss due to matrix dissolution, etc., and clarified the importance of the interface on the degradation of a GFRP panel.

In the present paper, we propose a quantitative evaluation method for the weight changes of the fiber/matrix interface of randomly oriented glass-fiber continuous strand mat reinforced unsaturated polyester panels immersed in hot water. The degradation behavior of the fiber/matrix interface is clarified by introducing a proposed evaluation method. The weight change mechanism of the randomly oriented GFRP panel immersed in hot water is discussed on the basis of the evaluated results of the weight changes of the interface.

Table 1. Composition of specimens used

Specimen	Type A	Type B
Resin matrix	Bisphenol based unsaturated polyester	
Reinforcement	Randomly oriented E-glass fiber continuous strand mat	
Filler	None	Calcium carbonate 15 phr
Molding method	Compression molding	

EXPERIMENTAL PROCEDURE

Materials used were two types of glass-fiber reinforced unsaturated polyester resin (types A and B) with different matrix composition. Two types of resin matrix based on bisphenol were used: unsaturated polyester resin with or without filler. Type A contained no filler and type B contained 15 phr calcium carbonate. Reinforcement was randomly oriented E-glass fiber continuous strand mat. The composition of the specimens is summarized in Table 1. Using these materials 300 mm square panels were fabricated by a compression molding method, and specimens were cut out from these panels.

Water immersion tests were conducted at 60 and 80°C with temperature controlled water baths. The periods of immersion were 3, 10, 30, 100, 300, 1000 and 3000 h. Weight changes due to immersion were determined by weighing 50 mm square specimens before and after immersion. Before immersion, all specimens were dried in vacuum at 100°C, and after that the specimens were immersed in hot water for a fixed period of time. After immersion, the wet specimen weight was measured and the specimens were dried again in a vacuum oven. After perfect drying, the dried specimen weight was determined. From these weight measurements, net weight gain (M_g) and weight loss (M_l) were obtained by:

$$M_g = (W_w - W_d)/W_o \qquad (1)$$

$$M_l = (W_o - W_d)/W_o$$

where W_o is the dried specimen weight before immersion, and W_w and W_d are the wet and the dried specimen weight after immersion. The neat resin specimens were also immersed in hot water and weight changes were evaluated in the same way as those of GFRP in order to compare with the weight changes of GFRP. For comparison with GFRP, M_g and M_l of the neat resin specimens were re-evaluated. Re-evaluated M_g and M_l for neat resin (M_{gR} and M_{lR}) are calculated on the assumption that only the resin matrix of GFRP affects the weight changes due to water immersion and that the fiber and the interface can be neglected for the weight changes of GFRP. M_{gR} and M_{lR} are expressed as:

$$M_{gR} = M_{gr} \times (1 - W_f)$$

$$M_{lR} = M_{lr} \times (1 - W_f) \qquad (2)$$

where M_{gr} and M_{lr} are experimental data of M_g and M_l for the neat resin specimen. M_{gR} and M_{lR} are the re-evaluated M_g and M_l of the neat resin, and W_f is the fiber weight fraction of GFRP.

RESULTS AND DISCUSSION

Weight changes in GFRP and neat resin

Figures 1 and 2 show the changes of the net weight gain M_g for GFRP and neat resin with the immersion time. The variation of M_g for GFRP indicated the same tendency as that for neat resin up to 100 h at 60°C and up to 30 h at 80°C. After these immersion times, the M_g for GFRP increased, whereas M_g for neat resin maintained a constant saturation level. As a result, the difference in M_g between GFRP and neat resin became greater as the immersion time became longer. The saturation level of M_g for neat resin was almost the same independent of water temperature. It is considered that only the matrix resin of GFRP absorbs the water before 100 h at 60°C and before 30 h at 80°C. Water absorption after these immersions may be due to the existence of glass fiber mat in GFRP. Glass fiber never absorbs water, while the fiber/matrix interface in GFRP can absorb water if the bonding between the fiber and the matrix is imperfect. Therefore the water absorption due to longer immersion may be caused by the degradation of the fiber/matrix interface. The M_g for GFRP in type A indicated the same tendency as type B at 60°C, and it was a little higher than in type B at 80°C.

Changes in the weight loss M_l for GFRP and neat resin with immersion time are shown in Figs 3 and 4. The M_l of neat resin was nearly equal to 0 up to 1000 h. In the same way the M_l of GFRP was nearly equal to 0 up to 300 h at 60°C and up to 100 h at 80°C. After these immersion times, however, M_l increased linearly against the square root of immersion time. The slope of M_l against the square root of time was almost the same
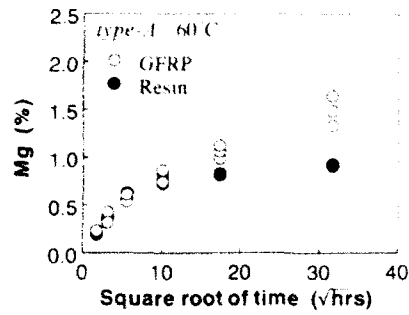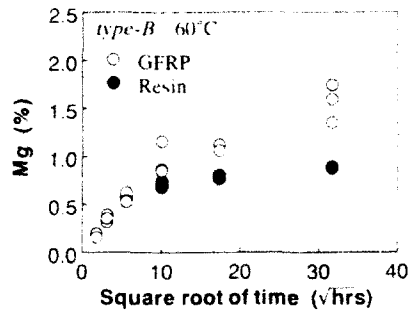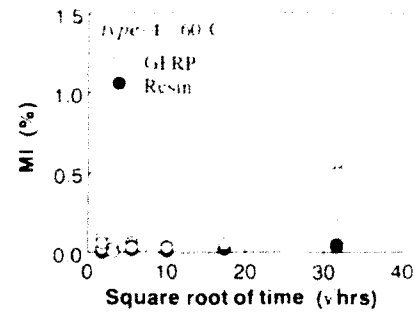
Fig. 1. Changes in net weight gain (M_g) for GFRP and neat resin at 60°C for (a) type A and (b) type B.

Fig. 3. Changes in weight loss (M_l) for GFRP and neat resin at 60°C for (a) type A and (b) type B.
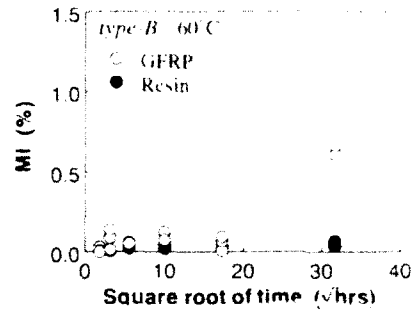

Fig. 2. Changes in net weight gain (M_g) for GFRP and neat resin at 80°C for (a) type A and (b) type B.
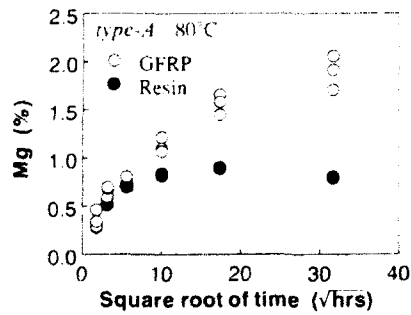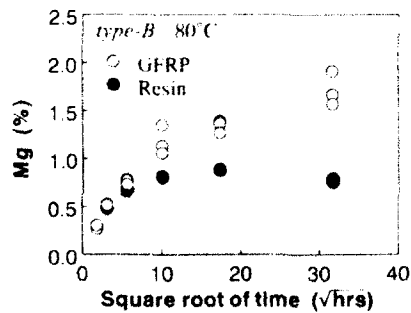

Fig. 4. Changes in weight loss (M_l) for GFRP and neat resin at 80°C for (a) type A and (b) type B.
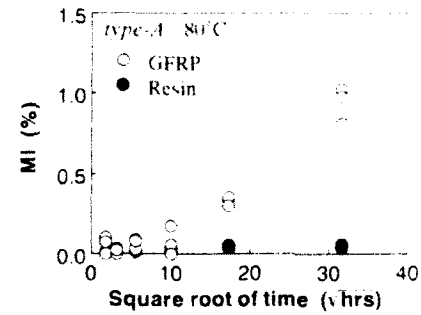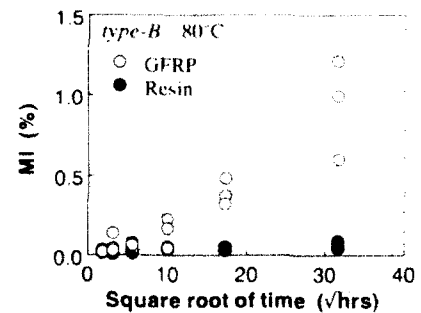
independent of water temperature. The slope of M_1 for GFRP in type B was higher than in type A. The neat resin hardly dissolved in water. Therefore the weight loss for GFRP may be induced by the degradation at the fiber/matrix interface.

Effect of degradation of fiber/matrix interface on weight change

Supposing that the fiber did not affect the weight change kinetics, the difference in weight changes between GFRP and neat resin may be considered to express the weight changes showing the existence of fiber/matrix interface. Therefore the weight change parameter for the fiber/matrix interface can be defined as follows:

$$M_{gI} = M_g - M_{gR}$$

$$M_{II} = M_1 - M_{1R}$$

(3)

where M_{gI} is the net weight gain of the fiber/matrix interface and M_{II} is the weight loss from the interface.

Figures 5 and 6 show the changes in M_{gI} against the square root of immersion time. M_{gI} increased almost linearly against the square root of immersion time after 100 h at 60°C and after 30 h at 80°C. This means that water penetration into the fiber/matrix interface occurred after 100 h at 60°C and after 30 h at 80°C and that water was absorbed only by the matrix resin before these immersion times. The extensive water penetration into the interface is considered to occur after water absorption in the matrix region reaches almost saturation level. The slope of M_{gI} at 80°C was greater than that at 60°C both for type A and type B. The water temperature affects the penetration speed of water into the interface. The slope of M_{gI} for type A at 60°C was almost the same as that of type B, however, it was greater than type B at 80°C. This phenomenon shows the difference in M_g for GFRP between type A and type B at 80°C. The filler mainly affects the weight gain due to water penetration into the fiber/matrix interface.

Figure 7 and 8 show the changes in M_{II} against the square root of immersion time. M_{II} at 60°C was almost 0 up to 300 h, and at 80°C it increased up to 100 h. After that M_{II} increased almost linearly against the square root of immersion time. The occurrence of M_{II} was delayed due to the presence of M_{gI}. Therefore it is considered that M_{II} is caused by degradation and chemical reaction such as hydrolysis due to absorbed water.
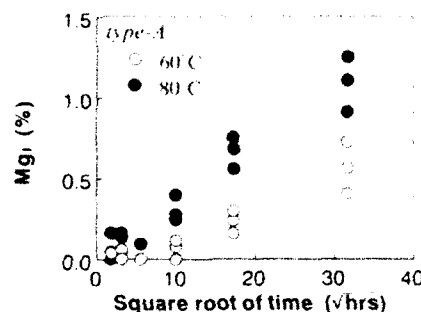

Fig. 5. Changes in net weight gain at interface M_{gI} for type A.
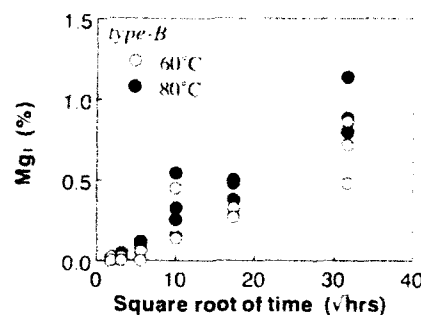

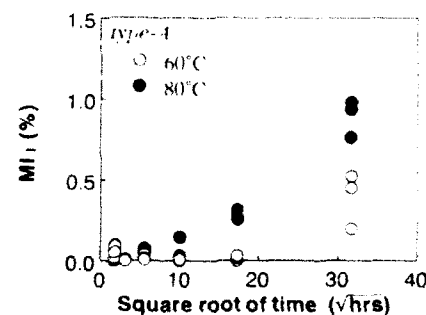**Fig. 6.** Changes in net weight gain at interface M_{gI} for type B.

Fig. 7. Changes in weight loss at interface M_{II} for type A.
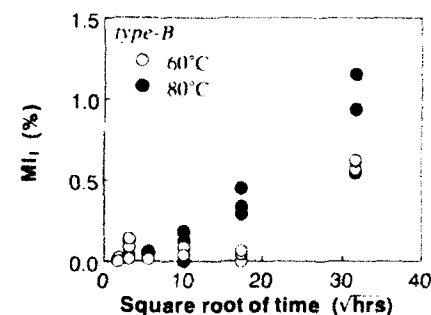

Fig. 8. Changes in weight loss at interface M_{II} for type B.

The debonding at the fiber/matrix interface occurs due to water penetration into the interface, and as a result, the matrix and the binder on the glass mat dissolve easily in water through the interface. The slope of M_{II} is almost the same independent of the water temperature and of the materials both for type A and type B. However, the immersion time for type B when M_{II} arose due to water immersion was shorter than for type A at both water temperatures. This difference is considered to be induced by the filler.

Weight change mechanism of GFRP immersed in water

The difference in M_g between GFRP and neat resin was remarkably large after 100 h at 60°C and after 30 h at 80°C. Therefore considerable water absorption into the interface is considered to occur after the above-mentioned immersion times. The M_l of neat resin was nearly equal to 0 up to 3000 h, while the M_l of GFRP increased after 300 h at 60°C and after 100 h at 80°C. Consequently the weight change of the randomly oriented GFRP used here can be classified into three phases as schematically illustrated in Fig. 9. In phase I, the weight gain was due to the water absorbed in the resin matrix only, however, a small amount of water was absorbed in the fiber/matrix interface. In phase II, weight gain due to water absorption into the interface occurred. After that phase, catastrophic degradation at the fiber/matrix interface resulted, and water absorption and matrix dissolution occurred simultaneously in phase III. Both in type A and type B at 60°C, phases I, II and III are defined as the
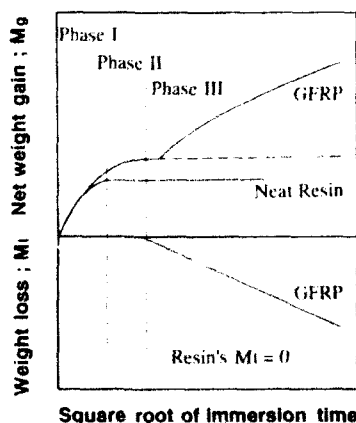
periods from 0 to 100 h, 100 h to 300 h, and over 300 h, respectively, from the experimental results shown in Figs 1 and 3. As with 80°C, phases I, II and III are the periods from 0 to 30 h, 30 h to 100 h, and over 100 h, respectively, shown in Figs 2 and 4. In phase I, water absorption in the matrix resin only occurred and the influence of the filler did not appear. In phase II, water absorption into the interface occurred and the M_{gI} of type B was greater than that of type A. After phase II, the influence of the filler appeared in the changes in M_{gI} and M_{II}, and more degradation of the interface occurred on type B than on type A. Therefore the filler influences the degradation of the fiber/matrix interface.

CONCLUSIONS

This study dealt with the weight changes of the interface and the weight change mechanisms of the randomly oriented E-glass fiber continuous strand mat reinforced unsaturated polyester panels. The weight changes were evaluated by introducing the weight gain due to water absorption (M_g) and the weight loss due to matrix dissolution (M_l). The weight changes in the fiber/matrix interface $(M_{gI}$ and $M_{II})$ were obtained from the difference in M_g and M_l between GFRP and neat resin.

Water absorption of the interface occurred after water absorption of the matrix resin reached saturation. Weight loss due to dissolution of binder on the glass-fiber mat and matrix from the interface occurred after water penetrated the interface. The debondings at the fiber/matrix interface occurred due to water penetration, and as a result, the binder and matrix dissolved easily in the water through the interface.

The weight changes of the GFRP panel were classified into three phases as follows:

Phase I: Only the resin matrix absorbed water.

Phase II: The fiber/matrix interface absorbed water.

Phase III: Water absorption into the fiber/matrix interface and matrix dissolution from the interface occurred simultaneously.

Fig. 9. Weight change behavior of randomly oriented GFRP panel.

REFERENCES

1. Shen, C. H. & Springer, G. S., Effects of moisture and temperature on the tensile strength of composite materials. *J. Comp. Mater.*, **11** (1977) 2–16.

2. Shen, C. H. & Springer, G. S., Environmental effects on the elastic moduli of composite materials. *J. Comp. Mater.*, **11** (1977) 250–64.

3. Ellis, B. & Found, M. S., The effects of water absorption on a polyester/chopped strand mat laminate. *Composites*, **14** (1983) 237–43.

4. Phillips, M. G., Prediction of long-term stress-rupture life for glass fibre-reinforced polyester composites in air and in aqueous environments. *Composites*, **14** (1983) 270–5.

5. Vaughan, D. J., Peek, R. C. Jr & Creech, M. H. Jr, The importance of the interface on water absorption in glass reinforced epoxy composites. *SPI 39th Annual Conference*, Session 4-G, 1984, pp. 1–1.

6. Janas, V. F. & McCullough, R. L., Moisture absorption in unfilled and glass-filled, cross-linked polyester. *Comp. Sci. Technol.*, **29** (1987) 293–315.

7. Wright, W. W., The effect of diffusion of water into epoxy resins and their carbon-fibre reinforced composites. *Composites*, **12** (1981) 201–5.

8. Hamada, H., Yokoyama, A., Maekawa, Z. & Morii, T., Weight change and mechanical properties of GRP panel in hot water. *Proc. ICCS-5* (1989) 259–77.

9. Morii, T., Tanimoto, T., Maekawa, Z., Hamada, H., Yokoyama, A., Kiyosumi, K. & Hirano, T., Effect of water temperature on hygrothermal aging of GFRP panel. *Proc. ICCS-6* (1991) 187–201.

The effects of environmental humidity after post cure on the optimal temperature path of polymer composites

R. S. Chen, G. S. Chen & J. R. Chen

Department of Engineering Science, National Cheng-Kung University, No. 1, University Road, Tainan, Taiwan, 70101

Previous studies on the optimal cool-down path of a composite laminate, were applied in this paper to a new element-humidity used for analysis of the residual stresses which develop in a composite material laminate after termination of cool down due to further exposure to a humid environment.

Computations were performed for AS4/3502 symmetric balanced cross-ply laminate. The viscoelastic behaviour and the constant expansion coefficients of temperature and moisture of hygrothermorheologically simple material have been considered and an optimal temperature path was obtained with the assistance of variations for yielding the minimal value for the average residual stress within the laminate. Furthermore, the experiment for measuring the residual stress by strain gauge is conducted in order to ensure the reliability of the theoretical analysis. The result of this paper gives further understanding of the humidity effect on composite material during its post cure process. Therefore, this study will be very helpful for the improvement of manufacturing industries.

INTRODUCTION

A composite material, which consists of fibres and epoxy is always fabricated as layers with different directions due to the various requirements of design. This leads to different thermal expansions in each direction. Therefore, control of the temperature path during the cure process is indeed important.[1-4] Furthermore, due to the process of moisture diffusion, swelling strains[5-8] develop within the composite which induce further residual stresses[9,10] in multi-directionally reinforced laminates. This humidity effect tends to be significant when the composite is exposed to environmental humidity after the post cure process.[11] This paper incorporates the humidity effect after fabrication to readjust the optimal path in the post cure.

ENVIRONMENTAL HUMIDITY

Governing equation of moisture diffusion

The moisture sorption behaviour of graphite/epoxy materials has been treated as a diffusion controlled process as described by Fick's Second Law.[5,6]

$$\frac{\partial m}{\partial t} = \frac{\partial}{\partial z}\left(C \cdot \frac{\partial m}{\partial z}\right) \tag{1}$$

where

t = time,

z = coordinate in the direction of the composite thickness,

$C = C(T)$ = moisture diffusion coefficient,

$m = m(z,t)$ = moisture content.

For a laminate with an initially uniform moisture content u_0 and symmetric boundary conditions $m(z = \pm h, t) = u_\infty$ where u_∞ is the equilibrium moisture content, the solution to eqn. (1) for a constant diffusion coefficient and boundary conditions can be expressed as follows:

$$m(z,t) - u_0 I_0(z,t) = u I(z,t) \tag{2}$$

where $I_0(z,t)$ and $I(z,t)$ are assumed as

$$I_0(z,t) = \begin{cases} F(z,t) \\ 1 - E(z,t) \end{cases}$$

and $\tag{3}$

$$I(z,t) = \begin{cases} 1 - F(z,t) \\ E(z,t) \end{cases}$$

in which

$$F(z,t) = 2 \sum_{n=1}^{\infty} \frac{(-1)^{n+1}}{P_n} \cos\left(\frac{P_n z}{h}\right) \exp(-P_n^2 t^*) \tag{4}$$

$$E(z,t) = \sum_{n=1}^{\infty} (-1)^{n+1} \left[\operatorname{erfc}\left(\frac{2n-1-z/h}{2\sqrt{t^*}}\right) + \operatorname{erfc}\left(\frac{2n-1+z/h}{2\sqrt{t^*}}\right) \right] \tag{5}$$

with

$$P_n = (2n-1)\pi/2$$
$$t^* = Ct/h^2$$

$$\operatorname{erfc}(x) = \frac{2}{\sqrt{\pi}} \int_x^{\infty} e^{-s^2} ds$$

where
 erfc = complement error function.
 h = half of thickness of the laminate.

Equations (4) and (5), the solutions for eqn (1) in terms of $E(z,t)$ and $F(z,t)$ are obtained by the separation of variables technique and the Laplace transform method, respectively. To achieve the computational efficiency, an efficient computational scheme for switching among these two forms has been proposed by Weitsman so as to minimize the numbers of terms required in Series (4) and (5) and obtain the moisture distribution to within the desired error tolerance. The scheme is based upon the observation in which Series (4) rapidly converges for the short time case due to the rapid decay of erfc, whereas Series (5) rapidly converges for the long time case. Weitsman also defined the following set of rules to maintain the accuracy of $(10)^{-16}$:

(a) for $\left(\frac{i-1}{2\lambda}\right)^2 < t^* < \left(\frac{i}{2\lambda}\right)^2$.

use i terms in Series $E(z,t)$

(b) for $\left(\frac{2}{\lambda}\right)^2 < t^* < \left(\frac{\delta}{81}\right)$.

use five terms in Series $F(z,t)$

(c) for $\frac{\delta}{(2i+1)^2} < t^* < \frac{\delta}{(2i-1)^2}$.

use i terms in Series $F(z,t)$

where $i = 1,2,3,4$, $\delta = 14.93$ and $\lambda = 5.877$.

Swell of composite material due to moisture sorption

The swelling strain for the graphite/epoxy composite due to moisture sorption perpendicular to the fibre direction (i.e. the transverse direction denoted by subscript L) is defined as the function in which the moisture content is beyond the initial value m_i, i.e.

$$\varepsilon_1 = \beta_1(m - m_i) \quad \text{when} \quad m > m_i$$
$$\varepsilon_1 = 0 \qquad\qquad \text{when} \quad m \le m_i \tag{6}$$

where
 ε_1 = transverse swelling strain.
 β_1 = transverse moisture expansion coefficient.
 m = moisture content.
 m_i = threshold moisture content.

For AS4/3502 graphite/epoxy material, the transverse moisture expansion coefficient β_1 is 0.00324 and the threshold moisture content m_i is 0.1%. Furthermore, the longitudinal swelling strain parallel to the fibre direction (denoted by subscript L) is negligible in comparison with the transverse swelling strain. The longitudinal moisture expansion coefficient β_1 is assumed to be zero for most cases.

Moisture diffusion coefficient and equilibrium moisture content

Springer[8] engaged in series of experiments on the moisture diffusion of the composite to obtain the moisture diffusion behaviour described by a simple mathematic model. A significant dependency of moisture diffusion coefficient on temperature and a weak dependency of moisture diffusion coefficient on moisture content have furthermore been revealed in his results. The moisture diffusion coefficient is therefore treated as a function of temperature:

$$C(T) = D_0 \exp(-A_0/RT) \tag{7}$$

where
 D_0 = permeability index,
 A_0 = activation energy for diffusion,
 R = gas constant,
 T = absolute temperature (K).

Meanwhile, the equilibrium moisture content u_∞ is the saturated moisture amount of the material which is dependent on the relative humidity surrounding the material.

$$\mu_\infty = H(RH\%)^p \tag{8}$$

where
RH = percentage relative humidity.
H, ρ = material constants.

THEORETICAL ANALYSIS

A symmetric cross-ply and viscoelastic composite laminate are considered which have been affected by a variated temperature $T(t)$ during the post cure and by a constant moisture content u_∞ in the environmental humidity after the termination of cool down. Due to the thickness of the composite laminate, temperature $T = T(t)$ is assumed to be spatially uniform but varies only with time. The process of moisture diffusion is thus uncoupled from that of thermal diffusion. The moisture content is a function of time and location (in the direction of thickness only) since the time required for reaching the saturated moisture content is rather long. Furthermore, the viscoelasticity of composite material can be solved through application of the correspondence principle. The HTSM properties are also introduced for temperature and moisture effects. The expansion coefficients of temperature and moisture are also finally assumed as being constant. The analytical processes are described as follows.

Linear elastic analysis

For a symmetric cross-ply laminate subjected to the effects of temperature and humidity, the relation between stress and strain in the individual orthotropic plies can be expressed as follows:

for the 0° layer (the layer with the fibre direction parallel to x-axis)

$$\sigma_x = Q_1(\varepsilon_x - \alpha_1 \Delta T - \beta_1 m_c)$$
$$+ Q_{11}(\varepsilon_y - \alpha_1 \Delta T - \beta_1 m_c)$$
$$\sigma_y = Q_{11}(\varepsilon_x - \alpha_1 \Delta T - \beta_1 m_c)$$
$$+ Q_1(\varepsilon_y - \alpha_1 \Delta T - \beta_1 m_c)$$

(9)

for the 90° layer (the layer with the fibre direction normal to x-axis)

$$\sigma_x = Q_T(\varepsilon_x - \alpha_1 \Delta T - \beta_1 m_c)$$
$$+ Q_{11}(\varepsilon_y - \alpha_1 \Delta T - \beta_1 m_c)$$
$$\sigma_y = Q_{11}(\varepsilon_x - \alpha_1 \Delta T - \beta_1 m_c)$$
$$+ Q_1(\varepsilon_y - \alpha_1 \Delta T - \beta_1 m_c)$$

where
Q = stiffness modulus.
α = thermal expansion coefficient.
β = swelling coefficient.
ΔT = temperature change.
m_c = effective moisture content ($= m - m_1$).
σ = stress.
ε = strain.

Subscripts x, y: reference system of laminates. Subscripts L, T: parallel and transverse to the direction of the fibres.

Since the laminate is assumed to be free of external loading, the net resultant force N of each point on the laminate must vanish. Namely,

$$N_x = \int_h^h \sigma_x \, dz = 0$$
$$N_y = \int_h^h \sigma_y \, dz = 0$$

(10)

where h is half thickness of composite laminate.
Substituting eqn (9) into eqn (10) we get

$$\varepsilon = \varepsilon_x = \varepsilon_y$$

$$\sigma = \sigma_x = -\sigma_y = -\frac{Q_1 Q_1 - Q_{11}^2}{Q_1 + Q_1 + 2Q_{11}} [(\alpha_1 - \alpha_1)\Delta T$$

(11)

$$+ (\beta_1 - \beta_1)m_c]$$

Incorporating the properties of graphite/epoxy into the above equation lead to the simplified form (such as $E_1 \sim 20 E_1$, $v_{11} \sim 20 v_{11}$ with $v_{11} = 0.28$)

$$\sigma = -r E_1 [(\alpha_1 - \alpha_1)\Delta T + (\beta_1 - \beta_1)m_c]$$

(12)

When considering the viscoelasticity of the resin, r becomes a function of time. However, in all practical cases, r is a weak function of time within the values ranging between 0.9 and 0.93. The expansion coefficient α_1 is also theoretically dependent on temperature. However, due to its weak dependence on T, α_1 constant is considered here in the present work.

Viscoelastic analysis

For the graphite/epoxy composite, an approximate expression for the transverse viscoelasticity modulus reads

$$E = E_T = E_0(\xi + t_0)^{-q}$$

(13)

where ξ is the reduced time.

A combined temperature–moisture shift factor can be introduced for analysing the effect of temperature and humidity on the composite due to consideration of the property of HTSM

$$a(z,s) = a(T(s), m(z,s)) = a_T(T) \cdot a_M(m) \qquad (14)$$

where $a_T(T)$ is the temperature related shift factor

$$a_T(T) = \exp(-T/A + B) \qquad (15)$$

$a_M(m)$ is the moisture related shift factor,

$$a_M(m) = \exp(-C_0 m + C_1) \qquad (16)$$

The reduced time ξ in eqn (5) therefore becomes

$$\xi(r) = \int_0^r \frac{ds}{a(z,s)} \qquad (17)$$

eqn (5) can be then expressed as

$$E = E_1[\xi(t)] = E_0\left\{ t_0 + \int_0^t \frac{ds}{a(z,s)} \right\}^{-q} \qquad (18)$$

Computations have been performed for AS4/3502. In this paper the viscoelastic properties and material constants of this graphite/epoxy composite are listed in Tables 1 and 2.

Table 1. The viscoelastic properties of the AS4/3502, graphite/epoxy

E_0 (kN/m²)	t_0 (min)	q	r	A (K)	B	C_0	C_1
$10^{10.05}$	1	0·00775	0·9	6·258	46·81	5·2	0·26

Table 2. The thermal expansion coefficients of the AS4/3502, graphite/epoxy

$\alpha T = \alpha_0 + \alpha_1 T$			
α_1 (cm/cm/K)		α_3 (cm/cm/K)	
α_0	α_2	α_0	α_2
$-0·484 \times 10^{-6}$	$0·72 \times 10^{-9}$	$9·5 \times 10^{-6}$	$0·41 \times 10^{-9}$

Table 3. The swelling coefficients and diffusion coefficients of the AS4/3502, graphite/epoxy

D_0	A_0/R	H	σ	m_∞	β_1	β_3
1·67	5480	0·002676	1·325	0·13%	0·00324	0·0

The optimal temperature path and residual stress for the curing process

Consider a symmetric cross-ply viscoelastic composite laminate (with a thickness of $2h$). During the cure process, the laminate is subjected to a variable temperature with the initial temperature T_1 and the final temperature T_R in a specified time interval t_c; after the cure process, as shown in Figs 1 and 2, it is affected by a fixed humidity u_∞ and the length of exposure Δt_c in the surrounding environment. Since the plate is thin, the temperature at each point of the composite can be assumed to be homogeneous, $T = T(t)$. Nevertheless, the marginal effect of the diffusion of moisture from the laminate can be ignored and only the moisture diffusion in the direction of the plate thickness is taken into account. The residual stress of the composite can hence be expressed as

$$-\sigma(z,t_c) = r \int_0^{t_c} E\left[\int_\tau^t \frac{ds}{a(T(s), m(z,s))} \right] \cdot \left[\alpha \frac{\partial}{\partial \tau}(T(\tau) - T_1) + \beta \frac{\partial}{\partial \tau} m_c(z,\tau) \right] d\tau \qquad (19)$$

where

$$\alpha = \alpha_1 - \alpha_3$$

$$\beta = \beta_1 - \beta_3$$

$$E_1\left[\int_\tau^t \frac{ds}{a(z,s)} \right] = E_1[\xi(t) - \xi(\tau)] = E_0\left\{ t_0 + \int_\tau^t \frac{ds}{a(z,s)} \right\}^{-q} \qquad (20)$$

$$t_c = t_1 + \Delta t_c$$

In eqn (19), stress is found to be a function of time and position in the laminate. This is because of the moisture diffusion in the composite laminate always resulting in spatially non-uniform stresses within each layer. Consequently, we confine our consideration to the average value of the residual stress σ_a, i.e.
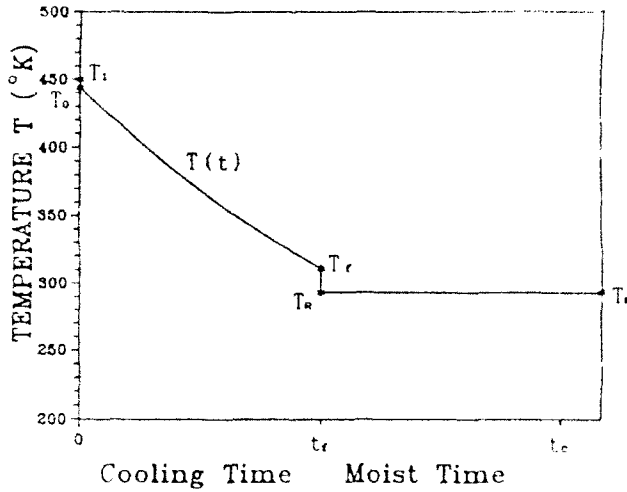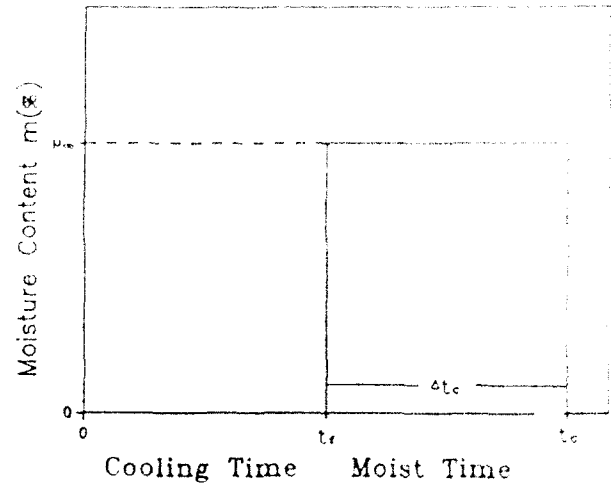
Fig. 1. Theoretical analysis for temperature path.

Fig. 2. Theoretical analysis for humidity fluctuation

$$-2h\sigma_a(t_c) = r \int_h^h \left\{ \left[\int_0^{t_o} \frac{ds}{a(T(s), m(z,s))} \right] \cdot \left[\alpha \frac{\partial}{\partial \tau} (T(\tau) - T_1) + \beta \frac{\partial}{\partial \tau} m_c(z,\tau) \right] \right\} dz \qquad (21)$$

In view of the results presented in Refs 3, 4 and 10, the temperature and humidity history are divided into four sections for integration. These are $t = 0$, $0 < t < t_c$, $t = t_t$ and $t_t < t < t_c$, respectively. Equation (21) can be revised to read

$$-2h\sigma_a(t_c) = r \left\{ \alpha(T_0 - T_1) \int_h^h E \left[\int_0^{t_t} \frac{ds}{a_1(T(s))} + \int_{t_t}^t \frac{ds}{a(T_R, m(z,s))} \right] dz \right.$$

$$+ \alpha(T_R - T_1) \int_h^h E \left[\int_{t_t}^t \frac{ds}{a(T_R, m(z,s))} \right] dz$$

$$+ \alpha \int_h^h \int_{t_c}^{t_c} E \left[\int_\tau^t \frac{ds}{a_1(T(s))} + \int_{t_t}^t \frac{ds}{a(T_R, m(z,s))} \right] \frac{\partial}{\partial \tau} \left[(T(\tau) - T_1) \right] d\tau \, dz$$

$$\left. + \beta \int_h^h \int_{t_c}^{t_c} E \left[\int_\tau^t \frac{ds}{a(T_R, m(z,s))} \right] \frac{\partial}{\partial \tau} m_c(z,\tau) \, d\tau \, dz \right\} \qquad (22)$$

By applying the method of calculus of variations,[3,4,10] the optimal temperature path of the minimum average residual stress can be derived.

Let $T(t)$ be the optimal path and designate $\tilde{T}(t) = T(t) + \varepsilon\eta(t)$ as an adjacent path, where ε is small value and $\eta(t)$ is an arbitrary function. $\tilde{\sigma}_a$ then becomes the average stress derived from $T(t)$ and $m(z,t)$ as

$$-2h\tilde{\sigma}_a(t_c) = r \left\{ \alpha(T_0 + \varepsilon\eta_0 - T_1) \int_h^h E \left[\int_0^{t_t} \frac{ds}{a_1(T(s) + \varepsilon\eta(s))} + \int_{t_t}^t \frac{ds}{a(T_R, m(z,s))} \right] dz \right.$$

$$+ \alpha(T_R - T_1 - \varepsilon\eta_1) \int_h^h E \left[\int_{t_t}^t \frac{ds}{a(T_R, m(z,s))} \right] dz$$

$$+ \int_{0}^{t_t} \int_h^h E \left[\int_\tau^t \frac{ds}{a_1(T(s) + \varepsilon\eta(s))} + \int_{t_t}^t \frac{ds}{a(T_R, m(z,s))} \right] dz \alpha \frac{\partial}{\partial \tau} \left[T(\tau) + \varepsilon\eta(\tau) - T_1 \right] d\tau$$

$$\left. + \beta \int_h^h \int_{t_c}^{t_c} E \left[\int_\tau^t \frac{ds}{a(T_R, m(z,s))} \right] \frac{\partial}{\partial \tau} m_c(z,\tau) \, d\tau \, dz \right\} \qquad (23)$$

where $\eta_0 = \eta(0)$; $\eta_1 = \eta(t_t)$.

To minimize the value of $\bar{\sigma}_a$, the differential of $\bar{\sigma}_a$ subject to ε must be zero, i.e.

$$\frac{d}{d\varepsilon}\left[-2h\bar{\sigma}_a\right]\Big|_{\varepsilon=0}=0 \tag{24}$$

Through the process of integration by parts, the optimal temperature path $T(t)$ with the open interval $0 < t < t_1$ can be obtained as the following nonlinear integro-differential equation

$$T'(t)=-\left(\frac{a_1'}{a_1 a_1''}\right)\frac{2h}{\int_h\left\{E'\left[\int_t^{t'}\frac{ds}{a_1(T(s))}+\int_{t_1}^{t}\frac{ds}{a(T_R,m(z,s))}\right]\Big/E''\left[\int_t^{t'}\frac{ds}{a_1(T(s))}+\int_{t_1}^{t}\frac{ds}{a(T_R,m(z,s))}\right]\right\}dz} \tag{25}$$

The magnitude of the initial discontinuity from T_1 to T_0 becomes

$$T_0-T_1=\frac{a_1(T_0)}{a_1'(T_0)} \tag{26}$$

The temperature path $T(t)$ obtained from eqns (25) and (26) can be substituted into eqn (19) so that the residual stress at any time can be obtained. Since the temperature and humidity in each interval is discontinuous, four time intervals are required for analysis of the residual stress as follows:

(a) $t_0=0^-$

$$-\sigma_a(t_0)=ra E_0(T_0-T_1) \tag{27}$$

(b) $0^-<t_1\le t_1^-$

$$-\sigma_a(t_1)=ra\left\{(T_0-T_1)E\left[\int_0^{t_1}\frac{ds}{a_1(T(s))}+\int_0^{t_1}E\left[\int_t^{t_1}\frac{ds}{a_1(T(s))}\right]\frac{\partial}{\partial\tau}(T(\tau)-T_1)d\tau\right\} \tag{28}$$

(c) $t=t_1^-$

$$-\sigma_a(t_1^-)=ra\left\{(T_0-T_1)E\left[\int_0^{t_1}\frac{ds}{a_1(T(s))}\right]+(T_R-T_1)E_0+\int_0^{t_1}E\left[\int_t^{t_1}\frac{ds}{a_1(T(s))}\right]\frac{\partial}{\partial\tau}T(\tau)-T_1 d\tau\right\} \tag{29}$$

(d) $t_1^-<t_2\le t_f$

$$-2h\sigma_a(t_2)=r\left\{a(T_0-T_1)\int_h E\left[\int_0^{t_1}\frac{ds}{a_1(T(s))}+\int_{t_1}^{t}\frac{ds}{a(T_R,m(z,s))}\right]dz\right.$$
$$+a(T_R-T_1)\int_h E\left[\int_{t_1}^{t'}\frac{ds}{a(T_R,m(z,s))}\right]dz+a\int_h\int_0^{t_1}E\left[\int_t^{t_1}\frac{ds}{a_1(T(s))}\right. \tag{30}$$
$$\left.+\int_{t_1}^{t}\frac{ds}{a(T_R,m(z,s))}\right]\frac{\partial}{\partial\tau}(T(\tau)-T_1)d\tau\,dz+\beta\int_h\int_{t_1}^{t_2}E\left[\int_t^{t'}\frac{ds}{a(T_R,m(z,s))}\right]\frac{\partial}{\partial\tau}m(z,\tau)\,d\tau\,dz\right\}$$

NUMERICAL ANALYSIS

The material adopted in this paper is AS4/3502 graphite/epoxy composite laminate with 12 symmetric cross-plies, and the thickness of each ply is 0·0148 cm. The initial temperature, the room temperature, and the average thermal expansion coefficient are assumed to be $T_1=450$ K, $T_R=293$ K and $a_{av}=(a(T_1)+a(T_R))/2$, respectively. Then, the theoretical solution for the optimal temperature path involves a nonlinear integro-differential equation. An iterative numerical method must be applied to find the distribution of the temperature path. The required steps are stated as follows.

Application of an iterative numerical method

First of all, the cooling time t_1 is divided into n incremental units

$$\Delta t = t_1/n \tag{31}$$

By guessing a value T_1^{-1} and applying eqn (25), then all following temperatures can be obtained, i.e. when $t = t_1$.

$$\frac{T_n - T_{n-1}}{\Delta T} = -\frac{a_1'T_n}{a_1'T_n + a_1''T_n} \cdot \frac{1}{\frac{1}{2h}\int_n^h \left\{ E'\left[\int_c \frac{ds}{a(T_R, m, z, s)}\right] + E''\left[\int_c \frac{ds}{a(T_R, m, z, s)}\right] \right\} dz} \tag{32}$$

where $T_n = T(t_1) = T_1$.

Using eqn (32), the value of T_{n-1} can be solved, when $t = t_1 - \Delta t$.

$$\frac{T_{n-1} - T_{n-2}}{\Delta t} = -\frac{a_1'T_{n-1}}{a_1'T_{n-1} + a_1''T_{n-1}}$$

$$\times \frac{1}{\frac{1}{2h}\int_n^h \left\{ E'\left[\int_c \frac{ds}{a_1(T, s)} + \int_c \frac{ds}{a(T_R, m, z, s)}\right] E''\left[\int_c \frac{ds}{a_1(T, s)} + \int_c \frac{ds}{a(T_R, m, z, s)}\right] \right\} dz} \tag{33}$$

Then the value of T_{n-2} is obtained. These steps are repeated until $t = t_1 - N\Delta t = 0$.

$$\frac{T_1 - T(0)}{\Delta t} = -\frac{a_1'T(0)}{a_1'T(0) + a_1''T(0)}$$

$$\times \frac{1}{\frac{1}{2h}\int_n^h \left\{ E'\left[\int_0^c \frac{ds}{a_1(T, s)} + \int_c \frac{ds}{a(T_R, m, z, s)}\right] E''\left[\int_0^c \frac{ds}{a_1(T, s)} + \int_c \frac{ds}{a(T_R, m, z, s)}\right] \right\} dz} \tag{34}$$

The value of $T(0)$ is obtained from eqn (30). However, the value obtained of $T(0)$ is generally not equal to the T_0 obtained from eqn (26). Therefore, a new guess for T_1^2 must be made to repeat the above steps. If $T_0 < T(0)$, then the new guess $T_1^2 < T_1^1$. Contrarily, if $T_0 > T(0)$, the new guess $T_1^2 > T_1^1$. These processes are repeated until the value of T_1 which satisfies $T(0) = T_0$ is obtained. Then the distribution of the optimal temperature path can be identified.

Furthermore, the residual stress can be obtained by eqns (27)–(30), where the integral form can be expressed by numerical equation:

$$\int_{t_0}^{t_1} F(\tau) \frac{\partial G(\tau)}{\partial \tau} d\tau = \frac{1}{2} \sum_{k=0}^{n-1} [F(t_k) + F(t_{k+1})] \cdot [G(t_{k+1}) - G(t_k)] \tag{35}$$

RESULTS AND DISCUSSION

To verify the reliability of the theoretical analysis, the symmetric cross-ply (0/90) composite laminate is placed on a hotpress in which the temperature is properly adjusted, and a humidifier is applied to simulate the humidity in the surrounding environment. The residual stress is measured by a strain gauge. Some results are summarized as follows.

Figures 3–6 indicate the optimal temperature path as well as the change of the accompanying residual stress on the specific t_1, RH and Δt_c. These figures show the discontinuity at the initial and final times but also a smooth continuous curve in the time interval. The final residual stress
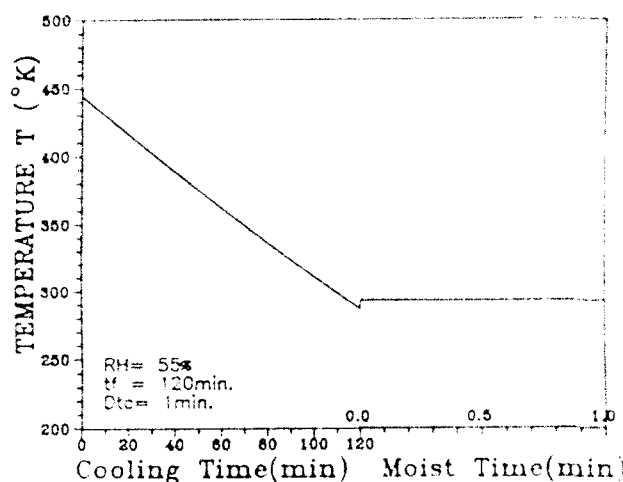
Fig. 3. The optimal cooling path T-t versus time t for AS4/3502 with 12 symmetric cross plies and cooling time $t_c = 120$ min, after cooling the relative humidity $RH = 55\%$ and the length of exposure $\Delta t_c = 1$ min.

Fig. 5. The optimal cooling path T-t versus time t for AS4/3502 with 12 symmetric cross plies and cooling time $t_c = 30$ min, after cooling the relative humidity $RH = 95\%$ and the length of exposure $\Delta t_c = 10$ min.

Fig. 4. The accompanying thermal stress σ-t versus time t for AS4/3502 with 12 symmetric cross plies and cooling time $t_c = 120$ min, after cooling the relative humidity $RH = 55\%$ and the length of exposure $\Delta t_c = 1$ min.
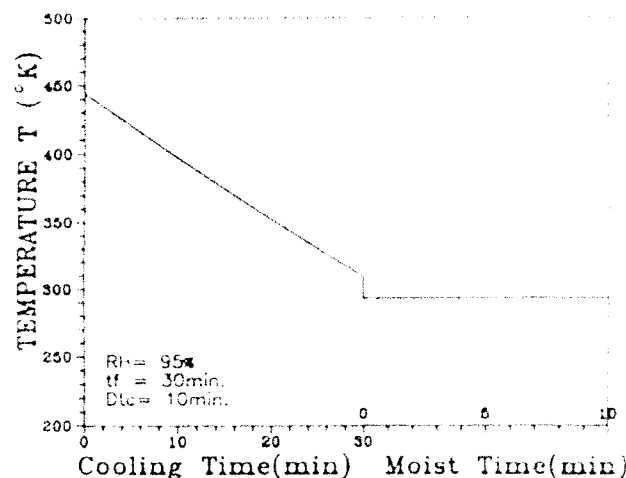

Fig. 6. The accompanying thermal stress σ-t versus time t for AS4/3502 with 12 symmetric cross plies and cooling time $t_c = 30$ min, after cooling the relative humidity $RH = 95\%$ and the length of exposure $\Delta t_c = 10$ min.
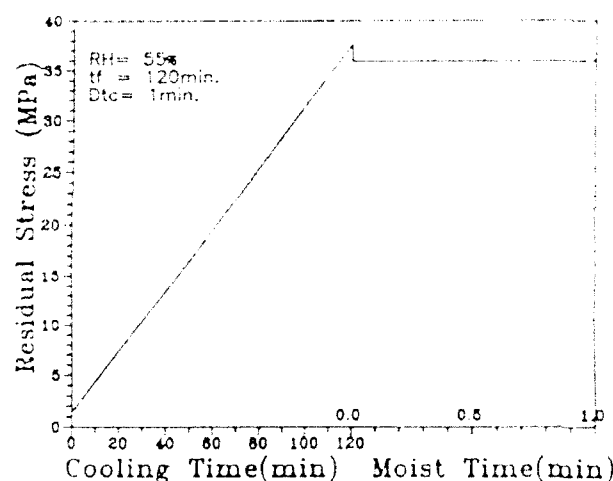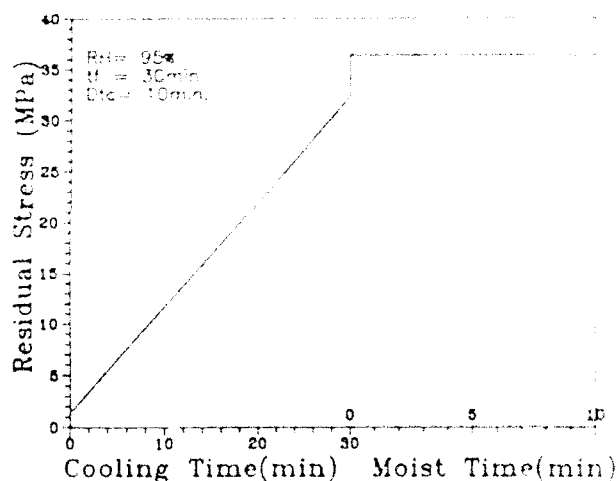
will meanwhile suddenly decrease if the final temperature T_f (i.e. $T(t_f)$) is below room temperature. Contrarily, the final residual stress will suddenly increase if the final temperature T_f is above the room temperature. Figure 7 indicates the relation between the final temperature $T(t_f)$ and $\log(t_f)$. Figure 8 shows the relation between the final residual stress $\sigma(t_f^*)$ and $\log(t_f)$. Figures 7 and 8 do not consider the effect of humidity after the cure. Figures 9 and 10 indicate the relation between the final temperature $T(t_f)$ and its final residual stress $\sigma(t_f^*)$ versus $\log(t_f)$ at various

exposure times under relative humidity $RH = 55\%$. By tracing the figure of $T(t_f)$ versus $\log(t_f)$, the value of T_f becomes higher in accordance with the higher RH, long Δt_c or shorter cooling time t_c. Besides, the figure of $\sigma(t_f^*)$ versus $\log(t_f)$ shows the curves almost coincide despite the value of the RH when the Δt_c is quite short (i.e. 1 min). This shows that the final residual stress $\sigma(t_f^*)$ can be controlled below some level by the control of the optimal temperature path.

In the laboratory, only the residual stress after fabrication can be measured. Therefore, the cool
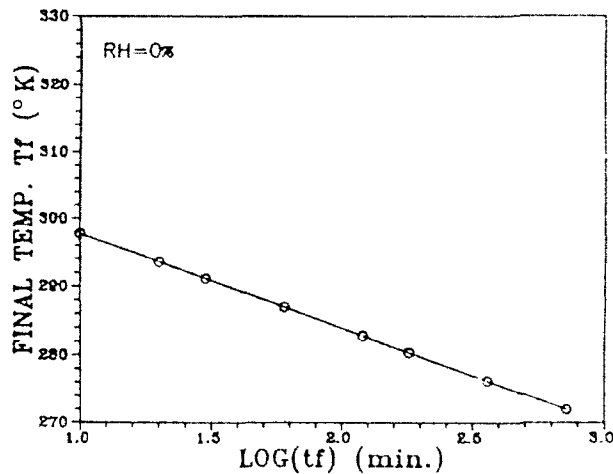
Fig. 7. The variation of $T(t_f)$ versus $\log t_f$ without humidity effect for 12 symmetric cross-ply laminates.
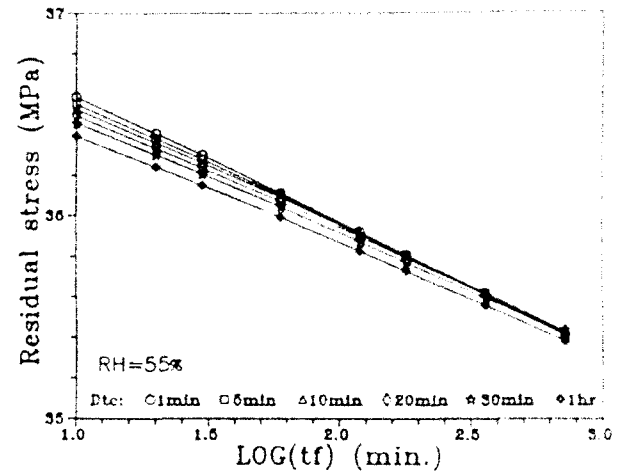

Fig. 10. The variation of $\sigma(t_f)$ versus $\log t_f$ under the various exposure time of environment humidity, $RH = 55\%$, for 12 symmetric cross-ply laminates.

Fig. 8. The variation of $\sigma(t_f)$ versus $\log t_f$ without humidity effect for 12 symmetric cross-ply laminates.
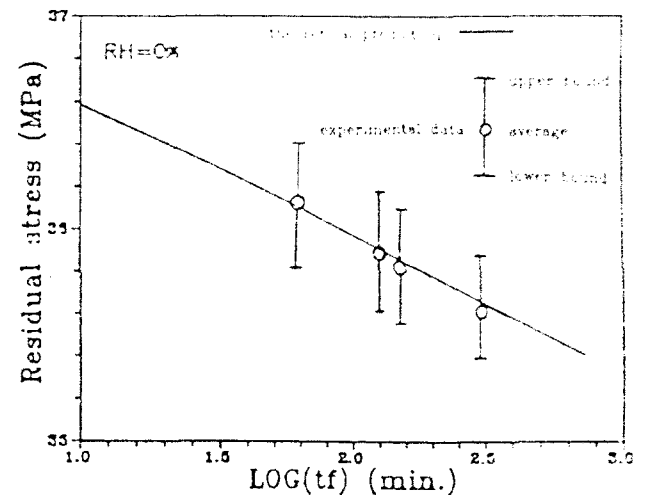
Fig. 11. Comparison of $\sigma(t_f)$ versus $\log t_f$ without humidity effect for 12 symmetric cross-ply laminates.

Fig. 9. The variation of $T(t_f)$ versus $\log(t_f)$ under various exposure times to environment humidity, $RH = 55\%$ for 12 symmetric cross-ply laminates.
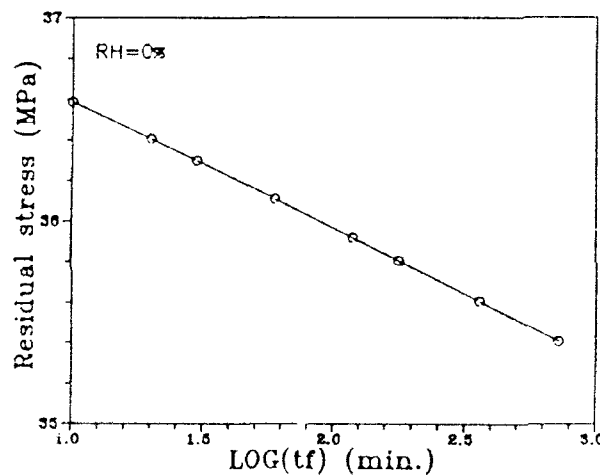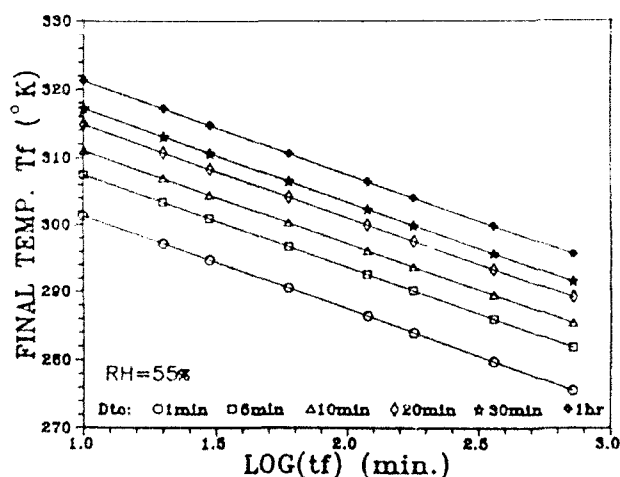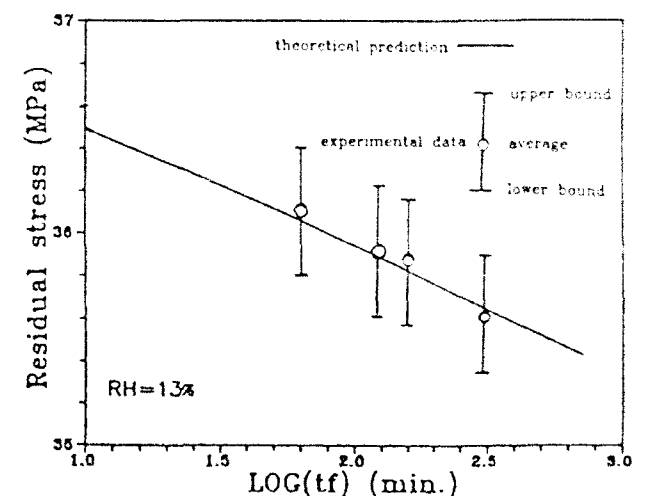

Fig. 12. Comparison of $\sigma(t_f)$ versus $\log(t_f)$ under an exposure time to environmental humidity of 10 min, and $RH = 13\%$ for 12 symmetric cross-ply laminates.

Fig. 13. Comparison of $\sigma(t_f^*)$ versus $\log(t_f)$ under an exposure time to environmental humidity of 5 min. and $RH = 35\%$ for 12 symmetric cross-ply laminates.

Fig. 14. Comparison of $\sigma(t_f^*)$ versus $\log(t_f)$ under an exposure time to environmental humidity of 1 min, and $RH = 55\%$ for 12 symmetric cross-ply laminates.

Fig. 15. Comparison of $\sigma(t_f^*)$ versus $\log(t_f)$ under an exposure time to environmental humidity of 5 min, and $RH = 75\%$ for 12 symmetric cross-ply laminates.
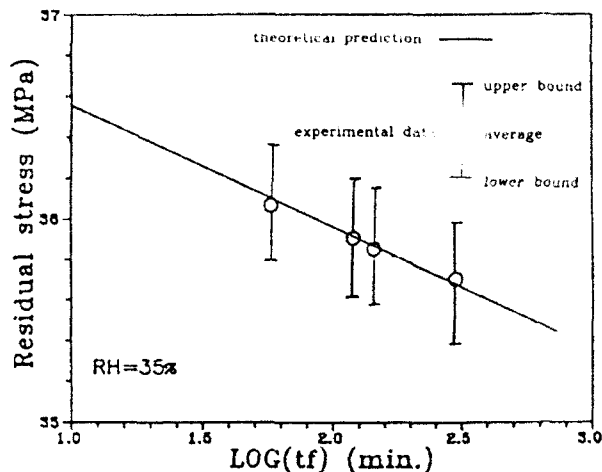

Fig. 16. Comparison of $\sigma(t_f^*)$ versus $\log(t_f)$ under an exposure time to environmental humidity of 1 min. and $RH = 95\%$ for 12 symmetric cross-ply laminates.
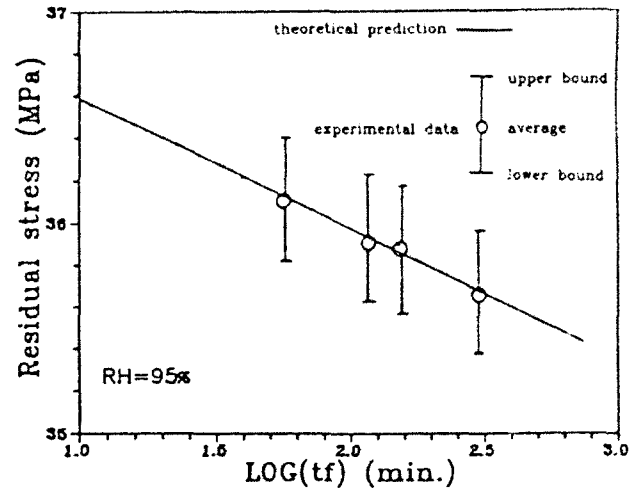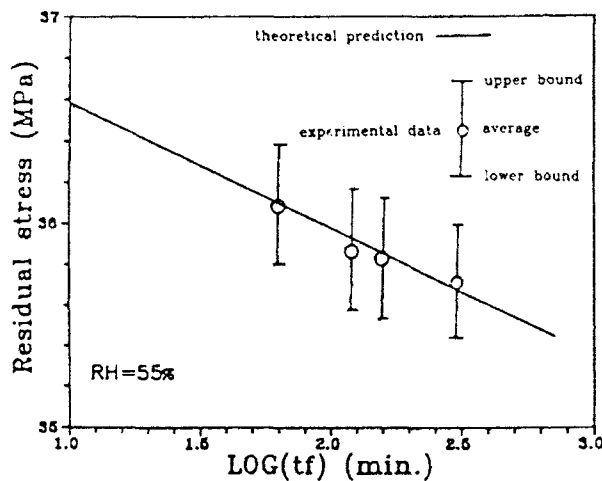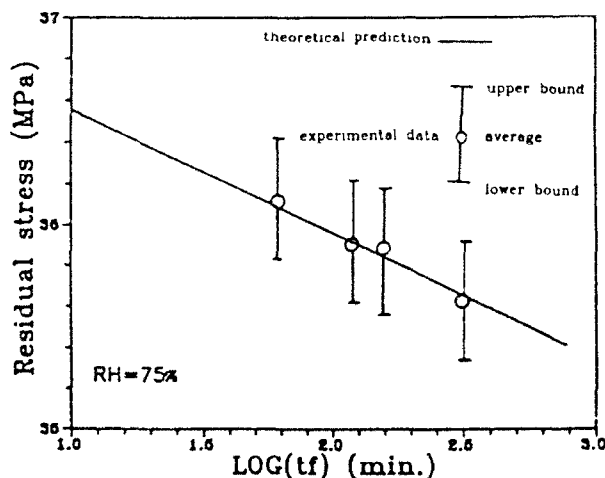
ing system of hot press must be adjusted by the theoretically derived temperature path, and the final residual stress is then measured by a strain gauge. Figures 13–16 show an approximate coincidence of the residual stress between the measured result experimentally obtained and the theoretical prediction. As a result, the accuracy of such a theoretical analysis can be recognized.

REFERENCES

1. Weitsman, Y., Residual thermal stresses due to cool down of epoxy resin composites. *Journal of Applied Mechanics*, **46** (1979) 563–7.
2. Gurtin, M. E. & Murphy, L. F., Optimal temperature paths for thermorheologically simple viscoelastic materials. *Quarterly Journal of Applied Mathematics*, **38** (1980) 179–80.
3. Weitsman, Y., Optimal cool-down in linear viscoelasity. *Journal of Applied Mechanics*, **47** (1980) 35–9.
4. Weitsman, Y. & Harper, B. D., Optimal cooling of cross-ply composite laminates and adhesive joints. *Journal of Applied Mechanics*, **49** (1982) 735–9.
5. Weitsman, Y., Effects of fluctuating moisture and temperature on the mechanical response of resin-plates. *Journal of Applied Mechanics*, **44** (1977) 571–6.
6. Hahn, H. T. & Kim, R. Y., Swelling of composite laminates. *Advanced Composite Materials — Environmental Effects, STP 658*, ed. J. R. Vinson. American Society for Testing and Materials, Philadelphia, PA, 1978, pp. 98–120.
7. Apicella, A., Nicolais, L., Astarita, G. & Drioli, E., Hygrothermal history dependence of moisture sorption kinetics in epoxy resins. *Polymer Engineering and Science*, **21** (1981) 18–22.
8. Springer, G. S., *Environmental Effects on Composite Materials*. Technomic Publishing Co., Westport, CN, 1981.

9. Flaggs, D. L. & Crossman, F. W., Analysis of the visco-elastic response of composite laminates during hygro-thermal exposure. *Journal of Composite Materials*, **15** (1981) 21.

10. Harper, B. D., On the effects of post cure cool down and environmental conditioning on residual stresses in composite laminates. PhD dissertation. Texas A&M University, 1983.

11. Hwang, Chao-Yi, The effect of humidity on the residual thermal stress of the fabricated viscoelastic composite material. Master's Thesis. Department of Engineering Science, National Cheng-Kung University, Taiwan, ROC, June, 1991.

12. Weitsman, Y., A rapidly convergent scheme to compute moisture profiles in composite materials under fluctuating ambient conditions. **15** (1981) 349–58.

Artificial damage techniques for low velocity impact in carbon fibre composites

M. P. Clarke & M. J. Pavier

Department of Mechanical Engineering, University of Bristol, Bristol, UK, BS8 1TR

Materials and techniques used in artificially induced damage are evaluated and compared. The damage induced by low velocity impacts is characterised using penetrant enhanced radiography and deply techniques. This information is used to construct specimens with simulated damage that will facilitate the study of damage growth. Specimens manufactured match quite closely the properties of specimens which contain actual damage.

1 INTRODUCTION

Carbon fibre composites are of great interest to engineers for applications that require low weight and high strength. Their use in primary structures, however, has been limited because of concern over their ability to sustain damage from low energy impacts without the damage being apparent except under extensive, and expensive examination. In many applications low velocity impacts are quite common; for example, stones thrown up from the runway hitting the wing of a plane or tools dropped during maintenance. The effect of this damage can be greater than that from a high energy impact that creates a neat puncture of the component, especially if the damage goes undetected and grows under subsequent loading.

1.1 Purpose of the work

It would be nice to simplify impact damage so that it is analysable, but would it be realistic? Can we replicate impact damage artificially and still get the same strength reduction? Damage caused by low velocity impact is complicated, containing fibre breaks, matrix cracks and ply delaminations. To study the effects of these defects the ability to control the type and quantity of damage in a specimen is crucial. In order to check the predictions from finite element analysis it is useful to have damage that is easy to model. A lot of work has been done using artificial damage, but very little published work has shown how realistic the artificial damage is.

1.2 Introduction to the paper

This paper looks at the techniques and materials used in implanting artificial damage and tests that were carried out to check their efficiency in replicating real damage. Real damage from impacts were inspected to give a measure of the extent and types of damage that would need implanting and then the specimens were manufactured. Comparisons were made between specimens with real and various levels of artificial damage and conclusions drawn.

2 ARTIFICIAL DAMAGE TECHNIQUES

2.1 Review of past methods

Artificial damage has been used extensively in specimens designed to measure material properties — for example an insert in a beam that encourages a starter crack in the double cantilever test for measuring G_{Ic}, and the end notch flexure for measuring G_{IIc}. In these cases the region of interest during measurements is not close to the damage.

Early work on artificially inserted damage sometimes removed the inserted material before testing so that you could be sure that the insert did not affect the behaviour of the specimen. This was possible because a through-the-width delamination allows access to the insert so that it can be pulled from the specimen. In this case you can be sure that the delamination faces are not bonded to

each other. It also allows you to do a 2D analysis.[1,2]

In reality damage caused by impacts is quite likely to be fully contained within a panel. This means that any insert that is used to replicate damage must be left *in situ*.[3]

2.2 Artificial delamination

2.2.1 Materials

The resin/fibre system chosen for these tests was T300/913c. T300 is an intermediate modulus fibre. The resin is a standard epoxy resin. The combination was chosen because it was a well-known composite and would allow us to concentrate on the damage.

Any materials chosen for the purpose of delamination must not affect the properties of the specimen. The dimensions of the insert must be such that it does not cause distortion in the laminate during manufacture — for example by causing sharp bends in the fibres or matrix rich regions. The insert must also be able to survive the regime of pressure and temperature that is used to cure the resin during the manufacture of the composite. Ideally, it should be easy to handle and inexpensive. Since the aim is to replicate damage surfaces which do not adhere to each other it would be better if the material had low adhesion without the requirement of additional release agents.

The basic criteria for the choice of material as inserts were:

- thickness — the thinner the better,
- low surface roughness and adhesion,
- resistance to adverse conditions,
- ease of use (handling and positioning of damage).

The materials chosen were aluminium foil, gold foil, PTFE tape and PTFE film. Two release agents were tried: petroleum jelly and Frekote[TM]. For some of the materials multiple layers of delaminant were used (see Table 1).

2.2.2 Techniques

A preliminary test was carried out using a glass fibre composite to check that inserts that were simulating a delamination did not move from position during the manufacturing process. Visible inspection showed that the assumption that the delamination was where it had been placed before cure was justified. In an opaque substance such as carbon fibre with a PTFE insert ultrasonic

Table 1. Possible candidates for use as delaminant

		Thickness μm
	Gold foil	3–6
	Aluminium foil	16
	PTFE tape	80
	PTFE film	10
For comparison	Diameter of typical carbon fibre	8

scanning or X-rays would not easily distinguish between resin and insert. When cutting specimens from large plates it is essential that you kmow where the damage is.

To determine the adhesion of the insert to the cured matrix two tests were used that measure interlaminar properties, and interlaminar strength (ILSS) test and a modified double cantilever beam test (DCB). The interlaminar shear test was inconclusive because of the transverse forces involved that swamped any effect in the plane of the damage. A modified DCB test was therefore employed (Fig. 1). In this test instead of using the insert as a starter crack the force necessary to pull the two faces apart was measured from the start. The initial force needed to start the opening was recorded and also the force–displacement curve. By repeating the test after the surfaces had been separated once we were able to see the contribution to the separation force provided by the resistance of the two beams to bending.

2.2.3 Results

Thin eight-ply unidirectional laminates 20 mm wide and 1 mm thick were used so that the contribution due to the adhesion of the artificial delamination would be large compared to that needed to bend the composite. Figure 2 shows the results of a DCB test on a specimen with two layers of aluminium foil delamination inserted. Table 2 shows the values of the force needed to initiate the debonding. A repeat of the experiment produced an almost identical trace for the PTFE, indicating that the adhesive force is smaller than can be measured by this experiment.

It should be noted that the use of a release agent can improve the effectiveness of an insert as a delamination, but if a liquid is used it is difficult to ensure that the agent is applied only in the region where it is required: this is why a release agent on its own was not tested. In the case of the PTFE a release agent is not necessary. PTFE tape was much easier to handle than the film, but was
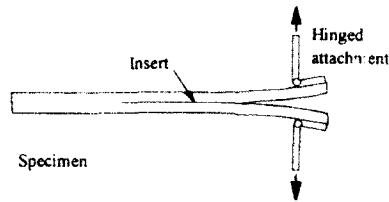
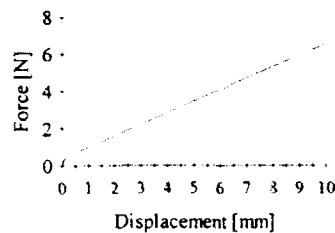Fig. 1. Adapted double cantilever beam test for measuring adhesion.

Fig. 2. Adhesive force on artificial delamination by double cantilever test.

Table 2. Force required in double cantilever beam test to pull surfaces apart

Delaminant	Thickness μm	No. of layers	Release agent	Breaking force N
None	—	—	—	> 2000
PTFE tape	80	2	None	450
PTFE tape	80	2	Frekote	34
PTFE film	10	2	None	0·3
PFTE film	10	1	None	0·3
Aluminium foil	16	2	Frekote	0·4
Aluminium foil	16	2	Petroleum jelly	25·0

later discovered to be porous — hence the large adhesive forces due to matrix bridging through the PTFE.

2.3 Ply cracks

A delamination is readily modelled by preventing bonding between two layers during curing. A real crack usually has space at the fibre break, so some way of preventing the matrix material from flowing into the gap must be devised. Also, a delamination is a large piece of damage (compared to the fibre dimensions) and so positioning is not a problem, whereas any material used to keep a crack open could more easily move during curing.

2.3.1 Techniques

We are concerned with finding a good method for inserting ply-cracks. It is important that the bro-

ken ends of the fibres are kept from overlapping either during laying up of the specimen or during curing (when resin is mobile). At the same time it is desirable that the amount of inserted material is kept to a minimum.

The ply-crack specimens were made by cutting a slot (0·5 mm by 25 mm) through two 0° plies before they were inserted in the specimen during laying up. The crack was held in place during the curing process by inserting aluminium foil or PTFE tape as shown in Fig. 3. Figure 4 shows a micrograph of a cross-section of the ply-crack after cure.

For measuring the effectiveness of artificial ply-cracks a standard tensile test was used. The ply cracks were simulated by cutting fibres prior to cure. The necessity of preventing ingress of matrix material into the crack was also investigated by using the PTFE film as a barrier (see Fig. 3).

The crack can fill with matrix material during manufacture so another technique that was tried was to apply a tensile load to the specimen to open the crack. The matrix plug in the crack is the weakest part of the specimen and if a delamination is present the strain should be sufficient to produce a crack in the matrix plug.

The effectiveness of ply-cracks can be determined by measuring the ultimate tensile stress for samples with and without cracks. Since the load is mainly carried by the 0° plies, the strength of the specimens should be proportional to the number of uncracked plies. Test specimens of width 12·5 mm and length 250 mm were cut from the cured plates such that the artificial damage was positioned centrally and across the whole width. Aluminium end tabs were adhesively bonded to the ends after the specimens had been abraded and de-greased using acetone. The adhesive used was Ciba-Geigy 2001, a cold curing adhesive.

2.3.2 Results

The strengths of specimens for the ply-crack testing are shown in Fig. 5.

These tests have shown that the undamaged specimens have an ultimate tensile stress of approximately 0·68 GPa which indicates that the lay-up and hot-press curing procedure has produced a reasonable quality of finished specimen. As expected the strength in tension is not affected much by delaminations when there is no crack present. When a crack *is* present the presence of a delamination does not affect the residual tensile strength. The presence of a PTFE filler in the crack does not reduce the residual strength. (In

some cases it increases it!) Having a broken ply in a plate weakens the plate more than not having the ply at all, probably because the fibre break is a source for further damage; an initiation point for failure.

It was noted during these tests that there was no indication that resin had penetrated between doubled layers of PTFE film. All the specimens broke in the test region.
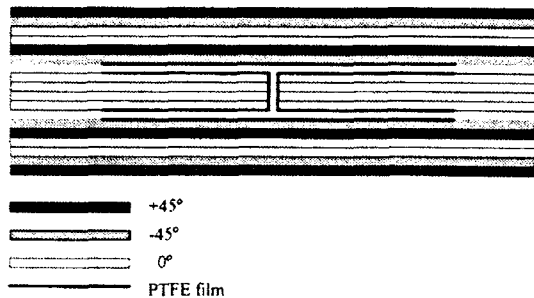

Fig. 3. Artificial delamination and crack across four plies, during lay-up. The layers are compressed during curing.

Fig. 4. Micrograph of the artificial delamination — cross-sectional view of gold foil insert (negative view).

3 EXAMINATION OF IMPACT DAMAGE

3.1 Introduction

Now that we can be sure that the artificial damage that we introduce into the specimen is a realistic simulation of real damage, we need to quantify the damage that occurs in a typical impact. This is done using radiography and a deply technique.

3.2 Creation of impact damage

The actual amount of damage incurred during impact will depend on the energy and velocity of the impactor, as well as the shape of the impact head (tup). In order to be able to compare the results with other research we have followed the CRAG standard.[4] The impactor has a variable mass to allow for the different energy of impact, and the tup has a diameter of 12·7 mm. Different materials will respond in different ways to the impact, and the lay-up of a composite affects the damage resistance. Our results are therefore limited in scope, but will allow us to compare the effect of real and artificial damage for this material and lay-up.

Impacts of energy 3, 5, 7, 9 and 12 J were used, and then the majority of the work carried out using specimens with 7 J impacts. This is because other work has shown that the compression after impact values does not increase greatly above this value, and at lower values the damage is limited.[5]

3.3 Examination of impact damage

After impact the plates were soaked with lead iodide solution, a dense liquid opaque to X-rays.
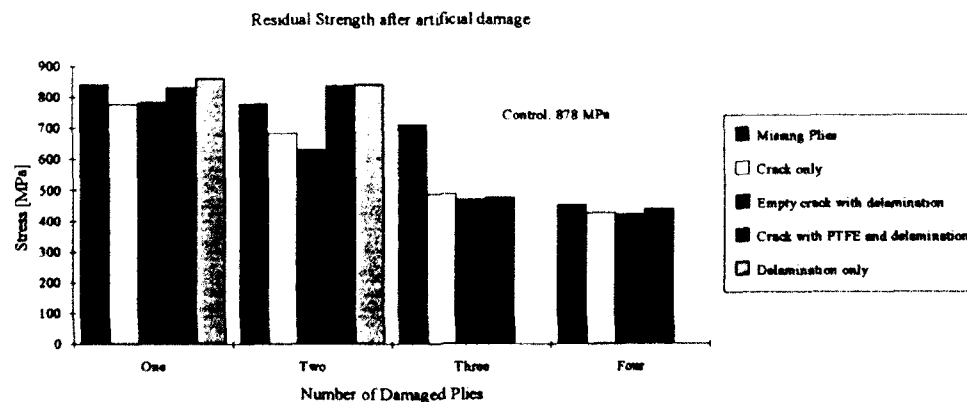

Fig. 5. Variation of strength with number of damaged plies.

After radiography some specimens were de-plied — the matrix burnt away and the individual plies unstacked. Various penetrants were used with the aim of leaving a deposit on the laminate to reveal the position of the delaminations. The information from these two methods allowed us to quantify the damage due to the impact.

3.3.1 Penetrant enhanced radiography

The contrast of an X-ray can be improved by adding an X-ray opaque substance to the areas that are damaged. Tetra-bromoethane (TBE) and di-iodobutane (DIB) are two very dense organic penetrants that have been used.[6-8] Lead iodide is an alternative to TBE, a mutagen, or DIB, an irritant. The solid is dissolved in equal volumes of water (a polar solvent) and isopropyl alcohol (a non-polar solvent) with a small amount of wetting agent (a linear alcohol alkoxylate) which reduces the surface tension of the solution.[8] An advantage of this particular mixture is that it has been shown to have no detrimental effect on the properties of the specimens of graphite/epoxy either at room temperature or at elevated temperatures.[8] This is helpful if you are studying delamination growth because the penetrant may stay in the specimen for some time as you continue experiments, gradually increasing the load or the number of fatigue cycles.

For those specimens where there was little surface cracking (low energies) a small hole was drilled through the impact point to allow the penetrant to flow into the damaged zone. Later, when testing specimens and recording delamination growth with loading, it was found to be helpful to drill a series of small holes and pump the penetrant in with a syringe. This reduced the time spent waiting for the penetrant to seep to the full extent of the delamination. (This reduces the effects it may have on the matrix).

3.3.2 Penetrant enhanced deply

One of the potentially most informative methods of evaluating damage in a specimen is a simple destructive examination technique that involves pyrolysing the matrix resin so that the plies of laminate can be unstacked. Harris[9] reports on the work that he has done on the materials T300/5208 and AS4/3502. In his work he was using a stacking sequence that did not have any adjacent plies with the same orientation: $[0°/\pm 45°/90°]$. This meant that there was only a slight difficulty in separating adjacent plies. In other work[10] there is no record of multiple plies of the same orientation

being separated from each other during the unstacking. This should be very difficult anyway, if the specimen has been made properly, as there should be no obvious matrix layer between similar plies.

Obviously, each material will need a different regime of heating and cooling to pyrolyse the matrix sufficiently to allow separation of the plies without causing damage to the fibres. The heating must be carried out in an inert atmosphere and precautions taken in handling the noxious fumes produced by the process. This method enables you to map the damage to fibres in individual layers and the pattern and size of delaminations between the successive plies of the laminate.

Freeman[10] reports on the use of gold chloride for revealing the delaminated area, but other authors have found that this is not always necessary. Gold chloride is expensive and seems to be unstable in solution so that the gold precipitates out. We have investigated other materials that might be suitable.

The criteria for a good penetrant are:

- soluble (in order to penetrate fully).
- inexpensive,
- capable of withstanding temperatures up to 420°C without boiling or decomposing, unless it leaves a deposit (gold chloride decomposes depositing a thin layer of gold).
- low expansion on heating so that is does not increase the amount of damage,
- it should leave a deposit clearly visible against the carbon fibres.

Unfortunately, none of the materials that fluoresce under ultraviolet light is capable of withstanding the temperatures needed for deplying. After consulation of reference books the following materials were tried: sodium sulphate (Na_2SO_4), calcium oxide (CaO), potassium(VI) chromate (K_2CrO_4) and magnesium sulphate ($MgSO_4$). The X-ray penentrant was also used (ZnI_2). All these materials are water soluble, though the calcium oxide did not dissolve easily. The addition of a wetting agent increases the penetration into the damaged areas.

3.4 Results

The X-rays produced good results for exposures of 200 s at 32 kV and 4 mA (distance from source, 60 cm), using Agfa Structurix D4 film.
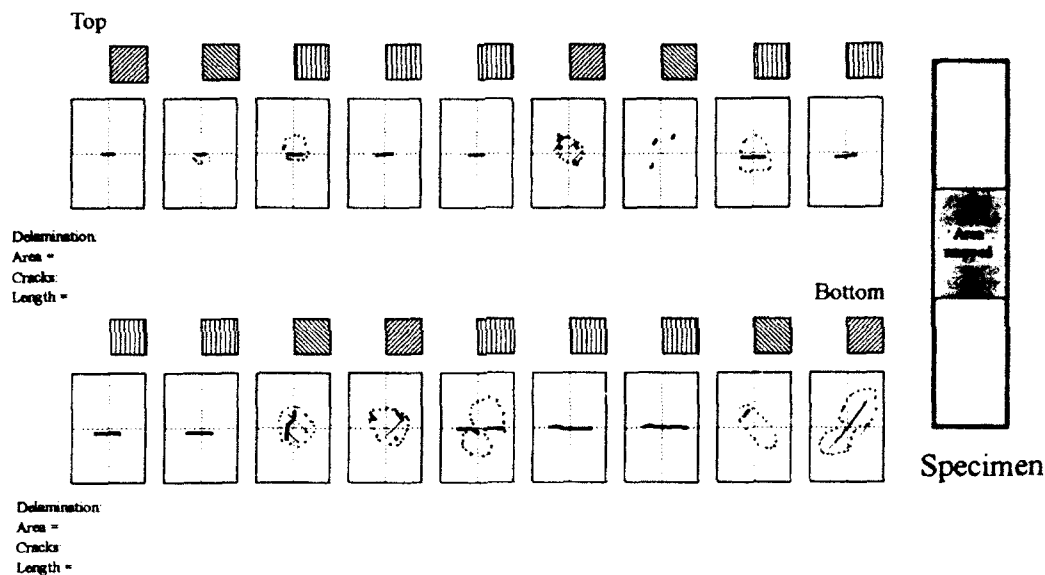
Fig. 6. Mapping of the damage from a 7 J impact. (Thick line = fibre crack, thin line = matrix crack, dotted line = edge of delamination).
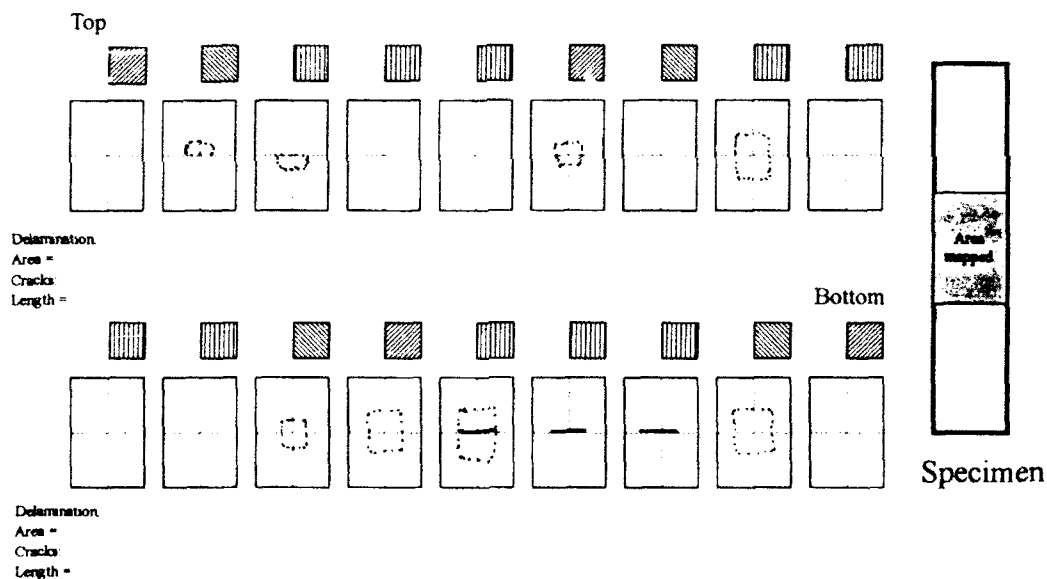
Fig. 7. Mapping function of implants for replicating damage from a 7 J impact. (Thick line = fibre crack, thin line = matrix crack, dotted line = edge of delamination).

In the deply method all penetrants left a deposit, but for some it was a loose powder that was easily dislodged, for example sodium sulphate. The most effective was calcium oxide, though the deposit was dark yellow rather than white. Zinc iodide left a mark on the fibres in the form of a dulling of the surface finish. This is clearly visible in the right lighting conditions. Overall, gold chlo-

ride is by far the best in terms of performance, but expensive. Zinc iodide was adequate, and if X-rays are also being taken, a suitable penetrant.

For T300/913c a regime of 418°C for 1 h was found to be effective for 18-plies (it would need less for a thinner plate). The composite was heated in an atmosphere of argon, supported on pins to ensure the whole plate would be pyrolysed

evenly and to allow the gaseous products to escape. A record of the results of delamination for 7 J impact is shown in Fig. 6.

4 FABRICATION OF ARTIFICIAL DAMAGE

Figure 7 shows the mapping of the artificial damage implanted in the specimens with the greatest damage. For other levels of damage the delaminations used were those on ply 17 and ply 14 (for the double delamination) and on ply 17 for the single delamination. In all cases the ply crack was a cut in plies 14-16 of length 25 mm.
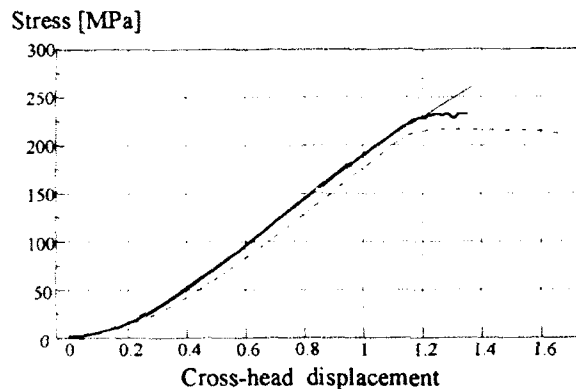
Stress [MPa]

Fig. 8. Realistic artificial damage compared to actual artificial damage. Artificial damage, ———: real damage, - - - : artificial damage: pre-stressed. ——. Failure occurs when load decreases by 20%.

5 COMPARISON OF REAL AND ARTIFICIAL DAMAGE

5.1 Results

Figure 8 shows the stress–displacement curves for the real damage and artificial damage (two delaminations and a ply crack) and the effect of opening the artificial ply crack. In compression ply-cracks do not affect the strength greatly, but opening the crack does seem to change the behaviour of the damage so that it is closer to the real damage.

Figure 9 shows how the level of damage and type of damage affects the residual compressive and tensile strengths. Realistic implanted damage is very close to real impact damage. More importantly, a simple double delamination and single crack is close to real damage.

5.2 Discussion

We can conclude from these tests that artificial damage in the form of PTFE film or aluminium foil with Frekote[TM] has a low enough adhesion to the resin to be a true representation of a crack in the matrix material. Once inserted the artificial damage remains in position during the manufacturing process. PTFE is to be preferred to aluminium because it does not require the addition of a release agent. A single layer of PTFE is sufficient to produce a debond and is better than a double
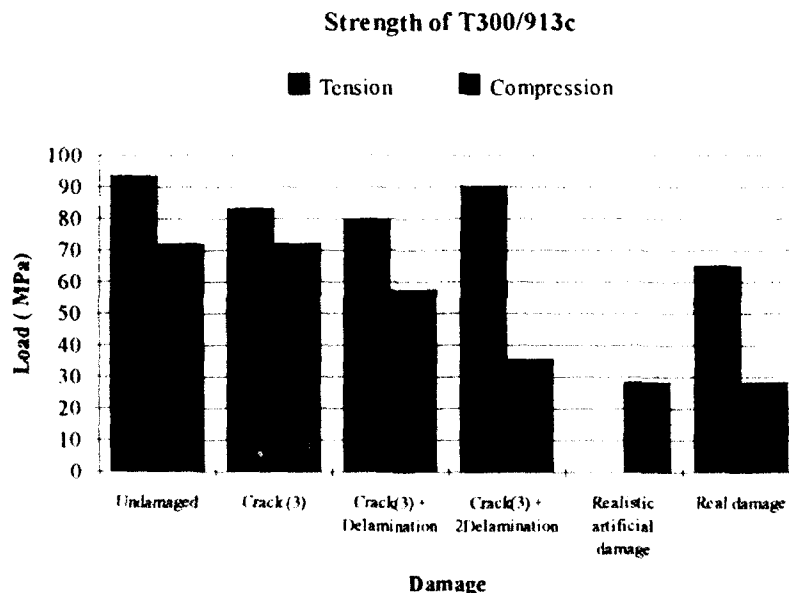
Strength of T300/913c

■ Tension   ■ Compression

Fig. 9. Comparison of residual strengths of damaged specimens.

layer because it is thinner. A PTFE insert for ply-cracks, to keep the crack open during the cure, is not necessary as pre-stressing the specimen opens the crack. The filling of the crack with resin does not improve the tensile strength of the specimen. The simpler form of artificial damage is suffi-ciently realistic for us to be justified in using it as a model which can be analysed easily using finite element methods, hence giving us a means of predicting the effects of damage.

6 CONCLUSIONS

The use of PTFE as a delaminant is justified as it produces an effective debond. Only one layer is necessary, no release agent is needed and posi-tioning is straightforward. Ply cracks can be simu-lated by simply cutting the fibres prior to curing the composite.

Radiography and deply are effective tools for characterising impact damage in composites, and are greatly enhanced by the use of suitable pene-trants. Gold chloride is very effective for deply work, but zinc iodide can be used for both.

Real damage is complex, but simplification in terms of the geometry and position of damage can be made whilst retaining realism.

Further investigation on the effect of position and geometry of implanted damage should reveal which areas of damage have the greatest influence on the strength of the specimen.

ACKNOWLEDGEMENTS

REFERENCES

1. Kutlu, Z. & Chang, F. K., Modelling compression failure of laminated composites containing multiple through-the-width delaminations. *Journal of Composite Materi-als*, **26** (3)(March 1992) 350–87.
2. Flanagan, G., Two-dimensional delamination growth in composite laminates under compression loading. *Composite Materials: Testing and Design (Eighth Confer-ence)*. STP 972, American Society for Testing and Mate-rials, Philadelphia, PA, 1988, pp. 180–90.
3. Whitcomb, J. D., Three-dimensional analysis of a post-buckled embedded delamination. *Journal of Composite Materials*, **23** (Sep., 1989) 862–89.
4. Curtis, P. (ed.), CRAG test methods for the measurement of the engineering properties of fibre rein-forced plastics. *RAE Technical Report*, **16** Feb. 1988 88012, 43–51.
5. Nettles, T. & Lance, D. G., The effects of compressive pre-loads on the compression-after-impact strength of carbon–epoxy. NASA Nov. 1992; TP3303, pp. 1–16.
6. Sendeckjy, G. P., The effect of tetrabromoethane-enhanced X-ray inspection on the fatigue life of resin-matrix composites. *Composites Technology Review*, **2** (1)(1980) 9–10.
7. Ratwani, M. M., Influence of penetrants used in X-ray radiography on compression fatigue life of graphite epoxy laminates. *Composites Technology Review*. **2** (2) (1980) 10–12.
8. Rummel, W. D., Tedrow, T. & Brinkerhoff, H. D., Enhanced X-ray stereoscopic NDE of composite mate-rials. Martin Marietta Corporation, Final Report. AFWAL-TR-80-3053, Contract No. 33615-79-C-3220, Wright Aeronautical Laboratories, 1980, AD A111303, p. 180.
9. Harris, C. E., Damage evaluation by laminate deply. 147–9.
10. Freeman, S. M., Characterization of laminae and inter-laminar damage in graphite/epoxy composites by deply technique. STP 787, American Society for Testing and Materials, Philadelphia, PA, 1982, pp. 50–62.

Impact damage evaluation on advanced stitched composites by means of acoustic emission and image analysis

C. Caneva, S. Olivieri, C. Santulli & G. Bonifazi

Dept. of Chemical and Materials Engineering, University of Rome 'La Sapienza', Via Eudossiana 18, 00184 Rome, Italy

Polymeric composites that are stitched reinforced show dissimilar behaviour, with respect to regular ones. In this paper the mechanical characteristics and different behaviours of stitched reinforced polymeric composites after impact tests are investigated using an alternative approach. Several factors such as grid size, stitching scheme and voids content modify the composite performances and the interlaminar delaminating processes. If, on the one hand, the stitching technique is used to prevent delaminating damage phenomena, then, on the other hand, the process itself introduces a sort of damage into the layers during the assembled preform, that has to be taken into account. Delaminating processes due to impact loads are considered and the post-impact behaviours and damage tolerance are investigated. Impact tests were performed at several energy levels known to have an appreciable damage on the specimens. Damage evaluation analysis was performed on post-impacted specimens using different techniques: as a first step, using a digitalised image technique, the damaged area was measured and different zone shape was evaluated, further compression tests were done to evaluate the material residual properties after impact. The results coming from compression tests do not reveal the better awaited behaviour of the stitched composites with respect to regular ones. On the other hand, the acoustic emission technique is capable of evidencing the different aspects of the stitching wire. The image acquisition technique represents a new experimental method able to fully characterise damage zones and gives more information on the interlaminar behaviour of composite material. This new technique joined to acoustic emission measurements allows important results on the residual life prediction of materials mechanical properties to be obtained.

INTRODUCTION

In comparison with traditional materials, composites suffer deterioration phenomena which from a mechanical point of view, are difficult to evaluate following fracture mechanics principles. A well-known difficulty in this field is to ascribe to some phenomena, such as fibre breakage or delamination, a value that can indicate the produced damage level, as regards structural properties of the material.

In other words, the question is to evaluate when deterioration phenomena (fibre breakage, delaminations and debonding) have a critical effect on mechanical behaviour in composites, and so to establish its residual life and damage tolerance.

In order to achieve this goal a large number of theoretical studies are nowadays available, concerning the modelling for different kinds of damage development and their effects on mechanical and structural properties, both from a dynamic and a cyclic point of view.

This approach nevertheless proved insufficient to interpret real damage phenomena, especially if the composite has a complex structure. This is what happens in the case of quasi-isotropic multi-strate laminates, sandwich structures, and stitched composites.

In such cases it is necessary to use experimental methods to prove the validity of models used to evaluate damage and to interpret mechanical test results.

Situations which evaluate damage and are considered to be particularly problematic are dynamic solicitation tests (impact test) and cyclic ones (fatigue test).

Beyond traditional methods of investigation, acoustic emission technology has been experi-

mented with for a long time, and it has proved to be very useful to monitor, in real time, damage initiation and propagation and giving more information on its critical condition state.[1]

In this work an evaluation methodology, based on image analysis and acoustic emission, is proposed to give an interpretation to the results obtained during a post-impact residual life evaluation test, performed on structural composites.

Image analysis characterises the impact effect, while post-impact compression test monitoring is carried out by acoustic emission.

The methodology has been tested on stitched laminates, which represent a new generation of advanced composite materials primarily for their wide range of application in the impact problems in aerospace applications.

The weakest point of a composite material realised in prepreg form, by a lay-up technique, is the low strength and the low capability to absorb damage due to impact load processes along the direction normal to the lay-up plane.

Moreover, laminated composites suffer from delamination processes caused by interlaminar stresses at the stress-free edges.

The stitched composites are tri-dimensional grids of bundles of fibres woven in-plane and stitched along the through-thickness direction with a wire made of the same or a different fibre.

This structure enhances the composite's resistance to delamination phenomena giving rise to more tough material and allowing it to absorb more impact energy.

METHODS AND MATERIALS

Test methodology is based on post-impact residual mechanical characteristics evaluation by compression testing, according to standards prescriptions.

Impact characterisation is performed, besides energy absorption curves, by observing the damaged area on material, using an image analysis technique.

Compression test monitoring is monitored by an acoustic emission technique in order to observe post-impact damage beginning and propagation loads, and to evaluate damage modality and critical conditions.

The method validity is verified by performing tests on E glass-epoxy laminates: with fibres content $V_f = 60\%$. Ten layers of fabric prepreg were employed, having a total laminate thickness of 3 mm.

Three types of laminate were employed, with the following reinforcement configurations:

(a) standard S;
(b) stitched St 05;
(c) stitched St 10.

With respect to standard (type a), the two kinds of stitched (types b, c) are realised using Kevlar 49 wire with a 5 mm stitching step: St 05 has a 5 mm square grid, while St 10 has a 10 mm square grid (Fig. 1).

The specimens were obtained from laminate plates made with a resin transfer moulding (RTM) technique, so as to have a good void control in order to emphasise the real stitching effects on the delamination process.[2]

Specimen dimensions were 150×90 mm.

IMPACT TEST

Materials underwent impact testing in accordance with ASTM D 3029. An impact test apparatus with a 0·5 in (1 in $\approx$ 2·54 cm) ball-bearing was utilised (Fig. 2).
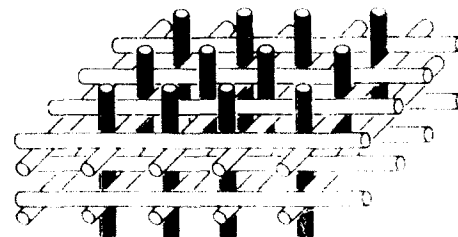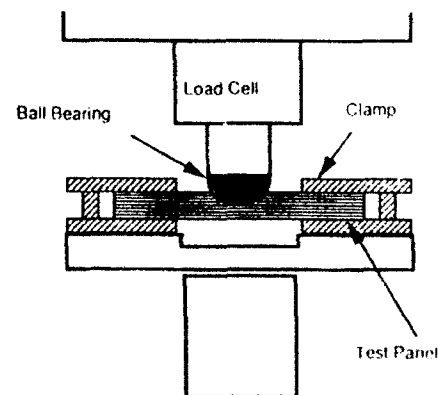

Fig. 1. Three-dimensional weave stitched.

plate shear specimen and loading arrangement

Fig. 2. Impact test apparatus.

Specimens are locked, by a pneumatic system, on a 1·5 in diameter annular bearing, in order to obtain full distribution of radial impact energy.

Maximum impact load and absorbed energy are measured (Fig. 3). Impact velocity, measured by photoelectric cell, was held at a constant value for all tests performed.

Three different impact energy levels were selected: 10, 18 and 22 J. For each type of material and energy level, five specimens were tested.

POST-IMPACT IMAGE ANALYSIS

Damaged areas in impact tested materials are detected by a high-definition telecamera and then digitalised, to be post-processed by an image analysis technique.

Thus, it is easy to distinguish different damage level areas by their different colouring and tone intensity, which are transformed in grey levels, on a 0–255 scale.

In order to obtain an immediate interpretation, four false colours were ascribed to post-processed images to represent typical damage levels.

False colours were: blue, azure, green and yellow.

Table 1 shows grey levels that are represented by the four false colours and damage phenomena connected with each of them.

COMPRESSION TEST MONITORING BY ACOUSTIC EMISSION

Compression tests were carried out on a Universal Instron machine. Specimens are locked on their four sides in a frame to avoid buckling (Fig.

4, as prescribed by ASTM D 695 and further recommended practices.

Loading velocity was 0·04 kN/s. The test is considered over when maximum load was exceeded. For test monitoring by acoustic emission, two piezoelectric resonant sensors type pzt 5A (R15) were applied on the specimens.

Acoustic emission detection was done by a LOCAN-AT PAC apparatus. Guard sensors were applied on specimens locking frame in order to obtain maximum measurement sensitivity and a high S/N (signal to noise) ratio, so to minimise external noise coming from compression machine. Acoustic emission parameters, which seem to be the more significant, are signal energy, amplitude, duration and counts.

Table 1

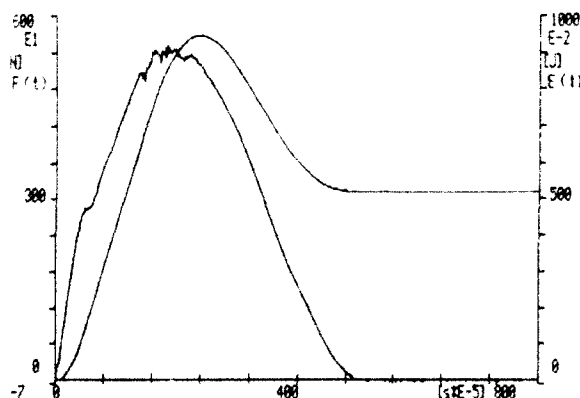| Colour	Grey level	Damage phenomenon
Blue	65	Matrix cracking, fibre failures and delaminations on whole thickness
Azure	76	Cracking related with *boundary effect* of broken fibres in impact area
Green	102	Cracking due to damage propagation along preferential lines: matrix cracking, delaminations
Yellow	127	Mostly delaminations with some matrix cracking

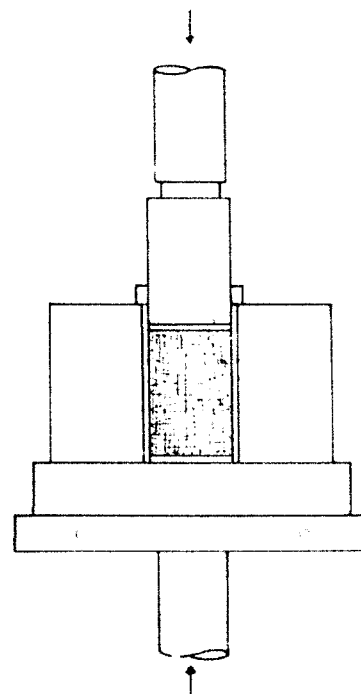

Fig. 3. Typical impact test curves (F(t), E(t)).

Fig. 4. Compression test apparatus.

RESULTS

Impact characterisation

In Figs 5–7 digitalised images are represented, regarding specimens impacted at the energy maximum level (22 J).
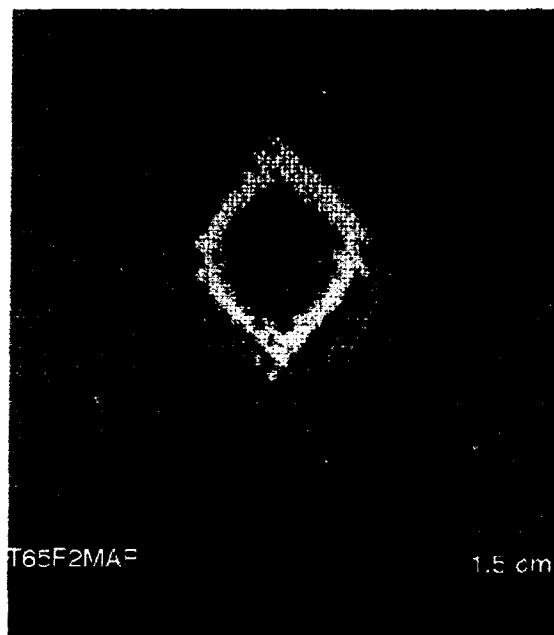

Fig. 5. Digitalised image of standard *S* after impact (22 J).

In these images it is easy to observe that impact area extension (internal blue area) never appreciably changes. Whole damage area has a larger extension, and it presents an irregular edge for stitched 05 (see Fig. 6). In this case damage concerns many grids surrounding impact area. Instead, in the case of stitched 10, delamination area seems to be limited only to grids effectively impacted (see Fig. 7).

In Table 2 damaged area dimensions are represented for the three materials at the different impact levels, normalised with respect to standard *S* impacted at 10 J.

It is clear from Table 2 that stitched 05 presents the larger damage, larger even than the standard. Damaged area always appears smaller in stitched 10, by as much as 50%.

In Figs. 8–10 typical damage level area distribution is reported for the three materials at the different impact levels.

In these graphs we can observe that, for impact at 10 J, blue damage area is never reached, while azure area is predominant for standard *S*, and yellow area for the two stitched 05 and 10 (see Fig. 8).

This seems to signify that the stitching effect is to contain well, at low energy impact, composite brittleness; nevertheless, we can note also that the damaged area is already greater for stitched 05 than for stitched 10.
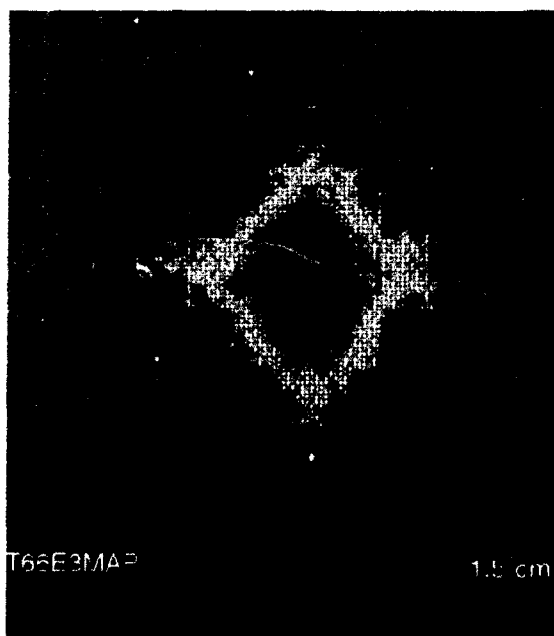

Fig. 6. Digitalised image of stitched 05 after impact (22 J).
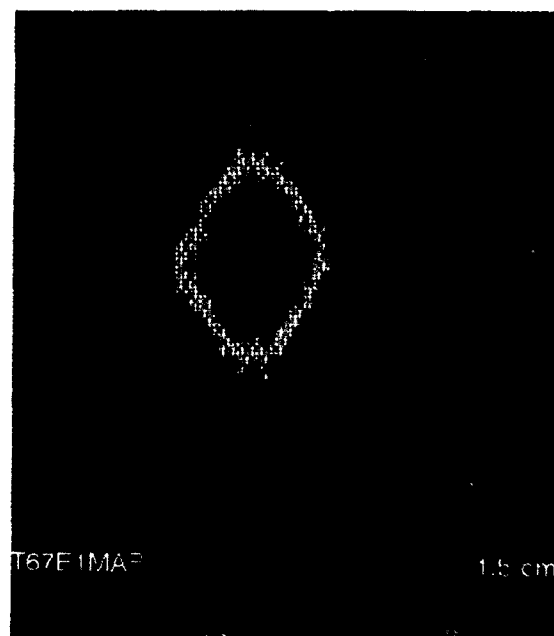

Fig. 7. Digitalised image of stitched 10 after impact (22 J).

This last consideration can be repeated and much more emphasised for higher energy impacts: in these cases, for all typical damage levels, the curve representing stitched 05 is much higher with respect to the other two curves, and so it is confirmed that stitched 05 is the more seriously damaged material by the impact process.

Residual life characterisation

Acoustic emission confirms that mechanical characteristics change for the three cases.

In standard *S* fracture is rather brittle with a sudden crack propagation. In fact acoustic emission events (see Fig. 11) are mostly concentrated in the final part of testing, in particular there is a very important energy peak close to ultimate load.

Table 2

Material	Impact energy		
	10 J	18 J	22 J
Standard *S*	1·0	2·5	3·6
Stitched 05	1·4	3·9	4·5
Stitched 10	0·6	1·9	2·3
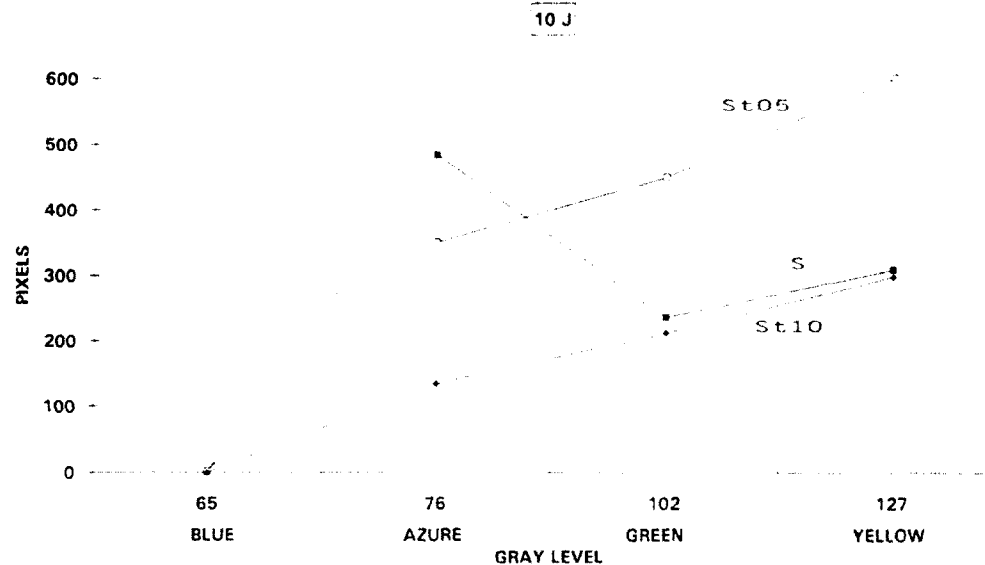
Fig. 8. Damage area distribution at 10 J impact.
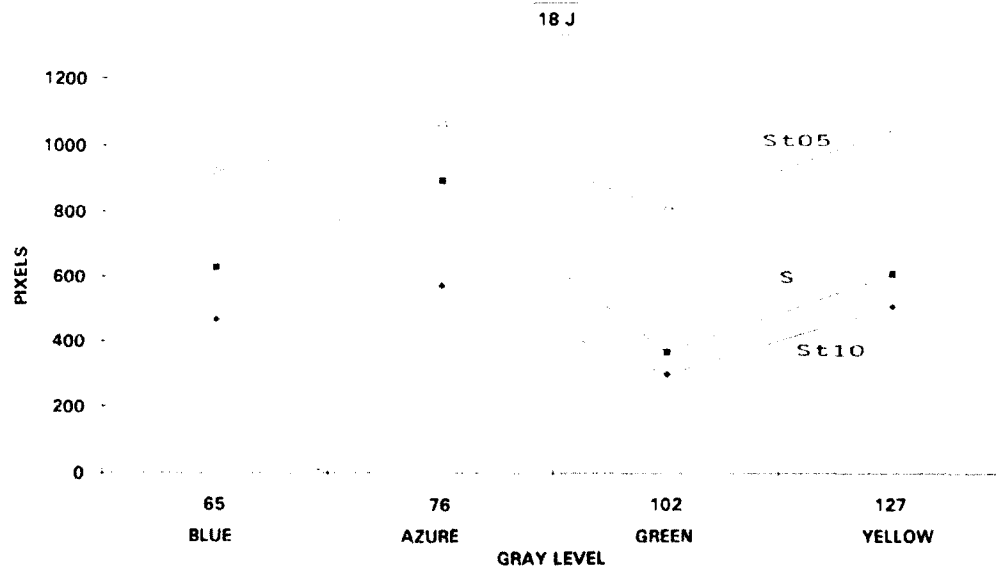
Fig. 9. Damage area distribution at 18 J impact.

22 J
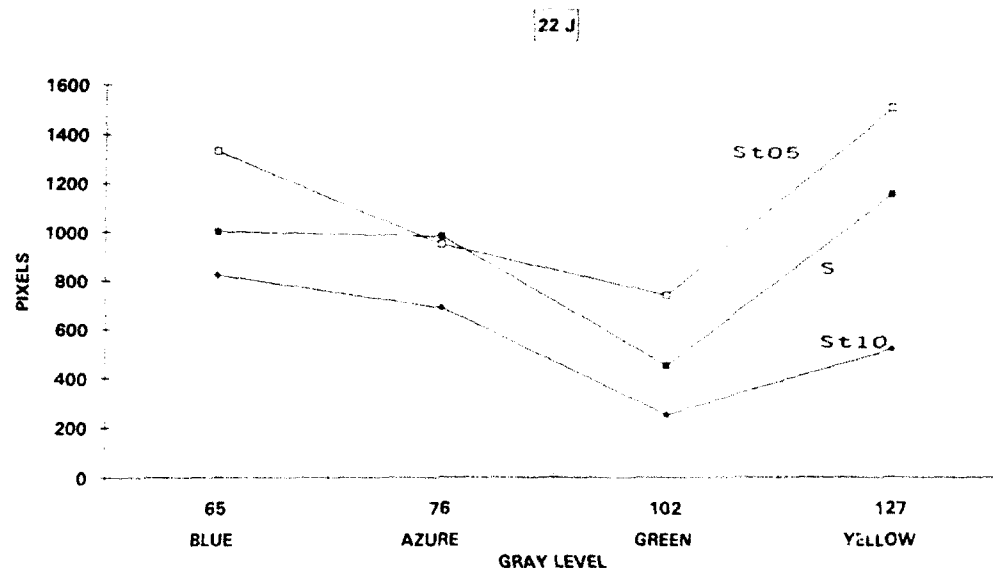
Fig. 10. Damage area distribution at 22 J impact.
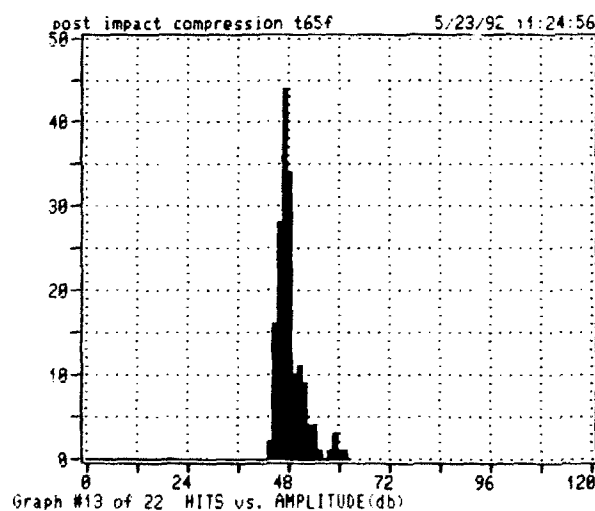
(a)
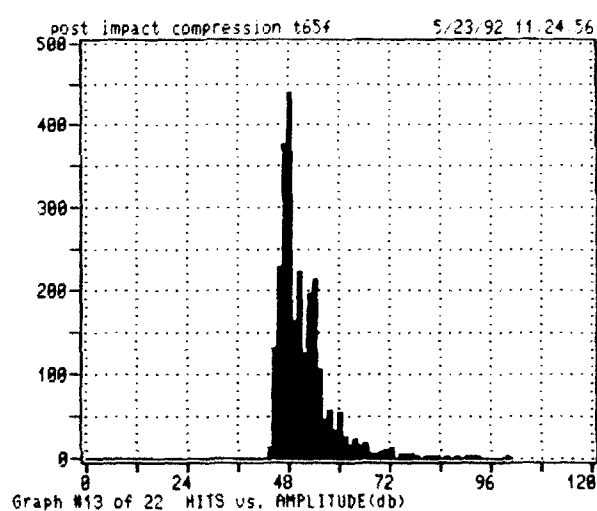
(b)

Fig. 11. Energy distribution in acoustic emission events (hits) for standard S.

From comparison with acoustic emission detected on the two types of stitched the following are noted.

(1) On stitched 05 high-amplitude phenomena (more than 70 dB) are very precocious in compression test, while they appear much later in stitched 10, and precisely only after having reached half the ultimate load (see Figs 12 and 13).

(2) Acoustic emission never stops during compression test on stitched 05, while it weakens and later vanishes on stitched 10. In this case, it resumes strongly only very close to the ultimate load.

(3) Events total amount is on an average 10^4 in stitched 10 and more than 2×10^4 in stitched 05.

(4) Cumulative energy and counts are four times larger in stitched 05 than in stitched 10.

We can thus affirm that in stitched 10 the initial phase of compression, when damage is contained
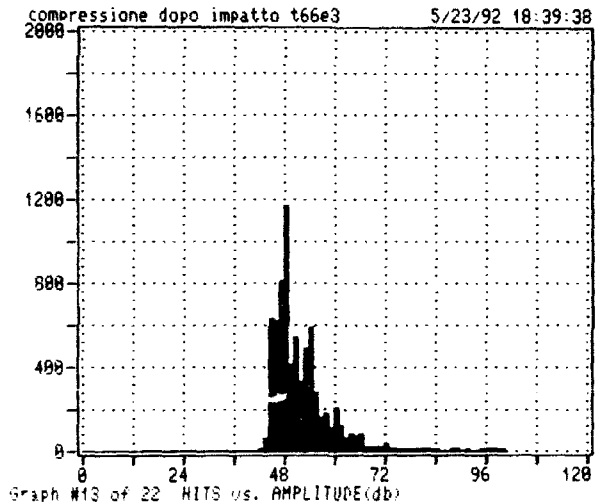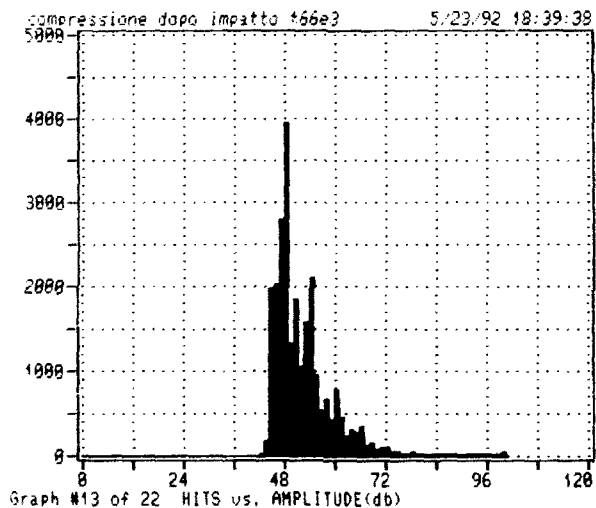
Fig. 12. Energy distribution in acoustic emission events (hits) for stitched 05.

Fig. 13. Energy distribution in acoustic emission events (hits) for stitched 10.

inside the grids and only impact damaged fibres fail, increases toughness at higher compression loads, while this does not happen with such emphasis in stitched 05.

In Table 3 are reported compression loads: from this table we note that it is not so easy to observe the importance of stitching effects in impacted materials by the mere mechanical test.

In fact, ultimate load values are rather dispersed and not very significant.

By combined use of image analysis and acoustic emission we can observe that stitching effect, on one side, increases the resistance to delamination, whereas on the other side, it may create

Table 3. Compression load (kN) versus impact energy for stitched and non-stitched composites

Material	Impact			
	00 J	10 J	18 J	22 J
Standard S	48	44	39	36
Stitched 05	41	37	36	31
Stitched 10	41	41	41	37

some local damage phenomena, that weaken reinforcement fibre.

This problem is clearly much more important when stitching concentration is greater, as in stitched 05.

We can also note, as a final consideration, that a mechanical test does not allow, if not supported by other techniques, to evaluate in a critical way residual life, especially if the material has a complex structure and can present some different types of damage in the same test.

In this case, in fact, the observation of ultimate compressive loads, does not show clearly the influence of stitching effect on damage after impact, and what happens to stitched materials when impact energy grows.

CONCLUSIONS

Using an image analysis technique to evaluate impact damage in close connection with acoustic emission technique to characterise post-impact residual life, we can obtain much more information on mechanical behaviour of materials having a complex structure.

This goal is achieved in two steps: first, by observing typical damage initiation and propagation in such material, and then by supporting

mechanical test results with some considerations on the real critical significance of a damage phenomenon.

These two techniques are also very useful for a combined use, because acoustic emission permits a closer and more profound observation of the damaged areas which appear to be critical in image analysis.

REFERENCES

1. Caneva, C., Bonora, N., Marchetti, M. & Mazzola, M., Acoustic emission behaviour of advanced stitched composites by RTM process under impact loads. Paper presented at the Fourth Int. Symp. on Acoustic Emission from Composite Materials (AECM4), 27-31 July, 1992, Seattle, WA, USA.
2. Caneva, C., Favuzzi, G., Mazzola, M., Russo, M. & Spoleti, M., RTM technology: characterization of fiber reinforcement critical parameters and a methodology to optimize processing conditions. *Journées Européennes des Composites* (Paris), 22 Avril 1992.
3. SACMA, *Recommended Test Method for Compression after Impact Properties of Oriented Fiber Resin Composites* SRM 2-88. Suppliers of Advanced Composite Materials Association, Arlington, VA, USA.

Numerical investigations of free edge effects in integrally stiffened layered composite panels

I. Skrna-Jakl & F. G. Rammerstorfer

Institute of Lightweight Structures and Aerospace Engineering, Vienna Technical University, Vienna, Austria

A linear finite element analysis is conducted to examine the free edge stresses and the displacement behavior of an integrally stiffened layered composite panel loaded under uniform inplane tension. Symmetric $(+\Phi, -\Phi, 0, -\Phi, +\Phi)$ graphite-epoxy laminates with various fiber orientations in the off-axis plies are considered. The quadratic stress criterion, the Tsai-Wu criterion and the Mises equivalent stresses are used to determine a risk parameter for onset of delamination, first ply failure and matrix cracking in the neat resin. The results of the analysis show that the interlaminar stresses at the $+\Phi/-\Phi$ and $-\Phi/0$ interfaces increase rapidly in the skin-stringer transition. This behavior is observed at the free edge as well as at some distance from it. The magnitude of the interlaminar stresses in the skin-stringer transition is strongly influenced by the fiber orientations of the off-axis plies. In addition, the overall displacements depend on the magnitude of the off-axis ply angle. It is found that for $\Phi < 30°$ the deformations of the stiffener section are dominated by bending, whereas for $45° < \Phi < 75°$ the deformations are dominated by torsion. The failure analysis shows that ply and matrix failure tend to occur prior to delamination for the considered configurations.

1 INTRODUCTION

The use of advanced fiber composites in airplane structures has increased significantly in recent years. First, parts of the cabin interior as well as secondary structures made of aluminum have been replaced by composite components. Nowadays the development of primary airplane structures, mainly for aircraft fuselages, using composite materials is taken in hand. Potential fuselage applications for composite materials are integrally stiffened skin-stringer panels.[1]

The design of structures using composite materials requires the understanding of a number of special features like 'free edge effects', which are characteristic for angle as well as cross-ply laminates, but are not observed in 'classical' metal structures. It is well known that at free edges of layered inhomogenous materials interlaminar stresses may occur due to the mismatch in material properties between adjacent layers.[2-5] In the region near the free edge the classical laminated plate theory is not valid because a triaxial state of stress is present. The interlaminar stresses may give rise to free edge delamination and failure of the laminate at lower loads than those predicted by the first-ply-failure-criterion. It depends

on the layup sequence and fiber orientations in the adjacent layers whether delamination or ply failure is the critical failure mode.

Free edge effects in composite plates under uniform extension have been analyzed by several investigators and a number of analytical approaches for the interlaminar stresses at free edges are available.[2-5] However, only limited work on integrally stiffened composite panels has been reported.[6] Hence, the present paper is focused at the interlaminar and free edge effects in the skin-stringer transition. In particular the influence of the fiber orientation on the above effects is studied and comparisons with the behavior in areas away from the stiffeners are discussed.

A numerical approach is presented, which uses the finite element method for investigating the free edge effects in an integrally stiffened composite panel in this respect. In addition, the stress distribution in the skin-stiffener transition at some distance from the free edge is determined. Symmetric $(+\Phi, -\Phi, 0, +\Phi, -\Phi)$ layups made of T300/5208 graphite-epoxy laminates[7,8] with various fiber orientations in the off-axis plies are considered. The interlaminar stresses in the stiffened structure as well as the displacements are computed as a function of the fiber orientation in

129

the off-axis plies. Furthermore, the quadratic failure criterion[9] and the Tsai–Wu criterion[11,12] are used to calculate risk parameters for delamination onset and first ply failure. As the applicability of the quadratic stress criterion depends on the accuracy of the stress results of the finite element analysis at the free edge, a non-stiffened panel is investigated first and the predictions of the quadratic stress criterion are compared with the results of a strain energy release rate criterion proposed by O'Brien.[8]

2 FINITE ELEMENT MODEL

The finite element model represents one periodic stiffener section of a thin-walled stiffened panel. Due to the non-symmetric fiber orientation in the laminates the whole stiffener is modelled. In order to minimize computer requirements a coupled three-dimensional (3D) solid-shell finite element approach is used. Most of the unstiffened panel parts are modelled with shell elements, and 3D solid elements are applied in the skin–stiffener transition to compute the triaxial stress state. To obtain detailed information on the stress distribution in the vicinity of the free edge, the 3D-mesh is refined towards the free edge (Fig. 1).

The connection between the 3D solid and shell elements is handled via multi-point constraints in correspondence with Mindlin–Reissner shell theory. The structure is loaded under uniform inplane tension of 445 N/mm transversally to the direction of the stiffener. On the side opposite to the free edge, the displacements in axial direction (parallel to the stiffener) are fixed, whereas the displacements in the vertical direction — except

on a horizontal nodeline — and the displacements in the load direction, except for one single node, are free. The material properties and strength values for the T300-5208 graphite–epoxy laminate and the neat resin are given in Table 1. The subscripts 1 and 2 indicate the inplane directions parallel and normal to the fibers, respectively.

3 INTERLAMINAR STRESSES

The results of the linear finite element analysis show that the interlaminar stresses at the $+\Phi/-\Phi$ and $-\Phi/0$ interfaces increase rapidly with s (see Fig 1) in the skin–stringer transition. In contrast to the behavior of the interlaminar stresses at the free edge of unstiffened composite panels, which vanish at some distance from the free edge, the interlaminar stresses in the skin–stiffener transition are observed at the free edge as well as at some distance from it. Figure 2 shows the different behavior of the interlaminar stresses observed in the skin–stringer transition (position A) and in the unstiffened parts of the panel (position B) along a horizontal nodeline parallel to the axis of the stiffener. The off-axis ply angle for this example is chosen to be 45°.

In the following section all stress results are discussed in eight specific points in the skin–stringer transition. Positions A_R and A_I at the $+\Phi/-\Phi$ interface and positions B_R and B_I at the $-\Phi/$ matrix interface are placed in an area where maximum interlaminar stresses were observed. Positions C_R and C_I at the $+\Phi/-\Phi$ interface and positions D_R and D_I at the $-\Phi/0$ interface are located in the panel away from the skin–stringer transition. In order to illustrate the free edge effect
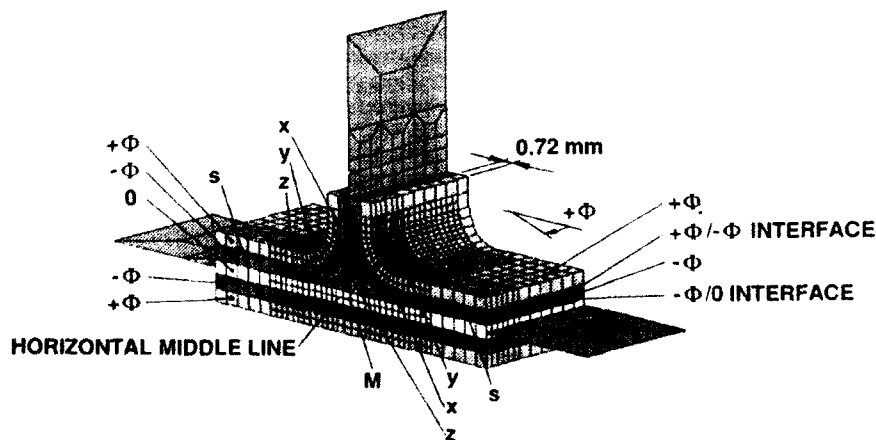

Fig. 1. Refined 3D-mesh at the free edge.

Table 1. Material properties and strength values for the T300-5208 graphite-epoxy laminate and the neat resin[a]

T300/5208 graphite-epoxy laminate

E_1	138000 MPa	σ^*_{11}		1513·5 MPa
$E_2 = E_3$	15000 MPa	σ^*_{11}		1696·2 MPa
$G_{12} = G_{13}$	5900 MPa	$\sigma^*_{22} = \sigma^*_{33}$		43·78 MPa
G_{23}	5953 MPa	$\sigma^*_{22} = \sigma^*_{33} = Z^t$		43·78 MPa
$\nu_{12} = \nu_{13}$	0·21	$\sigma^*_{12} = \sigma^*_{13}$		86·87 MPa
ν_{23}	0·254	$\sigma^*_{23} = Z^d = Z^c$		67·57 MPa

Neat resin

E	3450 MPa	ν	0·41
G	1340 MPa	σ	52·0 MPa

[a]Data taken from Refs 8 and 11.

Fig. 2. Interlaminar stresses at the skin–stringer transition (position A) and in the unstiffened part of the panel (position B).

Fig. 3. Positions A_L, A_R, B_L, B_R and C_L, C_R, D_L, D_R for interlaminar stress output.

on the magnitude of the interlaminar stresses, Figs 4 and 5 show the behavior of the interlaminar normal and major interlaminar shear stresses as a function of the fiber orientation in the off-axis plies at the free edge (denoted by [FREE EDGE]) as well as at some distance from it, which for the present work is chosen to be $-z = 5$ mm.

In the skin–stringer transition the magnitude of the interlaminar stresses (positions A_R, A_L, B_R, B_L) is strongly influenced by the fiber orientations of the off-axis plies. At some distance from the free edge both the interlaminar shear and normal stresses in the $+\Phi/-\Phi$ and the $-\Phi/$matrix interfaces are decreasing with increasing off-axis ply angle. The greatest influence of the free edge effects on the interlaminar shear as well as interlaminar normal stresses was found in the range of off-axis ply angles between $\Phi = 10°$ and $\Phi = 60°$. It depends on the interface, fiber orientation in the off-axis plies and the discussed position (A_R, A_L, or B_R, B_L) whether the free edge stresses decrease or increase when approaching the free edge. In the panel apart from the stiffener, interlaminar stresses are observed only near the free edge at all interfaces. There, the maximum interlaminar shear stress values are reached at ply angles between 10° and 50°, whereas the biggest interlaminar normal stresses occur at ply angles between 30° and 60°.

By comparing the influence of the free edge effects on the interlaminar stresses in the unstiffened parts of the panel with their behavior in the skin–stringer transition the following observations can be made for the $+\Phi/-\Phi$ and $-\Phi/0$ interfaces. The absolute as well as the relative change of the interlaminar shear stresses when approaching the free edge is much more pronounced in the unstiffened parts of the panel than in the skin–stringer transition. The relative change of the interlaminar normal stresses towards the free
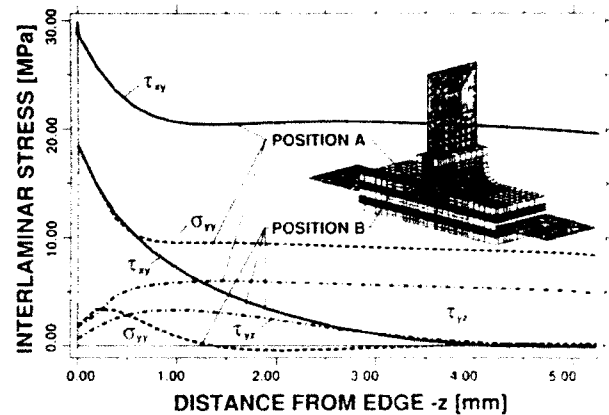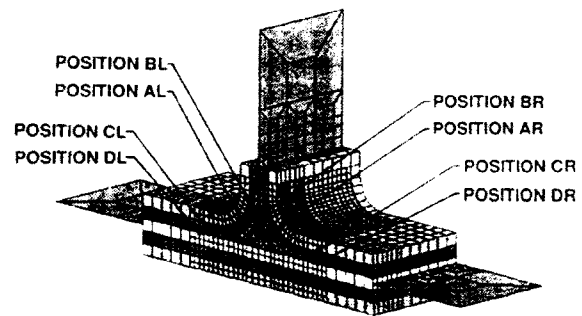
edge behaves as discussed above, whereas the absolute change at the $+\Phi/-\Phi$ interface is much higher in the skin–stringer transition than in the unstiffened parts of the panel. At the $-\Phi/0$ interface the maximum of the absolute change of the interlaminar normal stresses when approaching the free edge depends on the fiber orientation in the off-axis plies.

4 DEFORMATIONS

The overall displacements are predicted to be strongly influenced by the fiber orientation of the off-axis plies. The variation of the vertical displacements along the 'horizontal middle line' at the free edge, see Fig. 1, with the fiber angle in the off-axis plies is shown in Fig. 6. It can be seen that for $\Phi < 30°$ the deformations of the stiffener section are dominated by bending and for $45° < \Phi < 75°$ the deformations are dominated by torsion. The mode change occurs between $\Phi = 30°$ and $\Phi = 45°$.
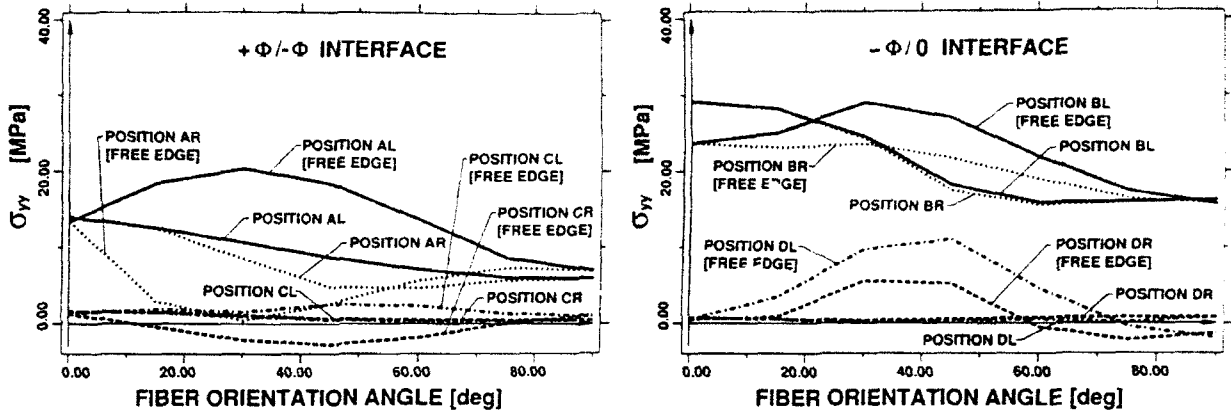
Fig. 4.   Interlaminar normal stresses at the $+\Phi/-\Phi$ and $-\Phi/0$ interfaces.
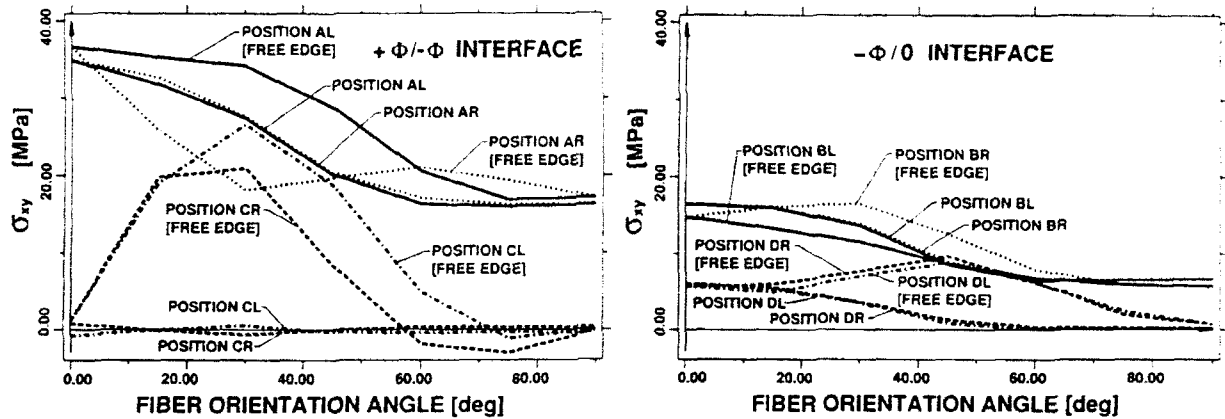
Fig. 5.   Interlaminar shear stresses at the $+\Phi/-\Phi$ and $-\Phi/0$ interfaces.
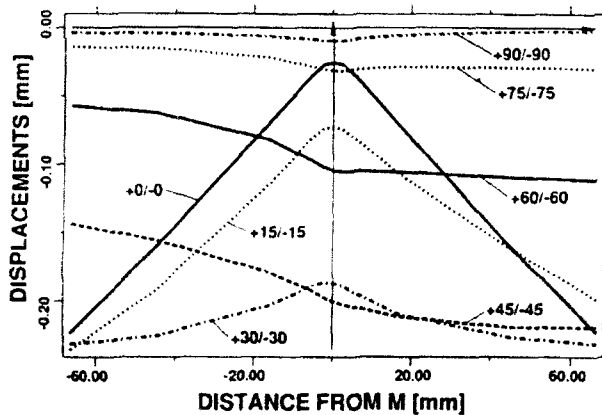
Fig. 6.   Vertical displacements at the free edge.

skin–stiffener transition from the neutral axis in the panel away from the stiffener. The vertical position of the neutral axis in the skin–stiffener transition depends on the fiber orientation of the off-axis plies as well as on the material properties and the size of the neat resin core. For $\Phi = 90°$ the neutral axis in the skin–stiffener transition lies above the neutral axis in the unstiffened panel parts, so that an inplane tension load transverse to the stiffener enforces a positive moment in the structure. In contrast, an off-axis ply angle of $\Phi = 0°$ induces a negative moment in the structure because the neutral axis in the skin–stiffener transition lies beneath the neutral axis in the unstiffened panel parts.

The different curvature of the horizontal middle line at the free edge of the deformed stiffener can be explained by the difference of the vertical position of the neutral axis in the

5 FAILURE CRITERIA

In the following section a brief description of three different failure criteria for delamination

onset, ply failure and matrix cracking is given. A risk parameter λ which will be used to examine the critical failure mode in the skin–stringer transition is defined for all three failure modes. Moreover, the application of the quadratic stress criterion and the Tsai–Wu criterion is tested on a non-stiffened layered composite panel.

5.1 Onset of delamination

To predict the onset of delamination, the following quadratic failure criterion proposed by Brewer and Lagace[9] is applied:

$$\left(\frac{\sigma_{yy}}{Z'^1}\right)^2 + \left(\frac{\sigma_{yz}}{Z'^2}\right)^2 + \left(\frac{\sigma_{zz}}{Z'}\right)^2 = 1 \tag{1}$$

Here σ_{yy}, σ_{yz} are the interlaminar shear stresses and σ_{zz} is the interlaminar normal stress at the free edge. Z'^1, Z'^2 and Z' are the interlaminar strength allowables. For further investigation a 'risk parameter' λ_{QSC} is defined:

$$\lambda_{QSC} = \sqrt{\left(\frac{\sigma_{yy}}{Z'^1}\right)^2 + \left(\frac{\sigma_{yz}}{Z'^2}\right)^2 + \left(\frac{\sigma_{zz}}{Z'}\right)^2} \tag{2}$$

$\lambda_{QSC} < 1$ no delamination

$\lambda_{QSC} = 1$ onset of delamination

$\lambda_{QSC} > 1$ delamination

The results of the quadratic stress criterion are strongly influenced by the accuracy of the interlaminar stresses at the free edge calculated in the finite element analysis and by the position selected for evaluation. Therefore, another failure criterion which does not depend on discrete stress results was employed to verify the predictions of the quadratic stress criterion. O'Brien[8] proposes a simple approach, employing strain energy release rates for characterizing the onset of delamination in an unnotched plane graphite epoxy laminate under static tension loading. The critical nominal strain, ε_c, of the specimen is derived as

$$\varepsilon_c = \sqrt{\frac{2G_c}{t(E_{LAM} - E^*)}} \tag{3}$$

where G_c is the critical strain energy release rate; t is the laminate thickness; E_{LAM} is the longitudinal stiffness of the undelaminated laminate calculated from laminate theory[13]; and E^* is the longitudinal stiffness of the laminate completely delaminated along one or more interfaces.

A value of 0.137 J/mm^2 is quoted[8] for the critical strain energy release rate of a T300-5208 graphite–epoxy laminate with an average ply thickness of $t_p = 0.14$ mm. The risk parameter λ_{SERRC}, which characterizes the initiation of delamination by using the strain energy release rate criterion, is defined as

$$\lambda_{SERRC} = \frac{F}{tb\varepsilon_c E_{LAM}} \tag{4}$$

$\lambda_{SERRC} < 1$ no delamination

$\lambda_{SERRC} = 1$ onset of delamination

$\lambda_{SERRC} > 1$ delamination

where F is the applied tension load; and b is the width of the specimen.

The strain energy release rate criterion is a handy method for calculating a risk parameter for delamination initiation. However, it should be kept in mind that the value of G_c may depend on the stacking sequence of the laminate as well as on the orientations of the plies which are joined at the delamination interface[8] and that it is strongly influenced by the layer thickness.[9]

O'Brien[8] used unstiffened plane laminates for his investigations. For comparison it is therefore necessary to compute the free edge stresses of a non-stiffened panel under uniform tension loading using the finite element method. The layup sequence, material properties, layer thickness, and mesh discretization are the same as discussed above for the stiffener section. The fact that the ply thickness in the panel is about five times that of the test specimen[8] used may be accounted for by increasing G_c to 0.205 J/mm^2 as observed by Brewer and Lagace.[9] A comparison between the risk parameters λ_{QSC} and λ_{SERRC} for delamination initiation at the $+\Phi/-\Phi$ and $-\Phi/0$ interfaces as a function of the off axis ply angle is shown in Fig. 7.

In the $-\Phi/0$ interface good agreement between the two criteria was found in the range of the off axis ply angles between $\Phi = 0°$ and $\Phi = 65°$, whereas in the $+\Phi/-\Phi$ interface, which actually is the delamination–prone interface, a difference of 30% between the risk parameters λ_{QSC} and λ_{SERRC} was observed. It can be seen that the value of G_c depends on the orientations of the plies which are joined at the interface. For the $-\Phi/0$ interface the chosen value of G_c is applicable whereas for the $+\Phi/-\Phi$ interface it is too small. A similar difference betwen the two criteria was observed by Brewer and Lagace[9] for thick $[+15/-15/0]_s$ laminates.
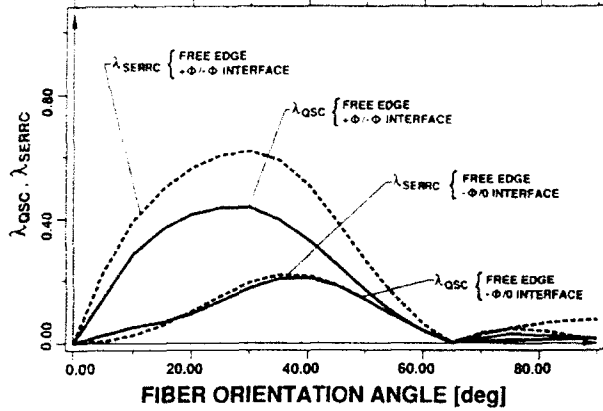
FIBER ORIENTATION ANGLE [deg]

Fig. 7. Comparison of the risk parameters λ_{QSC} and λ_{SERRC} at the $+\Phi/-\Phi$ and $-\Phi/0$ interfaces of the unstiffened panel.

5.2 Ply failure

A polynomial failure criterion proposed by Tsai and Wu[12] is used to determine first ply failure. The Tsai–Wu criterion is given by

$$F_1\sigma_{11} + F_2\sigma_{22} + F_3\sigma_{33} + 2F_{12}\sigma_{11}\sigma_{22}$$
$$+ 2F_{13}\sigma_{11}\sigma_{33} + 2F_{23}\sigma_{22}\sigma_{33} + F_{11}\sigma_{11}^2 + F_{22}\sigma_{22}^2$$
$$+ F_{33}\sigma_{33}^2 + F_{44}\sigma_{23}^2 + F_{55}\sigma_{13}^2 + F_{66}\sigma_{12}^2 = 1 \quad (5)$$

where

$$F_1 = \frac{1}{\sigma_{1t}^*} - \frac{1}{\sigma_{1c}^*} \qquad F_{11} = \frac{1}{\sigma_{1t}^*\sigma_{1c}^*}$$

$$F_2 = \frac{1}{\sigma_{2t}^*} - \frac{1}{\sigma_{2c}^*} \qquad F_{22} = \frac{1}{\sigma_{2t}^*\sigma_{2c}^*}$$

$$F_3 = \frac{1}{\sigma_{3t}^*} - \frac{1}{\sigma_{3c}^*} \qquad F_{33} = \frac{1}{\sigma_{3t}^*\sigma_{3c}^*}$$

$$F_{44} = \frac{1}{\sigma_{23}^*\sigma_{23}^*} \qquad F_{12} = -\tfrac{1}{2}\sqrt{F_{11}F_{22}}$$

$$F_{55} = \frac{1}{\sigma_{13}^*\sigma_{13}^*} \qquad F_{13} = -\tfrac{1}{2}\sqrt{F_{11}F_{33}}$$

$$F_{66} = \frac{1}{\sigma_{12}^*\sigma_{12}^*} \qquad F_{23} = -\tfrac{1}{2}\sqrt{F_{22}F_{33}}$$

with positive values for all σ_{xc}. The risk parameter for ply failure using the Tsai–Wu criterion is defined as follows:

$$\lambda_{TSWU} = \frac{1}{(K_1 \pm \sqrt{K_2})} \quad (6)$$

where

$$K_1 = \frac{-K_3}{2K_4}$$

$$K_2 = K_1^2 + \frac{1}{K_4}$$

$$K_3 = F_1\sigma_{11} + F_2\sigma_{22} + F_3\sigma_{33}$$

$$K_4 = 2F_{12}\sigma_{11}\sigma_{22} + 2F_{13}\sigma_{11}\sigma_{33} + 2F_{23}\sigma_{22}\sigma_{33}$$
$$+ F_{11}\sigma_{11}^2 + F_{22}\sigma_{22}^2 + F_{33}\sigma_{33}^2 + F_{44}\sigma_{23}^2$$
$$+ F_{55}\sigma_{13}^2 + F_{66}\sigma_{12}^2$$

$\lambda_{TSWU} < 1$ no ply failure

$\lambda_{TSWU} = 1$ first ply failure

$\lambda_{TSWU} > 1$ ply failure

The maximum value of λ_{TSWU} is taken into account.

Prior to the ply failure analysis of the skin–stringer transition the influence of the free edge stresses on the risk parameter λ_{TSWU} is examined in the nonstiffened panel, which was discussed before. Figure 8 shows the risk parameter λ_{TSWU} at the $+\Phi/-\Phi$ and the $-\Phi/0$ interfaces as a function of the off-axis ply angle. To illustrate the influence of the free edge, λ_{TSWU} is plotted at the free edge as well as at some distance from it.

In the 0°-ply at the $-\Phi/0$ interface the greatest influence of the free edge effect is found in the range of off-axis ply angles between $\Phi = 20°$ and $\Phi = 60°$. In contrast to the behavior of λ_{QSC}, which increases towards the free edge of the non-stiffened panel, λ_{TSWU} decreases. In the $-\Phi$-ply at the $-\Phi/0$ interface the difference between λ_{TSWU} at the free edge and λ_{TSWU} at some distance from the free edge is less than in the 0°-ply. For $\Phi < 35°$ the difference is negative and for $35° < \Phi < 65°$ it is positive.

At the $+\Phi/-\Phi$ interface λ_{TSWU} has the same value as in the $+\Phi$-ply and in the $-\Phi$-ply. In the range of off-axis ply angles between $\Phi = 10°$ and $\Phi = 60°$ λ_{TSWU} increases moderately when approaching the free edge. For $0° < \Phi < 10°$ and $60° < \Phi < 90°$ no edge effect is observed.

In addition, the upper limit line in Fig. 8 specifies the location and risk parameter of the first ply failure for any fiber orientation in the off-axis plies of the non-stiffened panel. It can be seen easily that for $10° < \Phi < 23°$ ply failure starts in the off-axis angle plies near the $+\Phi/-\Phi$ interface
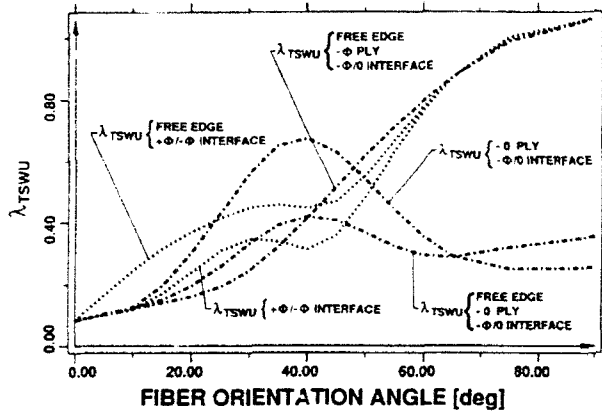
Fig. 8. Risk parameter λ_{TSWU} at the $+\Phi/-\Phi$ and $-\Phi/0$ interfaces of the unstiffened panel.

Fig. 9. Prediction of the critical failure mode in the unstiffened panel.

at the free edge, for $23° < \Phi < 48°$ first ply failure occurs in the $0°$-ply apart from the free edge and for $48° < \Phi < 65°$ first ply failure is found in the $-\Phi$-ply near the $-\Phi/0$ interface at the free edge. for $\Phi < 10°$ no particular location of the first ply failure can be predicted and for $\Phi > 65°$ ply failure is initiated in the $+\Phi$ and $-\Phi$ plies.

As all the risk parameters for delamination onset and ply failure are already determined it is easy to predict the critical failure mode of the unstiffened panel for any fiber orientation in the off-axis plies. Therefore, the values of the risk parameter for delamination onset calculated with the quadratic stress criterion are compared with the upper limit line of Fig. 8. Figure 9 shows that for

$0° < \Phi < 5°$	ply failure near the $+\Phi/-\Phi$ interface at the free edge
$5° < \Phi < 25°$	delamination in the $+\Phi/-\Phi$ interface at the free edge
$25° < \Phi < 48°$	ply failure in the $0°$-ply away from the free edge
$48° < \Phi < 65°$	ply failure in the $-\Phi$-ply near the $-\Phi/0$ interface at the free edge
$65° < \Phi < 90°$	ply failure in the $+\Phi$ and $-\Phi$ plies

are the critical failure modes.

5.3 Matrix cracking in the neat resin

As the neat resin is an isotropic material, the Mises equivalent stresses, $\bar{\sigma}$, are used for a first guess of failure by comparing them with the resin's strength, σ_{cru}, measured in the uniaxial tensile test. The Mises equivalent stress is a
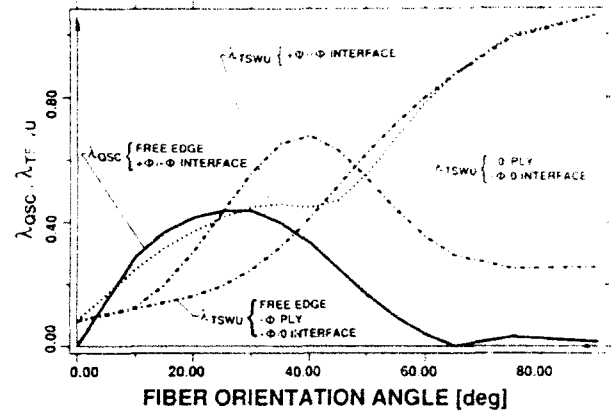
proper stress measure for yielding. However, in the configuration investigated here, it leads to similar results as would be derived by a certain maximum principal stress criterion. The risk parameter λ_{MIS} characterizes initiation of failure in the neat resin:

$$\lambda_{MIS} = \frac{\sigma_1}{\sigma_{cru}} \qquad\qquad 7$$

$\lambda_{MIS} < 1$	no matrix failure
$\lambda_{MIS} = 1$	first matrix failure
$\lambda_{MIS} > 1$	matrix failure

6 FAILURE ANALYSIS

A failure analysis is carried out to examine the critical failure mode in the skin–stringer transition. The quadratic stress criterion and the Tsai–Wu criterion are used to compute risk parameters for initiation of delamination and first ply failure. Additionally, Mises equivalent stresses are calculated in the neat resin core and compared with the critical uniaxial stress values.

To predict the onset of delamination the interlaminar stress results at the positions A_R, A_l and B_R, B_l in the skin–stringer transition and C_R, C_l and D_R, D_l in the panel away from the stiffener, which were already discussed before, are taken into account. Figure 10 shows the risk parameter λ_{QSC} as a function of the fiber orientation in the off-axis plies at the $+\Phi/-\Phi$ and $-\Phi/0$ ($-\Phi/$ matrix) interfaces. In order to illustrate the influence of the free edge effect, the magnitude of the risk parameter λ_{QSC} is plotted at the free edge as well as at some distance from it.
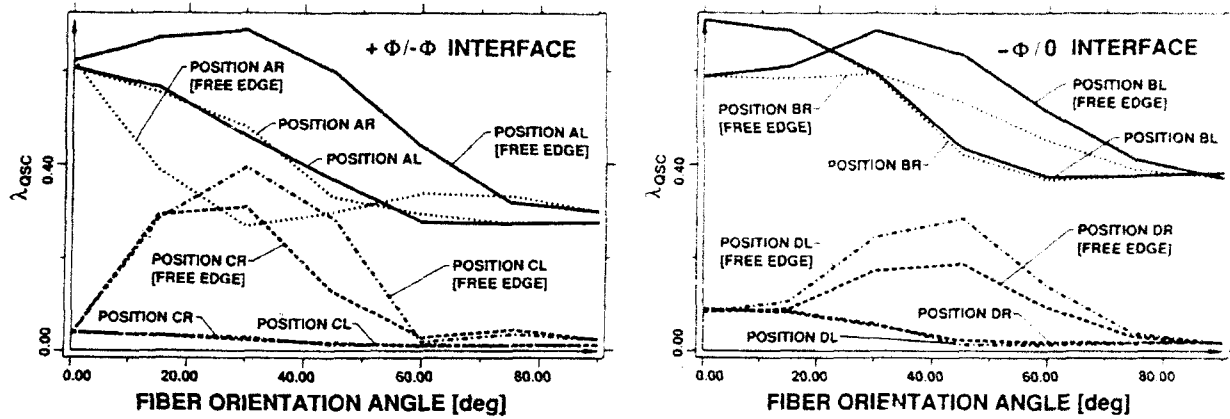
Fig. 10. Risk parameter λ_{QSC} at the $+\Phi/-\Phi$ and the $-\Phi/0$ interfaces in the skin–stringer transition.

It can be seen easily, that delamination will initiate in the skin–stringer transition because of the high values of the risk parameter. A comparison of the two diagrams in Fig. 10 shows that for

$0° < \Phi < 18°$ delamination starts in the $-\Phi/0$ interface at position B_l at some distance from the free edge

$18° < \Phi < 30°$ onset of delamination is observed in the $+\Phi/-\Phi$ interface at position A_l at the free edge

$30° < \Phi < 90°$ delamination initiates in the $-\Phi/0$ interface

It should be pointed out that delamination in the skin–stringer transition does not always initiate at the free edge $[0° < \Phi < 18°]$ as observed in the non-stiffened panels. Due to the fact that the magnitude of the risk parameter between $30° < \Phi < 90°$ in the skin–stringer transition is lowered by increasing the fiber angle in the off-axis plies, the onset of delamination can be prevented by an appropriate choice of the fiber orientation. However, ply failure and matrix cracking in the neat resin must be taken into account additionally to predict the critical failure mode.

Figure 11 shows the maximum values of the risk paramaters λ_{MIS} and λ_{TSWU} in the neat resin and in all $+\Phi$, $-\Phi$ and 0-plies of the skin–stringer transition as a function of the fiber orientation in the off-axis plies. As there are three $+\Phi$-plies and three $-\Phi$-plies in the layup sequence of the stiffener, the $+\Phi$ and $-\Phi$ plies which form the stiffener will be denoted in Fig.
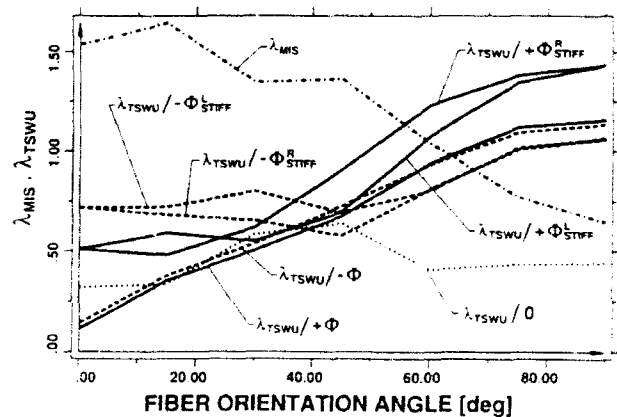
Fig. 11. Maximum values of λ_{MIS} and λ_{TSWU} in the skin–stringer transition.

11 as $+\Phi^R_{STIFF}$, $+\Phi^L_{STIFF}$ and $-\Phi^R_{STIFF}$, $-\Phi^L_{STIFF}$ depending on whether they are placed on the right side or left side (Fig. 1) of the geometric symmetry plane of the stiffener. In comparison with Fig. 10 it can be seen that the upper limit line of the λ_{MIS} curve and all λ_{TSWU} curves exceed the critical values of λ_{TSWU} for all considered fiber orientations. Hence, the critical failure mode is matrix cracking in the neat resin core for $0° < \Phi < 56°$ and ply failure in the $+\Phi^R_{STIFF}$-ply for $56° < \Phi < 90°$.

7 CONCLUSIONS

A finite element analysis of one periodic stiffener section of a thin-walled integrally stiffened composite panel under uniform inplane tension is presented. The behavior of the interlaminar stresses, displacements and the critical failure

mode as a function of the fiber orientation is investigated. In the skin–stringer transition high interlaminar stresses are observed at the free edge as well as at some distance from it. Depending on the fiber orientation and interface, interlaminar stresses are found either to decrease or increase when approaching the free edge. The study of the overall displacements of the stiffener shows that for $\Phi < 30°$ the deformation is dominated by bending and for $45° < \Phi < 75°$ it is dominated by torsion. The quadratic stress criterion, the Tsai–Wu criterion and the Mises equivalent stresses were used to predict the critical failure mode in the skin–stringer transition. For the considered configuration matrix cracking $(0° < \Phi < 56°)$ and ply failure $(56° < \Phi < 90°)$ will occur prior to delamination.

REFERENCES

1. Johnson, R., NASA/Boeing 777/ACTAS Programs Overview. Boeing Aerospace Co., 1992.
2. Pipes, R. B. & Pagano, N. J., Interlaminar stresses in composite laminates under uniform axial extension. *J. Comp. Mater.*, **4** 1970 538–48.
3. Wang, S. S. & Choi, I., Boundary-layer effects in composite laminates. Part 1: Free edge singularities. Part 2: Free edge stress solutions and basic characteristics. *J. Appl. Mech.*, **49** 1982 541–60.
4. Rose, C. A. & Herakovich, C. T., An approximate solution for interlaminar stresses in composite laminates. *J. Comp. Engng*, **3** 1993 271–88.
5. Christensen, R. M. & DeTeresa, S. J., Elimination minimization of edge-induced stress singularities in fiber composite laminates. *Int. J. Solids and Structures*, **29** 1992 1221–31.
6. Wang, J. T., Lotts, C. G., Davis, D. D. & Krishnamurthy, T., Coupled 2D–3D finite element method for analysis of a skin panel with a discontinuous stiffener. In *Proceedings of the AIAA/ASME/ASCE/AHS/ASC 33rd Structures, Structural Dynamics and Materials Conference*, Part 2. Paper No. 92-2474-CP, 1992, pp. 818–27.
7. Davila, C. G. & Johnson, E. R., Analysis for delamination initiation in postbuckled dropped-ply laminates. In *Proceedings of the AIAA/ASME/ASCE/AHS/ASC 33rd Structures, Structural Dynamics and Materials Conference*, Part 1. Paper No. 92-2226-CP, 1992, pp. 29–39.
8. O'Brien, T. K., Characterization of delamination onset and growth in a composite laminate. In *Damage in Composite Materials*, ASTM STP775, ed. K. L. Reifsnider. American Society of Testing and Materials, Philadelphia, PA, USA, 1982, pp. 140–67. *Engng Fracture Mech.*, **29** 1988 557–84.
9. Brewer, J. C. & Lagace, P. A., Quadratic stress criterion for initiation of delamination. *J. Comp. Mater.*, **22** 1988 538–48.
10. Garg, A. C., Delamination — a damage mode in composite structures. *Engng Fracture Mech.*, **29** 1988 557–84.
11. Reddy, J. N. & Pandey, A. K., A first-ply failure analysis of composite laminates. *J. Computers and Structures*, **25** 1987 371–93.
12. Tsai, S. W. & Wu, E. M., A general theory of strength for anisotropic materials. *J. Comp. Mater.*, **5** 1971 38–80.

On closed form solution for the elastic stress field around holes in orthotropic composite plates under in-plane stress conditions

N. Bonora, M. Costanzi & M. Marchetti

Aerospace Dept, University of Rome 'La Sapienza' Via Eudossiana 18, 00184 Rome, Italy

The present paper presents analytical work performed care of the Aerospace Department of the University of Rome 'La Sapienza'. Using the classical Airy's function solution method the expression of the stress-strain field, in a composite material, has been determined for different simple hole geometries in a closed form. The results have been compared with several extensive finite element calculations that confirm the accuracy of the theoretical solutions found.

1 INTRODUCTION

Discontinuities in a material or structure always represent a critical point because they alter locally the stress-strain field with the presence of relevant gradients. More generally, geometrical discontinuities, as notches or holes, modify significantly the stress field lines causing concentrations that can be critical and activate local damage phenomena. This situation can soon lead the component to failure even if the whole structure is subjected to a stress state far below the critical one.

Determination of the state of stress near notches or holes in homogeneous material has been solved by many authors for a large number of cases[1] that are commonly encountered in engineering design. For example, the stress field around a circular hole of radius a is given by:

$$\sigma_t = \frac{p+q}{2} \cdot f_1(r) - \frac{q-p}{2} \cdot f_2(r) \cdot \cos 2\theta \qquad (1)$$

$$\sigma_n = \frac{p+q}{2} \cdot f_3(r) + \frac{q-p}{2} \cdot f_4(r) \cdot \cos 2\theta \qquad (2)$$

$$\tau_{r\theta} = -\frac{q-p}{2} \cdot f_5(r) \cdot \sin 2\theta \qquad (3)$$

where p and q are the applied remote stress components in the x and y direction respectively and $f_i(r)$ $(i = 1,\dots,5)$ are functions of the radius r (Fig. 1).

On the edge of the hole $(r = a)$ the stress components become:

$$\sigma_r = \tau_{r\theta} = 0$$

$$\sigma_n = 3q - p, \qquad \theta = 0 \qquad (4)$$

$$\sigma_n = 3p - q, \qquad \theta = \frac{\pi}{2}$$

The ratio betwen the effective and nominal stress is commonly called the concentration factor. To know how the stress field is modified by the presence of geometrical discontinuities is useful in many engineering cases, such as riveted and bolted joints, passages for pipes, and inspection windows, etc.
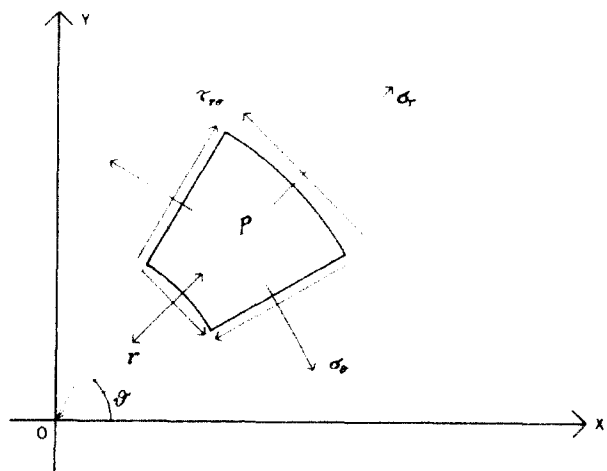

Fig. 1. Frame reference.

The identification of the concentration factor in composite materials is more difficult specially in the case of composite laminates where the constitutive equations are not simple and have to take account of several parameters such as stacking sequence, fibre and matrix properties, etc. Savin,[1] based on the works of Muskhelishvili[2] and Lekhnitskiy,[3] was one of the first to evaluate the stress field around discontinuities in orthotropic materials. Later, Sampath and Hulbert[4] developed a numerical procedure for the evaluation of the stress field in composite laminates weakened by multiple holes of different geometries.

Furthermore, this subject has been investigated by many researchers for possible application in aeronautic engineering. Venkayya et al.[5] analysed the effect of intensification around bolted joints in composite structures. Here, using a classic Airy solution method,[6] the expressions of the stress components, in a closed analytical form, for a generic composite plate were found for three classical cases: circular and elliptical hole and sharp crack. The solution was found using an Airy's function that takes into account the remote applied loads. The stress field equation has been determined for a symmetric balanced composite laminate and the results have been compared with finite element analysis. As a bench-mark test, the solution for a generic strongly orthotropic material has been also found.

2 THEORETICAL FORMULATION

In this section a rigorous analytical solution for the problem is given looking carefully at three different hole geometries: circular and elliptical hole and sharp crack in two different materials: strongly orthotropic material and a composite laminate. Sections 2.1 and 2.2 introduce the global notation and the general solution method. In Section 2.3 the final expressions for the cases examined are reported. More details on the analytical passages are reported in the Appendix.

2.1 Fundamental equations

Let us now consider a plate element in the orthogonal reference system xyz. The plate mid-plane is chosen to lay on the xy plane and the plate element has to be submitted to the following forces: the external force q, the normal resultant forces N_x and N_y, the shear resultant forces T_{xy}, T_{xz}, T_{yz} (for unit length) as shown in Fig. 2. The bending and twisting resultant moments are M_x, M_y, M_{xy} (for unit length) as in Fig. 3.

If u_0, v_0 and w_0 are the displacement components in the x, y, z directions respectively, the mid-plane strains vector, where the contribution of rotation is zero, can be written in the following form:

$$\{\varepsilon_0\} = \begin{Bmatrix} \varepsilon_{10} \\ \varepsilon_{20} \\ \gamma_{120} \end{Bmatrix} = \begin{Bmatrix} \dfrac{\partial u_0}{\partial x} \\[2ex] \dfrac{\partial v_0}{\partial y} \\[2ex] \dfrac{\partial u_0}{\partial y} + \dfrac{\partial v_0}{\partial x} \end{Bmatrix} \tag{5}$$

with the hypothesis that the element is not deformed under shear, i.e.

$$\theta_x = \frac{\partial w_0}{\partial x} \quad \theta_y = \frac{\partial w_0}{\partial y} \tag{6}$$
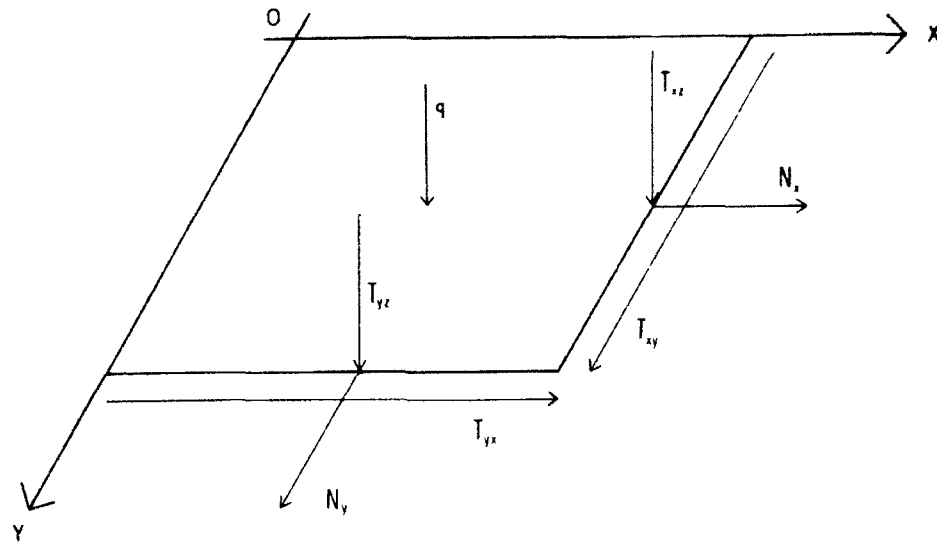
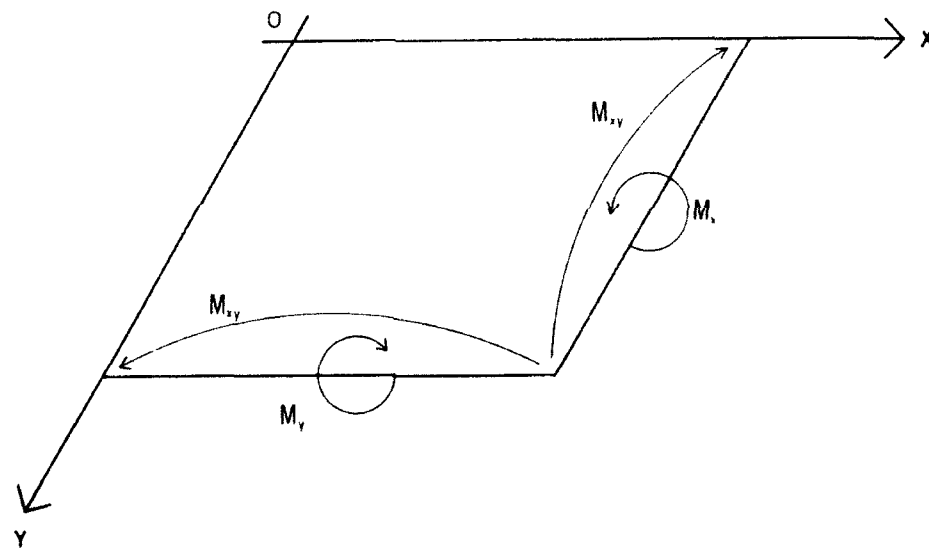**Fig. 2.**   Stresses for unit length components.

Fig. 3.   Moment notation.

then, the out-of-plane bending and twisting are given as:

$$\{x\} = \begin{Bmatrix} x_1 \\ x_2 \\ 2x_{12} \end{Bmatrix} = \begin{Bmatrix} \dfrac{\partial^2 w_0}{\partial x^2} \\[2ex] \dfrac{\partial^2 w_0}{\partial y^2} \\[2ex] 2\dfrac{\partial^2 w_0}{\partial x \partial y} \end{Bmatrix} \tag{7}$$

In the framework of the classical laminate theory, the relations between the normal resultant forces and moments with $\{\varepsilon_0\}$, $\{x\}$ vectors are linear and can be written in the following form (easily obtained from Hook's relations):

$$\{N\} = [A] \cdot \{\varepsilon_0\} - [B] \cdot \{x\} \tag{8}$$

$$\{M\} = [B] \cdot \{\varepsilon_0\} - [D] \cdot \{x\} \tag{9}$$

where

$$\{N\} = \begin{Bmatrix} N_x \\ N_y \\ T_{xy} \end{Bmatrix} \quad \{M\} = \begin{Bmatrix} M_x \\ M_y \\ M_{xy} \end{Bmatrix} \tag{10}$$

$$\{\varepsilon_0\} = \begin{Bmatrix} \dfrac{\partial u_0}{\partial x} \\[2mm] \dfrac{\partial v_0}{\partial y} \\[2mm] \dfrac{\partial u_0}{\partial y} + \dfrac{\partial v_0}{\partial x} \end{Bmatrix} \quad \{X\} = \begin{Bmatrix} \dfrac{\partial^2 w_0}{\partial x^2} \\[2mm] \dfrac{\partial^2 w_0}{\partial y^2} \\[2mm] 2\dfrac{\partial^2 w_0}{\partial x \partial y} \end{Bmatrix} \tag{11}$$

$$[A] = \begin{bmatrix} A_{11} & A_{12} & A_{13} \\ A_{12} & A_{22} & A_{23} \\ A_{13} & A_{23} & A_{33} \end{bmatrix} \tag{12}$$

$$[B] = \begin{bmatrix} B_{11} & B_{12} & B_{13} \\ B_{12} & B_{22} & B_{23} \\ B_{13} & B_{23} & B_{33} \end{bmatrix} \tag{13}$$

$$[D] = \begin{bmatrix} D_{11} & D_{12} & D_{13} \\ D_{12} & D_{22} & D_{23} \\ D_{13} & D_{23} & D_{33} \end{bmatrix} \tag{14}$$

Equations (8) and (9) can be written in the following semi-inverted form:

$$\{\varepsilon_0\} = [A]^{-1}\{N\} + [A]^{-1} \cdot [B]\{x\} = [a]\{N\} + [b]\{x\} \tag{15}$$

$$\{M\} = [B] \cdot [A]^{-1}\{N\} + ([B] \cdot [A]^{-1} \cdot [B] - [D])\{x\} = [b]^{\mathrm{T}}\{N\} + [d]\{x\} \tag{16}$$

It can be easily proved[6] that the out-of-plane shear resultant forces are given by:

$$T_{yz} = \frac{\partial M_y}{\partial y} + \frac{\partial M_{xy}}{\partial x} \quad T_{xz} = \frac{\partial M_x}{\partial x} + \frac{\partial M_{xy}}{\partial y} \tag{17}$$

Finally the system of equilibrium equations is given by:

$$\frac{\partial T_{xz}}{\partial x} + \frac{\partial T_{yz}}{\partial y} + \frac{\partial}{\partial x}\left(N_x \frac{\partial w_0}{\partial x}\right) + \frac{\partial}{\partial y}\left(T_{xy} \frac{\partial w_0}{\partial x}\right) + \frac{\partial}{\partial y}\left(N_y \frac{\partial w_0}{\partial y}\right) + \frac{\partial}{\partial x}\left(T_{xy} \frac{\partial w_0}{\partial y}\right) = -q$$

$$\frac{\partial N_x}{\partial x} + \frac{\partial T_{xy}}{\partial y} = 0 \tag{18}$$

$$\frac{\partial N_y}{\partial y} + \frac{\partial T_{xy}}{\partial x} = 0$$

and the additional compatibility condition is obtained applying the Schwarz theorem:

$$\frac{\partial^2 \varepsilon_{10}}{\partial y^2} + \frac{\partial^2 \varepsilon_{20}}{\partial x^2} - \frac{\partial^2 \gamma_{120}}{\partial y \partial y} = 0 \tag{19}$$

2.2 Airy's stress function for plates

It is well known that it is possible to solve the compatibility and equilibrium equations in terms of displacement variables using what is called Airy's function, defined by the following conditions:

$$N_x = \frac{\partial^2 U}{\partial y^2}$$

$$N_y = \frac{\partial^2 U}{\partial x^2} \tag{20}$$

$$T_{xy} = \frac{\partial^2 U}{\partial y \partial x}$$

Then, the problem is completely solved if the function U is determined. Equation (2) verifies the equilibrium conditions; substituting (20) in the compatibility equations we obtain a fourth order differential equation where U and w_0 are the unknowns:

$$a_{22} \frac{\partial^4 U}{\partial x^4} - 2a_{23} \frac{\partial^4 U}{\partial x^3 \partial y} + (2a_{12} + a_{33}) \frac{\partial^4 U}{\partial x^2 \partial y^2} - 2a_{13} \frac{\partial^4 U}{\partial x \partial y^3} + a_{11} \frac{\partial^4 U}{\partial y^4} + b_{21} \frac{\partial^4 w_0}{\partial x^4} + (2b_{23} - b_{31}) \frac{\partial^4 w_0}{\partial x^3 \partial y}$$

$$+ (b_{11} + b_{22} - 2b_{33}) \frac{\partial^4 w_0}{\partial x^2 \partial y^2} + (2b_{13} - b_{32}) \frac{\partial^4 w_0}{\partial x \partial y^3} + b_{12} \frac{\partial^4 w_0}{\partial y^4} = 0 \tag{21}$$

where a_{ij} and b_{ij} are the elements of the $[a]$ and $[b]$ compliance matrices defined in the previous section. Taking into account the geometrical symmetry of the laminate the equations can be reduced. If the laminate stacking sequence is symmetric with respect to the mid-plane, we have:

$$a_{22} \frac{\partial^4 U}{\partial x^4} - 2a_{23} \frac{\partial^4 U}{\partial x^3 \partial y} + (2a_{12} + a_{33}) \frac{\partial^4 U}{\partial x^2 \partial y^2} - 2a_{13} \frac{\partial^4 U}{\partial x \partial y^3} + a_{11} \frac{\partial^4 U}{\partial y^4} = 0 \tag{22}$$

and if the laminate is also balanced, that means for each lamina $\theta°$ oriented there is another lamina $-\theta°$ oriented with the same mechanical characteristics and thickness, the last equation becomes finally:

$$a_{22} \frac{\partial^4 U}{\partial x^4} + (2a_{12} + a_{33}) \frac{\partial^4 U}{\partial x^2 \partial y^2} + a_{11} \frac{\partial^4 U}{\partial y^4} = 0 \tag{23}$$

The solution for (23) is given in the form:

$$U = 2\mathrm{Re}[f_1(z_1) + f_2(z_2)] \tag{24}$$

where $f_1(z_1)$ and $f_2(z_2)$ are two arbitrary complex algebraic functions that have to be chosen in a more convenient way for the problem under investigation. The variables z_1 and z_2 are given as:

$$z_1 = x \pm s_1 y$$

$$z_2 = x \pm s_2 y \tag{25}$$

where $\pm s_1$ and $\pm s_2$ are the four purely imaginary roots of the characteristic equation associated, given as:

$$s_1 = iS_1 = i \sqrt{\frac{(2a_{12} + a_{33}) + \sqrt{(2a_{12} + a_{33})^2 - 4a_{11}a_{22}}}{2a_{11}}}$$

(26)

$$s_2 = iS_2 = i \sqrt{\frac{(2a_{12} + a_{33}) - \sqrt{(2a_{12} + a_{33})^2 - 4a_{11}a_{22}}}{2a_{11}}}$$

S_1 and S_2 take into account the material properties through the compliance elements a_{ij} ($i = \sqrt{-1}$). Once the Airy function is determined, going back to the equilibrium equations it is possible to find the expressions for the displacements:

$$u_0 = 2\text{Re}[(s_1^2 a_{11} + a_{12}) \cdot f_1'(z_1) + (s_2^2 a_{11} + a_{12}) \cdot f_2'(z_2)] + u_0^* - \omega y$$

(27)

$$v_0 = 2\text{Re}\left[\left(\frac{a_{22}}{s_1} + s_1 a_{12}\right) \cdot f_1'(z_1) + \left(\frac{a_{22}}{s_2} + s_2 a_{12}\right) \cdot f_2'(z_2)\right] + v_0^* + \omega y$$

(28)

and stress components in the mid-plane:

$$N_x = 2\text{Re}[s_1^2 f_1''(z_1) + s_2^2 f_2''(z_2)]$$

$$N_y = 2\text{Re}[f_1''(z_1) + f_2''(z_2)]$$

(29)

$$T_{xy} = -2\text{Re}[s_1 f_1''(z_1) + s_2 f_2''(z_2)]$$

where u_0^*, v_0^* and ω describe the rigid body modes in the xy plane. These terms disappear if sufficient boundary conditions are applied.

To solve completely the problem of the determination of the Airy's function it is now necessary to choose the $f(z)$ functions and apply the boundary condition for the geometry under investigation.

2.3 Circular, elliptical hole and sharp crack in an infinite plate

Let us now consider a composite plate that extends infinitely in both direction x and y. Let us say that the composite is also symmetric and balanced and that it is subjected to the remote loads N_{0x} and N_{0y} along the x and y direction respectively. That means

$$M_x = M_y = M_{xy} = T_{xz} = T_{yz} = w_0 = p \equiv 0$$

(30)

In addition, all the rigid body modes must be constrained. Sampath and Hulbert[4] using a truncated modified Laurent series, suggest for the functions $f(z)$ the following expressions:

$$f_1(z_1) = A' + A_0 \ln \zeta_1 + \Sigma_{k=1}^{N}[A_k \zeta_1^k + A_{-k} \zeta_1^{-k}]$$

(31)

$$f_2(z_2) = B' + B_0 \ln \zeta_2 + \Sigma_{k=1}^{N}[B_k \zeta_2^k + B_{-k} \zeta_2^{-k}]$$

(32)

where A_i and B_i are complex coefficients and ζ_1 and ζ_2 are functions of z_1 and z_2. The form of the mapping functions ζ is determined by the geometry of the problem.

Let us consider a circular hole, of given radius a, in the laminate so that its centre is in the origin of the xy reference frame (Fig. 4). The mapping functions for the first quadrant can be given as:

$$\zeta_1 = z_1 + \sqrt{z_1^2 - a^2 \cdot (1 + s_1^2)}$$

(33)

$$\zeta_2 = z_2 + \sqrt{z_2^2 - a^2 \cdot (1 + s_2^2)}$$

(34)

and we can pose:

$$\zeta_1^{-1} = z_1 - \sqrt{z_1^2 - a^2 \cdot (1 + s_1^2)}$$

(35)

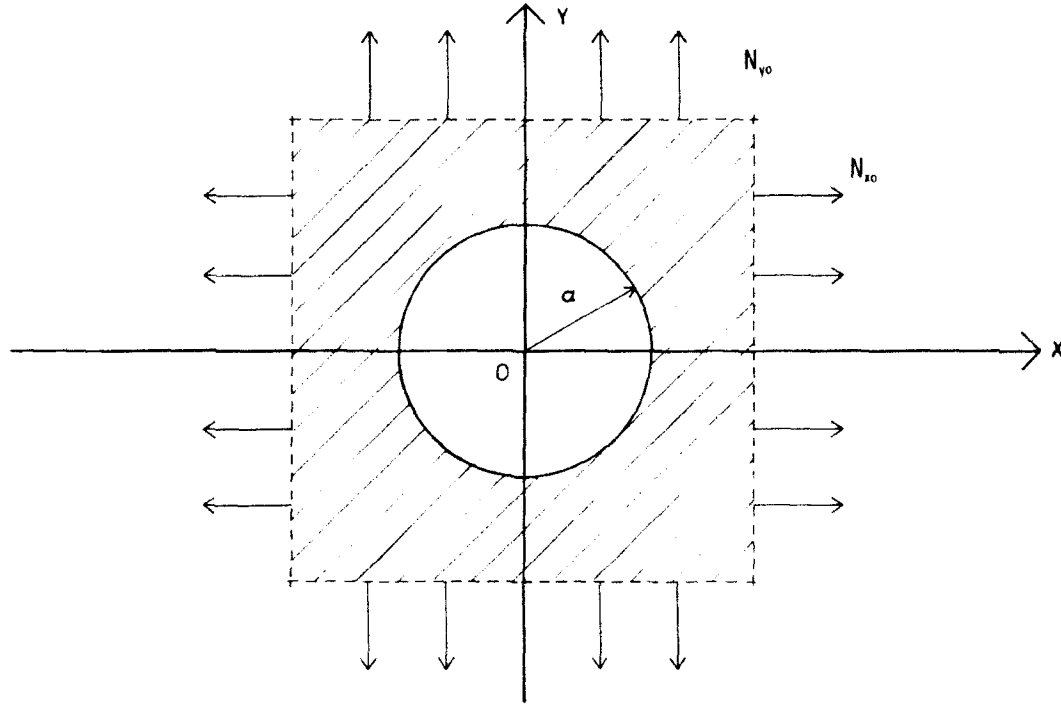$$\zeta_2^{-1} = z_2 - \sqrt{z_2^2 - a^2 \cdot (1 + s_2^2)}$$

(36)

Fig. 4. Plate with circular hole.

where the real constants $[a^2(1 + s_1^2)]^{-k}$ and $[a^2(1 + s_2^2)]^{-k}$ are already included in the complex constants A_{-k} and B_{-k} respectively.

The functions $f(z)$ are determined if $(4N + 4)$ coefficients of the series are known. The determination of these coefficients has been already proposed by Sampath and Hulbert. They suggest expanding the series up to the seventh term and then applying boundary conditions at a hundred points at least. This method requires, of course, a dedicated code and heavy numerical calculation even in very simple and common geometries, such as circular holes. The problem of determination of the stress–strain field around simple geometries has been treated also by Zhang and others.[7-10]

Here a closed form solution is proposed. We suggest a modified expression for the $f(z)$ functions that take into account the stress–strain field far away from the hole:

$$f_1(z_1) = A' + A_0 \ln \zeta_1 + \Sigma_{k=1}^{N} [A_k \zeta_1^k + A_{-k} \zeta_1^{-k}] + \frac{1}{4} \cdot \frac{N_{x0} - s_2^2 N_{y0}}{s_1^2 - s_2^2} \cdot z_1^2 \tag{37}$$

$$f_2(z_2) = B' + B_0 \ln \zeta_2 + \Sigma_{k=1}^{N} [B_k \zeta_2^k + B_{-k} \zeta_2^{-k}] + \frac{1}{4} \cdot \frac{N_{x0} - s_1^2 N_{y0}}{s_2^2 - s_1^2} \cdot z_2^2 \tag{38}$$

It can be demonstrated (see the Appendix) that, in our case, all the coefficients of the series disappear except the real parts of A_{-2} and B_{-2}.

For the sake of brevity we pose:

$$g_1(z_1) = \sqrt{z_1^2 - a^2 + \phi^2}$$

$$g_2(z_2) = \sqrt{z_2^2 - a^2 + \psi^2}$$

So, substituting in (29), the resultant forces around a circular hole (Fig. 5) in an infinite plate under in-plane loads are given by:

$$N_x = N_{x0} - \mathrm{Re} \left[\frac{a^2(1 + S_1) \cdot (N_{x0} - S_2 N_{y0}) \cdot S_1^2}{(S_1 - S_2) \cdot g_1(z_1) \cdot [z_1 + g_1(z_1)]} + \frac{a^2(1 + S_2) \cdot (S_1 N_{y0} N_{x0}) \cdot S_2^2}{(S_1 - S_2) \cdot g_2(z_2) \cdot [z_2 + g_2(z_2)]} \right] \tag{39}$$

$$N_x = N_{x0} + \mathrm{Re}\left[\frac{a^2(1+S_1)\cdot(N_{x0}-S_2 N_{y0})}{(S_1-S_2)\cdot g_1(z_1)\cdot[z_1+g_1(z_1)]} + \frac{a^2(1+S_2)\cdot(S_1 N_{y0}-N_{x0})}{(S_1-S_2)\cdot g_2(z_2)\cdot[z_2+g_2(z_2)]}\right] \tag{40}$$

$$T_{xy} = -\mathrm{Re}\left[\frac{i\cdot S_1\cdot a^2(1+S_1)\cdot(N_{x0}-S_2 N_{y0})}{(S_1-S_2)\cdot g_1(z_1)\cdot[z_1+g_1(z_1)]} + \frac{i\cdot S_2\cdot a^2(1+S_2)\cdot(S_1 N_{y0}-N_{x0})}{(S_1-S_2)\cdot g_2(z_2)\cdot[z_2+g_2(z_2)]}\right] \tag{41}$$

where $\phi = a^2 S_1^2$ and $\psi = a^2 S_3^2$.
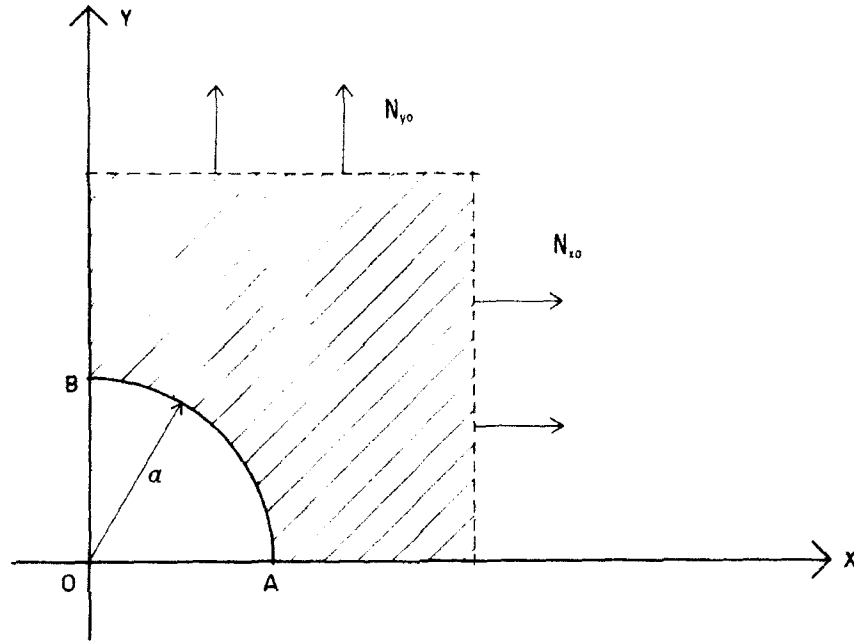

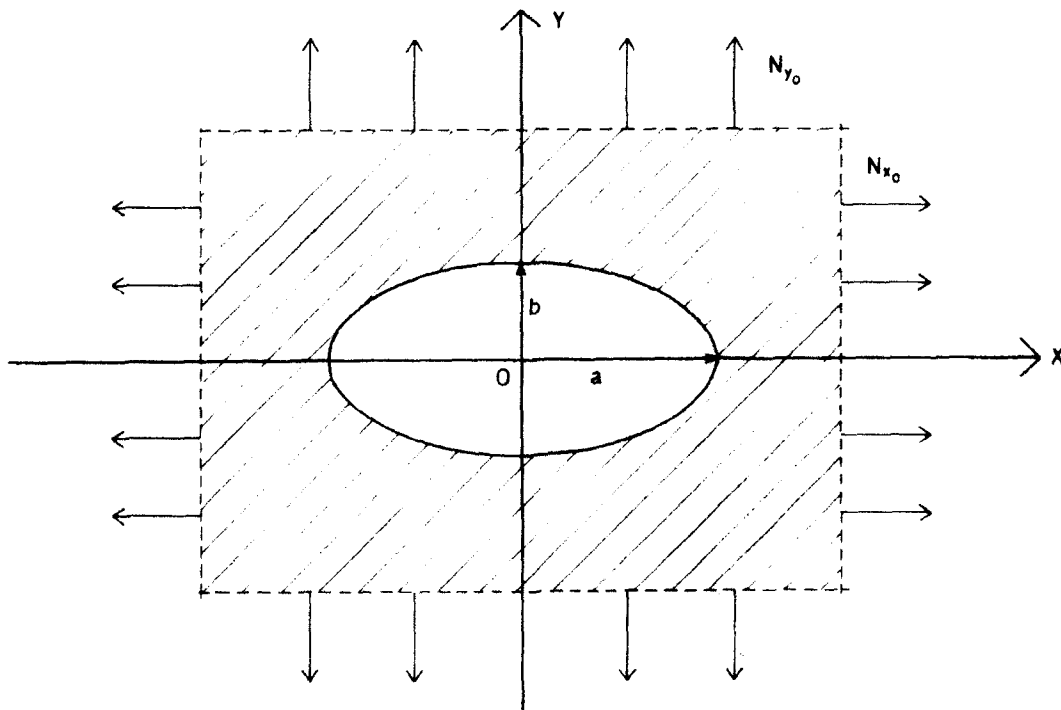Fig. 5.   Circular hole notation.

Fig. 6.   Plate with elliptical hole.

In the same way the stress field around an elliptical hole (Fig. 6) of given semi-axes a, along the x direction, and b, along the y direction, can be found:

$$N_x = N_{x0} - \text{Re}\left[\frac{S_1^2 \cdot (a + S_1 b) \cdot (bN_{x0} - aS_2 N_{y0})}{(S_1 - S_2) \cdot g_1(z_1) \cdot [z_1 + g_1(z_1)]} + \frac{S_2^2 \cdot (a + S_2 b) \cdot (aS_1 N_{y0} - bN_{x0})}{(S_1 - S_2) \cdot g_2(z_2) \cdot [z_2 + g_2(z_2)]}\right] \tag{42}$$

$$N_y = N_{y0} + \text{Re}\left[\frac{(a + S_1 b) \cdot (bN_{x0} - aS_2 N_{y0})}{(S_1 - S_2) \cdot g_1(z_1) \cdot [z_1 + g_1(z_1)]} + \frac{(a + S_2 b) \cdot (aS_1 N_{y0} - bN_{x0})}{(S_1 - S_2) \cdot g_2(z_2) \cdot [z_2 + g_2(z_2)]}\right] \tag{43}$$

$$T_{xy} = -\text{Re}\left[\frac{i \cdot S_1 \cdot (a + S_1 b) \cdot (bN_{x0} - aS_2 N_{y0})}{(S_1 - S_2) \cdot g_1(z_1) \cdot [z_1 + g_1(z_1)]} + \frac{i \cdot S_2 \cdot (a + S_2 b) \cdot (aS_1 N_{y0} - bN_{x0})}{(S_1 - S_2) \cdot g_2(z_2) \cdot [z_2 + g_2(z_2)]}\right] \tag{44}$$

where $\phi = b^2 S_1^2$ and $\psi = b^2 S_2^2$.

It is worth noting that if the plate is loaded only in the y direction, in correspondence with $A \equiv (a; 0)$ (Fig. 7) the intensification factor is:

$$\frac{N_y(a;0)}{N_{y0}} = 1 + \frac{a}{b} \cdot \frac{S_1 + S_2}{S_1 \cdot S_2} \tag{45}$$

that for $a = b$ (circular hole) and for $S_1 = S_2 = 1$ (isotropic material) eqn (44) gives the well known value of 3 [compare with (4)].

Using the expressions found for the elliptical hole, the stress field for a sharp crack (Fig. 8) can be easily determined just making the limit for $b \to 0$. Then follows:

$$N_x = N_{x0} + \text{Re}\left[\frac{S_1^2 \cdot a^2 S_2 N_{y0}}{(S_1 - S_2) \cdot g_1(z_1) \cdot [z_1 + g_1(z_1)]} - \frac{S_2^2 \cdot a^2 S_1 N_{y0}}{(S_1 - S_2) \cdot g_2(z_2) \cdot [z_2 + g_2(z_2)]}\right] \tag{46}$$

$$N_y = N_{y0} - \text{Re}\left[\frac{a^2 S_2 N_{y0}}{(S_1 - S_2) \cdot g_1(z_1) \cdot [z_1 + g_1(z_1)]} - \frac{a^2 S_1 N_{y0}}{(S_1 - S_2) \cdot g_2(z_2) \cdot [z_2 + g_2(z_2)]}\right] \tag{47}$$
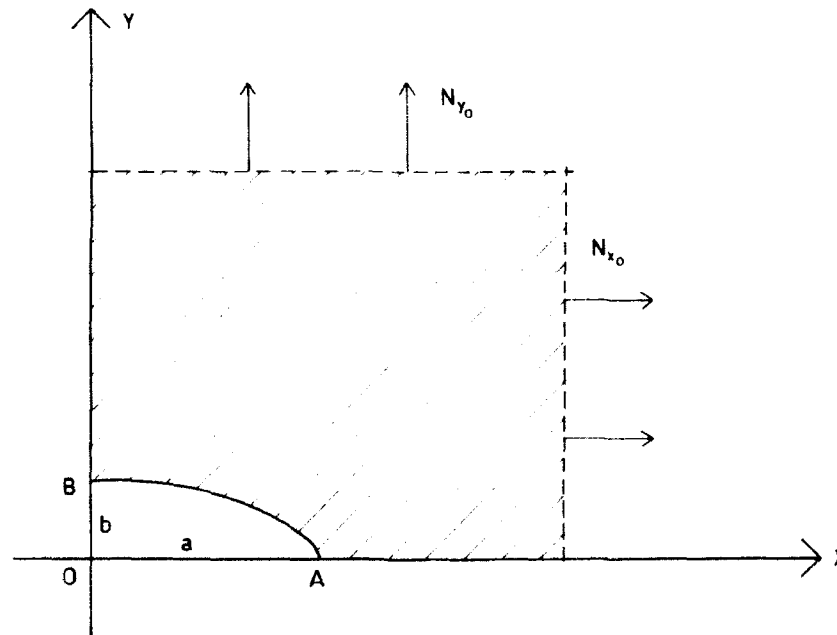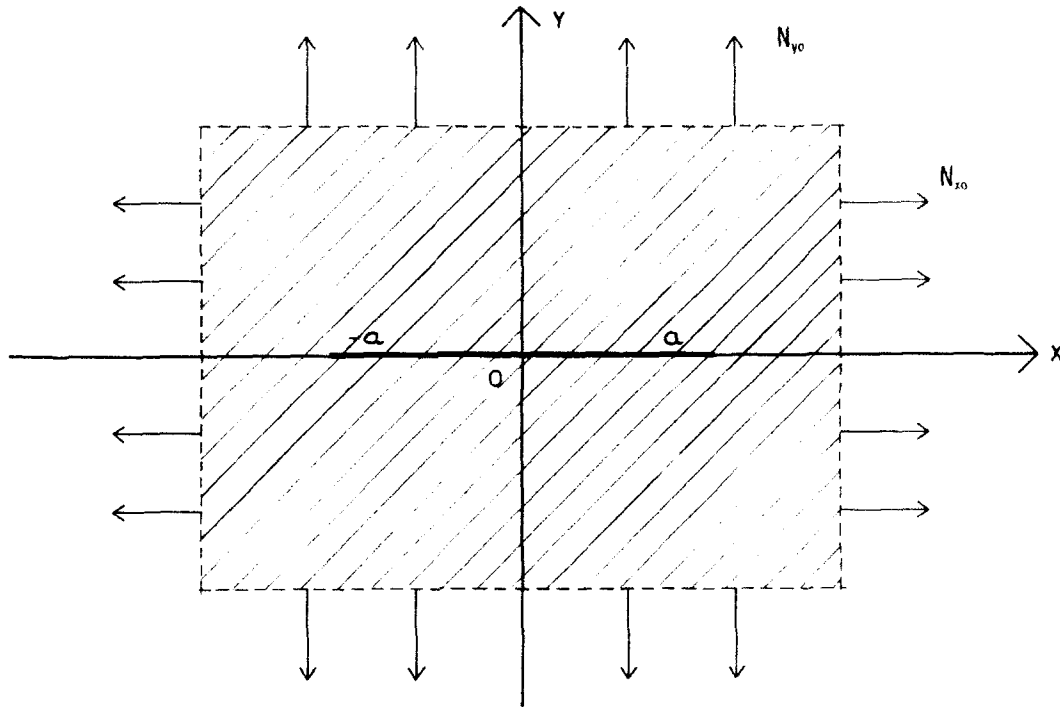

Fig. 7. Elliptical hole notation.

Fig. 8. Plate with sharp crack.

$$N_{xy} = + \mathrm{Re}\left[\frac{a^2 S_1 S_2 N_{y0}}{(S_1 - S_2) \cdot g_1(z_1) \cdot [z_1 + g_1(z_1)]} - i\,\frac{a^2 S_2 S_1 N_{y0}}{(S_1 - S_2) \cdot g_2(z_2) \cdot [z_2 + g_2(z_2)]}\right] \tag{48}$$

where $\phi = \psi = 0$ and $2a$ is the crack length. It is important to note that in the expression above the load N_{x0} does not appear in the stress intensification terms. That means that no intensification occurs if a panel with a central crack is loaded only along the crack direction.

3 COMPARISON BETWEEN THEORETICAL AND FEM RESULTS

To check the validity of the expressions found, the theoretical stress field was compared with finite element calculations for the three different cases described above. As a first test case, a strongly orthotropic plate with a central flaw was simulated. Only a quarter of the plate was modelled for sake of symmetry. In Figs 9–11 are reported the models used. In the calculation plane stress conditions were assumed and an isoparametric eight node, fully integrated element was employed. The material chosen was an unidirectional CFRP Epoxy Matrix composite, with 60% of fibre volume content. The values of the material properties are summarized in Table 1.

The plate thickness was always kept equal to 1 mm, the remote load applied in the y direction

was of 100 MPa in all cases; no remote load in the x direction was applied. To avoid size effect due to the finite plate dimension, the characteristic flaw dimension was chosen $\frac{1}{20}$ of the plate width, that means $a = 1$ mm for the sharp crack, $r = 1$ mm for the circular hole and $a = 1$ mm and $b = 0.5$ for the elliptical hole. For the plate with a circular hole, Fig. 12 shows the comparison between σ_x and σ_y along the x axis ($\theta = 0$) where the strongest stress intensification is expected. A very good agreement between the theory and the FEM analysis was found for each value of θ as also shown in Fig. 13 for the same components of stress along the y axis, i.e. at $\theta = 90°$. It is worth noting here that the stress intensification factor is equal to 2.5 instead of 3 as in the isotropic material. That can be easily explained taking into account the plate principal direction orientation: E_{22} concordant with the y axis. In Figs 14–17 are reported the
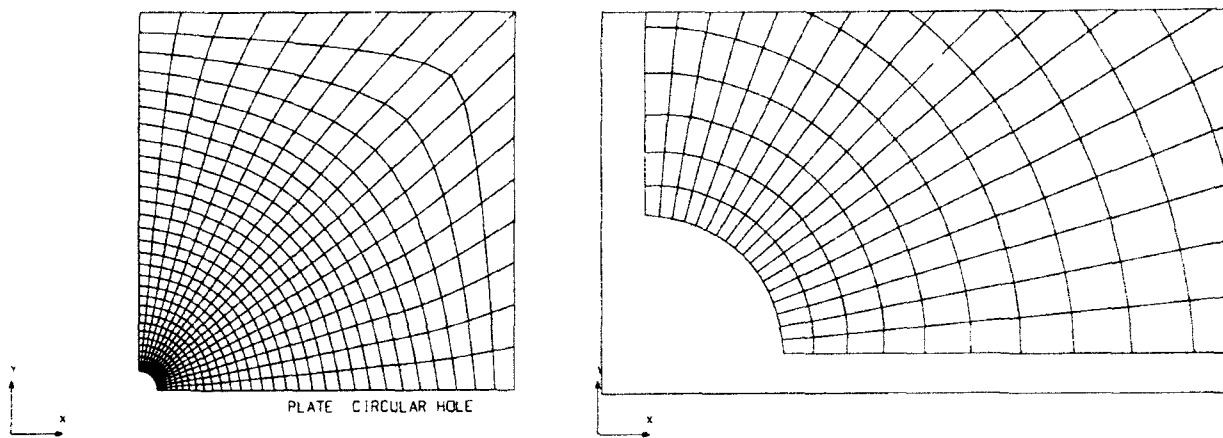
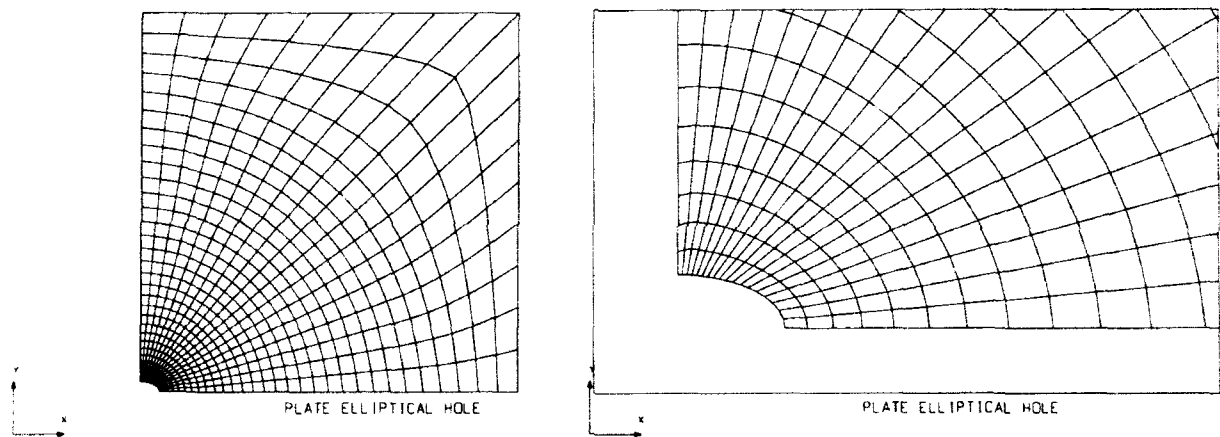**Fig. 9.** Circular hole FEM model and hole close up.

Fig. 10. Elliptical hole FEM model and hole close up.
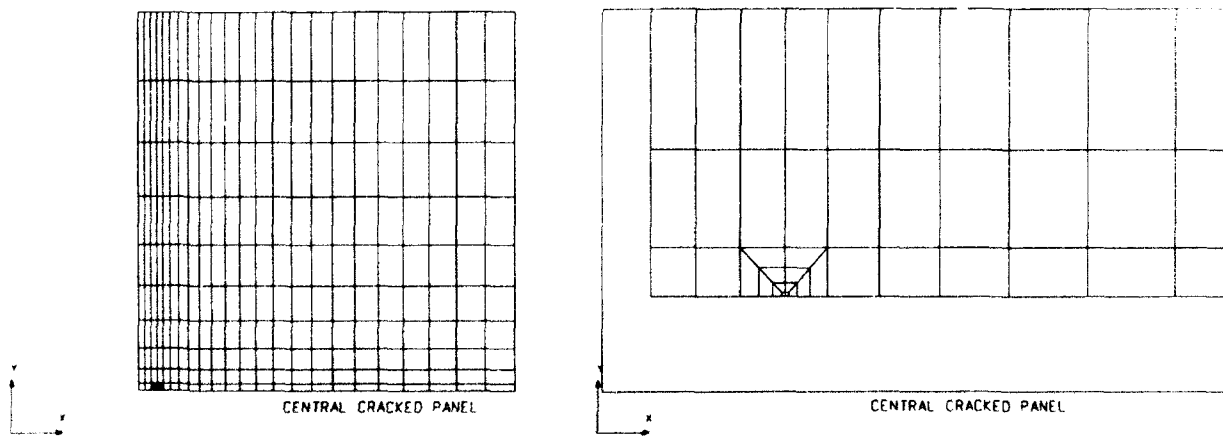
Fig. 11. Sharp crack FEM model and notch refinement.

Table 1. Orthotropic material properties

E_{11} (MPa)	E_{22} (MPa)	G_{12} (MPa)	ν_{12}	ν_{21}
130 000	6 900	4 480	0·27	0·0143
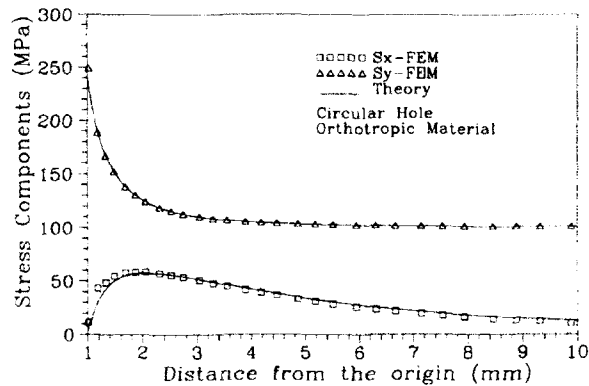
Fig. 12. Circular hole: stress components along the x axis in orthotropic material.
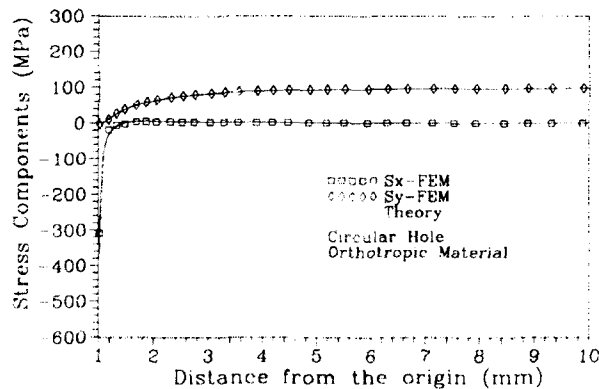
Fig. 13. Circular hole: stress components along the y axis in orthotropic material.
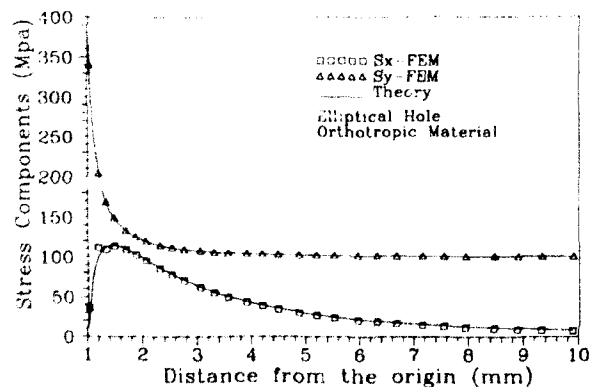
Fig. 14. Elliptical hole: stress components along the x axis in orthotropic material.

Fig. 15. Elliptical hole: stress components along the y axis in orthotropic material.

Fig. 16. Sharp crack: stress components along the x axis in orthotropic material.

Fig. 17. Sharp crack: stress components along the y axis in orthotropic material.

same comparison for the elliptical and sharp crack along the x and y axes respectively. The agreement is always well verified in all cases.

Then, the theory was applied to a symmetric and balanced composite laminate with the following stacking sequence: $[0,90,0,90]_s$; the layer thickness was 0·125 mm to have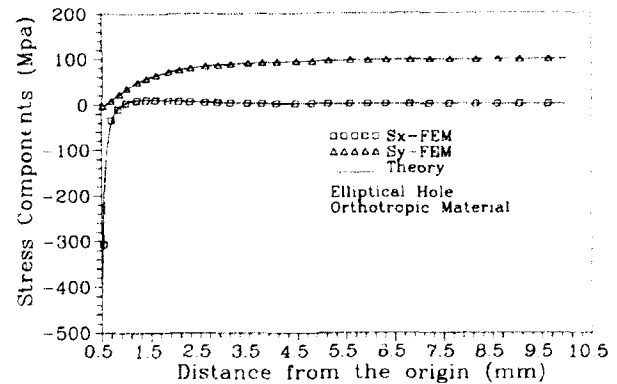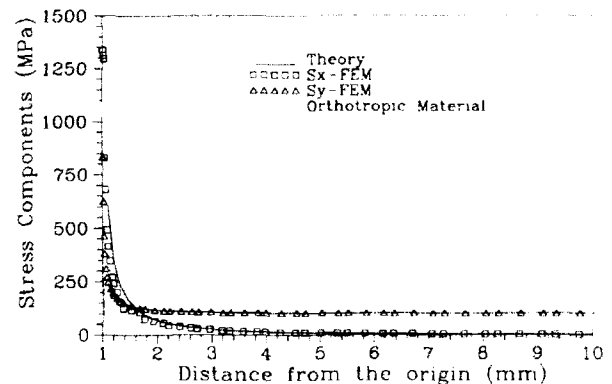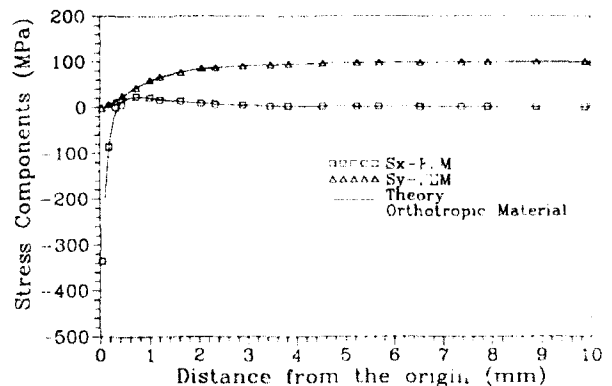 a total laminate thickness of 1 mm as in the orthotropic case. The laminate material is the same as the orthotropic case, the overall laminate properties are reported in Table 2.

The finite element calculation was performed using a three dimensional thin plate, multi-layer element with four nodes. In Figs 18–33 the comparison between the theoretical model (continuous line), and the FE results (dots) for the circular and the elliptical hole, along the x and y axes, is depicted. In every case the agreement between theory and numerical approach is very good. Some differences can be found in comparison on the calculus of the σ_{xx} stress component in the case of the elliptical hole. These discrepancies become more evident the more the free edge of the hole is approached. The differences and the limits of finite element calculations with respect to the theory are also given in evidence in Figs 34

and 35 where comparison of the shear τ_{xy} stress, in the function of the angle θ is given. In fact, even though the shear component is very well calculated by FEM far from any free edges (Fig.
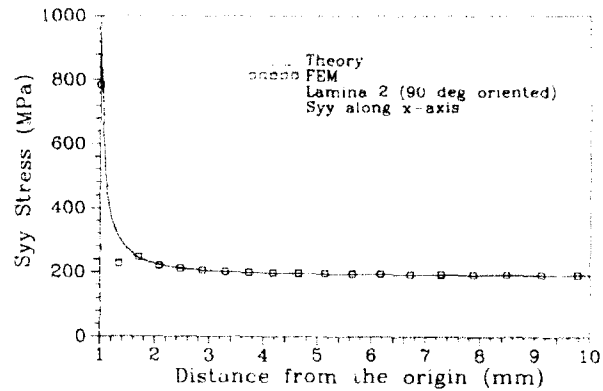
Fig. 19. Circular hole: σ_{yy} stress component along the x axis in composite laminate (lamina 2, 90° oriented).

Table 2. Composite laminate material properties (8 layers $[0,90,0,90]_s$)

In-plane constants				
E_{11} (GPa)	E_{22} (GPa)	G_{12} (GPa)	v_{12}	v_{21}
68·665	68·665	4·480	0·0272	0·0272

Flexural constants				
E_{11f} (GPa)	E_{22f} (GPa)	G_{12f} (GPa)	v_{12f}	v_{21f}
91·810	45·507	4·480	0·0411	0·0204

Fig. 20. Circular hole: σ_{xx} stress component along the y axis in composite laminate (lamina 2, 90° oriented).
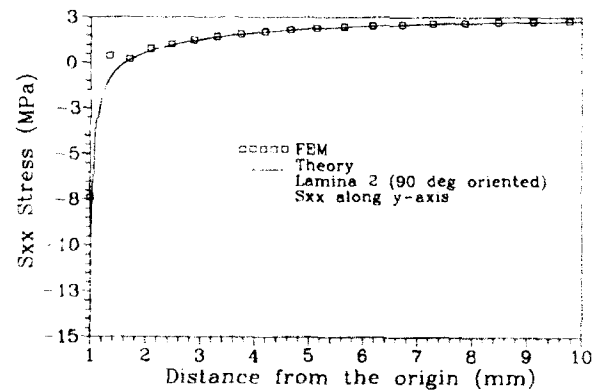
Fig. 18. Circular hole: σ_{xx} stress component along the x axis in composite laminate (lamina 2, 90° oriented).
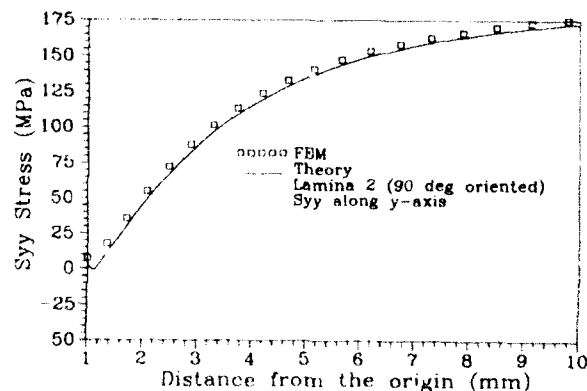
Fig. 21. Circular hole: σ_{yy} stress component along the y axis in composite laminate (lamina 2, 90° oriented).
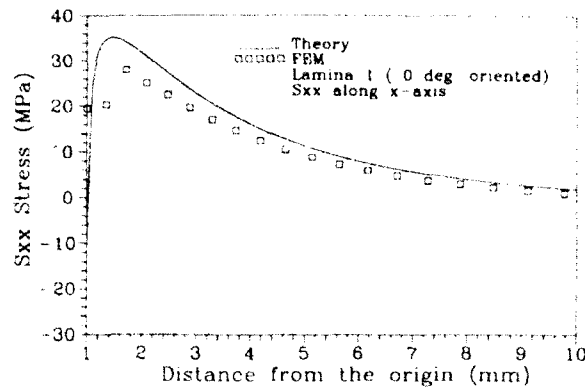
Fig. 22. Circular hole: σ_{xx} stress component along the x axis in composite laminate (lamina 1, 0° oriented).
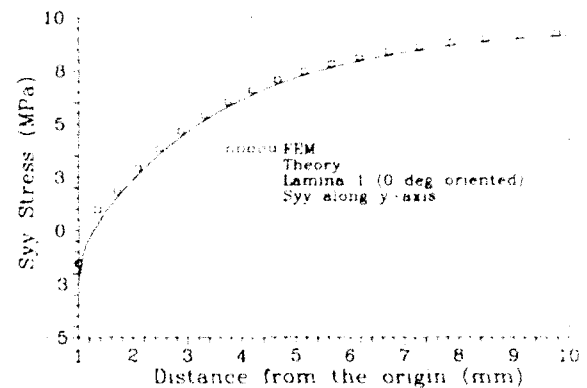
Fig. 25. Circular hole: σ_{yy} stress component along the y axis in composite laminate (lamina 1, 0° oriented).
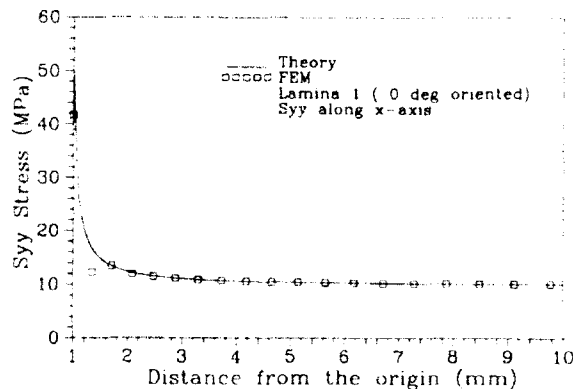
Fig. 23. Circular hole: σ_{yy} stress component along the x axis in composite laminate (lamina 1, 0° oriented).
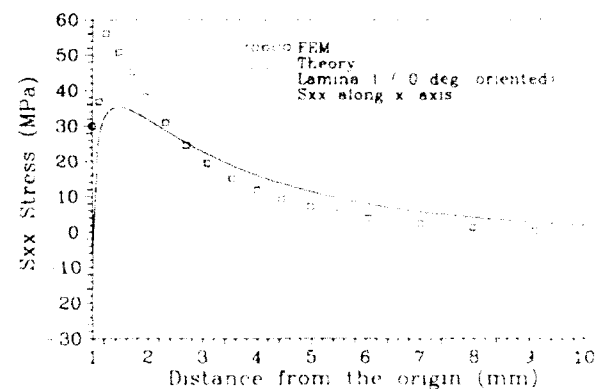
Fig. 26. Elliptical hole: σ_{xx} stress component along the x axis in composite laminate (lamina 1, 0 oriented)
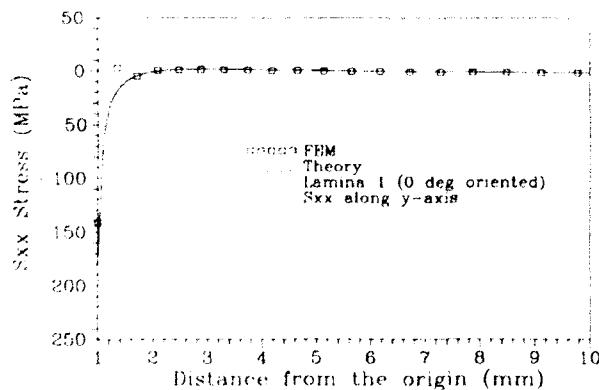
Fig. 24. Circular hole: σ_{xx} stress component along the y axis in composite laminate (lamina 1, 0° oriented).
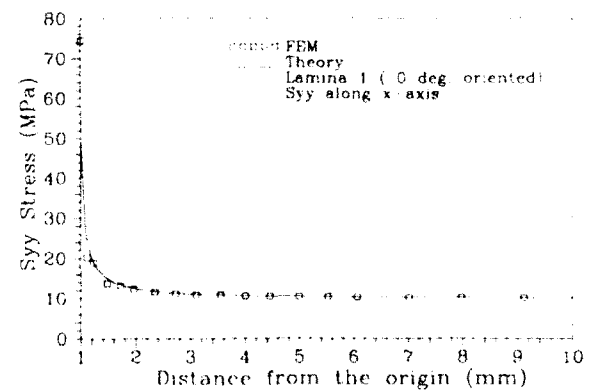
Fig. 27. Elliptical hole: σ_{yy} stress component along the x axis in composite laminate (lamina 1, 0 oriented).

34), the computation becomes more and more inaccurate approaching the body boundaries (Fig. 35). This limit is inner to the FE formulation for problems where composite materials are involved, a more accurate solution requires either an elevated order of the shape functions or a 3-D model with a very large number of degrees of freedom.
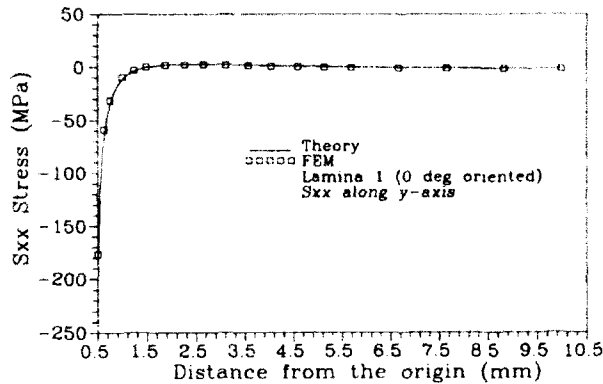
Fig. 28. Elliptical hole: σ_{xx} stress component along the y axis in composite laminate (lamina 1, $0°$ oriented).
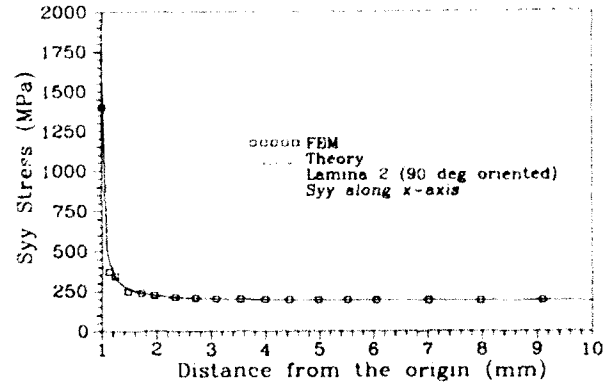
Fig. 31. Elliptical hole: σ_{yy} stress component along the x axis in composite laminate (lamina 2, $90°$ oriented).
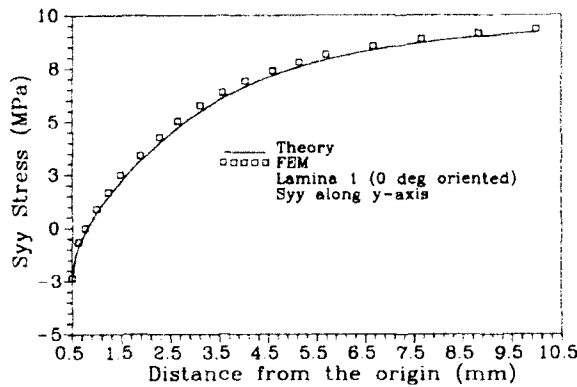
Fig. 29. Elliptical hole: σ_{yy} stress component along the y axis in composite laminate (lamina 1, $0°$ oriented).
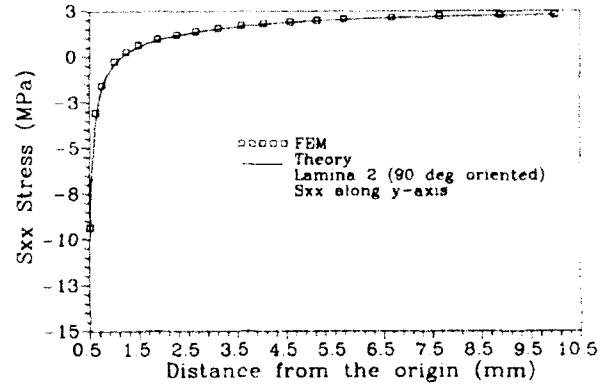
Fig. 32. Elliptical hole: σ_{xx} stress component along the y axis in composite laminate (lamina 2, $90°$ oriented).
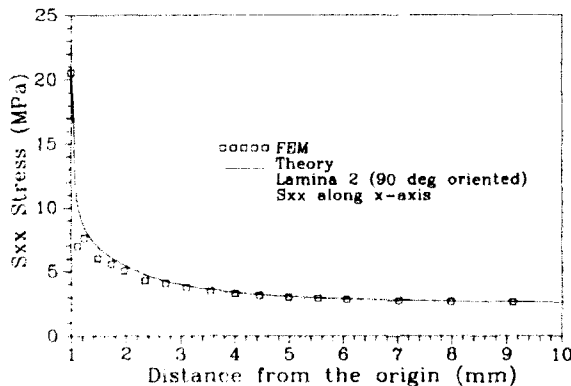
Fig. 30. Elliptical hole: σ_{xx} stress component along the x axis in composite laminate (lamina 2, $90°$ oriented).
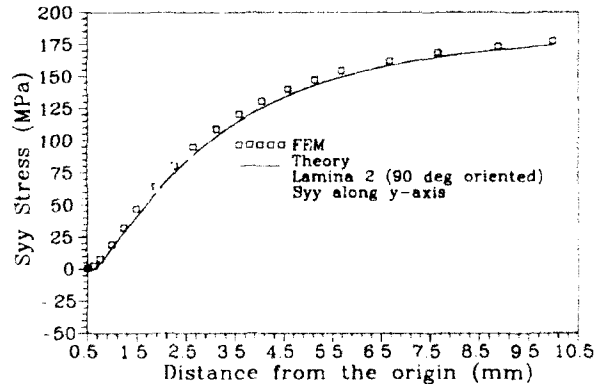
Fig. 33. Elliptical hole: σ_{yy} stress component along the y axis in composite laminate (lamina 2, $90°$ oriented).

4 CONCLUSIONS

An alternative analytical expression for the Airy's function has been proposed to determine the stress-field intensification around simple hole geometries. The analytical solution for the stress–strain field, in a closed form, was found for sharp crack, circular and elliptical hole. Extended finite element analyses have been performed to evaluate the accuracy and consistency of the
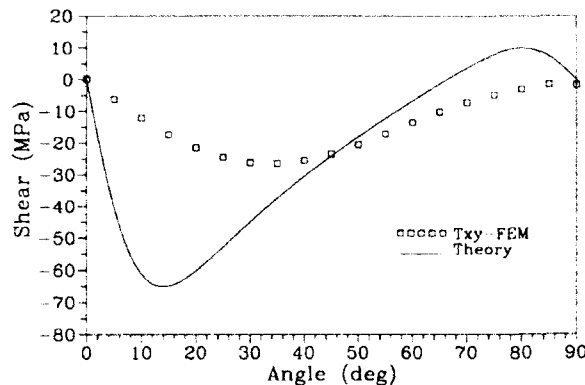
Fig. 34. Circular hole: τ_{xy} shear stress along the hole free edge in composite laminate.
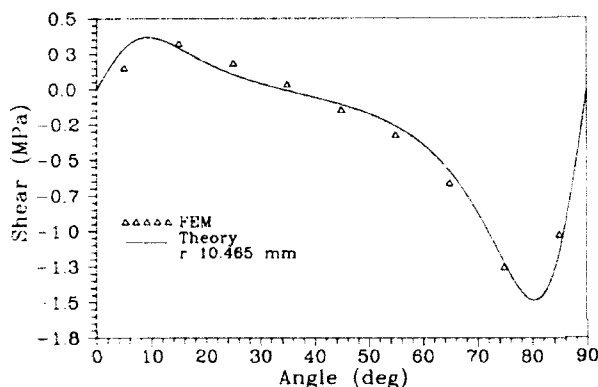
Fig. 35. Circular hole: τ_{xy} shear stress at distance $r = 10.465$ mm in composite laminate.

model proposed. A very good agreement has been found for a strongly orthotropic material and for a composite laminate, too.

The expressions found, even if they seem to be complex, can be easily plotted, for any angle or distance from the hole, just inferring the compli-

ance coefficients of the material under investigation. The model proposed highlighted the limits, difficulties and heavy computational costs necessary to solve accurately by FEM, also simple problems that involve composite materials.

ACKNOWLEDGEMENTS

REFERENCES

1. Savin, G. N., *Stress Concentration Around Holes* (translated from Russian). International Series of Monographs in Aeronautics and Astronautics. Pergamon Press, Oxford, 1961.
2. Muskhelishvili, N. I., An investigation of new integral equations in the plane theory of elasticity. *Dokl. Akad. Nauk. USSR*, **III** (2) (1934) 73.
3. Lekhnitskiy, S. G., *Anisotropic Plates* (translated from Russian). Gordon and Breach, New York, 1968.
4. Sampath, S. G. & Hulbert, L. E., Analysis of multiholed orthotropic laminated plates by the boundary-point-least-square method. *Transactions ASME* (May 1975).
5. AGARD, *Conference Proceedings No. 427: Behaviour and Analysis of Mechanically Fastened Joints in Composite Structures*. NATO.
6. Calcote, L. R., *The Analysis of Laminated Composite Structures*. Van Nostrand Reinhold, New York, 1969.
7. Kai-Da Zhang, & Ueng, C. E. S., Stresses around a pin-loaded hole in orthotropic plates with arbitrary loading direction. *Composite Structures*, **3** (2) (1985) 119–43.
8. Mangalgiri, P. D. & Dattaguru, B., A large orthotropic plate with misfit pin under arbitrarily oriented biaxial loading. *Composite Structures*, **6** (4) (1986) 271–81.
9. Jia-Keng Lin & Ueng, C. E. S., Stresses in a laminated composite with two elliptical holes. *Composite Structures*, **7** (1) (1987) 1–20.
10. Wei-Xun Fan & Jian-Guo Wu, Stress concentration of a laminate weakened by multiple holes. *Composite Structures*, **10** (4) (1988) 303–19.

APPENDIX

Our problem is completely solved if the following functions:

$$f_1(z_1) = A' + A_0 \ln \zeta_1 + \Sigma_{k=1}^{N}[A_k \zeta_1^k + A_{-k} \zeta_1^{-k}]$$

$$f_2(z_2) = B' + B_0 \ln \zeta_2 + \Sigma_{k=1}^{N}[B_k \zeta_2^k + B_{-k} \zeta_2^{-k}]$$

are known, i.e. the complex constants A_0, B_0, A_k, A_{-k} and B_{-k} are known. In general these coefficients can be found by some numerical method, by choosing an appropriate value for k. But in our case, they can be found with some simple considerations: all terms where $k > 2$ must go to zero because their second order derivatives are divergent to infinity and that would imply that stresses diverge too. As a consequence of this we have:

$$f_1(z_1) = A' + A_0 \ln [z_1 + \sqrt{z_1^2 - a^2 \cdot (1 + s_1^2)}] + \Sigma_{k=1}^2 \{A_k [z_1 + \sqrt{z_1^2 - a^2 \cdot (1 + s_1^2)}]^k$$

$$+ A_{-k} [z_1 - \sqrt{z_1^2 - a^2 \cdot (1 - s_1^2)}]^k\} + \frac{1}{4} \cdot \frac{N_{xo} - s_2^2 N_{yo}}{s_1^2 - s_2^2} \cdot z_1^2$$

$$f_2(z_2) = B' + B_0 \ln [z_2 + \sqrt{z_2^2 - a^2 \cdot (1 + s_2^2)}] + \Sigma_{k=1}^N \{B_k [z_2 + \sqrt{z_2^2 - a^2 \cdot (1 + s_2^2)}]^k$$

$$+ B_{-k} [z_2 - \sqrt{z_2^2 - a^2 \cdot (1 + s_2^2)}]^k\} + \frac{1}{4} \cdot \frac{N_{yo} - s_1^2 N_{xo}}{s_2^2 - s_1^2} \cdot z_2^2$$

Furthermore, the displacement field does not diverge to infinity when x and $y \to \infty$ if the coefficients are chosen in the form:

$$A_2 = B_2 = 0$$
$$A_0 = 2a^2(1 + s_1^2)A_{-2}$$
$$B_0 = 2a^2(1 + s_2^2)B_{-2}$$
$$A_{-2} \neq 0$$
$$B_{-2} \neq 0$$

The $f(z)'$ functions become:

$$f_1'(z_1) = A_1 \frac{z_1 + \sqrt{z_1^2 - a^2 \cdot (1 + s_1^2)}}{\sqrt{z_1^2 - a^2 \cdot (1 + s_1^2)}} - A_{-1} \frac{z_1 - \sqrt{z_1^2 - a^2 \cdot (1 + s_1^2)}}{\sqrt{z_1^2 - a^2 \cdot (1 + s_1^2)}}$$

$$+ 4A_{-2} [z_1 - \sqrt{z_1^2 - a^2 \cdot (1 + s_1^2)}] + \frac{1}{2} \cdot \frac{N_{xo} - s_2^2 N_{yo}}{s_1^2 - s_2^2} \cdot z_1$$

$$f_2'(z_2) = B_1 \frac{z_2 + \sqrt{z_2^2 - a^2 \cdot (1 + s_2^2)}}{\sqrt{z_2^2 - a^2 \cdot (1 + s_2^2)}} - B_{-1} \frac{z_2 - \sqrt{z_2^2 - a^2 \cdot (1 + s_2^2)}}{\sqrt{z_2^2 - a^2 \cdot (1 + s_2^2)}}$$

$$+ 4B_{-2} [z_2 - \sqrt{z_2^2 - a^2 \cdot (1 + s_2^2)}] + \frac{1}{2} \cdot \frac{N_{yo} - s_1^2 N_{xo}}{s_2^2 - s_1^2} \cdot z_2$$

In addition the symmetry conditions are given by

$$v_0 = 0 \qquad \forall(x, 0)$$
$$u_0 = 0 \qquad \forall(0, y)$$

Symmetry conditions can be verified only if the coefficients A_1, A_{-1}, B_1, B_{-1} and the imaginary part of A_{-2}, B_{-2} are equal to zero. According to this we have:

$$f_1'(z_1) = 4A_{-2} [z_1 - \sqrt{z_1^2 - a^2 \cdot (1 + s_1^2)}] + \frac{1}{2} \cdot \frac{N_{xo} - s_2^2 N_{yo}}{s_1^2 - s_2^2} \cdot z_1$$

$$f_2'(z_2) = 4B_{-2} [z_2 - \sqrt{z_2^2 - a^2 \cdot (1 + s_2^2)}] + \frac{1}{2} \cdot \frac{N_{yo} - s_1^2 N_{xo}}{s_2^2 - s_1^2} \cdot z_2$$

Differentiating again with respect to z we have:

$$f_1''(z_1) = -4A_{-2} \frac{a^2 \cdot (1 + s_1^2)}{\sqrt{z_1^2 - a^2 \cdot (1 + s_1^2)} \cdot [z_1 + \sqrt{z_1^2 - a^2 \cdot (1 + s_1^2)}]} + \frac{1}{2} \cdot \frac{N_{xo} - s_2^2 N_{yo}}{s_1^2 - s_2^2}$$

$$f_2''(z_2) = -4B_{-2} \frac{a^2 \cdot (1 + s_2^2)}{\sqrt{z_2^2 - a^2 \cdot (1 + s_2^2)} \cdot [z_2 + \sqrt{z_2^2 - a^2 \cdot (1 + s_2^2)}]} + \frac{1}{2} \cdot \frac{N_{yo} - s_1^2 N_{xo}}{s_2^2 - s_1^2}$$

Substituting s_1 and s_2 with iS_1 and iS_2 gives:

$$f_1''(z_1) = -4A_{-2} \frac{a^2 \cdot (1 - S_1^2)}{\sqrt{z_1^2 - a^2 + a^2 S_1^2} \cdot [z_1 + \sqrt{z_1^2 - a^2 + a^2 S_1^2}]} + \frac{1}{2} \cdot \frac{N_{xo} + S_2^2 N_{xo}}{S_2^2 - S_1^2}$$

$$f_2''(z_2) = -4B_{-2} \frac{a^2 \cdot (1 - S_2^2)}{\sqrt{z_2^2 - a^2 + a^2 S_2^2} \cdot [z_2 + \sqrt{z_2^2 - a^2 + a^2 S_2^2}]} + \frac{1}{2} \cdot \frac{N_{xo} + S_1^2 N_{xo}}{S_1^2 - S_2^2}$$

where the two coefficients A_{-2}, B_{-2} can be determined imposing the boundary conditions. In the case of a circular hole (Fig. 5):

$$A \equiv (a; 0) \to N_x = T_{xy} = 0$$

$$B \equiv (0; a) \to N_y = T_{xy} = 0$$

hence

$$N_x(a; 0) = N_{xo} + 8A_{-2} \cdot S_1 \cdot (1 - S_1) + 8B_{-2} \cdot S_2 \cdot (1 - S_2) = 0$$

$$N_y(0; a) = N_{yo} + 8A_{-2} \cdot (1 - S_1) + 8B_{-2} \cdot (1 - S_2) = 0$$

and solving the above equations gives (conditions on T_{xy} are automatically satisfied):

$$A_{-2} = \frac{S_2 \cdot N_{yo} - N_{xo}}{8(S_1 - S_2)(1 - S_1)}$$

$$B_{-2} = \frac{N_{xo} - S_1 \cdot N_{yo}}{8(S_1 - S_2)(1 - S_2)}$$

Finally the expressions for the derivatives become:

$$f_1''(z_1) = \frac{a^2 \cdot (1 + S_1) \cdot (N_{xo} - S_2 N_{yo})}{2 \cdot (S_1 - S_2) \cdot \sqrt{z_1^2 - a^2 + a^2 S_1^2} \cdot [z_1 + \sqrt{z_1^2 - a^2 + a^2 S_1^2}]} + \frac{1}{2} \cdot \frac{N_{xo} + S_2^2 N_{xo}}{S_2^2 - S_1^2}$$

$$f_2''(z_2) = \frac{a^2 \cdot (1 + S_2) \cdot (S_1 N_{yo} - N_{xo})}{2 \cdot (S_1 - S_2) \cdot \sqrt{z_2^2 - a^2 + a^2 S_2^2} \cdot [z_1 + \sqrt{z_2^2 - a^2 + a^2 S_2^2}]} + \frac{1}{2} \cdot \frac{N_{xo} + S_1^2 N_{xo}}{S_1^2 - S_2^2}$$

which with the set of equations (29) states the solution for the problem. The above expression is valid only in the first quadrant; the solution in the other quadrants can be obtained by mirroring the given one.

Now, following the same procedure it is possible to determine the stress–strain field for an elliptical hole (Figs 6 and 7) of given semi-axes a, along the x direction, and b, along the y direction. For this geometry the two $f'(z)$ functions are:

$$f_1''(z_1) = \frac{(a + S_1 b) \cdot (b N_{xo} - a S_2 N_{yo})}{2 \cdot (S_1 - S_2) \cdot \sqrt{z_1^2 - a^2 + b^2 S_1^2} \cdot [z_1 + \sqrt{z_1^2 - a^2 + b^2 S_1^2}]} + \frac{1}{2} \cdot \frac{N_{xo} + S_2^2 N_{xo}}{S_2^2 - S_1^2}$$

$$f_2''(z_2) = \frac{(a + S_2 b) \cdot (a S_1 N_{yo} - b N_{xo})}{2 \cdot (S_1 - S_2) \cdot \sqrt{z_2^2 - a^2 + b^2 S_2^2} \cdot [z_2 + \sqrt{z_2^2 - a^2 + b^2 S_2^2}]} + \frac{1}{2} \cdot \frac{N_{xo} + S_1^2 N_{xo}}{S_1^2 - S_2^2}$$

Stresses in rotating composite cylindrical shells

James Ting-Shun Wang & Chien-Chang Lin

Institute of Applied Mathematics, National Chung-Hsing University, Taichung, Taiwan 40227

Stresses in composite cylindrical shells rotating with a constant speed about their longitudinal axis are analyzed. Each ply or ply group is treated as a separate thin layer of homogeneous and orthotropic material under the interfacial stresses as surface loading. There is no limitation on the total thickness of the shell. The circumferential stress, motivated by the conventional thin shell theory, is assumed to vary linearly through the thickness of the layer. The radial stress is determined in terms of the circumferential stress through the equilibrium condition, and an average compatibility condition through the thickness of the thin layer is used. Numerical results using the present analysis show nearly perfect agreement with the exact solution for homogeneous and isotropic cylinders. Some results for cylinders having orthotropic layers are presented for illustrative purposes.

INTRODUCTION

Composite cylindrical shells have been used widely in many engineering applications. The conventional Kirchhoffean shell theory given in standard textbooks on thin elastic shells such as Refs 1 and 2 is applicable for thin composite shells. However for moderately thick shells, various theories accounting for the shear deformation effect are available. A brief discussion of previous works can be found in Ref 3. The authors[4] have presented a theory which has no limitation on the overall thickness of the cylinder. The analysis was made for determining interfacial stresses in cylinders under uniform internal and/ or external surface loading. The theory was based on a linearly varying circumferential stress distribution and an average compatibility condition through each thin layer of the shell, and continuous deformation along all interfaces showing accurate results given in Ref. 4. The concept of the analysis used in Ref. 4 is followed for studying the present problem.

THEORY

The theory is derived for the stress analysis of a complete cylinder which consists of a number of homogeneous ply groups. The cylinder is rotating with a constant speed about its longitudinal axis. Each ply group forming a layer is treated as an individual thin elastic shell of generally orthotropic material with interfacial stresses on the inner and outer surfaces of the layer as the boundary loading. The circumferential stress is assumed to vary linearly through the thickness of the layer as being guided by the usual thin shell theory. The radial stress is determined from the equilibrium equation. Such stress distribution is believed to be sufficiently accurate as the thickness of each layer can be taken far within the usual thin shell limitation. While the equilibrium condition is satisfied exactly, the compatibility condition is made to satisfy the average value through the thickness of each layer. With the equilibrium condition satisfied exactly and the compatibility condition satisfied on the average, the deformation and stresses in each layer can be expressed in terms of interfacial stresses along the exterior surfaces of each layer. When the continuity in deformation along each interface between adjacent layers is satisfied, a recurrence equation relating interfacial stresses at adjacent interfaces can be established. All stresses throughout the complete cylinder can be determined subsequently after satisfying boundary conditions at the inside and outside surfaces of the cylinder in conjunction with the recurrence relationship among interfacial stresses.

157

Basic equations

The equilibrium equation for the axisymmetric stress distribution in polar coordinates for a cylinder in the centrifugal field is

$$\frac{d}{dr}(r\sigma_r) - \sigma_\theta + mw^2 r^2 = 0 \tag{1}$$

where r and θ are radial and circumferential coordinates respectively, σ stands for the normal stress, m is the mass density of the shell, and w is the rotating speed. The subscript j identifying the layer number is suspended for the convenience of discussion. The circumferential stress is assumed to vary linearly through the thickness h of the layer as follows:

$$\sigma_\theta = \sigma_m + \frac{1}{h}\sigma_d(r-\rho) \tag{2}$$

where σ_m is the mean circumferential stress which is equal to one half the sum of the circumferential stresses σ_θ^+ and σ_θ^-. Superscripts + and - denote locations of outer and inner surfaces of the layer respectively. The subscript d denotes the difference in σ_θ^+ and σ_θ^-, and ρ is the radius of the mid-surface of the layer. Substituting eqn (2) into eqn (1) and integrating the resulting equation with respect to r, we obtain

$$\sigma_r = \sigma_m + \frac{1}{2h}\sigma_d(r-2\rho) - \frac{1}{3}mw^2 r^2 + \frac{C}{r} \tag{3}$$

The interfacial stresses at $r = R_i$ and R_o, determined from eqn (3), are

$$\sigma_r^- = \sigma_m - \frac{1}{2h}\sigma_d R_o + \frac{C}{R_i} - \frac{1}{3}mw^2 R_i^2 \tag{4}$$

$$\sigma_r^+ = \sigma_m - \frac{1}{2h}\sigma_d R_i + \frac{C}{R_o} - \frac{1}{3}mw^2 R_o^2 \tag{5}$$

where the subscripts o and i denote radii of outer and inner surfaces of the layer respectively. Subtracting eqn (4) from eqn (5), we obtain

$$C = \frac{1}{2h}[\sigma_d - 2[\sigma_r^+ - \sigma_r^-]]R_o R_i - \frac{1}{3h}mw^2(R_o^2 - R_i^2)R_o R_i \tag{6}$$

The stress, strain and displacement relations are

$$\varepsilon_r = \frac{du}{dr} = \frac{1}{E_r}\sigma_r - \frac{v_{\theta r}}{E_\theta}\sigma_\theta \tag{7}$$

$$\varepsilon_\theta = \frac{u}{r} = -\frac{v_{r\theta}}{E_r}\sigma_r + \frac{1}{E_\theta}\sigma_\theta \tag{8}$$

where ε stands for the extensional strain, E_r and E_θ are moduli of elasticity, $v_{\theta r}$ and $v_{r\theta}$ are Poisson's ratios. The compatibility equation is

$$r\frac{d\varepsilon_\theta}{dr} + \varepsilon_\theta - \varepsilon_r = 0 \tag{9}$$

The well known exact solutions for rotating cylinders of homogeneous and isotropic material can be found in standard textbooks on elasticity such as Refs 5–7 as follows:

$$\sigma_r = \frac{3+v}{8} mw^2 b^2 \left[1 + \left(\frac{a}{b}\right)^2 - \left(\frac{r}{b}\right)^2 - \left(\frac{a}{r}\right)^2 \right] \qquad (10)$$

$$\sigma_\theta = \frac{3+v}{8} mw^2 b^2 \left[1 + \left(\frac{a}{b}\right)^2 - \frac{1+3v}{3+v} \left(\frac{r}{b}\right)^2 + \left(\frac{a}{r}\right)^2 \right] \qquad (11)$$

where a and b are the outside and inside radii of the shell respectively.

Analysis

Integrating eqns (2) and (9) through the thickness of each layer, we arrive at the following relations:

$$\sigma_m h = R_o \sigma_r^- - R_i \sigma_r^- + \frac{1}{3} hmw^2 (R_o^2 + R_o R_i + R_i^2) \qquad (12)$$

$$\sigma_\theta \left[\left(\frac{1}{E_\theta} + \frac{1}{2E_r}\right)\beta - \frac{1}{2E_r} \right] + \left(\frac{1}{E_\theta} - \frac{1}{E_r}\right) \sigma_m H \beta = -\frac{1}{E_r}(\sigma_r^+ - \sigma_r^-) - \frac{1}{3}\beta \left(\frac{1}{3E_r} + \frac{v_{\theta r}}{E_\theta} mw^2 H(R_o^2 + R_o R_i + R_i^2)\right) \qquad (13)$$

where $H = h/\rho$ and

$$\beta = \frac{H}{[1-(H/2)^2]\ln 2 + H/2 - H}$$

which is close to 1 for small values of H. Substituting eqn (13) into eqn (12) and after some manipulation, we obtain

$$\sigma_d = \alpha^+ \sigma_r^- - \alpha^- \sigma_r^- + M_d$$

where

$$\alpha^+ = \left[\left(1 - \frac{E_r}{E_\theta}\right) \frac{R_o}{\rho} \beta - 1 \right] / \alpha^*$$

$$\alpha^- = \left[\left(1 - \frac{E_r}{E_\theta}\right) \frac{R_i}{\rho} \beta - 1 \right] / \alpha^* \qquad (14)$$

$$\alpha^* = \left(\frac{E_r}{E_\theta} + \frac{1}{2}\right) \beta - \frac{1}{2}$$

$$M_d = -\frac{mw^2 b^2}{3\alpha^*} \left\{ \left[\frac{E_r}{E_\theta}(1 + v_{\theta r}) - \frac{2}{3} \right] J\beta + 2 \left(\frac{\rho}{b}\right)^2 \right\} H$$

$$J = \frac{R_o^2 + R_o R_i + R_i^2}{b^2}$$

Equation (12) may be written in the following form:

$$\sigma_s = \frac{2R_o}{h}\sigma_r^+ - \frac{2R_i}{h}\sigma_r^- + M_s \qquad (15)$$

where $\sigma_s = 2\sigma_m$ and

$$M_s = \frac{2}{3} mw^2(R_o^2 + R_oR_i + R_i^2)$$

Adding and subtracting eqns (14) and (15), we obtain

$$\sigma_\theta^+ = \left(\frac{R_o}{h} + \frac{\alpha^+}{2}\right)\sigma_r^+ - \left(\frac{R_i}{h} + \frac{\alpha^-}{2}\right)\sigma_r^- + \frac{1}{2}(M_s + M_d) \tag{16}$$

$$\sigma_\theta^- = \left(\frac{R_o}{h} - \frac{\alpha^+}{2}\right)\sigma_r^+ - \left(\frac{R_i}{h} - \frac{\alpha^-}{2}\right)\sigma_r^- + \frac{1}{2}(M_s - M_d) \tag{17}$$

In order to maintain continuity in deformation at the general jth interface, we equate ε_θ requiring

$$\left(-\frac{\nu_{r\theta}}{E_r}\sigma_r^+ + \frac{1}{E_\theta}\sigma_\theta^+\right)_j = \left(-\frac{\nu_{r\theta}}{E_r}\sigma_r^- + \frac{1}{E_\theta}\sigma_\theta^-\right)_{j+1} \tag{18}$$

from which we arrive at the following recurrence equation relating interfacial radial stresses q_j at adjacent interfaces:

$$A_{j+1}q_{j+1} = B_jq_j + C_{j-1}q_{j-1} + F_j \tag{19}$$

where

$$A_{j+1} = \left(\frac{R}{h} - \frac{1}{2}\alpha^+\right)_{j+1}$$

$$B_j = \bar{E}_j\left(\frac{R}{h} + \frac{1}{2}\alpha^+ - \nu_{\theta r}\right)_j + \frac{R_j}{h_{j+1}} - \left(\frac{1}{2}\alpha^- + \nu_{\theta r}\right)_{j+1}$$

$$C_j = -\bar{E}_j\left(\frac{R_{j-1}}{h_j} + \frac{1}{2}\alpha_j^-\right)$$

$$F_j = -\frac{1}{2}[(M_s - M_d)_{j+1} - \bar{E}_j(M_s + M_d)_j]$$

$$\bar{E}_j = (E_\theta)_{j+1}/(E_\theta)_j$$

From the recurrence relations given in eqn (19), we can express the interfacial radial stress at any general jth layer in terms of q_1 and q_0 for j larger than 1 in the following general form:

$$q_j = D_jq_1 + G_jq_0 + V_j \tag{20}$$

where

$$D_2 = \frac{B_1}{A_2}, \quad G_2 = \frac{C_0}{A_2}, \quad V_2 = \frac{F_1}{A_2}$$

$$D_3 = \frac{B_2D_2 + C_1}{A_3}, \quad G_3 = \frac{B_2G_2}{A_3}, \quad V_3 = \frac{B_2V_2 + F_2}{A_3}$$

$$D_j = \frac{1}{A_j}(B_{j-1}D_{j-1} + C_{j-2}D_{j-2})$$

$$G_j = \frac{1}{A_j}(B_{j-1}G_{j-1} + C_{j-2}G_{j-2})$$

$$V_j = \frac{1}{A_j}(B_{j-1}V_{j-1} + C_{j-2}V_{j-2})$$

for $j \geq 4$. Solving q_1 from eqn (20) by taking $j = n$, we arrive at

$$q_1 = \frac{1}{D_n}(q_n - G_n q_0 - V_n) \tag{21}$$

where q_0 and q_n are boundary tractions at the inside and outside surfaces of the cylinder respectively. Once q_1 is determined for given q_0 and q_n, all other interfacial stresses can be systematically computed using eqn (20).

A simple model

The circumferential and radial stresses in a rotating homogeneous cylinder of isotropic materials are obviously tensile for the case where both the inside and outside boundary surfaces are free of tractions. However, some numerical results, obtained in examples considered later for a compressive shell having layers of ply groups of different fiber orientations, show that compressive interfacial radial stress also occurs. To give an approximate exploration of the possibility of interfacial radial stress being compressive in cylinders of layered construction, we consider a simple model for a cylinder made of two thin layers of different materials. From the exact solutions given in eqns (10) and (11), the maximum variation of circumferential stress through the thickness is less than 6·5% when the thickness h to the radius ratio is 1/20. The maximum variation is less than 1·5% when the ratio is 1/100. Therefore, the circumferential stress is considered to be uniform through the thickness of each layer in this model. The inner layer is labeled as number 1 layer, and number 2 for the outer layer as shown in Fig. 1. The equilibrium equations for the two layers having the same thickness h are

$$mhr_2^2 w^2 - qr_c = \sigma_2 h \tag{22}$$

$$mhr_1^2 w^2 + qr_c = \sigma_1 h \tag{23}$$

where σ_1 and σ_2 are circumferential stresses in layers 1 and 2 respectively. The corresponding r_1 and r_2 are the radii of the mid-surfaces of the layers. Adding eqns (22) and (23), we obtain

$$\sigma_1 + \sigma_2 = mw^2(r_1^2 + r_2^2) \tag{24}$$

In order to maintain continuity in deformation by equating circumferential strain, we obtain

$$E_2 \sigma_1 = E_1 \sigma_2 \tag{25}$$

where E_1 and E_2 are moduli of elasticity of the two layers. Equation (25) is valid because the radial stress is substantially smaller than the circumferential stress as the thickness of each layer is taken to be small
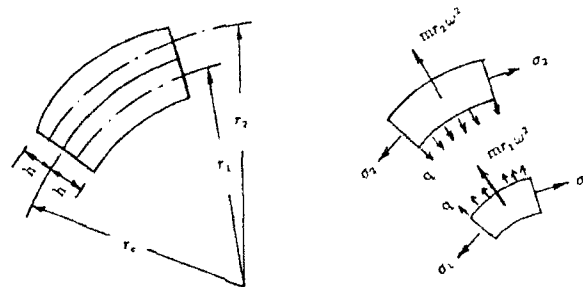

Fig. 1. A simple model.

with respect to its radius. By substituting eqn (25) into eqn (24), we obtain

$$\left(\frac{E_2}{E_1}+1\right)\sigma_1 = mw^2(r_1^2 + r_2^2) \tag{26}$$

Substitution of eqn (26) into eqn (23) yields the interfacial radial stress

$$q = \frac{mhw^2}{(E_1 + E_2)r_c}(E_1 r_2^2 - E_2 r_1^2) \tag{27}$$

where r_c is the radius of the surface at the interface. Equation (27) indicates that q may be positive or negative depending on the stiffness of the materials and radii of the two layers. From eqn (27), we conclude that

$$q > 0 \quad \text{if} \quad \frac{E_1}{E_2} > \left(\frac{r_1}{r_2}\right)^2$$

$$q = 0 \quad \text{if} \quad \frac{E_1}{E_2} = \left(\frac{r_1}{r_2}\right)^2 \tag{28}$$

$$q < 0 \quad \text{if} \quad \frac{E_1}{E_2} < \left(\frac{r_1}{r_2}\right)^2$$

in which we note that the ratio of r_2 to r_1 is nearly equal to 1 for thin layers, and the positive value of q corresponds to tensile stress. Consequently, radial stress could be tensile or compressive in rotating layered shells.

EXAMPLES

In order to partially check the accuracy of the present analysis, a rotating homogeneous cylinder made of isotropic material where exact solutions are available is used as the first example. Stresses are computed in terms of $p = mw^2 b^2$ for various a to b ratios. The Poisson's ratio is taken to be 0·25, and the total thickness of the cylinder is divided into 45 layers of the same thickness in the present analysis. Hence, the thickness of each layer is equal to $(a-b)/45$. Results for $a = 4b$ are given in Table 1. For this case the h to p ratio varies between 1/9 and 1/60. Layers near the inner boundary surface are close to the limit of the usual thin shell theory while layers near the outer boundary surface are far within the thin shell limit.

The results given in Table 1 show nearly perfect agreement between the present results and exact solutions. The interface numbers 0 and 45 correspond to locations at the inner and outer surfaces of the cylinder respectively.

As a second example, we consider a cylinder consisting of 45 layers of alternating ply groups of 0° and 90° fibers. All ply groups have the same thickness h, and the exterior layers are 90° ply groups. The fiber orientation angle is measured with respect to the longitudinal axis of the cylinder. The material properties $E_r = E_\theta = 2\cdot2 \times 10^6$ psi and $v_{\theta r} = 0\cdot21$ for 0° ply groups. $E_r = 2\cdot2 \times 10^6$ psi, $E_\theta = 20\cdot2 \times 10^6$ psi, and $v_{\theta r} = 0\cdot21$ for 90° ply groups are those used in Refs 8 and 9. Results for the radial and circumferential stresses at the locations of interfaces for a to b ratios ranging from 1·01 to 10 are computed. The thickness of each layer h is equal to $(a - b)/45$. Therefore, the h to p ratio for the thickest cylinder with $a = 10b$ ranges between 1/5 and 1/50. The ratio for the thinnest cylinder with $a = 1\cdot01b$ is about 1/4500. Numerical results for cylinders having a to b ratios equal to 1·1, 4 and 10 are given in Tables 2, 3 and 4.

The positive numbers in Tables 2-4 are tensile stresses and the negative sign denotes compressive. Two numbers are given for σ_θ at each interface location. They represent stress discontinuities in adjacent layers. The numerical results given in these tables indicate that all radial stresses at even number interface locations are algebraically smaller than those in their immediate

Table 1. Comparison of stresses in an isotropic cylinder (a = 4b)

Interface no.	σ_r/p Present	σ_r/p Exact	σ_θ/p Present	σ_θ/p Exact
0	0	0	13·1869	13·1875
1	0·7319	0·7311	12·3690	12·3703
2	1·3251	1·3239	11·6841	11·6858
3	1·8088	1·8074	11·1031	11·1051
4	2·2048	2·2032	10·6044	10·6065
5	2·5294	2·5278	10·1714	10·1736
:	:	:	:	:
10	3·4392	3·4378	8·6365	8·6386
15	3·6573	3·6563	7·6545	7·6563
20	3·5013	3·5006	6·9077	6·9092
25	3·1038	3·1033	6·2635	6·2648
30	2·5281	2·5278	5·6586	5·6597
35	1·8076	1·8074	5·0597	5·0607
:	:	:	:	:
40	0·9611	0·9610	4·4479	4·4487
41	0·7777	0·7777	4·3229	4·3237
42	0·5899	0·5899	4·1968	4·1976
43	0·3976	0·3976	4·0696	4·0704
44	0·2010	0·2010	3·9413	3·9421
45	0	0	3·8116	3·8125

Table 2. Stresses in a composite cylinder (a = 1·1b)

Interface no.	$\sigma_r \times 10^3/p$	σ_θ/p
0	0	2·0693
1	2·3605	2·0643 (0·2253)
2	0·6245	0·2243 (02·0585)
3	2·9305	2·0535 (0·2242)
4	1·1798	0·2232 (2·0477)
5	3·4302	2·0427 (0·2231)
:	:	:
10	2·4260	0·2200 (2·0160)
15	4·9072	1·9906 (0·2177)
20	3·1692	0·2146 (1·9651)
25	4·7635	1·9408 (0·2123)
30	2·3372	0·2091 (1·9163)
35	3·0986	1·8927 (0·2067)
:	:	:
40	0·0241	0·2036 (1·8690)
41	1·4063	1·8646 (0·2033)
42	−0·0689	0·2024 (1·8597)
43	0·7306	1·8554 (0·2022)
44	−1·2971	0·2013 (1·8504)
45	0	1·8462

Table 3. Stresses in a composite cylinder (a = 4b)

Interface no.	σ_r/p	σ_θ/p
0	0	12·1396
1	0·6685	11·3879 (1·3750)
2	0·6371	1·3175 (11·2096)
3	1·1325	10·6202 (1·3911)
4	1·0652	1·3589 (10·9121)
5	1·4605	10·4120 (1·4361)
:	:	:
10	1·7615	1·5426 (11·4399)
15	2·1731	11·7333 (1·7158)
20	2·0472	1·7648 (12·9309)
25	2·0700	12·9549 (1·8210)
30	1·6541	1·7491 (13·3684)
35	1·3404	12·8466 (1·6619)
:	:	:
40	0·6487	1·4540 (12·2815)
41	0·6097	12·0222 (1·4285)
42	0·3745	1·3598 (11·8664)
43	0·3171	11·6146 (1·3270)
44	0·0758	1·2537 (11·3835)
45	0	11·1394

Table 4. Stresses in a composite cylinder (a = 10b)

Interface no.	σ_r/p	σ_θ/p
0	0	28·0547
1	4·1092	23·6822 (3·5146)
2	3·7831	3·5258 (28·6567)
3	6·4231	25·6559 (4·2993)
4	5·8733	4·4375 (33·6732)
5	8·1550	30·9335 (5·2240)
:	:	:
10	10·0512	7·1296 (51·0940)
15	13·5231	58·7264 (9·2167)
20	13·2391	10·2059 (73·1861)
25	14·1646	76·1051 (11·1459)
30	11·6064	10·9890 (82·3246)
35	9·7443	79·8369 (10·6274)
:	:	:
40	4·8023	9·2331 (76·9452)
41	4·5491	74·9965 (9·0651)
42	2·7996	8·5640 (74·0460)
43	2·3840	72·1630 (8·3300)
44	0·5795	7·7870 (70·5244)
45	0	68·7085

adjacent odd number interface locations. This means that the interfacial stress is smaller at the interface where a 90° ply group is on the outer side of the 0° ply group than that where a 90° layer is on the inner side of the 0° layer. The trend is correct since E_θ for the 90° ply group is larger than that of the 0° ply group. For the same reason, the circumferential stress in the 90° layer is higher than those in the adjacent 0° layers as expected. While all interface radial stresses are positive for thicker shells, some negative radial stresses appeared in the thinnest case for $a = 1·1b$ as shown in Table 2. Negative radial stresses begin to occur at 36th interface location for $a = 1·05b$, and at all even interface locations for $a = 1·01$ cases.

CONCLUDING REMARKS

The theory presented in the study divides a composite circular cylindrical shell into a number

of thin layers of ply groups. Each layer is treated as an individual thin shell of orthotropic material. Interfacial stresses at the inner and outer surfaces are considered as the loading on the thin layer. Motivated by the usual thin elastic shell theory, the circumferential stress is assumed to vary linearly along the radial direction. The radial stress is determined from the equilibrium equation exactly, and the compatibility condition is satisfied on the average through the thickness of each thin layer of ply groups of composite materials. The theory leads to an analysis procedure allowing systematic calculations of all stresses in layered composite cylindrical shells in the centrifugal field. The theory is accurate as evidenced by the comparison made with numerical results to exact solutions of degenerated cases. While all tensile stresses occur in rotating homogeneous cylinders of isotropic materials, numerical results indicate that compressive radial stress may occur in cylinders of composite materials of layered constructions. A simple model presented in the study supports the fact that compressive stress could arise depending on the relative stiffness of the adjacent layers. All computations indicate that the procedure established for the analysis is effective, and has no limitation on the total thickness of the shell.

REFFRENCES

1. Kraus, H., *Thin Elastic Shells*. John Wiley, New York, 1967.
2. Timoshenko, S. & Woinowsky-Krieger, S., *Theory of Plates and Shells*. 2nd edn. McGraw-Hill, New York, 1959.
3. Reddy, J. N., *Energy and Variational Methods in Applied Mechanics*. John Wiley, New York, 1984.
4. Wang, J. T. S. & Lin, C. C., Interface stresses in laminated cylindrical shells. *Proceedings of the International Conference on Advanced Composites '93*, Wollongong, Australia, February 15-19, 1993.
5. Fung, Y. C., *Foundations of Solid Mechanics*. Prentice-Hall, Englewood Cliffs, NJ, 1965.
6. Timoshenko, S. P. & Goodier, J. N., *Theory of Elasticity*, 3rd edn. McGraw-Hill, New York, 1970.
7. Wang, C. T., *Applied Elasticity*. McGraw-Hill, New York, 1953.
8. Wang, A. S. D. & Crossman, F. W., Some new results on edge effect in symmetric laminates. *Journal of Composite Materials*, 11 (1977) 92-106.
9. Wang, J. T. S. & Dickson, J. N., Interlaminar stresses in symmetric composite laminates. *Journal of Composite Materials*, 12 (1978) 390-402.

A unified formulation of laminated composite, shear deformable, five-degrees-of-freedom cylindrical shell theories

K. P. Soldatos & T. Timarci

Department of Theoretical Mechanics, University of Nottingham, Nottingham, UK

The main objective of this paper is a theoretical unification of most of the variationally consistent classical and shear deformable cylindrical shell theories available in the literature. This is achieved by introducing into the shell displacement approximation certain general functions of the transverse coordinate which account for the incorporation of the transverse shear deformation effects. Avoiding having to provide a single choice of the forms of these 'shear deformation shape functions' before or during the variational formulation of the general theory, the present formulation leaves open possibilities for a multiple, a-posteriori specification of particular shear deformable shell theories. As a result, the classical Donnell-, Love- and Sanders-type shell theories as well as their well known uniform and parabolic shear deformable analogues are obtained as particular cases. Moreover, a generalized 'zig-zag' displacement model is presented which gives further multiple freedom in achieving continuous distributions of interlaminar stresses through the thickness of an unsymmetric cross-ply laminated cylindrical shell.

1 INTRODUCTION

The rapid increase in the industrial use of advanced homogeneous or laminated composite materials has necessitated and resulted in the formulation and analytical use of several two-dimensional, higher order theories suitable for the static and/or dynamic analysis of cylindrical shells. Most of them are refined, displacement based, theories which enable consideration of transverse shear deformation effects.

The development of such a refined shell theory is usually based on a displacement approximation which involves five unknown displacement components (degrees of freedom). Three of these are the ones involved in a corresponding classical shell theory (displacement components of a reference surface). The additional degrees of freedom are multiplied by a certain function of the transverse coordinate and are suitably superposed with the in-plane displacement field of a corresponding classical shell theory, accounting, thus, for the effects of transverse shear deformation.

The choice of such a shear deformation 'shape' function is not unique. It is based on the satisfaction of certain mechanical, material and/or geometrical constraints of the problem consid-

ered and, in general, characterizes the degree of sophistication or even the degree of accuracy of the resulting shell theory. Hence, different shape functions have been used over the years by different researchers.

The main objective of this paper is the development of a variationally consistent, static and/or dynamic shear deformable cylindrical shell theory which is independent of the choice of that 'shape' function. This is achieved by introducing general shape functions and, henceforth, avoiding having to provide a single choice of their forms before or during the variational formulation of the theory. Such a procedure leaves open possibilities for a multiple, a-posteriori specification of such a shear deformation shape function, while it eventually results in a theoretical unification of most of the classical and shear deformable cylindrical shell theories available in the literature.

Starting with an identically zero shape function, the widely used laminated composite classical shell theories of the Donnell-, Love- and Sanders-type can be obtained as particular cases. This is achieved by incorporating, where it is necessary throughout the theoretical formulation, certain tracers which have the form of Kronecker's deltas.[1] As a result, each five-degrees-of-freedom

shell theory produced on the basis of the proposed formulation is a transverse shear deformable analogue of one of the aforementioned classical shell theories.

Upon choosing a linear form of that function, a so-called uniform shear deformable shell theory[2-4] is obtained, while a particular cubic choice leads to a so-called parabolic shear deformable shell theory.[5-8] Nevertheless, different choices can be employed[9] and, with some of them, the analogues of certain refined shear deformable cylindrical shell theories[10,11] can also be obtained as particular cases of the proposed formulation. It is important to notice, that any of the choices consistent with Refs 2–10 leads to shell theories which violate continuity of transverse shear stresses at the material interfaces of a laminated composite shell. On the other hand, a choice consistent with Ref. 11 leads to shell theories which account for continuous interlaminar stresses at those material interfaces.

Consideration of this latter feature is of particular importance for the development of refined theories suitable for the static and dynamic analysis of laminated composite thin-walled structures. This is the direction in which the field is currently growing, with particular attention given to laminated composite beams[12] and plates[13-17] where geometrical simplicity facilitates theoretical modelling. However, with the proposed unified formulation, any choice which is consistent with Refs 12–16 can also lead to shear deformable, five-degrees-of-freedom, shell theories that account for interlaminar stress continuity. Hence, the second objective of this paper is the derivation of a generalized 'zig-zag' displacement model which gives multiple freedom in choosing continuous distributions of interlaminar stresses throughout the thickness of a cross-ply laminated cylindrical shell.

2 THEORY

Consider a circular cylindrical shell with a constant thickness h, and denote by R and L the radius and the axial length of its reference surface, respectively. Upon denoting the length parameters along the axial, circumferential and normal to that reference surface directions by x, s and z, respectively, consider further the curvilinear coordinate system $Oxsz$. Finally, assume that the shell considered is subjected to an external stress distribution, q, acting normally on its top surface.

The shell is constructed by either a homogeneous or a laminated composite elastic material having density ρ. Under this consideration, it is generally assumed[18,19] that there exists a strain energy density function, $V(\varepsilon_x, \varepsilon_s, \varepsilon_z, \gamma_{xs}, \gamma_{xz}, \gamma_{sz})$, such that:[20]

$$(\sigma_x, \sigma_s, \sigma_z, \tau_{xs}, \tau_{xz}, \tau_{sz})$$

$$= \left[\frac{\partial V}{\partial \varepsilon_x}, \frac{\partial V}{\partial \varepsilon_s}, \frac{\partial V}{\partial \varepsilon_z}, \frac{\partial V}{\partial \gamma_{xs}}, \frac{\partial V}{\partial \gamma_{xz}}, \frac{\partial V}{\partial \gamma_{sz}} \right] \quad 1$$

Denoting by U, V and W the shell displacement components, along the x, s and z directions, respectively, the present theoretical formulation starts with the superposition[5]

$$(U, V, W) = (U^c, V^c, W^c) + (U^a, V^a, 0) \quad 2$$

of two different displacement fields. The basic displacement field,

$$U^c(x, s, z; t) = u(x, s; t) - z w_{,x}$$

$$V^c(x, s, z; t) = [1 + (\delta_{11} + \delta_{S1}) z/R] v(x, s; t) - z w_{,s}$$

$$W^c(x, s, z; t) = w(x, s; t) \quad 3$$

produces in particular cases the displacement field used in classical shell theories of Donnell-, Love- and Sanders-type, by setting $T = D$, L and S, respectively.[1] Here, δ is the Kronecker symbol and t denotes time, while u, v and w represent unknown displacement components of the shell reference surface. The additional displacement field,

$$U^a(x, s, z; t) = \varphi_1(z) u_1(x, s; t)$$

$$V^a(x, s, z; t) = \varphi_2(z) v_1(x, s; t) \quad 4$$

dismisses the validity of the Kirchhoff–Love assumptions and, as will become apparent from the kinematic relations (5) and (6) below, it incorporates into the theory the effects of transverse shear deformation. For a notation convenience, it is assumed that $\varphi_1(z)$ and $\varphi_2(z)$ have dimensions of length. Imposing no further restrictions on the choice of these shape functions, an obvious multiple freedom is introduced in the choice of through-thickness displacement distributions.

Introduction of the displacement approximation (2)–(4) into the cylindrical-polar form of the kinematic relations of linear elasticity[20] yields:

$$\varepsilon_x = e_x^c + z k_x^c + \varphi_1(z) k_x^a, \quad \varepsilon_s = e_s^c + z k_s^c + \varphi_2(z) k_s^a$$

$$\gamma_{xs} = e_{xs}^c + z k_{xs}^c + \varphi_1(z) k_{xs}^a + \varphi_2(z) k_{xs}^a \quad (5)$$

$$\gamma_{sz} = \varphi_2'(z) e_{sz}^a, \quad \gamma_{xz} = \varphi_1'(z) e_{xz}^a, \quad \varepsilon_z = 0$$

where a prime denotes ordinary differentiation with respect to z and,

$$e_1^c = u_{,1}, \quad \varepsilon_1^c = v_{,1}, \quad e_{11}^c = u_{,1} + v_{,1}$$

$$k_1^c = -w_{,11}, \quad k_1^c = -w_{,11} + (\delta_{11} + \delta_{S1})v_{,1}/R$$

$$k_{11}^c = -2w_{,11} + (\delta_{11} + 3\delta_{ST}/2)v_{,1}/R - \tfrac{1}{2}\delta_{S1}u_{,1} \quad (6)$$

$$k_1^a = u_{1,1}, \quad k_1^a = v_{1,1}, \quad k_{11}^a = u_{1,1}, \quad k_{11}^a = v_{1,1}$$

$$(e_{1z}^a, e_{1z}^a) = (u_1, v_1)$$

Upon setting $T = D$, L or S, expressions (6(a)–(c)) are reduced to the conventional reference surface strains, changes of curvature and twist occurring in a classical shell theory of Donnell-, Love- or Sanders-type, respectively. The occurrence of the quantities defined by expressions (6, last two) is clearly due to transverse shear deformation effects. These represent additional strains, changes of curvature and twists of the shell reference surface, and are therefore appropriately denoted with e^a- or k^a-symbols, respectively.

In a close relation with expressions (1), the approximate stress field corresponding to the displacement approximation (2)–(4) is represented by introducing the following generalized stress components:

$$(\sigma_1^c, \sigma_1^c, \tau_{11}^c) = \left(\frac{\partial V_0}{\partial e_1^c}, \frac{\partial V_0}{\partial e_1^c}, \frac{\partial V_0}{\partial e_{11}^c}\right)$$

$$(\tau_{1z}^a, \tau_{1z}^a) = \left(\frac{\partial V_0}{\partial e_{1z}^a}, \frac{\partial V_0}{\partial e_{1z}^a}\right) \tag{7}$$

together with the following generalized moment components:

$$(m_1^c, m_1^c, m_{11}^c) = \left(\frac{\partial V_0}{\partial k_1^c}, \frac{\partial V_0}{\partial k_1^c}, \frac{\partial V_0}{\partial k_{11}^c}\right)$$

$$(m_1^a, m_1^a, m_{11}^a, m_{11}^a) = \left(\frac{\partial V_0}{\partial k_1^a}, \frac{\partial V_0}{\partial k_1^a}, \frac{\partial V_0}{\partial k_{11}^a}, \frac{\partial V_0}{\partial k_{11}^a}\right) \tag{8}$$

Under these considerations, the generalized force and moment resultants of the present theory are defined as follows:

$$(N_1^c, N_1^c, N_{11}^c) = \int_z \left(\frac{\partial V_0}{\partial e_1^c}, \frac{\partial V_0}{\partial e_1^c}, \frac{\partial V_0}{\partial e_{11}^c}\right) dz$$

$$= \int_z (\sigma_1^c, \sigma_1^c, \tau_{11}^c)\, dz$$

$$= \int_z (\sigma_1, \sigma_1, \tau_{11})\, dz \tag{9a}$$

$$(M_1^c, M_1^c, M_{11}^c) = \int_z \left(\frac{\partial V_0}{\partial k_1^c}, \frac{\partial V_0}{\partial k_1^c}, \frac{\partial V_0}{\partial k_{11}^c}\right) dz$$

$$= \int_z (m_1^c, m_1^c, m_{11}^c)\, dz$$

$$= \int_z (\sigma_1, \sigma_1, \tau_{11}) z\, dz \tag{9b}$$

$$(Q_1^a, Q_1^a) = \int_z \left(\frac{\partial V_0}{\partial e_{1z}^a}, \frac{\partial V_0}{\partial e_{1z}^a}\right) dz$$

$$= \int_z (\tau_{1z}^a, \tau_{1z}^a)\, dz$$

$$= \int_z [\tau_{1z}\varphi_2'(z), \tau_{1z}\varphi_1'(z)]\, dz \tag{9c}$$

$$(M_1^a, M_1^a, M_{11}^a, M_{11}^a)$$

$$= \int_z \left(\frac{\partial V_0}{\partial k_1^a}, \frac{\partial V_0}{\partial k_1^a}, \frac{\partial V_0}{\partial k_{11}^a}, \frac{\partial V_0}{\partial k_{11}^a}\right) dz$$

$$= \int_z (m_1^a, m_1^a, m_{11}^a, m_{11}^a)\, dz$$

$$= \int_z [\varphi_1\sigma_1, \varphi_2\sigma_1, \varphi_1\tau_{11}, \varphi_2\tau_{11}]\, dz \tag{9d}$$

where, for the derivation of these expressions, the chain rule of partial differentiation has been used.[18,19]

These definitions make clear that the resultants denoted with a superscript 'c' are the well known conventional force and moment resultants employed in classical plate and shell theories. They are therefore considered as resultants of a certain, basic part of the deformation in which the shell is deformed in accordance with the Kirchhoff–Love assumptions. Similarly, the set of the remaining force and moment resultants, denoted with a superscript 'a', is considered as describing a certain, additional part of the shell deformation which is due to the incorporation of the transverse shear deformation effects. During that part of the deformation, the shell reference surface is deformed in accordance with the pattern described by the set of the additional reference surface strains, curvatures and twists denoted with a superscript 'a' in eqns (6).

Upon employing Hamilton's principle, the following equations of motion are obtained:

$$N^c_{x,x} + N^c_{xs,s} - \frac{1}{2R} \delta_{ST} M^c_{xs,s} = I_1$$

$$N^c_{s,s} + N^c_{xs,x} + \frac{1}{R} [(\delta_{LT} + \delta_{ST})M^c_{s,s}$$

$$+ (\delta_{LT} + \tfrac{3}{2}\delta_{ST})M^c_{xs,x}] = I_2$$

$$- N^c_s/R + M^c_{x,xx} + 2M^c_{xs,xs} + M^c_{s,ss} = q + I_3 \qquad (10)$$

$$M^a_{x,x} + M^a_{xs,s} - Q^a_x = I_4$$

$$M^a_{s,s} + M^a_{xx,x} - Q^a_s = I_5$$

The inertia terms are defined as follows:

$$I_1 = [\rho_0 u - \rho_1 w_{,x} + \bar\rho^{11}_0 u_1]_{,tt}$$

$$I_2 = \{[\rho_0 + (2\rho_1/R + \rho_2/R^2)(\delta_{LT} + \delta_{ST})]v$$

$$+ (\rho_1 - \rho_2/R)w_{,s} + (\rho^{21}_0 + \bar\rho^{21}_1/R)v_1\}_{,tt}$$

$$I_3 = \{\rho_0 w - \rho_2(w_{,xx} + w_{,ss}) + \rho_1 u_{,x}$$

$$- [\rho_1 - (\delta_{LT} + \delta_{ST})\rho_2/R]v_{,s}$$

$$+ \bar\rho^{11}_1 u_{1,x} + \bar\rho^{21}_1 v_{1,s}\}_{,tt} \qquad (11)$$

$$I_4 = (\bar\rho^{11}_0 u + \bar\rho^{12}_0 u_1 - \bar\rho^{11}_1 w_{,x})_{,tt}$$

$$I_5 = \{[\bar\rho^{21}_0 + (\delta_{LT} + \delta_{ST})\bar\rho^{21}_1/R]v + \bar\rho^{22}_0 v_1$$

$$- \bar\rho^{21}_1 w_{,sx}\}_{,tt}$$

where

$$\rho_i = \int_l \rho z^i \, dz, \qquad (i = 0,1,2) \qquad (12a)$$

$$\rho_i^{\cdot \alpha\beta} = \int_l \rho[\varphi_\alpha(z)]^\beta z^i \, dz, \qquad (i = 0,1;\ \alpha,\beta = 1,2) \qquad (12b)$$

Moreover, Hamilton's principle yields the following boundary conditions imposed at the shell edges $x = 0, L$:

u prescribed or N^c_x prescribed,

v prescribed or $N^c_{xs} + (\delta_{LT} + \delta_{ST})M^c_{xs}/R$

   prescribed,

w prescribed or $M^c_{x,x} + 2M^c_{xs,s}$ prescribed,

$w_{,x}$ prescribed or M^c_x prescribed, $\qquad (13)$

u_1 prescribed or M^a_x prescribed,

v_1 prescribed or M^a_{xs} prescribed.

For an explicitly given form of the strain energy function, V_0, all force and moment resultants (9) can be expressed in terms of the five unknown degrees of freedom and their partial derivatives with respect to the spatial coordinates and time.

Hence, a subsequent introduction of these latter expressions into eqns (10) yields the so-called Navier-type equations of the present theory. In accordance with the number of the edge boundary conditions (13), these will form a twelfth-order system of partial differential equations.

As can easily be verified, the formulation presented has eventually resulted in a theoretical unification of most of the classical and shear deformable cylindrical shell theories available in the literature. Starting with identically zero shape functions, the widely used laminated composite classical shell theories of the Donnell-, Love- and Sanders-type are obtained as particular cases. Upon choosing these functions to be linear in z, a so-called uniform shear deformable shell theory[2-4] is obtained, while a particular cubic choice leads to a so-called parabolic shear deformable shell theory.[5-8] Nevertheless, different choices can be employed[9] and, with some of them, the analogues of certain refined shear deformable cylindrical shell theories[10,11] can also be obtained as particular cases of the present formulation.

3 CONTINUITY OF INTERLAMINAR STRESSES

Any choice of shape functions consistent with Refs 2-10 leads to shell theories which violate continuity of transverse shear stresses at the material interfaces of a laminated composite shell. On the other hand, a choice consistent with Ref. 11 leads to a layerwise linear distribution (zig-zag variation) of the in-plane displacement components which results in a continuous, linear variation of transverse shear stresses throughout the shell thickness. Such a zig-zag displacement approximation can be improved in a sense, as for instance, by Lee et al.[13] for corresponding problems dealing with cross-ply laminated flat plates. In Ref. 13, the improved zig-zag displacement model employed was selected in such a manner that the resulting continuous transverse shear stresses were parabolically distributed through the thickness of the laminated plate considered. The generalized 'zig-zag' displacement model proposed in this section gives further multiple freedom in appropriately choosing continuous distributions of interlaminar stresses through the thickness of a cross-ply laminated cylindrical shell.

Consider a thin cross-ply laminated circular cylindrical shell composed of an arbitrary

number, N, of perfectly bonded, coaxial specially orthotropic layers and denote with z_k the position of the material interface between its kth and $(k+1)$th layers $(k = 1,2,...,N-1)$. Denote further by R_k and $Q_{44}^{(k)}$ and $Q_{55}^{(k)}$ the middle surface radius and the transverse shear elastic moduli, respectively, of the kth layer $(k = 1,2,...,N)$. Under these considerations, the transverse shear stresses and strains are related as follows:

$$\tau_{xz}^{k} = Q_{44}^{(k)}\gamma_{xz}^{k}, \ \tau_{xz}^{(k)} = Q_{55}^{(k)}\gamma_{xz}^{(k)}, (k=1,2,...,N)$$
(14)

Consider next the kth layer as an independent cylindrical shell and, in a close relation with the displacement model (2)-(4), approximate its displacement components as follows:

$$U_k(x,s,z;t) = u_{0k} - zw_{,x} + f_{1k}(z)u_{1k}$$
(15a)

$$V_k(x,s,z;t) = [1 + (\delta_{LT} + \delta_{ST})z/R_k]v_{0k}$$
$$- zw_{,s} + f_{2k}(z)v_{1k}$$
(15b)

$$W_k(x,s,z;t) = w(x,s;t)$$
(15c)

where u_{0k}, u_{1k}, v_{0k} and v_{1k} are functions of x, s and t only. Equation (15b) makes clear that the middle surface of each particular layer has been selected as its reference surface. It is again assumed that $f_{1k}(z)$ and $f_{2k}(z)$ have dimensions of length. It is moreover emphasized that, although their forms may differ from layer to layer, their derivatives should take non-zero values at the shell material interfaces.

In what follows, a procedure is outlined according to which, independently of the choice of their forms, $f_{1k}(z)$ and $f_{2k}(z)$ $(k = 1,2,...,N)$ are connected in a manner that guarantees interlaminar continuity of both displacements and transverse shear stresses. To this end, the middle surface of the first layer is selected as the reference surface of the entire shell $(R = R_1)$. This is not an essential restriction but, in the present case dealing with unsymmetric cross-ply laminated shells, it is found convenient for the description of the outlined procedure. Nevertheless, for a different choice of the shell reference surface, the whole procedure can be appropriately modified.

In accordance with eqns (5) and (6), eqns (14) yield the following expressions for the transverse shear stresses in the kth layer:

$$\tau_{xz}^{k} = Q_{44}^{(k)}f_{2k}'(z)v_{1k}, \ \tau_{xz}^{(k)} = Q_{55}^{(k)}f_{1k}'(z)u_{1k}$$
(16)

Requiring continuity of these interlaminar stresses on the $(k-1)$th material interface yields $(k = 2,3,...,N)$:

$$u_{1k} = \frac{Q_{55}^{k-1}f_{1,k-1}'(z_{k-1})}{Q_{55}^{k}f_{1k}'(z_{k-1})}u_{1,k-1} = ... = A_k u_{11}$$
(17)

$$v_{1k} = \frac{Q_{44}^{k-1}f_{2,k-1}'(z_{k-1})}{Q_{44}^{k}f_{2k}'(z_{k-1})}v_{1,k-1} = ... = C_k v_{11}$$

where

$$A_k = \frac{Q_{55}^{k-1}}{Q_{55}^{k}}\frac{f_{1,k-1}'(z_{k-1})}{f_{1k}'(z_{k-1})}A_{k-1}, \ A_1 = 1$$
(18)

$$C_k = \frac{Q_{44}^{k-1}}{Q_{44}^{k}}\frac{f_{2,k-1}'(z_{k-1})}{f_{2k}'(z_{k-1})}C_{k-1}, \ C_1 = 1$$

Now inserting eqns (17) into the expressions (15) and requiring continuity of displacements at the $(k-1)$th shell material interface yields $(k = 2,3,...,N)$:

$$u_{0k} = u_{01} + B_k u_{11}$$
$$v_{0k} = D_k v_{01} + F_k v_{11} = v_{01} + F_k v_{11}$$
(19)

where $k = 2,3,...,N$.

$$B_k = \sum_{i=2}^{k}[A_{i-1}f_{1,i-1}(z_i) - A_i f_{1i}(z_i)]$$

$$D_k = \frac{[1 + (\delta_{LT} + \delta_{ST})z_{k-1}/R_{k-1}]}{[1 + (\delta_{LT} + \delta_{ST})z_k/R_k]}D_{k-1}, \ D_1 = 1$$
(20)

$$F_k = D_k \sum_{i=2}^{k}(E_i/D_i), \ F_1 = 0$$

$$E_k = [1 + (\delta_{LT} + \delta_{ST})z_{k-1}/R_k]^{-1}[C_{k-1}f_{2,k-1}(z_k)$$
$$- C_k f_{2k}(z_k)]$$

Inserting finally eqns (17)-(20) into eqns (15) yields the shell displacement approximations in the following form:

$$U_k(x,s,z;t) = u_{01} - zw_{,x} + [A_k f_{1k}(k) + B_k]u_{11}$$

$$V_k(x,s,z;t) = [1 + (\delta_{LT} + \delta_{ST})z/R_1]v_{01} - zw_{,s}$$
$$+ \{[1 + (\delta_{LT} + \delta_{ST})z/R_k]F_k$$
$$+ C_k f_{2k}(z)\}v_{11}$$
(21)

$$W_k(x,s,z;t) = w(x,s;t)$$

Hence, independently of the chosen forms of the shape functions f_{1k} and f_{2k} $(k = 1,2,...,N)$, a displacement approximation of the form (21) guarantees the desired continuity of both displacements and transverse shear stresses throughout the laminated shell thickness.

Under the present considerations $(R = R_1)$, a comparison of eqns (21) with the displacement approximations (2)–(4) yields,

$$\varphi_1(z) = [A_k f_{1k}(z) + B_k]$$

$$\varphi_2(z) = [1 + (\delta_{LT} + \delta_{ST})z/R_k]F_k + C_k f_{2k}(z) \qquad (22)$$

which relate the present refined displacement approximation to the unified shell theory presented in the preceding section. Inserting these forms of φ_1 and φ_2 in definitions (9d) and (12b), as well as their derivatives in definitions (9c), the constitutive equations and, therefore, the left-hand-sides of the five differential equations of motion (10) of the present unified shell theory can be expressed in terms of the same number of main unknown functions, u_{01}, u_{11}, v_{01}, v_{11} and w, and their derivatives with respect to the spatial coordinates. In such a case, u_{01}, u_{11}, v_{01}, v_{11} must also be inserted in place of the corresponding displacement functions appearing in eqns (11).

4 CLOSURE

A displacement based theory suitable for the static and dynamic analysis of transverse shear deformable circular cylindrical shells constructed of a homogeneous or a laminated composite elastic material has been presented. By introducing into the shell displacement approximation certain general functions of the transverse coordinate, which account for the incorporation of the transverse shear deformation effects, the present formulation has effectively resulted in a theoretical unification of most of the variationally consistent classical and shear deformable cylindrical shell theories available in the literature.

In more detail, the classical Donnell-, Love- and Sanders-type shell theories as well as their well known uniform and parabolic shear deformable analogues were obtained as particular cases of the proposed formulation. Moreover, having left the forms of the aforementioned 'shear deformation shape functions' unspecified, this formulation left open further possibilities for a multiple, a-posteriori specification of particular shear deformable shell theories. In particular, the generalized 'zig-zag' displacement model produced, as an application of the present analysis, gives further multiple freedom in achieving continuous distributions of interlaminar stresses through the thickness of an unsymmetric cross-ply laminated cylindrical shell.

For the free vibration problem of certain symmetric cross-ply laminated cylindrical shells, numerical results obtained on the basis of the present unified shell theory are presented in Ref. 21, for several choices of the shear deformation shape functions. These are also compared with corresponding numerical results obtained and tabulated in Ref. 22 on the basis of several two-dimensional shell theories, as well as with corresponding results based on an exact, three-dimensional vibration analysis.[23,24] According to the numerical comparisons made in Ref. 21, employing a linear form for the shape functions f_{1k} and f_{2k} introduced in the preceding section $(k = 1, 2, \ldots, N)$ yields essentially the values and corresponding wave numbers of all fundamental vibration frequencies obtained in Ref. 22 on the basis of Di Sciuva[11] shell theory. Moreover, it is further shown[21] that certain non-linear choices[9] of those shape functions lead to frequency predictions which are even closer to the corresponding exact frequencies of vibration.[24]

REFERENCES

1. Soldatos, K. P., A comparison of some shell theories used for the dynamic analysis of cross-ply laminated circular cylindrical panels. *J. Sound Vib.*, **97** (1984) 305–19.
2. Dong, S. B. & Tso, F. K. W., On a laminated orthotropic shell theory including transverse shear deformation. *J. Appl. Mech.*, **39** (1972) 1091–7.
3. Sinha, P. K. & Rath, A. K., Vibrations and buckling of cross-ply laminated circular cylindrical panels. *Aeron. Quart.*, **26** (1976) 211–18.
4. Hsu, Y. S., Reddy, J. N. & Bert, C. W., Thermoelasticity of circular cylindrical shells of laminated composite materials. *J. Thermal Stresses*, **4** (1981) 155–77.
5. Bhimaraddi, A., A higher-order theory for free vibration analysis of circular cylindrical shells. *Int. J. Solids Struct.*, **20** (1984) 623–30.
6. Reddy, J. N., A higher-order shear deformation theory of laminated elastic shells. *J. Appl. Mech.*, **51** (1984) 319–30.
7. Soldatos, K. P., Free vibration analysis of thickness shear deformable cross-ply laminated oval cylindrical shells. *Lect. Notes Engng*, **28** (1986) 324–32.
8. Soldatos, K. P., A refined laminated plate and shell theory with applications. *J. Sound Vib.*, **144** (1991) 109–29.
9. Soldatos, K. P., A transverse shear deformation theory for homogeneous monoclinic plates. *Acta Mech.*, **94** (1992) 195–220.
10. Touratier, M., A refined theory of laminated shallow shells. *Int. J. Solids Struct.*, **29** (1992) 1401–15.
11. Di Sciuva, M., An improved shear-deformation theory for moderately thick multilayered anisotropic shells and plates. *J. Appl. Mech.*, **54** (1987) 589–96.
12. Lee, K. H., Xavier, P. B. & Chew, C. H., Static response of unsymmetric sandwich beams using an improved zig-zag model. *Compos. Engng*, **3** (1993) 235–48.

13. Lee, K. H., Senthilnathan, N. R., Lim, S. P. & Chow, S. T., An improved zig-zag model for the bending of laminated composite plates. *Compos. Struct.*, **15** (1990) 137-48.

14. Savithri, S. & Varadan, T. K., Free vibration and stability of cross-ply laminated plates. *J. Sound Vib.*, **141** (1990) 516-20.

15. Savithri, S. & Varadan, T. K., Accurate bending analysis of laminated orthotropic plates. *AIAA J.*, **28** (1990) 1842-4.

16. Cho, M. & Parmerter, R. R., An efficient higher-order plate theory for laminated composites. *Compos. Struct.*, **20** (1992) 113-23.

17. Soldatos, K. P., A general laminated plate theory accounting for continuity of displacements and transverse shear stresses at material interfaces. *Compos. Struct.*, **20** (1992) 195-211.

18. Soldatos, K. P., Vectorial approach for the formulation of variationally consistent higher-order plate theories. *Compos. Engng.* **3** (1993) 3-17.

19. Soldatos, K. P., A four-degree-of-freedom cylindrical shell theory accounting for both transverse shear and transverse normal deformation. *J. Sound Vib.*, **159** (1992) 533-9.

20. Sokolnikoff, I. S., *Mathematical Theory of Elasticity.* McGraw-Hill, New York, 1956.

21. Soldatos, K. P. & Timarci, T., Vibrations of laminated composite cylindrical shells on the basis of a unified five-degrees-of-freedom theory. *Proc. 9th Int. Conf. Comp. Mater.*, Madrid, Spain, July 12-16, 1993.

22. Di Sciuva, M. & Carrera, E., Elastodynamic behavior of relatively thick, symmetrically laminated, anisotropic cylindrical shells. *J. Appl. Mech.*, **59** (1992) 222-4.

23. Soldatos, K. P. & Hadjigeorgiou, V. P., Three-dimensional solution of the free vibration problem of homogeneous isotropic cylindrical shells and panels. *J. Sound Vib.*, **137** (1990) 369-84.

24. Ye, J. Q. & Soldatos, K. P., Three-dimensional vibrations of laminated cylinders and cylindrical panels with a symmetric or an antisymmetric cross-ply lay-up. *Compos. Engng* (submitted).

Nonlinear analysis of laminated composite plates and shells including the effects of shear and normal deformation

V. E. Verijenko

Department of Mechanical Engineering, University of Natal, Durban 4001, South Africa

A nonlinear higher-order theory for laminated composite plates and shells with an arbitrary number and sequence of layers is presented. The theory takes into account both transverse shear and normal deformation and considers the elasto-plastic behaviour of the composite materials. The results presented illustrate first the importance of modelling the nonlinear behaviour of the material especially at high levels of loading, and secondly the importance of modelling both transverse shear and normal compression.

1 INTRODUCTION

The motivation for the current investigation arises from the fact that most engineering materials exhibit nonlinear stress–strain behaviour even at moderately low strains. Moreover it is well-known[1-4] that in the analysis of laminated composite structures, the use of the classical theory based on the Kirchoff–Love assumptions leads to substantial errors. Although numerous approaches have been suggested[3-5] to refine classical theory, the analysis of laminated structures with nonlinear stress–strain relations on the basis of higher-order theories has not been developed sufficiently.

In the present study the basic equations of a nonlinear higher-order theory for transversely isotropic laminated plates and shells are presented. This theory is based on the kinematic hypotheses which are not assumed *a priori* but are derived on the basis of an iterative technique. Material nonlinearity is included at the initial stage of the derivation of the theory when the kinematic hypotheses are formulated. This approach leads to a comprehensive consideration of material nonlinearity in the higher-order theory.

The nonlinear theory presented in this study is capable of treating laminated plates and shells with an arbitrary number and sequence of layers, and takes into account transverse shear and normal deformation. Numerical results illustrate that the influence of transverse shear and normal deformation is more pronounced in nonlinear analysis of laminated structures than it is in linear analysis.

2 DERIVATION OF THE KINEMATIC HYPOTHESES

The derivation of the nonlinear higher-order theory of plates and shells is based on kinematic hypotheses which reduce a three-dimensional problem in the theory of plasticity into a two-dimensional problem in the theory of plates and shells. The theory of plastic deformations of composite materials presented by Pobedrya[6] is employed in this study. In this theory, Lagrange's and Castiliano's principles are valid and the quasi-static problem may be solved efficiently using the method of elastic solutions.[7] This method is mathematically analogous to the extended Kantorovich method and exhibits good convergency.

The equations of the theory of plasticity for a transversely isotropic continuum may be expressed in a conventional form. The stress–strain relationship is given by

$$e'^k_{11} = \frac{1-v_k}{E_k} \frac{\sigma^k_{11}+\sigma^k_{22}}{2} - \frac{v'_k}{E'_k} \sigma^k_{33} + \frac{p_k}{P_k} \frac{\sigma^k_{11}-\sigma^k_{22}}{2}$$

$$e^k_{22} \rightleftharpoons e^k_{11} : \quad e^k_{33} = -\frac{v'_k}{E_k}(\sigma^k_{11}-\sigma^k_{22}) + \frac{1}{E_k} \sigma^k_{33}$$

$$e'^k_{12} = \frac{p_k}{P_k} \sigma^k_{12} ; \quad e^k_{13} = \frac{q_k}{Q_k} \sigma^k_{13} ; \quad e'^k_{23} = \frac{q_k}{Q_k} \sigma'^k_{23} \tag{1}$$

where the symbol $\rightleftharpoons$ indicates that the expression for e_{22} is of the same form as that for e_{11} with the provision that the subscript 11 is replaced with 22 and vice versa. A superscript or subscript k refers to the kth layer. Also, E_k and v_k are modulus of elasticity and Poisson's ratio in the plane of isotropy, and E'_k and v'_k are the corresponding constants in the transverse direction.

The 'secant' shear moduli for the kth layer are

$$\bar{G}_k = P_k/2p_k = G_k(1-\pi_k)$$

$$\bar{G}'_k = Q_k/2q_k = G'_k(1-\kappa_k) \tag{2}$$

where $G_k = E_k/2(1+v_k)$ and G'_k are the initial 'tangent' shear moduli and $\pi_k(p_k)$ and $\kappa_k(q_k)$ are plasticity functions which are zero if the material remains linearly elastic.

The 'secant' moduli may be found using the generalized stresses and strains,[b] viz.

$$P_k = \frac{\sqrt{2}}{2} \sqrt{(\sigma^k_{11}-\sigma^k_{22})^2 + 4(\sigma^k_{12})^2}$$

$$Q_k = \sqrt{(\sigma^k_{13})^2 + (\sigma^k_{23})^2} \tag{3}$$

and

$$p_k = \frac{\sqrt{2}}{2} \sqrt{(e^k_{11}-e^k_{22})^2 + 4(e^k_{12})^2}$$

$$q_k = \sqrt{(e^k_{13})^2 + (e^k_{23})^2} \tag{4}$$

Using eqn (2), π_k and κ_k may be expressed as

$$\pi_k = 1 - \frac{P_k}{2p_kG_k} ; \qquad \kappa_k = 1 - \frac{Q_k}{2q_kG'_k} \tag{5}$$

Clearly the plasticity functions π_k and κ_k defined in eqn (5) are functions of the stress and strain state of the kth layer. Therefore, the 'secant' moduli are also functions of the stress and strain state, viz. $\bar{G}_k = \bar{G}_k(x,z)$, $\bar{G}'_k = \bar{G}'_k(x,z)$.

The kinematic hypotheses are now derived using the above equations of the theory of plasticity. A laminated shell is defined in a curvilinear coordinate system x_1Ox_2 (see Fig. 1). The axes of the curvilinear orthogonal coordinates $x_i = $ constant $(i = 1,2)$ coincide with the principal lines of curvature and the coordinate $z = x_3$ is perpendicular to the reference surface x_1Ox_2 which is positioned arbitrarily in the sequence of layers. The shell is constructed of transversely isotropic elastic or elasto-plastic materials. The loads applied on the outer and inner surfaces $p^+ = p_s^+(x)$, $p^- = p_s^-(x)$ $(s = 1,2,3)$ are functions of the curvilinear orthogonal coordinates $x = \{x_1,x_2\}$.

In the following derivation a subscript after a comma denotes differentiation with respect to the variables following the comma.
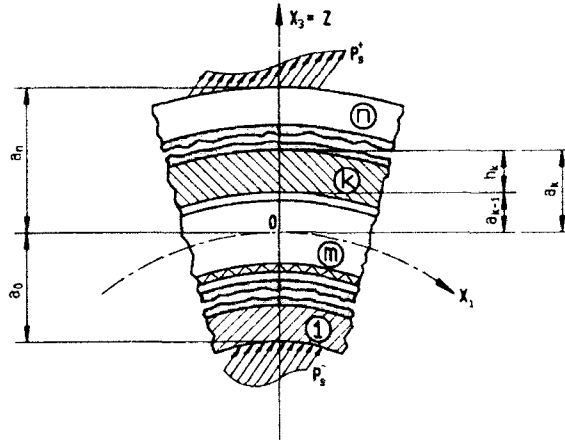
Fig. 1. Geometry of a laminated shell.

The loading conditions on the external surfaces $z = a_0$ and $z = a_n$ are written as

$$\sigma_{3}^{1} = -p_{s}^{-} \qquad (z = a_0, k = 1)$$

$$\sigma_{3}^{n} = p_{s}^{-} \qquad (z = a_n, k = n) \tag{6}$$

The layers are assumed to be rigidly bonded and the rigidity conditions for an arbitrary surface $z = a_{k-1}$ are given by

$$\sigma_{3}^{k} = \sigma_{3}^{k-1} \qquad \text{(static)}$$

$$u_{s}^{k} = u_{s}^{k-1} \qquad \text{(kinematic)} \tag{7}$$

In order to derive a higher-order theory for the stress and strain analysis of the multilayered shell described above, a model based on classical hypotheses must be derived in the first instance. Therefore eqns (1) are rewritten taking into account eqns (2) and assuming that $E_k' = G_k' = \infty$, viz.

$$e_{11}^{k} = \frac{1}{2G_k} \left(\frac{1 - \nu_k}{1 + \nu_k} \frac{\sigma_{11}^{k} + \sigma_{22}^{k}}{2} + \frac{1}{1 - \pi_k} \frac{\sigma_{11}^{k} - \sigma_{22}^{k}}{2} \right)$$

$$e_{22}^{k} \rightleftharpoons e_{11}^{k}; \quad e_{33}^{k} = 0$$

$$e_{12}^{k} = \frac{1}{2G_k(1 - \pi_k)} \sigma_{12}^{k}; \qquad e_{13}^{k} = 0; \qquad e_{23}^{k} = 0 \tag{8}$$

The tangential components of the stress tensor are determined using eqns (8) as

$$\sigma_{11}^{k} = \frac{2G_k}{1 - \nu_k} (e_{11}^{k} + \nu_k e_{22}^{k}) - G_k \pi_k (e_{11}^{k} - e_{22}^{k})$$

$$\sigma_{22}^{k} \rightleftharpoons \sigma_{11}^{k}; \qquad \sigma_{12}^{k} = 2G_k(1 - \pi_k)e_{12}^{k} \tag{9}$$

The linear and nonlinear terms in eqns (9) for the stresses are

$$\sigma_{11}^{k} = \frac{2G_k}{1 - \nu_k} (e_{11}^{k} + \nu_k e_{22}^{k})$$

$$\sigma_{22}^{k} \rightleftharpoons \sigma_{11}^{k}; \qquad \sigma_{12}^{k} = \frac{2G_k}{1 - \nu_k} (1 - \nu_k)e_{12}^{k} \tag{10}$$

and

$$\bar{\sigma}_{11}^{k} = 2 G_{k} \frac{\bar{e}_{11}^{k} - \bar{e}_{22}^{k}}{2}; \qquad \bar{\sigma}_{22}^{k} = \bar{\sigma}_{11}^{k}; \qquad \bar{\sigma}_{12}^{k} = 2 G_{k} \bar{e}_{12}^{k} \tag{11}$$

where $\bar{e}_{ij}^{k} = -\pi_{k} e_{ij}^{k}$ $(i,j = 1,2)$.

Equations (9) now may be rewritten as

$$\hat{\sigma}_{ij}^{k} = \sigma_{ij}^{k} + \bar{\sigma}_{ij}^{k}; \qquad i,j = 1,2 \tag{12}$$

For the derivation of the other components of the stress tensor, the equations of equilibrium of a shell[8] are considered and for the kth layer are

$$\sigma_{ij,j}^{k} + \sigma_{i3,3}^{k} = 0$$
$$\sigma_{33,3}^{k} + \sigma_{i3,i}^{k} - k_{ij}\sigma_{ij}^{k} = 0 \tag{13}$$

where k_{ij} are curvatures of the shell.

From eqns (12) and (13), the transverse shear stresses may be derived as

$$\sigma_{i3}^{k} = \sigma_{i3}^{k} + \bar{\sigma}_{i3}^{k} = -\left[\int_{a_{k-1}}^{z} \sigma_{ij,j}^{k}\, \mathrm{d}z + \int_{a_{k-1}}^{z} \bar{\sigma}_{ij,j}^{k}\, \mathrm{d}z \right] + \Phi_{ik} \tag{14}$$

where the constants of integration $\Phi_{ik} = \bar{\Phi}_{ik} + \breve{\Phi}_{ik}$ are obtained using eqns (6) and (7).

The linear components of the stresses in eqns (14) are determined by substituting eqns (10) and following the procedure described by Piskunov *et al.*,[9] viz.

$$\sigma_{i3}^{k} = \nabla w_{,i} f_{1k} + p_{i}^{-} f_{2k} + p_{i}^{+} f_{3k} \tag{15}$$

where ∇ is the Laplace operator; p_{i}^{-}, p_{i}^{+} are given functions of the external load; and $f_{sk}(z)$ $(s = 1,2,3)$ are functions which enable the given conditions on the external surfaces of the shell to be satisfied once the reference surface has been positioned arbitrarily through the sequence of the layers.

The functions f_{sk} are given by

$$f_{1k}(z) = f_{k}^{*} - f_{k} B_{1} B^{-1}; \qquad f_{2k}(z) = f_{k} B^{-1} - 1; \qquad f_{3k}(z) = f_{k} B^{-1}$$

$$f_{k}(z) = \int_{a_{0}}^{z} E_{0k}\, \mathrm{d}z; \qquad f_{k}^{*}(z) = \int_{a_{0}}^{z} E_{0k} z\, \mathrm{d}z$$

$$B = \int_{a_{0}}^{a_{n}} E_{0k}\, \mathrm{d}z; \qquad B_{1} = \int_{a_{0}}^{a_{n}} E_{0k} z\, \mathrm{d}z \tag{16}$$

where $E_{0k} = 2 G_{k}/(1 - \nu_{k})$.

The nonlinear components of the transverse shear stresses are defined as

$$\bar{\sigma}_{13}^{k} = -[\nabla w_{,1} \bar{f}_{1k} + (w_{,11} - w_{,22})\bar{f}_{2k} + 2 w_{,12}\bar{f}_{3k}]$$
$$\bar{\sigma}_{23}^{k} = -[\nabla w_{,2} \bar{f}_{1k} + 2 w_{,21}\bar{f}_{2k} + (w_{,22} - w_{,11})\bar{f}_{3k}] \tag{17}$$

where

$$\bar{f}_{1k}(x,z) = -\left(\int_{a_{0}}^{z} G_{k}\pi_{k} z\, \mathrm{d}z - \frac{B_{1}}{B} \int_{a_{0}}^{z} G_{k}\pi_{k}\, \mathrm{d}z \right)$$

$$\bar{f}_{2k}(x,z) = -\left(\int_{a_{0}}^{z} G_{k}\pi_{k,1} z\, \mathrm{d}z - \frac{B_{2}}{B} \int_{a_{0}}^{z} G_{k}\pi_{k,1}\, \mathrm{d}z \right)$$

$$\bar{f}_{3k}(x,z) = -\int_{a_0}^{z} G_k \pi_{k,2} z \, dz - \frac{\bar{B}_3}{\bar{B}} \int_{a_0}^{z} G_k \pi_{k,2} \, dz \Big)$$

$$\bar{B}_1 = \int_{a_0}^{a_n} G_k \pi_k z \, dz; \qquad \bar{B}_2 = \int_{a_0}^{a_n} G_k \pi_{k,1} z \, dz$$

$$\bar{B}_3 = \int_{a_0}^{a_n} G_k \pi_{k,2} z \, dz; \qquad \bar{B} = \int_{a_0}^{a_n} G_k \, dz \qquad (18)$$

Now the transverse shear stresses in eqns (14) may be rewritten as

$$\sigma_{13}^{(k)} = -\nabla w_{,1}(\bar{f}_{1k} - f_{1k}) + p_1^- f_{2k} + p_1^+ f_{3k} - (w_{,11} - w_{,22})\bar{f}_{2k} - 2w_{,12}\bar{f}_{3k}$$

$$\sigma_{23}^{(k)} = -\nabla w_{,2}(\bar{f}_{1k} - f_{1k}) + p_2^- f_{2k} + p_2^+ f_{3k} - 2w_{,21}\bar{f}_{2k} - (w_{,22} - w_{,11})\bar{f}_{3k} \qquad (19)$$

Substituting eqns (19) into the second equation of (13) the transverse normal stresses are derived as

$$\sigma_{33}^{(k)} = \sigma_{33}^{(k)} + \bar{\sigma}_{33}^{(k)}$$

$$= -\left[\int_{a_{k-1}}^{z} (\sigma_{i3,i}^{(k)} - k_{ij}\sigma_{ij}^{(k)}) \, dz - \int_{a_{k-1}}^{z} (\bar{\sigma}_{i3,i}^{(k)} - k_{ij}\bar{\sigma}_{ij}^{(k)}) \, dz \right] + \Phi_{3k} \qquad (20)$$

where the constants of integration $\Phi_{3k} = \bar{\Phi}_{3k} + \bar{\bar{\Phi}}_{3k}$ are determined using eqns (6) and (7).

The linear component of eqn (20) is obtained as[9]

$$\sigma_{33}^{(k)} = p_{i,i}^- f_{4k} + p_{i,i}^+ f_{5k} + p_3^- f_{6k} + p_3^+ f_{7k} + B_\sigma \qquad (21)$$

where p_3^-, p_3^+ are known functions of the normal components of the external loading and the function B_σ is given by

$$B_\sigma = B_\sigma(x,z) = k_{ij}\varepsilon_{ij}f_{8k} + k_{ij}\kappa_{ij}f_{9k} + (k_{11}\varepsilon_{22} - 2k_{12}\varepsilon_{12} + k_{22}\varepsilon_{11})f_{8k} + (k_{11}\kappa_{22} - 2k_{12}\kappa_{12} + k_{22}\kappa_{11})\bar{f}_{9k} \qquad (22)$$

where ε_{ij}, κ_{ij} are the deformations of the reference surface which may be expressed as

$$\varepsilon_{ij} = \tfrac{1}{2}(u_{i,j} + u_{j,i}) + k_{ij}w$$

$$\kappa_{ij} = -w_{,ij} \qquad (23)$$

The distribution functions of the transverse shear stress through the thickness of the laminated shell are given by

$$f_{4k}(z) = F_{1k}D_2 D_1^{-1} - F_{2k}; \qquad f_{5k}(z) = F_{1k}D_3 D_1^{-1} - F_{3k}$$

$$f_{6k}(z) = F_{1k}D_1^{-1} - 1; \qquad f_{7k}(z) = F_{1k}D_1^{-1}$$

$$f_{8k}(z) = f_k - F_{1k}BD_1^{-1}; \qquad f_{9k}(z) = f'_{1k} - F_{1k}B_1 D_1^{-1}$$

$$\bar{f}_{9k}(z) = \bar{f}'_k - F_{1k}B'_1 D_1^{-1}; \qquad F_{sk}(z) = \int_{a_0}^{z} f_{sk} \, dz$$

$$D_s = \int_{a_0}^{a_n} f_{sk} \, dz; \qquad f_{1k}(z) = \int_{a_0}^{z} E_{0k} \nu_k \, dz; \qquad \bar{f}'_k(z) = \int_{a_0}^{z} E_{0k} \nu_k z \, dz$$

$$\bar{B} = \int_{a_0}^{a_n} E_{0k} \nu_k \, dz; \qquad B'_1 = \int_{a_0}^{a_n} E_{0k} \nu_k z \, dz; \qquad s = 1,2,3 \qquad (24)$$

The nonlinear component of eqn (20) may be expressed as

$$\bar{\sigma}_{33}^{(k)} = \nabla w_{,1}\bar{f}_{4k} + \nabla w_{,2}\bar{f}_{5k} + 2w_{,12}\bar{f}_{6k} + (w_{,11} - w_{,22})\bar{f}_{7k} + \bar{B}_\sigma \qquad (25)$$

where

$$\bar{f}_{4k}(x,z) = \bar{F}_{2k} - \frac{\bar{D}_2}{\bar{D}_1}\bar{F}_{1k}; \qquad \bar{f}_{5k}(x,z) = \bar{F}_{3k} - \frac{\bar{D}_3}{\bar{D}_1}\bar{F}_{1k}$$

$$\bar{f}_{6k}(x,z) = \bar{F}_{4k} - \frac{\bar{D}_4}{\bar{D}_1}\bar{F}_{1k}; \qquad \bar{f}_{7k}(x,z) = \bar{F}_{5k} - \frac{\bar{D}_5}{\bar{D}_1}\bar{F}_{1k}$$

$$\bar{B}_o(x,z) = \bar{F}_{ok} - \frac{\bar{D}_o}{\bar{D}_1}\bar{F}_{1k}$$

$$\bar{F}_{pk}(x,z) = \int_{a_0}^{z} f^*_{pk}\, dz; \qquad p = 1,\dots,5$$

$$\bar{F}_{ok}(x,z) = \int_{a_0}^{z} k_{ij}\bar{\sigma}_{ij}^{k}\, dz; \qquad i,j = 1,2$$

$$\bar{f}_{ok} = \int_{a_{k-1}}^{z} k_{ij}\bar{\sigma}_{ij}^{k}\, dz; \qquad f^*_{1k}(x,z) = \bar{f}_{1k}; \qquad f^*_{2k}(x,z) = \bar{f}_{2k} + \bar{f}_{1k,1}$$

$$f^*_{3k}(x,z) = \bar{f}_{3k} + \bar{f}_{1k,2}; \qquad f^*_{4k}(x,z) = \bar{f}_{2k,2} + \bar{f}_{3k,1}; \qquad f^*_{5k}(x,z) = \bar{f}_{2k,1} - \bar{f}_{3k,2} \qquad (26)$$

The general equation for transverse normal stress may be written as

$$\sigma_{33}^{k} = p_{i,i}^{-}f_{4k} + p_{i,i}^{-}f_{5k} + p_3^{-}f_{6k} + p_3^{+}f_{7k} + \nabla w_{,1}\bar{f}_{4k} + \nabla w_{,2}\bar{f}_{5k} + 2\nabla w_{,12}\bar{f}_{6k} + (w_{,11} - w_{,22})\bar{f}_{7k} + B_o + \bar{B}_o \qquad (27)$$

Kinematic hypotheses are now formulated for the derivation of a nonlinear higher-order theory. According to the procedure described by Piskunov et al.,[9] eqns (10) and (11) for the stresses σ_{ij}^{k}, and eqn (27) for σ_{33}^{k} are substituted into eqn (1) for e_{33}^{k}. Then we may write

$$e_{33}^{k} = e_{33}^{k} + \bar{e}_{33}^{k} = \nabla w a_{1k} + u_{i,i}a_{2k} + p_{i,i}^{-}a_{3k} + p_{i,i}^{-}a_{4k} + p_3^{-}a_{5k} + p_3^{+}a_{6k} + B_o' + \nabla w_{,1}\bar{a}_{3k} + \nabla w_{,2}\bar{a}_{4k}$$
$$+ 2w_{,12}\bar{a}_{5k} + (w_{,11} - w_{,22})\bar{a}_{6k} + \bar{B}_o' \qquad (28)$$

where

$$a_{1k}(z) = v_{0k}'z; \qquad a_{2k}(z) = -v_{0k}'$$

$$\bar{a}_{qk}(z) = \bar{f}_{qk}/E_k'; \qquad a_{qk}(z) = f_{qk}/E_k'; \qquad q = 3,\dots,6; \qquad g = q + 1$$

$$B_o' = B_o/E_k'; \qquad \bar{B}_o' = \bar{B}_o/E_k'; \qquad v_{0k}' = E_k v_k'/E_k'(1 - v_k) \qquad (29)$$

Since $e_{33}^{k} = u_{3,3}^{k}$, the normal components of the displacement vector are obtained from eqn (28)

$$u_3^{k}(x,z) = w(x) + \int_{a_{k-1}}^{z} (e_{33}^{k} + \bar{e}_{33}^{k})\, dz + C_{3k} \qquad (30)$$

where the constants of integration C_{3k} may be determined from eqn (7) and the condition that $u_3^{m}(x,0) = w(x)$ for $z = 0$ ($k = m$).

Equation (30) may now be rewritten as

$$u_3^{k}(x,z) = w + \nabla w\varphi_{1k} + u_{i,i}\varphi_{2k} + p_{i,i}^{-}\varphi_{3k} + p_{i,i}^{+}\varphi_{4k} + p_3^{-}\varphi_{5k} + p_3^{+}\varphi_{6k} + \nabla w_{,1}\bar{\varphi}_{3k} + \nabla w_{,2}\bar{\varphi}_{4k} + 2w_{,12}\bar{\varphi}_{5k}$$
$$+ (w_{,11} - w_{,22})\bar{\varphi}_{6k} + C_o + \bar{C}_o \qquad (31)$$

where the distribution functions of the normal displacement through the thickness of the laminated shell are given by

$$\varphi_{qk}(z) = \int_0^z \alpha_{qk}\, dz; \qquad q = 1,\ldots,6$$

$$\bar{\varphi}_{qk}(x,z) = \int_0^z \bar{\alpha}_{qk}(x,z)\, dz; \qquad q = 3,\ldots,6$$

$$C_o = \int_0^z B'_o\, dz; \qquad C_o = \int_0^z B'_o\, dz; \qquad B'_o = B_o / E'_k \tag{32}$$

The tangential components of the displacement vector may be found from

$$u_{i,3}^k = 2e_{i3}^k - u_{3,i}^k \tag{33}$$

in conjunction with eqns (1), (2) and (19).

The shear deformations are given by

$$2e_{13}^k = \sigma_{13}/\bar{G}'_i = \nabla w_{,1}\varphi_k - p_1^- \varphi_{7k} - p_1^- \varphi_{8k} + \nabla w_{,1}\bar{\varphi}_k - (w_{,11} - w_{,22})\bar{\varphi}_{7k} - 2w_{,12}\bar{\varphi}_{8k}$$

$$2e_{23}^k = \sigma_{23}^k/\bar{G}'_k = \nabla w_{,2}\varphi_k - p_2^- \varphi_{7k} - p_2^- \varphi_{8k} + \nabla w_{,2}\bar{\varphi}_k - 2w_{,21}\bar{\varphi}_{7k} - (w_{,22} - w_{,11})\bar{\varphi}_{8k} \tag{34}$$

where

$$\varphi_k(x,z) = f_{1k}/\bar{G}'_k; \qquad \varphi_{7k}(x,z) = -f_{2k}/\bar{G}'_k; \qquad \varphi_{8k}(x,z) = -f_{3k}/\bar{G}'_k$$

$$\bar{\varphi}_k(x,z) = -\bar{f}_{1k}/\bar{G}'_k; \qquad \bar{\varphi}_{7k}(x,z) = \bar{f}_{2k}/\bar{G}'_k; \qquad \bar{\varphi}_{8k}(x,z) = -\bar{f}_{3k}/\bar{G}'_k \tag{35}$$

By substituting eqn (34) into eqn (33) and then integrating, the tangential components of the displacement vector are derived as

$$u_i^k = u_i - w_i z - \nabla w_i \varphi_{1k} - u_{i,t}\varphi_{2k} - p_{i,tt}\varphi_{3k} - p_{i,tt}\varphi_{4k} - p_{3,t}\varphi_{5k} - p_{3,t}\varphi_{6k} - p_1^- \varphi_{7k} - p_2^- \varphi_{8k} - \nabla w_{,i}\bar{\varphi}_{1ki}$$

$$- \nabla w_{,i}\bar{\varphi}_{2ki} - \nabla w_{,tt}\bar{\varphi}_{3k} - \nabla w_{,2i}\bar{\varphi}_{4k} - 2w_{,12i}\varphi_{5k} - (w_{,11} - w_{,22})_{,i}\varphi_{6k} - p_{1i}\bar{\varphi}_{7ki} - p_{2i}\bar{\varphi}_{8ki} - \Phi_o$$

$$i,j,t = 1,2; \qquad t \neq i \tag{36}$$

where

$$p_{11} = w_{,11} - w_{,22}; \qquad p_{12} = 2w_{,12}; \qquad p_{21} = 2w_{,21}; \qquad p_{22} = w_{,22} - w_{,11} \tag{37}$$

and

$$\psi_{1k}(x,z) = \int_0^z (\varphi_{1k} - \varphi_k)\, dz; \qquad \psi_{qk}(z) = \int_0^z \varphi_{qk}\, dz, \qquad q = 2,\ldots,6$$

$$\bar{\psi}_{gk}(x,z) = \int_0^z \varphi_{gk}\, dz, \qquad g = 7,8; \qquad \bar{\psi}_{2k1}(x,z) = \int_0^z \bar{\varphi}_{4k,1}\, dz$$

$$\bar{\psi}_{1k1}(x,z) = \int_0^z (\bar{\varphi}_{3k,1} - \bar{\varphi}_k)\, dz; \qquad \bar{\psi}_{qk}(x,z) = \int_0^z \bar{\varphi}_{qk}\, dz \qquad q = 3,\ldots,6$$

$$\bar{\psi}_{7k1}(x,z) = \int_0^z (\bar{\varphi}_{7k} + \bar{\varphi}_{6k,1})\, dz; \qquad \bar{\psi}_{8k1}(x,z) = \int_0^z (\bar{\varphi}_{8k} + \bar{\varphi}_{5k,1})\, dz$$

$$\psi_{1k2}(x,z) = \int_0^z (\bar{\varphi}_{4k,2} - \bar{\varphi}_k)\, dz; \qquad \psi_{2k2}(x,z) = \int_0^z \bar{\varphi}_{3k,2}\, dz$$

$$\bar{\psi}_{7k2}(x,z) = \int_0^z (\bar{\varphi}_{7k} + \bar{\varphi}_{5k,2})\, dz; \qquad \bar{\psi}_{8k2}(x,z) = \int_0^z (\bar{\varphi}_{8k} + \bar{\varphi}_{6k,2})\, dz$$

$$\Phi_o(x,z) = \int_0^z (C_{o,1} + \bar{C}_{o,2})\, dz \tag{38}$$

The above equations for e_{i3}^{k}, e_{33}^{k} and σ_{i3}^{k}, σ_{33}^{k} and eqns (36) and (31) are not relevant to the model based on the classical hypotheses since they only demonstrate the contradictions in this model, but are important for the derivation of a higher-order theory.

3 NONLINEAR HIGHER-ORDER THEORY

The derivation of a nonlinear higher-order theory of laminated plates and shells is based on kinematic hypotheses. Using eqns (31) and (36) these hypotheses are formulated as

$$u_i^k = u_i - w_{,i}z - x_{1,i}\psi_{1k} - x_{2,i}\psi_{2k} - x_{q,i}\psi_{qk} - x_{g,i}\psi_{gk} - \lambda_{1,i}\bar{\psi}_{1ki} - \lambda_{2,i}\bar{\psi}_{2ki} - \lambda_{q,i}\bar{\varphi}_{qk} - \lambda_{g,i}\psi_{gki}$$

$$i = 1,2; \qquad q = 3,...,6; \qquad g = 7,8$$

$$u_3^k = w + x_1\varphi_{1k} + x_2\varphi_{2k} + x_q\varphi_{qk} + \lambda_q\bar{\varphi}_{qk} \qquad q = 3,...,6 \tag{39}$$

where $u_i(x)$, $w(x)$ are unknown displacements of the reference surface, and $x_1(x)$, $x_2(x)$ are new unknown functions. The first of these functions, $x_1(x)$, is termed the 'shear function' and the second, $x_2(x)$, the 'compression function'.[9,10] In eqns (39) we also have

$$x_3(x) = p_{i,i}^{-}; \qquad x_4(x) = p_{i,i}^{+}; \qquad x_5(x) = p_3^{-}$$

$$x_6(x) = p_3^{+}; \qquad x_7(x) = p_i^{-}; \qquad x_{8i}(x)p_i^{+} \tag{40}$$

which may be determined directly from the given external loading. The distribution functions in eqns (39) are given in eqns (38).

In eqns (39) we also use the following notations for the given functions

$$\lambda_{1,i} = \nabla w_{0,i}; \qquad \lambda_{2,i} = \nabla w_{0,i}; \qquad \lambda_{3,i} = \nabla w_{0,1i}$$

$$\lambda_{4,i} = \nabla w_{0,2i}; \qquad \lambda_{5,i} = 2w_{0,12i}; \qquad \lambda_{6,i} = (w_{0,11} - w_{i,22})_i$$

$$\lambda_{7,i} = p_{1i}; \qquad \lambda_{8,i} = p_{2i}; \qquad i,t = 1,2; \qquad i \neq t \tag{41}$$

where $w_0(x)$ is a known function of the deflection determined from the solution obtained using the model based on the classical hypotheses. The solution of the 'nonclassical part' involves the determination of the unknown functions u_i, w, x_1 and x_2. The other functions in eqns (39) are known and are functions of the external load or of the 'classical part' of the solution.

Using the kinematic model (39) and Cauchy's equations, the transverse shear components of the strain tensor are obtained as

$$2e_{i3}^k = u_{i,3}^{\prime k} + u_{3,i}^k = x_{1,i}\varphi_k - x_{7,i}\bar{\varphi}_{7k} - x_{8,i}\varphi_{8k} + \lambda_{1,i}\bar{\varphi}_k - \lambda_{7,i}\bar{\varphi}_{7k} - \lambda_{8,i}\bar{\varphi}_{8k} = \Theta_i^{\prime\prime}\beta_{ik} + \bar{\Theta}_i^{\prime\prime}\bar{\beta}_{ik};$$

$$i = 1,2; \qquad t = 1,7,8 \tag{42}$$

where we have denoted

$$\beta_{1k} = -\varphi_k; \qquad \beta_{7k} = \varphi_{7k}; \qquad \beta_{8k} = \varphi_{8k}$$

$$\bar{\beta}_{1k} = -\bar{\varphi}_k; \qquad \bar{\beta}_{7k} = \bar{\psi}_{7k}; \qquad \bar{\beta}_{8k} = \bar{\varphi}_{8k} \tag{43}$$

$$x_{t,i} = -\Theta_i^{\prime\prime}; \qquad \lambda_{t,i} = -\bar{\Theta}_i^{\prime\prime}$$

The deformation in the normal direction is given by

$$e_{33}^k = u_{3,3}^k = x_1\alpha_{1k} + x_2\alpha_{2k} + x_q\alpha_{ql} + \lambda_q\bar{\alpha}_{qk} \qquad q = 3,...,6 \tag{44}$$

respectively, consider further the curvilinear
coordinate system $Oxsz$. Finally, assume that the
shell considered is subjected to an external stress
distribution, q, acting normally on its top surface.

$$\iota_s = e_s + zk_s + \varphi_1(z)k_{s}, \; \iota_t = e_t + zk_t + \varphi_2(z)k_t$$
$$\gamma_{ss} = e_{ss} + zk_{ss} + \varphi_1(z)k_{ss1} + \varphi_2(z)k_{ss2} \quad (5)$$
$$\gamma_{ts} = \varphi_2(z)e_{ts}^a, \; \gamma_{ts} = \varphi_1(z)e_{ts}^a, \; \epsilon_s = 0$$

and the tangential components of the strain tensor are given by

$$e_{11}^k = \varepsilon_{11} + \kappa_{11}z + \kappa_{1}^g \psi_{gk} + \Theta_1^t \psi_{tk,1} + k_{11}x_q\varphi_{qk} + \bar{\kappa}_{11}^t \bar{\psi}_{sk1} + \bar{\kappa}_{11}^p \psi_{pk} + \bar{\Theta}_1^s \bar{\psi}_{sk1,1} + \bar{\Theta}_1^p \bar{\psi}_{pk,1} + k_{11}\lambda_p\bar{q}_{pk}$$

$$e_{22}^k \rightleftharpoons e_{11}^k$$

$$e_{12} = \varepsilon_{12} + \kappa_{12}z + \kappa_{12}^g \psi_{gk} + \tfrac{1}{2}(\Theta_1^t \psi_{tk,2} + \Theta_2^t \psi_{tk,1}) + k_{12}x_q\varphi_{qk} + \tfrac{1}{2}\bar{\kappa}_{12}^s(\psi_{sk1} + \psi_{sk2}) + \bar{\kappa}_{12}^p \psi_{pk}$$
$$+ \tfrac{1}{2}(\bar{\Theta}_1^s \bar{\psi}_{sk1,2} + \bar{\Theta}_2^s \bar{\varphi}_{sk2,1}) + \tfrac{1}{2}(\bar{\Theta}_1^p \bar{\psi}_{pk,2} + \bar{\Theta}_2^p \bar{\psi}_{pk,1}) + k_{12}\lambda_p\bar{q}_{pk}; i,j=1,2; \quad g=1,\ldots,8;$$
$$t=1,7,8; \quad s=1,2,7,8; \quad q=1,\ldots,6; \quad p=3,\ldots,6 \quad (45)$$

In eqns (45) we also have

$$\kappa_{ij}^g = -x_{g,ij}; \quad \kappa_{11,2}^g - \kappa_{12,1}^g = 0; \quad \kappa_{22,1}^g - \kappa_{12,2}^g = 0$$

$$\bar{\kappa}_{ij}^g = -\lambda_{g,ij}; \quad \bar{\kappa}_{11,2}^g - \bar{\kappa}_{12,1}^g = 0; \quad \bar{\kappa}_{22,1}^g - \bar{\kappa}_{12,2}^g = 0$$

$$\bar{\Theta}_i^s = -\lambda_{s,i}; \quad \bar{\Theta}_i^p = -\lambda_{p,i}; \quad g=1,\ldots,8 \quad (46)$$

The components of the stress tensor can be found using the constitutive equations (1), except for the transverse normal stresses σ_{33}^k since they are not compatible with conditions (6) and (7). In order to satisfy these conditions, eqn (27) is taken as a hypothesis. Using the notation defined in eqns (40) and (41), for $B_{ij} = \bar{B}_{ij} = 0$ we can write

$$\sigma_{33}^k = x_q f_{q-1,k} + \lambda_q \bar{f}_{q-1,k} \quad q=3,\ldots,6 \quad (47)$$

The equations of equilibrium and the boundary conditions are derived using Lagrange's variational principle under the condition that the constitutive equations must comply with the transverse normal deformation e_{33}^k.

The equations of equilibrium are obtained as

$$N_{ij,i} + p_i = 0$$
$$M_{ij,ij} - k_{ij}N_{ij} + p_3 = 0$$
$$M_{ij,ij}^1 - T_{ij,i}^1 - Q_{i,i}^1 - Q_3^1 - k_{ij}N_{ij}^1 + p_3^1 = 0$$
$$M_{ij,ij}^2 - Q_3^2 - k_{ij}N_{ij}^2 - p_3^2 = 0 \quad (48)$$

and the boundary conditions as

$$(N_{hh} - N_{hh}^*)\delta u_h = 0$$
$$(N_{hl} - N_{hl}^*)\delta u_l = 0$$
$$(M_{hh,h} - 2M_{hl,l} + p_h - R_h^*)\delta w = 0$$
$$(M_{hh} - M_{hh}^*)\delta\omega_{,h} = 0$$
$$(M_{hh,h}^1 + 2M_{hl,l}^1 - (T_{hhh}^1 + T_{hll}^1) - Q_h^1 + p_h^1 - R_h^{*1})\delta x_1 = 0$$
$$(M_{hh,h}^2 + 2M_{hl,l}^2 + p_h^2 - R_h^{*2})\delta x_2 = 0$$
$$(M_{hh}^1 - M_{hh}^{*1})\delta x_{1,h} = 0$$
$$(M_{hh}^2 - M_{hh}^{*2})\delta x_{2,h} = 0 \quad (49)$$

The integral characteristics of the stresses due to internal forces and moments in eqns (48) and (49) are given by

$$N_{ij} = \int_{u_c}^{u_n} \sigma_{ij}^1 \, dz; \quad N_{ij}^p = \int_{u_c}^{u_n} \sigma_{ij}^k \varphi_{pk} \, dz; \quad Q_i = \int_{u_c}^{u_n} \sigma_{i3}^k \, dz$$

$$Q_i^1 = \int_{u_c}^{u_n} \sigma_{i3}^k \beta_{1k} \, dz; \quad M_{ij} = \int_{u_c}^{u_n} \sigma_{ij}^k z \, dz; \quad M_{ij}^p = \int_{u_c}^{u_n} \sigma_{ij}^k \psi_{pk} \, dz$$

$$Q_i^k = \int_{a_n}^{a_n} \sigma_{33}^k \alpha_{pk}\, dz; \qquad T_{ij}^1 = \int_{a_1}^{a_r} \sigma_{ij}^k \psi_{1k_j}\, dz; \qquad i,j,p = 1,2 \tag{50}$$

where the higher-order forces and moments which reflect the influence of the transverse shear and normal deformation, are denoted by superscripts.

Also, the generalized reactions in eqn (49) are given by

$$R_i^* = Q_{ii}^* + M_{hi,i}^*$$

$$R_i^{*p} = Q_{ii}^{*p} + M_{hi,i}^{*p}; \qquad p = 1,2$$

$$Q_i^{*p} = \int_{a_n}^{a_r} \sigma_{h3}^{0} q_{pk}\, dz \tag{51}$$

and generalized functions of external loads are denoted as

$$p_i = p_i^- + p_i^+$$

$$p_3 = a_0 p_{i,i}^- + a_0 p_{i,i}^+ + p_3^- + p_3^+$$

$$p_i^p = \psi_{p1}(a_0)p_{i,i}^- + \psi_{pn}(a_n)p_{i,i}^+ + q_{p1}(a_0)p_3^- + q_{pn}(a_n)p_3^+$$

$$p_{i_t} = a_0 p_{i_t}^- + a_n p_{i_t}^+$$

$$p_{i_t}^p = \psi_{p1}(a_0)p_{i_t}^- + \psi_{pn}(a_n)p_{i_t}^+; \qquad p = 1,2 \tag{52}$$

As in the linear higher-order theory,[9] the boundary conditions (49) are able to model constraints on the boundary of the reference surface ($z = 0$) and the constraints which model transverse shear and normal compression on the edge of the shell.

The equations given above define the nonlinear higher-order theory of laminated plates and shells and take into account the effects of transverse shear and normal deformation.

4 NUMERICAL RESULTS AND DISCUSSION

The solution of a nonlinear problem based on higher-order theory requires an iterative procedure in which for each level of loading, the nonlinear theory based on classical hypotheses is used as a first step and then the higher-order theory is applied.

A special scheme for the finite element implementation of the nonlinear higher-order theory and different types of finite elements have been developed.[11,12] Some examples are now presented to illustrate the application of the theory.

Consider a three-layered square plate which is simply-supported and whose bearing layers are aluminium and have the characteristics: Young's modulus $E = 7 \times 10^4$ MPa, ultimate strength $\sigma_{ult} = 230$ MPa, yield point $\sigma_{yp} = 100$ MPa and Poisson's ratio $\nu = 0.32$. The load is applied at the centre of the plate in steps of $\Delta P = 1.6$ kN up to a final value of $P = 8$ kN. The stress intensity law is given by

$$\sigma_i = \sigma_{ult}(1 - e^{-at})$$

where $a = 3G/\sigma_{ult}$.

The deflection of the centre of the plate versus the ratio G_R/G_f of the initial shear moduli of the bearing and filler layers is considered in order to study the influence of transverse shear. The thickness ratios $h/a = 1/5$, $1/10$, $1/25$ are considered. For comparison the filler layer is treated as both a linear and a nonlinear material.

The results of this study are shown in Figs 2(a) and 2(b) where the parameter C_n is the ratio of the deflections obtained using finite elements which include transverse shear to the deflections obtained using finite elements based on the classical hypotheses. Both of these elements allow for the nonlinear behaviour of the material. Figure 2(a) shows the results for a nonlinear filler material and Fig. 2(b) for a linear filler material. These graphs show the influence of transverse shear on plates for different thickness ratios under equal loading. When the ratio of the shear moduli of the bearing and filler layers is of the order one
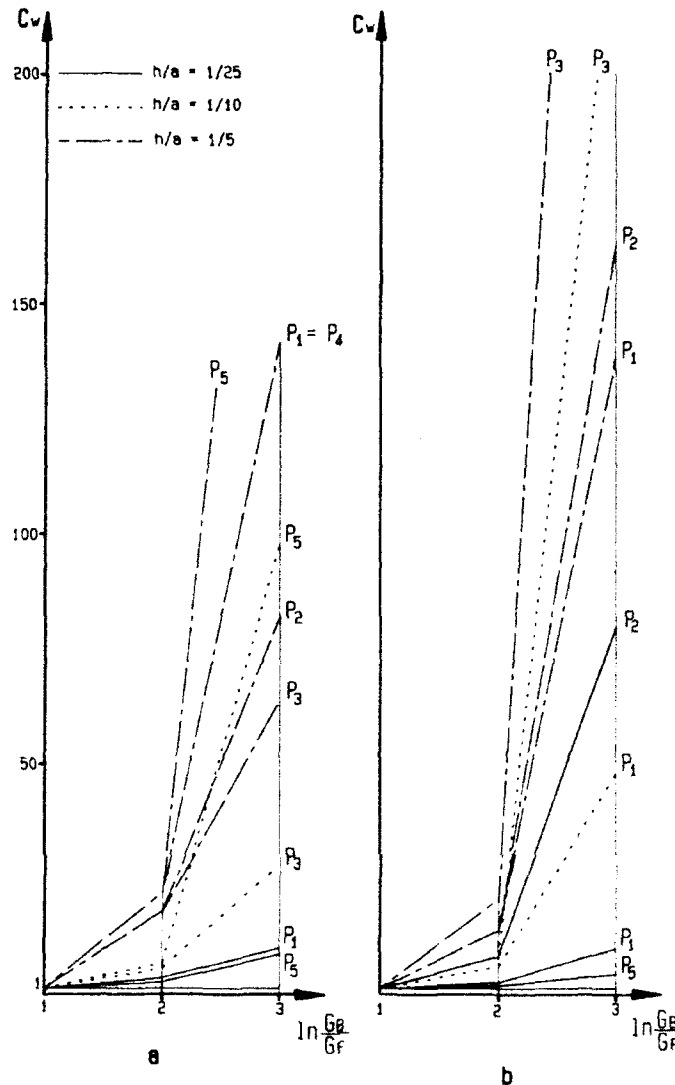
Fig. 2. Diagrams depicting the influence of transverse shear: (a) nonlinearly elastic filler material; (b) linearly elastic filler material.

In $G_B/G_f = 1$) the influence of transverse shear is negligible ($C_w = 1$). The appearance of a plastic zone in the bearing layers and sublayers of the filler layer leads to failure and we observe sharp increases in the value of C_w. This is caused by delamination.

The graphs in Fig. 2(b) show a decrease in the strength of the structure when the filler is treated as a linear material. The plate with the thickness ratio $h/a = 1/10$ fails on the third step of loading, whereas the plate with the thickness ratio $h/a = 1/5$ fails on the second step. For these plates, 'internal failure' is observed, i.e. internal sublayers of the filler layer fail before the bearing layers, and the influence of transverse shear increases and this leads to the failure of the structure as a whole.

In plates whose filler layer is treated as a nonlinear material, the structure fails simultaneously with the failure of the bearing and filler layers.

Consider a three-layered shell which is a slightly curved cylindrical panel. The shell is hinge-supported at its straight edges and free along the curved edges. The external layers have the same mechanical characteristics as the plate described above and the filler is subdivided into four layers which have the characteristics: $E = 34$ MPa, $\sigma_{ult,c} = 0.97$ MPa in compression and $\sigma_{ult,t} = 0.65$ MPa in tension. Finite elements which include both transverse shear and normal deformation were used in the analysis of this problem. In Fig. 3 the deflection of the centre of the shell is given for various thickness ratios and the levels of

loading. The filler layer is considered as a linear material (solid line) and as a nonlinear material (dashed line). In Fig. 3 it is clear that the treatment of the filler as a linear material tends to a decrease in the overall stiffness of the system when the load is moderately high.
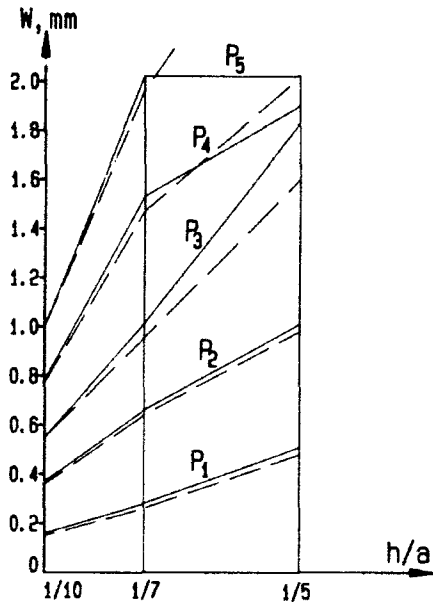
In order to study the influence of both transverse shear and normal compression, a plate with thickness ratio $h/a = 1/5$ is considered. In Fig. 4 the diagrams of the greatest normal deflections and stresses through the thickness at the centre of the plate are presented for the level of loading $P_3 = 4.8$ kN. The first value on the diagrams corresponds to nonlinear analysis and the second to linear analysis. Clearly the results obtained using the full model are substantially different even from those of the shear model. Moreover, a substantial difference exists between the results of the linear and nonlinear analyses. The model based on classical hypotheses is found to be inadequate for the analysis of such structures.

5 CONCLUSIONS

A new nonlinear higher-order theory of laminated plates and shells is presented. The theory takes into account transverse shear and normal deformation and is based on kinematic hypotheses in which material nonlinearity is included. The proposed theory is capable of treating plates and shells with an arbitrary number and sequence of layers which may differ significantly in their physical and mechanical properties.
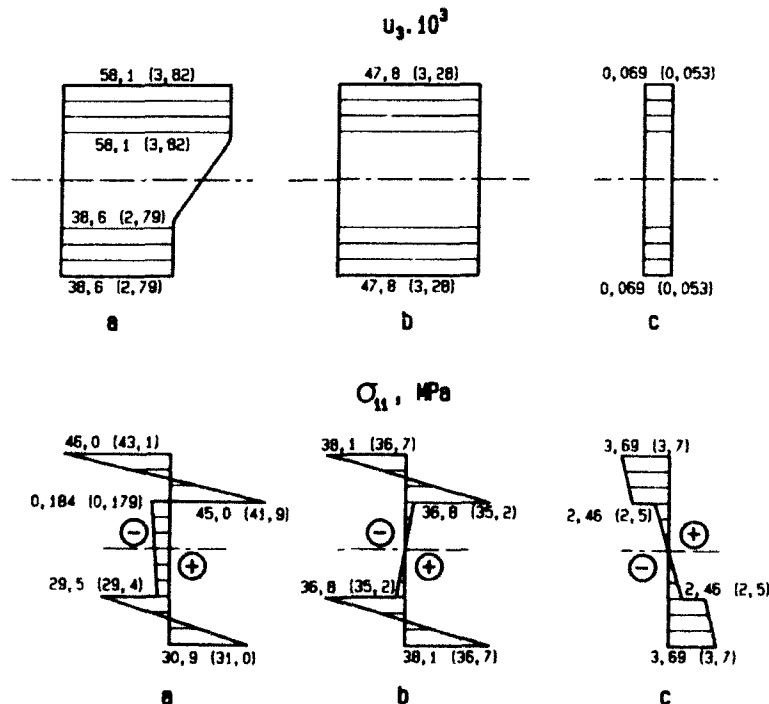

Fig. 3. Curves depicting the influence of transverse shear in the nonlinear analysis of shells.

Fig. 4. Diagrams of normal deflection u_3 and stresses σ_{11} at the centre of a sandwich plate: (a) model with transverse shear and normal compression; (b) model with transverse shear only; (c) classical model.

The results presented illustrate the importance of modelling the nonlinear behaviour of the materials especially at high levels of loading. The present study shows that the influence of transverse shear and normal deformation is more pronounced in the case of a nonlinear analysis.

REFERENCES

1. Bert, C. W., A critical evaluation of new plate theories applied to laminated composites. *Comp. Struct.*, 2 (1984) 329–47.
2. Piskunov, V. G. & Verijenko, V. E., *Linear and Nonlinear Problems in the Analysis of Laminated Structures.* Budivelnik, Kiev, 1986 (in Russian).
3. Noor, A. K. & Burton, W. S., Assessment of computational models for multilayered composite shells. *Appl. Mech. Rev.*, 43 (4) (1990) 67–97.
4. Reddy, J. N., On refined theories of composite laminates. *Meccanica*, 25 (4) (1990) 230–8.
5. Reddy, J. N., A general nonlinear third-order theory of plates with moderate thickness. *J. Non-Linear Mech.*, 25 (6) (1990) 677–86.
6. Pobedrya, B. E., *Mechanics of Composite Materials.* Moscow State University, Moscow, 1984 (in Russian).
7. Iluslin, A. A., *Plasticity.* USSR Academy of Science, Moscow, 1963 (in Russian).
8. Novozhilov, V. V., *Theory of Thin Shells.* Giossouzizdat-sudprom, Leningrad, 1962 (in Russian).
9. Piskunov, V. G., Verijenko, V. E., Adali, S. & Summers, E. B., A higher-order theory for the analysis of laminated plates and shells with shear and normal deformation. *Int. J. Engng. Sci.*, to appear in 1993.
10. Verijenko, V. E., Nonclassical theory of elasto-plastic strain of laminated transversely isotropic tapered shells. *Strength Mater.*, 19 (4) (1987) 547–53.
11. Verijenko, V. E., Adali, S. & Summers, E. B., Discrete-continuous scheme of FEM for analysing laminated composite shells and plates. *Proceedings of FEMSA92.* Cape Town, South Africa, 1992, pp. 589–600.
12. Verijenko, V. E., Adali, S. & Summers, E. B., Applications of refined theory in the numerical analysis of composite laminated structures. *International Conference on Computational Engineering Science.* Hong Kong, 1992, p. 248.

Calculation of effective moduli of fibrous composites with micro-mechanical damage

Y. W. Kwon

Department of Mechanical Engineering, Naval Postgraduate School, Monterey, CA 93943, USA

A micro-mechanics model for continuous fibrous composites was developed in order to determine the effective moduli of composites based on the material properties of their constituents, i.e. fiber and matrix materials. The model can calculate elastic or nonelastic effective moduli of composites depending on their constituents' behavior. Furthermore, micro-mechanical damage can also be considered in the present model to determine effective moduli. Predicted effective moduli from the present model compared very well with experimental data available elsewhere for both undamaged and damaged composites.

INTRODUCTION

Prediction of effective moduli of fibrous composites from material properties of their constituents, i.e. fiber and matrix materials, has been a major research concern. Many different micro-mechanics models[1-13] have been proposed to predict effective moduli. Most of these[1-6] were two-dimensional models for elastic deformation of composites. On the other hand, some micro-mechanics models have been proposed for the three-dimensional configuration and for material nonlinear behavior of composites.[7-13]

Dvorak and Bahei-El-Din[7] assumed cylindrical fibers with vanishing diameters in order to maintain the axial constraint of the constituents. They postulated that the fiber and matrix had the same stresses in all directions other than the longitudinal normal stress. Aboudi[8-10] considered a representative cell to model a fiber and a surrounding matrix. The fiber was assumed to be of rectangular shape and the cell was divided into four subcells. He used linear displacement fields within each subcell and imposed continuity of displacements at the cell and subcell interfaces on the average sense. As pointed out by Pecknold,[13] Aboudi's micro-mechanical model is conceptually a crude finite element model. More detailed micro-mechanical models were also considered using refined finite element discretizations of a typical repeating unit cell.[14,15] However, they are computationally intensive. Pecknold[13] proposed a simple unit cell model represented by serial and/or parallel springs.

All the works mentioned above computed stresses at the composite level. However, in order to investigate damage progress at the micro-mechanics level, computation of stresses occurring in the fiber and matrix are very beneficial. In addition, for a composite with plastic deformation of the matrix and elastic deformation of the fibers, calculations of fiber stresses and matrix stresses, respectively, are also useful to determine the state of stresses in each constituent. To this end, a new micro-mechanical model was developed by the author.[11,12] The model computes fiber and matrix stresses and uses a yield criterion for each constituent, if applicable, directly.

The previous model[11,12] was based on rather simple assumptions such as transverse normal stresses are the same for both fiber and matrix. In this paper, a refined micro-mechanics model is presented. The present model is more general than, but still as efficient as, the previous model.[11,12] The model can be used to predict composite material properties from elastic or nonelastic constituent material properties. Moreover, it can also be used to study the evolution and effects of micro-damage in composites.

The following sections describe the micro-mechanics model and some results. Both damaged and undamaged composites were considered. For undamaged composites, composite material properties were computed from constituents' material properties using the proposed model and their results were compared with experimental data. Transverse cracking was studied for damaged composites. Transverse

matrix cracking was observed in cross-ply composites by Broutman and Sahu.[16] After the observation, several investigators have studied the phenomenon analytically and experimentally. Highsmith and Reifsnider[17] conducted an experiment to measure the longitudinal stiffness reductions of various laminates. Later some analytical studies were performed to predict the stiffness reduction.[18-21] Talreja[18,19] used continuum damage mechanics. He represented damage as internal variables in a phenomenological approach. Hashin[20] used the principle of minimum complementary energy while Aboudi[21] solved a periodic crack problem. The present model is also used to predict the stiffness reduction.

MICRO-MECHANICS MODEL

Consider a unit cell made of a fiber and a surrounding matrix material. The fiber is assumed to have a square cross-section. Because of symmetry, a quarter of the unit cell is considered as shown in Fig. 1. The cell is divided into four subcells and the size of each subcell depends on the fiber volume fraction. The following development is based on average stresses and strains in a subcell. Stresses and strains at the composite level (or the unit cell level) are expressed

$$\bar{\sigma}_{ij} = v^f \sigma_{ij}^a + \sqrt{v^f}(1 - \sqrt{v^f}) \sigma_{ij}^b + \sqrt{v^f}(1 - \sqrt{v^f})$$
$$\times \sigma_{ij}^c + (1 - \sqrt{v^f})^2 \sigma_{ij}^d \qquad i,j = 1,3 \qquad (1)$$

$$\bar{\varepsilon}_{ij} = v^f \varepsilon_{ij}^a + \sqrt{v^f}(1 - \sqrt{v^f}) \varepsilon_{ij}^b + \sqrt{v^f}(1 - \sqrt{v^f})$$
$$\times \varepsilon_{ij}^c + (1 - \sqrt{v^f})^2 \varepsilon_{ij}^d \qquad i,j = 1,3 \qquad (2)$$

where $\bar{\sigma}_{ij}$ and $\bar{\varepsilon}_{ij}$ = composite stresses and strains, σ_{ij}^α and ε_{ij}^α = stresses and strains of a subcell (α = a, b, c or d), v^f = fiber volume fraction, and subcell 'a' represents a fiber and the rest of the subcells are matrix. The composite stresses or strains are determined by the volume average of the stresses and strains of the subcells.

Stress continuity at the subcell interfaces requires

$$\sigma_{22}^a = \sigma_{22}^b, \ \sigma_{22}^c = \sigma_{22}^d, \ \sigma_{33}^a = \sigma_{33}^c, \ \sigma_{33}^b = \sigma_{33}^d \qquad (3)$$

and

$$\sigma_{12}^a = \sigma_{12}^b, \ \sigma_{12}^c = \sigma_{12}^d, \ \sigma_{13}^a = \sigma_{13}^c, \ \sigma_{13}^b = \sigma_{13}^d,$$

$$\sigma_{23}^a = \sigma_{23}^b = \sigma_{23}^c = \sigma_{23}^d \qquad (4)$$

The coordinate system for eqns (3) and (4) is given in Fig. 1. Axis 1 indicates the fiber longi-
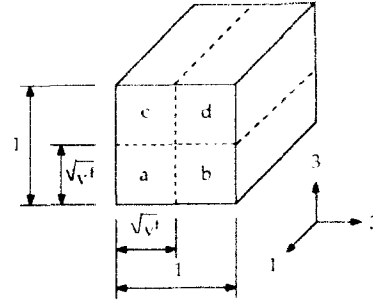

Fig. 1. A unit cell made of subcells.

tudinal direction and axes 2 and 3 are normal to the fiber direction. In addition, strains of subcells are postulated to satisfy the following relationship of deformation:

$$\varepsilon_{11}^a = \varepsilon_{11}^b = \varepsilon_{11}^c = \varepsilon_{11}^d, \ \varepsilon_{22}^a + \varepsilon_{22}^b = \varepsilon_{22}^c + \varepsilon_{22}^d,$$

$$\varepsilon_{33}^a + \varepsilon_{33}^c = \varepsilon_{33}^b + \varepsilon_{33}^d \qquad (5)$$

and

$$\varepsilon_{12}^a + \varepsilon_{12}^b = \varepsilon_{12}^c + \varepsilon_{12}^d, \ \varepsilon_{13}^a + \varepsilon_{13}^c = \varepsilon_{13}^b + \varepsilon_{13}^d \qquad (6)$$

The relationship among normal strains is based on the assumption that deformation of a unit cell is uniform although each subcell may have different normal strains.

A constitutive equation for each subcell can be expressed as

$$\sigma_{ij}^\alpha = E_{ijkl}^\alpha \varepsilon_{kl}^\alpha \qquad (i,j = 1, 2, 3 \text{ and } \alpha = a, b, c, d) \qquad (7)$$

The constitutive equation, eqn (7), is substituted into the stress continuity equations, eqns (3) and (4). The substitution results in stress continuity equations in terms of strain components of subcells. These expressions are solved along with the strain relations, eqns (5) and (6), simultaneously. This algebraic operation yields expressions for subcell strains in terms of average composite strains.

Subcell stresses in eqn (1) are replaced by subcell strains using the constitutive equation for subcells, eqn (7). This results in composite stresses expressed in terms of subcell strains. These subcell strains are then replaced by composite strains obtained in the previous paragraph. As a result, the composite stresses are given in terms of composite strains using the material properties of subcells. In other words, the effective material property at the composite level can be written in terms of the properties of the fiber and matrix materials. The properties of each constituent may be anisotropic, in general. For the elastic range,

subcells b, c and d in Fig. 1 may have the same material property because they are the matrix. For the plastic range, however, each subcell may have different material properties since they are dependent on the state of the stresses.

The procedure for analyzing the material non-linear deformation of a composite structure using the present micro-mechanics model can be summarized as given below. The procedure is described in conjunction with the finite element analysis.

(A) Initially assume elastic deformation and compute the effective material properties of the composite.

(B) Obtain the displacement field of the composite using the elastic effective material properties.

(C) Compute composite strains from the displacement field.

(D) Compute subcell strains (or strains at the constituent level) from the composite strains.

(E) Compute subcell stresses from the subcell strains. If there is yielding, the subcell stresses are modified.

(F) Compute composite stresses from the subcell stresses.

(G) Compute internal forces from the composite stresses. If the internal forces are not in equilibrium with the external forces, a residual is computed. With the residual forces, go back to (B) and repeat the process until the residual comes within a given tolerance.

RESULTS AND DISCUSSION

The effective moduli of the composites predicted by the present model were compared with experimental data available elsewhere. The first case was a graphite/epoxy composite. Graphite fibers were considered to be transversely isotropic and the epoxy matrix was considered to be isotropic. The corresponding properties are given below. The graphite fibers have longitudinal and transverse elastic moduli of 232 GPa and 15 GPa, respectively. Their longitudinal and transverse Poisson's ratios are 0·275 and 0·49, and the inplane shear modulus is 24 GPa. The epoxy material has an elastic modulus of 5·35 GPa and a Poisson's ratio of 0·354. Experimental results were given for this composite in Ref. 22 and they

are compared with present predicted values in Figs 2–6. Elastic moduli and shear moduli in both longitudinal and transverse directions respectively are compared as well as the transverse Poisson's ratio. The experimental and computed material properties of the graphite/epoxy composite show good agreement between them.

The next comparison was for a glass/epoxy composite. Both constituents were isotropic. The elastic modulus and Poisson's ratio for the glass
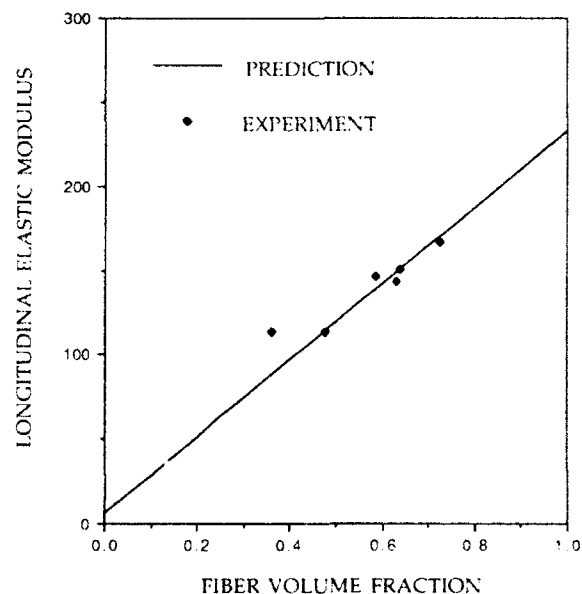

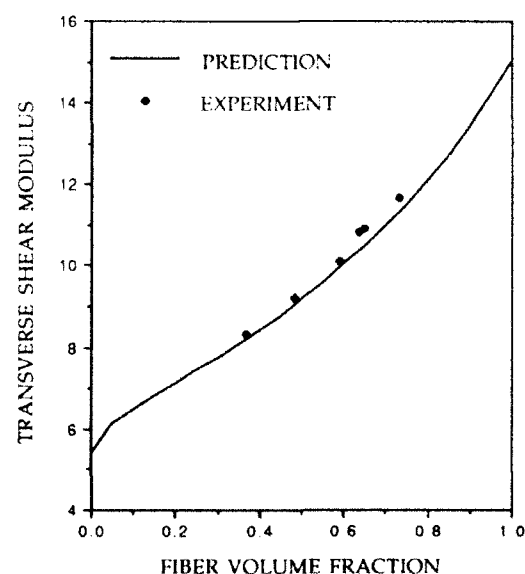Fig. 2. Longitudinal elastic modulus of a graphite/epoxy composite.

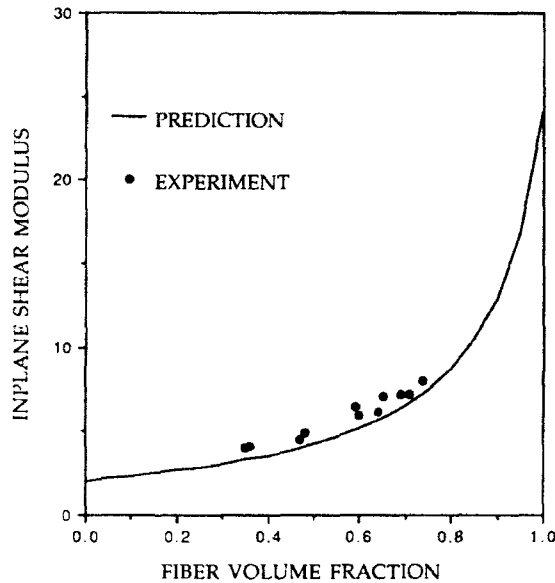Fig. 3. Transverse elastic modulus of a graphite/epoxy composite.

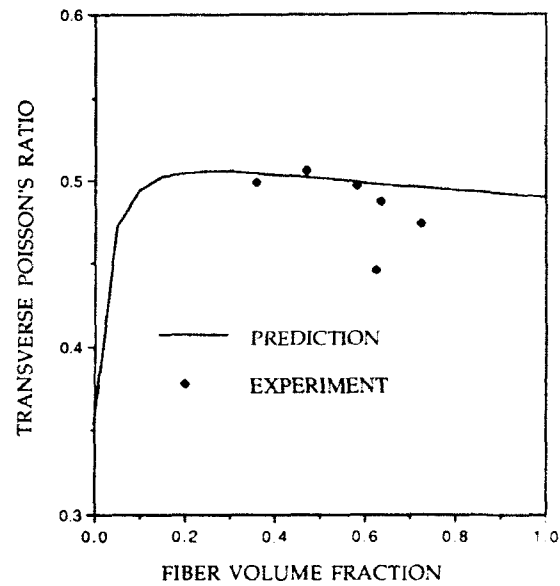**Fig. 4.** Inplane shear modulus of a graphite/epoxy composite.

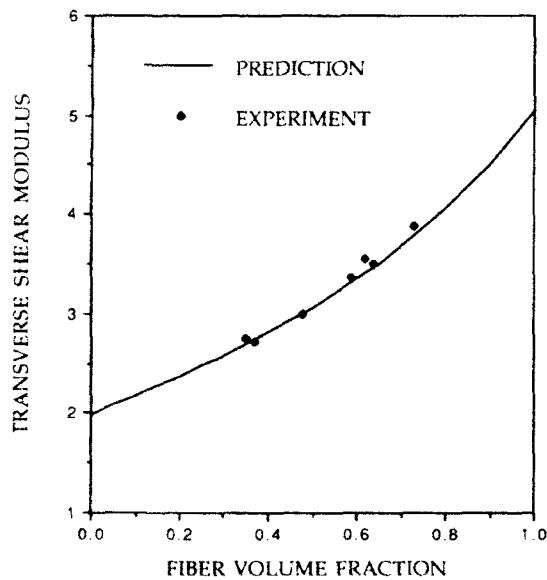**Fig. 6.** Transverse Poisson's ratio of a graphite/epoxy composite.

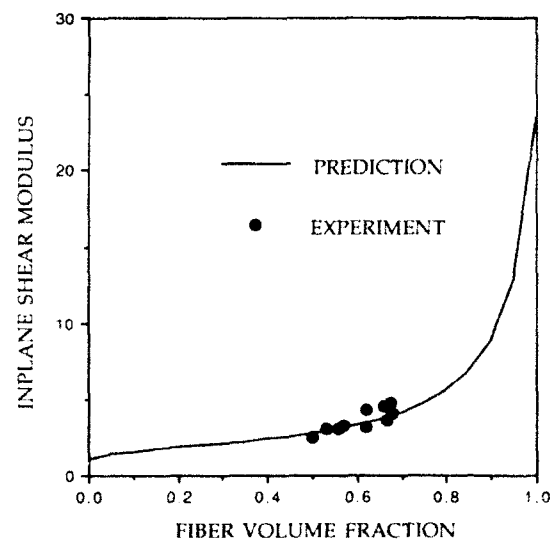**Fig. 5.** Transverse shear modulus of a graphite/epoxy composite.

Fig. 7. Inplane shear modulus of a glass/epoxy composite.

are 72·38 GPa and 0·2 while those for the epoxy are 2·75 GPa and 0·35. The present predicted value of transverse shear modulus was compared with the experimental data.[23] Comparison, as shown in Fig. 7, is very good.

The next cases considered damage in composites. The reduction in stiffness caused by matrix cracks was considered. Glass/epoxy composites of cross-plies [0/90]$_s$ and [0/90$_3$]$_s$ respectively were used for this study. Transverse matrix cracks

in the 90° layer, which was normal to the loading direction, reduced the longitudinal elastic modulus of the composites. Experimental data are available in Ref. 17. The material properties for the composite are elastic moduli of 41·7 GPa in the longitudinal direction and 13 GPa in the transverse direction, inplane and out of plane Poisson's ratios of 0·3 and 0·42, and inplane shear modulus of 3·4 GPa. The thickness of a layer is 0·203 mm. Because the composite properties were known but not the constituents' properties, the properties of each constituent were determined using the

present micro-mechanics model by trial and error. The result gave an elastic modulus of 72·5 GPa and a Poisson's ratio of 0·23 for the glass and an elastic modulus of 4·0 GPa and a Poisson's ratio of 0·35 for the epoxy with a fiber volume fraction of 0·5. The composite material properties using these constituent properties yielded the glass/ epoxy composite properties within an error of 3%.

The reduction in the longitudinal stiffness was computed for different crack densities (1/2L) using the finite element method and the present model. Here 2L denotes the longitudinal distance of periodically spaced damage zones containing transverse matrix cracks. Three-dimensional solid elements were used for the computation. Transverse matrix cracks in the 90° layer were modeled as described below. If the loading was in the direction of axis 2 in Fig. 1, then subcells b and d within the transverse crack zone were considered not to support normal stresses. As a result, the elastic

modulus in these subcells was reduced to a small value close to zero. The reduced stiffness ratio is plotted in terms of the crack density in Figs 8 and 9. The reduced stiffness ratio is equal to the cracked elastic modulus divided by the uncracked elastic modulus in the longitudinal direction. Overall, the present prediction compares well with the experimental data. Especially, the agreement was very good for a glass/epoxy composite with $[0/90]_s$.

CONCLUSIONS

A micro-mechanics model was presented in order to predict the effective material properties of composites based on their constituent material properties. Both the elastic and non-elastic deformations of composites can be analyzed using the present model. In addition, the model can include micro-mechanical damage in composites. For both cracked and uncracked composites, comparisons between the present predicted values and experimental data proved the accuracy of the present model.

Fig. 8. Stiffness reduction in a glass/epoxy composite of cross-ply due to transverse matrix cracks.
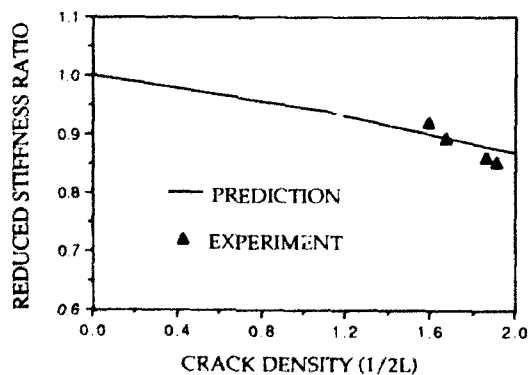
Fig. 9. Stiffness reduction in a glass/epoxy composite of [0/ 90/90/0] due to transverse matrix cracks.

REFERENCES

1. Ekvall, J. C., Elastic properties of orthotropic mono-filament laminates. ASME Paper 61-AV-56. Aviation Conference, Los Angeles, CA, March, 1961.
2. Tsai, S. W., Structural behavior of composite materials. NASA CR-71, July 1964.
3. Rosen, B. W., Dow, N. F. & Hashin, Z., Mechanical properties of fibrous composites. NASA CR-31, April, 1964.
4. Hashin, Z. & Rosen, B. W., The elastic moduli of fiber-reinforced materials. Paper No. 63-WA-175, *J. Appl. Mech., ASME* (June 1964).
5. Ekvall, J. C., Structural behavior of monofilament composites. *AIAA 6th Structures and Materials Conference*. Palm Springs, CA, April, 1965.
6. Noyes, J. V. & Jones, B. H., Analytical design procedures for the strength and elastic properties of multilayered fiber composites. *Proc. AIAA/ASME 9th Structures, Dynamics and Materials Conference*. Paper 68-336, 1968.
7. Dvorak, G. J. & Bahei-El-Din, Y. A., Plasticity analysis of fibrous composites. *J. Appl. Mech.,* **49** (June 1982) 327-35.
8. Aboudi, J., Closed form constitutive equations for metal matrix composites. *Int. J. Engng Sci.*, **25** (9) (1987) 1229-40.
9. Aboudi, J., Micromechanical analysis of composites by the method of cells. *Appl. Mech. Rev.*, **42** (7) (July 1989) 193-221.
10. Aboudi, J., Effective behavior of inelastic fiber-reinforced composites. *Int. J. Engng Sci.*, **22** (4) (1984) 439-49.
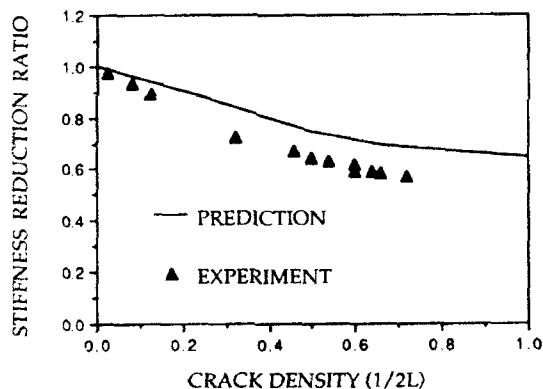
11. Kwon, Y. W.. Material nonlinear analysis of composite plate bending using a new finite element formulation. *Comput. Struct.*, **41** (5) (1991) 1111–17.

12. Kwon, Y. W. & Byun, K. Y.. Development of a new finite element formulation for the elasto-plastic analysis of fiber-reinforced composites. *Comput. Struct.*, **35** (5) (1990) 563–70.

13. Pecknold, D. A.. A framework for 3-D nonlinear modeling of thick-section composites. DTRC-SME-90/92, Ship Materials Engineering Department Research and Development Report. David Taylor Research Center.

14. Adams, D.. Elastoplastic behavior of composites. In *Mechanics of Composite Materials*, ed. G. P. Sendeckyi. Academic Press, New York, 1974, pp. 169–208.

15. Kelkar, A. D.. Brown, R. J. & Raju, I. S.. Evaluation of transverse mechanical properties of unidirectional composites by using finite element micromechanical analysis. In *Recent Advances in Structure Mechanics—1992*, ed. Y. W. Kwon & H. H. Chung. ASME PVP-Vol. 248/NE-Vol. 10, 1992, pp. 145–53.

16. Broutman, L. J. & Sahu, S.. Progressive damage of a glass reinforced plastic during fatigue. *SPI, 24th Annual Technical Conference*, Washington, DC, February 1969, Section 11-D.

17. Highsmith, A. L. & Reifsnider, K. L.. Stiffness-reduction mechanisms in composite laminates. In *Damage in Composite Materials*, ASTM STP 775, American Society for Testing and Materials, Philadelphia, PA, 1982, pp. 103–17.

18. Talreja, R.. Transverse cracking and stiffness reduction in composite laminates. *J. Comp. Mater.*, **19** (July 1985) 355–75.

19. Talreja, R.. Stiffness properties of composite laminates with matrix cracking and interior delamination. *Engng Fract. Mech.*, **25** (5/6) (1986) 751–62.

20. Hashin, Z.. Analysis of stiffness reduction of cracked cross-ply laminates. *Engng Fract. Mech.*, **25** (5/6) 1986 771–8.

21. Aboudi, J.. Stiffness reduction of cracked solids. *Engng Fract. Mech.*, **25** (5) (1987) 637–50.

22. Kriz, R. D. & Stinchcomb, W. W.. Elastic moduli of transversely isotropic graphite fibers and their composites. *Exp. Mech.* (Feb. 1979) 41–9.

23. Tsai, S. W. & Hahn, H. T.. *Introduction to Composite Materials*. Technomic, Westport, CN, 1980.

Effect of motion parameters on the tribological behaviour of ptfe-based composite

W. W. Marzouk

Faculty of Engineering and Technology, Minia University, Minia, Egypt

The effect of motion parameters such as average contact pressure, sliding speed and temperature on the tribological behaviour of polytetrafluoroethylene (ptfe) composite containing 60% by weight of bronze powder were studied and evaluated. The rotatable plan was utilized to get more accurate values of motion parameters. Measurements of friction, wear and temperature were carried out continuously during the wear process. The results showed that there are two regions of motion parameters where the wear intensity was minimum and the coefficient of friction attained its lowest value.

NOTATION

$b_0 - b_{23}$	The coefficient of regression function
H	Hardness of the steel surface (HRC)
I_r	Wear intensity (μm/km)
L	Friction distance (m)
N	Number of experiments
N_0	Number of experiments at central point
p	Average contact pressure (MPa)
R_r	Surface roughness of the steel counterpart (μm)
S	Number of the investigated factors
t_p	Initial temperature (°C)
t_f	Final temperature (°C)
v	Sliding speed (m/s)
$X_1 - X_3$	The input quantity in the experiments
$y_1 - y_3$	The output measured data
μ	Coefficient of friction
ρ	The value of stellar (sidereal) radius obtained in the rotatable plan for the polynomial of the second degree

INTRODUCTION

The extremely low coefficient of friction of polytetrafluoroethylene (ptfe) makes it an attractive material for lubrication of any type of sliding component. The usually quoted value of 0·04 for μ is lower than that for graphite, MoS_2 or any other known solid.[1] However, there are several properties of ptfe that limit its applicability. One fundamental defect of ptfe which limits its technical use is the higher wear rate. Also, ptfe is a poor conductor of heat; thus the excess heat generated under sliding is not readily dissipated and contributes to the decomposition of the ptfe.[2] It also has a relatively low compressive strength which results in the cold flow of ptfe films so that the tolerances of the bearing are changed. In thin film applications the films are removed to the point that the underlying surfaces are exposed.[3]

The wear of a polymeric material depends upon the sliding speed and the load conditions. In general, high loads and high speeds cause excessive wear. This is probably due to heating at the interface which may be high enough to cause melting or softening of the sliding polymer surface, thereby abruptly increasing the rate of wear. This kind of behaviour for ptfe has been observed by Lancaster.[4] Lontz and Kumnick[5] demonstrated that the wear rate of ptfe is directly proportional to the flexure modulus and inversely proportional to the yield strain. Kar and Bahadur[6] showed that the wear of ptfe-filled polyoxymethylene and unfilled polyoxymethylene is directly proportional to the normal load, sliding distance and surface energy, all raised to different powers greater than one, and inversely proportional to the modulus of elasticity raised to a much higher power.

The object of this work is to study the effect of the motion parameters average contact pressure, sliding speed and temperature (p, v, t_p) on the tribological behaviour of a ptfe-based composite containing 60% by weight of bronze powder.

193

ROTATABLE PLAN

This is one of the statistical programs used in multi-level design (five levels). It is used in the experimental data and is carried out according to the exact number of experiments, defined previously, and it distributes these data in a spherical shape so that the variance in the central point should be the same as in the other points surrounding the central point with radius ρ, where ρ is the value of stellar radius which depends on the degree of the polynomial and the number of experiments at the central point. The polynomial regression function contains three independent variables ($S = 3$), of the second degree ($R = 2$) with ten factors of regression function ($K = 10$). From the above mentioned terms can be calculated the following statistical values: coefficients of regression function, standard deviation of the remainder, variance estimation of the regression function and polynomial correlation factor. Lastly, the output at any values of the input independent variables could be calculated whether the experiments were carried out at these variables or not.

EXPERIMENTAL WORK

The pin on disc testing machine, Fig. 1, used previously[7] was employed. The tests were conducted at five planes according to a rotatable plan[8] to obtain identical variance of results both at the points on the surface of a sphere with radius $\rho = 1$ and at the central point of the plan. Selection of the number of experiments at the central point is required in order to obtain variance at the central point, the same as in the other points in the experimental plan with radius $\rho = 1$; the recommended number of experiments is $N_0 = 6$ where $0 \leq \rho \leq 1$,[8] practical acceptance is exactly as in the
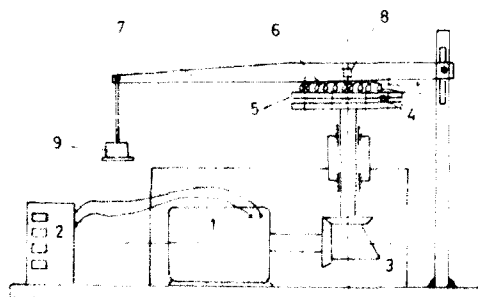

Fig. 1. Pin on disc machine (1, AC motor; 2, VLT frequency converter; 3, bevel gears; 4, testpiece; 5, counterpart; 6, electric heater; 7, lever; 8, strain gauge; 9, dead weight).

uniform plan. It was assumed that the star arm of the plan for the number of investigated factors $S = 3$ (contact pressure, sliding speed and initial temperature) was $a = \sqrt[4]{2^S} = 1.6817$ (these values selected on the basis of tabular recommendation.[8]

The overall number $N = 20$ tests was calculated using the relationship;

$$N = 2^S + 2S + N_0$$

N is number of experiments.
S is number of the investigated factors.
N_0 is number of experiments at the central point.

Moreover, after the initial investigations, the experiments were carried out at the following conditions:

— The hardness of the sliding surfaces of the counterparts (made of thermally improved steel 45) were $45 = \pm 1$ HRC and its surface roughness ranged from 0.13 to 0.16 μm.
— The samples were made of ptfe (its density is 2.18 g/cm^3, melting temperature is $327°$C) filled with 60% by weight of bronze (MB10, density 9.47 g/cm^3, grain size of $50-100$ μm) containing 30% Pb.

The following parameters were varied as follows:

— average contact pressure, $p = 0.05-1.95$ MPa;
— sliding speed, $v = 0.50-2.50$ m/s;

Table 1. The input variables (p, v, t_p) and output data (t_c, l_r, μ) of experiments

Exp. no.	X_1 p (MPa)	X_2 v (m/s)	X_3 t_p (°C)	y_1 t_c (°C)	y_2 l_r (μm/km)	y_3 μ
1	0.43	0.90	39	40	2.0	0.11
2	1.56	0.90	39	60	5.6	0.58
3	0.43	2.09	39	55	2.3	0.12
4	1.56	2.09	39	86	3.6	0.57
5	0.43	0.90	81	102	2.4	0.16
6	1.56	0.90	81	105	2.0	0.57
7	0.43	2.09	81	125	3.6	0.21
8	1.56	2.09	81	135	3.2	0.60
9	0.05	1.50	60	60	3.0	0.08
10	1.95	1.50	60	115	7.0	0.69
11	1.0	0.50	60	70	2.4	0.26
12	1.0	2.50	60	110	1.6	0.31
13	1.0	1.50	25	35	2.4	0.31
14	1.0	1.50	95	110	2.0	0.33
15	1.0	1.50	60	80	3.0	0.34
16	1.0	1.50	60	85	3.0	0.28
17	1.0	1.50	60	95	2.8	0.30
18	1.0	1.50	60	100	2.8	0.31
19	1.0	1.50	60	100	2.4	0.33
20	1.0	1.5	60	95	2.8	0.31

— initial temperature, $t_p = 25-95°C$;
— friction distance (length of action), $L = 5000$ m.

The flat end of the ptfe pins, which were 8 mm in diameter, were rubbed against the steel discs (counterparts) in the conditions of technically dry friction. The diameter of the frictional tracks on the discs was 60 mm. After the specimen had been mounted in the specimen holder, the pin was initially rubbed against 600 grade emery paper placed on the disc to ensure good contact between the pin and the disc. Before the wear test was started, the pin and disc surfaces had been cleaned by rubbing with a soft cloth dipped in ethyl alcohol. The coefficient of friction and wear intensity were obtained during the steady state stages of friction and wear, respectively.

The results obtained were interpreted using a computer routine with which the coefficients of

the polynomial regression function of the output quantities measured were determined. The simplified polynomial of the second degree of the three independent variables may be expressed as follows:

$$y = b_0 + b_1 X_1 + b_2 X_2 + b_3 X_3 + b_{11} X_1^2 + b_{22} X_2^2$$
$$+ b_{33} X_3^2 + b_{12} X_1 X_2 + b_{13} X_1 X_3 + b_{23} X_2 X_3$$

where

y is the output quantity of the experiments,

$b_0, \ldots, b_{23}$ are the coefficients of the regression function,

X_1, X_2, X_3 are the input quantities in the experiments.

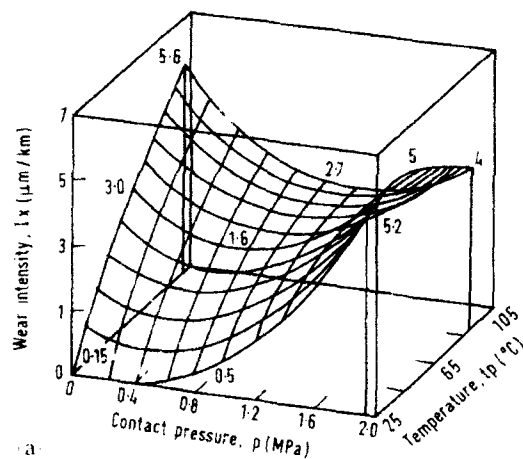The input variables X_1-X_3, and the measured output data, y_1-y_3, are shown in Table 1.
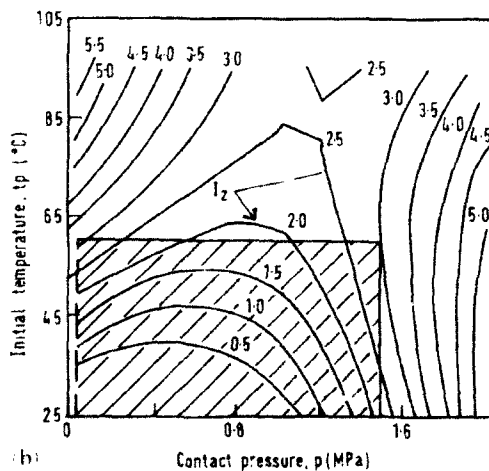
Fig. 2. Wear intensity of a ptfe-based composite sliding against a steel disc at a sliding speed of 2·5 m/s in two forms (a) spatial; (b) contour.
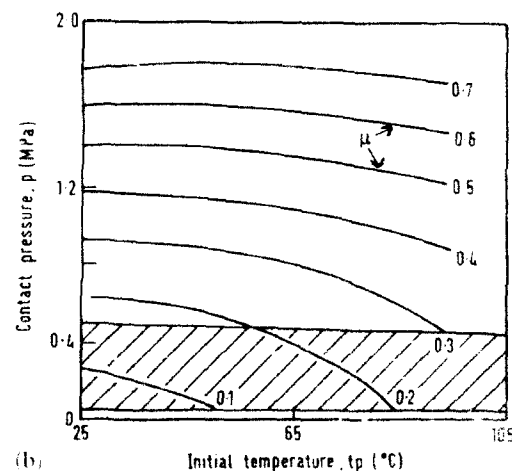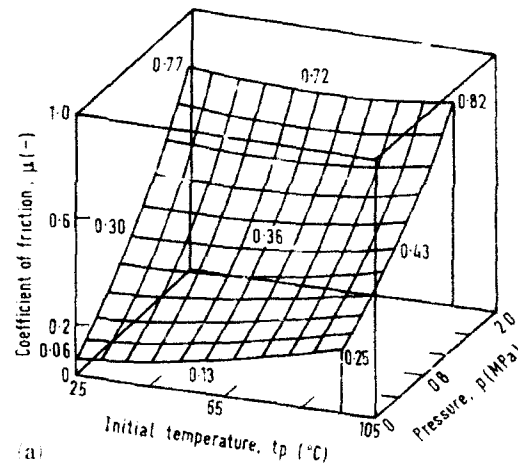
Fig. 3. Coefficient of friction of a ptfe-based composite sliding against a steel disc at sliding speed of 2·5 m/s in two forms: (a) spatial; (b) contour.

RESULTS AND DISCUSSION

The test results are presented in two forms: three dimensional (spatial) diagrams and contour forms. Wear intensity, I_z, coefficient of friction, μ, and final temperature, t_f, as functions of contact pressure, p, sliding speed, v, and initial temperature, t_p, are shown in Figs 2–9.

(a) The effect of motion parameters (p, v, t_p) on wear intensity and coefficient of friction

Figures 2 and 3 show the wear intensity and coefficient of friction versus the contact pressure and initial temperature at the sliding speed of 2·5 m/s. Figure 2(b) indicates that, at low initial temperature of 25°C, wear intensity starts to increase rapidly above a contact pressure of about 1 Mpa. At the high initial temperature of 95°C, increasing the contact pressure results in a gradual decrease

in wear intensity to about 50% of its initial value at 1 Mpa then it gradually increased with increase in pressure. Also, increasing initial temperature tends to a sharp increase in wear intensity at low pressure, but it tends to reduce wear intensity at high pressure.

Figure 3 shows that there is an increase in the coefficient of friction with increase in contact pressure regardless of the initial temperature. Figure 3(b) shows that the coefficient of friction increases gradually with increasing initial temperature and much more rapidly with increasing pressure. This may be attributed to the fact that, the coefficient of friction of ptfe is generally independent of temperature in the high temperature range."

Figures 2(b) and 3(b) show that there is a region of low initial temperature and low contact pressure where both the coefficient of friction and wear intensity are relatively low the hatched
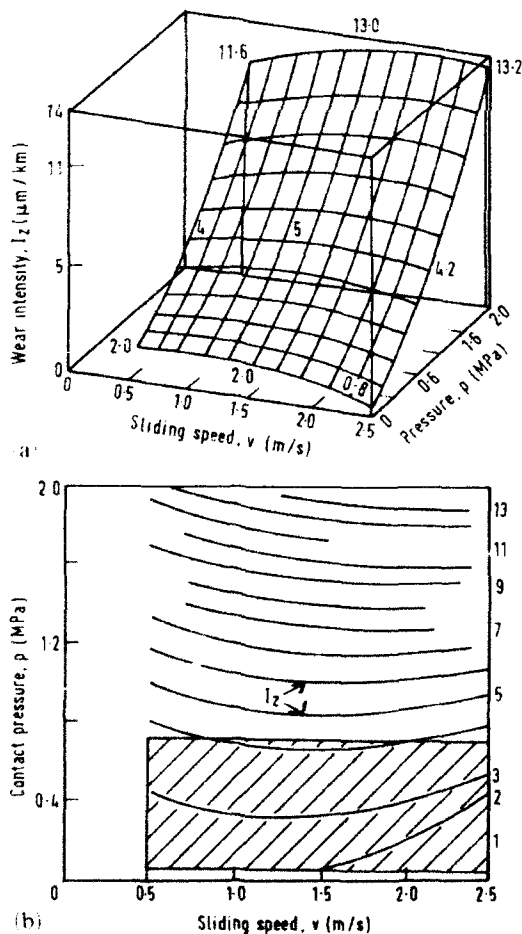

Fig. 4. Wear intensity of a ptfe-based composite sliding against a steel disc at initial temperature of 25°C in two forms (a) spatial; (b) contour.
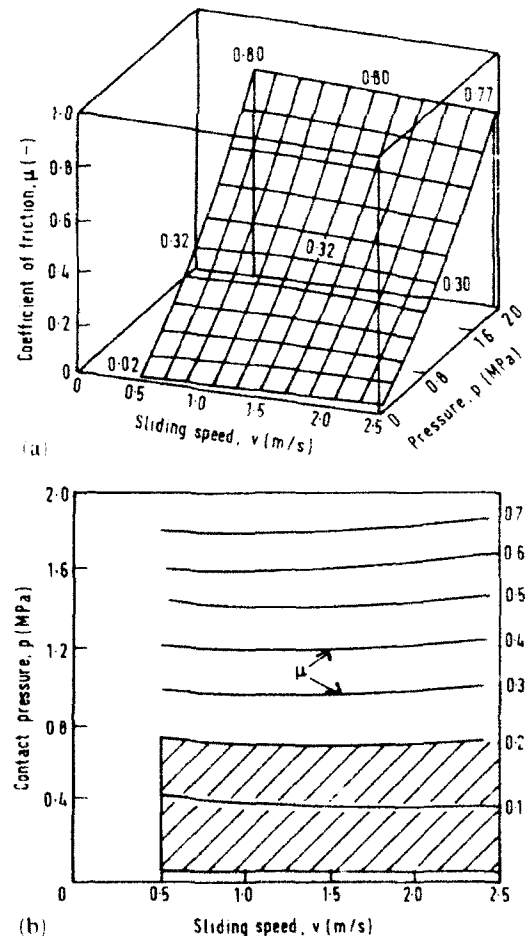
Fig. 5. Coefficient of friction of a ptfe-based composite sliding against a steel disc at initial temperature of 25°C in two forms: (a) spatial; (b) contour.
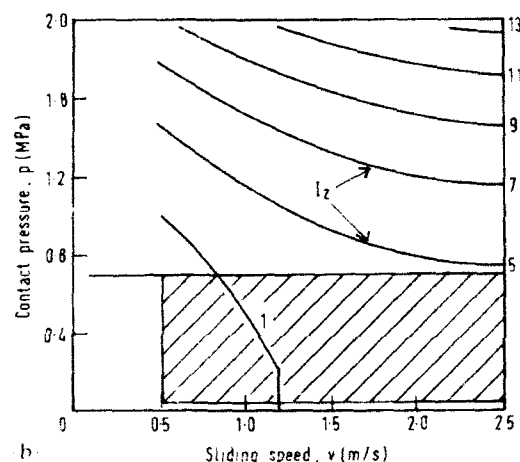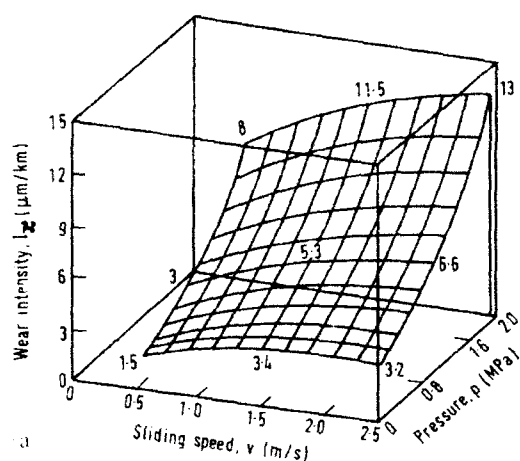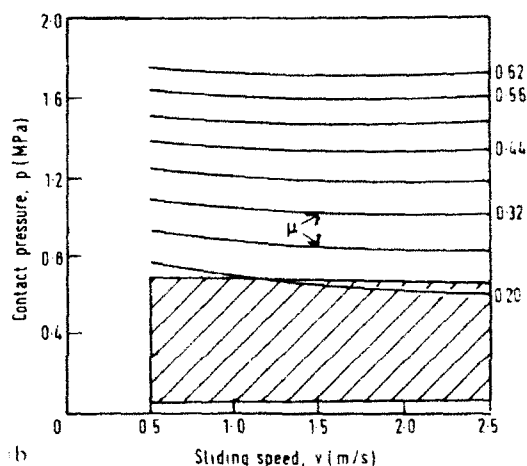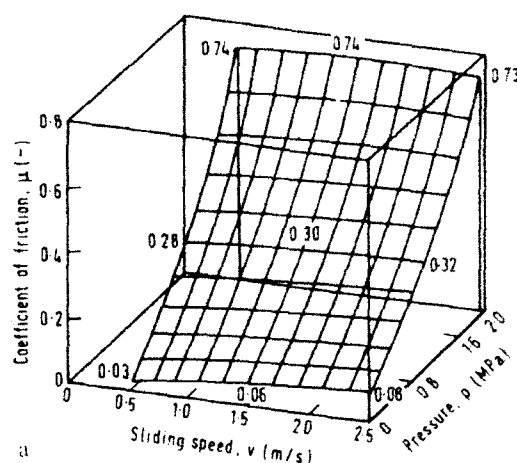
Fig. 6. Wear intensity of a ptfe-based composite sliding against a steel disc at initial temperature of 60°C in two forms: a spatial; b contour.
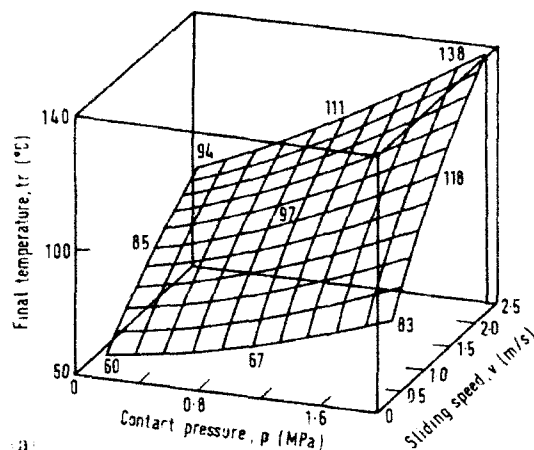

Fig. 7. Coefficient of friction of a ptfe-based composite sliding against a steel disc at initial temperature of 60°C in two forms: a spatial; b contour.

areas) where $I_z \leq 3$ μm/km at $P = 0.05-1.5$ MPa, t_p up to 60°C and $\mu \leq 0.3$ at $P = 0.05-0.5$ Mpa, t_p up to 100°C.

Figures 4 and 5 depict the results of wear intensity and coefficient of friction versus the sliding speed and contact pressure at an initial temperature of 25°C. It can be observed that wear intensity and coefficient of friction both increase with increasing contact pressure, regardless of the sliding speed. Increasing sliding speed has almost no effect on wear intensity and coefficient of friction. In Figs 4(b) and 5(b), can be seen another area of motion parameters (the hatched areas) where the wear intensity is a minimum and the coefficient of friction still has a low value ($I_z \leq 4$ μm/km and $\mu \leq 0.2$ at $p = 0.05-0.7$ MPa, $v = 0.5-2.5$ m/s and $t_p = 25$°C). This may be explained on the grounds of the mechanical-adhe-

sive theory of friction of thermoplastic polymers as follows: on the sliding surface of the steel counterpart, the spread-bronze metallic film is coated with a ptfe film which smoothes the surface resulting in a reduced degree of interaction between the bulk materials in contact, this tends to reduce friction.

The same effects, as in Figs 4 and 5, are shown in Figs 6 and 7 but at a relatively high initial temperature of 60°C. It is seen that there is less change in wear intensity and coefficient of friction with contact pressure and sliding speed at that temperature than at 25°C, however both have higher initial values. Also from Figs 6 and 7 it can be seen that, at severe friction conditions (high sliding speed and high contact pressure), the wear intensity and coefficient of friction attained high values ($I_z = 13$ μm/km and $\mu = 0.74$ at $v = 2.5$ m/s,
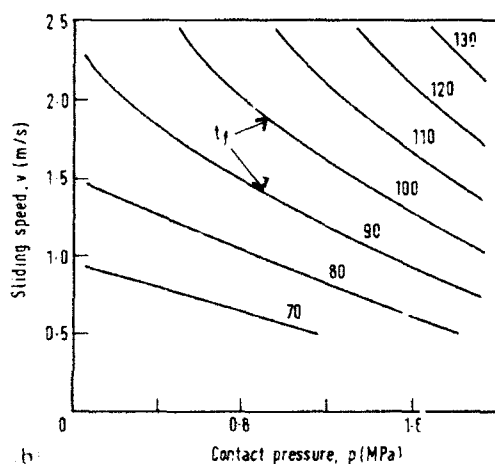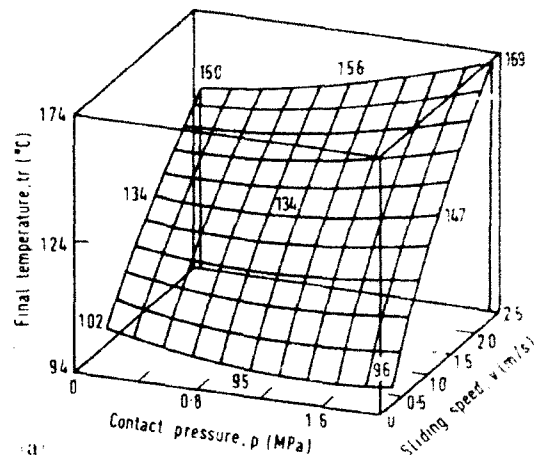
Fig. 8. Final temperature of a ptfe-based composite sliding against a steel disc at initial temperature of 60°C in two forms: (a) spatial; (b) contour.
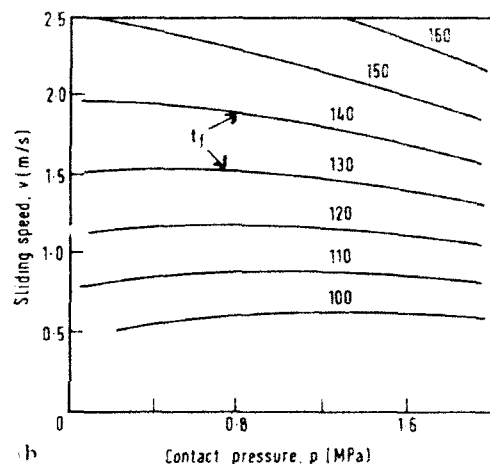
Fig. 9. Final temperature of a ptfe-based composite sliding against a steel disc at initial temperature of 95°C in two forms: (a) spatial; (b) contour.

$p = 2$ MPa and $t_p = 60°C$). This may be attributed to a partial degradation of ptfe resulting in an increase of metal to metal contact of the two sliding surfaces. This caused an increase in the adhesion contribution to the process of friction, increasing the friction coefficient and resulting in more rapid wear of the composite.[9,10]

(b) The effect of motion parameters (p, v, t_p) on the final temperature of friction

The effect of sliding speed and contact pressure on the resultant final temperature of friction is shown in Figs 8 and 9 from initial temperatures of 60°C and 95°C, respectively. It is obvious that the value of the final temperature is determined by the value of the initial temperature and by the fact that it increases with increasing sliding speed. Figure 8(a), $t_p = 60°C$, indicates that the final temperature increases with increasing contact pres-

sure and/or sliding speed. While, at 95°C, there is almost no effect of increasing contact pressure on the final temperature of friction except at high sliding speed, Fig. 9. On the other hand, increasing sliding speed tends to a gradual increase in the final temperature, regardless of the contact pressure.

CONCLUSIONS

From the conducted experimental friction and wear tests of ptfe filling with bronze powder rubbing against a steel counterpart at different motion parameters, the following conclusions could be drawn:

(1) There are two regions of motion parameters where wear intensity and the coefficient of friction both have low values. It is advantageous for the designer to predict

the values of wear intensity, coefficient of friction and final temperature of friction of that material if he knows the motion parameters and the inverse is correct.

(2) The final temperature increases with increasing contact pressure and/or sliding speed at relatively high initial temperature (60°C).

REFERENCES

1. Glauss, F. G., *Solid Lubricants and Self-Lubricating Solids*, Academic Press, New York, London, 1972, p. 200.
2. Buckley, D. H., *Friction, Wear and Lubrication in Vacuum*, NASA, Washington, DC, 1971, p. 138.
3. Braithwaite, R., *Solid Lubricants and Surfaces*, MacMillan, New York 1964, p. 179.
4. Lancaster, J. K., Estimation of the limiting *PV* relationships for thermoplastic bearing materials. *Tribology*, 4 (2) 1971 82-6.
5. Lontz, J. F. & Kumnick, M. C., Wear studies on molding of ptfe resins: considerations of crystallinity and graphite content. *ASLE Trans.*, 6 (4) 1963 276-86.
6. Kar, N. K. & Bahadur, S., The wear equation of unfilled and filled polyoxymethylene. *Wear*, 30 (3) 1974 337-48.
7. Ziemianski, K. & Capanidis, D., The mechanism of dry friction of polyoxymethylene against steel. *Wear*, 82 (1982) 717-32.
8. Manchak, K., *Technique of Plan Experiments*, WNT, Warsaw, Poland, 1976 (in Polish).
9. Tanaka, K. & Ueda, S., The mechanism of wear of ptfe above the melting point. *Wear*, 39 1976 323-33.
10. Bahadur, S. & Ludema, R. C., The viscoelastic nature of the sliding friction of polyethylene, polypropylene and copolymer. *Wear*, 18 1971 109-28.

Designing for damage tolerant bonded joints

R. Jones, W. K. Chiu & J. Paul

Defence Science and Technology Organisation, Airframes and Engines Division, Aeronautical Research Laboratory, 506 Lorimer St, Pt. Melbourne, Victoria 3207, Australia

This paper discusses the damage tolerant design methodology for adhesively bonded joints and bonded repairs. Attention is focused on the effects of rate dependence, creep, and strain/load holds on the load carrying performance of structural adhesives.

1 INTRODUCTION

The research undertaken as part of the Primary Adhesively Bonded Structure Technology (PABST) program[1] revealed that adhesively bonded structures are significantly more tolerant to large disbonds than had previously been thought. The PABST fuselage was made using 'development' tooling and contained a number of significant flaws. These flaws did not grow during testing.[2] Similarly, the environmental fatigue testing of representative coupons did not damage the adhesive bonds.[2]

Following this work it was shown (see Ref. 3) that externally bonded composite patches were an effective method of repairing cracked, or damaged, structural components. Whilst this repair methodology was first used to repair cracks in military aircraft it has recently been applied to civilian aircraft. An application to Boeing 727 and 747 aircraft is described in Refs 4 and 5, which outline a series of flight demonstrator programs, whilst repair to the keel beam of a Boeing 767 aircraft is described in Ref. 6. A summary of the relevant structural design consideration is given in Ref. 7.

In 1990, with the support of the Australian Civil Aviation Authority (CAA), a world wide study into the commercial application of this technology was performed, see Ref. 8. Thirty four organisations in eight countries, including 10 manufacturers and seven regulatory authorities were consulted. The following proposed design rules and procedures were subsequently adopted by the CAA: viz.

(1) Designs shall be substantiated against the Damage Tolerance provisions of the United States Federal Aviation Regulations (FAR) Part 25.571 at Amendment 45.

(2) The repair of any structural component which contains damage sufficient to reduce the aircraft structure to below design limit load residual strength shall not normally be attempted.

(3) Service time degradation, environmental and impact damage substantiation evidence shall be provided for the composite material and the structural bond, as appropriate to the design. This should include sufficient work to enable the composite repair to meet the intent of the damage tolerance requirements.

(4) Quality control considerations should include, for all critical areas, wedge testing of bond strips produced during the repair process.

The purpose of this report is to discuss the design methodology for the damage tolerant design of bonded joints and, by analogy, composite repairs to cracked metallic structural components.

In the CAA Airworthiness Advisory Circular it was stated that:

> ...civil requirements do not mandate an initial flaw approach. However, it is often convenient to do so and this may reduce the threshold fatigue testing requirement. This may be in recognition of leaving the initial crack in the metal unchanged but also may cover the presence of an unbonded region in the joint.

In light of these comments the initial PABST methodology, see Ref. 9, has recently been extended to include damage tolerance considerations, see Ref. 10. In Ref. 10 this work was sub-

stantiated by a series of fatigue test programs in which the joints contained either in-built disbonds and/or impact damage.

2 DESIGN METHODOLOGY

2.1 Maximum load carrying capacity

The results of the PABST test program led to the widespread acceptance of several simple formulae for calculating the maximum load carrying capacity of a bonded joint. For a symmetrical bonded joint, subjected to a uniform remote tensile stress, it was suggested[9] that failure will occur when W_{max}, the maximum value of the strain energy density in the bond, equals W_c, the maximum permissible value of the strain energy density of the adhesive as determined from a thick adherend test, i.e. when

$$W_{max} = W_c \qquad (1)$$

It was also shown, see Ref. 9, that for thin adherends the maximum load, P_{max}, that can be carried by the bond was related to W_{max} by the formulae:

$$W_{max} = P_{max}^2/(4ETt) \qquad (2)$$

Here E is the Young's modulus of the adherends (skin) whilst t and T are the thicknesses of the adhesive and the adherend respectively, see Fig. 1. Consequently, for a symmetrical 'thin skinned' bonded joint, subjected to a uniform remote tensile stress, the maximum load P_{max} that can be carried by the bond was given, see Ref. 9, as:

$$P_{max} = 2\sqrt{tW_c ET} \qquad (3)$$

The analysis used, in Ref. 9, to determine these formulae made no explicit allowance for the effects of load dwells or strain holds. This effect, which can be quite significant, is shown in Fig. 2 for the thin film adhesive FM73 at various strain rates. (Note that, as can be seen in Fig. 2, during a
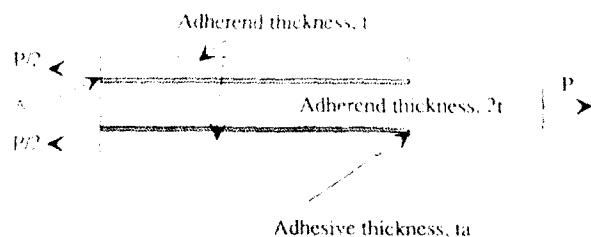
strain hold the stress decays to an asymptotic value which is independent of the strain rate and of the value at which the strain was held. As such these formulae are only applicable for loading which is strictly monotonic. This limitation can be removed by modifying eqn (3) as follows:

$$P_{max} = 2\sqrt{tET} |W_c - W^I| \qquad (4)$$

where W^I is the irreversible, i.e. inelastic, energy resulting from either a load dwell or a strain hold. In general W^I will depend on the loading rate. However, for strain holds the quantity W^I can be approximated by the formula:

$$W^I = (\sigma_e^2 - \sigma_{th}^2)/2E_a \qquad (5)$$

where E_a is the Young's modulus of the adhesive, σ_e is the maximum value of the von Mises equivalent stress in the adhesive and σ_{th} is the threshold, i.e. the endurance, level of the von Mises equivalent stress. As shown in Ref. 10 whilst the
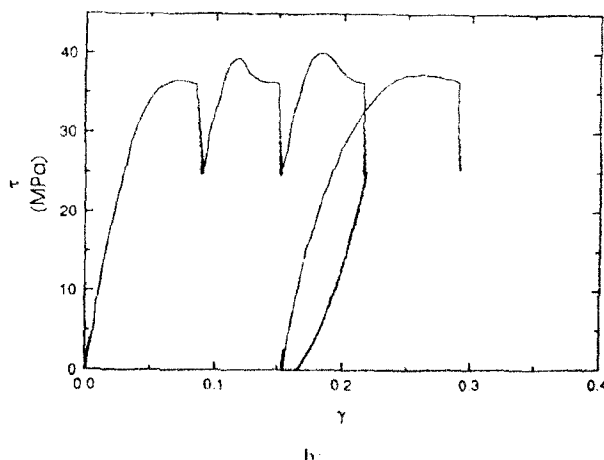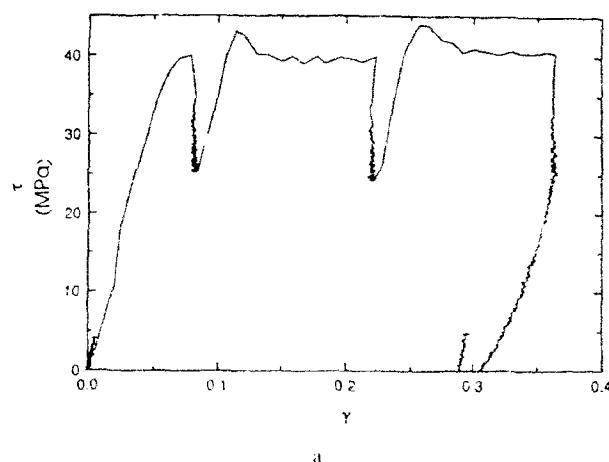

a

b

Fig. 2. Stress/strain response of FM73: (a) 8·80e-2/s; (b) 8·67e-3/s.

Fig. 1. Geometry of the lap joint.

von Mises equivalent stress σ_e is strain rate dependent the threshold stress σ_{th} is strain rate independent. (Here it should be noted that for pure shear problems σ_e^2 equals $3\tau^2$.)

A conservative estimate for P_{max} is obtained by using the value of σ_e obtained from test data at high strain rates. For FM73 this value, at room temperature, is approximately 40 MPa, see Ref. 10. For FM73 the room temperature 'threshold' stress σ_{th} is approximately 25 MPa, which corresponds to a 'threshold' energy W_1 of 0·416 MPa. As can be seen from Table 1 the 'threshold' stress corresponds to the lower limit of the yield (shear) stress, i.e. the value of the yield (shear) stress at vanishingly small strain rates.

During strain holds, which frequently occur during proof tests, in laboratory testing and in pressurised fuselage structures, the recoverable (i.e. elastic) strain energy is converted into irreversible energy, and as such is a direct reflection of the degradation of the adhesive. The boron/epoxy reinforcement (doubler) to a F111 wing pivot fitting is an interesting example which illustrates the importance of this effect. Here the doubler is bonded to the wind pivot fitting under load. In one instance, due to a problem in the application process, a doubler disbonded during a strain survey. This failure, which is documented in Ref. 11, did not occur instantaneously, upon commencement of the strain hold, and took a significant time to occur.

It is important to note the fundamental assumptions underlying eqn (3). These are:

(i) In the adherends (skin) the shear stress and the normal stress (peel) are negligible.
(ii) Each point in the adhesive lies on the same, i.e. unique, rate independent stress/strain curve.

The first assumption is only true for thin adherends. For 3·175 mm thick aluminium alloy skins it has been shown, both experimentally and analytically,[12] that this assumption is invalid over a distance of approximately 2 mm on either side

Table 1. Yield shear stress and elastic shear modulus of FM73 at various strain rates

Strain rate (s⁻¹)	Yield stress (MPa)	Shear modulus (MPa)
8·68e-5	26·78	753
8·78e-4	32·81	746
8·67e-3	35·94	766
8·80e-2	39·06	758

of the joint. In this region, which is the peak shear stress region, the inner adherend (skin) experiences significant compressive normal (peel) stresses. As such eqns (3) and (4) are only valid for thin skinned structures. For aluminium alloy skins they are questionable when the skin thickness is greater than approximately 3 mm.

The assumption that each point is on a single rate independent stress/strain curve is also questionable. As shown in Ref. 10 adhesives are strongly rate dependent. The linear elastic solution for the strain in the joint yields strains which vary from a minimum of zero in the centre of the joint to a maximum of

$$\gamma = \lambda_e \tau_{av} l / (2 G_e)$$

at the ends. Here $\tau_{av} l = P/2$, P is the applied load, τ_{av} is the average shear stress, G_e is the shear modulus of the adhesive and $\lambda_e^2 = 2G_e/Et_a$. If it took t_a s to apply the load then the strain rate in the adhesive would vary from zero, in the centre of the joint, to a maximum value of γ/t_a at the ends. As can be seen from Table 1 this would result in a significant range of the apparent 'yield stress'.

As a result of this effect each point in the adhesive can be expected to be on a different, time dependent, stress/strain curve. As load is shed from the adhesive at the ends of the joint, due to the onset of plasticity, it can be expected that, at points away from the ends, the local strain rate will increase. Consequently, it is anticipated that any given point in the adhesive will not remain on a single stress/strain curve. Initially it will, in general, lie on a 'low' strain rate curve and subsequently move to a series of 'higher' strain rate curves as the load increases. Whilst this effect may invalidate the formulae, derived in Ref. 9, for the shear stresses and strains the expression for the strain energy W remains unchanged. (This phenomenon will be clarified in Section 3.) As a result eqns (3) and (4) are still applicable.

2.2 Damage tolerance considerations

For bonded structures the PABST program revealed that, for thin skinned structures, the use of da/dn calculations, to life a bonded joint, is often inappropriate and, in some instances, potentially detrimental, see Ref. 2. For such structures the bond (joint) can be designed such that damage will not initiate. Furthermore, if the bond is found to contain damage, i.e. delaminations or disbonds, then this damage will not grow, even under

adverse environmental conditions, see Refs 2, 4, 8, 10, 13. In this case the joint should be designed such that the stresses and strains in the adhesive are below a limiting value, which is termed the 'threshold,' or endurance, value for the particular adhesive, see Ref. 10 and Chapters 4 and 6 in Ref. 3.

To address the damage tolerant requirements inherent in the CAA Airworthiness Advisory Circular it is possible to define the fatigue 'threshold' load P_t, and the associated fatigue 'threshold' strain ε_t, below which irreversible damage in the adhesive will not occur, see Ref. 10. For 'thin' adherends (skins) this is done, as in eqns (1) and (3), from the formulae:

$$P_t = 2\sqrt{t W_t E T} \qquad (7)$$

$$\varepsilon_t = 2\sqrt{W_t E t / T} \qquad (8)$$

where W_t is the 'threshold' value of the strain energy density of the adhesive, i.e. the value below which irreversible effects will not occur. The value of W_t can be determined experimentally using the thick adherend test specimen, see Ref. 10. In this case irreversible damage will not occur. For FM73 the 'threshold' stress is approximately 25 MPa, which corresponds to a 'threshold' energy W_t of 0·416 MPa, see Ref. 10.

For aerospace applications P_{max}, as calculated from eqn (3) should be greater than the ultimate load for the component and the value of $P_t(\varepsilon_t)$, calculated using eqns (7) or (8), should be greater than the limit load (strain). In general if the requirement for $P_t(\varepsilon_t)$ is met then the requirement for P_{max} will usually be satisfied. However, there will be instances when it is not possible to meet the requirement for $P_t(\varepsilon_t)$. In these cases the adhesive joint may still exhibit an adequate fatigue life. For bonded composite repairs this means that if FAR 25 (Part 25.571) and the associated damage tolerant requirements are to be met, see Section 1, then a more detailed fatigue analysis of the joint possibly including coupon tests, both with and without damage, in an aggressive environment, i.e. a hot wet 3·5–5% salt environment, may be required. However, it should be noted that for composite repairs the fatigue life of the repaired structure only needs to be greater than that of the undamaged structure.

As an example let us consider a typical 'thin skin' joint where $t = 0·2$ mm, $T = 1·2$ mm and $E = 70$ GPa. This results in a threshold strain ε_t of approximately 0·002 which, in many cases, would be above the limit strain for the component. (For a

typical wide-bodied transport aircraft the peak (limit) fuselage strain is approximately 0·0013, see Ref. 13.) To further illustrate the need to keep below the endurance level consider the case where this joint experiences a load spectra consisting of the following loading blocks: A strain excursion, in the (remote) adherend, with $\varepsilon_{min} = 0·00$ and $\varepsilon_{max} = 0·0031$ where the maximum strain is achieved in 0·59 s. (Using eqn (6) this corresponds to a maximum shear strain, in the adhesive, of approximately 0·052, and an associated strain rate of approximately 0·008 s^{-1}. This strain rate corresponds (approximately) to the fastest rate given in Table 1. At this rate the strain excursion corresponds to a stress excursion in the adhesive of approximately 39 MPa. This strain excursion is then followed by a 2-s strain hold, i.e. at $\varepsilon_{max} = 0·0031$, after which the specimen is unloaded to zero load.

The initial strain excursion produces, in the adhesive, very little inelastic strain. However, the 2-s strain hold results in an inelastic strain, in the adhesive, of approximately 0·019, which accumulates with each consecutive strain hold. However, the maximum strain that the adhesive can tolerate is approximately 0·7. Thus as a first approximation the joint can be expected to withstand of the order of 40 such blocks of loading, after which delamination damage can be expected to initiate. (A similar 'ratcheting' process can be seen in the experimental test data given in Ref. 10. This damage can subsequently be expected to result in fatigue failure. On the other hand taking, as a conservative estimate, W_c to be 25 MPa, we obtain P_{max}/T to be in excess of 1000 MPa, which is well above the strength of most aluminium alloys.

This example illustrates how a joint may fail in fatigue at a strain/stress well beneath the ultimate load carrying capacity of the joint and highlights the need to consider fatigue implications in the design process. By reducing ε_{max} the number of cycles that can be withstood is increased. However, if the skin thickness had been increased, to say $T = 3$ mm, then to achieve a similar degradation in the fatigue performance of the joint would require a lower value of ε_{max}, i.e. approximately 0·0018 for the case when $T = 3$ mm.

In previous sections we have seen that when designing a bonded joint, the stress/strain response of the adhesive plays a central role in determining both the load carrying capacity and the fatigue performance of the joint, see Refs 1, 2, 9, 10. An analytical representation for this rate dependent stress/strain response, which uses a

'State Variable' approach and which can be implemented on an IBM PC, is given in Ref. 10. The computational advantage of expressing the 'fatigue threshold' load P_t in terms of the quantity W_t, rather than the associated stress or strain threshold values, was discussed in Ref. 10 and will also be discussed in the next section.

3 RATE DEPENDENT ANALYSIS OF BONDED JOINTS

To evaluate the effect of the loading rate on the critical design variables we will consider the specific joint analysed in Ref. 14. Here, as in Ref. 14, the elastic shear modulus G_a of the adhesive was taken as 750 MPa, the overlap length, l, of the joint was 100 mm, the adhesive thickness, t, was 0·2 mm, and the adherend thicknesses, T, were 3·175 mm whilst the remote stress in the adherends was 900 MPa. An elastic, a traditional incremental elastic–plastic and an elastic–plastic rate dependent finite element analysis of this joint was performed using the mesh described in Ref. 14, see Fig. 3, with four elements across the adhesive layer. In this work the adhesive properties were taken to be as for FM73 with the strain rate dependence as measured in Ref. 10. Here it was found that for FM73 the slope of the post yield curve was essentially rate independent and was approximately 5 MPa. The strain rate dependence of the yield stress was given in Table 1. However, for comparative purposes a variety of post yield slopes were also considered, see Table 2.

For this geometry the maximum value of the strain energy density (work), was calculated from the results of an elastic, an incremental elastic–plastic and a rate dependent elastic–plastic analysis, see Refs 10, 15 for details. The resultant values are given in Table 2 for a remote stress in the adherends of 900 MPa. Here we see that the differences, in the calculated values for the strain energy, were approximately 5% and were similar to the differences given by the rate independent analysis. This work can thus be seen to support the fundamental assumption, underlying the simple design formulae developed in Ref. 9 as part of the PABST program, that although adhesively bonded joints are strongly rate dependent the maximum value of the critical design variable, i.e. the maximum value of the strain energy in the joint, is relatively rate independent.
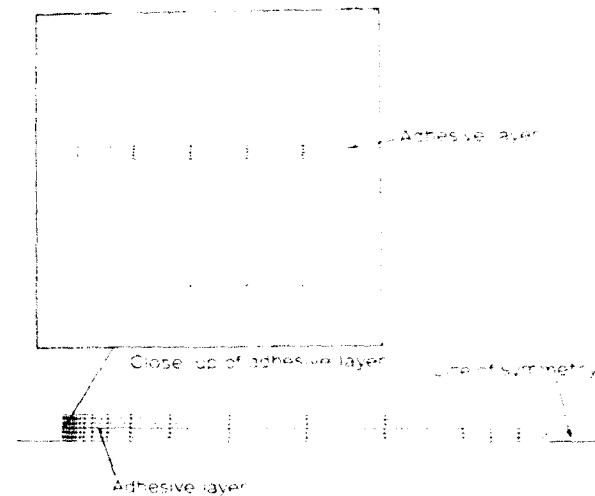

Fig. 3. Details of the finite element mesh.

Table 2. Effect of strain rate

	Rate independent solution					Rate dependent solution				
						$t_0 = 1$ s			$t_0 = 100$ s		
Yield stress MPa	Post yield slope (MPa)	Strain energy density (MPa)		%	Post yield slope (MPa)	Strain energy density (MPa)		%	Strain energy density (MPa)		%
		Elastic soln	Elastic–plastic soln			Elastic soln	Rate depent soln		Elastic soln	Rate depent soln	
68	5	20·936	19·451	7·6	5	20·936	18·682	11·0	20·936	18·606	11·0
68	50	20·936	20·444	2·4	50	20·936	20·362	2·7	20·936	19·034	9·1
68	100	20·936	20·792	0·6	100	20·936	21·364	2·0	20·936	19·521	6·7
68	400	20·936	21·981	4·7	400	20·936	19·524	6·7	20·936	21·702	3·6
68	800	20·936	22·029	4·9	800	20·936	20·894	0·2	20·936	20·623	1·5
100	50	20·936	22·389	6·4	—	—	—	—	—	—	—
140	50	20·936	24·724	18	—	—	—	—	—	—	—

Whilst the strain energy was relatively insensitive to strain rate effects the individual stress and strain components were not. This can be seen in Fig. 4 where, for point A, the equivalent stress–equivalent strain relationship is plotted for the two cases when the load was applied over 1 s and 100 s respectively.

At any given point, the strain rate and hence the associated stress–strain curve also vary with time. Once the inelastic irreversible process commences, there are three effects. Since the post-yield slope is small, the 'resistance' to any increase in load is lowered. This effect tends to increase the strain rate. However, as the yielded region becomes larger this 'local' region, which is less stiff, sheds load. This effect tends to reduce the local strain rate. Eventually, a 'steady state' level is reached. These three phenomena can be seen in Fig. 5, where the strain rate behaviour of the adhesive is plotted for points at various distances from point A. Initially the first effect dominates. Then as load shedding becomes more dominant the strain reduces to a steady state value. The
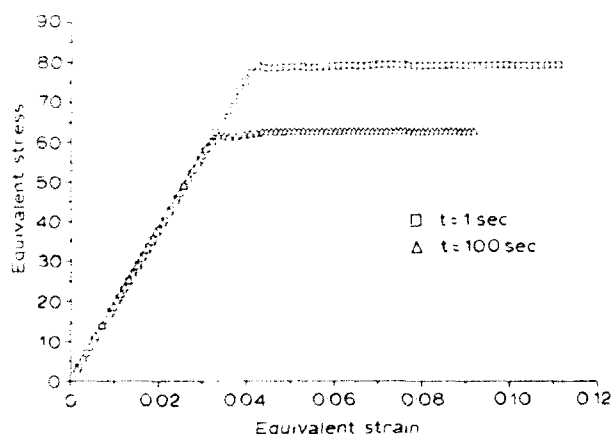
strain rate at each point in the adhesive is different and varies with time. It is thus apparent that no single stress–strain curve is applicable and that, at each point, the appropriate curve is determined by the local strain rate at that instant of time.

4 IMPLICATIONS FOR CO-CURED COMPOSITE JOINTS

The previous analysis has concentrated on adhesively bonded joints where the load is transmitted, via shear, through the adhesive layer. Symmetric co-cured composite joints are somewhat similar in that the load is transmitted via interlaminar shear in the composite. We also know that, in shear, composite materials behave in a fashion similar to adhesives, see Ref. 16. To illustrate this a simple two rail shear test was performed in accordance with ASTM test standard D4255-83 method A. The test specimen was a T300/914C graphite-epoxy laminate with a [0,90] ply configuration of dimensions 76 mm by 152 mm. The tests were performed in strain control. Tests were also performed during which the strain was held constant, until the stress reached its asymptotic value, at various strain levels. A typical shear stress–shear strain curve is given in Fig. 6. Here, after the second strain hold the specimen was unloaded and then reloaded at the same strain rate.

The composite behaviour, as given in Fig. 6, is quite similar to that shown in Fig. 2 for the thin film adhesive FM73. In both cases during a strain hold the stress relaxes to an asymptotic level regardless of the strain level. The slope of the 'reloading' curve, following either a strain hold or

Fig. 4. Equivalent stress–equivalent strain relationship.

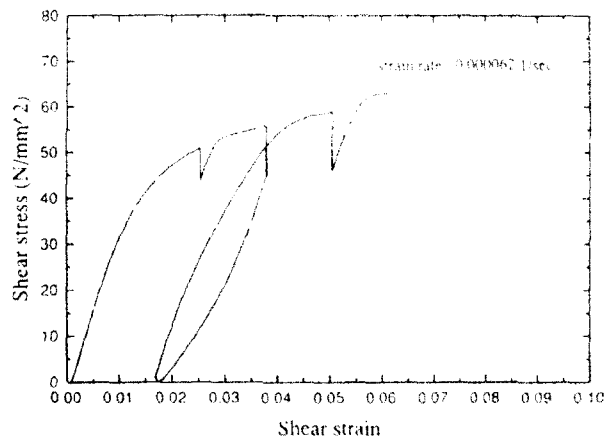Fig. 5. Strain rate–time relationship at various locations in the adhesive layer.

Fig. 6. Stress/strain response of T300/914.

unloading, is parallel to its initial elastic curve. This implies a 'traditional', i.e. metal-like, inelastic behaviour. As such conventional formulations for the load carrying capacity, and durability, of co-cured joints need to be extended to allow for this time dependent behaviour.

5 CONCLUSION

This report has presented the extended PABST philosophy for the damage tolerant design of adhesively bonded joints. In this approach the adhesive stresses and strains are kept beneath their threshold values. These threshold values have been presented for the thin film adhesive FM73, which is widely used in aerospace applications. The stress strain response of this adhesive, at various strain rates, together with the associated value of W, is presented in Ref. 10, as is an analytical representation for the rate dependent response.

REFERENCES

1. Thrall, F. W., Primary adhesively bonded structure technology (PABST): Design handbook for adhesive bonding. USAF Technical Report, AFFDL-TR-79-3119, 1979.

2. Hart-Smith, L. J., Design and analysis of bonded repairs for metal aircraft structures. *Bonded Repair of Aircraft Structures*, Chap. 3, ed. A. A. Baker & R. Jones. Martinus Nijhoff, Dordrecht, 1988.

3. Baker, A. A. & Jones, R., *Bonded Repair of Aircraft Structures*. Martinus Nijhoff, Dordrecht, 1988.

4. Bartholomeus, R. A., Paul, J. J. & Roberts, J. D., Application of bonded composite repair technology to civilian aircraft — 747 Demonstrator Program. *Proceedings International Conference on Aircraft Damage Assessment and Repair*, ed. R. Jones & N. J. Miller. Institution of Engineers Australia. ISBN BOOK 85825 537 5, July, 1991.

5. Taylor, J. L., The practicalities of ensuring the continued structural integrity of aging aircraft in an airline environment. *Proceedings International Conference on Aircraft Damage Assessment and Repair*, ed. R. Jones & N. J. Miller. Institution of Engineers Australia. ISBN BOOK 85825 537 5, July, 1991.

6. Jones, R., Bridgford, N., Molent, L. & Wallace, G., Bonded repair of multi-site damage. *Structural Integrity of Aging Airplanes*, ed. S. N. Atluri, S. G. Sampath & P. Tong. Springer Verlag, Berlin-Heidelberg, 1991, pp. 199-213.

7. Jones, R., Recent developments in advanced repair technology. *Proc. Int. Conf. on Aircraft Damage Assessment and Repair*, Melbourne, August 1991. Institution of Engineers Australia. ISBN BOOK 85825 537 5, July, 1991.

8. Torkington, C., The regulatory aspects of the repair of civil aircraft metal structures. *Proceedings International Conference on Aircraft Damage Assessment and Repair*, ed. R. Jones & N. J. Miller. Institution of Engineers Australia. ISBN BOOK 85825 537 5, July, 1991.

9. Hart-Smith, L. J., Adhesively bonded double lap joints. NASA Langley Research Center Report NASA CR-112235, January, 1973.

10. Chiu, W. K., Rees, D., Chalkley, P. & Jones, R., Designing for damage tolerant repairs. ARL Aircraft Structures Report 450, August, 1992.

11. Molent, L., Callinan, R. J. & Jones, R., Structural aspects of the design of an all boron epoxy reinforcement for the F111C Wing Pivot Fitting: Final Report. ARL, Aircraft Structures Report 436, September, 1992.

12. Heller, M., Williams, J. F., Dunn, S. & Jones, R., Thermo-mechanical analysis of composite specimens. *J. Composite Structures*, 11 1988 309-24.

13. Molent, L., Bridgford, N., Rees, D. & Jones, R., Environmental evaluation of repairs to fuselage lap joints. *Composite Structures*, 21 2 1992 121-30.

14. Chiu, W. K. & Jones, R., A numerical study of adhesively bonded joints. *International Journal of Adhesion and Adhesives* in press.

15. Kuruppu, M. D., Williams, J. F., Bridgford, N., Jones, R. & Stouffer, D. C., Constitutive modelling of the elastic plastic behaviour of 7050-T7451 aluminium alloy. *Journal of Strain*, 27 2 1992 85-92.

16. Cardon, A. H., Global and internal time dependent behaviour of polymer matrix composites. *Inelastic Deformation of Composite Materials*, ed. G. J. Dvorak. Springer-Verlag, New York, 1990, pp. 489-99.

Stress and strength analysis of composite joints using direct boundary element method

Chien-Chang Lin & Chuen-Horng Lin

Institute of Applied Mathematics, National Chung-Hsing University, Taichung, Taiwan

In this paper, the stress distribution and the strength of bolted joints of ortho-tropic composite plates under uniform loading are investigated. A direct boundary element method with quadratic isoparametric elements in conjunction with a fundamental solution derived by Rizzo and Shippy[1] is used. Plates with rigid bolts are treated as two-dimensional plane stress problems, and the bolt size is considered to be identical to the hole dimension. The prediction of the laminate strength is based on the Yamada-Sun[2] failure criterion. Some numerical results for various edge distances and material properties are presented for illustrative purposes.

NOTATION

D	Hole diameter
E	Edge distance
E_1	Young's modulus in the longitudinal direction
E_2	Young's modulus in the transverse direction
G_{12}	Shear density
H	Thickness of the plate
L	Length of the plate
R_{oc}, R_{ot}	Characteristic lengths
S	Shear strength of a cross-ply laminate
W	Width of the plate
X	Longitudinal tensile strength of each ply
v_{12}	Poisson's ratio

INTRODUCTION

Increasing applications of composite materials in aircraft structures have motivated the present investigation on the stress concentration and strength of bolted joints. Limited work in this area is available in the open literature, and the authors are not aware of any existing closed form solution for this problem concerning orthotropic plates. However, there are studies for stress and strength analysis for bolted joints of orthotropic plates using various numerical methods.

In 1979, Pyner and Matthews[1] made an experimental investigation on the strength of a variety of multi-hole joints. Their results were compared with the strength of single-hole joints. In 1980, Ogonowski[3] used the complex variable technique in conjunction with boundary collocation procedure to determine the stress concentration at a circular hole of a laminated finite plate. In 1982, Chang *et al.*[5] studied the stress distribution and the failure load of a laminate by using a finite element method. Using a computationally efficient finite element model, Lakshminarayana[6] in 1983 presented a study on the problem of a semi-circular edge-notch in a laminated composite plate of finite size under uniaxial tension. In 1984, Chang and Scott[7] presented the stress distribution in the laminate using a finite element method and the failure load and mode for a joint containing one or two pin-loaded holes. Also Zhang and Ueng[8] in 1984 used the complex stress function which satisfies the displacement boundary conditions along the hole to obtain an analytical solution of stress around a pin-loaded hole in an orthotropic laminate. In 1986, Mahayerin and Sikarskin[9] developed an efficient boundary element method for use in the analysis of mechanically fastened composite structures.

In this study, stress concentrations are determined by a direct boundary element method with quadratic isoparametric element formulation, and the fundamental solution for two-dimensional problems for orthotropic elastic material is used. For the strength of bolted joints of laminated orthotropic plate, the analysis is based on the characteristic curve for plate failure derived from the Yamada-Sun failure criterion. A comparison

of the numerical results based on the present method with other methods shows that the present direct boundary element method is significantly more efficient in computational time and cost for comparable accuracy.

STRESS ANALYSIS

Direct boundary element method

The direct BEM can most conveniently be formulated through the reciprocal work theorem. The theorem states that: if two distinct elastic equilibrium states $(\phi^*, t_i^*, u_i^*), (\phi_i, t_i, u_i)$ exist in a region V bounded by the surface S, the work done by the forces of the first system $(*)$ on the displacements of the second is equal to the work done by the forces of the second system on the displacements of the first $(*)$. Thus, according to Banerjee and Butterfield.[10]

$$\int_S t_i^*(x)u_i(x)\,ds(x) + \int_V \phi_i^*(z)u_i(z)\,dv(z)$$

$$= \int_S t_i(x)u_i^*(x)\,ds(x) + \int_V \phi_i(z)u_i^*(z)\,dv(z) \quad (1)$$

where x is a point on S and z is a point in V. Displacements, tractions, and body forces are u_i, t_i and ϕ_i, respectively, and the $(*)$ denotes those quantities corresponding to a unit force applied in an infinite solid.

We shall require the surface traction $t_i(x)$ at a point (x_i) on a surface with outward normal $n_i(x)$ determined from

$$t_i(x) = \sigma_{ij}(x)n_j(x) = F_{ik}(x, \xi)e_k(\xi)$$

$$\times u_i(x) = G_{ik}(x, \xi)e_k(\xi) \quad (2)$$

$$t_i^*(x) = F_{ik}(x, \xi)e_i^*(\xi) \quad (3)$$

Substituting eqns (2) and (3) in eqn (1), we obtain

$$\int_S F_{ij}(x, \xi)u_i(x)\,ds(x) + \int_V \delta_{ij}\delta(z, \xi)u_i(z)\,dv(z)$$

$$= \int_S t_i(x)G_{ij}(x, \xi)\,ds(x)$$

$$+ \int_V \phi_i(z)G_{ij}(z, \xi)\,dv(z) \quad (4)$$

in which we have made use of eqn 3 with the following manipulation for the unit force $\phi_i^* = e^*(z)$ in the second term on the left-hand-side of eqn (1):

$$\int_V e^*(z)u_i(z)\,dv(z) = \int_V e^*(\xi)\delta(z, \xi)u_i(z)\,dv(z)$$

$$= \int_V e^*(\xi)\delta_i u_i(z)\,dv(z) \quad 5$$

The $e^*(\xi)$ term is now common to all the integrals in eqn (1) and can be factored outside of each integral which allows us to write eqn (4). This term can further be simplified by noting that

$$\int_V \delta_{ij}\delta(z - \xi)u_i(z)\,dv(z)$$

$$= \int_V u_i(z)\delta(z, \xi)\,dv(z) = \beta u_i(\xi) \quad 6$$

in which the index $\beta = 1$ corresponds to points within V, $\beta = \frac{1}{2}$ corresponds to points on S, and $\beta = 0$ corresponds to points outside of S. Hence from eqn (4), we arrive at

$$\beta u_i(\xi) = \int_S [t_i(x)G_{ij}(x, \xi) - F_{ij}(x, \xi)u_i(x)]\,ds(x)$$

$$+ \int_V \phi_i(z)G_{ij}(z, \xi)\,dv(z) \quad 7$$

Since no body force is considered in the study, then

$$\beta u_i(\xi) = \int_S [t_i(x)G_{ij}(x, \xi) - F_{ij}(x, \xi)u_i(x)]\,dS(x) \quad 8$$

where x locates an interior point and ξ for a boundary point, t_i is the surface traction, and u_i is the displacement vector.

Fundamental solution

A symmetrically stacked laminated plate consisting of N orthotropic lamina subjected to inplane loads as shown in Fig. 1 is considered. The relationship between the inplane stress resultants and the strain components based on the classical
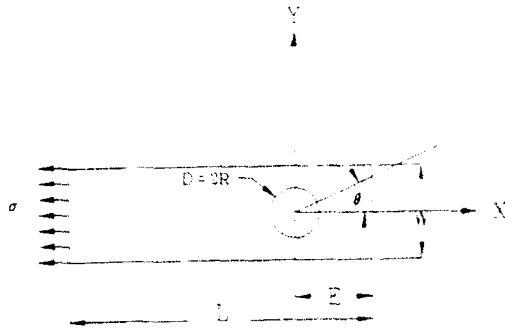
Fig. 1. Geometry and coordinates of a composite plate.

lamination theory is

$$\left\{\begin{array}{c} N_x \\ N_y \\ N_{xy} \end{array}\right\} = \left[\begin{array}{ccc} A_{11} & A_{21} & A_{61} \\ A_{12} & A_{22} & A_{62} \\ A_{16} & A_{26} & A_{66} \end{array}\right] \left\{\begin{array}{c} u_{x,x} \\ u_{y,y} \\ u_{x,y} + u_{y,x} \end{array}\right\} \qquad (9)$$

where

$$A_{ij} = \sum_{k=1}^{N} \overline{Q}_{ij}^{k} h_k$$

in which $\overline{Q}_{ij}^{k}$ are the reduced stiffnesses and h_k is the thickness of the kth layer.

If the A_{16} and A_{26} terms are zero, eqn (9) reduces to

$$\left\{\begin{array}{c} N_x \\ N_y \\ N_{xy} \end{array}\right\} = \left[\begin{array}{ccc} A_{11} & A_{21} & 0 \\ A_{12} & A_{22} & 0 \\ 0 & 0 & A_{66} \end{array}\right] \left\{\begin{array}{c} u_{x,x} \\ u_{y,y} \\ u_{x,y} + u_{y,x} \end{array}\right\} \qquad (10)$$

which is the constitutive equation for the plane elasticity problem for a specially orthotropic laminate.

The effective engineering properties for balanced and symmetric laminates are determined from the stiffness constants, A_{ij}. The effective longitudinal Young's modulus becomes $E_x = (A_{11}A_{22} - A_{12}^2)/A_{22}$, the transverse Young's modulus $E_y = (A_{11}A_{22} - A_{12}^2)/A_{11}$, the longitudinal Poisson's ratio $\nu_{xy} = A_{12}/A_{22}$, and the shear modulus $G_{xy} = A_{66}$.

The Hooke's law for plane stress distribution for orthotropic plates takes the form

$$u_{x,x} = s_{11}\sigma_x + s_{12}\sigma_y$$
$$u_{y,y} = s_{12}\sigma_x + s_{22}\sigma_y \qquad (11)$$
$$u_{x,y} + u_{y,x} = s_{66}\sigma_{xy}$$

in which

$$s_{11} = \frac{1}{E_x}; \quad s_{22} = \frac{1}{E_y}; \quad s_{12} = \frac{-\nu_{xy}}{E_x} = \frac{-\nu_{yx}}{E_y};$$

$$s_{66} = \frac{1}{G_{xy}}$$

are the compliance, the stress σ_{ij} and displacement gradients $u_{i,j}$ are mean values taken through the thickness of the laminate.

According to Rizzo and Shippy,[1] various quantities are taken as follows:

$$G_{11} = K_a(\sqrt{\alpha_1}A_2 \ln r_1 - \sqrt{\alpha_2}A_1 \ln r_2)$$
$$G_{12} = G_{21} = -K_a A_1 A_2(\theta_1 - \theta_2) \qquad (12)$$
$$G_{22} = -K_a\left(\frac{1}{\sqrt{\alpha_1}}A_1 \ln r_1 - \frac{1}{\sqrt{\alpha_2}}A_2 \ln r_2\right)$$

$$F_{11} = K_a\left(\frac{A_1}{\sqrt{\alpha_2}r_2^2} - \frac{A_2}{\sqrt{\alpha_1}r_1^2}\right)x_2 n_2$$

$$F_{12} = K_a\left(M_1\frac{A_2}{r_1^2} - M_2\frac{A_1}{r_2^2}\right)$$

$$F_{21} = K_a\left(M_1\frac{A_2}{\alpha_1 r_1^2} - M_2\frac{A_1}{\alpha_2 r_2^2}\right) \qquad (13)$$

$$F_{22} = K_a\left(\frac{A_1}{\sqrt{\alpha_1}r_1^2} - \frac{A_2}{\sqrt{\alpha_2}r_2^2}\right)x_2 n_2$$

in which

$$K_a = \frac{1}{2\pi(\alpha_1 - \alpha_2)S_{22}}$$

$$A_i = S_{12} - \alpha_i S_{22}$$

$$r_i = \sqrt{x_1^2 + \frac{x_2^2}{\alpha_i}}$$

$$\theta_i = \tan^{-1}\left(\frac{x_2}{\sqrt{\alpha_i}x_1}\right)$$

$$M_i = \sqrt{\alpha_i}x_1 n_2 - \frac{1}{\sqrt{\alpha_i}}x_2 n_1$$

where the values of α_i are generally real and positive for a large number of materials, and the present study is limited to this class of materials.

Stress and displacement of interior points

For solving boundary value problems in plane elasticity using the fundamental solution, displacement and traction at each boundary element are given. As a result, we will use the following equation with the known values of displacements and tractions from the boundary points:

$$u_i(\xi) = \sum_{l=1}^{n} \left(\int_{sl} G_{ij}(x, \xi) \, ds(x) \right) t_j'(x^k)$$

$$- \sum_{l=1}^{n} \left(\int_{sl} F_{ij}(x, \xi) \, ds(x) \right) u_j'(x^k) \qquad (14)$$

Once the displacements at interior points $j(x, \xi)$ are given, the stress at interior points can be determined from the following stress–strain relation.

$$\begin{Bmatrix} \sigma_x \\ \sigma_y \\ \sigma_{xy} \end{Bmatrix} = \begin{bmatrix} c_{11} & c_{21} & 0 \\ c_{12} & c_{22} & 0 \\ 0 & 0 & c_{66} \end{bmatrix} \begin{Bmatrix} u_{x,x} \\ u_{y,y} \\ u_{x,y} + u_{y,x} \end{Bmatrix} \qquad (15)$$

in which $c_{ij} = A_{ij}/H$ and H is the plate thickness.

While $u_{x,x}$, $u_{y,y}$, $u_{x,y} + u_{y,x}$ are unknown in eqn (15), they can be determined by using eqn (14), and the stress components may be expressed as follows:

$$\sigma_{ij} = \sum_{l=1}^{n} \left(\int_{sl} D_{ij} \, dS(x^k) \right) t_j'(x^k)$$

$$- \sum_{l=1}^{n} \left(\int_{sl} S_{ij} \, dS(x^k) \right) t_j'(x^k) \qquad (16)$$

in which

$$D_{ij} = [D_{1ij} \quad D_{2ij}], \qquad S_{ij} = [S_{1ij} \quad S_{2ij}]$$

$$D_{111} = c_{11} \frac{\partial G_{11}}{\partial \xi_1} + c_{12} \frac{\partial G_{21}}{\partial \xi_2}$$

$$D_{211} = c_{11} \frac{\partial G_{12}}{\partial \xi_1} + c_{12} \frac{\partial G_{22}}{\partial \xi_2}$$

$$D_{122} = c_{12} \frac{\partial G_{11}}{\partial \xi_1} + c_{22} \frac{\partial G_{21}}{\partial \xi_2}$$

$$D_{222} = c_{12} \frac{\partial G_{12}}{\partial \xi_1} + c_{22} \frac{\partial G_{22}}{\partial \xi_2}$$

$$D_{112} = c_{66} \frac{\partial G_{11}}{\partial \xi_2} + c_{66} \frac{\partial G_{21}}{\partial \xi_1}$$

$$D_{212} = c_{66} \frac{\partial G_{12}}{\partial \xi_2} + c_{66} \frac{\partial G_{22}}{\partial \xi_1}$$

$$S_{111} = c_{11} \frac{\partial F_{11}}{\partial \xi_1} + c_{12} \frac{\partial F_{21}}{\partial \xi_2}$$

$$S_{211} = c_{11} \frac{\partial F_{12}}{\partial \xi_1} + c_{12} \frac{\partial F_{22}}{\partial \xi_2}$$

$$S_{122} = c_{12} \frac{\partial F_{11}}{\partial \xi_1} + c_{22} \frac{\partial F_{21}}{\partial \xi_2}$$

$$S_{222} = c_{12} \frac{\partial F_{12}}{\partial \xi_1} + c_{22} \frac{\partial F_{22}}{\partial \xi_2}$$

$$S_{112} = c_{66} \frac{\partial F_{11}}{\partial \xi_2} + c_{66} \frac{\partial F_{21}}{\partial \xi_1}$$

$$S_{212} = c_{66} \frac{\partial F_{12}}{\partial \xi_2} + c_{66} \frac{\partial F_{22}}{\partial \xi_1}$$

STRENGTH ANALYSIS

For the determination of the strength of a bolted joint before failure, the failure strength and location of failure initiation may be predicted by adopting a failure criterion. The present study follows the failure criterion proposed by Yamada and Sun.[2] The criterion proposed below is based on the assumption that all constituent lamina fail in the form of cracking along the fiber directions and each lamina has substantially higher shear strength:

$$\left(\frac{\sigma_1}{X} \right)^2 + \left(\frac{\sigma_{12}}{S_c} \right)^2 = e^2; \begin{cases} e \geq 1 \text{ failure occurs} \\ e < 1 \text{ without failure} \end{cases} \qquad (17)$$

where σ_1 is the longitudinal stress, σ_{12} is the shear stress, X is the ply longitudinal strength and S_c is the ply shear strength measured from a symmetric cross-ply laminate.

Locations of failure are determined according to the characteristic curve established by Chang et al.[5] for loaded holes. The failure is considered to occur on the curve for the value of r of the charac-

teristic curve defined by the following equation:

$$r(\theta) = \frac{D}{2} + R_{ot} + (R_{oc} - R_{ot})\cos(\theta) \qquad (18)$$

in which R_{ot} and R_{oc} are experimentally determined characteristic lengths for tension and compression respectively.

To predict the failure or strength of a bolted joint, we first determine laminate stress resultants from the characteristic curve from which we can determine e from ply-by-ply lamina stresses. These e values are proportional to the applied load p, and the highest value of e governs the strength of the joint. When this maximum $e = 1$, the corresponding applied load $p = p_t$ is the failure load:

$$p_t = \frac{p}{e} \qquad (19)$$

NUMERICAL RESULTS AND DISCUSSION

The present analysis using a direct boundary element method in conjunction with quadratic isoparametric elements is an accurate and versatile approach for solving elastic orthotropic plate problems. Several numerical examples are presented here for illustrative purposes.

Isotropic plates

To demonstrate the accuracy of the method, the stress distribution in an isotropic annulus plate for which the exact solution can be found in any textbook in elasticity such as the book by Timoshenko and Goodier[11] is considered. The material properties are $E = 2.96$ MPa, and $v = 0.3$. Results for the annulus having an inside radius $r_1 = 10$ cm and of outside radius $r_2 = 20$ cm under the internal pressure $\sigma = 10$ MPa are shown in Fig. 2. They compare extremely well with the exact solution given in Ref. 11.

Orthotropic plates

We first consider an orthotropic rectangular plate with a circular opening under three types of loading considered in Ref. 12. They are case (1) tension in the principal direction, case (2) hydrostatic tension of a plate, case (3) constrained pressure of plate. The material properties are $E_1 = 1.2 \times 10^5$ psi, $E_2 = 0.6 \times 10^5$ psi, $G_{12} = 0.07 \times 10^5$ psi and $v_{12} = 0.6568$. The

analytical results for the problem were given previously by Leknitskii *et al.*[12] The present results, given in Table 1 compare extremely well with the exact solutions.

An orthotropic plate of finite width containing an unloaded hole is considered next. The analytical solutions for the problem were given previously by Whitney and Nuismer,[13] and Chang *et al.*[5] The material properties are $E_{11} = 149.8$ GPa, $E_{22} = 1$ GPa, $G_{12} = 5.39$ GPa and $v_{12} = 0.29$. The geometrical dimensions are $W/D = 3.0$, $E/D = 4$, $L/D = 14$ with the diameter $D = 49$ mm where W and L are the width and length of the plate respectively, and E is the edge distance from the centre of the hole. Results based on the present method as shown in Fig. 3 show excellent agreement with the existing analytical solutions.
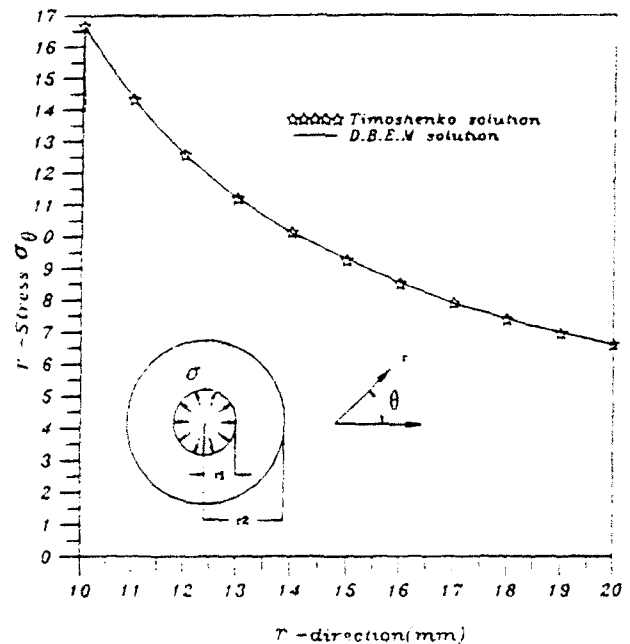

Fig. 2. Stress in the isotropic annulus plate under uniform internal pressure.

Table 1. Stresses in orthotropic plate with a circular opening

Loading type	σ_θ	Present solution (psi)	Exact solution[12] (psi)
Case (1)	Maximum	5·4694	5·454
	Minimum	−0·7172	−0·71
Case (2)	Maximum	4·0607	4·04
	Minimum	1·0915	1·09
Case (3)	Maximum	0·5389	0·56
	Minimum	−5·4025	−5·4

Finally, the strength of a plate made of T300/SP286(0/±45/90), with the same ply thickness of 1·067 mm is investigated. The material properties are given in Table 2, and the geometrical dimensions are $L = 100$ mm, $W = 25$ mm and $D = 10$ mm. Results on σ_x along the y-axis are shown in Fig. 4. Obviously, the high stress concentration
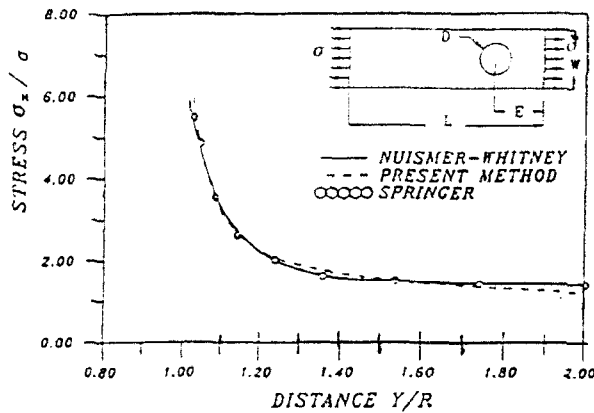
occurs at the edge of the hole. It is found that, when E/D is less than two, the longitudinal stress σ_x decreases across the width of the plate, and the stress reverses to compressive near the edge of the plate.

Similarly, the strength of a plate having two holes made of AS 3501–6(0/±45/90), with material properties given in Table 1, and ply thickness of 5·283 mm is studied. Results on σ_x along the y-axis are given in Fig. 5. Obviously, high stress concentration occurs at the edge of the hole. It is found that when E/D is less than two, the longitudinal stress σ_x decreases across the width of the plate, and the stress reverses to compressive near the edge of the plate.

Failure strength

The strength of a plate made of T300/SP286 with ply thickness of 1·067 mm is investigated. The results on the strength for $D = 10$ mm are shown in Fig. 6. Similarly, for the same problem for AS/3501 with ply thickness of 5·283 mm, results on the strength for $D = 10$ mm are given in Fig. 7. The strength at failure is small for E/D less than

Fig. 3.   Stresses in a uniformly loaded orthotropic plate with a free hole.
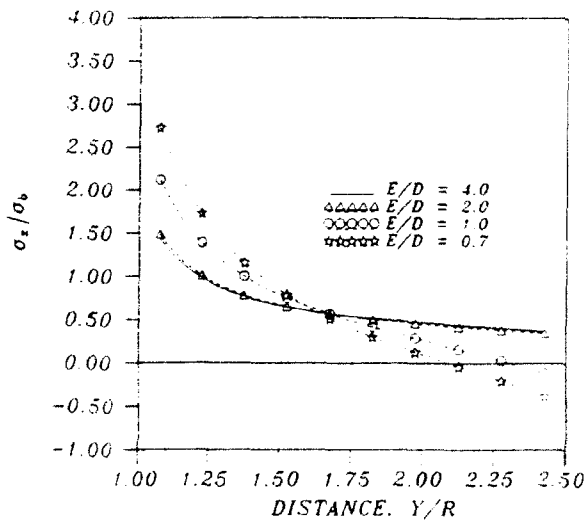
Fig. 4.   Stresses in a uniformly loaded T300/SP286 laminate with a loaded hole (where $\sigma_b = P/dt$).
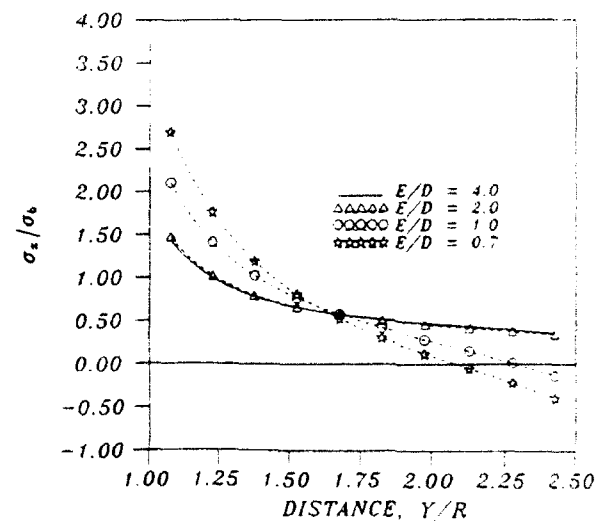
Fig. 5.   Stresses in a uniformly loaded AS/3501-6 laminate with a loaded hole (where $\sigma_b = P/dt$).

Table 2. Lamina material properties

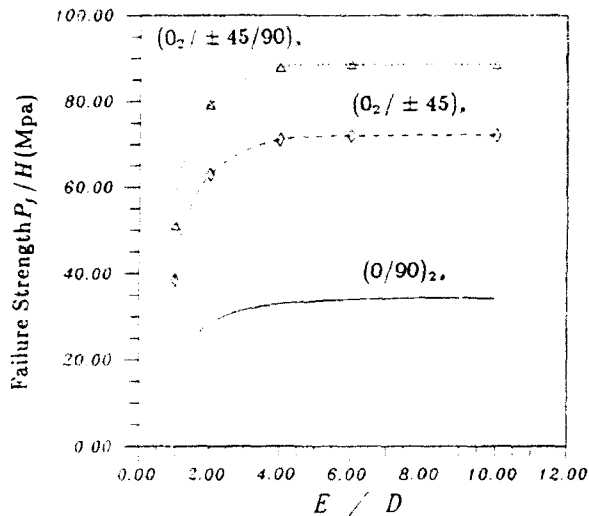|	E_1 (GPa)	E_2 (GPa)	G_{12} (GPa)	ν_{12}	X (GPa)	S (GPa)	R_{oc} (mm)	R_{ot} (mm)
T300/SP286	130·0	8·274	5·033	0·3	1·23	0·05	1·092	3·048
AS/3501-6	130·0	13·1	5·86	0·3	1·58	0·12	0·584	1·727

Fig. 6. The failure strength of T300/SP286 laminate under inplane stresses versus E/D ratio.
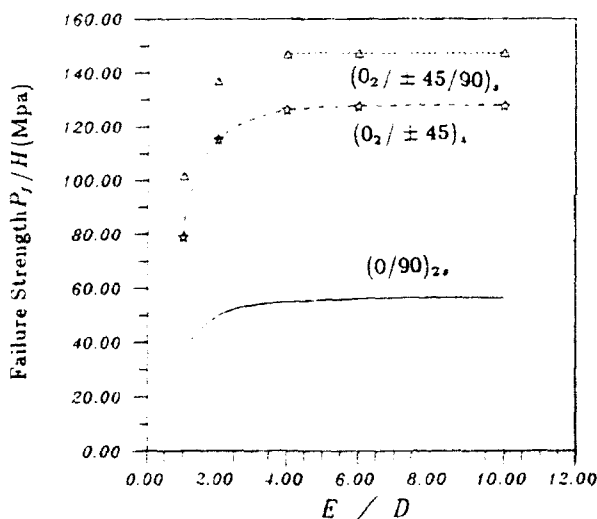

Fig. 7. The failure strength of AS/3501-6 laminate under inplane stresses versus E/D ratio.

two. For the three stacking sequences considered, the $(0_2/\pm45/90)_s$ laminate has the highest strength of P_1/H.

CONCLUSIONS

The method of analysis established in this study has been used to determine the stresses around a hole, and to predict the strength of a finite composite laminate. Based on the numerical results, the following conclusions can be made:

1. The present method using the direct boundary element with quadratic isoparametric element formulation requires less boundary conditions than the conventional boundary element method which saves computing time.
2. Solutions indicate that the E/D value should be larger than two for safe design.
3. The stress concentration increases when the E/D value decreases, and the maximum strength decreases when the E/D value decreases.
4. The laminate strength depends on material properties and stacking sequence of the laminate.

REFERENCES

1. Rizzo, F. J. & Shippy, D. J., A method for stress determination in plane anisotropic elastic bodies. *Journal of Composite Materials*, 4 (1970) 36–61.
2. Yamada, S. E. & Sun, C. T., Analysis of laminate strength and its distribution. *Journal of Composite Materials*, 12 (1978) 275–84.
3. Pyner, G. R. & Matthews, F. L., Comparison of single and multi-hole bolted joint in glass fiber reinforced plastic. *Journal of Composite Materials*, 13 (1979) 232–9.
4. Ogonowski, J. M., Analytical study of finite geometry plates with stress concentration. *AIAA Journal*, 18 (1980) 694–8.
5. Chang, F. K., Scott, R. A. & Springer, G. S. Strength of mechanically fastened composite joint. *Journal of Composite Materials*, 16 (1982) 470–94.
6. Lakshminarayana, H. V., Stress distribution around a semi-circular edge-notch in a finite size laminated composite plate under uniaxial tension. *Journal of Composite Materials*, 17 (1983) 357–67.
7. Chang, F. K. & Scott, R. A., Failure of composite laminates containing pin loaded holes—method of solution. *Journal of Composite Materials*, 18 (1984) 255–78.
8. Zhang, Kai-da & Ueng, C. E. S., Stress around a pin-loaded hole in orthotropic plates. *Journal of Composite Materials*, 18 (1984) 432–46.
9. Mahayerin, E. & Sikarskin, D. L., Boundary element study of loaded hole in an orthotropic plate. *Journal of Composite Materials*, 20 (1986) 375–89.
10. Banerjee, P. K. & Butterfield, R., *Boundary Element Method in Engineering Science*. McGraw-Hill, Berkshire, 1981.
11. Timoshenko, S. P. & Goodier, J. N., *Theory of Elasticity*. McGraw-Hill, New York, 1951.
12. Lekhnitskii, S. G., Tsai, S. W. & Cheron, T., *Anisotropic Plates*, Gordon and Breach, New York, 1968.
13. Whitney, J. M. & Nuismer, R. J., Stress fracture criteria for laminated composite containing stress concentrations. *Journal of Composite Materials*, 8 (1974) 253–65.

Adhesive interface element for bonding of laminated plates

Chien-Chang Lin & Tseng-Chung Ko

Institute of Applied Mathematics, National Chung-Hsing University, Taichung, Taiwan

An isoparametric adhesive interface element is used in the stress analysis of adhesive-bonded structures. The model assumes that transverse shear and peel stresses prevail in the adhesive layer. The analyses articulate separate responses of the plate, overlays and the adhesive. The stress distribution in the adhesive layer, obtained for lap joints, is found to be in agreement with those obtained by previous authors. To extend the use of bonded joints, the deflection of patched plates under transverse loading and the stress concentration in a plate having a center hole reinforced by a ring patch are also analyzed. The present element, together with the eight-node isoparametric plate element based on first order shear deformation theory used to model the plate and overlay patch, is found to have an advantage in solving problems of adhesive-bonded structures.

1 INTRODUCTION

Adhesive-bonded joints have widespread applications in aerospace structures due to their light weight and efficient load transfer characteristics. These can be metal to metal, metal to composite or composite to composite bonding. The use of adhesive in the bonding technique for composite structures has shown the feasibility of adhesive joining and stiffening of structural components subjected to severe environmental and loading conditions. For efficient designs of adhesive-bonded structures, a knowledge of the relationship between plates and adhesive layer is essential. Most of the existing studies[1-10] pertain to the analysis of bonded joints such as lap joints. In crack patching problems,[11,12] it is assumed that the plate and patch are membranes and the adhesive is a shear spring. However, it is not valid for single side patching because the bending effect is neglected. The realm of analysis is extended in this study. While an eight-node isoparametric plate element based on the first order shear deformation theory[13-15] is used to idealize the plate and overlay patch, a sixteen-node adhesive interface element for the adhesive layer is developed in the present work.

This paper presents a stress analysis method for adhesive-bonded structures under in-plane and transverse loading. The adhesive layers are assumed to be relatively thin and behave elasti-

cally as simple tension-shear springs connecting the plates and patches. Although the method is developed for lap-joints, patched plates and reinforcement of plate with hole, it can be readily extended to other bonded joint configurations. Numerical examples are provided to show the influence of the patch on the deflection of the locally patched plate and the stress distribution of a plate having a center hole reinforced by a ring patch. The present finite element solutions show good agreement with the published results. The element developed is quite general which can easily be employed for adhesive-bonded structures.

2 BONDING PROBLEM DESCRIPTION

For the elastic analysis of adhesive-bonded structures, the following assumptions are made: (1) deformations are small, and all constituent materials are homogeneous and linearly elastic; (2) the transverse normal modulus of adhesive is much lower than that of the plate and overlay patch, so that the transverse normal deformation of the plate and overlay is negligible in comparison with that of the adhesive; (3) the adhesive is under the antiplane stress state, i.e. $\sigma_x = \sigma_y = \tau_{xy} = 0$; (4) the peel and shear stresses along the thickness direction in the adhesive layer are assumed uniform.

217

Bonded structures including the plate, adhesive and overlay as shown in Fig. 1, may be viewed as a sandwich structural element. The displacement components of the adhesive u, v and w are obtained from the equilibrium equations expressed in terms of displacements, and the detailed formulation of the problem is presented here.

From assumptions (3) and (4), there are only three stresses and their associated strains in the adhesive. The stress–strain and strain–displacement relations are

$$\tau_{xz} = G_a\gamma_{xz}(x,y), \ \tau_{yz} = G_a\gamma_{yz}(x,y), \ \sigma_z = E_a\varepsilon_z(x,y) \quad (1)$$

$$\gamma_{xz} = \frac{\partial u}{\partial z} + \frac{\partial \omega}{\partial x}, \ \gamma_{yz} = \frac{\partial v}{\partial z} + \frac{\partial w}{\partial y}, \ \varepsilon_z = \frac{\partial w}{\partial z} \quad (2)$$

and the equilibrium equations are as follows:

$$\frac{\partial \tau_{yz}}{\partial z} = 0, \ \frac{\partial \tau_{xz}}{\partial z} = 0, \ \frac{\partial \tau_{xz}}{\partial x} + \frac{\partial \tau_{yz}}{\partial y} + \frac{\partial \sigma_z}{\partial y} = 0 \quad (3)$$

Integration of ε_z in eqn (2) with respect to z in conjunction with σ_z in eqn (1) results in

$$w(x,y,z) = \frac{z}{E_a}\sigma_z + w_0(x,y) \quad (4)$$

where $w_0(x,y)$ is the displacement in the adhesive at $z = 0$. Displacements u and v are obtained by integrating eqn (3) in conjunction with eqn (4). Along interfaces between patch and adhesive at $z = t_a$ and between plate and adhesive at $z = 0$, two independent continuity equations in the x and y directions respectively become:

$$\gamma_{xz} = \frac{1}{t_a}(u_1 - u_2 + h_1\psi_{1x} + h_2\psi_{2x})$$

$$\quad (5)$$

$$\gamma_{yz} = \frac{1}{t_a}(v_1 - v_2 + h_1\psi_{1y} + h_2\psi_{2y})$$

where E_a = Young's modulus of the adhesive, t_a = thickness of the adhesive, t_1 = thickness of the overlay patch, t_2 = thickness of the plate, u_1, v_1, w_1 = displacement components of the overlay, ψ_{1x}, ψ_{1y} = rotation components of the overlay, u_2, v_2, w_2 = displacement components of the plate, ψ_{2x}, ψ_{2y} = rotation components of the plate, $h_1 = \frac{1}{2}(t_1 + t_a)$, $h_2 = \frac{1}{2}(t_2 + t_a)$.

3 FINITE ELEMENT FORMULATION

Isoparametric plate elements with first order shear deformation are used for both the plate and overlay patch. They are made of fiber reinforced composites. Referring to the schematic of the isoparametric adhesive interface element as shown in Fig. 1, the adhesive is assumed to experience only the transverse shear stress τ_{xz}, τ_{yz} and normal stress σ_z. The total strain energy of an element of the bonded structure can thus be written as

$$\Pi_e = U_1^s + U_2^s + U_3^s + U_4^s = \frac{1}{2}\delta_s^T K_s\delta_s + \frac{1}{2}\delta_p^T K_p\delta_p + \frac{t_a}{2}G_a\int_\Omega (\gamma_{xz}^2 + \gamma_{yz}^2)\,dx\,dy + \frac{E_a}{2t_a}\int_\Omega (w_1 - w_2)^2\,dx\,dy$$

$$(6)$$

in which Ω represents the area of the adhesive, and γ_{xz} and γ_{yz} are the transverse shear strains corresponding to τ_{xz} and τ_{yz} respectively. Here K_p and K_s are, respectively, the element stiffness matrices of the overlay patch and plate. The transpose of the displacement vector δ_s for the plate is δ_s^T which is defined in terms of the nodal point displacements w_{1j}, u_{1j}, v_{1j} and rotations ψ_{1xj}, ψ_{1yj} ($j = 1, 2,....,m$) with $m = 8$ being the number of nodes, i.e.
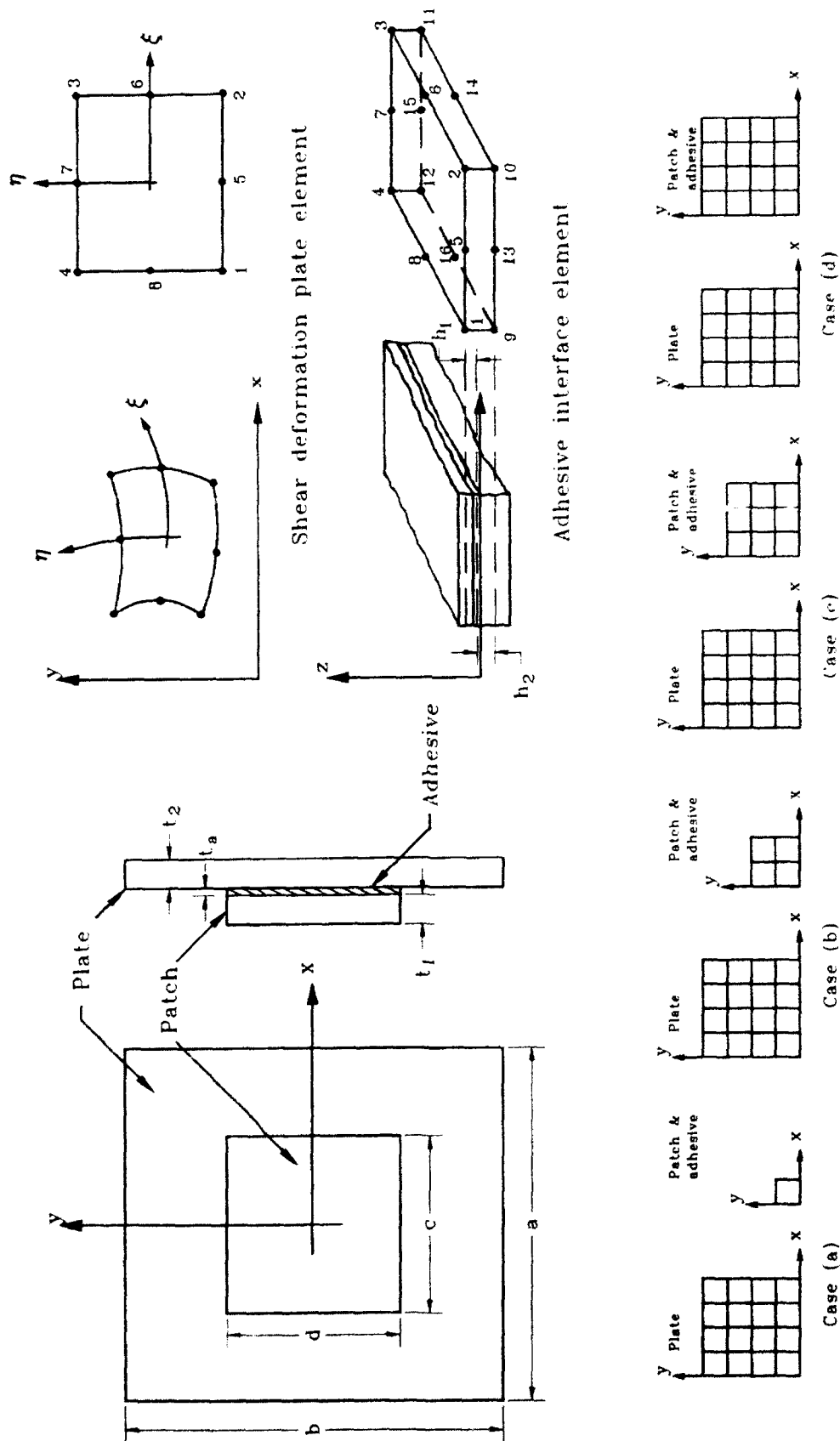
$$\delta_s^T = [w_{1i}, \psi_{1xi}, \psi_{1yi}, u_{1i}, v_{1i}], \ i = 1, 2, ..., 8$$

Similarly, the same applies to the displacement vector δ_p for the overlay patch such that

$$\delta_p^T = [w_{2i}, \psi_{2xi}, \psi_{2yi}, u_{2i}, v_{2i}], \ i = 1, 2, ..., 8$$

The evaluation of the area integrals U_3^s and U_4^s requires a knowledge of the shear strains γ_{xz} and γ_{yz} for the adhesive layer. The shear strains can be found from the relative displacements between the overlay patch and plate given in eqn (5). The generalized displacement can be written as

$$[q_i] = [w_1, \psi_{1x}, \psi_{1y}, u_1, v_1, w_2, \psi_{2x}, \psi_{2y}, u_2, v_2]$$

Shear deformation plate element

Adhesive interface element

Finite element grids

Fig. 1. Adhesively patched plate.

where

$$q_j = \sum_{i=1}^{s} q_{ji} f_i$$

for j ranging from 1 to 10, and f_i are shape functions. The vector $\{\delta\}$ contains the nodal displacements in both the overlay patch and plate as follows:

$$\{\delta\}^t = \lfloor w_{11}, \psi_{1x1}, \psi_{1y1}, u_{11}, v_{11}, w_{12}, \psi_{1x2}, \ldots, u_{28}, v_{28} \rfloor_{80 \times 1}$$

Without going into details, the area integrals in eqn (6) can be expressed in the form

$$U_3^c + U_4^c = \frac{t_a}{2} G_a \int_\Omega (\gamma_x^2 + \gamma_y^2) \, dx \, dy + \frac{E_a}{2 t_a} \int_\Omega (w_1 - w_2)^2 \, dx \, dy = \{\delta\}^t [K_a]\{\delta\} \tag{7}$$

From the strain and nodal displacement relationship, we have

$$\begin{Bmatrix} \gamma_{xz} \\ \gamma_{yz} \end{Bmatrix} = [B_s]\{\delta\}$$

$$w_1 - w_2 = [B_n]\{\delta\} \tag{8}$$

where

$$[B_s] = \frac{1}{t_a} \begin{bmatrix} 0 & h_1 f_1 & 0 & f_1 & 0 & \ldots & 0 & h_1 f_8 & 0 & f_8 & 0 & 0 & h_2 f_1 & 0 & -f_1 & 0 & \ldots & 0 & h_2 f_8 & 0 & -f_8 & 0 \\ 0 & 0 & h_1 f_1 & 0 & f_1 & \ldots & 0 & 0 & h_1 f_8 & 0 & f_8 & 0 & 0 & h_2 f_1 & 0 & -f_1 & \ldots & 0 & 0 & h_2 f_8 & 0 & -f_8 \end{bmatrix}_{80 \times 2}$$

$$[B_n] = \lfloor f_1 \ 0 \ 0 \ 0 \ 0 \ \ldots \ f_8 \ 0 \ 0 \ 0 \ 0 \ -f_1 \ 0 \ 0 \ 0 \ 0 \ \ldots \ -f_8 \ 0 \ 0 \ 0 \ 0 \rfloor_{80 \times 1}$$

The stiffness matrix due to the shear strain can be expressed as

$$[K_{ss}] = t_a G_a \int_{-1}^{1} \int_{-1}^{1} [B_s]^t [B_s] \det[J] \, d\xi \, d\eta \tag{9}$$

and the stiffness matrix due to the normal strain can be expressed as

$$[K_{ns}] = \frac{E_a}{t_a} \int_{-1}^{1} \int_{-1}^{1} [B_n]^t [B_n] \det[J] \, d\xi \, d\eta \tag{10}$$

where $[J]$ is the Jacobian matrix which is used to transform the physical coordinates (x,y) to the curvilinear coordinates (ξ, η). Both ξ and η range between -1 and $+1$. The matrix $[K_a]$ of an adhesive interface element for the adhesive layer given by

$$[K_a] = [K_{ss}] + [K_{ns}] \tag{11}$$

can be evaluated numerically using the 3×3 Gaussian point integration procedure.

Finally, by assembling the total stiffness of all elements of an adhesively bonded structure, we obtain the following equation:

$$[K] = \Sigma[K^e] = \Sigma[K_s] + [K_p] + [K_a] \tag{12}$$

and the stress analysis of bonded structures is established.

4 NUMERICAL EXAMPLES WITH DISCUSSION

A single lap joint under various loading conditions, a patched plate under transverse loading, and a plate with a center hole reinforced by a ring patch as shown in Figs 1, 3, 5, respectively, are considered as examples. The following material constants are used:

Boron–epoxy:

$$E_x = 2.234 \times 10^{11} \, \text{N/m}^2 \qquad (3.24 \times 10^7 \, \text{psi})$$

$$E_y = E_z = 2.413 \times 10^{10} \, \text{N/m}^2 \qquad (3.50 \times 10^6 \, \text{psi})$$

$$G_{xy} = G_{xz} = G_{yz} = 8.481 \times 10^9 \, \text{N/m}^2$$

$$(1.23 \times 10^6 \, \text{psi})$$

$$\nu_{xy} = 0.23$$

Aluminum:

$$E = 6.895 \times 10^{10} \, \text{N/m}^3 \quad (10^7 \, \text{psi})$$

$$\nu = 0.3$$

Adhesive:

$$E_a = 3.068 \times 10^9 \, \text{N/m}^2 \quad (4.45 \times 10^5 \, \text{psi})$$

$$G_a = 1.138 \times 10^9 \, \text{N/m}_2 \quad (1.65 \times 10^5 \, \text{psi})$$

The plate element based on the first order shear deformation theory is used to idealize the upper and lower adherend, and the adhesive interface element is used to idealize the adhesive. The thickness of adhesive is assumed to be 0.1016 mm in all cases.

For single lap joint problems: the finite element mesh used for the bonded region of a lap joint is shown in Fig. 2. Case (a) is a lap joint under tension as shown in Fig. 3(a). The calculated results are presented for aluminum to aluminum and aluminum to boron–epoxy combinations. Both shear and peel stresses in the adhesive are shown in Figs 3(a) and (b). As the upper adherend has the same thickness and material as the lower adherend with $t_1 = t_2 = 2.29$ mm, we obtain the symmetric stress distribution about the center of the bonded joint as shown in Fig. 3(a). The results are in close agreement with previously obtained analytical results given by Goland and Reissner.[1] For the combination where, the upper adherent boron–epoxy with $t_1 = 0.762$ mm and lower adherend is aluminum with $t_2 = 2.29$ mm as case (b), the stress concentration of peel stress σ and shear stress τ at $x = 0$ as shown in Fig. 3(b) are dramatically greater than those in Fig. 3(a). This is
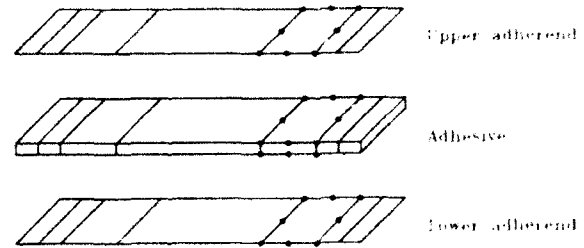
Fig. 2. Finite element idealization of single lap joint.

because of the smaller bending stiffness of the upper adherend. The results found in this example are in agreement with those given in Ref. 5. The discrepancies are mainly due to the modeling of the adhesive for which the peel stress includes the effect of axial strain in Ref. 5, but is neglected in this paper. Case (c) is a lap joint under bending, and case (d) is a lap joint under transverse shear. The high stress concentration at $x = 0$ for cases (c) and (d) are similar to case (b) as shown in Figs 3(c) and (d).

For patched plate problems: a square plate, $a = b = 508$ mm, reinforced by bonding an overlay patch with $c = d = 0.25a, 0.50a, 0.75a$ and $1.0a$, is considered. The patched plate subjected to a uniform transverse load $q = 1.0$ psi, and the finite element mesh are shown in Fig. 1. Numerical results, when compared with unpatched plates having a thickness of t, $2t$ and $2t + t_a$, show that the present analysis is reasonable and the total patching is quite workable. The following three cases with different boundary conditions and lamination schemes are considered for this purpose:

(i) A simply supported square aluminum plate is reinforced locally by bonding an aluminum patch. The plate and patch have the same thickness of $t = 5.08$ mm. The nondimensionalized deflection, $w' = w(t^3 E/qa^4)10^2$, of patched plate along x direction is shown in Fig. 4(a), and the maximum transverse displacements are given in Table 1. In the full plate patch case (d), the deflection is lower than the unpatched plate with $2t + t_a$ thickness. Since the simply supported line is on the neutral plane of the plate while the patch edge is free, the overall stiffness is larger than the unpatched case due to the shifting of the neutral plane. From the numerical results, we have found that the patching system is efficient. The reduction of deflection is about 30% by only patching $\frac{1}{16}$ of the plate area in case (a).
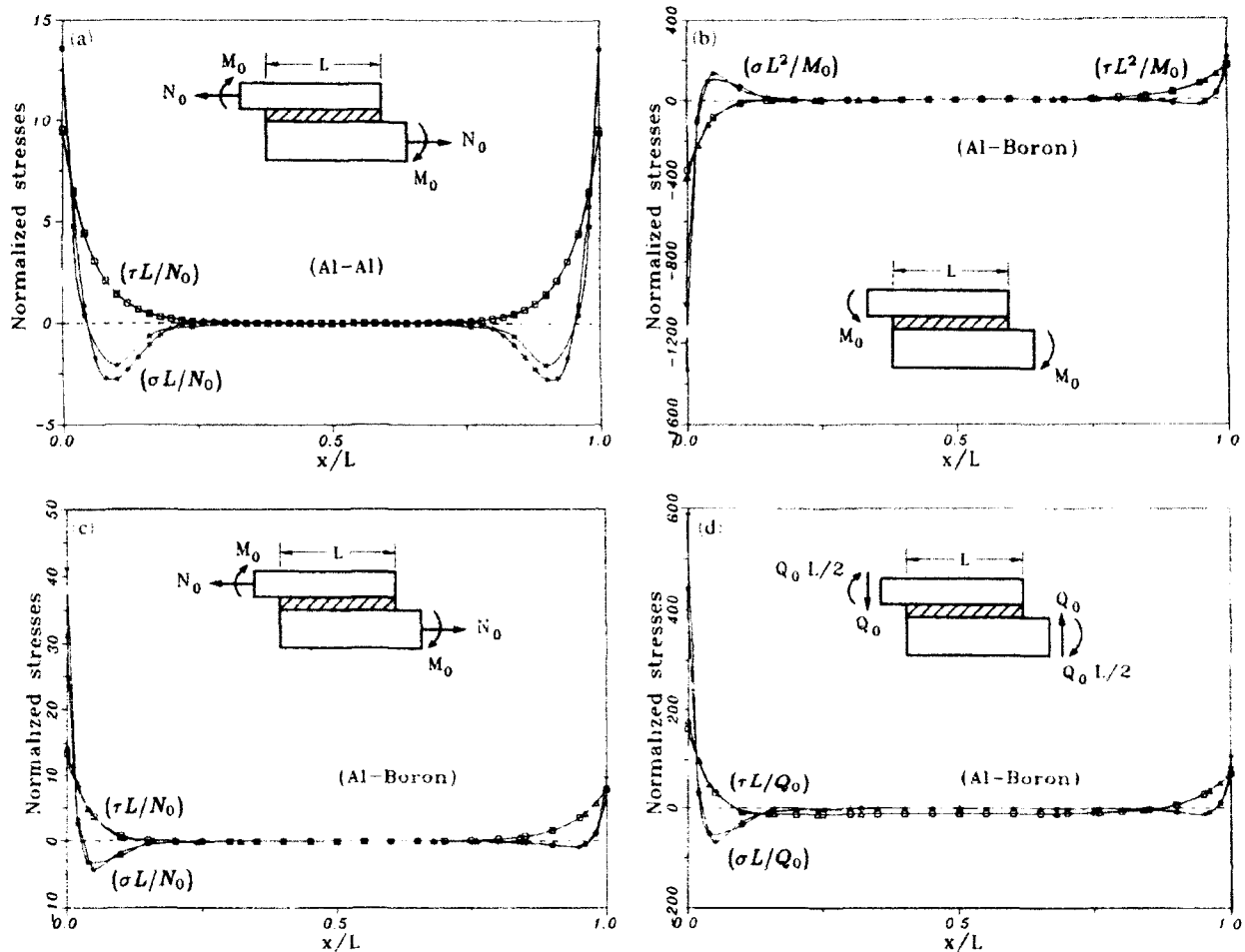
Fig. 3.   Stress distribution in the adhesive for a single lap joint. $L = 25.4$ mm, *****, peel stress. [1] for (Al–Al), [5] for (Al–boron); *****, peel stress, present; □□□□□, shear stress, [1] for (Al–Al), [5] for (Al–boron); △△△△△, shear stress, present).

(ii) For the same problem considered in (i) except the boundary condition is changed from simple support to clamped, the nondimensionalized deflection of the patched plate along the x direction is shown in Fig. 4(b), and the maximum transverse displacements are sorted in Table 2. Similarly, we also found that the local patching is efficient. In the full plate patch case (d), the plate and patch edges are all clamped. The deflection of patched plate is between the unpatched plates of $2t$ and $2t + t_a$ thicknesses, and the value is equal approximately to $\frac{1}{8}$ of the deflection of the unpatched plate with thickness t. This is reasonable.

(iii) A clamped square boron-laminated plate (0/90/0) reinforced locally by bonding a boron-laminated patch (0/90/0) is considered. The

thickness of each layer for plate and patch is 1.27 mm. The nondimensionalized deflection, $w^* = w(t^3 E_y/qa^4)10^3$, of the patched plate along the x direction is shown in Fig. 4(c) and the maximum transverse displacements are given in Table 3. In the full plate patch case (d), the deflection is slightly lower than the laminated plate with (0/90/0/0/90/0) stacking. From the numerical results, we notice the excellent efficiency of the patching system. The reduction of deflection is about 35% by only patching $\frac{1}{16}$ of the plate area in case (a).

For a plate having a center hole reinforced by a ring patch: a square plate with a center hole (radius = 25.4 mm) reinforced by a single and double ring patch (outer radius = 50.8 mm and
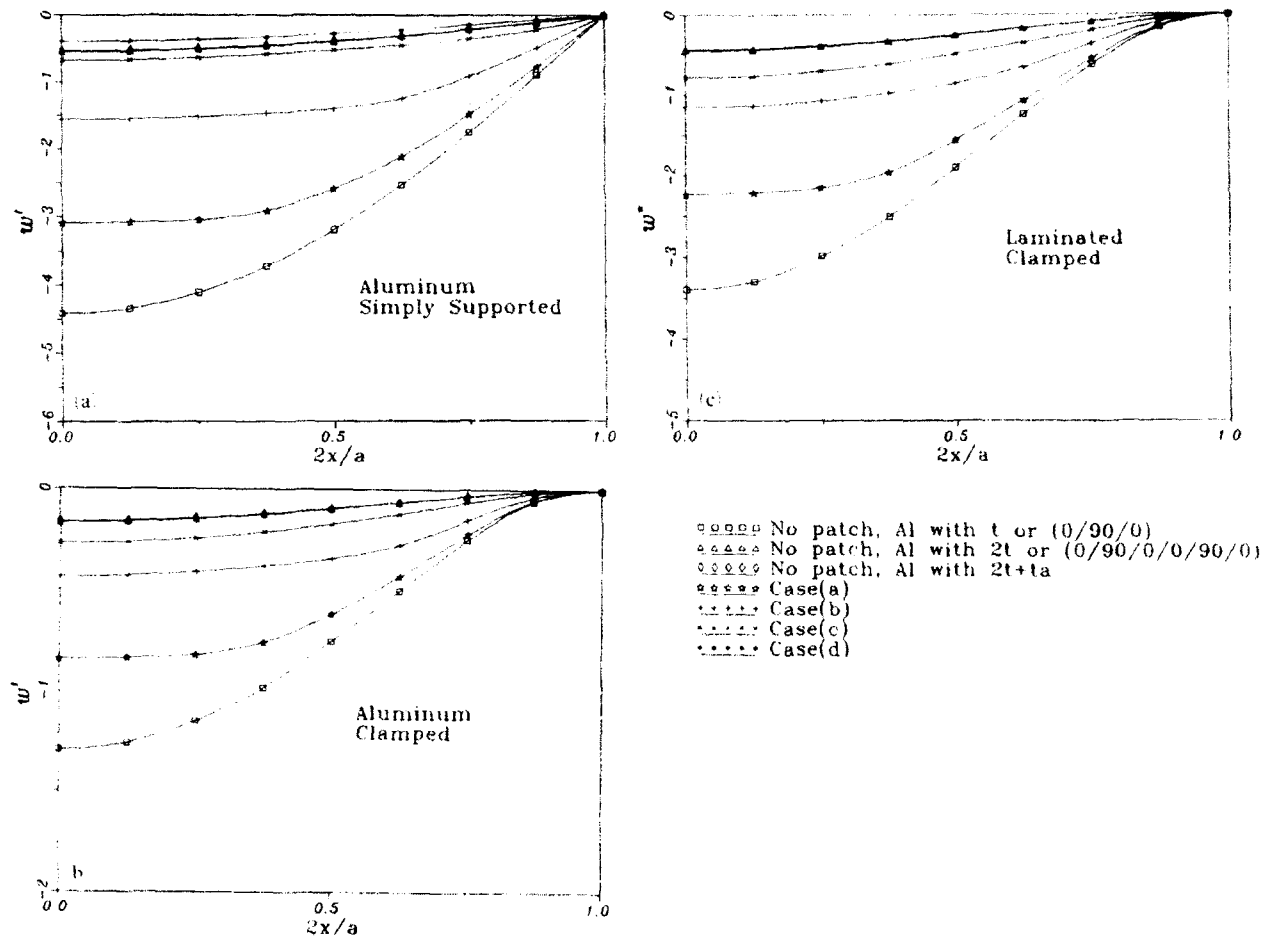
Fig. 4. The transverse deflection of patched plates.

Table 1. The center deflection of simply supported patched plates under uniform transverse load

Condition	Case	w'	Ratio down (%)
Unpatched	Thickness = t	−4·416	100
	Thickness = 2t	−0·554	12·54
	Thickness = 2t + t_a	−0·538	12·17
Patched	Case (a)	−3·088	69·94
	Case (b)	−1·562	35·36
	Case (c)	−0·677	15·32
	Case (d)	−0·395	8·945

Nondimensionalized deflection $w' = w(t^3E/qa^4)10^2$.

Table 2. The center deflection of clamped patched plates under uniform transverse load

Condition	Case	w'	Ratio down (%)
Unpatched	Thickness = t	−1·296	100
	Thickness = 2t	−0·167	12·88
	Thickness = 2t + t_a	−0·162	12·50
Patched	Case (a)	−0·840	64·84
	Case (b)	−0·435	33·56
	Case (c)	−0·268	20·71
	Case (d)	−0·163	12·57

Nondimensional deflection $w' = w t^3E/qa^4 10^2$.

inner radius = 25·4 mm) is considered. The plate is under uniform simple tension as shown in Fig. 5. The shaded area shown in Fig. 5 represents the patched region. The finite element mesh used for the ring-patched center hole plate is shown in Fig. 5. The patch materials used are aluminum and boron–epoxy, and the fiber direction is parallel to

the applied force. Numerical results show dramatic reductions of the stress concentration at the hole edge from the unpatched case, especially for double patched cases. Details are given in Tables 4 and 5. Owing to the bending effect, the single sided patches result in limited reduction in stress concentration even for a thick patch. The

double sided patches always have excellent patching efficiency even for thin patches. In this class of problems, because the patch only transfers part of the applied load which is not like the lap joint where the full load must be transferred, the stresses in the adhesive are not as critical.

5 CONCLUSIONS

An adhesive interface element and a first order shear deformation plate element are established for the analysis of adhesive-bonded structures. The analysis provides accurate and efficient calculations for the distribution of shear and peel stresses in the adhesive, and stresses and displacements in plates for a variety of adhesive-bonded structural problems subjected to various loading conditions. Results obtained in the study are in close agreement with previously obtained analytical results. Detailed finite element studies have confirmed that the adhesively patched method may upgrade the structural performance and dramatically reduce stress concentration for structures with cutouts. The present procedures

are simple to use, and provide realistic assessments of the stress distribution and deformation of the adhesive-bonded laminated plates.

ACKNOWLEDGEMENT

Table 4. Stress concentration factor for a center-hole plate with a Al-ring patch

Total patch thickness	Single side reinforcement	Double side reinforcement
No patch	3·091	3·091
0·254 mm	2·514	—
0·508 mm	2·466	2·392
1·016 mm	2·419	2·175
1·524 mm	2·408	1·994
2·032 mm	2·407	1·840
2·540 mm	2·401	1·708
3·556 mm	2·364	1·493
5·080 mm	2·256	1·255

Table 5. Stress concentration factor for a center-hole plate with a boron-ring patch

Total patch thickness	Single side reinforcement	Double side reinforcement
No patch	3·091	3·091
0·254 mm	2·721	—
0·508 mm	2·708	1·891
1·016 mm	2·587	1·515
1·524 mm	2·451	1·289
2·032 mm	2·321	1·134
2·540 mm	2·197	1·017
3·556 mm	1·966	0·8511
5·080 mm	1·675	0·6908

Table 3. The center deflection of clamped patched laminated plates (0/90/0) under uniform transverse load

Condition	Case	w*	Ratio down %
Unpatched	0/90/0	−3·398	100
	0/90/0/0/90/0	−0·451	13·28
Patched	Case a	−2·233	65·72
	Case b	−1·151	33·87
	Case c	−0·784	23·07
	Case d	−0·436	12·83

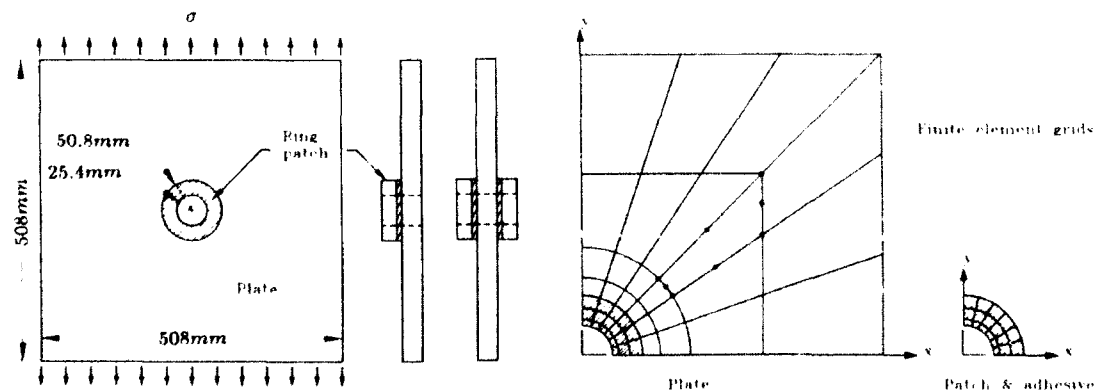Nondimensionalized deflection $w^* = w \cdot t \cdot E_z / qa^4 \cdot 10^3$.

Fig. 5. The plate with a center hole reinforced by ring patch.

REFERENCES

1. Goland, M. & Reissner, E., Stresses in cemented joints. *Journal of Applied Mechanics*, **11** 1944 A17–A27.
2. Renton, W. J. & Vinson, J. R., Analysis of adhesively bonded joints between panels of composite materials. *Journal of Applied Mechanics, ASME*, 1977 101–6.
3. Yuceoglu, U. & Updike, D. P., Stress analysis of bonded plates and joints. *Journal of the Engineering Mechanics Division, ASCE*, **106** 1980 37–56.
4. Renton, W. J. & Vinson, J. R., The efficient design of adhesive bonded joints. *Journal of Adhesion*, **7** 1975 175–93.
5. Delale, F., Erdogan, F. & Aydinoglu, M. N., Stresses in adhesively bonded joints: a closed-form solution. *Journal of Composite Materials*, **15** 1981 249–71.
6. Wah, T., Stress distribution in a bonded anisotropic lap joint. *Journal of Engineering Materials and Technology, ASME*, **95** 1973 174–81.
7. Adams, R. D. & Peppiatt, N. A., Stress analysis of adhesive-bonded lap joints. *Journal of Strain Analysis*, **9** 3 1974 185–96.
8. Nagesvara Rao, B., Sadasiva Rao, Y. V. K. & Yadagiri, S., Analysis of composite bonded joints. *Fibre Science and Technology*, **17** 1982 77–90.
9. Roberts, T. M., Shear and normal stresses in adhesive joints. *Journal of Engineering Mechanics, ASCE*, **115**, 1989 2460–79.
10. Yuceoglu, U. & Updike, D. P., Bending and shear deformation effects in lap joints. *Journal of the Engineering Mechanics Division, ASCE*, 1981 55–76.
11. Chu, R. C. & Ko, T. C., Isoparametric shear spring element applied to crack patching and instability. *Theoretical and Applied Fracture Mechanics*, **11** 1989 93–102.
12. Kuo, A. S., A two-dimensional shear spring element. *AIAA Journal*, **22** 10 1984 1460–4.
13. Whitney, J. M. & Pagano, N. J., Shear deformation in heterogeneous anisotropic plates. *Journal of Applied Mechanics, ASME*, 1970 1031–6.
14. Yang, P. C., Norris, C. H. & Stavsky, Y., Elastic wave propagation in heterogeneous plates. *International Journal of Solids and Structures*, **2** 1966 665–84.
15. Reddy, J. N., Free vibration of antisymmetric angle-ply laminated plates including transverse shear deformation by the finite element method. *Journal of Sound and Vibration*, **66** 1979 565–76.

Compressive and shear buckling analysis of metal matrix composite sandwich panels under different thermal environments

William L. Ko & the late Raymond H. Jackson

NASA Dryden Flight Research Facility, Edwards, CA, 93523-0273, USA

Combined inplane compressive and shear buckling analysis was conducted on flat rectangular sandwich panels using the Rayleigh–Ritz minimum energy method with a consideration of transverse shear effect of the sandwich core. The sandwich panels were fabricated with titanium honeycomb core and laminated metal matrix composite face sheets. The results show that slightly slender (along the unidirectional compressive loading axis) rectangular sandwich panels have the most desirable stiffness-to-weight ratios for aerospace structural applications; the degradation of buckling strength sandwich panels with rising temperature is faster in shear than in compression; and the fiber orientation of the face sheets for optimum combined-load buckling strength of sandwich panels is a strong function of both loading condition and panel aspect ratio. Under the same specific weight and panel aspect ratio, a sandwich panel with metal matrix composite face sheets has a much higher buckling strength than one having monolithic face sheets.

NOTATION

a	Length of sandwich panel (m) (in)
a_o	Edge length of square sandwich panel (m) (in)
a''_{mn}	Coefficients of characteristic equations (dimensionless)
A_{mn}	Fourier coefficient of trial function for w (m) (in)
b	Width of sandwich panel (m) (in)
D^*	Flexural stiffness parameter,

$$D = \frac{E_{11} I_s}{1 - \nu_{11}^2} , (m\,N)(in\text{-}lb)$$

D_{0x}, D_{0y}	Transverse shear stiffnesses of sandwich core in the x–z and y–z planes, $D_{0x} = G_{cxz} h_c$, $D_{0y} = G_{cyz} h_c$ (N/(m-rad)) (lb/(in-rad))
D_x, D_y	Longitudinal and transverse flexural stiffnesses, $D_x = E_x I_s$, $D_y = E_y I_s$ (m-N) (in-lb)

D_x, D_y	Panel flexural stiffnesses, $D_x = D_x / (1 - \nu_{xy} \nu_{yx})$, $D_y = D_y / (1 - \nu_{xy} \nu_{yx})$ (m-N) (in-lb)
D_{xy}	Panel twisting stiffness, $D_{xy} = 2 G_{xy} I_s$ (m-N) (in-lb)
E_{11}	Young's modulus of titanium material (N/m²) (lb/in²)
E_x, E_y	Young's moduli of face sheets (N/m²) (lb/in²)
G_{cxz}, G_{cyz}	Shear moduli of sandwich core (N/m²) (lb/in²)
G_{xy}	Shear modulus of face sheets (N/m²) (lb/in²)
h	Depth of sandwich panel = distance between middle planes of two face sheets (cm) (in)
h_c	Sandwich core depth (cm) (in)
i, j	Indices, 1, 2, 3,...
I_s	Moment of inertia, per unit width, of two face sheets taken with respect to horizontal centroidal axis (neutral axis) of the sandwich panel, $I_s = \frac{1}{2} t_s h^2 + \frac{1}{6} t_s^3$ (m³/m) (in³/in)
k_x, k_y	Compressive buckling factors in x- and y-directions, $k_x = \frac{N_x a^2}{\pi^2 D^*}$, $k_y = \frac{N_y a^2}{\pi^2 D^*}$ (for a = constant) (dimensionless)

k_{xy} Shear buckling load factor, $k_{xy} =$

$$\frac{N_{xy}a^2}{\pi^2 D^*} \text{ (for } a = \text{constant) (dimensionless)}$$

$\bar{k}_x, \bar{k}_y$ Modified compressive buckling load factors in x and y-directions,

$$\bar{k}_x = \frac{N_x a_0^2}{\pi^2 D^*} = k_x \frac{b}{a}, \quad \bar{k}_y = \frac{N_y a_0^2}{\pi^2 D^*} = k_y \frac{b}{a}$$

(for $ab = a_0^2 = $ constant) (dimensionless)

$\bar{k}_{xy}$ Modified shear buckling load factor,

$$\bar{k}_{xy} = \frac{N_{xy} a_0^2}{\pi^2 D^*} = k_{xy} = \frac{b}{a} \quad \text{(for} \quad ab = a_0^2$$

= constant) (dimensionless)

m Number of buckle half waves in x-direction

MMC   Metal matrix composite

n Number of buckle half waves in y-direction

N_x Normal stress resultants in x-direction (N/m)(lb/in)

N_y Normal stress resultants in y-direction (N/m)(lb/in)

N_{xy} Shear stress resultant (N/m)(lb/in)

P_x Compressive load in x-direction (N) (lb)

P_y Compressive load in y-direction (N) (lb)

Q Shear load (N)(lb)

t_s Thickness of sandwich face sheets (cm) (in)

T Temperature (°C)(°F)

Ti   Titanium

w Panel deflection (m) (in)

x, y, z Rectangular Cartesian coordinates

δ_{mnij} Special data function obeying $m \neq i$, $n \neq j$ $(m \pm i) = $ odd, $(n \pm j) = $ odd,

$$\delta_{mnij} = \frac{mnij}{(m^2 - i^2)(n^2 - j^2)}$$

θ Fiber angle (°)

ν_{ti} Poisson ratio of titanium material

ν_{xy}, ν_{yx} Poisson ratios of face sheets, also for sandwich panel

INTRODUCTION

Metal matrix composites (MMCs) have gained considerable popularity as one of the strongest candidates for hot structural applications. Typical hot structures are the airframes of hypersonic flight vehicles, gas turbine engine components, etc. The MMC system is attractive for hot structures because it can meet the structures' service requirements. Namely, MMCs can operate at elevated temperatures and provide specific mechanical properties (i.e. high strength and stiffness). Taya and Arsenault have discussed all aspects of the thermomechanical behavior of the MMC system in great detail.[1]

The principal application of MMCs in hypersonic flight vehicles is in the form of sandwich constructions with the laminated MMCs used as face sheets.[2] The sandwich structure offers low thermal conductivity in the sandwich thickness direction, a high stiffness-to-weight ratio, and the capability to reduce thermal stresses.

During service, the sandwich panel is under combined thermal and mechanical loading that could induce a critical situation of combined compressive and shear loading, the driving force of panel buckling. Before actual application of MMC sandwich panels as hot structural components, the buckling characteristics of the structural panels under different thermal environments must be fully understood. This paper analyzes the combined inplane-compressive and shear buckling behavior of MMC sandwich panels using the Rayleigh–Ritz minimum energy method and shows how the combined load buckling strength varies with temperature levels, fiber orientation, and panel geometry.

METAL MATRIX COMPOSITE SANDWICH PANEL

Figure 1 shows a rectangular sandwich panel of length a and width b, fabricated with a titanium (Ti) honeycomb core of depth h_c and laminated MMC face sheets of the same thickness t_s. The sandwich panel is simply supported at its four edges, and is subjected to combined inplane compressive and shear loadings. The problem is to calculate buckling interaction curves for the panel and to examine how the combined load buckling strength of the panel changes with (1) thermal environment, (2) fiber orientation, and (3) panel aspect ratio.
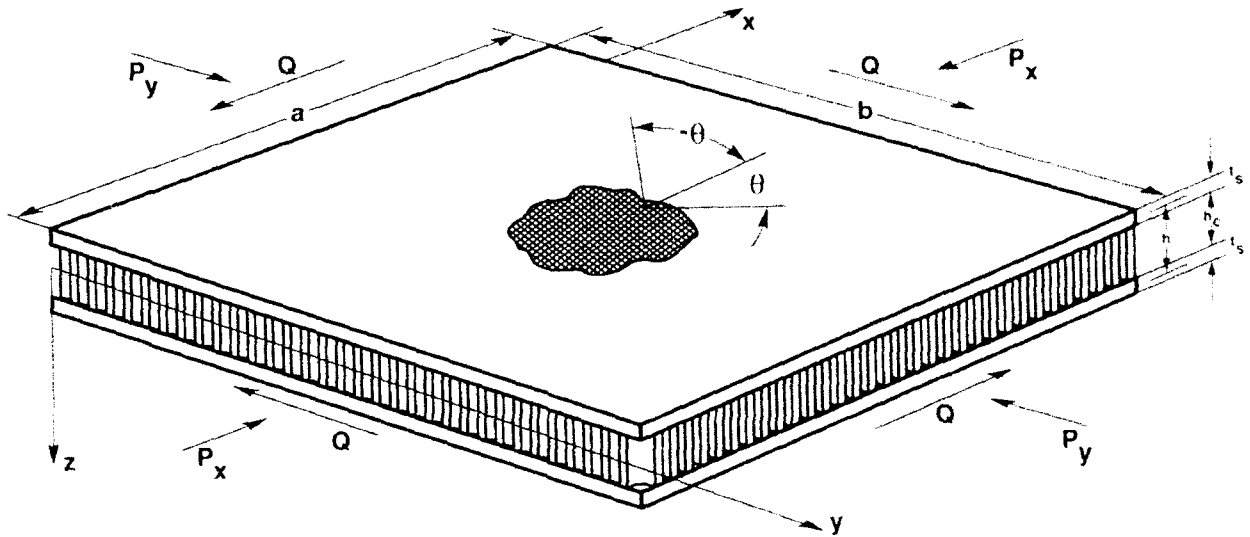
Fig. 1. Honeycomb-core sandwich panel with MMC face sheets subjected to combined compressive and shear loadings.

COMBINED-LOAD BUCKLING EQUATION

The combined-load (inplane compression and shear) buckling characteristic equation developed by Ko and Jackson[5] for a four-edge simply supported anisotropic rectangular sandwich panel may be written as

$$\frac{M_{mn}}{k_{xx}} A_{mn} + \sum_{i=1}^{\infty} \sum_{j=1}^{\infty} \delta_{mnij} A_{ij} = 0 \tag{1}$$

This equation was derived through the use of the Rayleigh–Ritz method of minimization of the total potential energy of the sandwich panel with the effect of transverse shear taken into consideration.

In eqn (1), A_{mn} is the undetermined Fourier coefficient of the assumed function for panel deflection w in the form

$$w(x, y) = \sum_{m=1}^{\infty} \sum_{n=1}^{\infty} A_{mn} \sin \frac{m\pi x}{a} \sin \frac{n\pi y}{b} \tag{2}$$

where a and b, respectively, are the length and the width of the panel and m and n, respectively, are the number of buckle half waves in the x- and the y-directions. The δ_{mnij} in eqn (1) is a special delta function defined as

$$\delta_{mnij} = \frac{mnij}{(m^2 - i^2)(n^2 - j^2)} \tag{3}$$

that obeys the conditions $m \neq i$, $n \neq j$, $(m \pm j) =$ odd and $(n \pm j) =$ odd. The stiffness factor M_{mn} in eqn 1 is defined as

$$M_{mn} = \frac{ab}{32} \left\{ k_x \left(\frac{m\pi}{a}\right)^2 + k_y \left(\frac{n\pi}{p}\right)^2 - \frac{a^2}{\pi^2 D^*} \left[a_{mn}^{11} + \frac{a_{mn}^{12}(a_{mn}^{23}a_{mn}^{31} - a_{mn}^{21}a_{mn}^{33}) + a_{mn}^{13}(a_{mn}^{21}a_{mn}^{32} - a_{mn}^{22}a_{mn}^{31})}{a_{mn}^{22}a_{mn}^{33} - a_{mn}^{23}a_{mn}^{32}} \right] \right\}$$

         ↑

     classical thin   transverse shear effect terms   4

     plate theory term

where the characteristic coefficients a_{mn}^{ij} $(i, j = 1, 2, 3)$ appearing in eqn (4) are defined as [3]

$$a_{mn}^{11} = \bar{D}_x \left(\frac{m\pi}{a}\right)^4 + (\bar{D}_x \nu_{yx} + \bar{D}_y \nu_{xy} + 2D_{xy}) \left(\frac{m\pi}{a}\right)^2 \left(\frac{n\pi}{b}\right)^2 + \bar{D}_y \left(\frac{n\pi}{b}\right)^4 \qquad (5)$$

$$a_{mn}^{12} = a_{mn}^{21} = -\left[\bar{D}_x \left(\frac{m\pi}{a}\right)^3 + \frac{1}{2}(\bar{D}_x \nu_{yx} + \bar{D}_y \nu_{xy} + 2D_{xy}) \left(\frac{m\pi}{a}\right) \left(\frac{n\pi}{b}\right)^2 \right] \qquad (6)$$

$$a_{mn}^{13} = a_{mn}^{31} = -\left[\bar{D}_y \left(\frac{n\pi}{b}\right)^3 + \frac{1}{2}(\bar{D}_x \nu_{yx} + \bar{D}_y \nu_{xy} + 2D_{xy}) \left(\frac{m\pi}{a}\right)^2 \left(\frac{n\pi}{b}\right) \right] \qquad 7$$

$$a_{mn}^{22} = \bar{D}_x \left(\frac{m\pi}{a}\right)^2 + \frac{D_{xy}}{2} \left(\frac{n\pi}{b}\right)^2 + D_{Qx} \qquad (8)$$

$$a_{mn}^{23} = a_{mn}^{32} = \frac{1}{2}(\bar{D}_x \nu_{yx} + \bar{D}_y \nu_{xy} + D_{xy}) \left(\frac{m\pi}{a}\right) \left(\frac{n\pi}{b}\right) \qquad (9)$$

$$a_{mn}^{33} = \bar{D}_y \left(\frac{n\pi}{b}\right)^2 + \frac{D_{xy}}{2} \left(\frac{m\pi}{a}\right)^2 + D_{Qy} \qquad (10)$$

EIGENVALUE SOLUTIONS

Equation (1) forms a system of an infinite number of simultaneous equations associated with different values of m and n. However, the number of equations written from eqn (1) may be truncated up to a certain finite number as required for the convergency of the eigenvalue solutions.

Because $(m \pm i) =$ odd and $(n \pm j) =$ odd (eqn (3)), then $(m \pm i) \pm (n \pm j) = (m \pm n) \pm (i \pm j) =$ even. Thus, if $(m \pm n) =$ even, then $(i \pm j)$ must be even also. Likewise, if $(m \pm n) =$ odd, then $(i \pm j)$ must be odd. Therefore, there is no coupling between the even and odd cases in each equation written from eqn (1) for a particular set of $\{m, n\}$. If the A_{mn} term in eqn (1) is for $(m \pm n) =$ even, then the A_{ij} terms in the same equation must be for $(i \pm j) =$ even also. If the A_{mn} term is for $(m \pm n) =$ odd, then the A_{ij} term must be for $(i \pm j) =$ odd also.

Thus, the set of simultaneous equations written from eqn (1) may be divided into two groups that are independent of each other: one group in which $(m \pm n)$ is even (symmetrical buckling), and the other group in which $(m \pm n)$ is odd (antisymmetrical buckling).[3-7] For the deflection coefficients A_{mn} to have nontrivial solutions for given values of k_x, k_y and b/a, the determinant of the coefficients of the unknown A_{mn} must vanish. The largest eigenvalue $1/k_{xx}$ thus found will give the lowest buckling factor k_{xx} as a function of k_x, k_y and b/a. Thus, a family of buckling interaction curves in the k_x-k_{xx} or in the k_y-k_{xx} space may be generated with b/a as a parameter. Representative characteristic equations (buckling equations) for 12 × 12 matrices written from eqn (1) are shown in eqns (11) and (12) for the cases $(m \pm n) =$ even and $(m \pm n) =$ odd.[3]

For $(m \pm n)$ = even (symmetric buckling):

i,j / m,n	A_{11}	A_{13}	A_{22}	A_{31}	A_{15}	A_{24}	A_{33}	A_{42}	A_{51}	A_{35}	A_{44}	A_{53}	
$m=1,n=1$	$\dfrac{M_{11}}{k_0}$	0	$\dfrac{4}{9}$	0	0	$\dfrac{8}{45}$	0	$\dfrac{8}{45}$	0	0	$\dfrac{16}{225}$	0	
$m=1,n=3$		$\dfrac{M_{13}}{k_0}$	$-\dfrac{4}{5}$	0	0	$\dfrac{8}{7}$	0	$-\dfrac{8}{25}$	0	0	$\dfrac{16}{35}$	0	
$m=2,n=2$			$\dfrac{M_{22}}{k_0}$	$-\dfrac{4}{5}$	$-\dfrac{20}{63}$	0	$\dfrac{36}{25}$	0	$-\dfrac{20}{63}$	$\dfrac{4}{7}$	0	$\dfrac{4}{7}$	
$m=3,n=1$				$\dfrac{M_{31}}{k_0}$	0	$-\dfrac{8}{25}$	0	$\dfrac{8}{7}$	0	0	$\dfrac{16}{35}$	0	
$m=1,n=6$					$\dfrac{M_{15}}{k_0}$	$-\dfrac{40}{27}$	0	$-\dfrac{8}{63}$	0	0	$-\dfrac{16}{27}$	0	
$m=2,n=4$						$\dfrac{M_{24}}{k_0}$	$-\dfrac{7}{35}$	0	$-\dfrac{8}{63}$	$\dfrac{8}{3}$	0	$-\dfrac{120}{147}$	$=0$
$m=3,n=3$				Symmetry			$\dfrac{M_{33}}{k_0}$	$-\dfrac{72}{35}$	0	0	$\dfrac{144}{49}$	0	
$m=4,n=2$								$\dfrac{M_{42}}{k_0}$	$-\dfrac{40}{27}$	$\dfrac{120}{147}$	0	$\dfrac{8}{3}$	
$m=5,n=1$									$\dfrac{M_{51}}{k_0}$	0	$\dfrac{16}{27}$	0	
$m=3,n=5$										$\dfrac{M_{35}}{k_0}$	$\dfrac{80}{21}$	0	
$m=4,n=4$											$\dfrac{M_{44}}{k_0}$	$\dfrac{80}{21}$	
$m=5,n=3$												$\dfrac{M_{53}}{k_0}$	(11)

For $(m \pm n)$ = odd (antisymmetric buckling):

i,j / m,n	A_{12}	A_{21}	A_{14}	A_{23}	A_{32}	A_{41}	A_{16}	A_{25}	A_{34}	A_{43}	A_{52}	A_{61}	
$m=1,n=2$	$\dfrac{M_{12}}{k_0}$	$-\dfrac{4}{9}$	0	$\dfrac{4}{5}$	0	$-\dfrac{8}{45}$	0	$\dfrac{20}{63}$	0	$\dfrac{8}{25}$	0	$-\dfrac{4}{35}$	
$m=2,n=1$		$\dfrac{M_{21}}{k_0}$	$-\dfrac{8}{45}$	0	$\dfrac{4}{5}$	0	$-\dfrac{4}{35}$	0	$\dfrac{8}{25}$	0	$\dfrac{20}{63}$	0	
$m=1,n=4$			$\dfrac{M_{14}}{k_0}$	$-\dfrac{8}{7}$	0	$-\dfrac{16}{225}$	0	$\dfrac{40}{27}$	0	$-\dfrac{16}{35}$	0	$-\dfrac{8}{175}$	
$m=2,n=3$				$\dfrac{M_{23}}{k_0}$	$-\dfrac{36}{25}$	0	$-\dfrac{4}{9}$	0	$\dfrac{72}{35}$	0	$-\dfrac{4}{7}$	0	
$m=3,n=2$					$\dfrac{M_{32}}{k_0}$	$-\dfrac{8}{7}$	0	$-\dfrac{4}{7}$	0	$\dfrac{72}{35}$	0	$-\dfrac{4}{9}$	
$m=4,n=1$						$\dfrac{M_{41}}{k_0}$	$\dfrac{8}{175}$	0	$-\dfrac{16}{35}$	0	$\dfrac{40}{27}$	0	$=0$
$m=1,n=6$				Symmetry			$\dfrac{M_{16}}{k_0}$	$-\dfrac{20}{11}$	0	$\dfrac{8}{45}$	0	$-\dfrac{36}{1225}$	
$m=2,n=5$								$\dfrac{M_{25}}{k_0}$	$-\dfrac{8}{3}$	0	$-\dfrac{100}{441}$	0	
$m=3,n=4$									$\dfrac{M_{34}}{k_0}$	$-\dfrac{144}{49}$	0	$\dfrac{8}{45}$	
$m=4,n=3$										$\dfrac{M_{43}}{k_0}$	$-\dfrac{8}{3}$	0	
$m=5,n=2$											$\dfrac{M_{52}}{k_0}$	$-\dfrac{20}{11}$	
$m=6,n=1$												$\dfrac{M_{61}}{k_0}$	(12)

where the nonzero off-diagonal terms in eqns (11) and (12) satsify the condition $m \neq i$, $n \neq j$, $(m \pm i)$ = odd. and $(n \pm j)$ = odd.

Notice that the diagonal terms in eqns (11) and (12) came from the first term of eqn (1), and the series term of eqn (1) given the off-diagonal terms of the matrices. The 12×12 determinant was found to give sufficiently accurate eigenvalue solutions.

NUMERICAL RESULTS

Numerical buckling studies were performed on sandwich panels having MMC face sheets of different fiber orientations. The loading in the y-axis was set to zero (i.e. $k_y = 0$, eqn (4)). Thus, the combined loading implies inplane uniaxial compression in the x-direction and shear.

Physical properties

The sandwich panels analyzed have the following geometry: $a = a_0 = 60.96$ cm (24 in) or $ab = a_0^2$, $b/a = 0.1-4$, $h = 3.0480$ cm (1.2 in), $h_c = h - t_s = 2.9667$ cm (1.1680 in), and $t_s = 0.08128$ cm (0.0320 in). The effective material properties used for the titanium honeycomb core are shown in Table 1, and the two types of laminated MMC face sheets investigated have the laminate properties listed in Table 2.

Finally, the value of D^* (eqn (4)), the room temperature material properties of Ti − 6-4, were used, namely, $E_{Ti} = 110.3161$ GPa (16×10^6 lb/in²), $v_{Ti} = 0.31$.

Table 1. Material properties of titanium honeycomb

Temperature °C (°F)	G_{xz} (GPa) (10⁵ lb/in²)	G_{yz} (GPa) (10⁵ lb/in²)
21·11 (70)	1·4365 (2·0835)	0·6505 (0·9435)
315·56 (600)	1·2480 (1·8100)	0·5652 (0·8197)
648·89 (1200)	0·8277 (1·2005)	0·4527 (0·6566)

Buckling curves

Conventional plots

In the conventional plots of buckling interaction curves, the panel length a is kept constant (i.e. $a = a_0 = $ constant). Figure 2 shows a family of buckling interaction curves calculated from eqn (1) for the sandwich panels with two different types of laminated face sheets. The buckling interaction curves are plotted for different panel aspect ratios b/a and different temperatures using data given in Tables 1 and 2. For $b/a = 0.7$, each buckling interaction curve is a combination of symmetric and antisymmetric buckling interaction curves. For compression-dominated loadings the panels will buckle antisymmetrically. For shear-dominated loadings the buckling mode is symmetrical. For $b/a = 1$ (square panel), all buckling interaction curves are continuous and are associated with symmetric buckling. The antisymmetric buckling interaction curves for $b/a = 1$ (not shown) which give much higher buckling loads, do not intersect with the symmetric buckling curves. For $b/a = 2, 3, 4$, the buckling interaction curves are discontinuous, and are the composite curves consisting of both symmetric and antisymmetic buckling interaction curve segments. For $b/a \leq 1$, the [45/−45/−45/45] lamination case has a higher combined buckling strength as compared with the [90/0/0/90] lamination case. As the temperature increases, the buckling strength of the latter decreases slightly faster than the former. For $b/a = 2$, the two lamination cases have comparable compression-dominated buckling strength. But for shear-dominated buckling, the [45/−45/−45/45] lamination case is slightly superior to the [90/0/0/90] lamination case. For $b/a = 3, 4$, the [90/0/0/90] lamination case has a slightly higher compression-dominated buckling strength than the [45/−45/−45/45] lamination. For shear-dominated bucklings, the reverse is true.
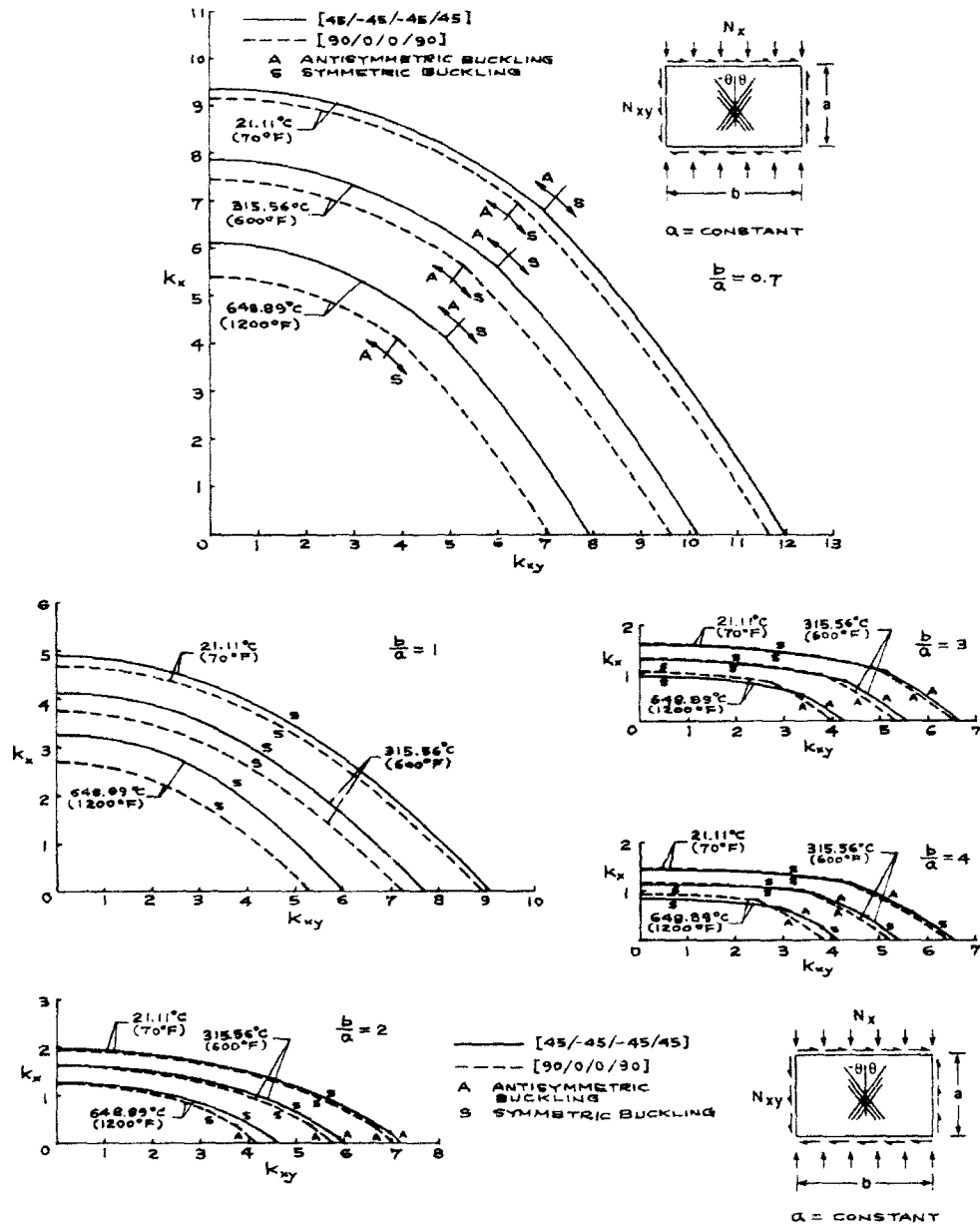
Table 2. Material properties of laminated MMC face sheets

Temperature (°C) (°F)	E_x (GPa) (10⁶ lb/in²)	E_y (GPa) (10⁶ lb/in²)	G_{xy} (GPa) (10⁶ lb/in²)	$v_{xy} = v_{yx}$
[90/0/0/90] laminate				
21·11 (70)	158·3581 (22·9679)	158·3581 (22·9679)	56·1923 (8·150)	0·2369
315·56 (600)	135·0573 (19·5884)	135·0573 (19·5884)	40·6791 (5·900)	0·2108
648·89 (1200)	110·8008 (16·0703)	110·8008 (16·0703)	24·1317 (3·500)	0·1634
[45/−45/−45/45] laminate				
21·11 (70)	145·8551 (21·1545)	145·8551 (21·1545)	64·0130 (9·2843)	0·2972
315·56 (600)	110·2837 (15·9953)	110·2837 (15·9953)	55·7731 (8·0892)	0·3555
648·89 (1200)	70·7457 (10·2608)	70·7457 (10·2608)	47·6193 (6·9066)	0·4658

Fig. 2. Buckling interaction curves for MMC sandwich panels at different temperatures; constant panel length.

Even though the [45/ − 45/ − 45/45] lamination case has lower values of bending stiffness $\{D_x, D_y\}$ (or $\{E_x, E_y\}$, Table 2) than the [90/0/0/90] lamination case, it has higher values of D_{xy} (or G_{xy}, Table 2) than the latter for all temperature levels. Because the combined-load buckling strength of panels depend not only on $\{D_x, D_y\}$ but also on D_{xy} (eqns (1), (4) and (5)–(10)), the combination of the values of D_x, D_y and D_{xy} happened to cause the |45/ − 45/ − 45/45| lamination case to have slightly superior buckling strength than the [90/0/0/90] lamination case.

Figure 3 compares the room temperature ($T = 21·11°C$ (70°F)) buckling interaction curves of the $b/a = 0·7$ sandwich panels fabricated with MMC face sheets (taken from Fig. 2) and with monolithic titanium face sheets, under the condition of equal panel specific weight.[3] Notice that through the fiber reinforcement of the face sheets, the buckling strength of the sandwich panel could be increased by 27% in pure uniaxial compression and by 22% in pure shear.

Figures 4 and 5, respectively, show the decrease in the compressive and shear buckling

strengths (k_x, k_{xy}) of the two types of MMC sand-
wich panels with increase in the panel aspect ratio
b/a. The compressive buckling strength k_x (Fig. 4)
decreases very sharply with the increase in b/a in

the region $b/a < 1$, and beyond $b/a = 2$, the rate of
decrease of k_x gradually dies out. For low panel
aspect ratio $(b/a < 0.75)$, the buckling mode is
antisymmetrical, and beyond $b/a = 0.75$, the panel
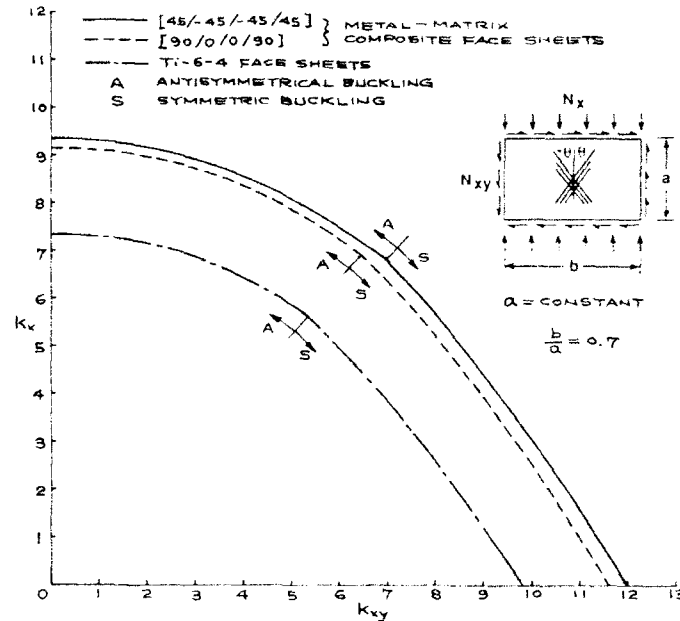
Fig. 3. Comparison of buckling strengths of honeycomb-core sandwich panels of same specific weight fabricated with different face sheet materials; $T = 21.11°C$ (70°F); constant panel length.
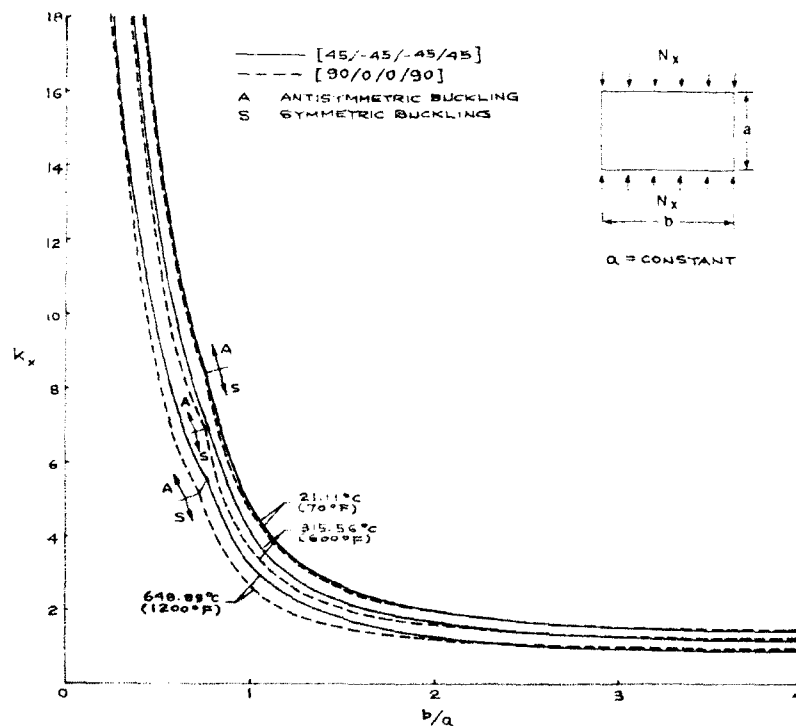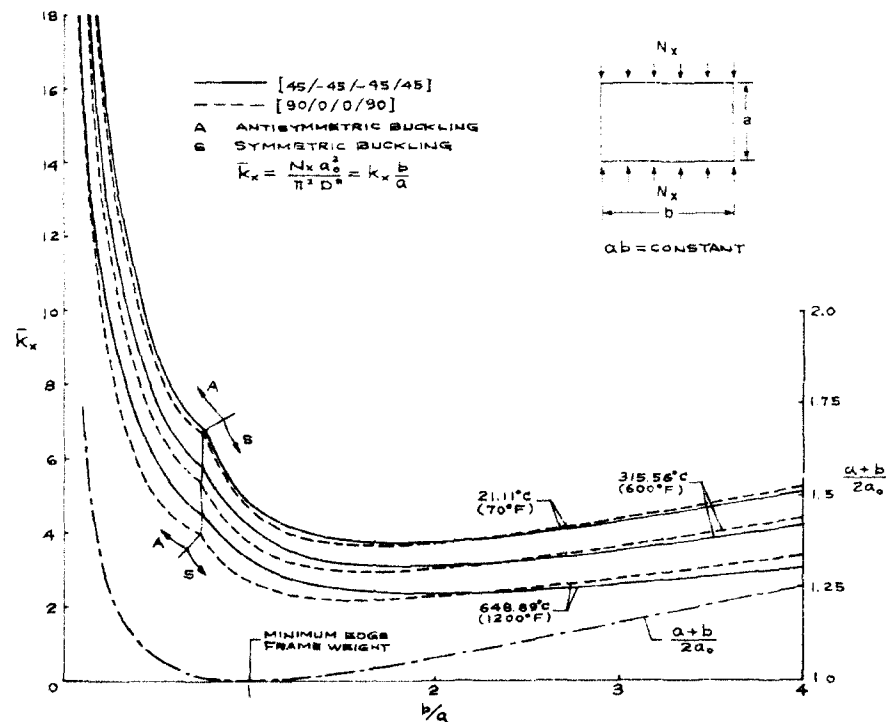

Fig. 4. Degradation of compressive buckling strengths of MMC sandwich panels with increasing temperatures and panel aspect ratios; constant panel length.
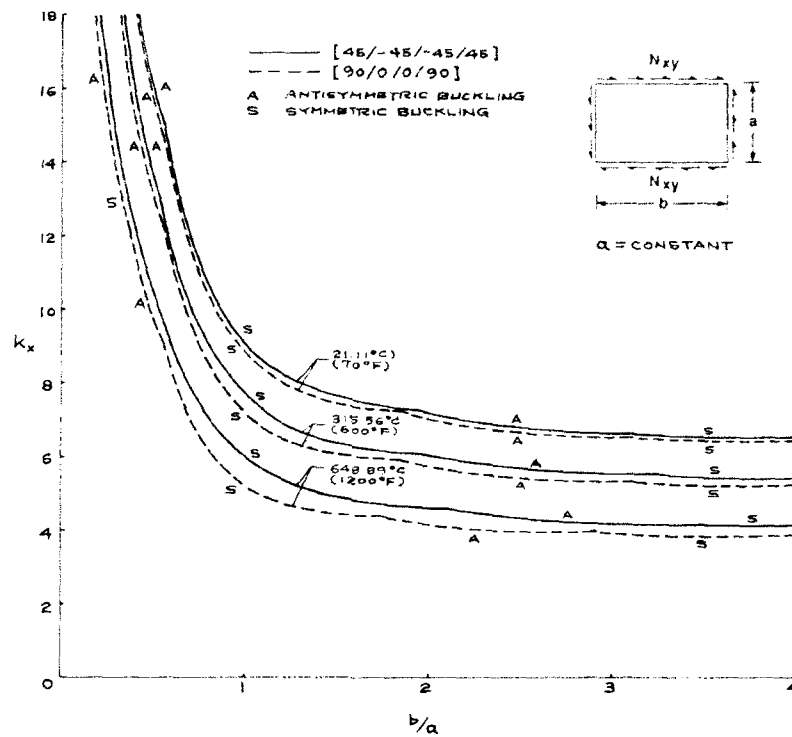
Fig. 5. Degradation of shear buckling strengths of MMC sandwich panels with increasing temperatures and panel aspect ratio; constant panel length.
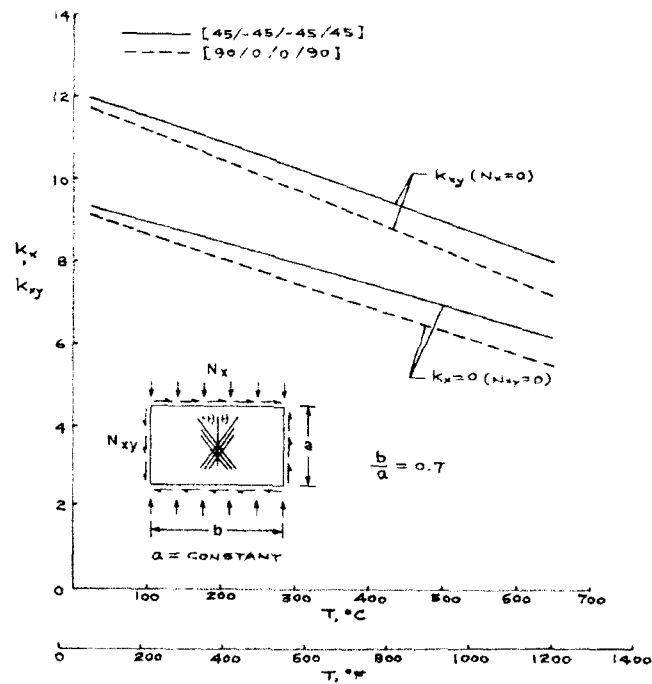
Fig. 6. Degradation of pure compressive and pure shear buckling strengths of MMC sandwich panels with increasing temperatures; $b/a = 0.7$; constant panel length.

will buckle symmetrically. The shear buckling strength k_{xy} (Fig. 5) is less sensitive to the change in b/a. All shear buckling curves shown in Fig. 5 are composite curves constructed with symmetrical and antisymmetrical buckling curves.

Figure 6 shows the degradation of k_x of pure compression, and k_{xy} of pure shear with the increase in temperature for the panel with aspect ratio $b/a = 0.7$. The [45/−45/−45/45] lamination case has a lower rate of degradation of k_x and k_{xy} with temperature than the [90/0/0/90] lamination case.

Modified plots

In the modified plots of the buckling curves, the panel area is kept constant $(ab = a_0^2 = \text{constant})$. The conventional plots shown in Figs 4 and 5 may not serve as ideal design curves for aerospace structural panels because, when the panel aspect

ratio b/a is changed (holding a constant), the panel weight (or panel area ab) is also changed accordingly. In aerospace structural designs, the main objective is structural optimization. That is, for a given panel weight, the objective is to search for a panel with optimum buckling strengths (or stiffness). For this reason, k_x and k_{xy} were recalculated as functions of b/a under the conditions $ab = a_0^2 = \text{constant}$ (instead of $a = a_0 = \text{constant}$). Figures 7 and 8 respectively show the modified buckling plots of $\bar{k}_x$ as a function of b/a and $\bar{k}_{xy}$ as a function of b/a when the panel area ab was held constant. In practical applications, the structural panels have to be supported by edge frames, and, therefore, the weight of the edge frames must be considered in the structural optimizations. If the cross-sections of the edge frames are kept constant, the edge frame weight becomes a function of edge length $2(a + b)$. Thus, in Figs 7 and 8 the
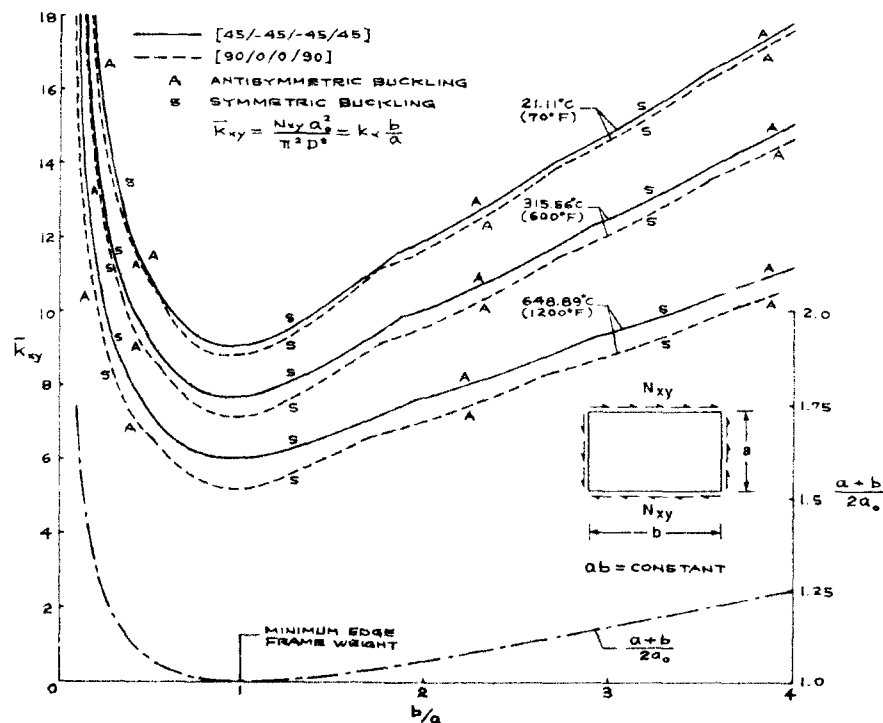

Fig. 7. Degradation of compressive buckling strengths of MMC sandwich panels with increasing temperatures and change of panel aspect ratio; constant panel areas.

Table 3. Panel aspect ratios at which $\bar{k}_x$ or $\bar{k}_{xy}$ is minimum

T (°C) (°F)	b/a for minimum at $\bar{k}_x$		b/a for minimum $\bar{k}_{xy}$	
	[45/−45/−45/45]	[90/0/0/90]	[45/−45/−45/45]	[90/0/0/90]
21·11 (70)	1·8	1·7	0·9	0·9
315·56 (600)	1·9	1·7	0·9	0·9
648·89 (1200)	2·0	1·6	1·0	1·0

dimensionless semi-edge length $(a+b)/2a_0$ was also plotted as a function of b/a. Figures 7 and 8 serve as design curves for selecting the optimum sandwich panel geometry (i.e. the panel aspect ratio b/a). A square panel ($b/a = 1$) has the minimum edge frame weight; however, it has comparatively low compressive buckling strength (Fig. 7), and it has practically the lowest shear buckling strength (Fig. 8). The aspect ratios b/a at which either $\bar{k}_x$ (Fig. 7) or $\bar{k}_{xy}$ (Fig. 8) becomes a minimum are listed in Table 3.

For pure compression (Fig. 7), the $[45/-45/-45/45]$ laminates have slightly higher compressive buckling strengths than the $[90/0/0/90]$ laminates in the region $b/a < 2.2$, and the reverse is true when $b/a > 2.2$. For pure shear (Fig. 8), the $[45/-45/-45/45]$ laminates are always superior to the $[90/0/0/90]$ laminates for the whole range of panel aspect ratios b/a. From Figs 7 and 8, it is noticed that the slender $(b/a < 1)$ rectangular panels are more efficient than the fat $(b/a > 1)$ rectangular panels. When the panel aspect ratio b/a is reduced from $b/a = 1$, one can improve the panel compressive buckling strength (Fig. 7) considerably with a slight edge frame weight penalty. The similar gain in shear buckling strength (Fig. 8) is less conspicuous. At higher

aspect ratios, the gains in values of $\bar{k}_x$ (Fig. 7) and $\bar{k}_{xy}$ (Fig. 8) are practically offset by the edge weight penalty (more severe in $\bar{k}_x$ curves (Fig. 7)).

Buckling interaction surfaces

Figure 9 shows three dimensional buckling surfaces plotted in $\{\bar{k}_x, \bar{k}_{xy}, b/a\}$ and $\{\bar{k}_x, \bar{k}_{xy}, b/a\}$ spaces for conditions $a = a_0 = $ constant (constant panel length), and $ab = a_0^2 = $ constant (constant panel area), respectively. This figure gives better visualization of the buckling behavior of the sandwich panels than the buckling plots shown in Figs 2, 4, 5, 7 and 8. For slender rectangular panels ($b/a < 1$), antisymmetric bucklings occur mostly in the compression-dominated regions. For wider panels ($b/a > 1$), the antisymmetric bucklings take place in the shear-dominated regions. In the neighborhood of $b/a = 1$, the lowest buckling modes are all symmetric ($m = n = 1$).

Effect of fiber orientations

Figure 10 shows the room temperature ($T = 21.11°C$ (70°F)) pure compression buckling strength ($\bar{k}_x$) of sanwich panel with $[\theta/-\theta/-\theta/\theta]$ laminated face sheets plotted as a function of fiber angle θ with panel aspect ratio b/a as a parameter. The peak value of $\bar{k}_x$ occurs at $\theta = 20°$ for the b/a

Fig. 8. Degradation of shear buckling strengths of MMC sandwich panels with increasing temperatures and change of panel aspect ratio; constant panel areas.

(a) a = constant.

(b) ab = constant.
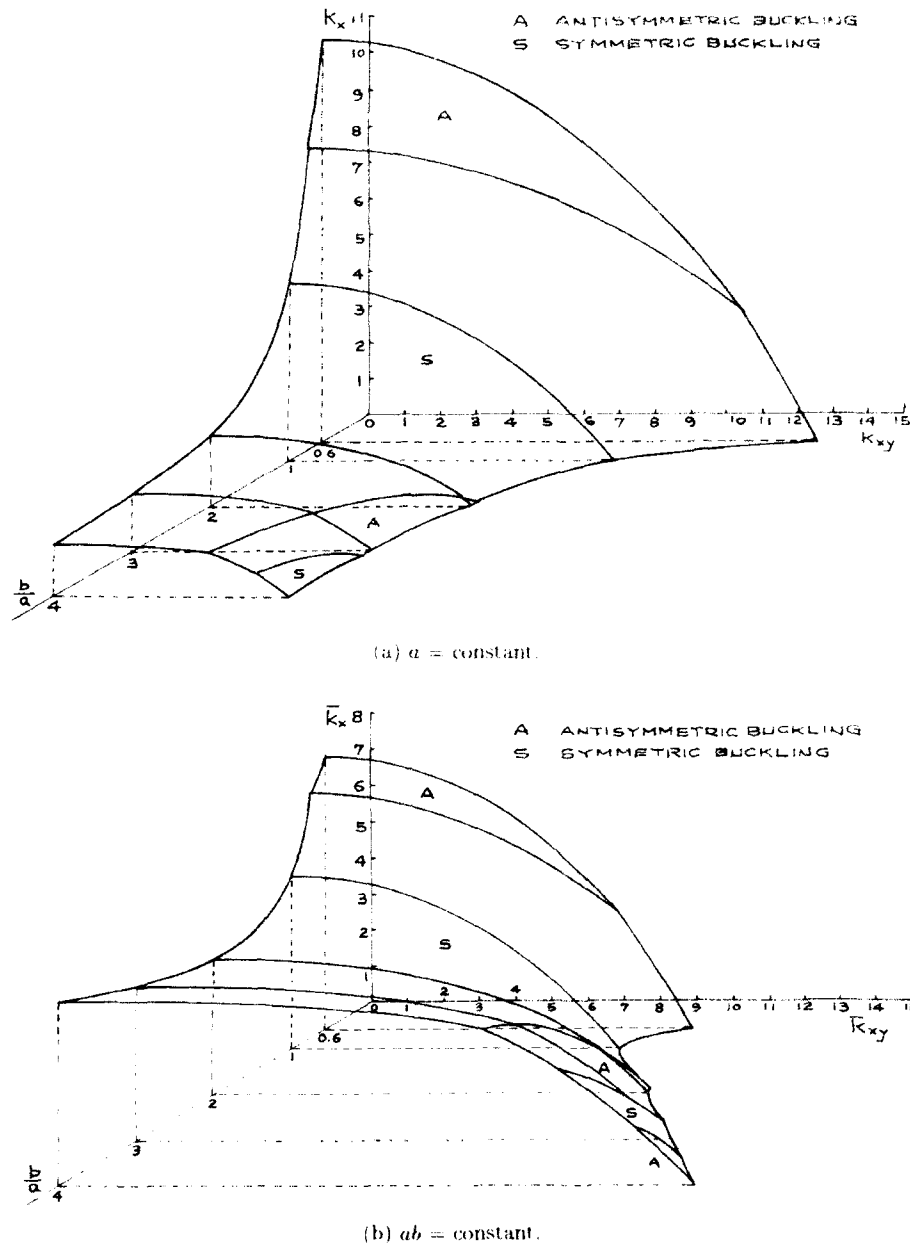
Fig. 9. Buckling interaction surfaces for MMC sandwich panels; [45/−45/−45/45] face sheets; T = 21·11°C (70°F).

= 0·7 panel, and migrates to θ = 60° for the b/a = 0·8 panel. In the neighbourhood of b/a = 1, the peak k_x point occurs near θ = 45°. As the value of b/a increases, the peak k_x point shifts toward θ = 0°.

This special feature of composite material was also seen in single laminated plates with symmetric angle-ply laminate[7] and antisymmetric angle-ply laminate.[8] Similar plots for pure-shear buckling strength (k_{xy}) are shown in Fig. 11. The maximum k_{xy} point occurs at θ = 45° for b/a ≤ 1

and gradually moves toward θ = 0° as the value of b/a increases beyond b/a = 1.

CONCLUSIONS

Combined compressive and shear buckling analysis was performed on flat rectangular sandwich panels fabricated with titanium honeycomb core and laminated metal matrix composite face sheets of [45/−45/−45/45] and [90/0/0/90] lamina-
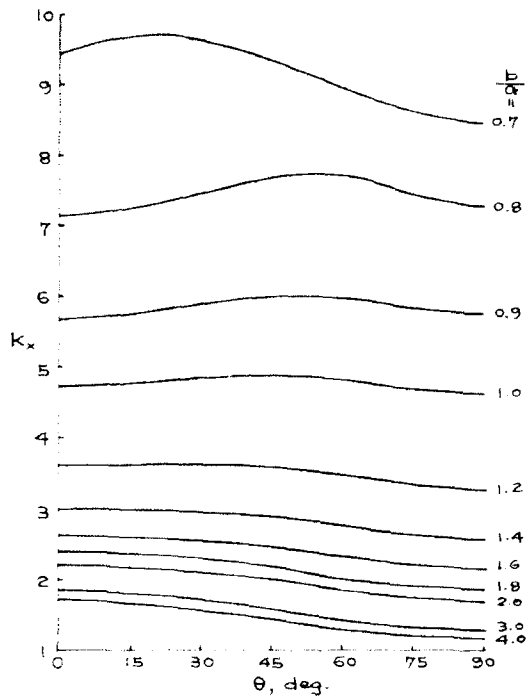
Fig. 10. Effect of fiber orientation on compressive buckling strengths of MMC sandwich panels: $T = 21 \cdot 11^\circ C (70^\circ F)$.

Fig. 11. Effect of fiber orientation on shear buckling strengths of MMC sandwich panels: $T = 21 \cdot 11^\circ C (70^\circ F)$.

tions. The results of the analysis may be summarized in the following.

1. The $|45/-45/-45/45|$ lamination case has slightly superior compressive buckling strength than the $|90/0/0/90|$ lamination case for panel aspect ratios $b/a < 2 \cdot 2$, beyond which the reverse is true.

2. The $|45/-45/-45/45|$ lamination case has shear buckling strength superior to the $|90/0/0/90|$ lamination case for the whole range of panel aspect ratios.

3. Through fiber reinforcement, the compressive and shear buckling strength may be increased from the monolithic face sheet case by about 27 and 22%, respectively.

4. Degradation of buckling strength of the sandwich panel with rising temperature is faster in shear than in compression.

5. The geometry of the desired high efficiency sandwich panels is slightly slender (i.e. $b/a < 1$) rectangular panels.

6. The optimum fiber orientation of the face sheets for the highest combined-load buckling strength of the sandwich panel is a

strong function of both loading condition k_x or k_{xy} and panel aspect ratio b/a.

REFERENCES

1. Taya, M. & Arsenault, R. J., *Metal Matrix Composites: Thermomechanical Behavior.* Pergamon Press, New York, 1989.

2. Tenny, D. R., Lisagor, W. B. & Dixon, S. C., Materials and structures for hypersonic vehicles. *J. Aircraft.* **26** 11 (Nov. 1989) 953–70.

3. Ko, W. L. & Jackson, R. H., Combined compressive and shear buckling analysis of hypersonic aircraft structural sandwich panels. NASA TM-4290, 1991. Also AIAA paper no. 92-2478-CP, presented at the 33rd AIAA/ASME/ASCE/AHS/ASC Structures, Structural Dynamics and Materials Conference, Dallas, Texas, April 13–15, 1992.

4. Bert, C. W. & Cho, K. N., Uniaxial compressive and shear buckling in orthotropic sandwich plates by improved theory. AIAA 86-0977, May, 1986.

5. Batdorf, S. B. & Stein, M., Critical combinations of shear and direct stress for simply supported rectangular flat plates. NACA TN-1223, 1947.

6. Stein, M. & Neff, J., Buckling stresses of simply supported rectangular flat plates in shear. NACA TN-1222, 1947.

7. Aston, J. E. & Whitney, J. M., *Theory of Laminated Plates.* Technomic Publishing Co., Westport, CT, 1970.

8. Jones, R. M., Morgan, H. S. & Whitney, J. M., Buckling and vibration of antisymmetrically laminated angle-ply rectangular plates. *J. Appl. Mech.*, **40** (4) (Dec. 1973) 1143–4.

Postbuckling analysis and imperfection sensitivity of metal matrix laminated cylindrical panels

Esther Feldman & Jacob Aboudi

Department of Solid Mechanics, Materials and Structures, Fleishman Faculty of Engineering, Tel Aviv University, Ramat Aviv, 69978, Israel

The postbuckling behaviour of metal matrix composite (MMC) laminated cylindrical panels under quasistatic in-plane loading is investigated. A micro-to-macro analysis is used to obtain the response of the composite structure. The micromechanical analysis allows us to establish the overall instantaneous elastic–viscoplastic behaviour of the MMC composite at each load increment. The macromechanical analysis provides the response of the geometrically imperfect cylindrical panel to the applied external loading.

Results are presented for unidirectional and antisymmetric angle-ply SiC/Ti composite panels, subjected to uniaxial compressive loadings. The effects of the panel curvature, initial imperfections and rate of loading on the postbuckling response are illustrated. Comparisons with the response of the corresponding perfectly elastic panels are shown.

1 INTRODUCTION

Curved panels, made of advanced composite materials, are now widely used in the design of aeronautical and aerospace constructions. Under working conditions, these structures might be submitted to in-plane forces that can cause instability phenomena. The important problems here are not only the determination of the lowest buckling loads and the corresponding modes of buckling, but also the study of the postbuckling behaviour of a structure and its sensitivity to the initial imperfections. Such a study would allow a deeper understanding of the behaviour of a structural element and better utilization of its load-carrying capability.

Many research works on different aspects of buckling and postbuckling behaviour of perfectly elastic composite curved panels have been reported in the literature. Comprehensive lists of references can be found, for example, in reviews by Leissa[1] and Simitses[2] and in the recent paper by Librescu and Chang.[3]

However, there are fewer works dealing with the buckling and postbuckling of inelastic composite curved panels. A finite element analysis of elastic–plastic laminated thin shells was presented by Liaw and Yang.[4] Where a survey of recent

developments in the finite element analysis of elastic–plastic response and buckling of laminated composite shells may also be found.

Metal matrix composites (MMC) are known as exhibiting elasto–plastic rate-dependent behaviour. The latter property is especially significant at high temperatures. Viscoplastic bifurcation buckling of metal matrix composite plates was investigated by Paley and Aboudi,[5] where a method for determination of the buckling load was proposed.

The present paper deals with the postbuckling behaviour of layered cylindrical panels, made of MMC materials, under in-plane loading. The analysis of such structures is difficult for three reasons. First, the metal matrix (for example, aluminium) exhibits elastic–viscoplastic behaviour. Second, there are complicated interactions between the inelastic matrix and the reinforcement. Third, due to the nonuniformity of the stress and strain fields in the postbuckling stage, the instantaneous properties of the composite not only change with time (as might occur in the prebuckling stage, e.g. Paley and Aboudi[6]), but they are difficult at the different points of the MMC structure at every instant of time.

The derivation of the instantaneous properties of composite at every point of the structure in the present investigation is based on the micro-

mechanical method of cells, proposed by
Aboudi.[6] This method establishes overall con-
stitutive relationships for MMC. The metal matrix
is modeled as an elastic–viscoplastic material, and
the fibres may be either elastic or viscoplastic.
The rate dependent behaviour of a metal matrix is
represented by means of the unified theory of
plasticity by Bodner and Partom.[7] This theory
does not require a yield criterion or distinguish
between loading and unloading, so that the elasto-
plastic equations have the same form at any point
of the structure during the whole process of defor-
mation.

In this paper simply supported unidirectional,
angle-ply and cross-ply rectangular cylindrical
panels, subjected to a uniaxial loading, are con-
sidered. The geometrically nonlinear quasistatic
behaviour of the panel is governed by the non-
linear differential equations in terms of stress
function Φ and out-of-plane displacement w, in
the framework of classical shell theory. The initial
imperfections are included. A method of solution
to the problem using Galerkin's procedure is pro-
posed. As a result a postbuckling equation is esta-
blished, which relates at each time increment the
value of the applied external axial load and the
value of the out-of-plane displacement.

The method proposed is illustrated for various
types of SiC/Ti composite panels. The panels are
subjected to a uniaxial compression, applied on
both edges. The results display the applied
external loading against the out-of-plane displace-
ment. The effects of panel curvature, material rate
sensitivity, ply orientation, initial imperfections
and mode of buckling on the postbuckling behavi-
our are studied. Comparisons with the cor-
responding postbuckling behaviour of cylindrical
panels, obtained by disregarding the viscoplastic
effects in the metal matrix, are presented.

2 THEORETICAL ANALYSIS

2.1 Constitutive equations of a unidirectional
metal matrix composite: a micromechanical
analysis

The analysis of a MMC panel requires a constitu-
tive law which describes the overall behaviour of
the single inelastic composite ply. The latter is a
unidirectional metal matrix composite whose
inelastic effects are caused by the plastic deforma-
tion of the metallic matrix phase. The requested
constitutive law can be established by a suitable

micromechanical approach which relies on the
fibre and matrix properties and analyses their
detailed interaction.

In this paper the micromechanical analysis
which describes the inelastic behaviour of the
unidirectional composite ply is based on the
method of cells developed by Aboudi.[6] In this
model the composite is assumed to be of a
periodic structure such that the detailed analysis
of a repeating volume element is sufficient for the
determination of the behaviour of the entire com-
posite.

In the framework of the method of cells, the
repeating volume element is divided into four sub-
cells, one being occupied by the elastic fibre,
whereas the other three subcells are occupied by
the inelastic metallic matrix. The detailed interac-
tion between the various subcells is accounted by
enforcing continuity of displacements and trac-
tions at the interfaces between the subcells, as well
as between neighbouring repeating cells. This, in
conjunction with microequilibrium conditions,
establishes the overall behaviour of the unidirec-
tional composite. The veracity and reliability of
the method of cells were extensively checked and
discussed with various theoretical and experi-
mental approaches in a review paper[8] and in the
monograph.[6]

The micromechanically established constitutive
law that describes the average behaviour of a
unidirectional metal matrix composite can be
written in the form (see Ref. 6, eqn (8.48))

$$\bar{\sigma}_{ij} = E_{ijkl}(\bar{\varepsilon}_{kl} - \bar{\varepsilon}^p_{kl}) \qquad i,j,k,l = 1,2,3 \qquad (1)$$

where $\bar{\sigma}_{ij}$, $\bar{\varepsilon}_{ij}$ and $\bar{\varepsilon}^p_{ij}$ are the stress, total strain and
plastic strain components of the bulk composite,
referred to a Cartesian system (x_1, x_2, x_3) in which
the unidirectional fibres are oriented in the x_1
direction. In eqn (1), E_{ijkl} are the components of
the effective elastic stiffness tensor of the unidi-
rectional composite, which are given explicitly in
terms of the fibre and matrix properties and the
fibre volume ratio. The composite plastic strain
$\bar{\varepsilon}^p_{ij}$ is given in a closed-form manner in terms of
the plastic deformations of the metallic matrix
subcells.

2.2 Response of an elastic–viscoplastic
cylindrical panel to axial loading:
a macromechanical analysis

Consider a shallow cylindrical panel of length a,
width b, thickness h and radius of curvature R
(see insert to Fig. 1 (later)). The panel consists of a

number of perfectly bonded layers. A layer is made of a unidirectional MMC material and is oriented at angle θ_k with respect to the panel axes (x, y) (k is the layer number).

The differential equations, which govern the moderately large deflection response of a geometrically imperfect cylindrical panel under quasistatic in-plane loading, can be written in the following form (see for example Simitses[9])

$$M_{xx,xx} + 2M_{xy,xy} + M_{yy,yy} + \frac{1}{R}\Phi_{,xx}$$

$$+ \Phi_{,yy}w_{,xx} - 2\Phi_{,xy}w_{,xy} + \Phi_{,xx}w_{,yy} = 0 \quad (2)$$

$$\varepsilon^0_{xx,yy} + \varepsilon^0_{yy,xx}\varepsilon^0_{xy,xy} = -\frac{1}{R}(w - w^0)_{,xx} - w_{,xx}w_{,yy}$$

$$+ (w_{,xy})^2 + w^0_{,xx}w^0_{,yy} - (w^0_{,xy})^2 \quad (3)$$

Here $\Phi(x, y, t)$ is the stress function, $w(x, y, t)$ and $w^0(x, y)$ are current and initial transverse displacements respectively, M_{xx}, M_{yy}, M_{xy} are the bending moments, ε^0_{xx}, ε^0_{yy}, ε^0_{xy} are middle-plane strains corresponding to the von Karman–Donnel nonlinear kinematic relations, and t is the time.

The following matrix notations are introduced:

$$\varepsilon^0 = [\varepsilon^0_{xx}\ \varepsilon^0_{yy}\ \varepsilon^0_{xy}]^T$$

$$\varepsilon = [\varepsilon_{xx}\ \varepsilon_{yy}\ \varepsilon_{xy}]^T$$

$$\chi = [\chi_{xx}\ \chi_{yy}\ \chi_{xy}]^T$$

$$= -[(w - w^0)_{,xx}\ (w - w^0)_{,yy}\ 2(w - w^0)_{,xy}]^T$$

$$\sigma = [\sigma_{xx}\ \sigma_{yy}\ \sigma_{xy}]^T \quad (4)$$

$$N = [N_{xx}\ N_{yy}\ N_{xy}]^T$$

$$= [\Phi_{,yy}\ \Phi_{,xx}\ (-\Phi_{,xy})]^T = \int_{-h/2}^{h/2}\sigma\, dz$$

$$M = [M_{xx}\ M_{yy}\ M_{xy}]^T = \int_{-h/2}^{h/2}\sigma z\, dz$$

where ε_{ij} and σ_{ij} are total strains and stresses in the composite, which are referred to the panel coordinates (x, y, z); N_{ij} are the membrane stress resultants.

In the framework of the classical plate theory,

$$\varepsilon(x, y, z, t) = \varepsilon^0(x, y, t) + z\chi(x, y, t) \quad (5)$$

In order to obtain the governing equations for the elastic–viscoplastic composite cylindrical

panel, we proceed with the consideration of the corresponding constitutive relationships. The total strain ε is presented as the sum of elastic (reversible) and plastic (irreversible) components: $\varepsilon = \varepsilon^{(e)} + \varepsilon^{(p)}$, where the elastic strain is related to the stress by the inverse Hooke's law, while the plastic strain components ε^p_{ij} are related to the plastic strains $\bar{\varepsilon}^p_{ij}$ of eqn (1) by the transformation of coordinates (x, y) to (x_1, x_2).

The plane stress constitutive equation for the kth layer has the form

$$\sigma^{(k)} = Q^{(k)}(\varepsilon - \varepsilon^{(p)}) \quad (6)$$

here $Q^{(k)}$ is the reduced stiffness matrix, which is derived from the material stiffness matrix $C^{(k)}$: $Q^{(k)}_{ij} = C^{(k)}_{ij} - C^{(k)}_{i3}C^{(k)}_{3j}/C^{(k)}_{33}$; $i, j = 1, 2, 6$. The matrix $C^{(k)}$ is obtained from the effective elastic stiffness matrix $E^{(k)}$ of eqn (1) through the transformation of coordinates (see Whitney,[10] for example).

From eqns (4)–(6) may be shown that

$$\varepsilon^0 = A^*N + B^*\chi + A^*N^p$$

$$M = -B^{*T}N + D^*\chi - B^{*T}N^p - M^p \quad (7)$$

where the matrices A^*, B^*, D^* are defined in Ref. 10 and the vectors N^p and M^p are the contributions, due to the existence of the plasticity effects, to the total stress and moment resultants.

In this work we shall consider the response of antisymmetric angle-ply or symmetric cross-ply laminated panels. For this case, retaining only the non-zero elements of the stiffness matrices, and taking into account relationships (4) and (7), one may write the expressions for ε^0 and M in terms of the stress function Φ, the transverse displacement w, and the vectors N^p and M^p. Substituting this expressions into eqns (2) and (3) yields the governing equations for the quasistatic response of the imperfect viscoplastic cylindrical laminated panel to an in-plane loading:

$$D^*_{11}(w - w^0)_{,xxxx} + 2(D^*_{12} + 2D^*_{66})(w - w^0)_{,xxyy}$$

$$+ D^*_{22}(w - w^0)_{,yyyy} - \frac{1}{R}\Phi_{,xx}$$

$$+ (2B^*_{26} - B^*_{61})\Phi_{,xxxy} + (2B^*_{16} - B^*_{62})\Phi_{,xyyy}$$

$$+ M^{(p)}_{xx,xx} + 2M^{(p)}_{xy,xy} + M^{(p)}_{yy,yy} + B^*_{61}N^{(p)}_{xy,xx}$$

$$+ 2[B^*_{16}N^{(p)}_{xx} + B^*_{26}N^{(p)}_{yy}]_{,xy} + B^*_{62}N^{(p)}_{xy,yy}$$

$$- \Phi_{,yy}w_{,xx} + 2\Phi_{,xy}w_{,xy} - \Phi_{,xx}w_{,yy} = 0 \quad (8)$$

$$A_{22}^* \Phi_{,xxxx} + (2A_{12}^* + A_{66}^*) \Phi_{,xxyy} + A_{11}^* \Phi_{,yyyy} =$$

$$-\frac{1}{R}(w - w^o)_{,xx} + (2B_{16}^* - B_{62}^*)(w - w^o)_{,xyyy}$$

$$+ (2B_{26}^* - B_{61}^*)(w - w^o)_{,xxxy} - w_{,xx} w_{,yy}$$

$$+ (w_{,xy})^2 + w_{,xx}^o w_{,yy}^o - (w_{,xy}^o)^2$$

$$+ \gamma_{xy,xy}^{(p)} - \gamma_{xx,yy}^{(p)} - \gamma_{yy,xx}^{(p)} \qquad (9)$$

where

$$\gamma_{xx}^{(p)} = A_{11}^* N_{xx}^{(p)} + A_{12}^* N_{yy}^{(p)};$$

$$\gamma_{yy}^{(p)} = A_{12}^* N_{xx}^{(p)} + A_{22}^* N_{yy}^{(p)}; \quad \gamma_{xy}^{(p)} = A_{66}^* N_{xy}^{(p)}.$$

Consider a simply supported panel, subjected to compressive uniaxial loading in the x direction. We'll stipulate the kinetic boundary conditions to be satisfied in the average sense:

$$x = 0, a: \frac{1}{b} \int_0^b \Phi_{,yy} \, dy = -P(t);$$

$$\int_0^b \Phi_{,xy} \, dy = 0; \quad w = 0; \quad \int_0^b M_{xx} \, dy = 0$$

$$\qquad (10)$$

$$y = 0, b: \int_0^a \Phi_{,xx} \, dx = 0;$$

$$\int_0^a \Phi_{,xy} \, dx = 0; \quad w = 0; \quad \int_0^a M_{yy} \, dx = 0$$

where $P(t)$ is the applied external load at time t.

An approximate solution to eqns (8–10) can be obtained by employing the Galerkin procedure. Suppose that the initial imperfection $w^o(x, y)$ has a simple sinusoidal shape compatible with the geometric boundary conditions, and assume that the transverse displacement $w(x, y, t)$ is of an analogous form:

$$w^o(x, y) = W_0 \sin \alpha^* x \sin \beta^* y;$$

$$w(x, y, t) = W(t) \sin \alpha^* x \sin \beta^* y \qquad (11)$$

where $\alpha^* = \pi m^*/a$, $\beta^* = \pi n^*/b$ and m^*, n^* are the modes of buckling.

After some lengthy manipulations one can establish the following postbuckling equation which relates the amplitude W of the transverse displacement to the applied axial load P:

$$c_0 + (c_1 - \alpha^{*2} P) W + c_2 W^2 + c_3 W^3 = 0 \qquad (12)$$

In this equation the coefficients c_i, $i = 0, \ldots, 3$ are

complicated expressions including, in particular, a number of line and surface integrals from the 'plastic' functions $N_{ij}^{(p)}$, $M_{ij}^{(p)}$.

To solve eqn (12), one needs to determine the coefficients c_i. This is performed in an incremental procedure. A three-dimensional regular grid with the coordinate points (x_i, y_j, z_k) is introduced, and at every time increment the aforementioned micromechanical analysis is performed at every grid point. As a result of this the values of the plastic strains ε_{ij}^p, needed for the next time increment, are available. After that all the values that form the expressions for c_i can be calculated.

3 APPLICATIONS

To illustrate the proposed method, consider the postbuckling response of SiC/Ti metal matrix laminated panels. The fibres are assumed to behave as perfectly elastic, whereas the matrix phase (Ti–6A–4V alloy) is considered as an elastic–viscoplastic work hardening material. Its inelastic behaviour is described by the unified viscoplasticity theory of Bodner and Partom.[7] The material parameters that characterize the SiC elastic fibres and the viscoplastic matrix at temperature $T = 315°C$ are given in the paper by Paley and Aboudi.[11]

The results are presented for square cylindrical panels $(a = b)$ of thickness $h = 28.5$ mm, with length-to-thickness ratio $a/h = 35$ and for different ratios a/R. All layers comprising a panel are of the same thickness and they are made of the same unidirectional MMC with the fibre volume fraction v_f.

The behaviour of composite panels is investigated by subjecting them to a quasistatic uniaxial compression $P(t)$ at both edges $x = 0$, a in such a manner that the rate of change of the transverse displacement $\dot{W}$ is constant. In each graph, representing the postbuckling response, two branches are shown: one branch corresponds to an initial imperfection W_0 and deflection rate $\dot{W}$, both directed outwards, i.e. $W_0 > 0$, $\dot{W} > 0$; and the second branch corresponds to W_0 and W, both directed inwards, i.e. $W_0 < 0$, $\dot{W} < 0$. A non-dimensional transverse displacement $\bar{W} = W/h$ and an average stress $\hat{\sigma} = P/h$ at the edges $x = 0$, a, are introduced. For convenience, the stresses are shown as positive in the figures. The elastic solutions obtained by neglecting the inelastic effects are presented in the figures by the dashed lines.

In Fig. 1 are shown the postbuckling curves $\hat{\sigma}$ versus $\tilde{W}$ for a cylindrical panel made of unreinforced titanium alloy (i.e. $v_f = 0$). The graphs relate to the lowest mode of buckling $(m^*, n^*) = (1, 1)$, and two values of rate loading: $|\dot{W}|/h = 1\ \text{s}^{-1}$ and $100\ \text{s}^{-1}$. Also shown in the figure is the corresponding elastic behaviour of the panel (obtained by neglecting the inelastic effects). It can be readily observed that the viscoplastic effects of the material are significant, and the ability of the viscoplastic panel to sustain loading, contrary to the case of the corresponding perfectly elastic structure, is limited. The effect of rate of loading, however, appears to be rather small.

Figure 2 presents the response of a unidirectional composite panel with $v_f = 0.3$, in which the external loading is applied in the direction of the fibres (i.e. for a lamination angle $\theta = 0°$). The graphs are shown for two values of initial imperfections: $|\tilde{W}_0| = 0.01$ and 0.1. It appears that in the present situation $(\theta = 0°)$ the effect of the initial imperfections on the postbuckling behaviour of the viscoplastic panel is similar to that exhibited in the perfectly elastic case.

The influence of the curvature a/R on the postbuckling response of the unidirectional composite panel, which is loaded in the fibre direction $(\theta = 0°)$, is illustrated in Fig. 3. The results are presented for $a/R = 0$ (i.e. a flat plate), 0.2 and 0.5. It can be readily observed that the viscoplastic effects increase with increase of curvature. This may be explained by the fact that in panels with
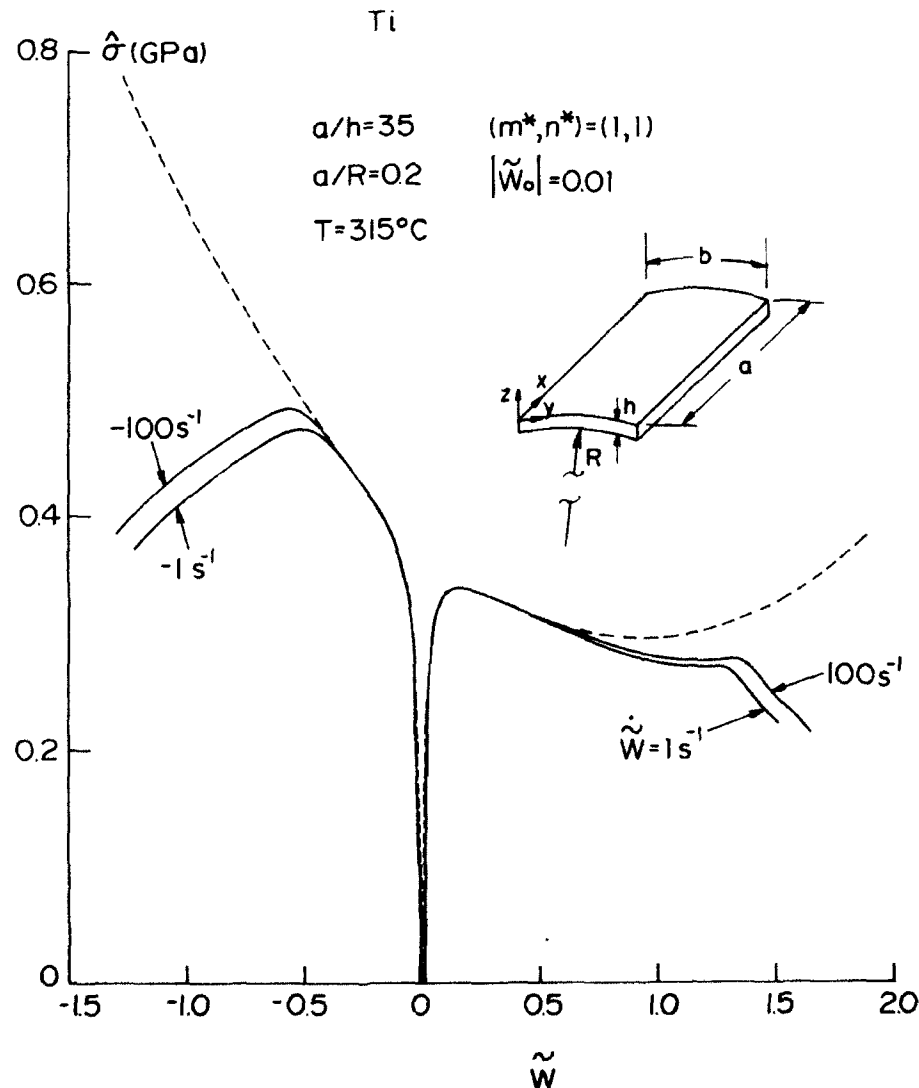
Fig. 1. The postbuckling curves (the applied stress versus maximum deflection) for a homogeneous cylindrical panel, made of titanium alloy only, at different rates of loading $\dot{W}/h$: (———) viscoplastic response; (– – –) elastic response.

Fig. 3. The influence of curvature a/R on the postbuckling behaviour of a unidirectional MMC panel, loaded in the fibre direction: (———) viscoplastic response; (– – –) elastic response.
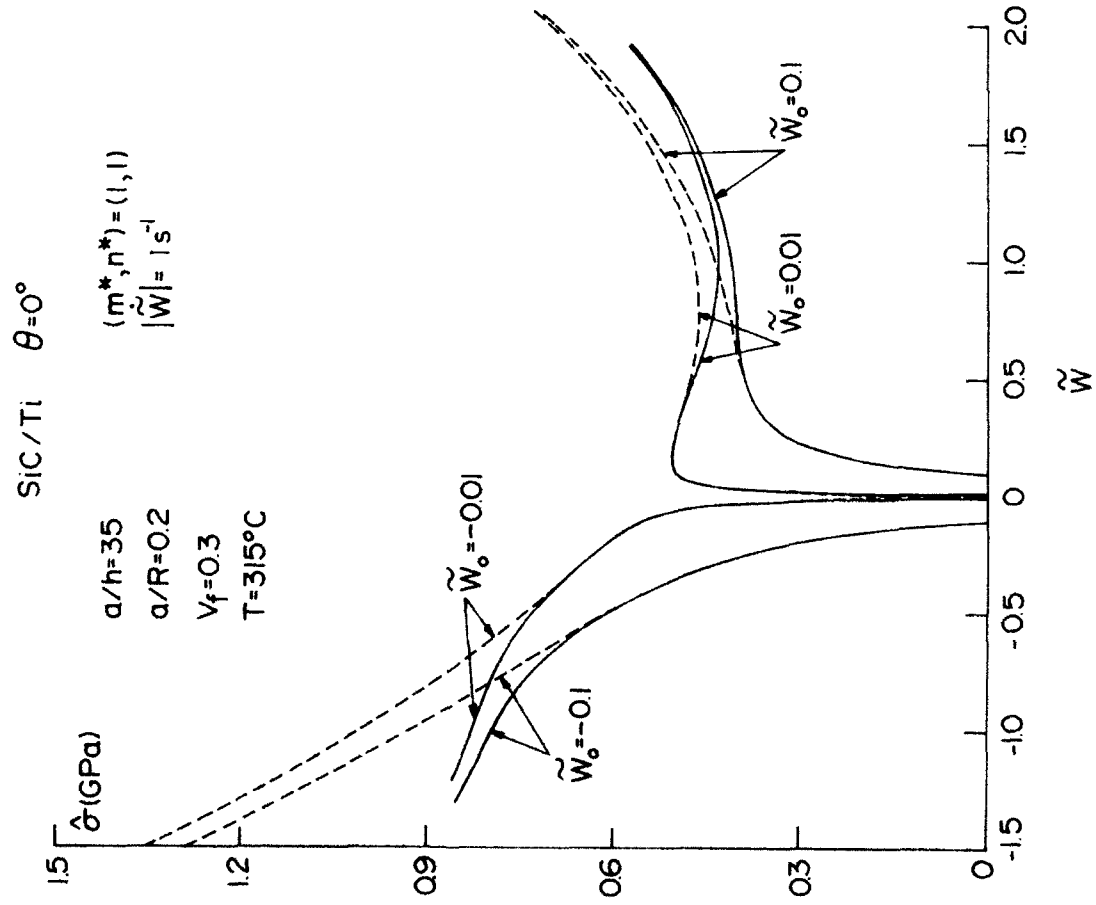
Fig. 2. The influence of initial imperfections W_0 on the postbuckling curves (applied stress versus maximum deflection) of a unidirectional MMC panel, loaded in the fiber direction: (———) viscoplastic response; (– – –) elastic response.
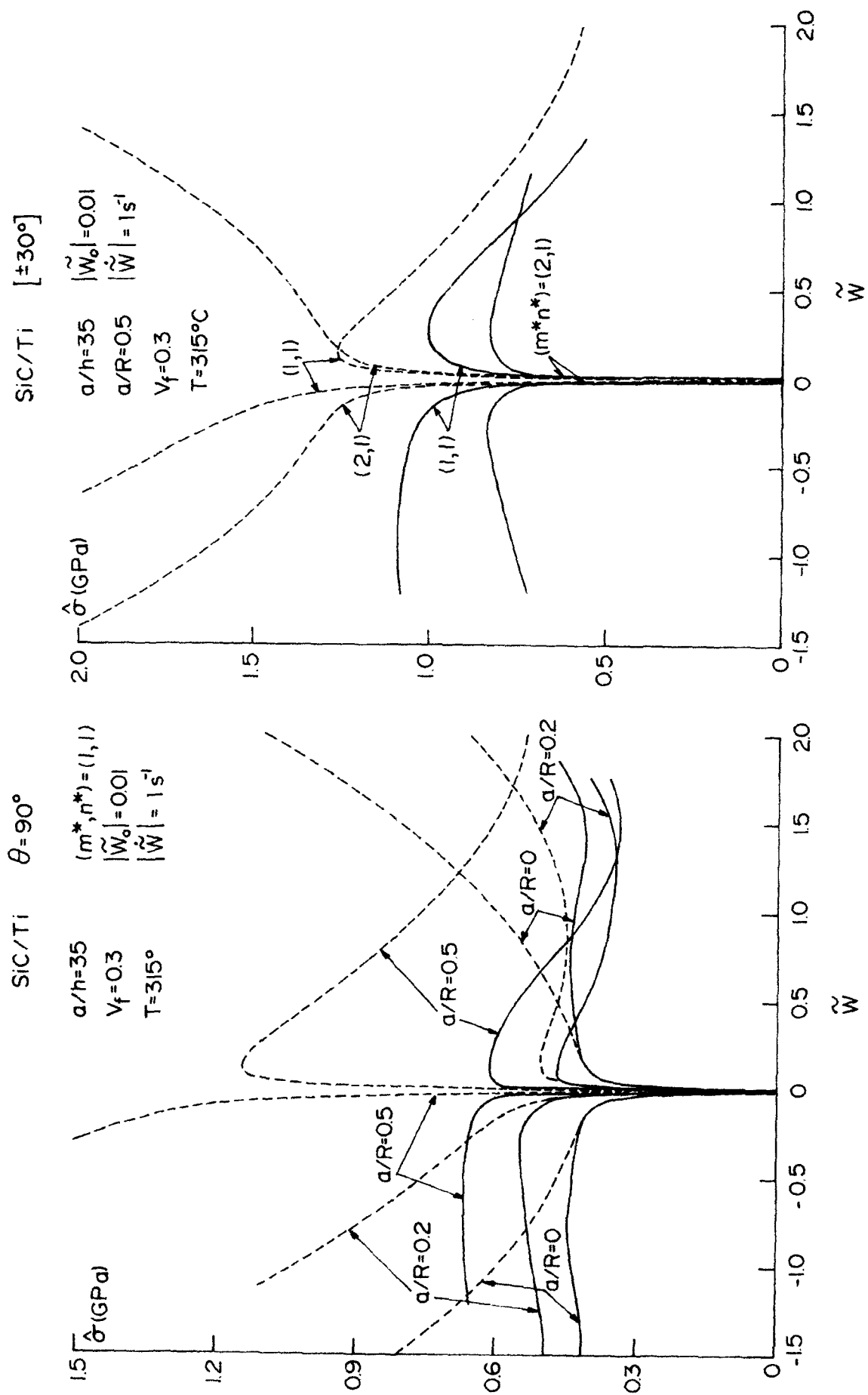
Fig. 4. The influence of curvature a/R on the postbuckling behaviour of a unidirectional MMC panel, loaded perpendicular to the fibre direction: ($-\!\!\!-\!\!\!-$) viscoplastic response; ($-\,-\,-$) elastic response.

Fig. 5. The postbuckling curves (applied stress versus maximum deflection) of a $[\pm 30°]$ MMC panel, for two modes of buckling (m^*, n^*): ($-\!\!\!-\!\!\!-$) viscoplastic response; ($-\,-\,-$) elastic response.

higher curvatures, higher stresses are developed for a given deflection. It can also be seen from the graphs, that the plate and the panel with $a/R = 0.2$ buckle in the elastic region. The panel with the higher curvature $a/R = 0.5$, however, buckles in the plastic region. It is worth mentioning that a composite panel, which is reinforced in the direction of external loading, can exhibit a considerable load-carrying capacity beyond the buckling load — contrary to the behaviour of the unreinforced panel, shown in Fig. 1.

Figure 4 demonstrates the influence of curvature a/R on the behaviour of a unidirectional composite panel, loaded perpendicular to the fibre direction ($\theta = 90°$). It is expected that in the present situation of matrix dominated behaviour, the viscoplastic effects are more significant than in the previously considered case ($\theta = 0°$). In addition, the increase in curvature leads to pronounced viscoplastic effects. The combined influence of matrix dominated behaviour and increase of curvature is displayed in Fig. 4. Note that whereas the panel with $a/R = 0.2$ in the case of loading in the fibre direction ($\theta = 0°$) buckles in the elastic region, it buckles presently ($\theta = 90°$) in the plastic region.

Until now we have discussed the behaviour of the buckling mode $(m^*, n^*) = (1, 1)$, which corresponds to the lowest buckling load for the plates and panels with $a/R = 0.2$ considered above. It is known, however, that as a cylindrical panel becomes more curved, the lowest buckling loads correspond to the higher modes of buckling. In fact, for the unidirectional panels with $a/R = 0.5$, considered in Figs 3 and 4, the buckling loads for the modes $(1, 1)$ and $(2, 1)$ are almost equal.

To illustrate the effect of higher mode of buckling, consider a two-layered $[\pm 30°]$ laminated panel with $a/R = 0.5$. If the viscoplastic effects are neglected, the critical buckling stress for the elastic structure $\hat{\sigma}_{cr}^{k}$ is equal to 1·33 GPa for the mode $(m^*, n^*) = (2, 1)$ and 1·47 GPa for the mode $(m^*, n^*) = (1, 1)$. The postbuckling responses of

these two modes for the viscoplastic $[\pm 30°]$ panel, as well as their perfectly elastic counterparts, are shown in Fig. 5. It is seen that whereas the elastic buckling stress for the mode $(2, 1)$ is only a little bit smaller than that for the mode $(1, 1)$, the difference between the corresponding viscoplastic buckling stresses is much greater. Furthermore, one may observe the characteristic difference between the postbuckling behaviour of symmetric $(m^* = 2)$ and antisymmetric $(m^* = 1)$ buckling modes. Note that the ability of the viscoplastic panel to bear loading is limited for both modes considered.

REFERENCES

1. Leissa, A. W., Buckling of laminated composite plates and shell panels. Flight Dynamic Laboratory, Wright Patterson Air Force Base, Dayton, Ohio, Report AFWAL-TR-85-3069, 1985.
2. Simitses, G. J., Buckling and postbuckling of imperfect cylindrical shells — a review. Appl. Mech. Rev., 39 (1986) 1517-24.
3. Librescu, L. & Chang, M.-Y., Imperfection sensitivity and postbuckling behaviour of shear-deformable composite doubly-curved shallow panels. Int. J. Solids Struct., 29 (1992) 1065-83.
4. Liaw, D. G. & Yang, T. Y., Elastic-plastic dynamic response and buckling of laminated thin shells. J. Comp. Mater., 25 (1991) 1039-63.
5. Paley, M. & Aboudi, J., Plastic buckling of metal matrix laminated plates. Int. J. Solids Struct., 28 (1991) 1139-54.
6. Aboudi, J., Mechanics of Composite Materials — A Unified Micromechanical Approach. Elsevier, Amsterdam, 1991.
7. Bodner, S. R. & Partom, Y., Constitutive equations for elastic-viscoplastic strain-hardening materials. J. Appl. Mech., 42 (1975) 385-9.
8. Aboudi, J., Micromechanical analysis of composites by the method of cells. Appl. Mech. Rev., 42 (1989) 193-221.
9. Simitses, G. J., Dynamic Stability of Suddenly Loaded Structures. Springer-Verlag, Berlin, 1990.
10. Whitney, G. M., Structural Analysis of Laminated Anisotropic Plates. Technomic, Lancaster, PA, 1987.
11. Paley, M. & Aboudi, J., Inelastic thermal buckling of metal matrix laminated plates. J. Therm. Stresses, 14 (1991) 479-97.

Scaling of impact damage in fiber composites from laboratory specimens to structures

Stephen R. Swanson

Department of Mechanical Engineering, University of Utah, Salt Lake City, Utah 84112, USA

Impact damage in fiber composite structures remains of much concern, and is often the limiting factor in establishing allowable strain levels. The complexity of impact damage formation usually dictates that experiments are required, but scaling of results from small laboratory scale specimens to large structures is not well understood. The following paper presents the results of an analytical and experimental investigation intended to develop procedures for prediction of damage formation and subsequent strength loss, with particular emphasis on scaling of results with respect to structure size. The experimental investigation involved both drop-weight and airgun impact on carbon/epoxy plates and cylinders. Five sizes of plates ranging from $50 \times 50 \times 1.072$ mm to $250 \times 250 \times 5.36$ mm, and two sizes of cylinders with diameters of 96.5 and 319 mm, were employed in the experimental program. Delamination was observed to increase with specimen size more than would be expected if stresses controlled the delamination extent, as would be predicted by fracture mechanics. Regions of broken fibers were observed in the impacted specimens, that were best correlated with the applied specimen stress or strains, independent of specimen size. It is seen that knowledge of the failure mechanisms involved is required to predict scaling of damage with confidence.

INTRODUCTION

Fiber composites are increasingly being used in large structures where in many cases the strength to weight and stiffness to weight are both important. Important questions in structural response must be answered by experiment. It is highly desirable to be able to conduct these experiments on scaled models, for reasons of time, convenience, and cost. Thus the question must be addressed as to whether the scaled model is representative of the final prototype, and just how to extrapolate the results with changes in scale. A well developed methodology exists to answer these questions, based on the theory of similitude.[1] In this methodology dimensionless groups are identified based on either dimensional analysis, or if possible, by examination of the governing differential equations involved in the problem at hand. Procedures of this type are, of course, well known in diverse fields. An application of scaling of this type was carried out by the author and co-workers for the problem of impact of fiber composite plates and cylinders. It was found that scaling of the linear response for both quasi-static and dynamic conditions could be well predicted over a range of specimen sizes, and thus the scaling was reasonably well understood. However the scaling of damage and failure mechanisms proved to be much more complicated.

The possibility of impact damage is an important consideration in the use of fiber composites. In early work, a number of investigators have determined the general susceptibility to impact damage of carbon fiber laminates, and demonstrated the forms of damage that result.[2-5] In further work, attempts were made to analyze the impact event. Sun and co-workers showed how the contact stiffness could be included in the analysis, and made finite element calculations of plate impact.[6,7] The nature of the damage resulting from impact has been discussed by a number of investigators. Boll et al.[8] have given detailed results of micrographs of sections taken from impacted specimens, indicating the widespread microcracking, delaminations, and fiber breakage that can result. Morton[9] and Jackson[10] have studied scaling in composites.

The difficulty in predicting the behavior of damage and failure with changes in scale is that the underlying failure mechanisms are not well understood. For example, it is sometimes consid-

249

ered that failure is related to maximum values of stress or strain components. Conversely, failure is often related to energetic principles as in the usual application of fracture mechanics. Frequently it is difficult to know which principles are applicable, and decisions are made based on the personal preference of the investigator. However the scaling behaviors of these two postulated failure mechanisms are quite different. As is well known, fracture mechanics involves a dependence on the absolute size of the crack, and thus scaled specimens containing a crack or flaw should exhibit a decrease in critical stress levels with an increase in size.

In the following, the previous experimental program on scaling of impact will be briefly reviewed. The scaling behaviors for two different failure mechanisms typical of fiber composites, that of delamination and of fiber breakage, will be examined with respect to changes with scale.

EXPERIMENTAL PROGRAM

Impact tests were carried out on 5 sizes of plates and 2 sizes of cylinders.[11-13] The plates varied from $50 \times 50 \times 1.027$ mm to $250 \times 250 \times 5.36$ mm. If the scale factor is termed λ, the dimensions of the plates were varied by $\lambda = 1,2,3,4$ and 5. The layup used in the plates was $[(\pm 72)_\lambda/0_{2\lambda}]_\lambda$. Geometric scaling was employed so that as many dimensions as possible were scaled with λ, including the exterior dimensions and the ply group thicknesses, but not the thickness of the fibers or individual plies. Tests were carried out using both drop-weight (pendulum) and an airgun apparatus, representative of quasi-static and dynamic conditions. The two cylinders were 96.5 mm and 319 mm ID respectively, and thus differed by a scale factor of 3.30. Again, both drop-weight and airgun experiments were employed.

Analysis procedures were developed for both the plate[11,14] and cylinder[15] impacts. The plate analysis was based on a Ritz procedure because of the boundary conditions employed in the tests, and used a finite difference integration in time. The cylinder analysis used Fourier series expansion of the displacements, coupled with Laplace transform techniques for the transient time effects.

Scaling of the linear structural response was established by examination of these governing differential equations. The coefficients were grouped into dimensionless parameters. A princi-

pal result was that if geometric scaling was used for the specimens and impactor geometry, constant values of peak strain, independent of specimen size, should result from impacts at a given constant value of impact velocity. Further, the time scale of impact should depend linearly on the geometric scale factor.

A total of approximately 400 impact tests were carried out on the plate specimens and 200 on the cylinders. Typical results for structural response are shown in Figs 1 and 2, taken from Refs 11 and
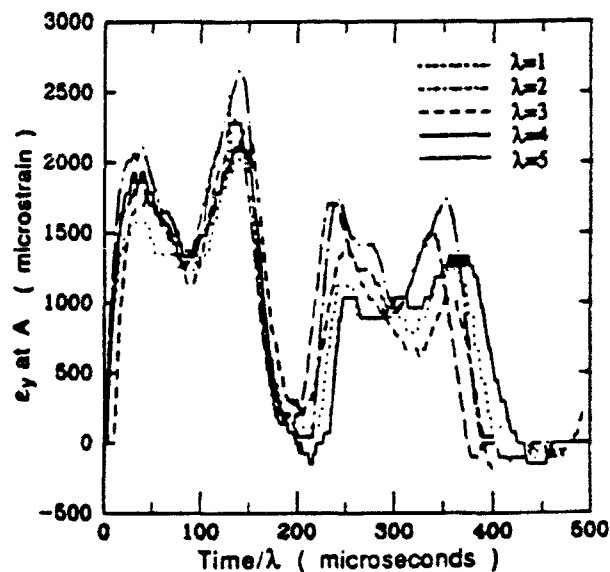
Fig. 1. Comparison of strain response at location A in impact tests on five different plate sizes. $V_0 = 5.47$ m/s (from Ref. 11).
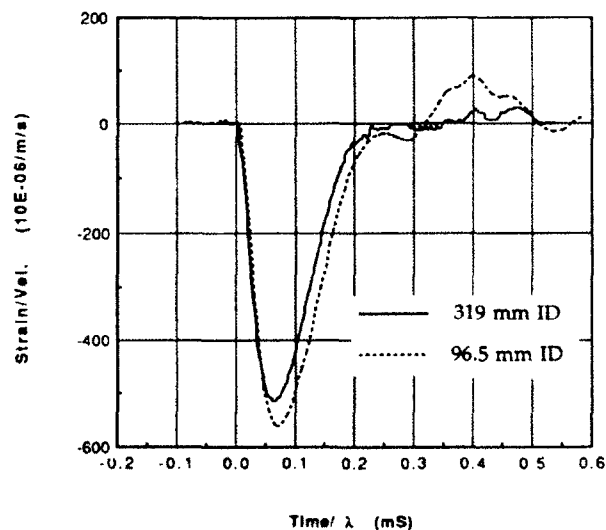
Fig. 2. Comparison of strain response H2 between 96.5 mm and 319 mm diameter cylinders (from Ref. 13).

13 for plates and cylinders. It can be seen that the response scales very well over the range of sizes examined experimentally. The peak strain values at a given value of impact velocity are constant over the range of specimen sizes, as predicted by the scaling theory. The time period of the impact is predicted to vary with the scale factor. As shown, normalizing the measured time scale by the scale factor gives good agreement over the range of specimen sizes. Additionally, it has been shown that the analysis procedures developed compared well with the experimental measurement of surface strains.[11,13]

The comparison between the drop-weight and the airgun experiments involves considerations apart from scaling issues. It is well known that for impacts in which the impactor and target act like a single degree of freedom system with the target behaving as a spring of negligible mass, the target response depends on the energy of impact and not on the specific values of impact mass and velocity. This is the well-known 'quasi-static' approximation for impact response. To facilitate comparisons of this type, the impact mass was decreased by a factor of 8 from pendulum to airgun, while the impact velocity was increased by a factor of 64. Thus the impact energies are the same for corresponding tests with pendulum and airgun tests. It was originally anticipated that the quasi-static analysis would be appropriate for the pendulum tests, and that the airgun experiments would display strong dynamic effects. The measured response of the airgun tests does display transient effects, however, the peak values of strain are very close to that which would be predicted by the quasi-static approximation. Calculations over a range of values of impact mass shows that rules can be established for the limits of the quasi-static approximation,[16] and that the airgun tests were on the border between quasi-static and dynamic. Further use of this will be made in the examination of the damage resulting from impact.

SCALING OF IMPACT DAMAGE

Damage was observed in the form of matrix cracks, delaminations and broken fibers. The delamination was measured by means of C-scan ultrasonic inspection. This measurement was quantified by computing the area of the image, which is thus an integration of delamination through the thickness. Nevertheless, this measured area seems to be an indication of the extent of the delamination sur-

rounding the impact site. The broken fibers were observed by thermally deplying the impacted specimens, and then inspecting under a low power microscope. The observations were quantified by specifying the length of the broken fiber region. Clearly this is not a very accurate measurement, however it is still believed to be representative of the extent of broken fibers.

Delamination

A typical set of results of the delamination measurement is shown in Fig. 3, where the delamination area is shown for the various sizes of plates, all impacted at a constant velocity. A line has been drawn in this figure indicating the delamination that would be expected if the delamination extent were controlled only by the stress distribution in the specimens. This line was constructed by drawing a line from the origin through the measured delamination extent for the smallest plate size. The logic for this is that the tests were designed so that the peak stresses and the relative stress distributions are the same for each specimen size, when impacted at a constant velocity. Thus, for example, if the delamination spread to a certain fraction of the specimen size for one of the plate sizes, it should also do so for all of the plate sizes. Thus the characteristic delamination length should vary linearly with specimen size. The consistent feature of all of the delamination results is that the measured delamination did not follow this trend, but exhibited a larger delamination area for the larger specimens.
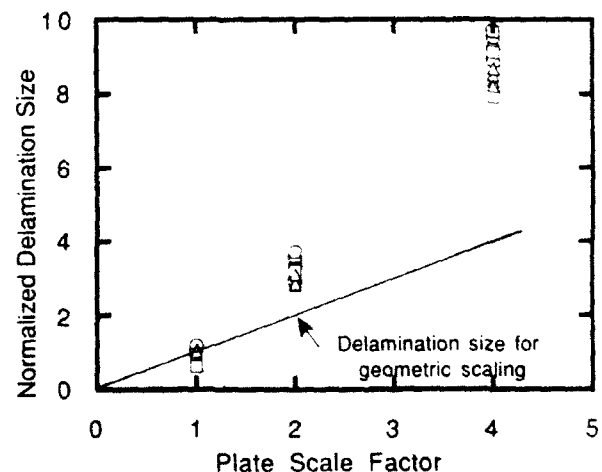
Fig. 3. Measured delamination size as a function of plate size in scaled dynamic impact tests, at impact velocity of 18.3 m/s (from Ref. 17)

The relative increase in delamination size with specimen size can be clearly seen in Fig. 3. The delamination results are consistent with a fracture mechanics interpretation of delamination, as has been discussed previously.[12] To see this, consider a generic expression for energy release rate given by

$$G = \sigma_0^2 \pi a f(a/w)/Q \qquad (1)$$

where G is the energy release rate for delamination, σ_0 is the applied stress, a is delamination size, $f(a/w)$ is a finite width geometry factor, and Q is an appropriate material stiffness constant. Noting that the applied stress is proportional to the impact velocity in the present experiments, it can be seen that the impact velocity required to produce a delamination size that is a given fraction of the specimen size should decrease with increasing specimen size. Specifically, the velocity to cause this relative delamination should decrease with the square root of specimen size. In fact, this relationship was observed, with velocities of 24·4 m/s, 18·3 m/s and 12·2 m/s giving the same relative extent of delamination in the 50 × 50, 100 × 100, and 200 × 200 mm plates, respectively.[12]

Evidence also exists that the initiation of delamination exhibits fracture mechanics scaling. To illustrate this, the delamination extent has been plotted as a function of impact velocity for the plate specimens in Fig 4 and the cylinders in Fig. 5, taken from Ref 17. Extrapolation of the delamination size to zero should give the velocity for delamination initiation. It appears that the velocity, and thus the stress, for initiation of delamination is dependent on the specimen size. As an explanation for this, it has been conjectured that the delamination initiates at microcracks,[18] and in the present case the ply group thickness, and thus the size of the microcrack, varies directly with the size of the specimen. Thus an energy release mechanism that initiates at microcracks may explain the size effect. Further discussion of this explanation for the size effect is given in Ref. 17.

Fiber breaks

As mentioned above, the plate specimens were thermally deplied and inspected under a low power microscope, and the length of the broken fiber regions noted. In the present tests a linear analysis indicates that the applied stress or strain levels are independent of specimen size, and only depend on the impactor velocity. Thus if the fiber
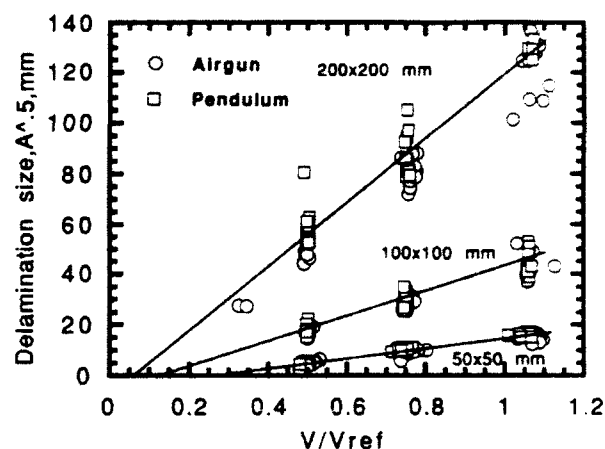
Fig. 4. Measured delamination size as a function of impact velocity in impact tests of plates. $V_{ref} = 24\cdot4$ m/s for airgun, 3·05 m/s for pendulum impact (from Ref. 17).
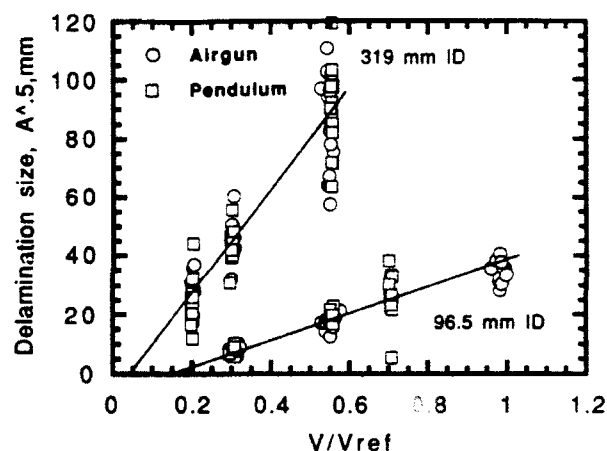
Fig. 5. Measured delamination size as a function of impact velocity in impact tests of cylinders. $V_{ref} = 61\cdot0$ m/s for airgun, 7·62 m/s for pendulum impact (from Ref. 17).

breaks were controlled by stress or strain levels, the length of the broken fiber region relative to the size of the specimen should depend only on input velocity and not on specimen size. A plot of the measured length of broken fibers is shown in Fig. 6 as a function of impact velocity for the pendulum tests. Extrapolating these values to zero length for the broken fiber region gives the critical velocity for initiation of the broken fiber regions. It can be seen that essentially the same critical velocity is estimated for all the plate sizes. This strongly suggests that the pendulum failure mechanism does not depend on the specimen size.

A similar plot is shown in Fig. 7, only now the broken fiber region length has been divided by the scale factor for the specimen. Consistent with the
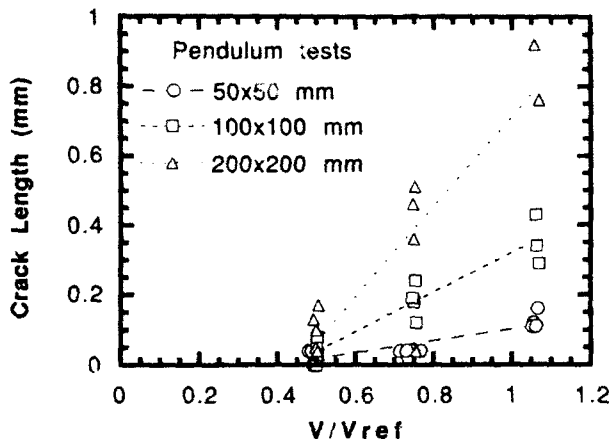
Fig. 6. Length of broken fiber region in 50, 100 and 200 mm plates after pendulum impact ($V_{ref} = 3.05$ m/s).
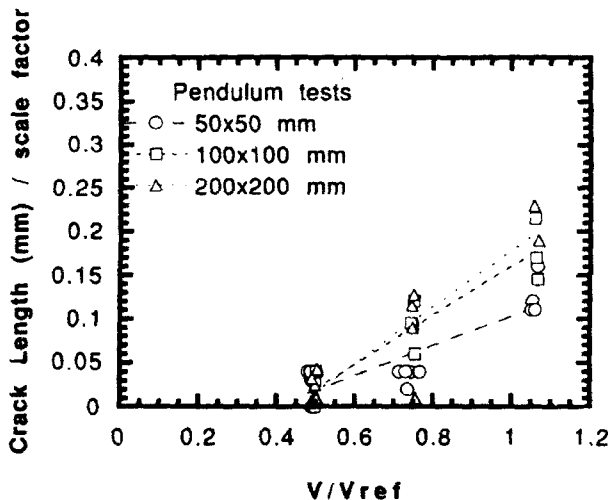
Fig. 7. Length of broken fiber region in 50, 100 and 200 mm plates after pendulum impact, normalized by scale factor ($V_{ref} = 3.05$ m/s).

previous figure, the velocity for the initiation of broken fibers is the same over the plate sizes. However, although the trends are masked somewhat by the data scatter, it is possible that the larger specimens seem to have developed larger relative broken fiber regions. Although conjectural, a possible factor in this may be the greater non-linearity in the larger specimens. This could arise because of the greater relative delamination in the larger specimens, as discussed previously. In any case, this effect is not large. Thus at least over the range of geometric scale factor considered in the experiments, the extent of the broken fiber regions appears to depend on stress or strain based criteria.

DISCUSSION

The major point of the present work is to examine the effects of geometric scale on damage and failure in impact of fiber composite structures. While scaling of the linear response appears to be reasonably well understood, scaling of failure mechanisms and damage is much more complicated. The experimental results appear to show that either the specific failure mechanisms involved must be well understood, or else a test program must be carried out in which size is considered as an explicit variable, if extrapolation to full scale structures is to be performed with any confidence.

In particular, the two forms of damage considered at present, that of delamination and fiber breakage, appears to have different trends with changes in size. Delamination exhibits a dependence on absolute size as would be expected from fracture mechanics considerations, while fiber breakage does not appear to exhibit this trend.

It is not surprising that delamination extent exhibits characteristics typical of fracture mechanics. It has long been considered that delamination propagation is governed by energy release rates and is an appropriate field for fracture mechanics methodology. The present results are thus consistent with this viewpoint, and do point out the implications for scaling from model to prototype.

The scaling behavior associated with fiber breakage is more controversial. There is considerable evidence that fiber breakage can be predicted on the basis of fiber direction stress or strain. For example, the author has been involved with experimental measurements of the ultimate failure of a number of carbon/epoxy laminates under biaxial stress loading, and it has been observed in all of these tests that the maximum fiber direction strain in a critical ply provides excellent correlation of the data.[19,20]

However when changes in stressed volume are considered, it is not clear just what theory to use. Weibull theory[21] is sometimes employed, in which the stressed volume of material is explicitly considered. However it should be noted that it is possible to confuse testing variables with size effects, and perhaps arrive at conclusions about scale effects that are not reliable in providing extrapolations. As an extreme case, consider the performance of the large size carbon/epoxy rocket motor cases that have been built. It was reported in Ref. 22 that the industry experience

seems to be that the delivered allowable stress or strain differs from that in test coupons by at most of the order of 20%, although the stressed volume differs by approximately a factor of a million. This evidence suggests that Weibull theory must be used carefully when applied to fiber composites. On the other hand, there seems to be ample evidence that the gradient of stress influences failure values, which has been sometimes interpreted as a Weibull effect.

The present data appear to show that the size of the specimen does not have a strong effect on the fiber failure values of stress or strain in impacted specimens, at least over the range of sizes included in the experiments. The evidence shown in Fig. 6 seems to show this quite clearly. However the trend to larger relative broken fiber regions with larger specimen size shown in Fig. 7 is not as well defined. As mentioned above, this trend may in fact depend on the greater degree of nonlinearity in the response in the larger specimens, due to the greater relative degree of delamination. Thus it is possible that the applied strains in the larger specimens are underpredicted by linear analysis to a greater degree than in the smaller specimens. This may explain the apparent tendency for larger broken fiber regions in the larger specimens, but not in the initiation of the broken fibers.

A major conclusion to be drawn from the above is that it is necessary to have specific knowledge of the failure mechanisms involved, as the scaling behaviors vary with the type of damage.

SUMMARY AND CONCLUSIONS

Impact tests have been carried out on five sizes of plates and two sizes of cylinders, using both pendulum and airgun tests. The goal of the program was to establish procedures to scaling of responses and damage formation with size. Scaling rules were developed by examination of the governing differential equations for dynamic impact. It was observed in the experimental results that the measured structural response agreed well with the predicted scaling behavior over the range of sizes of plates and cylinders. The impact damage exihibits complex scaling behavior. Delamination was seen to exhibit a dependence on absolute specimens size, as would be expected based on fracture mechanics criteria. Fiber breakage does not show this effect, and

appears to depend only on the applied stresses or strains, independent of specimen size.

REFERENCES

1. Goodier, J. N., Dimensional analysis. In *Handbook of Experimental Stress Analysis*, ed. M. Hetenyi. John Wiley, New York, 1950, pp. 1035–45.
2. Starnes, J. H., Rhodes, M. D. & Williams, J. G., Effect of impact damage and holes on the compressive strength of a graphite/epoxy laminate. *Nondestructive Evaluation and Flaw Criticality for Composite Materials*, ASTM STP 696, 1979, pp. 145–71.
3. Labor, J. D., Impact damage effects on the strength of advanced composites. *Nondestructive Evaluation and Flaw Criticality for Composite Materials*, ASTM STP 696, 1979, pp. 172–84.
4. Williams, J. G. & Rhodes, M. D., Effect of resin on impact damage tolerance of graphite/epoxy laminates. *Composite Materials: Testing and Design (Sixth Conference)*, ASTM STP 787, 1982, pp. 450–80.
5. Caprino, G., Residual strength prediction of impacted CFRP laminates. *J. Comp. Mater.*, **18** (1984) 508–18.
6. Sun, C. T. & Chen, J. K., On the impact of initially stressed composite laminates. *J. Comp. Mater.*, **19** (1985) 490–504.
7. Tan, T. M. & Sun, C. T., Use of statical indentation law in the impact analysis of laminated composite plates. *J. Composite Mater.*, **52** (1985) 6–12.
8. Boll, D. J., Bascom, W. D., Weidner, J. C. & Murri, J. C., A microscopy study of impact damage of epoxy-matrix carbon-fiber composites. *J. Mater. Sci.*, **21** (1986) 2667–77.
9. Morton, J., Scaling of impact-loaded carbon-fiber composites. *AIAA J.*, **26** (1988) 989–94.
10. Jackson, K. E., Scaling effects in the static large deflection response of graphite–epoxy beam columns. *Proc. 3rd Tech. Conf. on Composite Materials*, Seattle, Washington, 1988, pp. 655–66.
11. Qian, Y. & Swanson, S. R., Experimental measurement of impact response in carbon/epoxy plates. *AIAA J.*, **28** (1990) 1069–74.
12. Qian, Y., Swanson, S. R., Nuismer, R. J. & Bucinell, R. B., An experimental study of scaling rules for impact damage in fiber composites. *J. Comp. Mater.*, **24** (1990) 559–70.
13. Swanson, S. R., Smith, N. L. & Qian, Y., Analytical and experimental strain response in impact of composite cylinders. *Comp. Struct.*, **18** (1991) 95–108.
14. Qian, Y. & Swanson, S. R., A comparison of solution techniques for impact response of composite plates. *Comp. Struct.*, **14** (1990) 177–92.
15. Christoforou, A. P. & Swanson, S. R., Analysis of simply-supported orthotropic cylindrical shells subject to lateral impact loads. *J. Appl. Mech.*, **57** (1990) 376–82.

16. Swanson, S. R., Limits of quasi-static solutions in impact of composite structures. *Compos. Engng.*, **2** 1992 261–7.

17. Swanson, S. R., On impact damage in fiber composite structures. In *Damage Mechanics and Localization.* *AMD Vol. 142, MD Vol. 34. Proc. ASME WAM.* November, 1992, pp. 135–44.

18. Murri, G. B. & Guynn, E. G., Analysis of delamination growth from matrix cracks in laminates subjected to bending loads. *Composite Materials: Testing and Design (Eighth Conference).* ASTM STP 972, 1988, pp. 322–39.

19. Colvin, G. E. & Swanson, S. R., Characterization of the failure properties of IM7/8551-7 carbon-epoxy under multiaxial stress. *ASTME J. Engng Mater. Technol.*, **112** 1990 61–7.

20. Swanson, S. R. & Qian, Y., Multiaxial characterization of T800/3900-2 carbon-epoxy. *Comp. Sci. Technol.*, **43** 1992 197–203.

21. Felbeck, D. K. & Atkins, A. G., *Strength and Fracture of Engineering Solids.* Prentice-Hall, Englewood Cliffs, NJ, 1984.

22. Swanson, S. R., Strength design criteria for carbon-epoxy pressure vessels. *J. Spacecr. Rockets.* **27** 1990 522–6.

Delamination and matrix cracking of cross-ply laminates due to a spherical indenter

Sheng Liu

Department of Mechanical and Aerospace Engineering, Florida Institute of Technology, Melbourne, FL 32901, USA

An investigation was performed to study delamination growth induced by matrix cracks in cross-ply composites resulting from a spherical indenter. The major focus of the study was to understand fundamentally the damage mechanics in terms of matrix cracking and delamination growth, and interaction between them. A nonlinear three-dimensional finite element model based on an updated Lagrange formulation was developed during the investigation. An augmented Lagrangian method was utilized to model the delamination interface condition. A general contact node search algorithm was proposed which can handle complex contact conditions, such as arbitrary slippage and discontinuous curvature. The indentation resulting from the spherical rigid indenter was also modeled. Fracture mechanics was applied to determine the delamination propagation in three dimensions. The strain energy release rates were calculated by a crack-closure technique. The model was verified analytically and experimentally.

1 INTRODUCTION

It is well known that fiber-reinforced composites are vulnerable to transverse concentrated loads such as low-velocity impact, which can result in extensive delaminations and multiple matrix cracking.[1-11] Numerous experimental and analytical investigations have been performed to study the damage resulting from transverse loads. The analytical work previously developed has emphasized estimating the overall delamination sizes.[2,4,6,8,9,10,12] None of these models considered the detailed fracturing process during the formation of the damage.

Several investigators have indicated, based on their experiments, that for some ply orientations, surface matrix cracking could be produced without generating delaminations by carefully adjusting the impact velocity or the amount of the applied load. However, whenever there was a delamination, there were matrix cracks accompanied with the delamination. An energy threshold also exists below which no damage could be generated. Experiments have demonstrated that similar results obtained from low-velocity impact tests could be produced by quasi-static transverse loads.[1,3,5,7]

Jones *et al.*[11] and Josh and Sun[5] have suggested that matrix cracking is the initial impact damage mode. Basically, the initial matrix cracks have been classified by several investigators[5,6] into two types: the internal shear crack and surface bending crack. However, limited work has been performed in studying the interaction between matrix cracking and delamination.[13-15] The fracture modes controlling delamination growth of laminated composites subjected to transverse concentrated loads have not yet been adequately identified. Recently the author's 2-D study[16-19] showed that the initial matrix cracking affected significantly the growth of delamination. Delamination growth could be either stable or unstable depending upon the location of the initial matrix cracks. In 3-D, Lu and Liu[20] modeled an embedded circular delamination by a thin soft isotropic layer with a linear finite element method and showed that Mode I and Mode III fractures predominantly control the growth of the embedded delamination due to a point load. No matrix cracking was considered in the analysis.

Accordingly, the objective of this investigation was to study the damage mechanics of laminated composites subjected to transverse concentrated loading and to fundamentally understand the interaction between matrix cracking and delamination growth. To simplify the problem, only cross-ply laminated composite panels were studied, and the load was applied quasi-statically.

This paper will first present the analytical modeling. Comparison with the generated experimental data and numerical simulations will also be presented briefly. A detailed description of the analysis can be found in Ref. 19.

2 STATEMENT OF PROBLEM

Consider a cross-ply laminated composite plate subjected to a quasi-static transverse concentrated loading as shown in Fig. 1. The rectangular plates could be simply supported or clamped on any one of the edges and subjected to a transverse quasi-static concentrated load by a spherical indenter. The plates were assumed to contain a pre-existing small delamination located at the central loading area on the second 90/0 interface directly beneath the indenter. Two types of matrix cracking in conjunction with the delamination were considered in the study: a bending crack and a pair of shear cracks. Accordingly, for a given loading and boundary condition, four types of internal damage modes were studied: (1) delamination with no matrix cracks; (2) delamination induced by a bending crack; (3) delamination induced by shear cracks; and (4) delamination induced by both a bending crack and shear cracks, as shown in Fig. 2. Limited by the space, only surface crack is considered in this paper. A typical damage pattern of the laminate from an X-radiograph in shown in Fig. 3.

In this investigation, it was desired to determine:

(1) the effect of the initial matrix cracking on the propagation of the delamination in the plate,
(2) the delamination growth in the laminate at a given load,
(3) the fracture modes contributing to the delamination growth, and
(4) the contact information associated with the delamination growth.

Accordingly, the laminate containing a delamination with and without a pre-introduced matrix

Fig. 2. Four types of damage modes considered in this analysis: (1) delamination with no matrix cracks; (2) delamination induced by a bending crack; (3) delamination induced by shear cracks; and (4) delamination induced by both a bending crack and shear cracks.

Fig. 1. Description of the problem. A laminated composite panel subjected to a transverse load applied by a spherically-nosed indenter.

Fig. 3. An X-radiograph of a graphite/epoxy $[0_n/90_2]$ resulting from a quasi-static transverse loading.

crack in the 0° ply group was analyzed as shown in Fig. 4. A three-dimensional finite element method was developed for analyzing the problem. A brief description of the analysis will be given in the next section, however, details of the analysis can be found in Ref. 19.

3 METHOD OF APPROACH

As the local deformations of the laminate could be substantial due to the concentrated load, finite deformation theory was adopted in the analysis. The total potential energy of a laminate without damage under the given load can be described as

$$\Pi = \sum_{m=1}^{n_{pb}} \int_{o\Omega^m} W^m(E_{ij}^m)^o d\Omega - \int_{oS} {}^o\bar{T}_i \cdot u_i^o ds \qquad (1)$$

where n_{pb} is the total number of layers, $o\Omega^m$ is the cross-sectional area of the mth layer in the reference configuration, W is the strain energy function, u_i is the displacement vector, and ^oS is the boundary in the reference configuration where the tractions $^o\bar{T}_i$ are applied.

The components of the second Piola–Kirchhoff stress in the mth layer can be expressed by the constitutive relation as

$$S_{ij}^m = C_{ijkl}^m E_{kl}^m \qquad (2)$$

where E_{kl}^m are the components of Green's strain tensor. C_{ijkl}^m are the orthotropic material moduli for the mth layer.

Based on the virtual work principle, the following equation can be obtained from eqn (1) for an uncracked laminate:

$$\delta\Pi = \sum_{m=1}^{n_{pb}} \int_{o\Omega^m} S_{ij}^m \delta E_{ij}^{m\,o} d\Omega - \int_{oS} {}^o\bar{T}_i \cdot \delta u_i^o ds = 0 \qquad (3)$$

The above nonlinear equation is valid for any uncracked laminated composite undergoing finite deformations in three dimensions. However, for cracked laminates, eqn (3) cannot be applied directly because of the presence of crack interfaces generated inside the materials. The contact condition of the interfacial contact during loading must be included in the analysis.

Two type of contact are involved: the rigid-elastic contact between the indenter and the plate, and the elastic-elastic contact between the cracked/delaminated interfaces, as shown in Fig. 5. The local indentation resulting from a spherical indenter is very complicated and three-dimensional and could significantly affect the delamination growth and its interface deformation, especially when the delamination is small.

In order to prevent the contact surfaces from overlapping, an impenetrability condition must be specified and satisfied at all times along the contact interfaces. This condition requires that the shortest distance (defined as a gap g) between two contact surfaces must be greater than or equal to zero. Mathematically, the impenetrability constraint can be stated as $g \geq 0$. Upon contact, the contact force must also be less than or equal to zero $(\lambda_N \leq 0)$. Accordingly, the contact constraints for normal contact can be specified as

$$\left. \begin{array}{r} \lambda_N \leq 0 \\ g(u_i) \geq 0 \\ \lambda_N/g(u_i) = 0 \end{array} \right\} \qquad (4)$$

Fig. 4. The coordinate system used in the finite element analysis for a laminate containing a delamination and a bending crack.
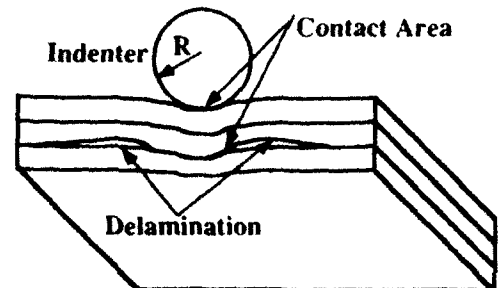
Fig. 5. Contact problem associated with a delaminated laminate subjected to an indenter.

This is the well-known Kuhn–Tucker condition for normal contact. The three equations in eqn (4) reflect, respectively, the compressive normal traction constraint, the impenetrability constraint, and the requirement that the pressure is nonzero only when $g = 0$. Accordingly, eqn (4) must be considered together with eqn (3) in order to analyze composites containing delaminations.

Several methods exist to implement the contact constraints. The most popular choices are the Lagrange multiplier method and the penalty method. Both methods have advantages and disadvantages (see discussions in Ref. 19). The Lagrange multiplier method was adopted previously by the author for the study of damage induced by a cylindrical indenter for analyzing the interaction between matrix cracking and delamination.[18] In this study, an augmented Lagrangian method was adopted. It has been shown to provide important advantages over the more traditional Lagrange multiplier and penalty methods. Detailed mathematical discussions can be found in Ref. 21. The augmented Lagrangian techniques have been known to provide almost exact enforcement of constraints while using finite penalty parameters, avoiding the ill-conditioning.

In the method of augmented Lagrangians, the Lagrange multiplier λ_N is initially chosen to be an arbitrary constant. If this constant is not the correct Lagrange multiplier, the contact constraint is not satisfied and minimization of the total potential energy of eqn (1) does not lead to the equation of equilibrium. Therefore, from a penalty function viewpoint, the total potential energy represented by eqn (1) needs to be further penalized by the following modified functional:

$$\bar{\Pi} = \Pi + \int_{\Gamma} \lambda_N^k g \, d\Gamma + \int_{\Gamma} \frac{1}{2} \epsilon_N g^2 \, d\Gamma \qquad (5)$$

where $\lambda_N^k \leq 0$ denotes the fixed estimate of the correct λ_N. The superscript k indicates that the search for the correct λ_N is an iterative process. The updated formula is

$$\lambda_N^{k+1} = (\lambda_N^k + \epsilon_N g) \qquad (6)$$

Therefore, the variational equation corresponding to eqn (5) can be derived as

$$\delta \Pi + \int_{\Gamma} (\lambda_N^k + \epsilon_N g) \, \delta g \, d\Gamma = 0 \qquad (7)$$

It is noted that the term $(\lambda_N^k + \epsilon_N g)$ plays the role of the Lagrange multiplier λ_N. If λ_N is the
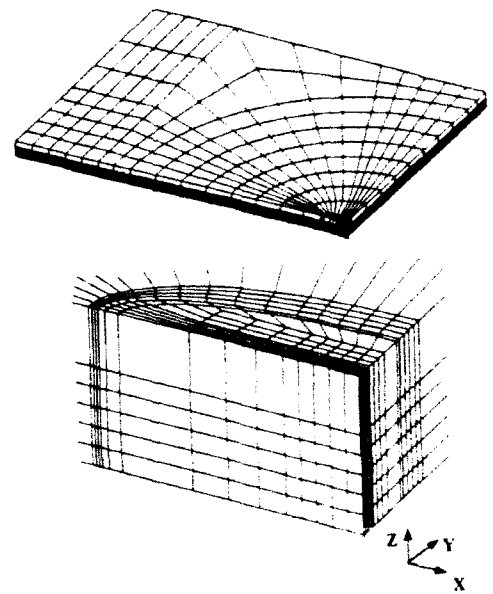
Fig. 6. Description of a typical finite element mesh used in the analysis.

correct multiplier, then $g = 0$ on Γ. Thus, in the case where the multipliers are correct, eqn (7) achieves exactly the same form as the standard Lagrange multiplier method, making it an exact penalization.

It is important to notice that eqn (7) is a non-linear equation due to the contact conditions and geometric nonlinearity. In general, then, it will be necessary to solve eqn (7) in an iterative manner. In practice, ϵ_N is chosen to be as large as practically possible without inducing ill-conditioning. The advantage of the current treatment over the penalty method was developed based on eqn (7), and an eight-node brick element was used. Due to symmetry, only a quarter of the laminate was analysed. A typical finite element mesh is shown in Fig. 6.

The initiation of delamination growth (onset of delamination growth) was predicted based on linear elastic fracture mechanics. The well-known virtual crack closure technique[22] served as the basis for the strain-energy release rate calculation. This procedure determines Mode I, Mode II and Mode III strain energy release rates (G_I, G_{II} and G_{III}) from the energy required to close the delamination over a small area.

Therefore, at any point on the delamination front, strain energy release rates can be calculated. Since the delamination growth can be attributed to a mixed mode fracture, the criterion for deter-

mining the initiation of the delamination growth was selected as[19]

$$\left(\frac{G_{\mathrm{I}}}{G_{\mathrm{IC}}}\right)^{\alpha} + \left(\frac{G_{\mathrm{II}}}{G_{\mathrm{IIC}}}\right)^{\beta} + \left(\frac{G_{\mathrm{III}}}{G_{\mathrm{IIIC}}}\right)^{\gamma} = E_{\mathrm{d}} \qquad (8)$$

for any point on the delamination front. Here, G_{IC}, G_{IIC} and G_{IIIC} are the critical strain energy release rates corresponding to Mode I, Mode II and Mode III fracture, respectively. It was assumed that G_{IC}, G_{IIC} and G_{IIIC} did not change with delamination size. Based on the previous two-dimensional study by the authors, $\alpha = 1$, $\beta = 1$, and $\gamma = 1$ were selected for this study, because they were found to provide the best fit to the experiments in two dimensions. It was assumed that $G_{\mathrm{IIIC}} = G_{\mathrm{IIC}}$,[23] because the value of G_{IIIC} has not been reported in the literature. Accordingly, delamination would start to propagate when $E_{\mathrm{d}} \geq 1$ at any point on the delamination front.

4 RESULTS AND COMPARISON

In order to verify the model, numerical solutions were generated and compared with existing analytical and numerical solutions. Overall, the agreements were very good. Due to limited space, verification can be found in Ref. 19. In the following, numerical simulations and experimental verification are presented and discussed.

For a $[0_6/90_2]_s$ layup, a long slender peanut-like shape of a delamination on the interface near the bottom surface was observed. A matrix crack (bending crack) in the bottom $0°$ ply group was also clearly seen from the X-radiograph given in Fig. 3. The left and right halves of the delaminations always grew in a relatively equal size.

In order to evaluate the damage propagation in $[0_6/90_2]_s$ composites due to transverse concentrated loading, both types 1 and 2 damage models were utilized to perform the numerical simulations. The type 1 model considered only a delamination without a bending crack, however, type 2 model considered both the delamination and the bending crack.

The mesh, deformation, and stress data generated from the finite element analysis were stored in standard post-processing files and transformed to the commercial code IDEAS[24] (licensed by Structural Dynamics Research Corporation). Figure 7 shows a close-up view of a deformed

cross-section $(X-Z, Y=0)$ of a $[0_6/90_2]_s$ composite at a load of 172 lbf. The local indentation due to the rigid indenter can be clearly observed in the figure. A relatively large sliding between the upper and lower surfaces of the delamination were also clearly shown in the figure.

A close-up side view of a deformed cross-section $(Y-Z, X=0)$ of a $[0_6/90_2]_s$ is shown in Fig. 8. The bending crack was open due to the applied load, which closely resembles the cylindrical bending of a $[90_m/0_n]_s$ beam containing a surface crack. The local indentation due to the rigid indenter and relatively large sliding between the upper lower surfaces of the delamination were also shown in the figure.

Figure 9 shows the comparison of the calculated total strain energy release rate G_{I} based on type 1 and 2 models for a laminate containing a small circular delamination with and without the surface matrix crack (bending crack). For the laminate containing the matrix crack, the value of
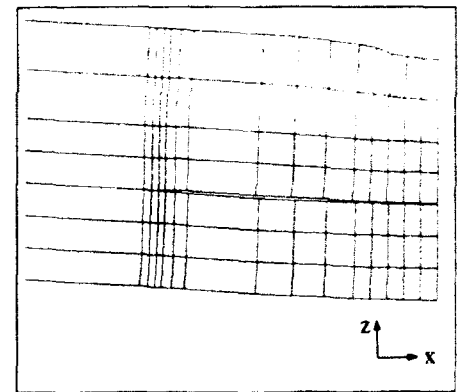
Fig. 7. Deformation of a cross-section $(X-Z, Y=0)$ of a $[0_6/90_2]_s$ composite with a surface matrix crack.
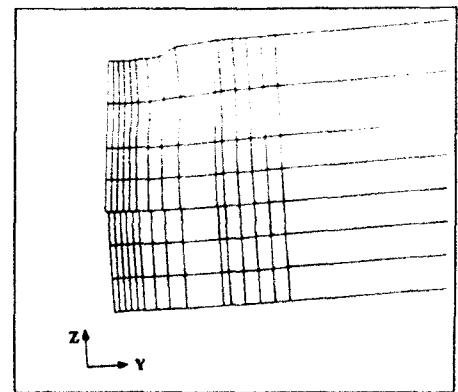
Fig. 8. Deformation of a cross-section $(Y-Z, X=0)$ of a $[0_6/90_2]_s$ composite with a surface matrix crack.

G_T along the delamination front near the location of the matrix crack increased significantly and reached a peak at the intersection between the matrix crack and delamination (at $\phi = 0°$). The value of G_T, however, decreased rapidly as the delamination front, where the value of G_T was calculated, moved away from the location of the matrix crack (ϕ approaches 90°).

A completely different distribution of the total strain energy release rate was obtained for the laminate containing no bending crack. Overall, the values of G_T obtained from the type 1 model were much smaller than those calculated by the type 2 model. Apparently, the laminate with the matrix crack could initiate the delamination growth at a much earlier loading stage than the one without. Once the delamination propagated, it would grow along the direction of matrix cracking.

Figure 10 shows the sequence of delamination growth in the laminate without the matrix crack predicted by the type 1 model based on the crack growth criterion (eqn (8)). The number shown in the bracket at the upper right corner of each sub-
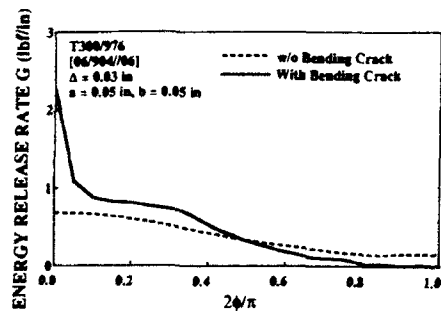
Fig. 9. Comparison of the calculated total strain energy release along a delamination front in a $[0_6/90_2]_s$ composite with or without a surface matrix crack.
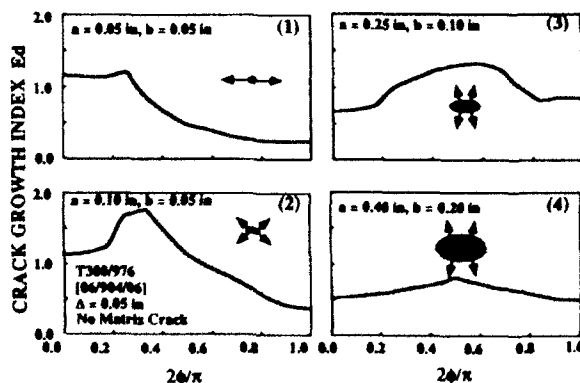
Fig. 10. The predicted delamination growth sequence in a $[0_6/90_2]_s$ composite without a surface matrix crack.

figure indicates the sequence. The sub-figures were generated by evaluating the strain energy release rate ratio E_d for various sizes of delaminations. First, the values of E_d were calculated for a small circular implanted delamination. If delamination growth was predicted ($E_d \geq 1$), then the delamination size was extended slightly along its major (X-direction, $\phi = 0°$) or minor (Y-direction, $\phi = 90°$) axis according to the predicted direction of delamination growth. In this analysis, the delamination was only allowed to grow into either a circular or an elliptical shape. Again, numerical calculations were re-performed to evaluate the strain energy release rates for the laminate with the new delamination. This procedure was repeated until the calculated strain energy release rate ratio was smaller than unity everywhere along the delamination front. The size of the final delamination was then considered to be the delamination shape corresponding to the given loading condition.

At 0·05 in of indenter displacement, the delamination tended to grow into an elliptical shape with major and minor axis ratio about 2 after a series of stable and unstable growth. However, the delamination shape predicted by the type 1 model was significantly different from the shape observed in the experiment. First, the well-known peanut-like delamination could not be predicted. Second, the predicted shape was fairly large instead of slender and was very different from the observed delamination shape with major and minor axis ratio about 5. And third, the applied load (or displacement) which initiated the delamination growth was much higher than the experimental one. It was noted that something was missing in the type 1 model for simulating the delamination growth due to a spherical indenter loading. It seemed to show that the type 1 model could not predict accurately the damage growth in this laminate due to a spherical indenter.

However, a completely different growth pattern was predicted by the type 2 model. First, at the same load, delamination growth was predicted to occur much earlier for the laminate containing the same small delamination given in Fig. 11(1). Figure 11 shows the sequence of the delamination growth in the laminate with the matrix crack predicted by the type 2 model.

At a fixed indenter displacement, Fig. 11 gives a final shape after a series of growth. After a substantial growth of the delamination along its major axis, Fig. 11(4) shows that the strain energy release rates started to increase near $\phi = 75°$ away
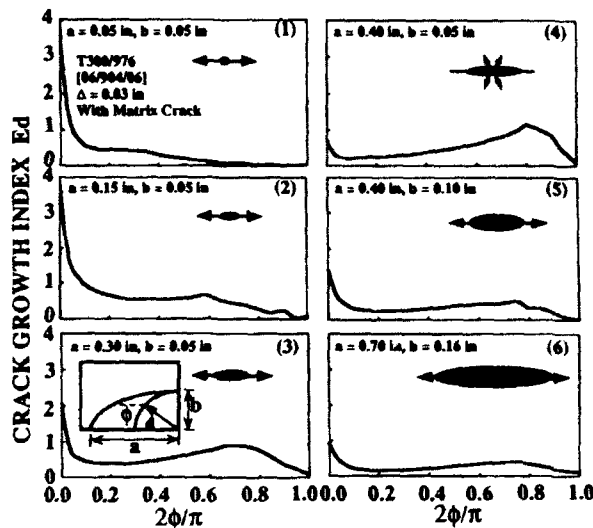
Fig. 11. The predicted delamination growth sequence in a composite containing a surface matrix crack.

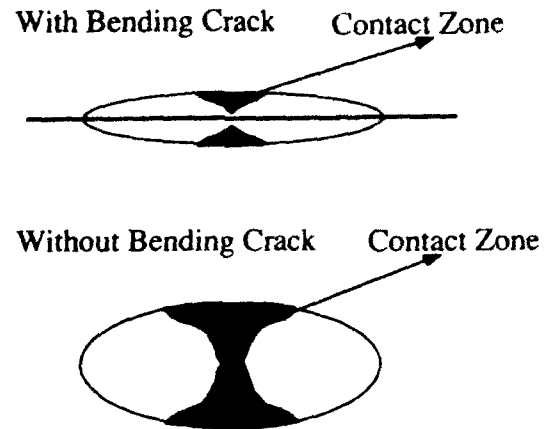With Bending Crack   Contact Zone

Without Bending Crack   Contact Zone

Fig. 12. Typical contact zone of a delamination in a $[0_n/90_2]_s$ composite containing an internal crack and/or a surface matrix crack.

from the matrix crack, initiating the expansion of the delamination along the minor axis. However, a slight expansion of the delamination along its minor axis as shown in Fig. 11(5) subsequently caused a significant increase of the strain energy release rates along the major axis. Hence, the delamination started to grow along the major axis again. Apparently, the growth of the delamination was predominantly controlled by the delamination front near the neighborhood where the matrix crack intersected with the delamination. It is worth noting that at $\phi = 90°$, strain energy release rates remained at a minimum regardless of the shape of the delamination. This observation implies that no delamination would grow in this area, leading the delamination to a peanut shape which was frequently observed from the experiments for this type of ply orientation, such as the one given in Fig. 3. This is also indicated from the actual contact area. Even the model allowed only the elliptical delamination shape, the actual contact area can be seen in Fig. 12, which coincided with the shape shown in Fig. 3. It is observed from Fig. 12 that the contact zones are significantly different with and without modeling the surface crack. Numerical experiments also showed that incorrect energy release rates would be calculated if the contact algorithm was not implemented.

Figure 13 shows the comparisons between the estimated delamination sizes in the x and y directions and the sizes measured from the experiments. The correlation between the experiments and the predictions was very good. Figure 14
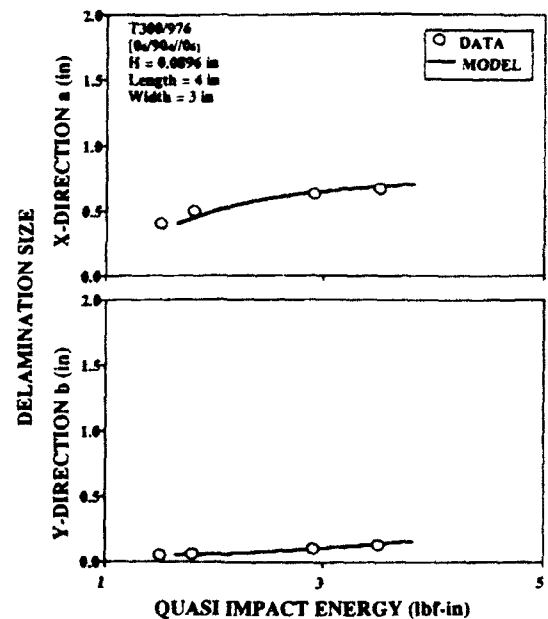
Fig. 13. Comparison of delamination sizes predicted and measured in a $[0_6/90_2]_s$ composite with respect to quasi-impact energy.

shows the calculated strain energy release rates of Modes I, II and III for the laminate containing a small and a large delamination with a surface matrix crack. Clearly, for the laminate containing the initial surface matrix crack, G_I (Mode I fracture) dominated the total strain energy release rate along the delamination front near the neighborhood where the surface matrix crack intersected with the delamination ($\phi = 0°$). This observation is also valid for a moderately large delamination, as shown in the same figure.

However, when the surface crack was ignored in the analysis, Modes II and III fractures dominated the total strain energy release rate along the delamination front for the laminate, as shown in Fig. 15. Although the contribution of each mode to the growth of the delamination strongly depended upon the current shape of the delamination, the presence of the matrix crack clearly played a very important role in the delamination growth. Therefore, it is very important that the initial matrix crack be considered in the analysis for understanding the damage mechanics and mechanism of laminated composites due to transverse loading.

5 CONCLUDING REMARKS

A finite element analysis was developed for analyzing cross-ply laminated composite plates subjected to transverse concentrated loading resulting from a spherical indenter. Based on the analysis, the following remarks can be made for the laminates studied:

(1) The initial matrix cracking affects significantly the growth of delamination resulting from transverse loading.
(2) The surface matrix crack induces the delamination to grow into a slender peanut shape.
(3) Mode I fracture contributes significantly to the growth of the delamination induced by a surface crack.
(4) Mixed mode fracture dominates the internal crack induced small delamination growth. Mode II governs the internal crack induced large delamination growth.

Additionally, it is noted that the proposed finite element analysis can also be extended to study other ply orientations and other loading conditions, such as delamination buckling, which are going to be reported in future publications.

Fig. 14. Comparison of the calculated strain energy release rates of Modes I, II, and III along a small and a large delamination front in a $[0_m/90_n]$ composite.
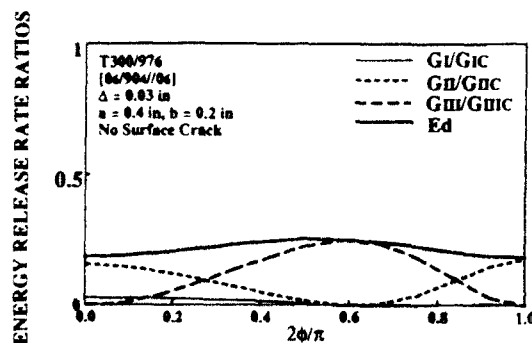
Fig. 15. The calculated strain energy release rates of Modes I, II, and III along a delamination front in a $[0_m/90_n]$ composite without a surface matrix crack.

REFERENCES

1. Finn, S. R. & Springer, G. S., *Composite Plates Impact Damage: An Atlas*. Technomic Publishing Co., Lancaster, PA, 1991.
2. Finn, S. R., Delaminations in composite plates under transverse static or impact loads. PhD thesis, Department of Aeronautics and Astronautics, Stanford University, CA, 1991.
3. Sjöblom, P. O., Hartness, J. T. & Cordell, T. M. On low-velocity impact testing of composite materials. *Journal of Composite Materials*, 22 (1988) 30–52.
4. Wu, H. T. & Springer, G. S. Measurements of matrix cracking and delamination caused by impact on com-

posite plates. *Journal of Composite Materials*, **22** (1988) 518–32.

5. Joshi, S. P. & Sun, C. T. Impact-induced fracture in quasi-isotropic laminate. *Journal of Composite Technology and Research*, **19** (1986) 40–6.

6. Choi, H. Y., Downs, R. J. & Chang, F. K., A new approach toward understanding damage mechanisms and mechanics of laminated composites due to low-velocity impact, Part I — Experiments. *Journal of Composite Materials*, **25** (8)(1991) 992–1011.

7. Poe, C. C. Jr, Simulated impact damage in a thick graphite/epoxy laminate using spherical indenters. NASA TM-100539, January, 1988.

8. Wu, H. T. & Springer, G. S., Impact induced stresses, strains and delaminations in composite plates. *Journal of Composite Materials*, **22** (1988) 533–60.

9. Liu, D. & Malvern, L. E., Matrix cracking in impacted glass/epoxy plates. *Journal of Computers and Structures*, **21** (1987) 594–609.

10. Gu, Z. L. & Sun, C. T., Prediction of impact damage region in SMC composites. *Composite Structures*, **7** (1987) 179–90.

11. Jones, S., Paul, J., Tay, T. E. & Williams, J. F., Assessment of the effect of impact damage in composites: some problems and answers. *Composite Structures*, **10** (1988) 51–73.

12. Choi, H. T., Wu, H. Y. T. & Chang, F. K. A new approach toward understanding damage mechanisms and mechanics of laminated composites due to low-velocity impact, Part II — Analysis. *Journal of Composite Materials*, **25** (8)(1991) 1012–38.

13. Sun, C. T. & Manoharan, M. G., Growth of delamination cracks due to bending in a [90₃/0₃/90₃] laminate. *Composite Science and Technology*, **34** (1989) 365–77.

14. Martin, R. H. & Jackson, W. C. Damage prediction in cross-plied curved composite laminates. NASA Technical Memorandum 104089, July, 1991.

15. Salpekar, S. A., Analysis of delamination in cross ply laminates initiating from impact induced matrix cracking. NASA Contract Report 187594, November, 1991.

16. Liu, S., Kutlu, Z. & Chang, F. K., Matrix cracking and delamination in laminated polymeric composites resulting from transversely concentrated loadings. *Proceedings of the 1st International Conference on Deformation and Fracture of Composites*, Manchester, UK, March 25–27, 1991, pp. 30/1–30/7.

17. Liu, S., Kutlu, Z. & Chang, F. K., Matrix cracking-induced stable and unstable delamination propagation in graphite/epoxy laminated composites due to quasi-static transverse concentrated load. *Composite Materials: Fatigue and Fracture (4th Symposium)*, 1991.

18. Liu, S., Kutlu, Z. & Chang, F. K., Matrix cracking and delamination propagation in laminated composites subjected to transversely concentrated loading. *Journal of Composite Materials* (submitted) (1991).

19. Liu, S., Damage mechanics of cross-ply laminated composites resulting from transverse concentrated loading. Phd thesis, Department of Mechanical Engineering, Stanford University, CA, 1992.

20. Lu, X. & Liu, D. Strain energy release rates at delamination front. *Proceedings of the American Society of Composites*, Fourth Technical Conference, Oct., 1989, pp. 277–86.

21. Luenberger, D. G., *Linear and Nonlinear Programming*. Addison-Wesley, Reading, MA, 1984.

22. Rybicki, E. F. & Konninen, M. F., A finite element calculation of stress intensity factors by a modified crack closure integral. *Engineering Fracture Mechanics*, **9** (1977) 931–8.

23. Chai, H., Mixed-mode fracture behavior of delaminated films. *Proceedings of the American Society for Composites*, Fourth Technical Conference, Oct., 1989, pp. 815–25.

24. Lawry, M. H., *I-DEAS Student Guide*. Structural Dynamics Research Corporation, Milford, OH, 1990.

25. Tsai, S. W. & Hahn, H. T., *Introduction to Composite Materials*. Technomic Publishing, Lancaster, PA, 1975.

A parametric study of residual strength and stiffness for impact damaged composites

Victor L. Chen, Hsi-Yung T. Wu

Composites, Transport Aircraft Technology, McDonnell Douglas Aerospace, Transport Aircraft, Long Beach, CA 90846, USA

&

Hsien-Yang Yeh

Department of Mechanical Engineering, California State University, Long Beach, CA 90840, USA

A parametric study of residual strength and stiffness for low-velocity impact damaged composites was performed. Possible compression after impact failure mechanisms, which may be caused by stiffness and strength degradation inside the damage region, were discussed. In order to understand the scaling effects on impact damage residual strength, finite element analysis was performed. With stiffness degradation inside the damaged area, the stress fields of small coupon and larger stiffened panels with the same damage were calculated numerically. The stress redistributions were found to be almost identical between the coupon and panels. This indicates that the stress redistribution is a local phenomenon, and will not be affected much by the existence of the stiffeners. It is believed that the residual strength of impact damaged composite structures is related more to the damage severity than to the load redistribution. The dependency of the stress concentration factor on the anisotropic engineering elastic constants of a laminate was extended from an analytical study by Lekhnitskii (*Anisotropic Plates*, Gordon and Breach Science Publishers, New York, USA, 1968).

INTRODUCTION

Laminated composite structures are generally susceptible to damage resulting from low-velocity impact. It is of vital interest to understand this mechanism because even non-detectable impact damage has been found to drastically reduce the strength of composite laminates. However, due to the complexity of impact damage which involves the interaction between dynamic matrix crack propagation and delamination growth, the current understanding is still very limited. Further, the question of how to predict residual strengths and stiffness about impact damaged composite structures is still not answered. Based on reported experimental results, an impactor with a hemispherical nose will produce a more or less circular damaged region. This damaged zone is expected to have reduced macroscopic stiffness and strength. Because of difficulties in directly measuring the stiffness and strength loss, a finite element parametric study is in order. The stress concentration factors with various laminate engineering elastic constants $\bar{E}_1$, $\bar{E}_2$, and $\bar{G}_{12}$ are also

evaluated using an analytical formula for anisotropic plate obtained by Lekhnitskii.[1]

The determination of stress concentration factors by linear elastic solutions is a classical problem, even for anisotropic materials. However, there is a renewed interest related to the causes of scaling effects on residual strength of impact-damaged composites. Figure 1 shows that the 4- or 5-in-wide (1 in ≈ 2·54 cm) coupons retain lower strength as compared to the larger stiffened panels when they were damaged by the same impact (same energy per thickness).[2] Traditionally, many argue that more complex structures (e.g. stiffened panels) provide alternative load paths, therefore retain higher residual strength (than coupons). However, C-scan results show that even a 100 ft-lb impact seldom causes damage arger than a 1 in disc in a ¼ in thick composite wing-skin panel. The damage size is small compared to the typical stringer spacing, and therefore all stress concentration diminishes within one skin bay. In other words, the stress distribution (within the skin bay) would be nearly identical to that within a coupon if the damages

were the same (size and severity). The scaling effects shown in Fig. 1 have to be explained by other means, but not by stress–load redistribution. The cause of the scaling effects that complex structures exhibit higher residual strength (after the same impact) will be further discused in a separate paper.[3]

To investigate the stress redistribution after impact damage, a parametric finite element study has been performed. Stiffness inside a circular damaged region is reduced to simulate the low-velocity impact damage. Results of this finite element analysis indicate that the stress redistribution is a local phenomenon and numerical calculation of stress concentration agrees with those obtained from the analytical predictions studied toward the end of this paper. This analytical parametric study indicates that laminate shear modulus $\bar{G}_{12}$, compared with $\bar{E}_1$ and $\bar{E}_2$, is a dominant factor in the variation of stress concentration factor. Through the variation of fiber orientation percentage in the laminate, the stress concentration factor could be reduced, thus, the residual strength after the low-velocity impact damage could be improved.

SCALING EFFECTS ON RESIDUAL STRENGTH OF IMPACT DAMAGED COMPOSITES

What structural designers often say about scaling effects are that complex structures are less affected by local damages (as compared to coupons).[2] This is reflected in Fig. 1 as having higher residual strength after the 'same impact' (defined by same energy per thickness). Such scaling effects are extremely important to composite aircraft structural design because the design stress–strain allowables are determined accordingly. There are two explanations: (i) complex structures can provide alternative load paths (stress redistribution), and (ii) complex structures can deflect and are damaged less during the impact (damage severity). Good understanding of scaling effects will help us in extrapolating coupon and element test data to predict compression after impact (CAI) behaviors of large structures. This is an appropriate goal in view of the pay-off culminating in economics via reduced panel testing.

To clarify the causes and their relative importance to scaling effects, steps were taken to sepa-
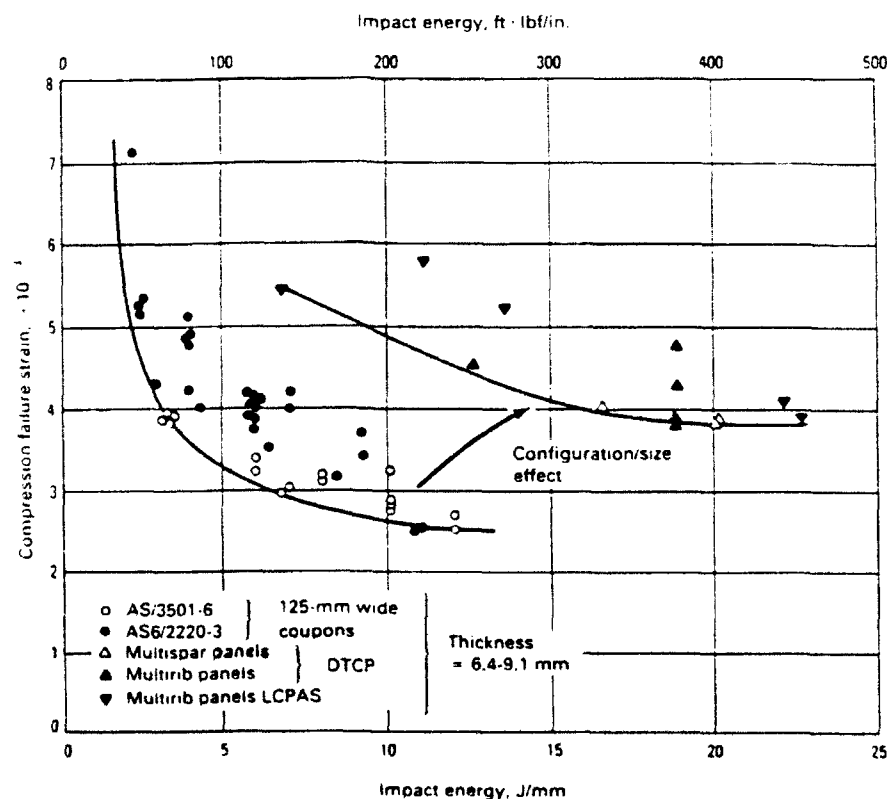
Fig. 1. Effect of test panel size/configuration on residual strength. (Adapted from Ref. 2.)

rate and better define the two explanations. Instead of using the rather ambiguous condition of the same impact level, we choose to model the 'same damage severity' (same geometry and material properties) into a 5×10 in coupon and stiffened panels with the same skin layup and thickness. The same end shortening strain is then applied to the quarter symmetric finite element models, with the damage modeled as a 1.5 in diameter disk retaining $X\%$ of the undamaged stiffness. Prior to detailed discussion on modeling and parametric studies, we shall look into the physics of this residual strength problem. If stress redistribution is the main cause of the scaling effects, one should expect major differences in stress distribution. In other words, the existence of the stringers should greatly lower the stress concentration in front of the damaged zone for the panel cases. If the stress distributions around the damages are similar for the coupon and the panels, one would be led to believe that damage severity is the main cause of the scaling effects. That is, the coupons and the panels must have damages of different severity to cause the difference in their residual strengths. Whether the 'same' impact' events (same impact energy per thickness in Fig. 1) resulted in different damages, and whether there is any other impact parameter that relates better to damage severity are not the subjects of this paper. We will only go through the damage modeling scenarios and concentrate on stiffness behaviors in the next two sections.

MODELING OF IMPACT DAMAGED COMPOSITES

A rigorous analytical residual strength prediction approach seems to have to start from detailed damage modeling. This is a difficult task, whether one does it by characterizing the observed damage or by simulating the impact event. Many researchers have compared the residual strengths of impact damaged specimens with the strengths of open-hole specimens.[4] The approach of treating the impact damaged area as a hole cut out of the laminates cannot capture the true characteristic of impact damaged composites. On the one hand, when damage growth prior to failure is insignificant, the damaged area is a weakened zone, but not necessarily as bad as a hole. On the other hand, if sub-laminate delamination/buckling is the main failure mechanism, an impact damage, usually associated with multiple delamination, can

be worse than a hole of the same size. To capture the latter, other researchers have used a sub-laminate buckling model with given delamination to relate the damaged area properties.[5,6] We made no attempt to resolve this task, nor to emphasize it in this paper. The following discussion is to point out the difficulties, and more importantly, to lead to a scenario that detailed damage modeling may not be as essential as it appears to the residual strength prediction.

Because impact damages are more critical under compressive loading, CAI cases are used for discussion. A typical CAI test used by Douglas Aircraft Company is the ST-1 described in NASA RP-1092.[7] We modeled the 5×10 in ST-1 CAI coupon with $X\%$ of the undamaged stiffness and $Y\%$ of the undamaged strength retained for the damaged area (Fig. 2). By comparing test data to the results of a parametric FEA study (varying X and Y), we expected to determine the values of X and Y for each damage case, including generalization to panel CAI. We encountered two major difficulties. (i) This seemingly simple model is quite complex, i.e. there is no restriction that X has to be the same as Y. Further, X and Y should be functions of positions rather than constants. (ii) ST-1 CAI coupon tests provide insufficient information in determining these functions, i.e. the ST-1 measurements reflect 'averaged' properties of the 5×10 in coupon, but not local properties of the damage.

The series of parametric studies did not lead us to a satisfactory means to determine X and Y for detailed damaged modeling. However, a few other findings are worthy of mentioning. First, for the entire range of stiffness variation, the stress redistribution is found to be a local phenomenon, which never goes beyond two or three times the damage size. Therefore, the overall stiffness behavior is not sensitive to the local stiffness (X). This suggests that the only experimental approach that may properly characterize the damage is to test narrow strips cut through the damaged area. Secondly, by varying X and Y independently, we found two competing failure mechanisms, and also obtained a feel for the implication of this competition. When low stiffness retention but high-strength retention was assumed, failure can initiate outside of the damaged zone due to stress concentration. When the opposite was assumed, high stiffness retained for the damaged zone causes little stress redistribution, and enough load still goes through the weak (small Y) damaged zone to initiate failure from within. Because of this

'competition' and the locality of stress redistribution, the collective behavior (e.g. calculated failure load) becomes less sensitive to X and Y individually. This suggests that detailed damage modeling (e.g. position dependent functions X and Y) may be circumvented for failure load prediction. Such an approach is consistent with the concept of continuum damage mechanics which treats the micro damage initiation and propagation as a macro-degradation process.[8] To speculate further, aside from damage growth, a single constant '$\bar{Y}$' indicating the collective strength retention, or the inverse of an equivalent stress concentration factor, may be sufficient for CAI strength description (Fig. 2). The stiffness behavior (stress distribution around the damage) is discussed further with numerical details in the next section.

CALCULATION OF STRESS REDISTRIBUTION USING FINITE ELEMENT METHOD

To investigate the stress redistribution of composites after impact damage, a paraametric finite element study has been performed. In the study, stress concentrations of a test coupon, two-stringer, and four-stringer stiffened panels with impact damage at the center are calculated. It is necessary to prove that the stress redistribution of damaged composites is a local phenomenon, and the stress redistributions between the test coupon and stringer-stiffened panels are similar.

The linear static analysis in MSC/NASTRAN version 67 was used for stress field calculations.[9] Dimensions of the test coupon, two-stringer, and four-stringer stiffened panels are shown in Fig. 3.

Standard material properties of graphite-epoxy composite[10] are used in the analysis, and they are shown in Table 1. The test coupon and the skin of stiffened panels are made of $[0/45/0/-45/90/-45/0/45/0]_{3s}$ laminate with a nominal thickness of 0·324 in. The 0° fiber orientation of the laminates is parallel to the stringer and applied load directions. The stringers of stiffened panels are made of the same material as the skin. The blade of stringers has $[0/45/0/-45/90/-45/0/45/0]_s$ layup with a height of 2 in and thickness of 0·468 in. The flange of stringers has $[0/45/0/-45/90/-45/0/45/0]_{2s}$ layup with a width of 2·94 in and thickness of 0·216 in. The flange of stringers is assumed to be bonded perfectly on the skin of panels.

The impact damage zones of test coupon and two stiffened panels are assumed to be circular with diameters equal to 1·5 in (Fig. 3), located at the center of each specimen. The stiffness inside these circular regions are reduced to simulate the low-velocity impact damage. Failure analysis will not be performed in the present study, therefore, material strength properties are not needed. Stress redistributions of coupon and panels with damage are calculated using finite element method. All stiffness (E_t, E_t, and G_{tt} of the lamina; therefore, $\bar{E}_1$, $\bar{E}_2$, and $\bar{G}_{12}$ of the laminate) retained inside the circular damage area are simultaneously varied from 0%, which is similar to a hole, to 100%, which is no damage, of the virgin material properties. Poisson's ratio (ν_{tt} of the lamina; therefore, $\bar{\nu}_{12}$ of the laminate) is assumed to remain unchanged for impact damaged composites. A same end-shortening strain

$$\frac{\Delta l}{l} = -4000 \ \mu\text{in/in}$$
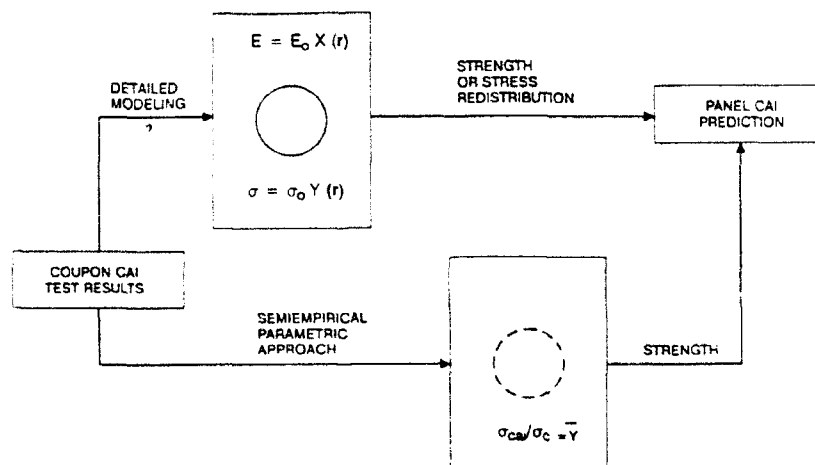
Fig. 2. Schematic of impact damage modeling.
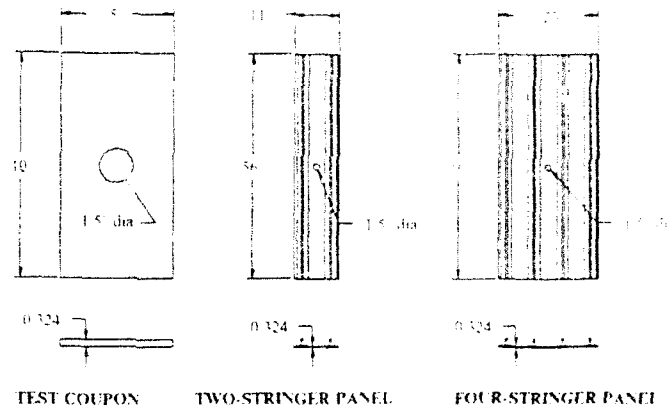
Fig. 3. Dimensions of test coupon and wing panels.

Table 1. Material properties of graphite epoxy[a]

$E_1 = 30 \times 10^6$ psi
$\nu_{12} = 0.25$
$E_2 = 0.75 \times 10^6$ psi
$G_{12} = 0.375 \times 10^6$ psi

[a]Adapted from ref. 10.

is applied to both the coupon and panels. Due to the symmetry, only one-quarter of structure is modeled. To illustrate the stress field redistributions due to impact damage, the results of minor principal stress, which is compressive, distributions of coupon and panels with 50% stiffness retained inside the circular damage area are plotted in Figs 4–6. From the calculation, the maximum stress concentrations appear at the boundary between damaged and intact areas. This finding is consistent with the conventional stress concentration study of composites with circular hole.[1]

In order to investigate the influence of impact damage severity to the stress redistribution of coupon and panels, the retained stiffness inside the circular damage zone is varied for stress field calculation. The stress concentrations of various retained stiffnesses inside the damage area are calculated and also compared with theoretical values of infinite plate with hole.[1] The results are plotted in Fig. 7 for infinite plate, coupon, and the panels. They show that the variations of the stress concentration between coupon and panels are as small as only 1%. Thus, we conclude that stress redistributions are similar for coupon and panels if they have the same magnitude of damage.

Buckling analysis is also performed for undamaged and impact damaged stiffened panels. It is found that the effects of the stiffness degradation within the impact damage area are too small to influence the first global buckling load and mode shapes of the whole stiffened panels.

STRESS CONCENTRATION FACTOR AND IMPACT DAMAGE RESIDUAL STRENGTH

From previous sections, one can conclude that the stress concentration factor (SCF) is an important indicator of the residual load-carrying capability. To recap this scenario, we recognize that the damages caused by impact are normally fiber breakage, matrix cracking, and delamination. These damages will certainly reduce local stiffness and strength of laminates. The stiffness reduction within the damage area will cause stress concentration near the interface of the intact and damaged areas under loading. This stress redistribution is critical for predicting the impact damage residual strength, while the SCF is the simplest indicator of the stress concentration. For the worst stiffness reduction (a hole), SCRF can be obtained analytically for infinite flat plates.[1] To economize engineering and computer time, a parametric study of SCF around circular holes is conducted for varying orthotropic plate properties. The results will provide information on relative severity of stress concentration for various laminates. Thus, within proper boundaries of laminate selection, designers could arrange the fiber orientation percentage in the laminate to minimize the SCF to improve the residual strength after impact.
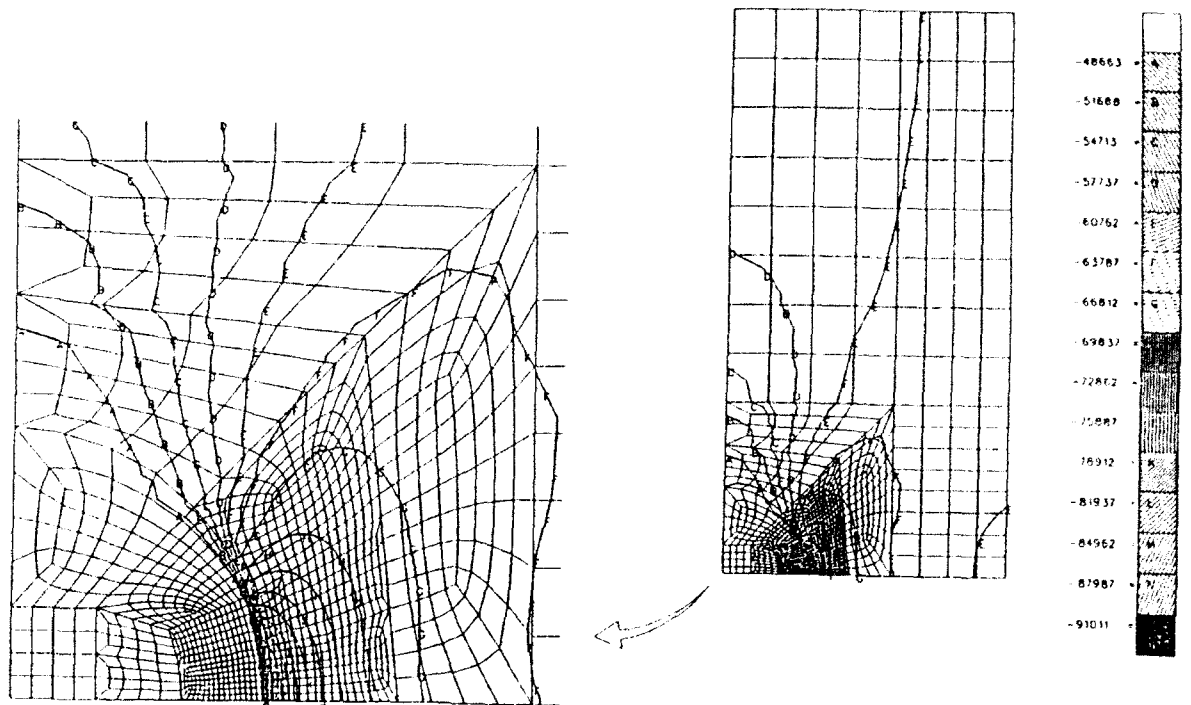
Fig. 4. Stress distribution of test coupon with 50% stiffness retained inside the 1·5 in circular damage area.
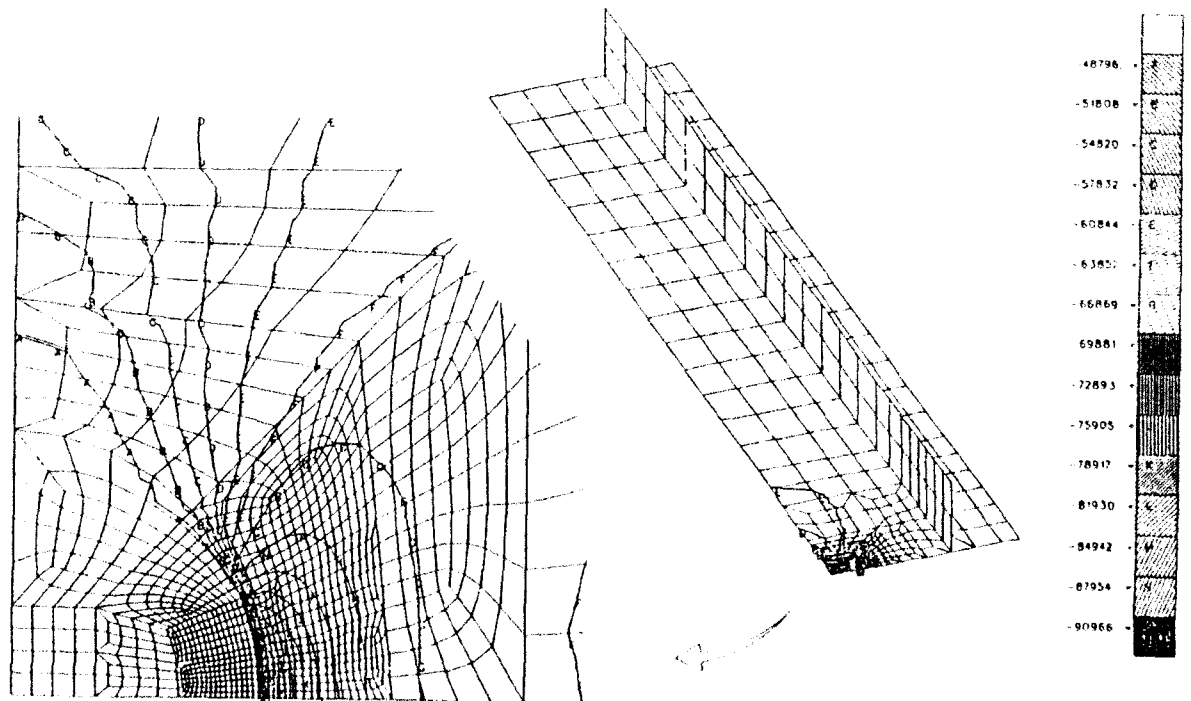
Fig. 5. Stress distribution of two-stringer panel with 50% stiffness retained inside the 1·5 in circular damage area.
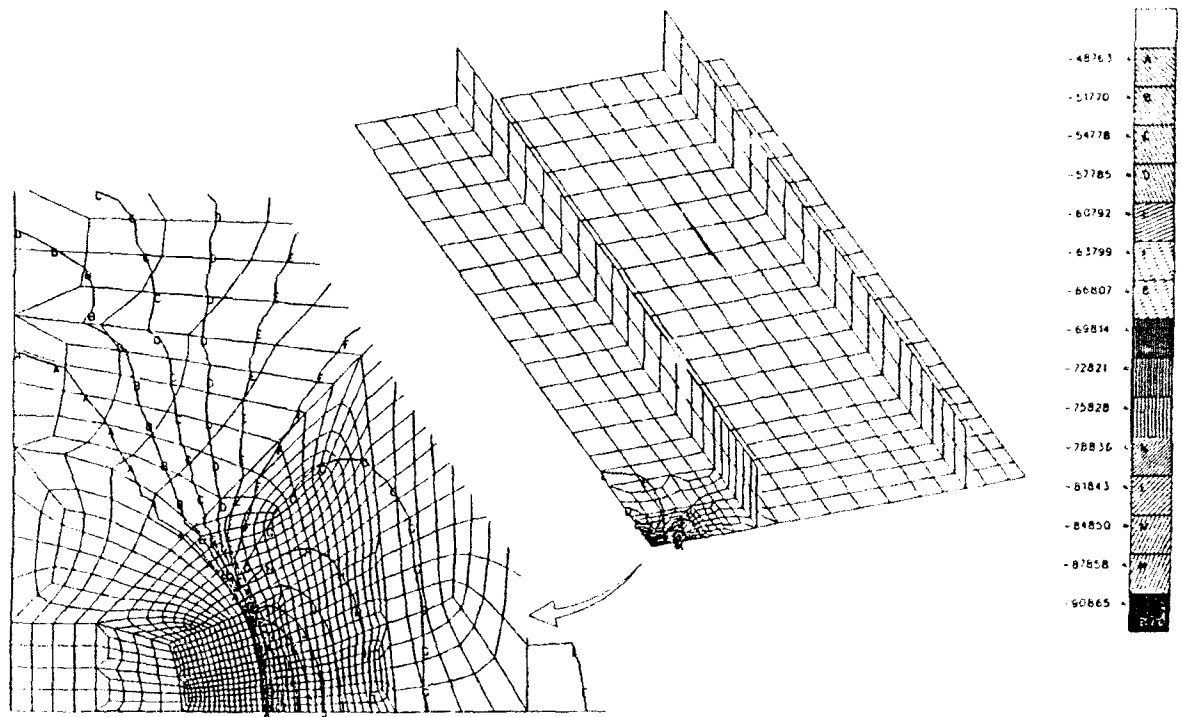
Fig. 6. Stress distribution of four-stringer panel with 50% stiffness retained inside the 1·5 in circular damage area.
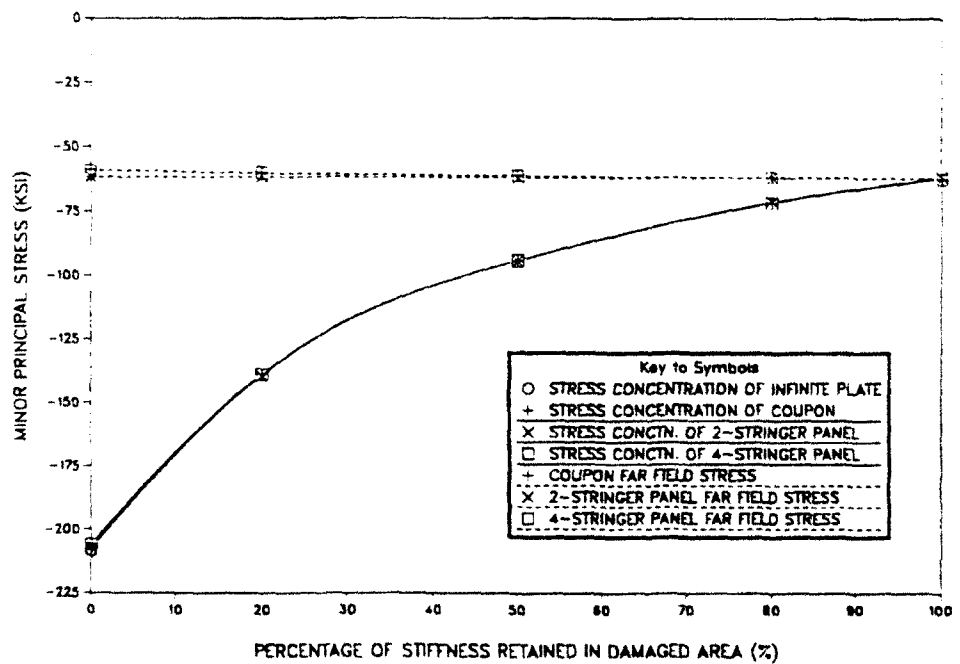
Fig. 7. Variation of stress concentration versus percentage of stiffness retained inside the impact damage area.

PARAMETRIC STUDY OF STRESS CONCENTRATION FACTOR

To investigate the stress concentration behavior of composites, a parametric study has been performed based on the anisotropic elastic infinite plate solution obtained by Lekhnitskii.[1] The stress concentration factor K can be expressed as

$$K = \frac{\sigma_a}{\sigma_\infty}$$

$$= ((-\cos^2 \phi + (k + n) \sin^2 \phi)k \cos^2 \alpha$$
$$+ ((1 + n) \cos^2 \phi - k \sin^2 \phi) \sin^2 \alpha$$
$$- n(1 + k + n) \sin \phi \cos \phi \sin \alpha \cos \alpha)$$

$$\bigg/ \bigg(\sin^4 \alpha + \frac{\bar{E}_1}{\bar{E}_2} \cos^4 \alpha$$

$$+ \frac{1}{4}\bigg(\frac{\bar{E}_1}{\bar{G}_{12}} - 2\bar{v}_{12}\bigg) \sin^2 2\alpha\bigg) \qquad (1)$$

where σ_a is the tangential stress along the circular hole at angular location α, σ_∞ is the far field stress acting at an angle ϕ with respect to the principal elastic axis '1' of the anisotropic plate shown in Fig. 8. The symbols k and n are product and sum of the complex roots of the anisotropic plate characteristic equation,[1-10] which are functions of $\bar{E}_1$, $\bar{E}_2$, $\bar{G}_{12}$ and $\bar{v}_{12}$.

Figure 9 shows clearly that, with fixed laminate Poisson's ratio $\bar{v}_{12}$, the SCF is lower for smaller $\bar{E}_1/\bar{E}_2$ value (stiffness ratio of the composite plate) and for larger $\bar{G}_{12}$ value (shear stiffness of the composite plate). The results of this parametric study indicate that shear stiffness, $\bar{G}_{12}$ is a dominant factor in the variation of SCF of the composite plate. In other words, adjusting shear stiffness may be an effective means to reduce SCF and to improve residual load carrying capability.

CONCLUSION

From the finite element analysis, the stress concentration appears near the interface of the intact and damaged areas. We also verify that the stress redistribution of damaged composites is a local phenomenon. The local stress distributions between the test coupon and stringer-stiffened panels are similar. This suggests that damage severity, not stress redistribution, is the main cause of the scaling effects. Even though this

indepth parametric study did not completely resolve the difficulty of impact damage modeling, it led to a better understanding of the damage residual strength performance.

A parametric study of the analytical solution about the SCF of composite plates indicates that the smaller $\hat{E}_1/\bar{E}_2$ value and larger $\bar{G}_{12}$ value will lower stress concentration. The shear stiffness $\bar{G}_{12}$ is the dominant factor in the variation of SCF of composite plate, therefore, it is a key factor to the failure mechanism of laminated composites.
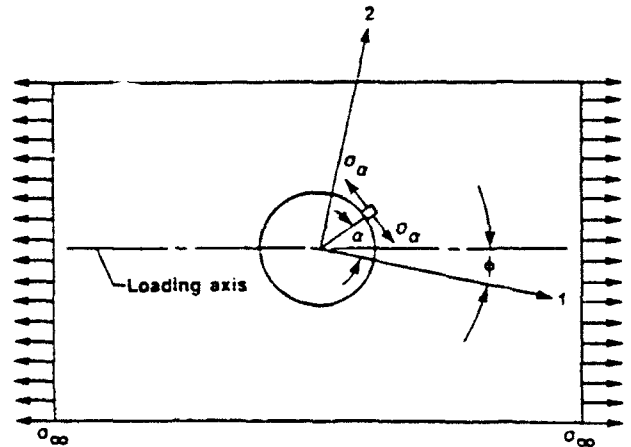
Fig. 8. Tension at an angle to a principal elastic axis 1 of an anisotropic plate with a circular hole.

$\bar{E}_1 = 15$ Msi
$\bar{E}_2 = 3, 6, 9, 12, 15$ Msi
$\bar{v}_{12} = 0.466$

$\bar{E}_2 = 3$ Msi

$\bar{E}_2 = 15$ Msi

$\bar{G}_{12}$ – Shear Modulus (Msi)
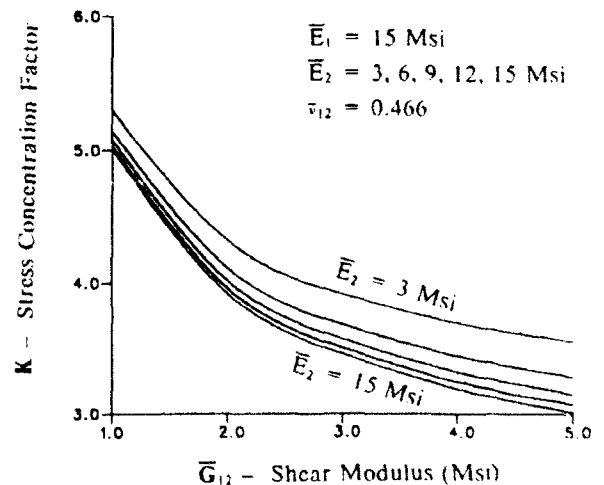
Fig. 9. Variation of stress concentration factor around circular hole in an infinite composite plate.

(IRAD) funding of the Composites Business Unit, McDonnell Douglas Aerospace, Transport Aircraft.

REFERENCES

1. Lekhnitskii, S. G., *Anisotropic Plates*. Gordon and Breach Science Publishers, New York, USA. 1968.
2. Horton, R. E. & McCarty, J. E., Damage tolerance of composites. In *Engineered Materials Handbook* (Vol. 1 — Composites). ASME International, Metals Park, OH, USA. 1988, p. 264.
3. Chen, V. L., Wu, H. T. & Kedward, K., Assessing the Impact Resistance of Contemporary Composite Structures, in progress.
4. Starnes, Jr. J. H., Rhodes, M. D. & Williams, J. G., The effect of impact damage and circular holes on the compressive strength of a graphite–epoxy laminate. NASA Technical Memorandum 78796, Oct. 1978.
5. Flanagan, G., 2-D delamination growth in composite laminates under compression loading. composite material-testing and design. In *8th Conference. ASTM STP 972*, ed. J. D. Whitcomb. Philadelphia. PA. USA. 1988, pp. 180–90.
6. Whitcomb, J. D., Mechanics of instability-related delamination growth. NASA Technical Memorandum 100622, May 1988.
7. ACEE Composites Project Office. Standard tests for toughened resin composites (rev. edn). NASA Reference Publication 1092. NASA Langley Research Center, Hampton, VA, USA. 1983.
8. Sidoroff, F., Damage mechanics and its application to composite materials. *Mechanical Characterization of Load Bearing Fibre Composite Laminates*, ed. Cardon & Verchery. 1985.
9. *MSC/NASTRAN User's Manual* (Version 67). The MacNeal–Schwendler Corporation, Los Angeles, CA, USA. Aug. 1991.
10. Jones, R. M., *Mechanics of Composite Materials*. Scripta Book Company, Washington, DC, USA, 1975. p. 70.
11. Yeh, H.-Y., Stress concentration around circular hole in a composite material specimen representative of the X-29A forward-swept wing aircraft. NASA Contractor Report 179435, Aug. 1988.

Identification of material properties of composite plate specimens

C. M. Mota Soares, M. Moreira de Freitas, A. L. Araújo

IDMEC, Instituto de Engenharia Mecânica, Pólo do IST, Av. Rovisco Pais, 1096 Lisboa Codex, Portugal

&

P. Pedersen

Department of Solid Mechanics, The Technical University of Denmark, Lyngby, Denmark

An indirect identification technique to predict the mechanical properties of composite plate specimens is presented. This technique makes use of experimental eigenfrequencies, the corresponding numerical eigenvalue evaluation, sensitivity analysis and optimization. The laminate analysis is formulated in terms of non-dimensional material parameters and the discrete model is based on the linear shear deformation theory of Mindlin. The constrained minimization of an error functional expressing the difference between measured higher frequencies of a plate specimen and the corresponding numerical ones is then carried out to find the desired optimum parameters. The required sensitivities with respect to changes in the non-dimensional material parameters have the option of being evaluated analytically, semi-analytically or alternatively by finite difference. Results which show the validation of the sensitivities and the limitations of the model to predict the required quantities and its range of application and accuracy are demonstrated through test cases.

1 INTRODUCTION

The use of composite materials in the project design of structures or structural components is increasing due to their strength to weight ratios, high stiffness to weight ratios, improved corrosion resistance, low specific gravity of fibers, low maintenance costs, etc. For specific applications the composite material is often tailored to meet certain design requirements and the mechanical properties are not available in general. Although these properties can be approximately estimated through the rule of mixtures[1] the safest and formal way of obtaining the required mechanical material data has been through experimental procedures using specific geometry specimens.

In this paper is described an indirect identification technique to predict the mechanical properties of composites which makes use of eigenfrequencies, experimental analysis of a composite plate specimen, corresponding numerical eigenvalue analysis and optimization techniques. An error functional expressing the difference between the measured higher eigenfrequencies of the plate specimen and the corresponding eigenfrequencies of the numerical model plate is established. This functional is then minimized to find the required mechanical properties. The eigenvalue analysis and the evaluation of sensitivities are carried out using a finite element model whose characteristics are derived for the linear shear deformation theory of Mindlin.[2] This work is closely related to the developments carried out by Pedersen[3] for thin composite plates using the classical theory assumptions of Kirchhoff and sensitivity analysis. Also Wilde and Sol[4] using Kirchhoff assumptions and a Bayesian parameters estimation method associated with a numerical model have developed an alternative technique based on experimental/numerical eigenfrequencies to estimate the mechanical properties of orthotropic specimens. More recently two alternative methods both requiring experimental eigenfrequency data have been published by Sol[5] and Wilde,[6] which do not follow the sensitivity analysis approach here proposed.

2 LAMINATE ANALYSIS

Considering the system referential cartesian axes x, y, z and the kth ply principal axes, X_1, X_2, X_3 (Fig. 1), the constitutive equations for a ply of a composite plate made of a finite number of orthotropic plies by neglecting the transverse normal stress effect can be represented as:

$$\{\sigma\}_k = [\bar{Q}]_k \{\varepsilon\}_k \tag{1a}$$

$$\{\sigma\}_k = \{\sigma_{xx}\ \sigma_{yy}\ \sigma_{yz}\ \sigma_{xz}\ \sigma_{xy}\}^t \tag{1b}$$

$$\{\varepsilon\}_k = \{\varepsilon_{xx}\ \varepsilon_{yy}\ \gamma_{yz}\ \gamma_{xz}\ \gamma_{xy}\}^t \tag{1c}$$

where $\{\sigma\}_k$ is the vector of stress components, $\{\varepsilon\}_k$ the vector of normal and shearing strain components, $[\bar{Q}]_k$ the material constitutive matrix transformed from X_1, X_2, X_3 to the x, y, z axes and t the transpose of a vector or matrix.

The mechanical properties of ply (k), consistent with the Mindlin plate model, are defined as E_1, E_2 the Young's modulus in the X_1, X_2 directions (X_1 being parallel to the fibers), G_{12}, G_{13}, G_{23} the transverse shear moduli in planes X_1–X_2, X_1–X_3, X_2–X_3, respectively and ν_{12} the major Poisson's ratio. It is also assumed that the ply is transversely isotropic, then $G_{12} = G_{13}$.

The coefficients of matrix $[\bar{Q}]_k$ can be represented as:

$$[\bar{Q}]_k = \frac{E_1}{8\alpha_o}[c]_k \tag{2a}$$

$$\alpha_o = 1 - \nu_{12}^2 \frac{E_2}{E_1} \tag{2b}$$

where matrix $[c]_k$ and α_o are here expressed in terms of nondimensional material parameters α_m ($m = 1, 2, 3, 4$). The terms of this matrix and the parameter α_o using the Vinson[1] index convention
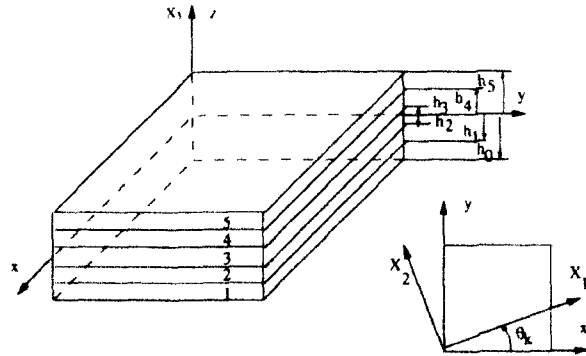
Fig. 1. Nomenclature for the stacking sequence and laminar coordinate system.

are given by:

$$c_{11} = 8 - \alpha_2[1 - \cos(2\theta_k)] - \alpha_3[1 - \cos(4\theta_k)]$$

$$c_{12} = c_{21} = \alpha_4 - \alpha_3\cos(4\theta_k)$$

$$c_{16} = c_{61} = \tfrac{1}{2}\alpha_2\sin(2\theta_k) + \alpha_3\sin(4\theta_k)$$

$$c_{22} = 8 - \alpha_2[1 + \cos(2\theta_k)] - \alpha_3[1 - \cos(4\theta_k)]$$

$$c_{26} = c_{62} = \tfrac{1}{2}\alpha_2\sin(2\theta_k) - \alpha_3\sin(4\theta_k)$$

$$c_{44} = \alpha_5 - [\tfrac{1}{2}(8 - \alpha_2 - 3\alpha_3 - \alpha_4) - \alpha_5]$$
$$\cos(2\theta_k) \tag{3}$$

$$c_{54} = c_{45} = [\tfrac{1}{2}(8 - \alpha_2 - 3\alpha_3 - \alpha_4) - \alpha_5]$$
$$\sin(2\theta_k)$$

$$c_{55} = \alpha_5 + [\tfrac{1}{2}(8 - \alpha_2 - 3\alpha_3 - \alpha_4) - \alpha_5]\cos(2\theta_k)$$

$$c_{66} = \tfrac{1}{2}(8 - \alpha_2 - \alpha_3 - \alpha_4) - \alpha_3\cos(4\theta_k)$$

$$\alpha_o = 1 - [(\alpha_4 - \alpha_3)/(8 - 2\alpha_2)]^2(4 - \alpha_2)/4$$

θ_k being the angle which axis X_1 of ply (k) makes with the system reference x axis. The non-dimensional material parameters are defined as:

$$\alpha_2 = 4 - 4(E_2/E_1)$$

$$\alpha_3 = 1 + (E_2/E_1)(1 - 2\nu_{12}) - 4(G_{12}/E_1)\alpha_o$$

$$\alpha_4 = 1 + (E_2/E_1)(1 + 6\nu_{12}) - 4(G_{12}/E_1)\alpha_o \tag{4}$$

$$\alpha_5 = 4(G_{23} + G_{12})\alpha_o/E_1$$

The inverse relations of eqn (4) are:

$$E_2/E_1 = (4 - \alpha_2)/4$$

$$G_{12}/E_1 = (8 - \alpha_2 - 3\alpha_3 - \alpha_4)/16\alpha_o$$

$$\nu_{12} = (\alpha_4 - \alpha_3)/(8 - 2\alpha_2) \tag{5}$$

$$G_{23}/E_1 = (2\alpha_5 - \tfrac{1}{2}(8 - \alpha_2 - 3\alpha_3 - \alpha_4))/8\alpha_o$$

The displacement field components at any point (x, y, z) on the composite plate, consistent with linear shear deformation theory are expressed as:

$$U(x, y, z) = u(x, y) - z\psi_x(x, y)$$

$$V(x, y, z) = v(x, y) - z\psi_y(x, y) \tag{6}$$

$$W(x, y, z) = w(x, y)$$

where u, v, w are the displacement components of a corresponding point in the middle surface in the x, y, z directions respectively and the ψ_x, ψ_y are the rotations of the normal to the middle plane along the y and x axes. The displacement field is related to the in-plane strains $\{\varepsilon_o\}$, curvatures $\{k\}$ and shearing strains $\{\gamma\}$ through the following

kinematic relations:

$$\{\varepsilon^o\} = \left[\frac{\partial u}{\partial x}, \frac{\partial v}{\partial y}, \frac{\partial u}{\partial y} + \frac{\partial v}{\partial x}\right]^t \quad (7a)$$

$$\{k\} = \left[-\frac{\partial \psi_x}{\partial x}, -\frac{\partial \psi_y}{\partial y}, -\frac{\partial \psi_x}{\partial y} - \frac{\partial \psi_y}{\partial x}\right]^t \quad (7b)$$

$$\{\gamma\} = \left[\frac{\partial w}{\partial x} - \psi_x, \frac{\partial w}{\partial y} - \psi_y\right]^t \quad (7c)$$

Integrating eqn (1) layer by layer through the cross-section of the composite plate one obtains the constitutive relations as:

$$\begin{bmatrix} \{N\} \\ \{M\} \\ \{Q\} \end{bmatrix} = \begin{bmatrix} [A] & [B] & [0] \\ [B] & [D] & [0] \\ [0] & [0] & [S] \end{bmatrix} \begin{bmatrix} \{\varepsilon^o\} \\ \{k\} \\ \{\gamma\} \end{bmatrix} \quad (8a)$$

$$A_{ij} = \frac{E_1}{8\alpha_o} \sum_{k=1}^{n} (h_k - h_{k-1})(c_{ij})_k; \quad i,j = 1,2,6 \quad (8b)$$

$$B_{ij} = \frac{E_1}{8\alpha_o} \sum_{k=1}^{n} (h_k^2 - h_{k-1}^2)(c_{ij})_k; \quad i,j = 1,2,6 \quad (8c)$$

$$D_{ij} = \frac{E_1}{8\alpha_o} \sum_{k=1}^{n} (h_k^3 - h_{k-1}^3)(c_{ij})_k; \quad i,j = 1,2,6 \quad (8d)$$

$$S_{ij} = \frac{E_1}{8\alpha_o} \frac{5}{4} \sum_{k=1}^{n} \left[h_k - h_{k-1} - \frac{4}{3}(h_k^3 - h_{k-1}^3)\frac{1}{h^2} \right]$$
$$(c_{ij})_k; \quad i,j = 5,4 \quad (8e)$$

$$\{N\} = \{N_x \ N_y \ N_{xy}\}^t; \quad \{M\} = \{M_x \ M_y \ M_{xy}\}^t;$$
$$\{Q\} = \{Q_x \ Q_y\}^t \quad (8f)$$

where the submatrices $[A]$, $[B]$, $[D]$, $[S]$ represent the extensional coupling, bending and shear material stiffnesses respectively, $\{N\}$, $\{M\}$, $\{Q\}$ are the vectors of the components of the in-plane stress resultants, bending moments, and transverse shear forces and n is the number of plies of the composite plate.

3 FINITE ELEMENT MODEL

For free harmonic vibrations, the equilibrium equations at the element level can be represented by:

$$K^e q^e = \omega^2 M^e q^e \quad (9)$$

where K^e, M^e and q^e are the element stiffness matrix, element consistent mass matrix and element displacement vector in the system axis x, y, z and ω^2 the eigenfrequency.

For node i of element e the sub-vector of the degrees of freedom is:

$$q_i^e = \{u_i^e; v_i^e; w_i^e; \psi_{xi}^e; \psi_{yi}^e\}^t \quad (10)$$

u_i^e; v_i^e; w_i^e being the nodal displacement of the middle plane with respect to the x, y, z axes respectively, and ψ_{xi}^e; ψ_{yi}^e the nodal rotations about the y and x axes.

For unsymmetrically stacked composite plates it can be shown following standard procedures via the virtual work principle that the element consistent mass and stiffness sub-matrices which link nodes i and j can be evaluated as:

$$M_{ij}^e = \int_{-1}^{+1} \int_{-1}^{+1} [N_i^e]^t [m][N_j^e] \det J \, d\xi \, d\eta \quad (11)$$

$$[m] = \sum_{k=1}^{n} [m]_k \quad (12a)$$

$$m_{11} = m_{22} = m_{33} = \rho_k(h_k - h_{k-1});$$

$$m_{44} = m_{55} = \frac{\rho_k}{3}(h_k^3 - h_{k-1}^3) \quad (12b)$$

$$m_{14} = m_{25} = \frac{\rho_k}{2}(h_k^2 - h_{k-1}^2) \quad (12c)$$

$$K_{ij}^e = \int_{-1}^{+1} \int_{-1}^{+1} \{[B_{mi}^e]^t[A][B_{mj}^e] + [B_{bi}^e]^t[B][B_{mj}^e]$$

$$+ [B_{mi}^e]^t[B][B_{bj}^e] + [B_{bi}^e]^t[D][B_{bj}^e] + [B_{si}^e]^t[S][B_{sj}^e]\}$$

$$\det J \, d\xi \, d\eta \quad (13)$$

where the non-zero coefficients of the symmetric matrix $[m]_k$ are shown above, ρ_k is the mass density of ply k and det J the determinant of the Jacobian matrix relating the natural coordinates ξ, η to the local coordinate derivatives. Matrices $[N^e]$, $[B_m^e]$, $[B_b^e]$ and $[B_s^e]$ relate the nodal degrees of freedom of the element to the generalized displacement field $\{u, v, w, \psi_x, \psi_y\}^t$, in-plane strains (eqn (7a)), curvatures (eqn (7b)) and transverse shear strains (eqn (7c)), respectively.[8,9] The element mass and stiffness matrix coefficients, eqns (11) and (13), are evaluated by Gaussian quadrature, with reduced integration on the stiffness transverse shear coefficients to avoid locking.

The system equilibrium equations are obtained in the usual way leading to an eigenvalue problem:

$$Kq_i = \omega_i^2 M q_i \qquad (14)$$

where K and M are the system stiffness and mass matrix and q_i the system eigenmode (i), which corresponds to the eigenfrequency ω_i^2.

When support conditions are not specified, as when a plate is assumed free in space, eqn (14) is modified through a sidestepping technique,[9] to avoid the singularity of matrix K.

Hence, the eigenvalue problem is replaced by an equivalent one as:

$$(K + \beta M)q_i = (\omega_i^2 + \beta) M q_i \qquad (15)$$

where $\beta > 0$ is of the order of magnitude of ω_i^2. In this work the initial guess is $\beta = \underline{\omega}_1^2$, $\underline{\omega}_1^2$ being the experimental fundamental eigenfrequency. A new value for β should be chosen before each new iteration of the optimization process. The prediction of β is efficiently carried out through a knowledge of the sensitivity of ω_1^2 with respect to the non-dimensional material parameters α_m by an expansion of first order through Taylor's series as:

$$\beta = \omega_1^2(\alpha_{2_{i-1}}, \alpha_{3_{i-1}}, \alpha_{4_{i-1}}, \alpha_{5_{i-1}}) \approx$$

$$\omega_1^2(\alpha_2, \alpha_3, \alpha_4, \alpha_5) + \frac{\partial \omega_1^2}{\partial \alpha_{2_i}}(\alpha_{2_{i-1}} - \alpha_{2_i})$$

$$\qquad (16)$$

$$+ \frac{\partial \omega_1^2}{\partial \alpha_{3_i}}(\alpha_{3_{i-1}} - \alpha_{3_i}) + \frac{\partial \omega_1^2}{\partial \alpha_{4_i}}(\alpha_{4_{i-1}} - \alpha_{4_i})$$

$$+ \frac{\partial \omega_1^2}{\partial \alpha_{5_i}}(\alpha_{5_{i-1}} - \alpha_{5_i})$$

i being the previous iteration.

4 DESCRIPTION OF THE IDENTIFICATION OPTIMIZATION PROBLEM

The identification technique aimed at finding the mechanical material properties of composite laminates takes advantage of the agreement between experimentally measured eigenfrequencies of a specimen plate hung on two thin elastic lines and the corresponding numerical model with free boundary conditions.

Let the experimentally obtained eigenfrequencies be designated by $\underline{\omega}_1^2, \underline{\omega}_2^2, \ldots, \underline{\omega}_i^2, \ldots, \underline{\omega}_I^2$, I being the number of measured eigenfrequencies. The corresponding numerical eigenfrequencies for a set of given material parameters α_m are repre-

sented by $C\omega_1^2, \ldots, C\omega_i^2, \ldots, C\omega_I^2$, where the constant C is chosen through the relation

$$C = \frac{\underline{\omega}_1^2}{\omega_1^2} \qquad (17)$$

to obtain agreement for the first eigenfrequency and to eliminate the influence of quantities which scale the set of eigenfrequencies.

The objective function Φ is defined as an error functional which depends on the higher order eigenfrequencies as:

$$\Phi = \sum_{i=2}^{I} (\underline{\omega}_i^2 - C\omega_i^2)^2 / \underline{\omega}_i^4 \qquad (18)$$

The optimization problem is formulated as the identification of the set of non-dimensional material parameters α_m which minimize the error functional:

$$\text{Min } \Phi(\alpha_2, \alpha_3, \alpha_4, \alpha_5) \geq 0 \qquad (19)$$

Subject to:

$$g_1 = -\alpha_2 < 0 \qquad \Leftrightarrow \quad (E_1/E_2 > 1)$$

$$g_2 = -\frac{(8 - \alpha_2 - 3\alpha_3 - \alpha_4)}{16\left\{1 - \left[\frac{\alpha_4 - \alpha_3}{8 - 2\alpha_2}\right]^2 \left(\frac{4 - \alpha_2}{4}\right)\right\}} < 0$$

$$\Leftrightarrow \quad (G_{12}/E_1 > 0)$$

$$g_3 = -\frac{\left(2\alpha_5 - \frac{1}{2}(8 - \alpha_2 - 3\alpha_3 - \alpha_4)\right)}{8\left\{1 - \left[\frac{\alpha_4 - \alpha_3}{8 - 2\alpha_2}\right]^2 \left(\frac{4 - \alpha_2}{4}\right)\right\}} < 0$$

$$\Leftrightarrow \quad (G_{23}/E_1 > 0) \qquad (20)$$

$$g_4 = \left| \frac{(\alpha_4 - \alpha_3)}{(8 - 2\alpha_2)} \right| - \sqrt{\frac{4}{(4 - \alpha_2)}} < 0$$

$$\Leftrightarrow \quad |v_{12}| - \sqrt{E_1/E_2} < 0$$

$$\alpha_i^l \leq \alpha_i \leq \alpha_i^u \qquad i = 2,3,4,5$$

g_i being inequality constraints and α_i^l, α_i^u the lower and upper side constraints respectively.

The optimization problem is solved by nonlinear mathematical programming techniques described by Vanderplaats[10] whose algorithms are incorporated in program ADS[11] (Automated Design Synthesis).

After the evaluation of the optimum values for the non-dimensional material parameters α_m $(m = 2,3,4,5)$ that satisfy eqn (19), the value of E_1

can be evaluated easily, since C and α_0 are known. The eigenvalue relation eqn (9) for mode q_1, which corresponds to the experimental eigenfrequency ω_1^2 can be written in an equivalent form; putting E_1 in evidence, yields:

$$E_1 K^* q_1 = \omega_1^2 M q_1 \tag{21}$$

$$C E_1^0 K^* q_1 = C \omega_1^2 M q_1 \tag{22}$$

hence

$$E_1 = C E_1^0 \tag{23}$$

E_1^0 being the initial guess value given to the Young's modulus in the major direction X_1 and E_1 the corresponding identified mechanical property. The remaining mechanical properties are then evaluated through the inverse relations in eqns (5). The optimum mechanical properties are valid on average for the entire specimen which contrasts with the majority of alternative direct methods where they are of local nature requiring a series of repetitive work to obtain reliable design data.

In the next section the evaluation of sensitivities required to accomplish the minimization of the error functional are discussed.

5 SENSITIVITY ANALYSIS

To minimize the error functional Φ, eqn (18), it is required to evaluate the sensitivities $\partial \Phi / \partial \alpha_m$ for $m = 2,3,4,5$. By differentiating the objective function (eqn (18)) with respect to α_m, yields:

$$\frac{\partial \Phi}{\partial \alpha_m} = -2C \sum_{i=2}^{I} \left(1 - \frac{C \omega_i^2}{\omega_i^2} \right)$$

$$\left[\left(\frac{\partial \omega_i^2}{\partial \alpha_m} - \frac{\omega_i^2}{\omega_i^2} \frac{\partial \omega_1^2}{\partial \alpha_m} \right) / \omega_i^2 \right], \quad (m = 2,3,4,5) \tag{24}$$

which requires the evaluation of the eigenfrequencies sensitivities with respect to the material non-dimensional parameters α_m:

$$\frac{\partial \omega_i^2}{\partial \alpha_m}, \qquad (i = 2,3,\ldots,I; \; m = 2,3,4,5) \tag{25}$$

These sensitivities are calculated through the numerical finite element model. Differentiating eqn (14) with respect to α_m and assuming that the eigenvectors are normalized through the relation $q_i^t M q_i$, yields:[12]

$$\frac{\partial \omega_i^2}{\partial \alpha_m} = q_i^t \left(\frac{\partial K}{\partial \alpha_m} - \omega_i^2 \frac{\partial M}{\partial \alpha_m} \right) q_i \tag{26}$$

where $\partial K / \partial \alpha_m$ and $\partial M / \partial \alpha_m$ are the system sensitivity stiffness and mass matrices with respect to perturbations in the non-dimensional parameters α_m. For the present situation $\partial M / \partial \alpha_m$ is considered as a null matrix, since it is independent of the material non-dimensional parameters.

Using the technique of obtaining the sensitivities at element level, for this particular application eqn (26) can be represented as:

$$\frac{\partial \omega_i^2}{\partial \alpha_m} = \sum_{l \in E} q_i^e \left(\frac{\partial K^{el}}{\partial \alpha_m} \right) q_i^{el} \tag{27}$$

E being the set of elements which are perturbed by the parameter α_m, $\partial K^e / \partial \alpha_m$ the sensitivity of the stiffness matrix of the element and q_i^e the element nodal eigenvector parameters for mode i and element l.

The sensitivities of the element stiffness matrix eqn (13) with respect to perturbations in the non-dimensional material parameters are evaluated as:

$$\frac{\partial K_{ij}^e}{\partial \alpha_m} = \int_{-1}^{+1} \int_{-1}^{+1} \left\{ [B_{mi}^e]^t \frac{\partial}{\partial \alpha_m} [A][B_{mi}^e] \right.$$

$$+ [B_{bi}^e]^t \frac{\partial}{\partial \alpha_m} [B][B_{mi}^e] + [B_{mi}^e]^t \frac{\partial}{\partial \alpha_m} [B][B_{bi}^e]$$

$$+ [B_{bi}^e]^t \frac{\partial}{\partial \alpha_m} [D][B_{bi}^e] + [B_{si}^e]^t \frac{\partial}{\partial \alpha_m} [S][B_{si}^e] \right\} \tag{28}$$

$$\det J \, d\xi \, d\eta$$

This is accomplished by differentiating analytically eqns (8b)–(8e) with respect to parameters α_m followed by matrices multiplication and integration using Gaussian quadrature.

Alternatively one obtains a semi-analytical solution for the evaluation of the eigenfrequencies sensitivities (eqn (27)) by calculating $\partial K^e / \partial \alpha_m$ approximately, using for instance a forward finite difference technique:

$$\frac{\partial K^e}{\partial \alpha_m} \cong \frac{K^e(\alpha + \Delta \alpha) - K^e(\alpha)}{\delta \alpha_m} \tag{29}$$

where $\alpha = [\alpha_2, \alpha_3, \alpha_4, \alpha_5]$ is the vector of non-dimensional parameters, $\delta \alpha_m$ is a small perturbation in α_m and $\Delta \alpha = [0,\ldots,\delta \alpha_m,\ldots,0]$.

As an alternative to these two methods, which differ only in the way matrix $\partial K^e/\partial \alpha_m$ is obtained. a so-called global finite difference (GFD) approximation can be carried out evaluating the eigenfrequencies sensitivities as:

$$\frac{\partial \omega_i^2}{\partial \alpha_m} \cong \frac{\omega_i^2(a + \Delta a) - \omega_i^2(a)}{\delta \alpha_m} \qquad (30)$$

which is easy to implement but less efficient with regard to CPU time, since two numerical analyses are required to evaluate each senstivity.

6 APPLICATIONS

6.1 Discrete model validation

A computer package with the objective of identification of the mechanical properties of multi-laminar composite plates has been developed and the eight node isoparametric composite plate element tested with regard to accuracy of the eigenfrequencies in accordance with benchmark for free vibrations of a typical square isotropic plate of dimensions $a \times a$. The following geometric and mechanical properties were used:[13]

$a = 10$ m, $h = 0.05$ m (thickness). $E = 200$ GPa (Young's modulus). $\nu = 0.3$ (Poisson's ratio). $\rho = 8000$ kg/m^3 (mass per unit volume).

The results for modes 4–9 are in perfect agreement both with an analytical solution and also with numerical results of several commercial codes shown in Morris.[13] Table 1 compares the results of the proposed model using a 4×4 regular mesh. with the corresponding analytical ones.[13] The maximum relative error related with ω_9 is -2.96%. When 6×6 and 8×8 regular meshes are considered then these relative errors are reduced to -2.13% and -0.08% respectively.

To compare the quality of the eigenfrequencies sensitivities with respect to changes in non-dimensional material parameters α_m a model using a regular mesh 4×4 and having the following characteristics has been used: four layered square plate $(a \times a)$, with stacking sequence $[0°, 90°, 90°. 0]$ and $a = 10$ m. $h = 0.1$ m $(h_0 = 0.05$ m. $h_1 = -0.025$ m. $h_2 = 0.0$ m. $h_3 = 0.025$ m. $h_4 = 0.05$ m). The mechanical properties were: $E_1 = 4.05$ GPa. $E_2 = 1.50$ GPa. $\nu_{12} = 0.23$, $G_{12} = G_{13} = 6.75$ GPa. $G_{23} = 2.7$ GPa and $\rho = 2100$ kg/m^3.

Table 1. Benchmark test — natural frequencies (Hz)

	Mesh	ω_4	ω_5	ω_6	$\omega_7 = \omega_8$	ω_9
	4×4	1·626	2·369	2·936	4·186	7·560
Present	6×6	1·621	2·360	2·925	4·180	7·402
	8×8	1·620	2·360	2·923	4·180	7·396
Analytical Morris[13]	—	1·622	2·360	2·922	4·233	7·416

Table 2. Eigenfrequency sensitivities $\dfrac{\partial \omega_i^2}{\partial \alpha_m}$ [rad^2/s^2]

	$m = 2$	$m = 3$	$m = 4$	$m = 5$
AN	$-191·25$	6·99	$-23·25$	0·239
SA	$-191·25$	6·99	$-23·25$	0·239
$\delta\alpha_m = 0·0001$				
GFD	$-191·25$	6·93	$-23·25$	0·236
$\delta\alpha_m = 0·0001$				

Removing the rigid body modes. Table 2 compares the eigenfrequency sensitivities for mode 2. $\omega_2 = 17.96$ rad/s (2·86 Hz). where the sensitivities of the element stiffness matrix with respect to parameters α_m are evaluated analytically (AN) and semi-analytically (SA) through eqns (28) and (29) respectively. Results are also shown for the global finite difference approximation (GFD) obtained using eqn (30).

These sensitivity results show that each of these techniques can be used with confidence in the optimization of composite mechanical parameters. The analytical sensitivity evaluation will be the option for the identification results presented in this paper. since in general they are always more accurate.[14,15]

6.2 Identification examples

Data for the six specimens which are being presented are shown in Table 3. The identification and comparison of reference and/or experimental versus optimized eigenfrequencies (after the removal of the rigid body modes) for specimens (SP) I–VI are presented in Table 4. The corresponding mechanical properties are shown and compared in Table 5.

Case I validates the range of application with regard to side/thickness (a/h) of a square steel plate, where the experimental frequencies were replaced by reference values obtained using the present model with an 8×8 regular mesh. These tests were carried out for several a/h ratios in the range 5–200. Results for the representative ratios

Table 3. Specimen data

Specimen	SP (I)	SP (II)	SP (III)	SP (IV)	SP (V)	SP (VI)
Material	Steel	Aluminium	Carbon-epoxy	Carbon-epoxy	Glass-epoxy	Carbon-epoxy
Dimension $x = a$ (m)	0·2	0·193	0·260	0·175	0·209	0·270
Dimension $y = b$ (m)	0·2	0·281	0·137	0·210	0·192	0·170
Overall thickness (m)	0·02; 0·002	0·00194	0·00234	0·00237	0·00259	0·00344
ρ_k (kg/m³)	8000	2688	1586	1564	2120	1513
Number of plies of equal thickness	1	1	16	16	16	8
Fiber orientation	—	—	$[0^0_{16}]_T$	(a)	(b)	$[0^0_8]_T$

(a) $[0°, -45°, 40°, 55°, 90°, -50°, -85°, 85°]_s$
(b) $[0°, -40°, 40°, 90°, 40°, 0°, 90°, -40°]_s$

Table 4. Natural frequencies (Hz)

SP	Mode i	1	2	3	4	5	6	7	8	9	10
	Reference value	1531·3	2281·3	2809·2	3844·5	3844·5	6675·8	6675·8	6712·4	7310·4	8162·8
	Optimum	1531·3	2283·6	2806·2	3844·5	3844·7	6671·9	6674·5	6710·4	7312·8	8156·8
	Error (%) $a/h = 10$	0·0	0·10	-0·11	0·0	0·0	-0·06	-0·02	-0·03	+0·03	-0·07
I	Reference value	81·0	118·0	146·1	209·0	209·0	368·4	368·4	382·3	417·3	465·8
	Optimum	81·0	118·1	146·1	209·0	209·1	368·5	368·5	382·3	417·3	465·8
	Error (%) $a/h = 100$	0·0	0·08	0·03	0·01	0·01	0·01	0·01	0·01	0·04	0·0
	Experimental	112·6	127·9	261·7	286·6	334·5	392·1	493·8	560·1	720·7	
II	Present (8 × 8)	112·6	127·5	263·4	284·4	334·3	391·8	497·7	558·7	725·2	
	Error (%)	0·0	-0·31	0·65	-0·77	-0·06	-0·08	0·79	-0·25	0·62	
	Experimental	136·7	312·5	329·1	419·7	431·8	707·8	877·0	910·6	963·4	1015·1
III	Present 8 × 8	136·7	314·0	333·5	419·2	428·2	719·4	874·7	909·8	956·1	1002·3
	Error (%)	0·0	0·47	1·34	-0·13	-0·84	1·64	-0·26	-0·09	-0·75	-1·26
	Experimental	245·9	263·4	516·6	569·0	680·7	799·0	1058·0	1147·0	1416·0	
IV	Present (8 × 8)	245·9	264·9	518·5	567·0	675·7	796·1	1054·1	1159·3	1410·4	
	Error (%)	0·0	0·58	0·37	-0·36	-0·73	-0·36	-0·37	1·07	-0·40	
	Experimental	172·5	250·2	300·6	437·9	443·6	760·3	766·2	797·4	872·6	963·4
V	Present (8 × 8)	172·5	250·5	299·4	439·6	443·0	755·5	771·7	804·3	878·7	962·7
	Error (%)	0·0	0·18	-0·43	0·57	-0·33	-0·14	0·21	0·88	0·71	-0·09
	Experimental	125·7	275·8	374·5	388·9	463·4	706·5	756·5	848·1	1051·5	1156·8
VI	Present (11 × 7)	125·7	275·3	373·6	390·8	463·6	699·2	761·2	846·2	1068·0	1131·0
	Error (%)	0·0	-0·17	-0·23	0·49	0·04	-1·03	0·63	-0·23	1·63	-2·23

$a/h = 10$ and $a/h = 100$, are shown. The material identification was carried out using the following initial guess: $E = E_1 = E_2 = 300$ GPa, $G = G_{12} = G_{13} = 125$ GPa and $v = v_{12} = 0·2$. The numerical reference values were obtained using the following mechanical properties: $E = 200$ GPa, $G = 76·9$ GPa, $v = 0·3$.

For specimens II–V the initial mechanical properties were: $E_1 = E_2 = 100$ GPa, $G_{12} = G_{13} = 50$ GPa and $v_{12} = 0·3$ and for example, VI, $E_1 = 100$ GPa, $E_2 = 10$ GPa, $G_{12} = G_{13} = 5$ GPa and $v_{12} = 0·2$.

From Table 4 it can be observed that the maximum relative error for the natural frequency is $-2·23\%$, corresponding to example VI, vibration mode 10, this frequency residual is due to specimen imperfections, namely non-uniform thickness.

From Table 5, case I, it can be seen that for the ratio $a/h = 10$ the agreement between the two sets of results is excellent. For the ratio $a/h = 100$ the value of the shear modulus in the plane perpendicular to the directions of the fibers, G_{23}, is not correctly predicted. From examples II–VI the

Table 5. Mechanical properties

SP	Method	Model	E_1 (GPa)	E_2 (GPa)	G_{12} (GPa)	G_{23} (GPa)	ν_{12}
		Micro $a/h=10$	200·2	200·1	76·9	76·8	0·3
I	Optimum	Micro $a/h=100$	200·2	200·2	76·9	102·0	0·3
	Reference value	Micro	200·0	200·0	76·9	76·9	0·3
II	Present (8 × 8)	Micro	68·7	68·1	24·6	26·9	0·34
	Pedersen[3]	Micro	69·5	67·8	24·5	--	0·34
III	Present (8 × 8)	Micro	126·3	10·5	6·1	6·5	0·24
	Pedersen[3]	Micro	127·0	10·6	6·06	—	0·29
	Present (8 × 8)	Micro	57·2	21·4	11·3	11·8	0·3
	Pedersen[3]	Micro	61·3	21·4	9·8	—	0·28
IV	Present (8 × 8)	Macro	36·9	34·0	14·1	11·5	0·26
	Experimental[3]	Macro	34·1	31·8	—	—	0·29
	Present (8 × 8)	Micro	57·2	21·4	11·3	11·8	0·30
	Pedersen[3]	Micro	61·3	21·4	9·8	—	0·28
V	Present (8 × 8)	Macro	36·9	34·0	14·1	11·5	0·26
	Pedersen[3]	Macro	37·4	34·0	13·9	--	0·28
	Experimental[3]	Macro	34·1	31·8	—	—	0·29
VI	Present (8 × 8)	Micro	98·3	7·7	3·8	6·1	0·23
	Experimental[3]	Macro	99·1	7·67	—	—	0·35

agreement between the alternative sets of results is very good, except for Poisson's ratio, which is not very sensitive to a material design perturbation in this variable. The shear modulus G_{23} is noticed to be always slightly larger than the plane shear modulus G_{12}, as expected.

The present macro model results were obtained by considering the specimens to be made of a unique ply of overall thickness h and

$$\theta = 1/n \sum_{k=1}^{n} \theta_k.$$

All optimum solutions have been achieved through modified feasible direction methods, implemented in optimizer ADS.[10,11]

Computational details regarding the optimization process are given in Table 6. The optimization has been carried out in a VAX 9000 computer. In the present paper only results dealing with specimens which are symmetric about the middle surface and having equal mechanical properties for the layers in the local referential, X_1, X_2, X_3 were shown. To overcome this limitation the present method of identification is being extended to contemplate more than one material and non-symmetric angle ply laminates.

Table 6. Computational information

Specimen (SP)	No. of iterations	CPU time (min)
I	19;24	30;37
II	13	22
III	38	51
IV	9	21
V	15	24
VI	11	47

7 CONCLUSIONS

The present discrete finite element model, based on the Mindlin plate theory when associated with experimental eigenfrequency identification is able to predict the mechanical properties of composite plate specimens within acceptable limits of accuracy. The sensitivity analysis required for the optimization process can be used with the three techniques although analytical or alternatively semi-analytical sensitivities are recommended.

The identification of mechanical properties E_1, E_2, G_{12} are always evaluated without major discrepancies. Some discrepancies are found in the identification of major Poisson's ratio ν_{12}. The value of the shear modulus G_{23} can only be pre-

dicted with confidence in the range of $5 \leq a/h \leq 10$. The mechanical properties evaluated through this technique are valid on average for the entire specimen.

The present model can predict the major properties of thin and moderately thick plate specimens, being advantageous to models based on the Kirchhoff theory which allow only thin test specimens.

Since the model is very dependent on good experimental eigenfrequencies, rectangular specimens of dimensions $a/b \cong 2$ are recommended to avoid very close eigenfrequencies which will make more difficult the identification process of the less sensitive mechanical properties such as Poisson's ratio v_{12}.

ACKNOWLEDGEMENTS

REFERENCES

1. Vinson, J. R. & Sierakowski, R. L., *The Behaviour of Structures Composed of Composite Materials*. Martinus Nijhoff, Dordrecht, 1986.
2. Mindlin, R. D., Influence of rotary intertia and shear on flexural motion of isotropic elastic plates. *Journal of Applied Mechanics*, 18 (1951).
3. Pedersen, P., In *Optimization Method Applied to Identification of Material Parameters, Discretization Methods and Structural Optimization — Procedures and Applications*, ed. H. A. Eschenauer & G. Thierauf. Springer-Verlag, Berlin, 1989, pp. 277–83.
4. Wilde, W. P. & Sol, H., Anisotropic material identification using measured resonant frequencies of rectangular composite plates. In *Composite Structures 4, Vol. 2*, ed. I. H. Marshall. Elsevier Applied Science, London, 1987, pp. 2317–24.
5. Sol, H., Indentification of the complex moduli of composite materials by a mixed numerical/experimental method. In *Composite Materials Design and Analysis*, ed. W. P. Wilde & W. R. Blain. Springer-Verlag, Berlin, 1990, pp. 267–79.
6. Wilde, W. P., Identification of the rigidities of composite systems by mixed numerical experimental methods. In *Mechanical Identification of Composites*, ed. A. Vautrin & H. Sol. Elsevier Applied Science, London, 1991, pp. 1–15.
7. Pedersen, P., On sensitivity analysis and optimal design for laminates. In *Mechanical Behaviour of Composites*, ed. Green & Micunovic. Elsevier, Amsterdam, 1987.
8. Owen, D. R. J. & Hinton, E., *Finite Elements in Plasticity*. Pineridge Press Ltd, Swansea, 1980, pp. 157–74.
9. Zienkiewicz, O. C., *The Finite Element Method in Engineering Science*, 2nd edn. McGraw-Hill, New York, 1971, pp. 349–51.
10. Vanderplaats, G. N., *Numerical Optimization Techniques for Engineering Design*. McGraw-Hill, New York, 1984.
11. Vanderplaats, G. N., *ADS — A Fortran Program for Automated Design Synthesis, Version 2.01*. Engineering Design Optimization Inc., St Barbara, CA, 1987.
12. Haftka, R. T. & Kamat, M., Finite elements on optimal structural design. In *Computer Aided Optimal Design: Structural and Mechanical Systems*, ed. C. A. Mota Soares. Springer-Verlag, Berlin, 1987, pp. 241–70.
13. Morris, A., *Selected Results from the NASFEMS Dynamics Working Group-Free Vibrations*, Benchmarks, Part 1, Benchmark, April, 1989.
14. Pedersen, P., Gengdong, C. & Rasmussen, J., On the accuracy problems for semi-analytical sensitivity analysis. *Mechanics of Structures and Machines*, 17 (1989) 241–7.
15. Barbosa, J. I., Mota Soares, C. M. & Mota Soares, C. A., Sensitivity analysis and shape optimal design of axisymmetric shell structures. *Computing Systems in Engineering*, 2 (5/6) (1991) 525–33.

Effect of the free edge finishing on the tensile strength of carbon/epoxy laminates

Sérgio Frascino Müller de Almeida

Department of Mechanical Engineering, Instituto Tecnológico de Aeronáutica, 12228-900 — São José dos Campos, Brazil

&

Geraldo Maurício Cândido

Composite Materials Division, EMBRAER — Empresa Brasileira de Aeronáutica 12225-180 — São José dos Campos, Brazil

High productivity can be achieved in the fabrication of composite laminates if molded edges are used. In this work, the fabrication process of laminates with this type of edge finishing is described. The stacking sequence effect for laminates with molded edges is experimentally studied and compared to that of laminates with machined edges. The tensile strengths of five different laminates fabricated with carbon epoxy unidirectional tape and woven fabrics were measured. It is shown that the strength of laminates with molded edges is about 10% lower than that of laminates with machined edges but less sensitive to stacking sequence. The presence of small pockets of pure resin near the free edge of laminates with molded edges causes a reduction in the tensile strength. The stacking sequence effect may be very pronounced for laminates with woven fabric layers and machined edges.

INTRODUCTION

Delamination initiated by free edge stresses may cause a severe reduction in the durability and damage tolerance of laminated composite structures. Edge delaminations appear as a consequence of the low interlaminar fracture toughness of laminated composites combined with the possible existence of high interlaminar stresses in the vicinity of free edges. Extensive research has been directed towards investigating design concepts to suppress edge delamination by increasing the fracture toughness and/or reducing the interlaminar stresses. Of course such methods are of practical interest only if they do not significantly penalize the weight and cost of the structure. Also, the stiffness of the laminate and its strength for all relevant types of loading must be preserved.

The simplest approach that has been proposed to control edge delamination is to choose an appropriate ply stacking sequence where the effect of interlaminar stresses is minimized according to some criterion. This method has the advantage of not affecting weight, cost and any

in-plane properties of the laminate. However, in general, it is not effective in applications where load reversal is present because interlaminar tensile normal stresses can not be avoided.

The fracture toughness in the vicinity of a free edge can be improved by stitching, braiding, or capping the edge. It has been shown that stitching can effectively arrest edge delamination but might have adverse effects on the strength and fatigue life of fiber dominated laminates. Braiding provides fiber reinforcement in the out-of-plane direction resulting in a dramatic increase in the interlaminar strength of the laminate. The resistance to edge delamination can also be improved by using a U-shaped cap along the edge. The use of any of these approaches may be limited by manufacturing constraints. Moreover, they may lead to a major increase in the cost of the structure because of the higher complexity of the manufacturing process and required inspection.

A number of design concepts have also been proposed to minimize the interlaminar stresses at the free edges thus improving the edge delamination resistance of the laminate. For example, by terminating critical plies at a certain distance from

the free edge, severe Poisson ratio mismatches between adjacent plies can be avoided, reducing the interlaminar stresses. Chan[3] demonstrated that the critical ply termination approach could suppress delamination as well as increase fatigue life. On the other hand, experimental results[7] indicate that the compressive strength of laminates with dropped plies may be significantly reduced due to the presence of thickness discontinuities.

Another technique to reduce the interlaminar stresses is the use of adhesive layers at the critical interfaces.[8,9] In this case, the mismatch of mechanical properties between adjacent layers is buffered by a thin layer of tough but unreinforced resin causing a reduction of both normal and shear interlaminar stresses. There is experimental evidence[8,9] that this technique may actually improve the static strength and fatigue life of composite laminates.

It has also been numerically demonstrated[10] that a reduction in the free edge interlaminar stresses can be achieved by reducing the fiber volume fraction near the free edge. Even though the theoretical results are very promising, this technique is very difficult to implement in practical applications.

Several other possibilities are available to the designer to improve the resistance of composite laminates to edge delamination. As mentioned earlier, for all of them there is a trade-off between effectiveness and cost/weight of the structure. In this work, a low cost fabrication process to produce carbon/epoxy laminates with a molded edge is studied. The strength of this type of laminate is investigated and a design approach to minimize free edge effects is proposed.

Also, the free edge effect for laminates with combined unidirectional tape and woven fabric reinforcements is experimentally evaluated. It is expected that the interlaminar stresses and laminate strength should be affected by the three dimensional nature of woven fabrics. Experimental data on the free edge effect for this type of laminate are scarce in the open literature even though woven fabrics are often used along with unidirectional tape in practical applications.

LAMINATES WITH MOLDED EDGES

A number of operations can now be automated to improve productivity in the manufacturing of composite structures. With the use of numerically controlled machines the pre-impregnated material can be automatically cut and laid on the mold producing high quality laminates. An additional gain in productivity is obtained if the material is cut to the exact required size eliminating the need for trimming the laminate edges and machining internal openings. In this work, this type of edge finishing will be designated as molded edge to indicate that it is the condition of the edge as the laminate is removed from the mold without trimming.

The use of molded edges in composite parts reduces manufacturing costs. However, the effect of this fabrication procedure on the strength of composite laminates must be evaluated. It will be experimentally demonstrated in this work that if the laminate construction is not adequate the use of molded edges may lead to a significant reduction in the laminate tensile strength.

The effect of the molded edge on the tensile strength is a consequence of the formation of resin rich regions near the edges. This occurs because, before the cure of the material, resin and fibers move towards the molded edge under the action of external pressure. As pointed out earlier, this may contribute to the reduction in the magnitude of the interlaminar stresses. On the other hand, the interlaminar fracture toughness near the molded edge may also decrease and the laminate strength may actually decrease as was experimentally observed. Therefore, the resulting arrangement of fibers and resin at the free edge is of paramount importance for the strength of the laminate.

The severity of the free edge effect in laminates with molded edges is assessed by comparison with that of laminates with machined edges. A family of delamination prone laminates is chosen and the effect of stacking sequence is characterized for laminates with molded edges and machined edges. The laminate with a machined edge was taken as a reference for comparison purposes because this type of edge finishing has been extensively investigated in the literature. Moreover, it has also been used as a reference to evaluate all the previously discussed design concepts to suppress edge delamination. The severity of the free edge effect is correlated to the arrangement of fibers and resin in the molded edge and compared to that of laminates produced with machined edges.

FABRICATION OF THE SPECIMENS

Five different families of laminates were produced using unidirectional carbon/epoxy tape and

Table 1. Mechanical properties of carbon/epoxy pre-impregnated material

Material	Unidirect. tape	Woven fabric
Longitudinal modulus, E_1 (GPa)	66·6	130·1
Transversal modulus, E_2 (GPa)	66·6	2·0
Shear modulus, G_{12} (GPa)	4·6	5·8
Poisson ratio, v_{12}	0·05	0·27
Longitudinal tensile strength (MPa)	6,3	1721
Transverse tensile strength (MPa)	678	43
Longitudinal compressive strength (MPa)	548	703
Transverse compressive strength (MPa)	548	133
In-plane shear strength, S_{12} (MPa)	122	88
Interlaminar shear strength, S_{13} (MPa)	69	84
Nominal thickness (mm)	0·35	0·18

eight harness satin weave carbon/epoxy fabric from Hexcell. The mechanical properties of the materials are given in Table 1. In order to minimize data dispersion all specimens were fabricated with material from the same batch.

The five families of laminates used in this work were chosen such that they are approximately equivalent in terms of in-plane mechanical properties according to Classical Lamination Theory. Since the nominal thickness of the fabric layer is approximately twice that of the unidirectional tape, in terms of in-plane stiffness, one layer of fabric is approximately equivalent to two orthogonal layers of unidirectional tape. The families of laminates produced are:

$$[90/90/0]_s, [90/0/90]_s, [0/90/90]_s, [(0, 90)/90]_s,$$

and

$$[90/(0, 90)]_s$$

One group of specimens was produced with machined edge and another with molded edge for each family of laminates. In order to produce the specimens with machined edge, five plates, one for each family, were manufactured. All plates were simultaneously cured at 180°C according to the cure cycle depicted in Fig. 1. After cure, five specimens were cut from each plate using a diamond saw. Each of the specimens had their edges carefully polished in a grinding machine. The finished specimens had a nominal width of 50 mm and nominal length of 350 mm as shown in Fig. 2.

The specimens with molded edge were manufactured using a specially developed mold. Five specimens with the same nominal dimensions of the specimens with machined edge could be simultaneously cured with the mold. The pre-impregnated layers were cut to a width slightly smaller than the nominal value to account for
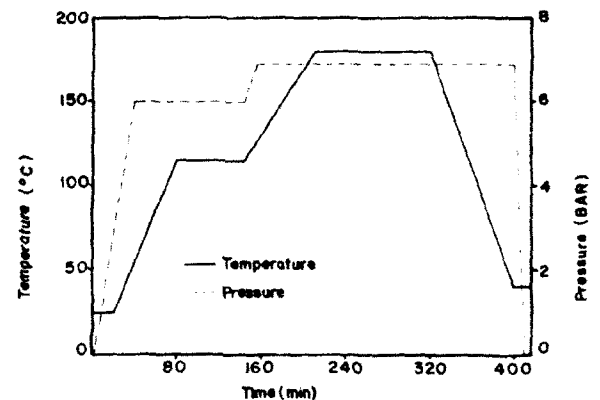
Fig. 1. Cure cycle.
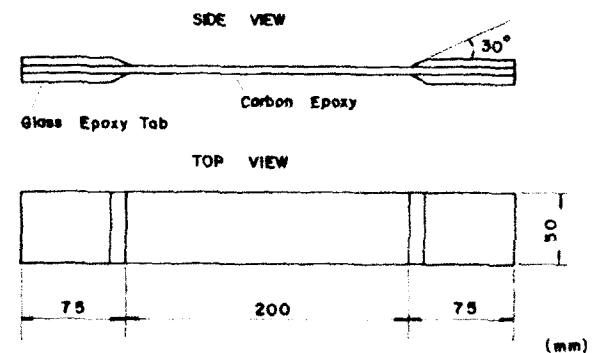
Fig. 2. Geometry of the specimen.

material accommodation and thermal expansion. After cure, using the same cure cycle as before, all the irregularities at the edge surface were gently removed with a fine sand paper. A total of six specimens with molded edge were produced for each family of laminates.

The tabs used for all specimens were produced with glass fiber reinforced epoxy and bonded to the specimens with structural adhesive cured at room temperature.

All specimens with machined and molded edges were inspected by ultra sound before testing to detect delaminations and other defects.

TEST RESULTS

The importance of the free edge effect for each type of edge finishing was characterized by evaluating the effect of stacking sequence on the tensile fracture stress of all laminates. The measurements were made in an Instron 4206 testing machine. All tests were conducted at laboratory room temperature with a stroke rate of 1·0 mm/min. The average strength measured for each group of specimens is depicted in Fig. 3. The lowest and highest measured values within each group are also included in the figure to characterize the data dispersion.

At least two cross-sectional optical micrographs were obtained for each specimen type to study the arrangement of fibers and matrix near the free edge. Figure 4 shows a typical micrograph (× 100) of the free edge of a specimen with machined edges. The specimen has a ply stacking sequence [90/0/90]. The figure shows that excellent finishing was obtained for the free edge surface with the fabrication procedure adopted. The same quality of edge finishing was obtained for all specimens with machined edges.

Figures 5–9 show a typical micrograph of each type of specimen with molded edge. It is readily apparent from the figures that longitudinal fibers (at 0°) can move laterally towards the edge under

the action of the external pressure in the autoclave. As a consequence, a small resin rich region reinforced only by longitudinal fibers is formed near the molded edge. This region typically spans
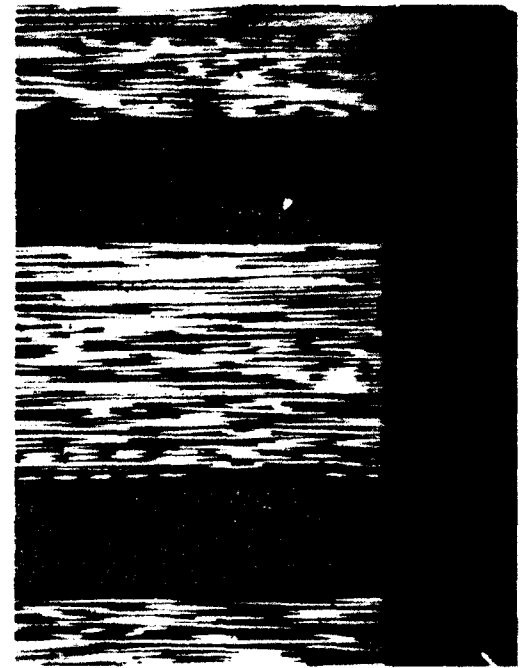
Fig. 4. Micrograph (× 100) of the free edge of a specimen with machined edges and ply stacking sequence [90/0/90].
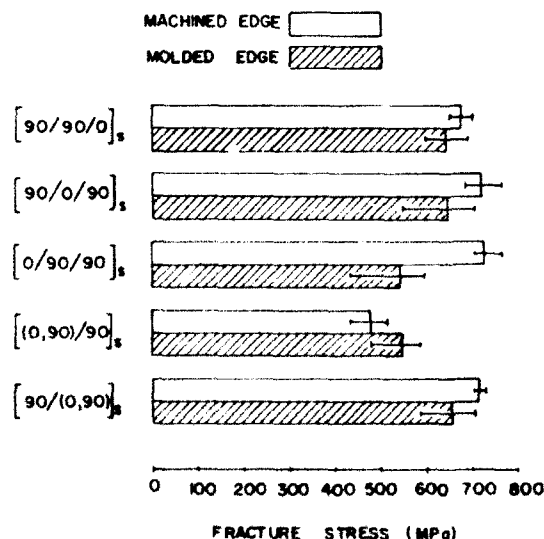
Fig. 3. Tensile fracture stress of the laminates.

Fig. 5. Micrograph × 100 of the free edge of a specimen with molded edges and ply stacking sequence [90/90/0].

Fig. 6. Micrograph (× 100) of the free edge of a specimen with molded edges and ply stacking sequence [90/0/90].

Fig. 8. Micrograph (× 100) of the free edge of a specimen with molded edges and ply stacking sequence [90/0. 90].
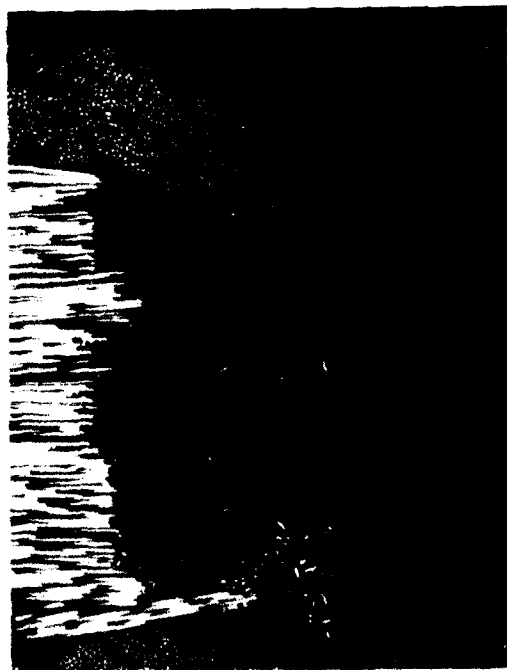
Fig. 7. Micrograph (× 100) of the free edge of a specimen with molded edges and ply stacking sequence [0/90/90].
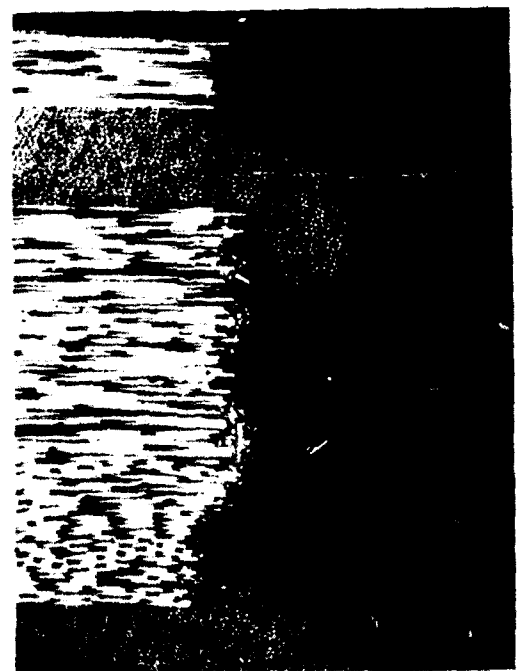
Fig. 9. Micrograph (× 100) of the free edge of a specimen with molded edges and ply stacking sequence [0, 90/90].

over a distance of about 0·3 mm from the edge. Depending on the stacking sequence, relatively large pockets of pure resin are formed near the edge.

It can be concluded from Figs 5 and 6 that for laminates [90/90/0] and [90/0/90] the longitudinal fibers move from the inner to the external layer forming a relatively homogeneous region of

resin reinforced by 0° fibers. On the other hand, Fig. 7 shows that for a [0/90/90]ₖ laminate the longitudinal fibers have a tendency to move from the external layer to the inner layer. However, this movement is prevented by the flow of the excess of resin from the inner layers and a large pocket of pure resin is formed.

Analysis of the micrographs of the laminates containing woven fabric plies leads to similar conclusions. Figure 8 shows that for laminate [90/(0, 90)]ₖ the molded edge is typically formed by resin reinforced by 0° fibers and small areas of pure resin. The molded edge of laminate [(0, 90)/90]ₖ, depicted in Fig. 9, clearly presents a large pocket of pure resin.

Comparing the micrographs of the laminates with molded edge to the measured tensile fracture stress, it can be concluded that there is a correlation between the existence of the pockets of resin at the molded edge and the tensile strength of the laminate. The laminates with molded edge that did not present a pocket of pure resin had an average strength varying from 643 to 656 MPa. Those laminates presenting pockets of pure resin had average strength from 542 to 547 MPa. This indicates that the existence of pockets of resin at the molded edge may reduce the laminate strength by about 15%.

It must also be pointed out that the data dispersion of strength of the laminates with molded edge is relatively low. If we consider that each specimen was produced independently, this indicates that the fabrication process used has good repeatability.

DISCUSSION AND CONCLUSIONS

The tensile fracture stress measured for the laminates [90/90/0]ₖ and [0/90/90]ₖ with machined edges (677 and 726 MPa, respectively) were almost identical to the results obtained by Lagace.[11] However, a large discrepancy was observed for laminate [90/0/90]ₖ. A fracture stress of 721 MPa was measured in this work and Ref. 11 reports a strength of 561 MPa. Therefore, for laminates produced with unidirectional tape and machined edges, Lagace measured a pronounced stacking sequence effect (up to 23%). Such an effect was not observed in this work probably due to the excellent free edge finishing obtained with the grinding machine. This indicates that a well polished free edge may sup-

press delamination. Obviously, this approach can not be used in most practical applications.

The data dispersion in fracture measurements is of great importance because it indicates whether the fabrication process is consistent or not. Moreover, it has a critical role in defining the design allowable for a part produced with such fabrication process. The experimental results show that data dispersion is smaller for laminates with machined edges than for laminates with molded edges. Of course, data dispersion would be larger if the specimens with machined edges were produced with production tools. But, even in this case, it is expected that the standard deviation would be smaller for laminates with machined edges than for laminates with molded edges. If we consider that each specimen with a molded edge was produced independently and most of them had to be cured separately, it can be said that the data dispersion for laminates with molded edges is still acceptable for composite manufacture.

A theoretical analysis of the free edge problem involving woven fabrics is very difficult because quasi-three-dimensional finite element models are not applicable. In this case, experimental analysis is the only source of data for design. The analysis of the strength of laminates fabricated with uni-directional tape combined with woven fabric lead to some interesting conclusions. Unlike what was expected, this type of laminate is very sensitive to the stacking sequence effect even for carefully machined edges. Due to the three-dimensional nature of woven fabrics, it is expected that the mismatch between elastic properties across the interface is not so severe and lower interlaminar stresses should develop. As a consequence, a higher resistance to edge delamination is expected. But the experimental results show that laminate [90/(0, 90)]ₖ is on average 33% stronger than laminate [(0, 90)/90]ₖ when machined edges are used. When molded edges are considered, this figure is reduced to 17%. Therefore, the stacking sequence effect for this type of laminate is more severe with machined edges than with molded edges. Also, laminate [(0, 90)/90]ₖ is the only one among the laminates tested that has lower strength with machined edges than with molded edges.

Severe Poisson mismatches across the interfaces must be avoided in the design of a laminate produced with machined edges. In this case, a tensile strength of the order of 720 MPa may be achieved for the laminates tested in this work. For laminates with molded edge, Poisson mismatch

does not seem to be an important factor. The design of the laminate must be such that no pockets of pure resin are formed at the free edge. If such pockets are not present the tensile strength will be of the order of 650 MPa for the configurations studied in this work. The existence of pockets of resin reduces the strength to a value of the order of 540 MPa. Therefore, the tensile strength of properly designed laminates with molded edges is about 10% lower than that of laminates with machined edges. On the other hand, laminates with molded edges are not as sensitive to stacking sequence effects.

The results of this work indicate that the use of molded edges is a promising alternative for the production of advanced composite laminates. The small loss in strength may be compensated by the higher productivity and the lower sensitivity to stacking sequence. However, further work is necessary to characterize the behavior of laminates with molded edges under compressive loads. Also, the fatigue behavior has to be investigated. Combinations of the molded edge approach with other techniques to improve edge delamination resistance must also be evaluated.

ACKNOWLEDGEMENTS

REFERENCES

1. Lagace, P. A., Delamination in composites: is toughness the key? *SAMPE Journal*, **22** (1986) 53-60.
2. Kim, R. Y. & Soni, S. R., Experimental and analytical studies on the onset of delamination in laminated composites. *Journal of Composite Materials*, **18** (1984) 70-80.
3. Chan, W. S., Design approaches for edge delamination resistance in laminated composites. *Journal of Composite Technology &Research*, **14** (1991) 91-6.
4. Mignery, L. A., Tan, T. M. & Sun, C. T., The use of stitching to suppress delamination in laminated composites. *Delamination and Debonding of Materials*, ASTM STP 876, ASTM, Philadelphia, PA, 1985, pp. 371-85.
5. Howard, W. E., Gossard, T. Jr & Jones, R. M., Composite laminate free-edge reinforcement with U-shaped caps. Part I: stress analysis. *AIAA Journal*, **27** (1989) 610-16.
6. Howard, W. E., Gossard, T. Jr & Jones, R. M., Composite laminate free-edge reinforcement with U-shaped caps. Part II: theoretical-experimental correlation. *AIAA Journal*, **27** (1989) 610-16.
7. Curry, J. M., Johnson, E. R. & Starnes, J. H. Jr. Effect of dropped plies on the strength of graphite-epoxy laminates. *AIAA Journal*, **30** (1992) 617-23.
8. Browning, C. E. & Schwartz, H. S., Delamination resistant composite concepts. *Composite Materials: Testing and Design (7th Conf.)*, ASTM STP 893, ASTM, Philadelphia, PA, 1986, pp. 256-65.
9. Chan, W. S., Rogers, C. & Aker, S., Improvement of edge delamination strength of composite laminates using adhesive layers. *Composite Materials: Testing and Design (7th Conf.)*, ASTM STP 893, ASTM, Philadelphia, PA, 1986, pp. 266-85.
10. Shiau, L. C. & Chue, Y. H., Free edge stress reduction through fiber volume fracture variation. *Composite Structures*, **19** (1991) 145-65.
11. Lagace, P. A., Notch sensitivity and stacking sequence of laminated composites. *Composite Materials: Testing and Design (7th Conf.)*, ASTM STP 893, ASTM, Philadelphia, PA, 1986, pp. 161-76.

Limit load carrying capacity for spherical laminated shells under external pressure

A. Muc, J. Ryś & W. Latas

Institute of Mechanics and Machine Design, Technical University of Cracow, ul. Warszawska 24,31-155 Kraków, Poland

The aim of the present paper is to discuss possible failure modes encountered in the analysis of multilayered laminated spherical shells having different shallowness parameters and subjected to external pressure. Two various approaches are proposed: the first based on the global buckling analysis and local determination of FPF for each individual layer in a laminate and the second postulating global investigations of both buckling as well as failure (in the sense of LPF) phenomena in laminated structures. The intersection of two curves corresponding to bifurcation buckling and breaking of fibres forms the limit load carrying capacity curve for the analysed shells. The first part of the work is devoted to the analytical prediction of the LLCC curves. Next, the theoretical results are compared with the numerical ones obtained with the use of strict geometrically nonlinear formulation for composite shells. Various types of materials are analysed herein, i.e. both unidirectional as well as woven roving composite materials. The analysis includes also some remarks dealing with the possibility of composite topology optimization in order to obtain the maximal LLCC.

1 INTRODUCTION

The design of structures, both isotropic or anisotropic, is always directed to the prediction of allowable loads which may be carried by plates and shells. These loads, determined with the use of various failure criteria, define the limit load carrying capacity (LLCC) of the analysed structures.

For shell structures made of FRP one can observe various types of possible failure modes which number is much higher than those for isotropic shells. It is obvious that this is mainly a result of a complex structure of composite shells. However, it is necessary to distinguish uniquely the levels of the analysis and the failure modes connected with them. In the broader sense one may describe the phenomena appearing at the level of the laminate. In this case as the types of failure modes most commonly encountered in practice one may list the following: (1) buckling (global or local), (2) ply failure (in the sense of first or last ply failure), (3) delamination (including delamination buckling), (4) material imperfections arising during production process (e.g. broken fibres, cracks in the matrix material, separation of

adjoining areas, holes and small, rigid inclusions. Each of them defines the individual LLCC for the composite structure (at the level of the laminate), whereas the lower bound of all individual failure loads (in the sense of the above criteria) can be used by a designer in order to identify the safe region and to establish a procedure for geometrical dimension calculations of the structure, and finally give the global LLCC.

The second level, narrower than the previous one, is directly associated with the phenomena appearing at the level of a single ply in the laminate. Utilizing this approach the failure modes of composite materials can be described as breaking of fibres, cracking of the matrix, debonding or bifurcation of individual fibres in the matrix. Each failure mode may lead to ply failure. However, the consequence of the individual failure mode will be of great importance in determining LPF. Thus, at the ply level, failure phenomena can be described by a variety of failure criteria connected directly with the type of failure mode — so called direct mode determining theories.

Since our analysis will be carried out at the level of the laminate it is necessary to emphasize

here that the FPF criteria used characterize only one possible failure mode at the narrower level of a ply, i.e. breaking of fibres.

The aim of the present paper is to determine and analyse the global LLCC taking into account buckling (the stability criterion) and ply failure (in the sense of the first ply failure) loads for doubly-curved laminated spherical shells of revolution, clamped at their edges and subjected to external pressure. The shell wall is built of N layers having identical material properties and thicknesses but they may have different fibre orientations θ_i with respect to an arbitrary shell meridian ($\theta_i = 0°$ denotes the direction parallel to the shell meridian).

In the first part of the work two different approaches for the determination of LLCC curves are presented and discussed. Then, we demonstrate the limits of possible FPF analysis for axisymmetric laminated shell or plated structures closed at the apex, based on the shallow shell equations. The last part of the paper deals mainly with numerical determination of the individual LLCC in the sense of FPF with the use of geometrically nonlinear shell theory. Various quadratic (polynomial) and linear (limit) FPF criteria are taken into consideration, such as the Tsai–Wu, the Hoffman, ε_{max}, σ_{max} criteria, in order to obtain the lower bound of the FPF pressures and finally, the lower bound is compared to pressures corresponding to bifurcation buckling.

In the literature shell failure analysis (in the sense of FPF criteria) has been carried out from the point of view of laminated shell theory. In this area different problems have been discussed in order to study the behaviour of composite shells having various forms (torispheres and hemispheres) and (or) loading and boundary conditions (see, for example, Refs 1–3). The present paper is an extension of considerations presented in Ref. 4.

2 VARIANTS OF PLY FAILURE ANALYSIS FOR THINWALLED STRUCTURES

Since buckling problems for doubly-curved laminated shells are broadly discussed in many papers (see, for example, Ref. 5) we do not intend to repeat it again. Briefly speaking, we employ here Sander's geometrically nonlinear relations (large deflections) based on the Love–Kirchhoff hypothesis and using a global approach both in buckling and FPF analysis. The solutions are obtained

numerically with the use of a computer code presented, for example, in Ref. 5.

FPF analysis of composite structures is a completely separate problem complicated, in addition, by the composite topology. The basic difficulty manifests itself in the formulation of the failure criteria for each individual ply in the laminate. Therefore, it requires the correct determination and representation of failure envelopes in the proper strain or stress spaces. In general, thinwalled composite shell deformations are completely described by the set S of M kinematical variables (their number depends on the type of kinematical hypothesis taken into consideration, $M = 3$ in our case) determined in the global coordinate system (x, y, z) connected with the curvilinear structure surface. The failure criterion is defined in the local coordinate system (ξ_i, η_i, z) connected with the ith layer in the laminate and is represented via the quadratic criterion in the following form:

$$\Psi(\sigma'^i) = \sigma'^i{}^{t} {}'^{r}A_i\sigma'^i + B_i\sigma'^i - 1 = 0 \qquad (1)$$

It forms a surface in the stress space σ'. The terms in the matrices A_i and B_i are evaluated experimentally. The subscripts (i) over the symbols denote values corresponding to the ith layer in the laminate, whereas $'$ means variables determined in the local coordinate system. The classical transformation law from the local to the global system allows one to obtain the analogous Ψ surface in the stress space σ:

$$\Phi(\sigma') = \sigma'{}^{t} {}'^{r}A\sigma' + B\sigma' - 1 = 0 \qquad (2)$$

The relationships used to transform stress and strain from one coordinate system to another are as follows:

$$\sigma' = [T'] \sigma'' \qquad (3)$$

and

$$\varepsilon' = [T'] \varepsilon'' \qquad (4)$$

where the transformation matrix $[T']$ is defined in the following way:

$$[T'] = \begin{bmatrix} m^2 & n^2 & -2mn \\ n^2 & m^2 & 2mn \\ mn & -mn & m^2 - n^2 \end{bmatrix}, \quad \begin{array}{l} m = \cos(\theta_i), \\ n = \sin(\theta_i) \end{array} \qquad (5)$$

The classical approach in the sense of FPF or LPF is based on the determination of all M kinematical variables, with the aid of analytical or numerical procedures, then evaluation of the strain tensor ε' in the (x, y, z) coordinate system.

the transformation of its components with the use of relations (4) to the material system and finally on the check whether the calculated stress field σ'^i belongs or not to the interior of the surface (1). The analysis should be carried out independently for each individual ith ply in the laminate. The sequence of procedures is drawn schematically on the left side of Fig. 1. The disadvantage of such an approach is obvious — the necessity of location of FPF for each layer separately. After FPF the configuration of the laminate is changed by the elimination of the ith layer which failed. LPF occurs after the structure is degraded to the point where it is no longer capable of carrying additional loads. In the LLCC analysis the problem becomes much more complicated as the bifurcation buckling phenomenon is taken into account. The elimination of a single layer in the laminate causes the structure to be thinner and it automatically accelerates the possibility of global buckling.

The other approach, demonstrated also in Fig. 1, is based directly on the relation (2). Assuming that the function $\Phi(\sigma')$ associated with possible failure modes may be treated in the identical way to the potential in the theory of plasticity and using Drucker's postulate, one can find the strains related to the stresses by means of the relations:

$$\varepsilon_{kl}^i = -\eta \frac{\partial \Phi}{\partial \sigma_{kl}'} \qquad (6)$$

In the theory of plasticity the above relation is called the flow law associated with the yield condition. In our case it implies that the strain vector suitably laid off in stress space is orthogonal to the FPF surface for the ith layer. However, the ortho-

gonality criterion is fully confirmed experimentally in plasticity only. Solving the linear system of eqns (6) with respect to the stress field σ_{kl}', and then inserting the result in eqn (2) one can determine the unknown coefficient η. Finally, the stress field on the failure surface Φ can be expressed by the following relation:

$$\sigma_{kl}' = F(\varepsilon_{kl}^i) \qquad (7)$$

where F denotes a nonlinear algebraic function. It is known that for thinwalled structures the stress resultants, represented by the matrix $[P]$, are commonly used in the description of their behaviour. Therefore, let us integrate eqn (7) over the thickness of the ith layer, then sum over the total number of layers N and finally the result can be written as:

$$[P]_{kl} = \sum_{i=1}^{N} \int_{z_i} \sigma_{kl}^i |z| dz = \sum_{i=1}^{N} \int_{z_i} F(\varepsilon_{kl}^i) |z| dz \qquad (8)$$

In this way one can determine the global failure envelope (in the sense of LPF) in the space of the stress resultants $[P]$ for the laminate having the prescribed composite topology. In addition, the proposed concept is based directly on the experimental data, i.e. it is necessary to know values of the strain field ε_{kl}^i corresponding to the failure of the ith layer in the laminate. The above method allows us also to compare easily the individual LLCC curves corresponding to bifurcation buckling or ply failure and to determine the global LLCC in the space of the stress resultants or in any subspace of $[P]$ arbitrarily chosen by the designer.

3 DEFORMATIONS OF LAMINATED SPHERICAL SHELLS

It is well known that one can easily find a great number of works dealing with the deformation analysis of orthotropic spherical shells. We would like to cite here as the reference the Grigorenko *et al.*[6] monograph giving a broad review of the state of knowledge in this area. Of course, one can simply adapt the results presented there to laminated composite shells which in the case of symmetric laminates are equivalent to orthotropic shells having material constants varying with fibre orientations θ_i. In general, such solutions are expressed by a hypergeometric series or other special functions (in the case of shallow spheres)

Set of kinematical variables - S

$\sigma(\text{or } \varepsilon)$

Experimental data $\Psi^{(i)}(\sigma') = 0$

$\sigma' = T^{-1}\sigma$

$\sigma = T\sigma'$

$\Psi^{(i)}(\sigma') > 0$

$\Psi^{(i)}(\sigma) = 0$

$\varepsilon^{(i)} = -\eta d\Psi^{(i)}/d\sigma$

$\Psi^{(i)}(\sigma') > 0$ N-1 layers

Ply failure or buckling

P envelope laminate

LLCC
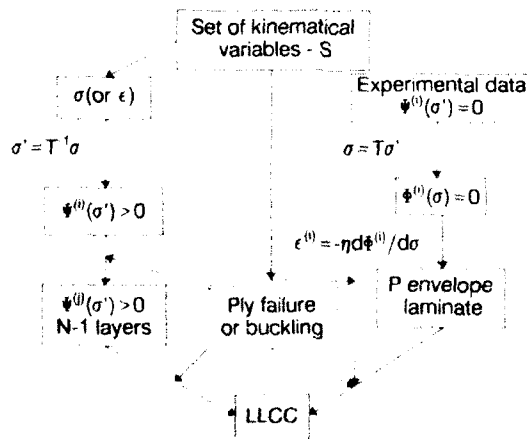
Fig. 1.

and take almost identical form to those presented by Flugge[7] for isotropic hemispheres. However, there is one difference involving a lot of problems. It can be easily explained with the help of Marguerre's shallow shell equations. In the case of axisymmetric deformations of shallow spherical shells made of unidirectional fibre reinforced plastics having mid-plane symmetry the first equation of equilibrium:

$$\frac{d(rN_r)}{dr} + N_o = 0 \tag{9}$$

can be expressed in the following explicit form:

$$r u_{,rr} + u_{,r} - \beta^2 \frac{u}{r} = f(w_{,rr}, w_{,r}, r) \tag{10}$$

where the orthotropy parameter β is defined as follows:

$$\beta = \sqrt{\frac{A_{22}}{A_{11}}} \tag{11}$$

u, w denote axial and normal displacements, respectively. r is the distance from the axis of symmetry and f is a function. The components of the strain fields are written in the classical form:

$$\varepsilon_r = \frac{du}{dr} + \frac{r}{R}\frac{dw}{dr} + \frac{1}{2}\left(\frac{dw}{dr}\right)^2, \quad \varepsilon_o = \frac{u}{r} \tag{12}$$

One can simply solve the homogeneous differential eqn (10)

$$u(r) = dr^\beta + br^{-\beta} \tag{13}$$

Since the displacements u finish at the apex of the shell the constant b must be identically equal to zero. Then, inserting the relation (13) into (12) one can find that both components of the strain field tend (or not) to infinity at the apex ($r = 0$) depending on the value of the orthotropy parameter β. It is obvious that for laminated shells closed at the apex the analysis of FPF or LPF may be carried out for such a composite topology which satisfies the inequality:

$$\beta \geq 1 \tag{14}$$

In the opposite case the application of any non-zero load may lead to early failure. The inclusion of geometrical nonlinearities into the considerations does not alter the above conclusion. Figure 2 presents the distributions of axial u (Fig. 2(a)) and normal displacements w (Fig. 2(b)) obtained
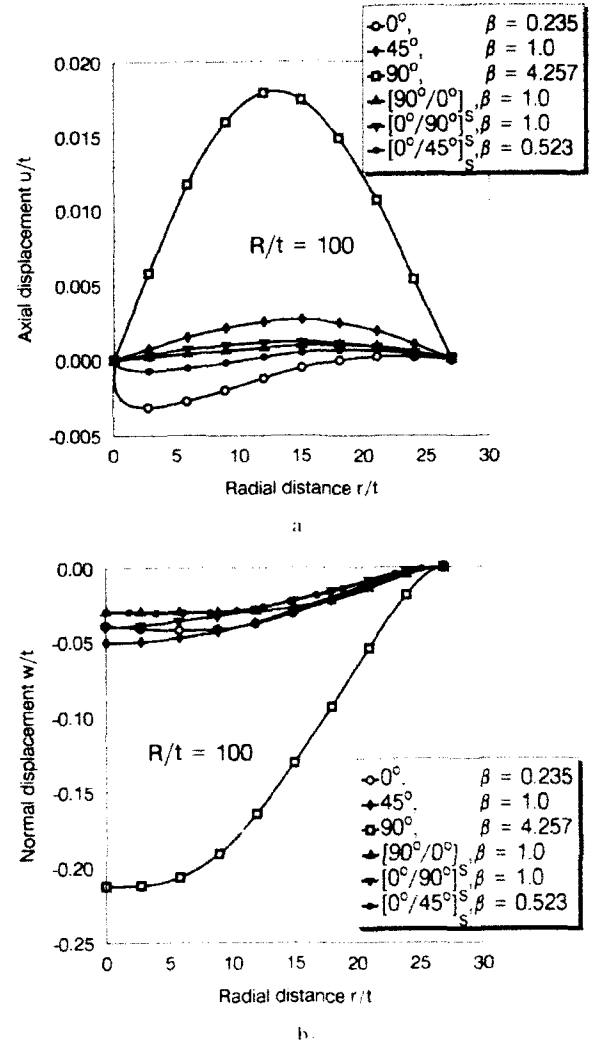
Fig. 2. Displacements of shallow $\lambda = 5$ spherical shells made of unidirectional CFRP. (a) Axial displacement u; (b) normal displacement w.

with the use of numerical procedures described in Ref. 5. As may be seen the parameter β changes the value of derivative du/dr from infinity ($\beta < 1$) to a positive number ($\beta \geq 1$). It is associated with the growth of the normal displacements w. An identical result can be obtained for deep shells. In that case the solution for axial displacements u is represented by a hypergeometric series multiplied by the function $\cos^\beta(\phi)$ that finally leads to the same conclusion as for shallow laminated shells. In general, for composite shells closed at the apex and having mid-plane symmetric orientations the condition (14) reduces significantly the field of kinematically admissible laminate configurations. This is very important from the viewpoint of any optimization problems in this area. On the other

hand, one can state that this is mainly the result of the inconsistency encountered herein in the shell theory. However, we do not intend to dwell on it in this paper.

4 NUMERICAL RESULTS

In order to illustrate the problems discussed above and explain the possible failure mechanisms of composite spherical shells a series of numerical examples have been solved. They have dealt with both woven roving composite materials and unidirectional ones. The mechanical properties of the materials discussed are given in Table 1.

By the simple analysis of all terms of the stiffness matrix one may notice that for unidirectional FRP their coefficients have no symmetry (from the definition) with respect to the angle θ in the interval of its admissible variations. However, due to the equality of E_1 and E_2 woven roving materials possess such a symmetry with respect to 45°. As will be seen later it may affect significantly the possible type of failure mode.

The procedure for determining the strength or buckling (LLCC) of the laminate involves an incremental load analysis. For a given load, the strains in each ply can be calculated with respect to the material (on axis) coordinates (eqns (3)–(5)). These strains (or stresses) are inserted into the appropriate failure criterion to determine if first ply failure has occurred within a lamina. It is checked independently on the top and bottom surfaces of each layers in the laminate. When failure does not occur, the external load increases until buckling is reached. Once the mode of failure (LLCC) is known, the numerical procedure is terminated, though for shells which fail in the sense of FPF the loading process may be continued up to LPF or buckling failure. If FPF occurs the structure is degraded and the total thickness of the shell wall is equal to $(N-1)t/N$ (Fig. 1). For angle-ply laminates having identical

fibre orientations $\pm\theta$ in each layer it leads automatically to FPF of the next layer (for the same value of the external load) and in this way it is equivalent to LPF. With the regard to buckling analysis the appearance of FPF reduces the shell resistance by the factor $(N-1/N)^2$.

All composite spherical shells analysed herein are described by the radius of curvature R, total thickness t and the shallowness parameter expressed in the following way:

$$\lambda = \sqrt[4]{12(1 - \nu_{12}\nu_{21})}\frac{a}{\sqrt{Rt}} \qquad (15)$$

Moreover, the failure pressures p_1 reported in the following figures are stated in their normalized form; they are related to the following value:

$$\bar{\lambda} = \frac{2\sqrt{E_1 E_2}}{\sqrt{3(1 - \nu_{12}\nu_{21})}}\left(\frac{t}{R}\right)^2 \qquad (16)$$

This is done to remove the effects of varying material constants and changing aspect ratios t/R.

Buckling and FPF analysis of spherical shells involves many geometric and material parameters. Therefore, generation of results which account for all effects requires extensive parametric studies. The results presented herein are restricted to specific numerical examples in order to illustrate the applicability of the present model, and to assess the effect of FPF and buckling on the global spherical shell resistance.

4.1 Woven roving composite materials

Since woven roving composite materials are characterized by identical values of Young's modulus in parallel and perpendicular directions to the fibres and buckling pressures p_b for composite clamped hemispheres can be represented in the same way as for isotropic shells:

$$p_b = 0.79\frac{2E}{\sqrt{3(1 - \nu^2)}}\left(\frac{t}{R}\right)^2 \qquad (17)$$

Table 1. Ply mechanical properties

Material	E_1	E_2	G_{12}	ν_{12}	X_t	X_c	Y_t	Y_c	S
	(GPa)				(MPa)				
Unidirectional CFRP	203	11·2	8·4	0·32	3500	1540	56	150	98
Unidirectional GFRP	38·6	8·27	4·14	0·26	1062	610	31	118	72
Woven roving GFRP	15·1	15·1	3·1	0·16	353	304	353	304	35

where in terms of composite materials constants E and ν are defined in the following way:

$$E = A_{11}/t = A_{22}/t = U_1 + U_3\cos(4\theta), \quad \nu = \frac{A_{12}}{A_{11}}$$

$$= \frac{U_4 - U_3\cos(4\theta)}{U_1 + U_3\cos(4\theta)} \qquad (18)$$

The dimensionless pressures p_t for the clamped angle-ply axisymmetric hemispherical shells having various fibre orientations related to an arbitrary shell meridian are compared with analytical predictions given by eqns (17) and (18) (Fig. 3). The set of numerical results shows the distributions of: bifurcation pressures (the wavelength number $n > 0$), pressures corresponding to axisymmetric collapse ($n = 0$) and those corresponding to FPF in the sense of Tsai–Wu's criterion (in the surrounds of $\theta = 45°$) being the lower bound of FPF pressures determined with the use of four criteria. As may be seen for the analysed ratio $t/R = 0.01$, bifurcation buckling loads are the global lower bound of the plotted curves and in this case correspond to the LLCC. In addition, that curve can be well approximated by the analytical solutions. However, for t/R ratios higher than 0.01, FPF is a dominating failure mode for the structure considered (Fig. 4). It is caused by the fact that buckling pressures are proportional to $(t/R)^2$ (a straight line in the plot), whereas FPF pressures are proportional to t/R (a hyperbola in fig. 4). The results are generated for the weakest and the strongest configurations of the shell wall (45° and

0°, respectively). Thus, one can state that for hemispheres made of woven roving composites bifurcation buckling forms completely the LLCC curve up to $t/R = 0.01$, and for $t/R \geq 0.02$, FPF precedes bifurcation buckling (for angle-ply laminates FPF is equivalent to LPF). In this case FPF always occurs at the clamped edge (identically as for isotropic shells) and is caused by compressive loads. Similar effects are observed for shallow spherical shells. However, for shallow shells the value of the t/R ratio has a much weaker influence on the appearance of the first ply failure, and its effect increases as the shallowness parameter λ increases.

For angle-ply laminates made of GFRP woven rovings (material 3 in Table 1), an arbitrary t/R ratio and the shallowness parameter λ, the maximal limit load (LLCC) is always reached at $\theta = 0°$. The same situation occurs for multilayered shells having various but symmetric with respect to mid-plane orientations. It may be simply obtained from eqn (17) and the results presented in Fig. 4. However, as the material properties of woven roving composites will change, the maximal limit load will be located in the interval [0°, 22.5°].

4.2 Unidirectional composite materials

It is well known that unidirectional composites may offer much higher maximal buckling and FPF resistance than structures made of woven roving composites due to the different values of Young's moduli E_1 and E_2. Figure 5 shows the effect of fibre variations on the LLCC for angle-ply spheri-
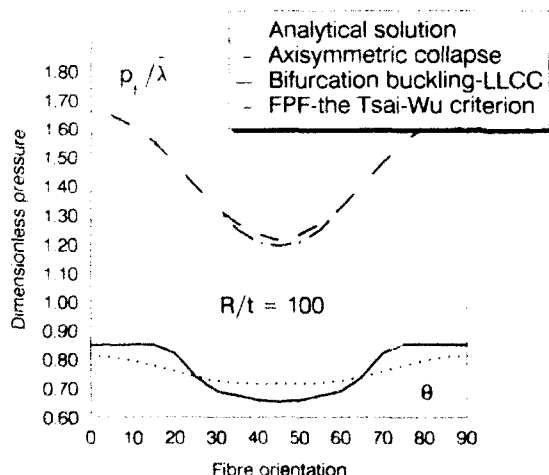
Fig. 3.   Distributions of failure pressures for angle-ply hemispheres made of woven roving GFRP.
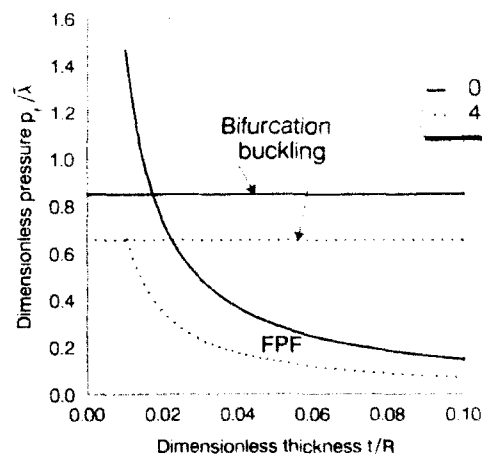
Fig. 4.   Influence of the t/R ratio on the type of failure mode

cal shells. As may be noticed both material properties of unidirectional FRP as well as the values of the shallowness parameters λ has visually no effect on the character of the LLCC curves, irrespective even of the t/R ratio. In the interval $[0°, 45°]$ the first ply failure always occurs at the shell apex; the values of the critical loads are very low. It is in very good agreement with the theoretical considerations presented in Section 3 of this paper. However, according to the results presented there the pressure p_f should be identically equal to zero in the analysed range of fibre orientation variations. In the plots presented the maximum is always reached for $\theta = 45°$ and it corresponds to the isotropic state $(A_{11} = A_{22}, D_{11} = D_{22})$. In this case the deep spherical shells (Figs 5(b), 5(c)) fail by a bifurcation buckling mode $n > 0$, whereas shallow shells (Fig. 5(a)) fail by axisymmetric collapse $(n = 0)$. For deep spherical shells as the value of the angle θ increases the failure mode switches to an axisymmetric one and, in addition a sharp drop in the limit load is noticed. This drop continues until it reaches a constant value. However, one can observe also a *narrow region* where FPF precedes axisymmetric collapse. It is worth noting that for the analysed aspect ratio $R/t = 100$ the curve corresponding to the axisymmetric collapse almost coincides with that for FPF in the sense of the Tsai–Wu criterion and in this way is denoted in Fig. 5. In the examples analysed the Tsai–Wu FPF criterion almost always gives the lowest values of the failure pressures. In general, the differences in the values of FPF pressures determined with the use of four failure criteria are almost negligible. It is obvious especially in Fig. 5(a), being the most representative plot which gives the possibility of distinguishing the values p_f for various FPF criteria analysed herein.

Similarly as for woven roving composite materials for thicker shells $(t/R \geq 0.02)$ FPF becomes the dominating failure mode and precedes bifurcation buckling. However, for unidirectional FRP a reduction in the pressure p_f is not proportional to the t/R ratio (Fig. 5(c)).

For various fibre orientations θ and the ratio $R/t = 50$ the type of fibres breaking is shown in Fig. 6. At $\theta = 45°$ the failure mode is typical for isotropic shells, occurs at the clamped edge and is caused by longitudinal compressive loads in the fibre direction. As the value of fibre orientations increases the rapid drop in the pressure p_f is associated with the alteration of failure mode and of its localization on the shell meridian. For $\theta = 50°$ FPF
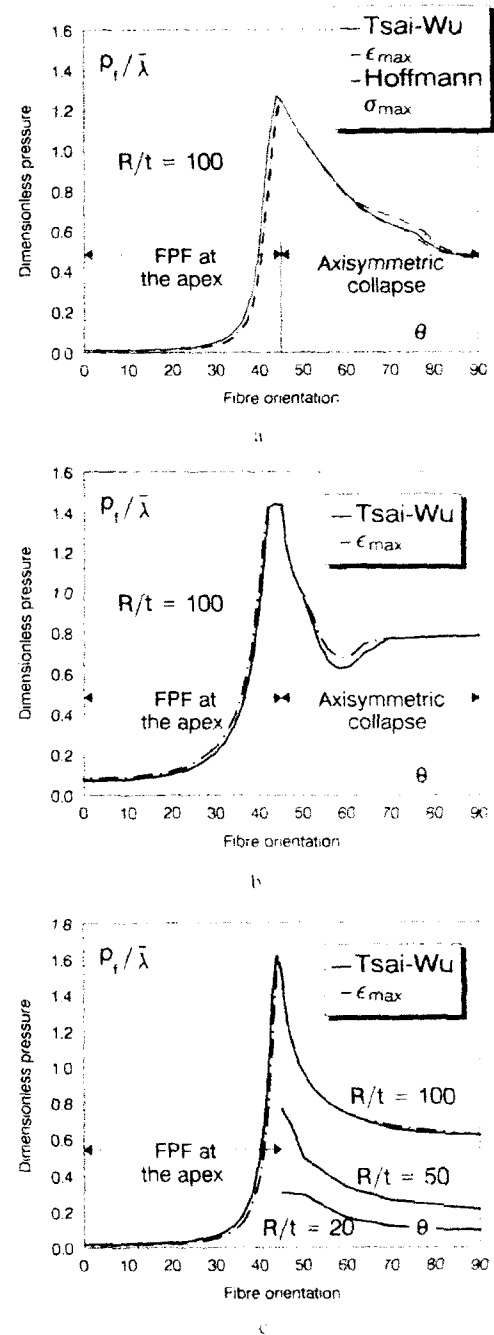
Fig. 5. Variations of limit load carrying capacity LLCC with fibre orientations: a—spherical cap $\lambda = 5$ — unidirectional CFRP; b—hemisphere — unidirectional GFRP; c—hemisphere — unidirectional CFRP.

occurs at the shell apex and is caused by tensile loads transverse to the fibre. Then, the position of FPF on the shell meridian moves from the apex to the clamped edge as the value of θ increases to 90°. It is worth remembering again that for angle-ply laminates FPF is automatically equivalent to LPF. Thus, the FPF position on the shell meridian
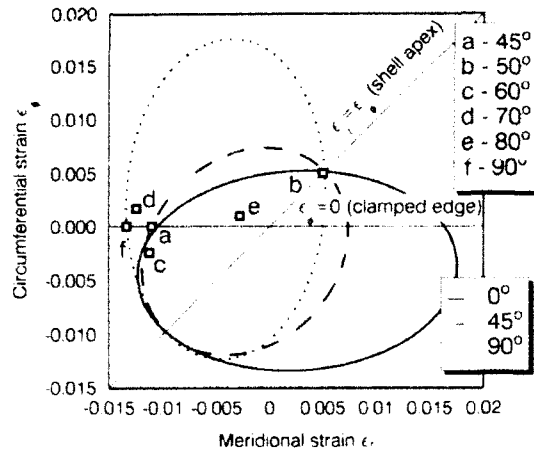
Fig. 6. Positions of FPF on the shell meridian for hemi-
spheres made of CFRP $t/R = 0.02$.

has no appreciable effect on the value of FPF limit
loads determined with the use of four failure
criteria. It seems that it is caused by the localiza-
tion of the FPF $\varepsilon_t - \varepsilon_o$ plane. The failure occurs in
the neighbourhood of the line $\varepsilon_t = \varepsilon_o$ or $\varepsilon_o = 0$
where the limit values for four criteria (linear or
quadratic) are almost identical (Fig. 6).

The analysis of angle-ply laminates is treated as
the starting point toward the analysis of multi-
layered unidirectional laminates especially from
the point of view of optimization (maximization)
of the pressures p_t corresponding to LLCC. In the
optimization of the buckling resistance of lami-
nated structures the commonly used approach
based on the lamination parameters scheme has
been introduced by Miki' and Fukunaga and
Vanderplaats.' For mid-plane symmetric lami-
nates they propose to introduce four independent
lamination parameters describing entirely the
composite topology. They are defined in the fol-
lowing fashion:

$$\xi_1 = \frac{1}{t} \int_{-t/2}^{t/2} \cos 2\alpha(z)\,dz,$$

$$\xi_2 = \frac{1}{t} \int_{-t/2}^{t/2} \cos^2 2\alpha(z)\,dz$$

$$\xi_9 = \frac{12}{t^3} \int_{-t/2}^{t/2} \cos 2\alpha(z)\,z^2\,dz,$$

$$\xi_{10} = \frac{12}{t^3} \int_{-t/2}^{t/2} \cos 2\alpha^2(z)\,z^2\,dz$$

(19)

where

$$\alpha(z) = \pm \theta_i \text{ for } t_i \leq z \leq t_{i+1} \qquad (20)$$

The feasible regions of in-plane and out-of-plane
lamination parameters are, respectively,
expressed as follows:

$$-1 \leq \xi_1 \leq 1, \; \xi_1^2 \leq \xi_2 \leq 1, \; -1 \leq \xi_9 \leq 1, \; \xi_9^2 \leq \xi_{10} \leq 1 \qquad (21)$$

and for the in-plane lamination parameters
(ξ_1, ξ_2) they form parabolas, whereas for out-of-
plane parameters (ξ_9, ξ_{10}) are restricted by the
values of ξ_1, ξ_2. A point on the parabola $\xi_2 = \xi_1$
corresponds to an angle-ply laminate $\pm \theta$. For
example the point (0,0) corresponds to a 45° lami-
nate and (0, 1) to a quasi-isotropic laminate.

As is demonstrated by Muc[1] the above para-
meters can be successfully used in the optimiza-
tion problems of buckling resistance for laminated
doubly-curved shells under external pressure.
However, such a procedure cannot be directly
repeated in the analysis of FPF since initial failure
of a single layer in the laminate depends entirely
on the stacking sequences and on the magnitude
of bending effects. For hemispheres made of uni-
directional CFRP and having the t/R ratio equal
to 0.01 the laminate [0°,90°], fails by bifurcation
buckling for $p_c = 4.98$ MPa, whereas for [90°,0°],
FPF occurs at the bottom surface and $p_c = 5.53$
MPa. However, on the plane (ξ_1, ξ_2) both lami-
nates are described by the same point (0,1).
Therefore, one can apply the lamination para-
meter plane for the presentation of optimization
results only but not for looking for the optimal
composite topology. In addition, it is worth men-
tioning here that the parabola (21) is cut off by the
restriction (14). Figure 7 is a plot of the maximal
pressures corresponding to the LLCC of four-
layered [θ₁, θ₂], hemispherical shells. As may be
seen the maximal LLCC is reached for the quasi-
isotropic state (the point (0,1)). Let us notice that
for angle-ply shells the fibre orientation 45° cor-
responding to the maximal LLCC represents also
the isotropic state.

5 CONCLUDING REMARKS

Two procedures are presented for the efficient
analysis of the limit load carrying capacity of
anisotropic shells of revolution closed at the apex.
From the point of view of FPF the limits of the
possible analysis for axisymmetric laminated
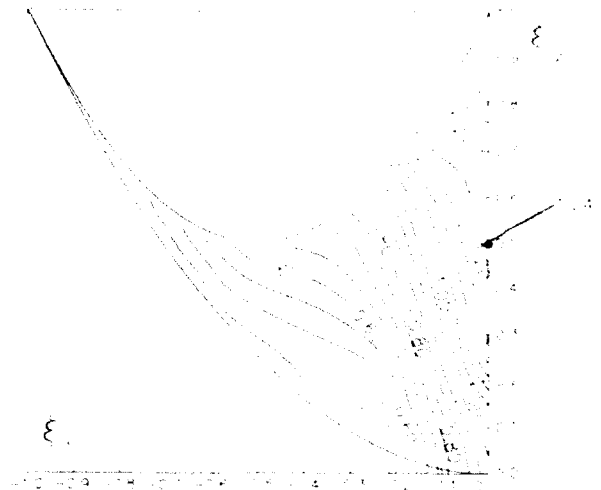
Fig. 7. Contour plots of the maximal LLCC for hemispherical shells made of CFRP $t/R = 0.01$.

shells closed at the apex are strictly determined by the value of the orthotropy parameter $\beta = \sqrt{A_{22}/A_{11}}$. If $\beta < 1$ then FPF always occurs at the apex even for infinitesimally small values of the external pressure. For the opposite case doubly-curved laminated shells can fail both by bifurcation as well as by breaking of fibres (FPF). The type of failure mode detected herein is primarily controlled by the value of the t/R ratio, and not by material properties or shallowness parameter λ. For $t/R \leq 0.01$ bifurcation buckling is a lower bound of possible failure pressures (in the sense of buckling and FPF criteria) and forms the LLCC curves for the structures analysed, whereas for $t/R \geq 0.02$ FPF is a dominating failure mode. The value of critical loads p_1 is not appreciably affected by the type of FPF criteria used in the analysis due to the localization of FPF on the strain plane in the global coordinate system. The numerical experience exhibits evidently that in the majority of cases the Tsai–Wu criterion gives the lower estimations of failure pressures. The exceptions occurs mainly for uni-directional composites and layers oriented at 45–50° where the criterion of maximal strains is the best (lowest) bound of failure pressures.

However, it has been found that the FPF is mainly associated with breaking of fibres on arbitrary points lying on the shell meridian—not only at the clamped edge as for isotropic shells—and is caused by longitudinal compressive loads or tensile loads transverse to the fibres.

The magnitude of limit loads (LLCC) is strictly connected with the composite topology. With regard to the possible increase of LLCC for spherical shells the optimization analysis has proved that quasi-isotropy is the best solution for unidirectional FRP.

ACKNOWLEDGEMENT

REFERENCES

1. Sacharov, A. S. *et al.*, Numerical modelling of failure for composite multilayered shells. *Mechanics of Composite Materials* 1989 459–65 (in Russian).
2. Galletly, G. D. *et al.*, Buckling of FRP domes under external pressure. *Composite Construction in Marine Structures*, London 1990 148–65.
3. Muc, A. & Szybiński, B., Failure and buckling analysis of doubly-curved shells made of FRP. *Textile Composites in Building Construction*, Paris 1992 237–47.
4. Muc, A., Failure modes of laminated axisymmetric shells of revolution subjected to external pressure. *Composite Structures — 5*, Elsevier, London, 1989, pp. 117–32.
5. Muc, A., Buckling of doubly-curved laminated shallow shells of revolution — formulation and numerical examples. *ZAMM*, **72** 1992 T67–72.
6. Grigorenko, J. M. & Vasilenko, A. T., *Methods of Shell Analysis, Vol. 4*, Kiev, 1981 (in Russian).
7. Flugge, W., *Theory of Shells*, Berlin, 1972.
8. Miki, M., Optimum design of fibrous laminated plates subjected to axial compression. *Proc. 3rd Japan–US Composite Materials Conf.*, Tokyo, 1986, pp. 673–81.
9. Fukunaga, H. & Vanderplaats, G. N., Stiffness optimization of orthotropic laminated composites using lamination parameters. *AIAA J.*, **29** 1991 641–8.
10. Muc, A., Optimization of composite topology for doubly-curved laminated shells under buckling constraints. *Proc. IUTAM Symposium Optimal Design with Advanced Materials*, Amsterdam, 1993, pp. 231–46.

Optimisation of laminated cylindrical pressure vessels under strength criterion

S. Adali, E. B. Summers & V. E. Verijenko

Department of Mechanical Engineering, University of Natal, Durban 4001, South Africa

An approach for the optimisation of symmetrically laminated cylindrical pressure vessels is presented. The analysis is based on the membrane theory of shells and the optimisation is carried out with respect to the fibre orientations and thickness distributions subject to the Tsai–Wu failure criterion. The approach is equally applicable to balanced and unbalanced symmetrically laminated shells. Two examples are considered which involve the design of cylindrical shells for maximum burst pressure and minimum weight. Numerical results are given for pressure vessels subject to internal pressure only and to a combination of internal pressure and liquid pressure. The effect of axial loading and torque on the designs is discussed.

1 INTRODUCTION

A major advantage of fibre-reinforced composite materials is the large number of design variables available to the designer. To realise this potential and to maximise the benefits which composites can offer, the design has to be tailored to the specific requirements of the problem. Optimisation of the design is an effective way of achieving this goal. The present article addresses the problem of optimally designing symmetrically laminated composite pressure vessels using fibre orientation and wall thickness as design variables. The lamination can be balanced or unbalanced. The balanced case refers to a lamination in which the layers with the same positive and negative fibre angles balance each other out.

Previous studies involving the optimisation of laminated pressure vessels include Refs 1–10. In Ref. 1, the minimum mass of fibres is determined subject to a tensile strength condition assuming inextensible fibres. Designs in Ref. 2 are based on Flügge's theory of shells with the Tsai–Hill failure criterion employed as the strength condition. Optimal designs based on criteria other than a failure one are given in Refs 3–5. Optimum shapes of filament-wound pressure vessels are determined subject to the Tsai–Hill failure criterion in Ref. 6. Optimal fibre orientations for cylindrical pressure vessels are obtained by Fuku-

naga and Chou for balanced stacking sequences. Karandikar *et al.* considered a multi-objective approach to the design of composite pressure vessels by including deflection, weight and volume in the performance index. In Refs 9 and 10, Donnell's shell theory is used to investigate the effect of temperature and fuzzy strength data, respectively, on the optimal design of laminated pressure vessels.

The present study is concerned with the optimisation of composite pressure vessels subject to the Tsai–Wu failure criterion and involving problems of maximum internal pressure and minimum weight. In the first problem, the fibre orientation is determined for balanced and unbalanced laminations to maximise the internal pressure. The effects of axial and torsional forces on the optimum design are discussed. It is shown that the axial force affects the optimum fibre angle differently for shells with single and multiple layers.

In the second problem, the design objective is the minimisation of the weight of a liquid-filled pressure vessel taking both the fibre orientation and the wall thickness as design variables. Both the constant and variable wall thickness cases are discussed. Comparative numerical results are presented for single and multiple layered vessels. It is noted that methods used in both design problems can be easily implemented in practical design situations.

305

2 BASIC EQUATIONS

The pressure vessel is modelled as a symmetrically laminated cylindrical shell of thickness H, length L and radius R, where R refers to the radius of the middle surface. The shell is constructed of an even number of orthotropic layers of equal thickness, t. The fibre orientation θ is defined as the angle between the fibre direction and the longitudinal axis x. The fibre angles are orientated symmetrically with respect to the middle surface such that $\theta_k = (-1)^{k-1}\theta$ for $k \leq n/2$ and $\theta_k = (-1)^k\theta$ for $k \geq n/2+1$ where $k = 1, 2, \ldots$, n is the layer number and n is the total number of layers. It is noted that $n = 2$ corresponds to a single lamina of thickness $H = 2t$ and fibre orientation θ. The coordinate axes x, ϕ and z refer to the longitudinal, circumferential and radial directions respectively, with the origin lying in the middle surface of the shell.

Due to the symmetry of the lamination, the force resultants in the geometric coordinate axes are given by

$$[N] = [A][\varepsilon] \tag{1}$$

where

$$[N] = \begin{pmatrix} N_x \\ N_\phi \\ N_{x\phi} \end{pmatrix}, \quad [A] = \begin{pmatrix} A_{11} & A_{12} & A_{16} \\ A_{12} & A_{22} & A_{26} \\ A_{16} & A_{26} & A_{66} \end{pmatrix},$$

$$[\varepsilon] = \begin{pmatrix} \varepsilon_x \\ \varepsilon_\phi \\ \gamma_{x\phi} \end{pmatrix} \tag{2}$$

In eqn (2), A_{ij} are the extensional stiffnesses given by $A_{ij} = H\bar{Q}_{ij}(\theta)$ for $i, j = 1, 2$ and $i = j = 6$, $A_{i6} = 2t\bar{Q}_{i6}(\theta)$ for unbalanced laminates and $A_{i6} = 0$ for balanced laminates with $i = 1, 2$. Also in eqn (2), ε_x, ε_ϕ and $\gamma_{x\phi}$ denote the normal and shear strains. Here $\bar{Q}_{ij}(\theta)$ is the transformed reduced stiffness component.

The stress–strain equations for the kth orthotropic layer are given by

$$[s^k] = [Q^k][\varepsilon] \tag{3}$$

where $[\varepsilon] = [A]^{-1}[N]$ from eqn (1), and

$$[s^k] = [\sigma_x^k \quad \sigma_\phi^k \quad \tau_{x\phi}^k]^T$$

denotes the stress vector in the $x\phi$ coordinate system.

The stress vector in the material coordinate system, denoted by $[\sigma^k] = [\sigma_1^k \quad \sigma_2^k \quad \tau_{12}^k]^T$, is obtained from the geometric stress vector s^k via the matrix transformation

$$[\sigma^k] = [T^k][s^k] \tag{4}$$

where $[T^k] = [T(\theta_k)]$ denotes the transformation matrix for the kth layer. From eqns (3) and (4) it follows that

$$[\sigma^k] = [T^k][Q^k][\varepsilon] \tag{5}$$

The design against failure is determined by employing a suitable failure criterion. In this study, the Tsai–Wu failure criterion[11] is used which stipulates that for non-failure the constraint

$$F_{11}\sigma_1^{k\,2} + F_{22}\sigma_2^{k\,2} + F_{66}\tau_{12}^{k\,2} + 2F_{12}\sigma_1^k\sigma_2^k$$
$$+ F_1\sigma_1^k + F_2\sigma_2^k - 1 \leq 0 \tag{6}$$

should be satisfied where the strength parameters F_{11}, F_{22}, F_{66}, F_{12}, F_1 and F_2 are given by

$$F_{11} = \frac{1}{X_t X_c}; \quad F_{22} = \frac{1}{Y_t Y_c}; \quad F_{66} = \frac{1}{S^2};$$

$$F_1 = \frac{1}{X_t} - \frac{1}{X_c}; \quad F_2 = \frac{1}{Y_t} - \frac{1}{Y_c}; \tag{7}$$

$$F_{12} = -\frac{1}{2}\sqrt{F_{11}F_{22}}$$

where X_t, X_c, Y_t and Y_c are the tensile and compressive strengths of the composite material in the fibre and transverse directions, and S is the in-plane shear strength.

The problem formulation and the performance index depend on the nature of the specific design problem. The problem statement involves maximizing or minimizing a cost function subject to the strength constraint given by eqn (6). The optimisation procedure is applied to two design problems.

3 DESIGN FOR MAXIMUM INTERNAL PRESSURE

We consider a cylindrical pressure vessel with closed ends and subject to an internal pressure p, axial force F and torque T. The first design problem involves determining the fibre orientation θ so as to maximise the internal pressure p for a given laminate thickness H under the forces F and T such that the optimal design satisfies the strength criterion in eqn (6).

3.1 Method of solution

The force resultants for this problem are given by

$$N_x = \frac{pR}{2} - \frac{F}{2\pi R}, \quad N_\phi = pR, \quad N_{x\phi} = \frac{T}{2\pi R^2}, \quad (8)$$

The vector $[N] = [N_x \; N_\phi \; N_{x\phi}]^t$ can be expressed as a sum of two components: one due to the internal pressure p, and the other due to the external forces F and T, namely

$$[N] = [N]_p p + [N]_f \qquad (9)$$

where $[N]_p$ is the coefficient vector of p, and $[N]_f$ incorporates the external forces. From eqns (8) and (9), it follows that

$$[N]_p = \begin{bmatrix} \frac{1}{2} \\ 1 \\ 0 \end{bmatrix} R, \quad [N]_f = \begin{bmatrix} -FR \\ 0 \\ T \end{bmatrix} \frac{1}{2\pi R^2} \qquad (10)$$

Similarly, the strain vector $[\varepsilon]$ may be expressed as

$$[\varepsilon] = [\varepsilon]_p p + [\varepsilon]_f \qquad (11)$$

where $[\varepsilon]_p = [A]^{-1}[N]_p$ and $[\varepsilon]_f = [A]^{-1}[N]_f$, which follows from eqns (1) and (9). Now the stresses in the material coordinates can be computed by inserting $[\varepsilon]$ from eqn (11) into eqn (5) which gives

$$[\sigma^k] = [\sigma^k]_p p + [\sigma^k]_f \qquad (12)$$

where

$$[\sigma^k]_p = [T^k][\bar{Q}^k_{ij}][\varepsilon]_p,$$
$$[\sigma^k]_f = [T^k][\bar{Q}^k_{ij}][\varepsilon]_f \qquad (13)$$

We substitute the stresses from eqn (12) into eqn (6) and obtain a quadratic failure criterion in terms of the internal pressure p as given by

$$\{F_{11}(\sigma^k_{1p})^2 + F_{22}(\sigma^k_{2p})^2 + F_{66}(\tau^k_{12p})^2$$
$$+ 2F_{12}\sigma^k_{1p}\sigma^k_{2p}\}p^2 + \{2F_{11}\sigma^k_{1p}\sigma^k_{1f}$$
$$+ 2F_{22}\sigma^k_{2p}\sigma^k_{2f} + 2F_{66}\tau^k_{12p}\tau^k_{12f} + 2F_{12}(\sigma^k_{1p}\sigma^k_{2f}$$
$$+ \sigma^k_{2p}\sigma^k_{1f}) + F_1\sigma^k_{1p} + F_2\sigma^k_{2p}\}p + \{F_{11}(\sigma^k_{1f})^2$$
$$+ F_{22}(\sigma^k_{2f})^2 + F_{66}(\tau^k_{12f})^2 + 2F_{12}\sigma^k_{1f}\sigma^k_{2f}$$
$$+ F_1\sigma^k_{1f} + F_2\sigma^k_{2f} - 1\} = 0 \qquad (14)$$

Solving the quadratic eqn (14) for the kth layer yields the burst pressure $p^k_{cr} = p^k_{cr}(\theta; F, T)$ corresponding to that layer. The burst pressure of the vessel is given by

$$p_{cr} = \min_k p^k_{cr}; \quad k = 1, 2, \ldots, n/2 \qquad (15)$$

If no positive real solution of eqn (14) exists, then the pressure vessel fails under external load only,

and the solution of the design problem does not exist as there is no feasible design satisfying eqn (6).

3.2 Optimal design problem

The design objective is the maximization of the burst pressure p_{cr} subject to the failure criterion, eqn (6). The optimisation is carried over the fibre orientation θ. The design problem can be stated as

$$p_{max} \overset{\text{def}}{=} \max_\theta p_{cr}(\theta; F, T) = \max_\theta \min_k p^k_{cr} \qquad (16)$$

where $p_{cr}(\theta; F, T)$ is given by eqn (15). The maximum burst pressure p_{max} is determined by solving the max–min problem of eqn (16) which also yields the optimal fibre orientation θ_{opt}.

The optimisation procedure involves the stages of evaluating the burst pressure p_{cr} for a given θ and iteratively improving θ_{opt} to maximise p_{cr}. Thus, the computatinal solution consists of successive stages of analysis and optimization until convergence is obtained. The optimisation stage employes the golden section method in determining θ_{opt}.

3.3 Numerical results for problem 1

The optimisation of the laminated pressure vessel is illustrated by considering a cylindrical shell of mean radius $R = 1$ m and thickness $H = 0.01$ m. The laminate is made of T300/5208 graphite/epoxy the elastic constants of which are $E_1 = 142$ GPa, $E_2 = 10.8$ GPa, $G_{12} = 5.49$ GPa, and $v_{12} = 0.3$. The strength values are $X_t = 1568$ MPa, $X_c = 1341$ MPa, $Y_t = 57$ MPa, $Y_c = 212$ MPa, and $S = 80$ MPa. The values for the material properties are taken from Ref. 12.

We first investigate the effect of fibre orientation on the burst pressure p_{cr} for different values of the axial force. Figure 1 shows the curves of p_{cr} versus θ for single-layered, four-layered and six-layered laminates with $T = 0$, $F = 0$ and 5 MN. It is noted that the results for the four-layered (balanced) laminate are applicable to balanced laminates with any number of layers. For single-layered construction, it is observed that $\theta_{opt} = 0$ for $F = 0$ and 90° for $F = 5$ MN. p_{cr} is much higher for multilayered laminates with the balanced case giving the highest burst pressure. The effects of the axial force and torque on θ_{opt} and p_{max} are investigated in Table 1. For single-layered laminates, $\theta_{opt} = 0$ for low values of F and jumps to 90° at a certain value of $F > 0$ which
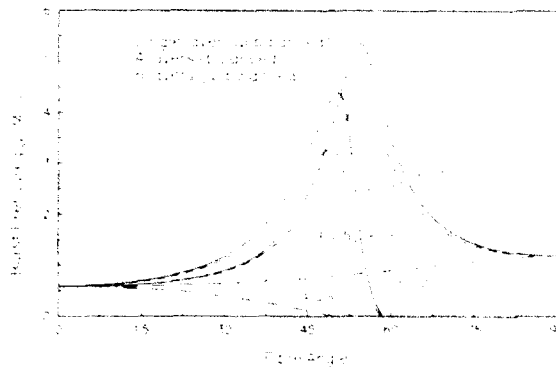
Fig. 1. Curves of burst pressure versus fibre angle with $T = 0$ problem 1.

Fig. 2. Surface of maximum pressure with respect to axial force and torque for a single-layered pressure vessel problem 1.

Table 1. Optimal fibre angles and maximum pressure (problem 1)

F MN	T MNm	Single layer unbalanced		Four layers balanced		Six layers unbalanced	
		θ_{opt}	p_{max} MPa	θ_{opt}	p_{max} MPa	θ_{opt}	p_{max} MPa
0	0	90·00	1·19	54·39	5·36	54·21	4·17
1	0	90·00	0·86	53·56	5·16	53·21	3·98
5	0	0·00	0·59	50·25	4·40	49·02	3·29
10	0	0·00	0·60	45·94	3·67	43·80	2·68
0	2	90·00	1·03	54·32	5·11	54·07	3·77
1	2	90·00	0·70	53·50	4·91	52·98	3·57
5	2	0·00	0·52	50·00	4·15	48·38	2·90
10	2	0·00	0·53	45·54	3·44	42·77	2·33
0	4	90·00	0·51	54·23	4·83	53·90	3·34
1	4	0·00	0·25	53·36	4·62	52·69	3·15
5	4	0·00	0·26	49·69	3·87	47·59	2·49
10	4	0·00	0·27	45·01	3·49	41·56	1·98

Fig. 3. Surface of maximum pressure with respect to axial force and torque for a four-layered pressure vessel problem 1.

depends on the amount of torque applied. For multilayered laminates, the fibres align themselves with the longitudinal axis x as F increases. This results is to be expected on physical grounds.

Failure surfaces with respect to maximum pressure are given in Figs 2 and 3 for single- and four-layered laminates, respectively. Figure 2 indicates that there is a sharp drop in p_{max} as F increases. Decrease in p_{max} with respect to torque is more gradual. For the balanced laminate with four layers, the failure surface as shown in Fig. 3 is rather flat with gradual decrease in p_{max} with increasing axial force and torque.

4 DESIGN FOR MINIMUM WEIGHT

As our second problem, we consider a circular cylindrical shell of length L filled with a liquid of specific weight ρ_l and under a given internal pres-

sure. The design problem involves optimizing the fibre orientation θ so as to minimise the weight of the liquid tank for a given pressure. It is noted that the weight of the tank can be evaluated in terms of the shell thickness H.

4.1 Method of solution

The force resultants for this problem are derived in Refs 13 and 14. For a cylindrical tank with bulkheads attached to the ends of the cylinder, these forces are

$$N_x = \frac{p_i R}{2} + \frac{\rho_l}{8} \cos\phi (4x^2 - L^2 - 2R^2)$$

$$N_\phi = p_i R - \rho_l R^2 \cos\phi \qquad (17)$$

$$N_{x\phi} = -\rho_l R x \sin\phi$$

where $P_c \geq \rho_l R$ is the pressure at the center of the cylinder and x is the longitudinal axis with the origin located at the mid-point such that $-L/2 \leq x \leq L/2$.

We note that $A_{ij} = H \eta_{ij} \bar{Q}_{ij}(\theta)$ where $\eta_{ij} = 1$ for $i, j = 1, 2$ and $i = j = 6$, $\eta_{i6} = 2/n$ for unbalanced laminates and $\eta_{i6} = 0$ for balanced laminates with $i = 1, 2$. We define a matrix $[a]$ such that $[a] = H^{-1}[A]$. Thus, $a_{ij} = \bar{Q}_{ij}(\theta)$ for $ij = 11, 12, 22$ and 66, and $a_{i6} = \eta_{i6} \bar{Q}_{i6}(\theta)$ for $i = 1, 2$. From eqn (1), it follows that $[\varepsilon] = H^{-1}[a]^{-1}[N]$ where $[N]$ is defined by eqns (2) and (17). Substituting $[\varepsilon]$ into eqn (5), we find

$$[\sigma^k] = H^{-1}[\sigma_0^k]$$ (18)

where

$$[\sigma_0^k] = T^k[\bar{Q}_0^k][a]^{-1}[N]$$ (19)

We substitute the stresses from eqn (18) into the strength constraint of eqn (6) and obtain a quadratic failure criterion in terms of the shell thickness H as given by

$$F_{11}\sigma_{10}^{k^2} + F_{22}\sigma_{20}^{k^2} + F_{66}\tau_{120}^{k^2} + F_{12}\sigma_{10}^k\sigma_{20}^k + F_1\sigma_{10}^k + F_2\sigma_{20}^k(H-H^2) = 0$$ (20)

The solution of eqn (20) gives for any x and φ the minimum shell thickness H_c^k corresponding to the failure of the kth layer. From eqn (20), it follows that the critical thickness $H_{cr} = H_{cr}(\theta; x)$ at a point x is given by

$$H_{cr} = \max_{\varphi, k} H_c^k; \quad k = 1, 2, \dots, n/2; \quad 0 \leq \varphi \leq 2\pi$$ (21)

It is noted that the critical thickness H_{cr} depends on the location x along the cylindrical shell as well as the internal pressure p_c and the specific weight ρ_l of the liquid.

4.2 Optimal design problem

The design objective for the cylindrical liquid tank problem is the minimisation of the shell weight with the thickness subject to the strength condition of eqn (6). The weight of the shell is given by

$$W(\theta) = 2\pi R \rho_l \int_{-L/2}^{L/2} H(\theta; x)\,dx$$ (22)

where ρ_l is the specific weight of the fibre composite material used in the construction of the tank.

Two distinct cases depending on whether the shell thickness is constant or variable over the length $-L/2 \leq x \leq L/2$ are considered.

Case I — Constant thickness tank

In this case $H = H(\theta)$ and the weight is given by

$$W(\theta) = 2\pi R L \rho_l H(\theta)$$ (23)

Since the weight is proportional to the thickness, it is sufficient to minimise $H(\theta)$ to obtain the minimum weight design. $H_{min}(\theta)$ for a given θ valid for all x is determined from

$$H_{min}(\theta) = \max_x H_{cr} = \max_x \max_{\varphi, k} H_c^k;$$
$$-L/2 \leq x \leq L/2, \quad 0 \leq \varphi \leq 2\pi$$ (24)

where H_c^k is determined from eqn (20).

Case II — Variable thickness tank

In this case $H = H(\theta; x)$ and the minimum thickness $H_{min}(\theta; x)$ at a point x for a given θ is defined by H_{cr} in eqn (21). Therefore, $H_{min}(\theta; x)$ is determined as the maximum of H_c^k given by eqn (21) at every point x producing a variable wall thickness. Thus

$$H_{min}(\theta; x) = \max_{\varphi, k} H_c^k; \quad 0 \leq \varphi \leq 2\pi$$ (25)

Due to symmetry, the thickness distributions are the same for $-L/2 \leq x \leq 0$ and $0 \leq x \leq L/2$. For this case, the weight is given by eqn (22).

In both cases, the design problem is to determine the optimal fibre orientation θ_{opt} so as to minimise the weight of the shell, namely

$$W_{min} = \min_\theta W(\theta)$$ (26)

with H_{min} obtained from eqn (24) in case I and from eqn (25) in case II. In eqn (26) $W(\theta)$ is given by eqn (23) for the constant thickness case and by eqn (22) for the variable thickness case.

The minimum weight problem is solved by determining the minimum thickness H_{min} satisfying the constraint of eqn (20) from eqn (24) (case I), or from eqn (25) (case II). The weight is minimised over the fibe orientation θ by using a one-dimensional numerical optimisation scheme, namely, the golden section method. Computations are continued until convergence is attained for θ.

4.3 Numerical results for problem 2

Numerical results are given for single- and four-layered laminated cylinders made of the same graphite/epoxy material defined by section 3.3. The numerical values are given for dimensionless quantities by introducing

$$X = x/L, \quad h = H/L, \quad r = R/L$$
$$p_0 = p_c/\rho_l R, \quad w = W/2\pi R L^2 \rho_l$$ (27)

From eqns (22) and (27), it follows that

$$w(\theta) = \int_{-1/2}^{1/2} h(\theta; X)\, dX \qquad (28)$$

We note that for the constant thickness shell (case I) $w(\theta) = h(\theta)$.

In Tables 2–5, subscripts c and v refer to the constant and variable thickness cases, respectively. In particular, $w_p(\theta)$ refers to the weight of a shell with the thickness function $H_{mn}(\theta; x)$

obtained from eqn (25) and the fibre orientation specified as θ.

The effect of increasing the internal pressure p_o on the optimal design is investigated in Tables 2 and 3 for single-layered constant and variable thickness shells, respectively. It is observed that θ_{opt} is 0° for low values of p_o and jumps to 90° as p_o increases. The weight difference between the constant and variable thickness shells decreases with increasing p_o. The right half of the tables is provided to compare the weight ratios of shells with specified and optimal fibre angles.

Table 2. Optimal fibre angles and minimum weight for a single-layered constant thickness pressure vessel (problem 2)

| | Single layer | | $w(\theta)/w_{min}$ | | | | |
| | | | θ | | | | |
p_o	θ_{opt}	$w_{min} \times 10^?$	0	30	45	60	90
1	0.00	90.44	1.00	1.36	1.37	1.27	1.29
2	0.00	128.14	1.00	1.24	1.22	1.11	1.07
3	90.00	157.93	1.08	1.23	1.20	1.07	1.00
4	90.00	178.62	1.19	1.30	1.24	1.10	1.00
5	90.00	199.31	1.28	1.35	1.28	1.12	1.00
6	90.00	220.00	1.36	1.39	1.31	1.14	1.00
8	90.00	261.38	1.47	1.46	1.35	1.17	1.00
10	90.00	302.77	1.55	1.51	1.39	1.19	1.00
20	90.00	509.76	1.75	1.64	1.47	1.25	1.00
30	90.00	716.76	1.84	1.70	1.51	1.27	1.00
40	90.00	923.77	1.89	1.73	1.53	1.28	1.00
50	90.00	1130.79	1.92	1.75	1.54	1.29	1.00
100	90.00	2165.87	1.99	1.79	1.57	1.31	1.00
200	90.00	4236.06	2.02	1.81	1.58	1.32	1.00

Table 4. Optimal fibre angles and minimum weight for a four-layered constant thickness pressure vessel (problem 2)

| | Four layers | | $w(\theta)/w_{min}$ | | | | |
| | | | θ | | | | |
p_o	θ_{opt}	$w_{min} \times 10^?$	0	30	45	60	90
1	44.96	24.88	3.64	2.33	1.00	2.78	1.69
2	48.72	30.64	4.18	2.78	1.14	2.47	4.48
3	49.84	34.77	4.91	3.24	1.30	2.37	4.54
4	50.50	38.52	5.53	3.63	1.43	2.31	4.64
5	50.93	42.20	6.06	3.97	1.55	2.27	4.72
6	51.22	45.93	6.50	4.24	1.65	2.24	4.79
8	51.60	53.65	7.15	4.65	1.79	2.17	4.87
10	51.82	61.76	7.59	4.92	1.89	2.11	4.90
20	52.52	106.27	8.42	5.44	2.06	1.88	4.80
30	52.97	152.05	8.68	5.60	2.11	1.77	4.71
40	53.30	197.86	8.83	5.68	2.14	1.72	4.67
50	53.51	243.64	8.92	5.74	2.16	1.69	4.64
100	53.94	472.46	9.10	5.85	2.20	1.62	4.58
200	54.16	929.98	9.20	5.92	2.22	1.58	4.56

Table 3. Optimal fibre angles and minimum weight for a single-layered variable thickness pressure vessel (problem 2)

| | Single layer | | $w_v(\theta)/w_{min}$ | | | | |
| | | | θ | | | | |
p_o	θ_{opt}	$w_{min} \times 10^?$	0	30	45	60	90
1	0.00	84.71	1.00	1.22	1.27	1.25	1.09
2	90.00	111.23	1.14	1.25	1.25	1.19	1.00
3	90.00	131.01	1.29	1.34	1.31	1.22	1.00
4	90.00	151.14	1.40	1.41	1.35	1.24	1.00
5	90.00	171.47	1.48	1.46	1.38	1.25	1.00
6	90.00	191.93	1.55	1.50	1.40	1.26	1.00
8	90.00	233.05	1.64	1.56	1.44	1.27	1.00
10	90.00	274.32	1.70	1.60	1.46	1.28	1.00
20	90.00	481.18	1.86	1.70	1.52	1.30	1.00
30	90.00	688.19	1.92	1.74	1.54	1.31	1.00
40	90.00	895.20	1.95	1.76	1.55	1.31	1.00
50	90.00	1102.22	1.97	1.78	1.56	1.31	1.00
100	90.00	2137.31	2.01	1.81	1.58	1.32	1.00
200	90.00	4207.49	2.03	1.82	1.59	1.32	1.00

Table 5. Optimal fibre angles and minimum weight for a four-layered variable thickness pressure vessel (problem 2)

| | Four layers | | $w_v(\theta)/w_{min}$ | | | | |
| | | | θ | | | | |
p_o	θ_{opt}	$w_{min} \times 10^?$	0	30	45	60	90
1	46.42	20.03	4.23	2.24	1.03	2.46	4.60
2	48.81	25.05	5.06	2.88	1.20	2.23	4.44
3	49.94	29.27	5.79	3.40	1.36	2.13	4.48
4	50.59	33.35	6.36	3.80	1.49	2.08	4.53
5	50.98	37.46	6.80	4.11	1.60	2.03	4.58
6	51.25	41.66	7.13	4.36	1.68	1.99	4.61
8	51.60	50.31	7.60	4.69	1.79	1.92	4.63
10	51.95	59.22	7.90	4.91	1.87	1.87	4.63
20	53.08	104.35	8.56	5.41	2.04	1.73	4.61
30	53.49	149.83	8.81	5.59	2.10	1.68	4.59
40	53.71	195.42	8.93	5.69	2.14	1.64	4.58
50	53.84	241.08	9.01	5.74	2.16	1.63	4.57
100	54.11	469.62	9.16	5.86	2.20	1.59	4.55
200	54.25	927.00	9.23	5.92	2.22	1.57	4.54

Tables 4 and 5 give the same information as Tables 2 and 3 for balanced four-layered shells. It is observed that as p_0 increases, the optimal fibre angle approaches θ_{opt} of the first problem with $F = T = 0$ (see Table 1). This is to be expected since the contribution of the liquid to resultant forces becomes less pronounced as the internal pressure increases (see eqn (17)) and problems 1 and 2 converge. Comparison of Tables 4 and 5 indicates that w_{min} values differ by about 20% for constant and variable thickness shells for small values of p_0. This difference decreases as p_0 increases and drops to less than 2% for $p_0 > 20$.

Figure 4 shows the optimal thickness distribution of the variable thickness shell with respect to the x axis and for increasing internal pressure.

5 CONCLUSIONS

A solution method is presented for the optimal design of symmetrically laminated cylindrical pressure vessels with balanced and unbalanced stacking sequences. The optimisation is carried out subject to the Tsai–Wu failure criterion.

Two design problems are solved. In the first problem, a cylindrical pressure vessel is optimised taking the fibre angle as the design variable to maximise the burst pressure. The effects of the axial force and torque on the optimal designs are investigated. In the second problem, a cylindrical vessel filled with a liquid and subject to an internal pressure is studied. The weight of the shell is minimised taking the fibre angle and the wall thickness as the design variables. Both constant and variable thickness shells are investigated. It is shown that the results for the second problem approach those

of the first problem as the internal pressure increases.

Numerical results are given for unbalanced single- and six-layered and balanced laminates noting that in the balanced case the number of layers does not affect the results. It is observed that fibre angles align themselves with the longitudinal axis as the axial force increases. Variable thickness shells are found to be about 20% more efficient than the constant thickness shells for low values of the internal pressure with the difference decreasing as this pressure increases. For single layer pressure vessels, the optimal fibre angle is found to be either $0°$ or $90°$ with the switch-over point depending on the magnitude of the axial force, torque or the internal pressure.

ACKNOWLEDGEMENT

REFERENCES

1. Pipkin, A. C. & Rivlin, R. S., Minimum-weight design for pressure vessels reinforced with inextensible fibres. *J. Appl. Mech.*, **30** 1963 103–8.
2. Chao, C. C., Sun, C. T. & Koh, S. L., Strength optimization for cylindrical shells of laminated composites. *J. Comp. Mater.*, **9** 1975 55–66.
3. Urazgil'dyaev, K. U., Design of equal-strength cylindrical shells of composite material. *Prikladnaya Mekhanika*, **13** 7 1977 121–4.
4. Tauchert, T. R., Optimum design of a reinforced cylindrical pressure vessel. *J. Comp. Mater.*, **15** 1981 390–402.
5. Fukunaga, H. & Uemura, M., Optimum design of helically wound composite pressure vessels. *J. Comp. Structures*, **1** 1983 31–49.
6. Eckold, G. C., A design method for filament wound GRP vessels and pipework. *Composites*, **16** 1 1985 41–7.
7. Fukunaga, H. & Chou, T. W., Simplified design techniques for laminated cylindrical pressure vessels under stiffness and strength constraints. *J. Comp. Mater.*, **22** 1988 1157–69.
8. Karandikar, H., Srinivasan, R., Mistree, F. & Fuchs, W. J., Compromise: an effective approach for the design of pressure vessels using composite materials. *Computers & Structures*, **33** 6 1989 1465–77.
9. Adali, S. & Yakar, B., Optimal design of laminated pressure vessels under internal pressure and temperature loading. In *Pressure Vessels and Components 1991, Proc of the 1991 Pressure Vessels and Piping Conference* PVP-Vol. 217, ASME, New York, USA, 1991, pp. 57–63.
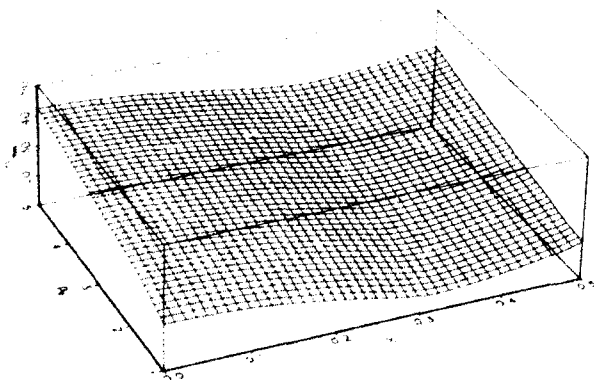
Fig. 4. Optimal thickness distribution with respect to x axis and internal pressure for a four-layered pressure vessel (problem 2).

10. Adali, S., Fuzzy optimization of laminated cylindrical pressure vessels. In *Composite Structures 6, Proc. of the 6th International Conference on Composite Structures.* Elsevier Applied Science, London, UK, 1991, pp. 249–59.

11. Datoo, M. H., *Mechanics of Fibrous Composites.* Elsevier Applied Science, London, UK, 1991.

12. Tsai, S. W. & Hahn, W. T., *Introduction to Composite Materials.* Technomic Publishing Company, Westport, CT, USA, 1980.

13. Flugge, W., *Stresses in Shells,* 2nd edn. Springer-Verlag, New York, USA, 1973.

14. Kraus, H., *Thin Elastic Shells.* John Wiley & Sons, New York, USA, 1967.

Development of the anthropomorphic robot with carbon fiber epoxy composite materials

Dai Gil Lee, Kwang Seop Jeong, Ki Soo Kim & Yoon Keun Kwak

Department of Precision Engineering and Mechatronics, Korea Advanced Institute of Science and Technology,
Taejon, Korea 305-701

The material for the robot structure should have high specific stiffness
stiffness/density to give positional accuracy and fast maneuverability to the
robot. Also, the high material damping is beneficial because it can dissipate the
structural vibration induced in the robot structure. This cannot be achieved
through conventional materials such as steel and aluminum because these two
materials have almost the same specific stiffnesses which are not high enough
for the robot structure. Moreover, steel and aluminum have low material
dampings.

Composites which usually consist of very high specific modulus fibers and
high damping matrices have both high specific stiffnesses and high material
dampings. Therefore, in this work, the forearm of an anthropomorphic robot
which has 6 degrees of freedom, 70 N payload and 0·1 mm positional accuracy
of the end effector was designed and manufactured with high modulus carbon
fiber epoxy composite because the magnitudes of the mass and moment of
inertia of the forearm of an anthropomorphic robot are most important due to
its farthest position from the robot base.

Two power transmission shafts which deliver the power of the motors
positioned at the rear of the robot forearm to the wrist and the end effector
were also designed and manufactured with high modulus carbon fiber epoxy
composite to reduce weight and rotational inertia. The mass reduction of the
manufactured composite forearm was 15·9 kg less than the steel forearm.

The natural frequencies and damping capacity of the manufactured
composite arm were measured by the fast Fourier transform method and
compared to those for the steel arm. From the test, it was found that both the
fundamental natural frequency and damping ratio of the composite arm of the
robot were much higher than those of the steel arm.

1 INTRODUCTION

The structure of a robot should have both high specific stiffness (E/ρ) and high damping in order to increase positional accuracy and dynamic performance.[1] If the thickness and the size of the robot structure are increased to stiffen the structure, the weight of the robot is also increased which requires larger motors to give the same acceleration. Even if aluminum rather than steel is used, the stiffness cannot be increased without weight increase because the specific stiffness of aluminum is almost the same as that of steel.

The specific modulus of the high modulus carbon fiber epoxy composite material can be increased to more than five times that of steel or aluminum if the stacking angle of fibers from the axis is less than 15°.[2] Also the carbon fiber epoxy

composite material has about 10 times the high damping which is necessary to dissipate the vibration of structures.[3] Therefore, the high dynamic performance and the high positional accuracy of the robot can be accomplished if the high modulus composite material is used in the robot structure; in other words the composite robot structure can have a higher payload with the same capacity motor with the same positional accuracy.

Asada[4] developed a direct-drive robot arm structure with the carbon fiber epoxy composite. He employed a hollow cylindrical shape for the robot arm structure. The cylindrical shape is good for torsional rigidity, but is not good for bending rigidity compared to the box-type structure. The box-type structure is more suitable for both bending and torsional rigidities and has been recommended for the machine tool structures.[5]

313

Lee et al.[1] designed and manufactured a four axis SCARA (Selectively Compliant Assembly Robot Arm) type direct-drive robot for assembly of the printed circuit board with a high modulus carbon fiber epoxy composite. The box-type shape was employed for the arm structure. The positional accuracy and dynamic performance of the composite SCARA robot arm were significantly improved compared to those of the aluminum arm.

The previous applications of composites to robot structures have been usually restricted to small direct-drive robots which have small payloads because the direct-drive robots do not have any gear trains for speed reduction. Whereas the conventional anthropomorphic robot uses gear trains composed of several spur and bevel gears to reduce the motor speed as well as to change the direction of motion. Because of gear trains, it has more complex arm structures. Also the power transmission shafts and bearings must be mounted inside or outside of the arm of the anthropomorphic robot. Since the anthropomorphic robot has a larger payload and working envelope as well as flexibility with the same capacity motor due to the motor speed reduction, it is widely accepted as an industrial robot for loading and unloading, painting, welding and assembly operations although it has complicated shapes, a backlash of gears and difficulty in control because of large friction and nonlinearity from the gear trains and other mechanisms.[6]

In this work, a six degree of freedom anthropomorphic robot arm with 70 N payload was designed and manufactured with high modulus carbon fibre epoxy composite. The deflection at the end effector of the arm was calculated to determine the size and the cross-section of the arm using the simple moment–curvature relationship of the beam which incorporates the composite properties. Also two power transmission shafts for the motion of the end effector were manufactured with high modulus carbon fiber epoxy composite. The composite arm and the composite transmission shafts were adhesively bonded to the gear box and the end effector.

The static performances of the composite forearm were compared to those of the steel forearm by measuring the weights and calculating the deflections of the end effector. The dynamic characteristics of the composite forearm were compared to those of the steel forearm by measuring vibrational impulse responses.

2 ROBOT SPECIFICATIONS

Figure 1 shows a photograph of the manufactured anthropomorphic robot. Its height and forearm length are about 2.0 m and 1.2 m, respectively, and its total weight is about 2000 N. The robot has six degrees of freedom. The pitch and roll motions of the end effector and the roll motion of the wrist are driven by the three motors (MO80) mounted at the rear of the forearm. The up–down and forward–backward motions are driven by the two motors (MO600) mounted in the back of the robot body. The whole robot structure can be rotated by the motor (MO600) mounted under the base which is not shown in Fig. 1. The MO80 motors have 150 W power and the MO600 motors have 700 W power. All the six motors are DC servo motors manufactured by Mavilor Company.

Figure 2 shows the assembled forearm configuration. The forearm consists of the three motors, the gear box, the arm, the wrist, the end effector and three hollow shafts for power transmission. From these components, the arm and the two outer power transmission shafts were manufac-
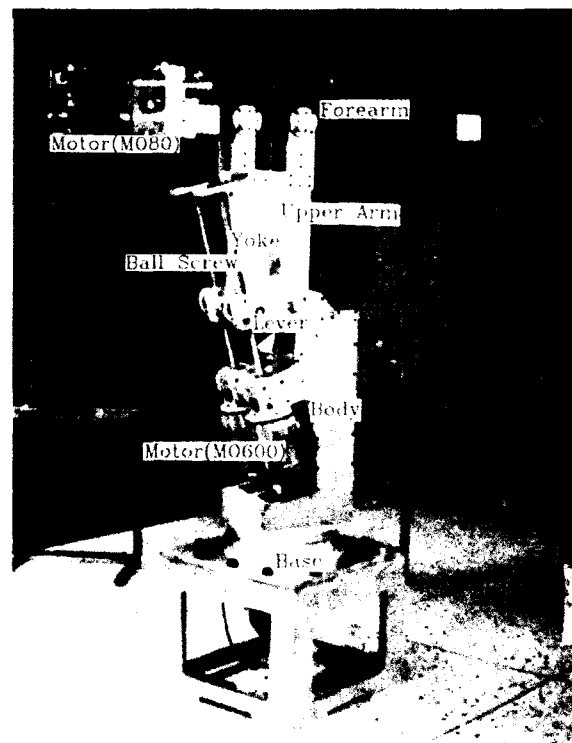
Fig. 1. Photograph of the manufactured anthropomorphic robot.

Motor & Gear Box
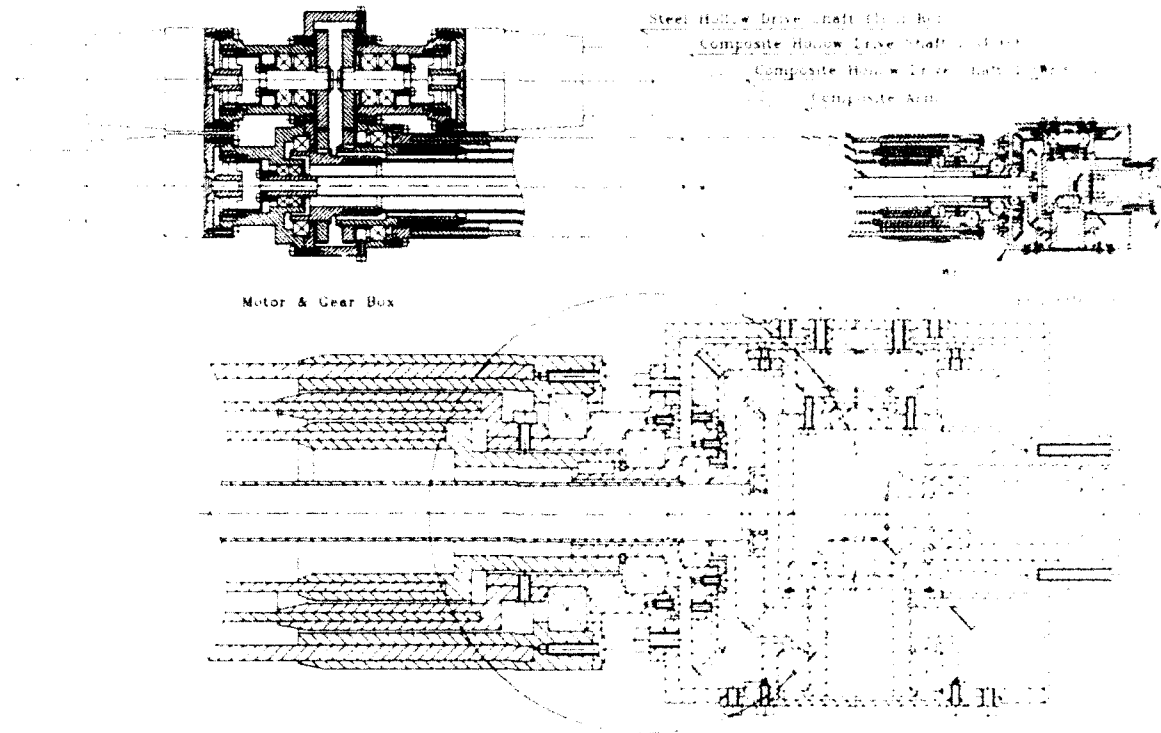
Fig. 2. Forearm configuration of the anthropomorphic robot

Table 1. Specifications of the anthropomorphic robot

		Specifications
Degrees of freedom		6
Payload		70 N
Position accuracy		±0.1 mm
Forearm length		800 mm
Upper arm length		600 mm
Length of the drive shafts	Tool roll	1007 mm
	Pitch	996 mm
	Wrist roll	976 mm
Range of rotation angles	Forearm	±50°
	Upper arm	±50°

tured with high modulus carbon fiber epoxy composite. Table 1 shows the specifications of the developed anthropomorphic robot.

3 DEFLECTION OF THE ROBOT ARM BY STATIC LOADS

The deflection of the end effector comes from the static weight of the robot, the payload and the inertia force due to the acceleration of the robot. In this work, the inertia force was not taken into consideration in calculating the deflection

because the maximum acceleration of the end effector of the robot was designed to be 3 m/s which was less than the gravitational acceleration 9.81 m/s².

Since the forearm's weight and the static payload effect directly the positional accuracy of the robot, the deflection of the forearm due to the forearm's own weight and the static payload was calculated using the simple moment-curvature relationship of the beam. Figure 3 shows the lumped mass distributions for the simple calculation of the deflection of the forearm, in which M_1 represents the combined weight of the arm and the three power transmision shafts, M_2 represents the combined weight of the wrist and the end effector, M_3 represents the combined weight of the motors and the gear box, and M_t ($= M_1 + M_2 + M_3$) represents the total weight of the forearm. The points C.M., B and E in Fig. 3 represent the center of mass, the pivot point between the upper arm and the forearm, and the pivot point between the yoke and the forearm, respectively. Then L_x, the length between the point B and the point C.M., can be calculated as follows:

$$L_x = \frac{(M_1 L_2 + M_2 L_x - M_3 L_m)}{M_t} \quad (1)$$
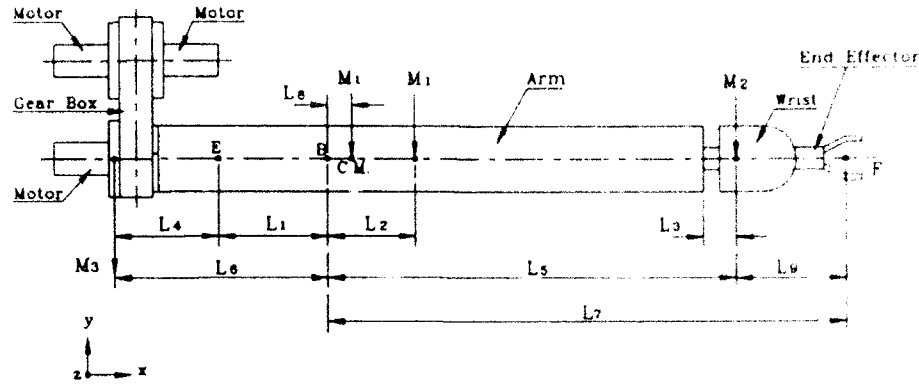
Fig. 3. Mass distributions of the forearm.
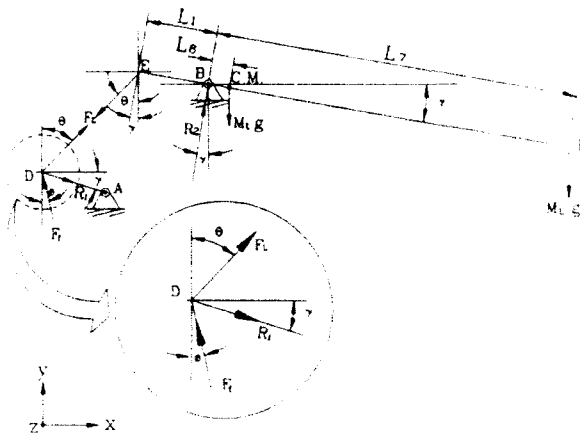
Fig. 4. Mechanical model of the forearm.

Figure 4 shows the free body diagram which depicts the force relationship between the forearm (EF), the yoke (DE) and the lever (AD). F_1 and F_t represent the forces from the ball screw and the forearm, respectively. R_1 and R_2 represent the forces from the pivot points A and B, respectively. γ represents the angle between the horizon and the forearm, whose range is $-50° - 50°$. ϕ represents the angle between the vertical and the ball screw, whose range is $0° - 16°$. θ represents the angle between the vertical and the yoke. M_t represents the equivalent mass of the payload.

Applying the force equilibrium equation to the point D in Fig. 4, the following relationships can be derived:

$$F_1 \sin \theta - F_t \sin \phi + R_1 \cos \gamma = 0 \qquad (2)$$

$$F_1 \cos \theta + F_t \cos \phi - R_1 \sin \gamma = 0 \qquad (3)$$

Eliminating R_1 from eqns (2) and (3), F_t can be derived as follows:

$$F_t = F_1 \frac{\cos(\theta - \gamma)}{\cos(\gamma + \phi)} \qquad (4)$$

From the moment equilibrium around the pivot point B, the following relationship can be derived:

$$F_t \cos(\theta - \gamma) = \left(M_t \frac{L_5}{L_1} + \frac{L_2}{L_1} \right) g \cos \gamma \qquad (5)$$

where g is the gravitational acceleration (9.81 m/s^2).

Eliminating F_t from eqns (4) and (5), the force F_1, which acts in the ball screw, can be derived in terms of M_t and M_1:

$$F_1 = \left(M_t \frac{L_5}{L_1} + M_1 \frac{L_2}{L_1} \right) \frac{g \cos \gamma}{\cos(\gamma + \phi)} \qquad (6)$$

The maximum deflection does not occur at $\gamma = 0°$ but around $0°$ because the deflection of the ball screw affects slightly the deflection of the end effector. However, the maximum deflection was calculated by assuming that it would occur when $\gamma = 0°$ because the axial deformation of the ball screw was designed to be small.

Figure 5(a) shows the kinematic mechanism of the forearm and its connected linkages. Figure 5(b) shows the deflection model of the forearm when $\gamma = 0°$. d_t and d_p represent the deflections of the end effector and the pivot point E, respectively. and d_b represents the component of the deflection of the ball screw perpendicular to the forearm, which is caused by the compliance of the ball screw.

The deflection d_a was calculated by the moment-curvature relationship of the beam as follows:

$$\frac{d^2 y}{dx^2} = \frac{M}{E_{11} I} \qquad (7)$$

where, M, E_{11} and I represent the moment in the forearm, the longitudinal Young's modulus of the
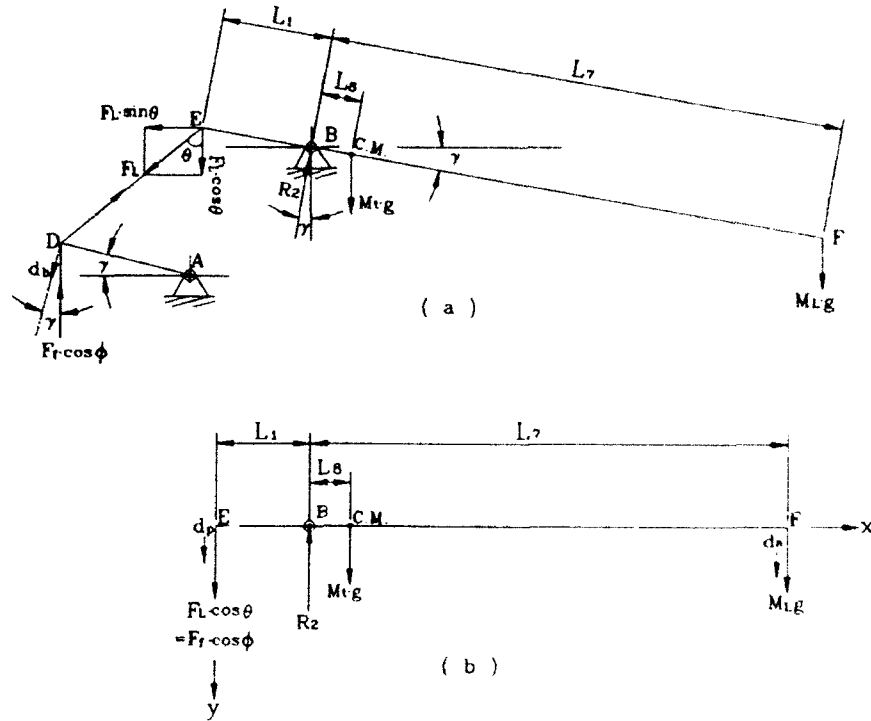
Fig. 5. Deflection model of the robot arm: (a) whole model of the robot arm; (b) model of the forearm when $\gamma = 0°$.

carbon fiber epoxy composite and the sectional second moment of inertia of the forearm, respectively. The moment $M(x)$ can be represented using the singularity function as follows:[8]

$$M = F_{\mathrm{f}} \cos \phi \langle x \rangle - R_2 \langle x - L \rangle + M_{\mathrm{t}} g \langle x - L_1 - L_8 \rangle \tag{8}$$

where the symbol $\langle \ \rangle$ represents the singularity function and x represents the distance from the point E. The force R_2 at the pivot point B can be calculated by the force equilibrium equation as follows:

$$R_2 = F_{\mathrm{f}} \cos \phi \left(1 + \frac{L_1}{L_7} \right) + M_{\mathrm{t}} g \left(1 - \frac{L_8}{L_7} \right) \tag{9}$$

Two boundary conditions for eqn (7) are as follows:

when $x = L_1, y = 0$ (10a)

when $x = 0, y = d_{\mathrm{p}}$ (10b)

Integrating eqn (7) with boundary conditions (10) after substituting for both eqns (8) and (9) into (7), the following deflection equation can be obtained:

$$y = \frac{F_{\mathrm{f}} \cos \phi}{6 E_{11} I} \left\{ x^3 - \left(1 + \frac{L_1}{L_7} \right) \langle x - L_1 \rangle^3 - L_1^2 x \right\}$$

$$+ \frac{M_{\mathrm{t}} g}{6 E_{11} I} \left\{ \langle x - L_1 - L_8 \rangle^3 - \left(1 - \frac{L_8}{L_7} \right) \langle x - L_1 \rangle^3 \right\}$$

$$+ \left(1 - \frac{x}{L_1} \right) d_{\mathrm{p}} \tag{11}$$

The deflection d_{p} at the point E can be expressed in terms of the deflection of the ball screw by assuming the yoke to be a rigid body. The deflection of the ball screw d_{c} due to the axial force F_{t} is expressed by the following equation:

$$d_{\mathrm{c}} = -\frac{F_{\mathrm{t}}}{K_{\mathrm{N}}} \tag{12}$$

where K_{N} represents the axial spring constant of the ball screw. Then, d_{h} the component of d_{c} perpendicular to the forearm is expressed as follows:

$$d_{\mathrm{h}} = d_{\mathrm{c}} \cos \phi = -\frac{F_{\mathrm{t}}}{K_{\mathrm{N}}} \cos \phi \tag{13}$$

Since the linkage ABED was designed to be a parallelogram, the deflection at the point E has the same deformation as at the point D. Therefore, the deflection d_p at $x = 0$ is expressed as follows:

$$d_p = d_b = -\frac{F_t}{K_N} \cos \phi \qquad (14)$$

Substituting for eqn (14) into eqn (11), the deflection $y(x)$ can be obtained as follows:

$$y = \frac{F_t \cos \phi}{6E_{11}I} \left\{ x^3 - \left(1 + \frac{L_1}{L_2}\right) (x - L_1)^3 - L_1^2 x \right\}$$

$$+ \frac{M_s g}{6E_{11}I} \left\{ x - L_1 - L_s)^3 - \left(1 - \frac{L_s}{L_2}\right) \right.$$

$$\times x - L_1)^3 \right\} - \left(1 - \frac{x}{L_1}\right) \frac{F_t}{K_N} \cos \phi \qquad (15)$$

The deflection of the end effector d_a can be obtained by substituting $L_1 + L_2$ for x as follows:

$$d_a = \frac{F_t \cos \phi}{3E_{11}I} (L_1^2 L_2 + L_1 L_2^2)$$

$$- \frac{M_s g}{E_{11}I} (2L_1^2 L_s - 3L_s L_2^2 + L_2^3)$$

$$+ \frac{F_t}{K_N} \cos \phi \left(\frac{L_2}{L_1}\right) \qquad (16)$$

4 PROPERTIES OF THE CARBON FIBER EPOXY COMPOSITE

The high modulus carbon fiber epoxy composite was chosen for both the arm and the power transmission shaft material. The unidirectional properties of the composite are as follows:

$E_L = 207$ GPa

$E_T = 13.8$ GPa

$G_{LT} = 5.9$ GPa

$\nu_{LT} = 0.28$

where the subscripts L and T represent the longitudinal and the transverse directions, respectively.

The composite arm was manufactured by hand lay-up of prepregs with stacking sequence $[\pm \alpha]_N$.

The composite transmission shaft was manufactured by the filament winding method with the winding angle $[\pm \alpha]_N$. The laminate engineering constants were calculated by the classical laminated plate theory[9] and Fig. 6 shows the variations of the longitudinal Young's modulus E_{11} and the shear modulus G_{12} versus the stacking angle α.

5 DESIGN AND MANUFACTURE OF THE COMPOSITE ARM

The design criterion of the static accuracy of the robot was that the deflection of the end effector should be less than 0.1 mm from the undeformed position when 70 N payload and gravity acted on the robot. The deflection of the end effector d_a in eqn (16) by the payload and the robot's own weight can be calculated if the sectional second moment I and the longitudinal Young's modulus E_{11} of the composite are known. The box-type section of the arm was chosen because of its high bending and torsional rigidity. The outside sectional size of the arm was chosen as 100×100 mm and the thickness of the arm was chosen as 5 mm. Then $I = 2.865 \times 10^{-6}$ m^4. The value of E_{11}, i.e. the stacking angle, was selected by taking into consideration the torsional rigidity of the arm. If the stacking angle is chosen as 0°, the longitudinal modulus becomes the maximum value. However, in that case both the shear modulus and the transverse modulus become the minimum values. Since the robot arm must withstand some torsional loads, the stacking angle of the composite arm must be larger than 0°. If the stacking angle is increased more than 15°, the longitudinal Young's modulus drops quickly. Therefore the stacking
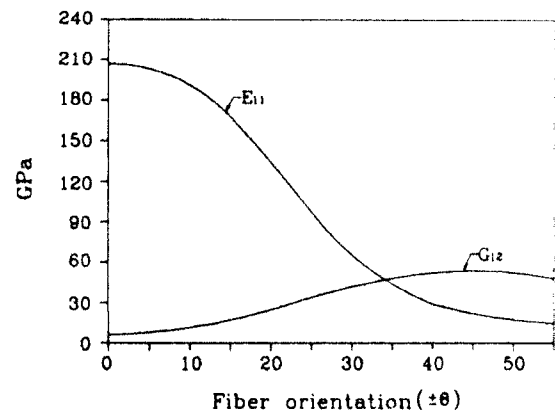
Fig. 6. Elastic moduli with respect to fiber orientation.

sequence $[\pm 15]_N$ was chosen for the prepreg lay-up. Then the value of the longitudinal Young's modulus E_{11} was 168 GPa.

6 DESIGN AND MANUFACTURE OF THE COMPOSITE TRANSMISSION SHAFTS

The angular deformations of the power transmission shafts affect the accuracies of the wrist and the end effector. In this work, the maximum angular deformation of the shaft was limited to $0.033°$ (0.58×10^{-3} rad). The relationship between the angular deformation Ψ and the applied torque T of the composite shaft is expressed by the following equation:[8]

$$\Psi = \frac{L}{G_{12}J} T$$

where L is the length of the shaft and J is the polar moment of the section. If the inner and outer diameters of the hollow shaft are d_i and d_o, respectively, then

$$J = \frac{\pi(d_o^2 - d_i^2)}{32}$$

Since the diameter of the shaft cannot be increased beyond the size limit of the forearm, the shear modulus G_{12} of the composite must be increased to reduce the angular deformation. The shear modulus can be increased by increasing the stacking or winding angle of the carbon fiber on condition that the fundamental natural frequencies of the shaft exceed the maximum rotational speed of the motor. Even though the maximum rotational speed of the motor was about 10 000 rev/min (167 Hz), the rotational speeds of the shafts were 2 Hz because the angular speed of the motor was reduced 80 times by a harmonic driver. Therefore, the winding angle $[\pm 45]_N$ was chosen for the filament winding angle without taking into

consideration the whirling of the shaft. Then the shear modulus of the composite was 54 GPa.

Figure 7 shows the relationship between the torque and the rotational speed of the motors (MO80) used for the end effector (pitch motion) and the wrist (roll motion). The motor torque at continuous 3000 rev/min use was 0.27 N m. This torque was increased to 20.5 N m by the harmonic driver whose efficiency was 96%. Table 2 shows the dimensions of the composite shafts and angular displacements when 20.5 N m was applied to the shafts. The calculated angular displacements satisfied the limitation of the angular deformation. The outside diameter of the composite shafts were 2 mm smaller than that of the steel shafts because the composite shafts required the tolerance for the fabrication of the double lap joints.

7 DESIGN AND MANUFACTURE OF THE JOINTS

Two different types of joints were designed and manufactured. In order to join the composite arm and the transmission shafts to the gear box and
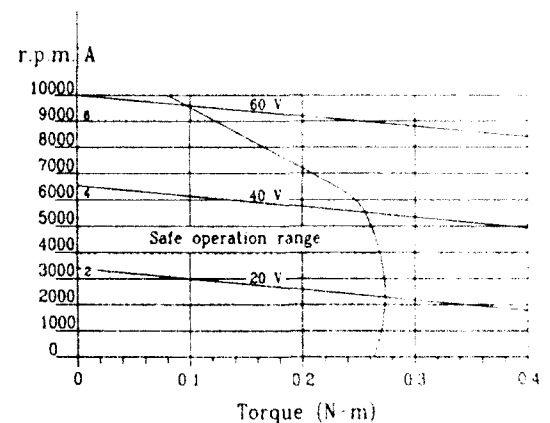
Fig. 7. Torque characteristics with respect to rev/min of MO80 motor.

Table 2. Dimensions and angular displacements of the steel and the composite hollow drive shafts

		Effective length (mm)	Outer diameter (mm)	Inner diameter (mm)	Shear modulus G_{12} (GPa)	Polar moment of section J (m⁴)	Angular displacement (radian)
Pitch	Steel	996	62	56	80	48.5×10^{-8}	0.53×10^{-3}
	Composite	996	60	50	54	65.8×10^{-8}	0.57×10^{-3}
Wrist roll	Steel	976	76	71	80	78.0×10^{-8}	0.32×10^{-3}
	Composite	976	74	66	54	108.1×10^{-8}	0.34×10^{-3}

the bearing housings, tubular adhesively bonded double lap joints were designed and manufactured. Also, the hybrid joint which uses both mechanical and adhesive joining was designed and manufactured to join the composite arm to the upper arm and the yokes.

The adhesive used is HYSOL EA 9309.2 NA whose properties are shown in Table 3. The adhesive is rubber-toughened and has a low viscosity before cure. The torque capacity of the adhesive joint decreases when the adhesive thickness is large because thermal residual stresses and voids become dominant as the adhesive thickness increases. Since Lee et al.[10] suggested that the adhesive thickness should be smaller than 0·15 mm, an adhesive thickness of 0·10 mm was chosen in this work. In order to determine the torque capacity of the adhesively bonded joint, the torque capacity was calculated by the method of Adams and Peppiatt.[11] Figure 8 shows the torque capacities of the joints versus joint lengths when HYSOL EA 9309.2 NA was used as the adhesive. When the adhesive thickness was 0·1 mm, the torque capacities saturated as the adhesive length became larger than 20 mm as shown in Fig. 8. Although 20 mm joint length was enough, 50 mm

joint length for the transmission shafts and 100 mm joint length for the forearm were chosen because the joining operation becomes difficult or the joint becomes weak due to bending moment as the joint length becomes smaller. The aluminum adherends for the double lap joints of the forearm and the transmission shafts were manufactured by electro-discharge machining. Figure 9 shows the joint components of the arm and the transmission shafts. Figure 10 shows the adhesively bonded composite arm and the transmission shafts.

Table 3. Properties of the HYSOL EA 9309.2 NA adhesive

Mixing ratio by weight (Part A : Part B)	100:22
Curing time	7 d (at 25°C)
	1 h (at 75°C)
Mixed viscosity	1500 P
Service temperature	80°C
Tensile modulus	1·20 GPa (at 25°C)
Poisson's ratio	0·4
Shear modulus	0·98 GPa (at 25°C)
Shear strength	30·0 MPa (at 25°C)
Lap shear strength	13·7 MPa (at 25°C)

(a)

(b)

(c)
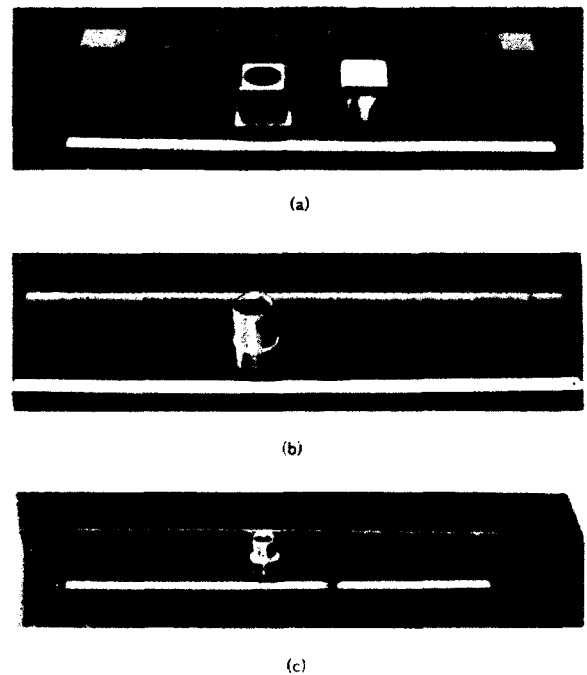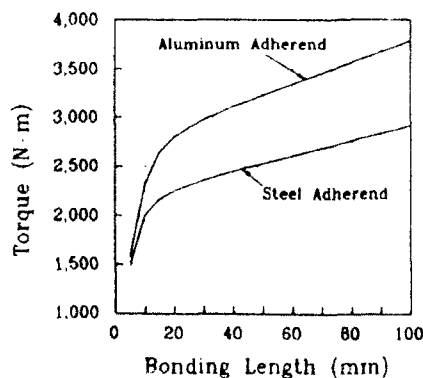
Fig. 9. Joint components of the composite arm and the hollow drive shafts: (a) arm and box type metal adherends; (b) drive shaft 1 and cylindrical metal adherends; (c) drive shaft 2 and cylindrical metal adherends.
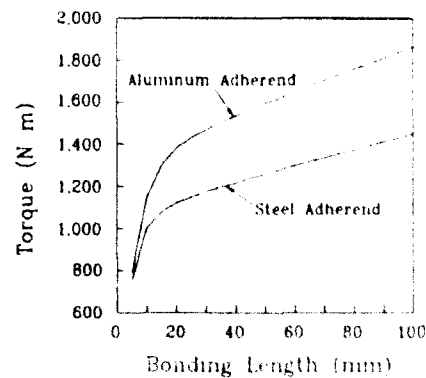
Fig. 8. Effects of bonding length on the maximum static torque transmission capability ($T_{tr,\kappa}$): (a) drive shaft 1; (b) drive shaft 2.

(a)

(b)

(c)
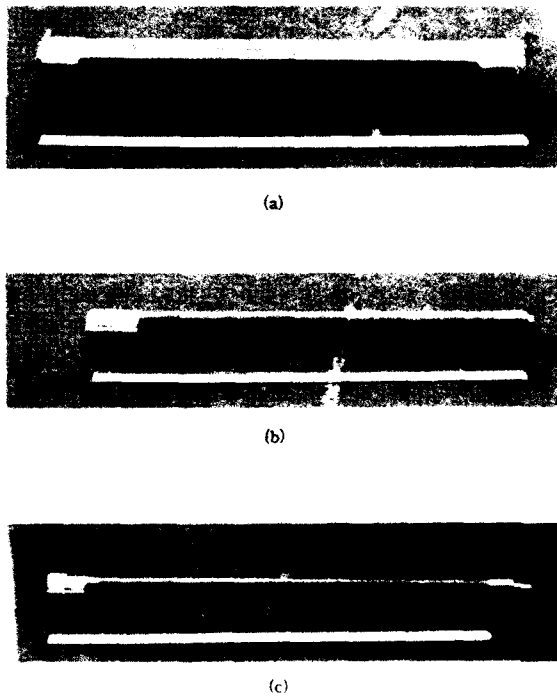
Fig. 10. Composite arm and hollow drive shafts after joining: a arm; b drive shaft 1; c drive shaft 2.

Fig. 11. Hybrid joint configuration of the composite forearm and the metal pivot shaft.

The joint between the composite forearm and the yoke and the joint between the composite forearm and the upper arm must sustain tensile forces as well as shear forces. Since the adhesively bonded joint is strong for shear forces but weak for tensile forces, a hybrid type joint which uses both mechanical and adhesive joining was designed and manufactured. The adhesively bonded part of the joint contributes in relieving the stress concentration due to holes fabricated for the mechanical joints. In this work the circular cup shaped steel plate which Nilsson[12] suggested to reduce the stress concentration of composite materials, was chosen as the reinforcement of the hybrid joint. Figure 11 shows the hybrid joint configuration and Fig. 12 shows the hybrid joint after joining.

8 COMPARISONS OF THE COMPOSITE FOREARM AND THE STEEL FOREARM

Figure 13 shows a photograph of the composite forearm and the steel forearm. The two forearms were designed to have the same size in order to compare the static and dynamic performances of the two forearms. However, the size of the composite forearm was a little different from the

Fig. 12. Joint for the composite forearm and the metal pivot shafts.
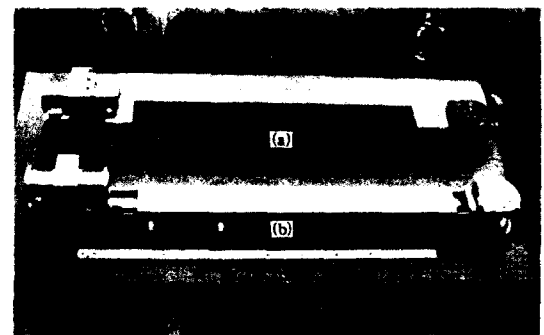
Fig. 13. Forearms of the anthropomorphic robot: a composite forearm; b steel forearm.

steel forearm because the composite forearm required the adhesive joining area. Table 4 shows the sizes and the second moments of area of the two forearms.

Table 5 shows the masses of the arms and the drive shafts. The mass of the composite arm was

3·1 kg and the composite transmission shafts for the wrist motion and the end effector pitch motion were 2·1 kg and 2·0 kg, respectively. The mass of the steel arm was 13·8 kg and the steel transmission shafts for the wrist roll motion and the end effector pitch motion were 4·8 kg and 4·5 kg, respectively. Therefore, the mass reduction of the composite forearm compared to the steel forearm was 15·9 kg.

Table 6 represents the mass distributions and lengths for the lumped model of Fig. 3. The spring constant K_N of the ball screw nut was 290 N/μm.[13] The Young's modulus of the steel was chosen as 207 GPa. Using these data and the equivalent mass of the payload $M_1 = 7$ kg, the deflection d_a of the end effector was calculated. From the numerical values, it was found that the maximum deflection of the arm occurred when $\phi = 8°$. The calculated maximum deflection of the end effector of the composite forearm $(d_{ac})_{max}$ and the calculated maximum deflection of the end effector of the steel forearm $(d_{as})_{max}$ were as follows:

$$(d_{ac})_{max} = 0.074 \text{ mm}$$

$$(d_{as})_{max} = 0.077 \text{ mm}$$

Table 4. Arm dimensions of the composite forearm and the steel forearm

		Composite	Steel
Arm	Inner area	90 × 90 mm²	91 × 91 mm²
	Outer area	100 × 100 mm²	100 × 100 mm²
	Thickness	5 mm	4 mm
	2nd moment of area	2·87 × 10⁻⁶ m⁴	2·36 × 10⁻⁶ m⁴

Table 5. Masses of the arms and the drive shafts of the forearms

	Arm	Drive shaft 1	Drive shaft 2
Composite	3·1 kg	2·1 kg	2·0 kg
Steel	13·8 kg	4·8 kg	4·5 kg

These two values satisfied the 0·1 mm deflection criterion.

Figure 14 shows the impulse frequency responses of the composite arm and the steel arm. The two arms were suspended in the air by nylon strings and the vibrational characteristics were obtained by fast Fourier transformation after giving an impulse to the arms. The equipment used was a FFT Signal Analyzer (B&K 2032), an impulse hammer (B&K 8202) and an accelerometer (B&K 4369). Figure 14(a) shows the vibrational responses in the 1·6 kHz base band and Fig. 14(b) shows the vibrational responses in the 200 Hz zoom band. The fundamental natural frequencies of the steel arm and the composite arm were 650 Hz and 1340 Hz, respectively and the damping ratios of the composite arm and the steel arm were about 0·007 and 0·001, respectively. From the experimental results, it can be concluded that the fundamental natural frequency and the damping ratio of the composite arm of the anthropomorphic robot were increased 2 and 7 times, respectively, compared to those of the steel arm of the robot.

9 CONCLUSIONS

A forearm of a six degrees of freedom anthropomorphic robot which has 70 N payload and 0·1 mm positional accuracy was designed and manufactured with high modulus carbon fiber epoxy composite material to reduce the weight of the arm and to increase the dynamic performance of the robot. Also, two power transmission shafts which deliver the power of the motors positioned at the rear of the forearm to the wrist and the end effector were also designed and manufactured with the high modulus carbon fiber epoxy composite material to reduce the rotational inertia. In order to join the composite forearm and the power transmission shafts to the gear box and the bearing housing, adhesively bonded double lap

Table 6. Masses and dimensions of the composite forearm and the steel forearm

	Composite forearm		Steel forearm	
Mass (kg)	$M_1 = 7.27$	$M_3 = 10.44$	$M_1 = 24.2$	$M_3 = 8.5$
	$M_2 = 27.01$	$M_4 = 44.72$	$M_2 = 28.3$	$M_4 = 61.0$
Dimension (mm)	$L_1 = 200.0$	$L_3 = 192.0$	$L_1 = 200.0$	$L_3 = 192.0$
	$L_2 = 13.0$	$L_4 = 173.4$	$L_2 = 13.0$	$L_4 = 173.4$
	$L_5 = 328.0$	$L_6 = 328.0$	$L_5 = 800.0$	$L_6 = 328.0$
	$L_7 = 1050.0$	$L_8 = 250.0$	$L_7 = 1050.0$	$L_8 = 250.0$

(a)

Mode	Frequency (Hz)	Damping Ratio
1	650	0.00098
2		

Mode	Frequency (Hz)	Damping Ratio
1	1,335 5	0 00723
2	1,347 6	0 00667

(b)
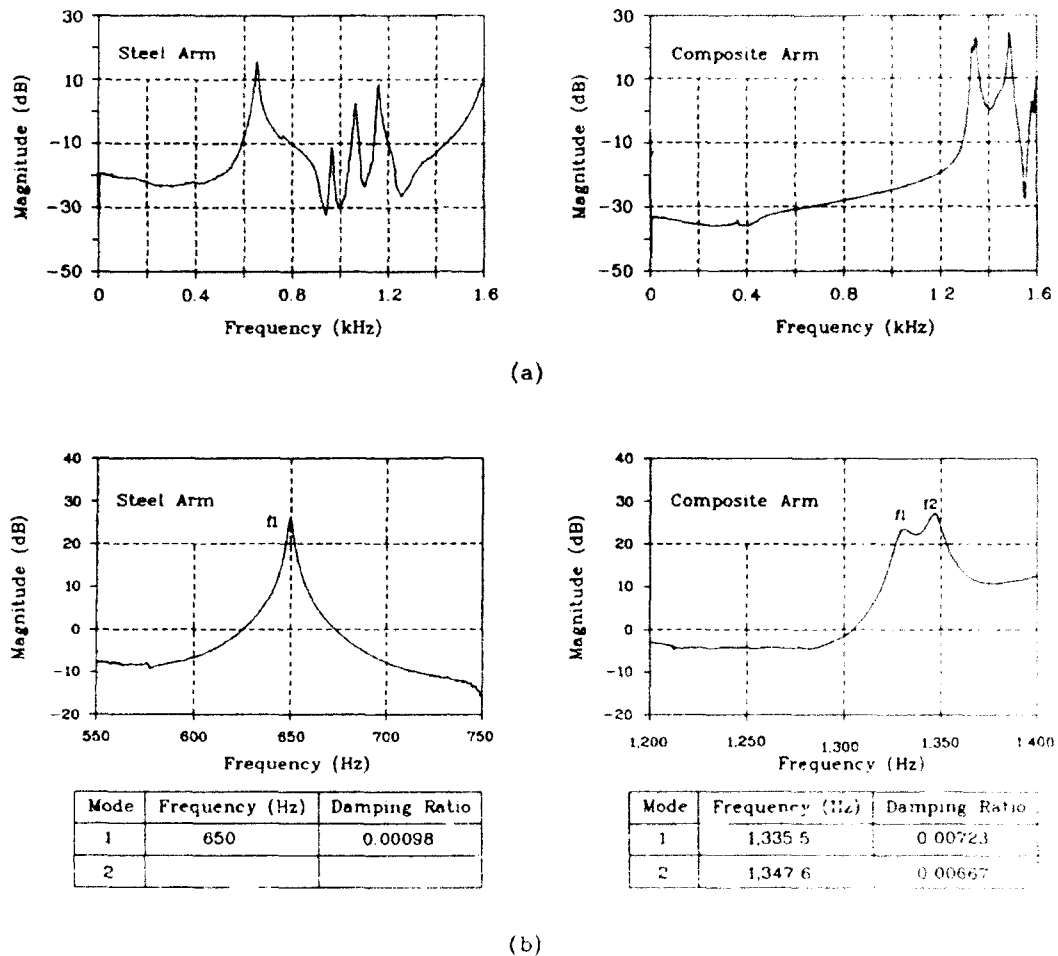
Fig. 14. Impulse frequency responses of the composite and steel arm: (a) represented in 1·6 kHz base band; (b) represented in 200 Hz zoom band.

joints and a hybrid joint which uses both mechanical and adhesive joining were designed and manufactured. A simple robot deflection equation of the end effector was derived to assess the deflection of the forearm by its own weight and the payload. The vibrational characteristics of the composite arm were tested by an impulse response and compared to those of the same size of the steel arm. From the calculated and experimental results, the following conclusions were made:

1. The mass of the composite arm was 3·1 kg and the composite transmission shafts for the wrist roll motion and the end effector pitch motion were 2·1 kg and 2·0 kg, respectively, whereas the mass of the steel arm was 13·8 kg and the steel transmission shafts for the wrist roll motion and the end effector pitch motion were 4·8 kg and 4·5 kg, respectively. Therefore, the mass reduction of the composite forearm was 15·9 kg.

2. The fundamental natural frequencies of the steel arm and the composite arm were 650 Hz and 1340 Hz, respectively and the damping ratios of the composite arm and the steel arm were 0·007 and 0·001, respectively.

3. The double lap joint and the hybrid joint which use both mechanical and adhesive joining were satisfactorily employed in joining the composite arm and the composite power transmission shafts to the gear box and the bearing housing.

REFERENCES

1. Lee, D. G., Kim, K. S. & Kwak, Y. K., Manufacturing of a SCARA type direct-drive robot with graphite fiber epoxy composite materials. *Robotica*, 9 (1991) 219–29.

2. Reugg, C. & Habermeir, J., Composite propeller shafts design and optimization. In *Advanced Composite Materials, 3rd Int. Conf. on Composite Materials, Vol 2*. Pergamon Press, Oxford, 1980, pp. 1740–55.

3. Vorlicek, P. L., Material damping of aluminum and graphite/epoxy in a simulated zero-gravity environment. SM thesis, Department of Aeronautics and Astronautics, Massachusetts Institute of Technology, Boston, MA, 1981.

4. Asada, H. & Youcef-Toumi, K., Direct-drive Robots. The MIT Press, Boston, MA, 1987, pp. 8-11.

5. Koenigsberger, F., Design Principles of Metal-Cutting Machine Tools. The Macmillan Company, New York, 1964, pp. 43-7.

6. Craig, J. J., Introduction to Robotics, Mechanics and Control, 2nd edn. Addison-Wesley, MA, Chapter 8, 1989.

7. Mavilor Motor Catalog, Mavilor Co., Ltd, Chicago, IL.

8. Popov, E. P., Engineering Mechanics of Solids. Prentice-Hall, Englewood Cliffs, NJ, 1990.

9. Jones, R. M., Mechanics of Composite Materials, McGraw-Hill, New York, Chapter 4, 1975.

10. Lee, D. G., Kim, K. S. & Im, Y. T., An experimental study of fatigue strength for adhesively bonded tubular single lap joints. Journal of Adhesion, 35 (1991) 39-53.

11. Adams, R. D. & Peppiatt, N. A., Stress analysis of adhesively bonded tubular lap joints. Journal of Adhesion, 9 (1977) 1-18.

12. Nilsson, S., Increasing strength of graphite/epoxy bolted joints by introducing an adhesively bonded metallic insert. Journal of Composite Materials, 23 (1989) 642-50.

13. THK LM System Catalog No. 100-1K, THK Co., Ltd, C-34, Tokyo, Japan, 1990.

A two-dimensional analysis of multiple matrix cracking in a laminated composite close to its characteristic damage state

D. Gamby & J. L. Rebière

Laboratoire de Mécanique & Physique des Matériaux, ENSMA, 20 rue Guillaume VII, F-86034 Poitiers Cedex, France

The proposed approach incorporates all the stress components of interest in each layer of a cracked cross-ply laminate. Its starting point is a very general distribution of the shearing stress in both types of layer, represented by a series, each term of which is the product of a trigonometric function in the axial co-ordinate, a hyperbolic function in the thickness coordinate and an undetermined coefficient a_{ij}; all the other stress components in each layer are deduced from the above by using the equilibrium equations, interface continuity conditions and traction boundary conditions. Minimizing the complementary energy of the whole laminate yields an algebraic system whose unknowns a_{ij} are the above coefficients. The validity of the proposed model is assessed by comparing the stress values it gives with those estimated through other semi-analytical models or a finite element method. Moreover, the series convergence is all the faster since the crack density is large, thus enabling careful investigation of the stress field when transverse cracking attains its saturation spacing.

1 INTRODUCTION

In the aeronautical industry, the design of structural parts often incorporates an estimation of the service life. Many aircraft development programmes involve the use of laminated composite materials made up of a polymer matrix and carbon long fibres. When specimens of such materials are subjected to a fatigue loading, several damage modes may occur in turn; the sequence of the various mechanisms, as well as their related growth rates, depend on many parameters: among other things, the elastic properties of each laminate ply, the stacking sequence, together with some geometrical characteristics such as the thicknesses of the off-axis and longitudinal layers, play a special role. In the cross-ply laminates investigated in Refs 1-3, the first observed damage mechanism is so-called transverse cracking, i.e. matrix cracking in off-axis plies. When the constraint due to the longitudinal plies is sufficient, transverse cracks do not significantly alter the mechanical properties of the laminate: their presence can be tolerated as long as their density is not too large. As early as 1977, several authors[4,5] remarked that the crack density on a specimen edge could not exceed some limiting

value beyond which the creation of new cracks became almost impossible. This saturation point of the transverse cracking phenomenon was called 'Characteristic Damage State' (CDS) by Reifsnider.[4] However, the evolution of this degradation mechanism has to be carefully monitored, as its saturation often announces the occurrence of other more harmful damage modes, such as delamination,[6] longitudinal splitting[7] or fibre breakages.

The initiation, growth and multiplication of matrix cracks in off-axis layers of composite laminates have been extensively investigated: numerous analytical or numerical models have been proposed to describe the stress distribution in cracked laminates; relationships between loading intensity on one hand, and crack density on the other, have also been derived. However, most studies are confined to cross-ply laminates and simple loading conditions; cracks are usually assumed to span the whole specimen width; the references we will quote do not constitute an extensive bibliography, but we hope them to be illustrative of the various kinds of modelling which can be encountered. A completely different type of approach relies on a purely phenomenological description of a cracked layer thought of as

made of an equivalent homogeneous material endowed with suitable internal or damage variables.[8-16] The aim of 'self-consistent' models is to provide theoretical estimates for the equivalent stiffnesses of cracked laminates.[17,18]

As regards the modelling of the local stress field distribution between two adjacent cracks, and at the level of a two-phase layer replaced by an equivalent homogeneous orthotropic elastic material, the available approaches can roughly be classified according to their refinement degree:

— The 'simplest' analyses (some of them are in fact fairly sophisticated!) lead to a differential equation governing some function (such as the average over a layer thickness of some displacement or stress component) of the 'longitudinal' coordinate (x) measured along an axis parallel to the loading direction, for a simple tensile loading, and perpendicular to the crack faces in the transverse layer of a cross-ply laminate:[1,2,19-31] most of the 'shear-lag' models come in this category. More often than not, the normal stress σ_{xx} is assumed to be constant through the thickness of each layer, i.e. along the (z) direction. Zhang, Fang and Soutis[32-33] attacked the difficult case of $[\pm\theta_m/90_n]_s$ laminates.

— Another type of approach is that of the would-be 'variational' models which rely on the principle of stationary potential/complementary energy for a kinematically/statically admissible displacement/ stress field. One of the major difficulties is to construct sufficiently general admissible fields. Such approaches usually lead to mathematical one-dimensional[34-43] or two-dimensional[44] models.

— Two- or three-dimensional descriptions of the displacement or stress distributions can also be achieved through finite element methods.[45-47] For various reasons, the results they provide are not always as reliable or useful as might be expected: for instance, it may occur that the traction-free condition on the crack faces is not accurately enforced.

— Other studies related to specific aspects of transverse cracking can be found in Refs 48–50.

Most of the above models give a good prediction of the stress field when the crack density is not too large. Close to the CDS, i.e. when the crack spacing has the same order of magnitude as the related layer thickness, it becomes important to get a description of the stress field which is as refined in the (z) direction as it is in the longitudinal (x) direction. Among the two-dimensional models, Ohira's approach,[51,52] deserves special attention, as it is the only one to lead to a partial

differential equation satisfied by the axial displacement considered as a function of both axial and thickness coordinates $(x$ and z respectively), thus yielding a stress distribution which qualitatively resembles that given by finite element analyses[45] (see Fig. 1).

In fact x and z now play similar roles, contrary to what happens in the above-mentioned one-dimensional models. Another analysis which does not favour the x-coordinate at the expense of the z-coordinate is that of Ref. 44.

The approach we propose goes beyond Ohira's model, as it does not rely on the description of a single displacement component; on the contrary, it incorporates all the stress components of interest in each layer of a cracked cross-ply laminate.

The model derivation is carried out in two stages: in the first stage, a very general distribution of the shearing stress is proposed. In the second stage, all the other stress components in each layer are deduced from the above by using the equilibrium equations, interface continuity conditions and traction boundary conditions. The so-obtained statically admissible stress field then depends on the still undetermined coefficients of the shearing stress distribution in the damaged layer. Minimizing the complementary energy of the whole laminate yields an algebraic system whose unknowns are the above coefficients.

The validity of the proposed approach is then assessed by comparing the stress values it gives with those estimated through other semi-analytical models, a finite element method, and some experimental results already obtained by earlier authors.

2 SHEARING STRESS DISTRIBUTION

2.1 Problem position

The structure at hand is a symmetric three-layer laminate whose mid-plane contains the x and y directions, whereas y and z denote the width and thickness directions respectively. In the central transverse layer, denoted by lamina 1, each matrix crack occupies a rectangle defined by

$$-\frac{b}{2} \leq y \leq \frac{b}{2}$$

$$-t_1 \leq z \leq t_1$$

$$x = (2p+1)l$$

$$p = 0,1,2\ldots$$

Normalized normal stress [0/(90)6]s laminate
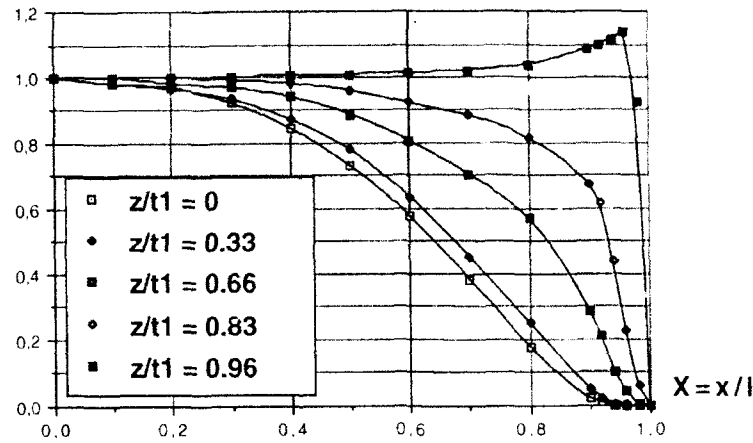
Fig. 1. Longitudinal normal stress in 90° ply, along *x*-axis, in a [0/90₂]ₛ laminate, for several values of thickness coordinate *z*, after Ref. 45.

where $2l$ is the constant spacing between two adjacent cracks, b is the plate width, $2t_1$ is the transverse layer thickness, t_2 denotes the thickness of each outer longitudinal layer, referred to as lamina 2, and $2t = 2(t_1 + t_2)$ is the plate total thickness. Due to the problem symmetries, attention is restricted to the unit cell (Fig. 2) defined by $0 \le x \le l, 0 \le y \le b, 0 \le z \le h$. L denotes the plate total length.

Two ratios will play an important role in the problem at hand:

— the constraint parameter $\lambda = t_2/t_1$

— the crack density $d = L/(2l)$

$\sigma_{ij}^{(i)}$ will denote the stress components in lamina (i).

The following boundary conditions have to be enforced on the cell faces:

- On the plane $z = 0$: $\sigma_{xz}^1 = 0$, $w^1 = 0$, where w^1 is the displacement component in the z-direction, related to lamina (1).
- On the plane $x = 0$: $\sigma_{xz}^i = 0$ and $u^i = 0$, where u^i is the axial displacement component (along x) in lamina (i) ($i = 1,2$).
- The plane $z = h = t_1 + t_2$ is a free boundary (in lamina (2)), on which: $\sigma_{zz}^2 = \sigma_{xz}^2 = 0$
- The face $x = l$ has to be divided into two parts:
  — the region $0 \le z \le t_1$ is a cracked surface where $\sigma_{xx}^1 = \sigma_{xz}^1 = 0$
  — the region $t_1 \le z \le h$ belongs to a plane of symmetry, whence: $u^2 = u$, where u is a constant, and $\sigma_{xz}^2 = 0$.
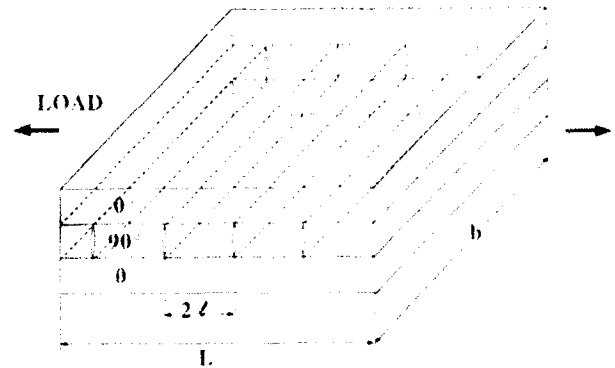
Fig. 2. Cracked laminate and unit cell.

In the basic variant of the model, a plane strain state with respect to the y-direction is assumed; in another variant, a plane stress state in the same direction will prevail; the actual mechanical state is expected to be close to a generalized plane strain state in the y-direction; it should lie between the two above simpler states.

2.2 Temporary kinematic assumptions

In order to construct a suitable basis for the shearing stress expressions, we shall provisionally use some fairly stringent assumptions concerning the displacement field $U^i(x, y, z)$ in each lamina (i). Once the desired basis is obtained, these assumptions can safely be discarded. Each displacement vector field U^i is assumed to be such that

$$U^i = u^i x + v^i y + w^i z$$

where

$$u^i = u^i(x,z), \quad v^i = v^i(y), \quad \varepsilon^i_{yy} = 0, \quad w^i = w^i(z)$$

2.3 Partial differential equation for $\sigma^{(i)}_{xz}$

As a consequence, σ^i_{xx}, u^i, w^i and σ^i_{xz} are related by:

$$\sigma^i_{xx} = C^i_{11}\frac{\partial u^i}{\partial x} + C^i_{13}\frac{\partial w^i}{\partial z} \tag{1}$$

$$\sigma^i_{xz} = C^i_{55}\frac{\partial u^i}{\partial z} \tag{2}$$

together with the equilibrium equation

$$\frac{\partial}{\partial x}\sigma^i_{xx} + \frac{\partial}{\partial z}\sigma^i_{xz} = 0 \tag{3}$$

Here, C^i_{kl} denote the stiffnesses in the orthotropic lamina i; $k, l = 1,...,6$. Eliminating u^i and σ^i_{xx} from eqns (1)–(3), while taking into account the condition $\partial/\partial x\, w^i = 0$, results in:

$$\frac{\partial}{\partial z}\sigma^i_{xz}(x,z) + R^i\frac{\partial^2}{\partial x^2}\sigma^i_{xz}(x,z) = 0 \tag{4}$$

where $R^i = \dfrac{C^i_{11}}{C^i_{55}}$

2.4 Shearing stress expressions

The most general shearing stress distribution which satisfies the above partial differential equation together with the boundary conditions bearing upon σ^i_{xz} at $x = 0$, $z = 0$, $x = l$, $z = h$ can be taken in the form of a Fourier series in the variable x, i.e.

$$\sigma^1_{xz} = \sum_q a_q \frac{\sinh(R^1\, q\pi z/l)}{\sinh(R^1\, q\pi h_1/l)}\sin(q\pi x/l) \tag{5}$$

$$\sigma^2_{xz} = \sum_q a_q \frac{\sinh(R^2\, q\pi(h-z)/l)}{\sinh(R^2\, q\pi h_2/l)}\sin(q\pi x/l) \tag{6}$$

The interface shearing stress is:

$$\sigma^1_{xz}(x,t_1) = \sigma^2_{xz}(x,t_1) = \tau(x) = \sum a_q \sin\left(q\pi\frac{x}{l}\right) \tag{7}$$

Although each of the above expansions (5) and (6) satisfies an equation of the type (4), its form is expected to be sufficiently general to represent the actual shearing stress distribution in each lamina with the desired accuracy. The sequence of undetermined coefficients $a_q; q = 1,...$ will be selected as the sole unknowns of the problem. From now on, the only assumption regarding the admissible stress field will be the form of the distribution of the shearing stress $\sigma^k_{xz}(x,z)$, $k = 1,2$ in each layer. Both expressions (5) and (6) meet the definite partial differential equation (4) whose origin will now intentionally be 'forgotten'. The derivation of Ohira's model[5] rests on a partial differential equation analogous to eqn (4) when the shearing stress σ^k_{xz} is replaced by the axial displacement in the transverse layer. Moreover, in his approach, one boundary condition bearing on the same shearing stress is not enforced. The model we propose is more general; as a consequence, once the stress components have been obtained, the related displacements can be deduced by the classical integration procedure, but there is no reason that these final displacements still have to meet the restrictive assumptions which were used to derive the partial differential equation (4) satisfied by σ^k_{xz}, notably $(\partial/\partial x)\, w^k \equiv 0$.

3 SECOND STAGE: PROBLEM SOLUTION

3.1 Statically admissible stress field

The statically admissible stress field incorporating the above shearing stress distribution is unique; its remaining components are obtained by integrating the equilibrium equations, taking into account the still unused boundary conditions. The plane strain condition $\varepsilon^k_{yy} = 0$ results in:

$$\sigma^k_{yy} = K^k_1 \sigma^k_{xx} + K^k_2 \sigma^k_{zz} \qquad (k = 1,2) \tag{8}$$

where K^k_j are functions of C^k_{ij} such that

$$\sigma^1_{yy}(x,z) = v_1(\sigma^1_{xx}(x,z) + \sigma^1_{zz}(x,z))$$

$$\sigma^2_{yy}(x,z) = v_2(\sigma^2_{xx}(x,z) + \sigma^2_{zz}(x,z))$$

From the equilibrium equations and boundary conditions:

$$\sigma = \frac{\partial}{\partial x} \int \sigma(x,z) \, dz, \quad \text{whence} \quad \sigma(x,z) = \sum f_q(z) \cos q\pi \frac{x}{l}$$

with

$$f_q(z) = a_q \left(-\frac{1}{R^2} \frac{\left|1 - \operatorname{ch} R^{-1} q\pi \frac{h-z}{l}\right|}{\operatorname{sh} R^{-1} q\pi \frac{t_2}{l}} \right)$$

and

$$\sigma = \sigma(x,t_1) + \frac{\partial}{\partial x} \int \sigma(x,z) \, dz$$

that is

$$\sigma(x,z) = \sum e_q(z) \cos q\pi \frac{x}{l}$$

where

$$e_q(z) = a_q \left[\frac{1}{R^2} \operatorname{th}\left(R^{-1} q\pi \frac{t_1}{2l} \right) + \frac{1}{R^2} \frac{\left[\operatorname{ch}\left(R^{-1} q\pi \frac{t_1}{l} \right) - \operatorname{ch}\left(R^{-1} q\pi \frac{z}{l} \right) \right]}{\operatorname{sh}\left(R^{-1} q\pi \frac{t_1}{l} \right)} \right]$$

The representation of the normal stress $\sigma_{13}^1(x,z)$ in the 90° layer is obtained by integrating one of the equilibrium equations over the interval $0 \le x \le l$; taking into account the traction-free condition on the crack surface. $\sigma_{13}^1(l,z) = 0$, results in

$$\sigma_{13}^1(x,z) = \frac{\partial}{\partial z} \int_x \sigma_{11}^1(x_1,z) \, dx_1.$$

Whence

$$\sigma_{13}^1(x,z) = C_0(z) + \sum_{n=1} C_n(z) \cos n\pi \frac{x}{l}$$

with

$$C_0(z) = -R^{-1} \sum_{q=1} a_q (-1)^q \frac{\operatorname{ch} R^{-1} q\pi z/l}{\operatorname{sh} R^{-1} q\pi t_1/l}$$

and

$$C_n(z) = a_n(R^{-1}) \frac{\operatorname{ch} R^{-1} n\pi z/l}{\operatorname{sh} R^{-1} n\pi t_1/l}$$

The expression of the normal stress $\sigma_{33}^2(x,z)$ is also obtained by integrating with respect to x the related equilibrium equation; by taking into account the boundary conditions at $x = 0$ and $x = l$, namely $u^2(l,z) = u, u^2$

$(\sigma, z) = 0$, $\forall z$, together with the plane strain state assumption, it can be shown that $\sigma_{11}^2(x,z)$ has an expression of the form:

$$\sigma_{11}^2 = \sigma_0 + \frac{\partial}{\partial z}\int_{x}^{l/2} \sigma_{13}^2(x',z)\,dx'$$

whence

$$\sigma_{11}^2(x,z) = \sigma_0 + \sum_{q=1} b_q(z)\cos q\pi\frac{x}{l}$$

where

$$b_q(z) = a_q - R^2\frac{\operatorname{sh} R^2 q\pi\frac{(h-z)}{l}}{\operatorname{sh} R^2 q\pi\frac{t_2}{l}}, \qquad \sigma_0 = \frac{u}{l\,S_{11}^2 + K_1^2\,S_{12}^2}$$

and S_{ij}^2 denote the compliances of lamina (k), owing to the fact that

$$u = \int_{-l}^{l} \varepsilon_{11}^2(x,z)\,dx = (S_{11}^2 + S_{12}^2 K_1^2)\sigma_0\int_0^l dx$$

and providing that

$$\int_{-l}^{l} \sigma_{11}^2(x,z)\,dx = 0$$

which is indeed the case. Displacement u is the problem datum.

3.2 Complementary energy

Due to the fact that the uniform displacement u is prescribed on a part of the cell boundary, the expression for the complementary energy has the form:

$$E_c = -W + ub\int_{z} \sigma_{11}^2(l,z)\,dz$$

where W is the cell strain energy, such that

$$W = b\int_0^l\int_0^l w^1(x,z)\,dx\,dz + b\int_l^h\int_0^l w^2(x,z)\,dx\,dz$$

in which the strain energy density in the $0°$ layer is expressed by:

$$2w^1 = \frac{(\sigma_{11}^1)^2}{E_A} + \frac{(\sigma_{22}^1)^2}{E_1} + \frac{(\sigma_{33}^1)^2}{E_A} + \frac{(\sigma_{13}^1)^2}{G_A} - \frac{2\nu_A}{E_A}[\sigma_{11}^1(\sigma_{22}^1 + \sigma_{33}^1)] - \frac{2\nu_1}{E_1}\sigma_{22}^1\sigma_{33}^1 \tag{9}$$

where E_A, ν_A, G_A, E_1, ν_1, G_1 respectively denote the axial Young's modulus, the associated axial Poisson's ratio, the axial shear modulus, the associated transverse Poisson's ratio and the transverse shear modulus. In order to take into account the plane strain state assumption, eqn (8) is substituted into eqn (9); one then has an expression of the form:

$$2w^2 = (\sigma_{11}^2)^2 a_1^2 + (\sigma_{22}^2)^2 a_2^2 + (\sigma_{33}^2)^2 a_3^2 + \sigma_{11}^2\sigma_{33}^2 a_4^2$$

where the coefficients a_i^k depend on the stiffnesses and compliances of layer k.

The strain energy density of the 90° layer is given by:

$$2w^1 = \frac{(\sigma_{11}^1)^2}{E_1} + \frac{(\sigma_{22}^1)^2}{E_3} + \frac{(\sigma_{33}^1)^2}{E_1} + \frac{(\sigma_{12}^1)^2}{G_1} - \frac{2\nu_3}{E_3}[\sigma_{11}^1(\sigma_{22}^1 + \sigma_{33}^1)] - \frac{2\nu_1}{E_1}\sigma_{22}^1\sigma_{33}^1 \qquad (10)$$

Similarly, when the plane strain condition is enforced, one arrives at an expression of the form:

$$2w^1 = (\sigma_{11}^1)^2 a_1^1 + (\sigma_{22}^1)^2 a_2^1 + (\sigma_{12}^1)^2 a_3^1 + \sigma_{11}^1\sigma_{22}^1 a_4^1$$

3.3 Problem equations

Minimizing the complementary energy with respect to the unknown coefficients a_q amounts to writing:

$$\frac{\partial}{\partial a_q} E_c = 0 \qquad (q = 1, 2, \dots) \qquad (11)$$

It is worth noting that the last term in the complementary energy,

$$A = u \int_\Sigma \sigma_{11}^2 l.z \cdot ds = ub \int_l^h \sigma_{11}^2 l.z \cdot dz$$

is such that

$$\frac{\partial}{\partial a_q}(A) = -ub\left[\frac{l}{\pi} \frac{(-1)^q}{q}\right]$$

If only Q terms are retained in each Fourier series expansion, the above conditions (11) yield a linear system of Q equations for the Q unknown coefficients a_q. This system has the form

$$\sum_{q=1}^{Q} B_{nq} a_q = D_n$$

in which the matrix B_{nq} exhibits no special symmetry.

In order to estimate the number Q of terms to be kept in the series expansions of the stress components, we investigated the rate at which the sequence (a_q) tends to zero in two extreme cases:

— Close to the saturation state of the transverse cracking, the length l (half-spacing between two neighbouring cracks) becomes very small: in practice, for a $[0_m, 90_p]_s$ cross-ply laminate such that $m + p = 8$, made of a T300/914 composite, the characteristic damage state is attained when $l = 0.2$ mm. Figure 3 shows the variation of a_q with q for this value of l.

It can be remarked that the first coefficients markedly prevail over the following ones, and that the terms of the related sequence rapidly tend to zero. In this first case, a good accuracy of the stress components can safely be expected, even when keeping a few terms of the Fourier series expansions.

— On the other hand, when the crack spacing is 'large' (for instance $l = 10$ mm), the terms of the sequence (a_q) tend to zero very slowly: if the same accuracy is demanded, ten times more terms as when $l = 0.2$ mm are needed (see Fig. 4)! In that case, it is more appropriate to resort to a model of the 'shear-lag' family.

4 NUMERICAL RESULTS

4.1 Stress distribution

In order to illustrate the marked dependence of the stress components on both axial and thickness coordinates close to the saturation state of the first damage mode, we present in Fig. 5 the distribution of the axial normal stress σ_{11}^k in each layer ($k = 1$ or 2) of a $[0_3, 90]_s$ laminate made up of T300/914 carbon/epoxy composite, for a crack spacing such that $l = 0.2$ mm. The stress values are
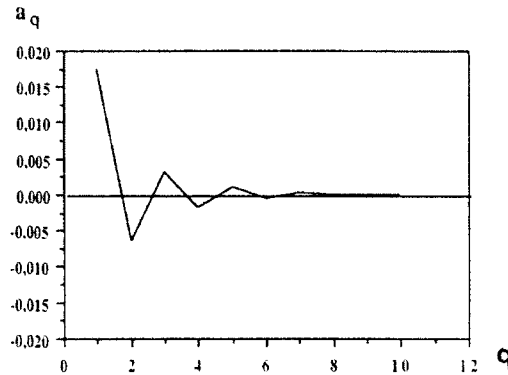
Fig. 3. Variation of the Fourier series coefficients a_q with q for $l = 0.2$ mm.
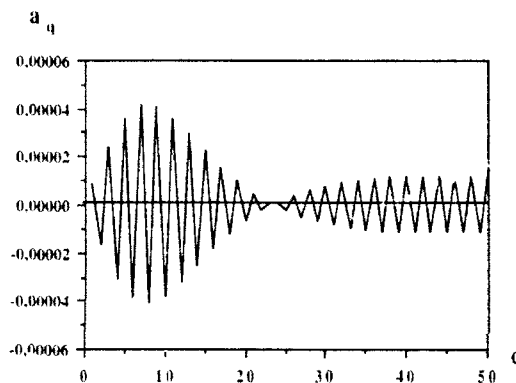
Fig. 4. Variation of a_q with q when $l = 10$ mm.

normalized by their related magnitudes σ_0^k in the uncracked state, as obtained by the classical laminate theory. As can be seen in Fig. 5, very sharp peak values are reached in the transverse layer close to the interface.

The starting point of our model is a given distribution of shear stresses σ_{xz}^k. Although the role of this stress component is essential when transforming the load from a damaged layer to the adjacent uncracked plies, in the vicinity of a transverse crack, few comparison elements pertaining to this stress component can be found in the literature. In most two-dimensional approaches, this distribution does not even satisfy all the problem boundary conditions. In Fig. 6, we superimposed both normalized distributions obtained by Ohira's model and ours: the latter can be spotted thanks to the zero traction condition met on the crack faces. Half the 90° layer alone is represented. The $[0,90_2]_s$ laminate is made of a T300/914 composite with a transverse crack spacing such that $l = 0.2$ mm.

4.2 Axial stiffness loss

When the constraint parameter λ is large enough, the decrease in the equivalent axial modulus E of the laminate due to matrix cracking is a small magnitude effect whose measurement requires great care; therefore, the prediction of axial stiffness loss according to the present model might be a good reflection of its refinement degree. The average $\bar{\sigma}_{xx}$ of the axial normal stress over the plate cross-section is such that

$$\bar{\sigma}_{xx} = \frac{1}{h} \int_0^h \sigma_{xx}^k(x,z)\, dz$$

Then the equivalent Young's modulus of the damaged laminate in the axial direction is defined by

$$E(l) = \frac{\bar{\sigma}_{xx}}{u/l}$$

After performing the integrations with respect to the thickness coordinate z in both types of layers, the resulting expression for $E(l)$ turns out to be independent on the axial coordinate x, namely:

$$E(l) = \frac{l}{uh}\left\{ \frac{l}{\pi}\sum_{q=1}^{\infty} a_q \frac{(-1)^q}{q} + \sigma_c t_2 \right\} \qquad (12)$$

By the way, eqn (12) is an example of the homogenization procedures that can be performed from the various 'local' stress component expressions given by the proposed model. The expression of $E(l)$ in terms of the sequence $\{a_q\}$ is remarkably simple. Stiffnesses or compliances of the homogeneous materials equivalent to the individual layers, damaged or not, can be expressed in terms of the crack spacing, in much the same way. Figure 7 shows the plot of relative axial stiffness variation E/E_0, where E_0 is the modulus in the undamaged state, against crack density $d = 1/(2l)$, according to the proposed model, Lim and Hong's shear-lag model[25] and experimental results.[53] It is worth noting the good achievement of Lim and Hong's model, in spite of the comparatively simple assumptions it relies on, as far as the equivalent axial modulus is concerned.

The relative axial stiffness variation predicted by a special two-dimensional finite element method[54] has also been compared in Fig. 8 with that given by the present model for a carbon/epoxy laminate, the constraint parameter of which is such that $\lambda = 7$. For a comparatively low value
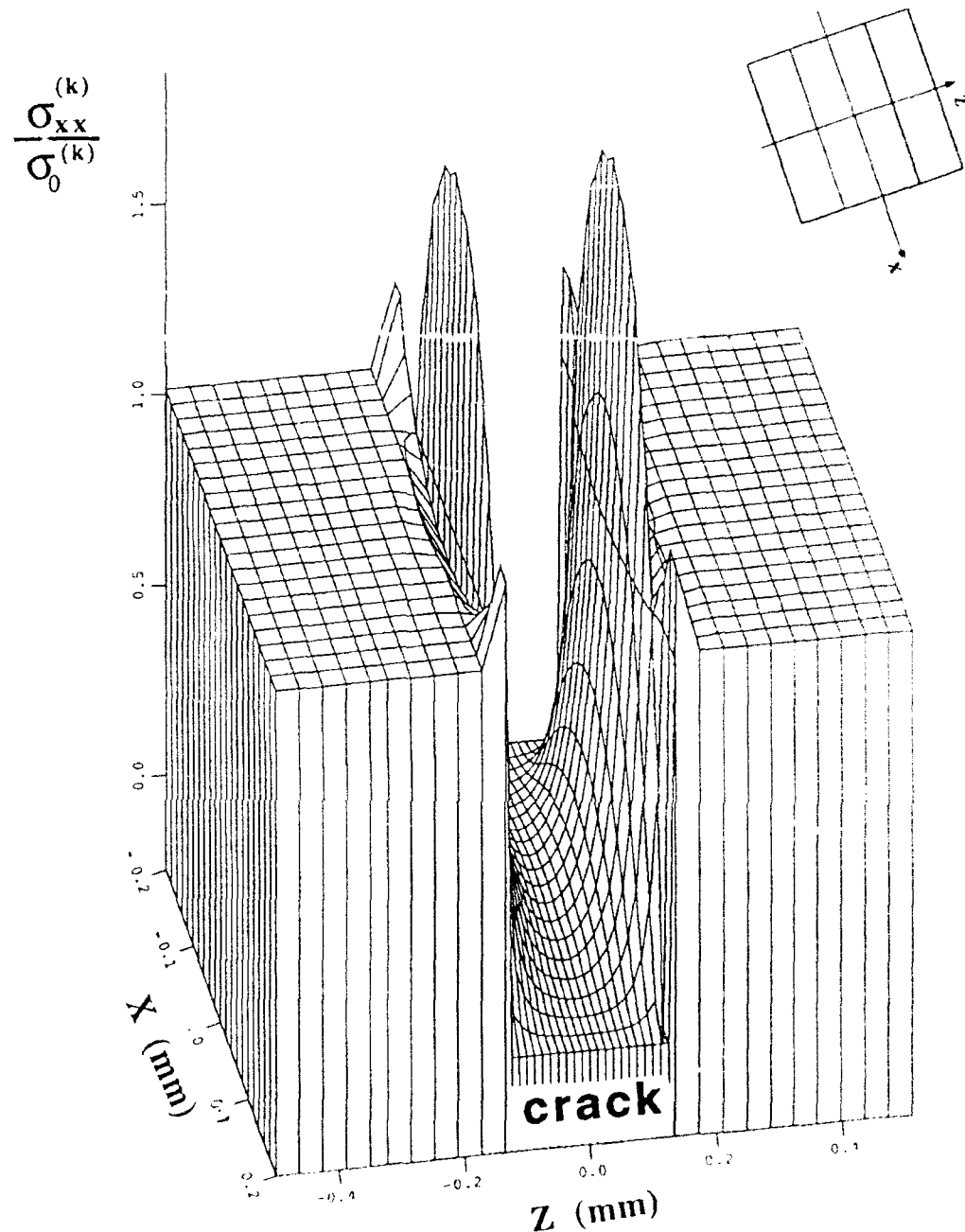
Fig. 5. Normalized normal stress σ_{xx}^k/σ_0^k in the three layers of a T300/914 carbon/epoxy $[0_3,90]_s$ laminate, for $l = 0.2$ mm.

of the crack density, this particular finite element method, in which a periodical stacking sequence is assumed, underestimates the stiffness loss.

5 DISCUSSION AND CONCLUSION

A plane stress state version of the model can easily be constructed by putting $K_I^{(k)} = 0$ in eqn

(8). In most situations, there is a very small difference in stress magnitudes between plane strain and plane stress states (see Ref. 55 for a quantitative comparison, at least in the case of the T300/914 composite); the 'actual' state can rightly be expected to lie between the above two extreme states. As the convergence of the series $\{a_q\}$ has been found to be all the faster since the crack density is large, the proposed model enables one
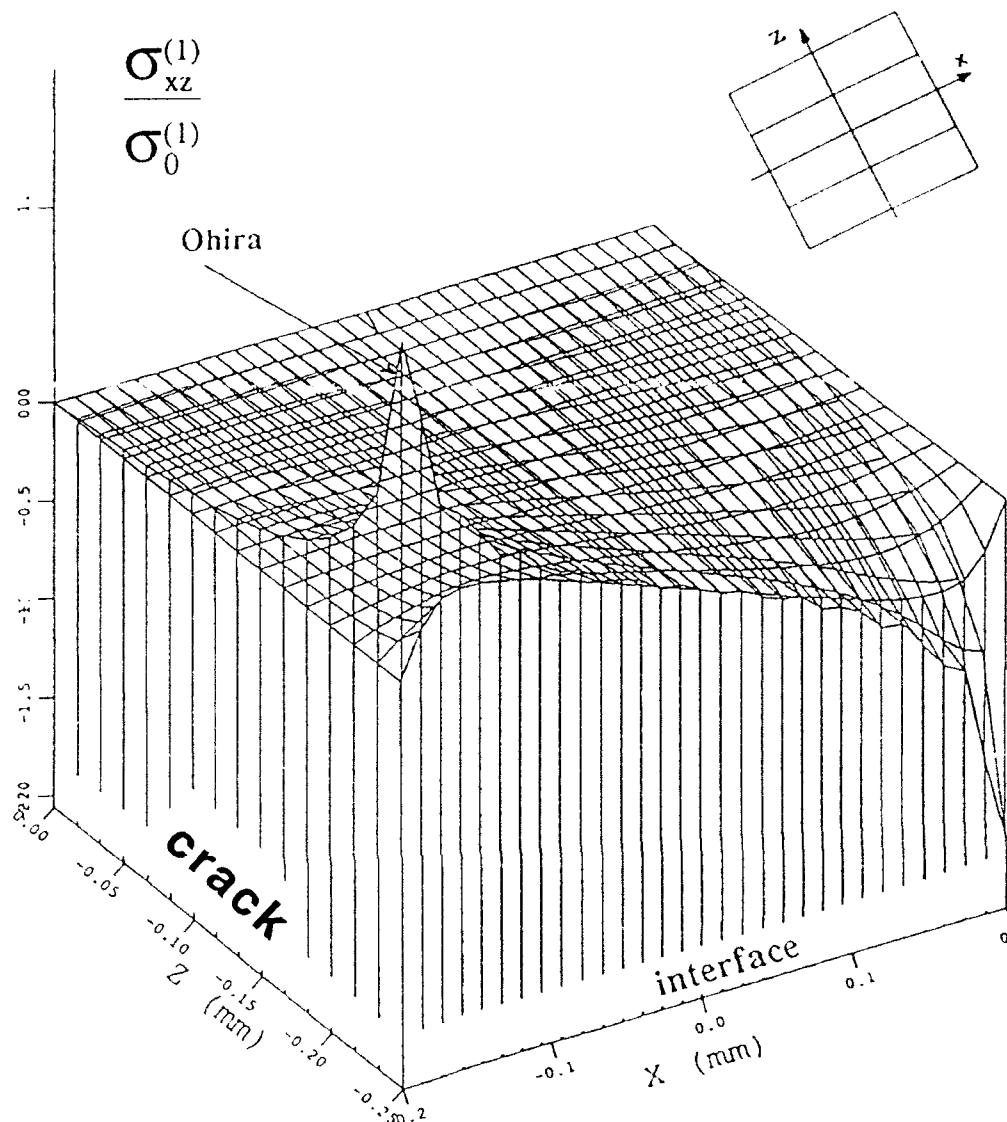
Fig. 6. Normalized shear stress $\sigma_{xz}^{1}/\sigma_0^k$ in the 90° half-layer as obtained by Ohira's model (peaked surface) and the present model (smoother surface).
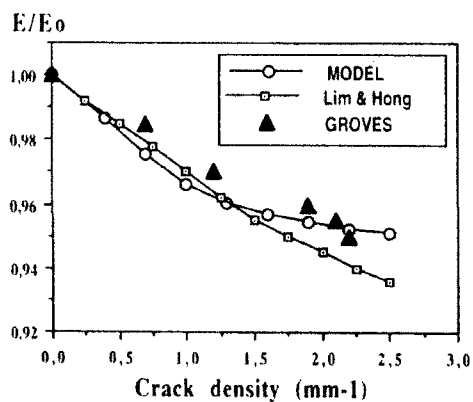
Fig. 7. Relative axial stiffness loss after: the proposed model, Lim and Hong's shear-lag model, and Groves' experimental results, for a graphite/epoxy $[0_2, 90_2]$ laminate.
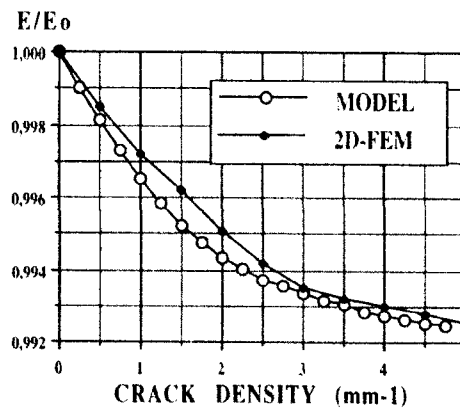
Fig. 8. Relative axial modulus of a damaged laminate versus crack density, for $\lambda = t_2/t_1 = 7$. Comparison of model with finite elements.

to carefully investigate the stress field when transverse cracking attains its saturation spacing.

Some of the simpler models, such as that of Refs 19 and 20, use as a starting point a linear shear stress distribution across each layer thickness: the proposed model is able to estimate the validity of this assumption (for more details, see Ref. 55). It also gives an expression of the often ignored normal stress σ_{zz} in the thickness direction, whose contribution to the calculation of the a_qs is not negligible.

Surprisingly, the proposed model cannot be fully assessed in relation to any absolute reference available in the literature, even finite element results, which are not always as reliable as they might seem: for instance, more often than not, some of the boundary conditions are not accurately enforced, even in sophisticated analyses such as that in Ref. 46.

Whatever the value of the constraint parameter, the marked variations of the stress components across the plate thickness are fully rendered, in accordance with the finite element predictions. The axial stiffness loss due to matrix cracking, as described by the present approach, is in good agreement with experimental results and calculations achieved from an analytical model. Finally, numerical investigations revealed that the stress magnitudes were fairly sensitive to small changes in the values of the parameters

$$(R')^2 = \frac{C_{11}'}{C_{55}'}$$

in eqn (4); in some cases, it might be useful to take advantage of this property so as to improve the model accuracy by slightly altering the values of these parameters.

REFERENCES

1. Hénaff-Gardin, C., Lafarie-Frenot, M. C., Brillaud, J. & El Mahi, A., Influence of the stacking sequence on fatigue transverse ply cracking in cross-ply composite laminates. In *ASTM Symp. Damage detection in composite materials*, ed. J. E. Masters, San Antonio, Texas, Nov. 1990, ASTM-STP1128, ASTM, Philadelphia, PA, 1992.

2. Lafarie-Frenot, M. C. & Hénaff-Gardin, C., Formation and growth of 90° ply fatigue cracks in carbon/epoxy laminates. *Composites Science and Technology*, **40** (3) (1991) 307–24.

3. Boniface, L. & Ogin, S. L., Application of the Paris equation to the fatigue growth of transverse ply cracks. *Journal of Composite Materials*, **23** (July 1989) 735–54.

4. Reifsnider, K. L., Some fundamental aspects of the fatigue and fracture response of composite materials. *Proc. 14th Annual Meeting of Soc. of Engineering Sc.*, Bethlehem, USA, 1977, pp. 373–84.

5. Garrett, K. W. & Bailey, J. E., Multiple transverse fracture in 90° cross-ply laminates of a glass fibre-reinforced polyester. *Journal of Material Science*, **12** 1977 157–68.

6. Whitcomb, J. D., Analysis of delamination growth near intersecting ply cracks. C.M.C. Report no. 91-1, Center for Mechanics of Composites, Texas A&M University, March 1, 1991.

7. Lafarie-Frenot, M. C., Hénaff-Gardin, C. & Urwald, F., Specificity of fatigue damage behaviour in carbon/epoxy cross-ply laminates. *IFS. FATIGUE 93*, Montreal, Canada, May 3–7, 1993.

8. Talreja, R., Yalvaç, S., Yats, L. D. & Wetters, D. G., Transverse cracking and stiffness reduction in cross-ply laminates of different matrix toughness. *Journal of Composite Materials*, **26** (11) Nov. 1992 1644–63.

9. Allen, D. H., Groves, S. E. & Harris, C. E., A thermomechanical constitutive theory for elastic composites with distributed damage. Part I — Theoretical development. *International Journal of Solids and Structures*, **23** (9) 1987 1301–18.

10. Ladevèze, P., A damage computational method for composite structures. *Computers and Structures*, **44** (1 2) 1992 79–87.

11. Renard, J., Modelling of a damaged composite specimen by a micro-macro numerical simulation. In *Advances in the Mechanics of Composite Structures*. ASME-IPCE Congress, New Orleans, 1990.

12. Shuxin Li, Cangru Jiang & Songlin Han, Modeling of the characteristics of fiber-reinforced composite materials damaged by matrix-cracking. *Composites Science and Technology*, **43** 1992 185–95.

13. Ousset, Y., Modèle homogénéisé d'une plaque composite présentant de la fissuration transverse. *La Recherche Aérospatiale* Mai–Juin 1991 33–47.

14. Chow, C. L. & Yang, F., A simple model for brittle composite lamina with damage. *Journal of Reinforced Plastics and Composites*, **11** March 1992 222–42.

15. Gudmundson, P. & Östlund, S., First order analysis of stiffness reduction due to matrix cracking. *Journal of Composite Materials*, **26** (7) 1992 1009–30.

16. Pyrz, R., A micromechanically-based model for composite materials with matrix cracks. *Composites Engineering*, **2** (8) 1992 619–29.

17. Laws, N., Dvorak, G. J. & Hejazi, M., Stiffness changes in unidirectional composites caused by crack systems. *Mechanics of Materials*, **2** (1983) 123–37.

18. Adali, S. & Makins, R. K., Effect of transverse matrix cracks on the frequencies of unsymmetrical, cross-ply laminates. *Journal of the Franklin Institute*, **329** (4) (1992) 655–65.

19. Nuismer, R. J. & Tan, S. C., Constitutive relations of a cracked composite lamina. *Journal of Composite Materials*, **22** (April 1988) 306–21.

20. Tan, S. C. & Nuismer, R. J., A theory of progressive matrix cracking in composite laminates. *Journal of Composite Materials*, **28** (July 1989) 1029–47.

21. Steif, P. S., Parabolic shear-lag analysis of a [0/90] laminate. In *Transverse Ply Crack Growth and Associated Stiffness Reduction during the Fatigue of a Simple Cross-Ply Laminate*, ed. S. L. Ogin, P. A. Smith & P. W. R. Beaumont. Report CUED/C/MATS/TR 105, Cambridge University, Engineering Department (Sept. 1984).

22. Han, Y. M., Hahn, H. T. & Croman, R. P., A simplified analysis of transverse ply cracking in cross-ply lami-

nates. *Composites Science and Technology*, **31** (1988) 165–77.

23. Han, Y. M. & Hahn, H. T., Ply cracking and property degradations of symmetric balanced laminates under in-plane loading. *Composites Science and Technology*, **35** (1989) 377–97.

24. Laws, N. & Dvorak, G. J., Progressive transverse cracking in composite laminates. *Journal of Composite Materials*, **22** (Oct. 1988) 900–16.

25. Lim, S. G. & Hong, C. S., Effect of transverse cracks on the thermomechanical properties of cross-ply laminated composites. *Composites Science and Technology*, **34** (1989) 145–62.

26. Dharani, L. R. & Tang, H., Micromechanics characterization of sublaminate damage. *International Journal of Fracture*, **46** (1990) 123–40.

27. Lee, J. W. & Daniel, I. M., Progressive transverse cracking of cross ply composite laminates. *Journal of Composite Materials*, **24** (1990) 1225–43.

28. Caslini, M., Zanotti, C. & O'Brien, T. K., Study of matrix cracking and delamination in glass/epoxy laminates. *Journal of Composites Technology and Research*, **9** (4) Winter 1987) 121–30.

29. Hénaff-Gardin, C. & Lafarie-Frenot, M. C., Fatigue transverse ply crack propagation in fiber reinforced composite laminates. In *Materials and Processing — Move into the 90's, Proc. of the 10th Int. SAMPE Conf.*, Birmingham, UK, ed. S. Benson, T. Cook, E. Trevin & R. M. Turner. Elsevier, Amsterdam, July, 1989, pp. 145–53.

30. MacCartney, L. N., Theory of stress transfer in a $0°-90°-0°$ cross-ply laminate containing a parallel array of transverse cracks. *Journal of the Mechanics and Physics of Solids*, **40** (1) (1992) 27–68.

31. Swanson, S. R., On the mechanics of microcracking in fiber composite laminates under combined stress. *Journal of Engineering Materials and Technology*, **111** (April 1989) 145–9.

32. Zhang, J., Fan, J. & Soutis, C., Analysis of multiple matrix cracking in $[\pm\theta_m/90_n]_s$ composite laminates — Part 1: In-plane stiffness properties. *Composites*, **23** (5) (1992) 291–8.

33. Zhang, J., Fan, J. & Soutis, C., Analysis of multiple matrix cracking in $[\pm\theta_m/90_n]_s$ composite laminates — Part 2: Development of transverse ply cracks. *Composites*, **23** (5) 1992) 299–304.

34. Vasil'ev, V. V., Dudchenko, A. A. & Elpat'evskii, A. N., Analysis of the tensile deformation of glass-reinforced plastics. *Mechanics of Polymers*, translated from *Mekhanika Polimerov*, **1** (Jan/Feb. 1970) 127–30.

35. Hashin, Z., Analysis of cracked laminates: a variational approach. *Mechanics of Materials*, **4** (1985) 121–36.

36. Hashin, Z., Analysis of stiffness reduction of cracked cross-ply laminates. *Engineering Fracture Mechanics*, **25** (5/6) (1986) 771–8.

37. Hashin, Z., Analysis of orthogonally cracked laminates under tension. *Journal of Applied Mechanics*, **54** (December 1987) 872–8.

38. Hashin, Z., Analysis of damage in composite materials. In *Yielding, Damage and Failure of Anisotropic Solids, EGF 5*, ed. J. P. Boehler. Mechanical Engineering Publications, London, 1990, pp. 3–31.

39. Nairn, J. A., The strain energy release rate of composite microcracking: a variational approach. *Journal of Composite Materials*, **23** (Nov. 1989) 1106–29.

40. Liu, S. & Nairn, J. A., Fracture mechanics analysis of composite microcracking: experimental results in fatigue. In *Composite Materials in Transition, Proc. American Society for Composites, 5th Technical Conference*, East Lansing, June 1990, pp. 287–95.

41. Pijaudier-Cabot, G. & Dvorak, G. J., A variational approximation of stress intensity factors in cracked laminates. *European Journal of Mechanics: A/Solids*, **9** (6) (1990) 517–35.

42. Varna, J. & Berglund, L., A model for prediction of the transverse cracking strain in cross-ply laminates. *Journal of Reinforced Plastics and Composites*, **11** (7) (1992) 708–28.

43. Yalvaç, S., Yats, L. D. & Wetters, D. G., Transverse ply cracking in toughened and untoughened graphite/epoxy and graphite/polycyanate crossply laminates. *Journal of Composite Materials*, **25** (Dec. 1991) 1653–67.

44. Lee, J. W., Allen, D. H. & Harris, C. E., Internal state variable approach for predicting stiffness reductions in fibrous laminated composites with matrix cracks. *Journal of Composite Materials*, **23** (Dec. 1989) 1273–91.

45. Jen, K. C. & Sun, C. T., Matrix cracking and delamination prediction in graphite-epoxy laminates. In *Composite Materials in Transition, Proc. American Society for Composites*, 5th Technical Conf., East Lansing, 12–14 June 1990. Technomic, Lancaster, PA, pp. 350–60.

46. Herakovich, C. T., Aboudi, J., Lee, S. W. & Strauss, E. A.,Damage in composite laminates: effects of transverse cracks. *Mechanics of Materials*, **7** (1988) 91–107.

47. Brillaud, J. & El Mahi, A., Numerical simulation of the influence of stacking sequence on transverse ply cracking in composite laminates. *Composite Structures*, **17** (1991) 23–35.

48. Yeh, J. R., The mechanics of multiple transverse cracking in composite laminates. *International Journal of Solids and Structures*, **25** (12) (1989) 1445–55.

49. Kaw, A. K. & Besterfield, G. H., Mechanics of multiple periodic brittle matrix cracks in unidirectional fiber-reinforced composites. *International Journal of Solids and Structures*, **29** (10) (1992) 1193–207.

50. Yang, W. & Boehler, J. P., Micromechanics modelling of anisotropic damage in cross-ply laminates. *International Journal of Solids and Structures*, **29** (10) (1992) 1303–28.

51. Ohira, H., Analysis of the stress distributions in the cross-ply composite transverse cracking. In *Fifth International Conference on Composite Materials, ICCM-V*, San Diego, ed. W. C. Harrigan, Jr. J. Strife & A. K. Dhingra. The Metallurgical Society (Jul.-Aug. 1985), pp. 1115–24.

52. Ohira, H., Shear lag analysis of stresses in cross-ply laminates after cracking of the inner layer. *Technology Reports of Kyushu University*, **57** (4) (August 1984) 477–84.

53. Groves, S. E., A study of damage mechanics in continuous fiber composite laminates with matrix cracking and internal delaminations. Dissertation submitted to the Graduate College of Texas A & M University, 1986.

54. El Mahi, A., Contribution à la modélisation numérique et expérimentale de l'endommagement par fissuration transverse des composites stratifiés. Influence de la séquence d'empilement. Doctoral thesis, Université de Poitiers, 1991.

55. Rebière, J. L., Modelling of the stress field due to fatigue cracks in a carbon/polymer laminate. Doctoral thesis, Université de Poitiers 1992. Available from the first author (D. Gamby).

56. Rebière, J. L. & Gamby, D., Analytical and numerical analyses of transverse cracking in a cross-ply laminate. Influence of the constraining effect. *Composite Structures*, **20** (1992) 91–101.

57. Gamby, D., Hénaff-Gardin, C. & Rebière, J. L., Modelling of the damage distribution along the width of a composite laminate subjected to a tensile fatigue test. In

2nd International Conference on Computer Aided Assessment and Control, Localized Damage II, ed. M. H. Aliabadi, D. J. Cartwright & H. Nisitani. Southampton, UK, 1–3 July 1992, Elsevier Applied Science, London, 1992, pp. 315–25.

58. Gamby, D. & Lafarie-Frenot, M. C., Evolution de la répartition de l'endommagement dans une éprouvette stratifiée soumise à un chargement de fatigue. In *Comptes-Rendus des 8èmes Journées Nationales sur les Matériaux Composites (JNC8-AMAC)*, Palaiseau, France, 16–18 novembre 1992, ed. O. Allix, J.-P. Favre & P. Ladevèze, pp. 483–93.

Thermal and mechanical fatigue analysis of CFRP laminates

C. M. Lawrence Wu

Department of Physics and Materials Science, City Polytechnic of Hong Kong, 83 Tat Chee Avenue, Hong Kong

$[0°/90°]_s$ and $[\pm45°]_s$ CFRP laminated plates were analysed using a finite element formulation for their fatigue behaviour. A fatigue criterion which is based on the laminate interlaminar stresses and the basic lamina fatigue parameters was used. Thermal effects were included in the formulation. In particular, initial thermal stresses resulting from the curing of the laminate were also included in the analysis. The results showed that both laminates had predicted S-N behaviour similar to that from experiments of past investigators. Also, the fatigue behaviour for the $[\pm45°]_s$ laminate between room temperature and the curing temperature were found to be the same. However, in the case of the $[0°/90°]_s$ laminate the fatigue strength at high temperatures was found to be lower than that at low temperatures.

1 INTRODUCTION

An important area of research on laminated plates has been the investigation of interlaminar stresses, especially at the free edge region. It has been mentioned in previous publications that a Carbon Fibre Reinforced Plastic (CFRP) laminate, when cured from the manufacturing temperature to room temperature, can result in initial thermal stresses in the laminate.[1] These stresses can be large, especially at the free edge region. To complicate the situation, when these initial thermal stresses are coupled with the mechanical stresses that result from an applied load, the free edge stresses are lowered or increased, depending upon the ply orientations in the laminate.

Under normal operating conditions a laminate can be subjected to cyclic loading and an understanding of the fatigue behaviour of laminates is therefore necessary. A number of past investigators have studied the fatigue behaviour of CFRP laminates by experiments.[2-5] In particular the fatigue behaviour of uni-directional, $[0°/90°]_s$ and $[\pm45°]_s$ laminates has been investigated. Results have been presented in the form of S-N curves similar to those of conventional materials. Experiments are usually time consuming and expensive and it is desirable to have available a computational method which can predict the fatigue life of symmetric angle-ply laminates. This paper describes an analysis for the investigation of the fatigue behaviour of symmetric laminates carried out using a finite element method that incorporates a fatigue criterion for anisotropic materials and thermal analysis of laminates. The results of the present analysis will be compared with those from experiments.

A formulation for the fatigue analysis of anisotropic materials will be described later in this paper. As a basis of the formulation, the fatigue data of a basic lamina along and transverse to the fibre direction as well as for the inplane shear are taken either from the results of past investigators or by estimation. At any point in the laminate, the stresses resulting from a loading case can be predicted by finite element analysis as described in previous publications.[1,6] The fatigue behaviour under a tri-axial state of stresses is different from that of a uni-directional case. A fatigue criterion, which is similar to a failure criterion, for a combined state of stress will be used. The fatigue criterion will predict, under the combined stresses at a point, the fatigue life in terms of the number of cycles to failure. This means that the criterion can predict failure locally. Conceptually each node in the finite element mesh will have their corresponding number of cycles to failure, N, at a certain applied load. Using the interlaminar stresses and the fatigue criterion to be defined later, N can be worked out at each node in the whole laminate. The minimum value of N for all nodes can be obtained and can then be taken as

the number of cycles to failure, N_f, for the laminate.

It was shown by previous investigators[7,8] that a finite-width laminate exhibited very high interlaminar stresses at the free edge under uniform axial strain loading. Fatigue failure was therefore expected to initiate at the free edge region. It was also shown that initial thermal stresses were present in a laminate after the curing process.[1] In this paper, $[0°/90°]_s$ and $[\pm 45°]_s$ composite laminates made up from Carbon Fibre Reinforced Plastic (CFRP) laminae were used as examples. The initial thermal stresses resulting from the curing of these laminated plates were included in the analysis. The nonlinear stress–strain response, as well as the resin layers between the plies in the laminate were also modelled in the analysis, as explained in Ref. 1. The nonlinear analysis on the laminates was based on that in Ref. 6 using a quasi-three-dimensional isoparametric finite element and an initial stress iteration method to tackle the problem of material nonlinearity. The initial thermal stresses of a laminate were first obtained by noting that after curing the laminate was cooled from its stress-free temperature to room temperature. Various uniform axial strains were then applied to the laminate to obtain the interlaminar stresses and finally the numbers of cycles to failure.

2 DESCRIPTION OF THE LAMINATE FREE EDGE PROBLEM

Consider the long, symmetric laminate shown in Fig. 1(a). It has four plies, each of thickness h and width $2h$, and is loaded with a uniform axial strain $\bar{\varepsilon}_x$ in the x-direction. Away from the ends the displacements u, v, w in the x, y, z, directions, respectively, in any $x = $ constant plane can be assumed to be:

$$u(x, y, z) = x\bar{\varepsilon}_x + U(y, z)$$
$$v(x, y, z) = V(y, z) \qquad\qquad (1)$$
$$w(x, y, z) = W(y, z)$$

The displacement field of eqns (1) should satisfy the equations of equilibrium and the stress-free conditions on the edges, $y = \pm b$, and the top and bottom surfaces, $z = \pm 2h$.

3 FORMULATION

The formulations of the quasi-three-dimensional finite element and the initial stress iteration method which are used in the present study can be found in Refs 1 and 6. The formulation to take into account the thermal stresses has also been given in Ref. 1. The fatigue criteria of the com-

(a) laminate subject to a uniform inplane strain

(b) mesh with resin layer

(c) definition of interfaces & surfaces
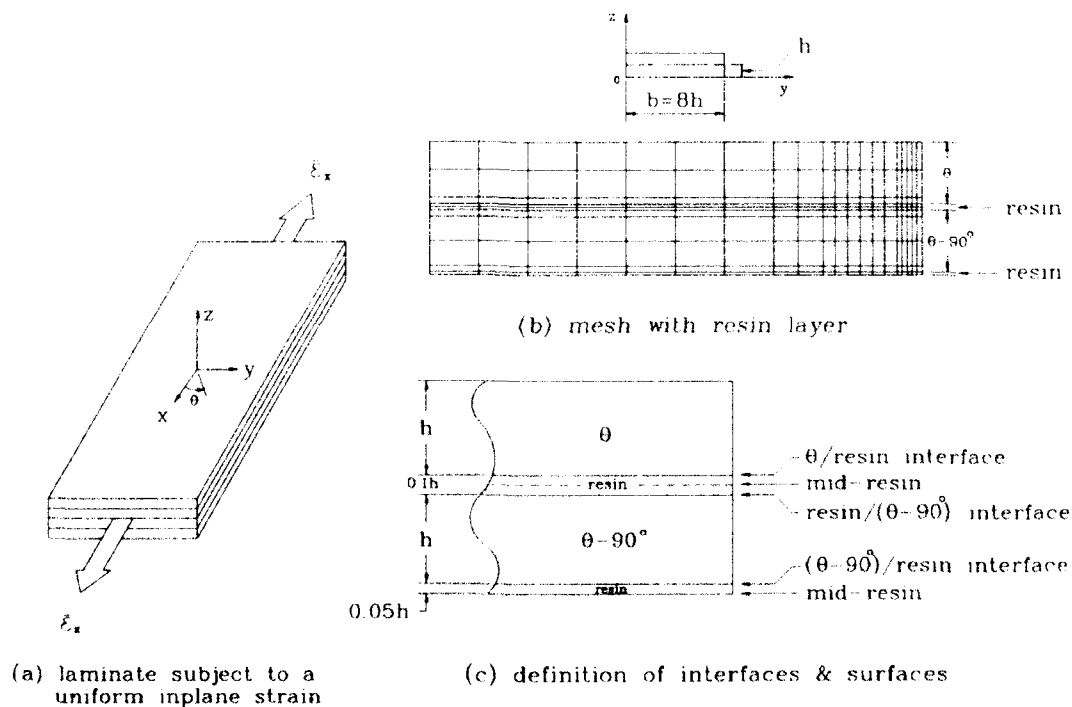
Fig. 1. Problem definition and finite element mesh.

posite lamina were compared by various authors and were summarised in Ref. 3. These criteria are not based on all stress components present in the laminate and a different approach is therefore adopted here. With this approach a new criterion is formulated by modifying the Tsai–Hill composite lamina yield criterion.[9] In the present formulation, we use functions X, Y, Z, Q, R and S, all are functions of N_f, so that X, Y and Z are the lamina peak stresses in the x-, y- and z-directions and Q, R and S are the lamina shear stresses with respect to shear stress components σ_{yz}, σ_{zx} and σ_{xy} respectively, all at N_f cycles of alternating applied stress. The relationship between X, Y, Z, Q, R, S and N_f are shown in Table 1. The fatigue criterion is therefore

$$f^2 = \frac{3}{2(F+G+H)}\left[F(\sigma_x - \sigma_z)^2\right.$$

$$+ G(\sigma_z - \sigma_y)^2 + H(\sigma_y - \sigma_x)^2$$

$$\left. + 2L\sigma_{yz}^2 + 2M\sigma_{zx}^2 + 2N\sigma_{xy}^2\right] = \bar{\sigma}^2 \qquad (2)$$

where σ_x, σ_y, σ_z, σ_{yz}, σ_{zx} and σ_{xy} are stresses in the lamina and the anisotropic parameters are defined as

$$F = \frac{1}{2}\left(\frac{1}{Y^2} + \frac{1}{Z^2} - \frac{1}{X^2}\right) \qquad L = \frac{1}{2Q^2}$$

$$G = \frac{1}{2}\left(\frac{1}{Z^2} + \frac{1}{X^2} - \frac{1}{Y^2}\right) \qquad M = \frac{1}{2R^2} \qquad (3)$$

$$H = \frac{1}{2}\left(\frac{1}{X^2} + \frac{1}{Y^2} - \frac{1}{Z^2}\right) \qquad N = \frac{1}{2S^2}$$

with the equivalent stress, $\bar{\sigma}$, given by

$$\bar{\sigma}^2 = \frac{3}{\frac{1}{X^2} + \frac{1}{Y^2} + \frac{1}{Z^2}} \qquad (4)$$

It is worth noting that in eqns (3), X, Y, Z, Q, R and S all are functions of N_f. So in eqn (2) f depends on N_f. From observation of the general behaviour of S–N curves, it follows that as N_f increases from a small value, f increases. When N_f is increased to a sufficiently large value so that $f = \bar{\sigma}$, fatigue failure occurs. In the present formulation, an iteration procedure is carried out to search for this value of N_f. At any point in the laminate, the stresses can be obtained from the finite element analysis. Using eqn (2) and the

iteration procedure, the corresponding value of N_f at which fatigue failure occurs at that point in the laminate can be obtained. For all nodal points in the laminate, their corresponding values of N_f are iterated and the minimum value of N_f is then obtained, and is taken to be the number of cycles to failure for the laminate.

Fatigue data in the form of S–N curves were taken, or derived, from Refs 2 and 3. Discrete values along these S–N curves were found and they are tabulated in Table 1. In particular, the CFRP lamina longitudinal data were obtained from Ref. 2, and the laminar transverse and shear data as well as the resin data were derived from data in Ref. 3. The lamina ultimate values of strains as well as the relationship between the thermal expansion and temperature in a CFRP lamina can be found in Ref. 1.

4 RESULTS AND DISCUSSION

Due to symmetry, it was only necessary to analyse the top right-hand corner of the laminate cross-section shown in Fig. 1(b). The mesh shown in this figure was used for analysis of the present $[0°/90°]_s$ and $[\pm 45°]_s$ laminates. In the present arrangement a resin rich layer was included between the θ and $90°-\theta$ layers and also between the middle two $90°-\theta$ layers. The reduction in modulus due to temperature change as well as due to the fatigue effects in the present case was neglected.

It was described earlier that under a specific loading on the laminate the interlaminar stresses could be obtained from finite element analysis. From these interlaminar stresses the number of cycles to failure at all nodal points in the laminate were obtained and the minimum of these values was taken as the number of cycles to failure for the laminate. In this investigation the number of cycles to failure for the laminates at various axial applied strains were obtained. They are now presented in the following two sections. For each type of laminate, thermal effects were also included to investigate for their behaviour at different temperatures.

4.1 The $[\pm 45°]_s$ laminate

Two cases were considered for this laminate. In the first case the laminate was considered to be stress-free at the curing temperature of 132°C. So at room temperature, interlaminar initial thermal stresses were present in the laminate.[1] On top of

C. M. L. Wu

these initial thermal stresses a uniform axial strain $\bar{\varepsilon}_x$ was applied to the laminate. At various applied strains the corresponding numbers of cycles to failure for the laminate were found as described before and the results are shown in Fig. 2. Also plotted on the same figure are the experimental results from Ref. 2 for the $[\pm 45°]_s$ laminate. The present method predicted higher values of N_f at high and low levels of alternating stresses. For a range between the high and low applied stresses, the present model predicted lower values of N_f. On the whole, the present results had a close correlation with the experimental ones in Ref. 2. The present model has provided a good method to estimate the fatigue failure in symmetrical laminates. The combination of the nonlinear analysis and the treatment of the free edge effects had probably provided a more realistic modelling of the real situation. Also, the inclusion of the initial thermal stresses due to the laminate curing process might have improved the correlation between the numerical and experimental results. For all applied strains, the minimum number of cycles to failure occurred at the free edge, close to the $-45°$/resin interface (see Fig. 1(c)) inside the $-45°$ layer.

The second case did not take into account the initial thermal stresses and the same method for finding the number of cycles to failure at various applied strains was carried out. The results showed that the numbers of cycles to failure for this case were different to those in the last case for the same applied strain at various locations in the laminate. However, the minimum number of cycles to failure was the same for the two cases and they occurred at the same position in the laminate, as discussed above. So the results shown in Fig. 2 represent the results for these two cases.

Table 1. S–N relationships

Lamina												
X (MPa)	1494.4	1494.4	1938.5	1900.4	1856.8	1787.4	1660.8	1283.7	1184.3	1142.1	1100.0	1068.6
N (cycles)	0	1000	4000	10000	21380	45709	10000	613823	1000000	2154435	4641588	10000000
Y, Z (MPa)	72.32	72.32	37.37	34.152	33.047							
N (cycles)	0	100	100000	1000000	10000000							
Q, R, S (MPa)	300.43	300.43	124.27	97.075	96.238							
N (cycles)	0	21	100000	1000000	10000000							
Resin												
X, Y, Z (MPa)	769.2	769.2	397.45	363.22	351.45							
N (cycles)	0	100	100000	1000000	10000000							
Q, R, S (MPa)	1099.2	1099.2	454.63	355.15	352.07							
N (cycles)	0	21	100000	1000000	10000000							

Fig. 2. S–N results of $[\pm 45°]_s$ laminate.

as far as the number of cycles to failure for the laminate is concerned.

It was mentioned that the minimum number of cycles to failure occurred at a position near the laminate free edge. It has been shown that the free edge stresses were very high under an applied strain in the x-direction.[1,6-8] The initial thermal stresses were small in magnitude in general but became large at the laminate free edge. However, they were still smaller in magnitude when compared with the mechanical stresses under the applied strain. So the initial thermal stresses were insignificant to the fatigue life of the laminate at the free edge. This explains why the number of cycles to failure for the two cases were the same.

The second case can be considered as the situation when the laminate is subjected to the same *temperature as the curing temperature*. Although practically the laminate will not be used at such an elevated temperature, the present case can be used to illustrate the fatigue behaviour of the laminate at a high temperature. Since the number of cycles to failure for the above two cases were the same, it follows that between room temperature and the curing temperature the fatigue behaviour of this laminate is the same.

4.2 The [0°/90°]ₛ laminate

Similar to the [±45°]ₛ laminate, the two cases with and without thermal effects included were considered for the [0°/90°]ₛ laminate. The results of the two cases are shown in Fig. 3. In the same figure the experimental results given in Ref. 2 are also plotted for comparison. For the first case, the initial thermal stresses were taken into account and the fatigue life at high stress levels was higher than that in Ref. 2. However, the fatigue life at low

stress levels was lower than that in Ref. 2. Nevertheless, the present results are close to the experimental data in Ref. 2. This indicates again that the initial thermal stresses are important in the prediction of laminate stress–strain behaviour. For all applied strains, the minimum number of cycles to failure occurred at the free edge, near the resin/90° interface (see Fig. 1(c)) inside the 90° layer.

In the second case the initial thermal stresses were not included and the *S–N* results in Fig. 3 indicate that the fatigue life is lower than that in the previous case. For example, at the same applied stress the laminate without initial thermal stresses included has a much smaller number of cycles to failure than the laminate with initial thermal stresses included. The minimum number of cycles occurred at the same position as in the previous case.

For the present laminate the initial thermal stresses were significant in magnitude when compared with the mechanical stresses. They also had the effect of increasing the overall stresses in the laminate. Consequently the *S–N* results for the case without the initial thermal stresses included were worse than those with initial thermal stresses included. As indicated above, this case without initial thermal stresses included can be taken as the case when the laminate is subjected to the same temperature when curing is taking place. It follows that the fatigue life of the [0°/90°]ₛ laminate at an elevated temperature is lower than that at room temperature.

5 CONCLUSION

A formulation for the fatigue analysis of anisotropic symmetric laminates has been described. Using this formulation the fatigue behaviour of [0°/90°]ₛ and [±45°]ₛ laminates was studied, based on the interlaminar stresses inside the laminate. The analysis took into account the initial thermal stresses in the laminate resulting from the curing procedure. The present results were close to the experimental data of past investigators. The [±45°]ₛ laminate was found to have the same *S–N* relationship at temperatures between the room temperature and the curing temperature. However, the [0°/90°]ₛ laminate was found to have a better fatigue life at room temperature than at an elevated temperature.

The present formulation provides a convenient method of life evaluation of symmetric angle-ply

Normalised Peak Stress (%)
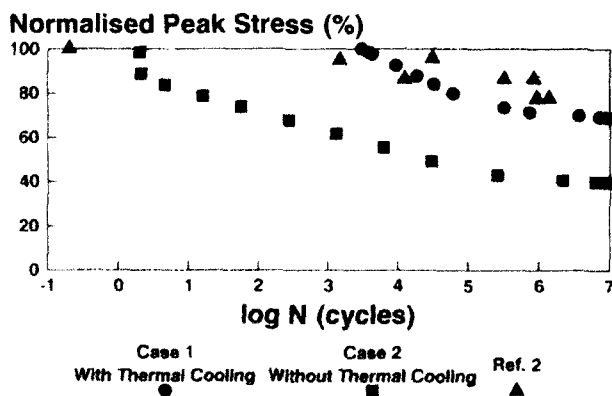
Fig. 3. *S–N* results of [0°/90°]ₛ laminate.

laminates. This will be useful for designers in situations such as choosing the type of laminate stacking sequence when designing a composite structure.

REFERENCES

1. Wu, C. M. L., Nonlinear thermal and mechanical analysis of edge effects in angle-ply laminates. *Computers & Structures*, **35** 1990 705–17.
2. Partridge, I. K. ed., *Advanced Composites*. Elsevier Applied Science, London, 1989.
3. Hahn, H. T., Fatigue behaviour and life prediction of composite laminates. *Composite Materials: Testing and Design* (5th Conf.), ASTM STP 674, ed. S. W. Tsai, ASTM, Philadelphia, PA, 1979, pp. 383–417.
4. Harris, B., *Engineering Composite Materials*. The Institute of Metals, London, 1986.
5. Curtis, P. T., An investigation of the mechanical properties of improved carbon fibre composite materials. RAE TR86021, 1986.
6. Wu, C. M. L., Nonlinear analysis of edge effects in angle-ply laminates. *Computers & Structures*, **25** 1987 787–98.
7. Pipes, R. B. & Pagano, N. J., Interlaminar stresses in composite laminates under uniform axial extension. *Journal of Composite Materials*, **4** 1970 538–48.
8. Pagano, N. J., On the calculation of interlaminar normal stress in composite laminate. *Journal of Composite Materials*, **8** 1974 65–81.
9. Hill, R., *The Mathematical Theory of Plasticity*. Oxford University Press, London, 1950.

Thermal buckling of bimodular sandwich beams

Tin Lan, Psang Dain Lin & Lien Wen Chen*

Department of Mechanical Engineering, National Cheng Kung University, Tainan, Taiwan, 70101

This paper presents a model that explores the thermal buckling of three-layer sandwich beams possessing thick facings and moderately stiff cores. Bimodular facings and core material are used. In contrast to conventional theory, the effects of transverse shear deformation in the facings as well as the effect of the stretching and bending action in the core on thermal buckling are considered. The governing equations are derived using the principle of minimum total potential energy and the fact that its second derivative is zero. The finite-element results are presented in order to investigate the effects of important parameters such as thickness, thermal expansion coefficients and moduli ratio on critical buckling temperatures.

1 INTRODUCTION

One of the most important and widely popular composite structures is that of the sandwich. As the core maintains a definite separation of two facings, the bending resistance of a sandwich structure is larger than a single facing. Although the volume of a sandwich structure is larger, it has the benefits of light weight and high bending resistance which has made the sandwich structure an important component in widespread applications.

The study of the sandwich structure was first addressed by Hoff and Mautner in 1945.[1] Many subsequent authors, such as March,[2] Hoff,[3,4] Libove and Batdorf,[5] Hemp[6] and Eringer[7] successively investigated its bending problems. Gordaninejad and Bert developed a new model for the sandwich beam,[8] and applied it in the study of vibration and bending problems.[9]

The thermal stress of the sandwich structure was investigated using the theory of elasticity by Bijlaard[10] and Pogorzeiski,[11] who subjected sandwich plates to thermal gradients. Ebcioglu,[12,13] using the principle of minimum total potential energy, determined the stress induced on the sandwich structure by transverse loadings, boundary forces and temperature gradients. Hussein et al.[14] considered the effects of inter-layer shear stresses on thermal stresses.

The concept of a bimodular material was introduced by Timoshenko,[15] who in 1941 considered

the flexural stresses of such a material undergoing pure bending. Tran and Bert,[16] using the transfer matrix method, studied the small bending deflection of homogeneous bimodular beams. Column buckling of general bimodular materials was considered by Rigbi[17] and Rigbi and Idan,[18] while the bifurcation buckling of a uniform, slender, cantilever column constructed of bimodular material was studied by Bert and Ko.[19] Dynamic analyses of bimodular beams known at present were investigated by Khachatryan,[20] Galoyan and Khachatryan,[21] Bert and Tran[22] and Rebello et al.[23] All of these works involved either free or forced vibrations.

This paper studies the thermal buckling of bimodular sandwich beams possessing thick facings and moderately stiff cores under uniform or tent-like temperature fields. The governing equations are derived using the principle of minimum total potential energy. The finite-element results are presented in order to study the effects of a number of important parameters on the critical buckling temperature.

2 FINITE ELEMENT FORMULATION

Consider a three-layer bimodular sandwich beam with total thickness h, and length l, as shown in Fig. 1. h_m is the thickness of the mth layer. x and z are respectively the Cartesian position coordinates along the length of the beam and normal to it, measured from the midplane of the beam. Based on the Duhamel–Neumann form of

*To whom correspondence should be addressed.

Hooke's law, the stress–strain relations of the mth layer are:

$$\begin{bmatrix} \sigma \\ \tau \end{bmatrix} = \begin{bmatrix} E_{km} & 0 \\ 0 & G_{km} \end{bmatrix} \begin{bmatrix} \varepsilon - \alpha \Delta T \\ \gamma \end{bmatrix} \qquad (1)$$

where ε and γ represent the axial normal and transverse shear strain respectively and σ and τ are their corresponding stresses; α is the thermal expansion coefficient, and ΔT is the temperature rise. Note that the subscript k of E_{km} and G_{km} refers to the sign of strain (k = t for tension and k = c for compression), while the subscript m denotes the layer number (see Fig. 1). In order to account for the transverse shear deformation effects, the Timoshenko displacement field is used:

$$u(x,z) = u_0(x) + z\Psi(x) \qquad (2a)$$

$$w(x,z) = w_0(x) \qquad (2b)$$

u_0 and w_0 are associated midplane displacements and Ψ is the bending slope. The displacement, u, is required in order to account for the lack of symmetry about the midplane, due to different facing thicknesses or bimodular material behaviour. With the assumptions that the material is not extensible in the thickness direction and that $w(x,z)$ is independent of z.[8] Consequently, the strain–displacement equations of linear elasticity are:

$$\varepsilon = \frac{\partial u}{\partial x} = \frac{\partial u_0}{\partial x} + z\frac{\partial \Psi}{\partial x} = \varepsilon_0 + z\kappa \qquad (3a)$$

$$\gamma = \frac{\partial w}{\partial x} + \frac{\partial u}{\partial z} = \frac{\partial w_0}{\partial x} + \Psi \qquad (3b)$$

As usual, the normal stress, moment, and transverse-shear stress resultants, each per unit width, defined respectively by:

$$\begin{bmatrix} N \\ M \\ Q \end{bmatrix} = \int_{h/2} \begin{bmatrix} \sigma \\ z\sigma \\ \tau \end{bmatrix} dz \qquad (4)$$

can be obtained by integration of stresses over the thickness h with eqn (1):

$$\begin{bmatrix} N \\ M \\ Q \end{bmatrix} = \begin{bmatrix} A & B & 0 \\ B & D & 0 \\ 0 & 0 & S \end{bmatrix} \begin{bmatrix} \varepsilon^0 \\ \kappa \\ \gamma \end{bmatrix} - \begin{bmatrix} N_t \\ M_t \\ 0 \end{bmatrix} \qquad (5)$$
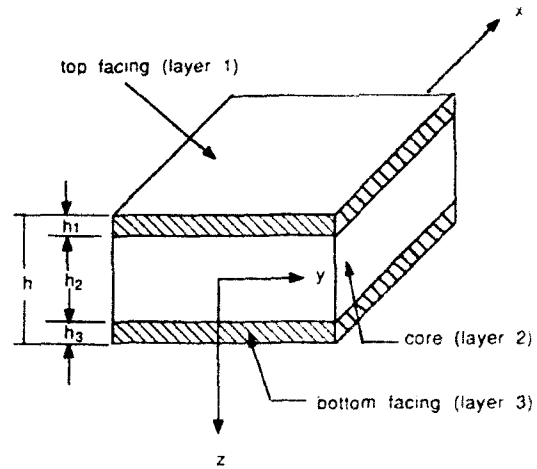
Fig. 1. Three-layer sandwich beam with composite facings.

where extensional stiffness A, flexural-extensional coupling stiffness B, flexural stiffness D, and transverse shear stiffness S (per unit width) for a laminate beam are defined as:

$$(A,B,D,S) = \int_{h/2} (E_{km}, zE_{km}, z^2 E_{km}, \kappa^2 G_{km}) \, dz \qquad (6)$$

The shear correction factor, κ^2, is obtained from the equilibrium equation of elasticity in the x–z plane and the concept of equivalent strain energy,[24] and is expressed as:

$$\kappa^2 = \frac{(AB - B^2)^2}{\left[\int_{h/2} G_{km} \, dz \right] \left[\int_{-h/2} (Ab - Ba^2)^2 \, dz \right]} \qquad (7)$$

where a and b are the extensional and flexural partial stiffnesses defined as

$$(z,b) = \int_{h/2} (1, z^*) E_{km} \, dz^* \qquad (8)$$

The thermal stress resultant, N_T, and the thermal moment resultant, M_T, are defined as:

$$(N_T, M_T) = \int_{-h/2}^{h/2} E_{km} \alpha \Delta T (1, z) \, dz \qquad (9)$$

The integration of eqns (6)–(9) were carried out in a piecewise fashion from one layer to the next, with account taken of the tension or compression within appropriate portions.

The problem was solved by a number of quadratic Lagrangian elements with three nodes and

nine degrees of freedom elements. The displacement components were approximated by the product of the shape function matrix, $[N_i]$, and the nodal displacement vector, $\{q_i^c\} = [u_{oi}\ w_{oi}\ \Psi_i]^T$, i.e.

$$\{q^c\} = \sum_{i=1}^{3} [N_i]\{q_i^c\} \tag{10}$$

The superscript 'c' indicates that these variables are defined on the element and are to be determined. The shape functions are given by:

$$N_1 = \frac{1}{2}\xi(\xi - 1) \tag{11a}$$

$$N_2 = 1 - \xi^2 \tag{11b}$$

$$N_3 = \frac{1}{2}\xi(\xi + 1) \tag{11c}$$

The midplane strains and curvatures on the element, e, can be rewritten as:

$$\{\varepsilon_o^c\} = \sum_{i=1}^{3} [B_{ti}]\{q_i^c\} \tag{12}$$

$$\{\kappa^c\} = \sum_{i=1}^{3} [B_{bi}]\{q_i^c\} \tag{13}$$

$$\{\gamma^c\} = \sum_{i=1}^{3} [B_{si}]\{q_i^c\} \tag{14}$$

$$\frac{\partial w_o^c}{\partial x} = \sum_{i=1}^{3} [B_{gi}]\{q_i^c\} \tag{15}$$

The strain matrices of $[B_{ti}]$, $[B_{bi}]$, $[B_{si}]$ and $[B_{gi}]$ are given by:

$$[B_{ti}] = [\partial N_i/\partial x\ 0\ 0] \tag{16a}$$

$$[B_{bi}] = [0\ 0\ \partial N_i/\partial x] \tag{16b}$$

$$[B_{si}] = [0\ \partial N_i/\partial x\ N_i] \tag{16c}$$

$$[B_{gi}] = [0\ \partial N_i/\partial x\ 0] \tag{16d}$$

The total potential energy, π, is the sum of the strain energy, π_1, and the work done by the applied distributed normal loading, π_2, i.e.

$$\pi = \pi_1 + \pi_2 \tag{17}$$

where

$$\pi_1 = \frac{1}{2}\int_R [N\varepsilon + Q\gamma]\, dx\, dz$$

$$= \sum_{e=1}^{n} \left\{ \frac{1}{2}\{q^c\}^T[K_s^c]\{q^c\} - \{q^c\}^T[F_T^c] \right\}$$

$$= \frac{1}{2}\{q\}^T[K_s]\{q\} - \{q\}^T[F_T]$$

$$\pi_2 = \frac{1}{2}\int_R \left[N\left(\frac{\partial w}{\partial x}\right)^2 \right] dx\, dz = \sum_{e=1}^{n} \frac{1}{2}\{q^c\}^T[K_G^c]\{q^c\}$$

$$= \frac{1}{2}\{q\}^T[K_G]\{q\}$$

with element structural stiffness matrix

$$[K_s^c] = \int_{-1}^{1} \left\{ [B_t]^T A[B_t] + [B_t]^T B[B_b] \right.$$

$$\left. + [B_b]^T D[B_b] + [B_s]^T S[B_s] \right\} |J|\, d\xi \tag{18}$$

element geometric stiffness matrix

$$[K_G^c] = \int_{-1}^{1} [B_g]^T N[B_g]|J|\, d\xi \tag{19}$$

element thermal load vector

$$[F_T^c] = \int_{-1}^{1} \left\{ [B_t]^T N_T + [B_b]^T M_T \right\} |J|\, d\xi \tag{20}$$

where $|J|$ is the determinant of the Jacobian transformation matrrix.

For the displacement field of prebuckling, minimization of π_1 with respect to the generalized displacement vector $\{q\}$ gives the following set of equations:

$$[K_s]\{q\} = [F_T] \tag{21}$$

For the critical buckling state corresponding to the neutral equilibrium condition, the second variation of total potential energy, π, must be set to zero which gives the following standard eigenvalue problem:

$$\|[K_s] + \lambda[K_G]\| = 0 \tag{22}$$

The product of λ and the initial guessed value ΔT is the critical buckling temperature, T_{cr}.

The different properties of the tension and compression of bimodular materials cause the neutral surface position to shift away from its geometric midplane. In the calculations, as the actual neutral surface positions were not known, an iterative technique was employed in order to compute their locations. The iteration procedure began with an assumed value of the neutral surface position. Dummy stiffness and thermal load were then computed from eqns (6) and (9) using these assumed values. After the eigenvalues and

eigenvectors were obtained, the new neutral surface locations were given by:

$$Z_n = -\varepsilon_o^*/\kappa^* = -(\varepsilon_o - \alpha\Delta T)/\kappa \qquad (23)$$

Using these new values, the stiffnesses for the next iteration are computed. This procedure is repeated until the differences between any two consecutive values of the neutral surface at all nodal points are smaller than one tenth of the thickness.

3 NUMERICAL RESULTS AND DISCUSSION

In this section, two sets of boundary conditions for beams subjected to either a uniform or tent-like temperature field are studied. For the sake of simplicity, the thermal expansion coefficient of the core is assumed to be zero since its value is in general, very small.

3.1 A beam hinged at both ends (denoted as H-H)

In this case, the midplane displacements, u_o and w_o, at both ends (i.e. $x = \pm l/2$) are zero.

3.1.1 A H-H beam under a uniform temperature field

The neutral surface of the core is located exactly at the midplane of the beam since strain ε_o is zero. Moreover, the strain of the facing having the smaller thermal coefficient is always negative. Consequently, the stiffness of the beam depends only upon the neutral surface of the other facing possessing the higher thermal coefficient.

The influence of the bimodular elastic moduli ratio (E_t/E_c) of the facing and the thermal expansion coefficient ratio, α_1/α_3, on the critical buckling temperature, T_{cr}, is shown in Figs 2 and 3. Note that by increasing α_1/α_3, the beam deflection also increases, and the section bending moment, the neutral position location, and the beam stiffness all change simultaneously. Note in Fig. 2 where $E_t > E_c$, the increase in the thermal expansion coefficient ratio and the shift in the neutral position, sharply changes the stiffness and the buckling temperature. The effect of α_1/α_3 on the critical buckling temperature for the case of $E_c > E_t$ is illustrated in Fig. 3. Note that a decrease in stiffness corresponds to a shift in the neutral position of the upper facing. Since E_t has more of
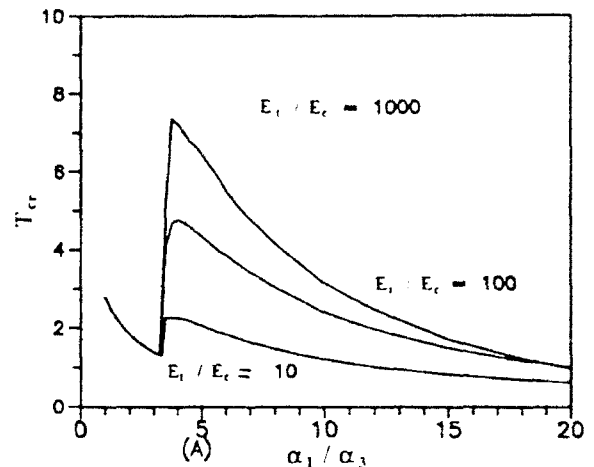
Fig. 2. Effect of transverse expansion ratio α_1/α_3 on thermal buckling load T_{cr} for various bimodulus ratios $(E_t > E_c)$ for H-H beam under uniform temperature field $(E_{c1} = E_{c3} = 1 \times 10^5, \ E_2 = 1 \times 10^2, \ \alpha_2 = 0, \ \alpha_3 = 1 \times 10^{-4}, \ G_{k1}/E_{k1} = 0.5, \ L = 600, \ h_1 = 3)$.
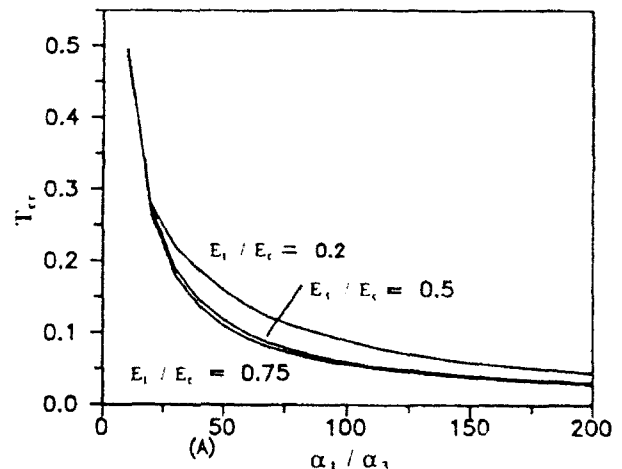
Fig. 3. Effect of α_1/α_3 on T_{cr} for various bimodulus ratios $(E_c > E_t)$ for H-H beam under uniform temperature field $(E_{c1} = E_{c3} = 1 \times 10^5, \ E_2 = 1 \times 10^2, \ \alpha_2 = 0, \ \alpha_3 = 1 \times 10^{-4}, \ G_{k1}/E_{k1} = 0.5, \ L = 600, \ h_1 = 3)$.

an influence on a decrease in thermal stress than on a decrease in stiffness, a lower E_t/E_c value corresponds to a higher critical buckling temperature.

The influence of the core's rigidity on the critical buckling temperature is presented in Fig. 4. Higher core rigidity is accompanied by a higher buckling temperature and a larger change in the neutral position.

The influence of the upper and lower facings' modulus ratio (E_3/E_1) and the thermal expansion ratio on the critical buckling temperature is dis-
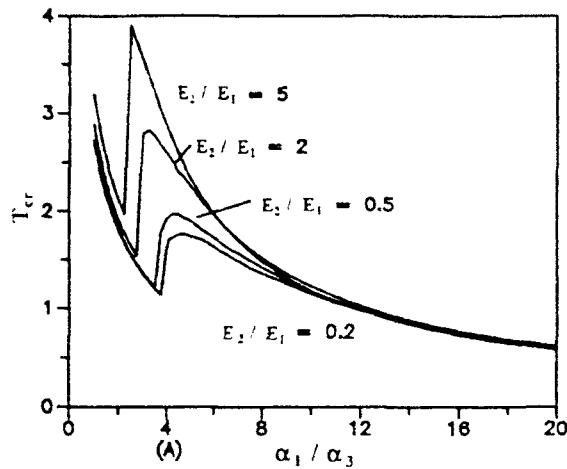
Fig. 4. Effect of α_1/α_3 and core moduli on T_{cr} for H-H beam under uniform temperature field $(E_{c1} = E_{c3} = 1 \times 10^5$, $E_{t1} = E_{t3} = 1 \times 10^6$, $\alpha_2 = 0$, $\alpha_3 = 1 \times 10^{-3}$, $G_{k1}/E_{k1} = 0.5$, $L = 600$, $h^1 = 3$).
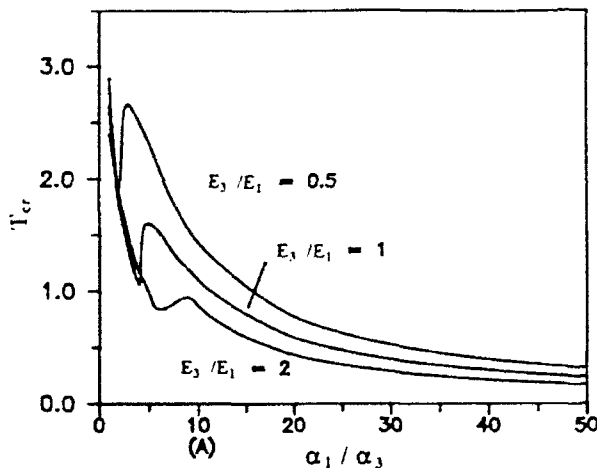
Fig. 5. Effect of α_1/α_3 and facing moduli on T_{cr} for H-H beam under uniform temperature field $(E_{c1} = 1 \times 10^4$, $E_{t1}/E_{c1} = 10$, $\alpha_2 = 0$, $\alpha_3 = 1 \times 10^{-3}$, $G_{k1}/E_{k1} = 0.5$, $L = 600$, $h_1 = 3$).

Fig. 6. Effect of α_1/α_3 and T_1/T_o on T_{cr} for H-H beam under tent-like temperature field $(E_{c1} = E_{c3} = 1 \times 10^5$, $E_{t1} = E_{t3} = 5 \times 10^5$, $E_2 = 1 \times 10^5$, $\alpha_2 = 0$, $\alpha_3 = 1 \times 10^{-4}$, $G_{k1}/E_{k1} = 0.5$, $L = 600$, $h_1 = 3$.

more of an effect on the critical buckling temperature.

3.1.2 A H-H beam under a tent-like temperature field

The tent-like temperature field is given by:

$$T(x) = \begin{cases} T_o + T_1(1 - 2x/l) \\ T_o + T_1(1 + 2x/l) \end{cases}$$

where T_o and T_1 are the uniform and gradient temperatures, respectively.

The influence of temperature distribution (T_1/T_o) and the thermal expansion ratio on the buckling behaviour of the bimodular sandwich beam under a nonuniform temperature is shown in Fig. 6. Note that a steep temperature gradient corresponds to a large change in the deflection and in the location of the neutral position. Likewise, a steep buckling temperature gradient corresponds to a large change in the stiffness.

The effect of the H-H beam thickness on the critical buckling temperature gradient is shown in

played in Fig. 5 where $E_t > E_c$. Note that a higher value of E_3/E_1 is accompanied by a lower buckling temperature. This phenomenon can be explained in terms of the lower facing's stiffness, an increase of which affects the location of the upper facings' neutral position, reducing the upper facing stiffness and that of the entire beam as well. Although the thermal stress is also reduced, it only decreases linearly with a change in the neutral position whereas the stiffness decreases by a power of three. A comparison of the effects of a change in the thermal stress and that of the stiffness reveals that the stiffness has

Fig. 7. In comparison with a homogeneous beam of the same facing material, the sandwich beam possesses lower stiffness and a highly buckling temperature gradient due to the low thermal expansion coefficient of its core. Note that in general, increasing the thickness of the core is an effective way of increasing the buckling temperature gradient.

3.2 A beam clamped at both ends (denoted as C-C)

Note that the displacements. u_0, w_0, and the bending slope Ψ are zero at both boundary ends. Also note that, in a uniform temperature field, the C-C beam will not deflect before buckling. Its curvature is zero and the whole beam is subjected to compression. Consequently, the extension modulus, E_{tm}, has no influence on its stiffness before buckling.

The critical buckling temperature of a C-C beam subjected to a nonuniform temperature field is illustrated in Figs 8–10. The influence of tem-

perature distribution on the unimodular beam's critical buckling temperature gradient (T_{1cr}) is shown in Fig. 8, while the influence of temperature distribution and the thermal expansion co-

Fig. 8. Effect of α_1/α_3 and T_1/T_0 on T_{1cr} for unimodular C-C beam under tent-like temperature field $(E = 1 \times 10^5$. $\alpha = 1 \times 10^{-4}$. $G/E = 0.5$. $L = 600$. $h = 9)$.
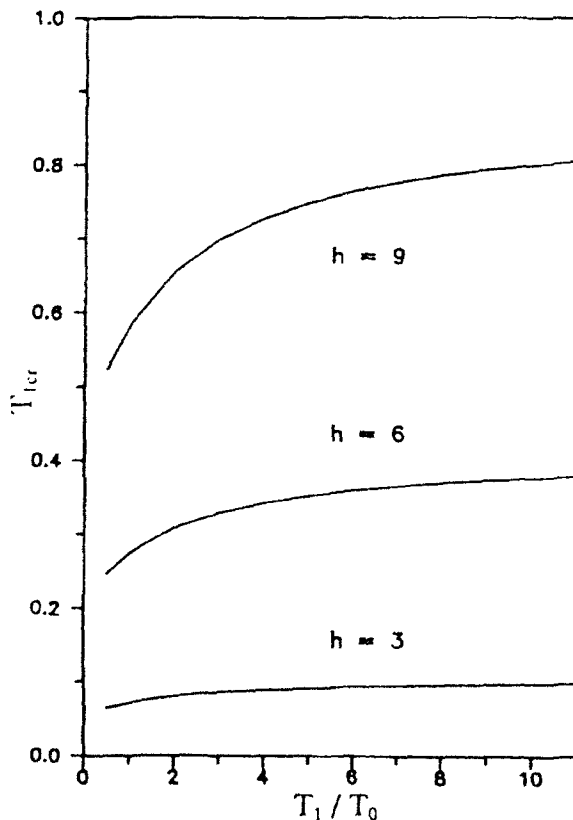
Fig. 7. Effect of thickness and T_1/T_0 on T_{1cr} for H-H beam under tent-like temperature field $(E_{c1} = E_{c3} = 1 \times 10^5$, $E_{t1} = E_{t3} = 5 \times 10^5$, $E_2 = 1 \times 10^2$, $\alpha_1 = 1 \times 10^{-3}$, $\alpha_2 = 0$, $\alpha_3 = 1 \times 10^{-4}$, $G_{k1}/E_{k1} = 0.5$, $L = 600$, $h_1 = 3)$.
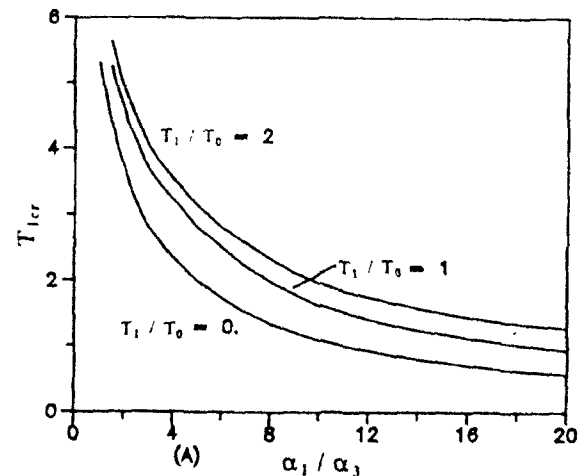
Fig. 9. Effect of α_1/α_3 and T_1/T_0 on T_{1cr} for C-C beam under tent-like temperature field $(E_c = 1 \times 10^4$, $E_1 = 2 \times 10^4$, $\alpha = 1 \times 10^{-4}$, $\alpha_2 = 0$, $\alpha_3 = 1 \times 10^{-4}$, $G_{k1}/E_{k1} = 0.5$, $L = 600$, $h_1 = 3)$.
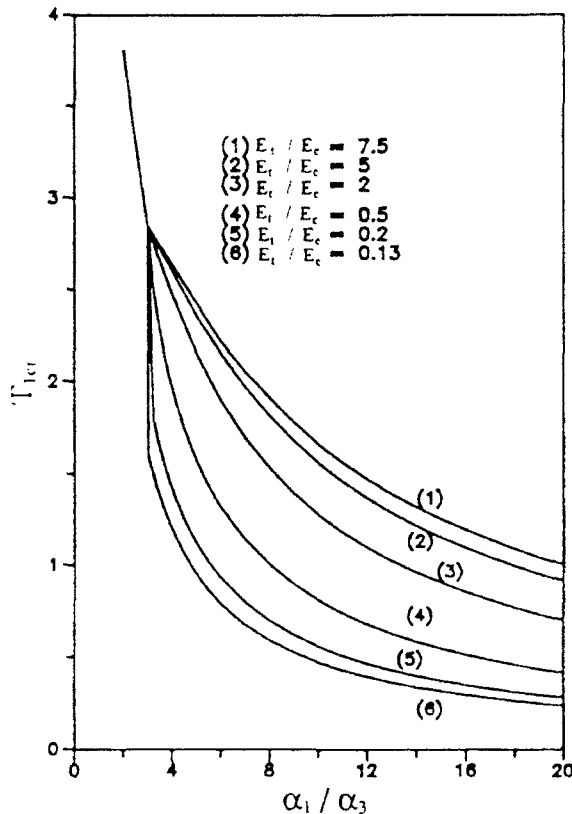
Fig. 16. Effect of a_1/a_3 and E_1/E_c on T_{1cr} for C-C beam under tent-like temperature field ($T_0 = 0$, $E_{11} = 1 \times 10^4$, $a_2 = 0$, $a_3 = 5 \times 10^{-5}$, $G_{k1}/E_{k1} = 0.5$, $L = 600$, $h_1 = 3$).

to differences in the thermal expansion coefficients of the facings. When this difference is large, the effects on stiffness, critical buckling temperature, and buckling temperature gradient are more pronounced.

(2) In a uniform temperature field, a H-H bimodular beam facing possessing a lower thermal expansion coefficient always undergoes compression, whereas the facing of a C-C bimodular beam is subjected to axial compressive strain and its stiffness remains unchanged until buckling.

(3) In a nonuniform temperature field, strain of a C-C beam varies in the axial direction. The thermal strain is nonsymmetric in the direction of thickness if the thermal expansion coefficients of the layers differ.

(4) Provided the core's thermal expansion coefficient is low, the best method for increasing sandwich stiffness and the critical buckling temperature gradient is to increase the core thickness.

ACKNOWLEDGEMENT

efficient ratio on the bimodular sandwich beam's critical buckling temperature are shown in Fig. 9. Figure 10 reveals that a C-C beam possessing a high modulus ratio and a lower thermal expansion coefficient ratio has higher critical buckling temperature gradient, T_{1cr}.

4 CONCLUSIONS

This paper investigated the thermal buckling of three-layer bimodular sandwich beams possessing thick facings and moderately stiff cores. The effects of transverse shear deformation in the facings as well as the effects of the stretching and bending action in the core on thermal buckling are considered. Two sets of boundary conditions, hinged or clamped at both ends, are studied under uniform or tent-like temperature fields. The following important conclusions were obtained:

(1) The stiffness of the bimodular sandwich beam varies with the temperature rise due

REFERENCES

1. Hoff, N. J. & Mautner, S. E., The buckling of sandwich type panels. *J. Aero. Sci.*, **12** (1945) 285.
2. March, H. W., Effects of shear deformation in the core of a flat rectangular sandwich panel. US Forest Product Laboratory, Report 1583, 1948.
3. Hoff, N. J. & Mautner, S. E., Bending and buckling of sandwich beams. *J. Aero. Sci.*, **15** (1948) 707–20.
4. Hoff, N. J., Bending and buckling of rectangular sandwich plates. NACA TN 2255, 1950.
5. Libove, C. & Batdorf, S. B., A general small deflection theory for flat sandwich plates. NACA TN 1526, 1948.
6. Hemp, W. S., On a theory of sandwich construction. ARCR & M 2672, March, 1948.
7. Eringer, A. C., Bending and buckling of rectangular sandwich plates. *Proc. 1st US Nat. Congr. Appl. Mech.*, 1951, pp. 381–90.
8. Gordaninejad, F. & Bert, C. W., A new theory for bending of thick sandwich beams. *Int. J. Mech. Sci.*, **31** (11/12)(1989) 925–34.
9. Rebello, C. A., Bert, C. W. & Gordaninejad, F., Vibration of bimodular sandwich beams with thick facings: a new theory and experimental results. *J. Sound Vib.*, **90** (3)(1983) 381–97.
10. Bijlaard, P. P., Thermal stresses and deflection in rectangular sandwich plates. *J. Aerosp. Sci.*, **26** (4) (1959) 210–18.

11. Pogorzeiski, J., Thermal deformations and stresses in rectangular sandwich panels with non-rigid cores. *Build. Sci.*, **4** (1969) 79-92.

12. Chang, C. C. & Ebcioglu, I. K., Thermoelastic behaviour of a simply supported sandwich plane under large temperature gradient and edge compression. *J. Aerosp. Sci.*, **28** (6) (1961) 480-92.

13. Ebcioglu, I. K., Thermo-elastic equation for a sandwich panel under arbitrary temperature distribution, transverse load and edge compression. *Proc. 4th US Nat. Cong. of Applied Mechanics*, ASME, New York, 1962, pp. 537-46.

14. Hussein, R., Ha, K. & Frazio, P., Thermal stresses in sandwich plates. *J. Therm. Stresses*, **12** (1989) 333-49.

15. Timoshenko, S., *Strength of Materials, Part 2, Advanced Theory and Problems*. Van Nostrand, Princeton, NJ, 1941.

16. Tran, A. D. & Bert, C. W., Bending of thick beams of bimodulus materials. *Comput. Struct.*, **15** (6) (1982) 627-42.

17. Rigbi, Z., The buckling of bimodular columns. *Acta Mech.*, **18** (1973) 317-32.

18. Rigbi, Z. & Idan, S., Buckling and immediate postbuckling behavior of bimodular columns. *J. Struct. Mech.*, **6** (1978) 145-64.

19. Bert, C. W. & Ko, C. L., Buckling of columns constructed of bimodular materials. *Int. J. Struct. Dynam.*, **10** (1982) 551-60.

20. Khachatryan, A. A., Longitudinal vibrations of prismatic bars made of different-modulus material. *Mech. Solids*, **2** (1967) 94-7.

21. Galoyan, A. G. & Khachatryan, A. A., On transversal vibration of beams made from different modulu material (in Russian). *Dokl. Akad. Nauk Armyanskoi SSr*, **66** (1967) 2-26.

22. Bert, C. W. & Tran, A. D., Transient response of a thick beam of bimodular material. *Earthqu. Engng Struct. Dynam.*, **10** (1982) 551-60.

23. Rebello, C. A., Bert, C. W. & Gordaninejad, F., Vibration of bimodular sandwich beams with thick facings: A new theory and experimental results. *J. Sound Vib.*, **90** (1983) 381-97.

24. Sun, L. X. & Hsu, T. R., Thermal buckling of laminated composite plates with transverse shear deformation. *Comput. Struct.*, **365** (5) (1988) 883-9.

Buckling and vibration of thin laminated composite, prismatic shell structures

S. Mohd

Pusat Pengajian Kejuruteraan Awam, Universiti Sains Malaysia, Kampus Cawangan Perak, 31750 Tronoh, Perak, Malaysia

&

D. J. Dawe

School of Civil Engineering, The University of Birmingham, Edgbaston, Birmingham, UK, B15 2TT

A description is given of the multi-term, finite strip analysis of the free vibration and buckling, under a system of applied biaxial direct and shear stresses, of thin, prismatic shell structures. The walls of the structure may be composite laminates with a general lay-up. The analysis is based on the use of Koiter–Sanders thin shell theory. Combinations of diaphragm, clamped and free conditions at the two ends of a structure are incorporated. The displacement field of a transversely-curved finite strip utilises Bernoulli–Euler beam functions in the longitudinal direction and quintic polynomial representations in the circumferential direction. The superstrip concept is used in conjunction with the modified Sturm sequence-bisection approach to provide an efficient analysis capability. Several applications involving flat plates, curved plates and complete cylinders are detailed.

1 INTRODUCTION

Prismatic plate and shell structures are important load-bearing structural components in various branches of engineering. Such prismatic structures may be made of metal or — in aerospace and marine engineering particularly — may be made of fibre reinforced composite laminated material. As part of the design process for such structures it is necessary to be able to predict accurately the vibrational and buckling behaviour. For such a prediction the finite strip method (FSM) offers an attractive blend of accuracy, economy and ease of modelling.

In recent years the FSM has been developed to a very considerable extent for analysis of the buckling and free vibration of prismatic plate structures whose component plates are flat. Reviews of this subject area are contained in recent publications[1,2] and analyses have been done on the basis of the use both of classical (thin) plate theory and of first-order shear-deformation plate theory. The FSM analysis of prismatic shell structures, i.e. circular cylindrical shells, assemblies of component plates some of which are transversely curved, etc., has received much less attention, though some studies are available in the

literature.[3-10] In these studies the development of strip properties is on the basis of thin shell theory, in which through-thickness shear effects are neglected, and the analyses all have one or another major restriction on their range of application.

The current development represents a major enhancement of earlier work by Dawe[5,6] and Morris and Dawe[7,8] wherein high-order curved finite strips were developed and used successfully in linear static, buckling (under biaxial direct stress) and vibration studies. In the earlier studies[6-8] dealing with buckling and vibration the shell material is isotropic, the ends of the shell are diaphragm supported and the analyses are of the single-term type, i.e. displacements vary purely sinusoidally along the structure length with nodal lines straight and parallel to the ends in any mode of buckling or vibration.

In the present work the developed FSM buckling and vibration capability is still based on the use of thin shell theory (that of Koiter[11] and Sanders[12]) and hence is strictly applicable only to thin-walled structures. Now, though, the walls of the structure may be fibre-reinforced composite laminates of arbitrary lay-up, the system of applied stresses may include shear stress as well as

353

biaxial direct stresses, and the conditions at the two ends of the structure may be any combination of diaphragm, clamped and free conditions. To accommodate these enhancements the displacements are of the multi-term type and Bernoulli–Euler beam functions are used in the longitudinal direction. The solution procedure now incorporates the powerful superstrip concept in conjunction with the modified Sturm sequence-bisection approach, in the manner described in earlier work concerning plate structures.[2]

The present study is part of a more general investigation into the use of the FSM to solve problems of buckling and vibration of shell structures. A related report[13] describes the development of a FSM capability based on the use of shear deformation shell theory.

2 FINITE STRIP ANALYSIS

2.1 General remarks

A curved-plate finite strip which is assumed to form part of a prismatic shell structure is shown in Fig. 1(a). The strip has a uniform radius of curvature R, thickness h, curved breadth b and length A. The local axes xyz are surface ones, i.e. axial (or longitudinal), circumferential and normal ones. The strip has four reference lines, numbered in Fig. 1(a), at which the degrees of freedom are located.

The finite strip may be subjected to the applied membrane stress system shown in Fig. 1(b), leading to buckling, or it may be undergoing harmonic motion whilst vibrating in a natural mode with circular frequency p (or both these influences may

be present, but this is not pursued further here). The applied stress system comprises uniform circumferential stress σ_y^0, uniform shear stress τ_{xy}^0, and axial stress σ_x^0 whose intensity around the strip may vary as a quintic polynomial distribution.

The displacements u, v, w shown in Fig. 1(a) are axial, circumferential and normal displacements at a point on the middle surface of the shell strip. These displacements are in fact perturbation displacements, i.e. they represent changes that occur at the instant of buckling following the application of the given inplane stress system at its critical level, or represent changes that occur during vibration about a datum position. In what follows, other quantities such as stresses and strains are to be understood, in a similar way, to be perturbation quantities (except, of course, for the prescribed stress components which are identified by the superscript 0).

2.2 Shell equations

The development of strip stiffness properties is based upon the use of the strain–displacement equations of Koiter–Sanders thin shell theory.[11,12] The linear expressions for the three significant insurface strain components are, at a general point,

$$\varepsilon_x = \partial u/\partial x - z\partial^2 w/\partial x^2$$

$$\varepsilon_y = \partial v/\partial y + w/R + z(-\partial^2 w/\partial y^2 + (1/R)\partial v/\partial y)$$

$$\gamma_{xy} = \partial u/\partial y + \partial v/\partial x + z(-2\partial^2 w/\partial x\partial y$$

$$+ [3\partial v/\partial x - \partial u/\partial y]/2R) \qquad (1)$$

In general the finite strip is assumed to be a laminate which is composed of a number of layers

(a)   (b)
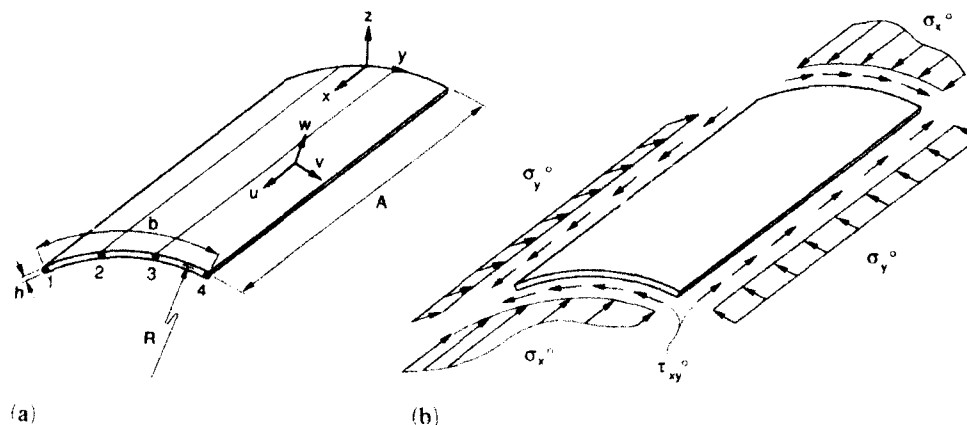
Fig. 1. A curved finite strip: (a) geometry and displacements; (b) applied stress system.

of unidirectional fibre-reinforced composite material. Making the usual assumptions, the stress–strain relationships at a general point for the *l*th layer are

$$
\begin{Bmatrix} \sigma_x \\ \sigma_y \\ \tau_{xy} \end{Bmatrix} = \begin{bmatrix} Q_{11} & Q_{12} & Q_{16} \\ Q_{12} & Q_{22} & Q_{26} \\ Q_{16} & Q_{26} & Q_{66} \end{bmatrix} \begin{Bmatrix} \varepsilon_x \\ \varepsilon_y \\ \gamma_{xy} \end{Bmatrix} \quad \text{or } \boldsymbol{\sigma} = \mathbf{Q}\boldsymbol{\varepsilon}
$$

(2)

where Q_{ij} are plane-stress reduced stiffness coefficients. The constitutive relationships for the laminate are obtained through use of eqns (1) and (2) and appropriate integration through the thickness, and are

$$
\begin{Bmatrix} N_x \\ N_y \\ N_{xy} \\ M_x \\ M_y \\ M_{xy} \end{Bmatrix} = \int_{-h/2}^{h/2} \begin{Bmatrix} \sigma_x \\ \sigma_y \\ \tau_{xy} \\ z\sigma_x \\ z\sigma_y \\ z\tau_{xy} \end{Bmatrix} dz =
$$

$$
\begin{bmatrix} A_{11} & & & & & \\ A_{12} & A_{22} & \text{Symmetric} & & & \\ A_{16} & A_{26} & A_{66} & & & \\ B_{11} & B_{12} & B_{16} & D_{11} & & \\ B_{12} & B_{22} & B_{26} & D_{12} & D_{22} & \\ B_{16} & B_{26} & B_{66} & D_{16} & D_{26} & D_{66} \end{bmatrix}
$$

$$
\times \begin{Bmatrix} \partial u/\partial x \\ \partial v/\partial y + w/R \\ \partial u/\partial y + \partial v/\partial x \\ -\partial^2 w/\partial x^2 \\ (1/R)\partial v/\partial y - \partial^2 w/\partial y^2 \\ -2\partial^2 w/\partial x\partial y \\ +(1/2R)(3\partial v/\partial x - \partial u/\partial y) \end{Bmatrix}
$$

or

$$
\mathbf{F} = \mathbf{L}\mathbf{e}
$$

(3)

Here N_x, N_y and N_{xy} are the membrane direct and shearing forces per unit length, and M_x, M_y and M_{xy} are the bending and twisting moments per unit length. The laminate stiffness coefficients are defined as

$$
(A_{ij}, B_{ij}, D_{ij}) = \int_{-h/2}^{h/2} Q_{ij}(1, z, z^2)\, dz \quad i,j = 1,2,6
$$

(4)

The form of the above constitutive equations is very general, allowing for full material coupling between in-surface and out-of-surface behaviours and for general anisotropy.

The strain energy, U, of the curved strip is

$$
U = \frac{1}{2}\int_V \boldsymbol{\sigma}^t \boldsymbol{\varepsilon}\, dV = \frac{1}{2}\int_V \boldsymbol{\varepsilon}^t \mathbf{Q}\boldsymbol{\varepsilon}\, dV
$$

(5)

where V denotes the volume of the strip. With the definitions given in eqns (1)–(4) U can also be expressed as

$$
U = \frac{1}{2}\int_{-b/2}^{b/2}\int_0^A \mathbf{e}^t \mathbf{L}\mathbf{e}\, dx\, dy
$$

(6)

This strain energy expression will not be presented in full here but clearly it includes the effects of in-surface stretching and shearing action, of out-of-surface bending and twisting action and of coupling between in-surface and out-of-surface actions.

If applied stress σ_x^0, σ_y^0 and τ_{xy}^0 are present, their potential energy arises from the action of the applied stresses on the corresponding second-order strains ε_x^{Nl}, ε_y^{Nl} and γ_{xy}^{Nl}. These strains are defined as

$$
\varepsilon_x^{Nl} = \frac{1}{2}\left[\left(\frac{\partial u}{\partial x}\right)^2 + \left(\frac{\partial v}{\partial x}\right)^2 + \left(\frac{\partial w}{\partial x}\right)^2\right]
$$

$$
\varepsilon_y^{Nl} = \frac{1}{2}\left[\left(\frac{\partial u}{\partial y}\right)^2 + \left(\frac{\partial v}{\partial y} + \frac{w}{R}\right)^2 + \left(\frac{\partial w}{\partial y} - \frac{v}{R}\right)^2\right]
$$

$$
\gamma_{xy}^{Nl} = \left[\frac{\partial u}{\partial x}\frac{\partial u}{\partial y} + \frac{\partial v}{\partial x}\left(\frac{\partial v}{\partial y} + \frac{w}{R}\right) + \frac{\partial w}{\partial x}\left(\frac{\partial w}{\partial y} - \frac{v}{R}\right)\right]
$$

(7)

and the potential energy, V_g, of the applied stresses is

$$
V_g = h\int_{-b/2}^{b/2}\int_0^A (\sigma_x^0 \varepsilon_x^{Nl} + \sigma_y^0 \varepsilon_y^{Nl} + \tau_{xy}^0 \gamma_{xy}^{Nl})\, dx\, dy
$$

(8)

If free vibration is taking place it is assumed that the displacements move with simple harmonic motion having a natural circular frequency p. In dealing with this problem it is convenient if we now regard the displacements as amplitudes of the motion and U as the maximum strain energy occurring during a cycle of the vibration. The maximum kinetic energy during the cycle is

$$
T = \frac{1}{2}p^2\rho\int_{-b/2}^{b/2}\int_0^A (u^2 + v^2 + w^2)\, dx\, dy
$$

(9)

2.3 The strip displacement field

The state of perturbation displacement in the buckled or vibrating finite strip, i.e. the strip displacement field, is defined by the variations over the middle surface of the strip of u, v and w. Each of these displacements is represented spatially as a summation of products of longitudinal (x-direction) series terms and circumferential (y-direction) polynomial functions. (In the dynamic problem u, v and w are regarded as amplitudes.) The specific spatial displacement field used here is

$$\begin{Bmatrix} u \\ v \\ w \end{Bmatrix} = \sum_i \begin{bmatrix} dF_i(x)/dx & 0 & 0 \\ 0 & F_i(x) & 0 \\ 0 & 0 & F_i(x) \end{bmatrix}$$
$$\times \begin{bmatrix} \Phi(y) & 0 & 0 \\ 0 & \Phi(y) & 0 \\ 0 & 0 & \Phi(y) \end{bmatrix} \begin{Bmatrix} A_1 \\ A_2 \\ \vdots \\ A_{18} \end{Bmatrix}$$

or

$$\delta = \sum_i s_i(x) \alpha(y) A_i \qquad (10)$$

The $F_i(x)$ longitudinal functions in $s_i(x)$ in eqn (10) are the Bernoulli–Euler beam functions which have been used frequently in the past in obtaining solutions to plate and shell problems by energy methods (see the monograph by Leissa[14] for shell studies), including by the finite strip method.[15] A beam function $F_i(x)$ is an expression for the deflection (w) of a beam when vibrating in a particular mode i. The beam has end conditions which correspond to a combination of simply supported, clamped and free ends, as is deemed appropriate to the conditions that prevail at the ends of the shell structure under consideration. Thus it appears logical to represent w in the x-direction for the finite strip by the series of $F_i(x)$ functions, and then, to maintain compatibility at longitudinal junctions in branched shells, it is necessary to represent v in the same fashion. The selection of the series of $dF_i(x)/dx$ functions to represent u longitudinally is somewhat more arbitrary, but has been used frequently in the past.[14] It is particularly appropriate for the case of diaphragm supports at both ends.

The summation on i in eqn (10) would ordinarily be consecutively from 1 to r but can be more selective, according to the nature of the problem being considered.

In eqn (10) the $\Phi(y)$ occurring in $\alpha(y)$ are each row matrices defined as

$$\Phi(y) = \begin{bmatrix} 1 & y & y^2 & y^3 & y^4 & y^5 \end{bmatrix} \qquad (11)$$

This indicates that u, v and w are each represented in the circumferential direction by quintic polynomial functions. (The merits of high-order displacement representation for analysing thin, deep shells have been established and discussed in Refs 5 and 6.) The column matrix A_i is the list of generalised displacement coefficients corresponding to the ith term of the longitudinal series. For each series term the generalised coefficients are related to appropriate polynomial degrees of freedom d_i by an equation of the type

$$A_i = C d_i \qquad (12)$$

where C is a square matrix of order 18. The column matrix of degrees of freedom for series term i is defined as

$$d_i = \{ u_1 \; v_1 \; w_1 \; \phi_1 \; u_2 \; v_2 \; w_2 \; \partial u/\partial y_2 \; \partial v/\partial y_2$$
$$u_3 \; v_3 \; w_3 \; (\partial u/\partial y)_3 \; (\partial v/\partial y)_3 \; u_4 \; v_4 \; w_4 \; \phi_4 \}$$
$$(13)$$

where

$$\phi = \frac{\partial w}{\partial y} - \frac{v}{R} \qquad (14)$$

is the rotation about the longitudinal axis. In eqn (13) the subscripts 1,2,3,4 relate to the strip reference lines 1,2,3,4 shown in Fig. 1(a).

Finally, on combining eqns (10) and (12) the strip displacement field can be expressed as

$$\delta = \sum_i s_i(x) \alpha(y) C d_i \qquad (15)$$

Of course, in effect the product $\alpha(y) C$ is a matrix of shape functions.

The conditions considered here at the ends of a shell structure are combinations of diaphragm-supported (or simply supported), clamped and free edges. At an end these conditions are defined as follows:

Diaphragm end:

$$v = w = N_x = M_x = 0 \qquad (16)$$

Clamped end:

$$u = v = w = \partial w/\partial x = 0 \qquad (17)$$

Free end:

$$N_x = N_{xy} + 3\frac{M_{xy}}{2R} = \frac{\partial M_x}{\partial x} + 2\frac{\partial M_{xy}}{\partial y} = M_x = 0$$
$$(18)$$
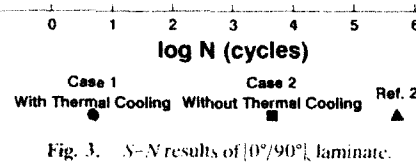
temperature and the curing temperature. How-
ever, the $[0°/90°]$ laminate was found to have a
better fatigue life at room temperature than at an
elevated temperature.

The present formulation provides a convenient
method of life evaluation of symmetric angle-ply

The Bernoulli–Euler beam functions used in the
strip displacement field satisfy explicitly the
necessary kinematic conditions at the ends. On
the other hand, the natural boundary conditions
are not satisfied explicitly, except in particular
cases, e.g. for structures with diaphragm ends and
made of orthotropic material. Of course explicit
satisfaction of natural boundary conditions is not
a requirement of the present approach and it is
only necessary that such conditions be allowed to
be satisfied as a result of the variational pro-
cedure. It is noted, however, that such allowance
is not always possible using the beam functions
and that then the displacement field is not strictly
admissible. This occurs, for instance, for aniso-
tropic structures with diaphragm ends.[2] The effect
is to introduce some degree of over-constraint at
the ends but not to an excessive extent.

At the exterior longitudinal edges of a structure
there is no difficulty in applying any specified
kinematic conditions, in the usual finite element
fashion, and there is no conflict in allowing any
required natural conditions to arise.

2.4 Strip matrices, superstrips and solution procedure

The displacement field defined in eqn (15) can be
used in conjunction with eqns (6), (8) and (9) to
establish expressions for the strain energy, poten-
tial energy of applied stresses, and kinetic energy
of a strip in their familiar quadratic forms as

$$U = \tfrac{1}{2}\,d^t k d \qquad (19)$$

$$V_g = \tfrac{1}{2}\,d^t k_g d \qquad (20)$$

and

$$T = \tfrac{1}{2}\,p^2 d^t m d \qquad (21)$$

Here k, k_g and m are the local stiffness, geometric
stiffness and consistent mass matrices, respec-
tively, and d is the column matrix of all local strip
degrees of freedom. The detailed development of
these matrices will not be given here but is avail-
able in the work of Mohd.[10] The strip has $18r$
degrees of freedom if it is assumed that r series
terms are used.

Multilevel substructuring techniques are used
to create so-called superstrips using the approach
developed earlier for the analysis of prismatic
plate structures.[2] A superstrip is an assembly of a
number of finite strips and one superstrip may
model a whole component curved plate or part of
a circular cylinder, subtending a large angle. Sub-

structuring is first employed at the level of the
individual finite strip to eliminate the degrees of
freedom at the two internal reference lines and
hence produce a strip which effectively has free-
doms only at its outside edges. Then repetitive
substructuring is used to create an assembly of 2^c
strips (where $c = 0, 1, 2, ...$) which is a superstrip
of order c, or simply a superstrip C. Typically we
may take $c = 5$, with Superstrip 5 being an
assembly of 32 finite strips but it is possible to use
up to $c = 10$, or 1024 strips, before beginning to
meet numerical difficulties. Whatever the value of
c, a superstrip ultimately has effective degrees of
freedom located only at its outside edges and
there are $8r$ such freedoms. There is no loss of
accuracy whatsoever involved in substructuring
out the very many internal freedoms associated
with a Superstrip C, i.e. the performance of a
Superstrip 5, say, is precisely that of an assembly
of 32 individual strips and hence is a very accur-
ate model. Moreover, superstrips can be created
with very little penalty as regards computation
time.

To assemble a model branched prismatic shell
structure from superstrips will require the trans-
formation of superstrip properties from the local
to a global configuration. In fact, two types of
transformation are catered for in the analysis, i.e.
the basic rotation transformation arising from the
fact that local axes will generally not coincide in
direction with a chosen set of global axes, and an
eccentricity transformation. Details of these trans-
formations will not be given here but are of similar
type to those considered earlier.[2]

Once the properties of all the superstrips
forming a structure are established in a global
configuration it is possible to assemble the struc-
ture stiffness, geometric stiffness and mass
matrices. Boundary conditions are applied along
longitudinal lines, as appropriate to the problem
under consideration. Then, symbolically, the final
set of equations for the structure has one of the
following two forms:

$$(K - p^2 M)D = 0 \qquad (22)$$

$$(K - f K_g)D = 0 \qquad (23)$$

Here eqn (22) relates to the free vibration prob-
lem whilst eqn (23) corresponds to the buckling
problem. K, K_g and M are the stiffness, geometric
stiffness and consistent mass matrices of the struc-
ture, respectively. D is the column matrix of struc-
ture degrees of freedom, p is a natural circular

frequency of vibration and f is a load factor governing buckling.

Because of the use of substructuring, the eigenvalue problem, of eqn (22) or eqn (23), is nonlinear. The practical solution of the set of equations to yield the natural frequencies or critical stresses proceeds in the manner described in detail in Ref. 2, and involves the use of an extended Sturm sequence-bisection approach.[17] This iterative approach is particularly well suited to the present analysis procedure and has the great merit that eigenvalues are determined automatically and with complete certainty. Once a particular eigenvalue is found the corresponding eigenvector D, representing the mode of vibration or buckling, is determined through the use of a random force vector.

3 APPLICATIONS

3.1 Vibration of isotropic, clamped curved plates

The vibration of a shallow, thin curved plate with all edges fully clamped has been considered by Olson and Lindberg[18] and by Petyt.[19] Details of the geometry and material properties of the plate are recorded in Table 1: B is the curved width of the plate. This table presents results obtained using the present FSM in the form of a convergence study, with the number of series terms used, for frequencies corresponding to the first four symmetric and the first four antisymmetric modes.

Table 1. Convergence of natural frequencies of a clamped, isotropic curved plate with number of series terms $A = 76.2$ mm, $B = 101.6$ mm, $R = 762$ mm, $h = 0.33$ mm, $E = 6.89 \times 10^{10}$ N/m², $\nu = 0.33$, $\rho = 2660$ kg/m³

Longitudinal terms	Frequency (Hz)			
Symmetric modes				
1	889.5	965.5	—	1789.3
1,3	879.7	961.1	—	1781.2
1,3,5	876.3	959.8	1287.9	1779.2
1,3,5,7	874.1	958.7	1286.9	1776.9
1,3,5,7,9	873.3	958.4	1286.7	1776.5
Ref. 18	869.6	957.6	1287.6	1779.6
Ref. 19	870	958	1288	1795
Antisymmetric modes				
2	1376.8	—	—	—
2,4	1374.9	1446.1	1759.8	—
2,4,6	1374.1	1444.5	1758.4	2990.6
2,4,6,8	1373.7	1443.6	1757.6	2289.5
2,4,6,8,10	1372.8	1442.4	1756.3	2288.3
Ref. 18	1363.2	1440.3	1755.6	2295.3
Ref. 19	1364	1440	1753	2300

These two kinds of mode have been analysed separately, using either only odd series terms or only even series terms, as appropriate, in the longitudinal direction. A single Superstrip 5 has been used across the curved plate.

The exhibited manner of convergence of the FSM results in Table 1 is very satisfactory and the comparison between the present results and those of Ref. 18 and 19 is good. It is noted that the comparative results of Olson and Lindberg are obtained using high-order triangular finite elements with properties based on shallow shell theory, whilst the comparative results of Petyt are obtained from what is described as an extended Rayleigh-Ritz method, on the basis of Flugge's shell theory.

3.2 Vibration of two-layered, simply supported, curved plates

The shallow curved plates considered here have simple supports on all edges. The plates are laminates of two-layer cross-ply construction and thus are orthotropic but unbalanced, with the B_{12} and B_{22} coupling stiffness coefficients present. Details of the curved plates are recorded in Table 2. Two curved plates are considered, corresponding to R/h values of 312.5 and 156.25.

Soldatos[20] has presented results for the first four modes of these two laminates, when in turn including or excluding the B_{12} and B_{22} coefficients. These results, like the present analysis, are based on the use of Koiter-Sanders thin shell theory. Results obtained using the present FSM are presented, along with those of Soldatos, in

Table 2. Frequency factors of two-layered, simply supported, curved plates $A = B$, $E_1/E_2 = 40$, $G_{12}/E_2 = 1$, $\nu_{12} = 0.25$, $\Omega = \rho A^2 (\rho E_1 h^2)^{1/2}$

Geometry		Mode designation		Frequency factor Ω			
B/h	R/h			Without B		With B	
		m	n	Present FSM	Ref. 20	Present FSM	Ref. 20
50	312.5	1	1	20.65	20.65	14.06	14.06
		1	2	54.66	54.66	32.42	
		2	1	56.43	56.43	35.45	
		2	2	77.26	77.26	47.95	—
50	156.25	1	1	24.37	24.37	19.16	19.15
		1	2	54.87	54.87	32.87	—
		2	1	61.61	61.61	43.35	—
		2	2	78.24	78.24	49.58	—

Table 2 and excellent comparison is exhibited. (In this table the quantities *m* and *n* are the numbers of half-waves in the *x*- and *y*-directions, respectively.) The FSM results are based on the use of one Superstrip 5 across the whole plate and on the use of two series terms longitudinally. (For this orthotropic curved plate two series terms give an exact longitudinal representation for modes with one or two longitudinal half-waves.) It is clear from Table 2 that the B_{ij} coupling coefficients have a major influence on frequency prediction for the two-layer panel.

3.3 Vibration of isotropic, cantilever cylinders

Sharma[21] has presented solutions, in the context of the use of Flugge's thin shell theory, for clamped-free circular cylinders. The details of one particular shell are recorded in Table 3. This table shows the manner of convergence of the present FSM results, for the fundamental frequency, with the number of series terms used up to $r = 6$. Four identical Superstrips 5 are used to model the full cylinder.

The natural frequency values for various modes of vibration are quoted in Table 4, from both the present FSM approach and that of Ref. 21. The FSM results are based on $r = 6$ and, for a mode with n circumferential half-waves, on modelling a portion of the cylinder of curved width $\pi R/n$ with one Superstrip 5. The results of

Ref. 21 are based on a Rayleigh–Ritz approach in which exact sinusoidal functions are used circumferentially and one clamped-free and one clamped-simple beam functions are used longitudinally. Comparison between the two sets of results is quite good and for all modes the present results are lower than those of Ref. 21.

3.4 Buckling of isotropic, flat, square plates

Here two cases of the buckling of isotropic, flat, square plates are considered. Case A concerns a plate with simply supported edges subjected to in-plane shear stress τ_{11}^0 whilst Case B concerns a plate with clamped edges subjected to biaxial direct stresses $\sigma_1^0 = \sigma_1^0$. Each plate is modelled with one Superstrip 5. Table 5 gives details of the convergence of the calculated FSM results with increase in the number of longitudinal series terms used. (For Case B only the odd terms in the series are used since the buckling mode is symmetric along the plate length.) Good convergence characteristics are indicated, to values which agree closely with comparative results.[22,23]

3.5 Shear buckling of anisotropic, simply supported, curved plates

Pallazoto and Straw[24] have conducted an analysis of the buckling under shear loading of anisotropic curved plates using a finite element approach in the context of modified Sanders' shell theory and incorporating a pre-buckling displacement function. For these curved plates $A = B$ and $A/h = 300$ The material properties are such that $E_1/E_t = 14$, $G_{Lt}/E_t = 0.5$, and $\nu_{Lt} = 0.25$. Two sets of 12-ply lay-up have been considered:[24] one is a symmetric lay-up $[+45_3/-45_3]$ with D_{16} and D_{26} coefficients present, and the other is an unsymmetric lay-up $[+45_6/-45_6]$ with B_{16} and B_{26}

Table 3. Convergence of the fundamental frequency f(Hz), for an isotropic cantilever cylinder
$A = 502$ mm, $R = 63.5$ mm, $h = 1.63$ mm, $E = 2.1 \times 10^{11}$ N/m², $\nu = 0.28$, $\rho = 7800$ kg/m³

r	1	2	3	4	5	6
f Hz	319.53	317.81	317.13	316.74	316.49	316.34

Table 4. Natural frequencies of an isotropic cantilever cylinder

n	Frequency (Hz)					
	$m = 1$		$m = 2$		$m = 3$	
	Present FSM	Ref. 21	Present FSM	Ref. 21	Present FSM	Ref. 21
2	316.3	318.1	947.6	1006.4	2337.2	2356.5
3	769.4	769.7	917.1	927.7	1465.1	1504.2
4	1462.9	1465.5	1520.7	1523.3	1715.7	1726.1
5	2365.9	2366.6	2404.4	2406.4	2506.6	2509.1
6	3468.7	3469.7	3502.6	3505.0	3579.8	3580.7

Table 5. Buckling of isotropic flat plates
$K_A = (\sigma_1^0)_{cr} hA^2/\pi^2 D$, $K_s = (\tau_{xy}^0)_{cr} hA^2/\pi^2 D$, $D = Eh^3/(1-\nu^2)$, $\nu = 0.3$

Case A		Case B	
r	K_A	r	K_s
2	10.388	1	5.340
3	9.378	3	5.308
4	9.366	5	5.305
5	9.334	7	5.304
6	9.332	9	5.303
Ref. 22	9.332	Ref. 23	5.300

coefficients present. In their finite element approach Pallazoto and Straw model the curved plates with flat, square elements each of which has 32 degrees of freedom, and they use a mesh of 18×18 elements. In the present FSM approach a single Superstrip 5 is used to represent the whole plate in the crosswise sense, and in the axial direction five series terms are used.

Results are presented in graphical form in Ref. 24 and hence graphical presentation is also made here. Figures 2(a) and 2(b) show the comparison between the FSM and FEM results for symmetric and unsymmetric lay-ups, respectively, in the form of plots of buckling stress versus h/R. There is good general agreement between the FSM and FEM results, although for deeper, symmetrically-laminated curved plates the predicted FSM buckling stresses for negative shear are quite significantly lower than are the FEM predictions. A particular feature of the shear buckling of anisotropic curved (or flat) plates is that positive and negative shear can yield markedly different values of buckling stress.

3.6 Buckling under axial loading of pear-shaped cylinders with diaphragm ends

The buckling under uniform axial stress of the pear-shaped cylinder shown in Fig. 3 has been studied by Bushnell[25] using an analysis based on the finite difference method used in conjunction with energy minimisation. The cylinder has diaphragm ends and is made of isotropic material. It has been found[25] that the lowest two buckling modes correspond, in turn, to buckling of the flat plate regions 1 and 3, with a single half-wave in

the axial direction. The isotropic pear-shaped cylinder has also been analysed by Dawe[6] in an earlier finite strip approach.

A convergence study has been conducted for this problem using the present FSM approach. The FSM modellings used are detailed in Table 6 and involve the use of superstrips of various orders, up to the use of one Superstrip 5 in each of parts 1-4 of the cylinder. In the longitudinal direction, corresponding to one half-wave, a single-term approach is suitable for this application. Details of the calculated FSM values of the first two buckling stresses are recorded in Table 7 together with the comparative solutions of Bushnell. It is seen that the FSM results converge rapidly to values which are very close to those of Ref. 25.

The scope of this application is now extended by changing the nature of the material from isotropic to composite laminate, whilst keeping all other details the same. The walls of the pear-shaped cylinder are now cross-ply laminates with a variable but even number, nl, of equal-thickness layers: they are thus unbalanced laminates with bending-stretching material coupling present through the B_{11} and B_{22} stiffness coefficients. It is assumed that prior to buckling there is no out-of-surface displacement and that a uniform axial stress is present at buckling. Two different types of material are considered, for both of which the value of E_1 is the same. The material properties are then defined as $E_1/E_1 = 10$, $G_{11}/E_1 = 0.33$, $\nu_{11} = 0.3$ for Material 1 and $E_1/E_1 = 39.8$, $G_{11}/E_1 = 0.49$, $\nu_{11} = 0.25$ for Material 2. For each of these materials Fig. 4 shows the variation of the lowest buckling stress with the number of layers in

Fig. 2. Shear buckling of simply supported, laminated curved plate: (a) symmetric lamination; (b) unsymmetric lamination $(K_x = (\tau_{xy}^0)_{cr} A^2 E_1/h^2)$.

Fig. 3. Cross-section of pear-shaped cylinder.

$$A = 0.80$$
$$R = 1.00$$
$$h = 0.01$$
$$v = 0.3$$
$$E = 1.0 \times 10^7$$

Table 6. FSM modellings for pear-shaped cylinder

Cylinder part	Number of finite strips					
	Model A	Model B	Model C	Model D	Model E	Model F
1	2	4	8	8	16	32
2	2	4	8	16	16	32
3	1	2	8	8	16	32
4	2	4	8	16	16	32

Table 7. Buckling stresses of isotropic pear-shaped cylinder

Finite strip model	Values of $10^5 \, \sigma''_{cr}/E$	
	First mode	Second mode
A	24·207	35·119
B	24·033	34·784
C	24·025	34·771
D	24·025	34·771
E	24·025	34·771
F	24·025	34·771
Ref. 25	24·02	34·74

Fig. 4. Buckling of cross-ply laminated pear-shaped cylinders of two materials $K = 10^5 \, \sigma''_{cr}/E_1$.

the structure may be composite laminates with arbitrary lay-up. The conditions at the two ends of the structure may be any combination of clamped, simply supported and free conditions. The super-strip concept has been incorporated into the development to provide a powerful and efficient solution capability.

A small range of applications, in which comparison is often made with existing solutions, has demonstrated the general validity of the developed procedures. It has been noted, though, that the use of beam functions to represent longitudinal variations of displacements is not always strictly correct and can lead to a degree of over constraint in some circumstances, notably when anisotropy is present.

The present finite strip approach is based on the context of the use of thin shell theory and this restricts its use to the analysis of thin structures. For thicker structures, particularly those made of composite laminate material, through-thickness shear deformation effects become significant. The development of a finite strip approach in the context of shear deformation shell theory is described elsewhere.[13,16]

the laminated wall. The horizontal lines shown in the figure represent the buckling stress when bending–stretching coupling is neglected, i.e. $B_{ij} = 0$. The results shown in Fig. 4 correspond to the use of model F in the FSM. Figure 4 reveals that the effect of bending–stretching coupling on buckling stress is very significant when the number of layers is small but dies out quite rapidly as the number increases, as expected.

4 CONCLUSIONS

The finite strip method has been developed for the prediction of natural frequencies and buckling stresses of prismatic shell structures. The walls of

REFERENCES

1. Dawe, D. J. & Craig, T. J., Buckling and vibration of shear deformable prismatic plate structures by a complex finite strip method. *Int. J. Mech. Sci.*, **30** (1988) 77–99.

2. Dawe, D. J. & Peshkam, V., Buckling and vibration of finite-length composite prismatic plate structures with

diaphragm ends. Part I: Finite strip formulation. *Comput. Meth. Appl. Mech. Engng*, 77 (1989) 1–30.

3. Viswanathan, A. V. & Tamekuni, M., Elastic buckling analysis for composite stiffened panels and other structures subjected to biaxial inplane loads. NASA CR-2216, 1973.

4. Viswanathan, A. V., Tamekuni, M. & Baker, L. L., Elastic stability of laminated, flat and curved, long rectangular plates subjected to combined inplane loads. NASA CR-2330, 1974.

5. Dawe, D. J., Static analysis of diaphragm-supported cylindrical shells using a curved finite strip. *Int. J. Num. Meth. Engng*, 11 (1977) 1347–64.

6. Dawe, D. J., Finite strip buckling analysis of curved plate assemblies under biaxial loading. *Int. J. Solids Struct.*, 13 (1977) 1141–55.

7. Morris, I. R. & Dawe, D. J., Free vibration of curved-plate assemblies with diaphragm ends. *J. Sound Vib.*, 73 (1980) 1–17.

8. Dawe, D. J. & Morris, I. R., Vibration of curved-plate assemblies subjected to membrane stresses. *J. Sound Vib.*, 81 (1982) 229–37.

9. Ashour, H. A. & Sobel, L. H., Buckling of prismatic structures under biaxial loading. *Comput. Struct.*, 12 (1980) 749–58.

10. Petyt, M. & Fleischer, C. C., Finite strip analysis of singly curved skin-stringer structures. *J. Sound Vib.*, 77 (1981) 561–71.

11. Koiter, W. T., A consistent first approximation in the general theory of thin elastic shells. In *Theory of Thin Elastic Shells*, ed. W. T. Koiter, North-Holland, Amsterdam, 1960.

12. Sanders, J. L., An improved first-approximation theory for thin shells. NASA Technical Report R24, 1959.

13. Mohd, S. & Dawe, D. J., Finite strip vibration analysis of composite prismatic shell structures with diaphragm ends (submitted for publication).

14. Leissa, A. W., Vibration of shells. NASA-SP-288, 1973.

15. Cheung, Y. K., *Finite Strip Method in Structural Analysis*. Pergamon Press, Oxford, 1976.

16. Mohd, S., Vibration and buckling analysis of laminated plate and shell structures by thin and shear deformable curved finite strips. PhD thesis, The University of Birmingham, 1990.

17. Wittrick, W. H. & Williams, F. W., A general algorithm for computing natural frequencies of elastic structures. *Q. J. Mech. Appl. Math.*, 24 (1971) 263–84.

18. Olson, M. D. & Lindberg, G. M., Dynamic analysis of shallow shells with doubly-curved triangular finite element. *J. Sound Vib.*, 19 (1971) 299–318.

19. Petyt, M., Vibration of curved plates. *J. Sound Vib.*, 15 (1971) 381–95.

20. Soldatos, K. P., A comparison of some shell theories used for the dynamic analysis of cross-ply laminated circular cylindrical panels. *J. Sound Vib.*, 97 (1984) 305–19.

21. Sharma, C. B., Calculation of natural frequencies of fixed free circular cylindrical shells. *J. Sound Vib.*, 35 (1974) 55–76.

22. Peshkam, V. & Dawe, D. J., Buckling and vibration of finite-length composite prismatic plate structures with diaphragm ends. Part II: Computer programs and buckling applications. *Comput. Meth. Appl. Mech. Engng*, 77 (1989) 227–52.

23. Timoshenko, S. P. & Gere, J. M., *Theory of Elastic Stability*, 2nd edn. McGraw-Hill, London, 1961.

24. Pallazoto, A. N. & Straw, A. D., Shear buckling of cylindrical composite panels. *Comput. Struct.*, 27 (1987) 689–92.

25. Bushnell, D., Stress, buckling and vibration of prismatic shells. *AIAA J.*, 9 (1971) 2004–13.

Influence of the prebuckling stress-field on the critical loads of inhomogeneous composite laminates

M. D. Pandey & A. N. Sherbourne

Department of Civil Engineering, University of Waterloo, Waterloo, Canada

The paper studies the uniaxial buckling behavior of composite laminates in which preselected variations of fiber spacing in the constituent laminae are adopted. Such laminates are referred to as inhomogeneous laminates because of the variable elastic stiffness along the coordinate axes. A non-uniform pre-buckling stress state observed even under constant uniaxial compression has a pronounced influence on the buckling behaviour of an inhomogeneous laminate. A procedure is summarized for computing the critical load of a laminate using the Ritz method which exploits an analogy between the bending and stretching formulations and utilizes Gram–Schmidt orthogonal polynomials. The paper illustrates that the variation in fiber spacing is an innovative way of increasing the critical load for a prescribed amount of fiber and highlights its remarkable sensitivity to the nature of fiber spacing, in-plane and out-of-plane boundary conditions, fiber type and the aspect ratio of the laminate.

1 INTRODUCTION

The concept of designing materials to desired forms of anisotropy and inhomogeneity by manipulating the micro-structural composition has inspired the development and applications of composite material laminates in engineering structures. The traditional approach to designing such laminates focusses on optimizing the orientation of fibers and the thickness of constituent laminae. Also, in the plane of a lamina, fibers are more or less uniformly distributed such that the assumption of a homogeneous, orthotropic material can be justifiably invoked, at least on a macroscopic scale. The possibility of introducing variations in the spacing of reinforcing fibers in constituent laminae for improving buckling resistance has been recently discussed in the literature.[1,2] Because of variable fiber spacing, the elastic stiffness is also variable along the coordinate axes; such laminates, therefore, are referred to as inhomogeneous laminates in this paper.

The non-uniform spatial distribution of fibers causing inhomogeneity requires an explicit derivation of the prebuckling stress-field and its subsequent inclusion in the buckling analysis since the assumption of a uniform uniaxial stress, commonly adopted for homogeneous materials, is now no longer valid. For a fixed quantity of fibers, a laminate design with variable fiber spacing reportedly offers considerable improvement over its homogeneous counterpart with uniform fiber spacing. Non-uniformity of the prebuckling stress-field, an important feature of an inhomogeneous laminate design, has a distinct influence on its critical load. It is easy to understand that the spacing of fibers is a major factor governing the distribution of stresses in the prebuckling state; this is further accentuated by other structural parameters such as boundary conditions, aspect ratio and elastic constants of the fiber. The paper critically examines uniaxial buckling behavior of unidirectional inhomogeneous laminates (Fig. 1) with the purpose of highlighting its sensitivity to the prebuckling stress-field and other intended parameters.

Six unidirectional laminate designs on the basis of six different fiber spacings along the y-axis (Fig. 1), as proposed by Leissa and Martin,[1] are analysed using a more general approach which exploits the classical analogy between the bending and stretching formulation[3] within the framework of the Ritz method.[2] The critical loads are computed not only on the basis of the actual prebuckling stress-fields but also on the assumption of a uniform stress-field as valid for homogeneous

designs. Naturally, the latter case does not require a formal computation of the prebuckling stress state. The advantages of variable fiber spacing and the discrepancies in the critical loads due to ignoring the non-uniformity of the stress state are illustrated for various cases.

2 ANALYSIS

The analytical treatment of the buckling problem consists of two steps, viz. the derivation of the prebuckling stress-field and the subsequent computation of the buckling load using the in-plane stress-field derived earlier. Within the framework of the Ritz method, a stress function formulation for plane-stress and a displacement formulation for buckling analysis are employed.[2]

2.1 Prebuckling stress analysis

The prebuckling stress state in an inhomogeneous laminate subjected to uniaxial compression. σ_{x_0} (Fig. 1), may be described by a stress function of the following form

$$F(X, Y) = F_p + \sum_{m=1}^{N} \sum_{n=1}^{N} A_{mn}\phi_m(X)\psi_n(Y) \qquad (1)$$

where F_p is the particular solution due to the applied stresses and $\phi_m(X)$, $\psi_n(Y)$, are orthogonal polynomials generated by the Gram–Schmidt method[4] to satisfy the prescribed stress boundary conditions. The in-plane stress-field can be expressed in terms of the stress functions using the relations

$$\sigma_x = F_{,yy}, \quad \sigma_y = F_{,xx}, \quad \text{and} \quad \sigma_{xy} = -F_{,xy} \qquad (2)$$

where the subscripts preceded by a comma denote partial differentiation with respect to the corresponding coordinates. Note that a and b are

0.5 a   0.5 a
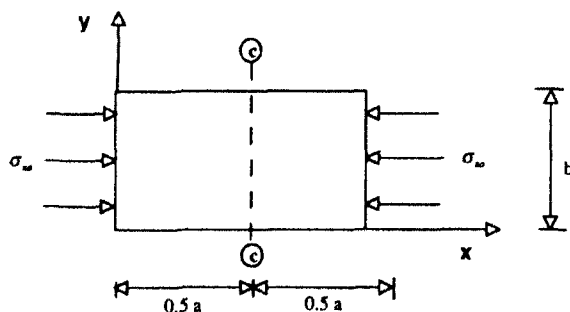
Fig. 1. Uniaxially loaded laminate.

plate length and width, respectively. $X = x/a$ and $Y = y/b$ are normalized coordinates.

The incremental potential energy under the plane-stress condition is given by[5]

$$U_p = \frac{1}{2} \int_0^1 \int_0^1 [C_{11}\sigma_x^2 + C_{22}\sigma_y^2 + 2C_{12}\sigma_x\sigma_y + C_{33}\sigma_{xy}^2]$$

$$dX\,dY \qquad (3)$$

where $C_{ij}(Y)$ are compliance coefficients defined as

$$C_{ij}(Y) = Q_{ij}^{-1}(Y), \qquad (i,j = 1.....3)$$

being functions of the Y coordinate due to non-uniform fiber distribution in that direction. $Q_{ij}(Y)$ are the usual orthotropic elastic constants given by

$$Q_{11} = \frac{E_x}{d}, \quad Q_{22} = \frac{E_y}{d}, \quad Q_{12} = v_{xy}\frac{E_y}{d},$$

$$Q_{33} = G_{xy}, \quad d = (1 - v_{xy}v_{yx})$$

where E_x, E_y are, respectively, the major and minor elastic modulus, v_{xy}, v_{yx} are major and minor Poisson's ratio and G_{xy} is the shear modulus. All the elastic constants, being a function of fiber volume fraction V_f, are now variable along the Y-coordinate. Now, substituting from eqn (2) into eqn (3) and minimizing the potential function. U_p, with respect to the coefficients A_{mn}, leads to the following system of linear simultaneous equations

$$\sum_{m=1}^{N} \sum_{n=1}^{N} [H_{mnij}]\{A_{mn}\} = -\sigma_{x_0}b^2\{P_{ij}\}(i,j = 1.....N)$$

$$(4)$$

The solution of the system of eqns (4) allows one to determine the prebuckling stress-field from eqn (2). The in-plane stiffness [H] and the load matrix {P} are given by Pandey and Sherbourne.[2] In computation $N = 10$, i.e. 100 terms are included in the stress function series (1).

2.1.1 In-plane boundary conditions

A sequence of Gram–Schmidt orthogonal polynomials can be constructed to satisfy the required end conditions using the following recurrence formulae[4]

$$\phi_2(X) = (X - B_2)\phi_1(X)$$

$$\phi_k(X) = (X - B_k)\phi_{k-1}(X) - C_k\phi_{k-2}(X)(k = 3,...,N)$$

where

$$B_k = \frac{\int_0^1 X\phi_{k-1}^2(X)\,dX}{\int_0^1 \phi_{k-1}^2(X)\,dX}, \quad C_\lambda = \frac{\int_0^1 \phi_{k-1}^2(X)\,dX}{\int_0^1 \phi_{k-2}^2(X)\,dX} \tag{5}$$

(1) Free (F) edges A free edge defined by $\sigma_x = \sigma_{x_0}$ and $\sigma_{xy} = 0$ at $X = 0, 1$ can be idealized by choosing coordinate functions that satisfy $\phi_m(x) = \phi_{m,x}(x) = 0$ at $X = 0, 1$. The first member of the orthogonal polynomial sequences in (5) would be

$$\phi_1(X) = a_1(X^2 - 2X^3 + X^4) \tag{6}$$

(2) Laterally restrained (R) edges A laterally restrained edge is defined as $\sigma_x = \sigma_{x_0}$, $\sigma_y = 0$ and $\sigma_{xy} \neq 0$ at $X = 0, 1$, for which, conditions $\phi_m(x) = \phi_{m,xx}(x) = 0$ at $X = 0, 1$, should be satisfied. Here, $\phi_1(X)$ is given by

$$\phi_1(X) = a_1(X - 2X^3 + X^4) \tag{7}$$

2.2 Buckling analysis

The potential energy of a uniaxially compressed orthotropic laminate at incipient buckling is given by

$$U_B = \frac{1}{2b^4}\int_0^1\int_0^1\left[\frac{1}{\beta^4}D_{11}W_{,xx}^2 + \frac{2}{\beta^2}D_{12}W_{,xx}W_{,yy}\right.$$

$$\left. + D_{22}W_{,yy}^2 + \frac{4}{\beta^2}D_{33}W_{,xy}^2\right]dX\,dY + b^2 t$$

$$\left[\frac{\sigma_x}{\beta^2}W_{,x}^2 + \sigma_y W_{,y}^2 + \frac{2\sigma_{xy}}{\beta}W_{,xy}\right]dX\,dY \tag{8}$$

where W is the out-of-plane displacement and $D_{ij} = Q_{ij}t^3/12\ (i,j = 1,\dots,3)$ is the laminate bending stiffness derived on the basis of Kirchhoff's plate theory.[6] Using displacement functions of the following form

$$W(X, Y) = \sum_{m=1}^{M}\sum_{n=1}^{M}B_{mn}f_m(X)g_n(Y) \tag{9}$$

and subsequently minimizing U_B with respect to coefficients B_{mn} results in a generalized eigenvalue problem

$$\sum_{m=1}^{M}\sum_{n=1}^{M}[E_{mnij}]\{B_{mn}\} = -\lambda b^2 t[G_{mnij}]\{B_{mn}\}$$

$$(i, j = 1,\dots,M) \tag{10}$$

in which λ is a load factor. Explicit expressions for elements of the stiffness matrix, E_{mnij}, and the geometric matrix, G_{mnij}, may be found elsewhere.[2] Buckling loads are computed using $M = 7$, i.e. 49 terms in the displacement function (9).

2.2.1 Boundary conditions

Two types of out-of-plane boundary conditions are considered.

(1) Simple (S) supports The conditions of zero displacement and moment at boundaries are satisfied by

$$W = \sum_{m=1}^{M}\sum_{n=1}^{M}\sin m\pi X \sin n\pi Y \tag{11}$$

(2) Clamped (C) supports A clamped support is specified by the conditions $W = W_{,x} = 0$ (say, at $X = 0, 1$) which can be satisfied by the following set of orthogonal polynomials

$$W = \sum_{m=1}^{M}\sum_{n=1}^{M}B_{mn}\phi_m(X)\psi_n(Y) \tag{12}$$

Using the duality of the bending and stretching formulations,[3] it can be shown[2] that the in-plane free boundary conditions and out-of-plane clamped conditions are simultaneously satisfied by an orthogonal polynomical sequence generated from eqns (5), (6) and (12). This feature, in essence, unifies the in-plane stress analysis and the buckling load calculation.

3 RESULTS AND DISCUSSION

Numerical results are obtained for two laminate aspect ratios, $a/b = 1$, 2 and three fiber types as listed in Table 1. Six fiber spacings (Table 2) as suggested by Leissa and Martin[1] are used. The boundary conditions are denoted by the letter S for simple, C for clamped, F for free and R for restrained in the following order: $x = 0$, $x = a$

Table 1. Material properties

Material	Elastic modulus (GPa)	Poisson's ratio (v)
Glass	73·09	0·22
Graphite	275·8	0·20
Boron	413·7	0·20
Epoxy	3·44	0·35

(loaded edges), $y=0$, $y=b$ (unloaded edges) such that support conditions denoted by say SSCC means loaded edges, $x=0$ and a are simply supported and unloaded edges, $y=0$ and b are clamped. Normalized buckling coefficients $(N_x = 12\sigma_{xo} b^2/E_f t^2)$ for simple (SSSS) and clamped (CCCC) laminates with free (FFFF) in-plane edge conditions are reported in Tables 3 and 4, respectively. Note that E_f is the fiber elastic modulus. Buckling coefficients are tabulated for the following three cases, (1) N_p: uniform fiber spacing, (2) N_x: variable fiber spacing and (3) N_{xu} inhomogeneous laminate under uniform pre-buckling stress state. In all the three cases, the total fiber volume remains constant.

Fiber spacing functions of type 1, 3 and 6 are plotted in Fig. 2 and corresponding stress distri-

butions are displayed in Figs 3 and 4 for free (FFFF) and laterally restrained (RRRR) in-plane BCs, respectively. In Figs 3 and 4, uniaxial stress distributions along a central section c–c, at $x = a/2$ (see Fig. 1) are presented for square and rectangular graphite–epoxy laminates. It is clearly seen that the variable fiber spacing introduces a varying degree of non-uniformity in the stress-field depending upon the spacing function. Fiber spacing of type 3 results in remarkably high stress concentrations, $\approx 1\cdot5\sigma_{xo}$, which may have serious implications in actual performance. It is interesting that, in rectangular laminates, the stress distribution tends to be more uniform with less pronounced peaks. However, it is noteworthy that the variation of V_f from 0 to 1, e.g. types 1–3 in Table 2, is not a practical case. For a benign fiber distribution, e.g. type 6, the stress variation is fairly uniform with $\sigma_x \approx \sigma_{xo}$. As shown in Fig. 4, for laminates with in-plane restrained (RRRR) edges, the nature of the stress distributions is significantly changed and stress concentrations are less severe.

3.1 Efficiency of inhomogeneous laminates

The efficiency of an inhomogeneous laminate can be estimated by comparing its buckling load (N_x) against that of an equal volume homogeneous counterpart (N_p). Thus,

Table 2. Fiber distribution functions

No.	Fiber spacing function $V_f(Y)$	$V_{f\,avg}(\%)$	$V_{f\,min}(\%)$ $(Y=0,1)$	$V_{f\,max}(\%)$ $(Y=0\cdot5)$
1	$4U$	67	0	100
2	$16U^2$	53	0	100
3	$64U^3$	40	0	100
4	$0\cdot5+U$	67	50	75
5	$0\cdot5+4U^2$	63	50	75
6	$0\cdot5+16U^3$	60	50	75

Note: $U = Y(1-Y)$, V_f = fiber volume fraction.

Table 3. Critical loads for simply supported (SSSS) laminates

Composite material	Fiber spacing type	N_p		N_x		Efficiency (%)		N_{xu}		Error (%)	
		$a/b=1$	$a/b=2$	$a/b=1$	$a/b=2$	$a/b=1$	$a/b=2$	$a/b=1$	$a/b=2$	$a/b=1$	$a/b=2$
Glass–epoxy	1	10·77	9·54	12·76	12·12	18·4	27	13·7	13·7	7·4	13·1
	2	8·41	7·13	9·83	8·62	16·8	20·9	11·03	11·03	12·2	27·9
	3	6·63	5·7	8·44	6·86	27·3	20·3	9·72	9·2	15·2	34·2
	4	10·77	9·54	11·13	9·83	3·4	3	11·25	10·26	1	4·3
	5	10·02	8·71	10·59	9·14	5·6	5	10·72	9·61	1·2	5·1
	6	9·51	8·17	10·26	8·77	8	7·3	10·4	9·22	1·2	5·2
Graphite–epoxy	1	7·77	3·86	9·37	5·61	20·7	45·6	9·71	6·23	3·6	11
	2	6·09	2·89	7·41	3·71	21·6	28·5	8·01	4·43	8·1	19·2
	3	4·66	2·25	6·28	2·95	34·5	31	7·04	3·71	12·1	26
	4	7·77	3·86	8·19	4·08	5·5	5·8	8·22	4·16	0·3	1·9
	5	7·26	3·53	7·86	3·83	8·1	8·5	7·89	3·92	0·4	2·2
	6	6·9	3·32	7·64	3·69	10·6	11	7·66	3·77	0·4	2·2
Boron–epoxy	1	7·39	3·13	8·9	4·5	20·4	43·7	9·14	4·89	2·7	8·7
	2	5·81	2·37	7·03	3·06	21·1	29·4	7·55	3·56	7·4	16·2
	3	4·43	1·83	5·87	2·45	32·6	34	6·55	3·01	12·3	23
	4	7·39	3·13	7·82	3·33	5·8	6·3	7·84	3·38	0·2	1·4
	5	6·92	2·88	7·51	3·14	8·5	9	7·53	3·19	0·3	1·6
	6	6·58	2·71	7·3	3·02	11	11·6	7·32	3·08	0·2	1·6

Table 4. Critical loads for clamped (CCCC) laminates

Composite material	Fiber spacing type	N_p		N_x		Efficiency (%)		$N_{\iota\upsilon}$		Error (%)	
		$a/b=1$	$a/b=2$	$a/b=1$	$a/b=2$	$a/b=1$	$a/b=2$	$a/b=1$	$a/b=2$	$a/b=1$	$a/b=2$
Glass–epoxy	1	35·6	22·6	40·98	23·84	15·1	5·5	45·07	28·5	10	19·4
	2	28·12	17·61	33	18·42	17·3	4·6	38·7	24·03	17·3	30·4
	3	22·03	13·87	28·35	15·67	28·7	13	34·74	21·61	22·5	37·9
	4	35·6	22·6	36·83	22·41	3·4	−0·8	37·38	23·34	1·5	4·2
	5	33·31	21·02	35·45	21·31	6·4	1·4	36·15	22·46	2	5·4
	6	31·69	19·93	34·6	20·71	9·2	4	35·33	21·92	2·1	5·8
Graphite–epoxy	1	29	12·95	35·15	14·95	21·2	15·4	36·42	17·02	3·6	13·8
	2	22·87	9·8	27·55	11	20·4	12·2	29·68	13·76	7·8	25·1
	3	17·46	7·58	19·75	9·01	13·1	18·8	23·71	12·02	20·1	33·4
	4	29	12·95	30·88	12·82	6·5	−1·1	31·02	13·17	0·4	2·8
	5	27·2	11·92	29·89	12·22	9·9	2·5	30·07	12·65	0·6	3·5
	6	25·9	11·23	29·18	11·9	12·7	6	29·36	12·34	0·6	3·7
Boron–epoxy	1	28·16	10·93	34·1	13	21·1	18·8	34·37	14·02	0·8	7·9
	2	22·3	8·32	24·11	9·76	8·2	17·2	24·21	10·37	0·4	6·3
	3	16·91	6·41	16·69	8·02	−1·3	25·2	14·86	6·6	−11	−17·8
	4	28·16	10·93	30·12	11·03	6·9	0·9	30·21	11·24	0·3	2
	5	26·43	10·1	29·15	10·56	10·3	4·6	29·27	10·82	0·4	2·5
	6	25·16	9·52	28·43	10·29	13	8·1	28·54	10·57	0·4	2·7

Fiber Spacing
— Type 1
— · Type 3
— · · Type 6
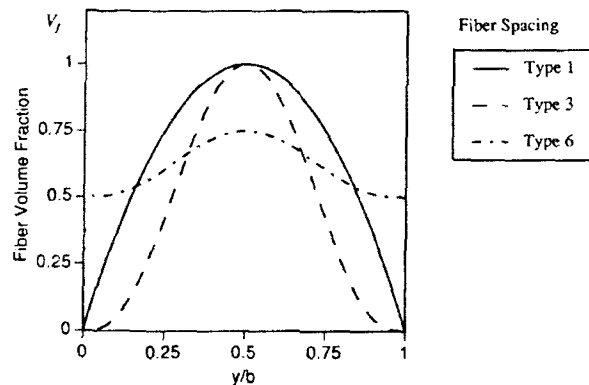
Fig. 2. Fiber spacing functions.

$$\text{Efficiency} = \frac{N_x - N_p}{N_p} \times 100 \qquad (13)$$

This efficiency is dictated by the chosen fiber spacing. For simply supported laminates, a cubic fiber distribution (type 3) increases the buckling load as much as 34% while a parabolic distribution seems to be optimal for rectangular laminates resulting in an increase of almost 45% in the case of graphite–epoxy composites. Clamped laminates follow a similar trend and display a pronounced dependence of efficiency on fiber type, i.e. material orthotropy, as well as aspect ratio. For example, the buckling load of a square boron–epoxy laminate is decreased by 2% for
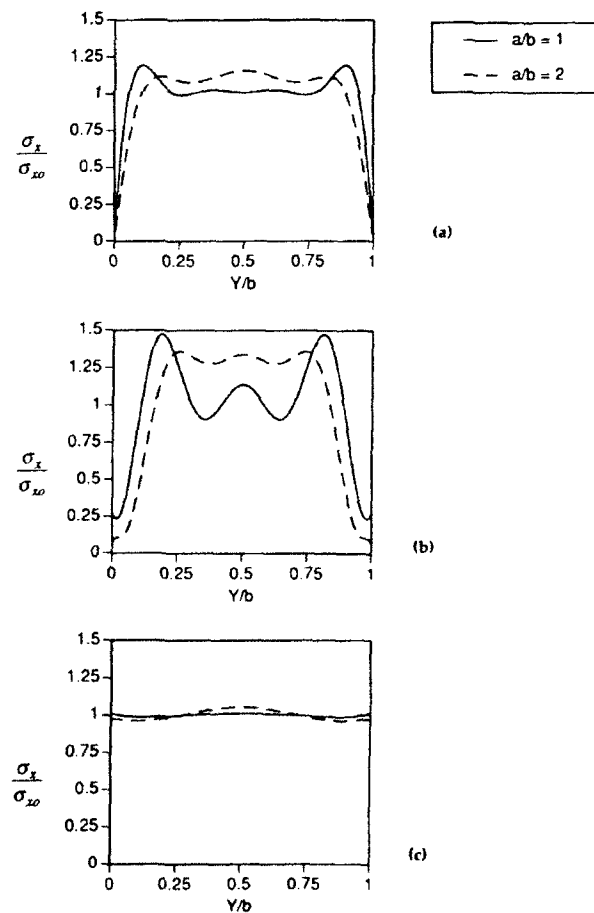
Fig. 3. Prebuckling stress-field: free (FFFF) in-plane BCs (a) fiber spacing 1; (b) fiber spacing 3; (c) fiber spacing 6.
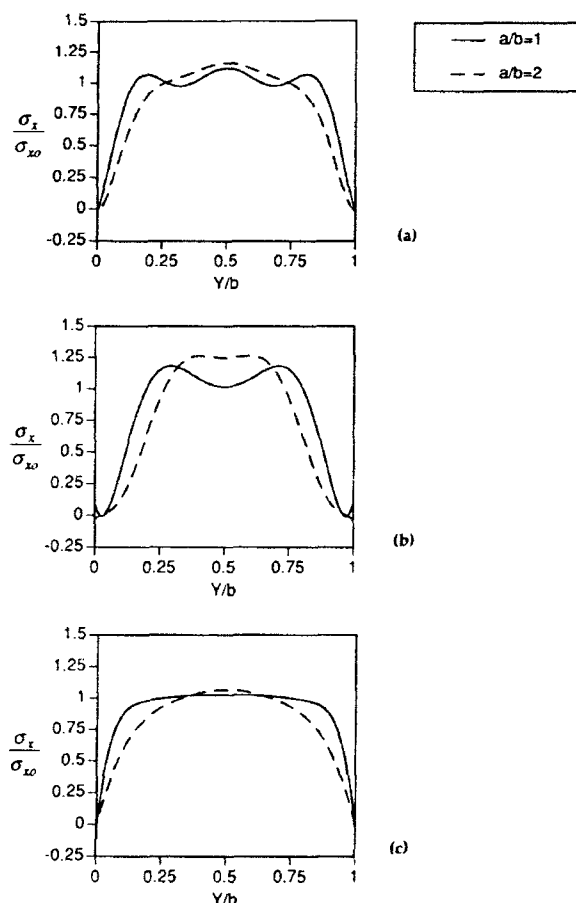
Fig. 4. Prebuckling stress-field: restrained (RRRR) in-plane BCs (a) fiber spacing 1: (b) fiber spacing 3: (c) fiber spacing 6.

fiber spacing of type 3; an increase of 25% is noted for rectangular laminates.

3.2 Effects of prebuckling stress-field

Buckling loads (N_{xu}) for inhomogeneous laminates are also computed ignoring the actual prebuckling stress field and imposing the assumption of a uniform stress field, $\sigma_x = \sigma_{xo}$, throughout the entire plate. The effect of prebuckling stress is quantified by comparing the actual buckling load N_x against N_{xu} and expressing it by an error parameter

$$\text{Error} = \frac{N_{xu} - N_x}{N_x} \times 100 \qquad (14)$$

The magnitude of the error term reflects, in some way, the sensitivity of the non-uniformity of the stress-field to the buckling load. In comparing square laminates, the error is much higher than for rectangular laminates, as high as 38% for a clamped glass–epoxy composite with type 3 fiber spacing. In cases of benign fiber distributions (types 4–6), the error is fairly small, not exceeding 5%. It is interesting to note that the assumption of a uniform prebuckling stress state consistently provides an upper bound (non-conservative) solution with the exception of clamped boron–epoxy laminates with type 3 spacing of fibers (Table 4). The fiber distributions which result in significant increases of the critical loads also admit considerable error upon imposing the assumption of a uniform stress-field; this highlights the importance of the formal computation of the prebuckling state for inhomogeneous laminates.

3.3 Effects of in-plane edge conditions

In Table 5, critical loads of simply supported (SSSS), graphite–epoxy laminates are presented for various combinations of free (F) and restrained (R) in-plane boundary conditions (BCs). Variations of in-plane BCs do not have a noticeable influence on the critical loads of square laminates despite significant changes in the stress-distribution in comparison to that corresponding to free edges as shown by Figs 3 and 4.

Table 5. Critical loads for SSSS laminates with various in-plane BCs

Fiber spacing type	Buckling coeff. (N_x)		Ratio of buckling coefficients (N_x/N_x) In-plane boundary conditions					
	FFFF		RRRR		FFRR		RRFF	
	$a/b = 1$	$a/b = 2$	$a/b = 1$	$a/b = 2$	$a/b = 1$	$a/b = 2$	$a/b = 1$	$a/b = 2$
1	9·37	3·85	1·03	1·64	1·03	1·63	0·98	1·44
2	7·4	2·89	1·08	1·54	1·08	1·54	0·98	1·26
3	6·27	2·25	1·13	1·66	1·13	1·66	0·98	1·29
4	8·19	3·85	1·01	1·15	1·01	1·13	0·99	1·05
5	7·85	3·53	1·01	1·17	1·01	1·15	0·99	1·08
6	7·63	3·32	1·01	1·2	1·01	1·18	0·99	1·1

However, rectangular laminates exhibit a remarkable increase in buckling loads, as high as 66% for type 3 fiber spacing. It should be noted that the restraining of the unloaded edges (FFRR case) is more effective than restraining the loaded edges (RRFF case) in terms of increasing the critical load.

4 CONCLUSIONS

The variation of fiber spacing proves to be an effective way of increasing the buckling load for a prescribed quantity of fibers. It results in a non-uniform prebuckling stress state, even under constant compression, which induces considerable change in the critical load of a laminate. However, the magnitude of such changes is highly dependent on other related structural parameters, namely, the nature of the spacing, fiber type, in-plane and out-of-plane boundary conditions and the laminate aspect ratio. It should be noted that a fiber spacing effective in increasing the critical load also results in remarkably high stress concentrations which raise concerns about its practicality and feasibility.

The paper emphasizes the accurate computation of the prebuckling stress-field since the assumption of a uniform stress state is likely to admit gross errors in the buckling analysis for highly inhomogeneous laminates. However, for benign fiber distributions, the non-uniformity of the stress-field is of such a mild degree that its formal computation is not justified on the grounds of attaining marginal accuracy at disproportionately high computational effort.

REFERENCES

1. Leissa, A. W. & Martin, A. F., Vibration and buckling of rectangular composite plates with variable fiber spacing. *Int. J. Comp. Struct.*, **14** (4) (1990) 339–57.
2. Pandey, M. D. & Sherbourne, A. N., Stability analysis of inhomogeneous fibrous composite plates. *Int. J. Solids Struct.*, **30** (1) (1992) 37–60.
3. Southwell, R. V., On the analogies relating flexure and extension of flat plates. *Quart. J. Mech. Appl. Math.*, **3** (3) (1950) 257–70.
4. Bhat, R. B., Natural frequencies of rectangular plates using characteristic orthogonal polynomials in Rayleigh–Ritz method. *J. Sound Vib.*, **102** (1985) 493–9.
5. Bassily, S. F. & Dickinson, S. M., The plane stress problem for rectangular regions treated using functions related to beam flexure. *Int. J. Mech. Sci.*, **19** (1977) 639–50.
6. Jones, R. M., *Mechanics of Composite Materials*. McGraw-Hill, New York, 1975.

Dynamic behavior of cross-ply laminated beams with piezoelectric layers

H. Abramovich
Faculty of Aerospace Engineering, Technion-IIT, 32000 Haifa, Israel

&

A. Livshits
The Israel Electric Corp. Ltd, IEC, Haifa, Israel

The dynamic behavior of cross-ply non-symmetric composite beams, having uniform piezoelectric layers is analysed. A first-order Timoshenko type analysis is applied to obtain the equations of motion, which include shear deformation, rotary inertia, bending–stretching coupling terms and induced axial strains caused by the piezoelectric material. Using the principle of virtual work, the coupled equations of motion and the relevant boundary conditions are obtained. For a laminated beam having uniform piezoelectric layers the induced strains appear only in the boundary conditions yielding time dependent ones. Therefore, a special procedure involving orthogonality of the coupled Timoshenko type natural vibrational modes of the beam is applied to help understanding of the dynamic behavior of the non-symmetric laminated beam and to investigate the influence of the induced strains (by the piezoelectric layers) on the dynamic behavior while keeping an 'open-loop' control. Typical types of laminates and piezoelectric materials are used to calculate natural frequencies and mode shapes. Numerical results for various parameters of laminated beams are presented to stress the better applicability and suitability of the present approach to the analysis of dynamic behavior of laminated composite beams with piezoelectric layers.

INTRODUCTION

In recent years, a considerable amount of research[1-5] has been done on intelligent structures. These are structures which are integrated with sensors and actuators to obtain active control. With the ability to control the response of a structure movement, the intelligent stucture will have three major applications, namely vibration control, shape control and damage deflection.

One of the primary materials considered for these intelligent structures is often laminated composites.[6,7] The advantages of using laminated composite materials include the ability to design the stiffness and strength of the laminate so as to keep the ratio of strength to weight maximum.

Piezoelectric materials, which exhibit mechanical deformation when an electric field is applied and/or produce voltage under strain, become increasingly important as sensors and actuators.[1,6-9]

Bonding or embedding[10] segments or layers of these materials in a laminated structure would allow the application of strains through which the deformation of the structure can be controlled and/or damped.[11]

To date, models of induced strain actuator/substrate system are very limited because most the researchers have concentrated their efforts on the implementation of control algorithms.[1,4,7,9,12] Most of the models in the literature are based on the classical lamination theories such as Kirchhoff's hypothesis for plates or the equivalent theory for beams, the Bernoulli–Euler theory,[7,12] both neglecting transverse shear deformations and rotary inertia. However, shear effects are significant for anisotropic beams because the ratio between the transverse shear modulus and the extensional modulus is between 1/20 and 1/50 for modern composites and between 1/2.5 and 1/3 for isotropic materials.[13,14] Use of refined shear-deformable theories including piezoelectric layers

are confined to plates[10,11,15] only, for static cases and very limited dynamic cases.

In the present work, the dynamic behavior of cross-ply non-symmetric (with symmetrical layup being only a simplified case) laminated composite beams, having uniform piezoelectric layers, is analysed. A first-order Timoshenko[13,14] type analysis is applied to obtain the equations of motion, which include shear deformation, rotary inertia, bending–stretching coupling terms and induced axial strains caused by the presence of the piezoelectric layers.

Using the principle of virtual work, the coupled equations of motion and the relevant boundary conditions are obtained. For a laminated beam having uniform piezoelectric layers the induced strains appear only in the boundary conditions, yielding time dependent ones. Therefore a special procedure involving orthogonality of the Timoshenko type natural vibrational modes of the

beam is applied to help understand the dynamic behavior of non-symmetric laminated beams with piezoelectric layers.

FORMULATION OF PROBLEM

Figure 1 shows a laminated composite beam referred to a system of Cartesian coordinates with the origin on the midplane of the beam and the x-axis being coincident with the beam axis. Two of the cross-ply layers are piezoelectric layers. We assume that the piezoelectric layer, thickness d, is negligible in comparison with the beam thickness, h, $d/h \ll 1$. The electro-mechanical behavior of the piezoelectric layer is described in Refs 1, 3, 4 and 12.

The displacements of the beam can be shown to be given by the following relations

$$U = u + z\psi \qquad\qquad (1)$$

$$W = w$$
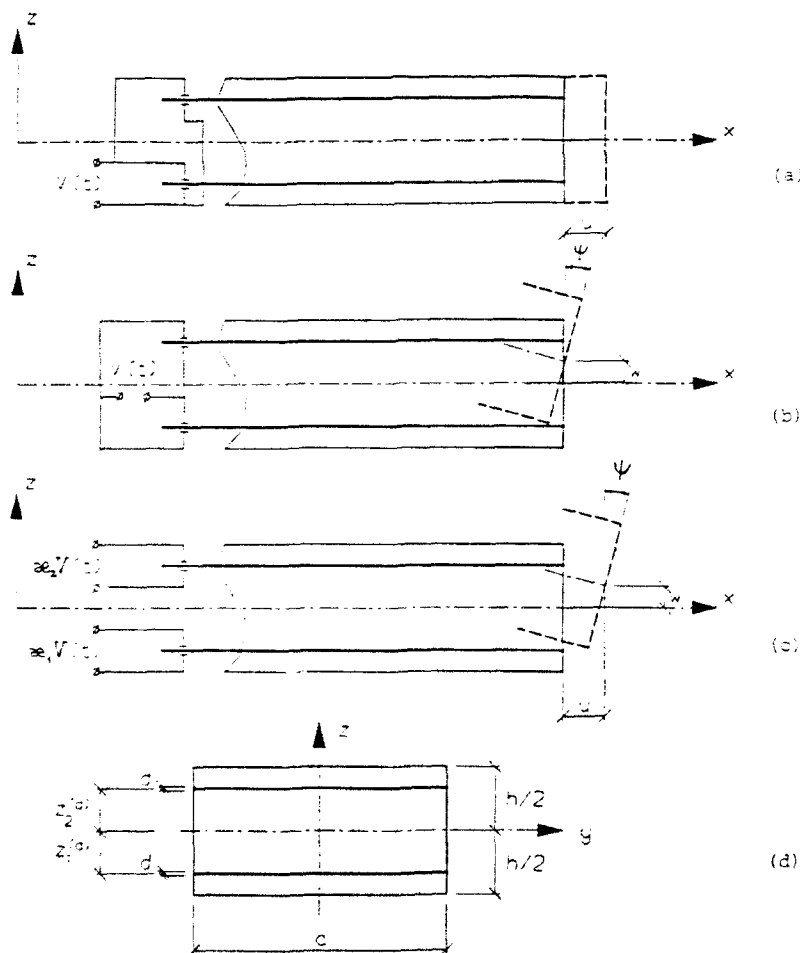
Fig. 1. A cross-ply laminate composite beam with piezoelectric layers; (a) symmetric case; longitudinal vibrations; (b) symmetric case; transversal vibrations; (c) non-symmetric case, coupled transverse–longitudinal vibrations; (d) cross-section.

where $u(x,t)$ and $w(x,t)$ are the axial and lateral displacements of a point on the midplane and $\psi(x,t)$ is the rotation of the normal to the midplane.

For the symmetric case having the piezoelectric layers at equal distance from midplane, $z_i^u = z_i^d$ and the special electric scheme (see Fig. 1a,b) the longitudinal and transverse vibrations of the beam are not coupled and may be described separately.

The classical strains, without external electric field are given by

$$\varepsilon_x = u' + z\psi' \qquad (2)$$
$$\gamma_{xz} = \psi + w'$$

where $'$ denotes partial derivation with respect to the span coordinate, x. The stress–strain relation for the piezoelectric material is similar to that of thermoelastic materials, with the thermal strain term being replaced by the piezoelectric induced strain. The actuation strain ε_i^d due to the external electric field is given by[3-12]

$$\varepsilon_i^d = \sum \frac{d_{31}}{d} \kappa_i V(t) \qquad (3)$$

where d_{31} is the appropriate static piezoelectric constant. $V(t)$ is the applied voltage and κ_i the control coefficient for the ith piezoelectric layer number.

The stress–strain relations for composite laminae are given by[13,14]

$$\sigma_x = \bar{Q}_{11} \varepsilon_x - \varepsilon_i^d$$
$$\tau_x = \bar{Q}_{55} \gamma_{xz} \qquad (4)$$

where $\bar{Q}_{11}$ and $\bar{Q}_{55}$ are the transformed material constants, depending on the material constants and on the angle θ between the fiber direction and the longitudinal axis of the beam. For cross-ply laminae the value of the angle θ is either $0°$ or $90°$. For this case the tranverse and torsional deformations can be shown to be uncoupled.[14,16]

The internal forces and moments acting on the cross-section of the beam are given by

$$(N_x, M_x) = \int_A \int \sigma_x (1, z)\, dA$$

$$Q_x = k \int_A \int \tau_x \, dA \qquad (5)$$

where $k = 5/6$ is a shear correction factor.[17] From relations (2)–(5) we can obtain the beam constitu-

tive equations:

$$N_x = A_{11} u' + B_{11} \psi' + E_{11} V(t)$$
$$M_x = B_{11} u' + D_{11} \psi' + F_{11} V(t) \qquad (6)$$
$$Q_x = A_{55}(\psi + w')$$

where

$$(A_{11}, B_{11}, D_{11}) = c \int_{-h}^{h} \bar{Q}_{11}(1, z, z^2)\, dz$$

$$A_{55} = kc \int_{-h}^{h} \bar{Q}_{55}\, dz \qquad (7)$$

$$(E_{11}, F_{11}) = -c \sum \bar{Q}_{11} \kappa_i d_{31}(1, z)$$

and c is the beam width.

The virtual work of the present problem is[8]

$$\delta\pi = \int_0^t \int_0^l \left[-N_x \delta u' + M_x \delta\psi' + Q_x \delta(\psi + w') + \right.$$
$$\left. I_1 \ddot{u} + I_2 \ddot{\psi})\delta u + I_1 \ddot{w}\delta w + (I_2 \ddot{u} + I_3 \ddot{\psi})\delta\psi \right]$$
$$dx\, dt = 0 \qquad 8$$

where

$$(I_1, I_2, I_3) = c \int_{-h}^{h} \rho (1, z, z^2)\, dz \qquad 9$$

ρ is the mass density of the beam material and $\cdot$ denotes partial derivation with respect to time, t. Using eqns (8) and carrying out the various variational operations yields the governing equations of motion for uniform cross-ply laminated composite beams with uniform spatial distribution of piezoelectric layers

$$A_{11} u'' + B_{11} \psi'' = I_1 \ddot{u} + I_2 \ddot{\psi}$$
$$A_{55} w'' + A_{55} \psi' = I_1 \ddot{w} \qquad (10)$$
$$B_{11} u'' - A_{55} w' + D_{11} \psi'' - A_{55} \psi = I_2 \ddot{u} + I_3 \ddot{\psi}$$

and the boundary conditions are:

$$A_{11} u' + B_{11} \psi' + E_{11} V(t) = 0 \quad \text{or} \quad u = 0$$
$$A_{55}(\psi + w') = 0 \quad \text{or} \quad w = 0 \qquad (11)$$
$$B_{11} u' + D_{11} \psi' + F_{11} V(t) = 0 \quad \text{or} \quad \psi = 0$$

SOLUTION OF EQUATIONS OF MOTION FOR A CANTILEVER BEAM

Introducing the non-dimensional span of the beam, ξ, and the non-dimensional time, τ, defined

by

$$\xi = \frac{x}{L} \qquad \tau = \omega_o t \tag{12}$$

where L is the length of the beam and ω_o is the fixed angular frequency, we obtain the non-dimensional generalized displacements

$$\{\bar{q}\} = \left\{ \frac{u}{L}, \frac{w}{L}, \psi \right\}^{\Gamma} \tag{13}$$

yielding the equations of motion in a matrix form:

$$[M]\{\ddot{\bar{q}}\} + [C]\{\bar{q}\} = 0 \tag{14}$$

where $[M]$ is mass matrix and $[C]$ is matrix differential operator, defined as

$$[M] = p_o^2 [M_o] \tag{15}$$

$$[M_o] = \begin{bmatrix} 1 & 0 & \eta^2 \\ 0 & b^2 & 0 \\ \eta^2 b^2 & 0 & r^2 b^2 \end{bmatrix},$$

$$[C] = - \begin{bmatrix} \xi_1^2 \partial_o^2 & 0 & \zeta^2 \partial_o^2 \\ 0 & \partial_o^2 & \partial_o \\ \zeta^2 b^2 \partial_o^2 & -\partial_o & b^2 \partial_o^2 - 1 \end{bmatrix} \tag{16}$$

$$(\cdot) = \frac{\partial}{\partial \tau}, \quad \partial_o = \frac{\partial}{\partial \xi}$$

are non-dimensional differential operators and the non-dimensional parameters are defined by

$$p_o^2 = \frac{\omega_o^2 I_1 L^4}{D_{11}} \qquad \xi_1^2 = \frac{A_{11} L^2}{D_{11}} \qquad b^2 = \frac{D_{11}}{A_{55} L^2}$$

$$r^2 = \frac{I_3}{I_1 L^2} \qquad \zeta^2 = \frac{B_{11} L}{D_{11}} \qquad \eta^2 = \frac{I_2}{I_1 L} \tag{17}$$

Defining the non-dimensional internal forces as:

$$(n_x, m_x, q_{xz}) = \left(N_x, \frac{M_x}{L}, Q_{xz} \right) \frac{L^2}{D_{11}} \tag{18}$$

yields the non-dimensional internal force vector $\{n\} = \{n_x, q_{xz}, m_x\}$ in a matrix form

$$\{n\} = [S]\{\bar{q}\} + \{F_o\} v(\tau) \tag{19}$$

where $[S]$ is a matrix differential operator defined as:

$$[S] = \begin{bmatrix} \xi_1^2 \partial_o & 0 & \zeta^2 \partial_o \\ 0 & \frac{1}{b^2} \partial_o & \frac{1}{b^2} \\ \zeta^2 \partial_o & 0 & \partial_o \end{bmatrix} \tag{20}$$

$$\{F_o\} = \{e_o, 0, f_o\}^{\Gamma}$$

$$(e_o, f_o) = \left(E_{11}, \frac{E_{11}}{L} \right) \frac{L^2 V_o}{D_{11}} \tag{21}$$

V_o is nominal voltage amplitude, $v(\tau) = V(t)/V_o$ is non-dimensional voltage–time function.

For a fixed non-movable end the boundary conditions[14] are $\{\bar{q}\} = 0$ and for a free end[13] they are $\{n\} = 0$. Therefore, for a cantilever beam the boundary conditions are given by:

$$\xi = 0 \qquad \{\bar{q}\} = 0$$
$$\xi = 1 \qquad \{n\} = 0 \tag{22}$$

which can be rewritten as

$$[R] \begin{Bmatrix} \{\bar{q}(0)\} \\ \{\bar{q}(1)\} \end{Bmatrix} = \{F\} \tag{23}$$

where $[R]$ is a 6×6 matrix

$$[R] = \begin{bmatrix} [E] & 0 \\ 0 & [S] \end{bmatrix} \tag{24}$$

$[E]$ is a unit 3×3 matrix and $\{F\}$ is the piezo-electric time-dependent vector

$$\{F\} = -\{\mathscr{F}_o\} v(\tau) \tag{25}$$

$$\{\mathscr{F}_o\} = \{0, 0, 0, e_o, 0, f_o\}^{\Gamma}$$

To obtain the solution of the beam vibrations problem having time-dependent boundary conditions, a special method of separation of variables[18,19] is adopted. We assume that the solution form is

$$\{\bar{q}\} = \{\tilde{q}\} + [\Gamma]\{F\} \tag{26}$$

where $[\Gamma]$ is a 3×6 matrix, to be determined later, and defined by

$$[\Gamma] = \{\{g_1(\xi)\}, \ldots, \{g_6(\xi)\}\} \tag{27}$$

Using the boundary conditions given by eqn (23) yields

$$[R] \begin{Bmatrix} \{\tilde{q}(0)\} \\ \{\tilde{q}(1)\} \end{Bmatrix} = \left([E]_{6 \times 6} - \begin{bmatrix} [E]_{3 \times 3} & [\Gamma(0)] \\ [S] & [\Gamma(1)] \end{bmatrix} \right) \{F\} \tag{28}$$

Assuming that the right-hand side of eqn (28) is zero, i.e.

$$\begin{bmatrix} [E]_{3\times3} & [\Gamma(0)] \\ [S] & [\Gamma(1)] \end{bmatrix} = [E]_{6\times6} \qquad (29)$$

The matrix system given by eqn (29) may be re-written as

$$\begin{Bmatrix} \{g_i(0)\} \\ [S]\{g_i(1)\} \end{Bmatrix} = \begin{Bmatrix} 0 \\ \vdots \\ \delta_{ii} \\ \vdots \\ 0 \end{Bmatrix}_{i=1,\dots,6} \quad, \ i=1,\dots,6 \qquad (30)$$

δ_{ii} is the Kronecker symbol. Solving an ordinary differential equation system like (30), yields the following form of the matrix $[\Gamma]$

$$[\Gamma] = \begin{bmatrix} 1 & 0 & 0 & \dfrac{1}{\zeta_1^2 - \zeta^4}\xi & 0 & -\dfrac{\zeta^2}{\zeta_1^2 - \zeta^4}\xi \\ 0 & 1 & -\xi & \dfrac{\zeta^2}{\zeta_1^2 - \zeta^4}\xi & b^2\xi & -\dfrac{\zeta_1^2}{\zeta_1^2 - \zeta^4}\xi \\ 0 & 0 & 1 & -\dfrac{\zeta^2}{\zeta_1^2 - \zeta^4}\xi & 0 & \dfrac{\zeta_1^2}{\zeta_1^2 - \zeta^4}\xi \end{bmatrix} \qquad (31)$$

Now the boundary conditions (28) for the general solution for $\{\bar q\}$ in eqn (14) are homogeneous and the equation for $\{\tilde q\}$ may be rewritten as

$$[M]\{\ddot{\tilde q}\} + [c]\{\dot{\tilde q}\} = -([M][\Gamma]\{\ddot F\} + [C][\Gamma]\{F\}) \quad (32)$$

Now the spatial and time variables can be separated using an eigenmode series. Let

$$\{\tilde q\} = \sum_{n=1}^{\infty} \{q_o^n\} T_n \qquad (33)$$

where $\{q_o^n (\xi)\}$ is the nth eigenform of the coupled vibration of the laminated composite beam with the respective eigenfrequency ω_n (or non-dimensional frequency p_n), and $T_n(\tau)$ is the time-dependent function.

Substitution of eqn (33) into eqn (32) and using Boubnov–Galerkin techniques (multiplication by the function $\{q_o^m\}^T$ and integration along the length of the beam) yields

$$\sum_n \left(\int_0^1 \{q_o^m\}^T [M]\{q_o^n\} \, d\xi \cdot \ddot T_n + \int_0^1 \{q_o^m\}^T [C] \right.$$

$$\left. \{q_o^n\} \, d\xi \times T_n \right) = -\left(\int_0^1 \{q_o^m\}^T [M][\Gamma] \, d\xi \cdot \{\ddot F\} \right.$$

$$\left. + \int_0^1 \{q_o^m\}^T [C][\Gamma] \, d\xi \cdot \{F\} \right) \qquad (34)$$

Taking into account the eigenmode behavior

$$[C]\{q_o^n\} = p_n^2 [M_o]\{q_o^n\}$$

and the orthogonality conditions

$$\int_0^1 \{q_o^m\}^T [M]\{q_o^n\} \, d\xi = p_o^2 \mu_n \delta_{mn}$$

$$\int_0^1 \{q_o^m\}^T [C]\{q_o^n\} \, d\xi = p_n^2 \mu_n \delta_{mn} \qquad (35)$$

where μ_n is the generalized mass of the nth eigenmode defined as

$$\mu_n = \int_0^1 \{q_o^n\}^T [M_o]\{q_o^n\} \, d\xi \qquad (36)$$

and δ_{mn} the Kronecker symbol, yields the equations for the time-dependent function, $T(\tau)$

$$\ddot T_n + \Omega_n^2 T_n = G_n \ddot v(\tau) + G_n^* v(\tau) \qquad (37)$$

where

$$\Omega_n^2 = \frac{p_n^2}{p_o^2} = \frac{\omega_n^2}{\omega_o^2}, \qquad G_n = \frac{1}{\mu_n}\{\hat G_n\}^T\{\mathcal{F}_o\}$$

$$G_n^* = \frac{1}{p_o^2 \mu_n}\{\hat G_n^*\}^T\{\mathcal{F}_o\}$$

$$\{\hat G_n\}^T = \int_0^1 \{q_o^m\}^T [M_o][\Gamma] \, d\xi$$

$$\{\hat G_n^*\}^T = \int_0^1 \{q_o^n\}^T [C][\Gamma] \, d\xi$$

Solution of eqns (37) with the initial conditions and eqns (26), (31) and (33) yields the full solution of the problem of vibrations of non-symmetrical cross-ply lamination composite beams with piezo-electric layers.

LAMINATED COMPOSITE BEAM WITH PIEZOELECTRIC LAYERS AS AN OPEN-LOOP CONTROL SYSTEM

Based on eqns (26), (31), (33), (37) and (38) we can get the structural scheme of the composite beam with piezoelectrical layers as an open-loop control system. The scheme is shown in Fig. 2. In Fig. 2, s is the Laplace variable and ε_n is the damping coefficient for the nth eigenmode of vibration, and usually $\varepsilon_n \ll \Omega_n$. Using the structural scheme, we can get the transfer function and, respectively, the amplitude-frequency and phase-frequency characteristics of the electro-elastic system for all the displacements of any point on the beam.

For a cantilever beam, the free end is more interesting. Using a normalized system of eigenmodes (with normalization condition $\bar{w}_n^{\prime\prime}(1) = 1$ for each n), yields the standard open-loop control system. Then, the classical methods of control theory may be used to lay out an active control loop.

NUMERICAL RESULTS

The study presents numerical results for cross-ply laminated composite beams having rectangular cross-section. The AS/3501-6 graphite–epoxy material properties used in the numerical results are:[13,14]

$$E_1 = 14 \cdot 5 \times 10^{10} \, \text{N/m}^2 \quad E_2 = 0 \cdot 96 \times 10^{10} \, \text{N/m}^2$$

$$\nu_{12} = 0 \cdot 3$$

$$G_{12} = G_{13} = 0 \cdot 41 \times 10^{10} \, \text{N/m}^2$$

$$G_{23} = 0 \cdot 34 \times 10^{10} \, \text{N/m}^2$$

The shear correction factor k is $5/6$ as commonly used in the literature.[17]

Two types of laminates were considered: a symmetrical one $[0°/0°]$ and a non-symmetrical one $[90°/0°]$. In the symmetrical case the longitudinal and transverse vibrations are not coupled. The relative thickness of the beam was $h/L = 1/10$. A comparison of the non-dimensional frequencies of the free vibrations for a cantilever beam with immovable ends is presented in Table 1. The first two mode shapes with a predominance of transverse vibrations (modes number 1 and 2) and the two first mode shapes with a predominance of longitudinal vibrations (modes 5 and 10, marked (*) in Table 1) are shown in Figs 3(a)–(d).

The influence of the non-dimensional radius of gyration r on the first three non-dimensional frequencies (p/p_0) of transverse vibrations for a symmetrical $[0°/0°]$ cross-ply beam is shown in Fig. 4(a). p_0 is the calculated frequency using the classical Bernoulli–Euler theory $(r = b = 0)$.

The graphs of the dependencies of non-dimensional frequencies (p/p_0) for a non-symmetrical $[90°/0°]$ laminated beam on the non-dimensional radius of gyration r are shown in Fig. 4(b). p_0 was calculated using the classical laminate (Bernoulli
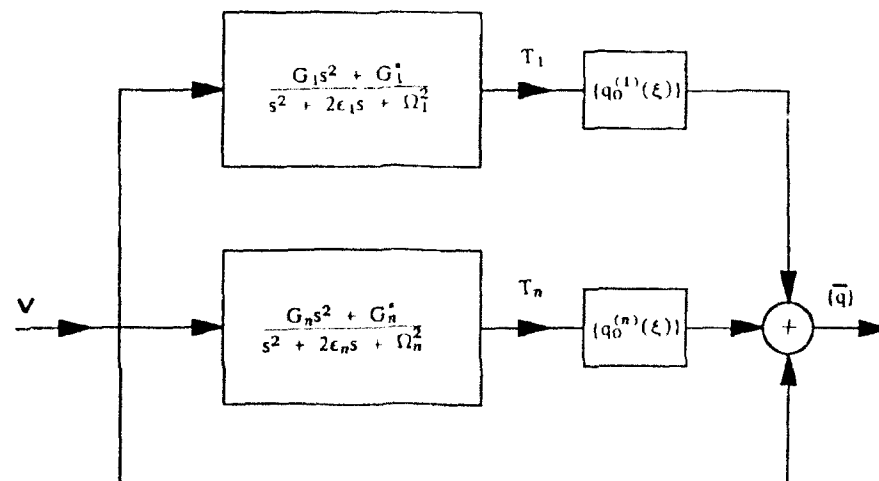
Fig. 2. Structural scheme of the open-loop control electroelastic system.

Table 1. Non-dimensional frequencies *p* for a cantilever beam (*L/h* = 10) for various types of laminates

Mode number *n*	Symmetrical case [0°/0°]	Non-symmetrical case [90°/0°]
1	3·2313	2·3201
2	14·650	12·696
3	31·648	30·484
4	48·799	50·326
5	54·414 [1]	54·479 *
6	65·999	72·724
7	82·801	94·812
8	99·479	116·47
9	115·894	137·75
10	132·250	144·28 *
11	148·320	161·68

[*n*]. *n*th mode of longitudinal vibrations.
*. mode with predominance of the longitudinal vibrations.

-Euler) theory, for a non-symmetric cross-ply laminated beam.[14]

The shear deformation and rotary inertia lower the frequencies with increase in *r* with a major influence on the high modes of vibration. This influence is greater in region $0 \le r \le 0.03$ for modes having a predominance of longitudinal vibrations (curve *n* = 5 in Fig. 4(b)).

The open-loop control system is influenced by the longitudinal/lateral stiffness ratio of the beam and the properties of the piezoelectric layers. A careful choice of this ratio and properties will enable the transfer of energy from the lateral vibrations to the longitudinal ones, yielding improved damping characteristics in the flexural direction. A parametric study to tune the coupled
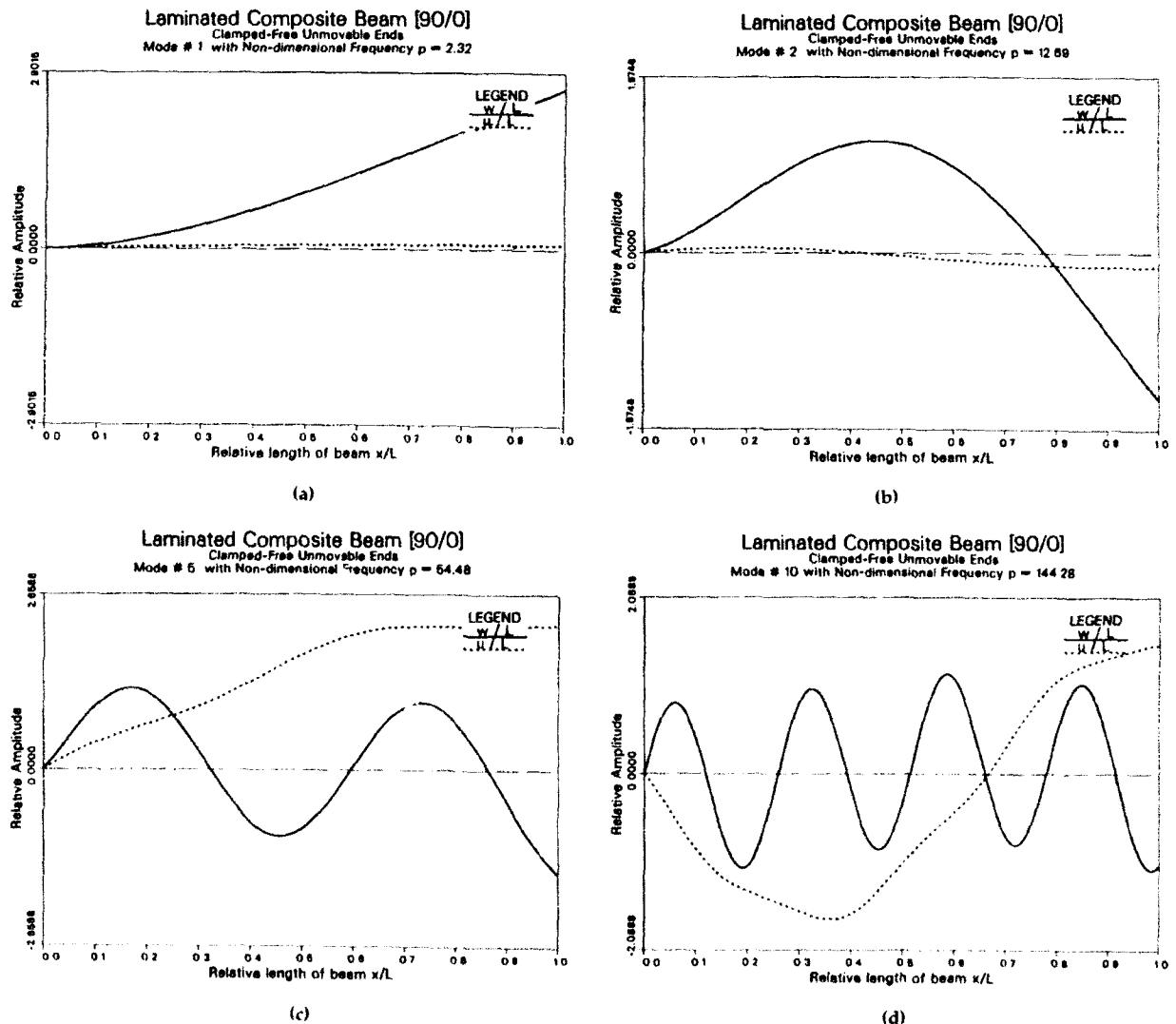
Fig. 3. Mode shapes of coupled transverse–longitudinal vibrations of a [90°/0°] cross-ply cantilever beam (*L/h* = 10): (a) 1st mode; (b) 2nd mode; (c) 5th mode; (d) 10th mode.
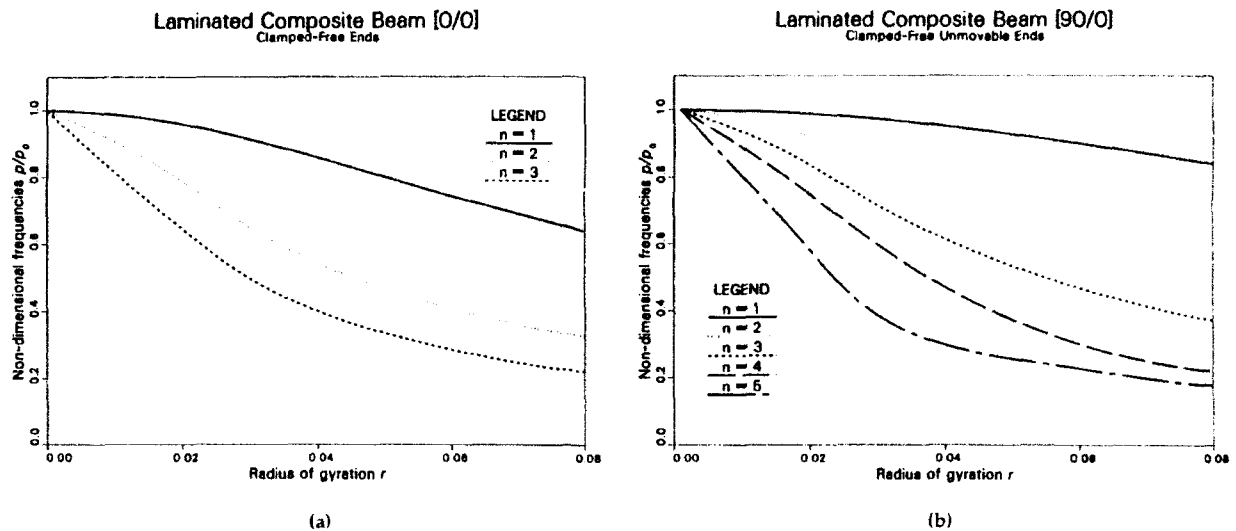
Fig. 4. Non-dimensional frequency (p/p_o) versus non-dimensional radius of gyration r for a composite cross-ply laminated cantilever beam: (a) symmetrical case $[0°/0°]$; (b) non-symmetrical case $[90°/0°]$.

properties of the laminated composite beam with the piezoelectric layers to obtain the minimum settling time of the flexural vibrations was initiated, with the results to be presented in the future.

CONCLUSIONS

The equations of motion of non-symmetric laminated composite beams having uniform piezoelectric layers have been formulated and solved, using a first-order shear deformation theory. The influence of longitudinal/flexural coupling was investigated for an open-loop control scheme.

Numerical results for various parameters of laminated beams are presented to stress the better applicability and suitability of the present approach to the analysis of dynamic behavior of laminated composite beams with piezoelectric layers.

REFERENCES

1. Crawley, E. F. & de Luis, J., Use of piezoelectric actuators as elements of intelligent structures. *AIAA J.*, 25 10 (1987) 1373–85.

2. Hagood, N. W., Chung, W. H. & von Flotow, A., Modelling of piezoelectric actuator dynamics for active structural control. *J. Intell. Mater. Syst. Struct.*, 1 (July 1990) 327–54.

3. Freyman, R. F. & Stumper, F., Active damping of a large lightweight structure using piezoelectric sensors and actuators. AIAA-91-1001-CP Paper, 1991, pp. 2852–64.

4. Hagood, N. W. & Crawley, E. F., Experimental investigation of passive enhancement of damping for space structures. *J. Guidance, Contr. Dynam.*, 14 6 (Nov–Dec. 1991) 1100–9.

5. Ehlers, S. M. & Weisshaar, T. A., Effect of adaptive properties on static aeroelastic control. AIAA-92-2526-CP Paper, 1992, pp. 914–24.

6. Anders, W. S., Rogers, C. A. & Fuller, C. R., Vibration and low frequency acoustic analysis of piecewise-activated adaptive composite panels. *J. Comp. Mater.*, 26 1 (1992) 103–20.

7. Wang, B. T. & Rogers, C. A., Laminate plate theory for spatially distributed induced strain actuators. *J. Comp. Mater.*, 25 4 (April 1991) 433–52.

8. Zhou, N., Sumali, H. & Cudney, H., Experimental development of piezofilm modal sensors and characterization of piezofilm strain rate gages. AIAA-91-1014-CP Paper, 1991, pp. 735–43.

9. Hagood, N. W. & von Flotow, A., Damping of structural vibrations with piezoelectric materials and passive electrical networks. *J. Sound Vib.*, 146 2 (1991) 243–68.

10. Chow, W. T. & Graves, M. J., Stress analysis of a rectangular implant in laminated composites using 2-D and 3-D finite elements. AIAA-92-2477-CP Paper, 1992, pp. 848–61.

11. Lin, M. W. & Rogers, C. A., Formulation of a beam structure with induced strain actuators based on an approximated linear shear stress field. AIAA-92-2524-CP Paper, 1992, pp. 896–904.

12. Bailey, T. & Hubbard, J. E., Jr. Distributed piezoelectric-polymer active vibration control of a cantilever beam. *J. Guidance*, 8 5 (Sept.–Oct. 1985) 605–11.

13. Abramovich, H., Shear deformation and rotary inertia effects of vibrating composite beams. *Comp. Struct.*, 20 165–73.

14. Abramovich, H. & Livshits, A., Free vibrations of non-symmetric cross-ply laminated composite beams. TAE Rep. No. 679, Faculty of Aerospace Engineering, Technion — IIT, Haifa 32000, Israel.

15. Pai, P. F., Nayfeh, A. H. & Oh, K., A nonlinear theory of laminated piezoelectric plates. AIAA-92-2407-CP Paper, 1992, pp. 577–85.

16. Stemple, A. D. & Lee, S. D., A finite element model for composite beams with arbitrary cross-sectional warping. AIAA-83-0773-CP Paper, 1987, pp. 304–13.

17. Rossi, R. E., Laura, P. A. A. & Maurizi, M. J., Numerical experiments on the effect of the value of the shear coefficient upon the natural frequencies of a Timoshenko beam. *J. Sound Vib.*, **154**(2)(1992) pp. 374–9.

18. Mindlin, R. D. & Goodman, L. E., Beam vibrations with time-dependent boundary conditions. *J. Appl. Mech., Trans. ASME*, **17**(1950) 377–80.

19. Hermann, G., Forced motions of Timoshenko beams. *J. Appl. Mech., Trans. ASME*, **77**(1955) 53–6.

Smart structures — vibration of composites with piezoelectric materials

S. M. Yang & J. W. Chiu

Institute of Aeronautics and Astronautics, National Cheng Kung University, Taiwan

A manufacturing technique is developed for embedding piezoelectric material in composite laminates while maintaining the structure strength and piezoelectric effectiveness. An ultrasonic C-scan test is applied to screen out the specimen with possible delamination along the interface of the piezoelectric material and glass fiber layer. It is shown that the problem of electrical insulation and piezoelectric material cracking can be prevented. In addition, tensile and static tests are conducted to validate the manufacturing technique. An analytical model is also presented to predict the natural frequencies and mode shapes of a composite structure with embedded piezoelectric materials. and the predictions are verified by modal testing.

1 INTRODUCTION

The stringent requirements of aerospace systems have created a need for smart structures, structures with built-in sensor/actuator and intelligence that can actively change its physical geometry and property. Application in aerospace systems includes: structure vibration suppression, structural shape control, attitude control, and acoustic noise suppression. In particular, a smart structure's adaptive nature to external stimuli makes it the best candidate in vibration and control applications. Recent research emphases have considered materials such as piezoelectric ceramics, piezoelectric polymers, electrorheological fluids, and shape memory alloys. This work focuses on one type of smart structures — vibration of aerospace composite structures with piezoceramic material.

With the pervasive application of composite structures in flight vehicles, the need to develop a technique to incorporate piezoelectric materials in composite laminates during the manufacturing process is necessary. Piezoelectric material can generate an electrical charge in response to mechanical strain, or conversely, can provide a mechanical strain as a result of the applied electrical field. The history and application of piezoelectricity can be found in Mason.[1] The major advantages of using piezoelectric material in smart structures include: (1) no magnetic field generated in the conversion of electrical energy into mechanical motion, (2) response time less than 1 ms, (3) high resolution in mechanical positioning, and (4) large force output, as much as 1000 N. For these reasons, applications of piezoelectric material to structure vibration and control have received considerable attention recently. Crawley and deLuis[2] and Crawley and Anderson[3] presented a mechanics model for the interaction of piezoelectricity with a one dimensional Euler–Bernoulli beam model. Two dimensional models of structures with piezoelectric material have also been developed by Lee[4] and Dimitriadis et al.[5] In addition, finite element models for piezoelectric material have been proposed by Nailon et al.[6] and Tzou and Tseng.[7] In spite of all the above work, however, examples and their applications have been limited to a one dimensional Euler–Bernoulli beam with piezoelectric materials. Lee and Yang[8] have recently shown both analytically and experimentally that the stiffness of a beam structure is influenced by the interaction between the piezoelectric actuation and structural vibration. But like many of the above, the work was conducted on isotropic structures with surface-bonded, piezoelectric materials. Analytical and experimental verification of composite smart structures are both necessary.

The use of smart structures in flight vehicle vibration control and flutter suppression is very promising for the low power consumption and high bandwidth of piezoelectric material. Recently, Ha et al.[9] have developed a finite ele-

ment formulation for composite laminates containing piezoelectric materials, but the experiment is conducted on a specimen with surface bonded piezoelectric material. Crawley and deLuis[2] have applied piezoelectric materials to three test specimens of cantilever beam: aluminum, glass/epoxy, and graphite/epoxy; their tensile tests show that the ultimate strength of the laminates is reduced by 20% when piezoelectric materials are embedded. However, the natural frequency, mode shape, and damping are not reported in their studies. In a similar work, Jenq et al.[10] have shown both computationally and experimentally that a one-end-cantilever, composite laminate can have a 10% natural frequency drop when a square cutout is present. Conversely, the embedding of piezoelectric materials in composite laminates can affect the natural frequencies and mode shapes as well. This paper presents an analytical model to predict the vibration characteristics of composite laminates with embedded piezoelectric materials, and manufacturing techniques are also developed for embedding piezoelectric materials inside glass fiber composite laminates. The smart structure specimens are tested to identify the effect of stiffness and inertia of the embedded piezoelectric materials on the natural frequencies and mode shapes.

2 ANALYTICAL MODEL

A prerequisite of effective structure vibration control is to understand the mechanics and dynamics of smart structures. An analytical model is developed to predict the vibration characteristics of composite laminates with embedded piezoelectric materials. The model incorporates the composite laminate model from Jenq et al.[10] and the piezoelectric model from Crawley and Anderson.[3] Consider a composite laminate consisting of N thin orthotropic layers of constant thickness, and each layer is oriented at an angle (θ_m) with respect to the plate coordinate axes where the xy plane coincides with the midplane of the plate. Based on the dynamic shear deformation theory of small strain and linear stress–strain assumptions, the displacement field can be expressed as

$$u_1(x, y, z, t) = u(x, y, t) + z\phi_x(x, y, t) \tag{1}$$

$$u_2(x, y, z, t) = v(x, y, t) + z\phi_y(x, y, t) \tag{2}$$

$$u_3(x, y, z, t) = w(x, y, t) \tag{3}$$

where t is time, u_1, u_2 and u_3 denote the displacements of a point in the x, y and z directions, respectively. u, v and w are the associated midplane displacements. ϕ_x and ϕ_y denote the rotations in the xz and yz planes due to bending. From Hamilton's principle, the equations of motion can be written as

$$\frac{\partial N_1}{\partial x} + \frac{\partial N_6}{\partial y} = I_1\ddot{u} + I_2\ddot{\phi}_x \tag{4}$$

$$\frac{\partial N_6}{\partial x} + \frac{\partial N_2}{\partial y} = I_1\ddot{v} + I_2\ddot{\phi}_y \tag{5}$$

$$\frac{\partial Q_1}{\partial x} + \frac{\partial Q_2}{\partial y} = q + I_1\ddot{w} \tag{6}$$

$$\frac{\partial M_1}{\partial x} + \frac{\partial M_6}{\partial y} - Q_1 = I_2\ddot{u} + I_3\ddot{\phi}_x \tag{7}$$

$$\frac{\partial M_6}{\partial x} + \frac{\partial M_2}{\partial y} - Q_2 = I_2\ddot{v} + I_3\ddot{\phi}_y \tag{8}$$

where I_1, I_2 and I_3 are the normal, couple normal-rotary, and rotary inertia coefficients, q represents the transverse distributed force. N_i, Q_i and M_i are stress and moment resultants given by the following equations

$$(N_i, M_i) = \int_{-h/2}^{h/2} (1, z)\,\sigma_i\,dz \tag{9}$$

$$(Q_1, Q_2) = \int_{-h/2}^{h/2} (\sigma_5, \sigma_4)\,dz \tag{10}$$

Note that $i = 1, 2, \ldots, 6$ and the stress component is denoted by σ_i, i.e. $\sigma_1 = \sigma_x$, $\sigma_2 = \sigma_y$, $\sigma_3 = \sigma_z$, $\sigma_5 = \sigma_{xz}$ and $\sigma_6 = \sigma_{xy}$.

With a four-node finite element formulation, the governing equation for each element can be written in matrix form as

$$M\ddot{x}^e + K^e x^e = f^e$$

where M^e and K^e are the element mass and stiffness matrix, respectively. f^e and x^e are the force and displacement vectors; $x^e = [u^e, v^e, w^e, \phi_x^e, \phi_y^e]^T$. The global governing equation can be obtained after assembling the equation of motion for each element,

$$(M_s + M_p)\ddot{x} + (K_s + K_p)x = f \tag{11}$$

where M and K are the system inertia and stiffness matrices; the subscripts s and p denote composite structure and piezoelectric material respec-

tively: and the components of $\mathbf{M}_v$ can be found in Jenq *et al.*[10] and Reddy.[11] The natural frequency and mode shape of a composite structure with embedded piezoelectric materials can then be determined by eqn (11) with the prescribed boundary conditions.

3 MANUFACTURING TECHNIQUE

Smart structure manufacturing techniques are developed for embedding piezoelectric materials inside glass fiber composite laminates. The composite laminates are made of S-glass/epoxy uni-directional pre-prag tape (Fiberite Hy-E 9134 B) with embedded piezoelectric material of high Curie temperature (APC840). Selection of the piezoelectric materials is to match both the elastic modulus and curing temperature of the composites because the curing process is limited by the Curie temperature of the piezoelectric materials. The mechanical properties of uni-directional laminates and the electro-mechanical properties of the piezoelectric material are listed in Tables 1 and 2, respectively. A cantilever plate of smart structure 30 cm × 14 cm × 0·12 cm is considered in this study. The laminate stacking sequence is [90/0], with six piezoelectric plates of 25·4 mm × 25·4 mm × 0·375 mm each, three on each side of the neutral axis. The pre-prag tapes are processed to have squares cut out for accommodating the piezoelectric plate, and the cross-section of the smart structure is shown in Fig. 1 in

which the third to fifth and eighth to tenth layers contain the piezoelectric plate. Note that the thickness of the piezoelectric plate is about three laminate layers.

The electrical lead is attached to the center of the top and bottom surfaces of the piezoelectric plate; no conductive epoxy is required for attaching the lead. A total of six electrical leads (M-line accessories 326 — DFV) is led through the adjacent layers to the edge of the cantilever end. In order to prevent the electrical leads from becoming brittle during the curing process, each lead goes through a needle (24G-1, 25 × 0·55 ϕ mm) located at the edge of the laminate plate. The smart structure is then hot pressed, vacuum bagged, and cured at about 180°C using the curing procedure shown in Fig. 2. After the curing process, the smart structure is inspected through the ultrasonic C-scan facility to screen out structurally defective specimens. Figure 3 shows a C-scan plot of a smart structure specimen in which the grey area around the piezoelectric plate indicates possible delamination.

4 STATIC AND VIBRATION TEST

The smart structure specimen is tested for its piezoelectric effectiveness by attaching a strain gauge to the top surface of the specimen adjacent to the piezoelectric materials. The embedded piezoelectric materials with DC voltage from a

Table 1. Mechanical properties of uni-directional laminates (S-glass/epoxy)

E_L	55·55 GPa
E_T	25·9 GPa
G_{LT}	7·7 GPa
G_{TT}	7·7 GPa
ν	0·26
ρ	1881 kg/m³

Table 2. Electro-mechanical property of piezoelectric material

Density g/cm³	7·6
Young's modulus (N/mm² × 10¹⁰)	6·8
Curie temperature (°C)	340
Mechanical Q	400
k_{33} %	0·35
d_{31} × 10⁻¹² m/V	-125
d_{33} × 10⁻¹² m/V	300
g_{31} × 10⁻³ V m/N	-10·5
g_{33} × 10⁻³ V m/N	26
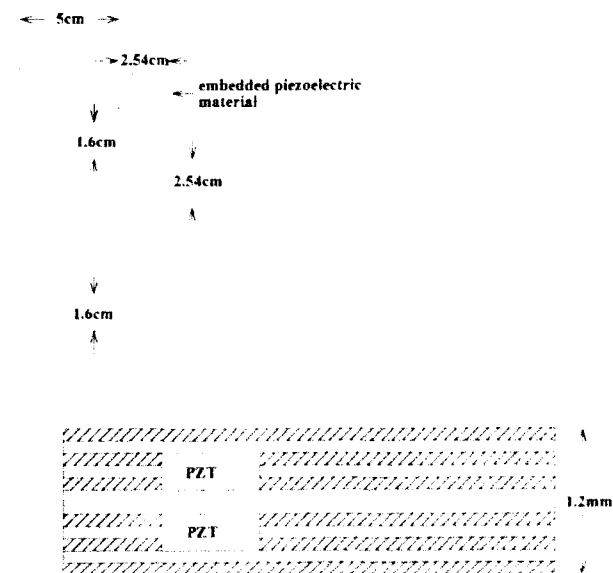
Fig. 1. Geometry and cross-section of the smart structure specimen of 30 cm × 14 cm × 0·12 cm.

power supply (HP6035A) serve as actuator, while the strain gauge measures the displacement. Figure 4 shows the piezoelectric effectiveness of the smart structure in which the mechanical strain increases to 80 μ in a rather linear relation when the DC voltage increases from 0 to 500 V. The smart structure specimen is further tested in a material test facility for its stress–strain curve and ultimate strength. These data are compared with those of a composite structure of the same layout but without piezoelectric materials. Figure 5 shows the stress–strain curve obtained from the composite laminate with and without embedded piezoelectric materials. The elastic modulus of a specimen without piezoelectric materials is about 52·5 GPa while that with is about 26·25 GPa. Their difference is contributed to the fact that the cross-section of the latter, in terms of fiber content is smaller than that of the former.
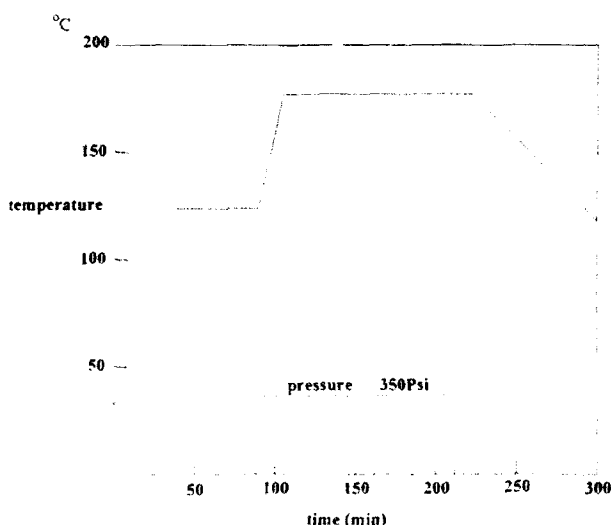
Effective vibration control application of a smart structure is impossible without knowing first its modal parameters. The modal parameters of a smart structure without external applied voltage are measured by using modal testing techniques for its natural frequency, damping, and mode shape. The objective is to identify the influence of embedded piezoelectric materials, such as material property, location, and size, on the vibration of a composite structure. Several transfer functions are measured on the same smart structure specimen for verification. A set of modal hammers and accelerometer is used to measure the input/output transfer function. In addition, the embedded piezoelectric materials are applied as sensor and actuator, and the accelerometer (B & K model 4373) is attached at the tip edge but off-center in order to measure the torsional mode as well. The transfer function can then be obtained by applying an AC voltage with sweeping frequency to the piezoelectric materials. Figure 6 shows the schematic diagram for smart structure modal testing.

The first three natural frequencies predicted from the analytical model are 12·90 Hz, 50·1 Hz and 80·1 Hz, respectively. The comparison of each modal testing and analytical prediction from the finite element method of eqn (11) is tabulated in Table 3. It is shown that the analytical prediction agrees quite well with all of the test results. Figure 7 shows the frequency response function obtained by using one embedded piezoelectric plate as actuator while three on the same side above the neutral axis act as sensors. The embedded piezoelectric materials can be successfully applied for in-situ actuator input and sensor measurement. The actuator capabilities are shown in Fig. 8 where the smart structure is excited at 80 VAC near the first natural frequency and the tip

Fig. 2. Curing process of the glass/epoxy in hot press.
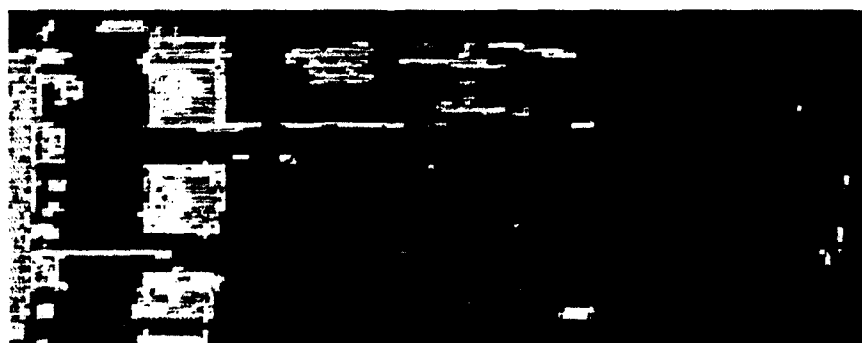
Fig. 3. C-scan plot of a smart structure specimen.
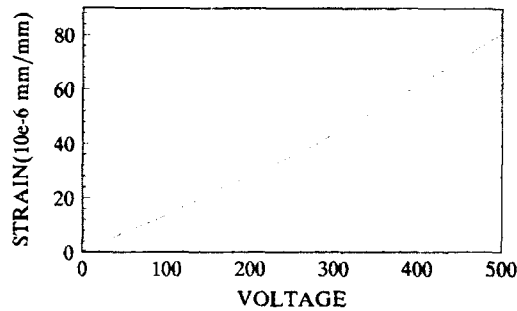
Fig. 4. Static test result of strain and applied voltage.
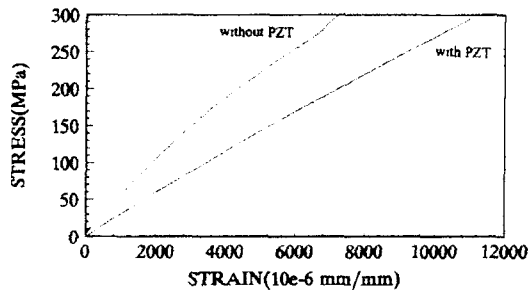
Fig. 5. Stress–strain curve of the composite laminate with and without embedded piezoelectric material.
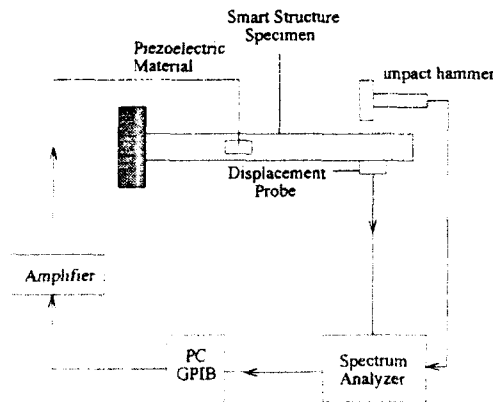
Fig. 6. Schematic of smart structure modal testing.

displacement is measured by a displacement sensor. It is shown that the manufacturing technique can prevent the problem of electrical insulation of the sensor/actuator, the cracking of piezoelectric material, and delamination of the laminates.

5 CONCLUSIONS

(1) An analytical model is developed to predict the vibration characteristics of smart structures, composite laminates with embedded piezoelectric materials. The modal parameters, including natural frequency and mode shape, are calculated to predict the influence of the embedded piezoelectric materials on the vibration of a composite structure.

(2) A manufacturing technique for embedding piezoelectric materials inside glass fiber composite laminates is also developed. The insulation techniques at the poles and leads of the piezoelectric materials should be considered to avoid electrical short. The smart structure specimens are tested for their static piezo-effectiveness, and they are also tested in a material test facility for stress–strain curve and ultimate strength. The ultrasonic C-scan is employed to screen out specimens with unsatisfactory delamination.

(3) The modal parameters of a smart structure without external applied voltage are measured by using modal testing techniques for natural frequency, damping, and mode shape. Experimental results indicate that the smart structure with external applied voltage can be effectively applied for vibration control.

(4) The embedded piezoelectric material is intended to serve as a strain sensor during the curing process; however, the experimental results show that the piezoelectric sensor is ineffective for measuring the DC signal. The need for an on-line

Table 3. Natural frequency of the smart structure specimen

	Type		ω_1	ω_2	ω_3
Analysis	Without PZT		12·76	49·9	79·5
	With PZT		12·9	50·1	80·1
Experiment	Input	Output			
	Impulse	Accelerometer	14 (8·5%)	46 (8·1%)	82 (2·4%)
	Impulse	PZT	14 (8·5%)	46 (8·1%)	82 (2·4%)
	PZT	Accelerometer	14 (8·5%)	47 (6·1%)	83·5 (4·2%)
	PZT	PZT	14 (8·5%)	46 (8·1%)	87 (8·7%)
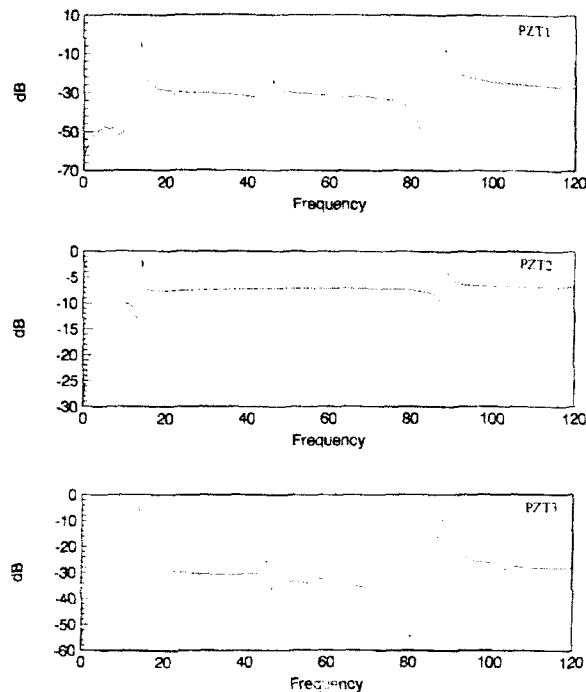
Fig. 7.   Frequency response function of the modal testing.
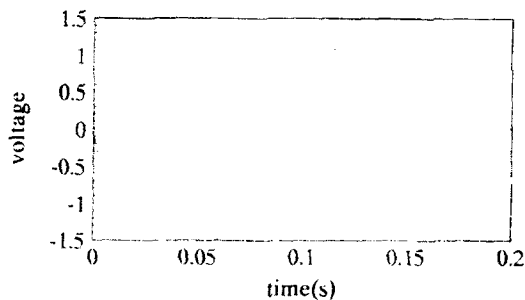
Fig. 8.   Tip response excited by the embedded piezoelectric actuator.

sensing technique by embedded piezoelectric sensor is yet to be developed. A piezoelectric sensor is physically equivalent to a capacitor; it is anticipated that further research is needed to

develop a charge amplifier circuit so as to measure the DC signal.

ACKNOWLEDGEMENT

REFERENCES

1. Mason, W. P., Piezoelectricity, its history and application. *J. Acoust. Soc. Amer.*, **70** (Dec. 1981) 1561–6.
2. Crawley, E. F. & deLuis, J., Use of piezoelectric actuators as elements of intelligent structures. *AIAA J.*, **25** (10) (1987) 1373–85
3. Crawley, E. F. & Anderson, E. H., Detailed models of piezoceramic actuation of beams. *J. Intell. Mater. Syst. Struct.*, **1** (1990) 4–25.
4. Lee, C. K., Theory of laminated piezoelectric plates for the design of distributed sensors/actuators. Part 1: Governing equations and reciprocal relationships. *J. Acoust. Soc. Amer.*, **87** (3) (1990) 1144–59.
5. Dimitriadis, E. K., Fuller, C. R. & Rogers, C. A., Piezoelectric actuators for distributed vibration excitation of thin plates. *J. Vib. Acoust.*, **113** (1991) 100–7.
6. Nailon, M., Coursant, R. H. & Besnier, F., Analysis of piezoelectric structures by a finite element method. *Acta Electron.*, **25** (4) (1983) 341–62.
7. Tzou, H. S. & Tseng, C. I., Distributed piezoelectric sensor/actuator design for dynamic measurement/control of distributed parameter systems: a piezoelectric finite element approach. *J. Sound Vib.*, **138** (1) (1990) 17–34.
8. Lee, Y. J. & Yang, S. M., Interaction of piezoelectric actuator and structural vibration. *J. Sound Vib.*, 1992 (submitted).
9. Ha, S. K., Keilers, C. & Chang, F. K., Analysis of laminated composites containing distributed piezoelectric ceramics. *J. Intell. Mater. Syst. Struct.*, **2** (1991) 59–70.
10. Jenq, S. T., Hwang, G. C. & Yang, S. M., On the natural frequency and mode shape of square cut-out composite laminates using holographic interferometry. *J. Comp. Sci. Technol.* (in press).
11. Reddy, J. N., *An Introduction to the Finite Element Method.* McGraw-Hill, New York, 1984.

Short- and long-term structural properties of pultruded beam assemblies fabricated using adhesive bonding

J. T. Mottram

Department of Engineering, University of Warwick, Gibbet Hill Road, Coventry, UK, CV4 7AL

Two beam assemblies fabricated using simple pultruded sections and adhesive bonding have been tested to determine their structural properties. The test configuration was three-point bending to simulate the most severe loading in a proposed application. Short-term stiffnesses are compared with those predicted using known section properties and linear elastic beam theory. Accelerated creep test data are used to determine long-term behaviour using Findley's linear viscoelastic theory. For the purpose of structural design, Findley's model is used to estimate the increase in maximum deflection due to a constant design loading of 1 week, 1 year and 10 years.

1 INTRODUCTION

The applications of pultruded sections in structural engineering are becoming more frequent.[1-3] Standard (e.g. 'I' hollow box and flat sheet) and non-standard prismatic sections are manufactured economically by pultrusion.[4,5] The pultrusion process is simple in principle; continuous fibre reinforcement in the form of alternate laters of randomly oriented mat and of uni-directional roving bundles are pulled through a thermosetting matrix impregnator and then on through a heated die. The die consolidates and forms the cured shape. The fibres for structural sections are usually of E-glass. The binding matrix is a mixture of thermosetting polyester resin and filler. The physical arrangement of the fibre reinforcement in the process gives the material anisotropic properties, with the highest properties in the direction of pull. Meyer[6] gives further details on the process. Motivating factors for using pultrudates are:[2,3] corrosion resistance; electromagnetic transparency; easier to assemble and maintain; saving in weight.

The majority of the applications[2,4] use pultruded sections as direct replacements for traditional structural steel sections. The differences in material properties ensure that identically shaped members of steel and pultruded material will behave differently. There is evidence from laboratory testing by the author[7-9] and others[10,11] that

optimum design is unlikely whilst pultruded sections are used as steel equivalents. The reason for this is that the dominant mode of failure with pultrudates is elastic buckling (local or global) and not material strength. They have, compared to steel sections, much higher strength-to-stiffness ratios. It therefore follows that open-sectioned members may need to be replaced by closed-sections ones which are less susceptible to buckling. The problem then faced by the engineer is to provide appropriate connections.

To overcome the problem, Maunsells Structural Plastic Group developed, over the last decade, an Advanced Composite Construction System (ACCS).[3,12-14] The ACCS has non-standard pultruded sections specific to its needs. Cross-sections for three components are shown in Fig. 1. The plank consists of a cellular system which uses effectively both the properties of the material and the pultrusion process. The plank and connectors are joined using mechanical interlocking and, if required, adhesive bonding.[3] The ACCS has been used to construct a bridge enclosure,[12] a 63 m footbridge[3] and a car wash porch.[14]

A second approach to providing structural members that are less susceptible to buckling is the subject of this paper. Instead of pultruding a complex non-standard closed-section requiring a large investment,[3,11-14] simple standard sections[4,5] may be joined along mating surfaces by adhesive bonding. Figure 2 illustrates a number of potential

$$Q_x = k \int_A \tau_x \, dA \qquad (5)$$

where $k = 5/6$ is a shear correction factor.[17] From relations (2)–(5) we can obtain the beam constitu-

Introducing the non-dimensional span of the beam, ξ, and the non-dimensional time, τ, defined

388   J. T. Mottram

Fig. 1.   Components of the Maunsell Advanced Composite Construction System.[12,13]

Fig. 2.   Potential bonded assemblies using simple prismatic sections.

assemblies using flat sheet, 'I' and channel sections. Such bonded assemblies with appropriate end connections could be used as beams, columns, panels, etc. The assemblies could be fabricated in workshops and transported to site for final erection. The potential applications for bonded assemblies is likely to be greater than the ACCS, as they may have optimum design for the specific loading to be transmitted.

Figure 3 shows the configuration of the closed-section bonded assembly which has been studied at Warwick University. It consists of two I-sections sandwiched between outer flat sheet plates. All mating surfaces are bonded. The adhesive used belongs to the family of toughened epoxies, as these adhesives have excellent structural properties. The assembly represents a beam section which may be repeated to construct a panel. Such panels may be used as a lightweight floor system in steel framed buildings. The floor system has always been one of the heaviest components of a building. Proposals for light weight systems using pultruded sections and concrete have been made by Hillman and Murray.[15] No test data on their systems have been published.

If bonded assemblies are to have structural applications, tests must be conducted to determine their structural performance. Presented in the paper are results of both short- and long-term tests. All three-point bend tests were conducted using the rig described in Ref. 9 and a DARTEC 9500 testing machine. The purpose of the tests was threefold:

i   To determine the reduction in short-term stiffness due to joining sections with adhesive bonding.

ii To monitor the creep behaviour of the assemblies and apply Findley's theory[10,16] to predict long-term deflections.

iii To monitor the integrity of the adhesive joints.

The low stiffness of the composite material makes deflection of beams the limiting state when determining safe working loads. The creep behaviour of beams subjected to working loads is known to
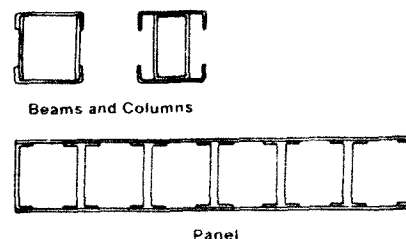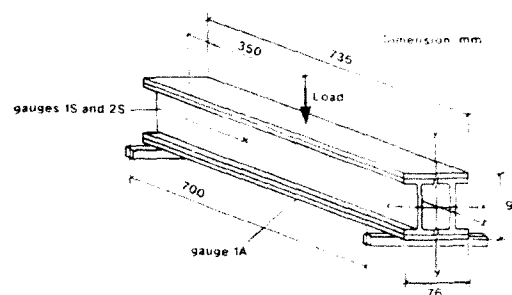
Fig. 3.   Three-point bend test and bonded assembly configuration.

give increased deflection.[10] It is, therefore important that we know how to account for the creep deflection by having a relevant and reliable creep model and its defining parameters. Presented in Sections 2–4 are details of the two specimens, test methods, data reduction methods and results.

2 SPECIMEN DETAILS

The two sections in the assembly see Fig. 3 were from the MMFG EXTREN 500/525 series.[4] The series consists of over 100 standard profiles. The resin is an isophthalic polyester; it is mixed with 10–15 parts per weight of filler (e.g. calcium carbonate), to form the matrix. The E-glass fibre reinforcement is continuous filament mat to impart transverse properties, and uni-directional roving bundles to give the essential longitudinal properties. Exact details of the reinforcement are not available as the manufacturer considers this information proprietary.

Each assembly had dimensions $735 \times 76 \times 90$ mm. They consisted of two side-by-side $3 \times 1.5 \times \frac{1}{4}$ in (76 × 38 × 6.25 mm) I-sections sandwiched between outer plates of $\frac{1}{4}$ in flat sheet. Tables 1

and 2 present the section mechanical properties.[4] Differences in the fibre reinforcement mean the two sections have different properties.

One Bonded Beam Assembly, BBAL, had the longitudinal direction (Table 2) of the flat sheets aligned with the I-sections. The second Bonded Beam Asembly, BBAT, had the transverse direction aligned with the I-sections.

The supplied sections had a surface coating of releasing agent, which along with the polyester surface veil directly below it must be removed by abrasion (e.g. shot blasting) before an adequate adhesive bond is achieved. This was confirmed by lap shear tests. These tests also showed that, once the releasing agent had been removed, failure was due to the adherend and not the 0·5 mm thick adhesive bond. All mating surfaces of the sections (see Fig. 3) were bonded using Permabond E32. This is a toughened cold cure two-part adhesive. It was chosen because it was easy to mix and spread, it had good flow control and thixotropy, and it had good gap filling capability. All these features made the E32 epoxy adhesive ideal for the bonded assemblies. To control the minimum bond thickness, lengths of 0·5 mm diameter copper wire were placed between the bonded surfaces.

Table 1. Minimum ultimate coupon properties of MMFG series 500/525 structural shapes

Property	ASTM test	Units	Longi-tudinal	Trans-verse
Tensile strength	D638	N mm^{-2}	210	50
Tensile modulus	D638	kN mm^{-2}	17	5·5
Compressive strength	D695	N mm^{-2}	210	103
Compressive modulus	D695	kN mm^{-2}	17	7
Shear strength	D2344	N mm^{-2}	31	31
Flexural strength	D790	N mm^{-2}	210	70
Flexural modulus	D790	kN mm^{-2}	14	5·5
Poisson's ratio	D3039		0·33	

Table 2. Minimum ultimate coupon properties of MMFG series 500/525 flat sheet

Property	ASTM test	Units	Longi-tudinal	Trans-verse
Tensile strength	D638	N mm^{-2}	138	70
Tensile modulus	D638	kN mm^{-2}	12·4	6·2
Compressive strength	D695	N mm^{-2}	165	114
Compressive modulus	D695	kN mm^{-2}	12·4	7
Shear strength	D2344	N mm^{-2}	41	41
Flexural strength	D790	N mm^{-2}	241	103
Flexural modulus	D790	kN mm^{-2}	13·8	7·6
Poisson's ratio	D3039		0·31	0·29

Strain gauges were attached to the surface of the specimens for creep data. The gauges were 3 mm FLA-3-11 (Tokyo Sokki Kenkyujo) having a yield strain > 2%. The adhesive was C-N adhesive. Figure 3 shows the positions of the gauges. The cross-ply gauges 1S and 2S were placed 160 mm from mid-span and at mid-depth of the web. They were oriented at ±45° to the z-axis (see Fig. 3). The axial strain gauge 1A was placed, at mid-breadth, on the underside of the tensile flange, directly below the loading nose. It was oriented in the z-direction.

3 THEORY AND TEST METHODS

3.1 Short-term tests

The purpose of these tests was to determine the stiffness of the assemblies and to find out if linear elastic beam theory, with section properties, can be used to predict short-term deflections. Figure 3 defines the cartesian axis system used to define beam properties. For a pultruded beam the ratio of the section longitudinal flexural modulus, $E_{z,u}(t)$, to the section shear modulus, $G_{xz}(t)$, is several times higher than it would be for the equivalent steel beam. As a result of this, the shear deformation contribution to the deflection should be included in the analysis. The term 'section' is used to distinguish a modulus specific to a beam from the 'material' or 'coupon' modulus determined using a standard test method. The two moduli are not necessarily equal,[a] and here, because we shall be considering creep, they are viscoelastic, and therefore, functions of time. Linear elastic beam theory for three-point bending gives the time-dependent central displacement $w(t)$ as

$$w(t) = w_b(t) + w_s(t)$$

$$= \frac{Pl^3}{48 E_{z,u}(t) I_u} + \frac{Pl}{4 K_s G_{xz}(t) A} \qquad (1)$$

where $w_b(t)$ is due to pure bending, and $w_s(t)$ is due to shear deformation. P is applied load. I_u is the second moment of area associated with moduli $E_{z,u}(0)$ (i.e. $t = 0$ h), A is the cross-section area, and l the beam span. The shear coefficient K_s attempts to overcome the inability of Timoshenko beam theory to account for the exact shear stress distribution over the cross-section. Several expressions evaluating K_s for multicelled thin-walled composite beams have been developed by

Bank.[17] However, none of the expressions can be used here because the beams consist of sections having different properties. It was therefore convenient to set $K_s = 1.0$, and use instead of A, the area of the two webs, A_w (i.e. $A_w = K_s A$ in eqn (1)).

For the short-term tests, where the time is taken as 0 h, eqn (1) may be expressed as

$$\frac{w}{Pl} = \frac{1}{48 E_{z,xx}(0) I_{xx}} l^2 + \frac{1}{4 G_{yz}(0) A_w} \qquad (2)$$

where $E_{z,xx}(0)$ and $G_{yz}(0)$ are initial section moduli.

The proven graphical procedure used to determine moduli ($E_{z,xx}(0)$ and $G_{yz}(0)$) with eqn (2) is detailed by Mottram.[9] Central load/central deflection, (P/w), gradients for the I-section and specimens BBAL and BBAT were measured at spans from 500 to 700 mm. The increment between each span was 50 mm. These data were used to construct a plot[9] of w/Pl against l^2. Equation (2) was used to obtain a linear regression fit to the plot whose gradient was $1/48 E_{z,xx}(0) I_{xx}$, and intercept was $1/4 G_{yz}(0) A_w$. Section moduli were then determined by inserting values for the geometric properties I_{xx} and A_w.

3.2 Long-term tests

The purpose of these tests was to determine the creep behaviour of the assemblies under normal laboratory conditions (22 ± 2°C and relative humidity 50 ± 5%). Such conditions of temperature and humidity may be expected for interior applications of bonded assemblies. For exterior applications, it is likely that environmental conditions will be more severe.

With a span of 700 mm, the specimen was loaded to 22·8 kN (i.e. 300 N per mm width) at a constant rate of 0·2 kN s^{-1}. This load corresponded to a factored design loading for a proposed application, that required a lightweight floor system with a span of 700 mm and a maximum slab depth of 100 mm. The dead load of the specimen was 0·034 kN and its effect on creep was negligible.

The end supports and loading nose of the bending rig had flat bearing surfaces[9] to minimise local stresses which cannot be alleviated by material yielding. The DARTEC machine was operated under load control, so that as the central deflection increased due to the creep, the load was kept constant. Figure 3 shows the positions of the

transducers. Central deflection was recorded by the stroke transducer in the DARTEC. Strain readings were monitored in real time using an Orion 3531D data logger. The repeatability of the instrument was ± 7 $\mu\varepsilon$. The surface strains were the maximum tensile, ε (gauge 1A) and the maximum shear strain, γ (average of sum of gauges 1S and 2S). The strains were recorded every 1 min for the first hour, 3 min for the next 9 h, and then every 15 min until the test was terminated. The test duration was 24 h.

The creep behaviour was described using Findley's linear viscoelastic power-law model.[14,16] The choice of the Findley theory follows recommendation by the American Society of Civil Engineers[18] who want to see their design procedure adopted. Findley's model has been used by Bank and Mosallam[10] to analyse long-term data from a beam in a full-sized pultruded U-frame. Other creep models are available. Holmes and Rahman[19] used three models, including Findley's, to study the creep of glass reinforced plastic box beams. They could not recommend one model to the exclusion of all others.

Using Findley's theory a time-dependent viscoelastic modulus may be obtained. This can be used to determine the overall deformation behaviour. Equation (1) shows that the deflection has the time-dependent terms due to pure bending $w_b(t)$, through modulus $E_{z,xx}(t)$, and due to shear deformation $w_s(t)$, through modulus $G_{yz}(t)$. We therefore need to develop the model to determine these time-dependent moduli.

The general form of Findley's creep power-law model is

$$\varepsilon = \varepsilon_0 + m(t/t_0)^n \qquad (3)$$

where ε is the time-dependent creep strain, ε_0 and m are functions of stress, n is independent of stress, t is time and t_0 is a constant taken as unity (i.e. 1 h in practice). Following the procedure given by Bank and Mosallam,[10] eqn (3) is used to develop expressions for the viscoelastic section moduli in eqn (1).

For example, the time-dependent flexural modulus $E_{z,xx}(t)$ is given by

$$E_{z,xx}(t) = \frac{E_{z,xx}(0) E_t}{E_t + E_{z,xx}(0)(t/t_0)^{n_t}} \qquad (4)$$

where $E_{z,xx}(0) = \sigma_0/\varepsilon_0$ is the short-term elastic modulus independent of time and $E_t = \sigma/m_t$ is a modulus which characterises the time-dependent behaviour.

Similarly, the time-dependent shear modulus $G_{yz}(t)$ is given by

$$G_{yz}(t) = \frac{G_{yz}(0)\,G_t}{G_t + G_{yz}(0)(t/t_0)^{n_g}} \quad (5)$$

where $G_{yz}(0) = \tau_0/\gamma_0$ is the short-term elastic modulus independent of time and $G_t = \tau/m_g$ is a modulus which characterises the time-dependent behaviour.

To determine the creep parameters m and n we use eqn (3). Its form for the axial (i.e. surface strain due to bending) creep modelling is

$$\varepsilon = \varepsilon_0 + m_e(t/t_0)^{n_e} \quad (6)$$

where subscript e derives from the Es in eqn (4) which define a flexural modulus. Equation (6) may be written as:

$$\log(\varepsilon - \varepsilon_0) = \log m_e + n_e \log(t/t_0) \quad (7)$$

Equation (7) gives a straight line when plotted on a log/log scale. When $t = 1$ h the ordinate is m_e, the gradient is n_e. The same procedure can be used to determine parameters m_g and n_g in eqn (5) from

$$\log(\gamma - \gamma_0) = \log m_g + n_g \log(t/t_0) \quad (8)$$

4 RESULTS AND DISCUSSION

4.1 Short-term tests

Separate tests gave the tensile modulus of the $\frac{1}{4}$ in flat sheet as: longitudinal (in pull-direction) 14·6 kN mm^{-2}; transverse 10·5 kN mm^{-2}. These compare with MMFG values in Table 2 of 12·4 and 6·2 kN mm^{-2}, respectively. The flexural moduli (Table 2), which are different, are not associated with the deformation of the flat sheets in the beams.

Using the procedure given in Section 3.1, two $3 \times 1·5 \times \frac{1}{4}$ in I-sections had mean initial section proerties of $E_{x,u}(0) = 31·15$ kN mm^{-2} and $G_{yz}(0) = 2·17$ kN mm^{-2}. In Table 1, the flexural modulus is 14 kN mm^{-2}. Its value is $< E_{x,u}(0)$ because it accounts for shear deformation and creep.[4]

The second moments of area for specimens BBAL and BBAT were calculated using the method of transformed sections.[20] This method was required because the flat sheet and I-section had different moduli. In the calculation, the effect

of the adhesive layer was ignored by assuming it was rigid and had no thickness. Specimen BBAL, with the flat sheet's longitudinal direction aligned with the I-sections had a $I_{xx} = 2·25 \times 10^6$ mm^4. Specimen BBAT, with the flat sheet's transverse direction aligned with the I-sections, had a $I_{xx} = 2·03 \times 10^6$ mm^4. These I_{xx}s were based on a flexural modulus $E_{x,u}(0) = 31·15$ kN mm^{-2}. For the purpose of obtaining the highest beam flexural rigidity $(E_{x,u}(t)I_{xx})$ it would have been better if the flat sheet had had the higher E modulus.

The procedure given in Section 3.1 was used with the specimens to determine their initial section moduli. In eqn (2) the I_{xx}s were those above and A_u was 810 mm^2. $E_{x,u}(0) = 29·2$ kN mm^{-2} and $G_{yz}(0) = 3·17$ kN mm^{-2} for BBAL. $E_{x,u}(0) = 28·7$ kN mm^{-2} and $G_{yz}(0) = 3·14$ kN mm^{-2} for BBAT. The section modulus G_{yz} was similar to the 'material' modulus using the Iosipescu shear test method.

The difference in $E_{x,u}(0)$ (29·2 and 28·7 kN mm^{-2}) between the assemblies and its assumed value for calculating I_{xx}s (31·15 kN mm^{-2}) provided a measure of the reduction in overall beam stiffness due to the adhesive bonding. Here, the reduction in stiffness was 7%. It follows that, for the purpose of structural design, a reduction of 10% in the flexural rigidity $E_{x,u}(0)I_{xx}$ should be adequate to account for the flexibility of the adhesive bonding.

4.2 Long-term tests

Each specimen was subjected to a number of creep tests as detailed in Section 3.2. At no time was there any indication of deterioration in the adhesive bond integrity. Following a test, recovery of a specimen to its initial state was just a matter of hours. Creep behaviour was monitored and results from one of the tests will now be presented. Using linear elastic beam theory the axial surface tensile stress, σ_0 (which remained constant), was 80 (BBAL) and 88 (BBAT) N mm^{-2}. From Table 2 the flat sheet has a tensile strength of longitudinal 138 and transverse 70 N mm^{-2}.

The initial central deflection, $w_{exp}(t)$, was between 4·0 and 4·5 mm (see Table 3). This short-term deflection was $\frac{1}{60}$th of the span, near the limit of $\frac{1}{100}$th for structural design.[4] At the end of 24 h, the growth in the central deflection was between 0·45 and 0·65 mm. This increase of over 10% in the deflection showed that creep was rapid, such that a creep test was accelerated. The highest

values were for specimen BBAT having an initial flexural rigidity $(E_{z,xx}(00)I_{xx})$ 0·89 of specimen BBAL.

Figures 4 and 5 are plots of eqns (7) and (8) using the strain data from gauge 1A, and gauges 1S and 2S on specimen BBAL. There is a good fit to Findley's model. For the axial creep behaviour Fig. 4 has gradient $n_e = 0·22$ and $m_e = 135 \times 10^{-6}$ $\mu\varepsilon$ (value of ordinate at $t = 1$ h). To complete eqn (4) for the time-dependent modulus $E_{z,xx}(t)$, we require the two moduli $E_{z,xx}(0)$ and E_t. The initial elastic modulus $E_{z,xx}(0) = \sigma_0/\varepsilon_0$, and is determined when $t = 0$ h. The relevant tensile strain was measured by gauge 1A, and was 3020 $\mu\varepsilon$. Hence, we have $E_{z,xx}(0) = 80/3020 \times 10^{-6} = 24·2$ kN mm^{-2}. This modulus is 17% less than the initial section modulus of 29·2 kN mm^{-2} (see Section 4.1). The reason for this discrepancy is unclear.

To predict the central deflection of an assembly using eqn (1), the objective of the analysis was to obtain the time-dependent moduli, $E_{z,xx}(t)$. It was, therefore, decided to take $E_{z,xx}(0) = 29·2$ kN mm^{-2}. The moduli $E_t = \sigma/m_e$. Following Bank and Mosallam[10] the stress was taken to be σ_0 (i.e. 80 N mm^{-2}); thus $E_t = 593·2$ kN mm^{-2}. The expression (eqn (4)) for the time-dependent longitudinal flexural modulus is

$$E_{z,xx}(t) = \frac{1·732 \times 10^7}{593·2 + 29·2 \times (t)^{0·22}} \qquad (9)$$

where t is in hours.

For the shear creep behaviour of BBAL Fig. 5 has a gradient $n_g = 0·24$ and $m_g = 180 \times 10^{-6}$ $\mu\varepsilon$. To complete eqn (5) for the time-dependent modulus $G_{xz}(t)$, we require the two moduli $G_{xz}(0)$

Table 3. Creep properties of bonded beam assemblies

Time (h)	0	1	10	24	168	8760	87600
Specimen BBAL							
$E_{z,xx}(t)$ (kN mm^{-2})	29·2	27·8	27·0	26·6	25·4	21·4	18·2
$G_{xz}(t)$ (kN mm^{-2})	3·15	2·83	2·66	2·53	2·23	1·57	1·15
$w_h(t)$ (mm)	2·48	2·60	2·68	2·72	2·85	3·38	3·98
$w_s(t)$ (mm)	1·56	1·74	1·85	1·95	2·21	3·14	4·28
$w(t)$ (mm)	4·04	4·34	4·53	4·67	5·06	6·52	8·26
$w_{exp}(t)$ (mm)	4·02	4·23	4·40	4·47			
Specimen BBAT							
$E_{z,xx}(t)$ (kN mm^{-2})	28·7	27·2	26·3	25·8	24·6	20·7	17·7
$G_{xz}(t)$ (kN mm^{-2})	3·15	2·87	2·68	2·59	2·33	1·62	1·17
$w_h(t)$ (mm)	2·80	2·95	3·05	3·11	3·26	3·88	4·53
$w_s(t)$ (mm)	1·56	1·72	1·84	1·90	2·11	3·04	4·21
$w(t)$ (mm)	4·36	4·67	4·89	5·01	5·37	6·92	8·74
$w_{exp}(t)$ (mm)	4·46	4·71	4·84	5·11			
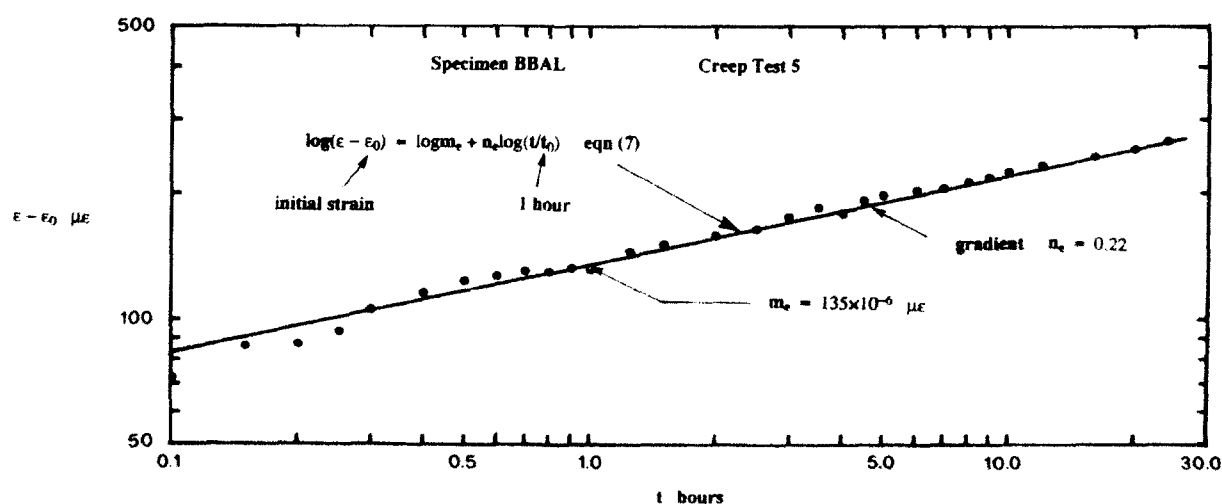
Fig. 4. Plot of axial creep for specimen BBAL and fit to Findley's model for parameter evaluation.
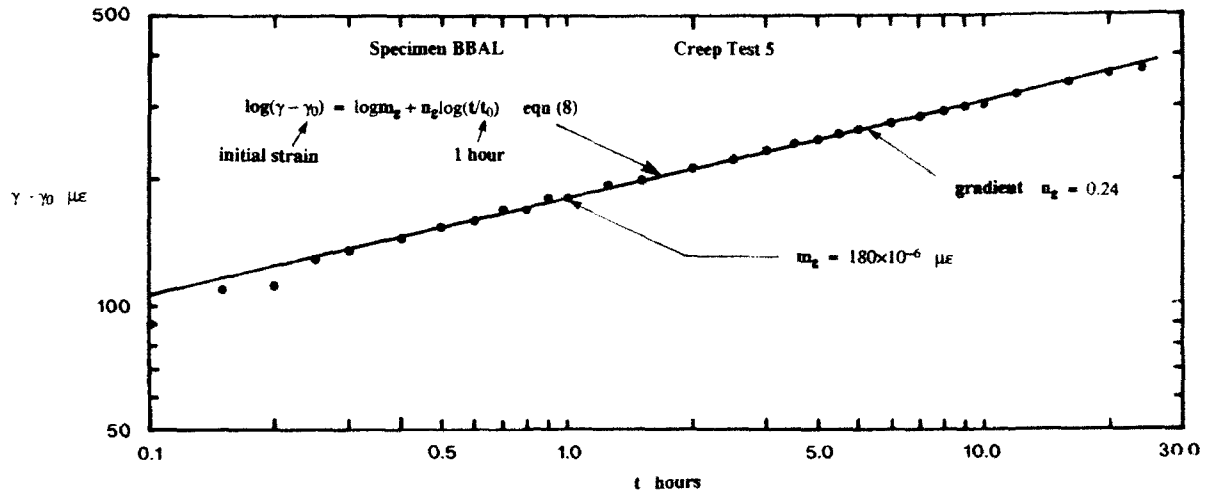
Fig. 5. Plot of shear creep for specimen BBAL and fit to Findley's model for parameter evaluation.

and G_t. The short-term elastic modulus $G_{vc}(0) = \tau_0/\gamma_0$, was taken to be that determined in Section 4.1. This gave $G_{vc}(0) = 3.15$ kN mm^{-2}. The moduli $G_t = \tau/m_g$, was determined by taking τ as the initial shear stress. This gave $\tau = \gamma_0 G_{vc}(0)$ and $G_t = (1580 \times 10^{-6} \times 3.15 \times 10^3)/180 \times 10^{-6} = 27.66$ kN mm^{-2}. The expression (eqn (5)) for the time-dependent shear modulus is

$$G_v(t) = \frac{8.71 \times 10^4}{27.66 + 3.15 \times (t)^{0.24}} \quad (10)$$

Figures 6 and 7 are plots of axial and shear creep strains for specimen BBAT. Using the procedure described above, we obtained

$$E_{vx}(t) = \frac{1.437 \times 10^7}{500.6 + 28.7 \times (t)^{0.21}} \quad (11)$$

and

$$G_v(t) = \frac{10.01 \times 10^4}{32.11 + 3.15 \times (t)^{0.25}} \quad (12)$$

The rate dependent creep parameter n is 0.21–0.25. Under tension loading, glass fibrous composites have parameter n typically in the range 0.16–0.22.[18]

In the creep test by Bank and Mosallam,[10] a 9 ft span $8 \times 8 \times \frac{3}{8}$ in WF beam was loaded in four-point bending. The constant load, equal to $\frac{1}{4}$ of that required to cause buckling failure, induced a maximum surface stress, σ_0, of only 12 N mm^{-2}. To determine creep behaviour using Findley's

model the duration of the test was thousands of hours. Using the procedure given in Section 3.2, the creep parameters were: axial, $m_e = 9.46 \times 10^{-6}$ $\mu\varepsilon$, and $n_e = 0.33$; shear, $m_g = 21.5 \times 10^{-6}$ $\mu\varepsilon$ and $n_g = 0.34$. As expected, the stress dependent parameter m is less than here. The rate dependent parameter n is, however, 50% higher.

Presented in Table 3 are predicted creep data for specimens BBAL and BBAT using eqn (1), with eqns (9)–(12). For a period up to 10 years and a constant load of 22.8 kN, the table gives the viscoelastic moduli $E_{vx}(t)$ and $G_v(t)$, bending deflection $w_b(t)$, shear deflection $w_s(t)$, and total central deflection $w(t)$ (i.e. $= w^b(t) + w_s(t)$). Following Bank and Mosallam,[10] who showed that Findley's theory satisfied creep data from a test of over 3500 h duration, it has been assumed that the data from a 24 h 'accelerated' creep test could be used to predict deflection after 87600 h (i.e. 10 years).

Shear deflection accounts for 40% of the initial deflection. After 87600 h, the shear deflection will be similar to the bending deflection. The total deflection, $w(t)$, will double in the 10-year period. The deflection of a bonded assembly will grow by 20% in 1 week and after 1 year the deflection will exceed the maximum design limit given by $\frac{1}{100}$ of the span.

Central deflections, $w(t)$, using the creep data and Findley's theory are found to be similar to the experimental deflections, $w_{exp}(t)$. The creep model should, therefore, provide a good estimation of deflection such that long-term safe working loads can be determined. To accomplish this,
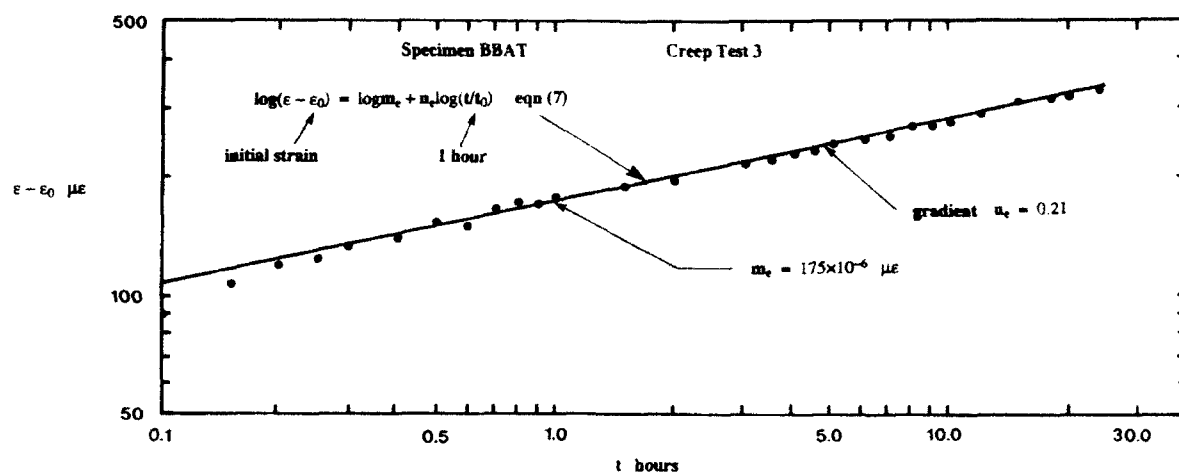
Fig. 6. Plot of axial creep for specimen BBAT and fit to Findley's model for parameter evaluation.
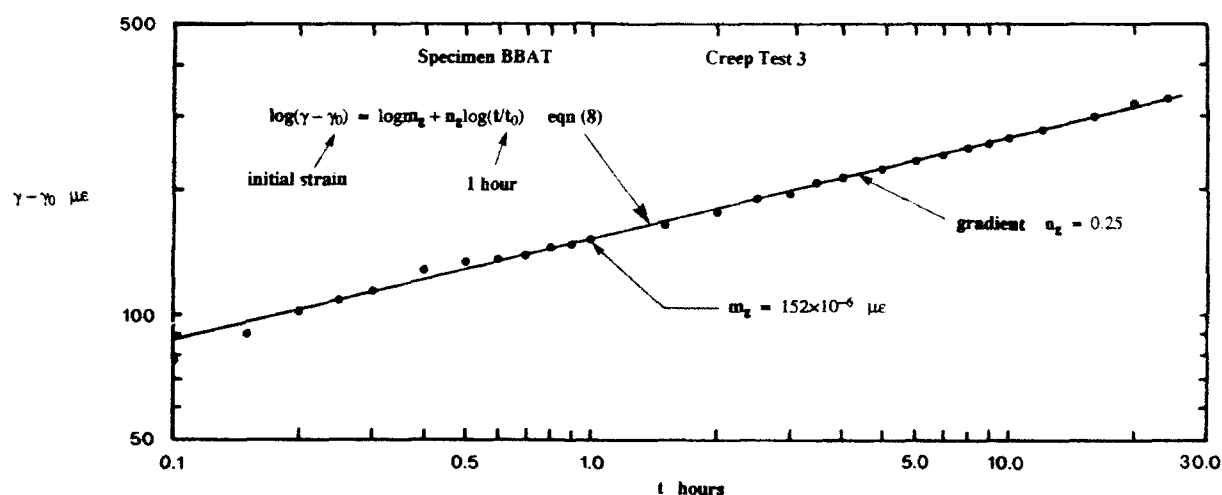
Fig. 7. Plot of shear creep for specimen BBAT and fit to Findley's model for parameter evaluation.

the design procedure would, however, require further testing at longer time durations and with different loadings. Such tests would be used to completely characterise the creep behaviour of the bonded beam assemblies. Further tests would also be necessary to study other long-term effects such as temperature, humidity, and fatigue.

5 CONCLUSIONS

1. It is practical to fabricate closed-sectioned structural assemblies from simple pultruded sections using adhesive bonding.
2. Connections between sections using adhesive bonding have been found to reduce the short-term stiffness of an assembly by about 10% from that calculated using linear elastic beam theory, section properties and a rigid adhesive.

3. Accelerated long-term tests (under normal laboratory conditions) have shown that the creep behaviour of an assembly was similar to that reported by Bank and Mosallam[10] for a pultruded WF beam.

4. Evidence has been given to show that Findley's creep theory is valid. This indicates that pultruded material has linear visco-elastic properties.

5. Using Findley's model and a factored design loading, the central deflection of a bonded assembly has been predicted to

grow by 25, 60 and 100% of its initial value in 1 week, 1 year and 10 years respectively.

6. As deflection limits safe working loads, the long-terms tests have shown that it will be necessary to develop a design procedure to take account of creep behaviour.

ACKNOWLEDGEMENTS

REFERENCES

1. Ballinger, C., Structural FRP composites. *Civ. Engng, ASCE*, **60**(7)(1990)63-5.

2. Barbero, E. & GangaRao, H. V. S., Structural applications of composites in infrastructure. Part 1. *SAMPE J.*, **27**(6)(1991)9-16.

3. NCE. Bridges. Link to a tee. *New Civ. Engng, London* (August, 1992), 20-3.

4. *MMFG Design Manual*. Extren fiberglass structural shapes design manual. MMFG Company Bristol, VA, 1989.

5. *Creative Pultrusions Design Guide*. Creative Pultrusion, Inc., Alum Bank, PA, 1989.

6. Meyer, P. W., *Handbook of Pultrusion Technology*. Chapman and Hall, London, 1985.

7. Mottram, J. T., Evaluation of design analysis for pultruded fibre-reinforced polymeric box beams. *Struct. Engr*, **69**(11)(1991)211-20.

8. Mottram, J. T., Structural properties of a pultruded E-glass fibre-reinforced polymeric I-beam. *Composite Structures 6, International Conference on Composite Structures*, September 9th-11th 1991. Paisley College of Technology, Elsevier Applied Science, London. 1991, pp. 1-28.

9. Mottram, J. T., Lateral-torsional buckling of a pultruded I-beam. *Composites*, **23**(1)(1992)81-93.

10. Bank, L. C. & Mosallam, A. S., Creep and failure of a full-size fibre-reinforced plastic pultruded frame. *Compos. Engng*, **2**(3)(1992)213-27.

11. Barbero, E., Ultimate bending strength of composite beams. *J. Mater. Civ. Engng, ASCE*, **3**(4)(1991) 292-306.

12. Head, P. & Churchman, A. E., Design, specification and manufacture of a pultruded composite flooring system. *Symposium Mass Production Composites*, 19th-20th September 1989. Imperial College, London. 1989, pp. 117-62.

13. Leonard, L., Rebuilding the infrastructure with advanced composites. *Adv. Compos.* (May/June, 1990) 43-7.

14. SERC. *Research in Building*, No. 9 Autumn, 1992, p. 8.

15. Hillman, J. R. & Murray, T. M., Innovative floor systems for steel framed buildings. *Proc. Conf. IABSE*, **60** (1990)672-5.

16. Findley, W. N., Mechanism and mechanics of creep in plastics. *SPE Jl* (January 1960) 57-65.

17. Bank, L. C. & Melehan, T. P., Shear coefficients for multicelled thin-walled composite beams. *Comp. Struct.* **11**(1989)259-76.

18. ASCE. *Structural Plastics Design Manual*. ASCE manuals and reports on engineering practice, No. 63, 1984.

19. Holmes, M. & Rahman, T. A., Creep behaviour of glass reinforced plastic box beams. *Composites*, **11**(2)(1980) 79-85.

20. Kong, F. K. & Evans, R. H., *Reinforced and Prestressed Concrete*. 3rd edn. Van Nostrand Reinhold, UK, 1987.

Analysis of sandwich plates using a mixed finite element

Chih-Ping Wu & Chen-Chung Lin

Department of Civil Engineering, National Cheng Kung University, Tainan, Taiwan 70101.

The stress and displacement analysis of the thick sandwich plate is presented here by using an interlaminar stress mixed finite element based on local high-order deformable theory. The displacements of a sandwich plate are assumed to be high order polynomial functions layer-by-layer through the plate thickness. Since the interlaminar stresses at the interface between layers in this finite element scheme are regarded as primary variables, they can then be accurately determined. The accuracy of this finite element scheme is checked by comparing the present results with 3-D elasticity solutions of a simply supported sandwich plate. The response of a thick angle-ply, fiber-reinforced plastic (FRP) faced sandwich with fully simple supports, subjected to a sinusoidal distribution of transverse load is evaluated. The present finite element results are compared with results obtained from other finite element schemes.

INTRODUCTION

The analysis of sandwich structures has received much attention resulting from the increasing application of sandwich structures to various industrial areas. Many research papers have been published on this topic. Rao[1] has respectively developed a bending theory of flat sandwich beams and plates. A sandwich-type shell theory has been formulated by Reissner.[2] Whitney[3] proposed a procedure to calculate the mechanical behavior of a thick laminated composite and sandwich plates by a first-order shear deformation theory which accounts for the effect of transverse shear deformation. The most important contribution has been made by Srinivas and Rao[4] and Pagano[5] who have presented the bending analysis of laminated composite/sandwich plates using the three-dimensional theory of elastic approach.

Many finite element models have been proposed for the analysis of sandwich structures due to the need of practical application. Pandya and Kant[6] presented a simple isoparametric finite element formulation based on a high-order displacement model for the bending analysis of sandwich structures. This high-order displacement model was also applied to the analysis of composite and sandwich cylindrical shells by Kant and Menon.[7] Rao and Meyer-Piening[8] developed a hybrid-stress finite element for the bending

analysis of thick sandwich plates with simply supported and clamped edges. An overview of various finite element models being proposed for the analysis of sandwich plates, was given by Ha.[9]

Here, an interlaminar stress finite element scheme based on a local high-order displacement model is presented for the analysis of sandwich structures. Since the local high-order displacement model is adopted, the effect of warping of the cross-section which is predominant in sandwich structures can be considered in the present formulation. In addition, the interlaminar stresses are treated as the primary parameters, one set of interlaminar stresses can be uniquely and accurately determined.

THEORY

In the present theory, the displacement components u_i, v_i and w_i of each layer are assumed in the following form:

$$u_i(x, y, z) = u_i^0(x, y) + z_i[\theta_x(x, y)]_i$$
$$+ z_i^2[\psi_x(x, y)]_i + z_i^3[\phi_x(x, y)]_i$$
$$v_i(x, y, z) = v_i^0(x, y) + z_i[\theta_y(x, y)]_i$$
$$+ z_i^2[\psi_y(x, y)]_i + z_i^3[\phi_y(x, y)]_i$$
$$w_i(x, y, z) = w_i^0(x, y) + z_i[\theta_z(x, y)]_i + z_i^2[\psi_z(x, y)]_i$$

$$(1)$$

where u_i^0, v_i^0 and w_i^0 are three mid-surface displacement functions. θ_x, θ_y and θ_z are three rotation functions and ψ_x, ψ_y, ψ_z, ϕ_x and ϕ_y are the other high order functions. z_i is measured from the middle surface of the ith layer.

The displacement continuity conditions at the interface between layers are regarded as the constraints in the present formulation due to the introduction of the local coordinates. The displacement continuity constraints between the ith and $(i+1)$th layers are given by

$$(f_x)_i = u_{i+1}^0 - u_i^0 - \frac{h_{i+1}}{2}(\theta_x)_{i+1} - \frac{h_i}{2}(\theta_x)_i$$
$$+ \frac{h_{i+1}^2}{4}(\psi_x)_{i+1} - \frac{h_i^2}{4}(\psi_x)_i$$
$$- \frac{h_{i+1}^3}{8}(\phi_x)_{i+1} - \frac{h_i^3}{8}(\phi_x)_i = 0$$

$$(f_y)_i = v_{i+1}^0 - v_i^0 - \frac{h_{i+1}}{2}(\theta_y)_{i+1} - \frac{h_i}{2}(\theta_y)_i$$
$$+ \frac{h_{i+1}^2}{4}(\psi_y)_{i+1} - \frac{h_i^2}{4}(\psi_y)_i$$
$$- \frac{h_{i+1}^3}{8}(\phi_y)_{i+1} - \frac{h_i^3}{8}(\phi_y)_i = 0 \qquad (2)$$

$$(f_z)_i = w_{i+1}^0 - w_i^0 - \frac{h_{i+1}}{2}(\theta_z)_{i+1} - \frac{h_i}{2}(\theta_z)_i$$
$$+ \frac{h_{i+1}^2}{4}(\psi_z)_{i+1} - \frac{h_i^2}{4}(\psi_z)_i = 0$$

The strain–displacement relationships based on the small deformation elasticity are then given by

$$(\varepsilon_x)_i = (\varepsilon_x^0)_i + z_i(K_x)_i + z_i^2(\Gamma_x)_i + z_i^3(H_x)_i$$
$$(\varepsilon_y)_i = (\varepsilon_y^0)_i + z_i(K_y)_i + z_i^2(\Gamma_y)_i + z_i^3(H_y)_i \qquad (3)$$
$$(\varepsilon_z)_i = (\varepsilon_z^0)_i + z_i(K_z)_i$$

and

$$(\gamma_{xy})_i = (\gamma_{xy}^0)_i + z_i(K_{xy})_i + z_i^2(\Gamma_{xy})_i + z_i^3(H_{xy})_i$$
$$(\gamma_{xz})_i = (\gamma_{xz}^0)_i + z_i(K_{xz})_i + z_i^2(\Gamma_{xz})_i \qquad (4)$$
$$(\gamma_{yz})_i = (\gamma_{yz}^0)_i + z_i(K_{yz})_i + z_i^2(\Gamma_{yz})_i$$

in which

$$[\varepsilon_x^0, \varepsilon_y^0, \varepsilon_z^0]_i = \left[\frac{\partial u^0}{\partial x}, \frac{\partial v^0}{\partial y}, \theta_z \right]_i$$

$$[K_x^0, K_y^0, K_z^0]_i = \left[\frac{\partial \theta_x}{\partial x}, \frac{\partial \theta_y}{\partial y}, 2\psi_z \right]_i$$

$$[\Gamma_x, \Gamma_y]_i = \left[\frac{\partial \psi_x}{\partial x}, \frac{\partial \psi_y}{\partial y} \right]_i \qquad (5)$$

$$[H_x, H_y]_i = \left[\frac{\partial \phi_x}{\partial x}, \frac{\partial \phi_y}{\partial y} \right]_i$$

and

$$[\gamma_{xy}^0, \gamma_{xz}^0, \gamma_{yz}^0]_i$$
$$= \left[\frac{\partial u^0}{\partial y} + \frac{\partial v^0}{\partial x}, \theta_x + \frac{\partial w^0}{\partial x}, \theta_y + \frac{\partial w^0}{\partial y} \right]_i$$

$$[K_{xy}, K_{xz}, K_{yz}]_i$$
$$= \left[\frac{\partial \theta_x}{\partial y} + \frac{\partial \theta_y}{\partial x}, 2\psi_x + \frac{\partial \theta_z}{\partial x}, 2\psi_y + \frac{\partial \theta_z}{\partial y} \right]_i$$

$$[\Gamma_{xy}, \Gamma_{xz}, \Gamma_{yz}]_i$$
$$= \left[\frac{\partial \psi_x}{\partial y} + \frac{\partial \psi_y}{\partial x}, 3\phi_x + \frac{\partial \psi_z}{\partial x}, 3\phi_y + \frac{\partial \psi_z}{\partial y} \right]_i$$

$$[H_{xy}]_i = \left[\frac{\partial \phi_x}{\partial y} + \frac{\partial \phi_y}{\partial x} \right]_i \qquad (6)$$

The displacement continuity constraints at the interface between layers (i.e. eqn (2)) are introduced into the potential energy functional of the laminates by the Lagrange multiplier method. The Lagrange multipliers, without a loss of generality, are taken to be the interlaminar stresses (i.e. τ_{xz}, τ_{yz} and σ_z) at the interface between layers. The modified potential energy functional is given by

$$\Pi_{mp} = \sum_{i=1}^{NL} \iint_A \int_{-h_i/2}^{h_i/2} \left[\frac{\sigma_x \varepsilon_x}{2} + \frac{\sigma_y \varepsilon_y}{2} + \frac{\sigma_z \varepsilon_z}{2} + \frac{\tau_{xy} \gamma_{xy}}{2} \right.$$
$$\left. + \frac{\tau_{xz} \gamma_{xz}}{2} + \frac{\tau_{yz} \gamma_{yz}}{2} \right]_i dz \, dA$$

$$- \iint_A [T_x u^* + T_y v^* + T_z w^*] \, dA$$

$$+ \sum_{i=1}^{NL-1} \iint_A [(\lambda_x)_i(f_x)_i + (\lambda_y)_i(f_y)_i$$

$$+ (\lambda_z)_i(f_z)_i] \, dA \qquad (7)$$

where T_x, T_y and T_z are the tractions applied at the upper surface, u^*, v^* and w^* are the displacement

components at upper surface, $(\lambda_x)_i$, $(\lambda_y)_i$ and $(\lambda_z)_i$ are respectively defined as the interlaminar stresses, i.e. τ_{xz}, τ_{yz} and σ_z, at the interface between ith and $(i+1)$th layers. NL denotes the total number of layers comprising the considered laminates.

The generalized stress and moment resultants of ith lamina can be obtained by performing the integration through thickness from bottom to top surfaces of this lamina and expressed by

$$
\begin{bmatrix} N \\ P \\ \cdots \\ M \\ \overline{M} \\ \cdots \\ Q \\ R \\ S \end{bmatrix}_i = \begin{bmatrix} D_m & \vdots & 0 & \vdots & 0 \\ \cdots\cdots\cdots\cdots \\ 0 & \vdots & D_b & \vdots & 0 \\ \cdots\cdots\cdots\cdots \\ 0 & \vdots & 0 & \vdots & D_s \end{bmatrix}_i \begin{bmatrix} \varepsilon \\ \Gamma \\ \cdots \\ K \\ H \\ \cdots \\ \gamma \\ K^* \\ \Gamma^* \end{bmatrix}
\tag{8}
$$

in which

$$N_i = \{N_x, N_y, N_z, N_{xy}\}_i^T$$

$$P_i = \{P_x, P_y, P_{xy}\}_i^T$$

$$M_i = \{M_x, M_y, M_z, M_{xy}\}_i^T$$

$$\overline{M}_i = \{\overline{M}_x, \overline{M}_y, \overline{M}_{xy}\}_i^T$$

$$Q_i = \{Q_x, Q_y\}_i^T \quad R_i = \{R_x, R_y\}_i^T \quad S_i = \{S_x, S_y\}_i^T$$

$$\varepsilon_i = \{\varepsilon_x^0, \varepsilon_y^0, \varepsilon_z^0, \gamma_{xy}^0\}_i^T \quad \Gamma_i = \{\Gamma_x, \Gamma_y, \Gamma_{xy}\}_i^T \tag{9}$$

$$K_i = \{K_x, K_y, K_z, K_{xy}\}_i^T \quad H_i = \{H_x, H_y, H_{xy}\}_i^T$$

$$\gamma_i = \{\gamma_{xz}^0, \gamma_{yz}^0\}_i^T \quad K_i^* = \{K_{xz}, K_{yz}\}_i^T$$

$$\Gamma_i^* = \{\Gamma_{xz}, \Gamma_{yz}\}_i^T$$

$[D_m]_i$ = membrane rigidity matrix of lamina i

$[D_b]_i$ = flexure rigidity matrix of lamina i

$[D_s]_i$ = shear rigidity matrix of lamina i

and

$$
\begin{bmatrix} N_x & N_y & N_z & N_{xy} & Q_x & Q_y \\ M_x & M_y & M_z & M_{xy} & R_x & R_y \end{bmatrix}_i
$$

$$
= \int_{-h/2}^{h/2} \begin{bmatrix} 1 \\ z \end{bmatrix} \{\sigma_x \ \sigma_y \ \sigma_z \ \tau_{xy} \ \tau_{xz} \ \tau_{yz}\}_i \, dz
$$

$$
\begin{bmatrix} P_x & P_y & P_{xy} \\ \overline{M}_x & \overline{M}_y & \overline{M}_{xy} \end{bmatrix}_i = \int_{-h/2}^{h/2} \begin{bmatrix} z^2 \\ z^3 \end{bmatrix} \{\sigma_x \ \sigma_y \ \tau_{xy}\}_i \, dz \tag{10}
$$

$$
[S_x \ S_y]_i = \int_{-h/2}^{h/2} z^2 [\tau_{xz} \ \tau_{yz}]_i \, dz
$$

FINITE ELEMENT FORMULATION

In the present finite element formulation, the total domain of the considered laminated composite/sandwich plate is discretized into NL layers (for the sandwich plate case, $NL = 3$) and then each layer domain is further discretized into NE elements such that

$$\Pi_{mp} = \sum_{i=1}^{NL} \sum_{e=1}^{NE} [\Pi_{mp}^e(\alpha_i, \beta_i)]_i \tag{11}$$

where

$$\alpha_i = \{u^0, v^0, w^0, \theta_x, \theta_y, \theta_z, \psi_x, \psi_y, \psi_z, \phi_x, \phi_y\}_i \tag{12}$$

and

$$\beta_i = \{\tau_{xz}, \tau_{yz}, \sigma_z\}_i \tag{13}$$

A nine-node quadratical C^0 isoparametric element is introduced in the present formulation. The spatial distribution of the primary displacement variables in lamina i and the interlaminar stresses at the interface between the ith and $(i+1)$th layers are respectively written as

$$\alpha_i = \sum_{j=1}^{ND=9} \Phi_j(\alpha_j)_i, \qquad i = 1, 2, \ldots, NL \tag{14}$$

and

$$\beta_i = \sum_{j=1}^{ND=9} \Phi_j(\beta_j)_i, \qquad i = 1, 2, \ldots, (NL-1) \tag{15}$$

where ND denotes the number of nodal points in the adopted element. Φ_j are the interpolating (or shape) functions associated with node j.

Substituting the previously assumed displacements and interlaminar stress functions into eqn (7), then after taking the first order variation of the present modified potential energy functional with respect to the primary variables (i.e. the generalized displacements and the interlaminar stresses at the interface between layers), we obtain the

stationary equilibrium equations as:

$$\sum_{i=1}^{NL} \sum_{c=1}^{NE} \sum_{j=1}^{ND} \begin{bmatrix} K_{II}^c & K_{III}^c & K_{IIII}^c \\ & K_{IIII}^c & K_{IIIII}^c \\ \text{symmetric} & & K_{IIIIII}^c \end{bmatrix}_i$$

$$\times \begin{bmatrix} \{a_j^c\}_i \\ \{\beta_j^c\}_i \\ \{\beta_j^c\}_i \end{bmatrix} = \begin{bmatrix} \{F_I^c\} \\ \{F_{II}^c\} \\ \{F_{III}^c\} \end{bmatrix}_i \qquad (16)$$

where

$$K_{II}^c = \int_{-1}^{1} \int_{-1}^{1} N^T DB |J| \, d\xi \, d\eta$$

$$K_{IIII}^c = \int_{-1}^{1} \int_{-1}^{1} (B_I - B_{II})^T B_{III} |J| \, d\xi \, d\eta$$

$$K_{IIIII}^c = \int_{-1}^{1} \int_{-1}^{1} (B_I + B_{II})^T B_{III} |J| \, d\xi \, d\eta$$

$$K_{IIII}^c = K_{IIIII}^c = K_{IIIIII}^c = 0 \qquad (17)$$

and

$$F_I^c = \int_{-1}^{1} \int_{-1}^{1} (B_I + B_{II})^T \begin{Bmatrix} T_x \\ T_y \\ T_z \end{Bmatrix} |J| \, d\xi \, d\eta$$

$$\text{when } i = NL$$

$$= 0 \qquad \text{when } i \neq NL$$

$$F_{II}^c = F_{III}^c = 0 \qquad (18)$$

NUMERICAL APPLICATIONS AND DISCUSSION

The presently mixed finite element scheme is used to study the displacement and stress of the fully simply supported sandwich plates, faced with an angle-ply fibre-reinforced plastic lamina and subjected to sinusoidal transverse loading (i.e. $T_x = T_y = 0$ and $T_z(x, y) = q_0 \sin \pi x/a \sin \pi y/b$). The geometric configuration of the considered sandwich plate is shown in Fig. 1. The mechanical properties of the face and core material are listed as follows.

For the face layer (orthotropic material):

$$E_L = 1.724 \times 10^8 \text{ kN/m}^2 (25 \times 10^6 \text{ psi})$$

$$E_T = 6.89 \times 10^6 \text{ kN/m}^2 (10^6 \text{ psi})$$

$$G_{LT} = 3.45 \times 10^6 \text{ kN/m}^2 (0.5 \times 10^6 \text{ psi})$$

$$G_{TT} = 1.378 \times 10^6 \text{ kN/m}^2 (0.2 \times 10^6 \text{ psi})$$

$$\nu_{LT} = \nu_{TT} = 0.25$$

where L and T mean the directions parallel and transverse to the fiber direction, respectively. ν_{LT} is Poisson's ratio measuring the ratio of transverse strain to normal strain under normal stress in the fiber direction.

For the core layer (transversely isotropic material):

$$E_{xx} = E_{yy} = 0.27 \times 10^6 \text{ kN/m}^2 (0.04 \times 10^6 \text{ psi})$$

$$E_{zz} = 3.45 \times 10^6 \text{ kN/m}^2 (0.5 \times 10^6 \text{ psi})$$

$$G_{xz} = G_{yz} = 0.41 \times 10^6 \text{ kN/m}^2 (0.06 \times 10^6 \text{ psi})$$

$$G_{xy} = 0.11 \times 10^6 \text{ kN/m}^2 (0.016 \times 10^6 \text{ psi})$$

$$\nu_{zx} = \nu_{zy} = \nu_{xy} = 0.25$$

The stress and displacement quantities are normalized in the same form as Pagano in order to compare the present results with Pagano's 3-D elasticity solutions.[5] They are written as

$$(\bar{\sigma}_x, \bar{\sigma}_y, \bar{\tau}_{xy}) = \frac{1}{q_0 S^2} (\sigma_x, \sigma_y, \tau_{xy})$$

$$(\bar{\tau}_{xz}, \bar{\tau}_{yz}) = \frac{1}{q_0 S} (\tau_{xz}, \tau_{yz}); \quad \bar{\sigma}_z = \frac{\sigma_z}{q_0}$$
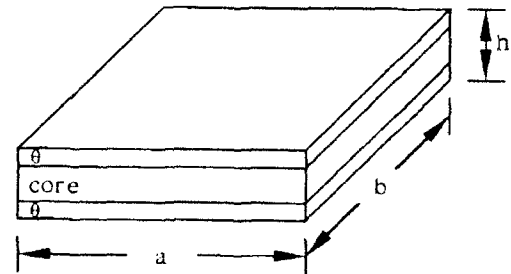
(a) [θ/core/θ] sandwich plate
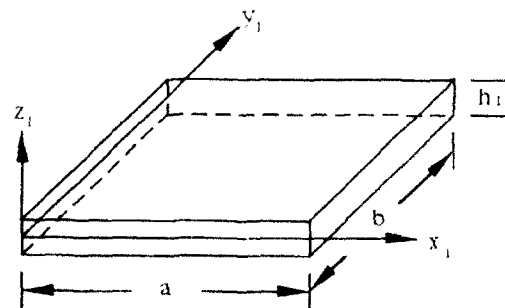
(b) The local coordinate system of ith layer

Fig. 1. Geometry and local coordinate system of the [θ/core/θ] sandwich plate.

$$\bar{u} = \frac{E_{\mathrm{T}} u}{q_0 h s^3}, \quad \bar{w} = \frac{100 E_{\mathrm{T}} w}{q_0 h s^4}$$

$$s = \frac{a}{h}, \quad \bar{z} = \frac{z}{h}$$

The reduced integration technique,[10] which means the 3×3 Gauss rule is used for the bending portion of the stiffness matrix and the 2×2 Gauss rule for the shear portion of the stiffness matrix, is adopted in this analysis. A quarter plate model with a 2×2 in-plane mesh is used for $[0°/\mathrm{core}/0°]$ and $[90°/\mathrm{core}/90°]$ sandwich plates, and a full plate model with a 4×4 in-plane mesh is used for $[\theta/\mathrm{core}/\theta]$ sandwich plates. The thickness ratio between the face and core layers of the considered sandwich plates is $0.1h:0.8h:0.1h$. The present element configurations of the displacements and interlaminar stresses are shown in Fig. 2.

The maximum stresses and deflections in the three layered rectangular laminate and square sandwich plates are respectively shown in Tables 1 and 2. The results obtained by the present FE
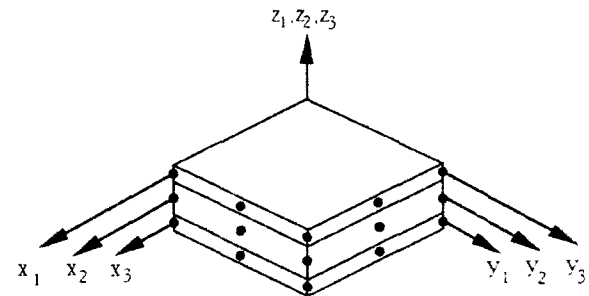
(a) Element configuration for displacements
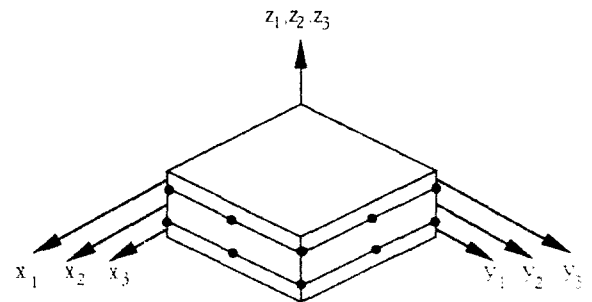
(b) Element configuration for interlaminar stresses

Fig. 2. Present element configuration

Table 1. Maximum stresses and deflections in three-layered rectangular ($b = 3a$) laminate

a/h	Source	$\bar{\sigma}_x\,a/2,b/2,1/2$	$\bar{\sigma}_y\,a/2,b/2,1/6$	$\bar{\tau}_{xy}\,0,0,1/2$	$\bar{\tau}_{xz}\,0,b/2,0$	$\bar{u}\,a/2,b/2,0$
2	Pagano[7]	2·130	0·230	−0·0564	0·257	8·170
	Present	2·220	0·236	−0·0596	0·267	8·163
	Rao and Meyer-Piening[9]	—	—	—	—	—
4	Pagano[7]	1·140	0·109	−0·0269	0·351	2·820
	Present	1·190	0·111	−0·0286	0·365	2·821
	Rao and Meyer-Piening[9]	0·934	0·107	−0·0266	0·387	2·752
10	Pagano[7]	0·726	0·0418	−0·0120	0·420	0·919
	Present	0·750	0·0412	−0·0129	0·450	0·917
	Rao and Meyer-Piening[9]	0·659	0·037	−0·0123	0·454	0·916

Table 2. Maximum stresses in a simply supported square sandwich plate

a/h	Source	$\sigma_x\,a/2,b/2,1/2$	$\bar{\sigma}_x\,a/2,b/2,0.4$	$\sigma_y\,a/2,b/2,1/2$	$\bar{\tau}_{xy}\,0,0,1/2$	$\bar{\tau}_x\,0,b/2,0$
4	Pagano	1·556	−0·233	0·2595	−0·1437	0·2390
	Present	1·548	−0·224	0·2413	−0·1339	0·2497
	Pandya and Kant[6]	1·523	−0·012	0·2414	−0·1419	0·2750
	Reddy and Chao[11]	0·865	—	0·1517	−0·0878	0·0994
	CLT	1·097	0·878	0·0543	−0·0433	0·3240
10	Pagano	1·153	0·628	0·1104	−0·0707	0·3000
	Present	1·210	0·669	0·1115	−0·0713	0·3177
	Pandya and Kant[6]	1·166	0·688	0·1052	−0·0692	0·3400
	Reddy and Chao[11]	1·015	—	0·0774	−0·0535	0·1112
	CLT	1·097	0·878	0·0543	−0·0433	0·3240
20	Pagano	1·110	0·810	0·0700	−0·0511	0·3170
	Present	1·173	0·861	0·0724	−0·0525	0·3530
	Pandya and Kant[6]	—	—	—	—	—
	Reddy and Chao[11]	1·051	—	0·0594	−0·0452	1·1400
	CLT	1·097	0·878	0·0543	−0·0433	0·3240

solutions, Pagano's 3-D elasticity solutions[5] and the results obtained from other finite element schemes[6,8,11] are also compared. It is observed that the present FE scheme gives much better prediction as compared to the other FE schemes in the literature. Figure 3 makes comparison between the present FE solutions and 3-D elas-

ticity solutions for the dependence of central deflection upon the side-to-thickness ratio a/h. The present FE results are in excellent agreement with 3-D elasticity solutions through the whole range of a/h including the very thick and thin plates. The variations of interlaminar shear and normal stresses contour at upper interface of $[\theta/\text{core}/\theta]$ sandwich plate with the change of fiber orientation angle θ are given in Figs 4 and 5. It is observed that the maximum interlaminar shear stress occurs at the locations $(x = 0, y = b/2)$ and $(x = a, y = b/2)$ in the $[0°/\text{core}/0°]$ sandwich plate and in the vicinity of these two locations while $0° < \theta < 90°$. The variation of interlaminar stress with the spatial coordinate is much more sensitive while θ approaches $0°$ than while θ approaches $90°$. The maximum interlaminar normal stress occurs at the location $(x = a/2, b/2)$. The influence of the change of fiber orientation angle θ on the variation of interlaminar normal stress is very insignificant.
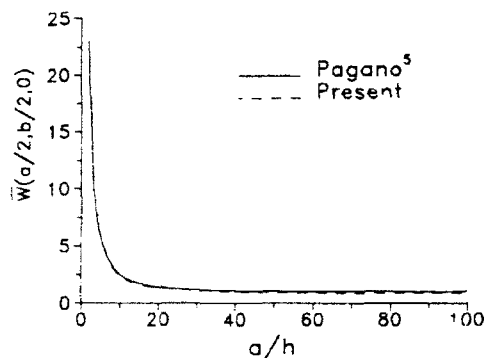
Fig. 3

(a) [0°/CORE/0°]

(b) [15°/CORE/15°]

(c) [30°/CORE/30°]

(d) [45°/CORE/45°]

Fig. 4

(e)[60°/CORE/60°]

(f) [75°/CORE/75°]

(g) [90°/CORE/90°]

Fig. 4 — *contd.*

(a) [0°/CORE/0°]

(b) [15°/CORE/15°]

Fig. 5

(C) [30°/CORE/30°]

(d) [45°/CORE/45°]

(e) [60°/CORE/60°]

(f) [75°/CORE/75°]

(g) [90°/CORE/90°]
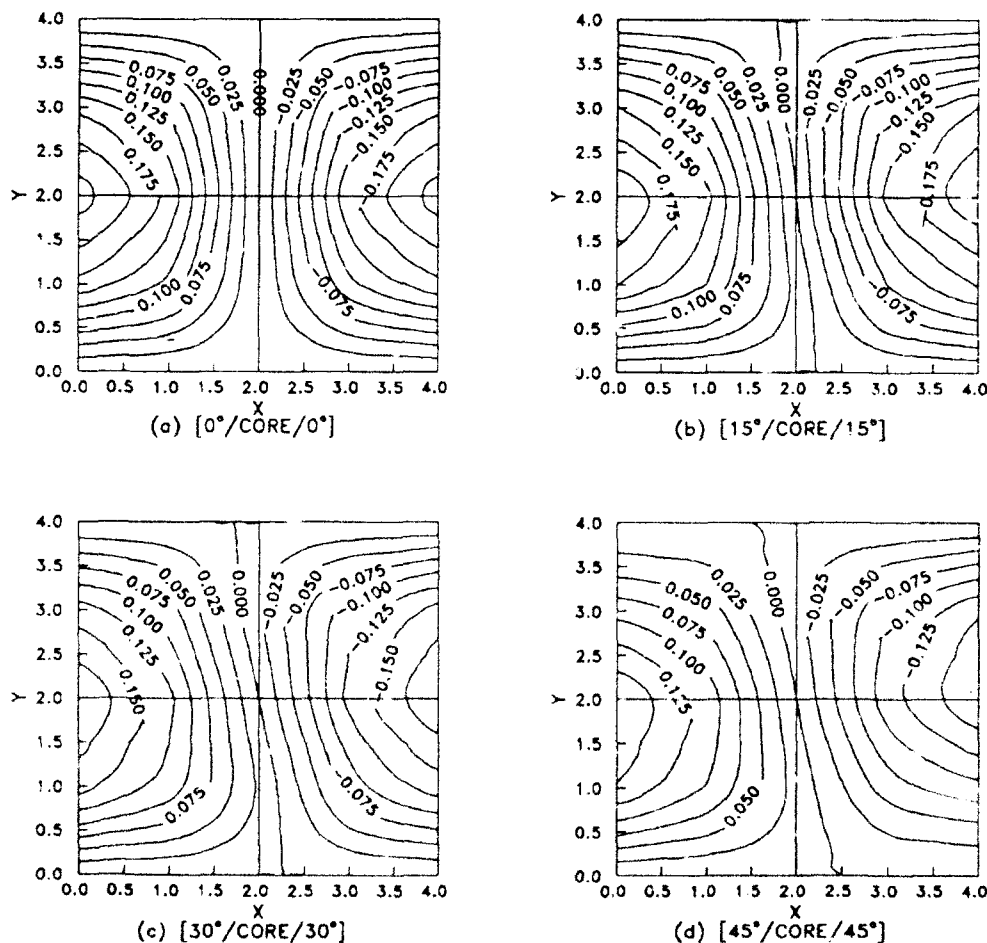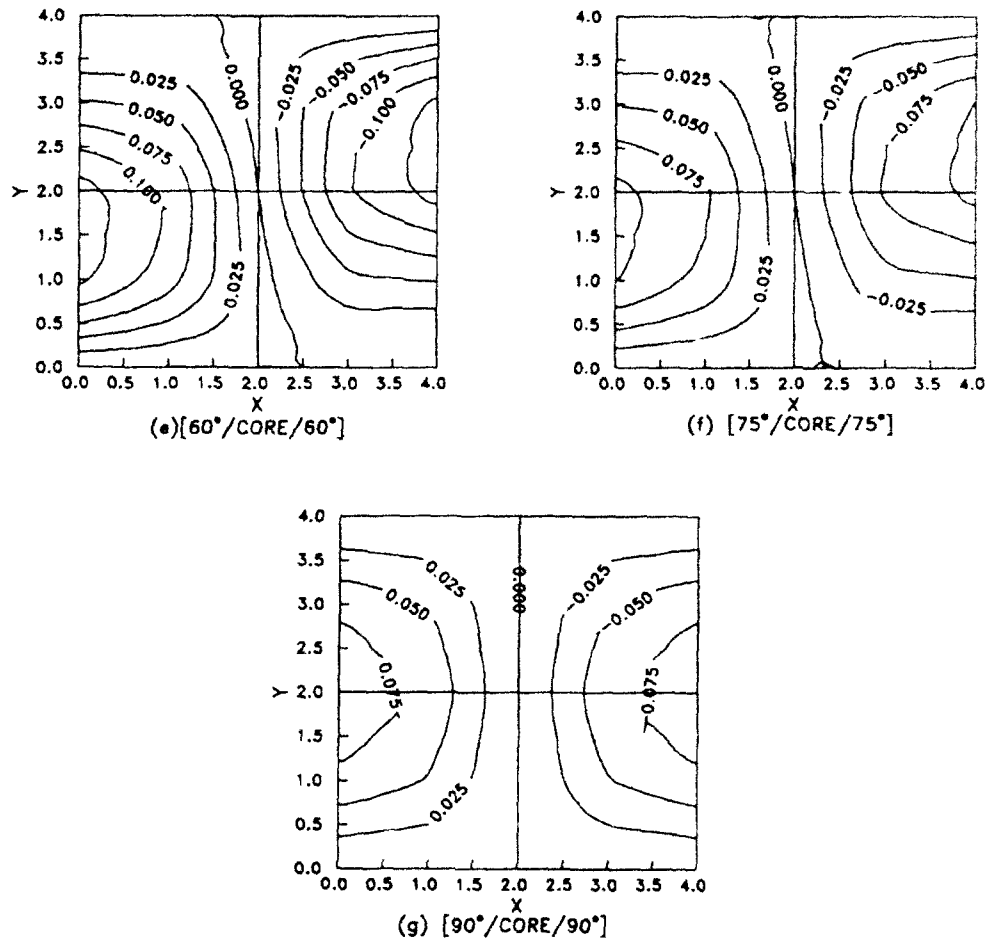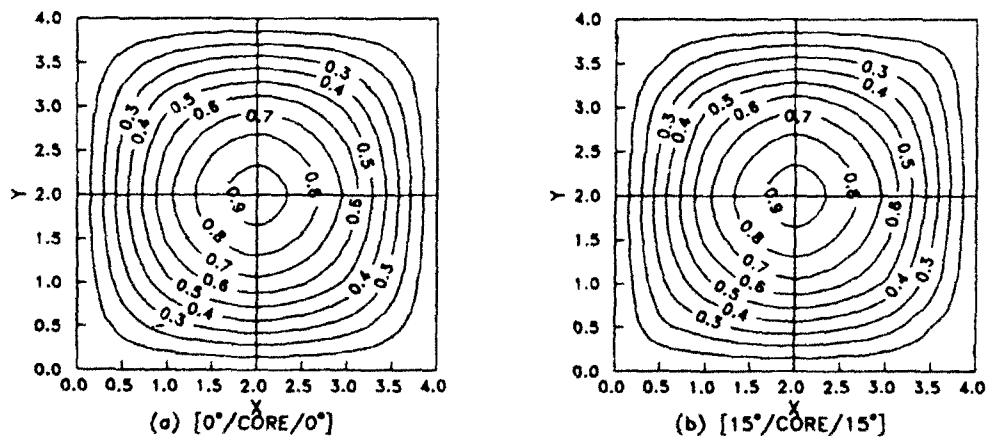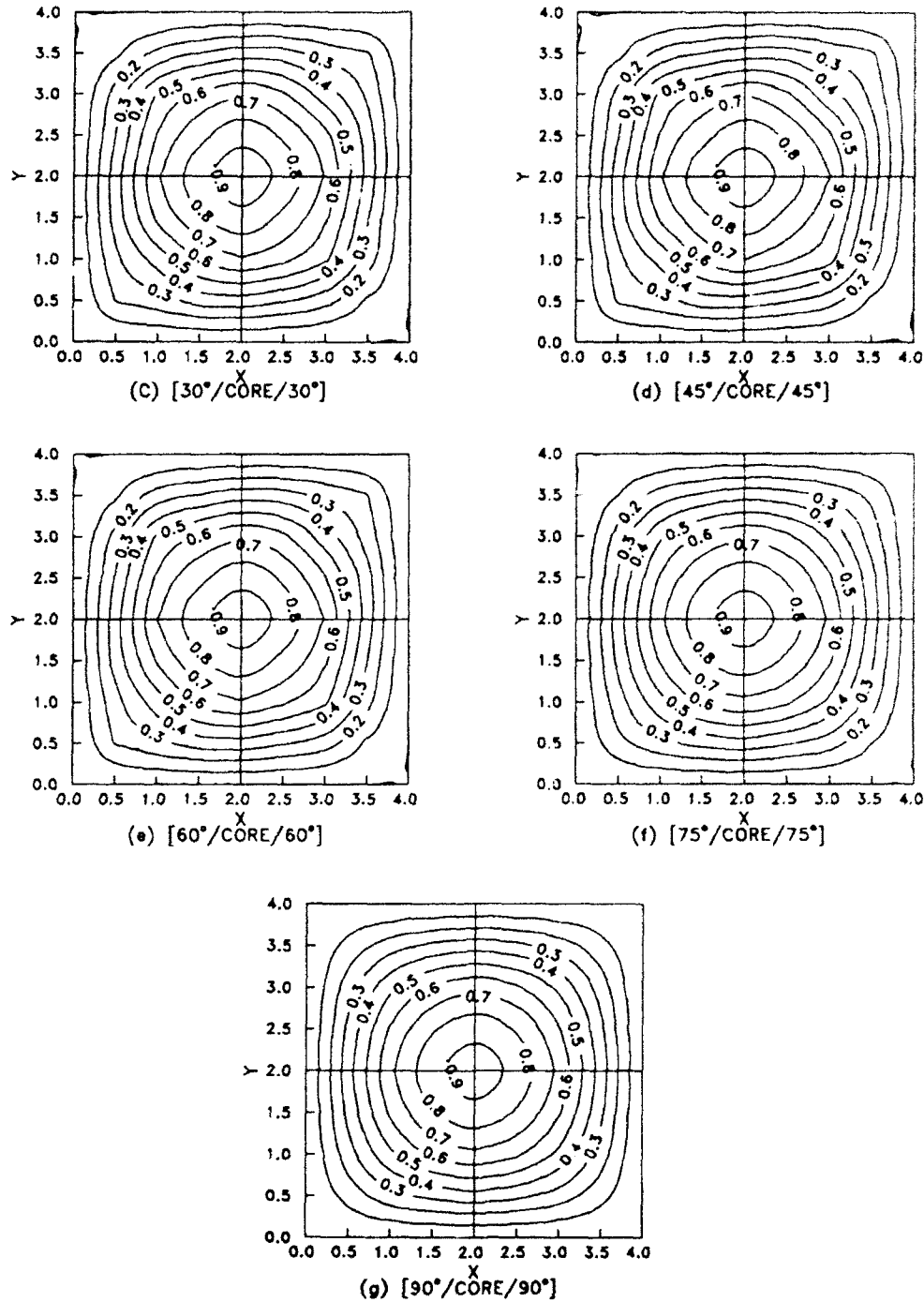
Fig. 5 — contd.

CONCLUSION

In this paper, the authors present a mixed finite element method based on a local high order lamination theory for the analysis of thick sandwich plates. The displacement and stress results obtained from the present FEM and from 3-D elasticity are in close agreement. Since the interlaminar stresses are treated as the primary variables, the present FE scheme also gives a very accurate estimation of interlaminar stress distribution at the interfaces. The influence of the fiber orientation angle θ on the variation of the interlaminar shear stress is much more significant than

on the variation of the interlaminar normal stress. The maximum interlaminar shear stress τ_{xz} occurs at the locations $(x = 0, y = b/2)$ and $(x = a, y = b/2)$ while $\theta = 0°$ and $90°$ and in the vicinity of these two locations while θ has the other values. The maximum interlaminar normal stress occurs at $(x = a/2, y = b/2)$ for any values of the fiber orientation angle θ.

REFERENCES

1. Rao, D. K., Buckling coefficients for FRP faced sandwich panels under combined loading. *AIAA J.,* **25** 1987 733–9.
2. Reissner, E., Small bending and stretching of sandwich-type shells. NACA Rept TN 1526 and NACA Rept 899, 1948.
3. Whitney, J. M., Stress analysis of thick laminated composite and sandwich plates. *J. Comp. Mater.,* **6** 1972 426–40.
4. Srinivas, S. & Rao, A. K., Bending vibration and buckling of simply supported thick orthotropic rectangular plates and laminates. *Int. J. Solids Struct.,* **6** 1970 1463–81.
5. Pagano, N. J., Exact solutions for rectangular bidirectional composites and sandwich plates. *J. Comp. Mater.* **4** 1970 20–34.
6. Pandya, B. N. & Kant, T., Higher-order shear deformable theories for flexure of sandwich plates — finite element evaluations. *Int. J. Solids Struct.,* **24** 1988 1267–86.
7. Kant, T. & Menon, M. P., Estimation of interlaminar stresses in fibre reinforced composite cylindrical shells. *Comput. Struct.,* **38** 1991 131–47.
8. Rao, K. M. & Meyer-Piening, H. R., Analysis of sandwich plates using a hybrid-stress finite element. *AIAA J.,* **29** 1991 1498–506.
9. Ha, K. H., Finite element analysis of sandwich plates: an overview. *Comput. Struct.,* **37** 1990 397–403.
10. Pugh, E. D. L., Hinton, E. & Zienkiewicz, O. C., A study of quadrilateral plate bending elements with 'Reduced' integration. *Int. J. Numer. Meth. Engng.* **12** 1978 1059–79.
11. Reddy, J. N. & Chao, W. C., Non-linear bending of thick rectangular laminated composite plates. *Int. J. Non-Linear Mech.,* **16** 1982 291–301.

Assessment of interlaminar stress distribution in CFRP laminates containing transverse crack using finite element model

Atsushi Yokoyama

Faculty of Education, Mie University, Kamihamacho, Tsu, Mie, Japan

Zen-ichiro Maekawa, Hiroyuki Hamada & Toshihiko Okumura

Faculty of Textile Science, Kyoto Institute of Technology, Matsugasaki, Sakyo-ku, Kyoto, Japan

Composite laminates have various failure modes mainly because of the heterogeneity of the material and the failure modes are influenced by the mechanical properties of the reinforcement and matrix. In particular, interlaminar delamination is the most severe failure mode which occurs in the matrix area in the interlamina. But, the mechanism of delamination cannot be understood by the assumption that the laminates are homogeneous. We propose a new finite element model which can represent the behaviour of the lamina and the interlamina independently. Consequently, the good analysis results expected by experimental results were obtained. Moreover, we estimate the effect of thermoplastic film which is inserted in the interlamina to prevent delamination.

1 INTRODUCTION

Carbon fibre reinforced plastics (CFRP) are being used for many aerospace structural components mainly because of their higher specific strength and specific stiffness compared to metals. Laminates, such as cross-ply, angle-ply and quasi-isotropic laminates, are gaining importance for real structural applications. But to use them efficiently, understanding the failure mechanism of these composite laminates is essential.

Composite laminates have various failure modes. In particular, matrix cracking and delamination are two primary failure modes often seen in composite laminates. The damage at the free edges of the laminate propagates and leads to premature failure of the laminate. Extensive research has been done on the failure mechanism of cross-ply and angle-ply laminates by the previous researchers. Hong and Kim[1] investigated the fact that delamination behaviour of cross-ply laminates depends on the stacking sequence of composite laminate. Kobayashi et al.[2] investigated the effect of temperature on the fracture mechanism of CFRP cross-ply laminates. Yalvac et al.[3] investigated the resistance of the cross-ply laminate to transverse ply cracking. Belglund et al.[4] investigated the failure mechanism of transverse layers using cross-ply laminates. Shuart[5] investigated the mechanisms of interlamina and in-plane shear failure of angle-ply laminates. On the other hand, the study relative to the failure mechanism of quasi-isotropic laminates is not conducted so frequently in comparison with cross-ply and angle-ply laminates. As an example, Garg[6] investigated the process of damage propagation of quasi-isotropic laminates using compact tension, centre-notched tension and three-point bending specimens. That is, little information is available on the fracture behaviour of quasi-isotropic laminates. Moreover, quasi-isotropic laminates have a complex stress state compared with cross-ply and angle-ply laminates.

There are various methods to evaluate the occurrence of delamination in composite laminates. Energy release rate is one of the parameters determining the occurrence of interlaminar delamination. Harikumar and Krishna Murty[7] investigated the onset and growth behaviour of delamination in laminates using the concept of strain-energy release rate. Kondo[8] investigated delamination onset strain associated with the growth of transverse crack tips. In recent years, the relation between delamination behaviour and

energy release rate has gradually become clearer by much research.

Another parameter determining the occurrence of interlaminar delamination is interlaminar stress. This method is more systematic compared with the method using energy release rate. Pipes and Pagano[9] were first to point out the existence of interlaminar stress on composite laminates. Especially in the case of quasi-isotropic laminates, the failure mode is very complex because of the interlaminar stress near the free edge of composite laminates.

To understand the mechanism of delamination, a knowledge of energy release rate and interlaminar stress is needed. Therefore, in the numerical analysis of delamination both energy release rate and interlaminar stress are used widely. In this study, interlaminar stress is adopted as the parameter determining the occurrence of interlaminar delamination.

At present, three-dimensional stress analysis is extensively used for the numerical analysis of delamination problems. Kim and Soni[10] predicted the onset of delamination either due to interlaminar normal stress σ_z or interlaminar shear stress τ_{xz}. Chen and Sun[11] investigated the interlaminar stress in composite laminates with and without delamination crack. However, the analysis is limited to a specific plane, which is perpendicular of the load direction.

Composite laminates undergo three-dimensional deformation, such as out-of-plane deformation, which depends on the stacking sequence. In the above method, the shear deformation of layers is ignored because of the assumption that the bond between two laminae is non-shear deformable. Shear stresses are developed on the faces of each layer. To understand delamination behaviour the whole geometry of composite laminates should be considered during modelling. Thus, it is desirable that these stress components are calculated by three-dimensional stress analysis for the whole of the laminate. Moreover, each layer of the laminate is assumed to be homogeneous. But the actual composite laminate is not homogeneous. For example, Chapin and Joshi[12] investigated the variation of residual thermal stress in graphite/epoxy laminates for three-dimensional analysis using three-dimensional solid elements. However this method did not consider the whole geometry of the laminate and the presence of interlamina for interlaminar stress analysis.

In this paper, a three-dimensional finite element model was proposed to investigate the occurrence of delamination. Using this analytical model interlaminar stress was calculated and the delamination behaviour of the composite laminates was investigated. Moreover the influence of introducing interleaf materials on the delamination behaviour of composite laminates was also investigated.

2 MODELLING

2.1 Modelling of the interlamina

As mentioned above, each interlaminar stress of composite laminates should be calculated by three-dimensional stress analysis. However, the state of stress near a free edge on composite laminates is not a plane stress state but a three-dimensional stress state. Therefore, for three-dimensional stress analysis it is necessary to understand the fracture mechanism of composite laminates.

One of the considerable problems of three-dimensional stress analysis is the expression of fracture modes. Generally, applying some fracture standard to judge the fracture of the elements is the most usual technique. Considering that composite laminates are homogeneous materials, applying the fracture standard to composite laminates is not desirable because the interlaminar delamination cannot be expressed under this assumption. Delamination is a complex phenomenon which results from various interlaminar stresses. To understand delamination behaviour, it is desirable to consider delamination as a microscopic failure mode. But, considering the calculation time on the computer, this assumption is not a good idea.

From another viewpoint, interlaminar delamination can be considered as the fracture of a resin area of the interlamina. Accordingly, if the existence of the interlamina can be assumed, interlaminar delamination can be expressed by the fracture of a resin area of the interlamina, that is, delamination can be treated as macroscopic a failure mode. However, most of the failure analyses of composite laminates which have been done, did not consider the distinction between the interlamina and other layers. That is, all layers of the laminate are replaced with homogeneous materials consisting of fibre and matrix. But this assumption can cause trouble because in the failure area one cannot distinguish between fibre breakage and matrix cracking; in other words, the fracture of a quasi-isotropic laminate caused by a

mixture of various fracture modes cannot be explained. Accordingly, the existence of inter-lamina must be considered. As an example, Hong and Kim[13] defined anisotropic layers and iso-tropic matrix layers respectively, and the matrix layers may be treated as a shear spring. However, this study did not distinguish between the material constants of fibre and resin. That is, it used the material constants of a composite material.

In this study, the resin layer at each interlamina was represented by separating each layer of composite laminate into fibre area and resin area. The concept of laminate modelling is shown in Fig. 1. In this figure, in the fibre area the fibre compacts. On the other hand, in the resin area the fibre does not exist at all. In the modelling of composite laminates including interlamina and other layers, it is necessary to know the thickness of the fibre layers and resin layers. In this study, the thickness of the fibre layers and resin layers is determined by the fibre volume fraction. The theoretical fibre volume fraction of a composite laminate V_f can be calculated in an equation where $2R$ is the centre-to-centre spacing of the fibres, and r is the fibre radius. This equation includes the assumption that the fibres have the same diameters and hexagonal arrangement. The maximum value of V_f is 90.7% when $r = R$, that is, the fibres are touching. In this concept, the thick-ness of the fibre area h_1 and that of resin area can be calculated easily in an equation. Where h_1 is the thickness of the carbon/epoxy prepreg sheet. V_{f0} is the fibre volume fraction of the composite laminate.

2.2 Modelling of transverse cracking

The failure mode of quasi-isotropic CFRP lami-nates under uniaxial tension depends on the stacking sequence. It is expected that the 90° layer breaks first. Generally, the fracture of the layers along the thickness in composite laminates is called transverse cracking. In this case, transverse cracking mainly means the fracture of the 90° layer. Transverse cracking in (0/45/−45/90) quasi-isotropic laminates is shown in Fig. 2. The interlaminar delamination is closely associated with the transverse cracking of the 90° layer. Hence it is essential to consider transverse crack-ing.

Transverse cracking can be considered as the fracture of the resin area in the 90° layer, similar to interlaminar delamination. It is considered that the interpretation of transverse cracking in the failure process of composite laminates is the key to better modelling of laminates. The manage-ment of transverse cracking in numerical analysis is very difficult. Transverse cracking can be con-sidered as a microscopic failure mode. Accord-ingly, it is appropriate that element division of the modelling corresponding with transverse cracking and the neighbourhood must be strictly con-ducted. But considering the calculation time on the computer, this assumption is not suitable for stress analysis of composite laminates. It is known that a laminate with a stacking sequence in which the 90° layer is located mid-layer occurs in trans-verse cracking. In this study, modelling of trans-verse cracking is conducted on the assumption that the transverse cracking absolutely occurs in the composite laminate in which the 90° layer is located mid-layer.

Now, interpretation of two types of transverse cracking was prepared. First, transverse cracking should be identically treated as a complete frac-ture because transverse cracking cannot transmit the stress component to another element. In this case, the elastic constant of the element which corresponds with transverse cracking, is defined as zero. Secondly, transverse cracking should be expressed by a decrease in stiffness of the ele-ments which correspond with it. If the elastic constant of the element which corresponds with

$$h_1 = h_0 \times \frac{V_{f0}}{90.7}$$
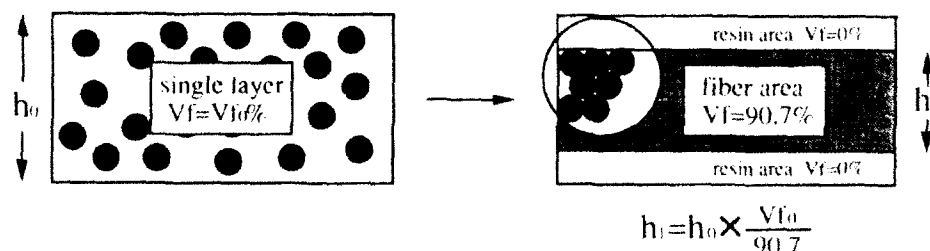
Fig. 1. The concepts of modelling on composite laminates.
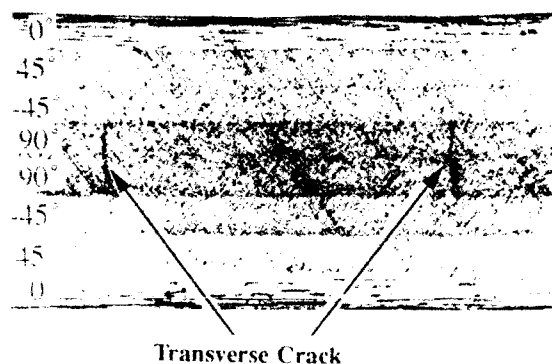
Fig. 2. Transverse cracking on quasi-isotropic CFRP laminates.

transverse cracking is zero. it is appropriate that that element does not exist. However, the existence of fibre and matrix in that element cannot be ignored, so that the elastic constant of the element which correponds with transverse cracking can not be defined as zero. Therefore, the element which occurs in transverse cracking does not break perfectly but decreases in stiffness. Craddock[15] describes the decrease in stiffness in composite laminates using a reduced modulus method. In this study, the decrease in stiffness when the element in the 90° layer breaks, is expressed by substituting the elastic constant, except for the X component, of the element which corresponds to the transverse cracking of neat resin.

In this paper, the applicability of the modelling which was obtained from the above mentioned interpretations was investigated. Then, numerical analysis was carried out according to the following three analysis conditions:

1. Numerical analysis is carried out by an analytical model without transverse cracking. When any element of the 90 layer has reached its limit in strength. analysis is continued by substituting the elastic constant of all elements which constitute the 90 layer with that of neat resin called Type A.

2. Numerical analysis is conducted by an analytical model without transverse cracking. When any element of the 90 layer has reached its limit in strength. analysis is continued by substituting the elastic constant of the broken elements of the 90 layer with the elastic constant of the neat resin called Type B.

3. Numerical analysis is conducted by analytical model with transverse cracking. The elements which correspond with transverse cracking are defined as zero, as mentioned above called Type C.

2.3 Analysis method

A three-dimensional analytical model of the laminates was made by laying-up of alternate layers of fibre and resin. The analytical model Type C is shown in Fig. 3. In this model, the X, Y, Z directions are defined as in Fig. 3. The analytical model, referred to as the quarter model, has the X-Y, X-Z planes defined as planes of symmetry. The shaped portion in this figure indicates transverse cracking. The occurrence of interlaminar delamination was judged by each interlaminar stress component of the X-Y plane. For the finite element model, a three-dimensional solid element such as an eight-node isoparametric element is used.
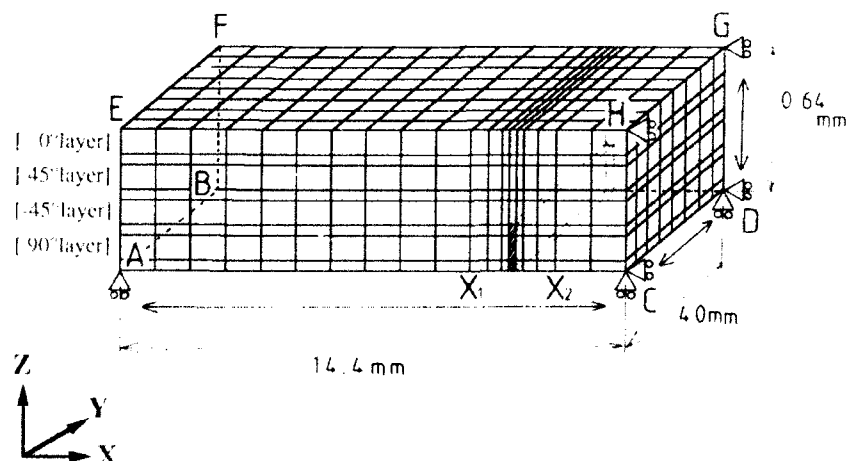
Fig. 3. Analytical model.

Table 1. Material constants of fiber and resin layers

	E_L kgf/mm²	E_T kgf/mm²	G_{LT} kgf/mm²	G_{TT} kgf/mm²	ν	ν
Fiber layer	27000	1200	1600	800	0.3	0.0135
Resin layer		350				0.3

Table 1 lists the mechanical properties of the carbon/epoxy composites used in this analysis. The material constants of the fibre layer were calculated using the material constants of the carbon/epoxy composite laminate by Uemura's approximate equation as follows.[16] The material constants of the fibre layer correspond with these values in the case of $V_f = 90.7\%$.

(1) Elastic moduli

$$E_L = E_f V_f + E_m V_m$$

$$\frac{1}{E_T} = \frac{D}{\Phi}\left[\frac{\pi}{2} + \frac{\gamma}{\sqrt{1-\alpha^2}} \ln\frac{1+\sqrt{1-\alpha^2}}{\alpha} + \frac{\delta}{\sqrt{1-\beta^2}}\right.$$

$$\left. \ln\frac{1+\sqrt{1-\beta^2}}{\beta}\right] + \frac{1-D}{E_m}$$

where

$$D = 2\sqrt{\xi}/\pi, \quad \xi = \sqrt{3}/2$$

$$\alpha = (\textcircled{2} + \sqrt{\textcircled{2}^2 - 4\textcircled{1}\textcircled{3}})/2\textcircled{1}$$

$$\beta = (\textcircled{2} - \sqrt{\textcircled{2}^2 - 4\textcircled{1}\textcircled{3}})/2\textcircled{1}$$

$$\gamma = (K_m \alpha D - \alpha^2\textcircled{1})/(\alpha - \beta)\textcircled{1}$$

$$\delta = (-K_m\beta D + \beta^2\textcircled{1})/(\alpha - \beta)\textcircled{1}$$

$$\textcircled{1} = (D/\xi)K_{tf}[K_{tf}K_{tt} - \nu_{tf}^2 K_{tt} + K_m(1 - \nu_m^2) - K_m K_{tt} + K_{tt} - 2\nu_{tf}\nu_m K_{tt}]$$

$$\textcircled{2} = -(D/\xi)K_m[2K_m(1 - \nu_m^2) - K_{tt} + K_{tt} - 2\nu_{tf}\nu_m K_{tt}]$$

$$\textcircled{3} = K_m^2(1 - \nu_m)^2$$

$$\textcircled{4} = (D^2/\xi)(K_{tt} - K_m)$$

$$K_m = E_m/(1 - \nu_m)^2$$

$$K_{tt} = E_{tt}/(1 - \nu_{tf}\nu_{ft})$$

$$K_{tt} = E_{tt}/(1 - \nu_{tf}\nu_{ft})$$

(2) Poisson's ratio

$$\nu_{tf} = \frac{D(\nu_{tf}K_{tt} - \nu_m K_m)}{K_{tt} - K_m}$$

$$+ \frac{\pi\xi K_m K_{tt}(\nu_m - \nu_{tf})}{2 (K_{tt} - K_m)^2}$$

$$- \frac{(\nu_m - \nu_{tf})\xi^2 K_m^2 K_{tt}}{D(K_{tt} - K_m)^2\sqrt{1-\epsilon^2}}$$

$$\ln\frac{1+\sqrt{1-\epsilon^2}}{\epsilon} + \nu_m(1 - D)$$

$$\nu_{tt} = \nu_{tf} E_T/E_L$$

where

$$\epsilon = \xi K_m/D(K_{tt} - K_m)$$

(3) Shear modulus

$$\frac{1}{G_{tt}} = \frac{\pi}{2(G_{tt} - G_m)} + \frac{\xi}{G_m} + \frac{1-D}{G_m}$$

$$- \frac{D}{G_m}\frac{\lambda^2}{\sqrt{1-\lambda^2}}\ln\frac{1+\sqrt{1-\lambda^2}}{\lambda}$$

where

$$\lambda = \xi G_m/D(G_{tt} - G_m)$$

where the subscripts f and m refer to the fibre and matrix; L and T refer to the fibre and transverse direction, respectively, and G_{tt} uses the half value of G_{tt} for convenience. The boundary conditions are shown in Fig. 3. In this model, the displacement in the X direction on the node of the plane CDGH, the displacement in the Z direction on the node of the plane ABCD, the displacement in the Y direction on the centre node of the line (A–B) were fixed respectively. In an ordinary tensile test, it seems that most of the tensile load is on the surface layer of laminates because both

ends of the specimen are fixed by a grip face. Therefore, concentrated load, which occurs when interlaminar delamination occurs, was at the node of the line (E–F), that is, on the node of the surface layer of laminates.

Stress analysis was carried out by a modified analysis model which follows the analysis conditions Type A, B and C, as mentioned above. The nonlinear analysis of fracture behaviour under a tensile load was carried out by the incremental load method. The interlaminar normal stress component (σ_z), interlaminar shear stress components (τ_{xz} and τ_{yz}), and Mises's equivalent stress component (σ_{Mises}) of each resin layer was calculated in order to judge whether or not interlaminar delamination had occurred. On these analysis results, adequate modelling of transverse cracking was obtained.

3 RESULTS AND DISCUSSION

The fracture development of resin layers in each analysis condition is shown in Fig. 4. The failure area is indicated by shading in this figure. The colour of the failure area darkened with increase of applied load, and, the applied load is at left side of each figure. In this study, when the Mises's equivalent stress of the resin element reached tensile strength of neat resin, the element was regarded as having broken down. Therefore, the increase in the failure area can be regarded as indicating the development of delamination. In the case of Type A, the failure area occurs at the free edge of a (45/–45) interlamina at first. Subsequently, the failure area occurred at the free edge of a (–45/90) interlamina; and, the development of the failure area was not observed in all interlamina. Type B indicated the same tendency as Type A. On the other hand, Type C shows the occurrence of the failure area at the free edge of a (45/–45) and (–45/90) interlamina in the load when the failure area occurs in Type A and Type B at first. The development of the failure area can be observed in (–45/90) and (45/–45) interlamina after the occurrence of the initial failure area. Failure area of Type C is greater than for Type A and Type B.

Mises's equivalent stress distribution in each analysis condition is shown in Fig. 5. The disruption indicates analysis of results when a 90° layer was ruptured in Type A and Type B the applied load is about 800 kgf. In this figure, the horizontal axis represents the location along the length of the laminates; the results are plotted for points along the length. These figures indicate the distribution of nearby transverse cracking from X_1 to X_2 in Fig. 3. Type A and Type B indicated constant stress distribution in all interlamina, whereas with Type C there was an increase in stress at the (–45/90) interlamina as the points approach transverse cracking. From these results, the development of interlaminar fracture cannot be expressed by the condition that transverse cracking is regarded as a decrease in stiffness, and it is difficult to understand the occurrence of
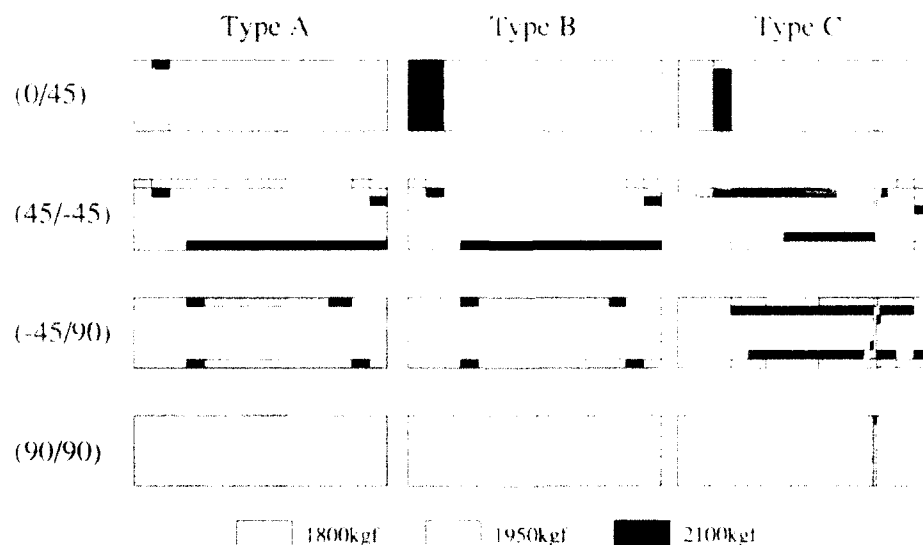
Fig. 4. Fracture development on each analytical condition.
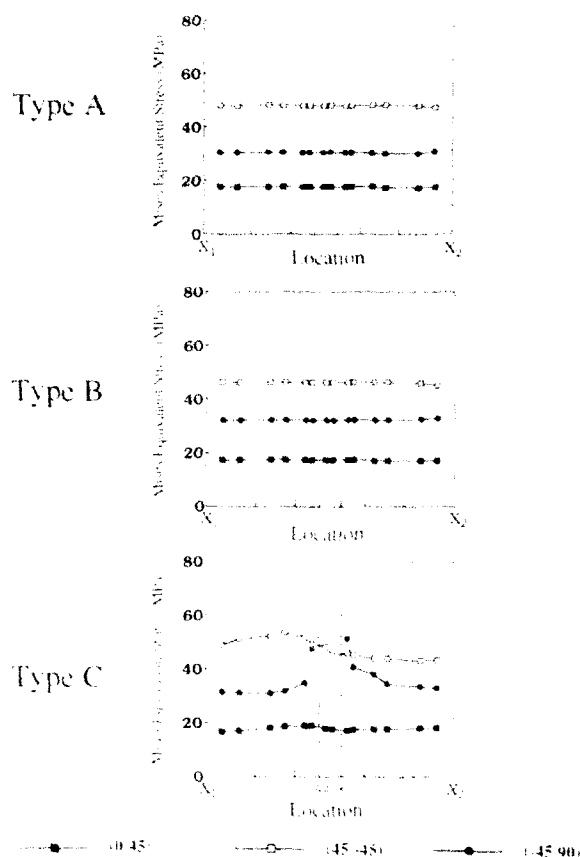
Fig. 5. Mises's equivalent stress distribution on each analytical condition.

Fig. 6. Interlaminar stress distribution of each interlamina.

delamination in the case of Type A and Type B. Therefore, Type C is the most effective in the modelling of transverse cracking.

From the analytical results of the development of the failure area, there is a possibility that interlaminar delamination occurs at either (−45/90) or (45/−45) interlamina. Considering Mises's equivalent stress distribution, interlaminar delamination of a laminate with the stacking sequence of [0/45/−45/90] occurs in the (−45/90) interlamina.

The stress component which causes interlaminar delamination has been investigated also. The distribution of interlaminar normal stress (σ_z) and interlaminar shear stress (τ_{xz} and τ_{yz}) are shown in Fig. 6 (applied load was 800 kgf). Both τ_{xz} and τ_{yz} are higher than σ_z. It was considered that interlaminar delamination occurs either due to τ_{xz} or τ_{yz} after transverse cracking occurs. The τ_{yz} was different for both the interlaminae (45/−45) and (−45/90). In the case of (−45/90) interlamina, τ_{yz} becomes high close to transverse cracking. Therefore, τ_{yz} has a great influence on the interlaminar delamination of composite laminates.

Fig. 7. Fracture aspect of quasi-isotropic CFRP laminate

Tensile tests were conducted in order to compare the analytical prediction with the experimental results. The laminates were made using unidirectional carbon/epoxy prepreg sheet (T800H/#2500, Toray industries, Inc.) and a vacuum bagging autoclave method. A quasi-isotropic stacking sequence of [0/45/−45/90] was used in the laminates. The tensile specimens were straight sided, 1·3 mm thick, 25 mm wide and 210 mm long, with end tabs. Tensile tests were conducted using an Instron testing machine. The interlaminar delamination of the laminates which were loaded to 82% of their tensile strength is shown in Fig. 7. Interlaminar delamination was

observed at −45/90 interlamina only. From this result, it can be concluded that the occurrence of interlaminar delamination of the laminates can be predicted by an analytical model with transverse cracking.

4 NUMERICAL ANALYSIS OF INTERLEAVED LAMINATES

4.1 Analytical model

Using the above analysis method the onset of interlaminar delamination can be predicted. The next step is to obtain an investigation method which prevents the onset of interlaminar delamination. According to Shiau and Chue[1] the interlaminar stress at the free edge of the composite laminates can be controlled by varying the fibre volume fraction. Kim[2] has shown that delamination of quasi-isotropic laminates can be prevented by reinforcing the free edges with glass-cloth woven fabric.

Another method of preventing delamination is by using a thermoplastic resin based film which is called an interleave. As an example, Lagace *et al.*[3] investigated the suppression effects of delamination by introducing a film adhesive interlayer.

In this study, the above analysis method was applied to quasi-isotropic CFRP laminates with polyethylene film interleaves. The stacking sequences of interleaved CFRP laminates are shown in Fig. 8. The shaded portions in this figure indicate film layers. For example, Type II has a film layer in each −45/90 interlamina. In this study, we ignored the change in the thickness of the laminate due to the presence of interleaved material. If the change in thickness is to be considered, then we must consider many other models which coincide with constituents of the laminates. To facilitate numerical analysis of interleaved CFRP laminates, the material constants of the resin layer were substituted for those of the interleaved film layer. The material constants of the films are given in Table 2. An analytical method of interleaved CFRP laminates was adopted for nonlinear analysis under tensile load. Using this method, each interlaminar stress and the development of failure at each interlamina was calculated. In this analysis, the load condition adopted was the incremental load method.

4.2 Results and discussion

The Mises equivalent stress distributions of each laminate are shown in Fig. 9. This distribution confirms the analysis results that the delamination occurs at an applied load of 1500 kgf. In this figure, the estimation of stress distribution is restricted to −45/90 interlamina mainly because interlaminar delamination was observed in this interlamina only. Except for Type II, the Mises stress of all other types becomes high close to transverse cracking. Especially, Type III indicates the highest stress in the neighbourhood of transverse cracking. Moreover, Type III has a non-symmetric stress distribution compared with Type I and Type IV.

Each interlaminar stress component of these laminates was also investigated. *Distributions of interlaminar normal stress* σ *and interlaminar*

Table 2. Material constants of interleaved films

Elastic modulus (kgf/mm)	3.0
Poisson's ratio	0.3

Fig. 9.   Mises's equivalent stress distribution of interleaved CFRP laminate.

| TYPE I | TYPE II | TYPE III | TYPE IV |
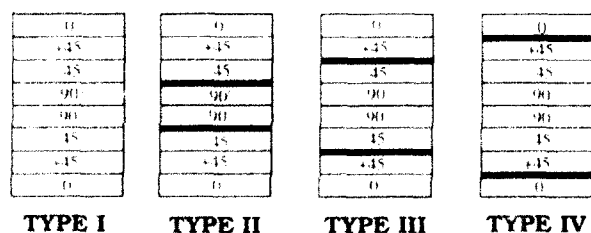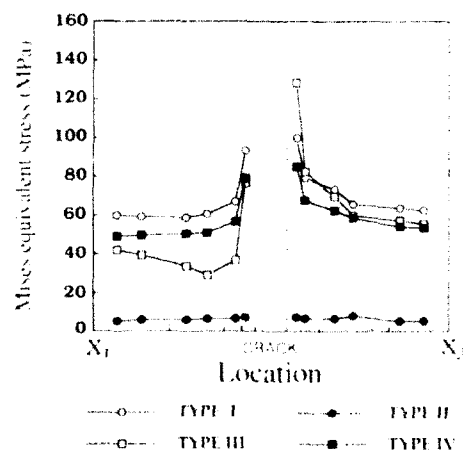
Fig. 8.   The stacking sequence of interleaved CFRP laminate.
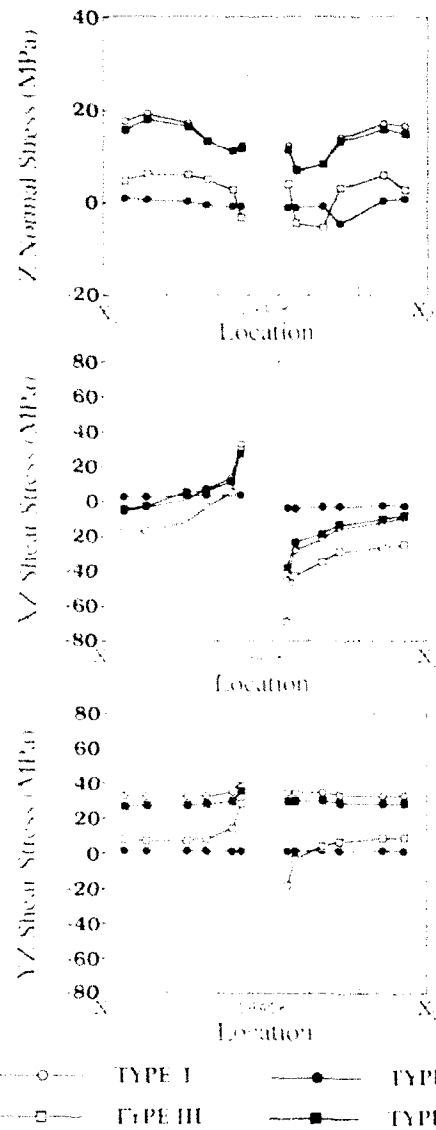
Fig. 10. Interlaminar stress distribution of interleaved CFRP laminate.

shear stress τ_{yz} and τ_{xz} are shown in Fig. 10. In the case of Type II, interlaminar stress is almost zero in all locations with respect to transverse cracking. Type IV indicates a similar stress distribution to Type I. In the case of Type III both τ_{yz} and τ_{xz} vary with respect to transverse cracking.

The fracture development of each resin layer is shown in Fig. 11. In Type II, the failure area is confined to only the free edge of (45/−45) interlamina. As a result, it is expected that the failure load of Type II is higher than that of Type I. In the case of Type IV, the failure area occurs at the free edges of (45/−45) and (−45/90) interlaminae. The failure area increases and coalesces with the neighbouring transverse cracking. The distribu-

tion of failure area is similar to that of Type I. But the growth of failure area is slower than that of Type I. Therefore, a higher failure load is expected in the case of Type IV compared to Type I. In the case of Type III, the failure area initially occurs near the transverse cracking and was not observed at the free edge of the laminate.

From these results, it seems that the stacking sequence for interlaminar delamination is only Type IV. Also, it is considered that Type III has a unique fracture process since the development of the failure area at (−45/90) interlamina differs from other laminates. Therefore, the fracture process of Type III was investigated in more detail. The tensile stress of each layer σ_i is tabulated in Table 3. The tensile stress values presented in this table were calculated for each layer in the vicinity of transverse cracking. The stress of Type III at the −45° layer is the highest compared to all other layers. Hence interlaminar delamination does not occur in Type III, however transverse cracking develops in the 45° layer. In the case of Type III, the layers between the interleaved film layers deformed independently since the transmission of shear force was suppressed by the film layers. Consequently, this laminate undergoes in-plane shear deformation which results in the loss of in-plane isotropy. It seems that this phenomenon is one of the reasons why the 45° layer of Type III breaks rapidly compared with other laminates. Hence it is expected that the strength of Type III laminates decreases.

A tensile test was carried out in order to compare experimental results with prediction results. The fracture aspects of Type II and Type IV which was loaded to 82% of tensile strength are shown in Fig. 12. Delamination was not observed in Type II whereas delamination of Type IV at (−45/90) interlamina was observed. Interlaminar delamination has not been observed in Type III. The tensile properties of interleaved laminates are tabulated in Table 4. The predicted estimates of ultimate tensile load agreed with the experimental results. It can be concluded that this analysis method can be applied to interleaved CFRP laminates.

5 CONCLUSIONS

Based on the results of this study, the following conclusions can be drawn.

1. It has been shown that by considering the whole geometry of the laminate, the fracture

	(0/45)	(45/-45)	(-45/90)
Type I			
Type II			
Type III			
Type IV			

1500 kgf   1800 kgf   2100 kgf
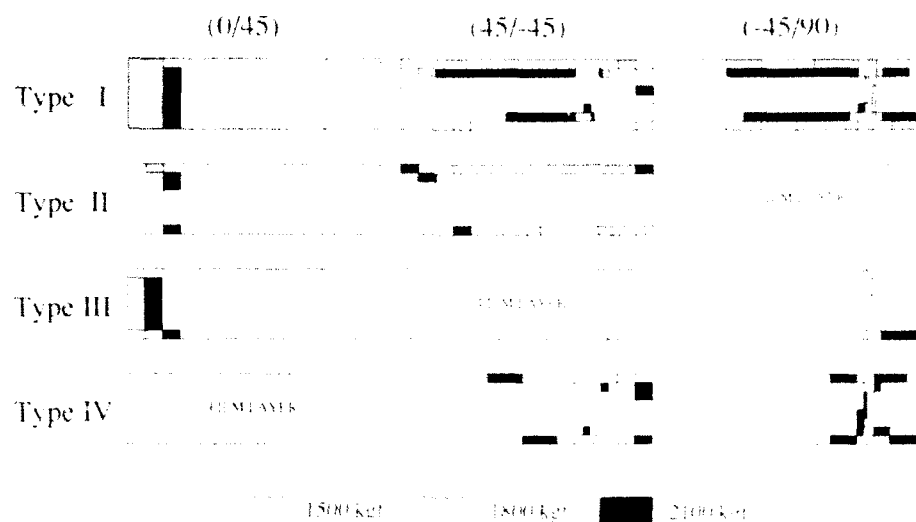
Fig. 11.   Fracture development on each interleaved CFRP laminate

Table 3. X normal stress in the vicinity of transverse crack-ing on each interleaved CFRP laminate

	X normal stress MPa			
	Type I	Type II	Type III	Type IV
0 layer	2117	2223	2202	2249
45 layer	262	262	214	212
-45 layer	308	259	358	261
90 layer	Transverse crack			

Table 4   Tensile properties of interleaved CFRP laminates

	Type I	Type II	Type III	Type IV
Maximum load kN	21.2	26.1	25.1	29.1
Coefficient of variation	8.7	3.8	2.8	1.9
Occurrence of delamination	Yes	No	No	Yes

Type II

Type IV

Damping Material Sheets — Cross Section (Type II)

Delamination — Damping Material Sheets — Cross Section (Type IV)
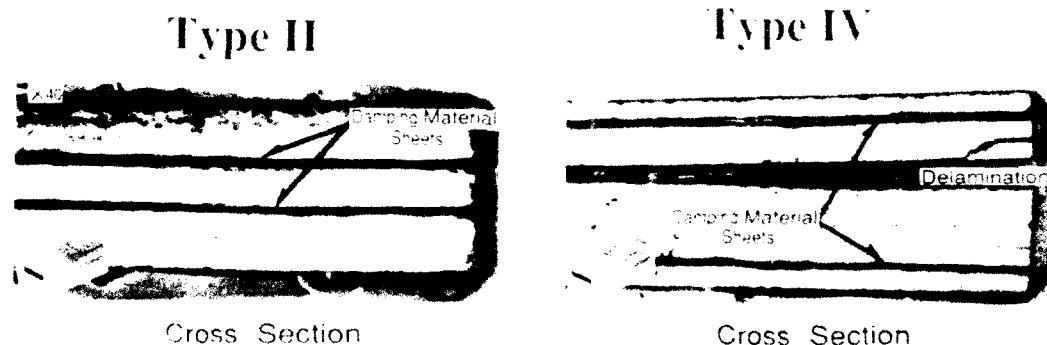
Fig. 12.   Fracture aspects of interleaved CFRP laminate Type II, Type IV

behaviour of the laminate can be predicted accurately using three-dimensional model-ling.

2. For accurate modelling, it is essential to consider the presence of the interlaminar resin layers and transverse cracking.

3. This three-dimensional analysis method is valid for understanding the delamination behaviour of interleaved CFRP laminates. Also the position of the interleaved film

layer with respect to laminate thickness is important in determining the delamination behaviour.

REFERENCES

1. Hong, C. S. & Kim, D. M., Mixed mode free-edge delamination on composite laminates. COMPOSIT Proceedings of ICCM/VIII, 28-D, 1991

2. Kobayashi, A., Ogihara, S. & Takeda, N., Microscopic studies on temperature-dependent failure process of conventional and toughened cross-ply laminates. *COMPOSITE Proceedings of ICCM/VIII*, 28-H, 1991.

3. Yalvac, S., Yat, L. D. & Wetters, D. G., Transverse ply cracking in toughened and untoughened graphite/epoxy and graphite/polycyanate crossply laminates. *Journal of Composite Materials*, 25 (12) 1991 1635–68.

4. Belglund, L. A., Varna, J. & Yarn, J., Transverse cracking and local delamination in $0_4/90_n$ and $90/0_1$ carbon fiber/toughened epoxy laminates. *Journal of Reinforced Plastics and Composites*, 11 (6) 1992 643–60.

5. Shuart, M. J., An analysis of shear failure mechanisms for compression-loaded $\pm \theta$ laminates. *Journal of Composite Materials*, 23 (3) 1989 251–64.

6. Garg, A. C., The fracture mechanics of some graphite fibre-reinforced epoxy laminates. Part 1: quasi-isotropic laminates *Composites*, 17 (2) 1986 141–9.

7. Harikumar, H. K. & Krishna Murty, A. V., On modeling of laminates containing free-edge delaminations. *Composite Science and Technology*, 42 1991 393–411.

8. Kondo, K., Energy release rate of delamination at transverse crack tips. *Proc. Japan-US CCM-IV*, ed. A. Kobayashi. Tokyo, 1990, pp. 169–76.

9. Pipes, R. B. & Pagano, N. J., Interlaminar stresses in composite laminates under uniform axial extension. *Journal of Composite Materials*, 4 1970 538–48.

10. Kim, R. Y. & Soni, S. R., Failure of composite laminates due to combined interlaminar normal and shear stress

    Proc. Japan-US, CCM-III, ed. K. Kawata, S. Umekawa & A. Kobayashi. Tokyo, 1986, pp. 341–50.

11. Chen, J. K. & Sun, C. T., Nonlinear analysis of interlaminar stress in graphite/epoxy laminates with and without delamination cracks. *Composite Structures*, 8 1987 271–85.

12. Chapin, C. M. & Joshi, S. P., Variation of residual thermal stresses in graphite/epoxy laminates. *COMPOSITE Proceedings of ICCM/VIII*, 30-D, 1991.

13. Hong, C. S. & Kim, K. S., An analysis of free-edge delamination in laminated composites under uniform axial strain. *ICCM-IV*, ed. T. Hayashi, K. Kawata & S. Umekawa. Tokyo, 1982, pp. 261–8.

14. Hull, D., *An Introduction to Composite Materials*, 1987.

15. Craddock, J. N., Behavior of composite laminates after first-ply-failure. *Composite Structures*, 3 1988 187–200.

16. Jemura, M. & Yamada, N., *Zairyo*, 24 257 1970 54–61 (in Japanese).

17. Shiau, L. C. & Chue, Y. H., Free edge stress reduction via variation of fiber volume fraction. *COMPOSITE Proceedings of ICCM/VIII*, 31-D, 1991.

18. Kim, P. Y., Prevention of free-edge delamination. *28th National Sampe Symposium*, 1983, pp. 200–9.

19. Lagace, P. A., Weems, D. B. & Brewer, J. C., Suppression of delamination via an interply adhesive layer. *Proc. Japan-US CCM-III*, ed. K. Kawata, S. Umekawa & A. Kobayashi. Tokyo, 1986, pp. 323–30.

Analysis of stiffness loss in cross-ply composite laminates

T. E. Tay & E. H. Lim

Department of Mechanical and Production Engineering, National University of Singapore, 10 Kent Ridge Crescent, Singapore 0511

The behaviour of laminated composite plates beyond first-ply failure has been the subject of much research work. It is well known that generally, the load-bearing capability of laminated composite plates can remain significant despite the presence of some damage in the plies. Traditionally, the ply-discount method has been used among analysts and designers, although the approach is generally regarded as too conservative. It is therefore desirable to develop models for the prediction of the mechanical properties of damaged composite laminates at various applied loads, and to be able to correlate the changes in properties with the amount of damage and cracking within each constituent ply. Generally, if the models are to be useful as predictive tools, they must be capable of not only sufficiently describing the damage state but also the nature of the damage evolution with loading. This 'evolution law' is often obtained through fracture analysis, although it should be noted that the diffused nature of cracks and the multiplicity of failure modes in composites in general greatly complicates the analysis. The problem of transverse matrix cracking in cross-ply laminates under uniaxial tension is considerably simpler because it is essentially dominated by mode I fracture. Thus it is necessarily the first step for any model aiming to predict stiffness losses in composite laminates. In this paper, a constitutive model of the damage state for composite laminates, first proposed by Allen et al., is used with a damage evolution criterion based on strain energy to predict the stiffness loss due to matrix cracking in cross-ply laminated composite plates. Although the constitutive model does not require the determination of many constants, the state of damage is described by a vector of internal state variables (ISV), which contains information on the crack geometry and fracture modes. A series of parametric finite element analyses was performed to determine the effects of relative ply thicknesses, crack density and crack opening profile on the vector of ISVs. A computer algorithm was written for the analysis of cross-ply laminates based on the damage evolution criterion proposed in this work. The results of the analysis compare favourably with experimental measurements of progressive stiffness loss in damaged cross-ply graphite-epoxy laminates obtained from other researchers.

INTRODUCTION

The process of damage evolution in composite laminates is generally very complex due to the multiplicity of failure modes such as transverse cracking, fibre-matrix interface debonding, fibre breakage and delamination. The use of fracture mechanics, especially in the realm of linear elastic fracture, has been very successful and well established for isotropic engineering materials because fracture in these materials (for linear elastic cases) can often be adequately characterized by a single parameter (for example, the stress intensity factor). However, attempts to apply similar fracture mechanics tools in the analysis of composite laminates have only met with limited success. Much of the effort at characterizing fracture in composites has been directed at the measurement of fracture toughnesses in laboratory test specimens. These serve as useful guides for comparison between different composite material specimens, but it remains unclear how the data from such tests can be used for the analysis of fracture in structural components. One reason is the considerable difficulty in determining the complex interactions between different failure modes and the effects of component size and geometry.

There have been attempts to model damage in composite laminates using damage and fracture theories.[1-4] For some types of diffused or distributed damage, a constitutive representation of the damage state may be most appropriate.[1] The use of fracture mechanics, however, is still necessary in order to establish criteria for damage progression. Numerous phenomenological models for the prediction of stiffness loss in composite laminates are available. Among the better known models based on continuum mechanics are those developed by Talreja[1] and Kachanov[2] (and applied to composite plates by Allen et al.[3]). These are particularly suitable for cases where the damage is fairly uniformly distributed throughout the lamina (e.g. transverse matrix cracking). However, the equations involved usually contain many constants which are not easily determined experimentally except in the simplest of cases. Hashin[5] developed an approximate variational method with admissible stress functions for cross-ply laminates, but the analysis has not been extended to laminates with other stacking sequences. One of the earliest developments is the shear lag model proposed by Highsmith and Reifsnider.[6] Although this model is quite simple and has been applied successfully to cross-ply laminates, it assumes the existence of an imaginary shear transfer layer whose properties are not readily defined or obtained through experiments. Experimentally, the monitoring and observation of damage progression in composites also involve cumbersome procedures.[6] The specimens are usually removed from the test rig after a predetermined number of fatigue cycles, dye-penetrated and X-rayed in order to determine the crack densities. It is not known whether the process of repeated dyeing and cleaning has any effect on the results. In any case, the procedure becomes impractical for even moderately thick laminates or laminates with more complicated stacking sequences other than cross-plies since adequate dye-penetration can no longer be ensured. It is not surprising then, that most published experimental data on rack densities have been limited to thin cross-ply laminates.

In this paper, a computer code based on the constitutive model of damage proposed by Kachanov[2] and Allen et al.[3] is used in conjunction with a simple kinematic representation of transverse crack profile to predict the stress–strain behaviour of damaged cross-ply laminates. A damage evolution criterion based on strain energy considerations is also proposed.

REPRESENTATION OF THE DAMAGE STATE

Currently, there are two well-known models on damaged composite laminates based on continuum damage mechanics (CDM). The first is due to Talreja,[1] who used a first order tensor of internal state variables (ISV) to describe the damage modes. By assuming the energy density in a cracked volume to be a function of the strain tensor and a damage vector, a set of constitutive equations with observable strains and an effective stress tensor can be constructed. However, this method requires the determination of ten constants for a general laminate containing matrix cracks. The number of constants is reduced to four in the case of cross-ply laminates.

A second model used by Allen et al.[3] also employs a set of ISVs described by second order tensorial quantities, originally proposed by Kachanov.[2] This model appears to require fewer constants and explicitly incorporates the crack kinematic features into the formulation for the ISVs. For these reasons, it is used in the work presented in this paper. In this model, the stress–strain relationship of a small volume of damaged material at ply level is assumed adequately described by the equation

$$\sigma_{ij} = C_{ijkl}\,\varepsilon_{kl} + I^{n}_{ijkl}\,\alpha^{n}_{kl} \qquad 1$$

where σ_{ij} are the applied stresses, C_{ijkl} are the stiffnesses of the undamaged material, ε_{kl} are the strains, I^{n}_{ijkl} are elements of the damage matrix, α^{n}_{kl} are the internal state variables, and $\eta = 1, 2, 3, \ldots$, refers to the damage modes. It was shown[3] that to a first approximation,

$$I^{n}_{ijkl} \approx C_{ijkl} \qquad 2$$

This assumption simplifies the theory considerably, leaving the unknown ISVs, α^{n}_{kl}, yet to be determined. Note that the entire description of the damage state is embedded in the second term of eqn (1). However, it is important to realize that eqn (1) does not provide any information on how that state of damage has been attained, i.e. the history of damage accumulation. Thus it is necessary to turn to fracture mechanics in search of suitable criteria for damage growth. Equation (1) is sufficiently general for use in the classical lamination theory (CLT) or some higher order theories. If the former is used, the damage in each ply can then be modelled separately.

The vector of resultant forces $\{N\}$ can be expressed in terms of the laminate midplane

strains $\{\varepsilon^o\}$ in the absence of bending–stretching coupling by:

$$\{N\} = [A]\{\varepsilon^o\} + \{D\} \tag{3}$$

where $[A]$ is the stiffness matrix of the laminate, defined for the kth ply by

$$A_{ij} = \sum_{k=1} (\bar{Q}_{ij})_k t_k \tag{4}$$

Here, $(\bar{Q}_{ij})_k$ are the transformed reduced material stiffnesses of the orthotropic layer, and t_k is the thickness of the ply. The following vectors are defined:

$$N = \int \{\sigma_x, \sigma_y, \tau_{xy}\}^T dz \tag{5}$$

$$\varepsilon^o = \int \{\varepsilon_x^o, \varepsilon_y^o, \gamma_{xy}^o\}^T dz \tag{6}$$

$$D = \sum \bar{I}_k \bar{a}_k t_k \tag{7}$$

where the subscripts x and y refer to the global co-ordinate system, while the subscripts 1 and 2 refer to the longitudinal and transverse material directions, respectively. The vector $\{D\}$ is known as the damage vector. t_k is the thickness of the kth ply and $\bar{a}_k$ is the transformed vector of internal state variables ISVs,[2,3] defined as

$$\bar{a}_k = \{a_{11}^T, a_{22}^T, a_{12}^T\} \tag{8}$$

The vector of ISVs can also be expressed in the material co-ordinate system:

$$a_k = \{0, a_{22}^T, a_{12}^T\} \tag{9}$$

It follows from eqn (2) that to an approximation,[3] if only modes I and II fracture is considered, the matrix $[I]_k$ in material co-ordinates is given by

$$I_k \approx - \begin{bmatrix} 0 & Q_{12} & 0 \\ 0 & Q_{22} & 0 \\ 0 & 0 & Q_{66} \end{bmatrix}_k \tag{10}$$

The matrix $[\bar{I}]_k$ is the transformed matrix in global co-ordinates. The ISVs $\{a\}_k$ embody the effects of crack geometry and distribution. The ISV for mode I cracking is defined as

$$a_{22}^T = \frac{1}{v} \int_s u_{22}^T n_{22}^T \, ds \tag{11}$$

where u_{22}^T is the crack opening displacement, n_{22}^T is the normal to the crack surface and v the unit crack volume. The integral is evaluated over the entire crack surface. The equivalent ISV for mode II may also be similarly defined:

$$a_{12}^T = \frac{1}{v} \int u_{12}^T n_{12}^T \, ds \tag{12}$$

where u_{12}^T is the crack sliding and n_{12}^T is a unit vector in the plane of the crack surface in the direction of shear.

Thus it is seen that the damage state is assumed adequately described by the damage vector $\{D\}$. The evaluation of the ISVs according to eqns (11) and (12) requires knowledge of the crack opening and sliding profiles, and the density at each load level. The former is obtained through FE analysis while the crack density can be obtained through a suitable damage evolution criterion. For cross-ply laminates, fracture in the transverse plies is dominated by mode I and therefore only the mode I ISV is relevant to the work presented here.

EVALUATION OF INTERNAL STATE VARIABLE

We assume that the transverse cracks within a damaged layer are uniformly distributed and that the behaviour of the laminate can be adequately represented by a repetitive unit volume of material containing a transverse crack as shown in Fig. 1. A series of finite element parametric studies has been performed in order to establish the effects of crack opening profiles, relative ply thicknesses and crack density on the stiffness of
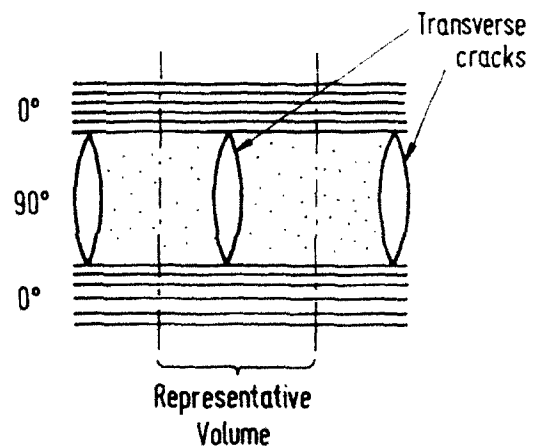
Fig. 1. Transverse cracks in 90° ply.

the laminate. Figure 2 shows an FE model of a quarter portion of the representative volume previously defined in Fig. 1. The region ABFC represents the 0° ply and FCED the 90° ply. The edges AB and ED are restrained from movement in the vertical direction and AF is restrained in the horizontal direction. A uniform displacement in the positive x-direction is applied to BCD. The half crack length extends from E to F, with the cracktip at F, which is at the interface between the 0° and 90° layers. The entire model consists of eight-noded isoparametric elements with ortho-tropic material properties obtained from Ref. 5 and given in Table 1.

The following non-dimensionalized parameters are defined:

$$\rho = t_i/l \qquad (13)$$

$$\theta = t_1/t_2 \qquad (14)$$

$$\delta = u_o/t_2 \qquad (15)$$

$$t = t_1 + t_2 \qquad (16)$$

where t_1 and t_2 are the thicknesses of the 0° and 90° plies, respectively. l is the distance between two adjacent transverse cracks, and u_o is the maximum crack opening displacement. Hence ρ and δ may be regarded as non-dimensionalized crack density and maximum crack opening displacement (COD), respectively. Since the analysis is linearly elastic, δ is directly proportional to the applied strain.

The results of the analysis are presented in Figs 3 and 4 for both graphite–epoxy and glass–epoxy

systems. From Fig. 3, it is seen that as the crack density ρ increases, δ decreases rapidly for a constant applied strain. On the other hand, Fig. 4 shows that as the ratio of the thickness of the 0° ply to that of the 90° ply increases, δ approaches a finite constant value. Although the curves are obtained for one value of applied strain, the results at other strains can be obtained by linear scaling.

Figure 5 shows the variation of the non-dimen-sionalized crack opening profile across the thick-ness of the 90° ply, obtained from the FE analysis. A fourth order polynomial fit of the nodal dis-placements is obtained such that

$$\frac{u(q)}{u_o} = 1 + C_1 q^2 + C_2 q^4 \qquad 17$$

where

$$q = \frac{2z}{t_2} \qquad 18$$

Substituting eqn (17) into eqn (11), performing the
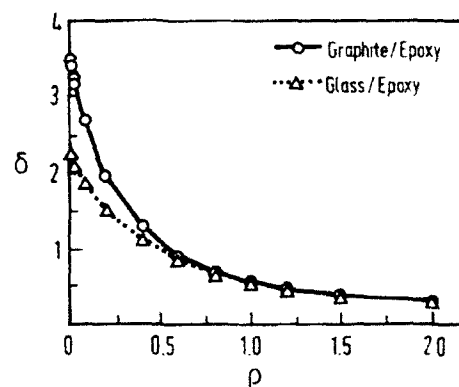
Fig. 3. Effect of crack density ρ on δ $\theta = $

Fig. 2. Finite element mesh.

Table 1. Material properties used in FE analysis, from Ref. 5

	E_1 (GPa)	E_2 (GPa)	G_{12} (GPa)	ν_{12}
Graphite–epoxy	142·0	9·85	4·48	0·3
Glass–epoxy	41·7	13·0	3·4	0·3
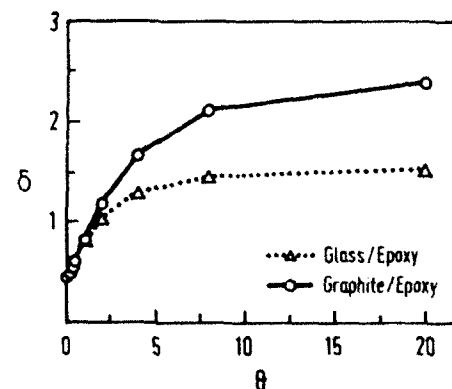
Fig. 4. Effect of thickness ratio θ on δ $\rho = 1$.
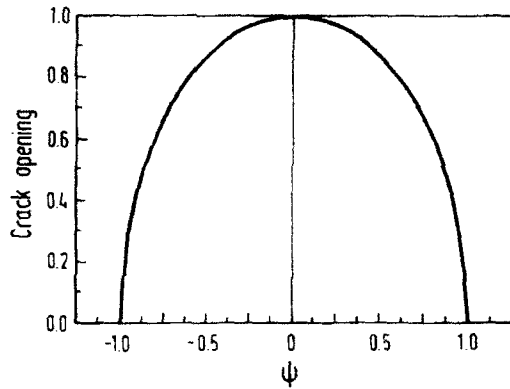
Fig. 5. Non-dimensionalized crack opening profile across thickness of 90° layer.

integration and assuming that the crack extends through the width b of the 90° ply, we have

$$a_{22} = \frac{u_o}{bl} \frac{b}{2} \int_{-1}^{1} (1 + C_1 q^2 + C_2 q^4) \, dq$$

$$= \frac{u_o}{l} (1 + C_1/3 + C_2/5) \tag{19}$$

As determined from Fig. 5, the constants C_1 and C_2 are -0.029 and -0.98, respectively. C_1 is negligible compared to unity, so that to a good approximation, eqn (19) reduces to

$$a_{22} = u_o \xi \tag{20}$$

where ξ is the crack density, defined as

$$\xi = \frac{1}{l} \tag{21}$$

Thus it is seen that the ISV for mode I transverse matrix cracking is completely determined if the maximum COD and the crack density are known.

DAMAGE EVOLUTION

The model is completed with the specification of the manner in which the damage accumulates with applied load. At any stage in the loading history, it is necessary to obtain ξ, the crack density. This is by no means a trivial exercise and different approaches have been suggested by researchers, although most employ fracture mechanics in some form. Variational-type analyses were used by Hashin[8] and Nairn,[9] although these were invariably restricted to cross-ply laminates. An interesting application of probabilistic fracture mechanics

was reported by Wang *et al.*[10] but this method also required extensive testing of a large number of specimens to determine the material coefficients used in the probability functions. Much research remains to be done in the formulation of a damage evolution criterion that is not only capable of predicting crack densities in cross-ply laminates, but also in laminates with general stacking sequences.

In this paper, a fracture or damage evolution criterion based on strain energy is proposed. Consider a symmetric cross-ply laminated composite plate of width b and length L, with the lay-up configuration $[0_p^\circ/90_q^\circ]_s$, where the subscripts p and q are integers. As the laminate is being loaded uniaxially in tension, the stress–strain curve obtained is linear until first-ply failure at A (see Fig. 6). A transverse crack is then introduced in the 90° layer and the crack density determined from eqn (21). The maximum COD corresponding to this crack density and laminate geometry can be obtained from the curves shown in Figs 3 and 4. These values are used in the computation of a_{22} according to eqn (20) and substituted into eqns (3) and (7). The result is a reduction in the effective stiffness of the laminate in the direction of the applied load, and this is represented by OF in Fig. 6. Upon further application of strain ϵ_o, the load path FB now reflects this reduction in stiffness. Note that the slope of the line OI corresponds to the stiffness of the laminate as determined by the ply discount method, where the contribution of the 90° layer to the load-bearing capacity of the laminate has been neglected. Hence OI represents the lower limit of the stiffness curves as far as damage in the 90° layer is concerned. Further fracture is assumed to have
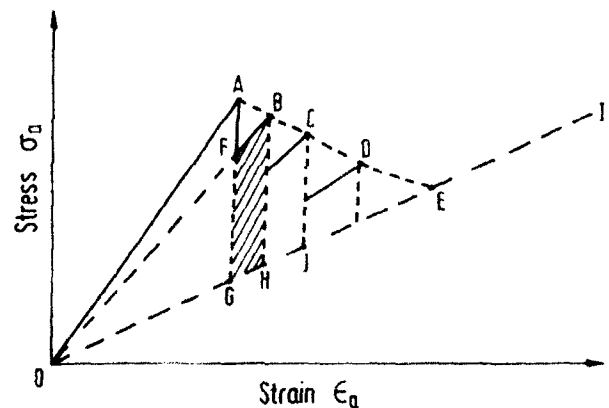
Fig. 6. Analysis of stiffness loss in damaged $[0_p^\circ/90_q^\circ]_s$ laminates.

occurred when, upon further application of strain, the area FBHG reaches a critical value. An additional transverse crack is formed and the effective stiffness further reduces to the slope of OC, which is calculated from eqn (3) and the updated a_{22}. Denoting the area FBHG by $(dW/dv)_i$ and defining the quantity U_i such that

$$U_i = \frac{tL}{t_2}\left(\frac{dW}{dv}\right)_i \tag{22}$$

a transverse crack is assumed to have formed when

$$U_i \geq G_{1c} \tag{23}$$

where G_{1c} is the mode I energy release rate for the formation of a transverse crack. This simple criterion can be easily implemented in any algorithm which employs lamination theory. The process of determining the transverse crack density is repeated for each successive matrix cracking using the same value of G_{1c}. Hence in Fig. 6 a series of points (A, B, C, D, ... , E) can be generated until the limit OI is reached, beyond which matrix cracking in the 90° layer no longer significantly influences the laminate stress-strain behaviour. As a typical analysis usually involves a large number of cracks, a computer code has been written to perform the calculations. It is noted that in practice, the intervals between the points A, B, C, etc., are very small and the curve appears smooth rather than discontinuous as shown schematically in Fig. 6.

COMPARISON WITH EXPERIMENTAL STRESS-STRAIN CURVES

The predictions of stiffness loss with damage for three graphite–epoxy laminates and one glass–epoxy laminate are compared with experimental stress–strain curves obtained by Daniel and Lee[11] (see Figs 7–10). Figures 7 and 9 show good agreement between theory and experiment, although the predicted curves have reached the limit determined by the ply discount theory at the applied strain of about 0·01. Both experimental curves from Daniel and Lee[11] show a stiffening of the laminates at high strains. This phenomenon is particularly pronounced in the $[0_2°/90_3°]_s$ laminate (Fig. 9) and may be due to stretching of the reinforcing fibres in the 0° plies. This effect is not considered in the present analysis. For the $[0°/90_3°]_s$ laminate, Fig. 8 shows that initially, the
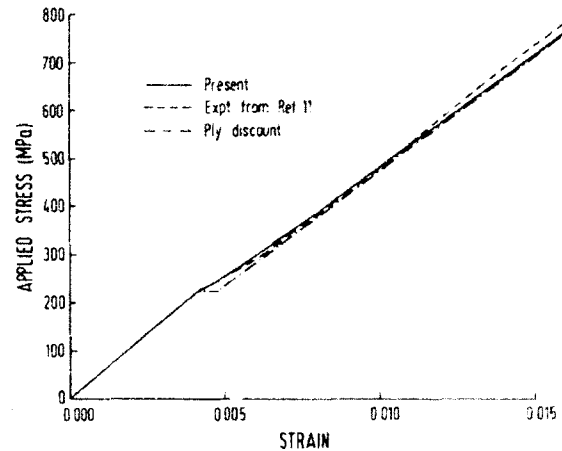
Fig. 7. Stress–strain curve for $[0/90]_s$ graphite-epoxy laminate.
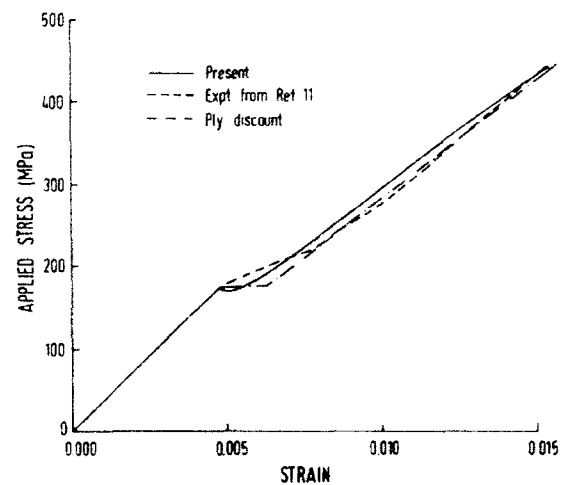
Fig. 8. Stress–strain curve for $[0/90]_s$ graphite-epoxy laminate.
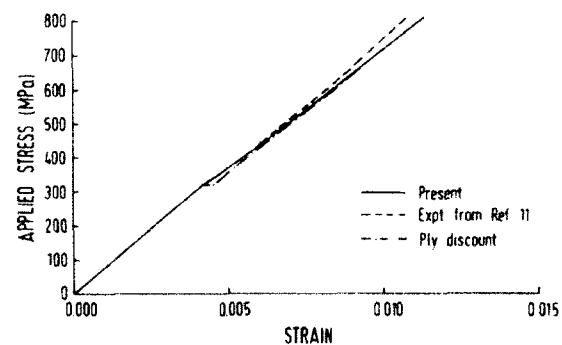
Fig. 9. Stress–strain curve for $[0_2/90_2]_s$ graphite-epoxy laminate.

prediction of stiffness loss after first-ply failure is greater than experimentally observed. However, better agreement is achieved with increasing applied strain. In this case, the predicted curve
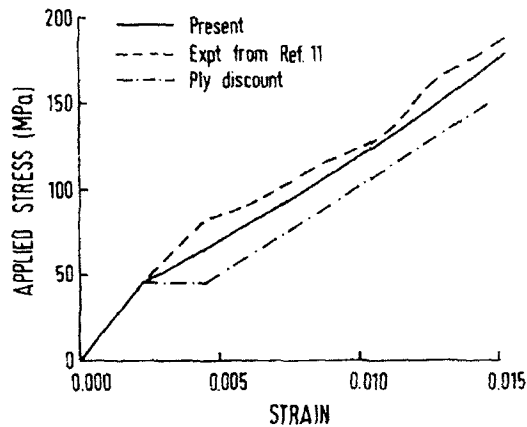
Fig. 10. Stress–strain curve for $0°/90°$, glass–epoxy laminate.

coincides with the ply discount prediction at an applied strain of about 0·018. The value of G_{Ic} used for transverse cracking of graphite–epoxy laminates is 228 J/m².[12] Finally, a comparison is also made with a $[0°/90°]_s$ glass–epoxy laminate in Fig. 10. The value of G_{Ic} in this case is taken to be 250 J/m².[13] The experimental stress–strain curve shows distinct knees. It is seen in Figs 7–10 that the predictions from the current model agree reasonably well with the available experimental data.

CONCLUSION

A computer algorithm based on a constitutive model of damage has been written and a criterion for damage progression in the 90° layer in cross-ply laminated composite plates has been proposed. The finite element method has been used to determine the effect of damage accumulation on the ISV used in the laminate equations. The predicted stress–strain curves compare reasonably well with experimental curves obtained from other researchers. Work is currently in progress to predict the stress–strain behaviour of constrained angle-ply laminates.

REFERENCES

1. Talreja, R., Internal variable damage mechanics of composite materials. In *Yielding, Damage and Failure of Anisotropic Solids*, EGF5, ed. J. P. Boehler. Mechanical Engineering Publications, UK, 1990, pp. 509–33.
2. Kachanov, M., Continuum theory of media with cracks. *Mekhanika Tverdogo Tela*, ASCE, 7 1972 54–9 in Russian.
3. Allen, D. H., Harris, C. E. & Groves, S. E., A thermo-mechanical constitutive theory for elastic composites with distributed damage — theoretical development. *Int. J. Solids Struct.*, 23 9 1987 1301–18.
4. Hashin, Z., Analysis of cracked laminates: a variational approach. *Mech. Mater.*, 4 1985 121–36.
5. Highsmith, A. L. & Reifsnider, K. L., Stiffness reduction mechanisms in composite laminates. In *Damage in Composite Materials*, ASTM STP 775, ed. K. L. Reifsnider. ASTM, Philadelphia, PA, 1982, pp. 103–17.
6. Masters, J. E. & Reifsnider, K. L., An investigation of cumulative damage development in quasi-isotropic graphite–epoxy laminates. In *Damage in Composite Materials*, ASTM STP 775, ed. K. L. Reifsnider. ASTM, Philadelphia, PA, 1982, pp. 40–62.
7. Crossman, F. W. & Wang, A. S. D., The dependence of transverse cracking and delamination on ply thickness in graphite–epoxy laminates. In *Damage in Composite Materials*, ASTM STP 775, ed. K. L. Reifsnider. ASTM, Philadelphia, PA, 1982, pp. 40–62.
8. Hashin, Z., Analysis of stiffness reduction of cracked cross-ply laminates. *Engng Fract. Mech.*, 25 1986 771–8.
9. Nairn, J. A., The strain energy release rate of composite microcracking: a variational approach. *J. Comp. Mater.*, 23 1989 1106–29.
10. Wang, A. S. D., Chou, P. C. & Lei, S. C., A stochastic model for the growth of matrix cracks in composite laminates. *J. Comp. Mater.*, 18 1984 239–54.
11. Daniel, I. M. & Lee, J. W., Damage development in composite laminates under monotonic loading. *J. Comp. Technol. Res.*, 12 1990 98–102.
12. Wang, A. S. D., Fracture mechanics of sublaminate cracks in composite materials. *Comp. Tech. Rev.*, 6 1984 45–62.
13. Laws, N. & Dvorak, G. J., Progressive transverse cracking in composite laminates. *J. Comp. Mater.*, 22 1988 900–16.

High strain rate compressional behavior of stitched and unstitched composite laminates with radial constraint

S. T. Jenq & S. L. Sheu

Institute of Aeronautics and Astronautics, National Cheng Kung University, Tainan, Taiwan.

This paper is concerned with the high strain rate compressional behaviour of glass/epoxy (Hy-E 9134B, Fiberite, USA) composite laminates with or without stitching reinforcement by untwisted Kevlar-49 threads (1140 denier). The split Hopkinson pressure bar (SHPB) apparatus is used in performing the high strain rate tests. Test data are analyzed in a manner similar to that reported by Hauser Exp. Mech., 6 (1966) 395. Specimens are tested at strain rates up to 10^3 s^{-1}. Unidirectional laminated parallelepiped samples are impacted along their fiber direction. Their high velocity compressive ductility is observed. Both $[0°]_{24}$ and $[0°/90°]_{6s}$ glass/epoxy circular specimens with disc diameters of 10 and 50·8 mm are transversely impacted by an input bar in order to study their high strain rate behavior. Moreover, two sets of stitched circular specimens with disc diameters of 10 and 50·8 mm are also examined. The effect of strain rate and radial constraint on the dynamic properties of stitched and unstitched GFRP laminated specimens and their associated damage patterns are described.

INTRODUCTION

Laminated composites have been widely used in such light weight and high strength structures as ground transportation vehicles, airplanes, and space satellites. Accordingly, there is a need for a detailed characterization of the behavior of fiber-reinforced composites subject to dynamic loading.[1] Although many invaluable papers emphasizing the dynamic behavior of metallic alloys can be found in the literature, and also in the proceedings of various conferences,[2-5] a limited amount of work, however, emphasizes the high strain rate behavior of laminated composites. For an extensive summary of material behavior at high strain rates, the reader is referred to Zukas et al.[6] A brief summary of the work related to the current research follows.

Sierakowski and Nevill,[7] working with an experimental program that systematically evaluated the deformation and fracture of steel wire reinforced epoxy composite systems subjected to impact loading, found that the rate effects depend upon composite constituent properties, geometric arrangement, volume fraction of reinforcement and the size of the reinforcing fibres. In addition, they found that maximum failure stress was dependent upon wire size, the volume percent of filament reinforcement and strain rate.

Harding and Welsh[8] examined a number of experimental techniques that had been previously employed in determining the mechanical behavior of composites under tensile impact loading. With a modified version of the tensile split Hopkinson pressure bar (SHPB) apparatus for tensile impact testing of carbon fibre reinforced plastics (CFRP) and glass fibre reinforced plastics (GFRP), they found that over strain rates of approximately 10^{-4}–10^3 s^{-1}, while the dynamic behavior of uni-directionally-reinforced CFRP is independent of strain rate, GFRP specimens demonstrated a dramatic increase in failure strength and elastic modulus at impact rates of strain.

Saka and Harding[10] also investigated the possible use of glass-reinforced layers in improving the impact resistance of all-carbon reinforced composite materials. Hybrid specimens with different weight fractions of carbon to glass were prepared and their impact responses at a tensile strain rate of about 1000 s^{-1} were compared with those obtained for similar all-carbon and all-glass specimens.

An extensive study of high velocity brittleness and ductility of Pyrex glass, metallic materials and composites was systematically conducted by

Kawata *et al.*[11] The dynamic tensile stress–strain relationships in the strain rate range up to 10^3 s^{-1} were obtained for these materials and their dynamic macromechanical characteristics discussed. In addition, the mechanisms of the various impact behavior/phenomena were discussed micromechanically. While GFRP specimens exhibited remarkable tensile high velocity ductility, CFRP specimens showed slight high velocity brittleness (strain rate insensitiveness).

The increase in flow stress relative to simple uniaxial compression for 2024-O aluminum plates subjected to symmetric quasi-static compression by steel punches and to dynamic compression by the Kolsky split Hopkinson bar was experimentally investigated by Liss *et al.*[12] For a specimen thickness to bar diameter ratio of 0·5, a constraint factor of 2·0 and 1·75 resulted under quasi-static and dynamic conditions, respectively.

The majority of the above mentioned work concentrated on the high strain rate tensile behavior of laminated composites. Note that the dynamic compressional behavior of GFRP with or without radial constraint at high strain rate loading has not been extensively studied. Although composite laminates possess high strength in the fiber direction, the lack of through-the-thickness reinforcement usually limits their use.[13] Improved delamination resistance in stitched composite plates subjected to low-velocity impact has been reported by Liu.[14] In 1985, Mignery *et al.*[15] demonstrated that although the effect of stitching on the ultimate tensile strength of graphite/epoxy laminates is not predictable, it can, however, effectively decrease the amount of delamination by checking the extent of cracking. Although the effect of stitching on the strength of composites and in improving their tolerance for impact damage has been reported,[16,17] the effect of stitching on the high strain rate behavior of composite laminates has however, been largely overlooked. The high strain rate compressional behavior of stitched and unstitched GFRP specimens with or without radial constraint is, accordingly, investigated in this work.

EXPERIMENTAL SETUP AND PROCEDURES

The high strain rate compressional tests were performed using the split Hopkinson pressure bar (SHPB) apparatus. A schematic drawing of the

test setup, containing an input, an output, and a throw-off bar, in addition to the associated electronic data recording devices is presented in Fig. 1. Each of the aforementioned bars possessed a diameter and length of 12·7 and 1000 mm, respectively and were made of DC53 steel alloy (Tatung Co., Taiwan). Prior to the tests, these bars were heat treated to a hardness of R_c 60–62, thereby ensuring that no permanent deformation would occur during the impact tests. The corresponding mechanical properties of these bars are summarized in Table 1. The striker bar (310 g), made of SAE 4130 steel, was fired onto the input bar by a pneumatic gun at impact velocities of 10–50 m/s. Two sets of unidirectional strain gauges (FLA-2-11, TML, Japan), with a gauge length of 2 mm, were installed on the input and output bars, respectively. In order to eliminate any bending waves, the gauges in each set were mounted, equi-distantly from the end of the bar, opposite to one another along their respective bar's axial direction. The specimen was placed between the input and output bars. The set of strain gauges mounted on the input bar were designed for measuring both incident and reflected stress waves, while their counterparts on
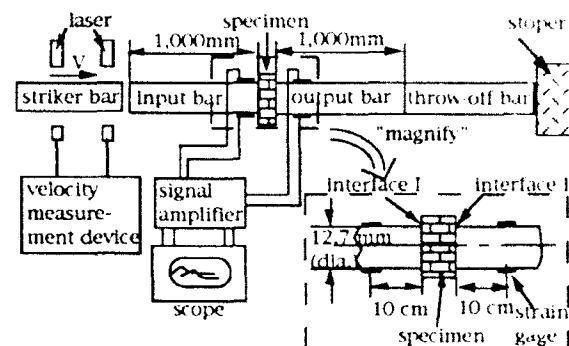
Fig. 1. A schematic representation of the split Hopkinson bar test setup.

Table 1. Mechanical properties and size of the striker, input and output bars

	Striker bar	Input and output bars
Material	SAE 4130	DC53[a] heat treated steel alloy
Diameter (d)	12·7 mm	12·7 mm
Length (l)	317 mm	1000 mm
Density (ρ)	7720 kg/m³	7870 kg/m³
Bar wave speed ($c = (E/\rho)^{1/2}$)	5174 m/s	5200 m/s
Yield strength	436·4 MPa	2880 MPa

[a]Manufactured by Tatung Co., Taiwan, ROC.

the output bar measured the transmitted stress wave. A four-channel signal amplifier and digital oscilloscope (4094C, Nicolet, USA) recorded these transient wave forms. The measured signals were then transferred through the general purpose interface bus (GPIB) to a personal computer for further analysis. In order to assure the accuracy and reproducibility of the measured wave forms, a set of split Hopkinson bar tests were performed on the 6061-O aluminum specimens. Satisfactory results were obtained.[18]

A total of four types of composite specimens were investigated. The geometry and fiber orientations of the samples are shown in Figs 2(a)–2(d). All tests were conducted at room temperature (approximately 25°C).

The first set of samples consisted of cured $[0°]_{64}$ glass/epoxy (Hy-E 9134B, Fiberite, USA) laminates that had been machined into rectangular parallelepipeds (8 × 6·5 × 6·2 mm in length, width, and thickness, respectively; Fig. 2(a)). A set of high strain-rate compressional (DP series) tests were performed on these specimens with the specific purpose of studying the dynamic

(a)

(b)

(c)

(d)

Fig. 2. Schematic drawing of the test specimens studied. Note that: (a) represents unidirectionally reinforced GFRP samples impacted along their fiber direction; (b) and (c) depict unidirectional and cross-ply GFRP laminates struck transversely by the input rod; and (d) represents the unidirectional GFRP samples with Kevlar fiber stitching reinforcement.

behavior of these unidirectionally reinforced GFRP samples impacted along the fiber direction. The second and third set of specimens, $[0°]_{64}$ and $[(0°/90°)_n]_s$ glass/epoxy (Hy-E 9134B, Fiberite) laminates shown schematically in Figs 2(b) and (c), respectively, were both machined into two different diameter (10 and 50·8 mm) circular discs. The AP and AR designations represent, respectively, the test series for 10 and 50·8 mm diameter $[0°]_{64}$ GFRP specimens, while the CP and CR designations represent, respectively, the test series for 10 and 50·8 mm diameter $[(0°/90°)_n]_s$ GFRP samples. These circular discs were impacted along their thickness direction. The fourth type of composite specimen incorporated Kevlar-49 untwisted fiber (1140 denier) sewn, via the horizontal balanced-lock-stitching method[17] with a sewing machine employing a stitch spacing and stitch step of 5 mm, perpendicular to the direction of the glass fiber in $[0°]_{64}$ glass/epoxy pre-preg (Hy-E 9134B, Fiberite). Again these stitched laminates were machined into two different diameter circular discs as above, with the 10 and 50·8 mm diameter specimens being used for the EP and ER test sets, respectively. A schematic representation of these stitched samples and the impact direction is shown in Fig. 2(d).

Note that the parallelepiped specimens were impacted along the fiber direction, while the circular specimens were impacted at the center of the disc along the direction of thickness. The circular unidirectional and cross-ply GFRP laminate specimens were examined with the specific purpose of studying the effect of radial constraint on their dynamic properties. In addition, the effect of stitching reinforcement on their high strain rate compressional behavior was also investigated. Prior to each test, the center line along the specimen, the input bar and the output bar were carefully aligned. All specimen surfaces were carefully finished in order to assure close contact between the specimen, and the input and output bars. The quasi-static mechanical properties of the unidirectional glass/epoxy laminates obtained with a MTS tester set at a strain-rate of $3 × 10^{-4}$ s^{-1} are shown in Table 2.
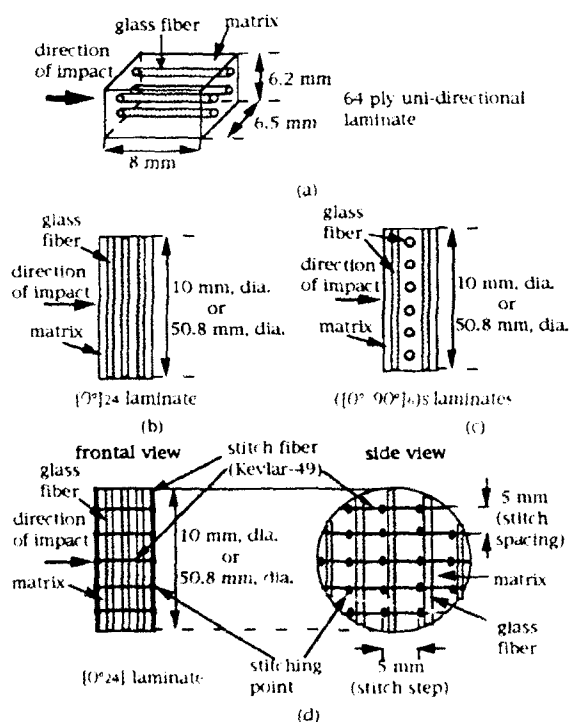
ANALYSIS

Due to the fact that the input and output bars remain in the elastic state at all times, stress and particle velocity can be accurately determined according to the measured strain. The measured

Table 2. The tensile and compressive quasi-static properties of (0°) and (90°) laminates

Description	Young's modulus (GPa)	Ultimate strength (MPa)	Strain rate (s⁻¹)
0° tensile properties	56·18 (48–62)[a]	1650 (1200–1600)[a]	3·3 × 10⁻⁴
0° compressive properties	54·2 (41–55)[a]	758 (560–700)[a]	1·0 × 10⁻³
90° tensile properties	18·9	42[a]	3·1 × 10⁻⁴
90° compressive properties	17·1	146	9·9 × 10⁻⁴

[a]Represents the material properties supplied by the manufacturer, page V.b-17, *Fiberite Materials Handbook*, ICI Fiberite, Tempe, AZ.
The neat resin tensile strength of Fiberite 934 epoxy is 27·6 MPa according to the *Fiberite Materials Handbook* (page V.b-5).

signals are analyzed based on the uniaxial stress wave theory detailed by Hauser[19] and Lindholm and Yeakley.[20] Considering the force equilibrium at interfaces I and II (refer to Fig. 1), the average stress in the specimen can be expressed as:

$$\sigma_{s} = \frac{\sigma_{i} - \sigma_{r} + \sigma_{t}}{2}\left(\frac{A_{1}}{A_{2}}\right) \qquad (1)$$

where $\sigma_i + \sigma_r$ and σ_t are measured by the gauges located on the input and output bars, respectively. The area of the input bar and the compressed area of the specimen are, respectively, represented by A_1 and A_2. The respective X_1 and X_2 displacements of interfaces I and II can be expressed as:

$$dX = \frac{\sigma}{\rho C} dt$$

$$X_{1} = \frac{1}{\rho C}\int_{0}^{t}(\sigma_{i} - \sigma_{r})\,dt \qquad (2)$$

$$X_{II} = \frac{1}{\rho C}\int_{0}^{t}\sigma_{t}\,dt$$

where ρ and C represent, respectively, the density and bar wave speed of the input and output bars, and a is the thickness of the specimen. From the equations shown above, the average strain in the specimen can now be expressed as:

$$\varepsilon_{avg} = \frac{X_{1} - X_{II}}{a} = \frac{1}{\rho C a}\left[\int_{0}^{t}(\sigma_{i} - \sigma_{r})\,dt - \int_{0}^{t}\sigma_{t}\,dt\right] \qquad (3)$$

The corresponding average strain rate is then:

$$\dot{\varepsilon}_{avg} = \frac{(\sigma_{i} - \sigma_{r}) - \sigma_{t}}{\rho C a} \qquad (4)$$

Based on eqns (2), (3) and (4), the dynamic stress–strain relationships can be computed from the measured wave forms.

RESULTS AND DISCUSSION

The unidirectionally reinforced glass/epoxy parallelepiped specimens (Fig. 2(a)) were tested at average strain rates of 980, 1350 and 2020 s⁻¹, which correspond, respectively, to the DP1, DP2, and DP3 tests. These samples were impacted along the fiber direction and their respective post-impact photographs are shown in Figs 3(a)–3(c). Note that the specimens have been shattered into small pieces, and that they possess a failure pattern quite different from that found from quasi-static compressional tests. Measured wave forms were analyzed based on the theory outlined in the analysis section. Curves A, B and C in Fig. 4 represent the dynamic stress–strain curves corresponding, respectively, to the DP1, DP2 and DP3 tests. The dynamic elastic modulus, ultimate stress and the corresponding strain were determined for each test and are listed in Table 3. Note that for unidirectional GFRP samples, the dynamic ultimate stress under DP3 test conditions is approximately two times higher than the (0°) quasi-static compressive strength. In addition, the dynamic elastic modulus of this specimen (under DP3 conditions) was found to be approximately 92% higher than the (0°) quasi-static elastic modulus.

The relationships between ultimate stress and the strain rate for the parallelepiped specimens

(a) (b) (c)
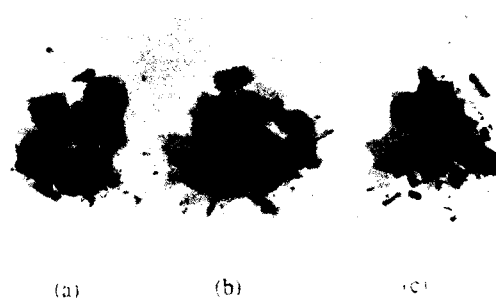
Fig. 3. Photographs of the damage pattern for the (a) DP1, (b) DP2, and (c) DP3 specimens.
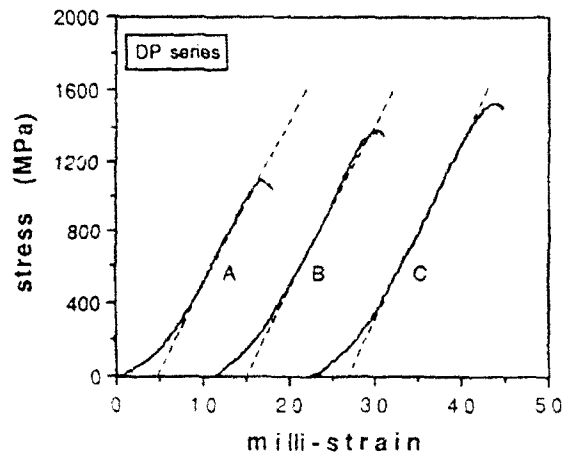
Fig. 4. Dynamic stress–strain curves for unidirectional GFRP specimens i.e. DP series impacted along their fiber direction.
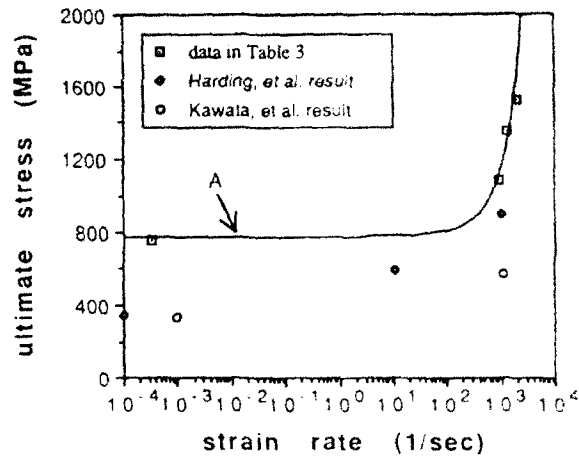
Fig. 5. A plot of ultimate stress versus strain rate for the DP test series curve A, and the test results from Harding and Welsh[ ] and Kawata *et al.*[ ] for GFRP.

Table 3. A summary of test results for the DP test series

Run no.	Average strain rate s	Young's modulus GPa	Maximum stress MPa	Failure strain	Note
SF1	1·0 × 10⁻⁴	54·2	758·0	0·009	Specimen failed
DP1	980	90·4	1080	0·017	Specimen failed
DP2	1350	96·53	1350	0·019	Specimen failed
DP3	2020	104·17	1520	0·024	Specimen failed

Represents the 0° quasi-static compressive properties of unidirectional GFRP sample.

Table 4. A summary of the test results for the AP and AR test sets

Run no.	Average strain rate s	Young's modulus GPa	Maximum stress MPa	Failure strain	Note
SM1	9·9 × 10⁻⁴	17·1	146·0	0·008	Specimen failed
AP1	3142	18·6	350·0	0·033	Specimen failed
AP2	3350	20·2	455·0	0·035	Specimen failed
AP3	6596	24·5	570·0	0·048	Specimen failed
AR1	1655	18·76	290·0	0·02	Specimen failed
AR2	2514	20·8	550·0	0·031	Specimen failed
AR3	4643	22·0	950·0	0·047	Specimen failed

Represents the 90° quasi-static compressive properties of unidirectional GFRP sample.

are shown by curve A in Fig. 5. Note that high velocity compressive ductility for these unidirectional GFRP specimens is observed. The high strain rate tensile test results reported by Harding and Welsh[ ] and Kawata *et al.*[ ] for GFRP specimens are also shown in Fig. 5. Note that in all cases, high velocity ductility is exhibited.

The $|0°|_{24}$ glass/epoxy circular disc laminates (Fig. 2(b)) were tested under the various strain rate conditions shown in Table 4. Two sets of unidirectional $|0°|_{24}$ GFRP laminates, possessing diameters of 10 mm (AP series) and 50·8 mm

(AR series), were impacted along their thickness direction with the specific purpose of investigating the effect of radial constraint on their dynamic properties. A total of six tests were performed for both the AP and AR series and their ultimate stress, corresponding strain, average strain rates, and dynamic elastic modulus results are summarized in Table 4. When specimens 10 mm in diameter were tested at average strain rates of 3000–7000 s⁻¹, they shattered into small pieces upon impact (refer to Figs 6(a)–6(c)). Under AR1 test conditions, the larger (50·8 mm in diameter)
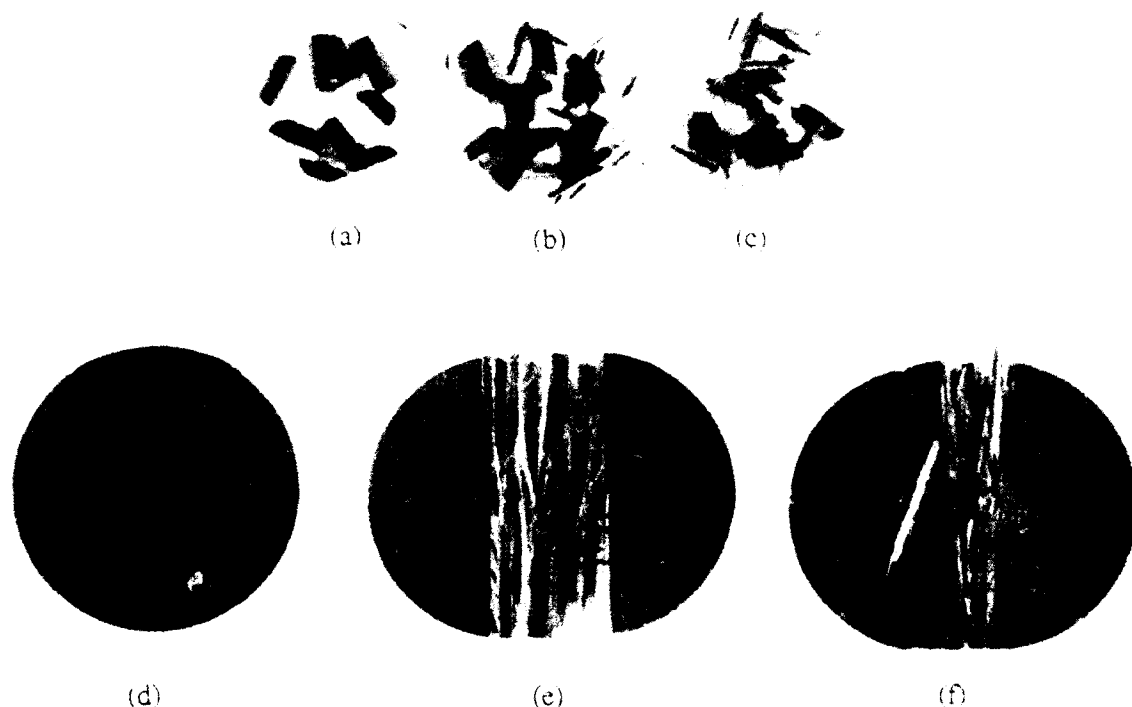
Fig. 6.   Photographs of the damage pattern for the a AP1, b AP2, c AP3, d AR1, e AR2, and f AR3 undirectionally reinforced specimens

specimens exhibited extensive edge-to-edge matrix cracks close to the region of impact Fig. 6 d . At strain rates higher than 2500 s⁻¹ AR2 and AR3 test conditions , the central impact region of the larger specimen split into several pieces. Note that the fibers in this region have broken and have spurred-out refer to Figs 6 e and 6 f .

Curves A, B and C in Fig. 7 a represent, respectively, the dynamic stress–strain relationships for the AP1, AP2 and AP3 tests. Similarly, curves A, B and C in Fig. 7 b represent, respectively, the dynamic stress–strain relationships for the AR1, AR2 and AR3 tests. A summary of the test results is listed in Table 4. An examination of this table reveals that the dynamic elastic modulus, ultimate stress and the associated strain increase with strain-rate for both the AP and AR test sets. The relationships between ultimate stress and average strain rate for the AP and AR test sets are shown in Fig. 8. The 'o' point in this figure corresponds to the transverse quasistatic compressive strength of a unidirectional GFRP specimen. Note that the ultimate stress of the larger diameter specimens at high strain rates

is greater than that of smaller specimens. The difference is due to the effect of radial constraint on the high strain rate chavior of the larger 0 specimens.

High strain rate tests for cross-ply 0 90   GFRP laminated samples were also conducted. A schematic representation of these specimens, including the impact direction, is shown in Fig. 2 c . Again, two different specimen diameters 10 mm, CP series, and 50·8 mm, CR series were examined, with two tests being conducted for each series. A summary of the test conditions that embody these two series is given in Table 5. Photographs of the impact damaged CP1 and CP2 specimens are shown in Figs 9 a and 9 b , respectively. Since the glass/epoxy laminates are partially transparent, their damage zones are easily examined with a strong back light. CP1 sample was tested at an average strain rate of 3168 s⁻¹. Note that its damage pattern is dominated by delamination, and that the damage zone is located about the circumferential edge of the specimen. When the same diameter specimen is, however, loaded with an averaged strain rate of 5394 s⁻¹ (the CP2 test), it shatters completely

into numerous small pieces. Large specimen (50·8 mm diameter) damage patterns, shown in Figs 9(c) and (d), exhibit an indented impacted region and extensive delamination zones stretching out

(a)

(b)

Fig. 7. Dynamic stress–strain curves for the AP (a) and AR (b) test sets, where the specimens were impacted along their thickness direction.

from the edge of this region to diameters of approximately 25 and 35 mm for the CR1 and CR2 specimens, respectively. In both cases, the central impacted region did not delaminate.

The dynamic compressional stress–strain curves for the CP and CR test sets are shown in Figs 10(a) and 10(b), respectively. In each case, curves A and B represent, respectively, test numbers one and two. A summary of the average strain rate, dynamic elastic modulus, maximum stress and its associated strain for the CP and CR test sets is presented in Table 5. An examination of this table reveals that the maximum stress for each test increases with loading strain rate. A plot of the strain rate versus maximum stress for the CP and CR test sets is presented in Fig. 11 and reveals that the effect of radial constraint on the maximum stress for these cross-ply specimens is limited: results in contrast to those found for the unidirectional GFRP specimens. An examination of Figs 8 and 11 reveals that for strain rates of 10^3–10^4 s^{-1}, the maximum stress for cross-ply

Fig. 8. A plot of ultimate stress versus strain rate for the AP and AR test sets.

Table 5. A summary of the test results for the CP and CR test sets

Run no.	Average strain rate (s^{-1})	Young's modulus (GPa)	Maximum stress (MPa)	Failure strain	Note
SM1	9·9 × 10^{-4}	17·1	146·0	0·008	Specimen failed
CP1	3168	21·97	861·0	0·049	Specimen delaminated
CP2	5349	26·8	1692	0·073	Specimen failed
CR1	2928	18·9	554·0	0·039	Specimen delaminated
CR2	5032	27·3	1107	0·055	Specimen delaminated

*Represents the 90° quasi-static compressive properties of unidirectional GFRP sample.

(a)   (b)

(c)   (d)
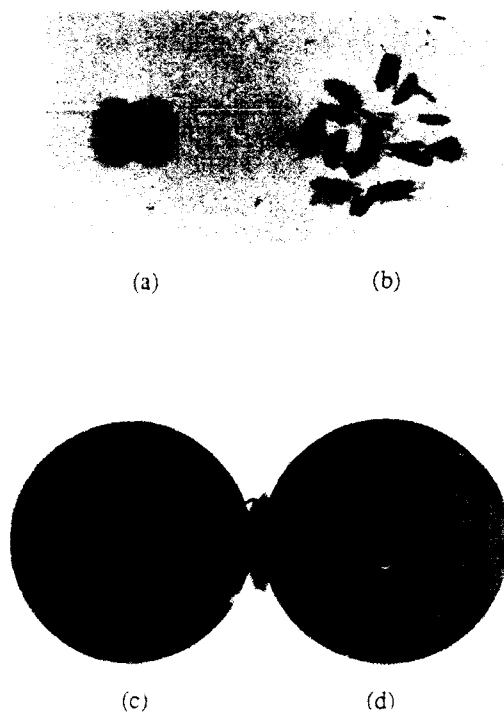
Fig. 9.   Photographs of the damage pattern for (a) CP1, (b) CP2, (c) CR1 and (d) CR2 specimens.

samples is about twice as high as that of unidirectional samples.

A plot of strain rate versus the elastic modulus for the AP, AR, CP and CR test sets is shown in Fig. 12. Note that the elastic modulus of cross-ply specimens increases with strain rate. Also note that the dynamic elastic modulus of the CR2 specimen loaded with a strain rate of 5032 s^{-1} is as much as 1·6 times higher than the transverse quasi-static compressive elastic modulus of an unidirectionally reinforced glass/epoxy specimen (Table 5). Moreover, Fig. 12 also indicates that for strain rates of 10^{-3}–10^{-1} s^{-1}, the effect of radial constraint on the dynamic elastic modulus of cross-ply GFRP laminates (the CP and CR series) is less significant than that of the high strain rate behavior of unidirectional GFRP laminated samples (the AP and AR series).

The last type of composite specimen incorporated Kevlar-49 untwisted fiber (1140 denier) sewn, via the horizontal balanced-lock-stitching method[14] with a sewing machine employing a stitch spacing and stitch step of 5 mm, perpendicular to the direction of the glass fiber in $[0°]_{24}$ glass/epoxy pre-preg (Hy-E 9134B, Fiberite). As above, two different specimen diameters (10 mm, EP series, and 50·8 mm, ER series) were studied.

(a)

(b)
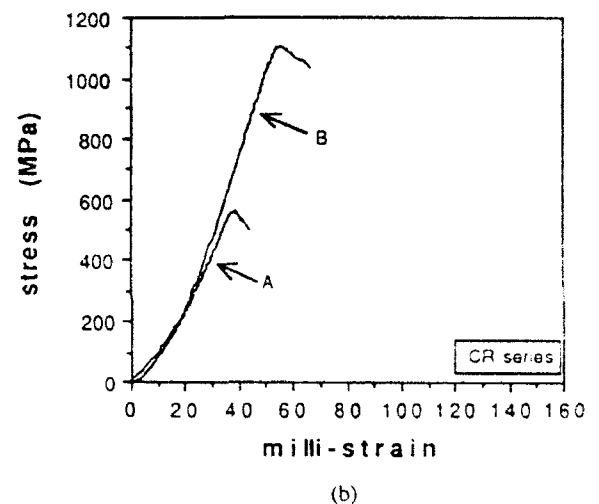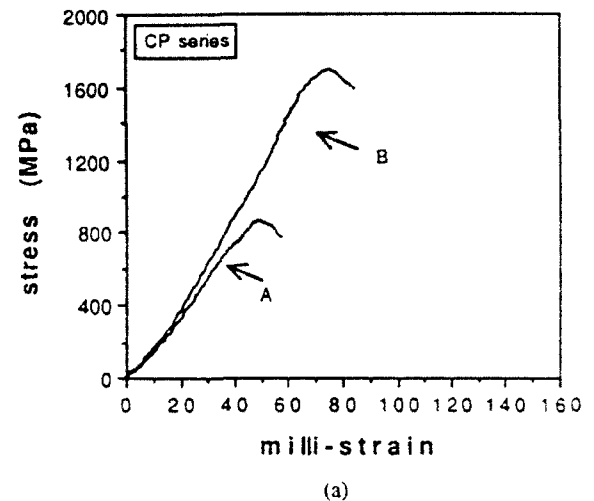
Fig. 10.   Dynamic stress–strain curves for the CP (a) and CR (b) test sets, where the cross-ply GFRP laminates were impacted along their thickness direction.
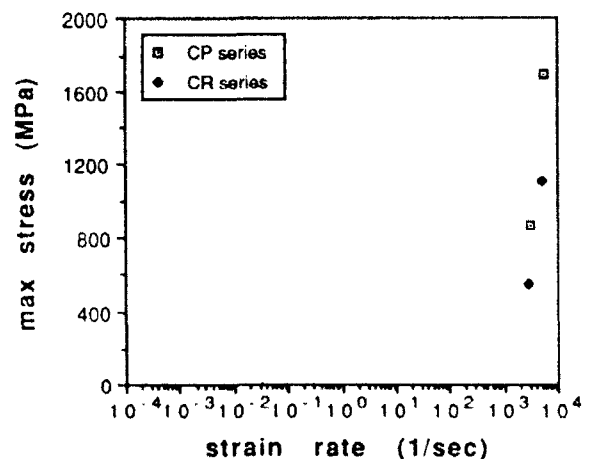
Fig. 11.   A plot of the maximum stress versus strain rate for the CP and CR test sets.
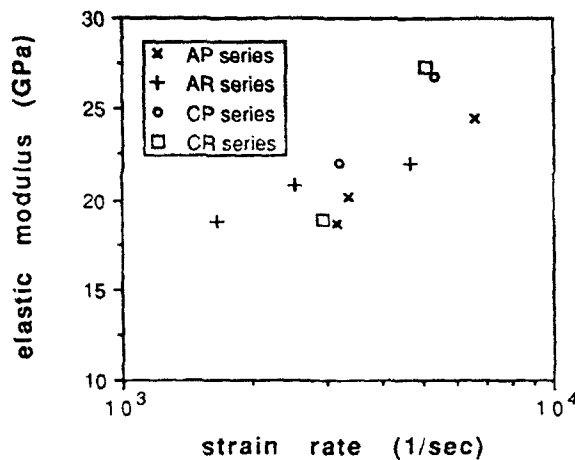
Fig. 12. A plot of the strain rate versus elastic modulus for the AP. AR. CP. and CR test sets.

with three dynamic compressional tests being conducted for each specimen diameter. A summary of the average strain rate, dynamic elastic modulus, and the ultimate stress for each test is listed in Table 6. Stitched specimens 10 mm in diameter shattered completely into small pieces upon impact, exhibiting those damage patterns shown in Figs 13(a)–13(c). The larger specimens exhibited broken stitched fibers especially near their stitching point, in addition to extensive edge-to-edge matrix cracks (see Figs 13(d)–13(f)).

The A, B and C dynamic stress–strain curves shown in Fig. 14(a) correspond, respectively, to the EP1, EP2 and EP3 tests. Similarly, the A, B and C dynamic stress–strain curves in Fig. 14(b) correspond, respectively, to the ER1, ER2, and ER3 tests. Again, note that dynamic ultimate stress increases with strain rate. Due to the effect of radial constraint, the dynamic ultimate stress for the larger diameter specimens is even higher than that for the smaller diameter samples. The relationship between ultimate stress and strain

rate for the AP, AR, EP and ER test sets is presented in Fig. 15. An examination of this figure indicates, however, that the ultimate stress for stitched specimens is less than that for unstitched specimens (AP and AR samples). This situation arises from the stitching process weakening the specimens, reducing their ultimate strength. Although the dynamic elastic modulus for the stitched specimens increases with strain rate as shown in Table 6, this value is only ⅓ to ½ that of the unstitched specimens. It is also found that the dynamic elastic modulus of the stitched specimens becomes less than the transverse quasi-static elastic modulus of the unidirectionally reinforced GFRP samples. A plot of the strain corresponding to ultimate stress versus strain rate for the AP, AR, EP and ER test sets is shown in Fig. 16. An examination of this figure reveals, however, that at strain rates of 10^3–10^4 s^{-1}, the dynamic ultimate strain of the stitched specimens is about 30–80% higher than that of the unstitched specimens.

CONCLUSIONS

The high strain rate compressional behavior of GFRP laminated (Hy-E 9134B, Fiberite) specimens with or without stitching reinforcement by Kevlar-49 untwisted threads was studied. High velocity ductility was verified for unidirectional glass/epoxy rectangular parallelepiped specimens when impacted along the fiber direction and the dynamic elastic modulus was found to be approximately 92% higher than the corresponding quasi-static test value. The dynamic elastic modulus and the ultimate or maximum stress for all specimens tested was found to increase with strain rate. The effect of radial constraint on increasing ultimate stress for stitched and unstitched unidirectionally reinforced GFRP specimens cannot be overlooked. Maximum stress values for 10 and 50·8

Table 6. A summary of the test results for the EP and ER test sets

Run no.	Average strain rate (s^{-1})	Young's modulus (GPa)	Maximum stress (MPa)	Failure strain	Note
SM1[a]	9.9×10^{-1}	17·1	146·0	0·008	Specimen failed
EP1	4150	8·2	252·0	0·042	Specimen failed
EP2	5500	8·3	338·0	0·046	Specimen failed
EP3	10400	13·4	450·0	0·063	Specimen failed
ER1	2180	9·9	369·0	0·04	Specimen failed
ER2	2900	10·6	471·0	0·057	Specimen failed
ER3	5280	14·1	755·0	0·062	Specimen failed

[a]Represents the 90° quasi-static compressive properties of unidirectional GFRP sample.

(a)   (b)   (c)

(d)   (e)   (f)
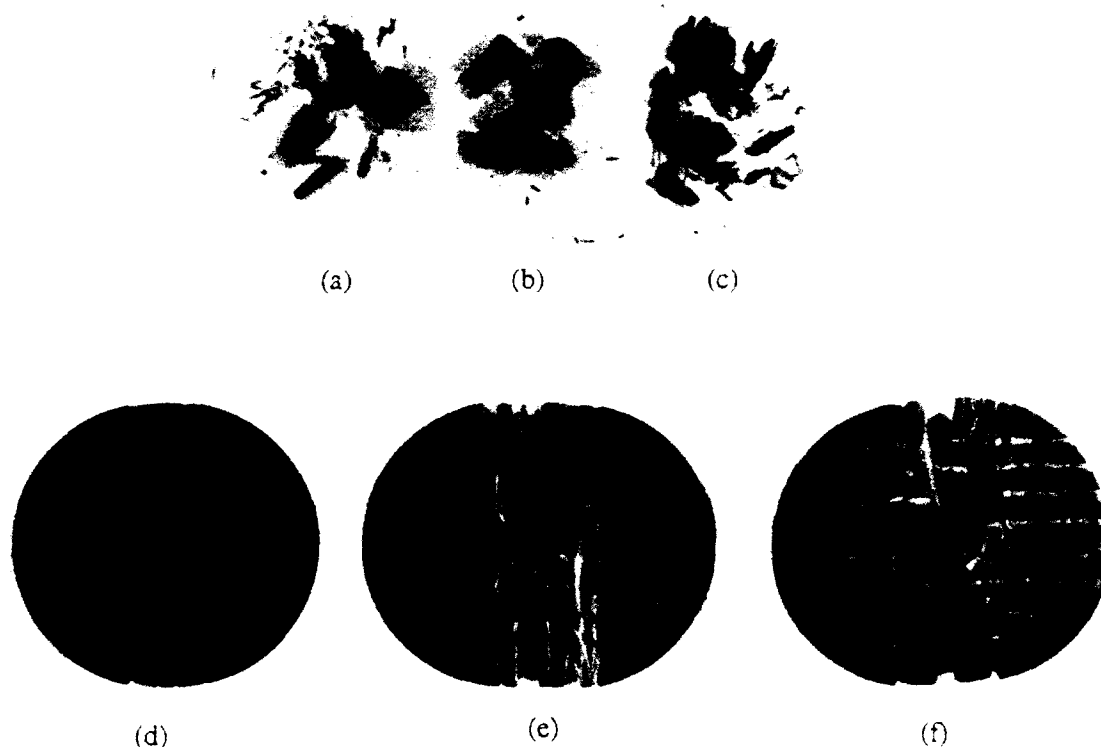
Fig. 13.   Photographs of the damage pattern for the (a) EP1, (b) EP2, (c) EP3, (d) ER1, (e) ER2 and (f) ER3 stitched GFRP specimens.

(a)   (b)
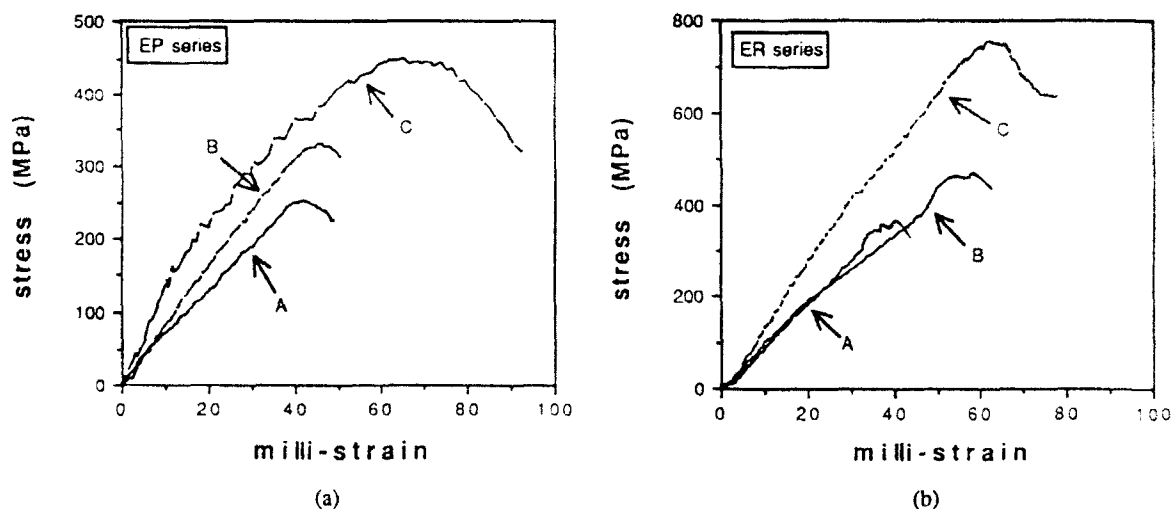
Fig. 14.   The dynamic stress-strain curves for the EP (a) and ER (b) test sets, where the stitched samples were impacted along their thickness direction.

mm diameter cross-ply GFRP specimens were found to be less sensitive to radial constraint. In addition, at strain rates of 10^3–10^4 s^{-1}, the maximum stress of cross-ply GFRP discs impacted along their thickness direction was found to be

about twice as high as that for unidirectionally reinforced GFRP discs. For strain rates of 10^3–10^4 s^{-1}, due to the fact that the stitching process introduced defects in the stitched samples, the dynamic ultimate stress for unidirectional
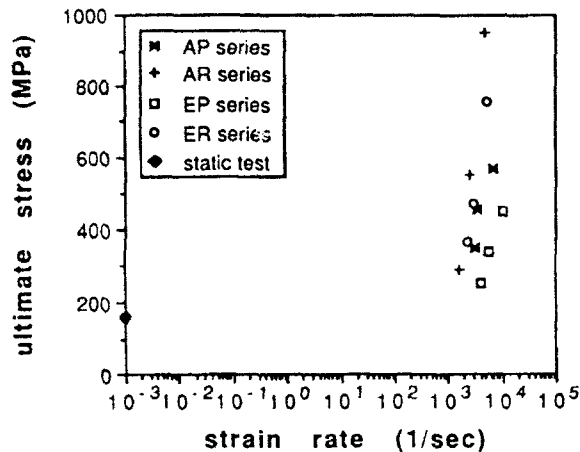
Fig. 15. A plot of ultimate stress versus strain rate for the AP, AR, EP and ER test sets.
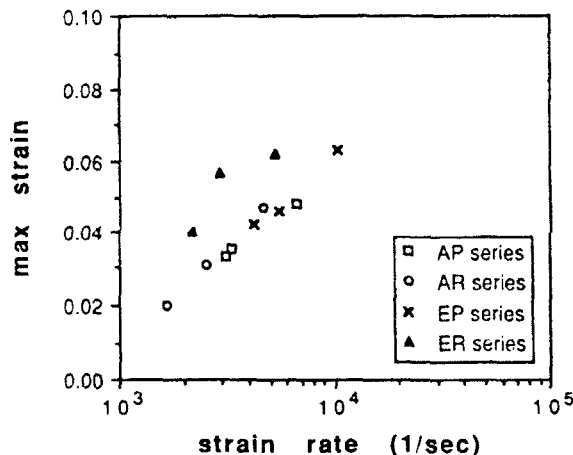
Fig. 16. A plot of strain rate versus strain corresponding to the ultimate stress for the AP, AR, EP and ER test sets.

GFRP samples with stitching reinforcement was found to be less than that for unidirectionally reinforced glass/epoxy samples. It was also found that the dynamic elastic modulus of the stitched specimens becomes less than the transverse quasi-static elastic modulus of the unidirectionally reinforced GFRP samples. The dynamic elastic modulus for stitched samples increased with strain rate: results similar to those found in unstitched specimens. Moreover, for stitched specimens, the maximum strain corresponding to the ultimate stress was found to be larger than that for unstitched specimens, and may enable the stitched specimens to absorb more deformation energy under high strain rate conditions.

REFERENCES

1. Armenakas, A. E. & Sciammarella, C. A., Response of glass-fiber-reinforced epoxy specimens to high rates of tensile loading. *Exp. Mech.*, **13** 1973 433–40.
2. Lindholm, S. Ulric ed., *Mechanical Behavior of Materials Under Dynamic Loads.* Springer-Verlag, New York, 1968.
3. Kanninen, *et al.* eds., *Inelastic Behavior of Solids.* McGraw-Hill, New York, 1970.
4. Harding, J. ed., *Mechanical Properties at High Rate of Strain.* Institute of Physics, No. 47, London, 1980.
5. Kawata, K. & Shioiri, J. eds., *Macro- and Micro-Mechanics of High Velocity Deformation and Fracture.* Springer-Verlag, New York, 1985.
6. Zukas, J. A. *et al.*, *Impact Dynamics.* John Wiley, New York, 1982.
7. Zukas, J. A. ed., *High Velocity Impact Dynamics.* John Wiley, New York, 1992.
8. Sierakowski, R. L. & Nevill, G. E. Jr. Dynamic compressive strength and failure of steel reinforced epoxy composites. *J. Comp. Mater.*, **5** 1970 362–77.
9. Harding, J. & Welsh, L. M., A tensile testing technique for fiber-reinforced composites at impact rates of strain. *J. Mater. Sci.*, **18** 1983 1810–26.
10. Saka, K. & Harding, J., The deformation and fracture of hybrid reinforced composites under tensile impact. *Proceedings of the IUTAM Symposium on MMMHVDF*, Tokyo, Japan, 1985, pp. 97–112.
11. Kawata, K. *et al.* Macro- and micro-mechanics of high-velocity brittleness and high-velocity ductility of solids. *Proceedings of the IUTAM Symposium on MMMHVDF*, Tokyo, Japan, 1985, pp. 1–26.
12. Liss, J., Goldsmith, W. & Hauser, F. E., Constraint to side flow in plates. *J. Appl. Mech.*, **50** 1983 694–8.
13. Tsu-Wei Chou, *Microstructural Design of Fiber Composites.* Cambridge University Press, Cambridge, 1992.
14. Dashsin Liu, Delamination resistance in stitched and unstitched composite plates subject to impact loading. *J. Reinf. Plast. & Comp.*, **9** 1990 59–69.
15. Mignery, L. A., Tan, T. M. & Sun, C. T., The use of stitching to suppress delamination in laminated composites, ASTM, STP 876, ASTM, Philadelphia, PA, 1985, pp. 371–85.
16. Xingwen Du, Fulin Xue & Zhenlong Gu, Experimental study of the effect of stitching on strength of a composite laminate. *Proceedings of International Symposium on Composite Materials and Structures*, Beijing, China, 1986, pp. 912–18.
17. Pelstring Michael, R. & Madan, Ram C., Stitching to improve damage tolerance of composites. *Proceedings of the 34th International SAMPE Symposium*, Covina, CA, 1989, pp. 1519–28.
18. Jenq, S. T. & Sheu, S. L., Experimental and numerical analysis of high strain-rate compressional behavior of 6061-O aluminum alloy. *Proceedings of the Ninth*

National Conf. Mech. Engrs, Kaoshung, Taiwan, ROC, 1992, pp. 551–8.

19. Hauser, F. E., Techniques for measuring stress–strain relations at high strain rates. *Exp. Mech.*, **6** (1960) 395–402.

20. Lindholm, U. S. & Yeakley, L. M., High-strain-rate testing: tension and compression. *Exp. Mech.*, **8** (1968) 1–9.

21. Kawata, K. *et al.*, Dynamic behavior analysis of composite materials. *Proceedings of Japan–US conf. on Composite Materials*, Tokyo, Japan, 1981, pp. 2–11.

A new local high-order laminate theory

Chih-Ping Wu & Chih-Shun Hsu

Department of Civil Engineering, National Cheng Kung University, Tainan, Taiwan 70101

A new local high-order deformable theory of laminated composite/sandwich plates is presented here. The displacement fields of each discrete layer were assumed in the present theory to be of a high-order polynomial series through layer-thickness. The displacement and traction continuity conditions at the interface between layers and the traction conditions at the outer surfaces were imposed as the constraint conditions, and introduced into the potential energy functional by the Lagrange multiplier method. The equations of motion and admissible boundary conditions were given on the basis of the present theory by using the generalized variational principle. Pagano's 3-D elasticity solutions of generally rectangular laminated composite/sandwich plates, fully simply supported, subjected to transverse sinusoidal loading were used for assessment of the present theory and other theories discussed in previous literature. The present theory was found to agree very closely with 3-D elasticity solutions.

1 INTRODUCTION

Proposing a new laminate theory which is capable of both accounting for the transverse shear or shear/normal deformation on the global behavior of composite structures and producing an accurate determination of the distribution of stresses produced in the composite structures under various loading conditions, has received much attention in the past. This topic[1-9] has been the focus of many previously published research papers. This is largely due to the fact that the influence of transverse shear/normal deformation is much more significant on the composite material than on the isotropic material.

Mindlin,[1] Ren,[2] Reddy,[3] Lo et al.,[4,5] and Sun and Whitney[6] have respectively proposed their global first-order or higher-order laminate theories for consideration of the effects of transverse shear or shear/normal deformation where the displacement fields were assumed as some kind of polynomial series across the entire laminate thickness. This displacement assumption results in discontinuous tractions at the interface between layers owing to the different elastic moduli for each layer. The first-order discrete-layer laminate theories[?] ave been previously presented by Mau[7] and Seide.[8] A general laminated plate theory without numerical applications was presented by Soldatos.[9] The most important contribution has been made by Pagano[10,11] who pre-

sented the bending analysis of laminated composite/sandwich plates using three-dimensional theory of elastic approach. These 3-D elasticity solutions provide a standard for assessing the new laminate theories. An excellent review of early laminate theories which considered the effects of transverse shear or shear/normal deformation was made by Noor and Burton.[12]

A local high-order laminate theory has been proposed by Wu and Kuo[13] where the high-order deformable model was used in each discrete layer composed of the entire laminate and only the displacement continuity conditions at interfaces were imposed as constraint conditions. A mixed finite element scheme based on this theory has been subsequently developed by Wu and Kuo.[14] A new local high-order laminate theory is presented in this paper for enhancement of Wu and Kuos' theory on the accuracy of transverse shear and normal stresses. This is attained through means of imposing both the displacement and traction continuity conditions at interfaces and the traction conditions at outer surfaces as constraint conditions in the local high-order deformable model. Pagano's 3-D elasticity solutions of the generally rectangular laminated composite plates being fully simply supported and subjected to transverse sinusoidal loads are used for assessment of the present theory, Wu and Kuos' theory, Ren's theory and Reddy's theory.

439

2 THEORY

2.1 Kinematical relationships

A local cartesian coordinate system in the present theory is located on the mid-surface of each individual lamina. The local displacement fields for a typical lamina i are expanded as a certain high-order polynomial series of thickness z_i and expressed by

$$u_i(x, y, z) = u_i^0(x, y) + z_i[\theta_x(x, y)]_i + z_i^2[\psi_x(x, y)]_i + z_i^3[\phi_x(x, y)]_i$$

$$v_i(x, y, z) = v_i^0(x, y) + z_i[\theta_y(x, y)]_i + z_i^2[\psi_y(x, y)]_i + z_i^3[\phi_y(x, y)]_i \qquad (1)$$

$$w_i(x, y, z) = w_i^0(x, y) + z_i[\theta_z(x, y)]_i + z_i^2[\psi_z(x, y)]_i$$

where u_i^0, v_i^0 and w_i^0 are three mid-surface displacement functions, θ_x, θ_y and θ_z are three rotation functions, and ψ_x, ψ_y, ψ_z, ϕ_x and ϕ_y are the other high-order functions. z_i is measured from the mid-surface of the ith layer.

The strain–displacement relationships are then given on the basis of small deformation elasticity as

$$(\varepsilon_x)_i = (\varepsilon_x^0)_i + z_i(K_x)_i + z_i^2(\Gamma_x)_i + z_i^3(H_x)_i$$

$$(\varepsilon_y)_i = (\varepsilon_y^0)_i + z_i(K_y)_i + z_i^2(\Gamma_y)_i + z_i^3(H_y)_i \qquad (2)$$

$$(\varepsilon_z)_i = (\varepsilon_z^0)_i + z_i(K_z)_i$$

and

$$(\gamma_{xy})_i = (\gamma_{xy}^0)_i + z_i(K_{xy})_i + z_i^2(\Gamma_{xy})_i + z_i^3(H_{xy})_i$$

$$(\gamma_{xz})_i = (\gamma_{xz}^0)_i + z_i(K_{xz})_i + z_i^2(\Gamma_{xz})_i \qquad (3)$$

$$(\gamma_{yz})_i = (\gamma_{yz}^0)_i + z_i(K_{yz})_i + z_i^2(\Gamma_{yz})_i$$

in which

$$[\varepsilon_x^0, \varepsilon_y^0, \varepsilon_z^0]_i = \left[\frac{\partial u^0}{\partial x}, \frac{\partial v^0}{\partial y}, \theta_z\right]_i$$

$$[K_x, K_y, K_z]_i = \left[\frac{\partial \theta_x}{\partial x}, \frac{\partial \theta_y}{\partial y}, 2\psi_z\right]_i$$

$$[\Gamma_x, \Gamma_y]_i = \left[\frac{\partial \psi_x}{\partial x}, \frac{\partial \psi_y}{\partial y}\right]_i \qquad (4)$$

$$[H_x, H_y]_i = \left[\frac{\partial \phi_x}{\partial x}, \frac{\partial \phi_y}{\partial y}\right]_i$$

and

$$[\gamma_{xy}^0, \gamma_{xz}^0, \gamma_{yz}^0]_i = \left[\frac{\partial u^0}{\partial y} + \frac{\partial v^0}{\partial x}, \theta_x + \frac{\partial w^0}{\partial x}, \theta_y + \frac{\partial w^0}{\partial y}\right]_i$$

$$[K_{xy}, K_{xz}, K_{yz}]_i = \left[\frac{\partial \theta_x}{\partial y} + \frac{\partial \theta_y}{\partial x}, 2\psi_x + \frac{\partial \theta_z}{\partial x}, 2\psi_y + \frac{\partial \theta_z}{\partial y}\right]_i \qquad (5)$$

$$[\Gamma_{xy}, \Gamma_{xz}, \Gamma_{yz}]_i = \left[\frac{\partial \psi_x}{\partial y} + \frac{\partial \psi_y}{\partial x}, 3\phi_x + \frac{\partial \psi_z}{\partial x}, 3\phi_y + \frac{\partial \psi_z}{\partial y}\right]_i$$

$$[H_{xy}]_i = \left[\frac{\partial \phi_x}{\partial y} + \frac{\partial \phi_y}{\partial x}\right]_i$$

2.2 Constraint conditions

The displacement and traction continuity conditions at the interface between laminae and traction conditions at outer surfaces are imposed as the constraint conditions in the present formulation. They are respectively written as follows: the displacement continuity constraints between the ith and $(i+1)$th layers are

$$(f_u)_i = u^0_{i+1} - u^0_i - \frac{h_{i+1}}{2}(\theta_x)_{i+1} - \frac{h_i}{2}(\theta_x)_i + \frac{h_{i+1}^2}{4}(\psi_x)_{i+1} - \frac{h_i^2}{4}(\psi_x)_i - \frac{h_{i+1}^3}{8}(\phi_x)_{i+1} - \frac{h_i^3}{8}(\phi_x)_i = 0$$

$$(f_v)_i = v^0_{i+1} - v^0_i - \frac{h_{i+1}}{2}(\theta_y)_{i+1} - \frac{h_i}{2}(\theta_y)_i + \frac{h_{i+1}^2}{4}(\psi_y)_{i+1} - \frac{h_i^2}{4}(\psi_y)_i - \frac{h_{i+1}^3}{8}(\phi_y)_{i+1} - \frac{h_i^3}{8}(\phi_y)_i = 0 \qquad (6)$$

$$(f_w)_i = w^0_{i+1} - w^0_i - \frac{h_{i+1}}{2}(\theta_z)_{i+1} - \frac{h_i}{2}(\theta_z)_i + \frac{h_{i+1}^2}{4}(\psi_z)_{i+1} - \frac{h_i^2}{4}(\psi_z)_i = 0$$

where $i = 1, 2, \ldots, (NL-1)$ and NL denotes the total number of layer composed of the considered laminae.

The traction continuity constraints between the ith and $(i+1)$th layers are

$$f_{xi} = (\tau_{xz})_{i+1} \Big|_{z_{i+1} = -h_{i+1}/2} - (\tau_{xz})_i \Big|_{z_i = h_i/2} = 0$$

$$f_{yi} = (\tau_{yz})_{i+1} \Big|_{z_{i+1} = -h_{i+1}/2} - (\tau_{yz})_i \Big|_{z_i = h_i/2} = 0 \qquad (7)$$

$$f_{zi} = (\sigma_z)_{i+1} \Big|_{z_{i+1} = -h_{i+1}/2} - (\sigma_z)_i \Big|_{z_i = h_i/2} = 0$$

where $i = 1, 2, \ldots, (NL-1)$.

The traction conditions at the top and bottom surfaces of the entire laminate are

$$f_{x,NL} = (\tau_{xz})_{NL} \Big|_{z_{NL} = h_{NL}/2} - T_x = 0$$

$$f_{y,NL} = (\tau_{yz})_{NL} \Big|_{z_{NL} = h_{NL}/2} - T_y = 0 \qquad (8)$$

$$f_{z,NL} = (\sigma_z)_{NL} \Big|_{z_{NL} = h_{NL}/2} - T_z = 0$$

and

$$f_{x0} = (\tau_{xz})_1 \Big|_{z_1 = -h_1/2} = 0$$

$$f_{y0} = (\tau_{yz})_1 \Big|_{z_1 = -h_1/2} = 0 \qquad (9)$$

$$f_{z0} = (\sigma_z)_1 \Big|_{z_1 = -h_1/2} = 0$$

2.3 Equations of motion

The displacement and traction continuity constraints at the interfaces and traction conditions at the outer surfaces (i.e. eqns (6)–(9)) are introduced into the potential energy functional of the laminate by using Lagrange multipliers. This modified potential energy functional Π_{mp} is then given by

$$\Pi_{mp} = \sum_{i=1}^{N} \iint \int_{h_i/2}^{h_i/2} \left[\frac{\sigma_x \varepsilon_x}{2} + \frac{\sigma_y \varepsilon_y}{2} + \frac{\sigma_z \varepsilon_z}{2} + \frac{\tau_{xy}\gamma_{xy}}{2} + \frac{\tau_{xz}\gamma_{xz}}{2} + \frac{\tau_{yz}\gamma_{yz}}{2} \right] dz\, dA - \iint \left(T_x u^* + T_y v^* + T_z w^* \right) dA$$

$$+ \sum_{i=1}^{N-1} \iint \left[(\lambda_{ui})(f_u)_i + (\lambda_{vi})(f_v)_i + (\lambda_{wi})(f_w)_i \right] dA + \sum_{i=0}^{N} \iint \left[\lambda_{xi} f_{xi} + \lambda_{yi} f_{yi} + \lambda_{zi} f_{zi} \right] dA \quad (10)$$

where T_x, T_y and T_z are the tractions applied at top surface of the entire laminate, u^*, v^* and w^* are the displacement components at the top surface. Applying the minimum potential energy principle (i.e. $\delta\Pi_{mp} = 0$), the integration is performed through the thickness from bottom to top surfaces of a typical lamina i. Following the standard variational operation, we obtain the equations of motion as:

$$\delta u: \left(\frac{\partial N_x}{\partial x}\right)_i + \left(\frac{\partial N_{xy}}{\partial y}\right)_i + (\lambda_{ui} - \lambda_{ui-1}) + Q_{1si}\frac{\partial}{\partial x}(\lambda_{xi} - \lambda_{xi-1}) + Q_{si}\frac{\partial}{\partial y}(\lambda_{xi} - \lambda_{xi-1}) = 0$$

$$\delta v: \left(\frac{\partial N_y}{\partial y}\right)_i + \left(\frac{\partial N_{xy}}{\partial x}\right)_i + (\lambda_{vi} - \lambda_{vi-1}) + Q_{ssi}\frac{\partial}{\partial y}(\lambda_{yi} - \lambda_{yi-1}) + Q_{si}\frac{\partial}{\partial x}(\lambda_{yi} - \lambda_{yi-1}) = 0$$

$$\delta w: \left(\frac{\partial Q_x}{\partial x}\right)_i + \left(\frac{\partial Q_y}{\partial y}\right)_i + (\lambda_{wi} - \lambda_{wi-1}) + Q_{4si}\frac{\partial}{\partial y}(\lambda_{zi} - \lambda_{zi-1}) + Q_{si}\frac{\partial}{\partial x}(\lambda_{zi} - \lambda_{zi-1})$$

$$+ Q_{ssi}\frac{\partial}{\partial y}(\lambda_{zi} - \lambda_{zi-1}) + Q_{si}\frac{\partial}{\partial x}(\lambda_{zi} - \lambda_{zi-1}) = 0$$

$$\delta\theta_x: \left(\frac{\partial M_x}{\partial x}\right)_i + \left(\frac{\partial M_{xy}}{\partial y}\right)_i - Q_x + \frac{h_i}{2}(\lambda_{xi} + \lambda_{xi-1}) + Q_{si}(-\lambda_{xi-1} + \lambda_{xi}) + Q_{si}(-\lambda_{xi-1} + \lambda_{xi})$$

$$+ Q_{1si}\frac{h_i}{2}\frac{\partial}{\partial x}(-\lambda_{xi-1} - \lambda_{xi}) + Q_{ssi}\frac{h_i}{2}\frac{\partial}{\partial y}(-\lambda_{xi-1} - \lambda_{xi}) = 0$$

$$\delta\theta_y: \left(\frac{\partial M_y}{\partial y}\right)_i + \left(\frac{\partial M_{xy}}{\partial x}\right)_i - Q_y + \frac{h_i}{2}(\lambda_{yi} + \lambda_{yi-1}) + Q_{4si}(-\lambda_{yi-1} + \lambda_{yi}) + Q_{si}(-\lambda_{yi-1} + \lambda_{yi})$$

$$+ Q_{ssi}\frac{h_i}{2}\frac{\partial}{\partial y}(-\lambda_{yi-1} - \lambda_{yi}) + Q_{si}\frac{h_i}{2}\frac{\partial}{\partial x}(-\lambda_{yi-1} - \lambda_{yi}) = 0$$

$$\delta\theta_z: \left(\frac{\partial R_x}{\partial x}\right)_i + \left(\frac{\partial R_y}{\partial y}\right)_i - N_{zi} + \frac{h_i}{2}[(\lambda_{zi} + \lambda_{zi-1}) + Q_{4si}(-\lambda_{zi-1} + \lambda_{zi})]$$

$$+ Q_{4si}\frac{h_i}{2}\frac{\partial}{\partial y}(-\lambda_{yi-1} - \lambda_{yi}) + Q_{ssi}\frac{h_i}{2}\frac{\partial}{\partial x}(-\lambda_{yi-1} - \lambda_{yi})$$

$$+ Q_{1si}\frac{h_i}{2}\frac{\partial}{\partial y}(-\lambda_{xi-1} - \lambda_{xi}) + Q_{si}\frac{h_i}{2}\frac{\partial}{\partial x}(-\lambda_{xi-1} - \lambda_{xi}) = 0$$

$$\delta \psi_{xi}: \left(\frac{\partial P_x}{\partial x}\right)_i + \left(\frac{\partial P_{xy}}{\partial y}\right)_i - 2 R_{xi} + \frac{h_i^2}{4}\left[(\lambda_{xi}) - (\lambda_{xi-1})\right] + (Q_{55})_i h_i \left[\lambda_{xi} + \lambda_{xi-1}\right] + (Q_{45})_i h_i \left[\lambda_{yi} + \lambda_{yi-1}\right]$$

$$+ (Q_{13})_i \frac{h_i^2}{4}\frac{\partial}{\partial x}\left[\lambda_{zi} - \lambda_{zi-1}\right] + (Q_{36})_i \frac{h_i^2}{4}\frac{\partial}{\partial y}\left[(\lambda_{zi}) - (\lambda_{zi-1})\right] = 0$$

$$\delta \psi_{yi}: \left(\frac{\partial P_y}{\partial y}\right)_i + \left(\frac{\partial P_{xy}}{\partial x}\right)_i - 2 R_{yi} + \frac{h_i^2}{4}\left[(\lambda_{yi}) - (\lambda_{yi-1})\right] + (Q_{45})_i h_i \left[\lambda_{xi} + \lambda_{xi-1}\right] + (Q_{44})_i h_i \left[\lambda_{yi} + \lambda_{yi-1}\right]$$

$$+ (Q_{23})_i \frac{h_i^2}{4}\frac{\partial}{\partial y}\left[\lambda_{zi} - \lambda_{zi-1}\right] + (Q_{36})_i \frac{h_i^2}{4}\frac{\partial}{\partial x}\left[(\lambda_{zi}) - (\lambda_{zi-1})\right] = 0$$

$$\delta \psi_{zi}: \left(\frac{\partial S_x}{\partial x}\right)_i + \left(\frac{\partial S_y}{\partial y}\right)_i - 2 M_{zi} + \frac{h_i^2}{4}\left[(\lambda_{zi}) - (\lambda_{zi-1})\right] + (Q_{33})_i h_i \left[\lambda_{zi} + \lambda_{zi-1}\right]$$

$$+ (Q_{13})_i \frac{h_i^2}{4}\frac{\partial}{\partial y}\left[\lambda_{xi} - \lambda_{xi-1}\right] + (Q_{55})_i \frac{h_i^2}{4}\frac{\partial}{\partial x}\left[(\lambda_{xi}) - (\lambda_{xi-1})\right]$$

$$+ (Q_{23})_i \frac{h_i^2}{4}\frac{\partial}{\partial y}\left[\lambda_{yi} - \lambda_{yi-1}\right] + (Q_{44})_i \frac{h_i^2}{4}\frac{\partial}{\partial x}\left[(\lambda_{yi}) - (\lambda_{yi-1})\right] = 0$$

$$\delta \phi_{xi}: \left(\frac{\partial M_x}{\partial x}\right)_i + \left(\frac{\partial M_{xy}}{\partial y}\right)_i - 3 S_{xi} + \frac{h_i^2}{8}\left[\lambda_{xi} + \lambda_{xi-1}\right] + (Q_{55})_i \frac{3h_i^2}{4}\left[-\lambda_{xi-1} + \lambda_{xi}\right]$$

$$+ (Q_{45})_i \frac{3h_i^2}{4}\left[-\lambda_{yi-1} + \lambda_{yi}\right] + (Q_{13})_i \frac{h_i^2}{8}\frac{\partial}{\partial x}\left[-\lambda_{zi-1} - \lambda_{zi}\right] + (Q_{36})_i \frac{h_i^2}{8}\frac{\partial}{\partial y}\left[-\lambda_{zi-1} - \lambda_{zi}\right] = 0$$

$$\delta \phi_{yi}: \left(\frac{\partial M_y}{\partial y}\right)_i + \left(\frac{\partial M_{xy}}{\partial x}\right)_i - 3 S_{yi} + \frac{h_i^2}{8}\left[\lambda_{yi} + \lambda_{yi-1}\right] + (Q_{45})_i \frac{3h_i^2}{4}\left[-\lambda_{xi-1} + \lambda_{xi}\right]$$

$$+ (Q_{44})_i \frac{3h_i^2}{4}\left[-\lambda_{yi-1} + \lambda_{yi}\right] + (Q_{23})_i \frac{h_i^2}{8}\frac{\partial}{\partial y}\left[-\lambda_{zi-1} - \lambda_{zi}\right] + (Q_{36})_i \frac{h_i^2}{8}\frac{\partial}{\partial x}\left[\lambda_{zi-1} - \lambda_{zi}\right] = 0 \qquad (11)$$

where $i = 1, 2, \ldots, NL$.

$$\delta(\lambda_{xi}): (f_{xi})_i = 0$$
$$\delta(\lambda_{yi}): (f_{yi})_i = 0 \qquad (12)$$
$$\delta(\lambda_{zi}): (f_{zi})_i = 0$$

where $i = 1, 2, \ldots, (NL - 1)$. And

$$\delta(\lambda_{xi}): (f_{xi})_i = 0$$
$$\delta(\lambda_{yi}): (f_{yi})_i = 0 \qquad (13)$$
$$\delta(\lambda_{zi}): (f_{zi})_i = 0$$

where $i = 1, 2, \ldots, NL$.

The generalized force and moment of a typical lamina i in eqns (11)–(13) are defined by

$$\begin{bmatrix} N_x & N_s & N_z & N_{xy} & Q_x & Q_y \\ M_x & M_s & M_z & M_{xy} & R_x & R_y \end{bmatrix}_i = \int_{-h_i/2}^{h_i/2} \begin{bmatrix} 1 \\ z \end{bmatrix} [\sigma_x \; \sigma_y \; \sigma_z \; \tau_{xy} \; \tau_{xz} \; \tau_{yz}]_i \, dz$$

$$\begin{bmatrix} P_x & P_y & P_{xy} \\ M_x & M_y & M_{xy} \end{bmatrix}_i = \int_{-h_i/2}^{h_i/2} \begin{bmatrix} z^2 \\ z^3 \end{bmatrix} [\sigma_x \; \sigma_y \; \tau_{xy}]_i \, dz \qquad (14)$$

$$[S_x S_y]_i = \int_{-h_i/2}^{h_i/2} z^2 [\tau_{xz} \; \tau_{yz}]_i \, dz$$

3 EXACT SOLUTIONS FOR SIMPLY SUPPORTED CROSS-PLY RECTANGULAR LAMINATES

The exact analytical solutions of the simultaneously partial differential equations in eqns (11)–(13) can be obtained for the generally rectangular cross-ply laminated composite/sandwich plates, with fully simple supports. The following elastic modulus for each layer is identical to zero:

$$(\bar{Q}_{16})_i = (\bar{Q}_{26})_i = (\bar{Q}_{36})_i = (\bar{Q}_{45})_i = 0 \qquad (15)$$

The 'simply supported' boundary conditions are assumed as follows:

$$\left.\begin{aligned}
u^{(i)} &= \theta_x^{(i)} = \psi_x^{(i)} = \phi_x^{(i)} = 0 \\
w^{(i)} &= \theta_z^{(i)} = \psi_z^{(i)} = 0 \\
N_x^{(i)} &= M_x^{(i)} = P_x^{(i)} = \bar{M}_x^{(i)} = 0 \\
\lambda_{xi} &= \lambda_{yi} = 0 \\
\lambda_{zi} &= \lambda_{zi} = 0
\end{aligned}\right\} \qquad \text{at } x = 0 \text{ and } x = a$$

$$\left.\begin{aligned}
u^{(i)} &= \theta_y^{(i)} = \psi_y^{(i)} = \phi_y^{(i)} = 0 \\
w^{(i)} &= \theta_z^{(i)} = \psi_z^{(i)} = 0 \\
N_y^{(i)} &= M_y^{(i)} = P_y^{(i)} = \bar{M}_y^{(i)} = 0 \\
\lambda_{xi} &= \lambda_{yi} = 0 \\
\lambda_{yi} &= \lambda_{zi} = 0
\end{aligned}\right\} \qquad \text{at } y = 0 \text{ and } y = b$$

(16)

The displacement variables for a typical lamina i and the Lagrange multipliers at the interface between the ith and $(i+1)$th layers are expanded in the double Fourier series as:

$$u = \sum_{m=1}^{\infty} \sum_{n=1}^{\infty} [(a_0)_{mn}^i + z_i (a_1)_{mn}^i + z_i^2 (a_2)_{mn}^i + z_i^3 (a_3)_{mn}^i] \cos \alpha x \sin \beta y$$

$$v = \sum_{m=1}^{\infty} \sum_{n=1}^{\infty} [(b_0)_{mn}^i + z_i (b_1)_{mn}^i + z_i^2 (b_2)_{mn}^i + z_i^3 (b_3)_{mn}^i] \sin \alpha x \cos \beta y$$

$$w = \sum_{m=1}^{\infty} \sum_{n=1}^{\infty} [(c_0)_{mn}^i + z_i (c_1)_{mn}^i + z_i^2 (c_2)_{mn}^i] \sin \alpha x \sin \beta y$$

$$(\lambda_x)_i = \sum_{m=1}^{\infty} \sum_{n=1}^{\infty} (\beta_0)_{mn}^i \cos \alpha x \sin \beta y$$

$$(\lambda_{l})_{i} = \sum_{m=1}^{\infty} \sum_{n=1}^{\infty} (\beta_{1})'_{mn} \sin \alpha x \cos \beta y$$

$$(\lambda_{u})_{i} = \sum_{m=1}^{\infty} \sum_{n=1}^{\infty} (\beta_{2})'_{mn} \sin \alpha x \sin \beta y$$

$$(\lambda_{v})_{i} = \sum_{m=1}^{\infty} \sum_{n=1}^{\infty} (\beta_{3})'_{mn} \cos \alpha x \sin \beta y$$

$$(\lambda_{x})_{i} = \sum_{m=1}^{\infty} \sum_{n=1}^{\infty} (\beta_{4})'_{mn} \sin \alpha x \cos \beta y$$

$$(\lambda_{z})_{i} = \sum_{m=1}^{\infty} \sum_{n=1}^{\infty} (\beta_{5})'_{mn} \sin \alpha x \sin \beta y$$

(17)

where $\alpha = m\pi/a$ and $\beta = n\pi/b$. The boundary conditions of the considered laminate are completely satisfied owing to the assumption of eqn (17). Substituting eqn (17) into eqns (11)–(13) yields one set of the simultaneously algebraic equations expressed in terms of the coefficients $(a_0)', (a_1)', (a_2)', (a_3)',$ $(b_0)', (b_1)', (b_2)', (b_3)'; (c_0)', (c_1)', (c_2)';$ and $(\beta_0)', (\beta_1)', (\beta_2)', (\beta_3)', (\beta_4)', (\beta_5)'$. Once the applied transverse loadings are written as a double Fourier series, those coefficients can be obtained for certain fixed values of m and n. Thus the bending problem of the laminated composite/sandwich plates is solved.

4 NUMERICAL APPLICATIONS AND DISCUSSION

The generally rectangular cross-ply laminates, with fully simple supports, subjected to sinusoidal transverse loading are evaluated here for the sake of validating the present laminate theory. The stress–displacement quantities are normalized in the following form of:

$$(\bar{\sigma}_x, \bar{\sigma}_y, \bar{\tau}_{xy}) = \frac{1}{q_0 s} (\sigma_x, \sigma_y, \tau_{xy})$$

$$(\bar{\tau}_{xz}, \bar{\tau}_{yz}) = \frac{1}{q_0 s}(\tau_{xz}, \tau_{yz}); \quad \bar{\sigma}_z = \frac{\sigma_z}{q_0}$$

(18)

$$\bar{u} = \frac{E_T u}{q_0 hs^3}, \quad \bar{w} = \frac{100 E_T w}{q_0 hs^4}$$

$$s = \frac{a}{h}, \quad \zeta = \frac{z}{h}$$

Tables 1 and 2 show static bending results for $[0°/90°/0°]$ cross-ply laminate composed of layers of equal-thickness, and aspect ratios of $b/a = 1$ and 3, respectively, and subjected to sinusoidal

transverse loading $T_{z|M} = q_0 \sin(\pi/a)x \sin(\pi/b)y$. The geometry, loading condition and local coordinate system of this considered problem are shown in Fig. 1. The lamina properties are assumed to be

$$E_L = 1.724 \times 10^8 \text{ kN/m}^2 (25 \times 10^6 \text{ psi})$$

$$E_T = 6.89 \times 10^6 \text{ kN/m}^2 (10^6 \text{ psi})$$

$$G_{LT} = 3.45 \times 10^6 \text{ kN/m}^2 (0.5 \times 10^6 \text{ psi}) \quad (19)$$

$$G_{TT} = 1.378 \times 10^6 \text{ kN/m}^2 (0.2 \times 10^6 \text{ psi})$$

$$\nu_{LT} = \nu_{TT} = 0.25$$

where L and T respectively indicate the directions parallel and transverse to the fiber direction, and ν_{LT} is the Poisson ratio measuring the ratio of transverse strain to normal strain under normal stress in the fiber direction. The comparisons between the present theory and 3-D elasticity and other laminate theories are illustrated for the dependence of the stress and displacement results at a certain critical location upon the side-to-thickness ratio of a/h. The present results are in excellent agreement with those of 3-D elasticity. The variations of transverse shear stress through the laminate thickness are respectively shown in Figs 2 and 3 at $s = 4$, 10 and 100 for a square $[0°/90°/0°]$ cross-ply laminate.

Table 1. Maximum stresses and displacement in the $[0/90/0]$ laminates ($a=b$)

a/h	Source	$\bar{\sigma}_x$ $a/2, b/2, h/2$	$\bar{\sigma}_y$ $a/2, b/2, h/6$	$\bar{\sigma}_z$ $a/2, b/2, h/2$	$\bar{\tau}_{yz}$ $0, b/2, 0$	$\bar{\tau}_{xz}$ $a/2, 0, 0$	$\bar{\tau}_{xy}$ $0, 0, h/2$	$\bar{w}$ $a/2, b/2, 0$
2	Pagano	1·436	0·669	1·0000	0·164	0·2591	0·0859	
	Present	1·4898	0·6850	1·0000	0·1665	0·2641	0·0872	5·0794
	Wu and Kuo	1·4352	0·6685	1·0836	0·1631	0·2620	0·0857	5·0636
4	Pagano	0·801	0·534	1·0000	0·256	0·2172	0·0811	2·006
	Present	0·8045	0·5357	1·0000	0·2568	0·2186	0·0811	2·0080
	Wu and Kuo	0·8019	0·5344	1·0721	0·2559	0·2180	0·0810	2·0068
	Ren	0·831	0·549		0·233	0·2140	0·0526	2·013
	Reddy	0·7345	0·5028		0·2024	0·1832	0·0397	1·9218
10	Pagano	0·590	0·285	1·0000	0·357	0·1228	0·0289	0·753
	Present	0·5907	0·2847	1·0000	0·358	0·1229	0·0288	0·7530
	Wu and Kuo	0·5908	0·2845	1·0698	0·3573	0·1228	0·0288	0·7530
	Ren	0·594	0·288		0·353	0·1220	0·0288	0·758
	Reddy	0·5684	0·2690		0·2447	0·1033	0·0277	0·7128
100	Pagano	0·539	0·181	1·0000	0·395	0·0828	0·0213	0·438
	Present	0·5393	0·1808	1·0000	0·3947	0·0828	0·0214	0·4327
	Wu and Kuo	0·5393	0·1808	1·0698	0·3947	0·0828	0·0214	0·4327
	Ren	0·539	0·181		0·395	0·0828	0·0214	0·438
	Reddy	0·5390	0·1806		0·2586	0·0828	0·0213	0·438
	CPT	0·539	0·180		0·395	0·0823	0·0213	0·4313

Table 2. Maximum stresses and displacement in the $[0/90/0]$ laminates ($b=3a$)

a/h	Source	$\bar{\sigma}_x$ $a/2, b/2, h/2$	$\bar{\sigma}_y$ $a/2, b/2, h/6$	$\bar{\sigma}_z$ $a/2, b/2, h/2$	$\bar{\tau}_{yz}$ $0, b/2, 0$	$\bar{\tau}_{xz}$ $a/2, 0, 0$	$\bar{\tau}_{xy}$ $0, 0, h/2$	$\bar{w}$ $a/2, b/2, 0$
2	Pagano	2·13	0·230	1·0000	0·257	0·0668	0·0564	8·17
	Present	2·2071	0·2320	1·0000	0·2603	0·0670	0·0569	8·1416
	Wu and Kuo	2·1305	0·2297	1·0741	0·2571	0·0668	0·0563	8·1606
4	Pagano	1·14	0·109	1·0000	0·351	0·0334	0·0269	2·82
	Present	1·1493	0·1097	1·0000	0·3523	0·0334	0·0269	2·8198
	Wu and Kuo	1·1454	0·1088	1·0717	0·3511	0·0334	0·0269	2·8209
	Ren	1·18	0·110		0·317	0·0308	0·0278	2·80
	Reddy	1·0359	0·1028		0·2724	0·0348	0·0263	2·6411
10	Pagano	0·726	0·0418	1·0000	0·420	0·0152	0·0120	0·919
	Present	0·7261	0·0419	1·0000	0·4204	0·0153	0·0120	0·9189
	Wu and Kuo	0·7262	0·0418	1·0707	0·4201	0·0152	0·0120	0·9189
	Ren	0·729	0·0420		0·415	0·0148	0·0122	0·920
	Reddy	0·6924	0·0398		0·2859	0·0170	0·0115	0·8622
100	Pagano	0·624	0·0253	1·0000	0·439	0·0108	0·0083	0·508
	Present	0·6244	0·0253	1·0000	0·4393	0·0108	0·0083	0·5077
	Wu and Kuo	0·6244	0·0253	1·0705	0·4393	0·0108	0·0083	0·5077
	Ren	0·624	0·0253		0·439	0·0108	0·0083	0·508
	Reddy	0·6240	0·0253		0·2886	0·0129	0·0083	0·5070
	CPT	0·623	0·0252		0·440	0·0108	0·0083	0·503

A fully simply supported sandwich plate with a thickness ratio of $h_{face}/h_{core} = 0·1h/0·8h$ and subjected to sinusoidal transverse loading is considered in Table 3. The material properties of the face layers are listed in eqn (19) and that of the core layer are given by

$$E_{11} = E_{22} = 0·27 \times 10^6 \text{ kN/m}^2 \,(0·04 \times 10^6 \text{ psi})$$

$$E_{33} = 3·45 \times 10^6 \text{ kN/m}^2 \,(0·5 \times 10^6 \text{ psi})$$

$$G_{13} = G_{23} = 0·41 \times 10^6 \text{ kN/m}^2 \,(0·06 \times 10^6 \text{ psi})$$

$$G_{12} = 0·11 \times 10^6 \text{ kN/m}^2 \,(0·016 \times 10^6 \text{ psi}) \tag{20}$$

$$\nu_{12} = \nu_{13} = \nu_{23} = 0·25$$

The maximum stresses and displacement obtained by the present laminate theory, Pagano's 3-D elasticity approach and other laminate theories in previous literature in the considered
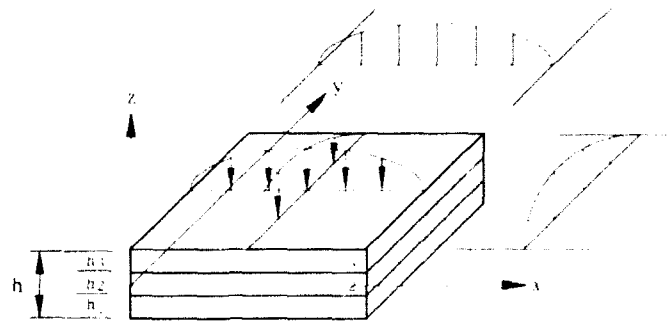
(a) Three-layer laminate

(b) i^{th} lamina (i=1,2 and 3)

Fig. 1. Geometry, local coordinate system and loading condition of the three-layer laminate.
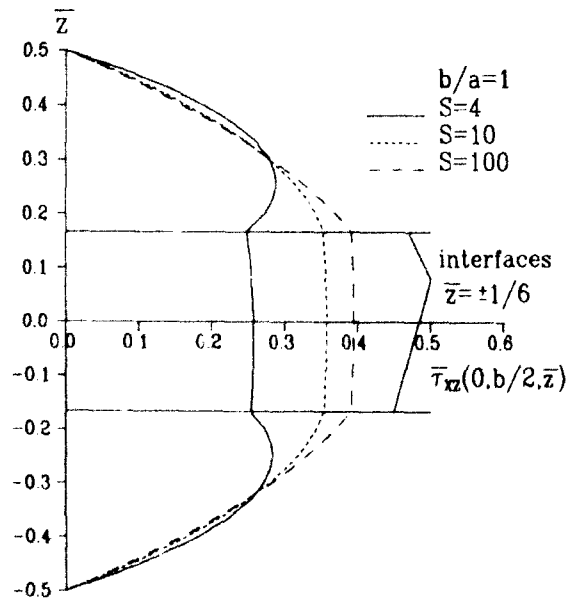
Fig. 2. Distribution of transverse shear stress through the thickness of [0°/90°/0°] laminated plate.
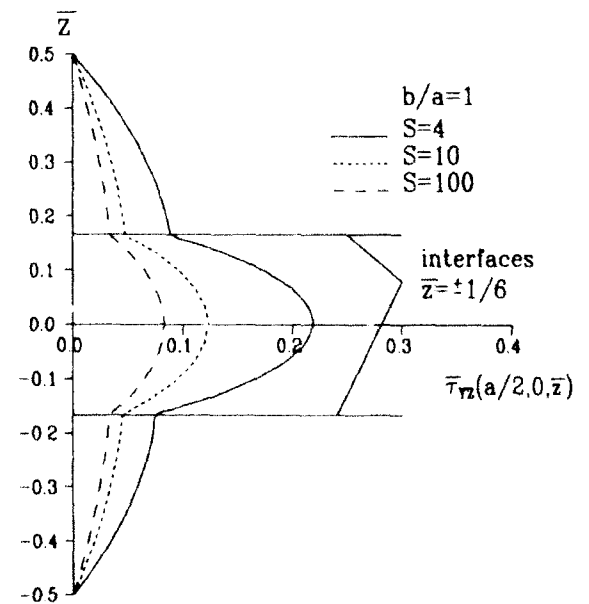
Fig. 3. Distribution of transverse shear stress through the thickness of [0°/90°/0°] laminated plate.

Table 3. Maximum stresses and displacement in a simply supported square sandwich plate (a = b)

a/h	Source	$\bar{\sigma}_x$ (a/2, b/2, 1/2)	$\bar{\sigma}_y$ (a/2, b/2, 1/2)	σ (a/2, b/2, 1/2)	$\bar{\tau}$ (0, b/2, 0)	$\bar{\tau}$ (a/2, 0, 0)	$\bar{\tau}$ (0, 0, 1/2)	$\bar{w}$ (a/2, b/2, 0)
4	Pagano[11]	1·556	0·2595	1·0000	0·2390	0·1072	−0·1437	7·596
	Present	1·4676	0·2307	1·0000	0·2397	0·1106	−0·1281	7·6451
	Wu and Kuo[13]	1·4679	0·2310	1·0177	0·2397	0·1106	−0·1281	7·6453
	Reddy and Chao[15]	0·867	0·1520	—	0·0993	0·1740	−0·0877	4·767
	FPT	0·906	0·1578	—	0·0995	0·0436	−0·0912	4·755
10	Pagano[11]	1·153	0·1104	1·0000	0·3000	0·0527	−0·0707	2·200
	Present	1·1446	0·1065	1·0000	0·2998	0·0534	−0·0686	2·2008
	Wu and Kuo[13]	1·1446	0·1066	1·0165	0·2998	0·0534	−0·0686	2·2008
	Reddy and Chao[15]	1·017	0·0776	—	0·1110	0·0950	−0·0533	1·560
	FPT	1·062	0·0806	—	0·1112	0·0238	−0·0553	1·557
20	Pagano[11]	1·110	0·0700	1·0000	0·317	0·0361	−0·0511	—
	Present	1·1078	0·0691	1·0000	0·3173	0·0363	−0·0505	1·2263
	Wu and Kuo[13]	1·1079	0·0691	1·0162	0·3173	0·0363	−0·0505	1·2263
	Reddy and Chao[15]	1·053	0·0595	—	1·140	0·076	−0·0450	1·0524
—	CPT	1·097	0·0543	—	0·3240	0·0295	−0·0433	0·8783

sandwich plate at s = 4, 10 and 20 are illustrated in Table 3. Again, the present results give much more accurate predictions of stress and displacement in the sandwich structures as compared to the other laminate theories presented in the literature.

5 CONCLUSIONS

A new local high-order deformable theory of laminated composite/sandwich plates was proposed in this paper. The local displacement fields presented here according to Pagano's work were indicated to be significantly more realistic as compared to the other global displacement fields proposed by previous researchers. The displacement and traction continuity conditions at the interfaces and the traction conditions at the outer surfaces in the present theory were completely satisfied. The present theory could be concluded here from observation of the numerical applications to perform excellent results for bending problems of the generally cross-ply laminates.

REFERENCES

1. Mindlin, R. D., Influence of rotary inertia and shear deformation on flexural motions of isotropic, elastic plates. ASME J. Appl. Mech., 18 (1951) 31–8.

2. Ren, J. G., A new theory of laminated plate. Comp. Sci. Technol., 26 (1986) 225–39.

3. Reddy, J. N., A simple higher-order theory for laminated composite plates. ASME J. Appl. Mech., 51 (1984) 745–52.

4. Lo, K. H., Christensen, R. M. & Wu, E. M., A high-order theory of plate deformation — Part 2: Laminated plates. ASME J. Appl. Mech., 44 (1977) 669–76.

5. Lo, K. H., Christensen, R. M. & Wu, E. M., Stress solution determination for high order plate theory. Int. J. Solids Struct., 14 (1978) 655–62.

6. Sun, C. T. & Whitney, J. M., Theories for the dynamic response of laminated plates. AIAA J., 11 (1973) 178–83.

7. Mau, S. T., A refined laminated plate theory. ASME J. Appl. Mech., 40 (1973) 606–7.

8. Seide, P., An improved approximate theory for the bending of laminated plates. Mech. Today, 5 (1980) 451–66.

9. Soldatos, K. P., A general laminated plate theory accounting for continuity of displacements and transverse shear stresses at material interfaces. Comp. Struct., 20 (1992) 195–211.

10. Pagano, N. J., Exact solutions for composite laminates in the cylindrical bending. J. Comp. Mater., 3 (1969) 398–411.

11. Pagano, N. J., Exact solutions for rectangular bidirectional composites and sandwich plates. J. Comp. Mater., 4 (1970) 20–34.

12. Noor, A. K. & Burton, W. S., Assessment of shear deformation theories for multilayered composite plates. Appl. Mech. Rev., 42 (1989) 1–10.

13. Wu, C. P. & Kuo, H. C., Interlaminar stresses analysis for laminated composite plates based on a local high order lamination theory. Comp. Struct., 20 (1992) 237–47.

14. Wu, C. P. & Kuo, H. C., An interlaminar stress mixed finite element method for the analysis of thick laminated composite plates. Comp. Struct. (accepted) (1992).

15. Reddy, J. N. & Chao, W. C., A comparison of closed-form and finite element solutions of thick laminated anisotropic rectangular plates. Nucl. Engng Des., 64 (1981) 153–67.

Dispersive waves in composites, a comparison between various laminated plate theories

W. J. N. Lima & A. M. B. Braga

Department of Mechanical Engineering, Pontifícia Universidade Católica do Rio de Janeiro, CEP 22453, Rio de Janeiro, Brazil

The exact Rayleigh–Lamb wave dispersion spectrum of laminated plates is obtained by applying a recursive algorithm developed for the analysis of stress waves in anisotropic layered media. Results from this benchmark problem are used in comparisons between the classical laminated plate, first-order shear deformation, and two higher-order shear deformation theories. Attention is paid to the effects of the number of layers, direction of propagation, and lay-up (symmetric or asymmetric), on the range of frequencies where these theories apply.

INTRODUCTION

Over the last two decades, considerable effort has been directed towards the development of approximate theories for the deformation of laminated composite plates. Thorough literature reviews are found in articles by Reddy,[1] Noor and Burton[2] and Kapania and Raciti,[3] to name only a few. In most cases, in order to assess the range of validity in the frequency domain of a given theory, comparisons are made with available exact results obtained from three-dimensional elasticity, such as those presented, for instance, in Refs 4–6. With a few exceptions, most of these results are restricted to simply-supported, rectangular, cross-ply laminates with a limited number of layers, and to the low-frequency/long-wavelength range. This paper presents a study on the limits of application in the frequency domain of laminated plate theories. This investigation is made via a wave dispersion analysis.

The dispersion spectrum of waves propagating in a composite plate calculated via a higher-order theory, has as many real branches as the number of kinematic variables used in the approximation of the displacement field. Within the range of frequencies where the theory is valid, each of these branches must have a counterpart in the Rayleigh–Lamb wave dispersion spectrum obtained from three-dimensional elasticity. A comparison between dispersion curves calculated through both methods allows one to assess the limits of validity of the laminated plate model, as well as to give evidence of the boundaries between different approximate theories.

This approach has been pioneered by Mindlin[7] in the evaluation of shear correction factors for his first order theory of homogeneous, isotropic plates. Nelson and Lorch[8] and Whitney and Sun[9] have also relied on comparisons between exact and approximated dispersion curves for the calculation of correction factors needed by their higher-order laminated plate theories. Valisetty and Rehnfield[10] have compared the first branch of the flexural wave dispersion spectrum obtained via a ply level analysis and other approximated theories with exact results reported by Kulkarni and Pagano.[5] These authors have studied laminates with up to five layers, and with a variety of lay-ups. Due to numerical stability problems, inherent in the method applied in the exact analysis presented in Ref. 5, the results from Kulkarni and Pagano are limited to the low-frequency range (wavelengths not shorter than twice the plate thickness).

Here, the exact Rayleigh–Lamb wave dispersion spectrum is obtained by applying a recursive algorithm developed for the analysis of stress waves in anisotropic layered media.[11,12] This algorithm is based on the discrete invariant imbedding technique, and has been shown to be stable over a wide range of frequencies, even in the presence of evanescent wave modes.[11] Due to the numerical stability of the algorithm, it is possible to obtain exact results for the whole frequency spectrum and for a variety of laminates.

These results are used in comparisons between the classical laminated plate theory, first-order shear deformation theory,[13] Reddy's refined third-order theory[14] and Lo et al.[15] first-order theory. The governing equations of the approximate theories are written in matrix form using a state variable approach, and the dispersion curves are constructed from the solution of the associated eigenvalue problem. Attention is paid to the effects of the number of layers, direction of propagation, and lay-up (symmetric or asymmetric), on the range of frequencies where these theories apply.

EXACT ANALYSIS

The field equations governing the linear, elastic motions of homogeneous anisotropic media are

$$\text{div } \boldsymbol{\sigma} = \rho \, \partial^2 \boldsymbol{u}/\partial t^2, \text{ and } \boldsymbol{\sigma} = \boldsymbol{C}{:}\boldsymbol{\nabla}\boldsymbol{u} \qquad (1)$$

where $\boldsymbol{\sigma}$ represents the Cauchy stress tensor, $\boldsymbol{u}$ the displacement field, and $\boldsymbol{C}$ the rank-4 elasticity tensor. Since we are concerned with laminated planar structures, it is convenient to employ as a field variable the traction $\boldsymbol{t} = \boldsymbol{\sigma}\boldsymbol{e}_z$, which must be continuous across planes parallel to the layering. Assuming plane harmonic motions in the form

$$f(x, z, t) = \bar{f}(z)\, e^{i(k_x x - \omega t)} \qquad (2)$$

where $f(x, z, t)$ represents any of the field variables, while ω is the angular frequency and k_x the wave-number in the x-direction, eqns (1) may be recast into a six-dimensional system of ordinary differential equations, written in matrix form as[16]

$$\frac{d}{dx}\,\bar{\boldsymbol{\xi}}(z) = i\boldsymbol{N}\bar{\boldsymbol{\xi}}(z), \text{ where } \bar{\boldsymbol{\xi}}(z) = \begin{Bmatrix} \bar{\boldsymbol{u}}(z) \\ i\bar{\boldsymbol{t}}(z) \end{Bmatrix} \qquad (3)$$

while the linear operator $\boldsymbol{N}$ is a real valued six-tensor depending upon the anisotropic material properties, and on the pair (ω, k_x). The matrix $\boldsymbol{N}$ for orthotropic media may be found in Ref. 16.

In order to obtain a solution for eqn (3), one must find the eigenvalues of $\boldsymbol{N}$. These six eigenvalues are the wave-numbers in the z-direction, and occur in pairs representing waves propagating or decaying in opposite directions of the z-axis.[16] We use the terms upgoing and downgoing when referring to these partial waves. The eigenvectors of $\boldsymbol{N}$ are the polarization vectors of these six waves.

A common practice in the description of the wave motion in layered media is the separation of the field variables into two parts, corresponding to the contributions of the upgoing and downgoing waves to the total fields. Using the subscripts 1 or 2 to represent, respectively, the upgoing or downgoing wave motions, we may write:

$$\bar{\boldsymbol{u}}(z) = \bar{\boldsymbol{u}}_1(z) + \bar{\boldsymbol{u}}_2(z), \text{ and } \bar{\boldsymbol{t}}(z) = \bar{\boldsymbol{t}}_1(z) + \bar{\boldsymbol{t}}_2(z) \qquad (4)$$

It may be shown that the fields $\bar{\boldsymbol{u}}_\alpha(z)$ and $\bar{\boldsymbol{t}}_\alpha(z)$ assume the following form[11,12] (no sum over repeated index)

$$\bar{\boldsymbol{u}}_\alpha(z) = \boldsymbol{W}_\alpha(z)\, \bar{\boldsymbol{u}}_\alpha(0), \text{ and } \bar{\boldsymbol{t}}_\alpha(z) = -i\omega \boldsymbol{Z}_\alpha \bar{\boldsymbol{u}}_\alpha(z)$$

$$\qquad (5)$$

where the $\boldsymbol{W}_\alpha(z)$ and $\boldsymbol{Z}_\alpha (\alpha = 1, 2)$ are (3×3) matrices constructed from the eigenvalues and eigenvectors of the six-dimensional system matrix $\boldsymbol{N}$.

Equations (4) and (5) completely describe the plane harmonic motions in homogeneous anisotropic media. The operator $\boldsymbol{W}_\alpha(z)$ is the propagator matrix that relates the upgoing ($\alpha = 1$), or downgoing ($\alpha = 2$), displacement field at a plane of coordinate z with its value at $z = 0$. The matrix $\boldsymbol{Z}_\alpha$ is the local impedance tensor of the upgoing ($\alpha = 1$) or downgoing ($\alpha = 2$) waves. The vectors $\bar{\boldsymbol{u}}_1(0)$ and $\bar{\boldsymbol{u}}_2(0)$ are the only unknown terms in the formalism represented by (4) and (5), and must be obtained from boundary conditions applied at planes normal to the z-axis.

Surface impedance tensor of a homogeneous plate

We now consider an infinite, homogeneous anisotropic plate of thickness h_1, which is bonded along its lower surface ($z = 0$) to a substrate characterized by the impedance tensor $\boldsymbol{G}_0$, i.e. along $z = 0^-$ (the plane immediately below the interface)

$$\bar{\boldsymbol{t}}(0^-) = -i\omega \boldsymbol{G}_0 \bar{\boldsymbol{u}}(0^-) \qquad (6)$$

We assume that $\boldsymbol{G}_0$ is given. If the layer is traction-free at the lower surface, we take $\boldsymbol{G}_0 = \boldsymbol{0}$. In general, the impedance $\boldsymbol{G}_0$ will depend on both ω and k_x. Since the layer is perfectly bonded to the substrate, both the displacement and traction must be continuous along the interface, i.e.

$$\bar{\boldsymbol{u}}(0^-) = \bar{\boldsymbol{u}}(0^+), \text{ and } \bar{\boldsymbol{t}}(0^-) = \bar{\boldsymbol{t}}(0^+) \qquad (7)$$

In this case, tractions and displacements at $z = h_1$, the top surface of the homogeneous layer, will be

related through the expression[11,12]

$$\bar{t}(h_1) = -i\omega G(h_1)\,\bar{u}(h_1) \tag{8}$$

where

$$G(h_1) = [Z_1 H(h_1) + Z_2][I + H(h_1)]^{-1} \tag{9}$$

and

$$H(h_1) = W_1(h_1)[Z_1 - G_0]^{-1}[G_0 - Z_2]\,W_2^{-1}(h_1) \tag{10}$$

Equation (8) expresses a linear relation between the traction and velocity fields at the plane $z = h_1$. The (3×3) operator $G(h_1)$ represents the surface impedance tensor of an anisotropic layer of thickness h_1 bonded to a substrate with impedance G_0.

Surface impedance tensor of a multilayered composite plate

We now consider a laminated composite plate which is in contact along its lower surface with a substrate of given surface impedance G_0. The n homogeneous layers have thicknesses $h_1, h_2, \dots, h_n$, and the total thickness of the laminated plate is h. The goal is to find an expression which is a generalization of (8) to the case of a multilayered plate. That is, we need to find the tensor G_n such that

$$\bar{t} = -i\omega G_n \bar{u} \tag{11}$$

where $\bar{t}$ and $\bar{u}$ are, respectively, the traction and displacement on the top of the plate.

We start by using the results of the last section to evaluate the impedance G_1 on the top of the first layer (for the sake of simplicity, we write $G_i = G(h_i)$; likewise, we write $H_i = H(h_i)$). We then proceed by employing this result to calculate G_2, the impedance on the top of the second layer, and so on, up to the nth layer. This procedure is summarized in the following algorithm:

Given G_0, ω and k_1:

For $j = 1$ to n repeat

$$H_j = W_1^j(h_j)[Z_1^j - G_{j-1}]^{-1}[G_{j-1} - Z_2^j] \\ \times (W_2^j(h_j))^{-1}$$

$$G_j = [Z_1^j H_j + Z_2^j][I + H_j]^{-1} \tag{12}$$

where $W_a^j(h_j)$ and Z_a^j are the propagator matrix and the local impedance of the upgoing ($a = 1$), or downgoing ($a = 2$), waves propagating in the jth layer. These (3×3) matrices are evaluated by

solving the eigenvalue problem for the N matrix of each homogeneous layer. A detailed analysis of this algorithm may be found elsewhere,[11] where its stability over a wide range of frequencies has been verified.

Rayleigh–Lamb waves in a composite plate

In this section, we consider an infinite, laminated composite plate which is traction-free on both surfaces. We are interested in generating the dispersion curves of plane waves that can propagate freely in the plate. In order to apply the algorithm (23), we choose $G_0 = 0$, which, according to eqn (6), guarantees that the lower surface of the plate is free of tractions. For each (ω, k_1) pair, we apply (23) to evaluate the impedance tensor G_n on the upper surface of the plate. From eqn (11), we conclude that the traction-free boundary condition will be satisfied only for those values of ω and k_1 such that the following equation holds:

$$\det G_n = 0 \tag{13}$$

This equation provides an implicit relation between the frequency ω and the wave-number k_1. It represents the dispersion equation of free waves that propagate in the plate in the absence of an external disturbance. The numerical results of eqn (13) will be compared with those predicted by different approximate plate theories.

APPROXIMATE THEORIES

The highest order laminated plate model considered in this paper is the third-order shear deformation theory introduced by Lo *et al.*[15] (TSDT), based on an assumed displacement field which, for time-harmonic motions, has the form

$$u_x(x, y, z, t) = [u(x, y) + z\phi_1(x, y) + z^2\psi_1(x, y) \\ + z^3\theta_1(x, y)]e^{-i\omega t}$$

$$u_y(x, y, z, t) = [v(x, y) + z\phi_2(x, y) + z^2\psi_2(x, y) \\ + z^3\theta_2(x, y)]e^{-i\omega t} \tag{14}$$

$$u_z(x, y, z, t) = [w(x, y) + z\phi_3(x, y) \\ + z^2\psi_3(x, y)]e^{-i\omega t}$$

Other theories may be considered particular cases of (14). The classical laminated theory (CLT), is obtained from expression (14) by assuming

$$\phi_1 = -\partial w/\partial x, \quad \phi_2 = -\partial w/\partial y, \quad \phi_3 = 0, \quad \psi_i = 0,$$

$$\text{and } \theta_i = 0 \tag{15}$$

for $i = 1, 2, 3$.

The first-order shear deformation theory[13] (FSDT) corresponds to

$$\phi_3 = 0, \quad \psi_t = 0, \quad \theta_1 = -\frac{4}{3h^2}\left(\phi_1 + \frac{\partial w}{\partial x}\right).$$

$$\phi_3 = 0, \quad \psi_t = 0, \quad \text{and} \quad \theta_t = 0 \qquad (16)$$

and

$$(17)$$

while Reddy's refined third-order theory[14] (RSDT) is obtained when we let

$$\theta_2 = -\frac{4}{3h^2}\left(\phi_2 + \frac{\partial w}{\partial y}\right)$$
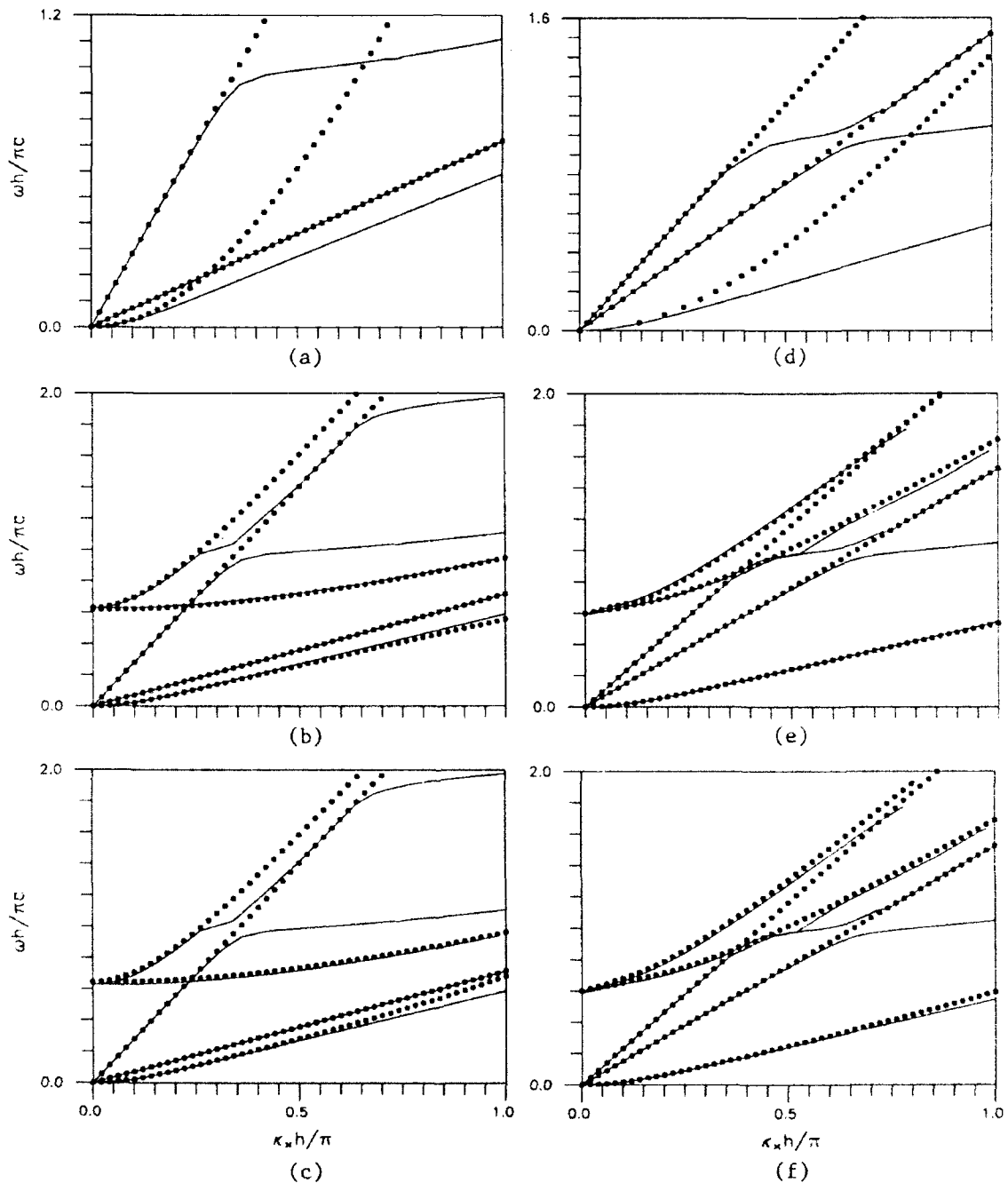
Fig. 1. Dispersion curves for a symmetric, cross-ply laminate with 15 layers: (a) CLT, $\varphi = 0°$; (b) FSDT, $\varphi = 0°$; (c) RSDT, $\varphi = 0°$; (d) CLT, $\varphi = 60°$; (e) FSDT, $\varphi = 60°$; (f) RSDT, $\varphi = 60°$.

Inertia coefficients and generalized forces are defined, respectively, as

$$I_k = \int_{-h/2}^{h/2} \rho z^{k-1}\, \mathrm{d}z, \quad \text{and} \quad R_j^k = \int_{-h/2}^{h/2} \sigma_j z^k\, \mathrm{d}z \tag{18}$$

where $\sigma_j (j = 1, 2, \ldots, 6)$ are the six components of the stress tensor. Stiffness coefficients are defined by

$$(A_{ij}, B_{ij}, D_{ij}, E_{ij}, F_{ij}, G_{ij}, H_{ij})$$

$$= \int_{-h/2}^{h/2} Q_{ij}(1, z, z^2, z^3, z^4, z^5, z^6)\, \mathrm{d}z \tag{19}$$

where Q_{ij} are the elastic constants in the plate coordinates — for CLT, FSDT and RSDT, they represent the plane-stress-reduced constants.

In the case of cylindrical bending, when all derivatives in the y direction vanish, the balance of linear momentum — in the absence of forcing terms — and constitutive equations for all four theories may be written in matrix form as[17]

$$\frac{\mathrm{d}}{\mathrm{d}x} \boldsymbol{\zeta} = M\boldsymbol{\zeta} \tag{20}$$

where the state vector, $\boldsymbol{\zeta}$, is defined as

$$\boldsymbol{\zeta}^{\mathrm{T}} = [u, v, -\mathrm{d}w/\mathrm{d}x, w, R_1^0, R_6^0, R_1^1, R_5^0] \quad \text{for CLT} \tag{21}$$

$$\boldsymbol{\zeta}^{\mathrm{T}} = [u, v, \phi_1, \phi_2, w, R_1^0, R_6^0, R_1^1, R_6^1, R_5^0] \quad \text{for FSDT} \tag{22}$$

$$\boldsymbol{\zeta}^{\mathrm{T}} = [u, v, \phi_1, \phi_2, -4(\mathrm{d}w/\mathrm{d}x)/3h^2, w, R_1^0, R_6^0,$$
$$R_1^1 - 4R_1^3/3h^2, R_6^1 - 4R_6^3/3h^2, R_1^3, R_5^0] \quad \text{for RSDT} \tag{23}$$

and

$$\boldsymbol{\zeta}^{\mathrm{T}} = [u, v, \phi_1, \phi_2, \psi_1, \psi_2, \theta_1, \theta_2, w, \phi_3, \psi_3,$$
$$R_1^0, R_6^0, R_1^1, R_6^1, R_1^2, R_6^2, R_1^3, R_6^3,$$
$$R_5^0, R_5^1, R_5^2] \text{ for TSDT} \tag{24}$$

Even though its size depends on the theory that is being applied, the system matrix M in eqn (20) can in all cases be partitioned into four real, square submatrices:

$$M = \begin{bmatrix} P & S \\ L & -P^{\mathrm{T}} \end{bmatrix} \tag{25}$$

where both S and L are symmetric. These matrices are presented in the Appendix for CLT,

FSDT and RSDT. The matrix M for TSDT may be found in Ref. 17. From the symmetries of S and L follows

$$JMJ^{\mathrm{T}} = -M^{\mathrm{T}}, \quad \text{where} \quad J = \begin{bmatrix} 0 & -I \\ I & 0 \end{bmatrix} \tag{26}$$

From (26), we conclude that the eigenvalues of M, which we denote by ik_i, occur in pairs of opposite
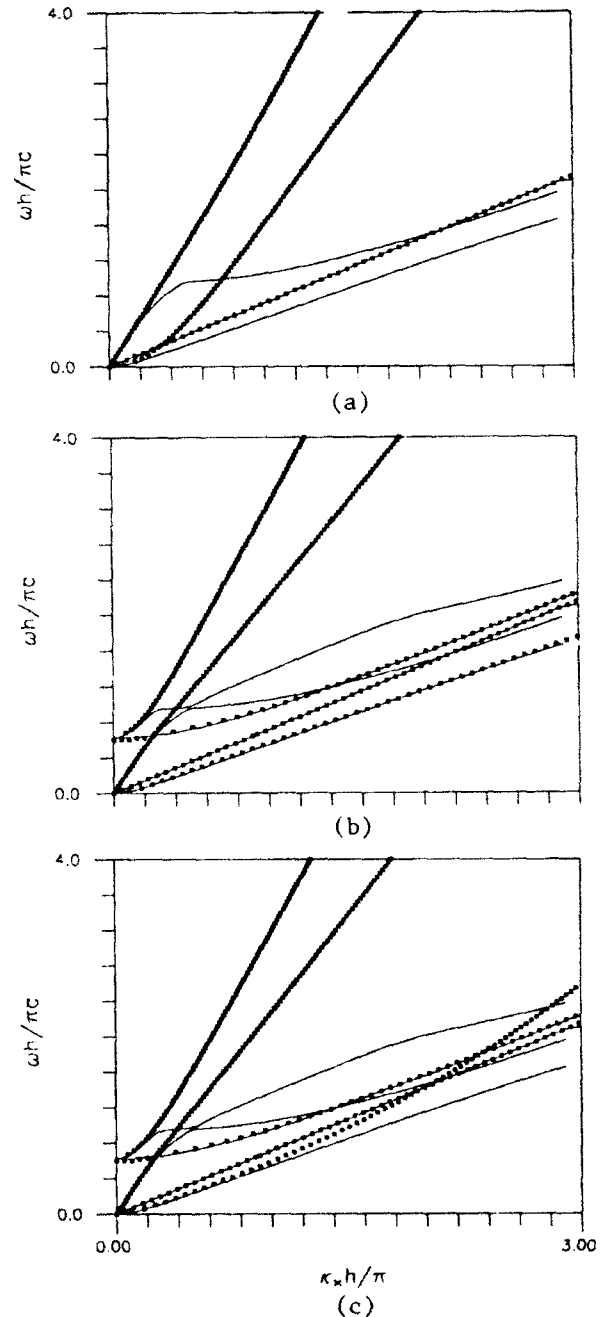
Fig. 2. Dispersion curves for a $(0°/90°/0°/90°)$ laminate: (a) CLT, $\varphi = 0°$; (b) FSDT, $\varphi = 0°$; (c) RSDT, $\varphi = 0°$.

sign.[17] It is clear that these eigenvalues are the wave-numbers associated with partial waves that propagate — or decay when k_x is complex — along the unloaded infinite plate. When solving a boundary value problem, these partial waves must be linearly combined in order to satisfy a proper set of boundary conditions. Next, we compare pairs formed by these eigenvalues and frequencies with the dispersion curves of Rayleigh–Lamb waves evaluated through the exact method presented in the preceding section

RESULTS AND DISCUSSION

The dispersion curves presented in this section have been obtained by plotting the nondimensional frequency, $\omega h/\pi \bar{c}$, versus the nondimensional wave-number $k_x h/\pi$, where $\bar{c} = \sqrt{Q_{33}/\rho}$ is a reference wave speed. The wavelength is $\lambda = 2\pi/k_x$. Except for the slowness plots in Fig. 4 below, the direction of propagation (x-direction)

makes an angle φ with the stiffer direction of the top layer in the laminate. In all plots, dotted lines correspond to approximate theories, while continuous lines are reserved for exact solutions. The following material properties have been used in all the calculations:

$$E_1 = 16E_2, \quad G_{12} = G_{13} = 0.57E_2, \quad G_{23} = 0.37E_2$$

and

$$\nu_{12} = 0.25.$$

The curves drawn in Fig. 1 are for a cross-ply, symmetric laminate with 15 layers. Figures 1(a–c) have been obtained for $\varphi = 0°$. In this case, the lower branch of the dispersion spectrum corresponds to a flexural wave, the second to an antiplane shear wave, and the third to an extensional wave. All three start from the origin. The fourth branch is associated with another antiplane shear wave and the fifth corresponds to the second flexural wave. Plots in Figs 1(d,e) are for $\varphi = 60°$. As expected, the flexural branch from CLT (Figs
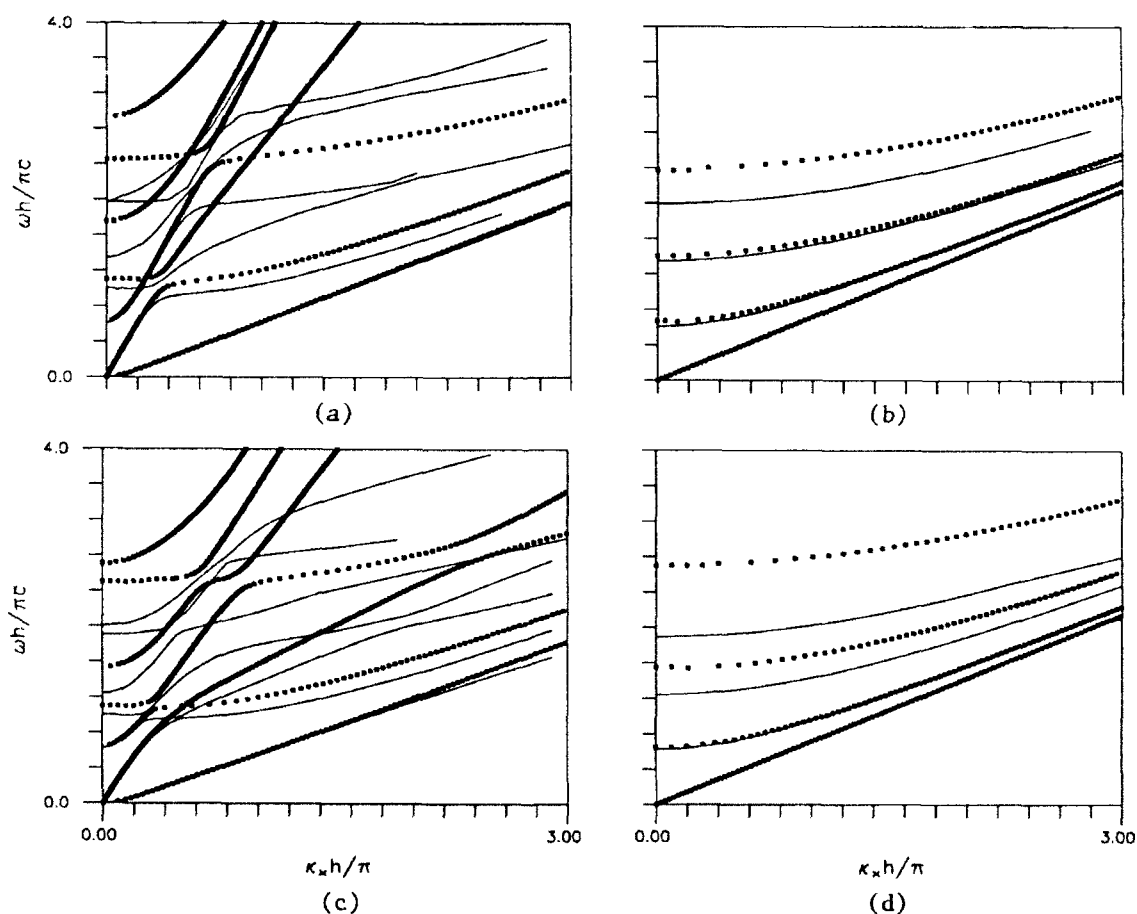
Fig. 3. Dispersion curves obtained via TSDT: (a) $(0°/90°/0°)$, $\varphi = 0°$; plane motions; (b) $(0°/90°/0°)$, $\varphi = 0°$, antiplane motions; (c) $(0°/90°/0°/90°)$, $\varphi = 0°$, plane motions; (d) $(0°/90°/0°/90°)$, $\varphi = 0°$, antiplane motions.

1(a) and 1(d)) matches the exact result only at very low frequencies. The shear-correction factor used for the FSDT results presented in Figs 1(b) and 1(e) has been calculated following Mindlin's approach.[7] We observe from Figs 1(c) and 1(f) that, as the wave-number becomes larger, the RSDT will predict higher frequencies for the lower flexural mode than the exact analysis or FSDT.

The results in Fig. 2 are for an antisymmetric laminate with four plies (0°/90°/0°/90°). The angle φ is 0°. Again, except for the first antiplane shear mode, results from CLT match the exact dispersion spectrum only in the low-frequency region. The shear correction factor $\pi^2/12$ was used for FSDT results in Fig. 2(b). The matching of the first three branches in Fig. 2(b) to exact results is remarkably good up to the nondimensional wave-number 3·0, which corresponds to a wavelength equal to $2h/3$. This is a much better result than

the one obtained from RSDT and shown in Fig. 2(c), whose first flexural branch matches the exact curve up to the nondimensional frequency 0·45, corresponding to a ratio $\lambda/h = 2$.

The first two plots in Fig. 3 present the dispersion spectrum of a (0°/90°/0°) plate calculated from TSDT. The results are for $\varphi = 0°$. In this case, plane and antiplane motions uncouple, and are plotted respectively in Figs 3(a) and 3(b). The first three branches of Fig. 3(a) and the first two of Fig. 3(b) can be identified with those obtained from both FSDT and RSDT. The results from these two theories for the three-ply laminate are not shown here, but we have observed that the agreement of the lower branches of TSDT with exact dispersion curves is better in this case. As the frequency increases, the matching of the higher branches of TSDT with those obtained from the exact analysis is very poor though, even for low wave-numbers (long wavelengths). The
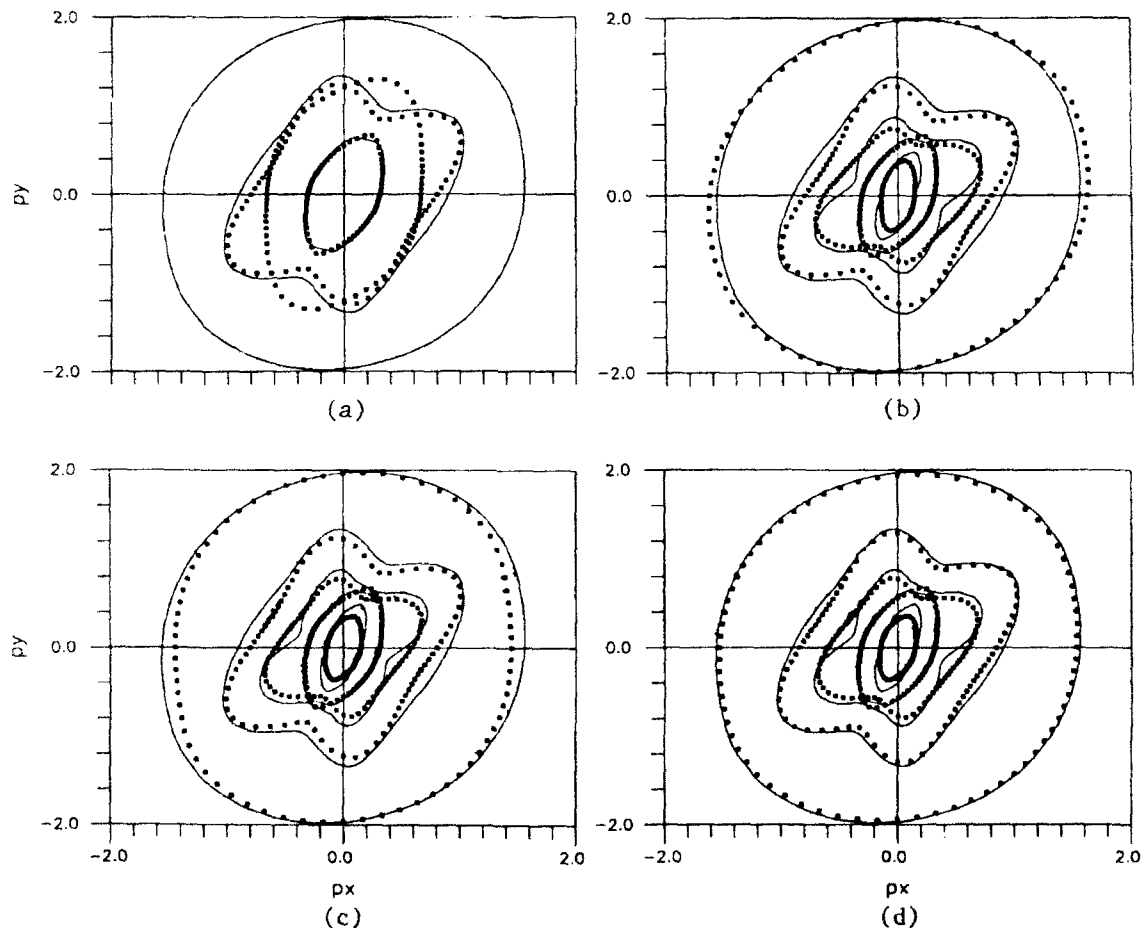
Fig. 4. Slowness curves for a (0°/45°/0°/45°/0°) laminate at $\omega h/\pi c = 0.8$: (a) CLT; (b) FSDT; (c) RSDT; (d) TSDT.

same conclusions regarding the TSDT results are reached for the plots in Figs 3(c) and 3(d), corresponding to a (0°/90°/0°/90°) plate.

Finally, we consider a (0°/45°/0°/45°/0°) laminate and observe the matching with exact results as we vary the angle of propagation φ. The plots in Fig. 4 correspond to slowness curves for a fixed frequency. They are obtained by dividing the nondimensional wave-number by the frequency, which yields the inverse of the phase velocity. Results are for $\omega h/\pi \bar{c} = 0.8$. The slownesses p_x and p_y represent the projections of the inverse of the phase velocity, $k_x \bar{c}/\omega$, on the x- and y-axes. The x-axis is parallel to the stiffer direction of the top layer in the laminate. The outermost and innermost curves correspond, respectively, to the first and second flexural modes. For all four theories considered, the agreement with exact results depends on the angle of propagation. Poorest results are again from the CLT. At this frequency, both the FSDT and RSDT provide very good estimates of the first flexural phase velocity for angles of propagation close to 90°. The best match is obtained from TSDT. The matching of the second flexural mode is poor for all three theories, except for angles φ close to 0°.

REFERENCES

1. Reddy, J. N., A review of the literature on finite-element modeling of laminated composite plates and shells. *Shock Vib. Digest*, 17 (4) (1985) 3-8.
2. Noor, A. K. & Burton, W. S., Assessment of shear deformation theories for multilayered composite plates. *Appl. Mech. Rev.*, 42 (1) (1989) 1-13.
3. Kapania, R. K. & Raciti, S., Recent advances in analysis of laminated beams and plates, part II: vibrations and wave propagation. *AIAA J.*, 27 (1989) 935-46.
4. Srinvas, S., Rao, J. & Rao, A. K., An exact analysis for vibration of simply-supported homogeneous and laminated thick rectangular plates. *J. Sound Vib.*, 12 (1970) 187-99.
5. Kulkarni, S. V. & Pagano, N. J., Dynamic characteristics of composite laminates. *J. Sound Vib.*, 23 (1972) 127-43.
6. Dong, S. B. & Nelson, R. B., On natural vibrations and waves in laminated orthotropic plates. *J. Appl. Mech.*, 39 (1972) 739-45.
7. Mindlin, R. D., Influence of rotatory inertia and shear on flexural motions of isotropic elastic plates. *J. Appl. Mech.*, 18 (1951) 31-8.
8. Nelson, R. B. & Lorch, D. R., A refined theory for laminated orthotropic plates. *J. Appl. Mech.*, 41 (1974) 177-83.
9. Whitney, J. M. & Sun, C. T., A higher order theory for extensional motion of laminated composites. *J. Sound Vib.*, 30 (1973) 85-97.
10. Valisetty, R. R. & Rehnfield, L. W., Application of ply level analysis to flexural wage propagation. *J. Sound Vib.*, 126 (1988) 183-94.
11. Braga, A. M. B., Wave propagation in anisotropic layered composites. PhD thesis, Stanford University, 1990.
12. Braga, A. M. B. & Herrmann, G., Free waves at a fluid/layered-composite interface. In *Elastic Wave Propagation and Ultrasonic Nondestructive Evaluation*, ed. S. K. Datta, J. D. Achenbach & Y. S. D. Rajapakse. Elsevier, Amsterdam, 1990, pp. 171-6.
13. Whitney, J. M. & Pagano, N. J., Shear deformation in heterogeneous anisotropic plates. *J. Appl. Mech.*, 37 (1970) 1031-6.
14. Reddy, J. N., A simple higher-order theory for laminated composite plates. *J. Appl. Mech.*, 51 (1984) 745-52.
15. Lo, K. H., Christensen, R. M. & Wu, E. M., A high-order theory of plate deformation. Part 2: laminated plates. *J. Appl. Mech.*, 44 (1977) 669-76.
16. Braga, A. M. B. & Herrmann, G., Floquet waves in anisotropic periodically layered media. *J. Acoust. Soc. Amer.*, 92 (1992) 1211-27.
17. Lima, W. J. N., Dispersive waves in laminated composite plates (in Portuguese). MSc thesis, Pontifícia Universidade Católica do Rio de Janeiro, 1993.

APPENDIX: MATRIX M

For CLT:

$P_{ij} = 0$ $(i, j = 1, \ldots, 4)$, except for $P_{43} = -1$

$L_{11} = L_{22} = L_{44} = -\omega^2 I_1$, $L_{33} = -\omega^2 I_3$, $L_{13} = L_{31} = -\omega^2 I_2$

$L_{12} = L_{21} = L_{14} = L_{41} = L_{23} = L_{32} = L_{24} = L_{42} = L_{34} = L_{43} = 0$

$S_{44} = S_{a4} = S_{4a} = 0$, $S_{a\beta} = K_{a\beta}$ for $a, \beta = 1, 2, 3$, where

$$K^{-1} = \begin{bmatrix} A_{11} & A_{16} & B_{11} \\ A_{16} & A_{66} & B_{16} \\ B_{11} & B_{16} & D_{11} \end{bmatrix}.$$

For FSDT:

$$P_{ij} = 0 \ (i, j = 1, \ldots, 5), \text{ except for } P_{53} = -1 \text{ and } P_{54} = -A_{45}/A_{55}$$

$$L_{11} = L_{22} = L_{55} = -\omega^2 I_1, \ L_{33} = -\omega^2 I_3, \ L_{44} = -\omega^2 I_3 + A_{44} - A_{45}^2/A_{55}$$

$$L_{13} = L_{31} = L_{24} = L_{42} = -\omega^2 I_2, \ L_{12} = L_{21} = L_{14} = L_{41} = L_{15} = L_{51} = 0$$

$$L_{23} = L_{32} = L_{25} = L_{52} = L_{34} = L_{43} = L_{35} = L_{53} = L_{45} = L_{54} = 0 \text{ and}$$

$$S^{-1} = \begin{bmatrix} A_{11} & A_{16} & B_{11} & B_{16} & 0 \\ A_{16} & A_{66} & B_{16} & B_{66} & 0 \\ B_{11} & B_{16} & D_{11} & D_{16} & 0 \\ B_{16} & B_{66} & D_{16} & D_{66} & 0 \\ 0 & 0 & 0 & 0 & A_{55} \end{bmatrix}$$

For RSDT:

$$P_{ij} = 0 \ (i, j = 1, \ldots, 6), \text{ except for } P_{65} = -3h^2/4$$

$$L_{11} = L_{22} = L_{66} = -\omega^2 I_1, \ L_{33} = -\omega^2 I_3 + \hat{A}_{55}, \ L_{44} = -\omega^2 I_3 + \hat{A}_{44}$$

$$L_{55} = -\omega^2 I_5 + 3h^2 \hat{A}_{55}/4, \ L_{13} = L_{31} = L_{24} = L_{42} = -\omega^2 I_2$$

$$L_{15} = L_{51} = -\omega^2 I_4, \ L_{34} = L_{43} = \hat{A}_{45}, \ L_{35} = L_{53} = -\omega^2 I_5 - 3h^2 \hat{A}_{55}/4$$

$$L_{12} = L_{21} = L_{14} = L_{41} = L_{16} = L_{61} = L_{23} = L_{32} = L_{25} = L_{52} = 0$$

$$L_{26} = L_{62} = L_{36} = L_{63} = L_{46} = L_{64} = L_{56} = L_{65} = 0$$

$$S_{66} = S_{6\alpha} = S_{6\alpha} = 0, \ S_{\alpha\beta} = K_{\alpha\beta} \text{ for } \alpha, \beta = 1, \ldots, 6, \text{ where}$$

$$K^{-1} = \begin{bmatrix} A_{11} & A_{16} & \hat{B}_{11} & \hat{B}_{16} & E_{11} \\ A_{16} & A_{66} & \hat{B}_{16} & \hat{B}_{66} & E_{16} \\ \hat{B}_{11} & \hat{B}_{16} & \hat{D}_{11} & \hat{D}_{16} & \hat{F}_{11} \\ \hat{B}_{16} & \hat{B}_{66} & \hat{D}_{16} & \hat{D}_{66} & \hat{F}_{16} \\ E_{11} & E_{16} & \hat{F}_{11} & \hat{F}_{16} & H_{11} \end{bmatrix}$$

and $\hat{B}_{ij} = B_{ij} - 4D_{ij}/3h^2$, $\hat{D}_{ij} = D_{ij} - 8F_{ij}/3h^2 + 16H_{ij}/9h^4$, $\hat{F}_{ij} = F_{ij} - 4H_{ij}/3h^2$, for $i, j = 1, 6$. $\hat{A}_{\alpha\beta} = A_{\alpha\beta} - 8D_{\alpha\beta}/h^2 + 16F_{\alpha\beta}/h^4$, for $\alpha, \beta = 4, 5$. $\hat{I}_2 = I_2 - 4I_4/3h^2$, $\hat{I}_3 = I_3 - 8I_5/3h^2 + 16I_7/9h^4$, $\hat{I}_5 = I_5 - 4I_7/3h^2$.

Optimum design for buckling of plain and stiffened composite axisymmetric shell panels/ shells

Biswajit Tripathy & K. P. Rao

Department of Aerospace Engineering, Indian Institute of Science, Bangalore, 560 012, India

The buckling of plain and discretely stiffened composite axisymmetric shell panels/shells made of repeated sublaminate construction is studied using the finite element method. In repeated sublaminate construction, a full laminate is obtained by repeating a basic sublaminate, which has a smaller number of plies. The optimum design for buckling is obtained by determining the layup sequence of the plies in the sublaminate by ranking, so as to achieve maximum buckling load for a specified thickness. For this purpose, a four-noded 48-dof quadrilateral composite thin shell element, together with fully compatible two-noded 16-dof composite meridional and parallel circle stiffener elements are used.

1 INTRODUCTION

Axisymmetric shell structures made of laminated composites are used extensively in many engineering applications. Buckling is one of the important modes of failure of shells when they are thin, as is the case most often in all aerospace applications. Buckling of composite cylindrical shell panels/shells has been attempted by many researchers,[1] showing the influence of various coupling terms, the panel aspect ratio, geometric nonlinearity and imperfections on the resultant buckling load. The buckling problem of conical shells made of orthotropic and composite materials has been solved by Hua and Dongxing[3] and Wang[4] respectively. In order to meet the stiffness and strength requirements, keeping in mind the minimum weight consideration, shells are stiffened. Addition of stiffeners may change the buckling load and mode of the structure entirely depending on the size and location of the stiffeners, material properties, loading and boundary conditions. Such a construction has to be modelled appropriately to represent the realistic behaviour of the shell. A fairly extensive review on the buckling of laminated composite plates and shell panels by Leissa[10] indicates that most of the research has been limited to unstiffened panels. This paper presents the work done on the buckling problem of laminated anisotropic axisymmetric shell panels/shells with laminated anisotropic stiffeners (in meridional and hoop directions) using the finite element method. A four-noded, 48-dof quadrilateral composite thin shell element with fully compatible two-noded, 16-dof meridonial stiffener element (MSE) and parallel circle stiffener element (PCSE) are used for the linear bifurcation analysis.

In designing a composite shell with composite stiffeners along meridional, and parallel circle directions, the designer has several parameters to contend with, such as geometry of the shell, fibre angles, the stacking sequence, spacing between stiffeners and their locations, etc. Among these, orientation angles and stacking sequence of the plies are found to have a significant effect on the buckling load of the structure. This makes it imperative to investigate ways to optimize the composite layup and exploit its directional property. It is found that attempts at optimization have been made only for simple cases of clamped or simply supported laminate composite circular cylindrical shells for which closed form solutions are available.[11,13] Not much information is available on the optimization of general stiffened composite shells for buckling, treating the ply angle distribution through the thickness as the design variable. In this paper a simple way to find the optimum layup scheme of plies in the shell and stiffener that will give the maximum buckling load

459

factor for a given geometry, loading and boundary conditions is proposed and several cases are addressed.

2 REPEATED SUBLAMINATE CONSTRUCTION AND SUBLAMINATE CODING

In the repeated sublaminate construction of composite laminates (Fig. 1), the basic sublaminate consisting of a few plies is repeated several times to obtain the desired thickness of the laminate. Such a construction results in better mixing of plies of different orientations leading to more damage tolerant laminates.[4] Besides, it also reduces manufacturing errors and is therefore employed in industry.

The buckling load of a shell panel/shell is mainly governed by its flexural stiffnesses D_{ij}. Both location and orientation of plies in a sublaminate have significant influence on these stiffnesses and hence on the resultant buckling load. Therefore, optimization of both location and orientation of plies in a sublaminate is needed to maximize the buckling load. A coding as developed by Tsai[12] for the laying up sequences of the plies in the sublaminate is followed in this paper. Details of the coding are given below.

The number of plies in a sublaminate are taken to be 6, 4 or 2. Four ply-orientation angles (θ_1, θ_2, θ_3, θ_4) are considered. Of these, the number of possible orientations of plies in 6, 4 and 2-ply sublaminates are assumed to be 3, 2 and 2 respectively. Thus the following layup schemes are examined:

(i) 40, 6-ply, tri-directional laminates represented by the code |4110|, |3210|,..., |0114| with the restriction that at least one ply must exist for each of the three angles in a sublaminate;

(ii) 18, 4-ply, bi-directional laminates represented by the code |3100|, |2200|,..., |0013| with the restriction that at least one ply must exist for each of the two angles considered in a sublaminate; and

(iii) 6, 2-ply, bi-directional laminates represented by the code |1100|,..., |0011| with the restriction that at least one ply must exist for each of the two angles considered in a sublaminate.

The sublaminate code designates the number of plies in the order of θ_1°, θ_2°, θ_3°, θ_4°. Thus |4110|
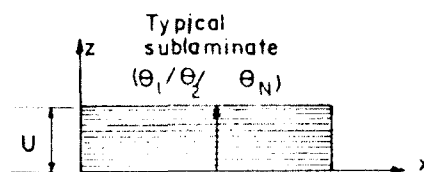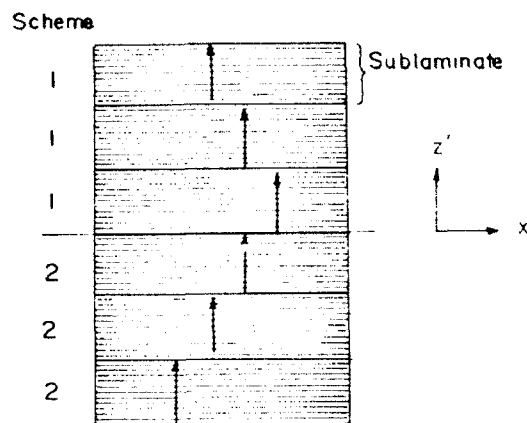
Fig. 1.   Repeated sublaminate construction.

Lay up scheme 1 — ($\Theta_1/\Theta_2/\Theta_3$ .... Θ_N)

Lay up scheme 2 — (Θ_N/Θ_{N-1} /Θ_{N-2} ... Θ_1)
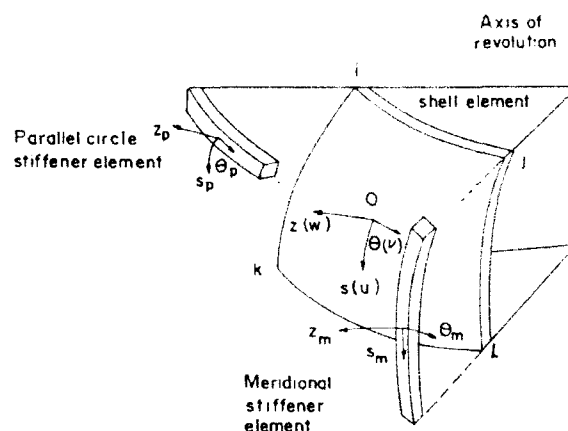
Fig. 2.   Parallel circle and meridional stiffener elements compatible with quadrilateral shell element.

designates $|(\theta_1)_4/\theta_2/\theta_3|$. There are altogether 64 sublaminates under this class.

As buckling is a phenomenon primarily governed by bending and twisting stiffnesses, the location of a ply with respect to the middle plane of the laminate is very important. So, each one of the 64 sublaminates with all possibilities of stack-

ing are considered. For example, in the case of the sublaminate $[\theta_1, \theta_2, \theta_3, \theta_4]$, there are 24 combinations possible such as $[\theta_1, \theta_2, \theta_3, \theta_4], [\theta_1, \theta_2, \theta_4, \theta_3], [\theta_1, \theta_3, \theta_2, \theta_4],\dots$ etc. Therefore we have for.
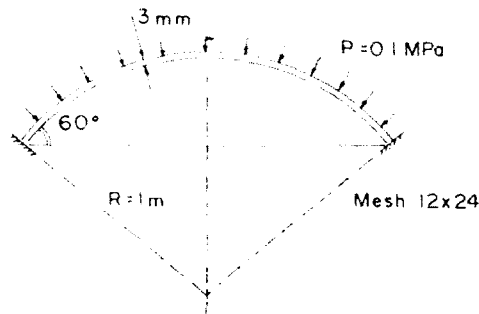
Fig. 3. Clamped spherical cap with uniform external pressure.

- 40, 6-ply sublaminates, 240 combinations.
- 18, 4-ply sublaminates, 36 combinations.
- 6, 2-ply sublaminates, 12 combinations

Thus in all, corresponding to the 64 groups of sublaminates, one would have 288 combinations to be considered. The following new notation is introduced to define these sublaminate layup schemes.

Integer 1 denotes θ_1 ply
Integer 2 denotes θ_2 ply
Integer 3 denotes θ_3 ply
Integer 4 denotes θ_4 ply

Thus a $[111123]$ layup scheme means $[\theta_1, \theta_1, \theta_1, \theta_1, \theta_2, \theta_3]$.

Table 1. Ranked coding for clamped spherical cap under uniform external pressure

Sl. No.	Code	λ	Sl. No.	Code	λ	Sl. No.	Code	λ
1	222344	6·751	97	334411	5·529	223	433331	4·587
2	222433	6·751				224	344441	4·587
3	224433	6·503				225	2223	4·582
4	223344	6·503	120	332111	5·397	226	2224	4·582
5	222243	6·469	121	221114	5·377	227	444133	4·552
6	222234	6·469	122	221113	5·377			
7	222334	6·416	123	442333	5·362			
8	222443	6·416	124	332444	5·362	247	1122	4·296
			125	444423	5·360	248	2221	4·260
			126	333324	5·360	249	144433	4·193
49	211444	5·864				250	133344	4·193
50	211333	5·864				251	133444	4·193
51	122444	5·823	149	422223	5·239	252	144333	4·193
52	122333	5·823	150	322224	5·239	253	2141	4·139
53	112244	5·806	151	441113	5·233	254	314444	4·070
54	112233	5·806	152	331114	5·233	255	413333	4·070
55	444421	5·804	153	411122	5·206			
56	333321	5·804	154	311122	5·206			
			155	422111	5·206	270	31	3·456
						271	341111	3·404
57	112333	5·798				272	431111	3·404
58	112444	5·798	190	333441	4·850	273	4433	3·380
59	443322	5·796	191	334441	4·850	274	3344	3·380
60	334422	5·796	192	443331	4·850	275	43	3·380
61	444412	5·788	193	443111	4·797	276	34	3·380
62	333312	5·788	194	334111	4·797			
63	344222	5·782	195	421111	4·781			
64	433222	5·782	196	321111	4·781	283	1333	3·300
			197	4442	4·777	284	1444	3·300
			198	3332	4·777	285	1114	3·162
90	111132	5·578	199	111134	4·760	286	1113	3·162
91	222241	5·562	200	111143	4·760	287	4111	2·745
92	222231	5·562				288	3111	2·745
93	433322	5·551						
94	344422	5·551	220	411333	4·593			
95	222114	5·531	221	333341	4·587			
96	222113	5·531	222	444431	4·587			

†Buckling load factor.

3 FINITE ELEMENT FORMULATION FOR BUCKLING

A doubly curved quadrilateral laminated aniso-
tropic shell finite element has been presented by
Venkatesh and Rao.[15] This is a four-noded ele-
ment of uniform thickness bound by two parallel
circles and two meridians of a shell of revolution.
Each of the three displacements of the reference
surface within the shell element is expressed as
products of one dimensional first order Hermite
interpolation polynomials. This leads to a 48-dof
element with 12-dof per node. A laminated aniso-
tropic meridional stiffener element (MSE) and a
parallel circle stiffener element (PSCE) have been
presented by Venkatesh and Rao.[16] Each is a two-
noded, 16-dof degenerated element derived from
the above shell element invoking line member
assumptions (Fig. 2).

Nonlinear strain–displacement relations and
the details of formulation of strain energy and the
geometric stiffness matrix for the shell and stif-
fener elements have been given in Ref. 17. The
stiffness matrix (elastic and geometric) of the stif-
fened shell is obtained by adding the respective
stiffness matrices of the shell and the stiffener
finite elements after suitable transformations are
made. These transformations take into account
the eccentricity between the shell and stiffener
axis systems and introduce the correct rotation
dof θ_z and θ_u.

The bifurcation buckling load is computed by
solving the eigenvalue problem given as

$$[K_1] + \lambda [K_G] = 0$$

where $[K_1]$ is the global elastic stiffness matrix and
$[K_G]$ is the global geometric stiffness matrix, which
not only depend on the geometry of the structure
but also on the initial applied loads. All 288 poss-
ible layup schemes given in Section 2 are consi-
dered and the corresponding buckling load
factors rank ordered. The layup is optimum if the
buckling load factor corresponding to it is a maxi-
mum.

4 OPTIMUM LAYUP FOR BUCKLING BY RANKING

The formulation and the computer code has been
checked for correctness by computing buckling
loads for several plain/stiffened shell panels/shells
with isotropic/orthotropic/layered composite

materials and subjected to various boundary
conditions and loadings. Comparisons made else-
where[17-20] with existing solutions in the literature
indicate good performance. Here optimization of
ply location and orientation in the sublaminate are
taken up to obtain maximum buckling loads for
three typical examples. The cases considered are:

1. clamped spherical cap under external pres-
   sure,
2. ring and stringer stiffened cylinder,
3. conical sandwich panel without and with
   hoop stiffeners.

The ply material used for all cases considered
for optimization is T300/N5208 graphite–epoxy.
Its properties are:

$E_1 = 181$ GPa
$E_t = 10.27$ GPa
$G_{lt} = 7.07$ GPa
$v_{lt} = 0.28$

The thickness of each ply is 0.125 mm. All 288
possible layup schemes for 6-, 4- and 2-ply sub-
laminates are considered for rank ordering. The
four ply angles are chosen as $0°$, $90°$, $45°$ and
$-45°$.
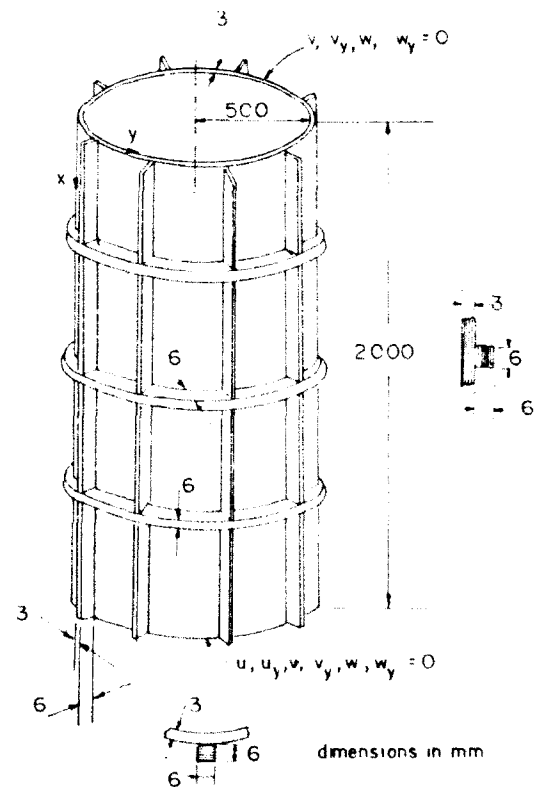
Fig. 4. Ring and stringer stiffened composite cylindrical shell.

Clamped spherical cap under external pressure

The geometry, loading and boundary conditions of the spherical cap considered, are given in Fig. 3. The rank ordered list of buckling load factors are given in Table 1. The optimum layup scheme for the sublaminate is [222344] or [90°/45°/−45°]. It can be seen from the table, that combination of 90°, 45° and −45° plies in the sublaminate, with ±45° plies placed away from the shell reference axis, gives higher buckling load factors. The layup scheme [431111] gives a minimum buckling load factor of 3·4 amongst all possible cases of 6-ply (tri-directional) sublaminates, whereas by reversing the layup scheme ([111134]), the buckling load factor obtained is 4·76 (~40% increase). Compared to the maxi-mum buckling load factor of 6·75 corresponding to the tri-directional 6-ply sublaminate layup scheme [222344], for bi-directional sublaminates (4-ply), the highest buckling load factor is 4·78 for the layup scheme [4442].

Ring and stringer stiffened cylinder

The geometry and boundary conditions of the stiffened cylinder are shown in Fig. 4. The thickness of the shell is 3 mm (12, 2-ply or 6, 4-ply or 4, 6-ply sublaminates) and the depth of each stiffener is 6 mm (24, 2-ply or 12, 4-ply or 8, 6-ply sublaminates). The stiffener laminae are considered to be parallel to the shell middle surface. For ply orientations of the cylinder and stringer sublaminates, the reference direction is along the

Table 2. Ranked coding for the axially compressed ring and stringer stiffened cylinder

Sl. No.	Code	λ[a]	Sl. No.	Code	λ	Sl. No.	Code	λ
1	113344	0·681	84	114422	0·485	218	222331	0·315
2	114433	0·681	85	311114	0·485	219	43	0·313
3	111433	0·674	86	222113	0·485	220	4433	0·313
4	111344	0·674	87	134444	0·484	·		
5	111334	0·664	88	113222	0·484			
6	111443	0·662	89	113322	0·482	240	4333	0·289
7	113444	0·656	90	314444	0·478	243	224441	0·285
8	443322	0·654	·			244	444421	0·282
9	114333	0·653				245	223331	0·281
10	311444	0·651	126	322211	0·441	246	333422	0·281
11	334422	0·650	127	1122	0·440	247	322444	0·280
12	114443	0·640	128	332444	0·440	248	333321	0·279
13	411333	0·635	129	444332	0·438	·		
14	113334	0·634	130	442333	0·437	·		
15	441133	0·614	131	433331	0·434	260	344442	0·257
16	111143	0·612	132	333442	0·433	261	224443	0·257
17	111134	0·609	133	1112	0·432	262	433332	0·256
18	331144	0·599	134	444413	0·432	263	324444	0·246
·			·			264	423333	0·245
·			·			265	444432	0·244
24	342222	0·577	144	332111	0·423	266	333342	0·243
25	224433	0·565	145	444112	0·421	267	234444	0·242
26	144433	0·562	146	233111	0·421	268	243333	0·241
27	133444	0·561	147	442211	0·420	269	444423	0·237
28	144333	0·560	148	333314	0·420	270	333324	0·236
29	222243	0·556	149	431111	0·419	271	244443	0·228
30	223344	0·556	150	224411	0·419	272	233334	0·227
·			151	122223	0·418	·		
·			152	341111	0·418	·		
76	333441	0·493	153	41	0·417	283	23	0·133
77	411122	0·493	154	333341	0·417	284	4442	0·132
78	311122	0·492	·			285	2233	0·132
79	334111	0·492	·			286	3332	0·132
80	222114	0·491	214	332221	0·323	287	2444	0·129
81	114222	0·488	215	144422	0·322	288	2333	0·129
82	211114	0·487	216	222441	0·321			
83	211113	0·486	217	133322	0·317			

[a] Buckling load factor.

length of the cylinder whereas for ply orientations of the ring sublaminates, the reference direction is along the circumference. Thus, code number 1 in a layup scheme will imply that fibres of that ply are aligned axially for the stringer and cylinder sublaminates, and are aligned along the circumference for ring sublaminates. As shown in the figure, the stiffeners are located eccentrically with respect to the shell middle plane. The stiffened shell is subjected to

(i) axial compression ($N_x = -10^6$ N/m);
(ii) axial compression and uniform external pressure ($N_x = -10^5$ N/m, $P_r = -10^5$ N/m^2).

The rank ordered buckling load factors (12 × 48 mesh) are given in Tables 2 and 3 respectively.

For the axially compressed eccentrically stiffened cylinder (Table 2), a |113344| or |0°/45°/−45°| sublaminate gives the best buckling performance with a buckling load factor (λ) of 0·681, compared to $\lambda = 0·227$ (corresponding to |233334| layup scheme), which is the lowest among the 6-ply tri-directional sublaminates. The layup scheme |2333| gives the overall lowest λ of 0·129 considering both bi-directional and tri-directional sublaminates. It is observed that by changing only the location of the plies of given orientations in the sublaminate, the buckling load is affected significantly. For example, by reversing the layup scheme |431111| ($\lambda = 0·420$) to |111134| ($\lambda = 0·609$), the buckling load factor goes up by 45%. Comparing the two layup schemes |224443| ($\lambda = 0·257$) and |224433|

Table 3. Ranked coding for the ring and stringer stiffened cylinder subjected to axial compression and uniform external pressure

Sl. No.	Code	λ*	Sl. No.	Code	λ*	Sl. No.	Code	λ*
1	114222	0·954	83	442211	0·726	174	233311	0·618
2	113222	0·952	84	322224	0·725	175	222344	0·616
3	111422	0·941	85	332211	0·725	176	222433	0·616
4	411222	0·940	86	222214	0·724	177	444421	0·613
5	111322	0·940	·	·	·	178	222443	0·612
6	311222	0·938	·	·	·	·	·	·
7	1122	0·932	100	222241	0·711	·	·	·
8	411122	0·919	101	332224	0·711	200	422333	0·597
·	·	·	102	222231	0·710	201	1113	0·596
·	·	·	103	333422	0·710	202	224441	0·593
20	114422	0·884	104	222411	0·709	203	1114	0·592
21	113322	0·882	105	222311	0·708	204	144333	0·592
22	111142	0·857	106	221144	0·707	205	133444	0·592
23	111132	0·857	107	221133	0·706	206	223331	0·592
24	144222	0·854	108	2111	0·702	207	3222	0·590
25	441122	0·853	·	·	·	208	144433	0·590
26	133222	0·852	·	·	·	·	·	·
·	·	·	118	411133	0·686	233	223444	0·566
·	·	·	119	311144	0·685	234	224333	0·565
40	21	0·800	120	333221	0·685	235	1444	0·562
41	112244	0·798	121	144442	0·681	236	1333	0·561
42	112233	0·797	122	114433	0·681	237	3311	0·560
43	111244	0·795	123	113344	0·681	238	4411	0·559
44	111233	0·794	124	133332	0·680	239	224443	0·559
45	441112	0·793	·	·	·	240	223334	0·558
46	331112	0·792	·	·	·	·	·	·
47	422221	0·782	150	331144	0·653	·	·	·
48	322221	0·781	151	442233	0·648	·	·	·
49	432222	0·778	152	332244	0·648	283	4333	0·475
50	342222	0·778	153	444412	0·647	284	3444	0·475
51	114142	0·778	154	333312	0·646	285	4443	0·471
52	144422	0·778	155	411113	0·645	286	3334	0·471
·	·	·	156	311114	0·645	287	2444	0·462
·	·	·	·	·	·	288	2333	0·458
80	444112	0·728	·	·	·	·	·	·
81	422223	0·727	172	433332	0·620	·	·	·
82	333112	0·727	173	244411	0·619	·	·	·

*Buckling load factor.
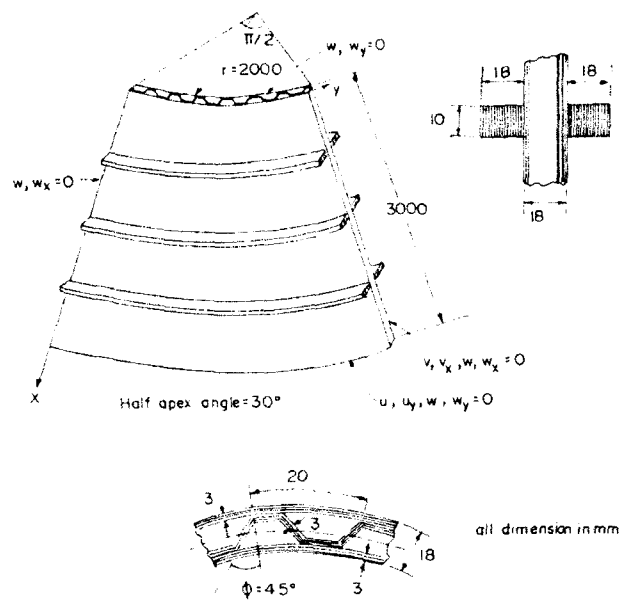
Fig. 5. Conical sandwich panel with hoop stiffeners.

($\lambda = 0.565$), it is seen that replacing a $-45°$ ply with a $45°$ ply increases the buckling load by more than 100%. It is also seen that sublaminates having an unequal number of $45°$ and $-45°$ plies combined with few $90°$ plies give a low buckling performance for this typical case. From this, it appears that bending–twisting coupling terms introduced by unbalanced $45°$ and $-45°$ plies lead to a substantial reduction of the buckling load. However, this coupling has a less pronounced effect on the buckling load when there are $0°$ plies in the sublaminate instead of $90°$ plies, along with the set of unbalanced $45°$ and $-45°$ plies. This is evident by considering the layup schemes |114443| ($\lambda = 0.640$) and |114433| ($\lambda = 0.681$).

This general trend is changed completely when the same stiffened cylinder is subjected to both axial compression (10^5 N/m) and uniform external pressure (10^5 N/m^2) as can be seen from the

Table 4. Ranked coding for sandwich conical panel without hoop stiffener

Sl. No.	Code	λ^*	Sl. No.	Code	λ^*	Sl. No.	Code	λ
1	342222	1·640	103	4442	1·297	202	444413	1·005
2	432222	1·640	104	221333	1·296	203	444431	1·004
3	322224	1·638	105	223331	1·294	204	344441	1·003
4	422223	1·637	106	2444	1·293	205	133334	0·998
5	222234	1·636	107	333342	1·293			
6	222243	1·636	108	433332	1·292			
.	.	.	.	.	.	227	332111	0·908
						228	233111	0·907
30	422221	1·520	126	2333	1·254	229	114443	0·901
31	222214	1·519	127	114422	1·215	230	113444	0·900
32	222241	1·518	128	441122	1·214	231	311444	0·899
33	334422	1·500	129	112244	1·212	232	444113	0·898
34	443322	1·500	130	442211	1·208	.	.	.
35	332244	1·496	131	221144	1·208			
36	442233	1·496	.	.	.	250	111132	0·769
.	.	.	149	4443	1·126	251	421111	0·768
55	322221	1·466	150	3444	1·124	252	241111	0·767
56	222213	1·465	151	133332	1·119	253	111443	0·767
57	222231	1·464	152	333312	1·117	254	111344	0·767
58	223334	1·461	153	333321	1·116	255	311112	0·767
59	422333	0·461	154	123333	1·115	.	.	.
60	224333	1·460	.	.	.	280	111134	0·608
61	144222	1·455	.	.	.	281	411113	0·605
.	.	.	175	111422	1·052	282	311114	0·605
			176	444211	1·052	283	431111	0·603
80	443332	1·357	177	411122	1·051	284	431111	0·603
81	333244	1·355	178	111224	1·050	285	1114	0·486
82	442333	1·354	179	1122	1·049	286	1113	0·485
83	233344	1·354	180	244411	1·049	287	4111	0·483
84	244333	1·353	.	.	.	288	3111	0·482
85	144422	1·338	.	.	.			
.	.	.	200	134444	1·006			
			201	314444	1·005			

*Buckling load factor.

Table 5. Ranked coding for the sandwich conical panel with hoop stiffeners

Sl. No.	Code	λ^a	Sl. No.	Code	λ^a	Sl. No.	Code	λ^a
1	342222	2·051	104	444432	1·647	203	444431	1·247
2	432222	2·051	105	344442	1·646	204	344441	1·246
3	322224	2·050	106	444423	1·646	205	133334	1·229
4	422223	2·050	107	221333	1·645	.	.	.
5	222234	2·048	108	223331	1·644			
6	222243	2·048	.	.	.	227	332111	1·137
.	.	.				228	233111	1·136
			126	2333	1·587	229	114443	1·116
30	442233	1·899	127	114422	1·543	230	113444	1·115
31	142222	1·897	128	441122	1·542	231	311444	1·114
32	412222	1·897	129	112244	1·540	232	444113	1·113
33	223344	1·897	130	442211	1·535	.	.	.
34	224433	1·897	131	221144	1·535			
35	122224	1·895	.	.	.	250	111132	0·965
36	422221	1·893	.	.	.	251	421111	0·964
.	.	.	149	133332	1·404	252	241111	0·963
.	.	.	150	333312	1·402	253	311112	0·963
56	23	1·858	151	333321	1·400	254	211113	0·958
57	122223	1·858	152	123333	1·399	255	321111	0·956
58	2233	1·857	153	213333	1·398	.	.	.
59	222144	1·856	154	4443	1·397			
60	322221	1·856	.	.	.	280	111143	0·757
61	223334	1·855	.	.	.	281	311114	0·754
.	.	.	175	444112	1·319	282	411113	0·754
.	.	.	176	112444	1·318	283	341111	0·751
80	333442	1·698	177	144433	1·318	284	431111	0·751
81	443332	1·698	178	223111	1·317	285	1114	0·610
82	444122	1·697	179	133444	1·317	286	4111	0·608
83	333244	1·696	180	444133	1·316	287	1113	0·606
84	442333	1·694	.	.	.	288	3111	0·603
85	233344	1·694	.	.	.			
.	.	.	200	134444	1·250			
.	.	.	201	314444	1·249			
103	122333	1·647	202	444413	1·248			

ᵃBuckling load factor.

rank ordered list given in Table 3. The layup scheme |113344| which was topping the ranked list for the axial compression case, is now in 123rd place. In this case, the highest buckling load factor is obtained by tri-directional 6-ply sublaminates with $\lambda = 0·954$ for a |114222| layup scheme which was in 81st place earlier. This is close to the highest buckling load factor obtained for bi-directional sublaminates (2-ply and 4-ply sublaminates) with $\lambda = 0·932$ for a |1122| layup scheme. For the case considered, a combination of 0° and 90° plies with no angle-ply (for bi-directional sublaminates) or one 45°/−45° ply (for tri-directional sublaminates) in the sublaminate seems to give the best buckling performance. Sublaminate layup schemes, containing large numbers of 45° and −45° plies give poor buckling load factors and find a place towards the end of the table. Like the previous case, here also reversing the layup scheme, for example |222411| to |114222|

changes the buckling load significantly (from 0·709 to 0·954); ~35%). These general trends however, are extremely difficult to predict *ab initio*.

Conical sandwich panel without and with hoop stiffeners

The geometry and boundary conditions of the stiffened panel are given in Fig. 5. First, the sandwich conical panel is considered without the hoop stiffeners and then the panel is modelled with the stiffeners to see the effect of the stiffeners on the rank ordered buckling loads. The loading is assumed to be: ($N_t = -10^5$ N/m, $P_f = -10^5$ N/m²). It is seen that (Tables 4 and 5) the optimum layup scheme |342222| (and the overall rank ordering) remains unchanged with addition of the hoop stiffeners. The maximum buckling load factor however, has increased from 1·640 to 2·051 (~25%)

in the process, which is appreciable considering the increase in weight of the panel (~ 1%) due to the addition of stiffeners.

5 CONCLUDING REMARKS

A four-noded, 48 dof doubly curved quadrilateral element together with a two-noded, 16 dof fully compatible meridional stiffener element (MSE) and parallel circle stiffener element (PCSE) are used for the linear bifurcation buckling analysis of plain/stiffened laminated anisotropic axisymmetric shell panels/shells. By using transformations which account for the eccentric placement of the stiffeners, problems of eccentrically stiffened shells of revolution have been solved. Determination of optimum layup scheme for buckling by ranking, of laminated composite axisymmetric shell panels/shells with/without laminated composite meridional and hoop stiffeners made of repeated sublaminate construction is presented. It is observed that both orientation and location of plies play a significant role in deciding the buckling load. For FRP shells subjected to general loading and boundary conditions, it is extremely difficult to predict the optimum layup scheme *a priori*, that will give the highest buckling load. In such cases, rank ordered tables such as those presented in this chapter, will be of significant practical use to the designer.

The finite element software developed can also handle buckling problems of eccentrically stiffened axisymmetric shell panels/shells of revolution with edge-stiffened cutouts whose boundaries coincide with meridians and parallel circles of the shell. Radially and/or circumferentially stiffened circular plates with/without stiffened cutouts with radial lines and parallel circles as boundaries can also be solved as a special case of the stiffened shell presented in this paper.

ACKNOWLEDGEMENTS

REFERENCES

1. Viswanathan, A. V., Tamekuni, M. & Baker, L. L., Elastic stability of laminated flat and curved, long rectangular plates subjected to combined inplane loads. Contractor Report, NASA CR-2330, 68, 1974.
2. Whitney, J. M., Buckling of anisotropic laminated cylindrical plates. *AIAA Journal*, 22 (1984) 1641–5.
3. Becker, M. L., Palazotto, A. N. & Khot, N. S., Instability of composite panels. *Journal of Aircraft*, 18 (1987) 739–43.
4. Jun, S. M. & Hong, C. S., Buckling behaviour of laminated composite cylindrical panels under axial compression. *Computers & Structures*, 29 (1988) 479–90.
5. Shaw, D. & Simitses, G. J., Instability of laminated cylinders in torsion. *Journal of Applied Mechanics*, 51 (1984) 188–91.
6. Simitses, G. J. & Han, B., Analysis of anisotropic laminated cylindrical shells subjected to destabilizing loads. Part I: Theory. *Composite Structures*, 19 (1991) 167–81.
7. Sheinman, I., Shaw, D. & Simitses, G. J., Nonlinear analysis of axially-loaded laminated cylindrical shells. *Computers & Structures*, 16 (1983) 131–40.
8. Hua, Z. & Dongxing, L., Mechanical analysis of the elastic buckling of an orthogonal anisotropic circular conical shell under uniform external pressure. *International Journal Pressure Vessel & Piping*, 48 (1991) 111–22.
9. Wang, T. K., General stability of composite circular shells. *Proc. of ICSTAD*, Vol. 1, Bangalore, India. Tata McGraw-Hill, India, 1990.
10. Leissa, A. W., Buckling of laminated composite plates and shell panels. AFWAL-TR-85-3069, Air Force Wright Aeronautical Laboratories, Wright-Patterson AFB, OH, 1985.
11. Sun, G. & Hansen, J. S., Optimal design of laminated composite circular cylindrical shells subjected to combined loads. *Journal of Applied Mechanics, Transactions of ASME*, 55 (1988) 136–42.
12. Nshanian, Y. S. & Pappas, M., Optimal laminated composite shells for buckling and vibration. *AIAA Journal*, 21 (1983) 430–7.
13. Onada, J., Optimal laminate configuration of cylindrical shells for axial buckling. *AIAA Journal*, 23 (1985) 1093–8.
14. Tsai, S. W., *Composite Design*, 4th edn. Think Composites, Sec. 9.8, 1988.
15. Venkatesh, A. & Rao, K. P., A doubly curved quadrilateral finite element for the analysis of laminated anisotropic thin shell revolution. *Computers & Structures*, 12 (1980) 825–32.
16. Venkatesh, A. & Rao, K. P., A laminated anisotropic curved beam and shell stiffening finite element. *Computers & Structures*, 15 (1982) 197–201.
17. Tripathy, B., Buckling of laminated anisotropic axisymmetric shells panels/shells with laminated anisotropic stiffeners. PhD thesis, Indian Institute of Science, Bangalore, India, 1992.
18. Rao, K. P. & Tripathy, B., Composite cylindrical panels — optimum layup for buckling by ranking. *Computers and Structures*, 38 (1991) 217–25.
19. Tripathy, B. & Rao, K. P., Curved composite beams — optimum layup for buckling by ranking. *Computers and Structures*, 41 (1991) 75–82.
20. Tripathy, B. & Rao, K. P., Stiffened composite axisymmetric shells — optimum layup for buckling by ranking. *Computers and Structures* (in press).

Buckling of open-section bead-stiffened composite panels

D. H. Laananen & S. P. Renze*

Department of Mechanical and Aerospace Engineering, Arizona State University, Tempe, Arizona 85287-6106, USA

Stiffened panels are structures that can be designed to efficiently support in-plane compression, bending, and shear loads. Although the stiffeners are usually discrete elements which are fastened or bonded to a flat or continuously curved plate, manufacturing methods such as thermoforming allow integral formation of the stiffeners in a panel. Such a configuration offers potential advantages in terms of a reduced number of parts and manufacturing operations. For thermoplastic composite panels stiffened by integrally formed open-section beads, the effects of bead spacing and bend cross-section geometry on the initiation of buckling under uniaxial compression and uniform shear loading were investigated. Finite elements results for a range of stiffened panel sizes and bead geometries are presented and compared with approximate closed-form solutions based on an effective flat plate size. Experimental verification of analytical predictions for one of the shear panels and one of the compression panels is described. Compensation of the forming tool to reduce the degree of initial curvature of the panels was found to be necessary.

INTRODUCTION

Stiffened panels are low-weight structural configurations which can be designed to efficiently support in-plane compression, bending, and shear loads. In conventional aircraft structures, the stiffeners, which typically have a C, Z, L, T or hat cross-section, are mechanically fastened or bonded to the panel. However, the use of discrete stiffeners adds cost and complexity due to a large number of parts and assembly operations. Manufacturing methods such as thermoforming make integral formation of the stiffeners in the panel as one piece an economically attractive alternative, although the resulting open-section bead has relatively low torsional rigidity. An example of a stiffened panel design which consists of repeating cells defined by closed-loop open-section beads is shown in Fig. 1.

A comprehensive survey of composite plate buckling by Leissa[1] indicated a lack of previous work addressing the issues concerned with the design of bead-stiffened thermoplastic shear webs. Rouse[2] presented experimental and analytical results for the shear loading of panels with one

or two parallel bend stiffeners extending the full panel length, for two bead widths. The effects of bead corner radii and other bead cross-section parameters upon the initial buckling load were not specifically addressed but are important design considerations for bead-stiffened panels.

The primary objective of the study reported in this paper has been to determine the effects of bead spacing and bead cross-section geometry upon the initial buckling load of a bead-stiffened thermoplastic composite panel. Part of this effort has been the determination of effective boundary conditions provided by the bead stiffener to the flat panel regions enclosed within the bead.
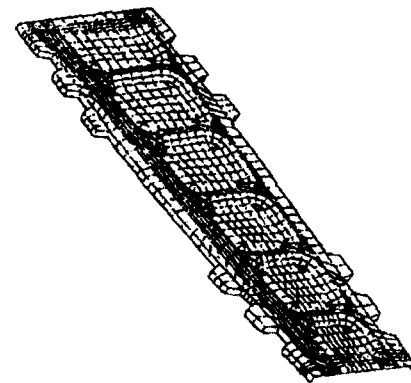
Fig. 1. Stiffened panel incorporating an open section bead.

*Present address: McDonnell Aircraft Company, St Louis, Missouri, USA.

The following section describes a parametric study which was performed using finite element analysis to assess the effects of different bead profile geometries, corner radii, and panel sizes upon the initial buckling load of panels loaded in shear and uniaxial compression. A basis for a simplified analysis methodology is developed in which the finite element results are bounded by approximate closed-form solutions after an effective flat panel size has been determined and load reduction techniques have been applied. Finally, the experimental program is discussed, including fabrication processes, test fixtures, and instrumentation used in the experimental verification of selected finite element results.

PARAMETRIC STUDY

A parametric study was performed using the PATRAN[3] finite element code to determine the cross-section geometry, corner radii, and panel sizes upon the initial buckling load. The specific panel configuration considered was a square panel containing a closed-loop, open-section bead, representing one cell or bay of the panel shown in Fig. 1. The parameters of interest, which are defined in Fig. 2, included the bead centerline spacing (CW), bead corner radius (CR), bead height (BH), and bead/pan radius (SR). The radius (BR) at the top of the bead was held constant at 12·7 mm.

The panels were modeled with general shell elements, four-node quadrilaterals, and three-node triangles, with six degrees of freedom per node. The material was a quasi-isotropic [0/90/45/−45], laminate of unidirectional AS4/APC2 thermoplastic composite. A symmetric quasi-isotropic laminate was chosen in order to avoid extension-bending coupling effects and to provide significant degrees of both longitudinal and shear stiffness. The eight-ply lay-up and the range of panel sizes were determined by the capabilities of available testing facilities to be used in the experimental phase of the project. The thickness of the laminate was assumed to be 1·06 mm, based on a nominal ply thickness of 0·132 mm. The material properties, shown in Table 1, were assumed to be orthotropic and homogeneous.

The clamped boundary conditions for the finite element model restrained out-of-plane displacements and rotations on all edges but allowed in-
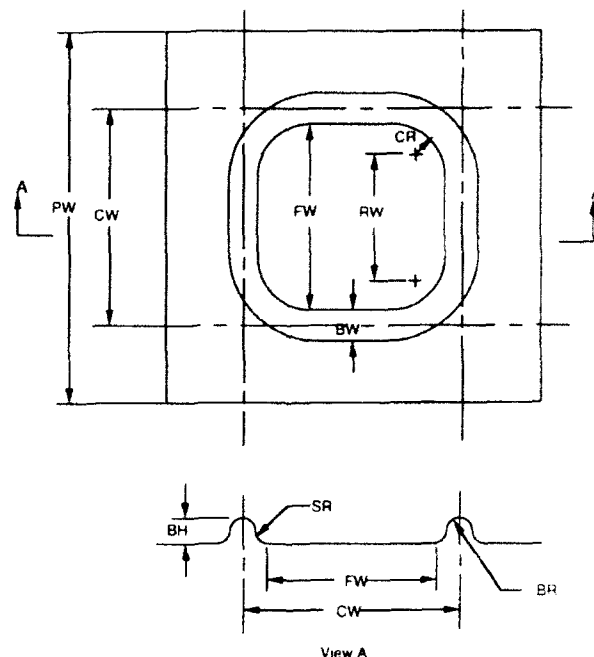
Fig. 2. Bead-stiffened panel geometry.

Table 1. AS4/APC2 lamina/laminate material properties

Property	Lamina/laminate
E_{11}/E_{22} (GPa)	120/76·5
E_{22}/E_{33} (GPa)	10·3/45·6
ν_{12}/ν_{11}	0·300/0·121
G_{12}/G_{13} (GPa)	5·10/8·14

[a]Flexural properties of [0/90/45/−45], laminate.

plane deformation, consistent with the actual conditions of the testing to be performed later. A constant shear force was applied on all edges in the conventionally defined positive direction, divided equally among the edge nodes. The critical buckling load was determined by multiplying the applied load by the eigenvalue returned from the finite element analysis. Elasticity solutions[4] for flat plates to calculate the stresses at the panel center confirmed correct application of the load. Geometric parameter values and results are listed in Table 2.

For the application of compressive loading, only one half of the panel was modeled, thus saving computational time and memory by utilizing symmetry. The boundary conditions were essentially the same as those utilized for the shear model. A compressive force was uniformly distributed along the nodes of the side parallel to the

Table 2. Parametric study shear panel geometry and results

Case	Corner radius CR (cm)	Pan interface radius SR (cm)	Bead height BH (cm)	Panel width RW (cm)	$(N_{xy})_{cr}$ without load reduction (kN/m)	$(N_{xy})_{cr}$ with load reduction (kN/m)	Closed-form soln. SS (kN/m)	Closed-form soln. CL (kN/m)
			PW = 43·2,		CW = 30·5 cm			
1S	3·05	1·27	2·54	19·3	22·9	9·75	9·26	17·7
2S	3·05	1·27	1·27	20·0	21·2	9·75	8·65	16·5
3S	3·05	1·27	0·635	21·0	16·7	8·21	7·81	14·9
4S	3·05	0·635	2·54	20·6	21·0	9·75	8·16	15·6
5S	3·05	0·318	2·54	21·2	20·3	9·60	7·67	14·6
6S	1·52	1·27	2·54	22·4	22·1	11·6	6·92	13·2
7S	0·76	1·27	2·54	23·9	21·2	12·0	6·06	11·6
			PW = 73·7,		CW = 61·0 cm			
8S	3·05	1·27	2·54	49·8	4·55	3·17	1·39	2·66
9S	1·52	1·27	2·54	52·8	4·47	3·29	1·24	2·36
10S	3·05	1·27	1·27	50·5	4·31	3·05	1·36	2·59
11S	1·52	1·27	1·27	53·5	4·40	3·19	1·21	2·29
			PW = 104,		CW = 91·4 cm			
12S	3·05	1·27	2·54	80·3	1·91	1·52	0·536	1·02
13S	1·52	1·27	2·54	83·3	1·87	1·56	0·497	0·94
14S	3·05	1·27	1·27	80·9	1·79	1·45	0·527	1·01
15S	1·52	1·27	1·27	84·0	1·77	1·49	0·490	0·933

symmetry axis. Stresses at the panel center confirmed correct application of the load based upon elasticity solutions for a flat panel. Parameter values and results are presented in Table 3.

CLOSED-FORM SOLUTIONS

Available solutions for the initial buckling of a flat, rectangular plate were used in an attempt to bound the preceding finite element solutions based on an effective flat panel size. The governing differential equation[5] for a flat, orthotropic plate subjected to uniform stress resultants N_x and N_{xy} is

$$D_{11} \frac{\partial^4 w}{\partial x^4} + 2(D_{12} + 2D_{66}) \frac{\partial^4 w}{\partial x^2 \partial y^2} + D_{22} \frac{\partial^4 w}{\partial x^4}$$
$$= N_x \frac{\partial^2 w}{\partial x^2} + 2N_{xy} \frac{\partial^2 w}{\partial y \partial x} \quad (1)$$

Solutions to this equation for plates with all edges either simply supported or clamped, under both uniaxial compression and shear, are well known. Approximate solutions for all four edges either simply supported or clamped are as follows:[6]

First, for uniaxial compression,

$$(N_x)_{cr} = \frac{\pi^2}{b^2} \sqrt{D_{11} D_{22}} \, K_c \quad (2)$$

where for simply supported edges,

$$K_c = \frac{m^2}{\lambda^2} + 2D_3 + \frac{\lambda^2}{m^2} \quad (3)$$

and for clamped edges,

$$K_c = 4 \left(\frac{1}{\lambda^2} + \lambda^2 + \frac{2}{3} D_3 \right) \quad (4)$$

For uniform shear loading,

$$(N_{xy})_{cr} = \frac{4}{b^2} \sqrt[4]{D_{11} D_{22}^3} \, K_s \quad (5)$$

where for simply supported edges $(\beta \le 1)$,

$$K_s = 8 \cdot 2 + 5 D_3 + 10^{0.3/\beta + B\beta}$$
$$A = -0 \cdot 27 + 0 \cdot 185 D_3 \quad (6)$$
$$B = 0 \cdot 82 + 0 \cdot 46 D_3 - 0 \cdot 2 D_3^2$$

Table 3. Parametric study shear panel geometry and results

Case	Corner radius CR (cm)	Pan interface radius SR (cm)	Bead height BH (cm)	Panel width RW (cm)	$(N_x)_{cr}$ without load reduction (kN/m)	$(N_x)_{cr}$ with load reduction (kN/m)	Closed-form soln. SS (kN/m)	Closed-form soln. CL (kN/m)
			PW = 43·2,	CW = 30·5 cm				
1C	3·05	1·27	2·54	19·3	52·0	3·31	3·96	13·0
2C	3·05	1·27	1·27	20·0	49·9	6·25	3·70	12·1
3C	3·05	1·27	0·635	21·0	22·6	6·36	3·34	10·9
4C	3·05	0·635	0·635	21·5	22·1	6·34	3·19	10·4
5C	3·05	0·318	0·635	21·8	21·9	6·39	3·10	10·1
6C	1·52	1·27	0·635	24·1	21·9	6·39	3·10	8·35
7C	0·76	1·27	0·635	25·6	20·8	7·32	2·26	7·39
			PW = 73·7,	CW = 61·0 cm				
8C	3·05	1·27	0·635	51·5	3·10	1·80	0·557	1·82
9C	1·52	1·27	0·635	54·6	3·01	1·87	0·496	1·63
10C	3·05	1·27	1·27	50·5	6·92	2·66	0·580	1·91
11C	1·52	1·27	1·27	53·5	6·74	2·73	0·515	1·69
			PW = 104,	CW = 91·4 cm				
12C	3·05	1·27	0·635	82·0	1·20	0·881	0·219	0·720
13C	1·52	1·27	0·635	82·0	1·19	0·909	0·205	0·669
14C	3·05	1·27	1·27	80·9	1·93	1·07	0·226	0·739
15C	1·52	1·27	1·27	84·0	1·91	1·10	0·208	0·686

and for clamped edges $(0.6 < \beta \leq 1)$,

$$K_s = K_0 + 10^{-4}(\beta^{-0.6} + B\beta^{-0.6})$$

$$K_0 = 19.3 + 8.45 D_3$$

$$A = -0.04 + 0.035 D_3 \tag{7}$$

$$B = 1.99 + 0.38 D_3$$

in which

$$\beta = (D_{11}/D_{22})^{1/4} \tag{8}$$

$$\lambda = (a/b)(D_{22}/D_{11})^{1/4} \tag{9}$$

$$D_3 = \frac{(D_{12} + 2D_{66})}{\sqrt{D_{11}D_{22}}} \tag{10}$$

and D_{11}, D_{22}, D_{12} and D_{66} are laminate flexural stiffness coefficients. These equations are valid for the square plates $(a = b)$ being modeled and for the first buckled mode shape in the form of one half-sine wave $(m = 1)$.

Independent verification of the approximate solutions given by eqns (2)–(10) for the specific laminate properties was performed by comparing the results with known analytical solutions for simply supported orthotropic plates loaded in uniform shear and uniaxial compression.[5] The results of eqns (2)–(10) were also compared with finite element results for a flat quasi-isotropic [0/90/45/−45], AS4/APC2 panel. The panel dimensions were arbitrarily assumed to be 36 cm

in length and width, with a thickness of 1·0 mm. The maximum error was calculated to be 13%. Finite element predictions for the same panel were compared with analytical results from eqns (2)–(4). The results for both a simply supported panel and a clamped panel agreed within 1%.

The same square, orthotropic panel with simply supported edges was used for comparison of shear buckling results from a Galerkin solution[5] with those of eqns (5) and (6). The analytical results from eqns (5)–(7) were also compared with finite element results. The maximum deviations for simply supported and clamped panels were 3 and 2% respectively.

These results indicated that eqns (2)–(10) were valid solutions of the governing differential eqn (1) for the panels being modeled, and, therefore, these solutions were used to calculate all further analytical results for this study. The close agreement between the finite element results and the results of eqns (2)–(10) also verified the representation of simply supported and clamped boundary conditions for the finite element models.

Equation (1) is valid for orthotropic laminates, i.e. laminates where D_{16} and D_{26} are zero, which is only approximately true for quasi-isotropic laminates of unidirectional plies. However, published criteria[7] were applied to demonstrate that, for the [0/90/45/−45], AS4/APC2 laminate, D_{16} and D_{26} were sufficiently small to be neglected.

thus confirming the applicability of the governing differential equation for an orthotropic plate as presented in eqn (1).

DETERMINATION OF EFFECTIVE FLAT PLATE SIZE

In the design of stiffened panels, it would be helpful to be able to determine an approximate buckling capability using closed-form solutions for a rectangular, orthotropic plate. Solutions for simply supported and clamped boundary conditions could represent upper and lower limits to the critical buckling load, provided that the appropriate flat plate length and width were used.

Referring to Fig. 2, three dimensions of the beaded panel which were considered as candidates for the effective flat plate edge length were the lengths CW, FW and RW. Determination of the most appropriate effective length was based on three criteria: (1) the finite element results should be bounded by the simply supported and clamped closed-form solutions, (2) the length was required to have a physical geometric interpretation, and (3) for every variation of a bead parameter, the length also had to change in a logical manner. For this study, the panel geometry was defined such that the bead centerlines were first located on the panel and then the open-section bead was modeled. As a result, the length CW remained invariant for certain bead parameter changes and thus did not satisfy the third condition. It was also determined that neither length CW nor FW satisfied the first condition since, for many cases, the finite element results exceeded the clamped closed-form solution by a significant margin. The length RW, on the other hand, satisfied all three criteria and thus was selected.

The finite element results were modified to account for the amount of the total applied load transmitted by the beads versus the quantity seen by the flat pan area enclosed within the bead. This was done by averaging the stress resultant along a line of nodes of length equal to RW, through the center of the panel. For panels loaded in compression, N_x was averaged, while for panels loaded in shear, N_{xy} was averaged.

ANALYSIS RESULTS

The closed-form solutions for flat, square plates loaded in shear and uniaxial compression, based
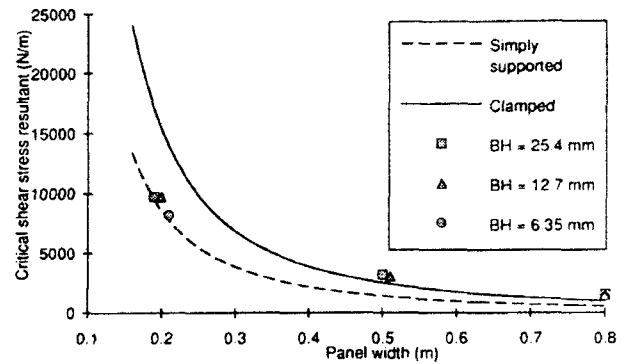
Fig. 3. Shear panel bead spacing and bead height effects (CR = 30 mm, SR = 12·7 mm).
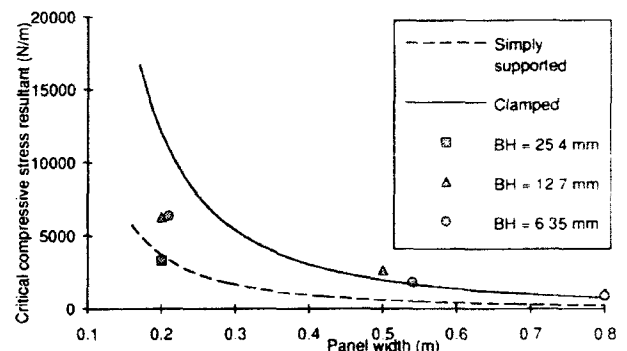
Fig. 4. Compression panel bead spacing and bead height effects (CR = 30 mm, SR = 12·7 mm).

upon the length RW, are plotted in Figs 3 and 4, respectively. The finite element solutions that involved variation of bead cross-section at each of three different panel sizes are also shown. As expected, when panel size was increased, the buckling load decreased. However, for small panels, the effective boundary conditions appear to be simply supported, while large panels would be better represented by clamped boundary conditions. The single finite element solution that falls below the simply supported curve is shown in Fig. 4 for bead height, $BH = 25$ mm. The deformed geometry results for this case showed local flange buckling or edge crippling in the area between the closed-loop bead and the load application of the panel edge. This indicated that the bead was so stiff that insufficient load was being transmitted through the bead into the flat pan region to initiate buckling there.

The effects of the radius at the bead–panel interface, SR, were not sigificant in terms of changes in the initial buckling load. However, referring to Fig. 2, SR can have a significant impact in terms of the formability of a panel. If the
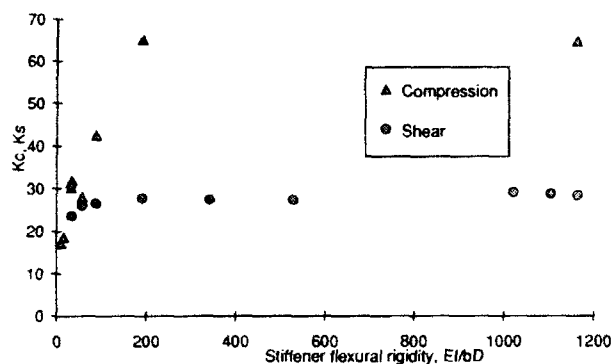
Fig. 5. Critical buckling load (normalized) *vs.* bead flexural rigidity.

radius SR is very small in relation to BH, BR and FW, then bridging of fibers across the radius may occur, resulting in an insufficiently consolidated or otherwise poor quality part. Decreasing the bead corner radius, CR, was found to produce small decreases in the total, unreduced buckling loads.

It has been demonstrated that for stiffened rectangular panels of isotropic material loaded in uniform compression[8] or shear,[9] critical buckling stress increases with increasing flexural rigidity of the stiffeners until a limiting value is reached, at which the stiffener remains essentially straight, acting as a nodal line for the buckled plate. Increasing the flexural rigidity beyond this critical value produces no further increase in the critical stress. It was further shown that increasing the stiffener torsional rigidity increased the critical value of flexural rigidity.[9]

The critical compressive and shear buckling loads calculated in the finite element parametric study are plotted in Fig. 5 as a function of normalized bead flexural rigidity, $E_x I / b D_{22}$, in which I is the moment of inertia of the bead cross-section with respect to an axis at the interface with the panel. The loads have been normalized using the following relationship developed from eqn (2):

$$K_{c,s} = N_{cr} b^2 / [\pi^2 (D_{11} D_{22})^{1/2}] \qquad (11)$$

For the plate aspect ratio $a/b = 1$ used in the parametric study, Fig. 5 indicates the critical values of bead flexural rigidity, beyond which no additional benefit in terms of buckling capability is realized. The bead geometry at this point would typically represent an optimum design, for further increasing the bead height would most likely either result in lower part quality or require higher forming pressure, thereby increasing cost. For the particu-

lar material, lay-up and thickness that were modeled in this investigation, the optimum bead height appears to be approximately 1·27 cm for a bead spacing of 30·5 cm or 2·54 cm for a bead spacing of 61·0 cm, for either compressive or shear loading.

EXPERIMENTAL VERIFICATION OF BUCKLING LOADS

In order to verify the critical buckling loads predicted by finite element analysis, four bead-stiffened panels of AS4/APC2 thermoplastic composite were manufactured and tested, two in uniaxial compression and two in shear. The [0/90/45/−45]$_s$ panels were fabricated with a 25-mm high bead corresponding to Cases 1S and 1C of the parametric study. Four flat panels were also manufactured with the same stacking sequence. Two of the flat panels were tested in compression, and two were tested in shear to verify the material properties and the boundary conditions used in the analysis.

The flat quasi-isotropic panels were manufactured in an autoclave at 390°C under 690 kPa pressure. The bead-stiffened panels were produced by double diaphragm forming at 380°C and 690–760 kPa. Shear test panels had two five-ply glass/epoxy tabs adhesively bonded along each edge prior to drilling for mounting in the shear test fixture.

Each test article was instrumented with strain gages at the center of the panel, both front and back, to monitor the state of strain in the panel and to determine the onset of buckling. The shear articles were instrumented with strain rosettes (0, 45, 90-deg orientation to the applied load) and the compression articles with biaxial gages (0, 90-deg orientation). The shear and compression test fixtures are illustrated in Figs 6 and 7, respectively. A modified Southwell technique[10] was used in plotting the load–strain data in order to obtain the critical buckling load.

The finite element code PATRAN was used to predict the initial buckling load of all test articles. The models were the same as in the parametric study discussed previously except for the input of the actual test specimen thickness and the actual outside dimensions.

The compression test articles were clamped by the test fixture on a 13-mm width around the perimeter. The resulting area (48 cm × 48 cm) inside the fixture was modeled as a panel with clamped
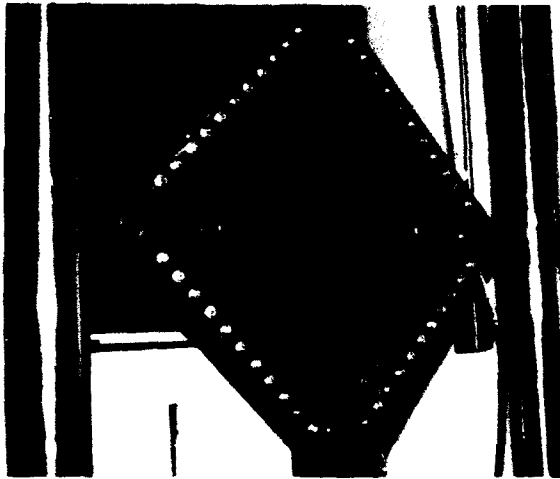
Fig. 6. Shear test fixture.

Fig. 7. Compression test fixture.

Table 4. Comparison of predicted buckling loads with test results

Panel No.	Configuration	Predicted load (kN)	Test result (kN)	% error
Compression				
1	Flat	1·36	1·44	6
2	Flat	1·36	1·40	3
4	Beaded	13·0	13·8	6
5	Beaded	13·0	14·9	12
8[a]	Beaded	11·6	12·1	4
12[a]	Beaded	11·6	10·5	11
Shear				
3	Flat	2·64	2·72	3
4	Flat	2·64	2·82	7
6	Beaded	13·2	6·58	100
7	Beaded	13·2	6·76	95
9[a]	Beaded	8·32	8·05	3
10[a]	Beaded	8·32	8·01	4

[a] Tool compensated to reduce panel initial curvature.

boundaries on all edges. The shear test articles were clamped by the 'picture frame' test fixture on a 38-mm width around the perimeter. The resulting panel area (43 cm × 43 cm) enclosed by the fixture was modeled as a panel clamped on all four edges.

The predicted buckling loads are compared with test results for compression and shear in Table 4. For the initial set of bead-stiffened panels, the measured buckling load was significantly less than that predicted by finite element analysis, particularly in the case of the shear specimens. In the region enclosed within the bead, all four of the stiffened panels were found to have an initial curvature with a maximum amplitude of approximately 2 mm, or nearly twice the panel thickness. Finite element analysis, including modeling of the temperature dependence of the material properties, was used to predict the initial curvature. The analytical results were then utilized in the design of a concave surface on the base block of the forming tool.[11] Four panels were fabricated with the compensated tool, and the amplitude of the resulting initial curvature was found to have been significantly reduced. Panels 8, 9, 10 and 12 in Table 4 were the stiffened panels that were produced with the compensated tool.

CONCLUSIONS

The results of a finite element parametric study performed on bead-stiffened panels loaded in uniform shear and compression showed that the geometric parameters that have the most significant effects upon the buckling load are the bead height and panel size. Increasing the bead height effectively increases the buckling load, while increasing the panel size decreases the buckling load as expected. However, as demonstrated previously for stiffened panels of isotropic material, there is a critical flexural rigidity, above which further increases in bead height will not be productive. The bead corner radius was found to have a small effect upon the initial buckling load in compression and in shear, but it is important to note that decreasing the bead corner radius can also be an important formability issue for panels with large bead heights.

A basis for a simplified analysis methodology was developed in which effective flat panel widths and load reduction techniques were used to bound finite element solutions with the limiting closed-form solutions for simply supported and clamped edges.

REFERENCES

1. Leissa, A. W., A review of laminated composite plate buckling. *Applied Mechanics Review*, **40** (1987) 575–91.
2. Rouse, M., Structural response of bead-stiffened thermoplastic shear webs. In *Proceedings of the First NASA Advanced Composite Technology Conference*, NASA CP-3104 Part 2, 1990, pp. 969–77.
3. *PATRAN™ User's Manual*. PDA Engineering, Costa Mesa, CA, 1990.
4. Timoshenko, S. P. & Goodier, J. N., *Theory of Elasticity*, 3rd edn. McGraw-Hill, New York, 1970.
5. Ashton, J. E. & Whitney, J. M., *Theory of Laminated Plates* Technomic Publishing Co., Stamford, CT, 1970.
6. Rockwell International Corporation, North American Aircraft Operations, *DOD/NASA Advanced Composites Design Guide*, Contract No. F-33615-78-C-3203, 1983.
7. Nemeth, M. P., Importance of anisotropy on buckling of compression-loaded symmetric composite plates. *AIAA Journal*, **40** (1986) 1831–5.
8. Bleich, F., *Buckling Strength of Metal Structures*, McGraw-Hill, New York, 1952.
9. Cook, I. T. & Rockey, K. C., Shear buckling of clamped and simply-supported infinitely long plates reinforced by transverse stiffeners. *Aeronautical Quarterly*, **13** (1962) 41–70.
10. Remeri, M. P. & Garrett, R. A., Postbuckling fatigue behavior of flat stiffened graphite-epoxy panels under shear loading. Report No. NADC-81168-60, Naval Air Development Center, Warminster, PA, 1982.
11. Renze, S. P. & Laananen, D. H., Reduction of composite panel initial curvature by tool compensation. *Journal of Thermoplastic Composite Materials*, **5** (1992) 287–303.

Vibration of composite-material cylindrical shells with ring and/or stringer stiffeners

Charles W. Bert, Chun-Do Kim

School of Aerospace and Mechanical Engineering, The University of Oklahoma, Norman, Oklahoma 73019-0601, USA

&

Victor Birman

Mechanical and Aerospace Engineering, University of Missouri-Rolla/University of Missouri-St Louis, Engineering Education Center, St Louis, Missouri 63121-4499, USA

Free vibration is analyzed for thin-walled circular cylindrical shells constructed of composite materials and provided with ring and/or stringer stiffeners. Numerical results are presented for graphite–epoxy shells: unstiffened and stiffened with rings only, stringers only, and both rings and stringers.

INTRODUCTION

In many applications of composite-material circular cylindrical shell structures, the use of advanced fiber-reinforced composite materials can be made even more efficient if axial (stringer) and circumferential (ring or bulkhead) stiffeners are used. This statement is valid for both aircraft and deep-diving submarine applications. Through the years, many analyses of isotropic circular cylindrical shells, reinforced with stringers alone or with rings alone, have appeared (for extensive reviews, see Bert and Egle[1] and Mukhopadhyay and Sinha[2]). There have also been some which treated both stringers and rings (cf. Egle and Sewall[3]). Likewise, there have been numerous analyses of smooth (unreinforced) composite-material shells; see the review by Bert.[4]

There appears to be a near void of published analyses concerned with vibration of composite-material shells reinforced with rings and/or stringers. (Prokopenko[5] considered such shells with symmetric ring reinforcements.) The purpose of the present paper is to fill this need by considering free vibrations, in both axisymmetric and unsymmetric modes, of circular cylindrical shells made of laminated composite materials and discretely reinforced with rings and/or stringers. Emphasis is placed on evaluation of the accuracy of various approximate theories by the use of

dimensionless tracer coefficients and on assessing the relative improvement in the lowest natural frequency due to ring stiffeners versus stringer stiffeners.

HYPOTHESES

The following hypotheses, widely used in thin shell analyses, are made:

1. Thin wall ($h/R \ll 1$). This implies no transverse shear and transverse normal deformation and no rotatory inertia.
2. A complete circular cylindrical shell of finite length and having no geometric imperfections is considered.
3. The vibration is assumed to involve sufficiently small amplitudes that geometric nonlinearity may be omitted.
4. Orthotropic, linear elastic materials having the same properties in tension and compression are considered.
5. Discrete ring and stringer stiffeners, equally spaced and with negligible torsional rigidity, are considered. The stiffeners are taken to be thin but the stiffener eccentricity is included.
6. The Sanders–Koiter best first-approximation shell theory and various simpler theories are considered.

7. The end conditions considered are simply supported without axial constraint at both ends.

DERIVATION OF EQUATIONS OF MOTION IN TERMS OF DISPLACEMENTS

Five different thin shell theories are employed. In order of descending accuracy and ascending simplicity, they are as follows:

1. the Sanders–Koiter best first-approximation theory,[6,7]
2. Love's first-approximation theory,[8]
3. Loo's approximation,[9]
4. Morley's approximation,[10]
5. Donnell's shallow shell theory.[11]

To present all five of the theories mentioned in a generalized manner, the concept of dimensionless tracer coefficients, as used by Bert and Kumar,[12] for instance, is applied. The values taken on by the various coefficients (C_i) for the respective theories are listed in Table 1.

The equations of motion, including both in-surface and radial inertias, are:[12]

$$N_{1,x} + N_{6,y} - (C_4/R) M_{6,y} = P u_{,tt}$$

$$N_{6,x} + N_{2,y} + (C_3/R) M_{6,x} + (C_1/R) M_{2,y} = P v_{,tt}$$

$$M_{1,xx} + 2 M_{6,xy} + M_{2,yy} - (N_2/R) = P w_{,tt} \qquad (1)$$

Here the M_i and N_i are stress couples (bending and twisting moments/unit width) and stress resultants (membrane forces/unit width) given by

$$(M_i, N_i) = \int_{-h/2}^{h/2} (z, 1) \sigma_i \, dz \quad (i = 1, 2, 6) \qquad (2)$$

The total mass per unit mid-surface area is given by

$$P = \int_{-h/2}^{h/2} \rho(z) \, dz + \sum_s \delta(y - y_s) \rho_s A_s$$

$$+ \sum_r \delta(x - x_r) \rho_r A_r \qquad (3)$$

where the symbol δ denotes the Dirac delta function.

Finally, A_s and A_r denote respective stringer and ring cross-sectional areas; $h \equiv$ shell thickness; $R \equiv$ mean radius of the shell; x, y, z are the axial, circumferential mid-surface, and outer thickness-direction normal position coordinates; u, v, w are the mid-surface displacements in the respective x,

Table 1. Listing of tracer coefficients associated with different thin shell theories

Theory	C_1	C_2	C_3	C_4
Sanders	1	1	3/2	1/2
Love	1	1	1	0
Loo	1	0	1	0
Morley	1	0	0	0
Donnell	0	0	0	0

y, z directions; ρ denotes density; and $(\ )_{,xy}$ denotes $\partial^2 (\ )/\partial x \, \partial y$, etc.

The laminated shell constitutive relations are

$$\begin{Bmatrix} N_i \\ M_i \end{Bmatrix} = \begin{bmatrix} A_{ij} & B_{ij} \\ B_{ij} & D_{ij} \end{bmatrix} \begin{Bmatrix} \varepsilon_j^0 \\ \kappa_j \end{Bmatrix} \quad (i, j = 1, 2, 6) \qquad (4)$$

Here ε_j^0 are the mid-surface strain components, κ_j are curvature changes, and the stiffnesses are determined in the usual way (cf. Jones[13]) as

$$\{A_{ij}, B_{ij}, D_{ij}\}$$

$$= \int_{-h/2}^{h/2} \{1, z, z^2\} Q_{ij}(z) \, dz \quad (i, j = 1, 2, 6) \qquad (5)$$

where Q_{ij} are the plane-stress-reduced material stiffness coefficients. In the present study, it is assumed that $A_{16} = A_{26} = B_{16} = B_{26} = D_{16} = D_{26} = 0$. Therefore, the shells considered here model exactly the following classes of lamination arrangement:

- shells with symmetrically or unsymmetrically laminated isotropic layers (A_{ij}, B_{ij} and D_{ij} all isotropic),
- shells with a single layer of bimodular orthotropic material,[12]
- symmetrically laminated cross-ply shells ($B_{ij} = 0$),
- antisymmetrically laminated cross-ply shells ($B_{22} = - B_{11}$ and $B_{12} = B_{66} = 0$).

Furthermore, the following classes are modeled approximately for the case of many layers (say, 10 or more):

- symmetric angle-ply shells (A_{16}, A_{26}, D_{16}/h^2, and D_{26}/h^2 negligible relative to other stiffnesses; $B_{ij} = 0$),
- antisymmetric angle-ply shells (B_{16}/h and B_{26}/h approach zero).

The total strain at an arbitrary position (x, y, z) is given by

$$\varepsilon_i(x, y, z) = \varepsilon_i^0(x, y) + z \kappa_i(x, y) \qquad (6)$$

In view of hypotheses 1 and 3, the mid-surface engineering strains may be expressed as

$$\varepsilon_1^0 = u_{,x}; \quad \varepsilon_2^0 = v_{,y} + (w/R); \quad \varepsilon_6^0 = u_{,y} + v_{,x} \quad (7)$$

The curvature changes, in view of hypothesis 1, are

$$\kappa_1 = -w_{,xx}; \quad \kappa_2 = -w_{,yy} + (C_2/R) v_{,y};$$
$$\kappa_6 = -2w_{,xy} + (C_3/R) v_{,x} - (C_4/R) u_{,y} \quad (8)$$

Neglecting the torsional stiffnesses of the stiffeners and allowing for the discrete nature of the stiffener spacing, one can write the constitutive relationships for the stiffeners as follows:

$$\{N_1^s, M_1^s\}$$
$$= \sum_s \delta(y - y_s) \int_{z^{(s)}} E_s\{1, z\}(\varepsilon_1^0 + z\kappa_1) b_s(z) \, dz \quad (9)$$

$$\{N_2^r, M_2^r\}$$
$$= \sum_r \delta(x - x_r) \int_{z^{(r)}} E_r\{1, z\}(\varepsilon_2^0 + z\kappa_2) b_r(z) \, dz$$

Here, z^s or z^r indicates integration throughout the entire depth of the corresponding stringer (s) or ring (r). b_s and b_r are stiffener widths, and E_s and E_r are stiffener elastic moduli.

The total stress resultants and stress couples are the sum of those of the shell and the stiffeners, i.e.

$$N_1 = \bar{N}_1 + N_1^s; \quad N_2 = \bar{N}_2 + N_2^r; \quad N_6 = \bar{N}_6,$$
$$M_1 = \bar{M}_1 + M_1^s; \quad M_2 = \bar{M}_2 + M_2^r; \quad M_6 = \bar{M}_6 \quad (10)$$

Substituting eqns (4), (7), (8) and (9) into eqns (10) yields the following expressions for the total stress resultants and stress couples in terms of the displacements:

$$N_1 = A_{11}u_{,x} + A_{12}(v_{,y} + R^{-1}w) - B_{11}w_{,xx}$$
$$\quad - B_{12}[w_{,yy} - (C_2/R) v_{,y}]$$
$$\quad + \sum_s \delta(y - y_s) E_s A_s (u_{,x} - z_s w_{,xx})$$

$$N_2 = A_{12}u_{,x} + A_{22}(v_{,y} + R^{-1}w) - B_{12}w_{,xx}$$
$$\quad - B_{22}[w_{,yy} - (C_2/R) v_{,y}]$$
$$\quad + \sum_r \delta(x - x_r) E_r A_r [v_{,y} + (w/R)$$
$$\quad - z_r(w_{,yy} - C_2 R^{-1}v_{,y})]$$

$$N_6 = A_{66}(u_{,y} + v_{,x})$$
$$\quad + B_{66}(-2w_{,xy} + C_3 R^{-1}v_{,x} - C_4 R^{-1}u_{,y}) \quad (11)$$

$$M_1 = B_{11}u_{,x} + B_{12}(v_{,y} + R^{-1}w)$$
$$\quad - D_{11}w_{,xx} - D_{12}(w_{,yy} - C_2 R^{-1}v_{,y})$$
$$\quad + \sum_s \delta(y - y_s)(E_s A_s z_s u_{,x} - E_s I_{os} w_{,xx})$$

$$M_2 = B_{12}u_{,x} + B_{22}(v_{,y} + R^{-1}w)$$
$$\quad - D_{12}w_{,xx} - D_{22}(w_{,yy} - C_2 R^{-1}v_{,y})$$
$$\quad + \sum_r \delta(x - x_r)[E_r A_r z_r(v_{,y} + R^{-1}w)$$
$$\quad - E_r I_{or}(w_{,yy} - C_2 R^{-1}v_{,y})]$$

$$M_6 = B_{66}(u_{,y} + v_{,x})$$
$$\quad + D_{66}(-2w_{,xy} + C_3 R^{-1}v_{,x} - C_4 R^{-1}u_{,y})$$

Here, I_{os} and I_{or} are the stiffener area moments of inertia about the shell mid-surface, and z_s and z_r are the distances between the stiffener centroids and the shell mid-surface.

Substitution of the complete constitutive expressions, eqns (11), into the equations of motion, eqns (1), yields a set of linear partial differential equations which can be expressed as

$$[\mathcal{L}]\{u, v, w\}^T = \{0\} \quad (12)$$

The elements of the linear differential operator matrix $\mathcal{L}$ are listed in Appendix 1.

SOLUTION OF THE EQUATIONS OF MOTION

The boundary conditions considered here are simply supported without in-surface constraint (SS3 conditions in the nomenclature of Hoff[14]) along its curved edges at $x = 0, L$:

$$N_1 = M_1 = w = v = 0 \quad (13)$$

Assuming normal modes, one can show that these boundary conditions are satisfied identically if the following displacements are used:

$$u = U \cos \alpha x \sin \beta y \cos \omega t,$$
$$v = V \sin \alpha x \cos \beta y \cos \omega t, \quad (14)$$
$$w = W \sin \alpha x \sin \beta y \cos \omega t$$

where $\alpha \equiv m\pi/L$, $\beta \equiv n/R$, and m and n are the axial half-wave number and the circumferential mode number, respectively.

Substitution of eqns (14) into eqn (12) yields a set of homogeneous algebraic equations in terms of U, V and W. Since vibrations are possible only if the determinant of this set vanishes, this requirement yields the frequency equation.

REDUCTION TO THE SMEARED CASE FOR CLOSELY SPACED STIFFENERS

In many applications, such as deep-diving submersibles and high-performance military aircraft, the stiffeners are spaced sufficiently close that the so-called 'smeared' approximation is valid. In this case, the actual stiffened composite-material shell is modeled by another hypothetical orthotropic shell with different effective properties.

Let l_r and l_s denote the center-to-center spacing of the rings and stringers, respectively. In the assumption of close spacing, one obtains

$$\sum_r \delta(x - x_r) = 1/l_r; \quad \sum_s \delta(y - y_r) = 1/l_s \qquad (15)$$

Then the effective inertia becomes

$$P = \rho h + (\rho_r A_r / l_r) + (\rho_s A_s / l_s) \qquad (16)$$

and the coefficients of the 3×3 frequency determinant are as listed in Appendix 2.

RESULTS AND DISCUSSION

Before proceeding to the composite-material and stiffened shells, some results are presented for unreinforced isotropic-material (steel) shells using properties listed in Table 2 (second column). In Table 3, the effects of L/R and h/R on the lowest natural frequency are shown according to the predictions of the five different shell theories considered. It can be seen that there is reasonably good agreement among all of the theories except

that at higher h/R and L/R, the Donnell theory predicts somewhat higher lowest natural frequencies than the other four theories.

The next case considered is an unreinforced composite-material shell made of hoop-wound, high-strength graphite–epoxy. The material properties are listed in the third column of Table 2. The frequency curves are shown in Fig. 1.

The next three figures (Figs 2–4) are for the cases of 10 ring stiffeners only, 15 stringers only, and the combination of 10 rings and 15 stringers. The shell geometry in all three figures is thin ($h/R = 0.02$) with a moderate length ($L/R = 4$). The stiffeners are assumed to be unidirectional graphite–epoxy with the same properties as listed for the shell. The stiffeners are considered to be smeared and stiffener parameter are $z_q/h = 3$ and $I_{oq}/A_q R^2 = 4.43 \times 10^{-3}$, where q denotes rings (r) or stringers (s).

The results of parametric studies for the baseline case of graphite–epoxy shells with 10 rings and 15 stringers are presented. In Table 4 is a study of the effect of omitting various in-surface inertias. In Fig. 5, all of the parameters mentioned in the preceding paragraph are held constant, except that the composite is assumed to be a many-layer regular angle-ply layup ($\pm \theta$). In Fig. 6, all of the parameters are constant as before, except that the L/R ratio is varied.

Table 2. Material properties used

Property	Material	
	Steel	High-strength graphite–epoxy
Major elastic modulus, E_1 (GPa)	203.4	151.0
Minor elastic modulus, E_1 (GPa)	203.4	10.55
Major Poisson ratio, ν_{11}	0.29	0.31
Shear modulus, G_{11} (GPa)	78.84	6.62
Specific gravity	7.86	1.52

Table 3. Comparison of the lowest natural frequencies (kHz) predicted by five different thin shell theories for various h/R and L/R values. Unreinforced steel shell; $R = 1.27$ cm; $m = 1$

Theory	h/R	0.050			0.010		
	L/R	1	4	10	1	4	10
	n	4	2	2	7	4	2
Sanders		41.37	10.13	3.713	3.812	0.9251	0.3667
Love		41.51	10.17	3.730	3.816	0.9261	0.3671
Loo		41.79	10.35	4.173	3.831	0.9439	0.3746
Morley		42.00	10.39	4.191	3.835	0.9449	0.3749
Donnell		42.29	10.62	4.714	3.851	0.9634	0.3848
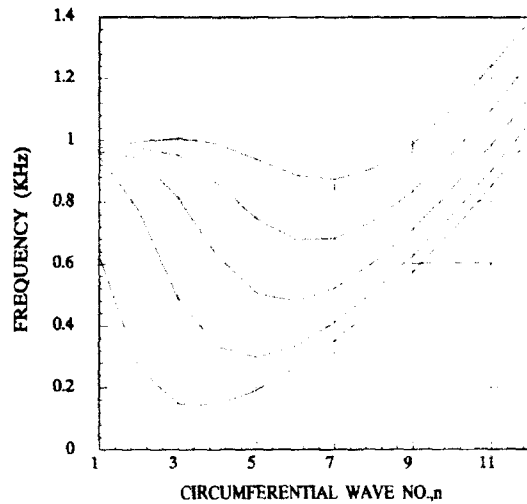
Fig. 1. The first five natural frequencies versus circumferential wave no. for an unreinforced shell constructed of circumferentially oriented, unidirectional graphite–epoxy (the axial mode numbers are 1 for the bottom curve, 2 for the next one, etc.) ($h/R = 0.02$, $L/R = 4$, $R = 1.27$ cm).
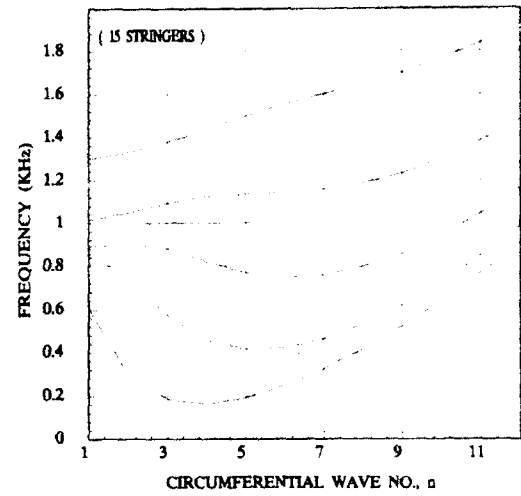
Fig. 3. The first five natural frequencies versus circumferential wave no. for the same shell shown in Fig. 1, but with the addition of 15 ring stiffeners.
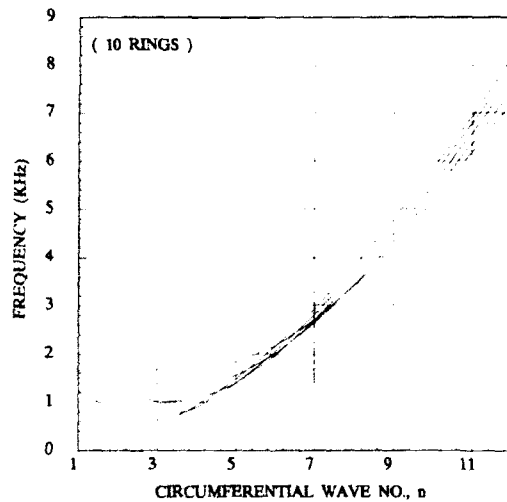
Fig. 2. The first five natural frequencies versus circumferential wave no. for the same shell shown in Fig. 1, but with the addition of 10 ring stiffeners. (The axial mode numbers range from 1 to 5, starting with the bottom at the left side of the figure.)
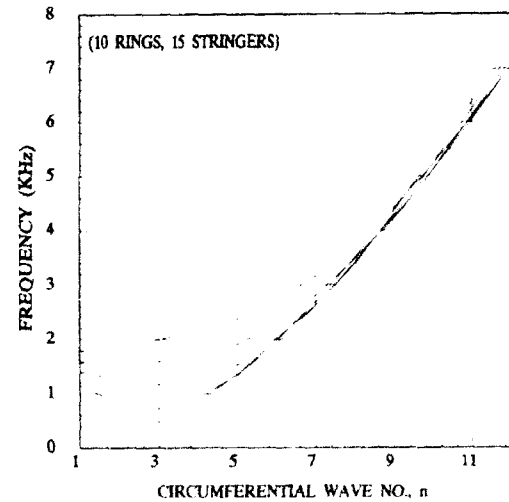
Fig. 4. The first five natural frequencies versus circumferential wave no. for the same shell shown in Fig. 1, but with the addition of 10 rings and 15 ring stiffeners.

Table 4. Comparison of the lowest natural frequencies (kHz) predicted by five different shell theories and inclusion or omission of various in-surface inertias ($h/R = 0.02$, $L/R = 4$, $R = 1.27$ cm). All occur at $m = 1$, $n = 2$

Theory	Including all translational inertias	Omitting axial inertia only	Omitting circumferential inertia only	Omitting both axial and circumferential inertias
Sanders	0.2969	0.2994	0.3408	0.3445
Love	0.2970	0.2995	0.3410	0.3446
Loo	0.2610	0.2633	0.3013	0.3047
Morley	0.2611	0.2634	0.3015	0.3049
Donnell	0.3214	0.3244	0.3724	0.3769
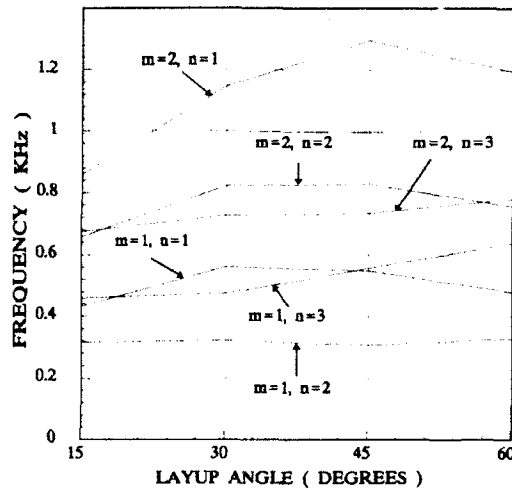
Fig. 5. The effect of layup angle on the natural frequencies of certain modes of an angle-ply composite-material shell; otherwise, the same as the one considered in Fig. 4.
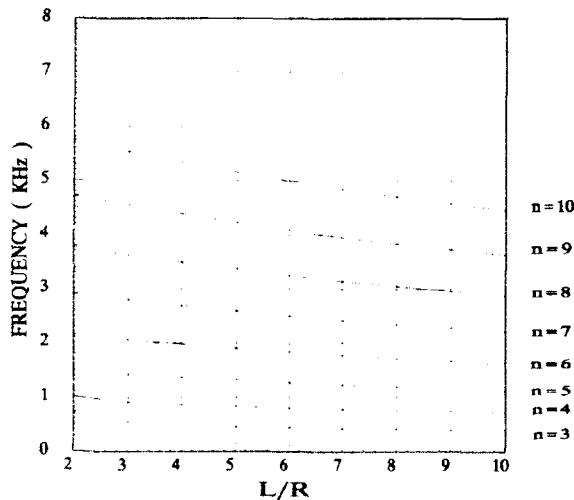
Fig. 6. The effect of cylinder aspect ratio, L/R, on the first nine natural frequencies corresponding to an axial mode number of unity. The shell is otherwise the same as the one considered in Fig. 4.

CONCLUSION

The analysis presented includes five different thin shell theories. For a reasonably wide range of

geometric parameters, all five theories are in reasonably close agreement. The analysis presented may be used to determine the lower natural frequencies of thin composite-material shells with ring and/or stringer stiffeners. As such, it may be useful for the preliminary design of dynamically loaded, stiffened, composite-material shells.

REFERENCES

1. Bert, C. W. & Egle, D. M., Dynamics of composite, sandwich, and stiffened shells. *J. Spacecr. Rockets*, **6** (1969) 1345–61.
2. Mukhopadhyay, M. & Sinha, G., A review of dynamic behavior of stiffened shells. *Shock Vib. Digest*, **24** (8) (1992) 3–13.
3. Egle, D. M. & Sewall, J. L., An analysis of orthogonally stiffened cylindrical shells with stiffeners treated as discrete elements. *AIAA J.*, **6** (1968) 518–26.
4. Bert, C. W., Recent advances in dynamics of composite structures. In *Proc. 4th Int. Conf. on Composite Structures, Vol. 2*, Paisley, Scotland. Elsevier Applied Science, London, 1987, pp. 2.1–2.17.
5. Prokopenko, N. Ya., Intrinsic oscillations of a reinforced laminar cylindrical shell. *Sov. Appl. Mech.*, **15** (1980) 821–7.
6. Sanders, J. L. Jr., *An Improved First-approximation Theory for Thin Shells*. NASA Report R-24, 1959.
7. Koiter, W. T., A consistent first approximation in the general theory of thin elastic shells. In *Proc. Symp. Theory of Thin Elastic Shells*. Amsterdam, North-Holland, 1960, pp. 12–33.
8. Love, A. E. H., *A Treatise on the Mathematical Theory of Elasticity*, 4th edn. Dover Publications, New York, 1944.
9. Loo, T. T., An extension of Donnell's equation for a circular cylindrical shell. *J. Aeronaut. Sci.*, **24** (1957) 390–1.
10. Morley, L. S. D., An improvement on Donnell's approximation for thin-walled circular cylinders. *Quart. J. Mech. Appl. Math.*, **12** (1959) 89–99.
11. Donnell, L. H., *Stability of Thin-walled Tubes Under Torsion*. NACA Report 479, 1933.
12. Bert, C. W. & Kumar, M., Vibration of cylindrical shells of bimodulus composite materials. *J. Sound Vib.*, **81** (1982) 107–21.
13. Jones, R. M., *Mechanics of Composite Materials*. Scripta, Washington, DC, 1975.
14. Hoff, N. J., Buckling of axially compressed circular cylindrical shells at stresses smaller than the classical ones. *J. Appl. Mech.*, **18** (1965) 542–6.

APPENDIX 1: LISTING OF LINEAR DIFFERENTIAL OPERATORS

The linear differential operators, $\mathcal{L}_{kl}$, appearing in eqn (12) are as follows:

$$\mathcal{L}_{11} \equiv \left[A_{11} + \sum_s \delta(y - y_s) E_s A_s \right] d_1^2 + [A_{66} - 2C_4(B_{66}/R) + C_4^2(D_{66}/R^2)] d_2^2 - P d_t^2$$

$$\mathscr{L}_{12} \equiv [A_{12} + A_{66} + C_2(B_{12}/R) + (C_3 - C_4)(B_{66}/R) - C_3 C_4(D_{66}/R^2)] d_x d_y$$

$$\mathscr{L}_{13} \equiv \mathscr{L}_{31} \equiv -\left[B_{11} + \sum_s \delta(y - y_s) E_s A_s z_s\right] d_x^3 - [B_{12} + 2B_{66} - 2C_4(D_{66}/R)] d_x d_y^2 + (A_{12}/R) d_x$$

$$\mathscr{L}_{21} \equiv [A_{12} + A_{66} + C_1(B_{22}/R) + (C_3 - C_4)(B_{66}/R) - C_3 C_4(D_{66}/R^2)] d_x d_y$$

$$\mathscr{L}_{22} \equiv [A_{66} + 2C_3(B_{66}/R) + C_3^2(D_{66}/R^2)] d_x^2 + \left\{A_{22} + (C_1 + C_2)(B_{22}/R) + C_1 C_2(D_{22}/R^2) + \sum_r \delta(x - x_r)\right.$$

$$\left.[E_r A_r[1 + (C_1 + C_2)(z_r/R)] + (E_r I_{0r}/R^2) C_1 C_2]\right\} d_y^2 - P d_t^2$$

$$\mathscr{L}_{23} \equiv -[B_{12} + 2B_{66} + C_1(D_{12}/R) + 2C_3(D_{66}/R)] d_x^2 d_y$$

$$\quad -\left\{B_{22} + C_1(D_{22}/R) + \sum_r \delta(x - x_r)[E_r A_r z_r + C_1(E_r I_{0r}/R)]\right\} d_y^3$$

$$\quad + \left[A_{22} + C_1(B_{22}/R) + \sum_r \delta(x - x_r) E_r A_r(1 + C_1 z_r R^{-1})\right] R^{-1} d_y$$

$$\mathscr{L}_{32} \equiv -[B_{12} + 2B_{66} + C_2(D_{12}/R) + 2C_3(D_{66}/R)] d_x^2 d_y$$

$$\quad -\left\{B_{22} + C_2(D_{22}/R) + \sum_r \delta(x - x_r)[E_r A_r z_r + C_2(E_r I_{0r}/R)]\right\} d_y^3$$

$$\quad + \left[A_{22} + C_2(B_{22}/R) + \sum_r \delta(x - x_r) E_r A_r(1 + C_2 z_r R^{-1})\right] R^{-1} d_y$$

$$\mathscr{L}_{33} \equiv \left[D_{11} + \sum_s \delta(y - y_s) E_s I_{0s}\right] d_x^4 + 2(D_{12} + 2D_{66}) d_x^2 d_y^2 + \left[D_{22} + \sum_r \delta(x - x_r) E_r I_{0r}\right] d_y^4$$

$$\quad - 2(B_{12}/R) d_x^2 - 2\left[(B_{22}/R) + \sum_r \delta(x - x_r) E_r A_r(z_r/R)\right] d_y^2 + (A_{22}/R^2) + \sum_r \delta(x - x_r)(E_r A_r/R^2) + P d_t^2$$

If all reinforcements are disregarded, the operators reduce to those given for an unstiffened shell by Bert and Kumar.[12] The operators are symmetric for the Sanders, Love, and Donnell theories, but not the Loo and Morley theories.

APPENDIX 2: LISTING OF COEFFICIENTS OF THE FREQUENCY DETERMINANT

For a circular cylindrical shell having closely spaced rings and/or stringers (spacings l_r and l_s), the coefficients of the 3×3 frequency determinant are:

$$C_{11} = -\{[A_{11} + (E_s A_s/l_s)] \alpha^2 + [A_{66} - 2C_4(B_{66}/R) + C_3^2(D_{66}/R^2)] \beta^2 - P\omega^2\}$$

$$C_{12} = -[A_{12} + A_{66} + C_2(B_{12}/R) + (C_3 - C_4)(B_{66}/R) - C_3 C_4(D_{66}/R^2)] \alpha\beta$$

$$C_{13} = -C_{31} = [B_{11} + (E_s A_s z_s/l_s)] \alpha^3 + [B_{12} + 2B_{66} - 2C_4(D_{66}/R)] \alpha\beta^2 + (A_{12}/R) \alpha$$

$$C_{21} = -[A_{12} + A_{66} + C_1(B_{12}/R) + (C_3 - C_4)(B_{66}/R) - C_3 C_4(D_{66}/R^2)] \alpha\beta$$

$$C_{22} \equiv -\{[A_{66} + 2C_3(B_{66}/R) + C_3^2(D_{66}/R^2)] \, \alpha^2 + \{A_{22} + (C_1 + C_2)(B_{22}/R) + C_1 C_2(D_{22}/R^2)$$
$$+ E_r A_r[1 + (C_1 + C_2)(z_r/R)] + C_1 C_2(E_r I_{or}/R^2)\} \, (\beta^2/l_r) - P\omega^2\}$$

$$C_{23} \equiv [B_{12} + 2B_{66} + C_1(D_{12}/R) + 2C_3(D_{66}/R)] \, \alpha^2\beta + [B_{22} + C_1(D_{22}/R) + (1/l_r)(E_r A_r z_r + C_1 E_r I_{or} R^{-1})] \, \beta^3$$
$$+ [A_{22} + C_1(B_{22}/R) + (E_r A_r/l_r)(1 + C_1 z_r R^{-1})] \, (\beta/R)$$

$$C_{32} \equiv -[B_{12} + 2B_{66} + C_2(D_{12}/R) + 2C_3(D_{66}/R)] \, \alpha^2\beta - [B_{22} + C_2(D_{22}/R) + (1/l_r)(E_r A_r z_r + C_2 E_r I_{or} R^{-1})] \, \beta^3$$
$$- [A_{22} + C_2(B_{22}/R) + (E_r A_r/l_r)(1 + C_2 z_r R^{-1})] \, (\beta/R)$$

$$C_{33} \equiv [D_{11} + (E_r I_{os}/l_s)] \, \alpha^4 + 2(D_{12} + 2D_{66}) \, \alpha^2\beta^2 + [D_{22} + (E_r I_{or}/l_r)] \, \beta^4 + 2(B_{12}/R) \, \alpha^2$$
$$+ 2[(B_{22}/R) + (E_r A_r z_r/l_r R)] \, \beta^2 + (A_{22}/R^2) + (E_r A_r/l_r R^2) - P\omega^2$$

The buckling of composite stiffened plates with some emphasis on the effects of fibre orientation and on loading configuration

J. Loughlan & J.-M. Delaunoy

Department of Aerospace Technology, College of Aeronautics, Cranfield Institute of Technology, Cranfield, Bedfordshire, UK, MK43 0AL

The bucking characteristics of some composite stiffened plates are determined in this paper using a finite strip approach. The finite strip formulation is able to predict the complex buckling modes associated with in-plane shear loading and the method of approach can allow for other loading configurations whose associated pre-buckling stresses are not so obviously realised.

Two loading conditions have essentially been considered in the paper, that of in-plane shear and that of partial edge loads being reacted by shear. The strip displacement fields before and after buckling are represented by algebraic polynomials across the strip and trigonometric functions along the strip length. The inclusion of sufficient harmonics in the appropriate displacement representations thus allows the distorted nodal lines of the shear buckling mode and the complex pre-buckled stresses associated with partial edge loads to be determined with relative ease.

INTRODUCTION

Many different analytical and solution procedures have been employed to determine the buckling behaviour of thin-walled metal and composite constructions and these include Finite Difference, Rayleigh–Ritz, Galerkin, Finite Element and Closed Form approaches to mention some. A method of analysis which has gained popularity over the years and is now being used quite extensively by many researchers, particularly for the buckling and vibration studies of prismatic flat plate structures, is that of the Finite Strip method. Although numerous investigations using the finite strip approach have been carried out during the past 20 years, mention is made here of only some, considered by the authors to be a representative sample of the type of research covered during this period.

The finite strip method has been used in the works of Plank and Wittrick[1] and Plank and Williams[2] on the buckling of longitudinally stiffened panels subjected to combined in-plane loading. The strip formulation employed can deal with isotropic or anisotropic materials but is based on an assumption with regard to the commonality of the buckle half-wavelength λ to all strip longitudinal lines which severely restricts the attainment of useful solutions in the presence of shear loading. The results presented in Refs 1 and 2 associated with in-plane shear loading are thus for infinitely long panels restricted to the local buckling mode only.

The vibrational characteristics of flat and single curved thin isotropic skin-stringer structures were determined by Petyt[3] and Petyt and Fleischer[4] using the finite strip method. The conventional simply supported rectangular flat strip was employed to model the flat skin structures whereas a rectangular planform singly curved finite shell strip was used to model the curved panel structures. Since the structures were not subjected to membrane force actions then coupling is eliminated between the different harmonics of the free vibration analysis and thus solutions could be determined corresponding to any specified individual harmonic.

To the author's knowledge the finite strip formulation developed by Graves Smith and Sridharan,[5] some 14 years ago, was the first of its kind to be able to examine the buckling behaviour of plate structures whose pre-buckling stress state could not be determined by simple deduction. The multi-term formulation developed was

applied to the problem of in-plane partial edge loading being reacted by shear in thin isotropic web plates. Using this formulation Graves Smith and Gierlinski[6] examined the behaviour of longitudinally stiffened isotropic web plates subjected to in-plane localised edge loads. Twelve significant harmonics were used in this work for the linear analysis to determine the pre-buckling stress variations and four harmonics were utilised to evaluate the buckling mode.

Several multi-term harmonic composite strip formulations have been developed by Dawe and Peshkam[7,8] who examined the effects of shear deformation and considered also the classical thin plate theory approach. The features of sub-structuring are outlined both at the local component flat level and at the structural assembly level. It is shown in Ref. 8 that highly accurate results can be determined by modelling each component flat of a structure by a single strip based on sub-structuring.

The compressive behaviour of singly curved composite stiffened panels has been studied by Snell and Greaves[9] through the use of finite strips with regard to buckling and experimentally with regard to strength. It is shown in this work that despite the presence of impact damage in some cases, the difference in test failure loads between otherwise identical panels was small.

The shear buckling behaviour of finite length stiffened panels has been examined by Loughlan[10,11] using a multi-term finite strip with the same perturbation displacement fields as those used by Graves Smith et al.[5,6] for the edge loading problem. The panels studied were comprised of plain flat outstands and consideration was given to isotropic[10] and composite[11] material construction.

In this paper the approach detailed in Refs 10 and 11, pertaining essentially to the simplified loading case of in-plane shear, is extended to allow for the effects of partial edge loading on thin composite stiffened plate structures. The pre-buckling stresses associated with partial edge loading are determined in the paper using a linear finite strip analysis and any number of significant harmonics can be utilised to represent the pre-buckling displacement field.

THEORETICAL DETAILS

The results given in this paper are those for thin laminated plates determined through the use of classical laminated plate theory and thus the effect

of shear deformation through the thickness of the laminate are neglected. To determine the buckling behaviour of thin stiffened plates manufactured from layered composite material the specialised technique known as the finite strip method is used in this paper. The finite strip approach has been shown[5] to yield considerable computing economy when compared with finite element methods.

The approach is considered favourable when dealing with the initial buckling or natural frequency characteristics of thin-walled prismatic structures. It assumes that the prismatic structure can be discretised into a number of longitudinal strips and that the displacement fields associated with each strip vary sinusoidally along the strip length and algebraically across the strip width. The geometry of a typical finite strip of layered composite material is shown in Fig. 1 indicating the coordinate axes system pertaining to the strip displacements u, v and w.

The strain energy U of a layered composite strip which has experienced a generalised interactive displacement field is given as follows:

$$U = \frac{1}{2} \int \int \{[\varepsilon_l^0]^T[A][\varepsilon_l^0] + 2[\varepsilon_l^0]^T[A][\varepsilon_{nl}^0]$$

$$+ 2[\varepsilon_l^0]^T[B][\psi] + 2[\varepsilon_{nl}^0]^T[B][\psi] + [\varepsilon_{nl}^0]^T[A][\varepsilon_{nl}^0]$$

$$+ [\psi]^T[D][\psi]\} \, dx \, dy \qquad (1)$$

In this expression $[\varepsilon_l^0]$ and $[\varepsilon_{nl}^0]$ are the linear and nonlinear components respectively of the middle surface strains $[\varepsilon^0]$ of the laminate and $[\psi]$ determines the middle surface bending and twisting curvatures. The $[A]$, $[B]$ and $[D]$ matrices are the usual in-plane, coupling and flexural stiffnesses of the composite material.
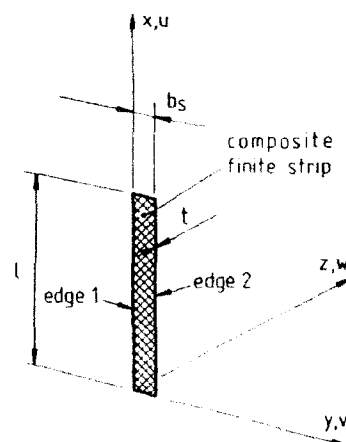
Fig. 1. Strip geometry and coordinate axes system.

For a laminate with a symmetric layup configuration the $[B]$ matrix is identically zero and since we are concerned only with the linearised eigenvalue problem, the post-buckling contribution to the strain energy is thus dispensed with at this stage to give:

$$U = \frac{1}{2} \int \int \{[\varepsilon_1^0]^T [A][\varepsilon_1^0] + [\psi]^T [D][\psi]\} \, dx \, dy$$

$$+ \int \int \{[\varepsilon_1^0]^T [A][\varepsilon_{nl}^0]\} \, dx \, dy \tag{2}$$

The strain energy component which accounts for the effect on strip stiffness of initial stresses can be written in terms of these stresses if these are known *a priori*. This is indeed the case for the more simplified loading cases such as pure compression or pure shear or combinations of compression and shear and thus for such cases we may write:

$$U = \frac{1}{2} \int \int \{[\varepsilon_1^0]^T [A][\varepsilon_1^0] + [\psi]^T [D][\psi]\} \, dx \, dy$$

$$+ t \int \int \{[\sigma]^T [\varepsilon_{nl}^0]\} \, dx \, dy \tag{3}$$

The stress matrix $[\sigma]$ thus describes the nature of the stresses acting on the strip prior to buckling and these can be considered as any combination of linearly varying σ_x and σ_y stresses coupled with a constant shear stress τ_{xy} as detailed in Fig. 2.

If the loading is of a more complex configuration then the pre-buckling stresses are, of course, unable to be deduced by simple inspection and thus an appropriate analysis procedure is required for their determination. In this paper the pre-buckling stresses pertaining to partial edge loading are determined by means of linear finite strip analysis in which the membrane displacements of the strips are considered to be of the form:

$$u = \sum_{m=1}^{M} [(1 - \eta)u_{1m} + \eta u_{2m}] \cos \frac{m\pi x}{l}$$

$$\tag{4}$$

$$v = \sum_{m=1}^{M} [(1 - \eta)v_{1m} + \eta v_{2m}] \sin \frac{m\pi x}{l}$$

where $\eta = y/b_s$ and the u_{1m}, u_{2m}, v_{1m}, v_{2m} are the nodal line connection quantities along the edges 1 and 2 of the strips and corresponding to the mth
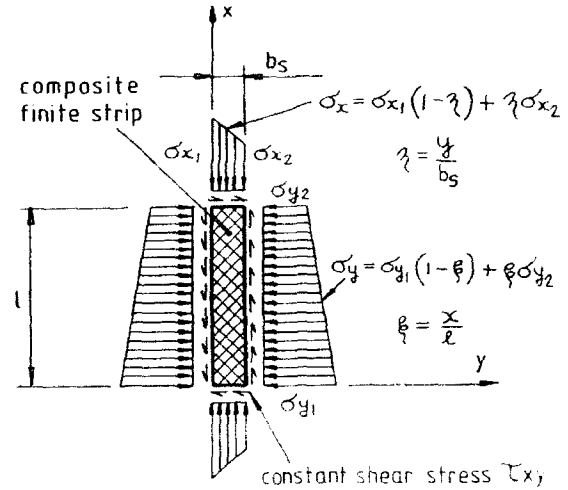
Fig. 2. Possible destabilising stress system acting on strip.

harmonic of the membrane displacement series in the pre-buckling analysis. M is the number of harmonics necessary to model the applied loading and to determine the corresponding internal membrane stress state with sufficient accuracy. The choice of displacements described by eqns (4) imposes some obvious restrictions on the application of such a strip formulation for linear membrane analysis. It has been found however that these displacements are particularly suitable for the partial edge loading problem.

Linear analysis solves for the nodal line displacements of the assembled structure in the usual manner associated with matrix displacement methods and thus the strains and stresses corresponding to these displacements are readily determined. The stress matrix $[\sigma]$ associated with partial edge loading is thus available for use in the energy expression of eqns (3) and the subsequent buckling analysis.

The middle surface strains ε^0 are described in terms of the strip displacements u, v and w by the expressions

$$\varepsilon_x^0 = \frac{\partial u}{\partial x} + \frac{1}{2}\left\{\left(\frac{\partial u}{\partial x}\right)^2 + \left(\frac{\partial v}{\partial x}\right)^2 + \left(\frac{\partial w}{\partial x}\right)^2\right\}$$

$$\varepsilon_y^0 = \frac{\partial v}{\partial y} + \frac{1}{2}\left\{\left(\frac{\partial u}{\partial y}\right)^2 + \left(\frac{\partial v}{\partial y}\right)^2 + \left(\frac{\partial w}{\partial y}\right)^2\right\} \tag{5}$$

$$\varepsilon_{xy}^0 = \frac{\partial u}{\partial y} + \frac{\partial v}{\partial x} + \left\{\frac{\partial u}{\partial x} \cdot \frac{\partial u}{\partial y} + \frac{\partial v}{\partial x} \cdot \frac{\partial v}{\partial y} + \frac{\partial w}{\partial x} \cdot \frac{\partial w}{\partial y}\right\}$$

The linear bending and twisting curvatures of the middle surface of the strip which cause additional linear strains at positions away from the middle surface through the strip thickness are given in terms of w as follows:

$$\psi_x = \frac{\partial^2 w}{\partial x^2}, \quad \psi_y = \frac{\partial^2 w}{\partial y^2}, \quad \psi_{xy} = 2\frac{\partial^2 w}{\partial x \partial y} \quad (6)$$

The displacements of the strip, over and above those associated with any pre-stress, i.e. the perturbation or buckling displacements, are described by the following functions;

$$u = \sum_{n=1}^{N} [(1-\eta)u_{1n} + \eta u_{2n}] \cos\frac{n\pi x}{l}$$

$$v = \sum_{n=1}^{N} [(1-\eta)v_{1n} + \eta v_{2n}] \sin\frac{n\pi x}{l} \quad (7)$$

$$w = \sum_{n=1}^{N} [(1-3\eta^2+2\eta^3)w_{1n} + b_\gamma(\eta-2\eta^2+\eta^3)\theta_{1n}$$

$$+ (3\eta^2-2\eta^3)w_{2n} + b_\gamma(\eta^3-\eta^2)\theta_{2n}] \sin\frac{n\pi x}{l}$$

where $\eta = y/b_\gamma$ and $u_{1n}, v_{1n}, w_{1n}, \theta_{1n}, u_{2n}, w_{2n}, \theta_{2n}$ are the perturbation displacement connection quantities along the edges 1 and 2 of the strip and corresponding to the nth harmonic of the buckling displacement series along the strip length.

Substituting for the appropriate derivatives of the displacements of eqns (7) into eqns (5) and (6) and then subsituting the resultant linear and non-linear components ε_l' and ε_{nl}' respectively of the middle surface strains along with the resultant curvatures ψ into eqns (3) and carrying out the integrations then gives the strain energy in terms of the displacement connection quantities or edge degrees of freedom of the strip. The strain energy for the strip is thus written;

$$U(\delta) = U_s(\delta) + U_\sigma(\delta) \quad (8)$$

where the first strain energy component is, of course, that which is associated with the conventional stiffness matrix of the strip and the second component is that which allows for the effect on stiffness of pre-stress. The displacement connection quanities at the strip edges and their associated force amplitudes corresponding to the nth harmonic of the postulated deflection series are shown in Fig. 3. The force and displacement amplitudes at the strip edges are thus described by
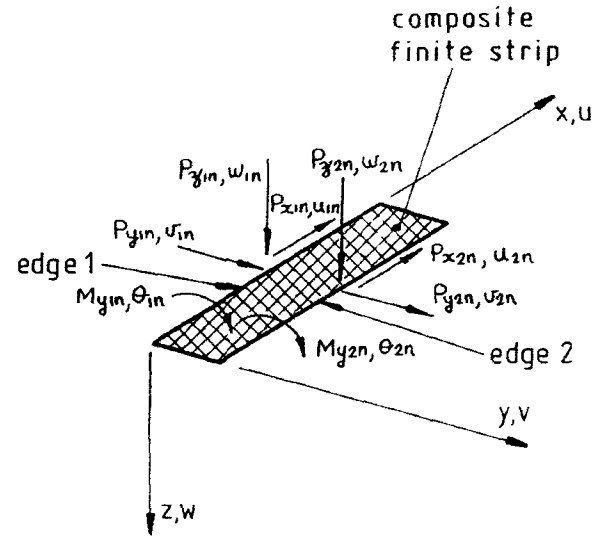
Fig. 3. Edge force and displacement amplitudes relating to Nth harmonic of perturbation deflection series.

the vectors $[F]$ and $[\delta]$ as follows:

$$[F]^T = [Px_{11}, Py_{11}, Pz_{11}, My_{11}, Px_{21}, Py_{21}, Pz_{21},$$

$$My_{21}... Px_{1N}, Py_{1N}, Pz_{1N}, My_{1N}, Px_{2N}, Py_{2N},$$

$$Pz_{2N}, My_{2N}] \quad (9)$$

$$[\delta]^T = [u_{11}, v_{11}, w_{11}, \theta_{11}, u_{21}, v_{21}, w_{21}, \theta_{21}...$$

$$u_{1N}, v_{1N}, w_{1N}, \theta_{1N}, u_{2N}, v_{2N}, w_{2N}, \theta_{2N}] \quad (10)$$

where N is the number of harmonics considered in the deflection series to be capable of the solution of the given problem. These force and displacement vectors are, of course, related through the stiffness of the strip and this is determined by invoking the Principle of Virtual Displacements in the form $Fr = (\partial U(\delta)/\partial \delta r)$ to give

$$[F] = [k + k\sigma][\delta] \quad (11)$$

The matrix $[k]$ is the conventional elastic stiffness of the strip pertaining to its in-plane and out-of-plane properties while the matrix $[k\sigma]$ is the initial stress stiffness matrix, or as it is often referred to, the geometric stiffness matrix of the strip.

So far we have determined the local stiffnesses $[k]$ and $[k\sigma]$ for an individual finite strip. The size of these local matrices is $8N \times 8N$ and it has been found that for shear or partial edge loading problems three longitudinal harmonics are sufficiently adequate to provide good accuracy.

It remains now to assemble or add together the stiffnesses of all strips that model the given structure in order to form the global elastic and geo-

metric stiffnesses [K] and [K_o] for the structure. This is undertaken in the usual manner associated with stiffness methods of analysis and after consideration of the constraint boundary conditions of the structure the final equations which relate to the active degrees of freedom of the structure are written:

$$[\bar{K}][\Delta] = ([K] + \lambda[K_o])[\Delta] = [P] \qquad (12)$$

The size of the structural matrices [K] and [K_o] in this system of equations depends, of course, on the number of strips engaged to model the given structure and on the number of longitudinal harmonics chosen to represent the displacement field of the strips as well as on the displacement constraints imposed.

The parameter λ in eqns (12) is an arbitrary scaler multiplier which describes the intensity of the existing membrane stresses acting on the structure. The geometric matrix [K_o] takes the sign of these stresses and if they are of a destablising nature then an increase in λ would result in a reduction of the total stiffness [$\bar{K}$] of the structure. The vector [P] is the global applied nodal line perturbation force amplitude and the [Δ] vector is the corresponding global displacement amplitude. It is possible to increase λ to such an extent that the total structural stiffness [$\bar{K}$] reduces to zero. This value of λ is that which describes the critical intensity of the membrane stresses required to cause buckling of the structure and if λ corresponds to this critical buckling value then it is possible to let the structure acquire the displacements [Δ] without application of the perturbation forces and eqns (12) thus become:

$$\{[K] + \lambda_{CR}[K_o]\}[\Delta] = 0 \qquad (13)$$

Although, in general, there is more than one value of λ_{CR} which satisfies eqns (13) and each has associated with it values of [Δ] defining the corresponding critical mode shape, the intensity of the membrane stress state to cause buckling is that which corresponds to the smallest value of λ_{CR} which satisfies these equations.

SOME ILLUSTRATIVE RESULTS

Results are given in the paper for both isotropic and composite material construction. The composite stiffened plates considered are assumed to be manufactured from high strength carbon–epoxy pre-impregnated ply sheets with a ply thickness of
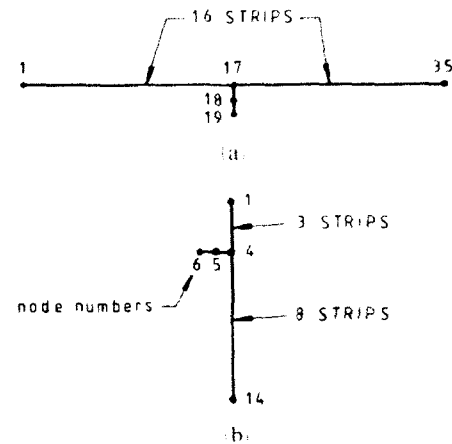
Fig. 4. Typical structural models used for solutions. a single transverse stiffener; (b) single longitudinal stiffener.

0·125 mm and with the following ply material properties:

$$E_1 = 140 \text{ kN/mm}^2, E_2 = 10 \text{ kN/mm}^2$$

$$G_{12} = 5 \text{ kN/mm}^2, \nu_{12} = 0·3$$

The finite strip models used to obtain the composite stiffened plate buckling solutions given in the paper are shown in Fig. 4. The two cases considered are, Fig. 4(a), a single centrally located transverse stiffener for the case of shear loading and Fig. 4(b) a single longitudinal stiffener located at ½ the depth of the plate from the loaded edge for the case of partial edge loading as indicated. Obviously a meaningful solution will depend to a large extent on the structural model utilised. It will depend on both the number of strips employed and on the number of longitudinal harmonics chosen to represent the perturbation or buckling displacements of the strip and for the case of partial edge loading, on the number of harmonics chosen to model the pre-buckling displacement field.

Figures 5 and 6 show the contour plots of the general and local shear buckling modes respectively of a thin plate skin reinforced by a centrally located transverse plain flat outstand. The aspect ratio of the plate is $a/b = 2$ and thus the centrally located stiffener divides the skin into two square plate regions as indicated. The buckling modes shown have been determined for isotropic construction and on the basis of using a finite strip model with fourteen strips representing the skin and two strips modelling the stiffener.

In Fig. 5 it is clearly indicated that the stiffener is substantially involved in the general shear

Fig. 5. General shear buckling mode

Fig. 6. Local shear buckling mode

buckling mode. The plot shown is for a stiffener to plate depth ratio $d/b = 0.02$ and for a stiffener to skin thickness ratio $t_s/t = 1.0$. Such a stiffener is particularly weak with regard to its in-plane bending stiffness and the plate is thus noted to buckle in a general fashion across the stiffener line. The distorted nodal lines of the buckling mode marked 0.0 are clearly evident. A close examination of the mode shape indicates substantial in-plane bending of the stiffener associated with a single half-wave along its length and also the presence of transverse bending and twisting of the stiffener associated with two half-waves along its length.

In Fig. 6 it is clear that the stiffener is of such proportions as to hold its attachment point to the skin as a nodal line. The distorted nodal lines of the buckling mode are also clearly evident. The plot shown is for the value of $d/b = 0.15$ and for the ratio of $t_s/t = 1.0$. The proportions of the stiffener are seen to subdue in-plane bending of the stiffener, however a close examination of the mode shape indicates the presence of transverse bending and twisting deformations of the stiffener and that these are associated with two half-waves along its length. It is noted from Figs 5 and 6 that in-plane shear loading is associated with complex buckling modes and thus in order to accurately

predict the distorted nodal lines of these modes using the finite strip method, several harmonics must be utilised in the postulated perturbation displacement series. Three harmonics were found to predict the modes of Figs 5 and 6 with good accuracy.

Figure 7 shows the partial edge loading of a square plate being reacted externally by shear along the two vertical edges of the plate. The partial edge loading is centrally located along the top edge of the plate and the width of the loading is $\frac{2}{9}$ of the plate depth. All edges of the plate are simply supported. The intensity of the applied loading is one unit as shown and the constant stress contour lines indicated are those which represent the internal σ_y pre-buckling stress pattern corresponding to this loading. As expected the stress pattern is noted to be symmetric about the plate vertical centreline and to have a high local intensity in the vicinity of the applied loading which then diminishes fairly rapidly to zero at the bottom edge of the plate. The stresses shown in Fig. 7 have been determined by utilising eleven strips to model the plate and six significant harmonics in eqns (4) to represent the pre-buckling displacement field.

The general buckling mode of the square plate subjected to partial edge loading is shown in Fig. 8. This has been determined on the basis of the pre-buckling stresses illustrated in Fig. 7 and by utilising two harmonics in the perturbation deflection series of eqns (7) to represent the buckling mode. The symmetry of the mode is obvious and it is also clear that the plate is more heavily buckled towards the loaded edge. The maximum

amplitude of the buckle is seen to occur at about $\frac{1}{4}$ the depth of the plate from the loaded edge.

To enhance the buckling capability of the plate a longitudinal stiffener is normally introduced in the region of high stresses and the optimum position of such a stiffener is considered to be at about $\frac{1}{5}$ of the plate depth from the loaded edge as indicated in Fig. 8.

It is clear that stiffeners in this location would be heavily involved in the buckling mode particularly if the stiffener depth were insufficient to enforce a nodal line. The deformed state of the stiffener in the buckling mode would thus be general or interactive in nature and the presence of both local and overall deflections would thus be evident.

Figure 9 shows the local buckling mode for the square plate subjected to partial edge loading. The
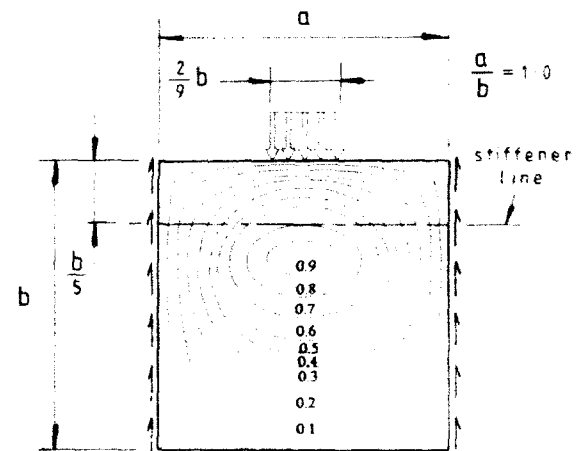
Fig. 8. General partial edge loading buckling mode.
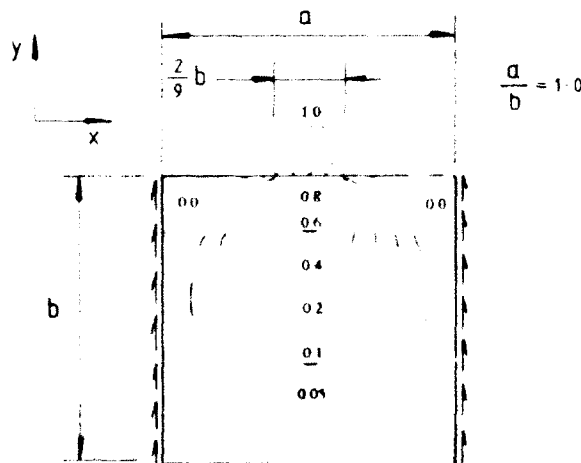
Fig. 7. Pre-buckling stresses resulting from partial edge loading.
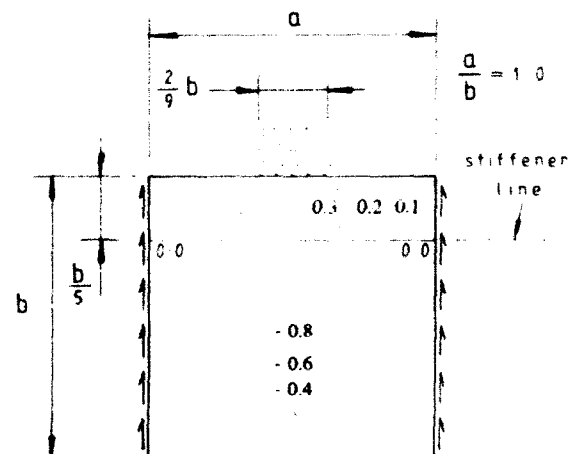
Fig. 9. Local partial edge loading buckling mode.

plate is now seen to buckle into two separate regions with the stiffener line being held as a nodal line. This mode was determined by utilising a stiffener in the form of a plain flat outstand symmetrically disposed about the plate mid-surface and with a stiffener depth to skin thickness ratio of $d/t = 18$ and a stiffener to skin thickness ratio of $t_s/t = 2$. Two additional strips were used in the structural model to represent the stiffener. This stiffener arrangement is just sufficient to hold the stiffener line as a nodal line and thus greater stiffener depths offer virtually no improvement in buckling capacity. A close examination of the buckling mode, taking note of symmetry, indicates that the local deflections of the stiffener are associated with a single half-wave along the stiffener length. The results discussed in Figs 7–9 have been determined for isotropic material construction.

With reference to composite material construction, Fig. 10 shows the single buckling capability of a plate stiffened by a single centrally located transverse stiffener. The skin is a 45° symmetric angle-ply configuration with 16 plies and the fibre orientation in the stiffener is symmetric cross-ply with consideration being given to 8, 16 and 24 plies in the stiffener respectively. The results shown in Fig. 10 have been determined on the basis of the structural model detailed in Fig. 4(a) and through the use of three harmonics to represent the buckling mode.

For the plate geometry considered the centrally located stiffener divides the skin into two square panel regions. For comparative purposes the shear buckling capacity of a simply supported square panel is indicated in Fig. 10 by the straight line whose value of $K_s = 13.57$. Also for comparative purposes the straight line whose value of $K_s = 14.86$ indicates the shear buckling capacity of a square panel with three sides simply supported and one side clamped. These two K_s levels are, of course, the lower and upper bound limits to the shear buckling capacity of the stiffened panel when the mode of buckling is local in nature and thus all curves are seen to lie between these limits at the higher stiffener depths.

It is shown in Fig. 10, as expected, that increasing the number of plies in the stiffener steadily improves the shear buckling performance of the panel at all stiffener depths and at the higher stiffener depths the curves are shown to move gradually towards the upper bound K_s value of 14.86 which, of course, is that relating to the case of a torsionally rigid connection at the skin–stiffener interface. It is of note that the levelling out of the curves is fairly well defined for the single stiffener
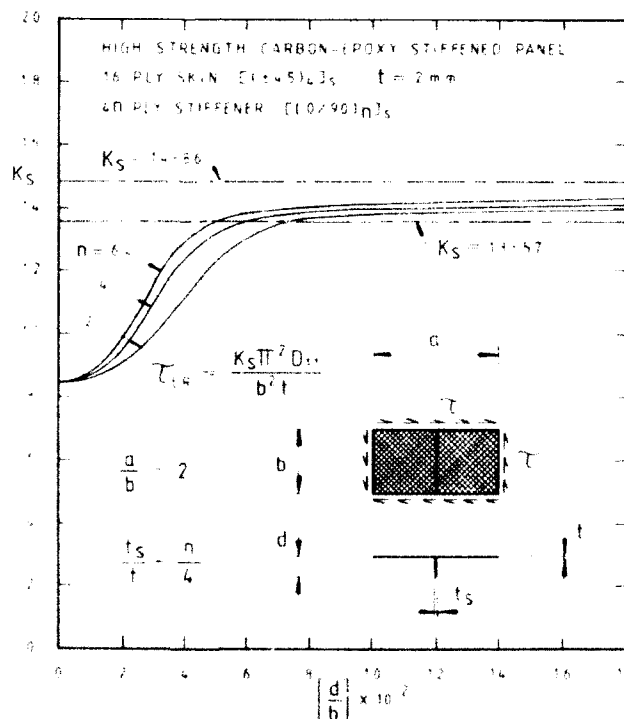
Fig. 10.   Shear buckling capacity of single transverse stiffener arrangement.

configuration and thus it would appear from Fig. 10 that it would be pointless to increase the stiffener depth above, approximately, the value of $d = 0.1b$ since, clearly, there is little or no gain to be made in the shear buckling resistance of the panel in doing so.

Figure 11 shows the buckling capacity of a square composite plate subjected to a central point load on its upper edge which is reacted externally by shear on the two vertical edges as shown. The plate is stiffened longitudinally by a plain flat outstand attached on one side and positioned at $\frac{1}{3}$ of the depth of the plate from the loaded edge as indicated. The results shown in Fig. 11 are based on the structural model of Fig. 4(b) and on the use of six significant harmonics for the pre-buckling stresses and two harmonics for the buckling mode. The skin is a 45° symmetric angle-ply configuration with four plies and the stiffener assumes the three different configurations of unidirectional, symmetric cross-ply and 45° symmetric angle-ply respectively such that the ratio $t_s/t = 1.0$ in all cases.

For a given structural weight, i.e. any given stiffener depth, it is clear that fibre orientation in the stiffeners can have a significant effect on buckling capacity. At the lower stiffener depths
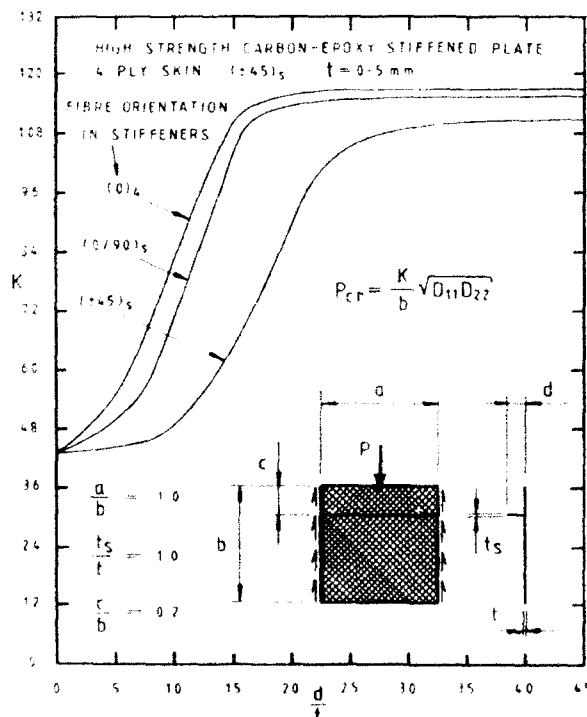
the buckling mode is general in nature and thus the stiffener is involved interactively with overall in-plane and local out-of-plane bending, this being associated with a single half-wave along the stiffener length. The stiffener lay-up configuration which provides the best combination of in-plane flexural stiffness and local through the thickness longitudinal and transverse bending stiffnesses should therefore be expected to provide the best response to buckling at the lower stiffener depths. The order of stiffener preference is thus shown in Fig. 11 to be unidirectional, cross-ply and 45° angle-ply respectively. This order of preference is seen to be unchanged at the higher stiffener depths where the mode of buckling is now local in nature and the local deflections of the stiffener are again associated with a single half-wave along the stiffener length.

CONCLUSIONS

A multi-term finite strip approach has been presented in this paper which is able to predict the complex buckling behaviour of stiffened plate structures manufactured from layered composite material. It is indeed necessary to utilise the multi-term approach in order to allow for the distorted nodal lines of the shear buckling mode and to determine the complex pre-buckled stresses associated with partial edge loads.

The results given in the paper for composite stiffened plates are those pertaining to the plain flat outstand attached to one side of the thin composite skin. Two loading conditions have been considered in the paper, that of in-plane shear and that of partial edge loading. For both loading cases considered it is shown that an optimum stiffener depth is realised as the buckling mode changes from being general to local in nature with increasing stiffener depth. Stiffener depths larger than the optimum are seen to provide a negligible variation in buckling capacity and thus such stiffeners serve only to increase structural weight for almost no gain.

It is shown that for any given structural weight the buckling performance of a composite stiffened plate can be considerably influenced by the orientation of the fibres in the stiffener. For the case of partial edge loading it is shown that the unidirectional stiffener provides the best response to buckling over the complete design range covering both general and local buckling whereas the 45° angle-ply stiffener performs poorly. It is consi-

Fig. 11. Effect of fibre orientation in single longitudinal stiffener arrangement.

dered that the use of unidirectional stiffeners would be impractical however since these would have the tendency to be associated with fibre splitting under the load and indeed from the results determined in the paper it is suggested that the symmetric cross-ply stiffener would be both efficient and practical over the complete design range for the partial edge loading case.

REFERENCES

1. Plank, R. J. & Wittrick, W. H., Buckling under combined loading of thin flat-walled structures by a complex finite strip method. *Int. J. Numer. Meth. Engng.*, **8** (1974) 323–39.
2. Plank, R. J. & Williams, F. W., Critical buckling of some stiffened panels in compression, shear and bending. *Aeronaut. Quart.*, **25** (1974) 165–79.
3. Petyt, M., Finite strip analysis of flat skin-stringer structures. *J. Sound Vib.*, **54** (4) (1977) 537–47.
4. Petyt, M. & Fleischer, C. C., Finite strip analysis of singly curved skin-stringer structures. *J. Sound Vib.*, **77** (4) (1981) 561–71.
5. Graves Smith, T. R. & Sridharan, S., A finite strip method for the buckling of plate structures under arbitrary loading. *Int. J. Mech. Sci.*, **20** (1978) 685–93.
6. Graves Smith, T. R. & Gierlinski, J. T., Buckling of stiffened webs by local edge loads. *J. Struct. Div., ASCE.*, **108** (ST6) (June 1982) 1357–66.
7. Dawe, D. J. & Peshkam, V., Buckling and vibration of finite-length composite prismatic plate structures with diaphragm ends: Part I, finite strip formulation. *Comput. Meth. Appl. Mech. Eng.*, **77** (1989) 1–30.
8. Peshkam, V. & Dawe, D. J., Buckling and vibration of finite-length composite prismatic plate structures with diaphragm ends: Part II. *Comput. Meth. Appl. Mech. Eng.*, **77** (1989) 227–52.
9. Snell, M. B. & Greaves, L. J., Buckling and strength characteristics of some CFRP stiffened curved panels. In *Aerospace Structures*, ed. J. Loughlan. Elsevier Applied Science, London, 1990, pp. 149–76.
10. Loughlan, J., The buckling and vibrational behaviour of some stiffened panels subjected to in-plane shear loading. In *Applied Solid Mechanics — 4*, ed. A. R. S. Ponter & A. C. F. Cocks. Elsevier Applied Science, London, 1991, pp. 275–302.
11. Loughlan, J., A finite strip analysis of the buckling characteristics of some composite stiffened shear panels. Submitted to *Composite Structures*. Elsevier Applied Science, London, 1993.

An evaluation of the edge solution for a higher-order laminated plate theory

M. Karama[a], **M. Touratier**[b] **& A. Idlbi**[a]

[a] *Laboratoire Génie de Production, CMAO — ENIT BP 1629 65016 Tarbes-Cedex, France*
[b] *Laboratoire de Mécanique des Structures — ENSAM 151, bd de l'Hôpital, 75013, Paris, France*

An analytical study was conducted to determine the edge effects upon a higher-order laminated plate theory due to Touratier (*Int. J. Engng Sci.*, **29** (1991) 911–16). The problem considered is a sandwich plate simply supported along two opposite edges and clamped along its two others. The plate is loaded in statics by a pressure upon its top surface and the load is 'sinusoidal-uniform'.

Results are presented for the transverse displacement and the stresses, using the theories of Kirchhoff–Love, Touratier and three-dimensional finite element computations. The results indicate clearly the importance of including transverse shear effects. Analytical calculations from the higher-order plate theory are in good agreement with three-dimensional finite element computations. Near to the clamped edges of the sandwich plate, a particular effect is shown upon the in-plane stresses, i.e. the Kirchhoff–Love theory.

INTRODUCTION

One of the major challenges in computational structural mechanics is the development of advanced models and numerical techniques in order to provide efficient tools exhibiting good interior and edge solutions, notably for composite plates. Then, these models may be used for the analysis and the design in composite structures.

The present work is in the composite plate field with interest focused on a refined shear deformation (called also higher-order) theory which has been published Touratier,[1] and a three-dimensional solid finite element analysis. This theory is described by the classical generalised displacements (as the first-order shear deformation theory or the Reissner–Mindlin theory) but uses a cosine variation of the transverse shear strains following the thickness direction of the plate. This choice for the transverse shear strains is new and has a three-dimensional justification.[1] One can prove that this type of theory may be seen as a generalisation of higher-order theories deduced from a polynomial expansion in respect to the thickness coordinate of the in-plane displacements. One of the interests of this type of theory is the lack of need of any shear correction factors as in the

Reissner–Mindlin theory. Then, the modelling of composite structures is facilitated.

In the present work, we emphasise the assessment of the edge solution from the theory presented in Ref. 1 and in comparison both with a 20-node three-dimensional solid finite element solution and the Kirchhoff–Love theory. Only one problem is presented. It is a sandwich plate which is simply supported along two opposite edges and clamped along the other two. The static load is uniform following the direction of the supported edges and sinusoidal along the direction of the clamped edges. Analytical computations according to this problem have been achieved using the MATHEMATICA[2] program while finite element calculations have been made with the ABAQUS[3] computer code. The numerical results indicate that the higher-order shear deformation theory is in good agreement with the three-dimensional solid finite element computations. The sandwich plate considered being thick, large deviations may be observed between the Kirchhoff–Love theory and the higher-order shear deformation theory. As is well known, the analysis in a normal plane to the midplane of the plate and the supported edges does not exhibit any special behaviour near to the simply supported boundaries. On the other hand,

in a normal plane both to the clamped boundaries and the midplane of the plate, end effects are shown by the higher-order theory near to the clamped edges.

THE HIGHER-ORDER PLATE THEORY IN BRIEF

Consider a plate Ω, of arbitrary shape, which is homogeneous and linearly elastic, in statics. All quantities refer to a fixed system of rectangular, Cartesian coordinates. A general point in this system is denoted by $(x_1, x_2, x_3 = z)$. Throughout, Latin and Greek indices take on the values 1, 2, 3 and 1, 2, respectively.

The main assumptions of the plate theory which have to be analysed are as follows.

(i) The domain Ω is of the form:

$$\Omega = \{(x_1, x_2, x_3 = z) \in R^3 / x_3$$
$$= z \in [-h/2, +h/2], (x_1, x_2)$$
$$\in A \subset R^2, \Phi \gg \text{Max}(x_3)\} \quad (1)$$

where Φ is the diameter of the plate, h its thickness and A its midplane.

(ii) The transverse normal stress $\sigma_{33} = 0$. (2)

(iii) The kinematics is of the form suitable for shear-bending:

$$U_a(x_1, x_2, z) = -z w_{,a} + f(z) \gamma_a^0(x_1, x_2)$$
$$U_3(x_1, x_2, z) = w(x_1, x_2) \quad (3)$$

where $w_{,a} = \partial w / \partial x_a$.

(iv) The perturbations are small (small displacements) and the material elastic. In kinematics (eqn (3)), the function $f(z)$ may be seen as a 'shear function', since γ_a^0 are the transverse shear strains at the midplane of the plate, defined by

$$\gamma_a^0(x_1, x_2) = \omega_a(x_1, x_2) + w_{,a}(x_1, x_2) \quad (4)$$

where ω_a are the rotations of the midplane normal about the x_a axes.

Expressions considered in the literature for $f(z)$ are those of

- Kirchhoff–Love, for which $f(z) = 0$ (5)

- Reissner,[1] Bollé,[5] Hencky,[6] Uflyang,[7] Mirdlin[8] for which $f(z) = z$ (6)

- Levinson,[9] Reddy,[10] for which $f(z) = z(1 - 4z^2/3h^2)$ (7)

- Touratier,[1] for which $f(z) = (h/\pi) \sin(\pi z/h)$ (8)

Only these two last expressions (eqns (7) and (8)) are associated with a refined shear deformation theory. Note that from Jemielita,[11] assumption[7] and some other analogue forms recalled in Jemielita 'was a starting point in the Vlassov's theory dated 1957'.

In this paper, we retain only expression (8). The boundary value problem associated in eqn (3) with eqn (8) is stated using a classic displacement variational principle, see Touratier.[1] Then, the shear-bending equilibrium equations from the present theory are in absence of body forces and in term of displacements; we note: $f_{,a} = \partial f / \partial x_a$

$$0 = -D_{11} w_{,1111} - 2(D_{12} + 2D_{66}) w_{,1122}$$
$$- D_{22} w_{,2222} + d_{11} \gamma_{1,111}^0$$
$$+ (d_{12} + 2d_{66})(\gamma_{1,122}^0 + \gamma_{2,211}^0) + d_{22} \gamma_{2,222}^0 + q \quad (9)$$

$$0 = -d_{11} w_{,111} - (d_{12} + 2d_{66}) w_{,122} - D_{11} \gamma_{1,11}^0$$
$$+ (D_{12} + D_{66}) \gamma_{2,12}^0 + D_{66} \gamma_{1,22}^0 - A_{55} \gamma_1^0 \quad (10)$$

$$0 = -d_{22} w_{,222} - (d_{12} + 2d_{66}) w_{,211} - D_{22} \gamma_{2,22}^0$$
$$+ (D_{12} + D_{66}) \gamma_{1,21}^0 + D_{66} \gamma_{2,11}^0 - A_{44} \gamma_2^0 \quad (11)$$

where q is the normal surface force density to the midplane of the plate.

Equation (9) is that of classical plate theory when $\gamma_a^0 = 0$ (no shear). At the edge of the midplane A of the plate boundary conditions may be prescribed. These are

'prescribe w or Q_a; ω_a or $M_{a\beta}$; $w_{,a}$ or $M_{a\beta}$' (12)

In these boundary conditions, generalised stresses in terms of displacements are for the orthotropic case:[1]

- classic resultant moments:

$$M_{11} = -D_{11} w_{,11} - D_{12} w_{,22} + d_{11} \gamma_{1,1}^0 + d_{12} \gamma_{2,2}^0$$
$$M_{22} = -D_{12} w_{,11} - D_{22} w_{,22} + d_{12} \gamma_{1,1}^0 + d_{22} \gamma_{2,2}^0$$
$$M_{12} = -2D_{66} w_{,12} + d_{66} (\gamma_{1,2}^0 + \gamma_{2,1}^0) \quad (13)$$

- refined resultant moments:

$$M_{11} = -d_{11} w_{,11} - d_{12} w_{,22} + D_{11} \gamma_{1,1}^0 + D_{12} \gamma_{2,2}^0$$
$$M_{22} = -d_{12} w_{,11} - d_{22} w_{,22} + D_{12} \gamma_{1,1}^0 + D_{22} \gamma_{2,2}^0$$
$$M_{12} = -2d_{66} w_{,12} + D_{66} (\gamma_{1,2}^0 + \gamma_{2,1}^0) \quad (14)$$

- shear forces:

$$Q_1 = A_{55} \gamma_1^0$$
$$Q_2 = A_{44} \gamma_2^0 \quad (15)$$

Constitutive coefficients in eqns (9)–(11) and (13)–(15) are defined by

$$D_{\mu\nu} = \int_{-h/2}^{+h/2} z^2 C'_{\mu\nu}\, dz;$$

$$\mathbf{D}_{\mu\nu} = \int_{-h/2}^{+h/2} C'_{\mu\nu}(f(z))^2\, dz$$

$$d_{\mu\nu} = \int_{-h/2}^{+h/2} C'_{\mu\nu} z f(z)\, dz;$$

$$\mathbf{A}_{\psi\varphi} = \int_{-h/2}^{+h/2} C_{\psi\varphi}(f_z)^2\, dz \qquad (16)$$

where $\mu\nu = 11, 22, 12, 66$ and $\psi\varphi = 44, 55$. Coefficients $C'\mu\nu$ are elastic coefficients involved by hypothesis (2). To obtain the classical thin plate theory, it is sufficient to take $f(z) = 0$ in expressions (16). Note that the first-order shear deformation theory is obtained by setting $f(z) = z$ and shear correction factors in $\mathbf{A}_{\psi\varphi}$. The present theory, because the choice of $f(z)$ by eqn (8) does not require shear correction factors.

THE PROBLEM CONSIDERED AND ITS ANALYTICAL SOLUTION

The problem considered to analyse the end effects is a sandwich orthotropic square plate from Srinivas and Rao.[12] The plate is simply supported along two opposite edges and clamped along its two other opposite edges. The plate is loaded by a pressure which is uniform following the direction of the simply supported edges and sinusoidal following the direction of the clamped edges. See Fig. 1 for all properties of the plate (geometry and material).

The partial differential equations describing the plate equilibrium must now be solved. The technique employed to solve eqns (9)–(11) with boundary conditions (12) is the Lévy technique,[13] since two opposite edges are simply supported, the two others being clamped. So, the plate displacements may have the forms (a is the length of the side of the square plate):

$$w(x_1, x_2) = W(x_2) \sin\left(\frac{\pi x_1}{a}\right) \qquad (17)$$

$$\gamma_1^0(x_1, x_2) = \Gamma_1(x_2) \cos\left(\frac{\pi x_1}{a}\right) \qquad (18)$$

$$\gamma_2^0(x_1, x_2) = \Gamma_2(x_2) \sin\left(\frac{\pi x_1}{a}\right) \qquad (19)$$

$$q(x_1, x_2) = q_0 \sin\left(\frac{\pi x_1}{a}\right) \qquad (20)$$

From eqns (3), (4) and (12), these forms for the displacement satisfy the requirements for edges which are simply supported at $x_1 = 0$ and $x_1 = a$ given by (easy to verify with eqns (13), (14) and (17)–(19)):

$$w(0, x_2) = w(a, x_2) = \gamma_2^0(0, x_2) = \gamma_2^0(a, x_2) = 0 \qquad (21)$$

$$M_{11}(0, x_2) = M_{11}(a, x_2) = \mathbf{M}_{11}(0, x_2) = \mathbf{M}_{11}(a, x_2) = 0 \qquad (22)$$

Equations (17)–(20) are used to simplify the equilibrium equations. So, substituting solutions (17)–(20) into equilibrium eqns (9)–(11) provides the following differential equation system:

$$-\alpha^4 D_{11} w + 2\alpha^2 (D_{12} + 2D_{66}) w_{,22} - D_{22} w_{,2222}$$
$$+ d_{11}\alpha^3 \Gamma_1 - (d_{12} + 2d_{66})(\alpha \Gamma_{1,22} + \alpha^3 \Gamma_{2,2})$$
$$+ d_{22}\Gamma_{2,222} = -q_0 \qquad (23)$$

$$\alpha^3 d_{11} w - \alpha(d_{12} + 2d_{66}) w_{,22} - \alpha^2 \mathbf{D}_{11}\Gamma_1$$
$$+ \alpha(\mathbf{D}_{12} + \mathbf{D}_{66})\Gamma_{2,2} + \mathbf{D}_{66}\Gamma_{1,22} - \mathbf{A}_{55}\Gamma_1 = 0 \qquad (24)$$

$$-d_{22} w_{,222} + \alpha^2 (d_{12} + 2d_{66}) w_{,2} + \mathbf{D}_{22}\Gamma_{2,22}$$
$$- \alpha(\mathbf{D}_{12} + \mathbf{D}_{66})\Gamma_{1,2} - \alpha^2 \mathbf{D}_{66}\Gamma_2 - \mathbf{A}_{44}\Gamma_2 = 0 \qquad (25)$$

where $\alpha = \pi/a$. This differential equation system is linear and its coefficients and derivatives are constant. Then a general solution for the homogeneous system (without the second member represented by the load q_0) is given by

$$W(x_2) = A \exp(px_2) \qquad (26)$$

$$\Gamma_1(x_2) = B \exp(px_2) \qquad (27)$$

$$\Gamma_2(x_2) = C \exp(px_2) \qquad (28)$$

where A, B, C are constants to be determined and p an unknown scalar. Reporting this solution in eqns (23)–(25) without their second member (i.e. $q_0 = 0$), we obtain a linear algebraic system of which a non-trivial solution for p is given by

$$\det(a_{ij}) = 0 \qquad (29)$$
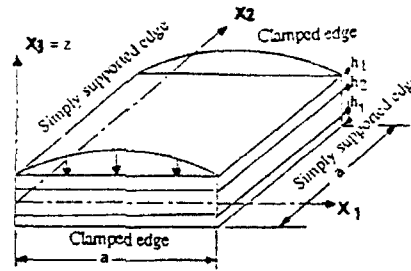
Geometrical properties of the square plate .

$a = 1 \, m \; ; h = 0,05 \, m \;$ and $h = 0,10 \, m$

$h_1 = 0,1 \, h \; ; h_2 = 0,8 \, h$ and $h = 2h_1 + h_2$

Three-dimensional elastic material properties of the square orthotropic sandwich plate (from [12])

C22 / C11 = 0,5431	C33 / C11 = 0,5301
C12 / C11 = 0,2331	C13 / C11 = 0,0107
C23 / C11 = 0,0882	C66 / C11 = 0,2629
C55 / C11 = 0,1599	C44 / C11 = 0,2668

$$\frac{\text{material properties of skins}}{\text{material properties of the core}} = 15$$

Fig. 1. Geometrical and material properties of the sandwich plate.

In eqn (29), a_{ij} are the coefficients of the algebraic system in A, B, C:

$$a_{11} = -a^4 D_{11} + 2a^2 p^2 (D_{12} + 2D_{66}) - p^4 D_{22}$$

$$a_{12} = a^3 d_{11} - a^2 p^2 (d_{12} + 2d_{66}) = a_{21}$$

$$a_{13} = -a^2 p (d_{12} + 2d_{66}) + p^3 d_{22} = -a_{31}$$

$$a_{22} = -a^2 D_{11} + p^2 D_{66} - A_{55}$$

$$a_{23} = ap (D_{12} = D_{66}) = -a_{32}$$

$$a_{33} = p^2 D_{22} + a^2 D_{66} - A_{44}$$

(30)

Classically, eqn (29) is a polynomial in p. Due to the higher-order theory, this polynomial has a degree eight, and has been factored using the MATHEMATICA² program. This can be reduced to an algebraic polynomial (bi-square polynomial) of order four. Its roots are computed from the MATHEMATICA program. For the geometrical and material properties of the problem considered, roots have been found real and positive. Finally, the general solution (26)–(28) is of the form

$$W(x_2) = A_1 \exp(p_1 x_2) + A_2 \exp(-p_1 x_2)$$
$$+ A_3 \exp(p_2 x_2) + A_4 \exp(-p_2 x_2)$$
$$+ (A_5 x_2 + A_6) \exp(p_3 x_2)$$
$$+ (A_7 x_2 + A_8) \exp(-p_3 x_2) \quad (31)$$

$$\Gamma_1(x_2) = B_1 \exp(p_1 x_2) + B_2 \exp(-p_1 x_2)$$
$$+ B_3 \exp(p_2 x_2) + B_4 \exp(-p_2 x_2)$$
$$+ (B_5 x_2 + B_6) \exp(p_3 x_2)$$
$$+ (B_7 x_2 + B_8) \exp(-p_3 x_2) \quad (32)$$

$$\Gamma_2(x_2) = C_1 \exp(p_1 x_2) + C_2 \exp(-p_1 x_2)$$
$$+ C_3 \exp(p_2 x_2) + C_4 \exp(-p_2 x_2)$$
$$+ (C_5 x_2 + C_6) \exp(p_3 x_2)$$
$$+ (C_7 x_2 + C_8) \exp(-p_3 x_2) \quad (33)$$

This solution indicates that roots of the bi-square characteristic equation (or bi-square characteristic polynomial) of the differential equation system are real and positive, but roots p_3^2 and p_4^2 are identical, while roots p_1^2 and p_2^2 are different.

Expressions (31)-(33) for generalised displacements require the evaluation of 24 separate constants for each set of boundaries in x_2. The algebraic system in A, B, C supplies obviously only two relations homogeneous for each value of the root in p, to be satisfied for all x_2. These give 16 relations and finally we have only eight unknown constants, for example, A_1, ..., A_8. The complete solution of the differential equation system is obtained by adding a particular solution due to the second member depending on the load q_0. Since this is constant, it is sufficient to try to satisfy the differential equation system with a constant as a particular solution. So, we have the complete solution of the differential equation system and now we have only to determine unknown constants, here A_1, ..., A_8. For this, we introduce boundary conditions following x_2. These are, since edges $x_2 = 0$ and $x_2 = a$ are clamped:

$$W(0) = W(a) = W_{,2}(0) = W_{,2}(a) = 0 \qquad (34)$$

$$\Gamma_1(0) = \Gamma_1(a) = \Gamma_2(0) = \Gamma_2(a) = 0 \qquad (35)$$

This achieves the determination of the complete solution of the problem considered.

AN EVALUATION OF THE INTERIOR AND EDGE SOLUTION

In this section we investigate numerical calculations from our higher-order theory, the classical thin plate theory of Kirchhoff–Love, and three-dimensional solid finite elements. The properties of the plate problem considered are presented in Fig. 1. The three-dimensional finite element model is described briefly now. The domain of the plate has been meshed using 20-node three-dimensional solid finite elements, see Fig. 2 for a

quarter of the plate due to symmetries of the problem. A convergence study has shown that this mesh is consistent with 600 elements in a quarter of the plate (six elements following its thickness). Finite element computations have been realised by using the ABAQUS[3] computer code. All results of the computations are presented in Figs 3–14. The following remarks are made, both for $a/h = 10$ and $a/h = 20$.
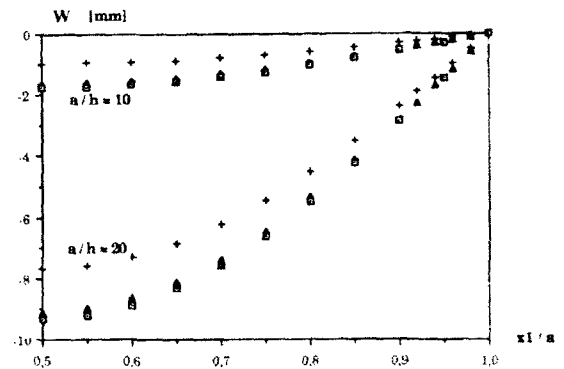
Fig. 3. Variation of the deflection of the plate following the line $x_2 = a/2$. ($\triangle$) Touratier; (+) Kirchhoff–Love; ($\square$) Abaqus.
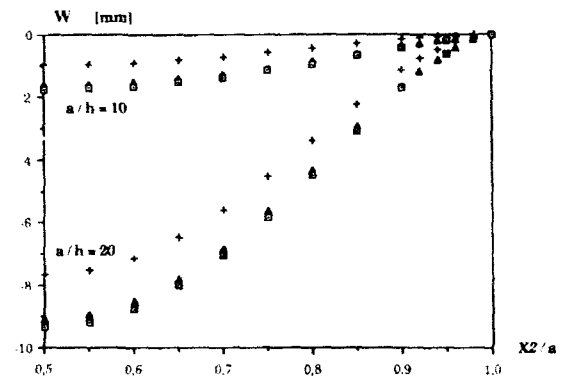
Fig. 4. Variation of the deflection of the plate following the line $x_1 = a/2$. ($\triangle$) Touratier; (+) Kirchhoff–Love; ($\square$) Abaqus.
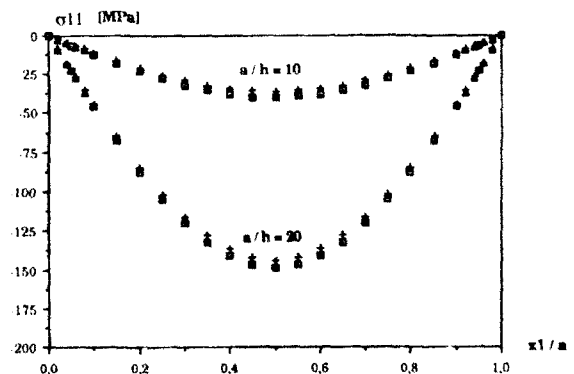
Fig. 5. Distribution of the normal stress σ_{11} along the line $x_2 = a/2$ and $x_3 = z = h/2$. ($\triangle$) Touratier; (+) Kirchhoff–Love; ($\square$) Abaqus.

Fig. 2. The three-dimensional solid finite element mesh for a quarter of the plate.
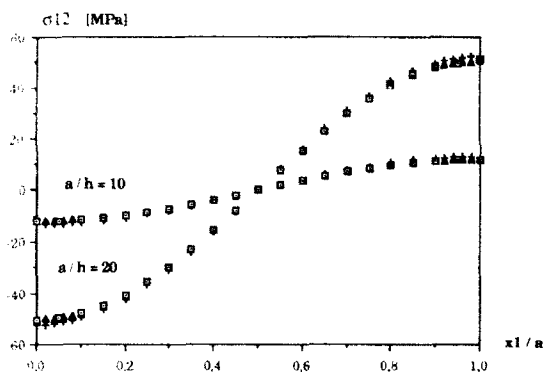
Fig. 6. Distribution of the in-plane shear stress σ_{12} along the line $x_2 = 3a/4$ and $x_3 = z = h/2$. ($\triangle$ Touratier; (+) Kirchhoff–Love; $\square$ Abaqus.
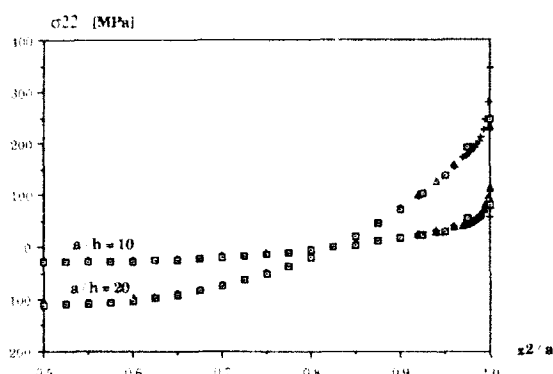
Fig. 7. Distribution of the normal stress σ_{22} following the line $x_1 = a/2$ and $x_3 = z = h/2$. ($\triangle$ Touratier; + Kirchhoff–Love; $\square$ Abaqus.
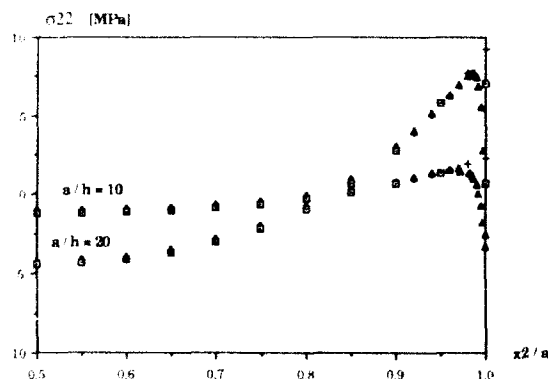
Fig. 8. Distribution of the normal stress σ_{22} following the in-core line $x_1 = a/2$ and $x_3 = z = 0.3h$. ($\triangle$) Touratier; (+) Kirchhoff–Love; ($\square$) Abaqus.

Fig. 9. Distribution of the in-plane shear stress σ_{12} along the line $x_2 = 3a/4$ and $x_3 = z = h/2$. $\triangle$ Touratier; + Kirchhoff–Love; $\square$ Abaqus.

Fig. 10. Distribution of the in-plane shear stress σ_{12} following the in-core line $x_1 = 3a/4$ and $x_3 = z = 0.3h$. ($\triangle$) Touratier; (+) Kirchhoff–Love; ($\square$) Abaqus.

(i) Transverse displacement w, see Figs 3 and 4.

A large deviation is observed between Kirchhoff–Love and Touratier theories due to significant transverse shear effects (the plate is sandwich and thick), especially
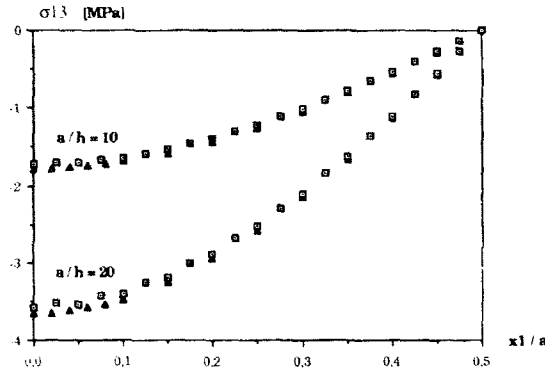
Fig. 11. Distribution of the transverse shear stress σ_{13} along the interface line $x_2 = a/2$ and $x_3 = z = 0$. ($\triangle$) Touratier; (+) Kirchhoff-Love; ($\boxdot$) Abaqus.
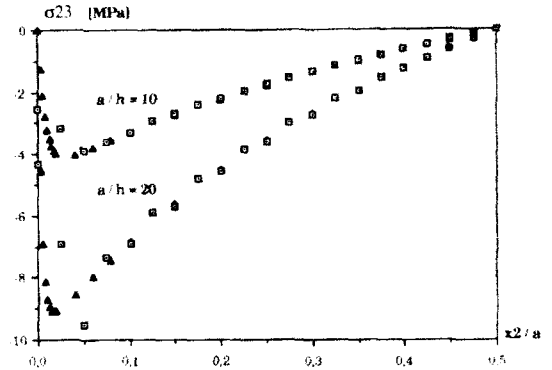
Fig. 14. Distribution of the transverse shear stress σ_{23} following the interface line $x_1 = a/2$ and $x_3 = z = 0$. ($\triangle$) Touratier; (+) Kirchhoff-Love; ($\boxdot$) Abaqus.
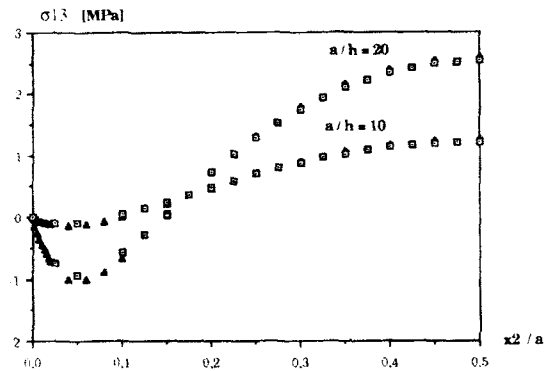
Fig. 12. Distribution of the transverse shear stress σ_{13} along the interface line $x_1 = 3a/4$ and $x_3 = z = 0$. ($\triangle$) Touratier; (+) Kirchhoff-Love; ($\boxdot$) Abaqus.
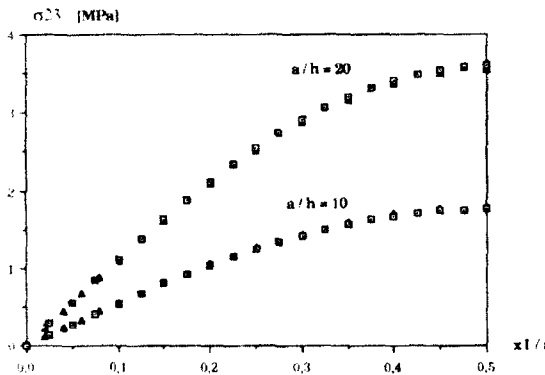
Fig. 13. Distribution of the transverse shear stress σ_{23} following the interface line $x_1 = 3a/2$ and $x_3 = z = 0$. ($\triangle$) Touratier; (+) Kirchhoff-Love; ($\boxdot$) Abaqus.

at the centre of the plate where the transverse displacement is maximum. This deviation is available for the distributions of the transverse displacement following the x_1 and x_2 coordinates.

(ii) In-plane stresses along the x_1 direction, see Figs 5 and 6.

A good agreement is observed between Kirchhoff-Love and Touratier theories for the distribution of the maximum stress σ_{11} and σ_{12}.

(iii) In-plane stresses along the x_2 direction, see Figs 7-10.

Figure 7 shows that good agreement between both theories considered is obtained except at the clamped edges where a serious deviation appears for the distribution of the maximum stress σ_{22}.

Then, Figs 8-10 show that a good agreement still exists between the two theories compared together except near to an edge zone in which a large deviation appears and the Kirchhoff-Love theory does not represent an 'edge effect' due to the combination of the clamped edges and the sandwich material of the plate. An analysis not shown here upon an homogeneous and isotropic plate has not given any edge effect as in Figs 8-10.

Note that the in-plane shear stress σ_{12} (Figs 9 and 10) furnishes the following result: the deviation between the Kirchhoff-Love theory and the Touratier theory near to the clamped edge is within a zone which is the boundary layer.

(iv) Transverse shear stresses along x_1 and x_2 directions, see Figs 11-14.

Along the coordinate x_1 (Figs 11 and 13) transverse shear stresses measured upon the midplane of the plate do not exhibit any of the well known edge effects. But along the coordinate x_2 (Figs 12 and

14) a clamped edge effect is observed, both for transverse shear stresses σ_{13} and σ_{23}. Note that the transverse shear stress σ_{13} (Fig. 11) gives in the in-plane shear stress a layer effect of which the thickness is of the order of the plate thickness (boundary layer). In the cases where an end effect has been observed, the zone thickness is always smaller than or equal to the thickness of the plate.

Finally, comparisons between three-dimensional solid finite element computations and the Touratier's theory show a good agreement on the problem considered.

CONCLUDING REMARKS

This study has shown the effects of significant boundary conditions upon the response of a sandwich plate for linearly elastic materials and in statics with small perturbations. For a thick plate made with orthotropic materials and clamped edges, results obtained from the Touratier plate theory indicate that edge effects appear near to the clamped edges in a layer of which the thickness is of the order of the plate thickness. The classical thin plate theory (Kirchhoff–Love) is not sensitive to these effects. Three-dimensional solid finite element computations have confirmed the good behaviour of the higher-order shear deformation theory[1] evaluated on significant boundary conditions. Future works are turned toward the analysis of other problems with significant bound-

ary conditions such that free edge conditions and the introduction of the transverse normal strain and stress.

REFERENCES

1. Touratier, M., An efficient standard plate theory. *Int. J. Engng Sci.*, **29** (1991) 911–16.
2. Wolfram, S., *MATHEMATICA, a System for Doing Mathematics by Computer.* 2nd edn. Addison-Wesley Publishing Company, 1991.
3. Hibbitt, Karlsson and Sorensen, *ABAQUS, Users' Manual.* Inc., 1989.
4. Reissner, E., The effect of transverse shear deformation on the bending of elastic plates. *J. Appl. Mech.*, **12** (1945) A69–77.
5. Bollé, E., Contribution au problème linéaire de flexion d'une plaque élastique. *Bulletin technique Suisse Romande*, **73** (1947) 281–98 and 293–8.
6. Hencky, H., Uber die berucksichtigung der schubverzerrung in ebenen platten. *Ing. Arch.*, **16** (1947) 72–6.
7. Uflyang, Y. S., The propagation of waves in the transverse vibrations of bars and plates. *Prikl. Mat. Mech.*, **12** (1948) 287 (in Russian).
8. Mindlin, R. D., Influence of rotatory inertia and shear on flexural motions of isotropic elastic plates. *J. Appl. Mech.*, **18** (1951) 31–8.
9. Levinson, M., An accurate simple theory of the statics and dynamics of elastic plates. *Mech. Res. Commun.*, **7** (1980) 343–50.
10. Reddy, J. N., A simple higher-order theory for laminated composite plates. *J. Appl. Mech.*, **51** (1984) 745–52.
11. Jemielita, G., On kinematical assumptions of refined theories of plates: a survey. *J. Appl. Mech.*, **57** (1990) 1088–91.
12. Srinivas, S. & Rao, A. K., Bending, vibration and buckling of simply supported thick orthotropic rectangular plates and laminates. *Int. J. Solids and Structures*, **6** (1970) 1461–81.
13. Palardy, R. F. & Palazotto, A. N., Buckling and vibration of composite plates using the Levy method. *Comp. Structures*, **14** (1990) 61–86.

Reliability analysis of nonlinear laminated composite plate structures

T. Y. Kam, S. C. Lin & K. M. Hsiao

Department of Mechanical Engineering, National Chiao Tung University, Hsin Chu 30050, Taiwan

A procedure for the reliability analysis of laminated composite plate structures subjected to large deflections under random static loads is presented. The nonlinear analysis of laminated composite plate structures is achieved via a corotational total Lagrangian finite element formulation which is based on the von Karman assumption and first order shear deformation theory. This formulation is applicable for the nonlinear analysis of plate structures with large rotations but moderate deformation and thus accurate enough to predict the behavior of the structures at the point of failure. The reliability assessment of laminated composite plate structures with random strength subjected to random loads is approached by the determination of limit state surfaces in load space. The limit space surfaces are obtained by performing a series of first ply failure analyses following different load paths in load space using the proposed nonlinear structural analysis technique and an appropriate failure criterion. A numerical technique is then proposed to evaluate the reliability of the plate structures. Examples of the reliability analyses of laminated plates with different layer orientations subject to random loads are given for illustration.

INTRODUCTION

The use of laminated composite materials in designing aircraft, space and marine structures has greatly enhanced the performance of such structures. In general, these structures are used in very severe environments, and for safety reasons they require very high reliability. Therefore, reliability analysis of laminated composite structures has gradually become an important subject of research in recent years. The reliability of laminated composite plates subjected to in-plane loads has been studied by a number of researchers.[1-3] Kam and Lin[4] have recently developed a stochastic finite element method for the reliability analysis of linear laminated composite plates subjected to transverse loads. As for the reliability analysis of nonlinear laminated composite plate structures, no work has been done in this area yet.

In this paper, a procedure for the reliability analysis of laminated composite plate structures subjected to large deflection under random static loads is presented. The nonlinear structural analysis is developed based on a corotational total Lagrangian finite element formulation using the von Karman assumption and first order shear deformation theory. The assessment of the reliability of laminated composite plate structures with random strength subjected to random loads is approached by the determination of limit state surfaces in load space. Numerical techniques are proposed to evaluate the failure probabilities of the layers and the plate as well. Examples of the reliability analyses of simply supported and cantilever laminated composite plates subject to random loads are given for illustration.

NONLINEAR LAMINATED COMPOSITE PLATE ANALYSIS

The plate under consideration is composed of a finite number of orthotropic layers of uniform thickness, with principal axes of elasticity oriented arbitrarily with respect to the plate axes. The x and y coordinates of the plate are taken in the midplane of the plate. The displacement field is assumed to be of the form

$$U_1(x,y,z,t) = U_0(x,y,t) + z\psi_x(x,y,t)$$
$$U_2(x,y,z,t) = V_0(x,y,t) + z\psi_y(x,y,t) \qquad (1)$$
$$U_3(x,y,z,t) = W(x,y,t)$$

where t is the time, U_x, U_y, U_z the displacements in the x, y, z directions, respectively, U_o, V_o, W the associated midplane displacements, and ψ_x and ψ_y the shear rotations. The strains in the von Karman plate theory can be expressed in the form

$$\varepsilon_x = \frac{\partial U_o}{\partial x} + \frac{1}{2}\left(\frac{\partial W}{\partial x}\right)^2 + z\frac{\partial \psi_x}{\partial x} = \varepsilon_x^o + z\kappa_x$$

$$\varepsilon_y = \frac{\partial V_o}{\partial y} + \frac{1}{2}\left(\frac{\partial W}{\partial y}\right)^2 + z\frac{\partial \psi_y}{\partial y} = \varepsilon_y^o + z\kappa_y \qquad\qquad 2$$

$$\varepsilon_s = \frac{\partial U_o}{\partial y} + \frac{\partial V_o}{\partial x} + \frac{\partial W}{\partial x}\frac{\partial W}{\partial y} + z\left(\frac{\partial \psi_x}{\partial y} + \frac{\partial \psi_y}{\partial x}\right) = \varepsilon_s^o + z\kappa_s$$

$$\varepsilon_4 = \psi_y + \frac{\partial W}{\partial x}, \qquad \varepsilon_3 = \psi_x + \frac{\partial W}{\partial y}$$

where ε_i^o $(i=x, y, s)$ are in-plane strains and κ_i bending strains. The associated Piola–Kirchhoff stress vector σ is

$$\sigma = \{\sigma_x, \sigma_y, \sigma_s, \sigma_s, \sigma_4\}^t \qquad\qquad 3$$

The constitutive equations for the plate can be written as

$$\begin{Bmatrix} N_i \\ M_i \end{Bmatrix} = \begin{bmatrix} A_{ij} & B_{ij} \\ B_{ij} & D_{ij} \end{bmatrix}\begin{Bmatrix} \varepsilon_i^o \\ \kappa_j \end{Bmatrix} \qquad (i,j=x,y,s)$$

$$\begin{Bmatrix} Q_2 \\ Q_1 \end{Bmatrix} = \begin{bmatrix} \bar{A}_{44} & \bar{A}_{45} \\ \bar{A}_{45} & \bar{A}_{55} \end{bmatrix}\begin{Bmatrix} \varepsilon_4 \\ \varepsilon_5 \end{Bmatrix} \qquad\qquad 4$$

Here N_i, M_i, Q_1 and Q_2 are the stress resultants defined by

$$(N_i, M_i) = \int_{-h/2}^{h/2} (1, z)\sigma_i\, dz, \qquad (Q_1, Q_2) = \int_{-h/2}^{h/2} (\sigma_s, \sigma_4)\, dz \qquad\qquad 5$$

The A_{ij}, B_{ij}, D_{ij} and $\bar{A}_{ij}$ $(i,j=4,5)$ are the in-plane, bending in-plane coupling, bending or twisting, and thickness-shear stiffness coefficients, respectively:

$$(A_{ij}, B_{ij}, D_{ij}) = \sum_{m=1}^{NL} \int_{z_m}^{z_{m+1}} Q_{ij}^m (1, z, z^2)\, dz \qquad\qquad 6$$

$$\bar{A}_{ij} = \sum_{m=1}^{NL} \int_{z_m}^{z_{m+1}} k_i k_j Q_{ij}^m\, dz$$

where z_m denotes the distance from the midplane to the lower surface of the mth layer, NL is the total number of layers, Q_{ij} are material constants, and k_i are the shear correction coefficents.

The basis of the formulation is the virtual work equation for a continuum written in a total Lagrangian coordinate system under the assumption of small strains and conservative loading as in Ref. 5

$$\int_v \delta\varepsilon^t \sigma\, dV = -\int_v \rho\delta U^t \ddot{U}\, dV + \int_{S_1} \delta U^t p\, dS \qquad\qquad (7)$$

where v is the undeformed volume, ρ is the mass density, $\ddot{u}$ the acceleration vector and p surface tractions acting over the undeformed area S_1.

The virtual work equation of the plate discretized into NE elements can be written as

$$\sum_{e=1}^{NE} \left\{ \int_{v_e} \delta\boldsymbol{\varepsilon}^t \boldsymbol{\sigma}\, dV + \int_{v_e} \rho\delta U^t \ddot{U}\, dV - \int_{s_e} \delta U^t \mathbf{p}\, dS \right\}_e = 0$$

where v_e, S_e are the volume and surface of an element, respectively. The midplane displacements u_0, V_0, W_0, ψ_x, ψ_y) within an element are given as functions of $5 \times q$ discrete nodal displacements and in matrix form they are expressed as

$$U = \sum_{i=1}^{q} \boldsymbol{\Phi}_i \mathbf{I} \mathbf{V}_{ei} = \boldsymbol{\Phi}\mathbf{V}_e$$

where q is the number of nodes for the element; $\boldsymbol{\Phi}_i$ are shape functions; $\mathbf{I}$ is a 5×5 unit matrix; and the nodal displacements $\mathbf{V}_{ei}$ are

$$\mathbf{V}_{ei} = (U_i, V_i, W_i, \psi_{xi}, \psi_{yi})^t \qquad (i = 1,\ldots,q)$$

In view of eqns (2)–(4) and (9), the virtual work equation, eqn (8), can be rewritten as

$$\sum_{e=1}^{NE} \left\{ \delta\mathbf{V}_e^t \left[\int_A \mathbf{B}^t \dot{\boldsymbol{\sigma}}\, dA + \int_{v_e} \boldsymbol{\Phi}^t \boldsymbol{\Phi} \ddot{\mathbf{V}}_{e} \rho\, dV - \int_{s_e} \boldsymbol{\Phi}^t \mathbf{p}\, dS \right] \right\}_e = 0$$

where A_e is the midplane area of an element and $\dot{\boldsymbol{\sigma}}$ the stress resultant. Through the assembling process, the nonlinear equilibrium equation of the plate may be expressed by

$$X = F_\sigma + F_1 - P = 0$$

where X is the unbalanced force vector. The internal nodal force F_σ and applied nodal force P are defined, respectively, as

$$F_\sigma = \sum_{e=1}^{NE} \left[\mathbf{a}^t \int_A \mathbf{B}^t \dot{\boldsymbol{\sigma}}\, dA \right]_e$$

$$F_1 = \sum_{e=1}^{NE} \left[\int_{v_e} \mathbf{a}^t \boldsymbol{\Phi}^t \boldsymbol{\Phi} \mathbf{a} \rho\, dV \right]_e \ddot{\mathbf{V}} = M\ddot{\mathbf{V}}$$

and

$$P = \sum_{e=1}^{NE} \left[\int_{s_e} \mathbf{a}^t \boldsymbol{\Phi}^t \mathbf{p}\, dS \right]_e$$

where $\mathbf{a}$ is the congruent transformation matrix and $\ddot{\mathbf{V}}$ global nodal acceleration vector. In case of dynamic analysis, the above nonlinear equilibrium equation can be replaced by the following incremental equilibrium equation.[6]

$$\Delta F_\sigma(t) + \Delta F_1(t) - \Delta P(t) = 0$$

The force increments in this equation can be expressed as

$$\Delta F_1 = F_1(t + \Delta t) - F_1(t) = M\Delta\ddot{\mathbf{V}}(t)$$

$$\Delta F_\sigma = F_\sigma(t + \Delta t) - F_\sigma(t) = K(t)\Delta\mathbf{V}(t)$$

$$\Delta P = P(t + \Delta t) - P(t)$$

where the tangent stiffness matrix

$$K(t) = \left[\frac{\partial F_\sigma}{\partial \mathbf{V}} \right]_t$$

The solution of the incremental equilibrium equation can be accomplished by utilizing

$$\Delta F_s - \Delta P = 0 \tag{17}$$

The load–displacement relation of the plate is obtained by using an incremental iterative method based on the Newton–Raphson method combined with constant arc length of incremental displacement vector. In the above nonlinear analyses, a corotational procedure is adopted to accommodate large rigid body rotations between two successive load increments and thus the iteration process can be expedited. Detailed description of the corotational procedure is reported in Ref. 7. The element employed in the following numerical demonstration is the nine-node Lagrangian element proposed by Pica *et al.*

LIMIT STATE EQUATION

A laminated composite plate is assumed to fail when any layer reaches a limit state. Failure of the plate is, therefore, determined from the first ply failure analysis, in which in-plane stresses and an appropriate failure criterion are adopted. For the purpose of comparison, three different failure criteria, namely, maximum work, maximum strain and maximum stress, will be used to construct the limit state equation in the plate reliability analysis. The limit state equations based on different failure criteria are expressed as:

a   Maximum work criteria

$$g = \frac{\sigma_1^2}{X_1} + \frac{\sigma_2^2}{X_c} - \left[\frac{\sigma_1}{X_1} + \frac{\sigma_2}{X_c} \right] \sigma_2 + \frac{\sigma_2^2}{Y_1} + \frac{\sigma_2^2}{Y_c} + \frac{\sigma_6^2}{S} - 1 = 0 \tag{18}$$

with

$$X = X \qquad \text{when} \qquad X \geq 0$$
$$X = 0 \qquad \text{when} \qquad X < 0$$

b   Maximum strain criterion

$$g = \varepsilon_1 - X_{1t} \cdot \varepsilon_1 + X_{1c} \cdot \varepsilon_2 - Y_{1t} \cdot \varepsilon_2 + Y_{1c} \cdot \varepsilon_6 - S_t \cdot \varepsilon_6 + S_t = 0 \tag{19}$$

c   Maximum stress criterion

$$g = \sigma_1 - X_1 \cdot \sigma_1 + X_c \cdot \sigma_2 - Y_1 \cdot \sigma_2 + Y_c \cdot \sigma_6 - S \cdot \sigma_6 + S = 0 \tag{20}$$

Here X_1, Y_1, X_c, Y_c, and S are, respectively, the tensile, compressive, and shear strengths of the unidirectional composite. The stress or strain components, σ_1, σ_2, σ_6, and ε_1, ε_2, ε_6, are referred to the material coordinate system. Failure occurs when $g \geq 0$.

RELIABILITY ANALYSIS

The reliability assessment of a laminated composite plate with random strength subject to random loads can be achieved by performing the following integration based on the weakest link hypothesis:

$$P_s = \prod_{i=1}^{M} \int \ldots \int_{g_i} f_i(\sigma_1, \sigma_2, \sigma_6, X_1, \ldots, S) \, d\sigma_1 \ldots dS \tag{21}$$

where P_s is reliability, $f_i(.)$ the joint probability density function of stresses and strength parameters for the ith layer, and integration is performed over the region where $g_i \leq 0$. In the above equation the assumption that a layer fails when the critical point in the layer reaches the limit state has been adopted.

In general, the stresses are statistically correlated and the above joint probability density functions are not available. Therefore, the reliability expressed in eqn (21) cannot be evaluated directly. Herein, the reliability is approached by the determination of limit state surface in load space. In the adopted load space formulation, the limit state for any layer of a plate subject to q random load variables, $(X_1, \ldots, X_q)$,

may be expressed as

$$G(X_1,\ldots,X_q) = 0 \tag{22}$$

The reliability of this limit state can be written as

$$P_s = \int\ldots\int_G f_X(x_1,\ldots,x_q)\,dx_1\ldots dx_q \tag{23}$$

in which f_X is the joint probability density function of the load variables. As an example, consider a layer subject to two random load variables, X_1 and X_2. The limit state function for this case is a curve in the X_1-X_2 plane as shown in Fig. 1, where the probability associated with the negative values of X_1 and X_2 is neglected. The integration of the probability distribution over the safe region ($G < 0$) gives the reliability of the layer. If the strengths X_1, Y_1,...,S of the layer are random rather than deterministic, the limit state function in load space will no longer be deterministic. Any limit state curve in load space represents a realization of the limit state function. For any loading path, corresponding to

$$\theta = \tan^{-1}\left(\frac{X_2}{X_1}\right)$$

in the X_1-X_2 plane, the conditional reliability and the conditional probability distribution of loading in that direction are $F_{R/\theta}(S,\theta)$ and $f_\theta(S,\theta)$, respectively. Using the theory of conditional probability, the conditional reliability for that load path can be obtained as

$$P_{s,\theta} = \int_0^\infty F_{R/\theta}(S,\theta)\,f_\theta(S)\,dS \tag{24}$$

where $P_{s,\theta}$ is the conditional reliability for the load path with angle θ away from the X_1-axis. The evaluation of $F_{R/\theta}(S,\theta)$ can be easily obtained using the Hasofer–Lind method[7] when the maximum work criterion of eqn (18) is adopted in the first ply failure analysis. If the maximum stress or strain criteria are adopted, the conditional reliability, assuming Weibull distributions for strengths, is obtained as, respectively,

$$P_{s,\theta} = \exp\left[-\left(\frac{\sigma_1}{a_{X_1}}\right) - \left(\frac{\sigma_1}{a_{X_2}}\right) - \left(\frac{\sigma_2}{a_{Y_1}}\right) - \left(\frac{\sigma_2}{a_{Y_2}}\right) - \left(\frac{\sigma_{12}}{a_S}\right)\right] \tag{25}$$

or

$$P_{s,\theta} = \exp\left[-\left(\frac{\sigma_1 - \nu_{12}\sigma_2}{a_{X_1}}\right) - \left(\frac{\sigma_1 - \nu_{12}\sigma_2}{a_{X_2}}\right) - \left(\frac{\sigma_1 - \nu_{21}\sigma_2}{a_{Y_1}}\right) - \left(\frac{\sigma_1 - \nu_{21}\sigma_2}{a_{Y_2}}\right) - \left(\frac{\sigma_{12}}{a_S}\right)\right] \tag{26}$$

Fig. 1. 2-D load space for deterministic structure.

where ν_{12}, ν_{21} are Poisson's ratios, and α, β are parameters of Weibull distributions. Here the polar co-ordinate system, $S-\theta$, is used for computing the total reliability of each ply in load space. In Fig. 2, the load space is first divided into N mutually exclusive and collectively exhaustive sectors with their vertices merging at the origin. Each sector is then divided into M quadrilaterals which are bounded in the radial direction from S_k to S_{k+1} ($k = 1, ..., M$). Assuming that a load path bisects the sector containing it and the conditional reliability in each quadrilateral is uniformly distributed, it can be shown that the total reliability is the sum of the conditional reliabilities in all quadrilaterals. In view of eqn (24), the total reliability in load space, P_s, can be written in the following summation form

$$P_s = \sum_{k=1}^{N} \sum_{i=1}^{M} \left\{ F_{R,S,\theta} \left(\frac{S_i + S_{i+1}}{2}, \frac{\theta_i + \theta_{i+1}}{2} \right) f_{S,\theta} \left(\frac{S_i + S_{i+1}}{2}, \frac{\sigma_i + \sigma_{i+1}}{2} \right) A_{ki} \right\}$$

(27)

where A_{ki} denotes the area of the jth quadrilateral in the ith sector. The reliabilities of the other layers can be evaluated following the above procedure.

NUMERICAL EXAMPLE

Before performing the reliability analysis of laminated composite plates, it is worth validating the proposed finite element method in analyzing nonlinear isotropic or laminated composite plate structures. First consider a simply supported square isotropic plate with length $a = 243.8$ cm, thickness $h = 0.635$ cm, Young's modulus $E = 7.031 \times 10^5$ N/cm², and Poisson's ratio $\nu = 0.25$ subject to uniform load $q = 4.882 \times 10^{-4}$ N/cm². In the finite element analysis, the plate was discretized into 4×4 elements and the center displacement–load relation was constructed. Figure 3 shows the present load–displacement curve in comparison with the results obtained by Akay[10] and close agreement between the two sets of results has been observed. Next consider the transient analysis of a simply supported square laminated composite plate with different lamination schemes subjected to suddenly applied uniform load $q = 5 \times 10^{-4}$ N/cm². The dimen-
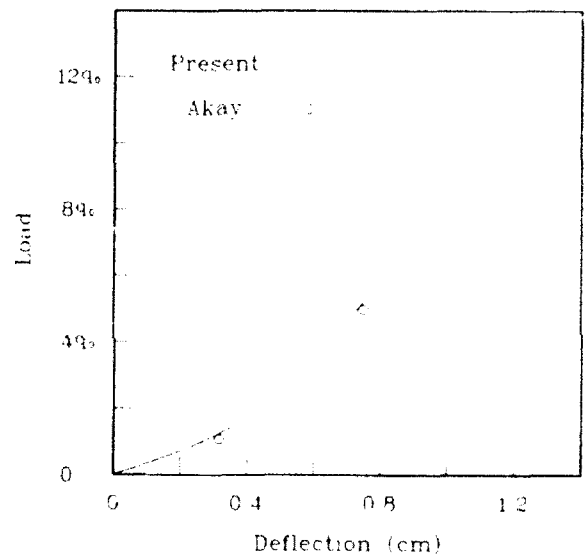
Fig. 3. Load–displacement curve of isotropic plate.
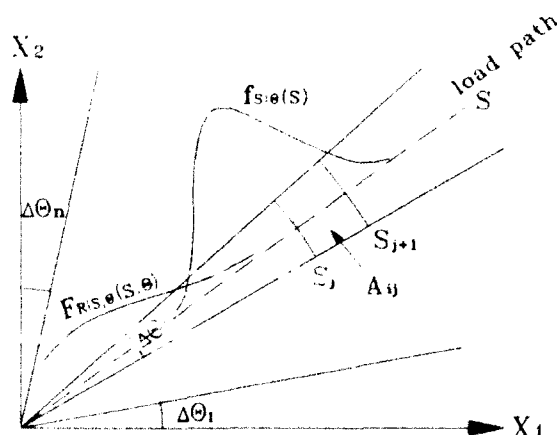
Fig. 2. 2-D load space of structure with random strength.
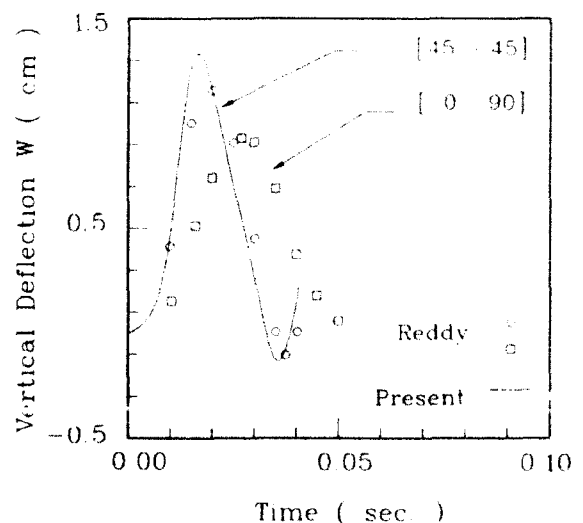
Fig. 4. Nonlinear transient response of laminated plates.
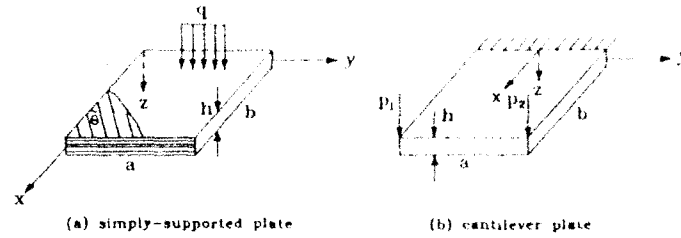
Fig. 5. Plate geometries, loading and boundary conditions

Table 1. Data used in the reliability analysis

	Simply supported		Cantilever plate
Geometry	$a = 10$ cm $b = 10$ cm $h = 0.4$ cm		$a = 6$ cm $b = 8$ cm $h = 0.4$ cm
Material properties	$E_1 = 13.238E + 6$ N/cm^2 $E_2 = 1.076E + 6$ N/cm^2 $G_{12} = 5.654E + 5$ N/cm^2 $G_{23} = 3.378E + 5$ N/cm^2 $G_{13} = G_{12}$ $\nu_{12} = 0.24$ $\nu_{23} = 0.49$		
Shape parameter[a]	$\beta_1 = 8.8$ $\beta_2 = 6.8$ $\beta_6 = 6.3$ $\beta_3 = 8.6$ $\beta_5 = 6.8$		
Scale parameter[a]	$\alpha_1 = 1.513E5$ $\alpha_2 = 4.378E3$ $\alpha_6 = 8.687E3$ $\alpha_3 = 1.69\ E5$ $\alpha_5 = 4.378E3$		

[a] Parameters of Weibull distribution for random strengths.

sions and material properties are assumed. respectively, to be: $a/b = 1$, $a/h = 10$, $E_1/E_2 = 25$, $G_{12} = G_{13} = 0.5E_2$, $G_{23} = 0.2E_2$, $\nu_{12} = 0.25$, and $\rho = 2.547 \times 10^{-6}$ Ns^2/cm^4. In the finite element discretization, a model of 4×4 mesh of nine-node elements was used. Figure 4 shows the plot of the center deflection versus time for two-layer, $[0°/90°]$, cross-ply and two-layer, $[45°/-45°]$, angle-ply plates in comparison with the results obtained by Reddy.[11] It is shown that the present method can yield very good results.

The forementioned reliability analysis was then applied to the reliability study of two laminated composite plates. The geometry of the plates is shown in Fig. 5. The dimensions, material properties, and strength statistics of the plates are given in Table 1. The simply supported angle-ply $[\theta/-\theta/\theta/-\theta]$ square plate was subjected to a random uniform load with mean and standard deviation, $\bar{q} = 25$ N/cm^2 and $\sigma_q = 5$ N/cm^2, respectively. The reliability of the plate was evaluated for q having been treated as a lognormal variate or normal variate. The results for the adoption of different failure criteria in the analyses are given in Fig. 6 for various fiber orientations. It is shown that the cases where q is log-
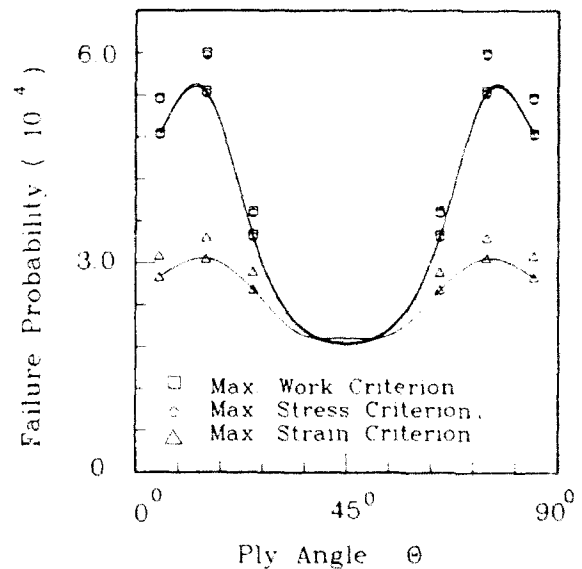
Fig. 6. Failure with probability of simply-supported plate with various ply angles (...... lognormal; ——— normal).

normal always yield higher failure probability. It is also noted that the maximum work criterion and the stress criterion give almost identical results. The optimum fiber orientation is 45° for the cases considered. Next, the reliability of the symmetri-
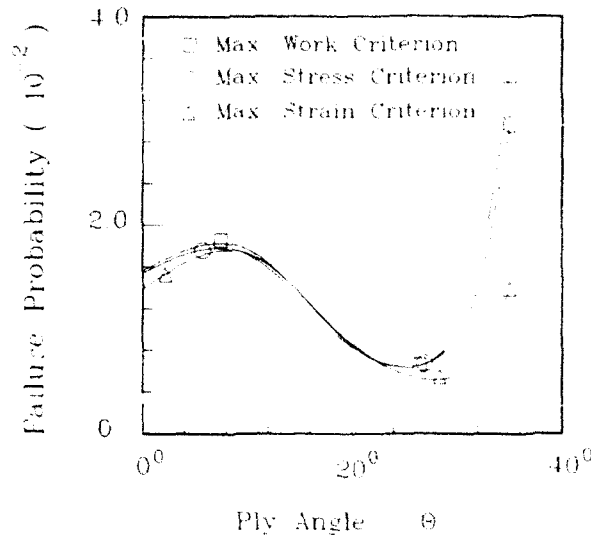
Fig. 7.   Failure probability of cantilever plate with various
ply angles.

cally laminated $[\theta/-\theta]$ cantilever plate in Fig. 5 b subjected to two random loads at the ends was considered. The two loads were assumed to be bi-variated lognormal with mean $\bar{P}_1 = \bar{P}_2 = 150$ N, standard deviation $\sigma_{P_1} = \sigma_{P_2} = 30$ N, and coefficient of correlation $\rho_{P_1 P_2} = 0.2$. The failure probabilities of the plate made up with different ply orientations were obtained for various failure criteria and the results are shown in Fig. 7. The optimal lamination is $[25°/-25°]$ for all the cases considered.

CONCLUSIONS

A method for the nonlinear analysis of laminated composite plate structures has been presented. Numerical examples were given to validate the accuracy of the proposed method. A procedure for reliability assessment of laminated composite plates with random strength subject to large deflections has also been proposed. The application of the proposed procedure on the reliability analysis of laminated composite plates was demonstrated by means of a number of examples. The effects of layer orientations on the reliability of laminated composite plates were investigated. Optimal ply orientations for the plates were determined.

ACKNOWLEDGEMENT

REFERENCES

1. Cassenti, B. N., Probabilistic static failure of composite materials. AIAA J., 22 (1) 1984 103-10.
2. Gederbaum, G., Lishalott, I. & Librescu, I., Reliability of laminated plates via the first-order second-moment method. Comp. Struct., 15 1990 161-7.
3. Duva, J. M., Lang, E. J., Miradech, I. & Herakovich, C. T., A probabilistic perspective on the failure of composite laminae. Appl. Mech. Rev., 1990 43.
4. Kam, T. Y. & Lin, S. C., Reliability analysis of laminated composite plates. Proc. NSC, Part A, 16 (2) 1992 163-71.
5. Washizu, K., Variational Methods in Elasticity and Plasticity. Pergamon Press, New York, 1982.
6. Clough, R. W. & Penzion, J., Dynamics of Structures. McGraw-Hill, New York, 1975.
7. Hsiao, K. M. & Hung, H. C., Large-deflection analysis of shell structure by using corotational total Lagrangian formulation. Comp. Meth. Appl. Mech. Engng., 72 1989 209-25.
8. Pica, A., Wood, R. D. & Hinton, E., Finite element analysis of geometrically nonlinear plate behavior using a Mindlin formulation. Comput. Struct., 11 1980 203-15.
9. Hasofer, A. M. & Lind, N. C., Exact and invariant second-moment code format. ASCE, J. Engng Mech., 92 1976 267-325.
10. Akay, H. U., Dynamic large analysis of plates using mixed finite elements. Comput. Struct., 11 1980 1-11.
11. Reddy, J. N., Geometrically nonlinear transient analysis of laminated composite plates. AIAA J., 21 (4) 1983 621-9.

Analysis of local bending effects in sandwich plates with orthotropic face layers subjected to localised loads

Ole Thybo Thomsen

Institute of Mechanical Engineering, Aalborg University, Aalborg, Denmark

This paper presents a method for the approximate analysis of local bending effects in sandwich plates with specially orthotropic face layers subjected to localised external loads. The local bending analysis is based on the assumption that the relative deflection of the loaded face against the deflection of the face not loaded can be modelled by application of an elastic foundation model. This is achieved by introducing a two-parameter elastic foundation model which takes into account the shearing interaction effects between the loaded face and the core material. An approximate solution to the complete problem is achieved by superposition of the local solution and an overall solution derived by application of classical sandwich plate theory. The results obtained are compared with finite element analysis results, and a good match between the solutions is observed. Finally a brief parametric study shows that the local bending effects are strongly influenced by the modular ratio and the thickness of the loaded face.

1 INTRODUCTION

Sandwich structures have become increasingly popular for structural design purposes over the last 30–40 years due to the possibility of obtaining very high stiffness to weight and strength ratios. However, although the sandwich concept has been accepted as an excellent way to design strong, durable and lightweight structures, which are especially efficient for transferring bending and buckling loads, a number of problems have been left more or less unattended, even by classical textbooks such as those by Allen[1] and Plantema.[2]

An area of significant practical importance, and belonging to this class of more or less unattended problems, is the so called indentation problem associated with local bending effects which are often experienced in connection with introduction or 'take-out' of external loads into sandwich panels.

It is a well known fact that sandwich panels are notoriously sensitive to failure by the application of localised loads such as point loads, line loads or distributed loads of high intensity. This pronounced sensitivity towards the application of localised loads is due to the associated inducement of significant local deflections of the loaded face into the core material of the sandwich plate, thus causing high local stress concentrations.

Relatively few references have been treating the problem of local bending effects in sandwich panels. Among these, Wiessman-Berman et al.[3] and Meyer-Piening[4] suggested the use of an elastic foundation model for the loaded face and the supporting core material, i.e. to consider the relative deflection of the loaded face against the face not loaded to be governed by an elastic foundation model. Both analyses[3,4] were based on the classical Winkler foundation model, which corresponds to the modelling of the core material as continuously distributed linear tension–compression springs.

Other investigations (analysis of low velocity impact on sandwich panels) such as Frostig et al.[5] and Ericsson and Sankar[6] used a formulation in which the core material was modelled as a special type of solid, where only the stiffness in the transverse direction is accounted for.

Two recent papers,[7,8] by the author of the present paper, also considered the local bending problem, and the approach suggested was also based on the application of an elastic foundation formulation. The method suggested, however, was different from the analyses introduced in the references cited[3,4] as the suggested elastic founda-

tion model accounts for the existence of shearing interaction between the loaded face and the core material of the sandwich panel. This additional feature allows for the calculation of the interface (between loaded face and core material) shear stresses, which may build up adjacent to the area of load application. For certain cases, these interface shear stresses are attributed significant importance (together with the interface transverse normal stresses) in the onset and development of failure.

The elastic foundation model suggested[5] is a two-parameter elastic foundation model, and it has been employed for sandwich beam analysis, whereas it has not been used for general sandwich plate analysis. The results obtained for sandwich beams, however, have been verified by comparison with finite element results[7] as well as experimental investigations.[6] Thus, it has been demonstrated that the elastic foundation approach is capable of giving a very good estimate of the stress concentrations induced by local bending in sandwich beams with very little computational effort involved.

None of the references cited above gives an explicit description of the onset and development of failure. Instead, they all restrict themselves to the development of different methods for structural analysis based on the somewhat unrealistic assumption of linear elastic behaviour of the constituent materials. Thus, the results obtained do not reflect the actual sequence of events leading to failure of the considered sandwich panel, but they do have the potential of giving valuable information about the fundamental mechanics of the local bending problem, as well as the parameters controlling the onset of failure.

The purpose of the present paper is to extend the two-parameter elastic foundation approach, presented and tested for sandwich beams,[5,6] to the analysis of rectangular sandwich plates with specially orthotropic (symmetric and balanced, if laminated faces are used) linear elastic face layers. The core material is assumed to be isotropic, homogeneous and linear elastic.

2 ELASTIC FOUNDATION ANALOGY

2.1 Formulation of governing equations using a three-parameter elastic foundation model

The present formulation is based on the assumption of an elastic foundation model, which does

take into account the existence of shearing interaction between the loaded face and the supporting core material. Figure 1 illustrates the considered problem: the loaded face with thickness t of a sandwich plate with length a and width b, and the supporting core material. The loaded face of the sandwich plate considered can be subjected to arbitrarily specified surface loads q_x, q_y, q_z along its upper surface.

It is suggested that the elastic response of the supporting core material is expressed by the following equations, which relate the deflections u, v, w of the loaded face to the interface stress components σ_z, τ_x, τ_y:

$$\sigma_z(x,y) = K_z w(x,y),$$

$$\tau_x = K_x u\left(x,y,-\frac{t}{2}\right)$$

$$\tau_y = K_y v\left(x,y,-\frac{t}{2}\right)$$

(1)

where K_z, K_x, K_y are the foundation moduli, $w(x,y)$ is the lateral displacement of the loaded face, $v(x,y,-t/2)$ is the displacement of the lower fibre of the loaded face in the y direction and $u(x,y,-t/2)$ is the displacement of the lower fibre of the loaded face in the x direction.

The core material is assumed to be isotropic, homogeneous and linear elastic, and the loaded face is assumed to be specially orthotropic i.e. the principal material directions coincide with the edges of the face plate (and linear elastic. It is suggested that the foundation moduli are expressed in accordance with Vlasov and Leontev[8] in
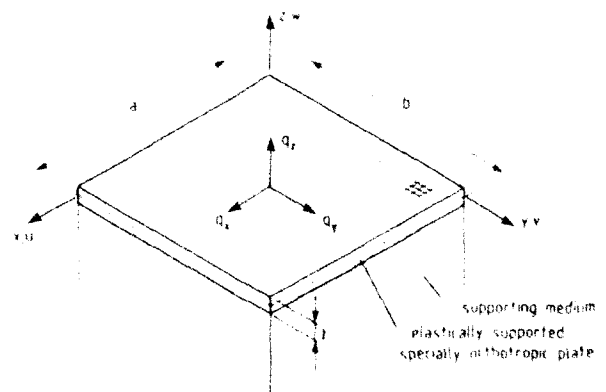
Fig. 1. Elastically supported, specially orthotropic face of rectangular sandwich plate

slightly modified form :

$$K_x = \frac{E_{cy}}{b(1-v_c^2)}\psi_1, \quad K_x = K_y = \frac{E_c b}{4v_c(1+v_c)}\psi_2 \quad 2$$

where

$$E_{cy} = \frac{E_c}{1-v_c^2}, \quad v_c = \frac{v_c}{1-v_c}$$

$$\psi_1 = \frac{\sinh\phi \cosh\phi + \phi}{\sinh^2\phi}$$

$$\psi_2 = \frac{\sinh\phi \cosh\phi - \phi}{\sinh^2\phi}$$

$$\phi = \frac{2\gamma c}{b}$$

In eqns 2 and 3, b is the width of the plate, γ is a factor dependent on the properties of the elastic foundation[10,11]; $\gamma = 1.5$ for the present case[10,11], c is the thickness of the core material i.e. the foundation depth, and subscript 'c' denotes 'core'.

The loaded face is modelled by application of the classical Kirchhoff theory of bending of plates. Thus, it is assumed that normals to the undeformed middle plane of the loaded face remain straight, normal and inextensional during deformation, so that transverse normal and shearing strains may be neglected in deriving the plate kinematic relations.

Referring to Fig. 2 for notation and sign convention, the face plate equilibrium equations can be written in the form (differentiation with respect to the spatial coordinates is denoted by a comma):

$$N_{x,x} + N_{xy,y} + q_x - \tau_x = 0, \quad N_{xy,x} + N_{y,y} + q_y - \tau_y = 0$$

$$Q_{x,x} + Q_{y,y} + q_z - \sigma_z = 0 \qquad (4)$$

$$M_{x,x} + M_{xy,y} + \frac{t}{2}(q_x + \tau_x) - Q_x = 0,$$

$$M_{xy,x} + M_{y,y} + \frac{t}{2}(q_y + \tau_y) - Q_y = 0$$

The plate kinematic relations may be written as (subscript 'o' denotes middle surface displacements):

$$u = u_o + z\beta_x, \quad v = v_o + z\beta_y, \quad w = w_o$$
$$\beta_x = -w_{,x}, \quad \beta_y = -w_{,y} \qquad (5)$$

The middle surface normal and shear strains, and curvature and twist components can be written as:
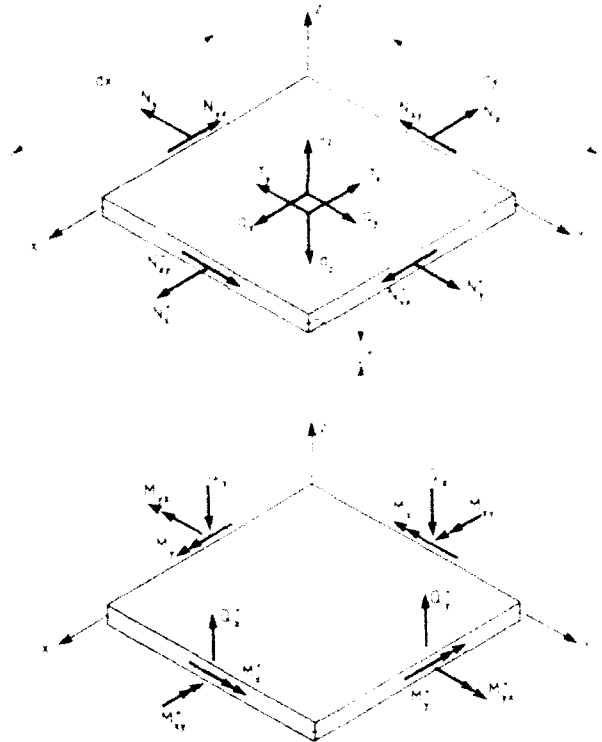
Fig. 2. Face plate element diagram, notation and sign convention.

$$\varepsilon_x = u_{o,x}, \quad \varepsilon_y = v_{o,y}, \quad \gamma_{xy} = u_{o,y} + v_{o,x}$$
$$\kappa_x = -w_{,xx}, \quad \kappa_y = -w_{,yy}, \quad \kappa_{xy} = -2w_{,xy} \qquad 6$$

The plate constitutive relations are formulated assuming linear elastic and specially orthotropic behaviour; if laminated faces are used, they are assumed to be symmetric and balanced :

$$\begin{Bmatrix} N_x \\ N_y \\ N_{xy} \\ M_x \\ M_y \\ M_{xy} \end{Bmatrix} = \begin{bmatrix} A_{11} & A_{12} & 0 & 0 & 0 & 0 \\ A_{12} & A_{22} & 0 & 0 & 0 & 0 \\ 0 & 0 & A_{66} & 0 & 0 & 0 \\ 0 & 0 & 0 & D_{11} & D_{12} & 0 \\ 0 & 0 & 0 & D_{12} & D_{22} & 0 \\ 0 & 0 & 0 & 0 & 0 & D_{66} \end{bmatrix} \begin{Bmatrix} \varepsilon_x \\ \varepsilon_y \\ \gamma_{xy} \\ \kappa_x \\ \kappa_y \\ \kappa_{xy} \end{Bmatrix} \quad 7$$

The A_{ij}'s ($i,j = 1,2,6$) in (7) are the extensional stiffnesses of the loaded face, and the D_{ij}'s ($i,j = 1,2,6$) are the bending stiffnesses (the A_{ij}, D_{ij} components can be derived from classical laminate theory[12]).

Equations (1)–(7) represent the complete set of equations governing the mechanical behaviour of the elastically supported face plate. From these equations it is possible, by proper manipulation, to formulate a system of three coupled partial dif-

ferential equations in the three unknown interface
stress components σ_z, τ_{xz}, τ_{yz}, or alternatively in u,
v, w:

$$D_{11}\sigma_{z,xxxx} + 2D_{12} + 2D_{66}\,\sigma_{z,xxyy} + D_{22}\sigma_{z,yyyy}$$

$$+ K_z\sigma_z - \frac{K_z t}{2}\left(\tau_{xz,x} + \tau_{yz,y}\right)$$

$$= K_z\left(q_t - \frac{t}{2}\,q_{,x} + q_z\right)$$

$$\frac{1}{K_x}\,A_{11}\tau_{xz,xx} + A_{66}\tau_{xz,yy} - \tau_{xz} + \frac{1}{K_z}\,\left(A_{12} + A_{66}\right)\tau_{yz,xy}$$

$$-\frac{t}{2K_z}\,\left(A_{11}\sigma_{z,x} + \left(A_{12} + 2A_{66}\right)\sigma_{z,xyy}\right) = -q_x$$

(8)

$$\frac{1}{K_x}\,\left(A_{12} + A_{66}\right)\tau_{xz,xy} + \frac{1}{K_z}\,\left(A_{22}\tau_{yz,yy} + A_{66}\tau_{yz,xx}\right)$$

$$-\tau_{yz} - \frac{t}{2K_z}\,\left(A_{22}\sigma_{z,yyy} + \left(A_{12} + 2A_{66}\right)\sigma_{z,xxy}\right) = -q_y$$

This completes the formulation of the set of equa-
tions governing the problem of the elastically sup-
ported, specially orthotropic face plate subjected
to arbitrary surface loads.

2.2 Derivation of local bending solution

As mentioned, the set of equations (8) represents
three coupled partial differential equations in the
unknowns σ_z, τ_{xz}, τ_{yz}, and for arbitrary surface load
and boundary conditions it is possible to obtain a
numerical solution by application of, for instance,
a finite difference solution scheme. Closed form
solutions, however, are only obtainable for pro-
blems characterised by very 'simple' types of
boundary conditions (simple support conditions).

For the class of problems considered in the
present paper (local bending effects in sandwich
plates subjected to localised loads) it turns out
that the actual type of boundary conditions of the
considered problem is of no importance, provided
that the area of external load application is far
away from the edges of the sandwich plate. This is
due to the fact that the local bending effects,
induced by highly concentrated loads, really are
local by their very nature (as will be demonstrated
later). Thus, the local disturbances of the overall
bending and shearing state in the sandwich plate

under consideration will typically show a very
steep decay so that the local bending effects will
not interfere with the edge effects.

From the above mentioned considerations it is
concluded that a closed form solution, based on
the assumption of simply supported edges of the
loaded face plate, will be able to model the local
bending problem satisfactorily for most practical
problems. Thus, it is assumed that the edges of the
considered face plate are simply supported, and
that the so called S2 boundary conditions[5] are
present (see Fig. 1):

$$x = 0, a: \quad w = 0, v = 0, M_x = 0, N_x = 0$$

$$y = 0, b: \quad w = 0, u = 0, M_y = 0, N_y = 0$$

(9)

If the external surface loads are expanded in
double Fourier series as follows:

$$q_z(x, y) = \sum_{m=1}^{\infty}\sum_{n=1}^{\infty} a_{mn}\sin\alpha x\sin\beta y$$

$$q_x(x, y) = \sum_{m=1}^{\infty}\sum_{n=1}^{\infty} b_{mn}\cos\alpha x\sin\beta y$$

(10)

$$q_y(x, y) = \sum_{m=1}^{\infty}\sum_{n=1}^{\infty} c_{mn}\sin\alpha x\cos\beta y$$

$$\alpha = \frac{m\pi}{a}, \quad \beta = \frac{n\pi}{b}$$

it is seen that separable solutions to the set of
equations (8), which also satisfies the S2 condi-
tions specified by (9), can be expressed in the
form:

$$\sigma_z(x, y) = \sum_{m=1}^{\infty}\sum_{n=1}^{\infty} A_{mn}\sin\alpha x\sin\beta y$$

$$\tau_{xz}(x, y) = \sum_{m=1}^{\infty}\sum_{n=1}^{\infty} B_{mn}\cos\alpha x\sin\beta y$$

(11)

$$\tau_{yz}(x, y) = \sum_{m=1}^{\infty}\sum_{n=1}^{\infty} C_{mn}\sin\alpha x\cos\beta y$$

Insertion of (10) and (11) into (8) yields three
linear algebraic equations from which the
unknown Fourier series coefficients A_{mn}, B_{mn},
C_{mn} can be determined.

The expressions derived for A_{mn}, B_{mn}, C_{mn} can
be written in the form:

$$A_{\ldots} = \frac{1}{F}\left[H\left(b_1 c_2 - b_2 c_1 + b_{\ldots}\left(a_2 c_1 - a_1 c_2\right)\right)\right.$$

$$\left. - c_{\ldots}\left(a_1 b_2 - a_2 b_1\right)\right]$$

$$B_{\ldots} = -\frac{1}{F}\left[H\left(b_1 c_2 - b_2 c_1 + b_{\ldots}\left(a_2 c_1 - a_1 c_2\right)\right)\right.$$

$$\left. - c_{\ldots}\left(a_1 b_2 - a_2 b_1\right)\right] \qquad (12)$$

$$C_{\ldots} = \frac{1}{F}\left[H\left(b_1 c_2 - b_2 c_1 + b_{\ldots}\left(a_1 c_2 - a_2 c_1\right)\right)\right.$$

$$\left. - c_{\ldots}\left(a_1 b_2 - a_2 b_1\right)\right]$$

where

$$F = a_1 b_2 c_2 - a_1 b_2 c_2 - b_1 a_2 c_2 + b_{\ldots} a_2 c_2$$

$$+ c_1 a_2 b_2 - c_{\ldots} a_2 b_2$$

$$H = K_1\left(a_{\ldots} - \frac{t}{2}\left(b_{\ldots}\alpha + c_{\ldots}\beta\right)\right)$$

$$a_1 = D_{11}\alpha^4 + \left(2 D_{12} + 2 D_{66}\right)\alpha^2\beta^2 + D_{22}\beta^4 + K_1$$

$$a_2 = \frac{K_1 t\alpha}{2}, \qquad a_3 = \frac{K_1 t\beta}{2}$$

$$b_1 = \frac{t}{2K_1}\left[A_{11}\alpha^2 + \left(A_{12} + 2A_{66}\right)\alpha\beta^2\right] \qquad (13)$$

$$b_2 = -\left[1 - \frac{1}{K_1}\left(A_{11}\alpha^2 + A_{66}\beta^2\right)\right]$$

$$b_3 = \frac{1}{K_1}\left(A_{12} + A_{66}\right)\alpha\beta$$

$$c_1 = \frac{t}{2K_1}\left[A_{22}\beta^2 + \left(A_{12} + 2A_{66}\right)\alpha^2\beta\right]$$

$$c_2 = -\frac{1}{K_1}\left(A_{12} + A_{66}\right)\alpha\beta$$

$$c_3 = -\left[1 - \frac{1}{K_1}\left(A_{22}\beta^2 + A_{66}\alpha^2\right)\right]$$

Thus, the solution to the problem of local bending of the loaded specially orthotropic face of a rectangular sandwich plate has been derived in terms of the interface stress components σ_z, τ_x, τ_y. From these, the other quantities of interest, such as the displacement components u, v, w, the stress and moment resultants N_x, N_y, N_{xy}, M_x, M_y, M_{xy}, and the in-plane stress components of the face plate σ_x^f, σ_y^f, τ_{xy}^f, can easily be derived by use of eqns 1, 5, 6 and 7. However, these details will be left out in the present paper.

2.3 Derivation of complete solution by superposition

A complete approximate solution to the problem of overall bending and shearing as well as local bending of a specific sandwich plate subjected to localised loads, is obtained by superposition of the local solution derived above and an overall closed form solution obtained by use of classical sandwich plate theory[1] or a finite element[1] solution based on sandwich plate or shell elements[2]. The approximate solution thus obtained, of course, will only describe the effects of local bending in the loaded face and the interface between the loaded face and the core material, i.e. no explicit information is obtained about the decay of the local bending effects down through the core material, and no information is available about whether the stress state of the lower face is affected of the local bending.

From a practical point of view, however, this is no serious drawback (provided the results for the loaded face are good), since the most critical part of a sandwich plate subjected to strongly localised loading is the loaded face (in the near vicinity of the area of external load application) and the interface between the face and the core.

The approximate complete solution to a specific problem can be represented in the form (displacements, in-plane face stresses, and interface stresses):

$$\begin{pmatrix} u \\ v \\ w \end{pmatrix}_{total} = \begin{pmatrix} u \\ v \\ w \end{pmatrix}_{overall} + \begin{pmatrix} u \\ v \\ w \end{pmatrix}_{local}$$

$$\begin{pmatrix} \sigma_x^f \\ \sigma_y^f \\ \tau_{xy}^f \end{pmatrix} = \begin{pmatrix} \sigma_x^f \\ \sigma_y^f \\ \tau_{xy}^f \end{pmatrix}_{overall} + \begin{pmatrix} \sigma_x^f \\ \sigma_y^f \\ \tau_{xy}^f \end{pmatrix}_{local} \qquad (14)$$

$$\begin{pmatrix} \tau_{zx}^{int} \\ \tau_{zy}^{int} \end{pmatrix}_{total} = \begin{pmatrix} \tau_{zx}^{int} \\ \tau_{zy}^{int} \end{pmatrix}_{overall} + \begin{pmatrix} \tau_x \\ \tau_y \end{pmatrix}, \quad \left(\sigma_z^{int}\right)_{total} = \sigma_z$$

For the purposes of the present paper, the overall solution part (denoted by subscript 'overall' in

[...] is obtained from classical sandwich theory including the contribution to the strain energy from the bending of the face plates, i.e. a theory valid for thick face sandwich plates, as derived by Ref. 1, to which the reader is referred for further details.

3 RESULTS AND DISCUSSION

In order to illustrate the applicability of the suggested approximate solution procedure, and to demonstrate the influence of certain characteristic parameters on the local bending effects, a few comparative results and a very brief parametric study will be presented in the following.

3.1 Comparison with finite element solution

The example chosen for the comparative study is the case of a simply supported specially orthotropic sandwich plate subjected to a central load P distributed uniformly over a small area. The geometry, material data and external load are as follows:

Geometry: $a = b = 500.0$ mm, $t = 3.0$ mm,
  $c = 30.0$ mm

Faces: $E_1 = 33.6$ GPa, $E_2 = 8.4$ GPa,
  $\nu = 0.32$, $G = 3.1$ GPa
  corresponding to one-layer unidirectional E-glass/epoxy laminate.
  $\rho_1 = \rho_2 = 4.0$

Core: $E_c = 0.1$ GPa, $\nu = 0.35$
  corresponding to PVC-foam,
  $\rho_c = 100.0$ kg/m

Load: $P = 1000.0$ N distributed over a small
  quadratic area, $A = 4.0$ mm.

The finite element model (FEM), which is generated using the general purpose finite element package ANSYS (version 4.4A), is made by use of isoparametric eight-node solid elements with three translational degrees of freedom in each node, and due to the symmetry of the problem only one quarter of the sandwich plate is considered. Two layers of elements are used for modelling the faces, and four layers of elements are used for modelling the core material of the sandwich plate. All together the number of nodes in the FEM model is 2304, and the number of elements is 1800. The FEM model is illustrated in Fig. 3, which shows one quarter of the sandwich plate in deformed configuration. The load in the FEM model is applied as a point load acting at the centre node of the plate ($x = 250$, $y = 250$).

The solution based on the elastic foundation approach, referred to as the EF solution, has been obtained by superposition of the local bending solution and a classical sandwich theory solution (referred to as the CST solution). In order to avoid singular bending moments (and thereby singular bending stresses in the faces), the external load P has been distributed uniformly over a small quadratic area with side lengths 2 mm, area 4 mm. The number of harmonics included in the double series expansions, eqns 10 and 11, needed to obtain convergence as well as a 'smooth' solution was 250.
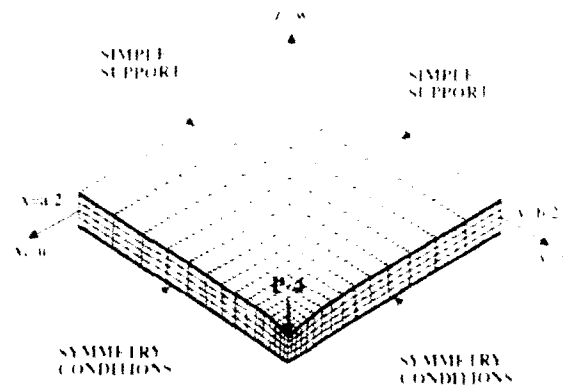
Fig. 3. FEM model of the sandwich plate in deformed configuration
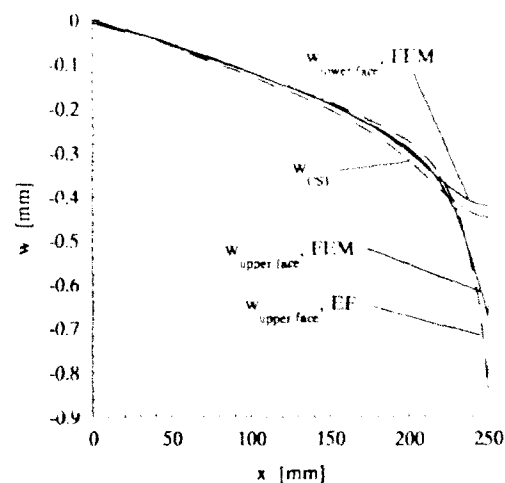
Fig. 4. Lateral deflections w of upper and lower faces for $0 \le x \le a/2 = 250$, $y = b/2 = 250$

Figure 4 shows the lateral deflections w of the upper and lower faces along the section defined by $0 \le x \le a/2 = 250$; $y = b/2 = 250$. From Fig. 4 it is observed that the FEM and EF solutions compare very well for the upper face of the sandwich plate, even though the EF solution predicts the maximum deflection to be somewhat larger than the FEM solution. The reason for this may be the fact that the FEM model is made with eight-node solid elements, which actually are not good enough for describing the local bending state near the centre of the plate with only two layers of elements through the face thickness. Better FEM results would have been obtained if 20-node solid elements were used instead. However, this was not possible with the ANSYS 4.4A version at hand due to severe restrictions with regard to the problem size allowed (maximum in core wave front allowed: 500). Nevertheless, the FEM results are expected to be quite good except very near the centre of the plate. Figure 4 also shows the w distribution of the lower face as obtained from the FEM solution, and it is seen that the results agrees very well with CST results, i.e. the decay of the local bending effects down through the core material is complete, which again means that the stress state of the lower face is unaffected by the local bending of the upper face.

Figure 5 shows the distribution of the transverse normal and shear stresses at the interface between the loaded face and the core material along the section $0 \le x \le a/2 = 250$, $y = b/2 = 250$. From Fig. 5 it is observed that the match between the predicted σ^{int} distributions is very close, even though it should be remembered that the FEM solution is obtained for a 'point load' situation whereas the EF solution is obtained for the case of a distributed load of very high intensity. The overall tendency observed from the two solutions is very clear: the peak value of σ^{int} is situated at the centre of the plate, and a very steep decay is seen as the distance from the plate centre is increased. About 1·5 sandwich plate thicknesses (thickness of sandwich plate: $c + 2t = 36$ mm) away from the plate centre the decay is complete, and no disturbances induced by local bending of the upper face are seen to be present. The interface distribution of shear stresses τ^{int}_{xz} is also shown in Fig. 5, and again it is observed that the two solutions match each other reasonably well. At the centre of the plate no interface shear stresses are present (due to the symmetry), and the peak value of τ^{int}_{xz} is situated some distance away from the centre of the plate (about 10–15 mm).
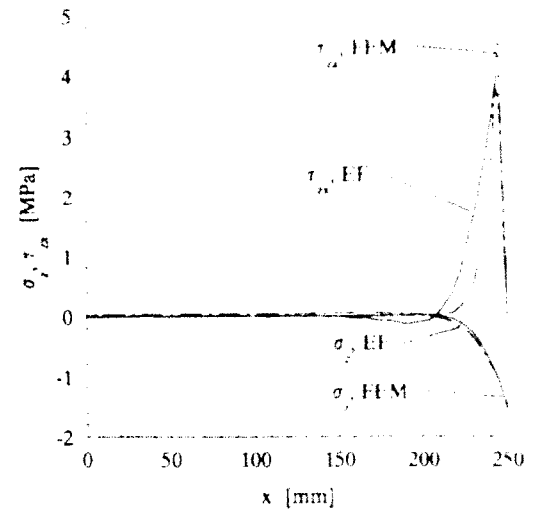
Fig. 5. Distribution of σ_z, τ_{xz} ($0 \le x \le a/2 = 250$, $y = b/2 = 250$)

After the peak value has been encountered. A very steep decay of τ^{int} takes place, and very rapidly the interface shear stress contribution induced by local bending fades out completely.

From both the σ^{int} and the τ^{int} distribution curves it is seen that the elastic response of the core material possesses a wavy harmonic nature along with a very steep decay, which means that the deflectional mode pattern can be attributed some characteristic wave-length.

The last comparative results to be included are given by Fig. 6, which shows the distribution of bending stresses σ^1_x in the upper and lower fibres of the loaded face along $0 \le x \le a/2 = 250$, $y = b/2 = 250$. Also with respect to the σ^1_x distributions a good match between the FEM and EF solutions is observed. Considering the results obtained for the upper fibre, it is seen that severe stress concentrations are present at the centre of the plate. The results obtained from the EF solution predicts the peak value of $(\sigma^1_x)_{upper\ fibre}$ to be about -170 MPa, whereas the CST solution predicts the peak value to be -35 MPa. Thus the local bending of the loaded face increases the peak value of $(\sigma^1_x)_{upper\ fibre}$ by a factor of nearly 5. The FEM results are very close to the EF results, but again attention should be focused on the load case modelled in the FEM model, which is a 'point load' case. This load case should actually provide singular stresses in the loaded face at the point of load application, but due to the relatively crude mesh and the application of eight-node solid elements, the results obtained lie very close to the EF

solution obtained for a load distributed uniformly over a small area.

Considering the σ_x^f distribution along the lower fibre of the loaded face, a very close match between the solutions is observed again, and a characteristic feature of the results obtained is that a tensile state of stress has been induced near the centre of the plate.

From the results included in Figs 4–6 it is seen that the match between the FEM and EF solutions is very convincing, and it is concluded that the elastic foundation approach is capable of supplying quite reasonable results, i.e. to give a good estimate of the severity of the stress concentrations induced by local bending effects. It should be noticed that the local bending effects contribute significantly to the stress state near the area of external load application, thus implying that CST-solutions will seriously underestimate the severity of the stress concentrations.

3.2 Parametric effects

In order to illustrate the influence of certain characteristic parameters on the local bending effects, the results of a brief parametric study will be presented. The problem considered is the loaded face of a sandwich plate subjected to a unit load ($P = 1.0$ N) distributed uniformly over a small area $A = 4.0$ mm². The loaded face is assumed to be composed of one layer of specially orthotropic material. In order to illustrate the effects of altering the degree of orthotropy, results will be pre-

sented for the case of isotropic face materials ($E_{11}/E_{22} = 1.0$) and for the case of face materials with $E_{11}/E_{22} = 4.0$.

Figure 7 shows the peak values of the interface transverse normal stresses $\sigma^{int}_{z\,peak}$ and the interface shear stresses $\tau^{int}_{xz\,peak}$ against the modular ratio E_{11}/E_c and the face thickness t ($t = 1.0, 2.0, 4.0$ mm) for the isotropic face material ($E_{11}/E_{22} = 1.0$) case. The overall tendency is that the higher the value of the modular ratio E_{11}/E_c the lower the value of the peak interface stress components, i.e. the more flexible the core material, compared to the face material, the lower the peak value of the interface stresses. Furthermore, it is observed that the peak values of the interface stresses decreases significantly as the thickness of the loaded face t increases, i.e. as the flexural rigidity of the loaded face increases.

Commenting on the results shown in Fig. 7, attention should be focused upon the fact that the elastic foundation approach becomes inadequate for handling the local bending problem for deformations of very short wave-length, which corresponds to the combination of very low values of the modular ratio E_{11}/E_c and low values of the face thickness t. The reason for this inadequacy is the fact that shearing interaction effects become increasingly important for deformations with short wave-lengths, and even though the two-parameter elastic foundation model does include shearing interaction effects, the model is sophisticated enough for describing deformations with

Fig. 6. Distribution of σ_x^f in the upper and lower fibres of the loaded face: $0 \leq x \leq a/2 = 250$, $y = b/2 = 250$.
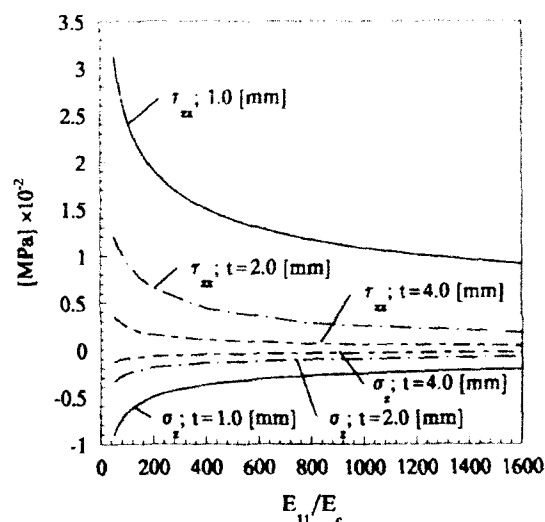
Fig. 7. $(\sigma^{int})_{peak}$, $(\tau^{int})_{peak}$ versus modular ratio E_{11}/E_c and face thickness t for isotropic face materials; $E_{11}/E_{22} = 1.0$; with unit load distributed uniformly over an area 4.0 mm².

very short wave-lengths. However, the overall parametric effects illustrated by Fig. 7 generally hold to be true.

Figure 8 shows the results of a parametric study similar to the study shown in Fig. 7 except that the ratio of orthotropy is set to $E_{11}/E_{22} = 4.0$. The overall tendencies shown by the curves of Fig. 8 are equivalent to the results shown in Fig. 8 as well. The only difference between the results shown in Figs 8 and 7 is that the peak stresses tend to increase about 30% as the ratio of orthotropy is increased from $E_{11}/E_{22} = 1.0$ to $E_{11}/E_{22} = 4.0$.

To conclude this section, it has been demonstrated that the local bending effects are strongly influenced by the modular ratio E_{11}/E_c and the face thickness t. Other parameters, such as the core thickness c and the sandwich plate span widths a and b, of course also influence the stress state in the sandwich plate, but as they primarily exert influence on the overall bending and shearing of the sandwich plates under consideration (in principle their influence is covered by classical sandwich theory, CST) they have not been included in the parametric study presented in this paper.

4 CONCLUSIONS AND FINAL COMMENTS

An approximate method of analysing the local stress and displacement fields in the near vicinity of localised external loads applied to the surface of specially orthotropic sandwich plates has been presented. The suggested solution procedure is based on the assumption that the relative deflection of the loaded face against the face not loaded can be modelled by use of a two-parameter elastic foundation model, which takes into account the existence of shearing interaction effects between the loaded face and the core material of the considered sandwich plate. Furthermore, it is assumed that the face behaves specially orthotropic and linear elastic, and that the core material can be considered as an isotropic linear elastic material.

The local stress and displacement fields derived by application of the two-parameter elastic foundation model can be superimposed on the stress and displacement fields derived by use of classical sandwich plate theory[1,2] (or alternatively a FEM solution based on the use of sandwich plate or shell elements).
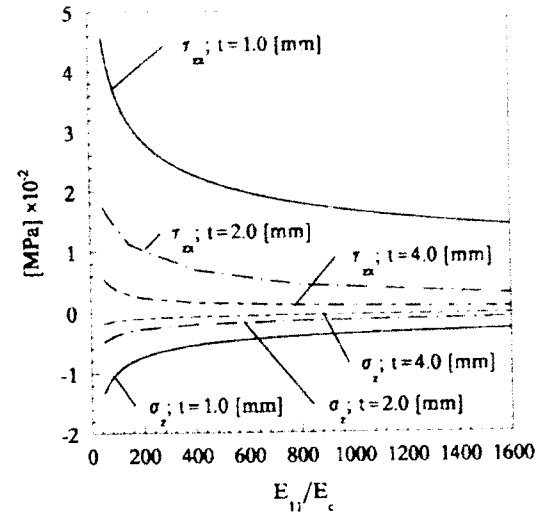
Fig. 8. σ^{ww}_{peak}, τ^{ww}_{peak} versus modular ratio E_{11}/E_c and face thickness t for specially orthotropic face materials; $E_{11}/E_{22} = 4.0$; with unit load distributed uniformly over an area 4.0 mm^2.

The applicability of the suggested solution procedure has been demonstrated by analysing the simple case of a quadratic sandwich plate with specially orthotropic face layers subjected to a central lateral load distributed uniformly over a small area (nearly a point load). The results obtained have been compared to a finite element solution (point load case), and a very good match between the two solutions has been observed. Thus, it has been demonstrated that it is possible to estimate, with a high degree of accuracy, the severity of the stress concentrations induced by local bending by application of a suitable elastic foundation formulation.

A brief parametric study has shown that the local bending effects are strongly influenced by the modular ratio (E_{11}/E_c for fixed value of E_{11}/E_{22}) as well as by the thickness t of the loaded face plate. The peak values of the interface stress components become very large for small values of the modular ratio and the face thickness, and it is further observed that the peak interface stresses decrease rapidly with increasing values of the modular ratio and the face thickness.

To conclude the paper a final comment about the limitations of the elastic foundation approach is appropriate. Obviously, the application of the elastic foundation approach for describing the local bending of the loaded face is not generally justified, as it is not possible to specify constant values of the foundation moduli (K_x, K_y, K_z)

which are appropriate for deformations of any wave-lengths. The reason for this is that the shearing deformations of the core material (foundation) become very influential for deformations with short wave-lengths. For practical structural sandwich panels, however, the bounds imposed by the somewhat vaguely formulated concept of 'deformations with short wave-lengths' are not likely to be active, since the typical face thicknesses $(0 \le t \le 10$ mm), and the typical modular ratios $(25 \le E_{11}/E_c \le 1500)$, will usually ascertain sufficiently large deflection wave-lengths to ensure that application of the elastic foundation approach will supply reasonable results.

If, on the other hand, the deflection wave-length for a specific problem is very long (exceeding the sandwich plate thickness seriously), it must be expected that the local bending effects may affect the bending state of the lower face seriously, i.e. the decay of the local disturbances through the thickness of the core material will not be complete. Thus, for sandwich plates characterised by very large values of the modular ratio and the face thickness, or by very small values of the core thickness ('thick face' sandwich plates), it may be expected that the quality of the elastic foundation approach will suffer a serious drawback.

ACKNOWLEDGEMENT

REFERENCES

1. Allen, H. G., *Analysis and Design of Structural Sandwich Panels*. Pergamon Press, Oxford, 1969.
2. Plantema, F. J., *Sandwich Construction*. John Wiley, New York, 1966.
3. Weissman-Berman, D., Petrie, G. L. & Wang, M.-H., *Flexural Response of Foam-Cored Sandwich Panels*. The Society of Naval Architects and Marine Engineers (SNAME), New York, November, 1988.
4. Meyer-Piening, H.-R., Remarks on higher order sandwich stress and deflection analyses. In *Sandwich Construction 1*, ed. K.-A. Olsson & R. P. Reichard. Proceedings of the 1st International Conference on Sandwich Construction, Stockholm, June 1989, pp. 107–27.
5. Frostig, Y., Baruch, M., Vilnay, O. & Sheinman, I., Bending of nonsymmetric sandwich beams with transversely flexible core. *ASCE J. Engng Mech.*, **117** 9 1991 1931–52.
6. Ericsson, A. & Sankar, A. V., Contact stiffness of sandwich plates and application to impact problems. In *Sandwich Construction 2*, eds K.-A. Olsson & D. Weissman-Berman. Proceedings of the 2nd International Conference on Sandwich Construction, University of Florida, March, 1992.
7. Thomsen, O. T., Further remarks on local bending analysis of sandwich panels using a two-parameter elastic foundation model. Report No. 40, Institute of Mechanical Engineering, Aalborg University, Denmark, March, 1992.
8. Thomsen, O. T., Analysis of local bending effects in sandwich beams subjected to localised loads. Submitted to *Thin-Walled Structures* July 1992.
9. Thomsen, O. T., Photoelastic investigation of local bending effects in sandwich beams. Report No. 41, Institute of Mechanical Engineering, Aalborg University, Denmark, May, 1992.
10. Vlasov, V. Z. & Leont'ev, N. N., *Beams, Plates and Shells on Elastic Foundations*, Moscow, 1960. English translation by Israel Program for Scientific Translation, Jerusalem, 1966.
11. Zhaohua, F. & Cook, R. D., Beam elements on two-parameter elastic foundations. *ASCE J. Engng Mech.*, **109** (6) December 1983 1390–402.
12. Jones, R. M., *Mechanics of Composite Materials*. McGraw-Hill, New York, 1975.

Eigen analysis of fiber-reinforced composite plates

A. M. Abd-el-Raouf,[a] E. E. El-Soaly,[b] S. M. Ghoneam[c] & A. A. Hamada[c]

[a]Engineering and Machine Department, Faculty of Engineering, Menoufia University, Shebin El-Kom, Egypt
[b]Mechanics and Elasticity Department, M.T.C., Cairo, Egypt
[c]Production Engineering and Machine Design, Menoufia University, Shebin El-Kom, Egypt

Composites plates of various orientation and thickness with fiber-reinforced plastics (FRP) find increasing applications in aerospace and automotive structures (due to their high strength, stiffness to weight ratios, and high damping characteristics). Determination of the dynamic characteristics and the investigation of such structures are essential not only in the design but also in manufacture development.

In the present paper, the eigen analysis of laminated square plates with various fiber orientations, various boundary fixations, and different stacking sequences has been presented and discussed. The experimental analysis and finite element techniques are utilized to study the effect of fiber orientation and boundary conditions on the dynamic characteristics of frequency and mode shapes. The vibrational system technique is utilized for experimental measurements. The results show agreement between experimental and theoretical investigations. Also, these results show a close connection between damping and stiffness characteristics in glass-fiber composites.

INTRODUCTION

Composite plates of various orientations with fiber-reinforced plastics (FRP) find increasing applications in aerospace and automotive structures due to their high strength, stiffness to weight ratios, and high damping characteristics. Determination of the vibration behavior of such components is necessary for either their design or engineering applications.

Studies in the area of the dynamic behavior of fiber-reinforced composites have been carried out by many investigators, and these have been reviewed extensively in review papers by Gibson and Plunket,[1] Gibson and Wilson,[2] Bert[3-6] and very recently by Plunket.[7] Chelladurai et al.[8] have carried out limited studies using a finite element method for square and rectangular orthotropic plates of constant thickness for two boundary conditions, for obtaining the fundamental frequency.

During the last two decades, the research and development of laminated composite structures has grown at an extremely rapid pace and it becomes an obvious trend that more and more composite materials will be used in the design of structures when the weight and strength are of primary consideration. The fundamental development in the mechanics of composite materials has been documented by Tsai and Hahn[9] and Jones.[10] The basic theory of the mechanics of composite materials, particularly for laminated plates, has been widely used in finite element formulations. Thus, it is common that existing isotropic and homogeneous finite elements also have the capability of treating laminate composite materials. A survey of recent research in the analysis of composite plates including finite element methods can be found in Reddy.[11]

Choice[12] has done limited studies on the dynamic response of planar frame composite structures using analytical and finite element solutions of simply supported beams. He shows that the finite element results are in very good agreement with analytical solutions. Also Sun et al.[13] present the development of an efficient finite element model for the analysis of laminated composite beams treated by a constrained viscoelastic layer. They show that the dynamic response is substantially improved by the use of damping treatments.

The activity and the effort in this field are on the increase for laminated construction, and on the form in which most of the fiber-reinforced

521

composite materials are employed. In addition they provide enough flexibility to the designer to vary the material properties significantly by changing the fiber orientation as well as the stacking sequence of the different layers of the composite laminate structures.

In the present work, five specimens (FRP) of square laminated plates with different types of orientation and boundary conditions, are studied and the correlation between experinental and numerical results is investigated.

The measurement of eigen parameters and damping properties, on laminated square plates with various lamina orientations, are carried out at different boundary conditions. The frequency response function (FRP) of the specimens used are recorded, hence frequency and amplitude are measured directly, and hence the damping factor is calculated using a half power band width method.

FINITE ELEMENT FORMULATION

The present formulation is based on four noded quadrilateral plate bending elements with three degrees of freedom, at each node. Numerical results have been computed for various orientations and boundary conditions. The data presented here include both the frequencies and mode shapes.

A typical square plate of dimensions 150 mm × 150 mm, with different fixations, CFFF, SSFF, CSFF, CCFF, SSSS along the edges of plate, is shown in Fig. 1. The figure shows the finite element grid with nine quadratic plate elements used. The element has twelve degrees of freedom with three degrees of freedom for each node, namely w, θ_x and θ_y, where w denotes the vertical deflection and θ_x and θ_y denote the slopes $\partial w/\partial y$ and $-\partial w/\partial x$ along y- and x-directions, respectively. The stiffness matrix of the element can be formulated as:[14]

$$[K]^e = t \int\int [B]^T [D][B]\,dx\,dy \qquad (1)$$

where t is thickness of plate, $[B]$ a strain matrix given by

$$[B] = \begin{bmatrix} -\partial^2/\partial x^2 \\ -\partial^2/\partial y^2 \\ -2\partial^2/\partial x \partial y \end{bmatrix} \cdot [N]$$

$[N] = [C] [A]^{-1}$ where $[N]$ is the matrix of the shape function, $[C]$ the interpolation function, $[A]$
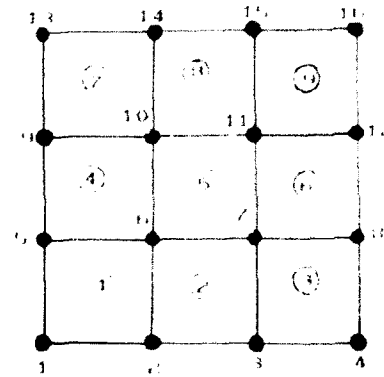
Fig. 1. Finite element grid and measuring positions

element geometry and $[D]$ is an elasticity matrix of laminated plate which can be computed according to Ref. 5, for different lamina orientation and layer thickness. The flexural coefficient D is expressed in terms of layers of stiffness as

$$D_{ij} = 1/3 \sum_{k=1}^{n} \bar{Q}_{ij} (h_k^3 - h_k^3) \qquad (2)$$

where

n is the number of layers,
$\bar{Q}_{ij}$ is the transformed reduced stiffness,
h_k is the thickness of the kth layer,
i,j are the indices varying from 1 to 3.

Consequently the mass matrix of the element can be formulated as:

$$[m]^e = \rho \int\int [N]^T[N]\,dx\,dy \qquad (3)$$

where ρ is density of fiber/polyester laminated plate.

A computer program has been developed to formulate the present composite plate element, 48 degrees of freedom in the case of FFFF of four edges of plate, 36 degrees of freedom in the case of CFFF, 24 degrees of freedom in the case of CCFF, 28 degrees of freedom in the case of CSFF, 32 degrees of freedom in the case of FFSS and 20 degrees of freedom in the case of SSSS. The elimination of w transformation, and the partitioned form of the stiffness and mass matrices are given respectively as

$$[K] = \left[\begin{array}{c|c} K_{tt} & K_{ts} \\ \hline K_{st} & K_{ss} \end{array}\right], \quad [m] = \left[\begin{array}{c|c} m_{tt} & m_{ts} \\ \hline m_{st} & m_{ss} \end{array}\right]$$

By the use of the condensation technique, the final results for the condensed stiffness matrix $[k]$ are

given by

$$|K| = K_{11} - K_{12}K_{22}^{-1}K_{21} \qquad (4)$$

The same procedure is carried out for the mass matrix

$$|m| = m_{11} - m_{12}m_{22}^{-1}m_{21} \qquad (5)$$

The program has been coded into IBM computer in quick Fortran language. The program computes the stiffness and mass matrices of any orientation and fixation of composite plates. The program computes the eigenvalues and eigenvectors. It finds the eigenvalues by computing the roots of the characteristic polynomial of any real square matrix in an iterative manner with an accuracy of 10^{-5} for five fixations namely: CFFF, CSFF, SSFF, CCFF and SSSS. The elements of the computed element stiffness and mass matrices are listed in the Appendix.

EXPERIMENTAL PROCEDURE

The experimental apparatus is shown in Fig. 2. The specimen is mounted in a test rig and excited by a B & K 4818 exciter, located at the central position of the test plate where all modes would be excited. The excitation signal feeds the analyzer through the amplifier 2708, and the excitation force can be measured by a force transducer 8200. The resulting vibration response is registered by a piezoelectric accelerometer type 4374, mounted on the specimen; the accelerometer signals are conditioned in the charge amplifier and feed to the dual channel signal analyzer 2032. The analyzer in conjunction with a fast fourier transform (FFT) gives the mathematical connection between time and frequency, successively displays the frequency response spectrum (FRS) and the coherence functions are registered in the desired frequency range.
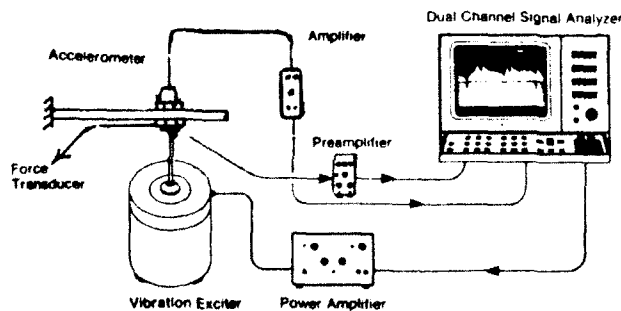
The test specimen is a square laminated plate of side length 150 mm and of thickness 5 mm. The fiber volume fraction is 56%. Five specimens were constructed and manufactured using a hand layout technique and the raw material was obtained from the Arab Company For Developed Materials, Maadi, Cairo. The mechanical properties of the composite unidirectional lamina calculated using the mixture rule, and the experimental test method are shown in Table 1.

MEASUREMENTS OF EIGENVALUES AND EIGENVECTORS

To study the effect of fiber orientation sequence on the dynamic behavior of a laminate, different boundary conditions are imposed on the specimen under the vibrational system mounted on the test rig. The specimen location in the test rig is ensured using tightened clamped and roller edges. Five laminated composite specimens with fiber orientation sequences 45/−45/0, 0/30/0, 0/5, 90/5 and 0/30/0/30/0, are fabricated to study the effect of fiber orientation sequence on the dynamic behavior of square laminated plate for different boundary conditions from an experimental and computational point of view. We execute our experimental study on five specimens which have different lamina orientation and boundary conditions. The accelerometer is attached at the desired measuring points using beeswax, according to Fig. 1. The amplitudes are measured in the normalized form at various points, the mode shapes are drawn for the first seven natural frequencies for different cases of boundary conditions imposed on the specimens.

The frequency response spectrum (FRS) is displayed by the analyzer, the average damping factor ζ is utilized to estimate seven frequency bands assuming damping linearly using half power bandwidth. The damping factor of a particular resonance can be calculated from the width of the

Fig. 2. Layout of vibration apparatus.

Table 1. Elastic moduli of E-glass polyester unidirectional composite lamina with $V_f = 0.56$

Elastic modulus	Experimental results	Results using mixture rule
E_1 (GPa)	40	40·983
E_2 (GPa)	8	8·373
G_{12} (GPa)	3·8	3·4
ν_{12}	0·25	0·20

resonance peak in the magnitude of the FRF,[16] where

$$\zeta = 1/2Q, \quad Q = w/w_d$$

The resonant frequency (w_d) and the width (w) can be found from the magnitude diagrams using the reference cursor. The value of the damping factor ζ is plotted against frequency and the effect of lamina orientation and boundary conditions are studied and discussed.

RESULTS AND DISCUSSION

The resonant frequencies, mode shapes and damping factors of square laminated composite plates (GRP) have been measured and analyzed for different lamina orientations and boundary conditions. The measured and computed values of the frequencies are given in Table 2. Comparison between the experimental and numerical results of the frequencies indicates good agreement.

Table 3 shows the variation of fundamental frequency, amplitude and damping factor for different lamina orientation at the same five layers; it can be seen that the amplitude of the specimen [45/−45/0] is relatively low compared with the others. This is due to the maximum stiffness at this orientation.

It can be noticed that the amplitude of the specimen [0/30/0/−30/0] is relatively high compared with the others, this is due to small stiffness value for this case of unsymmetry. For cases [0]5 and [90]5 the frequency must be equal in value theoretically. Table 2 shows a difference between the values of 2% in the case of [SSSS].

Figures 3 and 4 show mode shapes for a few selected cases of specimens. Figure 3 shows the first mode shapes for specimen [45/−45/0] for different boundary conditions. Figure 4 gives the first seven mode shapes for specimen [45/−45/0] simply supported along the four edges [SSSS].

As expected the measured natural frequencies are inversely proportional to the damping factor as shown in Fig. 5. In general, the damping factor

Table 2. Values of fundamental frequency in Hz for laminates for different boundary conditions (experimental and finite element results)

Boundary conditions	C—F F		S—S S		C—S		C—C		S—S	
Method	Exp.	FE	Exp.	FE	Exp.	FE	Exp.	FE	Exp.	FE
[45/−45/0]	32	33·42	64	65·5	96	97·6	144	145·2	248	249·5
[0/30/0]	28	31·56	44	46·2	84	86·5	124	126·5	240	241·5
[0]5	24	26·5	36	38·4	66	68·2	114	116·2	218	218·5
[90]5	20	22·6	32	33·4	59	62·5	96	98	216	218·2
[0/30/0/−30/0]	18	21·2	24	25·5	36	38·4	72	74·5	164	165·4

Table 3. Values of fundamental frequency, amplitude and damping factor for different boundary conditions (experimental results)

Boundary conditions		C—F F	S—S S	C—S	C—C	S—S
[45/−45/0]	Frequency	32 Hz	64 Hz	96 Hz	144 Hz	248 Hz
	Amplitude	48 dB	36 dB	32 dB	24 dB	20 dB
	Damp. factor	0·156	0·06	0·02	0·013	0·004
[0/30]	Frequency	28 Hz	44 Hz	84 Hz	124 Hz	240 Hz
	Amplitude	52 dB	41 dB	35 dB	27 dB	22 dB
	Damp. factor	0·196	0·07	0·04	0·024	0·006
[0]5	Frequency	24 Hz	36 Hz	66 Hz	114 Hz	218 Hz
	Amplitude	59 dB	44 dB	38 dB	29 dB	24 dB
	Damp. factor	0·22	0·12	0·06	0·035	0·009
[90]5	Frequency	20 Hz	32 Hz	59 Hz	96 Hz	216 Hz
	Amplitude	68 dB	64 dB	52 dB	38 dB	27 dB
	Damp. factor	0·25	0·18	0·084	0·046	0·015
[0/30/0/−30/0]	Frequency	18 Hz	24 Hz	36 Hz	71 Hz	164 Hz
	Amplitude	79 dB	65 dB	57 dB	40 dB	32 dB
	Damp. factor	0·33	0·2	0·166	0·06	0·024

Fig. 3. The first mode shape for specimen [45/ − 45/0] for different boundary conditions.
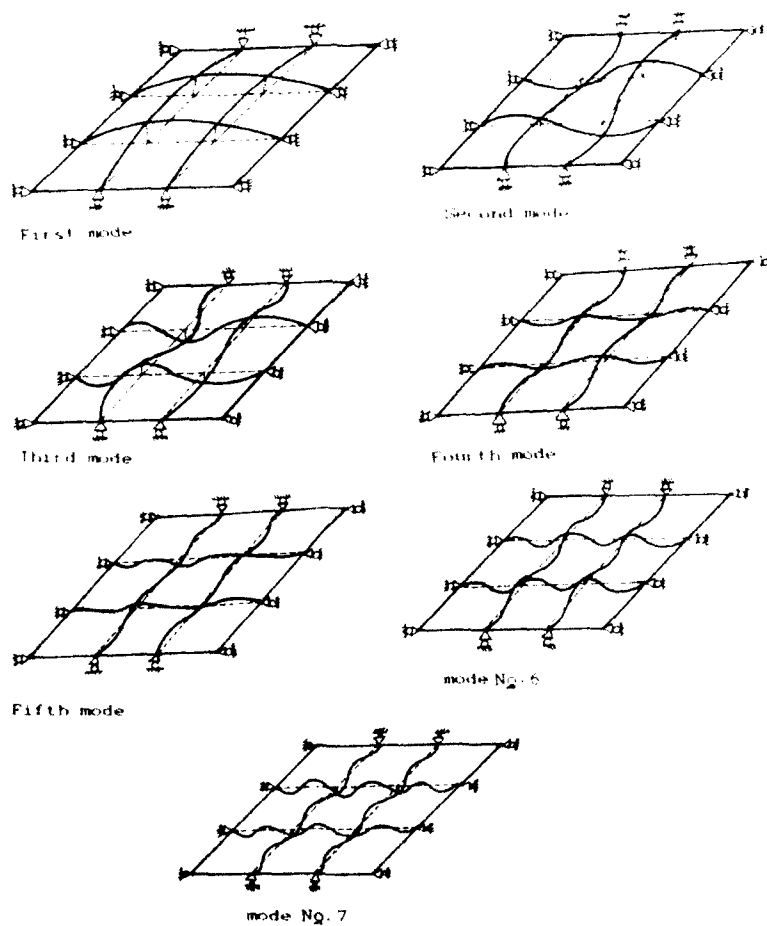
Fig. 4. The first seven mode shapes for specimen [45/ − 45/0] simply supported along the four edges [SSSS].

in composite materials is relatively high relative to bulk materials. It is difficult to control the value by variation of the mass and stiffness. From Fig. 5 it can be noticed that minimum values of the damping factor occur in the case of simply supported [SSSS] plates with different types of lamina orientation.

In all boundary conditions, it is observed that the damping factor is small for orientation [45/ −45/0] compared with other orientations. This is explained by the fact that fiber orientations in these directions are expected to increase the plate stiffness, and result in less energy dissipation. For orientation [0/30/0/ −30/0] the damping factor is high compared with other orientations. The unsymmetry decreases the plate stiffness, where the maximum energy dissipation results in a large system damping factor.

In addition, damping as a kind of energy dissipation may be primarily due to Coulomb friction due to slip in the unbonded regions of the fiber–matrix interface and one or a combination of the following: i) the fiber, ii) the matrix, iii) the fiber–matrix interface. The fibers do not contribute to the damping of a composite because of their low damping capacities but a large proportion of the stored energy must be in the matrix. Energy dissipation can occur at the fiber–matrix

interface either from relative slipping or from local stress concentration. The finite element results are typically higher than the experimental ones, as given in Table 2, and this is because of the effects of clamping pressure, air damping and transducers, and dissipation of energy at the matrix–fiber interface due to friction or impact which are not taken into consideration in the finite element model.

CONCLUSION

In the present study, the dynamic analysis of various lamina orientations of glass polyester laminates is investigated experimentally and verified analytically using the finite element method. Various specimens of different lamina orientations are fabricated utilizing a hand layout technique.

The results obtained from the present study indicate that:

1. The lamina orientation plays a dominant role for estimating the stiffness of laminated composite plates and a higher plate stiffness gives a higher frequency.

2. A finite element formulation is presented as a model for the analysis of laminated
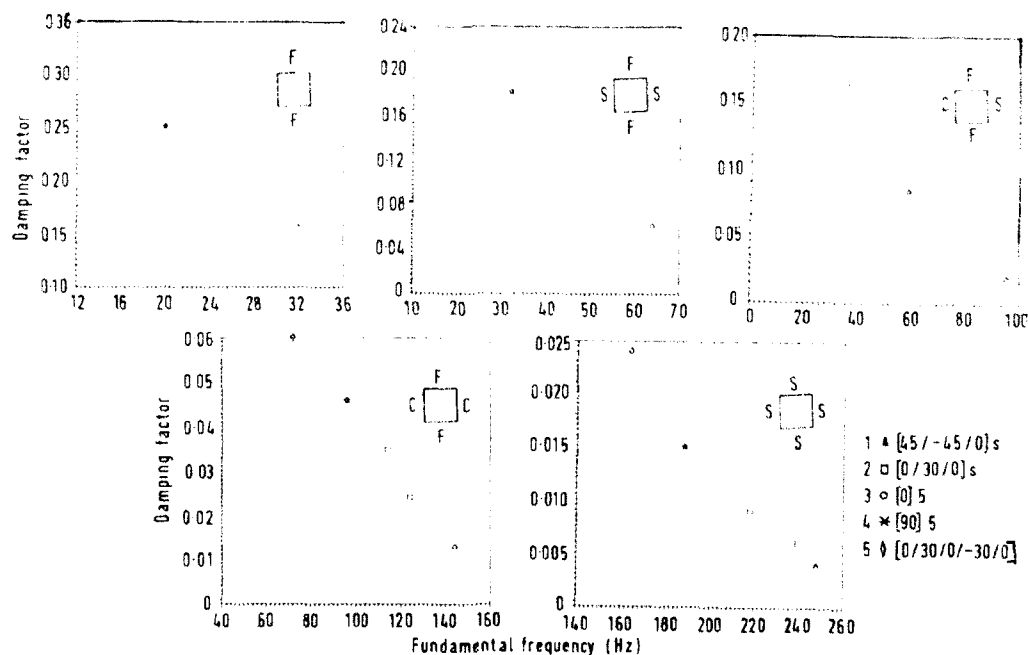
Fig. 5. The variation of damping factor with fundamental frequency for different lamina orientations.

composite plates. Eigenvalues and eigenvectors are directly obtained from the analysis. These results show good agreement with the experimental method.

(3) Damping in laminated composite plates is a kind of energy dissipation due to the matrix, fiber and matrix–fiber interface, either from relative slipping or from local stress concentration.

(4) The specimens of orientation sequence $[45/-45/0]_s$ have a relatively high frequency compared with the specimens of other orientation sequence with the same number of layers and boundary conditions. This is explained by the fact that such an orientation sequence is expected to make the plate more stiff.

(5) With the proper choice of fiber orientation, fiber and matrix materials for the composite, high values of the system damping factor for the various modes of symmetric vibration of the composite plate may be obtained.

REFERENCES

1. Gibson, R. F. & Plunket, R., Dynamics, stiffness and damping of fiber-reinforced composite materials. *Shock and Vibration Digest*, **9** 2 (February 1977).
2. Gibson, R. F. & Wilson, D. G., Dynamic mechanical properties of fiber-reinforced composite materials. *Shock and Vibration Digest*, **11** 10 (October 1979).
3. Bert, C. W., Damping of composite and sandwich panels. Part I. *Shock and Vibration Digest*, **8** 10 (October 1976).
4. Bert, C. W., Damping of composite and sandwich panels. Part II. *Shock and Vibration Digest*, **8** 11 (November 1976).
5. Bert, C. W., Composite materials: a survey of damping capacity of fiber-reinforced composites. In *Damping Applications for Vibration Control*, ed. P. J. Torvik. ASME: *AMD* **38** November 1980.
6. Bert, C. W., Vibrations of composite structures. *Recent Advances in Structural Dynamics. Proceedings*, ISVR, July, 1980.
7. Plunket, R., Damping mechanisms in fiber-reinforced laminates. *Mechanics of Composite Materials, Recent Advances. Proceedings*, 1982.
8. Chelladurai, T., Shastry, B. P. & Rao, G. V., Effect of fiber orientation behaviour of orthotropic rectangular plates. *Fiber Science and Technology*, **21** 1984 73–81.
9. Tsai, S. W. & Hahn, H. T., *Introduction To Composite Materials*. Technomic Publishing Co., Lancaster, PA, 1980.
10. Jones, R. M., *Mechanics of Composite Materials*. Scripta Book Co., Washington, DC, 1975.
11. Reddy, J. M., Survey of recent research in the analysis of composite plates. *Composite Technology Review*, **4** 3 1982.
12. Choice, R., Transient dynamic response of fiber-reinforced composite structures. *Proceedings of the AMI 5th Conf.*, 5–7 May, 1992.
13. Sun, C. T., Rao, V. S. & Sankar, B. V., Finite element analysis of intitially stressed, viscoelastically damped composite structural elements. *Current Advances in Mechanical Design & Production*. Fifth Cairo University MDP Conference, Cairo, Dec., 28–30, 1991.
14. Zienkiewicz, O. C. & Taylor, R. L., *The Finite Element Method*, 4th edn. McGraw-Hill, New York, 1989.
15. Bhagwan, B. A. & Lawrence, J. B., *Analysis and Performance of Fiber Composites*. John Wiley, New York, 1990.
16. Randall, R. B., *Application of B & K Equipment to Frequency Analysis*. Buerl and Kjear, 1977.

APPENDIX: ELEMENT STIFFNESS

The coefficient of the stiffness matrix k_{ij} according to eqn (1) is given by:

$$K_{ij} = \iint \sum_{r} \sum_{s} B_{ri} D_{rs} B_{sj}\, dx\, dy \quad (i, j = 1, 2, \ldots, n)$$

and according to eqn (2) the computed results of the coefficient D_{rs} of the flexibility matrix $[D_{ij}]$ for each case of the five specimens are as follows:

(1) $[45/-45/0]_s$

$$[D] = \begin{bmatrix} 170 & 96 & 0 \\ 96 & 176 & 0 \\ 0 & 0 & 115 \end{bmatrix}$$

(2) $[0]_5$

$$[D] = \begin{bmatrix} 41\cdot24 & 9\cdot8 & 0 \\ 9\cdot8 & 82\cdot4 & 0 \\ 0 & 0 & 38\cdot9 \end{bmatrix}$$

(3) [0/30/0]ₛ

$$[D] = \begin{bmatrix} 142 & 33 & 5\cdot1 \\ 33 & 90 & 1\cdot02 \\ 5\cdot1 & 1\cdot02 & 51\cdot5 \end{bmatrix} Nm$$

(4) [90]5

$$[D] = \begin{bmatrix} 97\cdot4 & 61\cdot1 & 0 \\ 61\cdot1 & 29\cdot4 & 0 \\ 0 & 0 & 8\cdot17 \end{bmatrix}$$

(5) [0/30/0/−30/0]

$$[D] = \begin{bmatrix} 34\cdot5 & 22\cdot3 & 0 \\ 22\cdot3 & 15\cdot07 & 0 \\ 0 & 0 & 4\cdot3 \end{bmatrix}$$

Element mass matrix for rectangular plate of unit thickness with sides a and b:

$$m = \frac{\rho ab}{176400}$$

	1	2	3	4	5	6	7	8	9	10
1	24336									
2	3432b	624b								
3	3432a	484ab	624a			Symmetric				
4	8424	2028b	1188a	24336						
5	2028b	486b	286ab	3432b	624b					
6	1188a	286ab	216a	3432a	484ab	624a				
7	2916	702b	702a	8424	1188b	2028a	24336			
8	702b	162b	169ab	1188b	216b	286ab	3432a	624b		
9	702a	169ab	162a	2028a	286ab	468a	3432a	484ab	624a	
10	8424	1188b	2028a	2916	702b	702a	8424	2028a	1188a	24336
11	1188b	216b	286ab	702b	162b	169ab	2028b	468b	286ab	3432b
12	2028a	286ab	468a	702a	169ab	162a	1188a	286ab	216a	3432a

In the present work $a = b = 0\cdot15$ m, $\rho = 1750$ kg/m³.

Large deflection initial failure analysis of angle-ply laminated plates

G. J. Turvey
Engineering Department, Lancaster University, Bailrigg, Lancaster, UK, L.. 4YR

&
M. Y. Osman
Mechanical Engineering Department, College of Engineering, PO Box 26, Athara, Sudan

A large deflection initial failure analysis of square angle-ply laminated plates subjected to uniform pressure loading is described. Approximate numerical solutions of the Mindlin laminated plate equations are derived using finite difference in conjunction with the Dynamic Relaxation (DR) technique. The solutions are scaled to satisfy the Tsai-Hill lamina failure criterion. The effects of plate slenderness, in-plane edge restraint and lay-up on the initial failure pressure and associated plate centre deflection are quantified for $\pm 45°$ laminated plates with simply supported and clamped edges. It is shown, particularly for thin plates, that in-plane edge restraint increases the initial failure pressure substantially, though changing the plate edge conditions from simply supported to clamped does not always increase the initial failure pressure.

NOTATION

a	Plate side length
A_{ij} $i,j = 1,2,6$	Plate extensional stiffness
A_i $i = 4,5$	Plate transverse shear stiffnesses
$[A]$	Matrix of plate extensional stiffnesses
$[A^*]$	Matrix of plate transverse shear stiffnesses
B_{ii} $i = 1,2$	Plate coupling stiffnesses
$[B]$	Matrix of plate coupling stiffnesses
D_{ij} $i,j = 1,2,6$	Plate flexural stiffnesses
$[D]$	Matrix of plate flexural stiffnesses
h_0	Plate thickness
k	Lamina number
k_u	Damping factor associated with the x co-ordinate direction
M_x, M_y, M_{xy}	Stress couples
$[M]$	Vector of stress couples
N_x, N_y, N_{xy}	Stress resultants
$[N]$	Vector of stress resultants
q	Transverse pressure
Q_x, Q_y	Transverse shear resultants
$[Q]$	Vector of transverse shear resultants
R, S, T	Transverse and in-plane shear strengths of a uni-directional lamina

s	Lamina surface number
u, v	Displacements in the x and y co-ordinate directions
w, w_c	Deflection and centre deflection respectively
x, y	Cartesian co-ordinates
$X_{t,c}, Y_{t,c}$	Longitudinal and transverse tensile/compressive strengths of a uni-directional lamina
$\beta \left(= \dfrac{a}{h_0} \sqrt{\dfrac{X_t}{E_1}} \right)$	Non-dimensional plate slenderness
Δt	Time increment
$\varepsilon_1^0, \varepsilon_2^0, \varepsilon_6^0$	Plate mid-plane strains
$\varepsilon_4^0, \varepsilon_5^0$	Plate mid-plane transverse shears
$[\varepsilon^0]$	Vector of plate mid-plane strains
$[\varepsilon^{*0}]$	Vector of plate mid-plane transverse shear strains
$\kappa_1^0, \kappa_2^0, \kappa_6^0$	Plate mid-plane curvatures
$[\kappa^0]$	Vector of plate mid-plane curvatures
ν_{11}	In-plane Poisson's ratio
ρ_u	Unit mass associated with the x co-ordinate direction
σ_1, σ_1	Longitudinal and transverse lamina direct stresses

530   G. J. Turvey, M. Y. Osman

| $\sigma_{11}, \sigma_{12}, \sigma_{12}$ | Lamina in-plane and transverse shear stresses |
| θ_x, ϕ | Rotation components of normal to plate mid-plane |

1 INTRODUCTION

The elastic flexural analysis of plates laminated
from long-fibre reinforced plastics such as CFRP
and GFRP carbon and glass fibre reinforced
plastics respectively is an active research topic
because of its importance to the development and
design of lightweight structures used in a wide
variety of engineering applications. Research
investigations of the flexural failure of laminated
plates that have been reported during the past 15
years are, by contrast, rather limited. It is, there-
fore, hardly surprising to realise that our under-
standing of laminated plate flexural failure
mechanics has not advanced significantly. One
aspect of flexural failure, viz. the onset or initia-
tion of failure has, however, been the subject of a
number of theoretical numerical investigations.
The approach adopted, which is akin to first yield
analysis of ductile metallic structures, is to scale
the elastic solution of the plate flexure problem
until it just satisfies an appropriate lamina failure
criterion. In these studies, exact, approximate
closed form and numerical solutions of the classi-
cal thin, first- and higher-order shear deformation
laminated plate bending equations have been
scaled, using simple linear and non-linear iterative
procedures, to satisfy a range of stress and strain
based lamina failure criteria and so provide initial
failure pressures and associated deflections. In
1980 Turvey[ ] presented several small deflection
initial failure analyses of uniformly loaded thin
plates and strips with cross and angle-ply lay-ups.
These analyses demonstrated, for unsymmetric
lay-ups, that the magnitude of the initial failure
pressure is direction dependent. Further small
deformation initial flexural and buckling failure
analyses of thin laminated plates were presented
by Adali and Nissen[ ] and Adali and Makins.[ ]
These two studies were concerned with thermal/
moisture and matrix crack distributions respec-
tively on the initial failure response.
    An approximate small deflection initial failure
analysis, based on a finite element analysis of the
Mindlin laminated plate equations, has been
presented recently by Reddy and Pandey.[ ] They
examined a number of lamina failure criteria in

their investigation and concluded that the
Tsai-Hill criterion was unsuitable for flexural
failure analysis. In Ref. 7 Turvey presented a small
deflection initial failure analysis for cross-ply
simply supported moderately thick laminated
plates based on the Tsai-Hill failure criterion and
used it to explore the effects of plate slenderness
on the initial failure response.
    Recently, Turvey and Osman developed a
finite-difference Dynamic Relaxation DR large
deflection analysis for orthotropic and laminated
Mindlin plates. They used it in Ref. 9 to carry out
both small and large deflection initial failure
analyses of the laminates described in Ref. 6 and
showed that small deflection analysis, when com-
pared with large deflection analysis, under-
estimates the initial failure pressure, especially
when the plates are thin. Moreover, they found
that the Tsai-Hill lamina failure criterion gave
similar predictions to all of the other failure
criteria used in the study. In their latest work,
Reddy and Reddy[ ] present finite element based
small and large deflection initial failure analyses
for moderately thick laminated plates which con-
firm the findings presented in Ref. 9, including the
assertion that the Tsai-Hill lamina failure
criterion is suitable for flexural failure analysis.
    Turvey and Osman[ ] quantified the effects of
slenderness and support conditions on the large
deflection initial failure pressures of cross-ply
laminated plates in an investigation completed
about 4 years ago. The present paper comple-
ments the latter one by presenting similar data for
angle-ply laminates. A brief introduction to the
governing Mindlin plate equations and the
Tsai-Hill failure criterion are presented first.
Thereafter, outlines of the numerical solution of
the governing plate equations and the procedure
used to scale the solution to satisfy the failure
criterion are given. The elastic properties and
strengths of the CFRP lamina are then introduced
and the scope of the initial failure analyses, i.e.
slenderness range, plate layups, etc., is outlined.
Finally, the detailed numerical results failure
pressures, associated plate centre deflections and
failure locations are presented and discussed.

2 LAMINATED MINDLIN PLATE EQUATIONS

In the DR analysis the Mindlin large deflection
plate equations, i.e. the equilibrium, strain-
displacement, curvature-displacement and con-

stitutive equations, retain their separate identities. It is, therefore, convenient in what follows to introduce these equations individually.

2.1 Equilibrium equations

The five equilibrium equations (two in-plane and three out-of-plane) are as follows:

$$\frac{\partial N_x}{\partial x} + \frac{\partial N_{xy}}{\partial y} = 0$$

$$\frac{\partial N_{xy}}{\partial x} + \frac{\partial N_y}{\partial y} = 0$$

$$\frac{\partial Q_x}{\partial x} + \frac{\partial Q_y}{\partial y} + N_x \frac{\partial^2 w}{\partial x^2} + 2N_{xy} \frac{\partial^2 w}{\partial x \partial y}$$

$$+ N_y \frac{\partial^2 w}{\partial y^2} + q = 0 \qquad (1)$$

$$\frac{\partial M_x}{\partial x} + \frac{\partial M_{xy}}{\partial y} - Q_x = 0$$

$$\frac{\partial M_{xy}}{\partial x} + \frac{\partial M_y}{\partial y} - Q_y = 0$$

Note, in the third of eqns (1) above the linear forms of the equilibrium equations are obtained by deleting the three terms

$$N_x \frac{\partial^2 w}{\partial x^2}, \quad 2N_{xy} \frac{\partial^2 w}{\partial x \partial y} \text{ and } N_y \frac{\partial^2 w}{\partial y^2}$$

2.2 Strain and curvature relations

The direct, in-plane shear and transverse shear strains of the plate mid-plane are expressed in terms of derivatives of the displacement and rotation components as follows:

$$\varepsilon_x^0 = \frac{\partial u}{\partial x} + \frac{1}{2}\left(\frac{\partial w}{\partial x}\right)^2$$

$$\varepsilon_y^0 = \frac{\partial v}{\partial y} + \frac{1}{2}\left(\frac{\partial w}{\partial y}\right)^2$$

$$\varepsilon_{xy}^0 = \frac{\partial u}{\partial y} + \frac{\partial v}{\partial x} + \frac{\partial w}{\partial x}\frac{\partial w}{\partial y} \qquad (2)$$

$$\varepsilon_{xz}^0 = \phi_x + \frac{\partial w}{\partial x}$$

$$\varepsilon_{yz}^0 = \phi_y + \frac{\partial w}{\partial y}$$

Likewise, the mid-plane curvatures and twist are expressed in terms of derivatives of the rotation components as follows:

$$\kappa_x^0 = \frac{\partial \phi_x}{\partial x}$$

$$\kappa_y^0 = \frac{\partial \phi_y}{\partial y} \qquad 3$$

$$\kappa_{xy}^0 = \frac{\partial \phi_y}{\partial x} + \frac{\partial \phi_x}{\partial y}$$

2.3 Constitutive relations for angle-ply lay-ups

The constitutive relations for shear deformable angle-ply laminated plates may be expressed as follows:

$$\{N\} = [A]\{\varepsilon^0\} + [B]\{\kappa^0\}$$

$$\{M\} = [B]\{\varepsilon^0\} + [D]\{\kappa^0\} \qquad 4$$

$$\{Q\} = [A^*]\{\varepsilon^{*0}\}$$

in which the stress resultant, shear stress resultant and stress couple vectors are:

$$\{N\}^T = \{N_x \ N_y \ N_{xy}\}, \quad \{M\}^T = \{M_x \ M_y \ M_{xy}\},$$

$$\{Q\}^T \{Q_x \ Q_y\}$$

and the in-plane strain, curvature and twist and the transverse shear strain vectors are:

$$\{\varepsilon^0\}^T = \{\varepsilon_x^0 \ \varepsilon_y^0 \ \varepsilon_{xy}^0\}, \quad \{\kappa^0\}^T = \{\kappa_x^0 \ \kappa_y^0 \ \kappa_{xy}^0\},$$

$$\{\varepsilon^{*0}\}^T = \{\varepsilon_{xz}^0 \ \varepsilon_{yz}^0\}$$

and the material stiffness matrices are:

$$[A] = \begin{bmatrix} A_{11} & A_{12} & 0 \\ A_{12} & A_{22} & 0 \\ 0 & 0 & A_{66} \end{bmatrix}$$

$$[B] = \begin{bmatrix} 0 & 0 & B_{16} \\ 0 & 0 & B_{26} \\ B_{16} & B_{26} & 0 \end{bmatrix}$$

$$[D] = \begin{bmatrix} D_{11} & D_{12} & 0 \\ D_{12} & D_{22} & 0 \\ 0 & 0 & D_{66} \end{bmatrix}$$

$$[A^*] = \begin{bmatrix} A_{44} & 0 \\ 0 & A_{55} \end{bmatrix}$$

The individual stiffnesses, $A_{11}, \ldots, A_{66}, B_{16}, B_{26}, D_{11}, \ldots, D_{66}$ and A_{44}^*, A_{55}^* are evaluated in the

usual way as described in Ref. 12. Note too, that for orthotropic plates $|B_{ij}| = 0$.

2.4 Boundary conditions

Equations (1)–(4) are solved for specific sets of plate edge conditions, which are specified in terms of prescribed values of the displacement, stress resultant, etc., components. For laminated Mindlin plates five conditions have to be defined along each edge. In consequence, it is possible to define several types of simply supported and clamped edge conditions, depending upon which particular displacement, etc., components are specified along the plate edge. As far as the present study is concerned the plates are considered to be either simply supported or clamped along all edges. Four types of simply supported and two types of clamped edge are considered. However, two of the simply supported edge conditions (SS3 and SS4) are only used in the computations undertaken to verify the DR plate analysis. The support conditions used in the large deflection failure study are designated respectively as: SS1, SS2, CC1 and CC2. Figure 1 shows the six sets of edge conditions. The principal difference between the type 1 and type 2 edge conditions is that in the former case in-plane displacements are suppressed, whereas in the latter they are not.

3 TSAI–HILL LAMINA FAILURE CRITERION

As shown previously by Turvey and Osman[2,3] there are a number of lamina failure criteria which may be used for initial flexural failure analyses. For the present study the following criteria were used: Maximum Stress, Maximum Strain, Hoffman, Tsai–Hill and Tsai–Wu. However, as similar failure pressures and deflections were obtained

with each, it is convenient to restrict attention to just one. Thus, all of the results presented in the paper have been derived from the Tsai–Hill lamina failure criterion. This criterion may be expressed in terms of lamina stresses as follows:

$$F_{11}\sigma_1^2 + 2F_{12}\sigma_1\sigma_T + F_{22}\sigma_T^2 + F_{44}\sigma_{LZ}^2 + F_{55}\sigma_{TZ}^2$$
$$+ F_{66}\sigma_{LT}^2 = 1 \tag{5}$$

in which the strength coefficients, F_{ij}, are defined as:

$$F_{11} = X_{tc}^{-2}, \; F_{12} = -X_{tc}^{-2}, \; F_{22} = Y_{tc}^{-2}, \; F_{44} = R^{-2},$$
$$F_{55} = S^{-2}, \; F_{66} = T^{-2}$$

and the subscripts, t and c, denote tensile and compressive strength values respectively.

4 DR SOLUTION OF THE MINDLIN LAMINATED PLATE EQUATIONS

The governing equations (1)–(4) are solved approximately using the DR algorithm. In order to be able to apply this algorithm, the equilibrium equations have first to be rendered quasi-dynamic through the addition of inertia and damping terms to their right hand sides. Thus, for example, the first of eqns (1) becomes:

$$\text{(LHS of (1a))} = \rho_u \frac{\partial^2 u}{\partial t^2} + k_u \frac{\partial u}{\partial t}$$

in which ρ_u and k_u are mass and damping terms respectively.

The acceleration and velocity terms in the above equation may now be replaced by the following approximations:

$$\frac{\partial^2 u}{\partial t^2} = \frac{1}{\Delta t}\left[\left(\frac{\partial u}{\partial t}\right)^a - \left(\frac{\partial u}{\partial t}\right)^b\right],$$

$$\frac{\partial u}{\partial t} = \frac{1}{2}\left[\left(\frac{\partial u}{\partial t}\right)^a + \left(\frac{\partial u}{\partial t}\right)^b\right]$$

and after re-arrangement the following velocity equation is obtained:

$$\left(\frac{\partial u}{\partial t}\right)^a = \frac{1}{(1+k_u^*)}\left[(1-k_u^*)\left(\frac{\partial u}{\partial t}\right)^b + \left(\frac{\Delta t}{\rho_u}\right)\text{(LHS of (1a))}\right]$$

in which the superscripts, a and b, denote the values after and before the time increment, Δt and $k_u^* = \frac{1}{2}k_u\Delta t\rho_u^{-1}$.

The remaining four equilibrium equations may be similarly transformed into initial value format.

In order to integrate the velocities and obtain displacements, an appropriate integration formula is required. The following simple formula is used:

$$u^a = u^b + \Delta t \left(\frac{\partial u}{\partial t}\right)^a$$

Thus, the velocity equations, i.e. the transformed equilibrium equations, the displacement integration equations, together with eqns (2)–(4) and the boundary conditions constitute the complete set of equations for the application of the DR algorithm. A somewhat more detailed account of the DR algorithm in the context of Mindlin plate analysis is given in Ref. 8.

To obtain numerical solutions, the equations have to be discretised. A conventional central finite-difference scheme was chosen. The finite-difference DR algorithm operates on the system of equations sequentially until the velocities become negligibly small and the static displaced configuration is achieved. Rapid decay of the velocities is ensured by appropriate choices of the damping factors and the use of fictitious densities. Further details of the latter may be found in Ref. 13.

5 INITIAL FLEXURAL FAILURE ANALYSIS

The approximate solution of the Mindlin laminated plate equations constitutes only a part of the initial flexural failure analysis. In order to determine the initial failure pressure and associated plate deflections, it is necessary to determine the particular approximate solution of the plate equations which just satisfies the Tsai–Hill failure criterion, i.e. eqn (5), at one (or in the case of symmetry at several) points. This is achieved by scaling the approximate solution. In the case of a small deflection solution, simple linear scaling may be used as explained in Ref. 9. On the other hand, it is necessary to use an iterative procedure (non-linear scaling) with a large deflection analysis. Details of a convenient iterative procedure are also given in Ref. 9.

6 VALIDATION OF INITIAL FAILURE ANALYSIS

A number of check analyses were undertaken to establish the accuracy of the initial failure results derived from the DR finite-difference solution of the Mindlin laminated plate equations. These consisted of comparisons of DR elastic small and large deflection solutions with alternative exact and approximate solutions. *It was found that the*

DR analysis solutions were in close agreement with these solutions (less than 1% difference provided a 5×5 mesh over one quarter of the plate was used. Where symmetry could not be exploited a 10×10 mesh over the whole plate gave results of similar accuracy. By applying only a small transverse pressure, it was possible to obtain small deflection initial failure results with the DR analysis. Thus, a series of small deflection initial failure analyses for single-layer orthotropic SS3 edge conditions) and two and four layer ±45° antisymmetric angle-ply square plates with SS3 edge conditions (see Fig. 1) were carried out. The plates were assumed to be laminated from unidirectional CFRP material with elastic modular and strength ratios as listed in Tables 1 and 2. Exact solutions, based on Fourier series analysis, were also computed for the same range of plate lay-ups. The DR approximate and Fourier exact initial failure pressures and associated plate centre deflections are listed in Table 3. Clearly, the DR initial failure results agree reasonably well with the exact results. It was, therefore, concluded that the DR analysis could be used with reasonable confidence to compute the main large deflection initial failure results of this study.

7 INITIAL FLEXURAL FAILURE RESULTS FOR ±45° ANGLE-PLY PLATES

As mentioned in the Introduction attention is focused on the effects of plate slenderness, edge support conditions and lay-up antisymmetry on the initial failure response of square CFRP plates. Thus, computations have been made for: plate span to thickness ratios in the range 10–50 (i.e. the practical range of thick to thin plates), two types of simply supported and clamped edge condition and symmetric and antisymmetric ±45° lay-ups. The large deflection initial failure results for the above range of parameters are presented in Tables 4 and 5 for the simply supported and clamped plates respectively. Also included in these tables are the failure initiation locations as well as the values of the square of the dimensionless plate slenderness,

$$\beta\left(= \frac{a}{h_0}\sqrt{\frac{X_t}{E_t}}\right)$$

In order to appreciate more clearly the effects of lay-up, slenderness, etc., on the initial failure
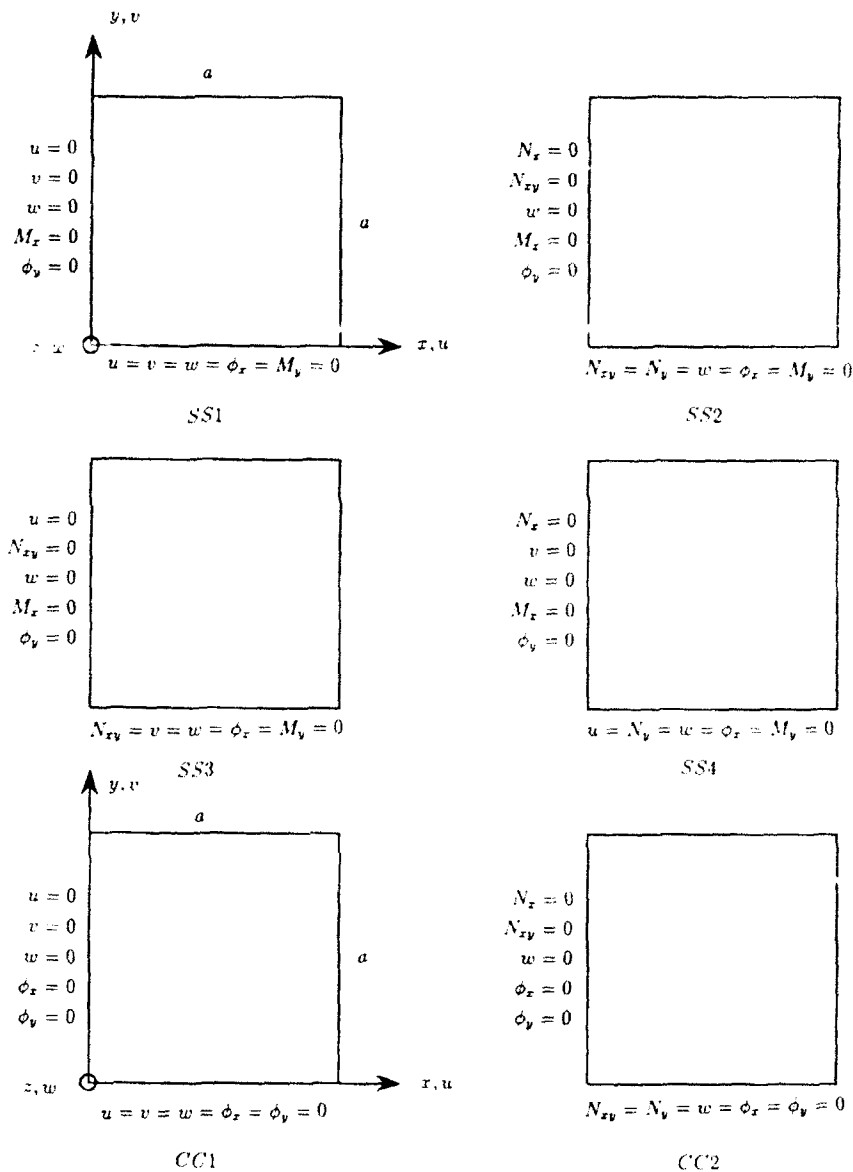
Fig. 1. Edge conditions for simply supported and clamped plates.

Table 1. Elastic properties of a uni-directional CFRP lamina

$\dfrac{E_1}{E_1}$	$\dfrac{G_{11}}{E_1}$	$\dfrac{G_{11}}{E_1}$	$\dfrac{G_{11}}{E_1}$	v_{11}
12·31	0·526	0·526	0·314	0·24

response it is helpful to plot initial failure pressures and associated plate centre deflections against β^2. This information is presented in Figs 2a and 2b for simply supported plates and in Fig. 2a and 3, it is clear 3 (initial failure pressures only) for clamped plates. Focusing attention on the initial failure pressure results first, i.e. Figs 2a and 3, it is clear that the dimensionless failure pressure increases with β^2. However, for both the SS2 and CC2 edge conditions, i.e. the in-plane free conditions, the failure pressure appears to show an almost linear increase with β^2, irrespective of whether the lay-up is symmetric or antisymmetric. The non-dimensional initial failure pressure versus β^2 relationship for plates with SS1 and CC1 edge conditions, i.e. in-plane fixed edges, is quite different, being markedly non-linear.

Looking at the results for simply supported edge conditions in more detail, it is evident from Fig. 2a that when the lay-up is antisymmetric the difference between the initial failure pressure for in-plane fixed and free edge conditions may be very large. For example, in the case of a thin two-layer plate, i.e. $\beta^2 = 10.175$, the initial failure pressures differ by a factor approaching three. Even when coupling is diminished, as in the case of a four-layer antisymmetric plate, this factor still exceeds two. However, in the absence of bending–shearing coupling (cf. the four-layer symmetric angle-ply plate), changing the in-plane edge restraint from fixed to free in a thin simply supported plate ($\beta^2 = 10.175$) increases the initial failure pressure only by about 50% and this effect diminishes rapidly as the plate becomes thicker.

Turning now to the associated plate centre deflections for simply supported $\pm 45°$ angle-ply plates shown in Fig. 2a, it is clear that although in-plane fixed and free edge conditions result in large differences in initial failure pressures for thin plates, this is not reflected in correspondingly large differences in plate centre deflections. For the four-layer symmetric angle-ply plate, it is evident that the degree of in-plane edge restraint does not affect the deflection at which failure initiates. Similarly, for slender two- and four-layer antisymmetric angle-ply plates in-plane fixity only increases/decreases the associated centre deflection by a few percent.

Considering now the initial failure pressures for clamped angle-ply plates, i.e. Fig. 3, it is clear that the same general trends as for simply supported plates are evident, viz. increasing the degree of in-plane edge restraint raises the initial failure pressure significantly for thin plates. However, for clamped plates, there is no significant difference between the associated plate centre deflections regardless of the degree of in-plane edge restraint and whether the plate is moderately thick or thin (see Table 5).

It is of interest to compare the effects of flexural edge restraint on the *initial failure results for these angle-ply plates*. Thus, referring to Figs 2a and 3,

Table 2. Strength ratios of a uni-directional CFRP lamina

$\dfrac{X}{Y}$	$\dfrac{X}{Y}$	$\dfrac{Y}{Y}$	$\dfrac{R}{Y}$	$\dfrac{S}{Y}$	$\dfrac{I}{Y}$
34·6	38·7	1·000	1·543	1·984	1·984

Note: $\dfrac{E_1}{Y} = 245.7$.

Table 3. Comparison of DR and exact small deflection initial failure analysis results for uniformly loaded square plates with simply supported edge conditions (shear correction factors = $\tfrac{5}{6}$)

Lay-up	$\dfrac{qa^4}{E_1 h^4}$	$\dfrac{w_c}{h}$	$\dfrac{x}{a}$	$\dfrac{y}{a}$	k	s	$\dfrac{h_c}{a}$	Plate edge conditions
Orthotropic	5·669	0·0819	0·5	0·3	1	3	0·1	SS3
	5·584	0·0812	0·5	0·3	1	3		
	154·98	1·8615	0·5	0·3	1	3	0·02	
	150·20	1·8109	0·5	0·2	1	3		
$45°/-45°$	3·212	0·0570	0·0	0·0	1	1	0·1	SS4
	3·322	0·0595	0·1	0·1	1	1		
	79·076	1·2467	0·0	0·0	1	1	0·02	
	83·296	1·3241	0·1	0·1	1	1		
$45°/-45°/45°/-45°$	7·488	0·0777	0·0	0·0	1	1	0·1	SS4
	7·277	0·0761	0·2	0·2	1	1		
	180·77	1·5213	0·0	0·0	1	1	0·02	
	188·97	1·5974	0·2	0·2	1	1		

[a] k = lamina number (starting from upper loaded plate surface).
[b] s = lamina failure surface (1 denotes upper and 3 lower surface).
[c] DR approximate analysis results.
[d] DR results computed with a 5 × 5 uniform mesh over a quarter of the plate.
[e] Exact analysis (series solution) results.
[f] DR results computed with a 10 × 10 uniform mesh over the whole plate.
[g] DR results computed with a 10 × 10 uniform mesh over the whole plate.

Table 4. DR large deflection initial failure results for uniformly loaded, square, simply supported (SS1 and SS2 edge conditions) angle-ply laminated plates (shear correction factors = ⅚)

Lay-up	$\dfrac{a}{h_o}$	$\dfrac{qa^4}{E_1 h_o^4}$	$\dfrac{w_c}{h_o}$	$\dfrac{x}{a}$	$\dfrac{y}{a}$	k	s	β
	10	4·506[a]	0·0593	1·0	0·2	1	1	0·407
		3·198[b]	0·0570	0·0	1·0	2	3	
	20	18·191	0·2006	1·0	0·2	1	1	1·628
		12·127	0·1959	1·0	1·0	2	3	
(45°/−45°)	30	43·479	0·3980	0·2	1·0	1	1	3·663
		25·868	0·4006	0·0	0·0	2	2	
	40	89·661	0·6240	0·8	0·0	1	1	6·512
		43·672	0·6415	0·0	0·0	2	3	
	50	171·36	0·8643	0·0	0·9	1	1	10·175
		65·581	0·8988	0·0	0·0	2	3	
	10	2·530	0·0279	1·0	1·0	1	1	0·407
		2·512	0·0277	1·0	1·0	4	3	
	20	9·433	0·0876	0·0	0·0	1	1	1·628
		9·329	0·0874	0·0	0·0	4	3	
(45°/−45°/−45°/45°)	30	21·628	0·1873	0·0	0·0	1	1	3·663
		20·570	0·1858	1·0	1·0	4	3	
	40	41·363	0·3245	0·0	0·0	1	1	6·512
		36·467	0·3226	0·0	0·0	4	3	
	50	74·428	0·4967	0·0	0·0	1	1	10·175
		57·000	0·4930	0·0	0·0	4	3	
	10	8·171	0·0796	0·5	0·5	4	4	0·407
		7·388	0·0767	1·0	0·0	4	3	
	20	32·828	0·2533	0·5	0·5	4	3	1·628
		27·830	0·2446	0·0	0·0	4	3	
		32·828	0·2533	0·5	0·5	4	3	
(45°/−45°/45°/−45°)	30	84·918	0·5190	0·5	0·5	4	3	3·663
		58·914	0·4913	0·0	0·0	4	3	
	40	194·50	0·8417	0·9	0·0	1	1	6·512
		99·744	0·7910	0·0	0·0	4	3	
	50	383·90	1·1604	0·9	0·0	1	1	10·175
		148·32	1·1070	0·0	0·0	4	3	

[a] SS1 results.
[b] SS2 results.
Values computed with a 10×10 uniform mesh over the whole plate.
Values computed with a 5×5 uniform mesh over a quarter plate.
Values computed with a 10×10 uniform mesh over the whole plate.

it is noticeable that in the case of the symmetric four-layer plate, changing the edge condition from simply supported to clamped produces a very large increase in the initial failure pressure (irrespective of in-plane edge restraint and slenderness). The situation for two- and four-layer antisymmetric angle-ply plates is markedly different, i.e. changing from simply supported to clamped edge conditions produces a reduction in the initial failure pressure when there is full in-plane fixity and an increase when there is no in-plane restraint.

In the last figure of the paper, i.e. Fig. 4, the effect of changing the flexural edge restraint (in the presence of full in-plane fixity) on the associated plate centre deflection is shown. In all cases, the deflections at the initiation of failure are larger for simply supported than for clamped plates. For example, the centre deflection of a simply supported four-layer antisymmetric angle-ply plate is nearly twice that of the corresponding clamped plate. The differences in deflection, though substantial, are not as large for the other two lay-ups considered.

Table 5. DR large deflection initial failure results for uniformly loaded, square, clamped (CC1 and CC2 edge conditions) angle-ply laminated plates (shear correction factors = $\frac{5}{6}$)

Lay-up	$\dfrac{a}{h_0}$	$\dfrac{qa^4}{E_1 h_0^4}$	$\dfrac{w}{h_0}$	$\dfrac{x}{a}$	$\dfrac{y}{a}$	k	s	p^2
$(45°/-45°)$	10	4·002[a]	0·0319	0·0	0·6	1	1	0·407
		4·285[b]	0·0341	0·4	1·0	1	1	
	20	17·010	0·1044	0·4	1·0	1	1	1·628
		17·237	0·1056	0·4	1·0	1	1	
	30	41·000	0·2320	0·5	0·0	1	1	3·663
		39·176	0·2261	0·4	1·0	1	1	
	40	80·300	0·4061	1·0	0·5	1	1	6·512
		71·500	0·4021	0·6	1·0	2	3	
	50	150·40	0·6237	0·0	0·5	1	1	10·175
		115·62	0·6279	0·4	0·0	2	3	
$45°/-45°/45°/-45°$	10	6·633	0·0381	0·6	1·0	1	1	0·407
		6·633	0·0381	0·6	1·0	1	1	
	20	32·201	0·1234	0·6	1·0	1	1	1·628
		31·999	0·1232	0·6	1·0	1	1	
	30	79·133	0·2658	1·0	0·6	1	1	3·663
		76·698	0·2652	0·4	0·0	1	1	
	40	158·00	0·4685	0·4	0·0	1	1	6·512
		142·20	0·4668	0·6	1·0	1	1	
	50	287·38	0·7148	0·0	0·4	1	1	10·175
		230·34	0·7206	0·6	1·0	1	1	
$45°/-45°/45°/-45°$	10	7·084	0·0391	0·4	1·0	1	1	0·407
		7·265	0·0401	0·0	0·6	1	1	
	20	30·925	0·1154	0·6	0·0	1	1	1·628
		31·327	0·1169	1·0	0·4	1	1	
	30	74·494	0·2480	0·6	0·0	1	1	3·663
		72·268	0·2429	0·6	0·0	1	1	
	40	143·28	0·4352	0·0	0·5	1	1	6·512
		132·68	0·4284	0·0	0·6	1	1	
	50	252·89	0·6667	0·5	0·0	1	1	10·175
		215·36	0·6749	0·0	0·6	1	1	

[a] CC1 results.
[b] CC2 results.
Values computed with a 10×10 uniform mesh over the whole plate.
Values computed with a 5×5 uniform mesh over a quarter plate.
Values computed with a 10×10 uniform mesh over the whole plate.

8 CONCLUDING REMARKS

The authors have presented an approximate large deflection initial failure analysis, based on Mindlin laminated plate theory, of uniformly loaded square angle-ply plates. The results of a parameter study for thick and thin $\pm 45°$ laminates show that the initial failure pressures are increased significantly by suppressing in-plane displacements at the plate edges, especially when the plates are thin. It is further shown, in the case of simply supported plates, that the associated centre deflection at the initiation of failure is either unaffected or is marginally increased as a result of suppressing in-plane edge displacements. For clamped plates the associated plate centre deflections are not influenced by the degree of in-plane restraint at the edge of the plate. Perhaps the most significant finding to emerge from the study is that when the plate lay-up is antisymmetric, changing the flexural support conditions from simply supported to clamped does not necessarily result in an increase in the initial failure pressure. Only when the flexural support conditions are changed in the presence of full in-plane edge restraint does this arise, otherwise a decrease in failure pressure occurs.
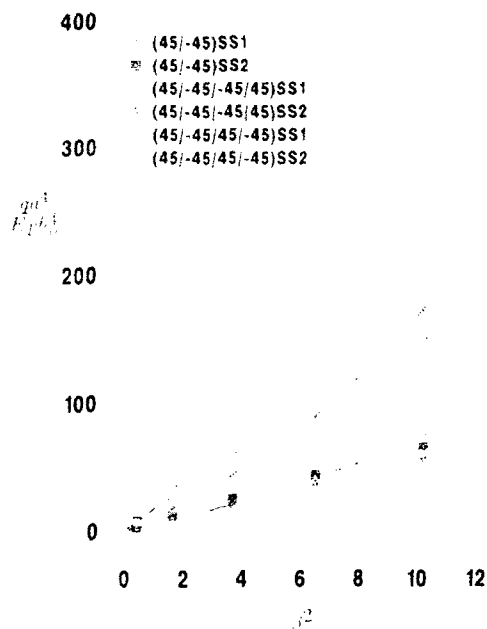
Fig. 2a. Initial failure pressure versus plate slenderness simply supported angle-ply laminates.
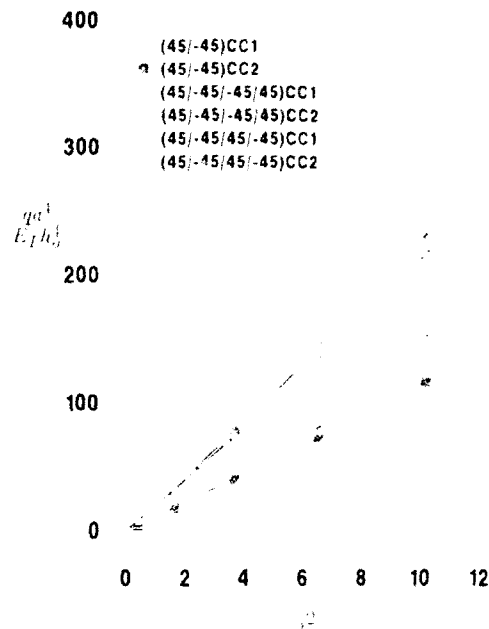
Fig. 3. Initial failure pressure versus plate slenderness clamped angle-ply laminates.
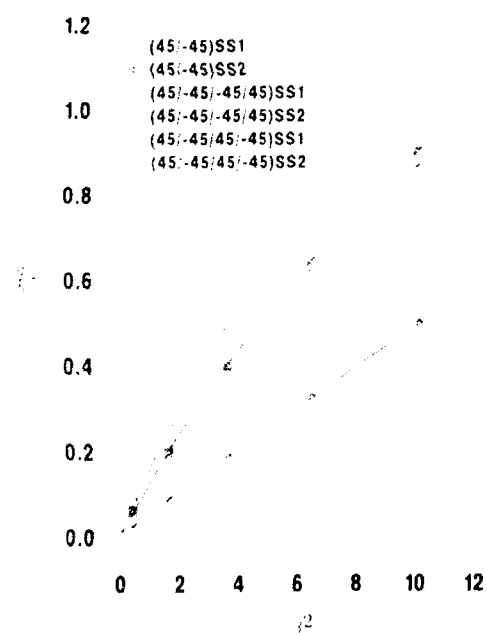
Fig. 2b. Associated plate centre deflection simply supported angle-ply laminates.
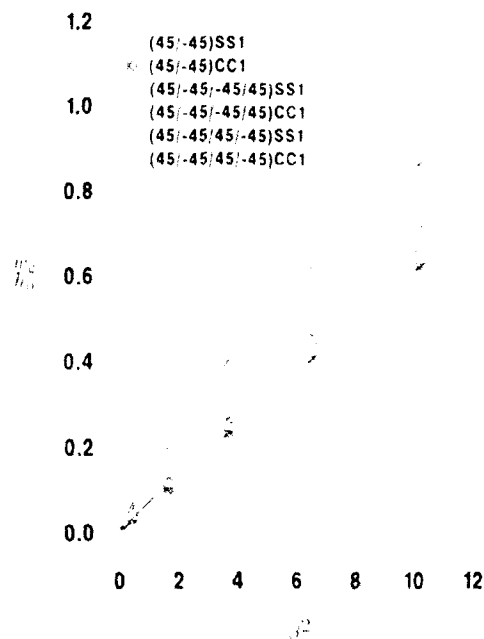
Fig. 4. Comparison of associated plate centre deflections versus plate slenderness for angle-ply laminates with SS1 and CC1 edge conditions.

ACKNOWLEDGEMENTS

REFERENCES

1. Turvey, G. J., An initial flexural failure analysis of symmetrically laminated cross-ply rectangular plates. *International Journal of Solids and Structures*, **16** (5) (1980) 451–63.

2. Turvey, G. J., Flexural failure analysis of angle-ply laminates of GFRP and CFRP. *Journal of Strain Analysis*, **15** (1) (1980) 43–9.

3. Turvey, G. J., A study of the onset of flexural failure in cross-ply laminated strips. *Fibre Science and Technology*, **13** (5) (1980) 325–36.

4. Adali, S. & Nissen, H., Micromechanical initial failure analysis of symmetrically laminated cross-ply plates. *International Journal of Mechanical Sciences*, **29** (1) (1987) 83–92.

5. Adali, S. & Makins, R. K., Buckling of unsymmetrical cross-ply laminates with matrix cracks. *International Journal of Mechanical Sciences*, **33** (10) (1991) 851–61.

6. Reddy, J. N. & Pandey, A. J., A first-ply failure analysis of composite laminates. *Computers and Structures*, **25** (3) (1987) 371–93.

7. Turvey, G. J., Effects of shear deformation on the onset of flexural failure in symmetric cross-ply laminated rectangular plates. In *Composite Structures 4, Vol. 2*, ed. I. H. Marshall. Elsevier Applied Science, Chapter 11, 1987, pp. 2.141–2.163.

8. Turvey, G. J. & Osman, M. Y., DR large deflection analysis of orthotropic Mindlin plates with simply-supported and clamped-edge conditions. *Composite Engineering*, **1** (4) (1991) 235–48.

9. Turvey, G. J. & Osman, M. Y., Exact and approximate linear and nonlinear initial failure analysis of laminated Mindlin plates. In *Composite Structures 5*, ed. I. H. Marshall. Elsevier Applied Science, London, Chapter 4, 1989, pp. 133–71.

10. Reddy, Y. S. N. & Reddy, J. N., Linear and non-linear failure analysis of composite laminates with transverse shear. *Composites Science and Technology*, **44** (3) (1992) 227–55.

11. Turvey, G. and Osman, M., Large deflection initial failure of laminated rectangular plates. *Developments in the Science and Technology of Composite Materials*, ed. A. R. Bunsell, P. Lamicq & A. Massiah. Elsevier Applied Science, London, 1989, pp. 321–33.

12. Jones, R. M., *Mechanics of Composite Materials*, McGraw-Hill Kogakusha, Tokyo, 1975.

13. Cassell, A. C. & Hobbs, R. E., Numerical stability of dynamic relaxation analysis of non-linear structures. *International Journal of Numerical Methods in Engineering*, **10** (6) (1976) 1407–10.

Static stress analysis of composite spur gears using 3D-finite element and cyclic symmetric approach

S. Mohamed Nabi & N. Ganesan

Machine Dynamics Laboratory, Department of Applied Mechanics, Indian Institute of Technology, Madras 600 036, India

It is more realistic to include the effect of adjacent teeth stiffness while evaluating the root stresses of a gear which is a rotationally periodic structure. This requires very large core and computational time. In the present analysis an attempt has been made to compare the root stresses with and without considering the effects of adjacent gear teeth stiffnesses using the concept of cyclic symmetry. Further, an attempt has been made to study the performance of a composite spur gear using the above approach. It is found that the root structure predicted by the method of cyclic symmetry is less for both isotropic and orthotropic spur gears.

1 INTRODUCTION

Fibre reinforced composite materials are being used for different structural components in space vehicles, aircraft and automobiles. Transmission gears made of composite materials have been used in some types of washing machines, gear pumps, etc. It has been reported in the literature that the life of a heavy duty gear pump in a chemical industry showed an increase of 1000 h when the conventional material is replaced by reinforced composite material.[1] Because of this and other advantages such as lower weight/stiffness ratio, composite gears may replace conventional material gears in power transmission systems. In the literature it is found that the boundary condition used for the study of gear tooth stresses is that either the base of the gear tooth is fixed or the sides are fixed, or both, none of which is correct. In reality the base of a gear tooth is fixed and the sides are subjected to the internal reactions of both teeth on either side of the teeth under study. Analysis of gears with such a boundary condition is possible only by making use of the concept of cyclic symmetry.

A cyclic symmetric structure is a rotationally periodic structure. Such a structure may operate with or without cyclic symmetric loading. Wildheim[2] derived this principle and applied it to the vibrations of a rotating regular polygon. Thomas[3] has used this approach for the dynamics of turbine blades and alternator end windings. The above authors have used conventional solution procedures, whereas the entire stiffness and mass matrices are assembled and used in the solution procedure. This type of analysis requires larger core (memory) for storage. Finite element analysis using a two dimensional element and the cyclic symmetric approach for an isotropic spur gear was carried out by Ramamurti and Ananda Rao.[4] Single tooth finite element analysis of composite gear was done by Vijayarangan and Ganesan.[5]

In the present work an attempt has been made to analyse the variation of tensile stresses on the load surface, which are responsible for the catastrophic failure of a gear tooth. Isotropic and composite materials are considered in the analysis. In the finite element model three dimensional eight noded brick elements with three degrees of freedom per node have been used. Usually the structural stiffness matrix of any system is in banded form. In the present case, the analysis uses one gear tooth with the coupling stiffnesses of the adjacent gear teeth. This inclusion makes the stiffness matrix fully populated. But the use of a conventional full matrix assembly procedure is inefficient and the core needed for such analysis is very high. Hence to solve this problem the out-of-core technique, namely, Potter's scheme has been used in the solution procedure, which uses the partition-wise assembly technique.

2 STIFFNESS AND FORCE EVOLUTION

2.1 Stiffness description

A gear wheel is a rotationally periodic structure having a number of identical substructures equal to the number of teeth in the gear. This periodicity of the gear teeth is explained in Fig. 1. Here, N is the number of teeth in the gear and n is number of stations considered in a single tooth. In the present model a gear tooth is divided into six (n) radial divisions. The number of nodes in each division will be different as explained in the figure. As described earlier, in the present case the stiffness matrix is a fully populated matrix and it is a hermitian matrix also. The static equilibrium for the gear wheel analysis can be represented as follows:

$$\begin{bmatrix} B_1 A_1 0 & & & A_n^1 k_1 \\ A_1 B_2 A_2 & & & 0 \\ & \cdots A_n^1 & B_n & A_n \\ A_n^1 k_2 0 & 0 & A_n & B_n \end{bmatrix} \begin{Bmatrix} z_1 \\ z_2 \\ z_n \\ z_n \end{Bmatrix} = \begin{Bmatrix} g_1 \\ g_2 \\ g_n \\ g_n \end{Bmatrix}$$

$$(1)$$

where B_i is a symmetric submatrix of a single station considered in a substructure and A_i is a coupling stiffness submatrix between two adjacent stations. g_i and z_i are displacement and force vectors of a single station.

$$k_1 = e^{-i\mu}; \quad k_2 = 1/k_1 \text{ and } i = 1, 2, 3, \ldots, n$$

μ is the angle subtended at the centre by the sides of the gear tooth under consideration which can be obtained as $2\pi/N$.

2.2 Force and displacement evaluation

In the present case, a gear wheel with unit contact ratio has been assumed. The loading on one gear
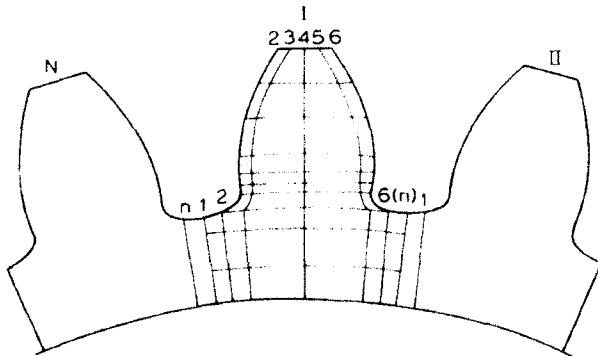
Fig. 1. Finite element model.

tooth and zero loads on all other teeth leads to asymmetric loading. A method of analysis of asymmetric loading has been presented in Ref 6 and is explained here. The load acting on that tooth is expressed as several Fourier harmonics. For each harmonic the analysis of the repeating sector (one tooth) is carried out. The total response is obtained as sum of the individual harmonic responses.

Since the stiffness of a cyclic symmetric structure is in polar coordinates, the forces are also expressed in the same coordinate system.

$$F(r, \mu, z) = f_1 e^{i\mu} + f_2 e^{i\mu} + \ldots + f_n$$

$$2$$

where $f(r, z)$ are coefficients corresponding to the jth harmonic and f_n is the axisymmetric component.

If $b_1, b_2, \ldots, b_n$ are the loads in the repeated structures $1, 2, \ldots, N$ then the corresponding Fourier components are given by

$$\begin{Bmatrix} b_1 \\ b_2 \\ b_n \end{Bmatrix} = \begin{bmatrix} e^{i\mu} & e^{2i\mu} & \ldots & 1 \\ e^{i\mu} & e^{4i\mu} & \ldots & 1 \\ \vdots & \vdots & & \vdots \\ 1 & 1 & & 1 \end{bmatrix} \begin{Bmatrix} f_1 \\ f_2 \\ f_N \end{Bmatrix}$$

$$3$$

The Fourier coefficients are to be evaluated for each structural degree of freedom to determine the load vector corresponding to each individual harmonic. The load on each degree of freedom can be represented as

$$b_{ik} = \sum_{r=1}^{N} f_{rk} e^{i(r-1)r\mu}$$

$$4$$

where f_{rk} is the component of the Fourier harmonic and $e^{i(r-1)r\mu}$ is the factor that links the force of the system of one structure to another.

In a spur gear the load acts on only one tooth (in this case, as contact ratio unity) and is uniformly distributed along the line of contact.

$$b_{1k} = P, \quad b_{2k} = b_{3k} = \ldots b_{nk} = 0$$

$$(5)$$

and

$$f_{1k} = f_{2k} = \ldots = f_{nk} = P/N$$

Using the procedure as prescribed in the next section, the displacements of the gear teeth under consideration are obtained. These displacements are extrapolated to the adjacent teeth based on wave propagation theory in the following way.

$$u_i = e^{i\mu}(u_{i-1})$$

$$(6)$$

The total displacement of each tooth is arrived at by summation of all the displacements obtained for different harmonic loads. The real and imaginary parts of the displacements obtained will be equal and opposite. All stress calculations are done in real mode only.

3 SOLUTION PROCEDURE

The static equilibrium of each station can be represented as follows.[5] For the first station

$$C_1 d_o + B_1 d_1 + A_1 d_2 = g_1 \qquad (7)$$

where B_1 and A_1 are stiffness submatrices of the stations, C_1 is the coupling stiffness matrix between successive stations, d is the nodal displacement, g is the force vector. Equation (7) can be written in general form

$$C_i d_{i-1} + B_i d_i + A_i d_{i+1} = g_i$$
$$i = 2, 3, 4, \ldots, n \qquad (8)$$

Equations (7) and (8) can be modified to

$$d_1 = -P_1 d_2 + q_1 + Q_1 d_o$$

and

$$d_i = -P_i d_{i+1} + q_i + Q_i d_o \qquad i = 2, 3, \ldots, n \qquad (9)$$

where

$$P_1 = B_1^{-1} A_1$$
$$q_1 = B_1^{-1} g_1$$
$$Q_1 = -B_1^{-1} C_1$$
$$P_i = (B_i - C_i P_{i-1})^{-1} A_i \qquad (10)$$
$$q_i = (B_i - C_i P_{i-1})^{-1} (g_i - C_i q_{i-1})$$
$$Q_i = (B_i - C_i P_{i-1})^{-1} C_i Q_{i-1} \qquad i = 2, 3, \ldots, n$$

The equilibrium at the nth station is

$$d_n = -P_n d_{n-1} + q_n + Q_n d_o \qquad (11)$$

Because of cyclic symmetry

$$d_{n+1} = d_1 \qquad (12)$$

Hence

$$d_n = (1 - Q_n)^{-1} q_n - (1 - Q_n)^{-1} P_n d_1 \qquad (13)$$

Equations (7) and (8) after simplification give

$$d_1 = -\bar{P}_1 d_2 + \bar{q}_1 \qquad (14)$$

where

$$\bar{P}_1 = [B_1 - C_1 (1 - Q_n)^{-1} P_n]^{-1} A_1$$
$$\bar{q}_1 = [B_1 - C_1 (1 - Q_n)^{-1} P_n]^{-1}$$
$$\times [g_1 - C_1 (1 - Q_n)^{-1} g_n] \qquad (15)$$

similarly

$$d_i = -\bar{P}_i d_{i+1} + \bar{q}_i$$
$$\bar{P}_i = [B_i - C_i (1 - P_{i-1})]^{-1} A_i \qquad (16)$$
$$\bar{q}_i = [B_i - C_i (1 - P_{i-1})]^{-1} [g_i - C_i q_{i-1}]$$
$$i = 2, 3, \ldots, n$$

The above equation can be written for the nth station

$$d_n = -\bar{P}_n d_{n-1} + \bar{q}_n \qquad (17)$$

Equation (13) can be substituted in (17)

$$d_n = -\bar{P}_n d_1 + \bar{q}_n \qquad (18)$$

Comparing eqns (13) and (17) we can obtain

$$d_1 = [\bar{P}_n - (1 - q_n)^{-1} P_n] \times [\bar{q}_n - (1 - Q_n) q_n] \qquad (19)$$

Substituting eqn (19) in eqn (18) we can arrive at the value of d_1 and with back substitutions into eqn (16) we can arrive at other unknown displacements.

4 RESULTS AND DISCUSSION

The above solution procedure is used to solve a static equilibrium equation for a carbon-steel material and a glass-epoxy material spur gear. Their material properties are given in Table 1. The gear tooth parameters used in this work are given in Table 2. A uniform load of 245.25 N/mm length of the face width of the gear tooth was assumed to act at the tip as shown in Fig. 2. This uniformly distributed load was lumped at the nodes. The load and node details are explained in the same figure. The considered spur gear sector

Table 1. Material properties

S. No.		Steel	Glass-Epoxy
1	E_1 (N/mm²)	206 010·0	37 866·0
2	E_2 (N/mm²)	206 010·0	8 112·9
3	G_{12} (N/mm²)	79 235·4	4 061·3
4	ν_{12}	0·3	0·26
5	Density (kg/mm³)	7·81E−10	1·81E−10
6	X (N/mm²)	353·2	981
7	Y_1 (N/mm²)	353·2	3·44
8	S (N/mm²)	176·6	88·3

Table 2. Gear tooth parameters

S. No.	Parameter	Value
1	Pressure angle	20°
2	Module (mm)	10
3	Addendum	1 m
4	Dedendum	1·25 m
5	Root-fillet radius	0·3 m
6	Rim thickness	1·25 m
7	Number of teeth	20
8	Face width	11 m
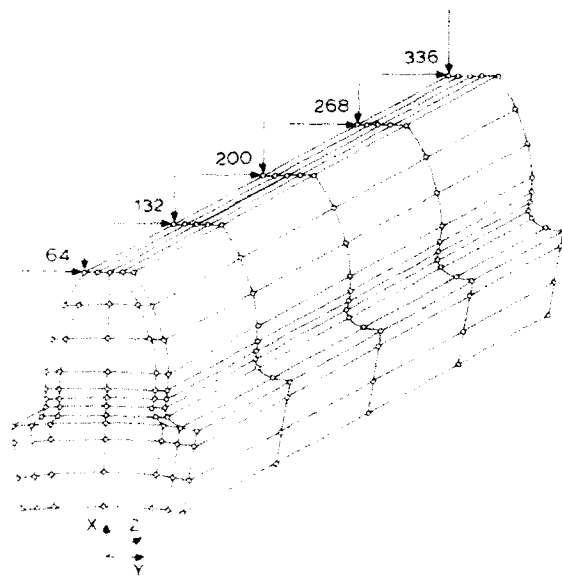
Fig. 2. Overall finite element model of gear tooth sector.

in the cyclic symmetric approach has an included angle of 18° (u). The stiffness matrix of the system is obtained by using eight noded brick elements with three degrees of freedom per node. They are u, v and w displacements along the three mutually perpendicular directions. First the analysis of a steel spur gear has been carried out. The calculated stresses are compared with the existing AGMA analytical method and with conventional single tooth finite element analysis. A comparison of obtained maximum σ_x of three methods are shown below.

(i) Analytical method (Agma equation): 140 N/mm

(ii) Single tooth finite element analysis: 122 N/mm

(iii) Cyclic symmetric approach: 97·2 N/mm.

A comparison of displacements in the u, v and w and stresses in the perpendicular directions are given in Table 3. The inclusion of the stiffness of

an adjacent gear tooth has resulted in a reduction of gear tooth stress σ_x.

A spur gear made of composite material (glass-epoxy) with radial fibre orientation has also been analysed. The displacements obtained (u, v, w) have been plotted in Figs 3–5. The maximum displacements from tip to root along load surface have been compared in Table 3 for both the cyclic symmetric and the single tooth approach. The stresses along the fibre direction (L), the other two perpendicular directions (T, Z) and the shear stresses in the LT, TZ, ZL planes are transformed from the calculated stresses along the geometrical axes. The stresses are plotted in Figs 6–11. It may be seen from these figures that the variation of displacement and stresses of both steel and com-

Table 3. Comparison of results cyclic symmetric approach and single tooth finite element analysis

		Cyclic symmetry	Conventional approach
u	S	0·3600E − 02	0·5417E − 02
	C	0·2674E − 01	0·4074E − 01
v	S	0·2874E − 01	0·2472E − 01
	C	0·2931E + 00	0·2863E + 00
w	S	0·2581E − 02	0·6432E − 03
	C	0·2976E − 02	0·7612E − 02
σ_x	S	0·9720E + 02	0·1220E + 03
	C	0·1080E + 03	0·1382E + 03
σ	S	−0·4401E + 02	−0·3800E + 02
	C	0·5056E + 02	0·4074E + 02
σ	S	−0·1546E + 02	−0·3369E + 02
	C	0·4900E + 02	0·4838E + 02
τ_{xy}	S	0·4867E + 02	0·3898E + 02
	C	0·5683E + 02	0·4876E + 02
τ	S	0·7864E + 00	−0·5000E + 00
	C	0·2320E + 00	−0·4600E + 00
τ	S	0·4987E + 00	0·2960E + 01
	C	0·3872E + 00	−0·8700E + 00

S, mild steel; C, composite material.
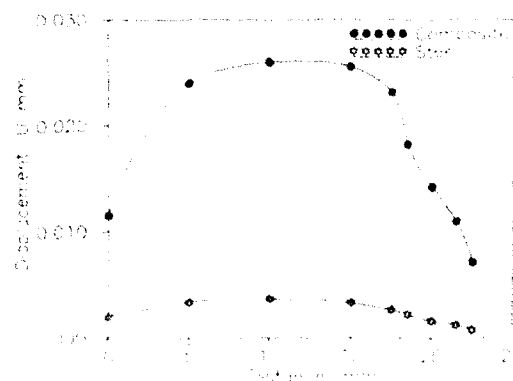
Fig. 3. Variation of u with distance from tip to root along load surface.

Mindlin laminated plate equations, has been presented recently by Reddy and Pandey. They examined a number of lamina failure criteria in

In the DR analysis the Mindlin large deflection plate equations, i.e. the equilibrium, strain displacement, curvature displacement and con-
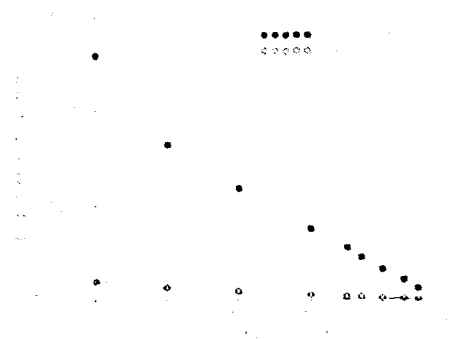
Fig. 4. Variation of τ with distance from tip to root along load surface
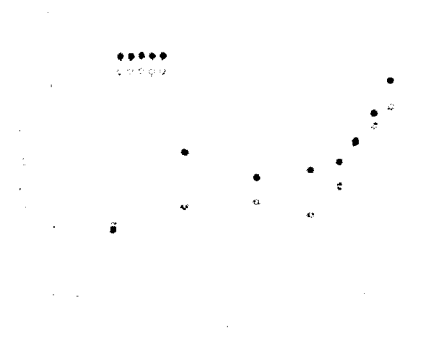
Fig. 7. Variation of σ with distance from tip to root along load surface
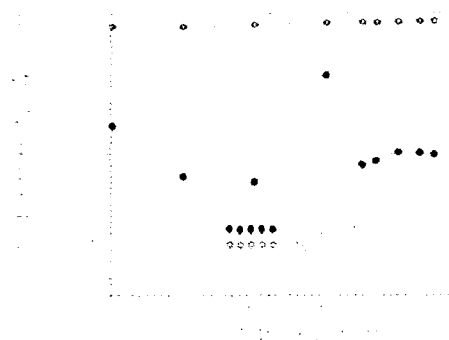
Fig. 5. Variation of σ with distance from tip to root along load surface.
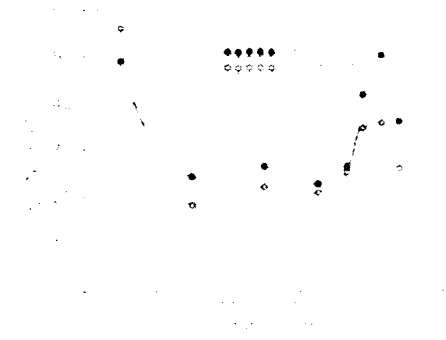
Fig. 8. Variation of σ with distance from tip to root along load surface.
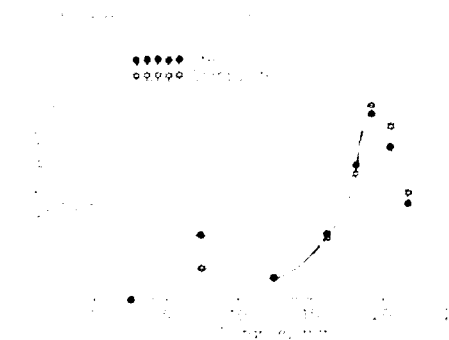
Fig. 6. Variation of σ_1 with distance from tip to root along load surface
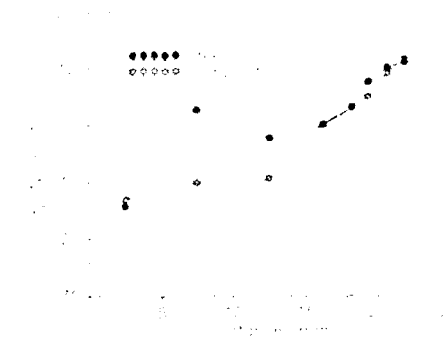
Fig. 9. Variation of σ_2 with distance from tip to root along load surface.

posite gears are similar. Here the normal stress along the fibre direction (σ_1) is lower compared to that for single tooth analysis. But the shear stress (σ_{11}) predicted by using the cyclic symmetric approach is higher. Usually, in a composite

material a combination of different stresses is a critical factor for the designer. Hence the Tsai-Hill theory has been used to calculate the factor of safety of the gear. The element at which the normal stress in the 1-direction is maximum has been
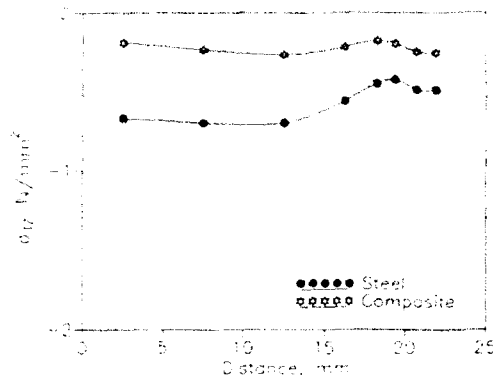
Fig. 10. Variation of σ_{12} with distance from tip to root along load surface.
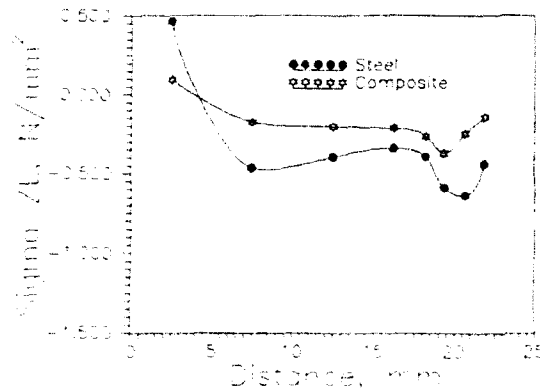
Fig. 11. Variation of σ_{21} with distance from tip to root along load surface.

identified. The factor of safety at that element has been calculated for both approaches. The lowest factor of safety occurs at tip of the gear teeth. The calculated lowest factor of safety for the two

approaches are:

(i) Conventional approach: 1·4600
(ii) Cyclic symmetric approach: 1·5513.

5 CONCLUSION

The effect of adjacent teeth stiffness on the stiffness of the gear tooth under consideration has been studied. It is found that the inclusion of the above stiffness results in a reduction of normal stress in the fibre direction. The normal stresses in the other two directions are found to increase slightly. But the factor of safety calculations predict higher values for the cyclic symmetric approach than the single tooth finite element analysis.

REFERENCES

1. Phillips 66 company. Advanced Composites Division. *Composites*, **18** Nov. 1987 354.
2. Wildheim, J., Vibration of rotating circumferentially periodic structures. *Quarterly Journal of Mechanical and Applied Mathematics*, **34** 1981 213-29.
3. Thomas, D. L., Dynamics of rotationally periodic structures. *International Journal of Numerical Methods in Engineering*, **14** 1979 81-102.
4. Ramamurti, V. & Ananda Rao, M., Dynamic analysis of spur gear teeth. *Computers & Structures*, **29** 5 1988 831-43.
5. Vijayarangan, S. & Ganesan, N., Stress analysis of a composite spur gear using finite element approach. To be published in *Computers & Structures*.
6. Ramamurti, V., *Computer Aided Mechanical Design and Analysis*. Tata McGraw-Hill, New Delhi, 1992.
7. Shigley, J. E. & Mischke, C. R., *Mechanical Engineering Design*. McGraw-Hill, New York, 1989.
8. Jones, R. M., *Mechanics of Composite Materials*. Scripta Book Company, Washington, DC, 1975.

A damage mechanics tool for laminate delamination

L. Daudeville & P. Ladevèze

Laboratoire de Mécanique et Technologie, ENS de Cachan/CNRS/Univ. P. et M. Curie, 61 avenue du Président Wilson, 94235 Cachan Cedex, France

A simplified method based upon damage mechanics for the delamination analysis of carbon–resin composites is presented. In the neighbourhood of a laminate structure quasi-straight edge, damage is taken concentrated on the interface between layers. The finite element code EDA, acting as a post-processor of an elastic laminate shell computation, allows the onset and propagation forecast of delamination. First numerical simulations of delamination are given and compared with experimental results from literature.

1 INTRODUCTION

The degradation modes of carbon–resin laminates e.g. T300-914 can be split into two classes. On the one hand, intralaminar damages: transverse matrix cracking, fibre–matrix debonding, fibre ruptures. On the other hand, delamination, i.e. degradation of the link between layers. Laminate structures being thin (plates or shells), the stress state far away from the edge zones (free edges, zones of force application) is a plane stress state, whereas the stress state can be three-dimensional in the edge zones. Thus, delamination, a phenomenon of layer debonding due to possible stresses that are normal to the shell surface, occurs principally in the edge zones of laminate structures.

Numerical rupture simulation of a laminate structure, taking into account all the progressive degradation phenomena, leads to a time dependent three-dimensional non-linear problem. Nowadays, finite element calcualtions under a classical laminate theory and combined with stress criteria,[1] are generally used for the rupture forecast far away from the edge zones. Such an approach can be discussed because such criteria cannot well describe the different damage phenomena.

For the delamination analysis, more especially for the onset forecast of a free edge crack, computation methods of elastic edge effects[2–4] are generally used as post-processors of an elastic laminate shell computation. They are associated to criteria based upon the average of normal stresses along a characteristic distance from the free edge.[5] Progressive degradations are not yet taken into account. In addition, delamination does not always occur where stresses are maxima and the intrinsic feature of the distance from the free edge can be discussed when geometry and stacking sequence vary. Linear fracture mechanics, i.e. computation of an energy release rate G and its comparison with a critical value G_c, is generally used for crack propagation study.[6,7] Nevertheless, fracture mechanics cannot be used for crack onset study.

Progressive degradation modelling allows one to predict accurately the structure behaviour until rupture: that is damage mechanics of composites.[8–11] Numerical methods based upon damage mechanics proposed by Ladevèze,[11] acting as post-processors of an elastic laminate shell computation have been developed for the forecast of (i) rupture far away from the edge, (ii) rupture in the vicinity of a circular hole, and (iii) delamination near a quasi-straight edge.

Method (iii) is presented. The general ideas of that computational tool were first presented in Ref. 12. We present now the development and the first results of this simplified method that allows the forecast of delamination onset and its propagation on a short distance. Damage phenomena are taken concentrated on the interfaces between the layers. The edge is quasi-straight, thus the

547

initial three-dimensional problem becomes a two-dimensional one set into a band perpendicular to the edge.

The laminate is modelled as a stacking of homogeneous elastic layers connected by elastic with damage interfaces. The interface is a two-dimensional entity which ensures stress and displacement transfers between layers. The degradation effect is taken into account through the relative variations of the interface elastic moduli. An interface with damage has also been used recently by Schellekens[13] for delamination simulation of a laminate under tension. The interface modelling of this author is principally based upon numerical considerations. The interface modelling we propose has already been presented. In the previous presentation,[14] for the particular example of a double cantilever beam DCB, a link has been established between damage mechanics of the interface and fracture mechanics giving a mechanical interpretation to that modelling. Note that the crack length was considered large compared with the beam thickness. In the present paper, the numerical simulation of the DCB test is performed with no initial crack. The finite element method is used. Due to damage, the structure may present a critical state. A method[15,16] in which crack opening displacement is controlled, allows such a limit point to be passed.

Numerical simulations of delamination, computed with the post-processor edge damage analysis (EDA), are given in the framework of (i) a DCB beam: study of onset and propagation of delamination, and (ii) a specimen under tension: study of delamination onset near the free edge. The proposed numerical simulations allow a comparison with experimental results from literature for the identification and the checking of the modelling.

2 DELAMINATION ANALYSIS BY DAMAGE MECHANICS

2.1 Laminate modelling

The laminate is modelled as a stacking (i) of homogeneous layers, and (ii) of interfaces connecting layers (see Fig. 1).

All damage phenomena are taken concentrated on the interface. The principal features of the interface are as listed below.
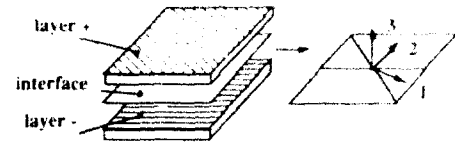
Fig. 1. Interface

- *Its behaviour is assumed orthotropic* — the influence of the adjacent layers on the interface damage behaviour is taken into account through the fibre direction bisectors that are supposed to be the directions of orthotropy. The constitutive law links the normal stresses to the jump of displacement between layers, its expression in elasticity is

$$\begin{pmatrix} \sigma_{13} \\ \sigma_{23} \\ \sigma_{33} \end{pmatrix} = \begin{pmatrix} k_1^0 & 0 & 0 \\ 0 & k_2^0 & 0 \\ 0 & 0 & k_3^0 \end{pmatrix} \begin{pmatrix} u_1 \\ u_2 \\ u_3 \end{pmatrix}$$

with

$$\left| \begin{array}{l} [U] = U^+ - U^- = u_1 N_1 + u_2 N_2 + u_3 N_3 \\ \text{jump of displacement between the } + \text{ and } - \text{ layers} \end{array} \right.$$

Note the particular cases:

$$\begin{cases} k_1^0 = k_2^0 = k_3^0 = 0 \\ \quad \text{complete debonding between layers} \\ k_1^0 = k_2^0 = k_3^0 = \infty \\ \quad \text{perfect bonding} \end{cases}$$

- *Damage is unilateral in the 3 direction* — for the normal to the shell direction (mode I) there is no damage under compression.
- *Relative variations of stiffness are the damage indicators* — three internal variables d are associated to the three stiffness moduli k_i^0.
- *The interface behaviour is assumed to be elastic with damage* — that is at first, an inelastic behaviour can also be introduced.[17]

The thermodynamical potential is the strain energy:

$$E_D = \frac{1}{2} \left(\frac{\langle -\sigma_{33} \rangle_+^2}{k_3^0} + \frac{\langle \sigma_{33} \rangle_+^2}{k_3^0(1-d_3)} \right. \\ \left. + \frac{\sigma_{13}^2}{k_1^0(1-d_1)} + \frac{\sigma_{23}^2}{k_2^0(1-d_2)} \right)$$

$\langle \cdot \rangle_+$ denotes the positive part.

The variables Y_{di}, that are similar to the energy release rate introduced in fracture mechanics, are conjugated to d_i: $Y_{di} = \partial E_D / \partial d_i$

$$Y_{d3} = \frac{1}{2} \frac{\sigma_{33}^2}{k_3^0 (1 - d_3)^2}$$

mode $3 \equiv$ mode I

$$Y_{d1} = \frac{1}{2} \frac{\sigma_{31}^2}{k_1^0 (1 - d_1)^2} ; \quad Y_{d2} = \frac{1}{2} \frac{\sigma_{32}^2}{k_2^0 (1 - d_2)^2} ;$$

mode 1   mode 2

Note that modes 1, 2 and 3 are here relative to the axes of orthotropy, contrary to the fracture mechanics classical appellation that refers to crack opening directions.

2.1.1 A first choice for the damage evolution law

The evolution of the three damage variables is linked because the same micro-cracks participate to damage. Damage evolution is assumed to be governed by

$$Y = \sup_{t \leq \tau} \left(Y_{d3} + \gamma_1 Y_{d1} + \gamma_2 Y_{d2} \right) \qquad \gamma_1, \gamma_2 \text{ coupling factors}$$

Damage evolution law is

$$\begin{cases} d_3 = w(Y) & \text{if } d_3 < 1 & d_3 = 1 \text{ otherwise} \\ d_1 = \gamma_1 w(Y) & \text{if } d_1 < 1 \text{ and } d_3 < 1 & d_1 = 1 \text{ otherwise} \\ d_2 = \gamma_2 w(Y) & \text{if } d_2 < 1 \text{ and } d_3 < 1 & d_2 = 1 \text{ otherwise} \end{cases}$$

with

$$w(Y) = \left(\frac{Y - Y_0}{Y_c - Y_0} \right)^n$$

where Y_0 is threshold energy, Y_c is critical energy, n is characteristic parameters of the damage evolution law of the interface.

2.2 Link with fracture mechanics

Classical tests of fracture mechanics[18] allow us to obtain the three inter-laminar fracture toughnesses G_{Ic}, G_{IIc}, G_{IIIc}, relative to the modes I, II and III. G_{Ic}, G_{IIc}, G_{IIIc} are different.[19]

Under the assumption that G_c is a constant parameter (there is no R-curve effect), G_c is a characteristic interface parameter. G_c can be interpreted as the necessary work per unit surface for the interface debonding. Then, it can be dependent (for instance under pure mode I $\equiv$ mode 3) on the characteristic parameters of the interface modelling.

$$G_{Ic} = \int_0^{u_{3c}} \sigma_{33} d|u_3| \qquad \text{with } |u_{3c}| = |u_3|\big|_{d3 = 1} : \text{the interface is locally cracked}$$

G_{Ic} is, therefore, the area under the curve $\sigma_{33} - |u_3|$ (see Fig. 2). In pure mode I one finds

$$G_{Ic} = Y_0 + \frac{n}{n+1} (Y_c - Y_0)$$

For the identification under pure modes 2 or 3, one assumes that the crack opening direction coincides with a bisector of adjacent fibre directions. In that case one finds (mode II $\equiv$ mode 1 and mode III $\equiv$ mode 2):

$$G_{\alpha c} = Y_0 \left(\frac{2}{\gamma_i} - 1 \right) + \frac{1}{\gamma_i^{1/(n+1)}} \left(1 - \frac{1}{\gamma_i^{n+1}} (Y_c - Y_0) \right) \qquad \text{with } \begin{cases} \alpha = \text{II, III} \\ i = 1, 2 \end{cases}$$

The above relations allow a first identification of damage evolution law parameters.

Note that delamination modelling through an interface with damage includes the notion of process zone given by some authors, because damage varies continually in the vicinity of the crack tip. The process zone length depends on the structure (the damaged zone at the crack tip is different for DCB beams with layers at $0°$ and $90°$).

3 NUMERICAL STRATEGIES

3.1 The boundary layer problem

3.1.1 Problem formulation in elasticity

The laminate shell, of thickness $2h$, occupies the domain $\Omega = \Omega_1 \cup \Omega_2$ (see Fig. 3).

When the thickness $2h$ is weak compared with the transverse dimensions, the three-dimensional displacement–stress solution (U, σ) of the elastic problem set on Ω can be written as follows:[20]

$$\begin{cases} U = U_P + U_F \\ \sigma = \sigma_P + \sigma_F \end{cases} \text{with} \begin{cases} (U_P, \sigma_P): \text{solution of a shell problem} \\ (U_F, \sigma_F): \text{solution localised near the edge } \partial\Omega_2 \end{cases}$$

Notably because of the layer constitutive law discontinuity, the following boundary condition is not respected on the edge $\partial\Omega_2$:

$$\forall z \in [-h, h] \quad \sigma_P(z)n = F(z)$$

where F and n denote the force density and the normal. Hence (U_F, σ_F) is added to the valid solution far away from the edge $\partial\Omega_2(U_P, \sigma_P)$ such that (U, σ) satisfies the equations and boundary conditions of the three-dimensional problem. (U_F, σ_F) is localised near $\partial\Omega_2$, thus the edge effect solution (U_F, σ_F) can be computed in post-processor of a shell computation set on Ω_2. If, in addition, the radius of curvature of the edge $\partial\Omega_2$ is large compared with the thickness, the variations of (U_F, σ_F) along the tangent direction y are negligible, the problem becomes set into a band $\mathscr{B}$ of which the length is in order of the thickness $2h$.

The problem $(\mathscr{P})$ to solve becomes: find (U_F, σ_F)

(i) $\quad U_F \in \mathscr{U} = \{V/V = 0 \text{ on } \partial\Omega_1 \cap \mathscr{B}\}$

(ii) $\quad \forall V \in \mathscr{U}. \displaystyle\int_{\mathscr{B}} \sigma_F \varepsilon(V) \, dS = \int_{\partial\Omega_2 \cap \mathscr{B}} RV \, ds$

(iii) $\quad \sigma_F = \mathscr{F}(\varepsilon(U_F))$

The force R applied on the edge $\partial\Omega_2 \cap \mathscr{B}$ of the structure is the residue of external forces and of the shell solution:

$$R = F - \sigma_P n$$

(i) means that (U_F, σ_F) is localised and (iii) is the constitutive law.
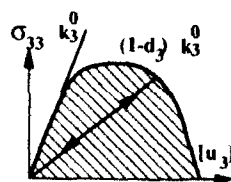
Fig. 2. Interface elastic with damage behaviour (mode 1 traction).
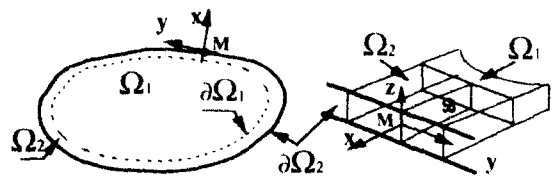
Fig. 3. Boundary layer.

3.1.2 Solving the boundary layer problem in the non-linear case

In the proposed modelling of the laminate, only the interfaces can be damaged due to edge effect normal stresses. The interfaces taking no part in the computation of $(\mathbf{U_P}, \boldsymbol{\sigma_P})$, it is possible to apply the principle of superimposed stress for the computation of $(\mathbf{U_E}, \boldsymbol{\sigma_E})$.

The problem $(\mathscr{P})$ to solve becomes a non-linear time dependent problem set into the band $\mathscr{B}$.

We compared the damage states near the free edge obtained by two non-linear computations of a specimen submitted to tension along the x direction (see Fig. 4).

The first computation C_1 has been carried out by resolution of problem $(\mathscr{P})$. The second one C_2 has been a reference computation because it allows us to have the exact three-dimensional solution by searching the displacement under the form proposed by Pipes and Pagano.[22]

$$\mathbf{U}(x, y, z): \begin{cases} u(y, z) + \varepsilon x \\ v(y, z) \\ w(y, z) \end{cases}$$

C_1 and C_2 results are rigorously equal. That confirms it is possible to apply the principle of superimposed stress in that particular case where non-linearities are taken concentrated on interfaces.

3.2 A Riks-like method

Due to damage on interfaces, an instability point may appear. That critical point cannot be passed with a Newton method that pilots the computation in terms of 'force' (see Fig. 5). A Riks-like method[15,16] allows to control the computation and pass such a limit point.

Current step:

$$\mathscr{F}: \begin{cases} \mathscr{K}_{it} \delta_i = \lambda_{i-1} \mathbf{F} - \mathbf{f}(\mathbf{U}_i) & \text{By the Newton method: } \delta\lambda_i = 0 \\ \lambda_{i-1} = \lambda_i + \delta\lambda_i & \text{By the Riks method the load factor is released, it is then} \\ \text{constraint: } g(\delta\lambda_i) = 0 & \text{necessary to impose a constraint: } g(\delta\lambda_i) = 0 \end{cases}$$

Riks[15] and Crisfield[16] propose a constraint $g(\delta\lambda_i) = 0$ that concerns the norm of the global vector δ_i. Such a global constraint may lead to a non-convergence when damage localises. To ensure a good convergence we propose to use a local constraint that considers only the more significant degrees of freedom in the increase of damage.

Note α is the closer node of the Gauss point where the increase of damage has been the more important at the initial step (β is the node located on the same interface but on the adjacent layer). n (1, 2 or 3) is the mode of principal damage (see Fig. 6).

The local constraint consists in imposing a constant value for the jump of displacement between α and β along the n direction.

$$(\delta_i)_n^\alpha - (\delta_i)_n^\beta = 0 \qquad \text{for } i \geq 1$$
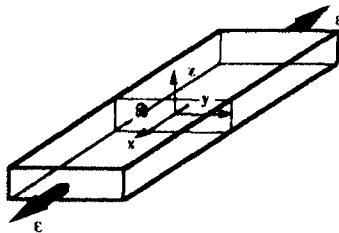
Fig. 4. Specimen under tension.
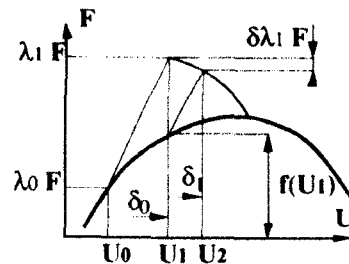
Fig. 5. Riks-like method.

3.3 A method for a large number of layers

The operator $\mathcal{K}_a$ (see ($\mathcal{S}$)) can be the tangent structural stiffness matrix $\mathcal{K}_t$ or the secant one $\mathcal{K}_s$ i.e. computed through an elastic with damage behaviour). Solving ($\mathcal{S}$) can be carried out with the direct Crout method. In the case of a large number of layers, that method may be expensive because of $\mathcal{K}$ matrix size. We propose then to use the conjugate gradient method with use of a conditioner.

$$\mathcal{K}_a = \mathcal{K}_t$$

In the iterative Riks algorithm, the linear systems to solve can be written under the form

$$\mathcal{K}_t \mathbf{X} = \mathbf{R} \qquad \text{with } \mathcal{K}_t = \mathcal{K}_{cou} + \mathcal{K}_{int}$$

$\mathcal{K}_{cou}$ and $\mathcal{K}_{int}$ are respectively the contributions of layers ($\mathcal{K}_{cou}$ is a constant matrix) and of interfaces $\mathcal{K}_{int}$ is a non-constant matrix because the interfaces can damage). The conjugate gradient method consists in a series of iterating resolutions of

$$\mathcal{K}_{cou} \mathbf{Z}_{n-1} = \mathbf{R} - \mathcal{K}_t \mathbf{X}_n$$

The matrix $\mathcal{K}_{cou}$ (conditioner) being diagonal by units, the resolution is parallel on each layer.

4 NUMERICAL SIMULATIONS OF DELAMINATION

4.1 Identification of model parameters

The characteristic parameters of the interface modelling are $k_1^0, k_2^0, k_3^0, Y_0, Y_c, n, \gamma_1, \gamma_2$.

The interface can be considered as a rich resin zone of weak thickness e_1 compared with the layer thickness e_c. By this analogy and by considering that $e_1/e_c \ll 1$, the interface constitutive law can be expressed as

$$\begin{pmatrix} \sigma_{13} \\ \sigma_{23} \\ \sigma_{33} \end{pmatrix} = \begin{pmatrix} k_1^0 & 0 & 0 \\ 0 & k_2^0 & 0 \\ 0 & 0 & k^0 \end{pmatrix} \begin{pmatrix} |u_1| \\ |u_2| \\ |u_3| \end{pmatrix}$$

$$\text{with } \begin{cases} k_1^0 = \dfrac{2G_{13}}{e_1} \\ \\ k_2^0 = \dfrac{2G_{23}}{e_1} \\ \\ k_3^0 = \dfrac{E_3}{e_1} \end{cases} \qquad (1)$$

where G_{13}, G_{23}, E_3: elastic moduli of the rich resin zone, they can be chosen equal to the homogenised layer moduli.

The identification of the other parameters can be carried out by the use of classical fracture mechanics tests[21] results for the mode I (specimen DCB see Fig. 7), the mode II (specimen ENF) and

the mode III (specimen SCB). The use of toughness values issued from literature[19] is difficult because those values can present, for the same material (for instance, T300-5208), an important divergence. For the following simulations, we identified the parameters by comparison with experimental results.

4.2 The DCB

We have simulated the DCB test with the EDA program for a comparison with the experimental results[23] (the simulation of the DCB test is not a boundary layer problem).

The studied structure is constituted of 48 layers of thickness $e_c = 0.1375$ mm and of T300 fibres with an M10 resin. The numerical simulation has
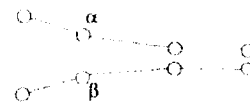
Fig. 6. Concerned nodes by the local constraint.
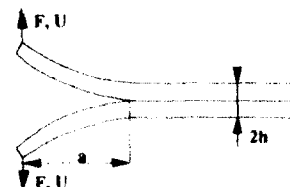
Fig. 7. DCB test.

been carried out with no initial crack, whereas the experimental specimen had an initial crack of 28·5 mm. The authors[23] found $G_{Ic} = 450$ J/m² and the following elastic moduli (the elastic moduli relative to the normal direction 3 are supposed to be equal to those in the transverse direction 2).

$E_{11} = 123\,680$ MPa

$E_{22} = E_{33} = 8990$ MPa

$G_{12} = G_{13} = G_{23} = 3770$ MPa

$\nu_{12} = \nu_{13} = \nu_{23} = 0.22$

We have chosen k_3'' by eqn. (1):

$$e_f = \frac{e_c}{5} \Rightarrow k_3'' = 3.27 \times 10^5 \text{ MPa/m}$$

Y_0, Y_c, n values satisfy the following relationship:

$$G_{Ic} = Y_0 + \frac{n}{n+1}(Y_c - Y_0) \tag{2}$$

In view of numerical results, one finds

- the numerical simulation predicts quite well the experimental results since the crack length (simulation) reaches the experimental initial crack length;
- Y_0, Y_c, n values have an influence on the F, U curve (see Fig. 8), at the condition these values satisfy eqn (2);
- by the knowledge of the load F associated to the crack length a, it is possible to compute the critical energy release rate G_{Ic} (by the area method[15]).

One finds the experimental value of G_{Ic} and one verifies that the critical energy release rate is independent of the crack length (see Fig. 9). This result has been verified experimentally[23] and theoretically established[14] for an initial crack

which is large compared with the thickness $2h$. The important point is the numerical simulation predicts this result even if the crack length is short.

4.3 Delamination near the free edge of a specimen under tension or compression

We compared our simulations of delamination near the free edge of a specimen under tension or compression (see Fig. 4) with first experimental results[5,24] for mode I delamination (on the midplane interface) of a T300-5208 material (see Table 1). Then, we also compared our results with experimental ones[25] for mixed mode of delamination of a T300-1034C (see Table 2). The
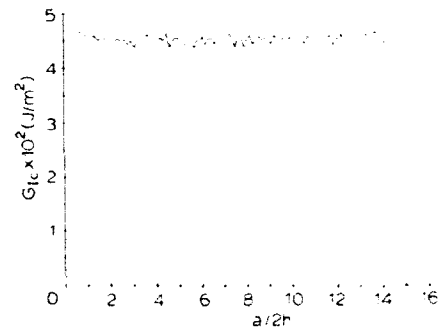
Fig. 9. G_{Ic}–a curve.

Table 1. Mode I delamination

Laminate	t_{exp}	t_{cal}
±45, 0, 90	0·53	0·53
±45, 0, 90	0·45	0·38
±45, 0, 90	0·36	0·32
0, ±45, 90	0·66	0·61
45, 0, −45, 90	0·54	0·57
±30, 90	0·39	0·43
±30, 90	0·36	0·39

"Data taken from Refs 5 and 23.

Table 2. Mixed mode delamination

Laminate	Interface	t_{exp}	t_{cal}
±45, 90, 0	90, 0	0·71	0·77
90, ±30	30, −30	−0·27	−0·28
90, ±15	15, −15	−0·34	−0·36
0, ±30	30, −30	−0·54	−0·65
0, ±30	30, −30	−0·35	−0·4
0, ±30	30, −30	0·85	0·73
0, ±15	15, −15	−0·51	−0·6
0, ±15	15, −15	−0·35	−0·45
0, ±15	15, −15	0·57	0·5

"Data taken from Ref. 25.
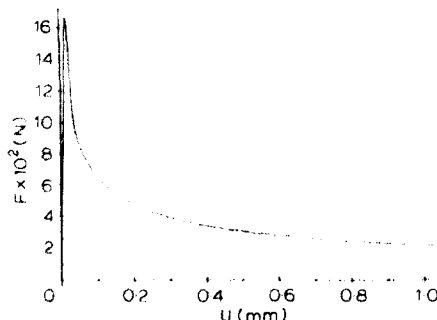
Fig. 8. F–U curve.

authors[5,25] propose the same elastic moduli for both materials T300-5208 and T300-1034C.

$$E_{11} = 138\,000 \text{ MPa}$$

$$E_{22} = E_{33} = 9700 \text{ MPa}$$

$$G_{12} = G_{13} = G_{23} = 5500 \text{ MPa}$$

$$\nu_{12} = \nu_{13} = 0.3, \quad \nu_{23} = 0.6$$

We have chosen the interface stiffnesses by eqn (1) and $e_1 = e_c/5$.

First, we have identified under mode I (T300-5208) the parameters Y_c, Y_0 and n with the $(\pm 45, 0, 90)_s$ laminate. Secondly, we have identified the parameters γ_1 and γ_2 under mixed mode (T300-1034C) such that the results are quite good. So, we assumed that both T300-5208 and T300-1034C damage behaviours were close.

The calculated strain (ε_{cal}) in the tables corresponds to the maximum of strain of the strain-crack length curve (see Fig. 10).

5 CONCLUSION

The analysis of delamination near an edge of a laminate structure by damage mechanics has been presented. The basic assumptions of this method — the edge is quasi-straight, damage is taken concentrated on interfaces between layers — lead to a simplified method for the delamination onset and propagation forecast. The identification of characteristic parameters of the interface modelling can be carried out by use of classical fracture mechanics tests. The finite element program EDA is independent of finite element codes, it acts as a post-processor of an elastic laminate shell com-

putation. Note there is no mesh dependency because the treated problem is plane and damage is concentrated on interfaces. The first comparisons of numerical simulations with experimental results are quite good.

REFERENCES

1. Tsai, S. W. & Wu, E., A general theory of strength for anisotropic materials. J. Comp. Mater., 5 1971 58-80.
2. Engrand, D., A boundary layer approach to the calculation of transverse stresses along the free edges of a symmetric laminated plate of arbitrary width under in plane loading. Comp. Structures, 1981 247-61.
3. Dumontet, H., Study of a boundary layer problem in elastic composite materials. M.A.N., 20 1986 265-86.
4. Bar-Yoseph, P., On the accuracy of interlaminar stress calculation in laminated plates. Comp. Meth. Appl. Mech. Eng., 36 1983 309-29.
5. Kim, R. Y. & Sony, S. R., Experimental and analytical studies on the onset of delamination in laminated composites. J. Comp. Mater., 18 1984 70-6.
6. Wang, A. S. D., Fracture analysis of interlaminar cracking. Interlaminar Response of Composite Materials Composite Material Series, Vol. 5, ed. N. J. Pagano. Elsevier Science Publishers, 1989, pp. 69-109.
7. Wang, A. S. D., Slomania, M. & Bucinell, R. B., Delamination crack growth in Composite Laminates. Delamination and Debonding of Materials, ed. W. S. Johnson. ASTM STP876, Washington, DC, USA, 1985, pp. 135-67.
8. O'Brien, T. K., Characterisation of delamination onset and growth in a composite laminate. Damage in Composite Materials, ed. K. L. Reifsnider, ASTM-STP775, Washington, DC, USA, 1982, pp. 140-67.
9. Talreja, R., Damage development in composites: mechanisms and modelling. J. Strain Anal., 24 1989 215-22.
10. Allen, D. H., Groves, S. E. & Harris, C. E., A cumulative damage model for continuous fibre composite laminates with matrix cracking and interply delaminations. Composite Materials: Testing and Design, ed. J. D. Withcomb. ASTM-STP972, Washington, DC, USA, 1988, pp. 57-80.
11. Ladevèze, P., Allix, O. & Daudeville, L., Mesomodelling of damage for laminate composites: application to delamination. In IUTAM Symposium on Inelastic Deformation of Composites Materials, Troy, ed. G. J. Dvorak. Springer-Verlag, 1990, pp. 607-22.
12. Allix, O., Daudeville, L. & Ladevèze, P., Delamination and damage mechanics. Mechanics and Mechanism of Damage in Composites and Multi-Materials, ed. D. Baptiste. ESIS Publication 11, London, UK, 1991, pp. 32-41.
13. Schellekens, J. C. J. & De Borst, R., Numerical simulation of free edge delamination in graphite epoxy specimen under uniaxial extension. In Sixth International Conf. on Composite Structures ICCS6, ed. I. H. Marshall. Elsevier Science Publishers, 1991, pp. 647-57.
14. Allix, O. & Ladevèze, P., Interlaminar interface modelling for the prediction of delamination. Comp. Structures, 22 (1992) 235-42.
15. Riks, E., An incremental approach to the solution of snapping and buckling problems. Int. J. Solids and Structures, 15 (1979) 524-51.
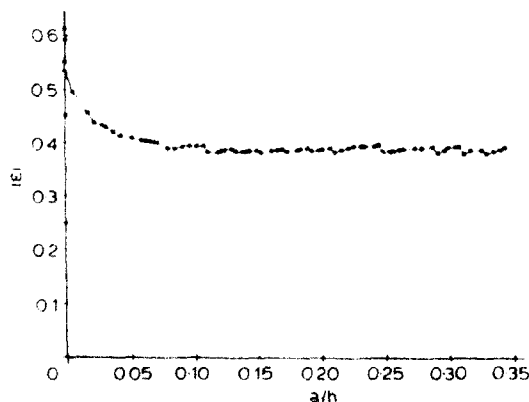
Fig. 10. ε–a curve for a $(0, \pm 45, 90)_s$ laminate: delamination on the mid-plane interface.

16. Crisfield, M. A., An arc-length method including line searches and accelerations. *Int. J. Num. Methods Eng.*, **19** 1983 1269-89.

17. Corigliano, A., Formulation, identification and use of interface models in the numerical analysis of composite delamination. Submitted to *Int. J. Solids and Structures*, 1992.

18. Whitney, J. M., Experimental characterisation of delamination fracture. In *Interlaminar Response of Composite Materials* Composite Material Series, Vol. 5, ed. N. J. Pagano. Elsevier Science Publishers, 1989, pp. 161-250.

19. Sela, N. & Ishai, O., Interlaminar fracture toughness and toughening of laminated composite materials: a review. *Composites*, **20** 1989 423-35.

20. Nesa, A., Abisror, A. & Bunsell, A. R., On cracking in a unidirectional glass-epoxy composite: toughness and damage mechanisms.

21. Fredrichs, K. O. & Dressler, R. F., A boundary layer theory for elastic plates. *Comm. Pure and Appl. Math.*, **14** 1961 1-33.

22. Pipes, R. B. & Pagano, N. J., Interlaminar stresses in composite laminates under axial extension. *J. Comp. Mater.*, **4** 1970 538-48.

23. Laksimi, A., Benzeggagh, M. L., Jing, G., Hecini, M. & Roelandt, J. M., Mode I interlaminar fracture of symmetrical cross-ply composites. *Comp. Sci. Technol.*, **41** 1991 147-64.

24. Rodini, B. T. & Eisenman, J. R., An analytical and experimental investigation of edge delamination in composite laminates. In *Proc. 4th Conf. Fibrous Comp. San Diego*, ed. Lenoe & Oplinger & Burke, 1978, pp. 441-57.

25. Kim, R. Y. & Sony, S. R., *Delamination of Composite Laminates Stimulated by Interlaminar Shear*. ASTM-STP893, Washington, DC, USA, 1986, pp. 286-307.

Carbon composite repairs of helicopter metallic primary structures

Michael L. Overd

Westland Helicopters Ltd, Westland Works, Yeovil, UK BA20 2YB

The main load path of the EH101 helicopter fuselage consists of I- and C-section frames and beams, machined from light alloy forgings and plate. A full-scale fatigue test of the airframe is being carried out as part of the structural substantiation programme. In order to minimise the fatigue test down-time, Westland opted to use composite materials for the repairs of fatigue failures.

Repairs use a wet lay-up of ±45° carbon fabric for shear webs and pre-cured, bonded-on unidirectional carbon–epoxy strips, for the flanges. Where it was necessary to use fasteners in the flanges, ±45° carbon fabric was introduced. In this way, complex frame shapes have been accommodated. Such repairs can be generated rapidly and applied *in situ*, in the test rig.

Fatigue testing of the repaired airframe continues. The oldest repair has experienced the equivalent of 16 400 flying hours of low frequency (manoeuvre) loading plus 0·86 × 10⁶ cycles of high frequency (rotor generated) loading. To-date, none of the repairs has failed.

Four case studies illustrating the simple methods used to design and instal the repairs are presented, together with their fatigue performance to date. The case study experience is then translated into general design rules which could be used in service. The applicability and limitations of the techniques are also presented.

1 INTRODUCTION

The main load path structure of the EH101 helicopter fuselage consists of I- and C-section frames and beams, machined from light alloy forgings and plate. A full-scale fatigue test of the airframe is being carried out as part of the structural substantiation programme.

To minimise the test down-time, carbon composite materials have been used to repair fatigue failures. This paper gives examples of the various failures and the way in which they have been repaired. The repair design methodology is described together with the fatigue performance of the repairs to-date. The case study experience is then used to generate general repair design rules.

2 AIRFRAME TEST CONFIGURATION

Figures 1–3 are photographs of the test showing details of the airframe and rig structure. There are three levels of load applied to the test:

(i) Low Level Manoeuvre Loads, following an assumed flight profile.

(ii) Medium Level Manoeuvre Loads, which are 1·3 times higher than low level.

(iii) High Frequency Loads, which are applied to induce fretting of joints and simulate blade passing vibration. In this case the test excitation is limited to the vertical axis but the vibratory amplitude is adjusted to give representative strains in the two main lift frames.

3 REPAIR CASE STUDIES

3.1 Lightening hole failure No. 1

3.1.1 Failure details
Figures 4 and 5 show general views of a shear web failure with two cracks propagating at 45° from a lightening hole. Several examples of this failure mode have occurred on the test due to the interaction of shear bending and direct stresses.

Fig. 1. Side view of the EH101 Airframe Fatigue Test.
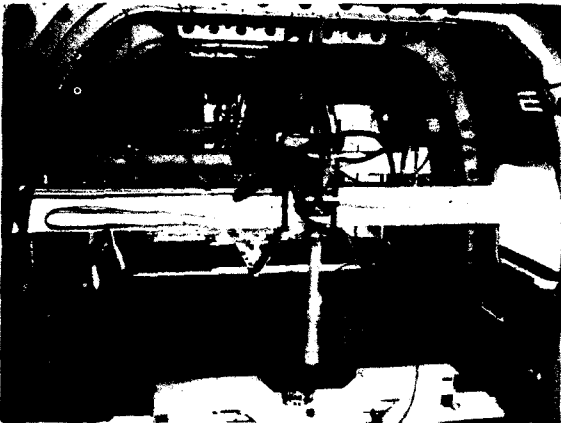
Fig. 2. Internal view of the EH101 Airframe Fatigue Test.
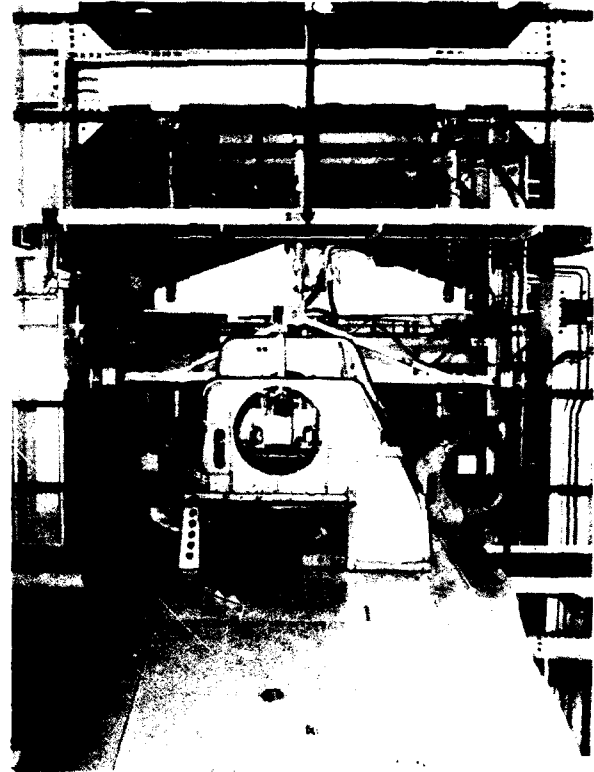
Fig. 3. Top structure of the EH101 Airframe Fatigue Test.

Detailed finite element modelling of these failures has demonstrated that the large lightening hole size relative to the shear web causes higher than expected stress concentrations. Figure 6 shows that the upper crack propagated along the junction between the outer flange and the web. Similarly, Fig. 7 shows the lower crack propagated along the junction between the inner flange and the web. A small central U-shaped section has then torn through the inner flange as shown in Fig. 5. This crack propagation behaviour is due to the presence of Brazier loading associated with the flange curvature.

3.1.2 Repair design

The requirement was for a repair which could be easily installed *in situ*, restore the load carrying capability of the web, prevent the adjacent holes from failing and also stop the cracks from propagating. Wet lay-up 833 style woven carbon at
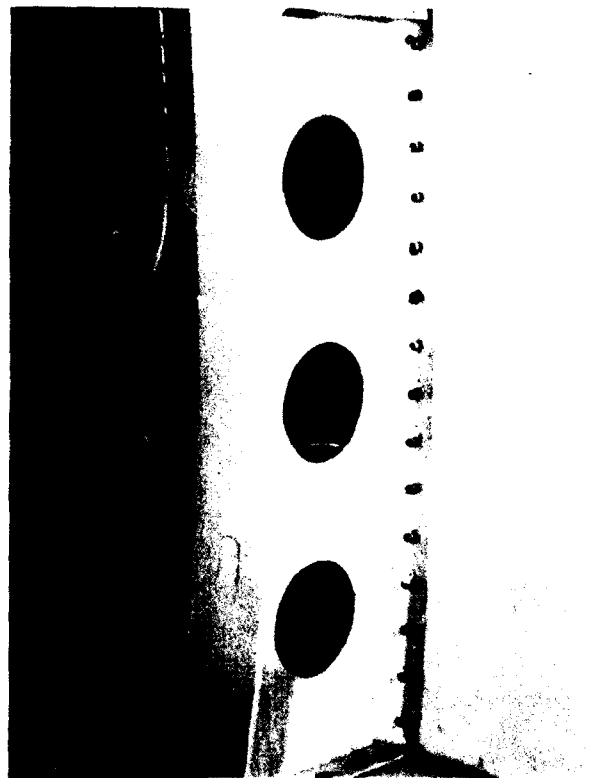
Fig. 4. View of lightening hole failure No. 1 showing damage to shear web and inner flange.

ii Single tooth finite element analysis 122
N mm

iii Cyclic symmetric approach: 97·2 N/mm.

A comparison of displacements in the *z*, *r* and *w*
and stresses in the perpendicular directions are
given in Table 3. The inclusion of the stiffness of

Fig. 3   Variation of growth distance from tip to root along
load at tip.
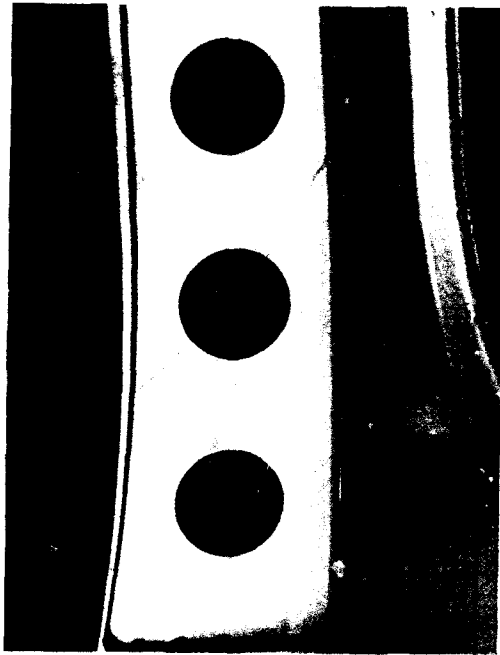
Fig. 5.   View of lightening hole failure No. 1 showing crack
trajectories in web.
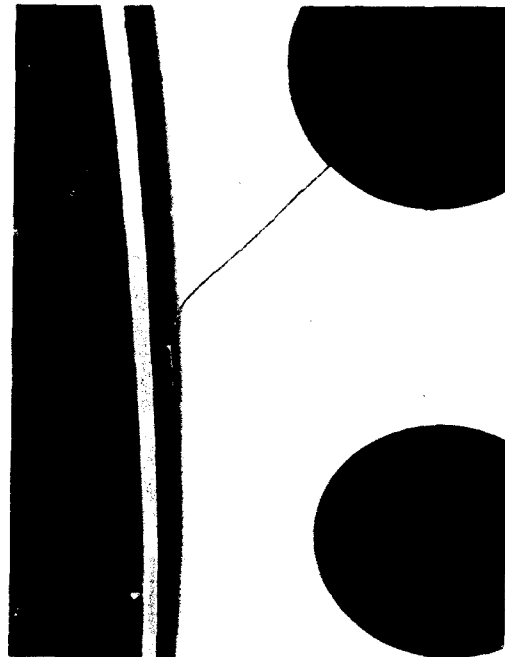
Fig. 7.   View of lightening hole failure No. 1 showing crack
propagation along inner flange.
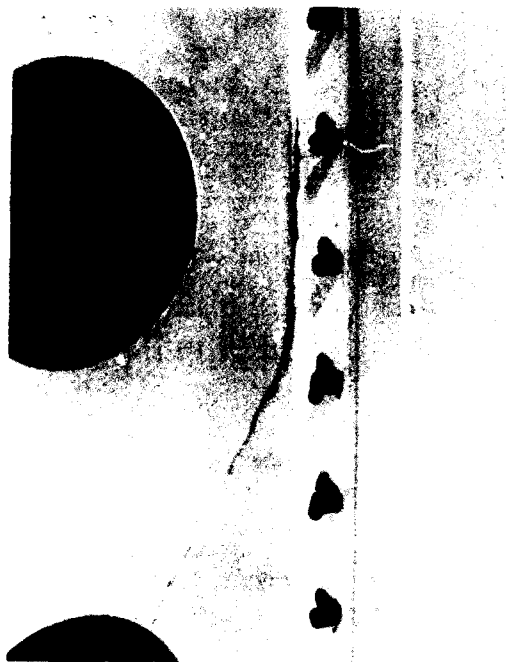
Fig. 6.   View of lightening hole failure No. 1 showing crack
propagation along outer flange.

±45° was used for the web repair. The initial
repair design philosophy was to reduce the local
strains by a factor of approximately two. There-
fore, the total thickness of repair patch required
was 4 mm compared with an original web thick-
ness of 2·5 mm since the woven carbon has a
slightly higher shear modulus.

The *S–N* curves in Fig. 8 compare the fatigue
performance of the wet lay-up repair with the
frame material. This figures shows the frame
failure point. It can be seen that a factor of four
reduction of local stress is required for the repair
to be acceptable. This is achieved by completely
covering the lightening hole and thus eliminating
the stress concentration together with the increase
in thickness of carbon against aluminium. This
confirms the carbon repair thickness.

The 5·5 mm thick inner flange was repaired
using pre-cured unidirectional (u/d) carbon strips,
totalling 4 mm thick, cold bonded to the flange
using paste adhesive. This thickness was chosen to
give a working strain of 1000 ± 1000 μstrain
assuming the carbon to take all of the flange load.
The endurance level of u/d carbon is approxi-
mately ±3400 μstrain at *R* = 0 in moulded com-
ponents. The chosen repair working strain level
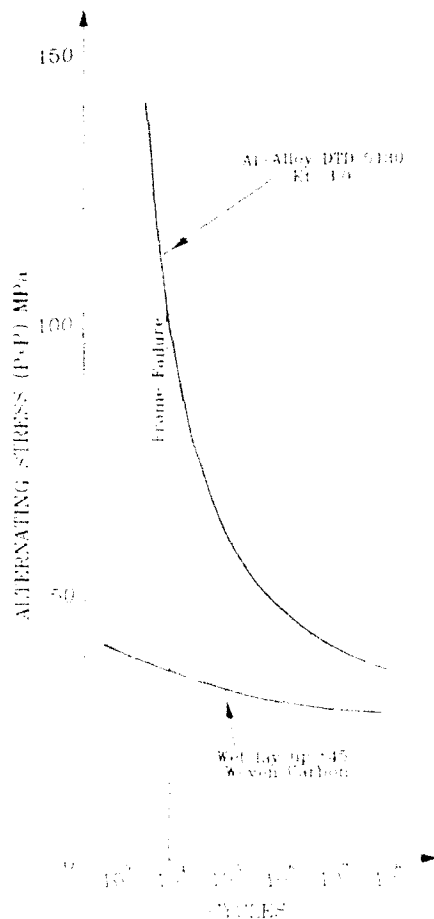
Fig. 8.   Comparison of DTD 5130 with wet lay-up ±45 woven carbon

Fig. 9.   Repair of lightening hole failure No. 2

therefore, allows a considerable margin to account for any deterioration in fatigue performance due to the repair process. The repair is shown in Fig. 9.

3.1.3 Repair process
The repair process was as follows:

a   Crack tips were stop drilled.
b   Rivets through cracked flanges were removed.
c   Paint was stripped from the repair vicinity and the anodic layer was reactivated within 3 h of subsequent bonding operations.
d   For the repair of the broken flange, u/d strips, 0·5 mm thick, were manufactured from four plies of pre-impregnated GRAFIL XAS 10K/Epoxy Fibredux 913 material cured at 125°C. These were then
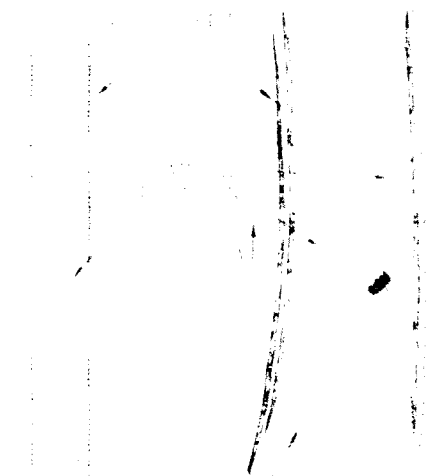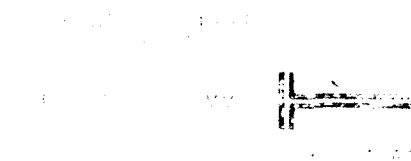
cold bonded to the flanges using paste adhesive whilst applying consolidation pressure using a vacuum bag.
e   For the repair of the shear web, the ±45 Brochier 833 carbon fabric was applied by wet lay-up with room temperature paste adhesive. The lightening holes were filled with Rohacell foam and consolidation pressure was applied using a vacuum bag.
f   Rivets were then re-installed with rivet burrs on the carbon side.

3.1.4 Repair performance
To date this repair has survived the following fatigue test cycles:

High frequency — 0·86 × 10⁶ cycles
Low Level Manoeuvre — 41 000 cycles
Medium Level Manoeuvre — 2207 cycles

This is more than the original structure achieved and is equivalent to approximately 16 400 h mean life. Although the test is conducted at factored loads, this life assessment makes none of the usual

allowance for:

(a) material scatter,
(b) moisture degradation,
(c) temperature degradation.

3.2 Lightening hole failure No. 2

3.2.1 Failure details

Figure 10 shows another shear web failure with one crack propagating from the lightening hole. Unlike the previous example, this crack did not propagate along the web to the flange junction due to the absence of significant Brazier loads. Instead, the crack propagated into the flange causing its complete failure. This failure section is subject to higher direct stresses than the previous example and so a slightly different repair technique was required.

3.2.2 Repair design

The failed flange was 7·5 mm thick and was repaired using 5 mm of pre-cured u/d carbon strips. Figure 11 compares the fatigue performance of u/d carbon with that of plain/lightly notched DTD 5130 plate and illustrates that

5 mm of u/d carbon is more than adequate providing that there is sufficient bond area to transfer the load. The mean fatigue strength of cold bond adhesives is about 5 ± 5 MPa and this figure is used to size the bond area. With all repairs, the plies are stepped off at the shallowest angle that space allows, with 5 mm steps taken as a minimum.

The shear web was repaired in a similar manner to that described above. However, eight plies per side of wet lay-up 0/90° woven carbon were also applied to the web close to the flange to restore its end load carrying capability. The wet lay-up $\pm 45°$ shear plies were then applied over the 0/90 plies. Figure 12 shows the repair.

3.2.3 Repair process

The repair process was as in Section 3.1.3 except that the 0/90 woven plies were bonded first. The $\pm 45°$ plies were then applied over the 0/90 plies.
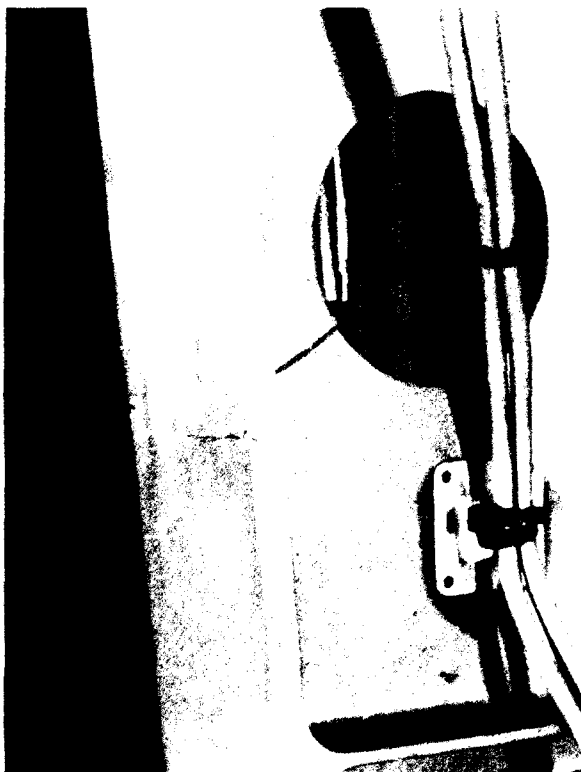
Fig. 10. View of lightening hole failure No. 2.
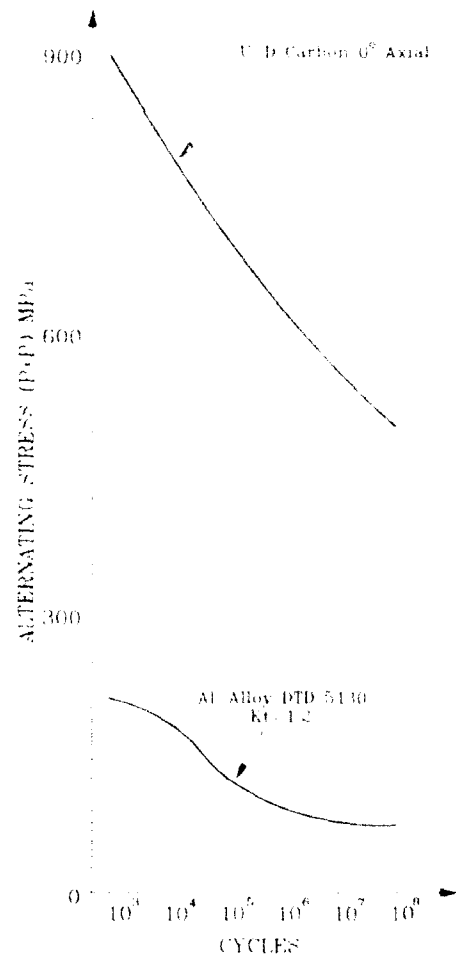
Fig. 11. Comparison of DTD 5130 with u/d carbon.

Fig. 12.   Repair of lightening hole failure No. 2.

Fig. 13.   View of curved flange failure.
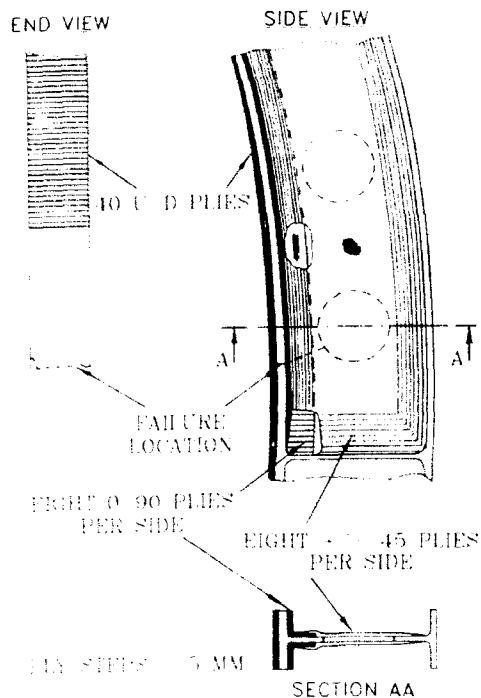
3.2.4 Repair performance

To date this repair has survived the following fatigue test cycles:

High Frequency — 0.52×10^6 cycles
Low Level Manoeuvre — 24 450 cycles
Medium Level Manoeuvre — 2207 cycles

This is equivalent to approximately 9800 h mean life without applying composite factors.

3.3 Curved flange failure

3.3.1 Failure details

Figure 13 shows a failure from the edge of a curved inner flange where it joins with a vertical stiffener. A three dimensional finite element model demonstrated that the failure was caused by a curved beam effect. The natural tendency of curved beam flanges is to warp out of plane. The vertical stiffener was preventing this from occurring leading to a local stress concentration as shown in Fig. 14.

3.3.2 Repair design

The repair of this failure was very similar to that described in Section 3.1.2 above. The flange thickness was 2 mm and 2 mm thickness of pre-cured u/d packs were used. Wet lay-up woven

Fig. 14.   3D FEM results showing stress concentration at curved flange failure point.

carbon at 0/90° was nested into the web/flange function to react Brazier loads and then eight plies of wet lay-up woven carbon at ±45° was overlaid into the web. Figure 15 shows the repair. The repair process was as in Section 3.2.3.

3.3.3 Repair performance
To date this repair has survived the following fatigue test cycles:

High Frequency — 0.86×10^6 cycles
Low Level Manoeuvre — 37 038 cycles
Medium Level Manoeuvre — 2207 cycles

This is more than the original structure achieved and is equivalent to approximately 14 800 h mean life without applying full composite factors.

3.4 Tapered flange failure

3.4.1 Failure details
Figures 16 and 17 show views of a failure at the thinnest point of a tapered flange. Only one side of the flange was failed. Strain gauge results have shown that this area is subject to higher-than-expected out-of-plane loads.

3.4.2 Repair design
The repair was similar to those described above. The failed flange was 3·5 mm thick and so 3 mm of pre-cured u/d carbon strips were cold bonded

to the outside face. This was to achieve a factor of 2·0 reduction in strain in the aluminium. Eight plies of wet lay-up 0/90 woven carbon were again nested into the web/flange angle. Since most of the shear web was still intact only four plies of ±45° woven carbon were overlaid into the web. The repair process was as in Section 3.2.3. Figure 18 shows the repair.

Fig. 16. View of tapered flange failure.
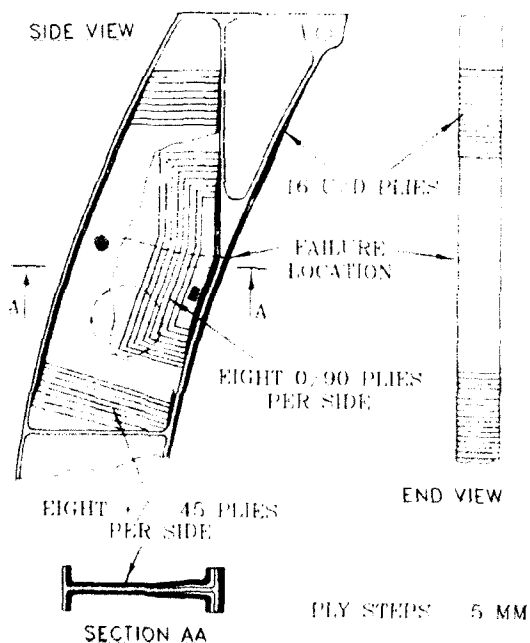
Fig. 15. Repair of curved flange failure.

Fig. 17. Close up view of tapered flange failure.
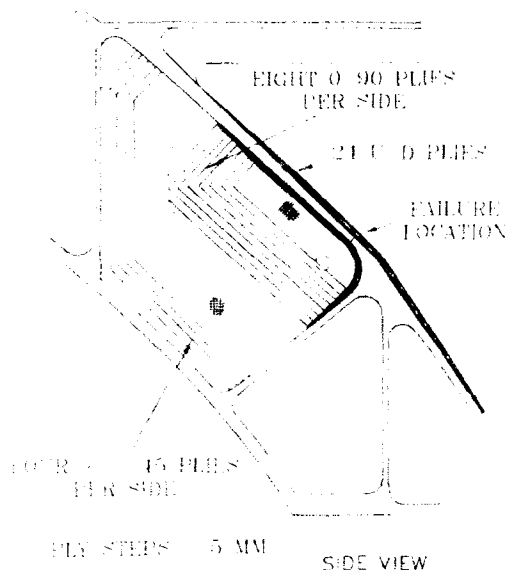
Fig. 18.   Repair of tapered flange failure.

3.4.3 Repair performance

To date the repair has survived the following fatigue test cycles:

High Frequency — 0.64×10^6 cycles
Low Level Manoeuvre — 24450 cycles
Medium Level Manoeuvre — 2207 cycles

This is equivalent to approximately 9800 h mean life without applying full composite factors.

4 REPAIR DESIGN RULES

4.1 General

It is desirable for the design experience gained from the case studies (and other repairs) to be translated into general repair design rules. These could then be applied to similar failures without the need for further analysis. The following sections, therefore, propose conservative design rules. Clearly, however, failures may vary widely and so sound engineering judgement is required when applying these rules.

4.2 Shear webs

Shear webs may be repaired using the original web thickness of wet lay-up woven carbon at ± 45° applied to each side of the web, i.e. a total of twice the original web thickness. If the crack is contained well within the web this repair is suf-

ficient. If, however, the crack has reached the edge of the shear web or propagated into or along the flange, then 0/90° woven carbon is also required. This should be applied to form a nested angle between the web and flange. The thickness requirement of 0/90° is the same as that of ±45°. Plies running into the web should be stepped off at a minimum of 5 mm.

4.3 Flanges

Flanges may be repaired using pre-cured u/d strips cold bonded in place. The thickness required is 70% of the original flange thickness. The bond length either side of the failure must be at least 16 times the flange thickness before the plies start stepping off. Plies should be stepped off at 5 mm per ply. If the failure location does not permit such a large bond area then fasteners must be used to transfer the load into the repair material. In this case ±45° woven carbon plies would need to be interleaved with the u/d strips to give significant lug strength. The same thickness again of ±45° would be required, doubling the total repair thickness.

5 IN-SERVICE APPLICATION POTENTIAL

The case studies illustrate the types of failures which can be repaired by this method. Most of the geometries have been complicated three dimensional shapes which would have been difficult to repair using metal. All have been installed *in situ* at room temperature. This makes them ideal for in-service application.

In addition, the repairs are lightweight: the heaviest repair weighs 0.82 kg to reinforce a shear web 600 mm × 125 mm. However, the repairs described above have all been conducted on primary structural items in which exist a high degree of damage tolerance. WHL do not consider that these techniques are currently applicable to GRADE A VITAL parts such as dynamic components.

6 LIMITATIONS

6.1 Bond strength

The limiting factor of the repair technique is the strength of the adhesive. Where insufficient bond area is available, or the bond is subject to peel

loads, fasteners are needed in addition to the bond. These may introduce stress concentrations into previously unnotched sections and so careful design is required.

6.2 Process control

As with all composite material applications, process control is very important: to ensure good bond strength and consolidation; and to reduce material strength ariability.

6.3 Inspection

Repairs should be readily inspectable to ensure that they have been satisfactorily installed and to monitor their continued integrity. The fatigue test repairs have generally been inspected by 'coin tap' but ultrasonic inspection has also been used.

6.4 Qualification

Providing a general repair 'formula' presents a problem for the airworthiness qualification of individual repairs. To-date none of the repairs have failed and consequently no data are available regarding possible failure modes. The failure modes may be slow and progressive or instantaneous. Consequently an approach based on either damage tolerance or safe life may be appropriate depending on the results of further testing.

7 CONCLUSIONS

Composite repairs have been successfully installed on the EH101 main load path fatigue test. Repair designs were quickly generated and were applied *in situ*. The design experience has been translated into general design rules. The performance of the repairs to date indicate that the techniques are viable for in-service use.

ACKNOWLEDGEMENTS

On design methods for bolted joints in composite aircraft structures

Tomas Ireman, Tonny Nyman & Kurt Hellbom

Saab Military Aircraft, S-581 88 Linköping, Sweden

The problems related to the determination of the load distribution in a multi-row fastener joint using the finite element method are discussed. Both simple and more advanced design methods used at Saab Military Aircraft are presented. The stress distributions obtained with an analytically based method and an FE-based method are compared. Results from failure predictions with a simple analytically based method and the more advanced FE-based method of multi-fastener tension and shear loaded test specimens are compared with experiments. Finally, complicating factors such as three-dimensional effects caused by secondary bending and fastener bending are discussed and suggestions for future research are given.

1 INTRODUCTION

Mechanically fastened joints are one of the most important elements in aircraft structures. Regardless of material combination in the parts joined, the joint is a critical element whose design is vital for the overall structural performance. Improper design may lead to overweight or structural problems and high life cycle costs of the aircraft. For joints in composite structures this is even more pronounced because of their inability to yield, the low transverse strength, the anisotropy and their sensitivity to temperature and moisture.

Typical applications of mechanically fastened joints in composite aircraft structures are the skin to spar/rib connections in, for example, a wing structure, the wing to fuselage connection and the attachment of fittings, etc. Examples of such joints from the fighter aircraft JAS 39 Gripen are shown in Fig. 1.

Mechanically fastened joints are difficult to design due to the many parameters and complex phenomena such as contact and friction involved in the behaviour of the joints. To include all parameters in an analysis of a general joint is almost impossible even with the most powerful computers of today. It is therefore necessary to reduce the problem to manageable size by conservative assumptions and proper design rules.

In the design of bolted joints in composite structures, as in the design of any structural element, there is a need for both simple and ad-

vanced methods for analysis and failure prediction. The simple methods are used in preliminary design, optimization and to sort out critical joints.

In Fig. 2 the overall design procedure for the case when FEM is used in each step is presented. First, the internal load distribution in the joint is determined. The more important the joint is considered to be the more detailed modelling is performed. Then, the local stress distribution around the fastener is determined by a detailed FE analysis or by analytically based methods and the
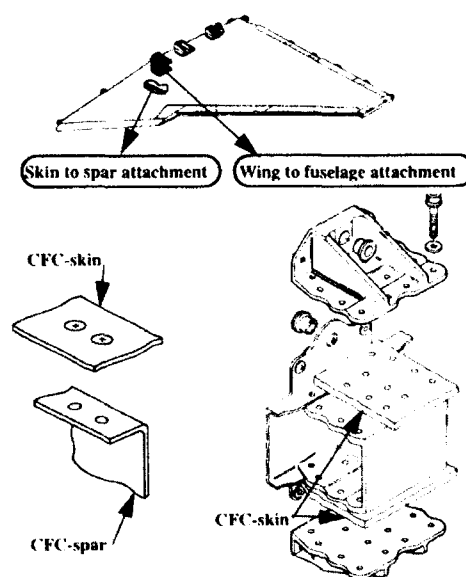
Fig. 1. Examples of bolted composite joints in JAS 39 Gripen.

strength is predicted using appropriate failure criteria.

In a secondary joint or in a preliminary design the load distribution is often determined using hand calculation methods and the strength prediction is performed using design diagrams.

2 LOAD DISTRIBUTION ANALYSIS

The purpose of load distribution analysis is to calculate the load distribution between the fasteners in a multi-fastener joint and the load distribution around a cut-out part of the laminate around the fastener. There are many problems associated with this type of calculation and the purpose of this section is to point out some of them. The discussion below is concentrated on load distribution analysis with FEM because in a joint with complicated geometry and loading this is considered to be the best way to determine the load distribution. However, in the design of secondary joints, preliminary design and design of primary joints with simple geometry and loading, hand calculations based on equilibrium considerations and simple computer programs may be sufficient.

Load distribution analyses are often performed on large structures which result in rather coarse meshes and simplified modelling of the joints. The contact between the members in the joint is usually ignored in the model. The hole is reduced to a point and the fastener, or a group of fasteners, is represented by a spring or beam element. If a group of fasteners is represented by a single spring or beam element it is necessary to perform the load distribution analysis in two steps.

In order to make a correct prediction of the load distribution, the finite element representing the fastener must be given the correct flexibility (1/stiffness). When determining and using flexibility data some difficulties occur due to the approximations presented above. To be able to predict the correct fastener displacement, it is not sufficient just to assign an experimentally known fastener flexibility (bolt constant) to the finite element representing the fastener. The fastener displacement consists partly of the fastener deformation, partly of the deformation at the hole edges of the parts. In the same way the 'fastener displacement' in the FE model depends on the deformation in both the element representing the fastener and the elements representing the parts. The latter does not represent the situation in the experiment because of the simplification made in the FE

model that the hole is omitted. This makes the contribution to the fastener displacement from the parts very mesh dependent. If the mesh in the parts is refined the net becomes more flexible and a stiffer 'fastener element' is required to obtain the correct fastener displacement and, in the case of a multi-fastener joint, the correct load distribution between the fasteners.

Considerable improvements in the prediction of the fastener displacement and secondary bending can be made by modelling the hole as shown by Edlund.[1] The price of the improvements is of course higher modelling and computing costs.

The other part of the load distribution analysis is the determination of the loading on a cut-out part of the laminate around the fastener. If this is done by hand it can be difficult to obtain a load case in equilibrium with the limited information from a coarse mesh.

3 DETAILED STRESS ANALYSIS USING ANALYTICALLY BASED METHODS

The method of complex functions developed by Muskhelishvili[2] extended to anisotropic materials by Lekhnitskii[3] and Savin[4] has been used by

(a) JAS 39 Gripen

(b) Load distribution analysis

c) Local stress analysis
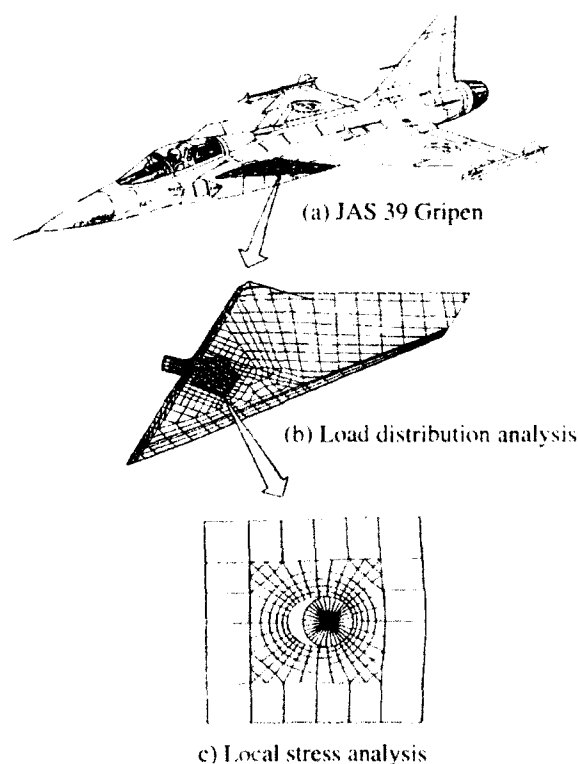
Fig. 2. Overall design procedure.

several authors to obtain the stress distributions in plates with loaded and unloaded holes. In the case of a rigid pin in an infinite plate, a major work was performed by de Jong[5] who also included friction between pin and plate. The additional complexity with an elastic pin has been considered by Hyer *et al.*[6] Finite geometry effects have been considered by using the collocation method[7] and the boundary integration method.[8] The basic equations of the anisotropic theory of elasticity for an infinite plate with a circular opening are reviewed below and the solution of the frictionless contact problem of an infinite plate loaded by a rigid pin is presented.

3.1 Basic equations

The two-dimensional stress field in an elastic plate can be found by determining Airy's stress function, $F(x, y)$ that satisfies the biharmonic equation for anisotropic materials

$$A_{22} \frac{\partial^4 F}{\partial x^4} - 2A_{26} \frac{\partial^4 F}{\partial x^3 \partial y} + (2A_{12} + A_{66}) \frac{\partial^4 F}{\partial x^2 \partial y^2}$$
$$- 2A_{16} \frac{\partial^4 F}{\partial x \partial y^3} + A_{11} \frac{\partial^4 F}{\partial y^4} = 0 \qquad (1)$$

where A_{ij} are the laminate compliances. Airy's stress function can be written as

$$F(x, y) = 2\mathrm{Re}(F_1(z_1) + F_2(z_2)) \qquad (2)$$

where $F_1(z_1)$ and $F_2(z_2)$ are analytic functions of the complex characteristic coordinates z_1 and z_2 defined as

$$z_k = x + \mu_k y, \quad k = 1, 2 \qquad (3)$$

where μ_1 and μ_2 are the roots to the characteristic equation associated with eqn (1).
By introducing the complex functions

$$\phi_k(z_k) = \frac{dF_k}{dz_k} \qquad (4)$$

the following expressions for the stresses and displacements can be derived from the definition of Airy's stress function and the kinematic relations

$$\sigma_x = 2\mathrm{Re}(\mu_1^2 \phi_1'(z_1) + \mu_2^2 \phi_2'(z_1)) \qquad (5)$$

$$\sigma_y = 2\mathrm{Re}(\phi_1'(z_1) + \phi_2'(z_1)) \qquad (6)$$

$$\tau_{xy} = -2\mathrm{Re}(\mu_1 \phi_1'(z_1) + \mu_2 \phi_2'(z_2)) \qquad (7)$$

$$u = 2\mathrm{Re}(p_1 \phi_1(z_1) + p_2 \phi_2(z_2)) \qquad (8)$$

$$v = 2\mathrm{Re}(q_1 \phi_1(z_1) + q_2 \phi_2(z_2)) \qquad (9)$$

where the primes denote differentiation with respect to z_k and

$$p_1 = A_{11}\mu_1^2 + A_{12} - A_{16}\mu_1$$

$$p_2 = A_{11}\mu_2^2 + A_{12} - A_{16}\mu_2$$

$$q_1 = \frac{A_{12}\mu_1^2 + A_{22} - A_{26}\mu_1}{\mu_1}$$

$$q_2 = \frac{A_{12}\mu_2^2 + A_{22} - A_{26}\mu_2}{\mu_2} \qquad (10)$$

The general form of $\phi_k(z_k)$ for the solution of the stress problem is

$$\phi_k(z_k) = A_k \ln z_1 + B_k z_k + \sum_{n=1}^{\infty} b_n^k z_k^{-n} \qquad (11)$$

where A_k, B_k and b_n^k are constants determined by the boundary conditions. The last part of eqn (11) can be identified as the holomorphic part which is single valued and tends to zero at infinity. In the case of an open hole in an infinite plate the constants A_k are zero while in the case of a loaded opening in an infinite plate the constants B_k are zero. In the first case the constants B_k are determined by introducing the remaining part of eqn (11) into eqns (5)–(7) with the condition that the stresses at infinity should be recovered.

3.2 Boundary conditions

In order to simplify the treatment of the boundary conditions new complex variables ζ_k are introduced as

$$\zeta_k = \frac{z_k \pm \sqrt{z_k^2 - R^2(1 + \mu_k^2)}}{R(1 - i\mu_k)} \qquad (12)$$

where R is the radius of the circular opening. The transformations in eqn (12) have the feature that they map the contour of the opening to a unit circle in the ζ_1 and ζ_2 planes, i.e. $\zeta_1 = \zeta_2 = e^{i\alpha} = \sigma$ on the contour of the opening.
For the case of a loaded opening in an infinite plate, eqn (11) can be written as

$$\phi_k(z_k) = C_k \ln \zeta_k + \sum_{n=1}^{\infty} c_n^k \zeta_k^{-n} \qquad (13)$$

where the last part is the holomorphic part denoted ϕ_n^k in the sequel.

The boundary conditions for the external forces can be expressed as

$$2\mathrm{Re}(\phi_1(z_1)+\phi_2(z_2)) = -\int_0 Y_\nu\,ds + k_1 \qquad (14)$$

$$2\mathrm{Re}(\mu_1\phi_1(z_1)+\mu_2\phi_2(z_2)) = \int_0 X_\nu\,ds + k_2 \qquad (15)$$

where X_ν and Y_ν are the external forces per unit area at the edge. s is an arbitrary arc length on the contour of the opening and k_1 and k_2 are integration constants depending on the start point for the integration.

In the case of a pin-loaded infinite plate the multi-valued part $C_k \ln \xi_k$ will yield the resultant forces P_x and P_y for a complete cycle round the hole boundary. Together with the condition that the displacements must be single-valued when completing a whole cycle, this gives the necessary equations for determining the constants C_k

$$C_1 + C_2 - \bar{C}_1 - \bar{C}_2 = \frac{P_x}{2\pi it}$$

$$\mu_1 C_1 + \mu_1 C_2 - \bar{\mu}_1 \bar{C}_1 - \bar{\mu}_2 \bar{C}_2 = -\frac{P_y}{2\pi it}$$

$$p_1 C_1 + p_2 C_2 - \bar{p}_1 \bar{C}_1 - \bar{p}_2 \bar{C}_2 = 0$$

$$q_1 C_1 + q_2 C_2 - \bar{q}_1 \bar{C}_1 - \bar{q}_2 \bar{C}_2 = 0 \qquad (16)$$

where the bars denote the conjugates of the marked quantities and t is the laminate thickness.

By using the first two parts of eqns (16) and expressing the holomorphic part as a power series in σ the boundary conditions (14) and (15) can be written as

$$2\mathrm{Re}(\phi_1(z_1)+\phi_2(z_2)) = -\int_0 Y_\nu\,ds = \frac{P_y\theta}{2\pi t}$$

$$+ \sum_{m=1} (a_m \sigma^m + \bar{a}_m \sigma^{-m}) \qquad (17)$$

$$2\mathrm{Re}(\mu_1\phi_1(z_1)+\mu_2\phi_2(z_2)) = \int_0 X_\nu\,ds = -\frac{P_x\theta}{2\pi t}$$

$$+ \sum_{m=1} (\beta_m \sigma^m + \bar{\beta}_m \sigma^{-m}) \qquad (18)$$

where a_m and β_m are coefficients from the tractions at the edge, X_n and Y_n. θ is the angle corresponding to s.

Identification between eqns (13), (17) and (18) gives the following expressions for the holomorphic parts in terms of the coefficients a_m and β_m.

$$\phi_0^1(z_1) = \sum_{m=1} \frac{\bar{\beta}_m - \mu_2 \bar{a}_m}{\mu_1 - \mu_2}\,\xi_1^{-m} \qquad (19)$$

$$\phi_0^2(z_2) = \sum_{m=1} \frac{\bar{\beta}_m - \mu_1 \bar{a}_m}{\mu_1 - \mu_2}\,\xi_2^{-m} \qquad (20)$$

In the general case of an infinite plate with a circular opening with radius R_2 loaded by a pin with radius R_1, different boundary conditions should be satisfied in different regions of the loaded edge as shown in Fig. 3.

In the different regions the following boundary conditions apply:

No-slip region:

$$u_r^{\mathrm{plate}} - u_r^{\mathrm{pin}} = \delta\cos\alpha - \Delta R(1-\cos\alpha)$$

$$u_\theta^{\mathrm{plate}} - u_\theta^{\mathrm{pin}} = -(\delta + \Delta R)\sin\alpha \qquad (21)$$

Slip-region:

$$u_r^{\mathrm{plate}} - u_r^{\mathrm{pin}} = \delta\cos\alpha - \Delta R(1-\cos\alpha)$$

$$|\tau_{r\theta}| = \mu|\sigma_r| \qquad (22)$$

No-contact region:

$$\sigma_r = 0$$

$$\tau_{r\theta} = 0 \qquad (23)$$

where

$$\delta = u_r^{\mathrm{plate}}(0) - u_r^{\mathrm{pin}}(0) \qquad (24)$$

and

$$\Delta R = R_2 - R_1 \qquad (25)$$
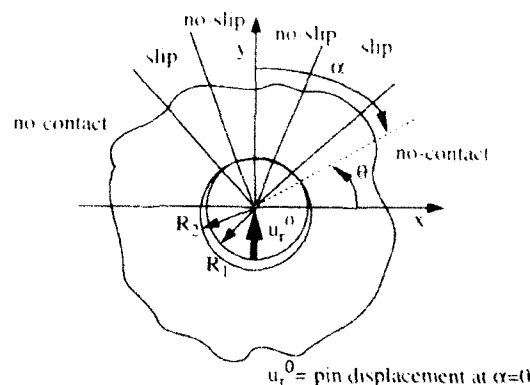
Fig. 3. Different regions at pin-plate interface.

i.e. δ is evaluated at $\alpha = 0$ and ΔR is the radial clearance. The subscripts r and θ refer to the radial and tangential directions respectively and μ is the friction coefficient.

3.3 Determination of the contact stress distribution

As in the work by de Jong[5] it is assumed that the pin and the hole can be in contact for angles in the interval $0 \le \theta \le \pi$ only. To be able to express unsymmetric contact pressures a sine-series is used in the interval $(0, \pi)$ together with the condition that the radial stress should be zero elsewhere.

$$N_s = p_0 \sum_{n=1} a_n \sin n\theta \quad 0 \le \theta \le \pi \quad (26)$$

$$N_s = 0 \quad \pi < \theta < 2\pi \quad (27)$$

Equations (26) and (27) can be expressed by a Fourier series

$$N_\theta = \frac{A_0}{2} + \sum_{m=1} A_m \cos m\theta + B_m \sin m\theta \quad (28)$$

The Fourier coefficients A_m, B_m are then easily expressed in terms of the coefficients, a_n, in the sine-series. By introducing eqn (28) into the boundary conditions, eqns (17) and (18), it is possible to relate the complex coefficients α_m and β_m to the real coefficients A_m and B_m.

$$\alpha_m = \frac{R}{4m}[(B_{m+1} - B_{m-1}) - i(A_{m+1} - A_{m-1})]$$

$$\beta_m = \frac{R}{4m}[(A_{m+1} - A_{m-1}) - i(B_{m+1} - B_{m-1})] \quad (29)$$

Thus the holomorphic part of $\phi_k(z_k)$ is completely determined through eqns (19) and (20). If friction is included a similar assumption for the shear stress distribution can be made and the same procedure as for the contact stress applied. To enforce the interface conditions between pin and plate, the displacements and stresses σ_r, $\tau_{r\theta}$ must be expressed in the coefficients of the sine-series, a_n, via eqns (5)-(9) and appropriate transformations.

As in Ref. 5 the loading is performed by giving the y-component of the resulting bolt force, P_y, i.e. the bolt is given an unknown displacement in a known direction. In the case when the direction of the bolt load and one of the principal material directions coincide, the contact stress distribution

is symmetric and P_y is equal to the bearing load, otherwise the component P_x of the bearing load is determined as part of the solution.

The distribution of the contact area and the slip-region if friction is included are determined through an iteration procedure. An initial contact area is assumed and the unknown coefficients a_n in eqn (26) are determined by the collocation method in which the contact conditions are satisfied in a finite number of collocation points corresponding to the unknown coefficients a_n. When the coefficients a_n are determined the contact stress distribution obtained is examined. If, for example, tension stresses are obtained at the edges of the distribution, the contact arc is too large and a smaller contact arc is tried.

4 SIMPLE ANALYTICALLY BASED DESIGN METHOD

4.1 Simple stress analysis using a fixed contact stress distribution

In order to simplify the stress analysis, a fixed contact stress distribution in the form of a sine distribution is assumed. Thus eqn (28) takes the form

$$N_\theta = \frac{4p_0}{\pi} \sin \theta \quad (30)$$

with

$$p_0 = \frac{P}{dt} \quad (31)$$

where P is the bolt load, d is the bolt diameter and t is the laminate thickness. The stress functions ϕ_k are then determined by solving the equation system (16) to obtain the non-holomorphic part and through eqns (29), (19) and (20) to obtain the holomorphic part.

The stress distribution for a more general case than a loaded hole, where the stresses at the hole edge are reacted at infinity, is obtained with the technique introduced by de Jong.[9] The solutions for tension/compression and shear loaded infinite plates with open holes are superimposed on the loaded hole case, as shown in Fig. 4.

4.2 Failure prediction

In this section the failure criteria used in the simple analytically based method are presented. Those
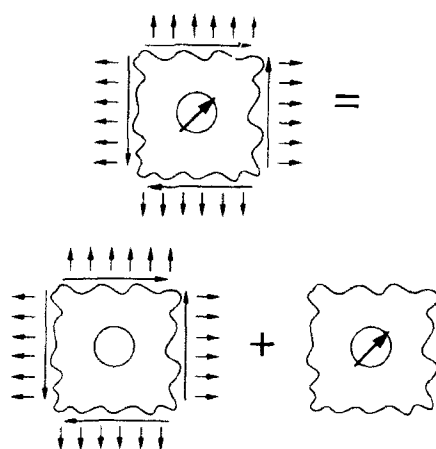
Fig. 4. Superposition of different solutions.

criteria are simple and require a smaller amount of testing than the more advanced criteria which will be presented in Section 5.3. It is of course possible to use the criteria in Section 5.3 together with the simplified stress analysis presented in the previous section.

By prescribing minimum edge distances and bolt spacing and applying some layup restrictions, the only failure modes which have to be considered are the bearing and net-section failure modes.

The failure load for the two different failure modes are predicted using two different failure criteria, one for net-section failure and one for bearing failure. The two failure criteria are both based on the same allowable far field strain for bolted joints, ε_B.

Net-section failure is predicted using a stress criterion in which the tangential stress on the hole edge is compared with the allowable tangential stress, σ_n^{all}, determined as

$$\sigma_n^{all} = E_n K_t \varepsilon_B \qquad (32)$$

where E_n is the tangential E-modulus in the point considered and K_t is the stress concentration factor with respect to the direction to the current evaluation point. The failure criterion is usually evaluated in the eight points around the circumference where fibres touch in a laminate containing $0°$-, $90°$- and $\pm 45°$-plies. Bearing failure is predicted with a stress criterion in which the maximum radial stress on the edge of the hole is compared with an allowable radial stress, σ_r^{all}, determined as

$$\sigma_r^{all} = E_r f \varepsilon_B \qquad (33)$$

where E_r is the radial E-modulus in the point considered and f is an empirically determined layup correction factor. The layup correction factor, f, is determined from bearing tests with different laminates and is expressed as a function of the square root of the ratio between the tangential and radial E-moduli. If this factor is assumed to be material independent, which seems to be reasonable at least for the same type of materials, e.g. carbon composites, the only strength parameter required is the allowable strain, ε_B. Therefore, this method is very useful for preliminary design and design of joints in secondary structures, where materials with insufficient design data for a more rigorous prediction may be used.

Through-thickness effects due to, for example, secondary bending and fastener bending in single shear joints are accounted for through empirically determined correction factors.

5 DESIGN METHODS INCLUDING SOLUTION OF THE CONTACT PROBLEM

Two methods, in which the solution of the frictionless contact problem is included are presented below. The two methods differ only in the stress analysis part. In the first method the two-dimensional anisotropic elasticity theory presented in Section 3 is used to obtain the stress distribution while in the second method this is done by FEM.

5.1 Analytically based local stress analysis

The local stress analysis of an infinite plate loaded with a rigid pin including the solution of the contact problem and an infinite plate with an open hole loaded at infinity is presented in Section 3. In order to obtain a more general loading case with both bearing and by-pass loading, the expressions for the displacements for the case with the open hole are added to the case with a pin loaded hole before the contact conditions in eqn (22) are imposed, i.e. the contact problem is solved for the case when both bearing and by-pass loads are present.

5.2 Local stress analysis with FEM

Two-dimensional FE analyses have been used in a number of studies[10-21] to determine the stress distribution in the vicinity of the hole. Only a few authors[22-24] have performed three-dimensional analyses.

The FE-based design method, COBOJ[17] consists of three parts: a model generation part in which the FE model is generated automatically, the FE analysis itself and a failure prediction part.

The FE analysis is performed with the FE system ASKA and includes a solution of the frictionless contact problem between the bolt and the hole. The contact algorithm in ASKA is developed by Torstenfelt[25] and is based on a nodal point iteration technique. The type of FE model used is shown in Fig. 2(c). The model consists of two parts, one fixed part close to the hole including the fastener which is common in all models and one flexible part which can be adjusted to the part cutout from the load distribution analysis model.

5.3 Failure prediction

Various types of failure criteria have been used to predict the strength of mechanically fastened joints. The characteristic distance approach introduced by Whitney and Nuismer[26] has been frequently used.[11-13,17,27] Another approach is to use progressive failure theories either by removing failed plies[18] or by elastoplastic modelling.[14,19,20]

As in the simple design method the only failure modes considered are net-section or bearing failure. For the prediction of net-section failure a variant of the 'Point Stress Criterion', PSC, introduced by Whitney and Nuismer[26] is used. The PSC assumes failure to occur when the tangential stress at a fixed distance, d_0, from the hole boundary reaches the unnotched strength, σ_0, of the laminate with respect to the tangential direction. The unnotched strength, σ_0, for the laminate is predicted with the maximum strain criterion and the characteristic distance as a function of layup and hole diameter is determined from experiments. In a general loading case it is assumed that failure initiates at points on the hole boundary having touching fibres. The failure criterion is evaluated at the radial distance, d_0, from these points. The bearing failure strength prediction follows the concept proposed by Chang et al.[12] who assume that failure occurs when the Yamada-Sun[28] failure criterion is satisfied in any point on a characteristic curve. The Yamada-Sun failure criterion states that failure occurs when

$$\left(\frac{\sigma_1}{X}\right)^2 + \left(\frac{\tau_{12}}{S}\right)^2 \geq 1 \qquad (34)$$

where σ_1 and τ_{12} are the longitudinal and shear stresses in a ply, X is the longitudinal tension or compression strength depending on the current

loading situation and S is the shear strength. In contrast to the approach proposed by Chang et al.,[12] who assumed a cosinusoidal shape of the characteristic curve, no restrictions are put on the shape of the curve. Instead, the characteristic curve is determined from bearing tests with different layups and FE analyses. The FE analyses are performed with models generated with the same mesh generator as in the design procedure. The failure load for each test specimen is applied to the FE model and the curve along which the Yamada-Sun failure criterion is satisfied with equality is determined. The characteristic curve is then determined as the curve along which the failure is predicted for each specimen as good as possible without being unconservative. The bearing tests are performed with the fasteners torque tightened finger tight. The characteristic curve can also be dependent on the hole diameter and tests with different hole diameters must therefore be included in the test program.

In a general loading case failure is predicted by evaluating the Yamada-Sun failure criterion in a number of points along the characteristic curve which are symmetrically located with respect to the bolt load direction.

6 DESIGN DIAGRAMS

For simple loading cases the easiest design method to use is the design diagram. Hart-Smith[29,30] presents a number of different diagrams determined from experiments.

Instead of performing experiments to obtain design diagrams, the computer based design methods presented in the previous sections can be used to generate design diagrams of different types. The two types of design diagrams used at Saab Military Aircraft are shown in Figs 5 and 6.

In the first diagram the bearing strength for different layups within the $0°/90°/\pm45°$ family can be determined. The diagrams can be determined for different degrees of bypass loading. The other diagram is of the bearing-bypass type introduced by Hart-Smith[31] which has also been used in the study by Crews and Naik.[32] The bearing-bypass diagram is only valid for one layup but can be used for design in any uniaxial bearing-bypass situation.

7 NUMERICAL RESULTS

The analytically based method including the solution of the contact problem and the FE-based

method have been used to calculate the stress distributions in three different bearing loaded laminates. In the analytically based method, 40 collocation points in the interval $-90° \leq \phi \leq 90°$, have been used to determine the contact stress distribution. The laminate properties in terms of engineering elastic material constants are shown in Table 1. The elastic properties have been calculated with classical laminate theory using the properties

of the Ciba-Geigy T300/914C graphite/epoxy material system with 65% fibre volume.

The geometry and loading of the analysed laminates are shown in Fig. 7. In all cases the bolt diameter, d, is 6·0 mm and the radial clearance, ΔR, is 0·021 mm which is a mean value for the clearance in the commonly used ISO fitting H10/f7. In the calculations with the FE-based method, the bolt was considered elastic with $E = 110$ GPa and $\nu = 0·29$ while the analytically based method is limited to a rigid bolt. The applied bearing stress, p_0, defined in eqn (31) is 300 MPa.

The calculated normalized contact stress distributions and the tangential stress distribution for the three different laminates are shown in Figs 8 and 9. ABM and FEM indicate results obtained with the Analytically Based Method and the FE-based Method respectively.

The radial and tangential stress distributions in the bearing and net-section planes respectively are shown in Figs 10 and 11.

It can be seen from Figs 8–11 that the general agreement between the stress distributions obtained with the analytically and FE-based methods is good. The greatest differences are obtained for the 0°-dominated laminate. This laminate is probably more sensitive to the differences in the contact solution methodology used in the two methods. Another reason for the deviations between the two methods is the approximate treatment of the finite width in the analytically based method. The somewhat physically unrealistic ten-

Fig. 5.   Design diagram for allowable bearing stress.

Laminate	E_x GPa	E_y GPa	G_{xy} GPa	ν_{xy}
A	99·2	35·5	8·5	0·24
B	35·5	99·2	8·5	0·08
C	51·5	51·5	19·3	0·33
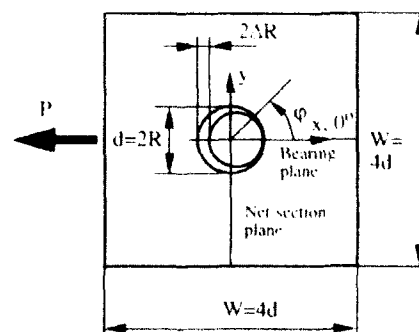
Bypass stress, σ_{bp} (MPa)

Fig. 6.   Bearing-bypass diagram.

Fig. 7.   Geometry and loading of the analysed laminates.

Fig. 8.   Contact stress distribution.

Fig. 10.   Radial stress distributions in the bearing plane

Fig. 9.   Tangential stress distribution.
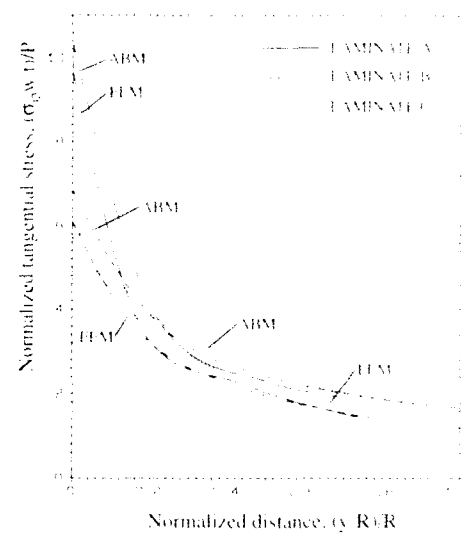
Fig. 11.   Tangential stress distributions in the net section plane

sile stresses at the edge of the contact surface, see Fig. 8, obtained with the FE-based method indicate that the mesh is too coarse to accurately determine the contact stress distribution.

8 PREDICTIONS

In order to demonstrate the failure prediction capability of the simple analytically based method

and the FE-based method, the strength of three different test specimens has been predicted. The test specimens are shown in Figs 12–14 and the laminate properties in terms of engineering elastic material constants are shown in Table 2. The test specimens are chosen to be more representative of joints in real aircraft structures than the simple coupons used to determine characteristic distances.

Stacking sequence:
[0°/90°/45°/135°/0°/45°/135°/90°/90°/45°/135°/0°/45°/135°/90°/0°]$_{s2}$
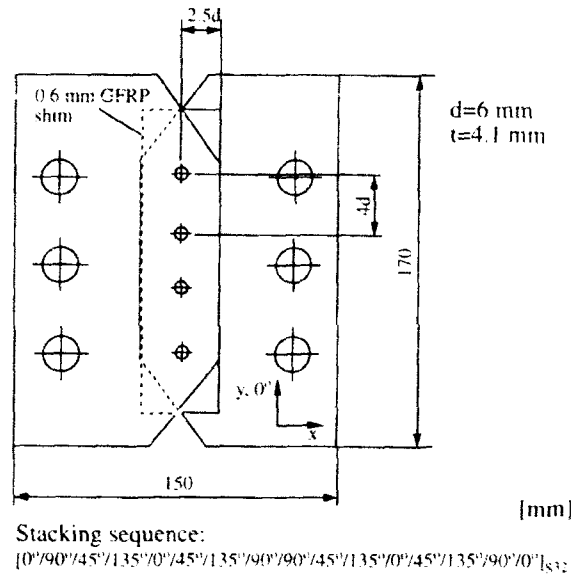
Fig. 12. Specimen A: Shear loaded joint with a single row of fasteners.

Stacking sequence:
[0°/90°/45°/135°/0°/45°/135°/90°/90°/45°/135°/0°/45°/135°/90°/0°]$_{s2}$
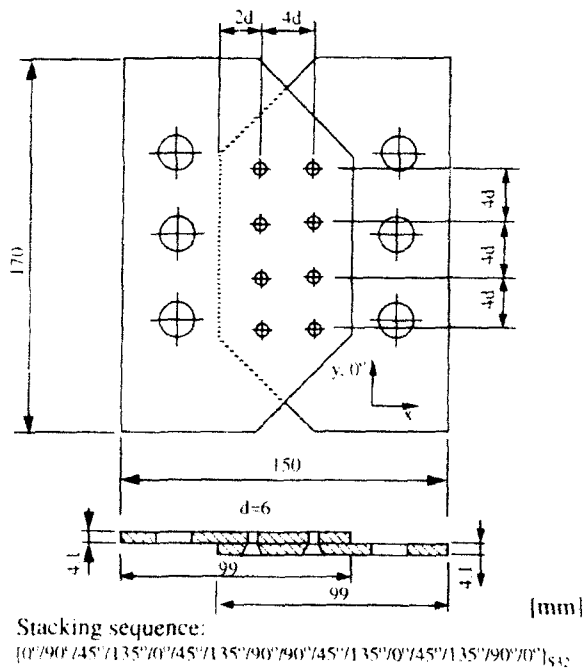
Fig. 13. Specimen B: Shear loaded joint with two rows of fasteners.

Fig. 14. Specimen C: Tension loaded joint with two rows of fasteners.

Table 2. Properties of laminates used in test specimens

Specimen	E_x GPa	E_y GPa	G_{xy} GPa	ν_{xy}
A	51·5	51·5	19·3	0·33
B	51·5	51·5	19·3	0·33
C	42·7	73·1	15·2	0·20

Table 3. Strength predictions

Specimen	F^{EXP}	Δ^{SAM}	F^{SAM}	Δ^{FEM}	F^{FEM}
A	B	0·92	N	0·85	N
B	N	0·63	N	0·77	N
C	N	0·76	N	0·90	N

etc., and in the numerical examples in the previous section. In the strength predictions presented below no corrections for through-thickness effects have been made because the test specimens are selected so that these effects are small. However, in the design of a joint in a real structure such a correction would have been made.

The load distribution in the joints has been determined from FE analyses following the description in Section 2. The fastener flexibility used has been determined from measurements in the tests.

The results from the failure predictions with the two methods in terms of the ratio between the experimental and predicted failure loads are shown in Table 3. Δ is the ratio between predicted and experimentally obtained failure load, F is the failure mode indicated with B for Bearing failure and N for Net-section failure and the superscripts SAM and FEM indicate the type of method, Simple Analytically based Method and FE-based Method respectively.

From Table 3 it can be seen that the predictions with both methods are conservative compared with the experiments but the wrong failure mode is predicted for specimen A and that the simple method seems to be more conservative at least in the last two

cases. One source of the conservatism is that the fasteners in the test specimens were torque tightened 5–6 N m while the design method assumes finger tight torque tightening (~0·5 N m). The reason for the prediction of the wrong failure mode for specimen A is probably ignorance of the through-thickness effects, i.e. in the case of shear loading and the non-uniform stress distribution through the thickness caused by the bending and tilting of the fastener.

9 CONCLUDING REMARKS

Each step in the design procedure of a mechanically fastened joint or in any design procedure is equally important, therefore the research efforts should be directed to improve the weakest links in the design chain. The load distribution analysis must be considered as such a part due to many difficulties associated with the representation of the joint in the load distribution FE model. Another important area for improvements which is strongly related to the load distribution analysis is the presence of through-thickness effects. In addition to more basic research including three-dimensional FE analyses and experimental studies on simple cases, more advanced modelling techniques using macro elements which are capable of calculating relevant measures of secondary bending and fastener bending, are needed in the load distribution analysis.

As shown by the comparison of stress distributions between the analytically based method in which the contact problem is solved and the FE-based method in Section 7, the analytically based method proves to be a good alternative to the FE-based method for simple loading cases. It should be pointed out that the computing time for the analytically based method is only a fraction of the computing time for the FE-based method. It should also be noted that the complexity in the analytically based stress analysis increases rapidly when the assumptions such as infinite width and rigid bolt are removed and if friction is included. Therefore it is believed that there will always be a need for the FE-based method to handle complex loading cases and geometries.

With the failure criteria presented in this paper it is possible to fairly well predict the strength of mechanically fastened joints with moderate through-thickness effects, i.e. non-uniform stress distribution through the thickness of the laminate. The failure criteria based on experimentally determined characteristic distances give somewhat

better predictions than the simple criteria but require a considerable number of experiments to determine the necessary parameters. Therefore, there is a strong need for failure criteria which require fewer experimentally determined parameters and are capable of predicting the strength of a joint with sufficient accuracy. Again three-dimensional modelling in which the interlaminar stresses can be considered will be important.

Even in the future three-dimensional modelling will probably not be a commonly used tool in the design of mechanically fastened joints due to the complexity and the need for computer power. There will always be a need for simple and fast methods such as design diagrams and analytically based computer programs for the large volumes of joints in an aircraft. Only for critical primary joints, advanced three-dimensional FE models can be useful in the design. Another interesting application of more advanced modelling and failure prediction is to generate correction factors for, for example, through-thickness effects, which can be used together with two-dimensional analyses in the design.

REFERENCES

1. Edlund, A., A nonlinear finite element analysis of the secondary bending in composite bolted joint. Report LiTH-IKP-Ex-531 (in Swedish) Linköping Institute of Technology, Department of Mechanical Engineering, Linköping, 1985.
2. Muskhelisvili, N. I., *Some Basic Problems of the Mathematical Theory of Elasticity*. Nordhoff Ltd, Groningen, Holland, 1953.
3. Lekhnitskii, S. G., *Anisotropic Plates*, translated from the second Russian edition by S. W. Tsai & T. Cheron. Gordon and Breach, New York, 1968.
4. Savin, G. N., *Stress Distributions Around Holes*. NASA TT F-607, 1970.
5. de Jong, T., On the calculation of stresses in pin-loaded anisotropic plates. TU Delft, Report LR-529, November, 1987.
6. Hyer, M. W., Klang, E. C. & Cooper, D. E., The effect of pin elasticity, clearance, and friction on the stresses in a pin-loaded orthotropic plate. Virginia Tech CCMS-85-04 VPI-E-85-09, 1985.
7. Ramkumar, R. L., Saether, E. S. & Appka, K., Strength analysis of mechanically fastened composite structures. AGARD conference proceedings No. 427, Madrid, Spain, 27–29 April, 1987.
8. Naidu, A. C. B., Dattaguru, B., Mangalgiri, P. D & Ramamurthy, T. S., Analysis of a finite composite plate with smooth rigid pin. *Composite Structures*, 11 (1989) 197–216.
9. de Jong, T., Stresses around pin-loaded holes in elastically orthotropic or isotropic plates. *Journal of Composite Materials*, 11 (1977) 313–31.
10. Waszak, J. P. & Cruse, T. A., Failure mode and strength predictions of anisotropic bolt bearing specimens. *Journal of Composite Materials*, 5 (1971) 421–5.

11. Agerwal, B. L., Static strength prediction of bolted joint in composite material. AIAA/ASME/ASCE/AHS, 20th Structure/Structural Dynamics and Materials Conference, St Louis, MD, April, 1979, pp. 303–9.

12. Chang, F-K., Scott, R. A. & Springer, G. S., Failure of composite laminates containing pin loaded holes — method of solution. *Journal of Composite Materials*, **18** 1984 255–78.

13. Chang, F-K., Scott, R. A. & Springer, G. S., Failure strength of nonlinearly elastic composite laminates containing a pin loaded hole. *Journal of Composite Materials*, **18** (1984) 464–77.

14. Yogeswaren, E. K. & Reddy, J. N., A study of contact stresses in pin-loaded orthotropic plates. *Computers & Structures*, **30** (1988) 1067–77.

15. Ramamurthy, T. S., Analysis of interference fit pin joints subjected to bearing bypass loads. *AIAA Journal*, **28** 1990 1800–5.

16. Eriksson, L. I., Contact stresses in bolted joints of composite laminates. *Composite Structures*, **6** 1986 57–75.

17. Eriksson, I., An analysis method for bolted joints in primary composite aircraft structure. Agard Conference Proceedings No. 427, Madrid, Spain, 27–29 April, 1987.

18. Jurf, R. A., Behaviour of bolted joints in composite laminates. Ph D dissertation, University of Delaware, Newark, DE, June, 1986.

19. Jurf, R. A. & Vinson, J. R., *Failure Analysis of Bolted Joints in Composite Laminates, Composite Materials: Testing and Design* Ninth Volume, ed. S. P. Garbo ASTM STP 1059, American Society for Testing and Materials, Philadelphia, PA, 1990, pp. 165–90.

20. Tsujimoto, Y. & Wilson, D., Elasto-plastic failure analysis of composite bolted joints. CCM-85-09, University of Delaware, Newark, DE, 1985.

21. Chang, F-K. & Chang, K-Y., Post-failure analysis of bolted composite joints in tension or shear-out mode failure. *Journal of Composite Materials*, **21** 1987 809–33.

22. Arnold, W. S., Marshall, I. H., Wood, A. J. & Mously, R. F., Observations on bolted connections in composite structures. *Composite Structures*, **13** 1989 133–51.

23. Mattews, F. L., Wong, C. M. & Chryssafitis, S., Stress distribution around a single bolt in fibre-reinforced plastic. *Composites* July 1982 316–22.

24. Johansson, S., A three-dimensional finite element contact analysis of a bolted joint. Report LiTH-IKP-Ex-650, Linköping Institute of Technology, Department of Mechanical Engineering, Linköping, 1987.

25. Torstenfelt, B., Finite elements in contact and friction applications. PhD thesis, Division of Solid Mechanics and Strength of Materials, Department of Mechanical Engineering, Linköping University, Sweden, 1985.

26. Whitney, J. M. & Nuismer, R. J., Stress fracture criteria for laminated composites containing stress concentrations. *Journal of Composite Materials*, **8** 1974 253–65.

27. Curtis, A. R. & Grant, P., The strength of carbon fibre composite plates with loaded and unloaded holes. *Composite Structures*, **2** 1984 201–21.

28. Yamada, S. E. & Sun, C. T., Analysis of laminate strength and its distribution. *Journal of Composite Materials*, **12** 1978 275–84.

29. Hart-Smith, L. J., Mechanically fastened joints for advanced composites. Phenomenological considerations and simple analysis. Douglas paper 6748A, McDonnel Douglas Corporation, 1978.

30. Hart-Smith, L. J., Design and analysis of bolted and riveted joints in fibrous composite structures. Douglas paper 7739, McDonnel Douglas Corporation, 1986.

31. Hart-Smith, J. L., Bolted joints in graphite-epoxy composites. NASA-Langly Contract Report NASA CR-144899, 1977.

32. Crews, J. H., Jr & Naik, R. H., Combined bearing and bypass loading on a graphite/epoxy laminate. *Composite Structures*, **6** 1986 21–40.

Mechanical bending behaviour of composite T-beams

A. Silva,[a] J. Travassos,[b] M. M. de Freitas[a] & C. M. Mota Soares[a]

[a]CEMUL, Instituto Superior Técnico, Av. Rovisco Pais, 1096 Lisboa Codex, Portugal
[b]INDEP, S.A., Rua Fernando Palha, 1802 Lisboa Codex, Portugal

A study of the design and mechanical behaviour of co-cured T-beams subjected to very high loading is presented. The T-beams were made by press moulding from pre-pregs of uni-directional glass or carbon fibre and glass fabric reinforced high performant epoxy matrix. Each type of beam was instrumented with strain gauges in the web and flange in order to carry out experimental four point bending tests. Analytical and numerical studies were also performed to compare experimental versus numerical and analytical results and to establish the suitability of a simplified bending theory for statically determinate composite beams constructed from laminated composite panels. The maximum carrying loads in the beam layers were evaluated experimentally and analytically using the Tsai-Wu failure criterion. Results showing the suitability of the simplified beam theory are presented and discussed.

INTRODUCTION

The use of composite materials is continuously increasing for a variety of purposes because of the potential benefits of decreased weight and increased stiffness. In the case of laminated composite materials, made of long fibres in polymer matrix, the bending behaviour can be enhanced by the use of reinforcements, a procedure also used in metallic structures. For plates and shells, these reinforcement structures are in general beams that are riveted or bonded to the structure. Recently, the use of co-cured beams in plates became an attractive procedure, as it helps to minimize manufacturing time and eventually to maximize structural performance.

The analytical tools available to predict the mechanical behaviour of beams are based on the Bernoulli–Euler theory of bending[1] or, alternatively on Timoshenko beam theory, while for plates Kirchhoff[2] or Mindlin[3,4] theories are used associated with analytical or numerical methods. The lay-up for a beam made up of composite plates respectively for the flange and web are not the same, since in the co-cured junction non-symmetrical lay-up occurs whose mechanical behaviour is affected by coupling effects of bending and tension.

Some work related to the experimental investigation of coupled deformations in thin-walled composite beams has been reported by Nixon.[5] Chandra et al.[6,7] Also Bank[8] presented modifications to a beam theory for the bending and twisting of composite material open-section beams. The theory has been formulated in terms of effective laminate properties to describe the overall beam deformation under bending, twisting and axial extension.

More recently Bank and Cofie[9] and Smith and Bank[10] carried out experimental verification of a modified theory for thin-walled open-sections for anisotropic composite beams, applied to symmetric and antisymmetric glass/polyester I-beams. These beams were tested under transverse loading and end-moments, using a cantilever model to evaluate induced twist, out-of-plane and in-plane lateral and transverse deflection respectively. A good correlation has been reported between experimental, analytical and numerical analysis carried out using a finite element model.

In the sequence of the work presented by Bank and Cofie[9] and Smith and Bank,[10] the present developments are an extension of the former by predicting analytically the failure of T composite beams using the Tsai–Wu failure criterion[2] applied to glass and hybrid (carbon and glass) fibre composites. The experimental results are compared with the simplified composite beam theory and alternatively with a finite element model using plate elements. Different dimensions,

lay-up and materials are considered, with and without hybrid lay-ups to establish the range of application of the analytical and numerical calculations.

MATERIALS

The materials used in the beam manufacture are unidirectional and fabric pre-pregs of glass or carbon fibres on an epoxy resin matrix:

- unidirectional pre-pregs of E-glass on a high performant epoxy resin R367 manufactured by STRUCTIL (France).
- unidirectional pre-pregs of T300 (Toray) on a high performant epoxy resin R367 manufactured by STRUCTIL (France).
- fabric pre-pregs of E-glass on epoxy resin manufactured by Hexcel-Genin (France).

The nominal mechanical properties of the laminated material for a 50% V_f (fibre volume) are listed in Table 1 where E is the Young's modulus.

v the Poisson's ratio, G the shear modulus, and the subscript L denotes the direction of the fibres and the subscript T the direction perpendicular to the fibres. In Table 2 are listed the tensile (subscript T), compressive (subscript C) and shear strength S of the laminate material.

Table 1. Elastic properties

Material	E_L GPa	E_T GPa	v_{LT}	G_{LT} GPa	Thickness mm
VEE45, R365	39·25	4·5	0·29	3·0	0·35
CTE45, R365	117·25	8·2	0·35	3·1	0·49
1581-ES-67	22·0	22·0	0·28	2·85	0·24

Table 2. Mechanical properties

Material	L_t MPa	L_c MPa	I_t MPa	I_c MPa	S MPa
VEE45, R365	1250	600	35	141	63
CTE45, R365	1270	1130	42	141	63
1581-ES-67	400	390	400	390	150

FABRICATION OF T-BEAMS

T-beams were manufactured from the pre-pregs by press moulding, simulating the fabrication of co-cured plates reinforced with beams. This manufacturing procedure, shown schematically in Fig. 1, ensures that the web and the upper flange of the beam are designed with symmetrical lay-up but the flange (upper and lower flanges) is composed of the previous symmetrical lay-up together with a half lay-up (lower flange) of the web. The following characteristics (dimensions and stacking sequences) were obtained for each beam tested (Fig. 2):

S4.1   60(web) × 40(flange) mm, with radius of curvature 3 mm between web and flange, made of unidirectional (ug) and fabric (fg) glass fibre, with 50% V_f and the following stacking sequences:

Web $- [45_{fg}, 0_{ug}, 45_{fg}, (0_{ug})_2, 45_{fg}, 0_{ug}]_s$

Flange $- [((0_{fg}, 45_{fg})_3, 0_{ug})_2, 0_{ug}, 45_{fg}, (0_{ug})_2, 45_{fg}, 0_{ug}, 45_{fg}]_t$

S4.2   60(web) × 40(flange) mm, with radius of curvature 3 mm between web and flange, made of unidirectional (ug) and fabric (fg) glass fibre, with 50% V_f and the following stacking sequences:

Web $- [45_{fg}, 0_{ug}, 45_{fg}, (0_{up})_2, 45_{fg}, 0_{ug}]_s$

Flange $- [((45_{fg}, 0_{fg}), 45_{fg})_2, 0_{ug}, 45_{fg}, (0_{ug})_2, 45_{fg}, 0_{ug}, 45_{fg}]_t$

S4.3   60(web) × 40(flange) mm, with radius of curvature 3 mm between web and flange, made of unidirectional carbon (uc) and fabric (fg) glass fibre, with 50% V_f and the following stacking sequences:

Web $- [45_{fg}, 0_{uc}, 45_{fg}, (0_{uc})_2, 45_{fg}, 0_{uc}]_s$

Flange $- [((0_{fg}, 45_{fg})_3, 0_{fg})_2, 0_{uc}, 45_{fg}, (0_{uc})_2, 45_{fg}, 0_{uc}, 45_{fg}]_t$

S4.4   Identical to S4.1, but with 43% V_f.
S4.1.5   Identical to S4.1 but with radius of curvature 5 mm between web and flange.
S4.1.7   Identical to S4.1 but with radius of curvature 7 mm between web and flange.
S4.1(40 × 40) Identical to S4.1 but with 40(web) × 40(flange) mm.

The manufacturing procedure used was press moulding with steel moulds where the laminate thickness was imposed, giving an accurate control of % V_f. The pressure, temperature and time of curing were used according to the pre-preg manufacturer's instructions.

FLEXURAL TESTS

All 60 × 40 mm T-beams were instrumented with five strain gauges, as schematically represented in Fig. 3. They were loaded in a mechanical testing machine, in four point bending to achieve uniform bending moment in the middle section, where the strain gauges were placed. All the specimens had a test span of 300 mm. At least three T-beams of each type were tested to final fracture.
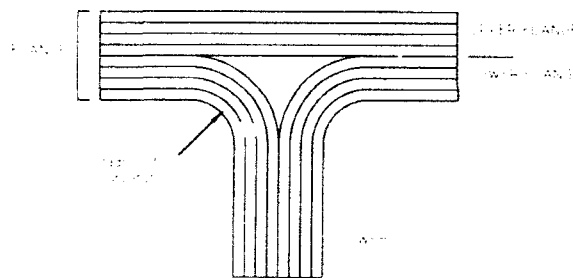
Fig. 1.   Schematic representation of beam cross-section.
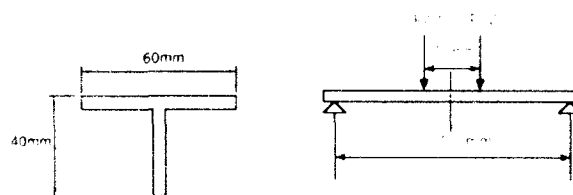
Fig. 2.   Typical beam section and experimental setup.
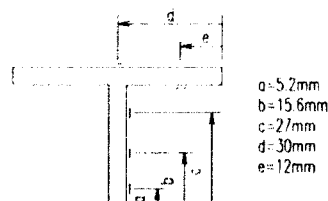
Fig. 3.   Location of strain gauges on the 60 × 40 mm beams.

SIMPLIFIED COMPOSITE BEAM THEORY

The classical beam theory is used in the design of structures built up of beams such as I, T, L, W or other types of beams, although they are actually made of thin panels. In the case of the T-beams, they are made of two panels, as Fig. 4 shows. Each panel has a 'panel coordinate system' (1, 2), other than the 'global coordinate system' (x, y, z) of the beam. For a general panel, there is a constitutive relation[2] in the form of eqn (1).

$$
\begin{Bmatrix} \varepsilon_1 \\ \varepsilon_2 \\ \varepsilon_6 \end{Bmatrix} =
\begin{bmatrix}
\dfrac{1}{E_1} & \dfrac{-\nu_{12}}{E_2} & \dfrac{\nu_{16}}{E_6} \\[2mm]
\dfrac{-\nu_{21}}{E_1} & \dfrac{1}{E_2} & \dfrac{\nu_{26}}{E_6} \\[2mm]
\dfrac{\nu_{61}}{E_1} & \dfrac{\nu_{62}}{E_2} & \dfrac{1}{E_6}
\end{bmatrix}
\begin{Bmatrix} \sigma_1 \\ \sigma_2 \\ \sigma_6 \end{Bmatrix}
\qquad (1)
$$

The stresses σ_1, σ_2 and σ_6 are average stresses across the panel thickness, and $\varepsilon_6 = 2\varepsilon_{12}$. The mechanical constants are average mechanical constants across the thickness.[2] The Young's modulus E_1 is the in-plane longitudinal modulus, obtained from the laminate in-plane stiffness coefficients (the 'A' matrix) which is obtained from the layer stiffness coefficients (the 'Q' matrix) depending on the mechanical constants of each layer.[2] The mechanical constants E_2 and E_6 are obtained in the same manner, as well as ν_{16} and ν_{26}, the in-plane normal coupling effects and ν_{61} and ν_{62}, the in-plane shear coupling effects.

Since the section of interest in the beam is the middle one and that section is under pure bending only, the expressions presented will serve for this particular case.

In the case of pure bending, an assumption is made in which the deformations due to the shear strains do not affect the linear axial normal stress distribution. If a couple is applied to the beam along the z-axis, then the classical form for the
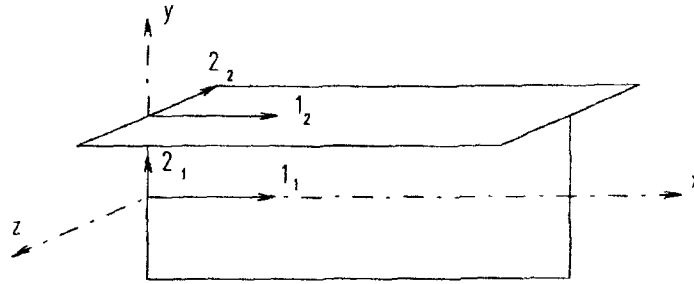
Fig. 4.   Coordinate systems on T-beams.

stress distribution is[1]

$$\sigma_\cdot = \frac{M_z y}{I_z} \qquad (2)$$

where M_z is the bending moment and I_z and y are, respectively, the second moment of area about the neutral axis and the distance from the neutral axis. Since in pure bending the only existing stress is the stress σ_x then, $\sigma_x = \sigma_1$ and use of eqn (1) yields

$$\varepsilon_1 = \frac{1}{E_1}\,\sigma_1 = -\frac{M_z y}{E_1 I_z} \qquad (3)$$

One has to notice that, in a composite beam, there is only one component of stress, but there is a shear strain along with the axial strain, although this shear strain is not used in this work.

For beams with different mechanical constants in the web and flange, the section is transformed as indicated by Bank.[11]

The average stress across the panel σ_1 is thus given by

$$\sigma_1 = \varepsilon_1 E_1 = -\frac{M_z y}{I_z} \qquad (4)$$

The stresses in the individual layers inside the panel will be given by[1]

$$\sigma_{1_i} = \varepsilon_1 E_1 = -\frac{M_z y}{E_1 I_z}\,E_1 \qquad (5)$$

where the subscript i denotes the ith layer.

FAILURE CRITERION

There are a considerable number of failure criteria throughout the literature.[12,14] Some involve stress failure criteria, others involve strain failure criteria, and others yet use energy failure criteria. In the first stage of this work, the Tsai–Wu criterion was preferred.

The Tsai–Wu energy criterion states that failure will occur if the following conditions are satisfied

$$F_i\sigma_i + F_{ij}\sigma_i\sigma_j = 1 \qquad i,j = 1,2,\dots,6$$

$$ \qquad (6)$$

$$F_{ii}F_{jj} - F_{ij}^2 \geq 0 \qquad i,j = 1,2,\dots,6$$

where for the special case of bi-dimensional anisotropic materials such as composite material layers, eqn (6) and its quantities F_i and F_{ij} are given by[2]

$$F_1\sigma_1 + F_2\sigma_1 + F_{11}\sigma_L^2 + F_{22}\sigma_T^2 + F_{66}\sigma_{LT}^2 + 2F_{12}\sigma_1\sigma_T = 1 \qquad (7)$$

$$F_1 = \frac{1}{L_t} - \frac{1}{L_c} \qquad F_{11} = \frac{1}{L_t L_c} \qquad F_2 = \frac{1}{T_t} - \frac{1}{T_c} \qquad F_{22} = \frac{1}{T_t T_c} \qquad F_{12} = -\frac{1}{2\sqrt{L_t L_c T_t T_c}} \qquad F_{66} = \frac{1}{S^2}$$

and the quantities $L_t L_c T_t T_c$ are the tensile and compressive maximum stresses in the respective directions in the (L, T) coordinate system, while S is the maximum shear stress in the layer.

In the present case, there is only one component of stress σ_x in the (x, y, z) global coordinate system. Noting that, for the web of the beam, $\sigma_x = \sigma_1$, each layer has a unique stress component in the x direction given by eqn (5). Depending on the fibre orientation in the ith layer, the Young's modulus in the x

direction in the same layer will be given by[1]

$$E_x = \cfrac{1}{\cfrac{\cos^4\theta_i}{E_L} + \cfrac{\sin^4\theta_i}{E_T} + 2\cos^2\theta_i\sin^2\theta_i\left(\cfrac{1}{2G_{LT}} - \cfrac{\nu_{LT}}{E_L}\right)} \qquad (8)$$

where θ_i is the angle between the (x, y) and (L, T) coordinate systems.

The stress σ_x must then be transformed to the (L, T) coordinate system,[2] yielding:

$$\begin{Bmatrix} \sigma_L \\ \sigma_T \\ \sigma_{LT} \end{Bmatrix}_i = \begin{bmatrix} \cos^2\theta & \cos^2\theta & 2\cos\theta\sin\theta \\ \cos^2\theta & \cos^2\theta & -2\cos\theta\sin\theta \\ -\cos\theta\sin\theta & \cos\theta\sin\theta & \cos^2\theta - \sin^2\theta \end{bmatrix}_i \begin{Bmatrix} \sigma_x \\ 0 \\ 0 \end{Bmatrix} \qquad (9)$$

Introducing eqns (5), (8) and (9) into (7) one obtains the maximum load in the layer, according to Tsai–Wu.

FINITE ELEMENT MODEL

A finite element model of the T-beam (Fig. 5) was built up using the commercial program COS-MOS[15] for personal computer use. The beam was constructed of quadrilateral and triangular generic plate-shell elements so called SHELL4L and SHELL3L with layered input and six degrees of freedom per node. The elements are based on Mindlin theory with linear C^0 fields and using the concept of decomposing the deformation into well-defined bending and shear modes.[16]

The loads were distributed across the flange of the beam, and the mesh was refined around the location of the loads using a total of 3293 degrees of freedom, 550 nodes and 504 elements.

Particular attention was given to the application of boundary conditions to simulate the experimental test. The beam was left free to displace axially at one end and the flange was constrained in the transverse direction in the nodes where loads are applied. The web was left completely free to deform and bend in all directions.

RESULTS AND DISCUSSION

Figure 6 shows an axial strain profile obtained from the five strain gauges attached to the surface at the centre position of the T-beam S4.3, a beam composed of hybrid layers, tested in four point bending. No significant deviation of the linearity of the experimental data obtained is observed for the two loads presented with no modifications with respect to the location of the neutral axis.

Similar results were obtained for the other T-beams mentioned previously.

These tensile and compressive strains were calculated using the simplified beam theory and the finite element model. Figures 7a–7e and Table 3 show the comparison between the strains obtained for a load of 10 kN, experimentally and calculated (analytically and numerically) for all
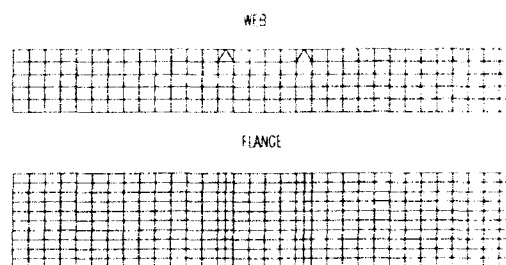
Fig. 5. Finite element mesh used for numerical calculations.
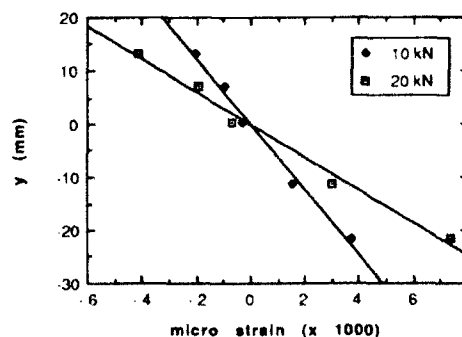
Fig. 6. Experimental data from S4.3 beam with 10 and 20 kN applied loads.
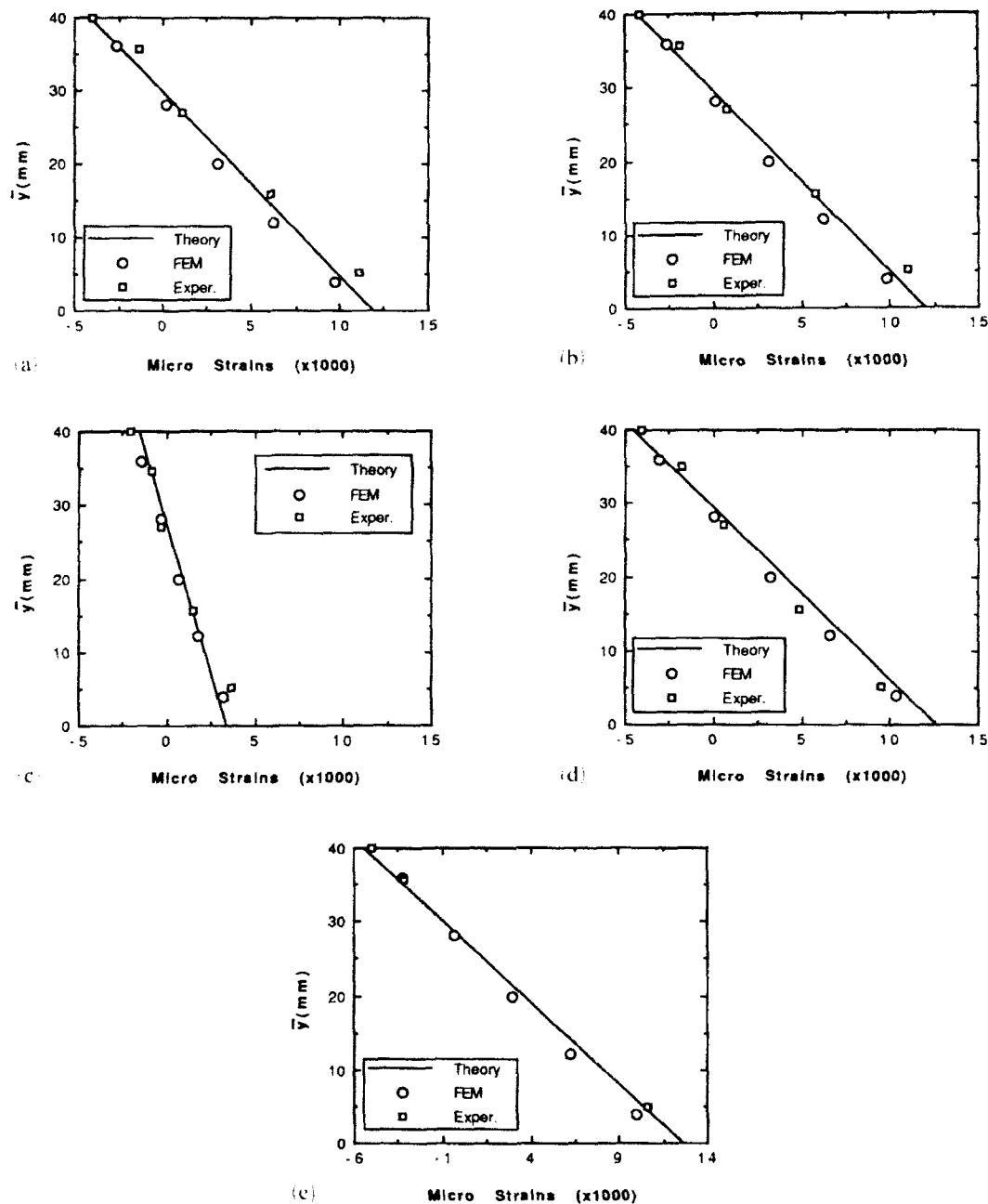
Fig. 7.   (a) S4.1 beam strain versus distance from bottom of web, ȳ, for 10 kN load; (b) S4.2 beam strain versus distance from bottom of web, ȳ, for 10 kN load; (c) S4.3 beam strain versus distance from bottom of web, ȳ, for 10 kN load; (d) S4.4 beam strain versus distance from bottom of web, ȳ, for 10 kN load; (e) S4.1 40 × 40 mm beam strain versus distance from bottom of web, ȳ for 10 kN load.

types of beams tested. No significant scatter is observed between the results for each T-beam, showing that, despite the existence of a non-symmetrical lay-up in the flange of the beam and the different theories used for the beam calculation, the analytical, numerical and experimental results are in good agreement. Concerning the position of the neutral axis, a maximum difference of 4% is

obtained for the hybrid composite T-beam and smaller values are obtained for the other type of beams. The finite element model always calculates the lowest value location of the neutral axis below the flange of the beam.

As expected, all the T-beams presented failure in tension on the web, with loads presented in Table 4 (average values of three beams tested).

Table 3. Comparison of analytical, numerical and experimental results for a 10 kN applied load

Beam	Method	Neutral axis location (mm)	$\varepsilon_{max} \times 10^{5}$	$\varepsilon_{min} \times 10^{5}$
S4.1	Theory	29·83	11·94	−4·07
	FEM	28·64	11·0	−4·38
	Experimental	30·51	13·08	−4·06
S4.2	Theory	29·59	12·01	−4·23
	FEM	28·64	11·0	−4·38
	Experimental	29·78	12·83	−4·4
S4.3	Theory	27·47	3·38	−1·54
	FEM	25·34	3·62	−2·09
	Experimental	26·77	4·3	−2·13
S4.4	Theory	29·42	12·66	−4·56
	FEM	28·2	11·78	−4·93
	Experimental	28·91	11·26	−4·32
S4.1– 40×40	Theory	27·86	12·60	−5·49
	FEM	27·53	11·41	−5·17
	Experimental	28·31	12·79	−5·28

Table 4. Experimental maximum carrying loads

	Maximum experimental loads (N)
S4.1	22 622
S4.2	22 073
S4.3	31 981
S4.4	23 054
S4.1.5	22 955
S4.1.7	21 876
S4.1–40×40	21 160

Fig. 8. Typical load–displacement diagrams of 1 S4.3 beams and 2 S4.1 beams until failure.

Table 5. Theoretical and experimental failure loads for S4.1 and S4.4 beams

Beam	Maximum load N		
	Theory		Experimental
	Unidirect.	Fabric	
S4.1	26 173·7	24 207·1	22 622
S4.3	31 479·2	85 601·4	31 981
S4.4	24 587·0	22 721·2	23 054

Figure 8 shows two load–displacement curves obtained on the failure tests of the T-beams S4.1 and S4.3, manufactured respectively with glass only and hybrid composite materials. A different failure behaviour is observed. For the S4.1 beam and all the T-beams made of glass composite materials, the failure is characterized by a certain amount of plastic behaviour before failure. For the hybrid T-beam a sudden failure occurs during the elastic loading. This behaviour can be explained, calculating the stresses in each layer by the simplified beam theory and applying the Tsai–Wu criterion of failure. Table 5 shows the maximum load predicted for each layer of the web of the T-beams S4.1, S4.3 and S4.4, together with experimental results. It can be seen that for the hybrid T-beam, the unidirectional carbon layers present the lowest value of the load, while for the other two beams all the layers present similar values of failure loads.

No significant influence on the maximum load obtained at failure was observed for the beams tested with different curvature radius between the web and the flange, as shown in Table 4. Neither the simplified beam theory nor the finite element calculations can simulate this behaviour since it is not possible for the modelling of the curvature radius on the beams. Nevertheless, it must be remarked that a different failure behaviour can be expected for out of plane bending.

CONCLUSIONS

The study of the mechanical behaviour in four point bending, of co-cured T-beams made of composite materials allowed the following conclusions:

—There is a significantly good correlation between analytical (beam theory), numerical (finite element) and experimental results.

—The beam theory is applicable to this type of beam and loading where non-symmetrical lay-up exists.

—The Tsai–Wu failure criterion, with stresses calculated analytically, can predict with accuracy the failure of the beams.

—For in-plane bending, the radius of curvature between the flange and the web has no influence on the final maximum load of the beam.

ACKNOWLEDGEMENTS

REFERENCES

1. Gay, D., Matériaux Composites, 3rd edn. Hermes, 1991.
2. Tsai, S. W. & Hahn, H. T., Introduction to Composite Materials. Technomic, Lancaster, PA, 1980.
3. Mindlin, R. D., Influence of rotary inertia and shear on flexural motion of isotropic elastic plates. J. Appl. Mech., 18 (1951) 31–8.
4. Noor, A. K. & Burton, W. S., Assessment of computational models for multilayered anisotropic plates. Composite Structure, 14 (1990) 233–65.

5. Nixon, M. W., Extension-twist coupling of composite circular tubes with application to tilt rotor blade design. In Proc. AIAA 28th Structures, Structural Dynamics and Material Conf., AIAA paper 87-0772, Monterey, CA. 6–8 April, 1987.
6. Chandra, R., Stemple, A. D. & Chopra, I., Thin-walled composite beams under bending, torsional, and extensional loads. J. Aircraft, 27 (1990) 619–26.
7. Chandra, R. & Chopra, I., Experimental and theoretical analysis of composite I-beams with elastic couplings. In Proc. AIAA 32nd Structures, Structural Dynamics and Material Conf., Baltimore, MD, 8–10 April, 1991, pp. 1050–65.
8. Bank, L. C., Modifications to beam theory for bending and twisting of open-section composite beams. Composite Structures, 15 (1990) 93–114.
9. Bank, L. C. & Cofie, E., A modified beam theory for bending and twisting of open-section composite beams—numerical verification. Composite Structures, 21 (1992) 29–39.
10. Smith, S. J. & Bank, L. C., Modifications to beam theory for bending and twisting of open-section composite beams—experimental verification. Composite Structures, 22 (1992) 169–77.
11. Bank, L. C., Shear coefficients for thin walled composite beams. Composite Structures, 8 (1987) 47–61.
12. Vinson, J. R. & Sierakowski, R. L., The Behaviour of Structures Composed of Composite Materials. Martinus Nijhoff, Dordrecht, 1986.
13. Hart-Smith, L. J., A scientific approach to composite laminate strength prediction. Composite Materials: Testing and Design. 10th Volume. ASTM STP 1120, 1992, pp. 142–69.
14. Wu, E. M., Phenomenological anisotropic failure criterion. In Mechanics of Composite Materials, Vol. 2, ed. G. P. Sendeckyj. Academic Press, New York, 1974, pp. 353–431.
15. COSMOS/M User Guide*. Structural Research and Analysis Corporation, 1987.
16. Belytschko, T. & Stolarski, H., A Cº triangular plate element with one-point quadrature. International Journal on Numerical Methods in Engineering, 20 (1984) 787–802.

Torsional response of inhomogeneous and multilayered composite beams

Marco Savoia & Nerio Tullini

University of Bologna, Istituto di Tecnica delle Costruzioni, Viale Risorgimento 2, 40136, Bologna, Italy

The elastic response of inhomogeneous orthotropic beams with general cross-section and subject to uniform torsion is investigated. The problem is formulated both in terms of the warping and of the Prandtl stress function. Moreover, the exact solution for rectangular orthotropic beams constituted by any number of layers is derived, making use of a series form which is unaffected by unstable behaviours. Several examples are presented, showing that approximate solutions based on simplified kinematical models can yield very poor estimates of the torsional rigidity. Finally, it is shown that the plating of homogeneous beams by means of thin carbon or glass fibre-reinforced laminae can be used to make the torsional rigidity 8–10 times as much.

1 INTRODUCTION

Problems concerning the elastic response of inhomogeneous anisotropic beams often arise in many engineering fields, for instance in the analysis of plated wood beams[1] and composite rotor blades.[2] In this paper, the torsional response of composite beams of arbitrary cross-section is analysed. The beam considered consists of prismatic components joined along their side surfaces. Making use of the Prandtl stress function, expressions are derived for calculating the shear stress distributions, the cross-sectional warping and the torsional rigidity. It should be remembered that cross-sectional warping can be the starting point for deriving one-dimensional theories for composite beams under more complex boundary and loading conditions.[3-5]

The exact solution for the uniform torsion of rectangular multilayered orthotropic beams is presented, making use of a series form which is unaffected by unstable behaviours even for low ratios of thickness to width. At present, exact solutions are available only for two-layered isotropic,[6] symmetric sandwich isotropic[7] and homogeneous anisotropic[8] cross-sections. For orthotropic laminates, to the authors' knowledge, only approximate solutions based on the Reissner–Mindlin theory (FSDT) have been proposed.[9] It is shown that FSDT results are very poor when compared with the exact solution; in particular FSDT underestimates the torsional

rigidity especially for thick laminates constituted by a low number of plies with very dissimilar elastic properties (as is the case of plated wood or cross-ply fibre-reinforced cross-sections). Finally, a design formula for the evaluation of the torsional rigidity of sandwich beams is presented, which is accurate over the whole range of thickness-to-width ratios.

2 BASIC STATEMENTS

Consider a prismatic beam of general cross-section and composed of orthotropic media. The beam is referred to a right-handed orthogonal co-ordinate system $(0; x_1, x_2, x_3)$, where the x_1 and x_2 axes lie in the root cross-section $(x_3 = 0)$ and x_3 is the centroidal axis. The cross-section of the beam consists of S regions of area A_s, corresponding to different materials, with external boundary Γ_e^s and interfaces Γ_i^s (see Fig. 1). For each layer the orthotropy axes are assumed to coincide with the reference axes. Moreover, K holes are present in the cross-section, having areas A_c^k and boundaries Γ_c^k. Finally, we assume that the boundary Γ^s of the sth layer is a piecewise C^1 curve, and that no points of the interfaces are shared by more than two layers.

Within the framework of the St Venant problem, tangential force distributions at the two ends are considered, whose resultants reduce to two twisting moments M_t, so that the beam is subject
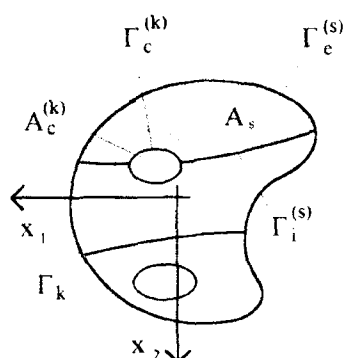
Fig. 1. A general inhomogeneous cross-section.

to uniform torsion. The problem of the elastic equilibrium of such a beam leads to the following differential problem:

A Equilibrium equation. traction-free equations for the lateral and the hole boundaries, stress continuity condition at the layer interfaces, stress balance at the ends of the beam:

$$\tau_{31,1} + \tau_{32,2} = 0 \qquad \text{in } A, \qquad (1)$$

$$\tau_{31} n_1 + \tau_{32} n_2 = 0 \qquad \text{on } \Gamma_e^s \text{ and } \Gamma_c^k \qquad (2)$$

$$[\tau_{31} n_1 + \tau_{32} n_2] = 0 \qquad \text{on } \Gamma_i^s \qquad (3)$$

$$\iint_A \tau_{31} \, dA = 0; \quad \iint_A \tau_{32} \, dA = 0;$$

$$\iint_A (\tau_{32} x_1 - \tau_{31} x_2) \, dA = M_t \qquad (4)$$

B Strain-displacement relations and constitutive law, displacement compatibility at the interfaces:

$$\tau_{31} = G_{13} (u_{3,1} + u_{1,3}); \ \tau_{32} = G_{23} (u_{3,2} + u_{2,3})$$

$$\text{in } A, \qquad 5$$

$$[u_1] = [u_2] = [u_3] = 0 \qquad \text{on } \Gamma_i^s \qquad 6$$

where the symbol [ ] stands for jump of the argument reported inside. For multiply-connected regions eqns (1)–(6) have to be supplemented by the condition of single-valuedness of displacement components. This condition can be fulfilled by imposing the vanishing of the following line integral taken along any closed circuit Γ_k surrounding a hole of the cross-section[10] (see Fig. 1):

$$\oint_{\Gamma_k} du_1 = \oint_{\Gamma_k} du_2 = \oint_{\Gamma_k} du_3 = 0 \quad \text{for } k = 1, \dots, K \qquad (7)$$

3 GENERAL SOLUTION OF TORSION PROBLEM FOR COMPOSITE ORTHOTROPIC BEAMS

The solution to differential problems (1)–(7) can be obtained either in terms of the torsion warping function or making use of the Prandtl stress function. As usual in the analysis of uniform torsion problems, the assumption is made that all transverse sections remain undeformed in their planes and that an axial warping takes place, constant along the beam. Hence, the displacement field is case in the form:

$$u_1 = -\Theta x_2 x_3; \quad u_2 = \Theta x_1 x_3; \quad u_3 = \Theta \omega_s(x_1, x_2)$$

$$(8)$$

where Θ is the angle of relative twist and ω_s is the torsional warping of the sth layer. Making use of the constitutive equations (5) and of eqns (8) the non-zero stress components take the form:

$$\tau_{31}^s = G_{13}^s \Theta (\omega_{s,1} - x_2); \quad \tau_{32}^s = G_{23}^s \Theta (\omega_{s,2} + x_1)$$

$$(9)$$

Hence, substituting eqn (9) in the governing equations (1), the following generalised Laplace equation for the sth region is obtained:

$$G_{13}^s \omega_{s,11} + G_{23}^s \omega_{s,22} = 0 \qquad \text{in } A, \qquad (10)$$

Equation (10) shows that the warping function ω_s reduces to a harmonic function for transversely isotropic materials, where $G_{13} = G_{23}$. Analogously, substituting eqns (8) and (9) in the boundary, interface and monodromy conditions (2), (3), (6) and (7) yields:

$$G_{13}^s \omega_{s,1} n_1 + G_{23}^s \omega_{s,2} n_2 = G_{13}^s x_2 n_1 - G_{23}^s x_1 n_2$$

$$\text{on } \Gamma_e^s \text{ and } \Gamma_c^k$$

$$[G_{13}^s \omega_{s,1} n_1 + G_{23}^s \omega_{s,2} n_2]$$

$$= [G_{13}^s x_2 n_1 - G_{23}^s x_1 n_2] \quad \text{on } \Gamma_i^s$$

$$[\omega_s] = 0 \qquad \text{on } \Gamma_i^s$$

$$\oint_{\Gamma_k} d\omega = \sum_s \int_{\Gamma_k} \omega_{s,1} \, dx_1 + \omega_{s,2} \, dx_2 = 0$$

$$\text{for } k = 1, \dots, K \qquad (11)$$

where $\Gamma_k = \cup \Gamma_k^s$.

The torsion problem can be stated in an alternative way by defining a potential function Ψ_s (Prandtl stress function) so as to satisfy identically

In order to demonstrate the failure prediction capability of the simple analytically based method

material constants are shown in Table 2. The test specimens are chosen to be more representative of joints in real aircraft structures than the simple coupons used to determine characteristic distances.

the equilibrium equation (1):

$$\tau_{31} = \Theta \Psi_{,2} \qquad \tau_{32} = -\Theta \Psi_{,1} \qquad (12)$$

By equating the RHS's of eqns (9) and (12), the relation between the warping and the stress function is obtained:

$$\omega_{,1} = \frac{\Psi_{,2}}{G_{13}} + x_2 \qquad \omega_{,2} = -\frac{\Psi_{,1}}{G_{23}} - x_1 \qquad (13)$$

and making use of the Schwarz integrability theorem $(\omega_{,12} = \omega_{,21})$ the following generalised Poisson equation is obtained, defined over the sth layer:

$$\frac{1}{G_{23}} \Psi_{,11} + \frac{1}{G_{13}} \Psi_{,22} = -2 \qquad \text{in } A_s \qquad (14)$$

In Ref. 11 the St Venant' problem for anisotropic rectangular multilayered cross-sections, based on the two Lekhnitskii stress functions, has been formulated making use of a direct integration technique. For orthotropic layers the governing equations are uncoupled and one of the field equations reduces to eqn (14), unless an integration coefficient at the RHS exists which depends on the layer considered. It is easy to verify that, to assure the continuity of in-plane displacements, this coefficient is independent of the layer and coincides with the unit twisting angle Θ.

Equations (12) show that, for each layer, the level lines of the stress function are also the lines of shearing stress $\tau = \tau_{31}, \tau_{32}$. Hence, eqn (2) implies that the stress function, for the sth layer, assumes constant values over the external boundary Γ and over the hole contours. By imposing the stress and displacement continuities at the intersection points between interfaces and the external and the hole contours it can be shown that the stress function is constant over the whole external boundary $\cup \Gamma_0$ and over Γ_i; moreover it is continued at the interfaces. Only one constant value can be arbitrarily fixed (for instance $\Psi_0 = 0$ at the external boundary), whereas all the remaining constants over the holes must be determined. The stress-free condition (2) and the continuity conditions of the interlaminar shearing stress (3) and of the axial displacement (6) at the interfaces give:

$$\Psi = 0 \qquad \qquad \text{on } \Gamma_0$$

$$\Psi = c^k \qquad \qquad \text{on } \Gamma^k \qquad (15)$$

$$\Psi = 0; \quad \omega = 0 \qquad \text{on } \Gamma_i$$

where the c^k are constant values for each hole, irrespective of the number of layers. Moreover, making use of eqn (13), the monodromy condition of axial displacements (7) around the kth hole can be written in terms of the stress function as follows:

$$-\int_{\Gamma_k} \left(\frac{\Psi_{,1}}{G_{23}} n_1 + \frac{\Psi_{,2}}{G_{13}} n_2 \right) d\tilde{s} = 2 A_k$$

$$\text{for } k = 1, \ldots, K \qquad (16)$$

where A_k is the area surrounded by the closed circuit $\Gamma_k = \cup \Gamma_k^s$ (see Fig. 1), n_1 and n_2 are the cosines of the inward normal and $\tilde{s}$ is a curvilinear co-ordinate lying on Γ_k.

Finally, making use of eqn (12) it can be verified that the stress balance at the ends of the beam (4, left and centre) are identically fulfilled, whereas from eqn (4, right) the following expression for the unit twisting angle is obtained:

$$\Theta = \frac{M}{G_r J}$$

where

$$G_r J = 2 \iint \Psi \, dA + 2 \sum c^k A^k \qquad (17)$$

represents the torsional rigidity for the composite orthotropic beam and G_r is a reference shear modulus.

In the following section the case of a rectangular multilayered cross-section will be analysed, where the exact solution to eqns (14)–(16) can be obtained.

4 RECTANGULAR MULTILAYERED CROSS-SECTION

Consider a rectangular laminated cross-section (Fig. 2), constituted of S orthotropic layers having two orthotropy directions parallel to the edges of the cross-section (cross-ply lamination scheme). The height, the width and the area of the cross-section are denoted by $H = h_S - h_0$, $B = 2b$ and $A = BH$, where h_0 and h_S are the co-ordinates of the bottom and the top of the cross-section. Moreover, h^s, h_{s-1} and h_s are the height and the coordinates of bottom and top interfaces of the sth layer.

Making use of the Fourier method, the differential problem (14) and (15) is solved in terms of
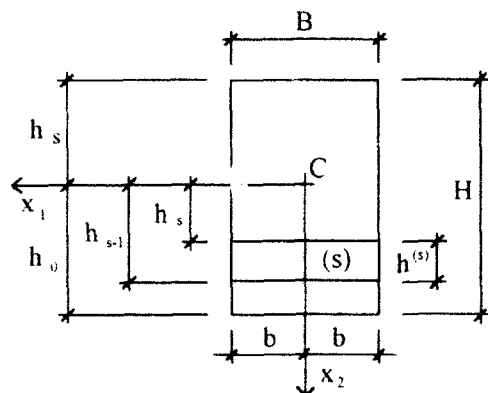
Fig. 2. The rectangular multilayered cross-section.

eigenfunction expansion of the corresponding elliptic boundary value problem. For a rectangular layer this expansion is given by a linear combination of trigonometric functions of x_1 and unknown functions of x_2. Then, taking into account eqn (15, top) at the lateral faces, the Prandtl function for the sth layer can be cast in the form:

$$\Psi = G_{23}^s B^2 \sum_{n=0}^{\infty} \frac{q_n}{\alpha_n^3} \left[1 - \psi_{sn}(x_2)\right] \cos \alpha_n \frac{x_1}{B} \quad (18)$$

where $q_n = 8(-1)^n$ and $\alpha_n = (2n+1)\pi$. By substituting eqn (18) into the field equation (14) a second order total differential equation for the unknown function $\Psi_{sn}(x_2)$ is obtained, whose solution can be cast in the form:

$$\psi_{sn}(x_2) = a_{sn} \cosh \beta_{sn} \frac{x_2}{H} + b_{sn} \sinh \beta_{sn} \frac{x_2}{H}$$

$$\text{for } s = 1, \ldots, S \text{ and } n = 1, \ldots, \infty \quad (19)$$

where the following positions have been made:

$$\beta_{sn} = \alpha_n \eta_s, \quad \eta_s = \mu_s \frac{H}{B}, \quad \mu_s = \sqrt{\frac{G_{13}^s}{G_{23}^s}} \quad (20)$$

By integrating eqns (13) and making use of the condition $u_3(x_1, x_2) = -u_3(-x_1, x_2)$, the axial warping for the sth layer can be written as:

$$\omega_s(x_1, x_2) = x_1 x_2 - \frac{B^2}{\mu_s} \sum_{n=0}^{\infty} \frac{q_n}{\alpha_n^3} \omega_{sn}(x_2) \sin \alpha_n \frac{x_1}{B} \quad (21)$$

where

$$\omega_{sn}(x_2) = a_{sn} \sinh \beta_{sn} \frac{x_2}{H} + b_{sn} \cosh \beta_{sn} \frac{x_2}{H} \quad (22)$$

The unknown coefficients a_{sn} and b_{sn} are determined by making use of the boundary conditions in eqns (15). Due to the linear independence of the trigonometric functions appearing in eqn (18), eqns (15) give, for each n:

$$\psi_{1n}(h_0) = 1; \qquad \psi_{Sn}(h_S) = 1$$

$$[G_{23}^s \psi_{sn}(h_s)] = [G_{23}^{s+1} \psi_{s+1,n}(h_s)]; \quad [\omega_{sn}(h_s)/\mu_s] = 0 \quad (23)$$

Finally, the torsional rigidity for a multilayered rectangular cross-section can be obtained by substituting eqns (18) and (19) into (17), so obtaining:

$$G_t J_t = \frac{1}{3} B^3 H \sum_{s=1}^{S} G_{23}^s (\delta_s - S_s) \quad (24)$$

where the following positions have been made:

$$\delta_s = \frac{h^s}{H}$$

$$S_s = \frac{192}{\eta_s^3} \sum_{n=0}^{\infty} \frac{1}{\alpha_n^5} \left[a_{sn} \cosh \beta_{sn} \left(\frac{h_s}{H} + \frac{\delta_s}{2}\right) \right.$$
$$\left. + b_{sn} \sinh \beta_{sn} \left(\frac{h_s}{H} + \frac{\delta_s}{2}\right) \right] \sinh \beta_{sn} \frac{\delta_s}{2} \quad (25)$$

For aspect ratios $\eta_s < 1$ it is convenient to write eqn (24) in a different form, where the minor dimension of the cross-section is up to three:

$$G_t J_t = \frac{1}{3} BH^3 \sum_{s=1}^{S} G_{13}^s \frac{\delta_s - S_s}{\eta_s^2} = \frac{1}{3} BH^3$$

$$\times \sum_{s=1}^{S} G_{13}^s K_s \quad (26)$$

It is well known that the calculation of the series reported in eqn (25, bottom) and, consequently, of the layer coefficients $K_s = (\delta_s - S_s)/\eta_s^2$ in eqn (26), is unstable for low aspect ratios H/B, so that approximate models have been proposed when the number of layers increases. For instance, for a homogeneous cross-section with $\eta = 0.01$ the summation in eqn (26) takes the form $(1 - 0.9999\ldots)/(0.01)^2$; to evaluate eqn (26) up to n significant figures, the summation (25) must be computed up to $n+4$ significant figures. But the accuracy of the series in eqn (26) can be definitely improved by setting:

$$K_s = \delta_s + \frac{S_{Ks}}{\eta_s^2}; \quad S_{Ks} = (1 - \eta_s^2)\delta_s - S_s \quad (27)$$

In this way the non-dimensional thickness δ_s of the sth layer is up to three. Finally, making use of the following hyperbolic series:

$$1 - \eta^2 = 192 \sum_{n=0}^{\infty} \frac{1}{\alpha_n^5} \left[\frac{1}{\eta} \tanh \frac{\alpha_n \eta}{2} \right.$$
$$\left. - \eta^3 \tanh \frac{\alpha_n}{2\eta} \right] \qquad (28)$$

which can be obtained in the homogeneous case $(S = 1, \delta_1 = 1)$ by expressing the indifference condition of the stress function with respect to a rotation of $\pi/2$ about the x_3 axis. Then, K_t can be written as:

$$K_t = \delta_s^3 - 192 \sum_{n=0}^{\infty} \frac{1}{\alpha_n^5} \left(\eta_s \delta_s^4 \tanh \frac{\alpha_n}{2\eta_s \delta_s} \right.$$
$$\left. - \frac{1}{\eta_s^3} \tanh \beta_m \frac{\delta_s}{2} \right) - S_{C_s} \qquad (29)$$

which is unaffected by unstable behaviours.

5 EXAMPLES

In this section some examples are presented, concerning the torsional response of sandwich isotropic and orthotropic cross-sections. The ratios between the shear moduli of external (1) and internal (2) layers are denoted by:

$$R_G = \frac{G_{23}^1}{G_{23}^2}; \quad \mu = \frac{\mu_1}{\mu_2} \qquad (30)$$

The first examples refer to two isotropic sandwich cross-sections with a non-dimensional external thickness $\delta_1 = h^1/H = 1/4$, aspect ratios $H/B = 1/2$ and 2, and ratio between the shear moduli of the layers equal to $R_G = 10$. Figures 3(a), 4(a) and Table 1 show the lines of shearing stress and some distributions of shear stress components. Moreover, the corresponding warping functions $\omega(x_1, x_2)$ are reported in Figs 3(b) and 4(b). The torsional rigidities for sections having the same cross-sectional area and $H/B = 0.001 \div 100$ have been reported in Figs 5(a) and 5(b) for $R_G = 10$ and 100. It is worth noting that, even though the two sections have the same amount of the two different materials, the stress distributions, the axial warping and, consequently, the torsional rigidities are completely different. For instance, for $R_G = 10$ the cross-section of Fig. 3

has a torsional rigidity 62% higher than that of Fig. 4, whereas for $R_G = 100$ it has a rigidity 2.4 times lower. Figure 5(b) distinctly shows that, for two special values of the aspect ratio, the torsional rigidity presents two relative maximum values, corresponding to two completely different behaviours. In fact, for $H/B > 1$ (Fig. 4(a)) some of the lines of shearing stress close up in the two stiffer external layers, whereas for smaller values (Fig. 3(a)) the lines of shearing stress close over the whole section. This circumstance suggested us to develop a simple approximate formula for the torsional rigidity of sandwich beams as the sum of two simplified scheme. In scheme I only the two stiff external layers are considered, adopting for them the formulas giving the torsional rigidity of rectangular homogeneous layers. In scheme II the laminate section is idealised as a hollow rectangular section, constituted by the two external layers and two ideal layers in the correspondence of the soft layer. Assuming for the soft layer a linear variation of the shear stresses and making use of equivalence considerations, the thickness of these ideal layers has been estimated as equal to $0.211 \, B$. A simple evaluation of the corresponding torsional rigidity can be performed by considering it as a thin tubular cross-section. Assuming a linear variation of the stress function over the thickness[10] and making use of eqns (16) and (17), the following expressions for the torsional rigidity of a closed thin-walled section, of variable thickness b, constituted of S layers made of transversely isotropic material connected in series, is derived:

$$J_t = \frac{4 A_m^2}{\rho}$$

where

$$\rho = G_t \sum_{s=1}^{S} \int_{\Gamma_s} \frac{d\xi}{G_t b(\xi)} \qquad (31)$$

where A_m is the area surrounded by the middle-line $\Gamma_m = \cup \Gamma_m^s$.

The dashed lines in Figs 5(a) and 5(b) represent the torsional rigidities corresponding to the two simplified schemes as well as to the sum of them. Note that the error with respect to the exact solutions (24) and (26) is less than 20% over the whole range of H/B aspect ratios; this error is essentially due to the simple scheme adopted for the hollow section. In the same figures the solution proposed in Ref. 9 is reported. This solution is
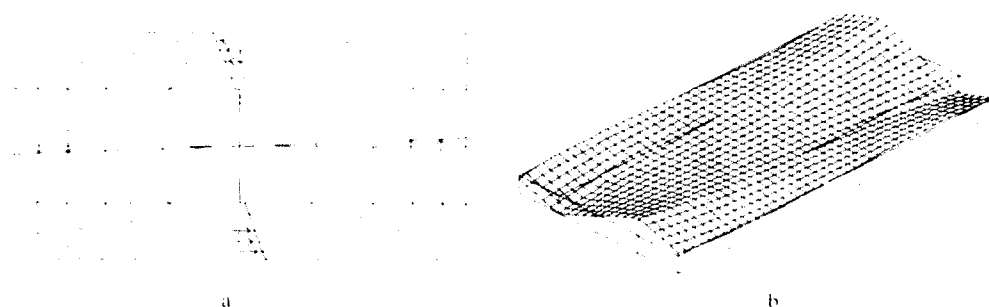
Fig. 3. a Lines of shearing stress and distributions of shear stress components; b cross-sectional warping, for an isotropic sandwich cross-section with a non-dimensional external thickness $\delta_1 = h^1/H = 1/4$, aspect ratio $H/B = 1/2$, and ratio between the shear moduli of the layers $R_G = 10$.
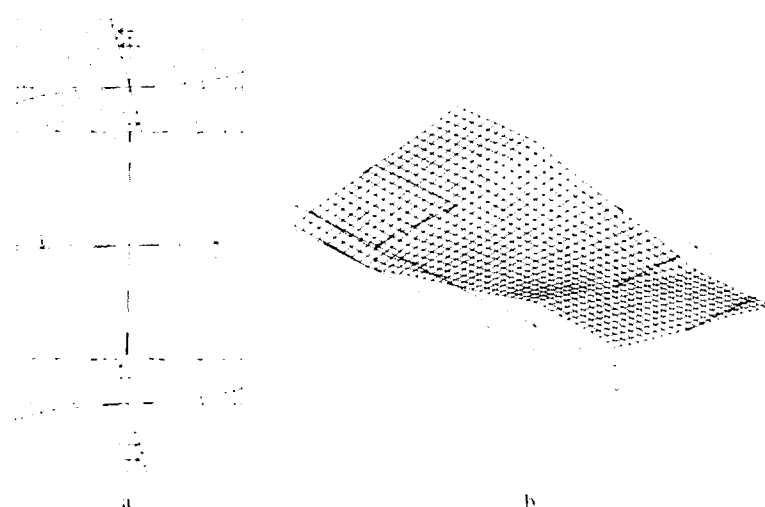
Fig. 4. a Lines of shearing stress and distributions of shear stress components; b cross-sectional warping, for an isotropic sandwich cross-section with a non-dimensional external thickness $\delta_1 = h^1/H = 1/4$, aspect ratio $H/B = 2$, and ratio between the shear moduli of the layers $R_G = 10$.

Table 1. Some characteristic values of the shear stress components

	$(0, H/2)$	$(0, h^-/2)$	$(0, h^-/2)$	$(b, 0.35h)$	$(b, 0)$
Fig. 3 a	5·99	1·12	0·11		1·93
Fig. 4 a	8·50	5·60	0·56	6·90	1·92
Fig. 6 a	65·15	62·65	0·63		1·78

$\tau = (\ldots) \dfrac{V}{AL}$, where $L = H$ if $H/B < 1$; $L = B$ if $H/B > 1$.

based on the Reissner–Mindlin theory, and the axial warping is assumed to be proportional to $x_1 x_2$. It is evident that these results are completely unreliable even for sufficiently thin laminates $H/B \cong 1/10$, due to the too simple displacement representation adopted. Finally, the plating of homogeneous beams by means of thin fibre-reinforced laminae is analysed. This technique is also used to increase the torsional rigidity in order to prevent the lateral instability phenomena of slender wood beams, especially during the installation processes. Laminae reinforced by means of two families of carbon fibres at $\pm 45°$ with respect to the beam axis are considered. The shear moduli adopted for wood (2) and fibre-reinforced laminae (1) are the following:

Fig. 6. (a) Lines of shearing stress and distributions of shear stress components for FRP-reinforced wood rectangular cross-section with $\delta = h / H = 1/100$ and $H/B = 1/2$; (b) increment of torsional rigidity of wood cross-section due to the plating by means of FRP laminate with $\delta = h / H = 1/100$ and $1/50$.

Fig. 5. Torsional rigidity for isotropic sandwich cross-sections having the same area for $\delta = h / H = 1/4$ and $R_G = 10$ (a) and $R_G = 100$ (b).

$$G_{13}^1 = G_{23}^1 = 0.66 \text{ GPa}; \quad G_{13}^2 = 66 \text{ GPa},$$

$$G_{23}^2 = 6.6 \text{ GPa} \tag{32}$$

so that $\mu_1^1 = 10$, $\mu_2^2 = 1$ and $\mu^2 = 10$, $R_G = 10$. The lines of shear stress for $H/B = 1/2$, $\delta_1 = 1/100$,

and the increment of torsional rigidity due to the plating are reported in Figs 6(a) and 6(b). Figure 6(b) refers to sections with the same amount of fibre-reinforced material used for the plating. It is worth noting that plating in the correspondence of the longer faces of the beam is more effective. For instance, for a section with ratio equal to 10 between height and width and adopting $\delta_1 = 1/50$, the torsional rigidity is increased up to 10 times by plating the long faces of the section $H/B = 0.1$, whereas it is increased 16% only by plating the two short faces $H/B = 10$.

ACKNOWLEDGEMENTS

REFERENCES

1. Plevris, N. & Triantafillou, T. C., FRP-reinforced wood as structural material. *J. Mater. Civ. Engng, ASCE,* **4** 1992 300-17.
2. Giavotto, V., Borri, M. *et al.,* Anisotropic beam theory and applications. *Comput. Struct.,* **16** 1983 403-13.
3. Laudiero, F. & Savoia, M., Shear strain effects in flexure and torsion of thin-walled beams with open or closed cross-sections. *Thin-Walled Struct.,* **10** 1990 87-119.
4. Ie, C. A. & Kosmatka, J. B., On the analysis of prismatic beams using first-order warping functions. *Int. J. Solids Struct.,* **29** 1992 879-91.
5. Savoia, M., Laudiero, F. & Tralli, A., A refined theory for laminated beams — Part 1: A new high order approach. *Meccanica,* **27** 1993.
6. Muskhelishvili, N. J., *Some Basic Problems of the Theory of Elasticity,* 4th edn. Noordhoff, The Netherlands, 1963.
7. Cheng, S., Wei, X. & Jiang, T., Stress distribution and deformation of adhesive-bonded laminated composite beams. *J. Engng Mech. ASCE,* **115** 1989 1150-62.
8. Lekhnitskii, S. T., *Theory of Elasticity of an Anisotropic Elastic Body.* Holden-Day, San Francisco, CA, 1963.
9. Tsai, C. L., Daniel, I. M. & Yaniv, G., Torsional response of rectangular composite laminates. *J. Appl. Mech. ASME,* **57** 1990 383-7.
10. Sokolnikoff, I. S., *Mathematical Theory of Elasticity.* McGraw-Hill, New York, 1956.
11. Wang, S. S. & Choi, I., Boundary layer effect in composite laminates: Part 1: Free edge singularities. *J. Appl. Mech. ASME,* **49** 1982 541-8.

AUTHOR INDEX

SUBJECT INDEX

INSTRUCTIONS TO AUTHORS

Submission of papers

Submission of a manuscript implies that it is not being considered contemporaneously for publication else-where. Submission of a multi-authored manuscript implies the consent of all the participating authors. All papers should be written in English. All papers will be independently refereed.

Manuscripts should be sent to the Editor, to a local member of the Editorial Board, or to the publisher.

Types of contributions

Research papers; review articles; case studies; technical notes; book reviews; reports of conferences and meetings; letters to the Editor.

Manuscripts

Three copies should be provided, in double-spaced typing on pages of uniform size, with a wide margin at the left. Generally, the size of the manuscript should not exceed 6000 words or about 12 printed pages. Each paper should be provided with an Abstract of about 100–150 words, reporting concisely on the purpose and results of the paper.

Wherever possible, authors should consult an issue of the journal for style and layout. The Editor reserves the right to adjust style to certain standards of uniformity.

The SI system should be used for all scientific and laboratory data; if, in certain instances, it is necessary to quote other units, these should be added in parentheses. Temperatures should be given in degrees Celsius. The unit 'billion' (10^9 in America, 10^{12} in Europe) is ambiguous and should not be used.

Tables, references and legends to illustrations should be typed on separate sheets and placed at the end of the paper. Footnotes should be avoided if they contain information which could equally well be included in the text.

Disks

For papers produced using a word-processor or T_EX, please submit a disk with the **final revised version** of the manuscript. The file on disk should correspond exactly to the hard copy. The operating system and the word-processor used should be specified clearly.

Illustrations or chemical structures in electronic format may be supplied provided that the file format and the program used to produce them is clearly indicated and that a hard copy is also supplied.

More detailed guidelines and further information are available from the publisher.

References

References to published work should be numbered sequentially in order of citation and given in the text by a superscript numeral, with a reference list, in numerical order, at the end of the paper. The list should give name(s) and initial(s) of author(s) and the exact title of the paper or book. For journals there should follow the title, volume number, year of issue and initial and final page numbers of article. For books there should follow the name(s) of the editor(s) (if appropriate), the name of the publisher and the town and year of publication. Where appropriate, initial and final page numbers should also be quoted. All references in this list should be indicated at some point in the text and vice versa. Unpublished data or private communications should not appear in the reference list.

Illustrations

The *original* and two copies, which may be of a reduced size, of each illustration should be provided. Line drawings may be submitted in any medium providing that the image is black and very sharp. They should preferably all require the same degree of reduction; large diagrams, more than four times final size, are discouraged due to handling difficulties. The type area of the journal is 177 mm wide · 240 mm deep, in two columns per page, each 85 mm wide, and lettering should therefore be large enough to be legible after reduction of the illustration to fit (ideally 7pt lettering after reduction). Photographs should be submitted as contrasting black-and-white prints on glossy paper. Each illustration must be clearly numbered and the name(s) of the author(s) of the paper written on the reverse side.

Proofs

The author (or the selected author where several are involved) will receive a set of proofs for checking. No new material may be inserted in the text at the time of proof reading unless accepted by the Editors. All joint communications must indicate the name and full postal address of the author to whom proofs should be sent.

Page charges and offprints

There will be no page charges. Twenty-five offprints of each paper will be supplied free of charge. Additional copies can be ordered at current printing prices.

COMPOSITE
STRUCTURES

VOL. 25 NOS 1-4 1993

Special Issue: Seventh International Conference on Composite Structures

END
FILMED
10-93
DTIC